

**Space Experiment Design/Lower
and Middle Atmosphere Modeling**

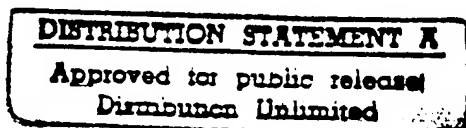
Final Report
SAIC 94/1041

February 23, 1994

[S]



Science Applications International Corporation
An Employee-Owned Company



DTIC QUALITY INSPECTED 3

19950925 018

DTIC QUALITY INSPECTED 3

94 5 03 11 4

12

**Space Experiment Design/Lower
and Middle Atmosphere Modeling**

Final Report
SAIC 94/1041

February 23, 1994



DISTRIBUTION STATEMENT A

Approved for public release
Distribution Unlimited

Accession For	
NTIS CRA&I	<input checked="checked" type="checkbox"/>
DTIC TAB	<input type="checkbox"/>
Unannounced	<input type="checkbox"/>
Justification	
By <i>per Oti</i>	
Distribution /	
Availability Codes	
Dist	Avail and/or Special
A-1	

**Space Experiment Design/Lower
and
Middle Atmosphere Modeling**

Final Report
SAIC 94/1041

February 23, 1994

Submitted to:

Naval Research Laboratory
Washington, DC 20375-5000

Prepared by:

Ellis Hyman, Principal Investigator
and
Jainn Jong Shi

Prepared Under:

Contract No. N00014-89-C-2234

DTIC QUALITY INSPECTED 3

TABLE OF CONTENTS

I.	DISCUSSION	1
II.	DEVELOPMENT AND APPLICATION OF FOUR-DIMENSIONAL DATA ASSIMILATION	1
II.1	Introduction	1
II.2	Application of Bratseth Scheme for the Analysis of Gale Data	2
II.3	Application of the Vertical Mode Initialization With and Without Diabatic Heating	4
II.4.	Four Dimensional Data Assimilation of Gale Data	6
III.	UTILIZATION OF ODW AND SSM/I DATA IN THE ANALYSIS OF TROPICAL AND EXTRA-TROPICAL CYCLONES.....	8
III.1	Introduction	8
III.2.	ERICA IOP-4 Case	8
III.3.	Hurricane Florence (1988) Case.....	10
III.4.	Hurricane Hugo (1989) Case	12
IV.	NUMERICAL INVESTIGATION OF THE OUTFLOW LAYER OF TROPICAL CYCLONES.....	13
V.	NUMERICAL SIMULATIONS OF MONSOON RAINFALL WITH THE NRL/NCSU REGIONAL NESTED MODEL	14
VI.	REFERENCES	18
APPENDICES		
Appendix A Application of the Bratseth Scheme for the Analysis of GALE Data Using a Mesoscale Model		
Appendix B Four-Dimensional Data Assimilation of Gale Data Using a Multivariate Analysis Scheme and A Mesoscale Model with Diabatic Initialization		
Appendix C Diabatic Initialization Test Using the Naval Research Laboratory Limited-Area Numerical Weather Prediction Model		
Appendix D Tests of Initialization Procedures With the NRL Limited Area Numerical Weather Prediction Model		

Appendix E Application of Vertical-Mode Initialization to a Limited-Area Model
in Flux Form

Appendix F An Examination of Four Dimensional Data-Assimilation
Techniques for Numerical Weather Prediction

Appendix G SSM/I Observations of ERICA IOP 4 Marine Cyclone: A
Comparison with In Situ Observations and Model Simulation

Appendix H Applications of SSM/I Data in the Analysis of Hurricane Florence
(1988)

Appendix I Numerical Investigation of the Interaction Between Hurricane
Florence (1988) and Its Upper-Level Environment

Appendix J Enhancement of Objective Analysis of Hurricane Florence (1988)
with Dropsonde Data

Appendix K Special Sensor Microwave/Imager (SSM/I) Observations of
Hurricane Hugo (1989)

Appendix L Sensitivity of Monsoon Rainfall Predictions to Initialization
Procedures

I. DISCUSSION

The work performed by Science Applications International Corporation (SAIC) on this contract, "Space Experiment Design/Lower and Middle Atmosphere Modeling", Contract Number N00014-89-C-2234, SAIC Project Number 01-0157-13-0952, focused predominantly on code development and analysis associated with mesoscale atmospheric forecasting. The work was substantially enhanced by a subcontract to Dr. Sethu Raman and his staff at the North Carolina State University (NCSU). This effort was in support of the programs of the Remote Sensing Physics Branch of NRL's Remote Sensing Division, specifically the Branch Section headed by Dr. Rangaro Madala. Administration of the contract was in the Space Science Division with Ms. Deborah McIntire serving as the Contracting Officer's Technical Representative (COTR). It covered the period from October 1, 1989 to December 31, 1993. In the following sections we will describe each of the topics investigated and the results obtained. Much of the research work has resulted in journal publications and NRL Memorandum Reports in which the research is described in detail. These reports are included in this Final Report in Appendices.

II. DEVELOPMENT AND APPLICATION OF FOUR-DIMENSIONAL DATA ASSIMILATION

II.1 Introduction

A four-dimensional data assimilation scheme was developed through the collaborative research effort between North Carolina State University (NCSU) and SAIC in support of this program at NRL. Four-dimensional data assimilation, in the context of numerical weather prediction, is the process of specifying initial conditions for the integration of a numerical forecast model. In this process, new observational data are merged, using a prescribed analysis procedure, with the ongoing integration of the prediction model. Data analysis and model prediction, along with model initialization, make up the major components of the data-assimilation process. A short-range model forecast serves as a first guess for the subsequent analysis. The overall purpose of this research is to develop a method of data assimilation, which includes a cost-effective multivariate analysis scheme, accounts for diabatic effects in the model initialization, and uses a fine-resolution mesoscale model. The goal is to produce improved analyses of mesoscale circulations resulting in more reliable

forecasts of coastal frontogenesis/cyclogenesis and associated precipitation. Another goal is to investigate the impact of assimilating high-frequency observational data using a mesoscale model.

II.2 Application of Bratseth Scheme for the Analysis of Gale Data

The objective analysis scheme developed for use with the NRL limited area weather prediction model utilizes the Bratseth scheme, in which the data weights are dependent on the covariance between observations, are reduced in regions of higher data density, and include observational errors. We have devised a computationally inexpensive method for linking the mass and momentum fields; the method is different from earlier methods reported in the literature (Cressman 1959, Lorenc et al. 1991, for example). The key element of the method involves obtaining the gradient of the geopotential change from the change in an estimated geostrophic wind at each iteration to enhance the initial univariate analysis of the geopotential. We use the initial univariate wind analysis to provide only the starting estimate of the geostrophic wind for the first iteration. For subsequent iterations, the geostrophic wind is estimated from the updated geopotential gradient. After this enhancement of the geopotential, the univariate wind analysis is updated for the change in the geostrophic wind.

An evaluation of the NRL objective analysis scheme has been accomplished using a data set from the Genesis of Atlantic Lows Experiment (GALE) for the Intensive Observational Period 2 (IOP-2). The use of a prior model forecast as a first guess for the analysis was crucial in obtaining mesoscale features in the analysis. Such features were not produced by our earlier procedure, which used a Barnes (1973) scheme to enhance the National Meteorological Center (NMC) hemispheric analyses (Chang et al. 1989, Shi et al. 1991). Over the region of the eastern United States, where there is a large amount of data, the Barnes scheme produced as good an analysis as the Bratseth (1986) scheme when the same first guess forecast is used. The Bratseth scheme was superior in the other regions where it could adjust for the variable data density. Our simple geostrophic method for linking the mass and wind field analyses provided tighter gradients in these fields, particularly in the regions of lower data density outside of the eastern United States.

For the second IOP of GALE, the vertical circulations were derived from the analyses by application of the vertical mode initialization scheme of Bourke and McGregor (1983). Superior mesoscale vertical circulations were produced in the coastal low and upper tropospheric jet streaks with the new NRL analysis scheme as compared to that derived from the earlier Barnes enhancement of the NMC hemispheric analyses. These circulations clearly demonstrated the interaction of the coastal low with the entrance region of a jet streak in the upper troposphere. The cooperation of the secondary circulations in two jets during offshore cyclogenesis is also shown. The capability of producing such mesoscale circulations using these analysis and initialization schemes is important for providing accurate initial conditions for generating forecasts with the limited area model.

The research described in this subsection (and in subsections 3 and 4) is described in greater detail in the Ph.D. thesis by Dewey E. Harms submitted to NCSU's Department of Marine, Earth, and Atmospheric Sciences in Raleigh, North Carolina in 1992. The thesis is entitled "Four-Dimensional Data Assimilation of Gale Data Using a Multivariate Analysis Scheme and a Mesoscale Model with Diabatic Initialization." An abstract of this research appears below.

Abstract

A method of assimilating 3-hourly sounding data is developed and successfully tested in this study. First, the successive corrections scheme of Bratseth (1986), which converges to optimum interpolation, is applied for the numerical analysis of data collected during the Genesis of Atlantic Lows Experiment (GALE). Univariate analyses of the mass and wind field are produced. The coupling of the mass and wind field is achieved by further iterations of the geopotential utilizing improving estimates of the geostrophic wind to extrapolate the geopotential to the grid points. The univariate wind analysis is then corrected for the new geostrophic wind.

Next, diabatic forcing is incorporated into a vertical mode initialization scheme to provide more realistic initial conditions and to shorten the spinup time of the Naval Research Laboratory/ North Carolina State University (NRL/NCSU) mesoscale model. Latent-heating profiles are computed from 'spun-up' model-generated and observed rainfall. The latent heating is distributed in the vertical according to the cumulus convective parameterization scheme (Kuo scheme) of the model. Compatibility

between the specific heating during initialization and the heating during early model integration is retained by merging the model integrated rainfall and heating rates with those rates from the initialization.

Finally, the multivariate, successive correction analysis scheme and the diabatic initialization procedure are combined with the NRL/NCSU model to form an intermittent data-assimilation system. Assimilations of the GALE data over a 2 1/2-day period were performed with differing update cycles of 3, 6, and 12 h. Twelve-hour NMC hemispheric analysis served as the "no assimilation" control case for comparison. The assimilation of 3-hourly GALE data led to large decreases in background forecast rms errors and smaller decreases in analysis rms error. Better consistency in time was achieved between forecasts and analyses in the assimilation experiments. Rainfall prognoses from the assimilated states verified reasonably well with the observed rainfall and showed much more rapid spinup and better overall patterns than did the "no assimilation" precipitation forecasts.

This research is also described in a publication in Monthly Weather Review (1993) by Sashegyi, et al. and is included in this report in Appendix A. Additional details are described in an NRL Memorandum Report (1992) included here in Appendix B.

II.3 Application of the Vertical Mode Initialization With and Without Diabatic Heating

A vertical mode initialization scheme following that of Bourke and McGregor (1983) was developed for use with the NRL model. Filtering conditions are applied to the model dynamical equations to derive the linear diagnostic equations for the mass divergence and geopotential, which are solved iteratively for the first three vertical modes of the numerical model. These modes have phase speeds that are much faster than those of meteorological systems. The further condition that the linearized potential vorticity is unchanged by the procedure is required to compute the vorticity. The observed wind and temperature are first interpolated to the sigma surfaces of the model. The iterative procedure is then used to compute incremental changes to the generalized geopotential, mass divergence and vorticity for the first three vertical modes of the numerical model. As is customary, we keep the

geopotential, temperature and pressure fixed at the lateral boundaries in the scheme. To provide a boundary condition for the divergence, however, an approximate divergence at the boundary is computed using the thermodynamic equation. In our scheme, changes in the tangential wind along the lateral boundaries are consistent with the computed changes in the vorticity and mass divergence. The procedure provides a balanced vertical motion field and produces smaller changes to the initial mass and wind fields compared to the static initialization. The scheme was tested on two grids of differing domain size and grid resolution. Convergence of the scheme was rapid with the lower resolution US grid, with three iterations of the scheme being sufficient for convergence. With the smaller GALE grid of higher resolution and sloping topography along two boundaries, the convergence of the scheme was slower and in fact the mass divergence did not converge for the third mode. However, by smoothing the topography in a boundary zone of five degrees, the convergence of the scheme was much improved. In both cases, changes in the mass and wind fields were still small after three iterations.

Integration with initial conditions, initialized with the vertical mode initialization procedure, prevented gravity wave oscillations without producing a mean drift in the surface pressure and provided a balanced vertical motion field. On the coarse US grid, little difference was found between integration using either of the lateral boundary treatments. However, some low amplitude long period oscillations in the surface pressure remained in the interior of the domain and some noise was generated in the vertical motion at the lateral boundaries when the Perkey Kreitzberg scheme was used. On the smaller GALE grid, some noise was produced in the vertical motion in the boundary zone by both schemes. In the interior, the Davies scheme produced a smoother variation of the surface pressure. When the Davies scheme was used with integration starting from uninitialized data and boundary values, an initial shock in the surface pressure was damped in the first four hours. However a small drift in the surface pressure was produced. This indicated that the boundary values used with the Davies scheme should be as balanced as possible for the numerical model, being initialized or derived from integration on a larger grid or with another model. Similar 12 to 48 hour forecasts were again produced with the various experiments.

For grids of high resolution such as our GALE grid, and especially when fine scale topography is used along the boundary, it is recommended that no

more than three iterations of the vertical mode scheme be used in practice. For grids of even higher resolution, only the first two modes may be able to be initialized, with possibly no more than three iterations used with the scheme. Some improvement, however, can be expected by smoothing the topography in the boundary zone or using a nested model to provide more accurate boundary values for the mass divergence for the inner nested grids.

After the vertical model initialization had been successfully tested with the NRL limited area numerical model, diabatic forcing was incorporated into the vertical mode initialization scheme (DVMI) to provide more realistic initial conditions and to alleviate the spinup time of the NRL limited area numerical model. Latent heating profiles are computed from 'spun-up' model-generated convective rainfall. The latent heating is distributed in the vertical according to the cumulus convective parameterization scheme (Kuo scheme) of the model. Compatibility between the specified heating during initialization and the heating during early model integration is retained by merging the model integrated rainfall and heating rates with those rates from the initialization.

The results of a case study from GALE indicated that model spinup of forecast rainfall can be substantially reduced when diabatic initialization with merging of heat/rain is used. The initializations and forecasts were performed in this study for the mid-latitudes, which dictates a relatively short spinup. In the data-sparse tropics spinup can be expected to be much greater. In the tropical case DVMI with merging will be critical in reducing spinup time.

Several papers have been published that provide a more detailed description of this research. In addition to the Harms dissertation described in II.2., they include: Harms, et al. (1993) in Monthly Weather Review found here as Appendix C, Sashegyi and Madala (1990) in an NRL Memorandum Report, here as Appendix D, and Sashegyi and Madala (1993) in Monthly Weather Review in Appendix E.

II.4. Four Dimensional Data Assimilation of Gale Data

A four dimensional data assimilation (FDDA) was developed to generate initial conditions for the NRL mesoscale model. This data-assimilation system consists of a multivariate, successive correction objective analysis, a diabatic vertical mode initialization (DVMI), and a mesoscale numerical forecast. The development of FDDA for limited areas is being driven by a need to optimally

utilize data from the new observing systems of the 1990s. In this study, the FDDA was used to assimilate 3-hourly data collected during GALE, which was conducted over the southeastern U.S. during the winter of 1986.

The performance of the assimilation system was evaluated by means of data-fitting statistics and subjective comparisons of assimilated states and subsequent forecasts. The assimilated background forecast rms error for all analysis variables decreased significantly as the length of the update cycle shortened, i.e. as additional asynoptic, high-density GALE data were assimilated. The same was true for the analysis error of geopotential. This decrease in background and analysis error clearly showed that the inclusion of the 3-hourly GALE data had a positive impact on the assimilation. The analysis errors of the wind components and relative humidity varied little between the different experiments, due most likely to relatively large observational error in the wind and humidity. The background and analysis rms errors changed little when diabatic heating was included in the vertical mode initialization, suggesting that the inclusion or exclusion has minimal impact on the assimilation of these first-order variables. The assimilation with a 3-hourly update cycle revealed that the background forecast error generally increases as the period from the previous synoptic update to the current analysis/forecast cycle increases. With only small insertions of data at the asynoptic cycles (as compared to complete data sets at the synoptic hours), the effectual background forecast duration of successive update cycles increases between synoptic updates for geopotential.

The results of this study showed that the assimilation of GALE data in a mesoscale model was successful in producing significantly improved analyses and subsequent forecasts that were more consistent in time. The results also indicated that a small area of higher temporal data resolution can, when they are assimilated with a high-resolution mesoscale prediction model, lead to improved assimilated states and better forecasts. However, the impact of the GALE data on the forecasts was generally greater when mesoscale circulations were important, such as in the interaction of the coastal front and the upper-level jet during the period prior to rapid cyclogenesis. When the large-scale synoptic system became dominant, the 3-hourly data had less impact in the subsequent forecasts.

Further details are included in the Harms dissertation described in Section II.2, in Appendix B, and have been published by Harms, et al. (1992) in

the Bulletin of the American Meteorological Society; the latter is included in this report as Appendix F.

III. UTILIZATION OF ODW AND SSM/I DATA IN THE ANALYSIS OF TROPICAL AND EXTRA-TROPICAL CYCLONES

III.1 Introduction

Data from the Special Sensor Microwave/Imager (SSM/I) launched by the Defense Meteorological Satellite Program (DMSP) were analyzed and used to infer important meteorological parameters of Hurricanes Florence (1988) and Hugo (1989) as well as an extra-tropical cyclone that developed during IOP-4 of the Experiment on Rapidly Intensifying Cyclones over the Atlantic (ERICA). These parameters include rainfall rates, integrated water vapor (IWV), marine surface wind speeds and 85 Gigahertz brightness temperatures used for center fixing the tropical cyclones. Omega-Dropwindsonde (ODW) data collected by the Hurricane Research Division of the Atlantic Oceanographic and Meteorological Laboratory (AOML/HRD) during Synoptic Flow Experiments on 8-9 September 1988 were also analyzed to study Hurricane Florence (1988).

The SSM/I retrieved parameters were compared to in situ observations and model simulation. These parameters were also assimilated into the numerical model to improve the model simulation of Hurricane Florence (1988). The ODW data were used to enhance the National Meteorological Center/Regional Analysis and Forecast System (NMC/RAFS) 2.5° analysis at 0000 UTC 9 September 1988 for the numerical study of Hurricane Florence (1988). The principal results of the collaborative research between NCSU and SAIC in support of this program at NRL are described in the following subsections.

III.2. ERICA IOP-4 Case

The SSM/I retrieved meteorological parameters during the IOP-4 on 4 January 1989 of the ERICA were analyzed. Qualitative and quantitative comparisons of SSM/I retrievals with Geostationary Operational Environmental Satellite (GOES) imagery, conventional observations, and results produced by NRL's limited-area numerical model were made to examine the spatial

relationship of the SSM/I retrieved fields to the rapid intensifying storm and the associated fronts.

SSM/I rainfall was found along and ahead of the cold and warm fronts with heavy precipitation within frontal bands during the mature stage of the storm. The spatial pattern and characteristics of SSM/I precipitation closely resembled those simulated by the model. Both the warm and cold front were found to be located near the area of the strongest gradient in IWV. In the warm sector, there is an area of IWV greater than 40 mm, an amount supported by model simulations. Both SSM/I rain rates and IWV distribution were found to be useful in locating the cold and warm fronts. There was good agreement on the relationship of frontal locations to the precipitation patterns and IWV gradients. Most of the high-wind area near the storm center was obscured by clouds for marine surface wind retrieval. SSM/I-retrieved marine winds outside the cloud shield were compared to ship- and buoy-reported winds. It was found that the retrieved wind estimates were within $0-3 \text{ ms}^{-1}$ of in situ observation over areas of slow wind shifts. The errors became larger in regions of rapid wind shifts.

A description of this research has been presented as a PhD thesis by Randall J. Alliss to the Department of Marine, Earth, and Atmospheric Sciences of NCSU in Raleigh, North Carolina (1992) entitled, "The Utilization of SSM/I DATA in the Analysis of Tropical and Extra-Tropical Cyclones". An abstract follows.

Abstract

Recently, remote sensing of tropical and extra-tropical storms has been enhanced via data from the Special Sensor Microwave/Imager (SSM/I) launched by the Defense Meteorological Satellite Program (DMSP) in June 1987. Data obtained from SSM/I was analyzed and used to infer important meteorological parameters of Hurricanes Hugo (1989) and Florence (1988) as well as a mid-latitude cyclone which developed during Intensive Observational Period (IOP)-4 of the Experiment on Rapidly Intensifying Cyclones over the Atlantic (ERICA). These parameters include rainfall rates, integrated water vapor, marine surface wind speeds and 85 Gigahertz brightness temperatures used for center fixing the tropical cyclones.

In this study, the utility of the SSM/I as a supplemental source of data in tropical and extra-tropical cyclones is evaluated. Results indicate that increases in SSM/I derived total latent heat release and increases in heavier rainfall rates near the center are associated with the intensification of both Hugo and Florence.

SSM/I winds give a good description of the surface wind field of both Florence and the IOP-4 storm, outside areas of deep convection. SSM/I integrated water vapor is found to be particularly useful in locating the surface fronts associated with the IOP-4 cyclone. In addition, storm structure characteristics inferred from SSM/I of the ERICA IOP-4 storm compare well with the numerical results produced by the Naval Research Laboratory mesoscale model.

Because SSM/I parameters were useful in observing the structure of these storms and compared well with in situ observations and model simulations, the applications described herein could be valuable in augmenting current analysis techniques of tropical and extra-tropical cyclones.

Additional details can be found in a published paper by Chang, et al. (1993) in Monthly Weather Review; the paper appears in this report as Appendix G.

III.3. Hurricane Florence (1988) Case

SSM/I observations of rainfall have been used to analyze the precipitation patterns associated with Hurricane Florence of 1988. Based upon SSM/I precipitation estimates, the intensification of Florence was accompanied by increases in the average rainfall, the relative contribution of heavier rainfall, and the total latent heat release. Unfortunately, any lag between the maximum total latent heat release (TLHR) and minimum pressure could not be determined from these SSM/I observations due to Florence making landfall. SSM/I observations of Florence's precipitation field and its trend during intensification support those seen in the much larger and more intense Hurricane Hugo, which will be discussed in the next section.

The wind field associated with Florence was analyzed using SSM/I wind speed data. SSM/I estimated winds at 0000 UTC 9 September were generally lighter than an Omega-Dropwinsonde (ODW) enhanced wind analysis. Conversely, SSM/I derived wind speeds at 1200 UTC 9 September were slightly stronger than in situ observations over the Gulf of Mexico but were well within ground truth specification. Due to the presence of heavy precipitation and cloud liquid water near the inner-core region, maximum wind estimates from SSM/I were unreliable. The ability of SSM/I 85 GHz imagery to provide much improved estimates of the location of Florence's center was clearly shown.

Center position estimates using SSM/I imagery compared much better to the National Hurricane Center (NHC) best track data than GOES IR imagery estimates.

Numerical experiments were conducted to assess the impact of the ODW data and SSM/I retrieved rain rates in the analysis and prediction of Hurricane Florence (1988). The ODW data were used to enhance the initial analysis that was based on the NMC/RAFS 2.5° analysis at 0000 UTC 9 September 1988. The SSM/I retrieved rain rates at 0000 and 1200 UTC 9 September 1988 were assimilated into NRL's tropical cyclone model during model integration.

Results showed that the prediction with the ODW enhanced initial analysis was improved over the case without the ODW data. The 24 h track and intensity forecast errors were reduced by 80% and 70%, respectively. Results also revealed that the assimilation of the SSM/I retrieved rain rates reduced the critical landfall location forecast error by about 50% (from 2.9° to 1.5° latitude), and the landfall time by 7 hours (from 9 hours to 2 hours) compared to the forecast when the NMC/RAFS 2.5° initial analysis was not enhanced. This study also showed that the assimilation of SSM/I retrieved rain rates improved the forecast error of the landfall time by two hours (from 2 hours to 0 hours) and made no improvement on the forecast error of the landfall location when the ODW enhanced analysis was used. The study concluded that numerical predictions of tropical cyclones can benefit from assimilations of the ODW data and SSM/I retrieved rain rates.

Further details can be found in the Alliss thesis referred to in Section III.2. In addition, this work has been described in a publication by Alliss, et al. (1993) in the Journal of Applied Meteorology and is included in this report in Appendix H. In addition, this work is described in the PhD dissertation by Jainn Jong Shi presented to the Department of Marine, Earth, and Atmospheric Sciences of NCSU in Raleigh, North Carolina in 1993. It is included in this report as Appendix I. Finally, this research was presented at the Nineteenth Conference on Hurricanes and Tropical Meteorology of the American Meteorological Society (1991). A reprint is included here as Appendix J.

III.4. Hurricane Hugo (1989) Case

SSM/I rainfall rates and 85 GHz imagery were instrumental in observing Hugo's convective organization and precipitation patterns. Rainfall rates measured by SSM/I just prior to landfall strongly support those observed at reporting stations along the Georgia-South Carolina coastlines. These results indicate that rain data obtained by SSM/I may be useful in providing forecasts for precipitation amounts over coastal areas as tropical cyclones make landfall. It was found that the total latent heat release (TLHR) calculated from SSM/I rainfall rates was comparable to estimates made by Rodgers and Adler (1981) who studied other tropical cyclones using the Nimbus Electrically Scanning Microwave Radiometer (ESMR-5). Furthermore, observations showed that as the TLHR increased with time so did the intensity of Hugo. Because of the poor temporal resolution, any lag present between the TLHR and the cyclone intensity was impossible to determine. The contribution of heavier rainfall rates to the total storm rainfall was calculated and observed to increase as Hugo intensified. It was found that higher rainfall rates occurred closer to the inner-core region during times of intensification. The areal coverage of higher rainfall rates was also observed to increase during times of intensification. Maximum rainfall rates in the eyewall region were found to increase as the minimum observed central pressure decreased. Poor temporal resolution prevented an estimation of the lag between the convection and minimum pressure. With three sensors currently in orbit, more frequent observations of tropical cyclones might help in determining this lag time.

The utility of SSM/I 85 GHz imagery in estimating the low-level center has also been demonstrated in this study. The usefulness of SSM/I data for this application was most beneficial when the eye of Hugo was obscured by clouds and at night when GOES imagery was unavailable. Furthermore, in the event that GOES becomes inoperative, a situation forecasters might face soon, or during times when no airborne reconnaissance data is available, SSM/I observations may become increasingly important for operational use.

Details of this research can be found in the Alliss thesis described in Section III.2, and in the publication by Alliss, et al. (1992) in *Monthly Weather Review*. The latter appears here as Appendix K.

IV. NUMERICAL INVESTIGATION OF THE OUTFLOW LAYER OF TROPICAL CYCLONES

The Naval Research Laboratory's tropical cyclone model was used to investigate the interaction between Hurricane Florence (1988) and its upper-tropospheric environment. Results from this study were documented in the Ph.D. dissertation by J.J. Shi referred to in Section III.3 and included as Appendix I. The research was supported by this program.

The model was initialized with the NMC/RAFS 2.5° analysis at 0000 UTC 9 September 1988, enhanced by the ODW data mentioned in the previous sections through an objective analysis. The model was then integrated for 24 hours valid for the period of time from 0000 UTC 9 September to 0000 UTC 10 September 1988. During the model integration, the SSM/I retrieved rain rates at 0000 UTC 9 September were assimilated into the model at 0-3 hour and the SSM/I rain rates at 1200 UTC 9 September at 9-15 hour. Diagnosis of the 200 mb level structure of the 12h forecast valid at 1200 UTC 9 September 1988 showed that the outflow layer was highly asymmetric with an outflow jet originating at approximately three degrees north of the storm. In agreement with the result of an idealized simulation, there was a thermally-direct, circum-jet secondary circulation in the jet entrance region and a thermally indirect one in a reversed direction in the jet exit region in this real case simulation. In several previous studies, it was postulated that an approaching westerly jet had modulated the convection and intensity variations of Florence.

In a variational numerical experiment, the approaching westerly jet was de-bogused by repeatedly setting the meridional wind component and zonal temperature perturbations to zero at the jet-level in the normal mode initialization procedure. These experiments showed that the sudden burst and collapsing of Florence's inner core convection was highly correlated with the position of the upper-tropospheric westerly jet. These experiments also suggested that the approaching of the upper-tropospheric westerly jet was crucial to the intensification of Florence's inner core convection between 1000 and 1500 UTC September 9 that occurred prior to the deepening of the minimum sea level pressure (from 997 to 987 mb) between 1200 UTC 9 September and 0000 UTC 10 September.

V. NUMERICAL SIMULATIONS OF MONSOON RAINFALL WITH THE NRL/NCSU REGIONAL NESTED MODEL

The NRL/NCSU regional nested-grid model was used to simulate monsoon rainfall. Results from this study were documented in the Ph.D. dissertation by K. V. Alapati presented to the Department of Marine, Earth, and Atmospheric Sciences of NCSU in Raleigh, North Carolina in 1993. The abstract of the paper, entitled "Numerical Simulations of Monsoon Rainfall with the NRL NCSU Regional Nested Grid Model" appears as follows.

Abstract

The short-range prediction of monsoon circulations and associated weather is a challenging problem. Two important processes which affect the dynamics as well as the thermodynamics of the monsoon are (a) the cumulus convection and (b) the energy and the mass transfer in the atmospheric boundary layer. From the modeling point of view, horizontal and vertical resolutions, numerical techniques and data preparation are important components. As an essential tool, a limited area numerical model with different boundary layer parameterizations and vertical grid resolutions, different cumulus convection parameterization schemes is developed to simulate various physical processes and rainfall associated with the Asian summer monsoon. The model developed for this research is based on a version of the Naval Research Laboratory's nested grid model.

Two different cumulus parameterization schemes, one developed by Kuo and the other by Betts-Miller, are used to simulate the orographic-convective rainfall associated with the Western Ghats during two different periods of the monsoon during which rainfall was moderate to heavy. First GARP Global Experiment (FGGE) data are used for the model development and to test the performance of the Kuo and the Betts-Miller scheme. First numerical simulation indicated that both the Kuo and the Betts-Miller schemes give half the observed rates of rainfall with the coarse horizontal resolution. The Kuo scheme gives better rainfall rates with increased horizontal (nested domain) while Betts-Miller scheme gives rainfall of about two to three times the observed rates. In the second numerical simulation during which large rainfall rates are observed, poor initial conditions appear to have affected the rainfall predictions. Rainfall rates predicted are higher in the nested domain (higher horizontal resolution) than those in the coarse-grid domain and the rates are somewhat similar with the both the Kuo and Betts-Miller scheme. However, large scale flow and monsoon depression are better simulated with the Kuo scheme as compared with the Betts-Miller scheme in both the numerical simulations.

A better resolution data set, obtained from the European Centre for Medium Range Weather Forecast center (ECMWF) is used to critically evaluate the performance of the Kuo and Betts-Miller scheme. Comparison of the model predictions with the observations indicate that the monsoon depression and associated rainfall is better simulated with the Kuo scheme. Predicted location of the heat low and intensity of the depression with the Kuo scheme agrees better with the observations. With the Betts-Miller scheme predicted heat low was located over northern Arabian Sea and has developed into a spurious intense tropical cyclone giving rise to large rainfall rates. Water vapor budget indicates that model predictions of rainfall and evaporation stabilized and there exists a balance between them after 30 h of integration with the Kuo scheme. Predicted evaporation far exceeded the rainfall with the Betts-Miller scheme. Also, differences between the model predictions and the analyzed data indicated that the atmosphere is more moist with the Betts-Miller scheme. The above three experiments thus indicated that the model predictions with the Kuo scheme are far superior than with the Betts-Miller scheme.

Sensitivity of the ten-layer model to the observed and climatological sea surface temperatures (SSTs) in the context of short-range prediction of monsoon rainfall was also studied. Presence of positive anomalies of about 1 to 2°C in the observed SSTs cause the evaporation to increase over the surrounding oceans and local acceleration of the winds. Area averaged rainfall is about 10% larger for the observed SSTs as compared to that obtained using the climatic SSTs. Comparison of the forecast errors in the zonally averaged atmospheric temperatures between these two experiments indicates that there is a net heating of the atmosphere while the differences of specific humidity were negligibly small. Simulations with uniformly increased climatic SSTs by 2°C indicated qualitatively similar results. Since SSTs are uniformly increased the SST gradients are preserved although there is a reduction in the surface pressure. As expected, predicted latent heat fluxes are much higher than that in the simulations with climatic SSTs. Increased evaporation caused higher rainfall rates and stronger circulation patterns over the convectively active regions. These results indicate that the short-range prediction of monsoon weather is sensitive to the small variations in the SSTs.

Diabatic forcing is incorporated into a vertical mode initialization scheme to improve the initial conditions. Analyzed gridded rainfall data are used to specify the vertical latent heating in the diabatic initialization scheme. Results indicate that the model predicted significantly higher rainfall rates when the initial conditions are obtained using a diabatic initialization scheme. Also, predicted rainfall rates are persistently higher almost throughout the period of simulation with a considerable increase during

the first nine hours of integration. Use of diabatic initialization scheme lead to the prediction of stronger winds, stronger circulation patterns associated with the cumulus convection, and higher latent heat fluxes from surrounding oceans, leading to higher rainfall rates.

A sixteen-layer model is developed to study the effect of improved boundary layer physics and increased vertical grid resolution. As observed, the sixteen layer model predicted significant diurnal variation of the height of the boundary layer over land and very little over the oceans. Increased vertical resolution and inclusion of better boundary layer physics reduced the errors in the predicted fields particularly in the lower troposphere. Monsoon depression and the associated rainfall are better simulated by the sixteen-layer model. In general, results indicate an overall improvement in the model predictions.

As described in the above abstract, two different cumulus parameterization schemes, one developed by Kuo and the other by Betts-Miller, were incorporated into the NRL/NCSU regional nested-grid model and used to simulate the orographic-convective rainfall associated with the western Ghats in two different periods of the monsoon during which rainfall was moderate to heavy. Data from the First GARP Global Experiment (FGGE) and the European Centre for Medium Range Weather Forecast (ECMWF) were used for the model development and to test the performance of the two different cumulus parameterization schemes. Comparison of the model predictions with observations indicated that the monsoon depression and associated rainfall was better simulated with the Kuo scheme. The predicted location of the heat low and the intensity of the depression agreed better with the observations using the Kuo scheme. The predicted heat low with the Betts-Miller scheme was located over the northern Arabian Sea and developed into a spurious intense tropical cyclone giving rise to large rainfall rates. With the Betts-Miller scheme, the predicted evaporation far exceeded the rainfall. Also, differences between the Betts-Miller scheme model predictions and the analyzed data indicated that the atmosphere contained more moisture than measured. Results from this study thus indicated that the model predictions with the Kuo scheme were far superior than those with the Betts-Miller scheme.

Diabatic forcing was also incorporated into a vertical mode initialization scheme to improve the initial conditions for this study. Analyzed gridded rainfall data were used to specify the vertical latent heating in the diabatic initialization scheme. Results indicated that the model predicted significantly

higher rainfall rates when a diabatic initialization scheme was used to obtain the initial conditions. The predicted rainfall rates were persistently higher throughout the period of the simulation with a considerable increase during the first nine hours of integration. Use of a diabatic initialization scheme led to the prediction of stronger winds, stronger circulation patterns associated with the cumulus convection, and higher latent heat fluxes from the surrounding ocean, leading to higher rainfall rates.

This work has been described in more detail in a paper published in Atmospheric Research (1993) by Alapaty, et al. It is included in this report as Appendix L.

VI. REFERENCES

- Alapati, K., R. V. Madala, and S. Raman, 1993: Sensitivity of monsoon rainfall predictions to initialization procedures. *Atmos. Research*, **30**, 157-170.
- Alliss, R. A., S. Raman, and S. W. Chang, 1992: Special Sensor Microwave/Imager (SSM/I) observations of Hurricane Hugo (1989). *Mon. Wea. Rev.*, **120**, 2723-2737.
- , G. D. Sandlin, S. W. Chang and S. Raman, 1993: Applications of SSM/I data in the analysis of Hurricane Florence (1988). *J. Appli. Meteor.*, **32**, 1581-1591.
- Barnes, S. L., 1973: Mesoscale objective map analysis using weighted time-series observations. NOAA Technical Memorandum, ERL NSSL-62, Norman, OK, 60 pp.
- Bourke, W., and J. L. McGregor, 1983: A nonlinear vertical mode initialization scheme for a limited area prediction model. *Mon. Wea. Rev.*, **111**, 2285-2297.
- Bratseth, A. M., 1986: Statistical interpolation by means of successive corrections. *Tellus*, **38A**, 439-447.
- Cressman, G., 1959: An operational objective analysis system. *Mon. Wea. Rev.*, **87**, 367-374.
- Chang, S., K. Brehme, R. Madala and K. Sashegyi, 1989: A numerical study of the East Coast snow storm of February 10-12, 1983. *Mon. Wea. Rev.*, **117**, 1768-1778.
- , R. J. Alliss, S. Raman, and J. J. Shi, 1993: SSM/I observations of ERICA IOP 4 marine cyclone: a comparison with in situ observations and model simulation. *Mon. Wea. Rev.*, **121**, 2452-2464.
- Harms, D. E., S. Raman, and R. V. Madala, 1992a: An examination of four-dimensional data assimilation techniques for numerical weather prediction. *Bull. Amer. Meteor. Soc.*, **73**, 425-440.
- , K. D. Sashegyi, R. V. Madala, and S. Raman, 1992b: Four dimensional data assimilation of GALE data using a multivariate analysis scheme and a mesoscale model with diabatic initialization. Tech Rep. NRL/MR/4223-92-7147, 219 pp.
- , R. V. Madala, S. Raman, and K. D. Sashegyi, 1993: Diabatic initialization tests using the Naval Research Laboratory limited-area numerical weather prediction model. *Mon. Wea. Rev.*, **121**, 3184-3190.

- Lorenc, A. C., R. S. Bell and B. MacPherson, 1991: The Meteorological Office analysis correction data assimilation scheme. *Quart. J. Roy. Meteor. Soc.*, **117**, 59-89.
- Rodgers, E. B., and R. F. Adler, 1981: Tropical cyclone rainfall characteristics as determined from a satellite passive microwave radiometer. *Mon. Wea. Rev.*, **109**, 506-521.
- Sashegyi, K. D., and R. V. Madala, 1990: Tests of initialization procedures with the NRL limited area numerical weather prediction model. NRL Memorandum Report 6648, Washington, D. C., 88 pp.
- , and -----, 1993: Application of vertical mode in initialization to a limited area model in flux form. *Mon. Wea. Rev.*, **121**, 207-220.
- , D. E. Harms, R. V. Madala, and S. Raman, 1993: Application of the Bratseth scheme for the analysis of GALE data using a mesoscale model. *Mon. Wea. Rev.*, **121**, 2331-2350.
- Shi, J. J., S. Chang, K. Sashegyi and S. Raman, 1991: Enhancement of objective analysis of hurricane Florence (1988) with dropsonde data. Preprints, *Nineteenth Conference on Hurricanes and Tropical Meteorology*, Amer. Meteor. Soc., May 6-10, Miami, FL, 335-337.

Appendix A

Application of the Bratseth Scheme for the Analysis of GALE Data Using a Mesoscale Model

Application of the Bratseth Scheme for the Analysis of GALE Data Using a Mesoscale Model

KEITH D. SASHEGYI*

Science Applications International Corporation, McLean, Virginia

DEWEY E. HARMS

Department of Marine, Earth and Atmospheric Sciences, North Carolina State University, Raleigh, North Carolina

RANGARAO V. MADALA

Naval Research Laboratory, Washington, D.C.

SETHU RAMAN

Department of Marine, Earth and Atmospheric Sciences, North Carolina State University, Raleigh, North Carolina

(Manuscript received 14 April 1992, in final form 15 February 1993)

ABSTRACT

The successive correction scheme of Bratseth, which converges to optimum interpolation, is applied for the numerical analysis of data collected during the Genesis of Atlantic Lows Experiment. A first guess for the analysis is provided by a 12-h forecast produced by integrating a limited-area model from a prior coarse operational analysis. Initially, univariate analyses of the mass and wind fields are produced. To achieve the coupling of the mass and wind fields, additional iterations on the geopotential are performed by extrapolating the geopotential to grid points, using improving estimates of the geostrophic wind. This improved geostrophic wind is then used to update the geostrophic component of the initial univariate wind analysis. Use of a background forecast produces much improved mesoscale structures in the analysis. Enhanced gradients of the geopotential and larger wind shears are the result of the coupling of the mass and wind fields, particularly in regions of lower data density. Application of the vertical mode initialization scheme of Bourke and McGregor is used to diagnose the divergent component of the mesoscale circulations produced with the analysis scheme.

1. Introduction

During the 1960s and 1970s, the most widely used objective analysis technique in operational data assimilation and forecast systems was the method of successive corrections. This type of analysis was first introduced by Bergthórsson and Döös (1955), and a number of versions have been developed by Cressman (1959), Barnes (1973), and others. It is still widely used for the analysis of mesoscale systems in the research community (e.g., Koch et al. 1983; Benjamin and Seaman 1985). However, these successive correction schemes possessed a couple of undesirable attributes. First the analysis always converges to the data,

which should not be the case when errors exist in the data and the background. Second, observations in regions of high data density are given excessive weight relative to observations in areas of low data density.

In the 1980s, emphasis shifted in the operational community toward the more mathematically complex and computationally expensive method of statistical interpolation, better known as optimal interpolation. With optimal interpolation, analysis errors are minimized with respect to the spatial structure of observational and forecast errors. A concise review of objective analysis can be found in Schlatter (1988). Recently, the method of optimum interpolation has been applied with success to operational limited-area modeling systems (DiMego 1988; Benjamin 1989; Mills and Seaman 1990). In these limited-area forecast systems using optimal interpolation the length scales of the correlation functions are usually reduced from those used with global models to provide more detail at the smaller scales (DiMego 1988).

A paper by Bratseth (1986) has caused a recent resurgence of the successive correction method. He in-

* Current affiliation: Naval Research Laboratory, Washington, D.C.

Corresponding author address: Dr. Keith Sashegyi, Remote Sensing Physics Branch, Code 7220, Naval Research Laboratory, Washington, D.C. 20375-5351.

roduced a successive correction scheme, in which the solution converges toward the solution obtained by optimal interpolation. His technique alleviates the aforementioned shortcomings of previous successive correction methods by using the correlation function for the forecast errors to derive weights that are reduced in regions of higher data density. Additionally, the Bratseth method requires much less computational expense than do optimal interpolation methods. Therefore, it is very attractive for use for a limited-area forecast system when only limited resources are available. This approach to successive correction methodology is currently being used operationally in a multivariate analysis for the limited-area forecast system at the Norwegian Meteorological Institute (Grønås and Midtbø 1987). After a number of iterations of the scheme, the length scale of the correlation functions is further reduced for subsequent iterations to speed the convergence of the scheme at the smaller scales (Grønås and Midtbø 1987; Seaman 1988). A further advantage of reducing the length scale of the correlation function with increasing iteration is that the geostrophic coupling of the geopotential and the wind can be relaxed for the smaller scales (Bratseth 1986). An algorithm similar to the Bratseth scheme has been applied at the U.K. Meteorological Office to directly insert data into both the global and regional models (Lorenc et al. 1991). With each iteration of the U.K. Meteorological Office scheme, the mass and wind variables are updated in a sequential fashion. To maintain balance in their models, changes to the geostrophic component of the wind are derived from any mass changes; the wind changes are nondivergent, and the divergence during integration is damped.

A simplified multivariate, successive correction objective analysis scheme using the Bratseth method has been developed at the U.S. Naval Research Laboratory (NRL) to analyze high-resolution datasets obtained from such field experiments as the Genesis of Atlantic Lows Experiment (GALE), which occurred from 15 January through 15 March 1986. Our scheme also sequentially couples the analyses of mass and wind but in a manner very different from the U.K. Meteorological Office scheme. During the intensive observing periods (IOPs) of GALE, more frequent upper-air soundings were taken at selected National Weather Service sites over the eastern United States, supplemented by additional sites along the coast, dropsondes deployed from aircraft offshore, and a denser set of surface observations (Dirks et al. 1988; Raman and Riordan 1988).

To better use this data, a prior forecast generated by the NRL limited-area weather prediction model is used, as in the operational limited-area models, to provide a first guess for the analysis scheme. The model consists of a fine grid covering the eastern United States and Atlantic offshore, with a resolution of about 55 km, nested inside a coarse grid covering the continental

United States and western North Atlantic with a resolution of about 170 km. A prior operational analysis is used to provide the initial conditions for integrating the NRL limited-area model. The analysis covers a similar region as the fine grid but at a lower resolution of 1.5° in latitude and longitude. The analysis grid spacing is consistent with the average upper-air station spacing of about 350 km over the eastern United States. By using such a high-resolution model to generate realistic mesoscale features for the first guess, the resulting analysis should be of a higher resolution than would be possible if a first guess were not used. To remove bad data or data inconsistent with the scales resolved by the numerical model, an efficient quality control procedure was implemented in a manner similar to DiMego (1988).

In this paper, we give a general description of our objective analysis method and provide a qualitative evaluation of the scheme using data from the second IOP of GALE. Results with our new analysis scheme are compared to a Barnes (1973) scheme that was used in the past to enhance large-scale operational analyses (Chang et al. 1989; Shi et al. 1991). The vertical-mode initialization scheme of Bourke and McGregor (1983) is used to diagnose the divergent circulations associated with the analyzed mesoscale features and upper-level jet streaks. The interaction of these secondary circulations in the jet streaks can be important for cyclone development (e.g., Uccellini et al. 1984; Uccellini and Kocin 1987). The impact the new scheme has on these derived mesoscale circulations is tested and compared with the earlier Barnes scheme.

2. The NRL objective analysis scheme

We use a simplified application of the Bratseth scheme compared to the full multivariate implementation used at the Norwegian Meteorological Institute by Grønås and Midtbø (1987). In our scheme, we first perform univariate analyses of the mass and wind fields using the successive correction approach of Bratseth (1986). We analyze for the deviations from a first-guess field, which is derived from a prior 12-h forecast generated by our limited-area model. To provide the coupling between the wind and mass fields, we use the analyzed wind as an initial estimate of the geostrophic wind for a further iteration on the geopotential. The geostrophic wind is used to extrapolate the geopotential to the gridpoint locations, in a fashion similar to Cressman (1959). In each subsequent iteration, an improved geostrophic wind estimate is then defined by the new geopotential gradient, and not by the original wind as was widely used with the Cressman scheme. This change in the geostrophic wind estimate is then used to update the geostrophic component of the initial univariate wind analysis, as in Kistler and McPherson (1975). Further iterations of the wind analysis are performed to enhance the ageostrophic component of the

wind. The initial univariate temperature analysis can then be corrected for the new geopotential thicknesses.

To test the scheme, a set of surface data and upper-air soundings were obtained for the second IOP of GALE from the GALE Data Center (GDC) at Drexel University (Mercer 1987). The data were provided at 10-mb levels from the surface up to 100 mb, and covered a domain over the eastern United States and western North Atlantic from 115° to 45°W and from 10° to 60°N. A higher density of upper-air soundings and surface data is found in the inner GALE region covering the Carolinas and southern Virginia from the Gulf Stream to the Appalachians. The analysis grid covered the data domain with a resolution of 1.5° in latitude and longitude, extending from 116° to 44°W and from 9° to 61.5°N. The initial conditions for the 12 h forecast of our limited-area model are derived from operational analyses obtained at 12-h intervals on a 2.5° hemispheric grid from the National Meteorological Center (NMC). A quality control of the data prior to the analysis is used to remove any data that are inconsistent with this forecast first guess, are not supported by neighboring observations, or are of a scale too small to be resolved by the analysis scheme. In areas without data, such as over the ocean and around the lateral boundaries of the analysis grid, bogus data are derived from the NMC analysis at that analysis time. The analyses are performed on pressure surfaces every 50 mb from 1000 to 100 mb. In a zone along the lateral boundaries of the analysis grid, the analyzed corrections are further merged with corrections to the first guess derived from the NMC analysis. The resulting corrections are bicubically interpolated to the model horizontal fine grid and added to the first guess for display on pressure surfaces. The components of our analysis scheme are

- (i) limited-area model forecast,
- (ii) data preparation and quality control,
- (iii) univariate analysis of the mass and wind field,
- (iv) enhancement of the geopotential gradient,
- (v) enhancements of the wind field and temperature gradient, and
- (vi) boundary values and interpolation to model grid.

We now briefly describe each of these components in turn. More details can be found in the report by Harms et al. (1992).

a. Limited-area model forecast

The limited-area model was developed at the Naval Research Laboratory and is detailed in several NRL technical memorandum reports by Madala et al. (1987), Sashegyi and Madala (1990), and Harms et al. (1992). This is a primitive equation model in terrain-following sigma coordinates having a doubly nested grid network. A coarse grid covers a domain including

the continental United States from 40° to 140°W and 10° to 70°N, with a horizontal resolution of 2° longitude (170 km at 40°N) \times 1.5° latitude (166.5 km). The coarse grid provides the lateral boundary conditions for an inner fine grid, which covers a smaller domain including the eastern half of the United States and extending out over the Gulf Stream from 58° to 102°W and 23.5° to 56.5°N with a finer horizontal resolution of 0.67° longitude (56.7 km at 40°N) \times 0.5° latitude (55.5 km). In the vertical, both grids use ten equally spaced sigma levels. Model topography for both grid domains is obtained from the U.S. Navy's 10-min global topographical data. For each model grid point, the average is computed over the grid square with one standard deviation added, and the result smoothed. Climatological mean sea surface temperatures for the month of January of 1° resolution, taken from Reynolds (1982), are interpolated to the model grids. A sea-ice boundary is derived from the U.S. Navy climatological sea-ice boundaries for the months of January and February.

To provide the first guess for the data quality control and analysis we integrate our limited-area forecast model for 12 h starting from a prior NMC analysis. The NMC 2.5° hemispheric analyses are interpolated to the horizontal model grids using Lagrangian cubic polynomial interpolation. The interpolated analyses are then initialized separately on both coarse and fine grids for the first three vertical modes of the numerical model using the vertical mode scheme of Bourke and McGregor (1983), as applied to the NRL model (Sashegyi and Madala 1993). This scheme generates a balanced divergent part of the wind field, while producing only small changes in the geopotential and vorticity. For the coarse grid, lateral boundary values for the model integrations are derived from these initialized NMC analyses by linear interpolating in time.

b. Data preparation and quality control

An efficient quality control procedure has been developed for use with the analysis scheme, similar to those at operational weather centers. After checking the upper-air soundings for hydrostatic consistency, we smooth the soundings in the vertical and recompute consistent geopotentials. The temperatures and the u and v wind components are averaged over 20-mb intervals, weighted by the log of pressure for the temperatures and by the mass for the u and v wind components. The humidities, which are more noisy (C. Kreitzberg 1987, personal communication), are smoothed by averaging over 50-mb intervals using the mixing ratios weighted by the mass. Data are retained at 50-mb levels to be more representative of our ten-layer model vertical resolution. For efficiency, the soundings are sorted into 5° latitude-longitude boxes for each pressure level from sea level to 100 mb.

As in the regional analysis at NMC (DiMego 1988),

we perform a "gross" check and a "buddy" check, in which observations with large deviations from the first guess or from neighboring observations are removed. In the gross check, those upper-air observations that differ in magnitude by more than four standard deviations from the first guess are rejected. For sea level pressure a limit of two and a half times the standard deviation is used. Estimates of the standard deviation of the observations from the first-guess forecast are obtained by adding a forecast error growth to the observational error. The values used were slight modifications to those used at operational centers (Dimego 1988; Shaw et al. 1987) and are listed in Table 1. For sea level pressure, an observational error of 1.5 mb is used with forecast error growth of 1.0 mb in 6 h. For the remaining quality control procedures and the analysis, only the deviations of the data from the first guess are retained. As shown by Bratseth (1986), close observations slow the convergence of the iterative scheme. To speed the convergence of the scheme, close observations are replaced by an average "super" observation (superob). To further prevent isolated data from adversely affecting the analysis by aliasing to the larger analysis scales, any remaining isolated observations are also eliminated. In data-sparse regions over the ocean, we use additional bogus soundings, derived from the difference between the first-guess forecast and the NMC 2.5° hemispheric analysis, for the analysis time of interest. To match the resolution of the NMC analysis, we use two bogus soundings spaced 5/3° apart in latitude and longitude in each empty 5° data box in the interior.

c. Univariate analysis of the mass and wind field

In the first univariate analysis step, sea level pressure, geopotential, temperature, and humidity corrections to the first guess are successively adjusted at each iteration using the Bratseth (1986) scheme. In this scheme estimates of both the interpolated correction and an observation correction are computed using the iterative formulas. For the geopotential corrections, the interpolated value ϕ_x at the grid point x is given by

$$\phi_x(k+1) = \phi_x(k) + \sum_{j=1}^n \alpha_{xj} [\phi_j^o - \phi_j(k)], \quad (1)$$

while the new estimate of the value of the observation correction is given by

$$\phi_i(k+1) = \phi_i(k) + \sum_{j=1}^n \alpha_{ij} [\phi_j^o - \phi_j(k)], \quad (2)$$

where ϕ_j^o is the value of the observation, $\phi_x(k)$ and $\phi_j(k)$ are the interpolated values at the grid point and the estimate of the observation value, respectively, for the k th iteration. The sum is over all the n observations. The starting corrections $\phi_x(1)$ and $\phi_j(1)$ are zero. The weights, which are dependent on the covariance of the corrections to the first guess, are in each case given by

TABLE 1. Standard deviation of the observational errors and forecast error growth (in parentheses) for a 6-h forecast period.

Pressure (mb)	Height (m)	Temperature (°C)	Relative humidity (%)	u, v wind (m s ⁻¹)
1000	5 (8)	1.8 (0.6)	13 (2)	2.5 (1.1)
950	5 (8)	1.8 (0.6)	13 (2)	2.5 (1.1)
900	5 (8)	1.8 (0.5)	13 (2)	2.5 (1.1)
850	6 (8)	1.5 (0.5)	13 (2)	2.5 (1.1)
800	6 (8)	1.5 (0.4)	13 (2)	2.5 (1.1)
750	6 (8)	1.4 (0.3)	12 (2)	2.5 (1.2)
700	6 (8)	1.3 (0.3)	12 (2)	2.5 (1.2)
650	6 (8)	1.2 (0.3)	12 (3)	3.0 (1.3)
600	7 (9)	1.0 (0.3)	12 (3)	3.0 (1.4)
550	8 (10)	1.0 (0.3)	13 (3)	3.0 (1.5)
500	9 (12)	1.0 (0.3)	13 (4)	3.0 (1.6)
450	10 (14)	1.0 (0.4)	13 (4)	3.5 (1.6)
400	12 (16)	1.0 (0.5)	13 (4)	3.5 (1.7)
350	14 (17)	1.0 (0.5)	15 (4)	4.0 (1.7)
300	14 (18)	1.0 (0.6)	17 (4)	4.0 (1.6)
250	14 (18)	1.5 (0.6)	—	4.0 (1.6)
200	15 (18)	1.8 (0.5)	—	4.0 (1.5)
150	18 (18)	1.8 (0.6)	—	4.0 (1.4)
100	20 (17)	2.0 (0.7)	—	3.5 (1.3)

$$\alpha_{xj} = \frac{\overline{\phi_x^i \phi_j^o}}{m_j \sigma^2} = \frac{\rho_{xj}}{m_j} \quad (3)$$

$$\alpha_{ij} = \frac{\overline{\phi_i^i \phi_j^o}}{m_j \sigma^2} = \frac{(\rho_{ij} + \epsilon^2 \delta_{ij})}{m_j}, \quad (4)$$

where the covariances are defined in terms of a correlation function ρ for the true values ϕ^i , ϵ^2 is the ratio of the observation error variance σ_e^2 to the first-guess (forecast) error variance σ^2 , and m_j is a "local data density" at the observation location. Here δ_{ij} represents the Kronecker delta function, which is defined to be unity for $i = j$, and zero otherwise. For the forecast error variance, we use the same variance used in the quality control for the variance of the observations from the first-guess forecast (see Table 1). Further, the data density m_i at an observation location is defined by

$$m_i = \frac{1}{\sigma^2} \sum_{j=1}^n \overline{\phi_i^o \phi_j^o} = \sum_{j=1}^n \rho_{ij} + \epsilon^2. \quad (5)$$

With observation errors included, the estimate of observation is not equal to the analyzed value interpolated to the observation location, but it converges rapidly to the value of the observation itself (Bratseth 1986). However, if there is no observation error, the analyzed value and the observation estimate are both the same value.

We model the correlation function $\rho(r)$ for the geopotential corrections as a Gaussian,

$$\rho(r) = e^{-r^2/d^2}, \quad (6)$$

which is a function of the distance r . The length scale d for the correlation function is defined by 600 km, similar to that used at NMC in the regional model

(DiMego 1988). After the first three or four iterations the length scale is reduced to 330 km for one additional iteration, to speed convergence of the scheme (see also Grønås and Midtbø 1987). After the first pass of our analysis scheme, the data are again checked for inconsistency with the first-pass analysis. Any inconsistent data, which differ by more than 2.5 times (1.5 times for sea level pressure) the standard deviation from the first pass, are removed and the first pass is repeated. The same correlation function is used for the univariate analysis of sea level pressure, temperature, and relative humidity.

For the univariate analysis of wind corrections to the first-guess wind field, different correlation functions are used. The functional form of the correlation functions ρ_u and ρ_v used for the components of the wind field are given by

$$\rho_u = \left[1 - \frac{(y - y_j)^2}{d_u^2} \right] \rho(r) \quad (7)$$

$$\rho_v = \left[1 - \frac{(x - x_j)^2}{d_u^2} \right] \rho(r), \quad (8)$$

where $\rho(r)$ is the correlation function for the geopotential, (x, y) and (x_j, y_j) are the Cartesian positions of an arbitrary point and an observation, respectively,

$$\phi_x(k+1) = \phi_x(k)$$

$$+ \sum_{j=1}^n \alpha_{xj} \{ \phi_j^o - \phi_j(k) - c_j(y - y_j) f_j [u_{g,j}(k) - u_{g,j}(k-1)] + c_j(x - x_j) f_j [v_{g,j}(k) - v_{g,j}(k-1)] \}, \quad (9)$$

and the observation estimate $\phi_i(k+1)$ is

$$\phi_i(k+1) = \phi_i(k)$$

$$+ \sum_{j=1}^n \alpha_{ij} \{ \phi_j^o - \phi_j(k) - c_j(y_i - y_j) f_j [u_{g,j}(k) - u_{g,j}(k-1)] + c_j(x_i - x_j) f_j [v_{g,j}(k) - v_{g,j}(k-1)] \}, \quad (10)$$

where ϕ_j^o is the value of the observation, $\phi_j(k)$ is the observation estimate, and $u_{g,j}(k)$ and $v_{g,j}(k)$ are estimates of the geostrophic wind correction at the observation point for the k th iteration. Here $u_{g,j}(k-1)$ and $v_{g,j}(k-1)$ are the prior estimates of the value of the geostrophic wind at the observation point. In the above, f is the Coriolis parameter and c is a geostrophy factor that reduces to zero near the equator. For the next iteration, an improved estimate of the geostrophic wind correction is computed at the grid points from the new interpolated values of the geopotential given by Eq. (9). Values $u_{g,j}(k+1)$ and $v_{g,j}(k+1)$ of the geostrophic wind at the observation point are then computed by linear interpolation. For the four iterations a single correlation scale d of 600 km is used. In this way, we correct the larger scales only, without changing the smaller scales that are not as geostrophic.

In computing the new estimates of the geostrophic

and d_u is a further length scale. The correlation functions for the wind components can be derived from the correlation function $\rho(r)$ for the geopotential, in which case the length scale d_u is given by the length scale d used for $\rho(r)$ (Grønås and Midtbø 1987). Here we have chosen to use the modified length scale d_u of 700 km, which fits the length scale found by Hollingsworth and Lönnberg (1986) where the transverse correlations in the wind reach zero. These correlation functions effectively give smaller weights across the direction of the wind than along it, without having to compute wind direction, as in Benjamin and Seaman (1985). After three to four iterations, the length scales d and d_u are reduced to 330 and 380 km, respectively, for one more iteration to, again, speed convergence.

d. Enhancement of the geopotential gradient

A further four iterations are used for the geopotential correction, using improving estimates of the geostrophic wind at each iteration to extrapolate the geopotential correction to the grid points. An initial estimate of geostrophic wind is obtained from the previous univariate u, v wind corrections by linear interpolation. The interpolated value $\phi_x(k+1)$ at the grid point is now given after the k th iteration by

wind components $u_{g,x}, v_{g,x}$ from the new geopotential ϕ_x at the grid points, the same geostrophy factor c and a modified Coriolis parameter f^* are used, where

$$u_{g,x} = -\frac{c}{f^*} \frac{\partial \phi_x}{\partial y} \quad (11)$$

$$v_{g,x} = \frac{c}{f^*} \frac{\partial \phi_x}{\partial x}. \quad (12)$$

The geostrophy factor c depends on the latitude θ in degrees as

$$c = \begin{cases} 1, & \text{for } |\theta| > 30^\circ \\ 0.5(1 + \cos 12\theta), & \text{for } 15^\circ \leq |\theta| \leq 30^\circ \\ 0, & \text{for } |\theta| < 15^\circ, \end{cases} \quad (13)$$

and f^* only differs from f in a 15° latitude band around the equator where its magnitude is given by that at 15°N , and it has the same sign as f .

e. Enhancements to the wind and temperature gradients

Following Kistler and McPherson (1975), we adjust the geostrophic part of the corrections to the wind field to match the new corrections for the geopotential. That is, the univariate wind corrections are modified by adding the difference in the geostrophic wind between the enhanced and univariate analysis of the geopotential. In this way the enhanced horizontal shear of the geostrophic wind is preserved in the wind analysis. A further four univariate passes of the wind analysis are then performed to improve the corrections for the ageostrophic component of the wind. After the corrections have been computed at all pressure levels of the analysis, the univariate temperature corrections are adjusted to match the computed thickness corrections.

f. Boundary values and interpolation to model grid

In a nine-point zone along the lateral boundaries of our analysis grid, we merge the analyzed corrections with values interpolated from the NMC analysis. The analyzed corrections in the first six points closest to the boundary are replaced by the NMC values, while a linear weighting of (0.25, 0.75), (0.5, 0.5), (0.75, 0.25) is used to merge the next three interior analyzed values with the NMC values. The final corrections are then bicubically interpolated to the horizontal fine grid of the model and added to the first guess for display of the final analysis on pressure surfaces.

For use on the forecast model grid, the analysis corrections are also interpolated to the sigma levels of the

model. An initial estimate of new surface pressure is first computed from the analyzed full fields on the pressure levels. The surface pressure of the background forecast is similarly computed from the temperature and height on the pressure levels. The difference in surface pressure between the two is then added to the original surface pressure of the background forecast to obtain the corrected surface pressure. The analysis deviations are then linearly interpolated in the vertical to the model sigma levels and added to the first-guess model forecast. The thermodynamic variables (temperature and humidity) are interpolated to the model sigma levels, assuming they are linear in log of pressure, while wind components are interpolated assuming they are linear in pressure. A balanced divergent part of the wind can then be obtained by applying the initialization procedure described in Sashegyi and Madala (1993).

3. Testing the analysis scheme

Analyses were made with the new scheme using the surface and atmospheric sounding data collected during IOP 2 of GALE for the period 0000 UTC 23 January to 1200 UTC 28 January 1986. During this period, cold-air damming occurred east of the Appalachians and a coastal front developed along the east coast of the United States, followed by cyclone development off Cape Hatteras. This range of mesoscale and synoptic-scale features occurred in the region of data coverage and provided an ideal test of the new scheme. The mesoscale features produced with the new scheme could also be compared to the mesoscale analyses of this period by Bosart (1988) and Doyle and Warner (1990). The NMC hemispheric analyses will provide a comparison for the synoptic-scale features produced with our new scheme. The impact of the different components of our new scheme are demonstrated using the analysis for 1200 UTC January 25. The effect of

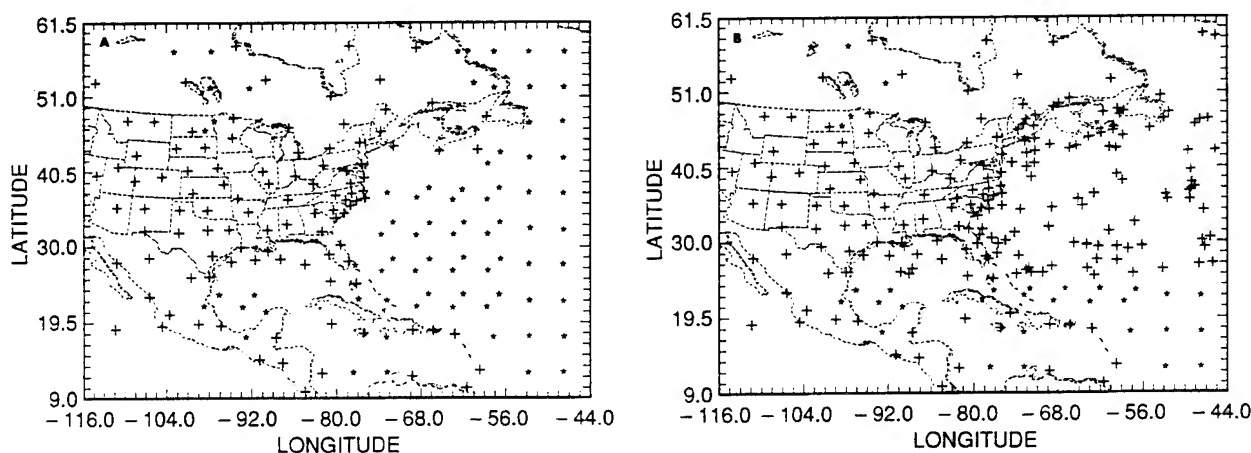


FIG. 1. The location of the data after quality control at 1200 UTC 25 January for (a) the geopotential height at 500 mb and (b) the sea level pressure. The observations are indicated by the plus sign, while bogus values are indicated by the asterisk. The analysis grid is indicated by the tick marks along the domain boundary.

reducing the width of the correlation function and of using superobs is also tested.

For 1200 UTC January 25, the locations of the data that remain after the quality control are shown in Fig. 1 on the domain of the analysis grid. The locations of the observations are shown by the crosses, while the stars show the NMC bogus data, which have been added in data-sparse regions. The analysis grid is indicated by the small tick marks every 1.5° along the latitude and longitude axes. With the 500-mb geopotential height data, few superobs were required but many NMC bogus soundings were added over the ocean. With the sea level pressure data, many more observations were available, many of which have been averaged and replaced by superobs.

To provide a fair comparison on the synoptic scales at the same resolution as our new analysis scheme, the NMC 2.5° hemispheric analyses are themselves enhanced by applying the Barnes (1973) scheme we have used in Chang et al. (1989) to this GALE data. In this application of the Barnes (1973) scheme, a two-step correction of the deviations of the GALE data from the NMC hemispheric analyses are performed using Gaussian weighting defined according to the criterion of Koch et al. (1983). Using an average spacing for the upper-air data over the eastern United States of 350 km, the criterion gives a length scale [d in Eq. (6)] of about 500 km for the Gaussian weighting function for the first pass and 275 km for the second pass. As in Shi et al. (1991), the same quality control described in section 2b is also applied here to the data using the standard deviation of the observational errors listed in Table 1. The first pass for this enhancement of the NMC fields is performed here on the same grid as the new analysis. However due to the decreasing data density outside the region of the eastern United States, the second pass of the Barnes scheme must be limited to a smaller domain, if aliasing is not to occur. The region for the second pass is bounded by longitudes 108° , 68° W and latitudes 25.5° , 49.5° N for the upper-air data, and 22.5° , 49.5° N for the sea level pressure data. A linear weighting is then used to merge the first and second passes over four more analysis grid points inside the second-pass domain. In contrast, this restriction is not necessary with the Bratseth scheme, which adjusts the weights for the changing data density over the whole analysis domain. The synoptic situation during GALE IOP 2 is now described using these enhanced NMC analyses.

a. Description of the synoptic situation

Riordan (1990) and Doyle and Warner (1990) describe in detail the development of the coastal front during GALE IOP 2. With the movement of a cold front off the east coast of the United States at 1200 UTC 23 January, a wedge of cold air is formed behind the front between the Appalachian Mountains and the

coast in the next 24 h. The temperature gradient across the coastline is enhanced by the strong sensible heating of the air over the Gulf Stream (Warner et al. 1990). In the subsequent onshore easterly flow behind the cold front, a coastal front develops offshore along the Carolina coast, and by 1200 UTC on 25 January, a 1000-km-long coastal front paralleled the coastline. The easterly flow regime can be seen in the enhanced NMC analysis for 1000 mb shown in Fig. 2a on the model's horizontal fine grid. The enhanced NMC analysis is, however, unable to resolve the strong thermal gradient along the coast. In the upper levels of the atmosphere, a broad, long-wave trough was present over the central United States at this time (Fig. 2b). During the next 24 h, the trough moved eastward and deepened rapidly due to a second short-wave digging southward in the long-wave trough. By 0000 UTC 26 January, the coastal front extended from Georgia to southern New England and a weak low moved up the coast along the front, reaching the Chesapeake Bay by 1200 UTC 26 January (Fig. 2c). In the next 12 h the coastal low merges with a weak trough, seen in Fig. 2c, moving eastward from the Great Lakes.

The disturbance that ultimately became the first of the major cyclones of GALE was present (Fig. 2a) as a minor frontal wave in extreme southeast Texas at 1200 UTC 25 January. Aloft a major short wave was digging southeastward in the long-wave trough. The surface disturbance remained weak as it advanced along the Gulf coast, and on 26 January the surface wave weakened further as it moved across Georgia. In response to the strong upper-level short wave reaching the East Coast, a new center formed off Cape Hatteras, which deepened rapidly as it moved north, as it combined with the preexisting waves associated with the northward-moving coastal low and eastward-moving trough. By 1200 UTC 27 January, the well-developed low pressure center can be seen (Fig. 2d) crossing the New England coast.

b. Impact of the new scheme

We demonstrate the impact of each of the components of our new analysis scheme with the analysis for 1200 UTC 25 January. The first-guess for the analysis is generated by a 12-h forecast with our limited-area model, where the initial conditions are derived from the NMC 2.5° hemispheric analysis for 0000 UTC 25 January 1986. The resulting first guess is illustrated in Fig. 3, which shows the sea level pressure, 1000-mb winds and temperature, and the 500-mb prediction of height, wind, and temperature on the model's horizontal fine grid. The model has produced a strong wedge of cold air and strong ridging east of the Appalachians (Fig. 3a). The strong temperature gradient along the Carolina coast in the region of strong onshore flow shows conditions favorable for the development of a coastal front. The 1200 UTC 25 January analysis

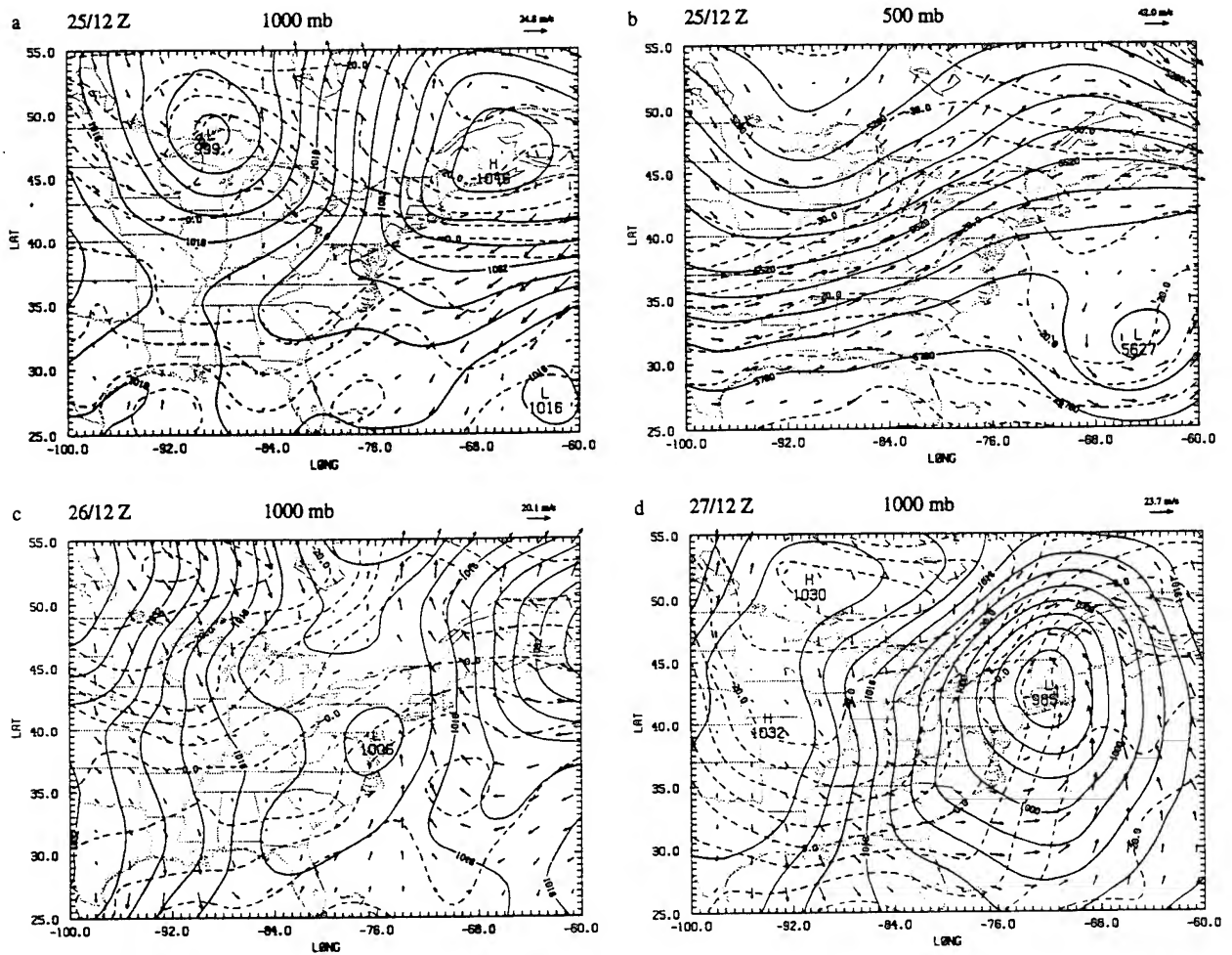


FIG. 2. (a) Sea level pressure (mb), temperature ($^{\circ}\text{C}$), and winds at 1000 mb, and (b) geopotential height (gpm), temperature ($^{\circ}\text{C}$), and winds at 500 mb for the enhanced NMC analysis for 1200 UTC 25 January. Here (c) and (d) are as in (a) except for 1200 UTC 26 and 27 January, respectively. Contours of sea level pressure are 4 mb and 5°C for temperature at 1000 mb. At 500 mb, contours are 60 gpm for geopotential and 2.5°C for temperature. Maximum wind vectors indicated by labeled arrow in meters per second. Model horizontal grid indicated by small tick marks along axes.

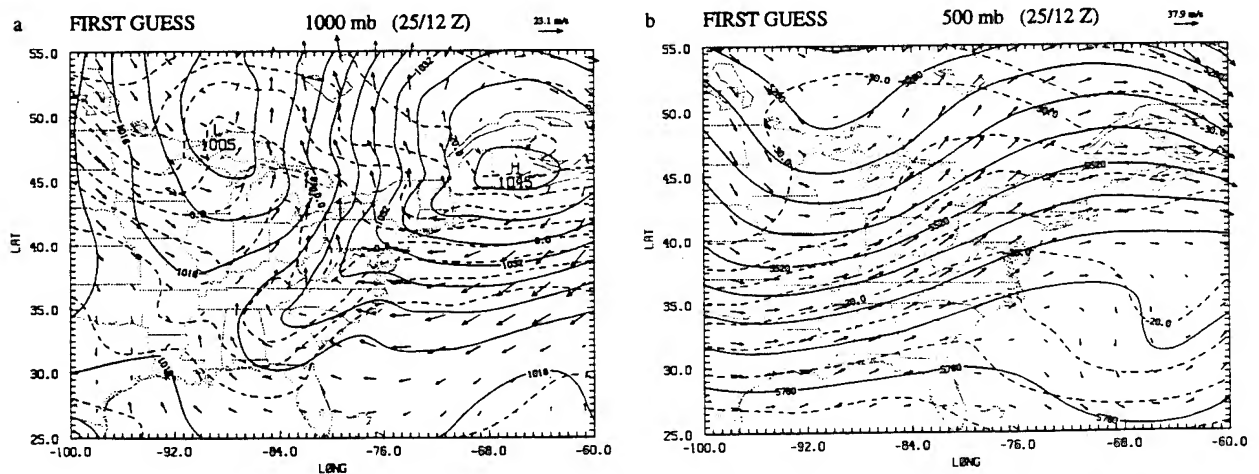


FIG. 3. The first guess at 1200 UTC 25 January for (a) sea level pressure (mb), 1000-mb temperature ($^{\circ}\text{C}$), and winds; and for (b) geopotential height (gpm), temperature ($^{\circ}\text{C}$), and winds at 500 mb. Contours as in Fig. 2.

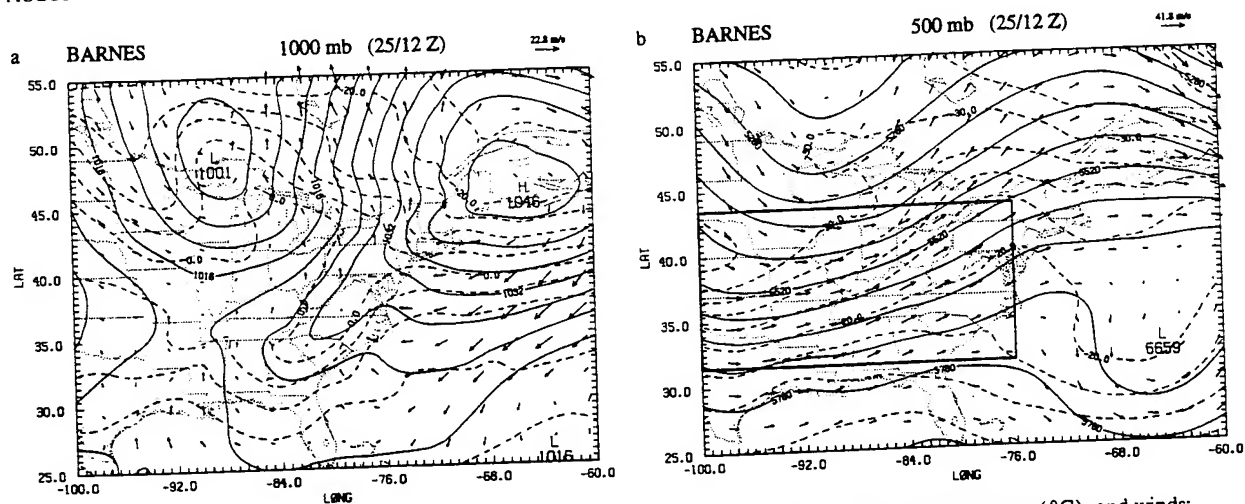


FIG. 4. The Barnes analysis at 1200 UTC 25 January for (a) sea level pressure (mb), 1000-mb temperature ($^{\circ}\text{C}$), and winds; and for (b) geopotential height (gpm), temperature ($^{\circ}\text{C}$), and winds at 500 mb. Contours as in Fig. 2.

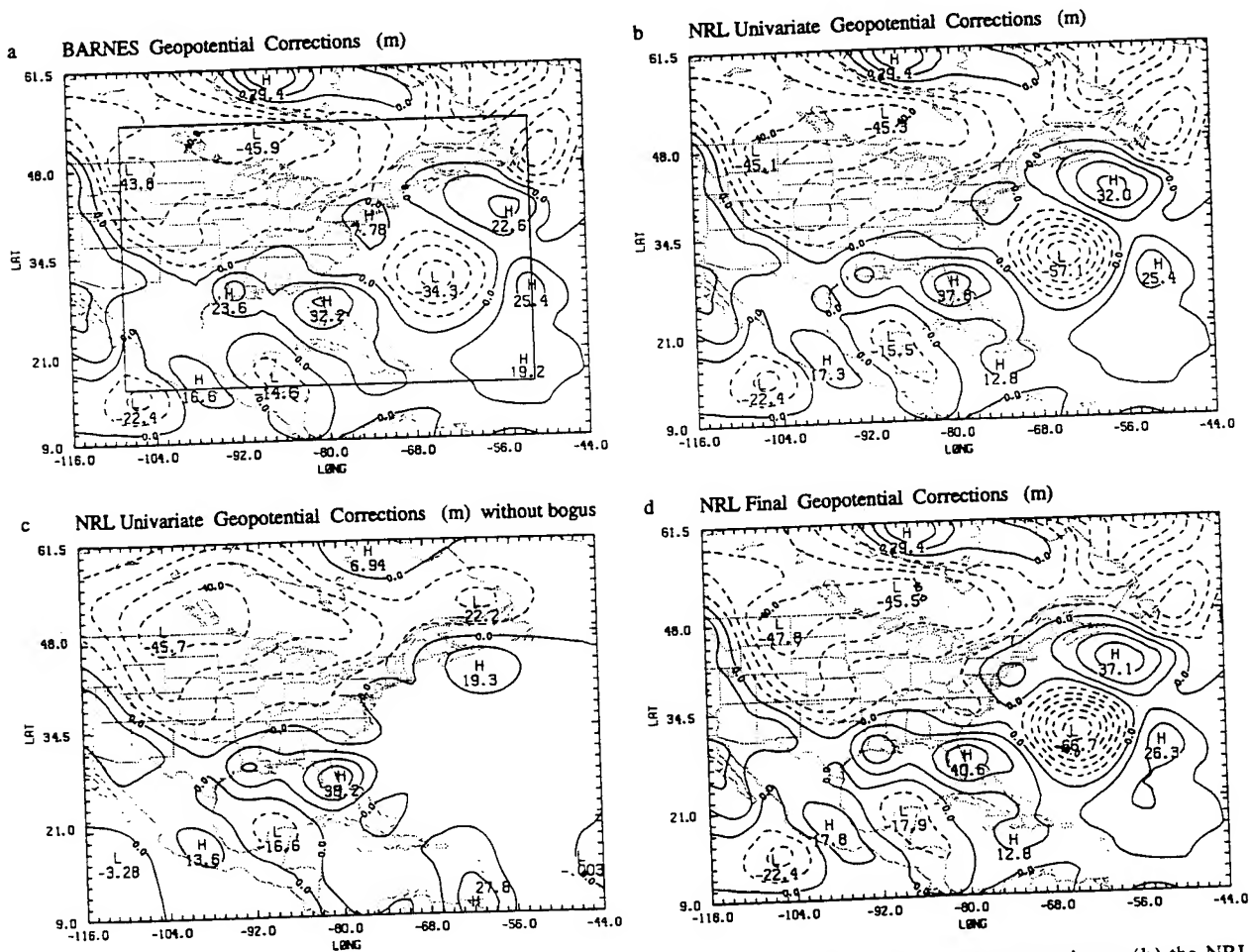


FIG. 5. The geopotential height corrections (gpm) at 500 mb for 1200 UTC 25 January with (a) the Barnes scheme, (b) the NRL univariate analysis, (c) the NRL univariate analysis without bogus data, and (d) the NRL multivariate analysis. Contours of geopotential corrections are every 10 gpm. Analysis grid points indicated by the tick marks along the axes.

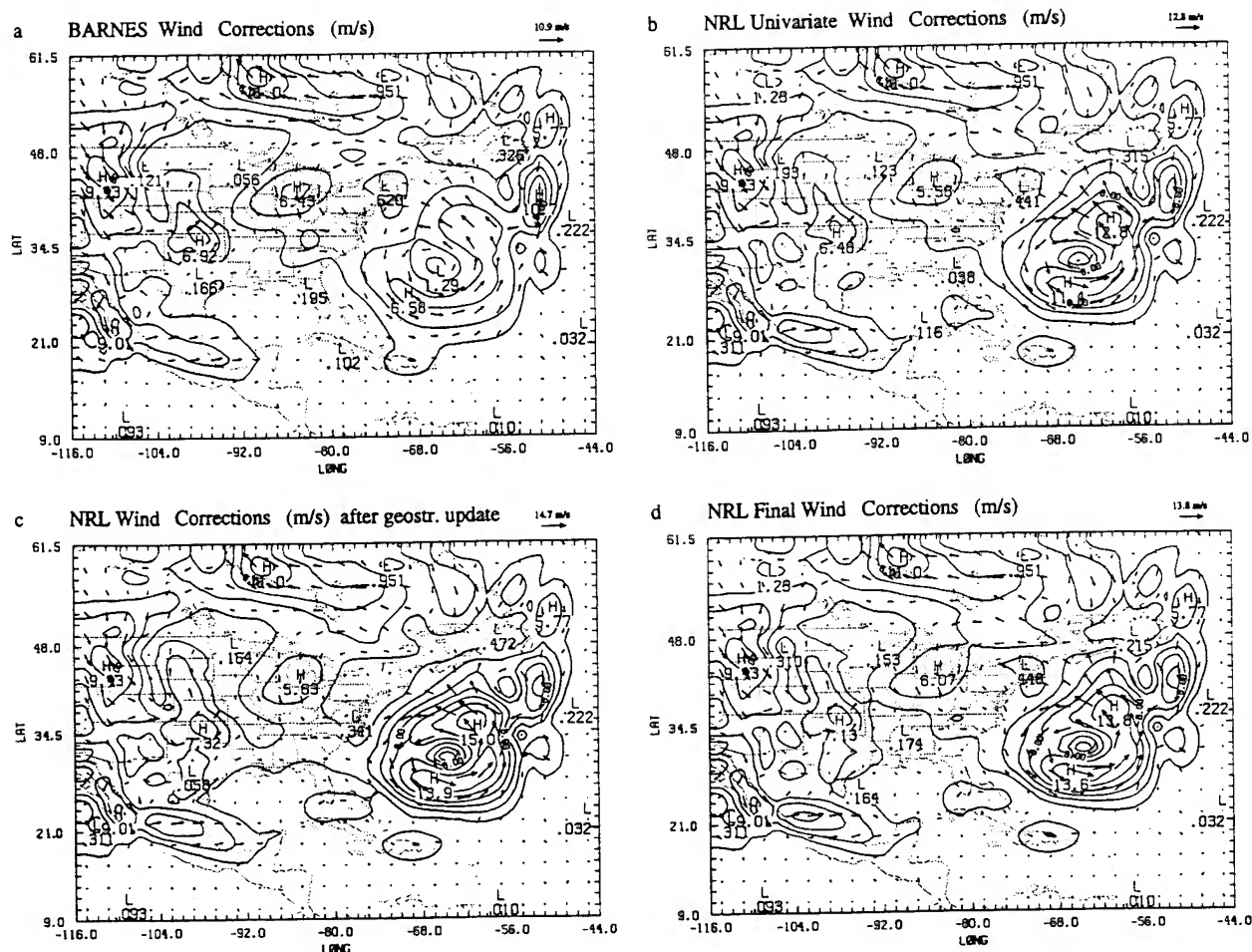


FIG. 6. The wind corrections (m s^{-1}) at 500 mb for 1200 UTC 25 January with (a) the Barnes scheme, (b) the NRL univariate analysis, (c) the NRL analysis after updating the geostrophic wind, and (d) the NRL multivariate analysis. Contours of wind speed corrections are every 2 m s^{-1} .

of Doyle and Warner (1990) verifies that the cold-air damming and coastal front with the strong onshore flow were indeed present (see Fig. 2b of Doyle and Warner). This tight thermal gradient along the coast could not be resolved in our enhanced NMC analysis shown in Fig. 2a. However, the low of 1005 mb over Lake Superior is too weak in the first guess (Fig. 3a) when compared to the enhanced NMC analysis (Fig. 2a). Aloft at 500 mb, the long-wave trough over the eastern United States in Fig. 3b is also too weak, and model forecast has failed to produce the cutoff low over the western Atlantic, which can be seen in the enhanced NMC analysis in Fig. 2b. The cutoff low in the enhanced NMC analysis is about 70 m deeper than the weak trough present in the first guess.

The improvement achieved alone by using a model-generated background field is first illustrated by repeating the Barnes analysis (which was used earlier for the enhancement of the NMC hemispheric analysis) using the aforementioned 12-h model forecast as the

background field. The resulting Barnes analysis for 1000 and 500 mb is shown in Fig. 4. The surface low over Lake Superior is corrected to within a millibar in Fig. 4a, and the cold-air damming and strong temperature gradient from the first guess are retained. Aloft at 500 mb, both the long-wave trough and the low off the coast have been correctly deepened in Fig. 4b. We can also see that the -30°C temperature contour has been shifted eastward in closer agreement with the enhanced NMC analysis in Fig. 2b. Therefore, in the region over the eastern United States, where there is a large amount of data, the Barnes scheme using the limited-area model forecast as a first guess, is able to produce a good synoptic-scale analysis and retain the mesoscale cold wedge and tight temperature gradient along the coast from the first guess. But the cutoff low over the western Atlantic in the Barnes analysis is still too weak by some 32 m when compared to the enhanced NMC analysis. However, the cutoff low does lie outside of the region influenced by the second pass of the

Barnes scheme (see beginning of section 3). The region fully updated by the second pass is shown by the solid rectangle inside Fig. 4b.

In Figs. 5 and 6, we compare the analysis corrections for the 500-mb geopotential height and winds after each of the remaining components of the new analysis scheme with that produced by the Barnes scheme. The figures show the entire region of the analysis grid, with the analysis grid points indicated by the small tick marks along the axes. The geopotential and wind corrections to the first guess obtained with the Barnes scheme are shown in Figs. 5a and 6a. The six-point region around the boundary, where analyzed values are replaced with values interpolated from the NMC 2.5° hemispheric analysis, is indicated by the solid rectangle in Fig. 5a (see section 2f). The deepening of the long-wave trough and a strong cutoff low are readily apparent in the geopotential height corrections in Fig. 5a. The winds around the cutoff low are strengthened in Fig. 6a, and an ageostrophic flow south of the Great Lakes is produced. In Figs. 5b and 6b we compare the result after the initial univariate analysis of the geopotential height and wind is carried out with the new analysis scheme as described in section 2c. The only change is that the Bratseth scheme is used for the analysis instead of the Barnes scheme. In the data-rich area over the eastern United States, only small differences are found in the 500-mb geopotential height and wind corrections. The maximum in the ageostrophic flow south of the Great Lakes is somewhat weaker with the Bratseth scheme. Over the western Atlantic, the cutoff low is much deeper when using the Bratseth scheme, which is able to adjust the weights for the changing data density and can be applied without restriction over the whole analysis domain. The influence of the bogus data used in the analysis can be seen in Fig. 5c, which shows the 500-mb geopotential corrections produced when no bogus data are used with the Bratseth scheme. The bogus data clearly define the cutoff low over the western Atlantic in Fig. 5b, providing a good check of our scheme.

The impact of using the wind information to extrapolate the geopotential heights in the second stage of the new scheme (section 2d) is demonstrated in Fig. 5d. The cutoff low is seen to be further deepened. The long-wave trough over the central United States is also deepened somewhat and heights are lowered over the Carolinas. After updating the geostrophic component of the wind field for the new geopotential height corrections (section 2e), we see the winds around the cutoff low in Fig. 6c are also strengthened with a stronger wind shear to the south of the low center. With the enhancement of the ageostrophic flow in the final stage of the scheme (section 2e), the intensity of the wind maxima around the south and western sides of the cutoff low have been reduced in Fig. 6d, but the wind shear is maintained. The reduction in the peak winds is not surprising, since the geostrophic wind is an over-

estimate of the actual wind in a low. The ageostrophic flow from the Great Lakes to the coast has also been strengthened somewhat.

c. Convergence of the new scheme

We illustrate in Fig. 7 the rate of convergence of the Bratseth (1986) scheme for our case with a fixed correlation length scale of 600 km for the univariate analysis of the 500-mb geopotential height at 1200 UTC 25 January. The curves in the figure show the root-mean-square (rms) errors for both the analyzed values and the observation estimates (computed here as differences from the observation values), as a function of the iteration number. With increasing iteration, the observation estimate rapidly approaches the value of the observation, while the analyzed value rapidly converges to a value different from the observation but the same as that which would be produced by optimum interpolation (Bratseth 1986). As described in section 2c, the length scale of the correlation function is reduced to 330 km after just four iterations in our case to speed the convergence of the scheme. A large decrease results in the magnitude of the rms errors for both the analyzed value and observation estimate of the 500-mb geopotential, as shown by the crosses in Fig. 7. The rms error for the analyzed values is then within 5% of the optimum value that is produced after 100 iterations with a fixed length scale. The differences between the analyzed fields produced in either case are small.

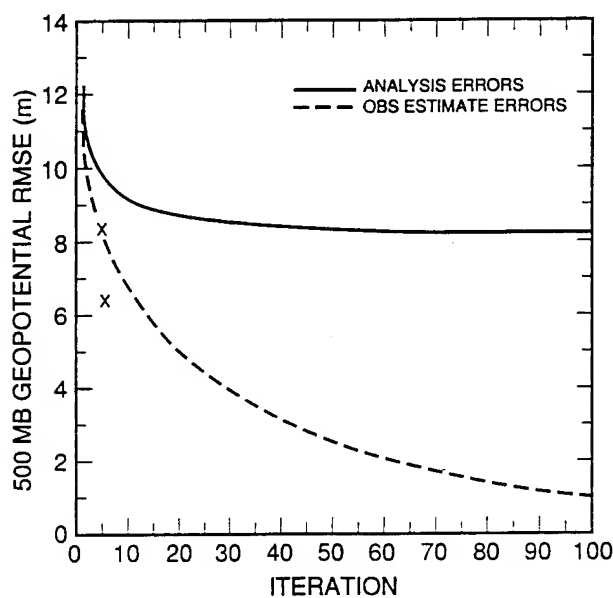


FIG. 7. The rms errors for the analyzed values [derived from Eq. (1)] at the observation locations (solid curve) and for the observation estimates obtained using Eq. (2) (dashed curve) for the geopotential at 500 mb, as a function of the iteration number. The rms errors obtained after just four iterations followed by a further iteration with a reduced length scale are indicated by the "X".

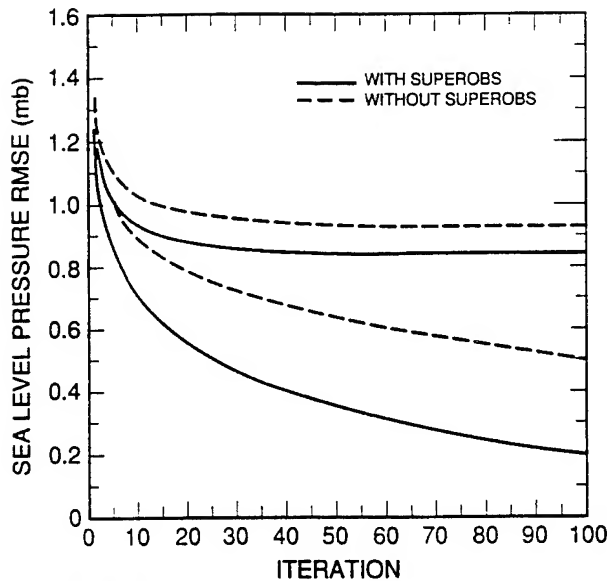


FIG. 8. As in Fig. 7 but for the rms errors of sea level pressure for the case with superobs (solid curve) and without superobs (dashed curve).

In Fig. 8, we illustrate the influence that using superobs has on the rate of convergence of the scheme for the sea level pressure data. The figure compares the rms errors for the analyzed values and the observation estimates of the sea level pressure at the data locations, for cases when superobs are used (solid curve) and when they are not used (dashed curve). Without the superobs, the rate of convergence of the observation estimate is much slower due to the many closely spaced observations (see Bratseth 1986). Even with the superobs, however, the resulting optimum analyses of the sea level pressure (produced after 100 iterations) differ from each other by only 10% in the rms error.

4. Results

The analyses with the new scheme of the cold-air damming, coastal front, subsequent capture of a weak coastal low by a jet streak and the cyclogenesis offshore are described. The results are compared with the enhanced NMC analyses produced with our old Barnes scheme in section 3a. Mesoscale features produced in the new scheme are compared with those described by Bosart's (1988) detailed hand analyses and by Doyle and Warner (1990). Application of the vertical-mode initialization scheme on both the enhanced NMC analyses and our new analyses is used to compare the mesoscale vertical motions and ageostrophic wind derived for each case.

a. Cold-air damming and coastal front

The final 1000-mb analysis produced with the new scheme of the cold-air damming and coastal frontogenesis at 1200 UTC 25 January is shown in Fig. 9a. The analysis has retained the cold-air damming and the temperature contrast along the East Coast, which was produced by the model forecast. In fact, the differences between this 1000-mb analysis in Fig. 9a and that using the Barnes scheme shown in Fig. 4a are small. However, the temperature gradient across the cold front south of the low center over Lake Superior is somewhat stronger with the new analysis. In the new 500-mb analysis shown in Fig. 9b, both the long-wave trough and the cutoff low of 5625 m are in close agreement with the enhanced NMC analysis shown in Fig. 2b. However, as shown in the preceding section, the cutoff low produced with the Barnes scheme in Fig. 4b was much weaker. The -30°C isotherm in the new analysis is east of Lake Superior in agreement with the enhanced NMC analysis in Fig. 2b, whereas the Barnes analysis in Fig. 4b has it lagging to the west around Lake Superior. A jet streak can be seen at 250 mb in

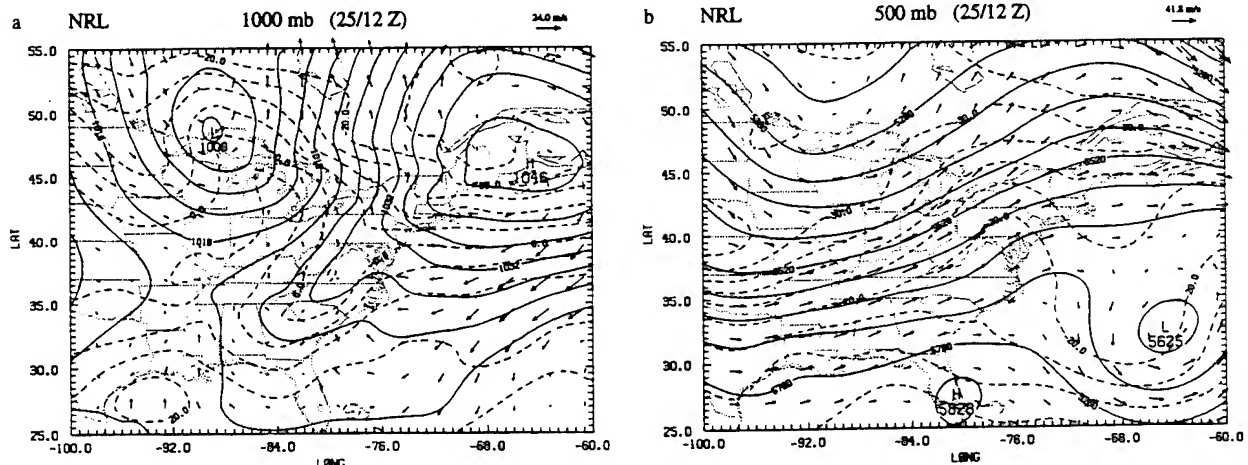


FIG. 9. The NRL analysis for 1200 UTC 25 January of (a) sea level pressure (mb), 1000-mb temperature ($^{\circ}\text{C}$), and winds, and of (b) the geopotential height (gpm), temperature ($^{\circ}\text{C}$), and winds at 500 mb. Contours as in Fig. 2.

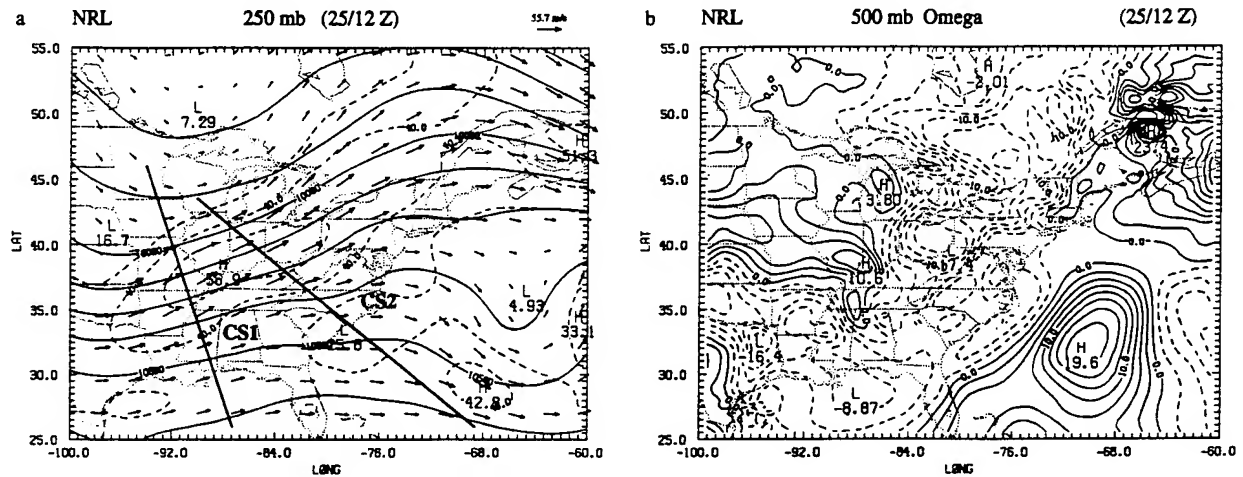


FIG. 10. The NRL analysis for 1200 UTC 25 January of (a) the geopotential height (gpm), temperature ($^{\circ}\text{C}$), and winds at 250 mb, and of (b) the vertical velocity (mb h^{-1}) at 500 mb. Contours of geopotential are every 120 gpm, and isotachs above 30 m s^{-1} are shown every 10 m s^{-1} . Vertical motion of magnitudes 20 mb h^{-1} or less are contoured every 2.5 mb h^{-1} .

Fig. 10a on the east side of the long-wave trough in the polar jet stream. The subtropical jet stream lies farther to the south across Florida and south of the cutoff low.

The field of vertical motion at 500 mb, which has been derived from the NRL analysis by application of the vertical-mode initialization procedure, is shown in Fig. 10b. Strong ascent from Ohio northeastward on the east side of the long-wave trough and strong subsidence west of the cutoff low are found in close agreement with that that can be derived from the enhanced NMC analysis (not shown). However, the major difference is that the rising motion associated with the developing coastal front along the Carolina coast in

the first-guess field is also retained in the NRL analysis. Also two separate centers of rising motion, associated with the surface cyclone located on the southeast Texas coast and the secondary circulation of the upper-level jet's entrance region, are evident over eastern Texas and northern Mississippi. In contrast, only a broad region of ascent can be derived from the enhanced NMC analysis.

To further show the secondary circulations associated with the entrance region of the upper-level jet and the coastal front, cross sections were produced using the initialized fields derived from the new NRL analysis at 1200 UTC 25 January. The locations of the

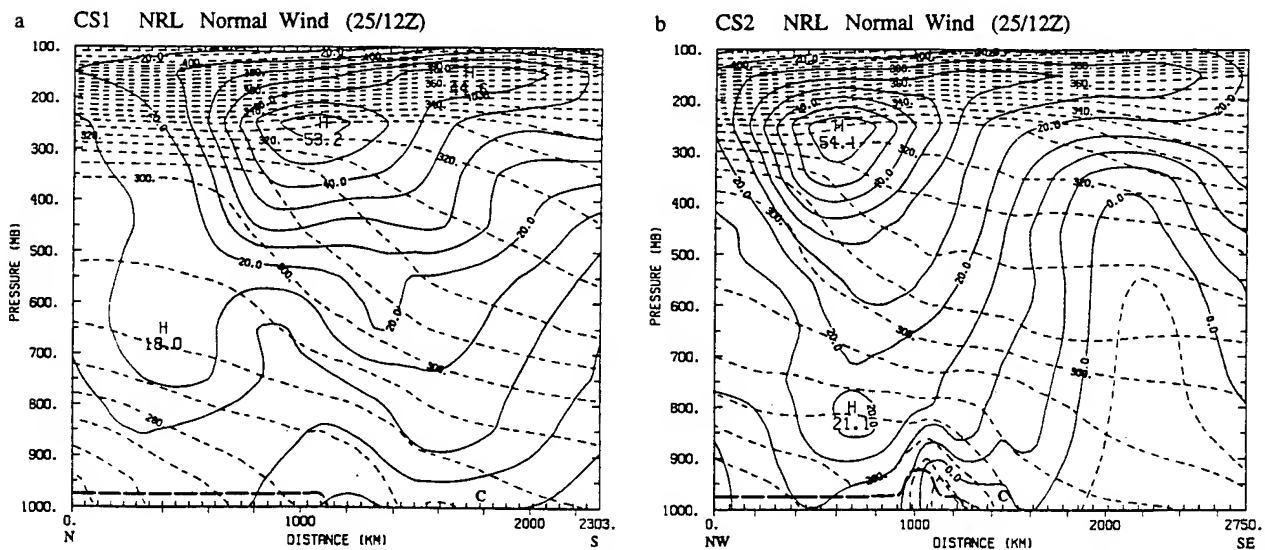


FIG. 11. The wind normal to the plane of the cross sections (a) CS1 from 46°N , 94°W to 26°N , 87.3°W and (b) CS2 from 43.5°N , 90°W to 26°N , 68.7°W for the NRL analysis at 1200 UTC 25 January. Contours every 5 m s^{-1} . The potential temperature (K) is also shown by the dashed contours every 5 K in the troposphere. The position of the model grid points every 0.5° in latitude are shown by the inner tick marks, and coastline by the "C."

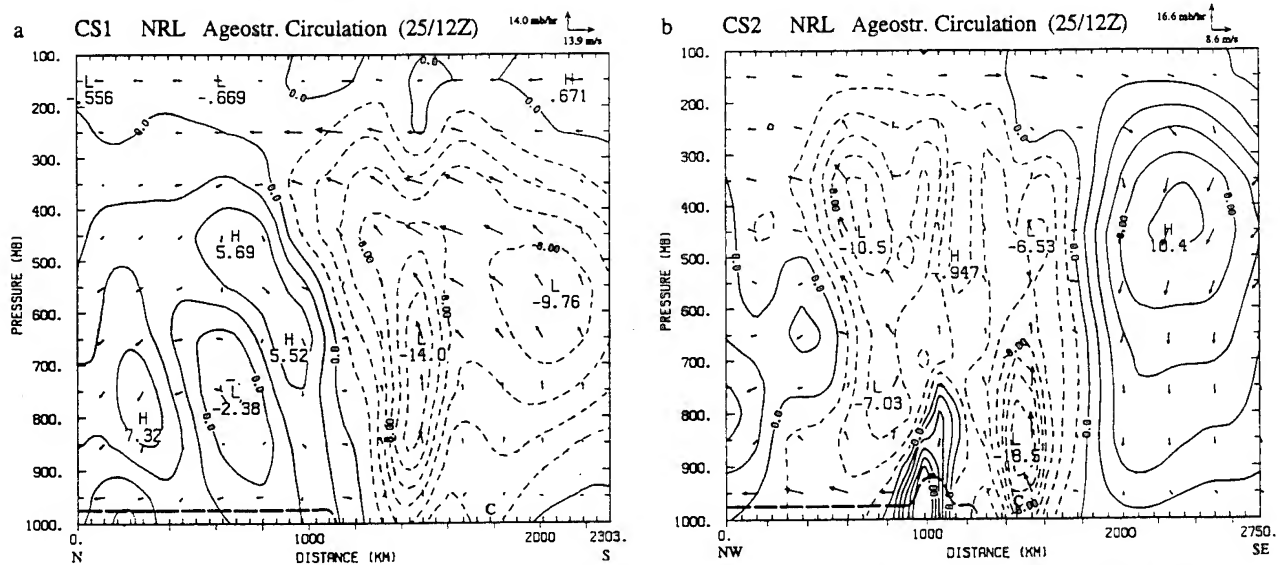


FIG. 12. As in Fig. 11 but for the vertical motion and ageostrophic wind in the plane of the cross sections (a) CS1 and (b) CS2. Contours of the vertical motion are every 2 mb h⁻¹. Scale of vectors indicated by labeled arrows.

two cross sections are displayed in Fig. 10a. Cross section CS1, which extends from Minnesota to the central Gulf of Mexico, cuts across the entrance region of the upper-level polar jet. In Fig. 11a, the wind speed normal to cross section CS1 shows the core of the polar jet at 250 mb and the subtropical jet lying farther to the south at 150 mb. A narrow region of ascending motion with a maximum ascent of 14 mb h⁻¹ can be seen in Fig. 12a over northern Mississippi in the right rear flank of this polar jet. Aloft, a strong southerly ageostrophic flow across the jet is followed by weaker subsidence to the north. Such a thermally direct circulation in the rear of the jet streak is well known (e.g., Uccellini and

Johnson 1979; Keyser and Shapiro 1986). Weaker ascent associated with the subtropical jet stream to the south is also evident in the figure. In comparison, the secondary circulation produced by the enhanced NMC analysis has a broader region of ascending motion in the rear of the polar jet streak (Fig. 13a). The second cross section CS2, which is perpendicular to the Carolina coast, cuts across the region of the coastal front and through the polar jet aloft. The cold air trapped between the coast and the Appalachians can be seen in Fig. 11b, with the jet core aloft to the northwest. The low-level jet west of the Appalachians in the figure provides the inflow to the low pressure system over

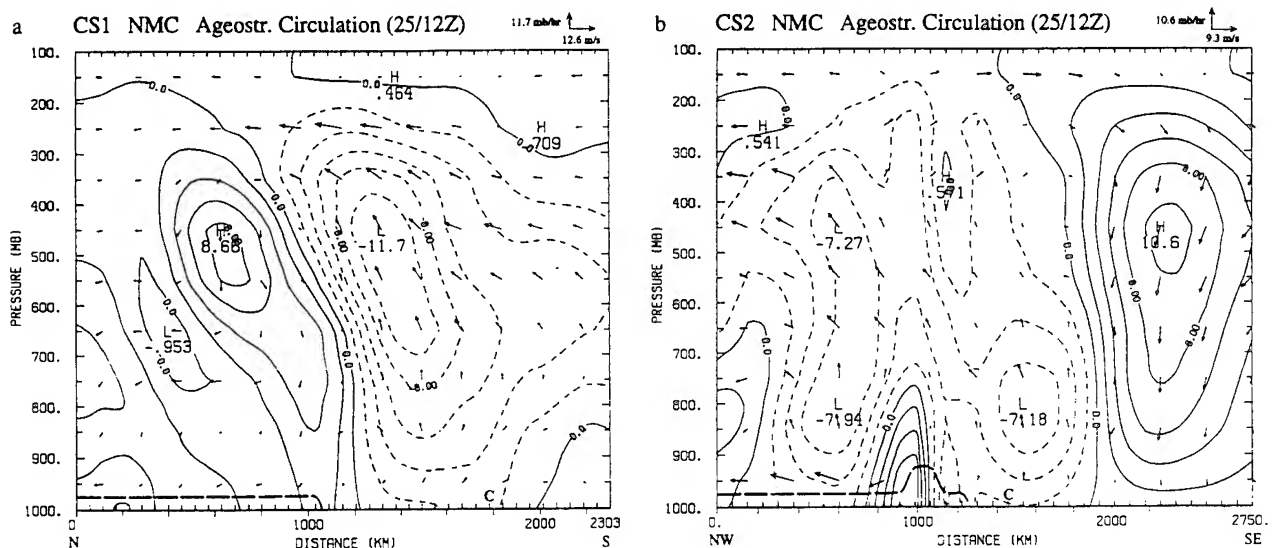


FIG. 13. The vertical motion and ageostrophic wind in the plane of the cross sections (a) CS1 and (b) CS2 for the enhanced NMC analysis. Contours as in Fig. 12.

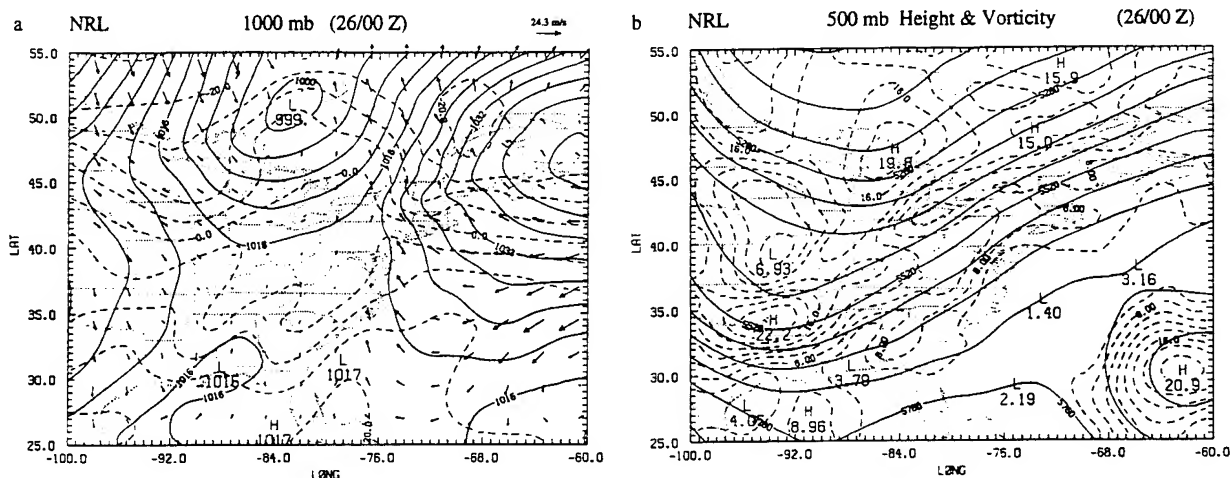


FIG. 14. The NRL analysis for 0000 UTC 26 January of (a) sea level pressure (mb), 1000-mb temperature ($^{\circ}\text{C}$), and winds; and of (b) the geopotential height (gpm), absolute vorticity ($\times 10^{-5} \text{ s}^{-1}$) at 500 mb. Contours of vorticity are every $2 \times 10^{-5} \text{ s}^{-1}$ for values above $6 \times 10^{-5} \text{ s}^{-1}$.

Lake Superior (Fig. 9a). In Fig. 12b, shallow ascent with maximum of 18.5 mb h^{-1} , which is associated with the coastal front generated in the first-guess forecast, can be seen in a narrow band at the coastline. This ascent is in good agreement with that shown by Doyle and Warner (1990) in their cross section normal to the coastal front (see their Fig. 15). The subsidence west of the cutoff low in the subtropical jet stream and ascent east of the approaching upper-level trough can also be seen in Fig. 12b. The coastal front circulation is much stronger and more well defined with the new analysis than the circulation shown in Fig. 13b, which is derived from the enhanced NMC analysis.

b. Interaction of jet streak with coastal front

By 0000 UTC January 26, the coastal front had developed from Georgia to southern New England in an onshore easterly flow regime and led to the erosion of the cold dome east of the Appalachians (Doyle and Warner 1990). The strong thermal gradient associated with the coastal front is seen along the coast of the Carolinas in the NRL 1000-mb analysis illustrated in Fig. 14a. In this case, the NRL analysis was able to significantly sharpen the temperature contrast between the Carolina coast and the Appalachians compared to that which was produced by the first-guess forecast (see

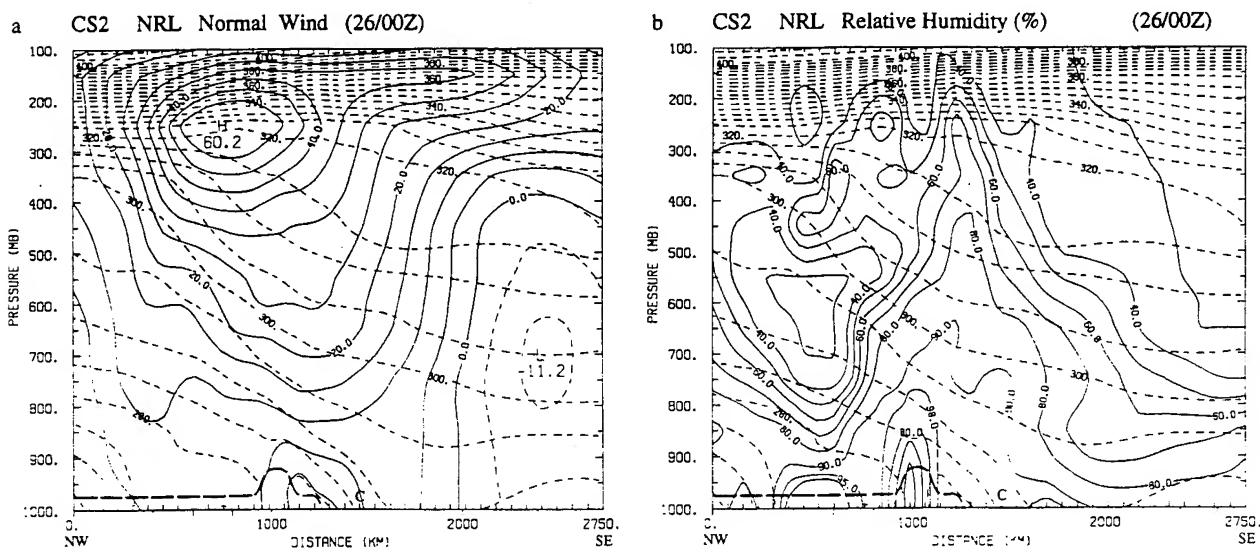


FIG. 15. (a) The wind normal to the plane of cross section CS2 and (b) the relative humidity (%) in the plane of the same cross section for the NRL analysis at 0000 UTC 26 January. Contours as in Fig. 11.

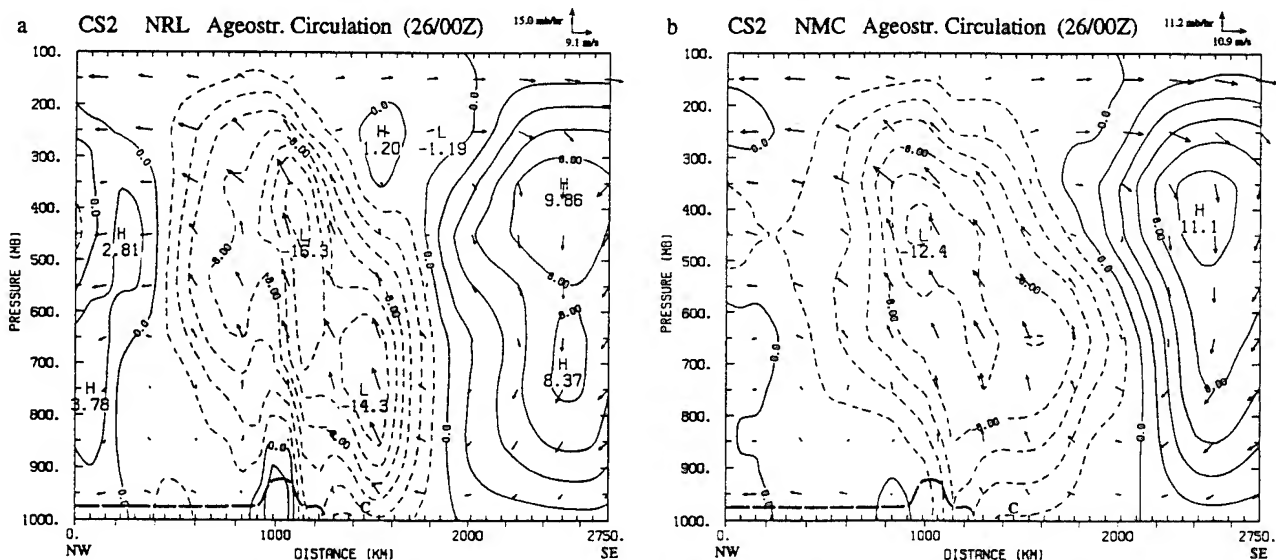


FIG. 16. The vertical motion and ageostrophic wind in the plane of cross section CS2 at 0000 UTC 26 January for (a) the NRL analysis and for (b) the enhanced NMC analysis. Contours as in Fig. 12.

Harms et al. 1992). The weak coastal low, which developed at the southern end of the coastal front (Bosart 1988; Doyle and Warner 1990), is also indicated in our analysis. The surface low associated with the a major short wave can be seen along the Alabama coast. This short wave can be seen as a strong vorticity maximum at the base of the long-wave trough at 500 mb in Fig. 14b. The polar jet across the eastern United States is strengthening as the short wave over the Great Lakes is moving eastward, producing a confluent flow into the jet. A weaker vorticity maximum can be seen over Georgia in the region of the interaction of the secondary circulation in the entrance region of the strengthening jet with the weak low on the coastal front.

This interaction of the secondary circulation in the entrance region of the jet with the weak coastal low at the southern end of the coastal front can be seen in the cross section CS2 across the coast shown in Figs. 15 and 16. Figure 15a shows the strengthening winds in the jet at 250 mb, while the ageostrophic flow and vertical motion are shown in Fig. 16a. A deep circulation can be seen linking the coastal low with the easterly ageostrophic flow across the upper-level jet. A further component of the circulation is linked to the subsidence west of the cutoff low in the subtropical jet stream to the southeast. Much weaker ascent is found in the lower troposphere when using the enhanced NMC analysis to derive the circulation (Fig. 16b). High

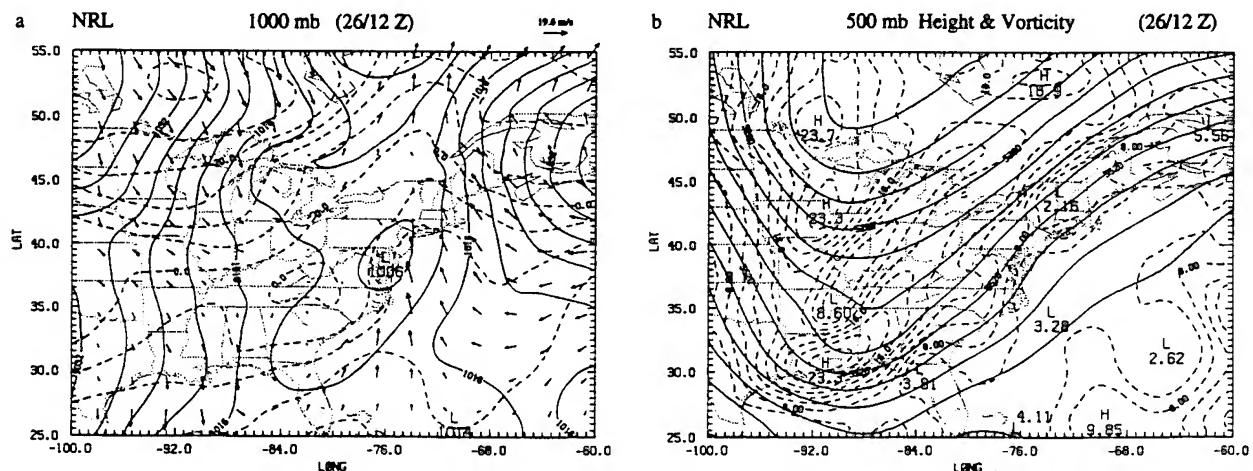


FIG. 17. The NRL analysis for 1200 UTC 26 January of (a) sea level pressure (mb), 1000-mb temperature ($^{\circ}\text{C}$), and winds, and (b) the geopotential height (gpm), absolute vorticity ($\times 10^{-3} \text{ s}^{-1}$) at 500 mb. Contours as in Fig. 14.

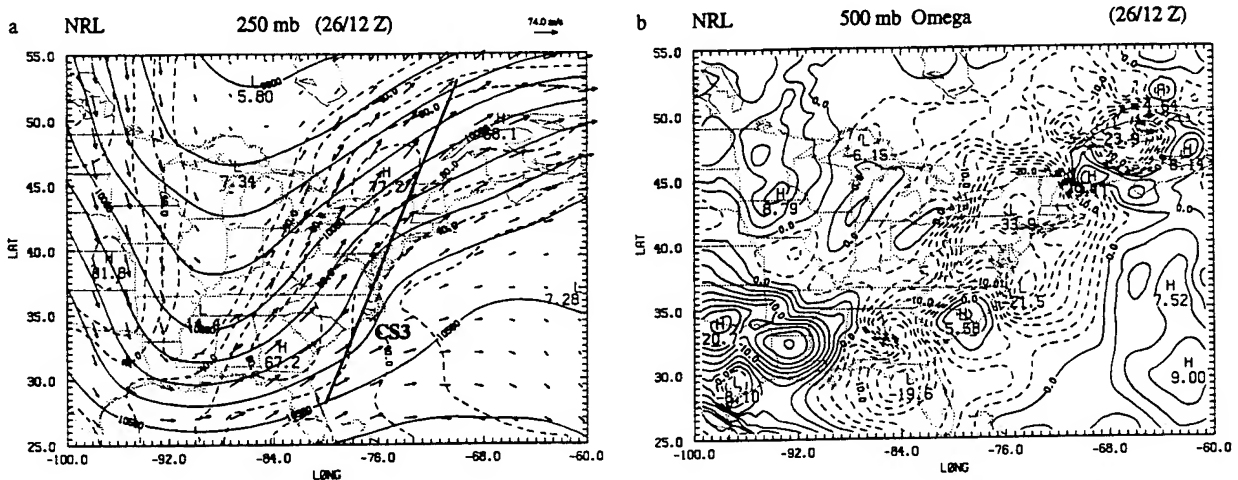


FIG. 18. (a) The geopotential height (gpm), temperature ($^{\circ}\text{C}$), and winds at 250 mb; and (b) the vertical velocity (mb h^{-1}) at 500 mb for the NRL analysis at 1200 UTC 26 January. Contours as in Fig. 10.

humidities of greater than 90% are analyzed in Fig. 15b over the coastal front, consistent with developing precipitation observed in the region (Doyle and Warner 1990).

c. Cyclogenesis offshore

The 1000-mb analysis for 1200 UTC 26 January in Fig. 17a shows the coastal low has moved north to the Chesapeake Bay and is merging with a large region of weak low pressure over the northeast. Over the Great Lakes, a secondary wave is developing along a strong front. The surface pressure is falling over the southeast as the strong southern short wave aloft can be seen

reaching the base of the long-wave trough in Fig. 17b. The short wave from the Great Lakes has merged with the northern jet as it moved northeastward, contributing to stronger vorticity gradients over the St. Lawrence River in the right rear flank of the jet. The weak vorticity maximum from Georgia (Fig. 14b) has moved northeastward to southwest Virginia in Fig. 17b, with the coastal low moving ahead of it. Figure 18a shows the northern jet approaching the top of the ridge and the southern jet at the base of the long-wave trough at 250 mb. At 500 mb, two strong centers of ascent can be seen to have developed in Fig. 18b over New York State below the right rear flank of the northern jet, as it strengthened, and off Cape Hatteras to the southeast

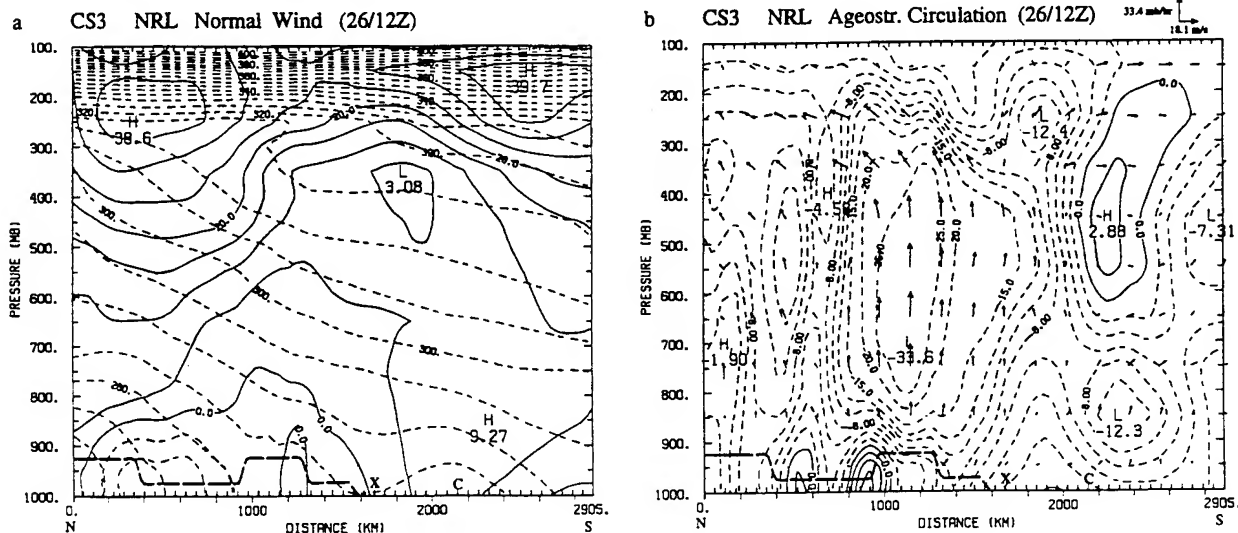


FIG. 19. (a) The wind normal to the cross section CS3 from 53°N , 70°W to 28°N , 80°W and (b) the vertical motion (mb h^{-1}) and ageostrophic wind (m s^{-1}) in the plane of cross section for 1200 UTC 26 January. Contours as in Figs. 11 and 12 except that contours of vertical motion less than -12 and -40 mb h^{-1} are every 5 and 15 mb h^{-1} , respectively.

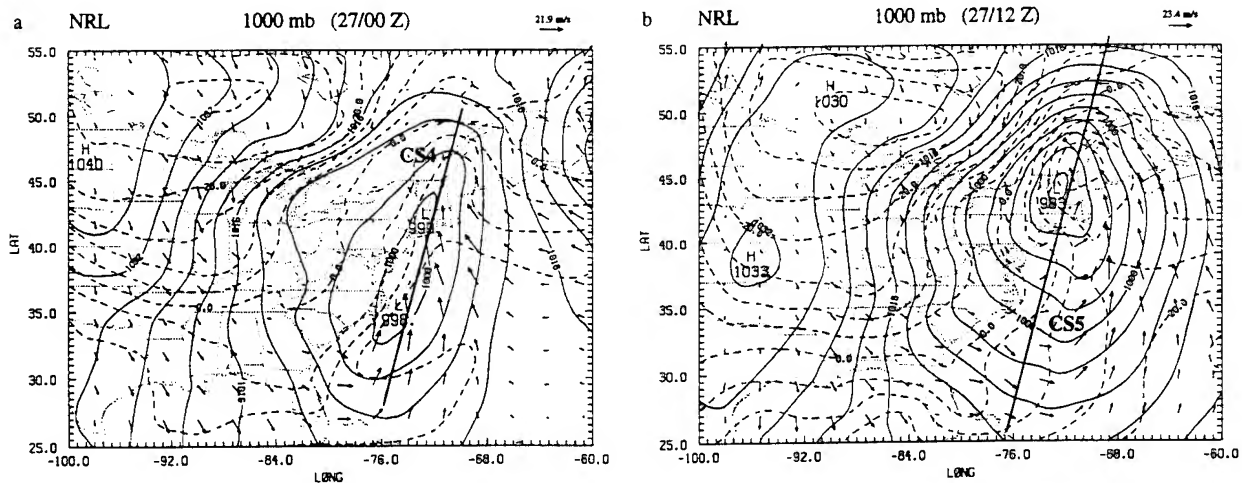


FIG. 20. The sea level pressure (mb), 1000-mb temperature ($^{\circ}\text{C}$), and winds for the NRL analysis at (a) 0000 UTC and (b) 1200 UTC on 27 January. Contours as in Fig. 2.

of the center of the coastal low as it moved with the jet. The region of ascent over Florida is in response to the exit region of the southern jet at the base of the long-wave trough.

The merging of the circulations associated with the entrance region of the northern jet and the coastal low are illustrated in a cross section CS3 along the coastline cutting through the northern jet and coastal low (see Fig. 18a). The northern jet at 250 mb and the subtropical jet stream to the south at 150 mb can be seen in the wind normal to the cross section in Fig. 19a. The corresponding ageostrophic circulation in the plane of the cross section is shown in Fig. 19b. A strengthened direct secondary circulation in the entrance region of the northern jet can be seen with maximum ascent of 33.6 mb h^{-1} and southerly ageostrophic flow aloft to the north. The northerly ageostrophic flow aloft to the south in the upper troposphere is associated with the subtropical jet stream. The position of the coastal low is shown by the "X" to the rear of the region of strongest ascent in the northern jet's secondary circulation. Ascent at the southern end of the cross section is associated with the exit region of the approaching jet at the base of the long-wave trough.

The 1000-mb analyses for 0000 and 1200 UTC 27 January are shown in Figs. 20a and 20b. They show the development of a new low off Cape Hatteras, which moves northward and deepens rapidly to overshadow the earlier coastal low. Cross sections CS4 and CS5 are taken along the coast to show the evolution of the secondary circulations associated with the two jets during this period. The positions of the jets for each cross section can be seen in Figs. 21a and 21c, and the corresponding ageostrophic circulations in Figs. 21b and 21d. The positions of the lows are indicated by the "X" in the figures. As the southern jet rounds the long-wave trough and crosses the coast at 0000 UTC, the new

low can be seen developing beneath strong ascent and northerly ageostrophic flow aloft in the exit region of this jet (Fig. 21b). The circulation associated with the northern jet and surface low is a separate circulation to the north at this stage. The rapid development of the new low in the next 12 h can be seen in Figs. 21c and 21d to be associated with the movement of the southern jet and its secondary circulation northward. By 1200 UTC, this secondary circulation in the southern jet has caught up with the circulation in the entrance region of the northern jet, so that they cooperate in strengthening the ascent in the rapidly developing low. Such cooperation has been found in other cases analyzed by Uccellini and Kocin (1987).

5. Summary and conclusions

During the last decade optimal interpolation replaced successive correction methods as the dominant objective analysis technique in operational weather forecasting systems. However, with the advent of Bratseth's (1986) analysis scheme, which converges to the optimal interpolation solution, the less expensive approach of successive correction has become a powerful and attractive alternative analysis method. The objective analysis scheme developed for use with the NRL limited-area weather prediction model uses the Bratseth scheme, in which the data weights are dependent on the covariance between observations, are reduced in regions of higher data density, and include observational errors. We have devised a computationally inexpensive method for linking the mass and momentum fields that is different from earlier methods reported in the literature (e.g., Cressman 1959; Lorenc et al. 1991). The key element is obtaining the gradient of the geopotential change from the change in an estimated geostrophic wind at each iteration to enhance the initial

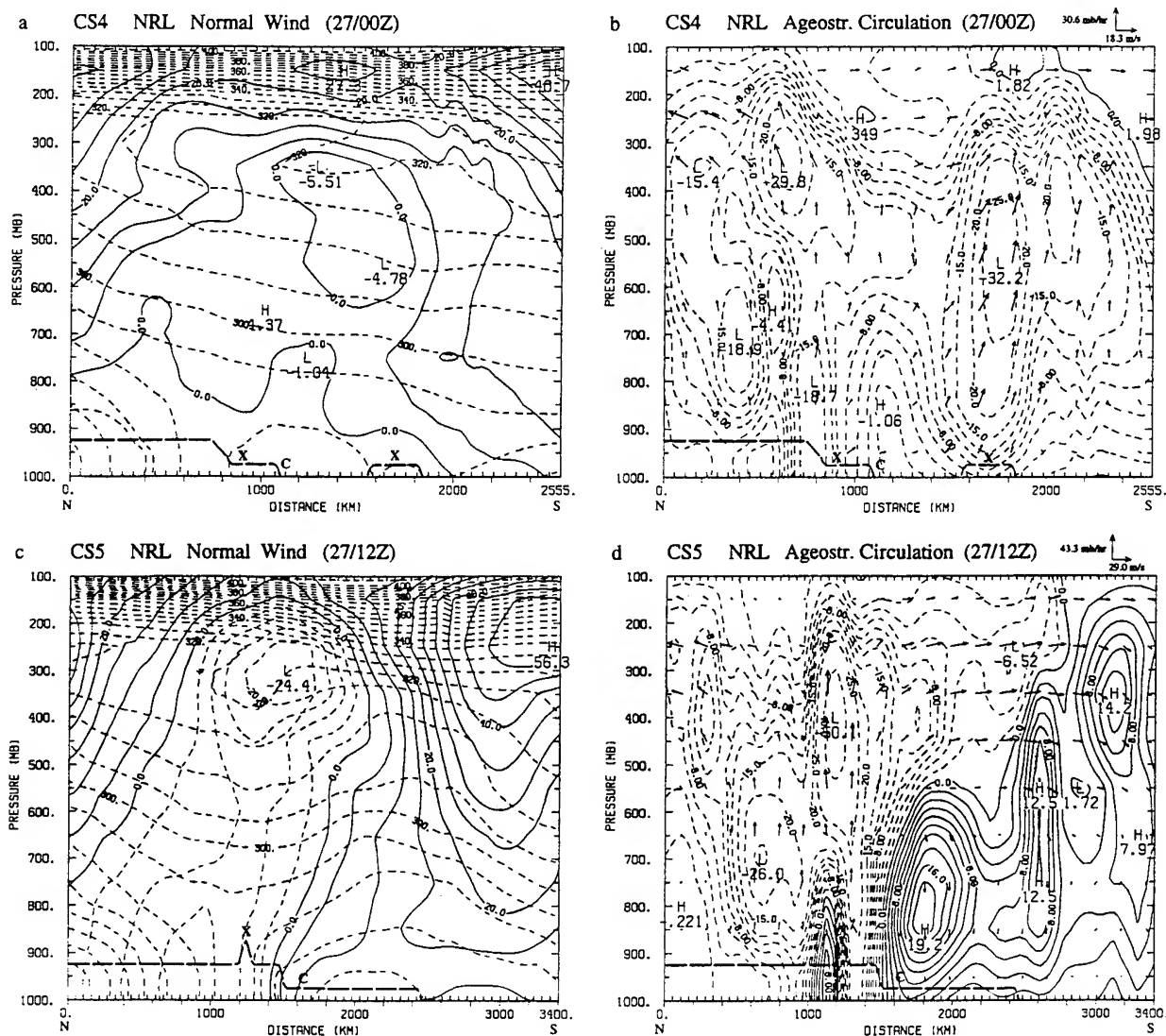


FIG. 21. (a) The wind normal to a cross section CS4 from 50.5°N, 70°W to 28°N, 76°W and (b) the vertical motion (mb h⁻¹) and ageostrophic wind (m s⁻¹) in the plane of cross section CS4 for the NRL analysis at 0000 UTC 27 January. Here (c) and (d) are the same as (a) and (b) but for cross section CS5 from 55.5°N, 68.7°W to 25.5°N, 76.7°W at 1200 UTC 27 January. Contours as in Fig. 19.

univariate analysis of the geopotential. We use the initial univariate wind analysis to provide only the starting estimate of the geostrophic wind for the first iteration. For subsequent iterations, the geostrophic wind is estimated from the updated geopotential gradient. After this enhancement of the geopotential, the univariate wind analysis is updated for the change in the geostrophic wind.

An evaluation of the NRL objective analysis scheme has been accomplished using a GALE IOP 2 dataset. The use of a prior model forecast as a first guess for the analysis was crucial in obtaining mesoscale features in the analysis. Such features were not produced by our earlier scheme, which used a Barnes (1973) scheme to enhance NMC hemispheric analyses (Chang et al. 1989; Shi et al. 1991). Over the region of the eastern

United States, where there is a large amount of data, the Barnes scheme produced as good an analysis as the Bratseth (1986) scheme, when the same first-guess forecast is used. The Bratseth scheme was more superior in the other regions where it could adjust for the changing data density. Our simple geostrophic method for linking the mass and wind-field analyses provided tighter gradients in these fields, particularly in the regions of lower data density outside of the eastern United States.

For the second IOP of GALE, the vertical circulations were derived from the analyses by application of the vertical-mode initialization scheme of Bourke and McGregor (1983). Superior mesoscale vertical circulations were produced in the coastal low and upper-tropospheric jet streaks with the new NRL analysis

scheme when compared to that derived from the earlier Barnes enhancement of the NMC hemispheric analyses. These circulations clearly demonstrated the interaction of the coastal low with the entrance region of a jet streak in the upper troposphere. The cooperation of the secondary circulations in two jets during offshore cyclogenesis is also shown. Being able to produce such mesoscale circulations using these analysis and initialization schemes is important for providing accurate initial conditions for generating forecasts with the limited-area model. Future work will use these improved analyses with the initialization scheme to test assimilating the GALE data in a limited-area analysis-forecast system.

Acknowledgments. This research was sponsored by NRL's basic research program and by SPAWAR of the U.S. Navy. The first author was supported at Science Applications International Corporation under Contract N00014-89-R-HB08 with NRL, and the second author was supported as a graduate student at North Carolina State University by the U.S. Air Force. Part of the computer time was provided by the North Carolina Super Computing Center, Research Triangle Park.

REFERENCES

- Barnes, S. L., 1973: Mesoscale objective map analysis using weighted time-series observations. NOAA Tech. Memo., ERL NSSL-62, Norman, OK, 60 pp.
- Benjamin, S. G., 1989: An isentropic meso-scale analysis system and its sensitivity to aircraft and surface observations. *Mon. Wea. Rev.*, **117**, 1586-1603.
- , and N. L. Seaman, 1985: A simple scheme for objective analysis in curved flow. *Mon. Wea. Rev.*, **113**, 1184-1198.
- Bergthórssón, P., and B. R. Döös, 1955: Numerical weather map analysis. *Tellus*, **7**, 329-340.
- Bosart, L. F., 1988: Coastal frontogenesis and cyclogenesis during GALE IOP #2. Preliminary Reports. GALE/CASP Workshop, Virginia Beach, VA, NCAR 75-93. [Available from GALE Project Office, P.O. Box 3000, Boulder CO 80807.]
- Bourke, W., and J. L. McGregor, 1983: A nonlinear vertical mode initialization scheme for a limited area prediction model. *Mon. Wea. Rev.*, **111**, 2285-2297.
- Bratseth, A. M., 1986: Statistical interpolation by means of successive corrections. *Tellus*, **38A**, 439-447.
- Chang, S., K. Brehme, R. Madala, and K. Sashegyi, 1989: A numerical study of the East Coast snow storm of 10-12 February 1983. *Mon. Wea. Rev.*, **117**, 1768-1778.
- Cressman, G., 1959: An operational objective analysis system. *Mon. Wea. Rev.*, **87**, 367-374.
- DiMego, G. J., 1988: The National Meteorological Center regional analysis system. *Mon. Wea. Rev.*, **116**, 977-1000.
- Dirks, R. A., J. P. Kuettner, and J. A. Moore, 1988: Genesis of Atlantic Lows Experiment (GALE): An overview. *Bull. Amer. Meteor. Soc.*, **69**, 148-160.
- Doyle, J. D., and T. T. Warner, 1990: Mesoscale coastal processes during GALE IOP 2. *Mon. Wea. Rev.*, **118**, 283-308.
- Grønås, S., and K. H. Midtbø, 1987: Operational multivariate analyses by successive corrections. Collection of papers presented at WMO/IUGG numerical weather prediction symposium, Tokyo, 4-8 August 1986. *J. Meteor. Soc. Japan*, 61-74.
- Harms, D. E., K. D. Sashegyi, R. V. Madala, and S. Raman, 1992: Four-dimensional data assimilation of GALE data using a multivariate analysis scheme and a mesoscale model with diabatic initialization. NRL Tech. Memo. Rep., No. 7147, Naval Research Laboratory, Washington D.C., 236 pp. [NTIS A256063.]
- Hollingsworth, A., and P. Lönnberg, 1986: The statistical structure of short-range forecast errors as determined from radiosonde data. Part I: The wind field. *Tellus*, **38A**, 111-136.
- Keyser, D., and M. A. Shapiro, 1986: A review of the structure and dynamics of upper-level frontal zones. *Mon. Wea. Rev.*, **114**, 452-499.
- Kistler, R. E., and R. D. McPherson, 1975: On the use of a local wind correction technique in four-dimensional data assimilation. *Mon. Wea. Rev.*, **103**, 445-449.
- Koch, S. E., M. DesJardins, and P. J. Kocin, 1983: An interactive Barnes objective map analysis scheme for use with satellite and conventional data. *J. Climate Appl. Meteor.*, **22**, 1487-1503.
- Lorenc, A. C., R. S. Bell, and B. MacPherson, 1991: The Meteorological Office analysis correction data assimilation scheme. *Quart. J. Roy. Meteor. Soc.*, **117**, 59-89.
- Madala, R. V., S. W. Chang, U. C. Mohanty, S. C. Madan, R. K. Paliwal, V. B. Sarin, T. Holt, and S. Raman, 1987: Description of the Naval Research Laboratory Limited Area Dynamical Weather Prediction Model. NRL Tech. Memo. Rep., No. 5992, Naval Research Laboratory, Washington, D.C., 131 pp. [NTIS A182780.]
- Mills, G. A., and R. S. Seaman, 1990: The BMRC regional data assimilation system. *Mon. Wea. Rev.*, **118**, 1217-1237.
- Mercer, T. J., 1987: *Genesis of Atlantic Lows Experiment (GALE): Data Users Guide*. GALE Data Center, Department of Physics and Atmospheric Science, Drexel University, 106 pp.
- Raman, S., and A. J. Riordan, 1988: Genesis of Atlantic Lows Experiment: The planetary-boundary-layer subprogram of GALE. *Bull. Amer. Meteor. Soc.*, **69**, 161-172.
- Reynolds, R. W., 1982: A monthly averaged climatology of sea surface temperatures. NOAA Tech. Rep., NWS-31, Climate Analysis Center, National Weather Service, Washington, D.C., 35 pp.
- Riordan, A. J., 1990: Examination of the mesoscale features of the GALE coastal front of 24-25 January 1986. *Mon. Wea. Rev.*, **118**, 258-282.
- Sashegyi, K. D., and R. V. Madala, 1990: Tests of initialization procedures with the NRL limited area numerical weather prediction model. NRL Tech. Memo. Rep., No. 6648, Naval Research Laboratory, Washington D.C., 88 pp. [NTIS A223549.]
- , and —, 1993: Application of vertical mode initialization to a limited area model in flux form. *Mon. Wea. Rev.*, **121**, 207-220.
- Schlatter, T. W., 1988: Past and present trends in the objective analysis of meteorological data for nowcasting and numerical forecasting. Preprints, *Eighth Conf. on Numerical Weather Prediction*, Baltimore, MD, Amer. Meteor. Soc., J9-J25.
- Seaman, R. S., 1988: Some real data tests of the interpolation accuracy of Bratseth's successive correction method. *Tellus*, **40A**, 173-176.
- Shaw, D. B., P. Lönnberg, A. Hollingsworth, and P. Undén, 1987: Data assimilation: The 1984/85 revisions of the ECMWF mass and wind analysis. *Quart. J. Roy. Meteor. Soc.*, **113**, 533-566.
- Shi, J. J., S. Chang, K. Sashegyi, and S. Raman, 1991: Enhancement of objective analysis of Hurricane Florence (1988) with dropsonde data. Preprints, *19th Conf. on Hurricanes and Tropical Meteorology*, Miami, Amer. Meteor. Soc., 335-337.
- Uccellini, L. W., and D. R. Johnson, 1979: The coupling of lower tropospheric jet streak and implications for the development of severe convective storms. *Mon. Wea. Rev.*, **107**, 682-703.
- , and P. J. Kocin, 1987: The interaction of jet streak circulations during heavy snow events along the east coast of the United States. *Wea. Forecasting*, **2**, 289-308.
- , —, R. A. Petersen, C. H. Wash, and K. F. Brill, 1984: The Presidents' Day cyclone of 18-19 February 1979: Synoptic overview and analysis of the subtropical jet streak influencing the pre-cyclogenetic period. *Mon. Wea. Rev.*, **112**, 31-55.
- Warner, T. T., M. N. Lakhtakia, J. D. Doyle, and R. A. Pearson, 1990: Marine atmospheric boundary layer circulations forced by Gulf Stream sea surface temperature gradients. *Mon. Wea. Rev.*, **118**, 309-323.

Appendix B

Four-Dimensional Data Assimilation of Gale Data Using a Multivariate Analysis Scheme and A Mesoscale Model with Diabatic Initialization



NRL/MR/4223-92-7147

**Four-Dimensional Data Assimilation of Gale Data
Using a Multivariate Analysis Scheme and
A Mesoscale Model with Diabatic Initialization**

DEWEY E. HARMS

*Department of Marine, Earth and Atmospheric Sciences
North Carolina State University
Raleigh, North Carolina 27695-8208*

KEITH D. SASHEGYI AND RAO V. MADALA

*Atmospheric/Ocean Sensing Branch
Center for Advanced Space Sensing*

AND

SETHU RAMAN

*Department of Marine, Earth and Atmospheric Sciences
North Carolina State University
Raleigh, North Carolina 27695-8208*

REPORT DOCUMENTATION PAGE			Form Approved OMB No. 0704-0188	
Public reporting burden for this collection of information is estimated to average 1 hour per response, including the time for reviewing instructions, searching existing data sources, gathering and maintaining the data needed, and completing and reviewing the collection of information. Send comments regarding this burden estimate or any other aspect of this collection of information, including suggestions for reducing this burden, to Washington Headquarters Services, Directorate for Information Operations and Reports, 1215 Jefferson Davis Highway, Suite 1204, Arlington, VA 22202-4302, and to the Office of Management and Budget, Paperwork Reduction Project (0704-0188), Washington, DC 20503.				
1. AGENCY USE ONLY (Leave Blank)	2. REPORT DATE October 6, 1992	3. REPORT TYPE AND DATES COVERED		
4. TITLE AND SUBTITLE Four-Dimensional Data Assimilation of Gale Data Using a Multivariate Analysis Scheme and a Mesoscale Model with Diabatic Initialization			5. FUNDING NUMBERS	
6. AUTHOR(S) Dewey E. Harms*, Keith D. Sashegyi, Rao V. Madala, and Sethu Raman*				
7. PERFORMING ORGANIZATION NAME(S) AND ADDRESS(ES) Naval Research Laboratory Washington, DC 20375-5320			8. PERFORMING ORGANIZATION REPORT NUMBER NRL/MR/4223-92-7147	
9. SPONSORING/MONITORING AGENCY NAME(S) AND ADDRESS(ES)			10. SPONSORING/MONITORING AGENCY REPORT NUMBER	
11. SUPPLEMENTARY NOTES *Department of Marine, Earth and Atmospheric Sciences North Carolina State University Raleigh, North Carolina 27695-8208				
12a. DISTRIBUTION/AVAILABILITY STATEMENT Approved for public release; distribution unlimited			12b. DISTRIBUTION CODE	
13. ABSTRACT (Maximum 200 words) A method of assimilating 3-hourly sounding data is developed and successfully tested in this study. First, the successive corrections scheme of Bratseth (1986) which converges to optimum interpolation, is applied for the numerical analysis of data collected during the Genesis of Atlantic Lows Experiment (GALE). Next, diabatic forcing is incorporated into a vertical mode initialization scheme to provide more realistic initial conditions and to shorten the spinup time of the Naval Research Laboratory/North Carolina State University (NRL/NCSU) mesoscale model. Latent-heating profiles are computed from 'spun-up' model-generated and observed rainfall. Finally, the multivariate, successive correction analysis scheme correction analysis scheme and the diabatic initialization procedure are combined with the NRL/NCSU model to form an intermittent data-assimilation system. Assimilations of the GALE data over a 2 1/2-day period were performed with differing update cycles of 3, 6, and 12 h. Twelve-hour NMC hemispheric analyses served as the "no assimilation" control case for comparison. The assimilation of 3-hourly GALE data led to large decreases in background forecast rms errors and smaller decreases in analysis rms error. Rainfall prognoses from the assimilated states showed much more rapid spinup and better overall patterns than did the "no assimilation" precipitation forecasts.				
14. SUBJECT TERMS Help Help Help Help Help Help			15. NUMBER OF PAGES 236	
			16. PRICE CODE	
17. SECURITY CLASSIFICATION OF REPORT UNCLASSIFIED	18. SECURITY CLASSIFICATION OF THIS PAGE UNCLASSIFIED	19. SECURITY CLASSIFICATION OF ABSTRACT UNCLASSIFIED	20. LIMITATION OF ABSTRACT SAR	

TABLE OF CONTENTS

	Page
ACKNOWLEDGEMENTS.....	v
LIST OF TABLES.....	vi
LIST OF FIGURES.....	vii
LIST OF SYMBOLS.....	xiii
 1. INTRODUCTION.....	 1
 2. LITERATURE REVIEW OF DATA ASSIMILATION.....	 4
2.1 Introduction.....	4
2.2 Quality Control.....	9
2.3 Objective Analysis Techniques.....	11
2.4 Initialization Techniques.....	15
2.5 Various Data-Assimilation Methods.....	23
2.6 Comparison of Operational Assimilation Techniques.....	29
2.7 FDDA Research: Implications and the Future.....	33
 3. NRL/NCSU MESOSCALE MODEL.....	 36
3.1 Dynamics of the Model.....	36
3.2 Numerics of the Model.....	39
3.2.1 Split-Explicit Time Integration.....	42
3.2.2 Lateral Boundary Conditions.....	43
3.3 Physics of the Model.....	44
3.3.1 Planetary Boundary Layer.....	44
3.3.2 Horizontal Diffusion.....	45
3.3.3 Cumulus Convection.....	46
3.3.4 Large-Scale Precipitation.....	47
3.3.5 Dry Convective Adjustment.....	48
3.3.6 Surface Parameters.....	49
3.4 Model Initialization.....	49

4. APPLICATION OF THE BRATSETH SCHEME FOR THE ANALYSIS OF GALE DATA.....	53
4.1 Introduction.....	53
4.2 The NRL/NCSU Objective Analysis Scheme.....	56
4.2.1 Data Preparation and Quality Control.....	57
4.2.2 Analysis Interpolation.....	62
4.3 Testing the Analysis Scheme.....	71
4.3.1 Experimental Design.....	72
4.3.2 The Synoptic Situation.....	74
4.4 Results.....	77
4.4.1 Comparisons of 25/12Z Analyses.....	77
4.4.2 Comparisons of Model Forecasts (25/12Z - 26/12Z).....	87
4.4.3 Comparisons using 26/00Z and 26/12Z Cases.....	102
4.5 Summary.....	122
5. DIABATIC INITIALIZATION EXPERIMENTS WITH CONVECTIVE HEATING.....	124
5.1 Introduction.....	124
5.2 Diabatic Heating in Model Initialization.....	126
5.3 Experimental Design.....	130
5.4 Results.....	131
5.4.1 Comparison of Initialized Vertical Velocity.....	131
5.4.2 Forecast Precipitation Comparisons.....	134
5.5 Summary.....	135
6. IMPACT OF ASSIMILATING 3-HOURLY GALE DATA.....	139
6.1 Introduction.....	139
6.2 The Data Assimilation System.....	142
6.3 Experimental Design.....	145
6.4 Results.....	153

6.4.1 Statistical Evaluation and Discussion.....	153
6.4.2 Subjective Evaluation and Discussion.....	164
7. CONCLUSIONS.....	204
8. LIST OF REFERENCES.....	208

ACKNOWLEDGEMENTS

This work was supported by the Naval Research Laboratory and the Division of Atmospheric Sciences, National Science Foundation under Grant ATM-88-01650. Part of the computer time was provided by the North Carolina Supercomputing Center, Research Triangle Park, North Carolina. We would like to express our thanks and appreciation to the United States Air Force and, in particular, the Air Force Institute of Technology and Air Weather Service for their financial support to the first author. Appreciation is also extended to Dr. Gerald Watson, Dr. Allen Riordan, and Dr. Ping-Tung Shaw for their assistance.

LIST OF TABLES

Table		Page
4.1	Standard deviation of the observational errors and forecast error growth for a 6-h forecast period in parentheses.....	60
4.2	Analysis and forecast test cases.....	73
6.1	Average number of observations, before and after quality control and creation of super observations, in each analysis time window.....	149
6.2	Data-assimilation experiments.....	151
6.3	Standard deviation of the observational errors and updated forecast error growth for a 6-h forecast period in parentheses.....	162

LIST OF FIGURES

Figure		Page
2.1	Successive reduction of wind error using a direct insertion of height data in a barotropic model. Corresponding results using height as well as from the derived geostrophic winds (McPherson 1975).....	8
2.2	Surface pressures for individual grid points for first 12 h of prognosis using an uninitialized analysis, after initializing two vertical modes, and after initializing two vertical modes using Dirichlet boundary conditions and Neumann boundary conditions (Bourke and McGregor 1983).....	18
2.3	Time trace of height field with no initialization and after two iterations of the implicit nonlinear normal mode initialization scheme (Temperton 1988).....	20
2.4	Gravity-wave activity (before and after initialization) for five vertical modes of a baroclinic model (Sugi 1986).....	21
2.5	Intermittent data assimilation using an analysis-forecast cycle (Bengtsson 1975a).....	24
2.6	A schematic of the assimilation-forecast cycle for various experiments (Ramamurthy and Carr 1987).....	30
3.1	Model domain with smoothed model topography for the coarse (outer) grid and the GALE (fine) grid.....	40
3.2	Horizontal staggered C-grid and vertical grid network utilized in the model for the simple case of $K = 2$	41
4.1	The location of the data for the geopotential height at 500 mb and the sea level pressure (SLP) after quality control.....	63

4.2	The rms of the differences between the observation estimate (and the analysis value interpolated to the observation point) and the observation value for the geopotential at 500 mb.....	67
4.3	SLP and 1000-mb temperature and winds at 25/12Z, 26/12Z, and 27/12Z, and 500-mb geopotential, temperature, and winds at 25/12Z from the NMC analysis.....	75
4.4	SLP and 1000-mb temperature and winds and 500-mb geopotential, temperature, and winds at 25/12Z from case 4.1 and NRL analysis.....	78
4.5	250-mb geopotential, temperature, and winds at 25/12Z from case 4.1, NRL analysis, and NMC analysis.....	81
4.6	500-mb absolute vorticity and vertical motion at 25/12Z from case 4.1 and the NRL analysis.....	84
4.7	500-mb absolute vorticity and vertical motion at 25/12Z from the NMC analysis.....	86
4.8	The magnitude of the wind normal to CS1 and CS2 at 25/12Z for the NRL analysis.....	88
4.9	Ageostrophic circulation in CS1 at 25/12Z for NRL and NMC analyses....	89
4.10	Ageostrophic circulation and relative humidity in CS2 at 25/12Z for NRL and NMC analyses.....	90
4.11	Six-hour forecast of SLP, surface air temperature, and 1000-mb winds valid at 25/18Z for cases 4.4 and 4.3.....	93
4.12	GALE analysis of SLP deviation (from 1000 mb), surface temperature and wind for 25/18Z by Bosart (1988).....	94

4.13	Six-hour forecast of 500-mb vertical motion at 25/18Z for cases 4.3 and 4.4.....	95
4.14	Twelve-hour forecast of SLP and 1000-mb temperature and winds, and forecast of 6-h precipitation valid at 26/00Z for cases 4.3 and 4.4.....	96
4.15	Six-hour accumulation of observed precipitation valid at 26/00Z.....	99
4.16	Twelve-hour forecast of ageostrophic circulation and relative humidity in CS2 valid at 26/00Z for cases 4.3 and 4.4.....	100
4.17	SLP and 1000-mb temperature and winds from case 4.4 and NRL analysis and 500-mb absolute vorticity from from NMC and NRL analyses at 26/00Z.....	103
4.18	Wind normal to and relative humidity in CS2 for the NRL analysis and ageostrophic circulation in CS2 for NRL and NMC analyses at 26/00Z.....	105
4.19	Forecast precipitation (26/00Z - 26/06Z) for cases 4.5 and 4.6 and observed precipitation (26/00Z - 26/06Z).....	108
4.20	Twelve-hour forecast of SLP and 1000-mb temperature and winds and 250-mb geopotential, temperature, and winds at 26/12Z from case 4.5 and forecast precipitation (26/06Z - 26/12Z) for cases 4.5 and 4.6.....	110
4.21	Twelve-hour forecast for case 4.5 of wind normal to and ageostrophic circulation in CS3 and CS4 valid at 26/12Z.....	112
4.22	SLP and 1000-mb temperature and winds; 250-mb geopotential, temperature, and winds; and 500-mb absolute vorticity and vertical motion from NRL analysis at 26/12Z.....	115
4.23	Wind normal to and ageostrophic circulation in CS3 and CS4 from NRL analysis valid at 26/12Z.....	117

4.24	SLP and 1000-mb temperature and winds for a 12-h forecast valid at 27/00Z and a 24-h forecast valid at 27/12Z for case 4.7.....	119
4.25	12- and 24-h forecasts for case 4.7 of wind normal to and ageostrophic circulation in CS5 and CS6, respectively.....	120
5.1	Vertical motion fields for 500 mb valid at 27/00Z from 12-h forecast of case 5.1, after DVMI (case 5.2), and after AVMI (case 5.3).....	132
5.2	Forecasts of accumulated total precipitation (26/00Z - 26/06Z) originating from DVMI and AVMI.....	136
6.1	The locations of surface and upper-air data at 26/00Z and 26/03Z.....	147
6.2	Average analysis and background-forecast rms errors for geopotential from the 0000 and 1200 UTC update cycles.....	154
6.3	Average analysis and background-forecast rms errors for geopotential from the 0600 and 1800 UTC update cycles.....	156
6.4	Average analysis and background-forecast rms errors for u- wind component from the 0000 and 1200 UTC update cycles.....	157
6.5	Average analysis and background-forecast rms errors for v- wind component from the 0000 and 1200 UTC update cycles.....	158
6.6	Average analysis and background-forecast rms errors for relative humidity component from the 0000 and 1200 UTC update cycles.....	159
6.7	Average analysis and background-forecast rms errors for geopotential from the all update cycles of 06DI and 06AI.....	160
6.8	Average analysis and background-forecast rms errors for geopotential from 03DI for 03/15, 06/18, 09/21, and 12/00Z updates cycles.....	163

6.9	SLP, 1000-mb temperature and wind analyses at 25/12Z from control and 12DI.....	166
6.10	GALE analysis of sea-level pressure deviation (from 1000 mb), surface temperature and wind for 25/12Z by Bosart (1988).....	167
6.11	1000-mb specific humidity analyses at 25/12Z from control and 12DI.....	168
6.12	500-mb relative humidity analyses at 26/00Z from control, 12DI, 06DI, and 06AI.....	169
6.13	500-mb vertical velocity analyses at 26/00Z from control, 12DI, 06DI, and 06AI.....	172
6.14	Wind normal to CS2 at 26/00Z from control and 12DI.....	174
6.15	Ageostrophic circulation in CS2 at 26/00Z from control and 12DI.....	175
6.16	SLP, 1000-mb temperature and wind analyses at 27/00Z from 03DI and control, and at 27/03Z from 03DI.....	178
6.17	Wind normal to CS7 at 27/00Z from 03DI; ageostrophic circulation at 27/00Z from 03DI and control, and at 27/03Z from 03DI.....	180
6.18	SLP, 1000-mb temperature and wind analyses at 27/12Z from control and 03DI.....	183
6.19	Ageostrophic circulation in CS6 at 27/12Z from control and 03DI.....	184
6.20	Six-hour forecasts of SLP, surface air temperature, and 1000-mb winds valid at 26/06Z from control, 12DI, and 06DI.....	185
6.21	Same as Fig. 10, but for 26/06Z.....	188

6.22	Forecasts of precipitation (26/00Z - 26/06Z) from control, 06DI, and 06AI; and observed precipitation (26/00Z - 26/06Z).....	189
6.23	Forecasts of precipitation (26/06Z - 26/12Z) from control, 12DI, and 06DI; and observed precipitation (26/06Z - 26/12Z).....	191
6.24	Forecasts of precipitation (26/12Z - 26/18Z) from control, 12DI, and 06DI; and observed precipitation (26/12Z - 26/18Z).....	194
6.25	Six-hour forecasts of SLP and 1000-mb temperature and winds valid at 26/18Z from control, 12DI, 06DI, and 03DI.....	196
6.26	Forecasts of precipitation (26/12Z - 26/18Z) from control, 12DI, and 06DI (forecast start time of 26/12Z); and observed precipitation.....	199
6.27	12- and 24-h forecasts of SLP and 1000-mb temperature and wind valid at 27/00Z and 27/12Z, respectively, from control and 03DI.....	201

LIST OF SYMBOLS

α_{ij}	analysis weight for the observational estimate
α_{xj}	analysis weight for the interpolated grid point value
c	geostrophy factor
c_p	specific heat at constant pressure for dry air [$\text{J kg}^{-1} \text{K}^{-1}$]
D	mass divergence [$\text{kg m}^{-1} \text{s}^{-3}$]
\tilde{D}	vertically integrated mass divergence [$\text{kg m}^{-1} \text{s}^{-3}$]
D_c	vertically averaged moistening rate [kg s^{-5}]
d	correlation length scale [m]
E	moisture flux [$\text{kg m}^{-2} \text{s}^{-1}$]
ϵ^2	ratio of observation error variance to forecast error variance
f	Coriolis parameter [s^{-1}]
F	forcing terms representing physical processes
Φ	generalized geopotential [m]
ϕ	geopotential [m]
ϕ_s	surface geopotential [m]
ϕ^*	average geopotential on a sigma surface [m]
g	acceleration of gravity [m s^{-2}]
h_x	map factor for horizontal x coordinate
h_y	map factor for horizontal y coordinate
H	sensible heat flux [$\text{K kg m}^{-2} \text{s}^{-1}$]
H_s	surface sensible heat flux [$\text{K kg m}^{-2} \text{s}^{-1}$]
K_H	diffusion coefficient [$\text{m}^2 \text{s}^{-1}$]
κ	ratio ($\kappa = R/c_p$)
L_c	latent heat of condensation [J kg^{-1}]

λ_k	square of phase speed of the the free gravity modes [$\text{m}^2 \text{s}^{-2}$]
M	horizontal moisture convergence [$\text{kg m}^{-1} \text{s}^{-3}$]
M_t	total horizontal moisture convergence [$\text{kg m}^{-1} \text{s}^{-3}$]
m_j	local data density
P_c	convective precipitation [cm]
P_L	large-scale non-convective precipitation [cm]
p	atmospheric pressure [$\text{kg m}^{-1} \text{s}^{-2}$]
p_0	standard reference level of 1000 mb
p_s	surface pressure [$\text{kg m}^{-1} \text{s}^{-2}$]
q	specific humidity [kg kg^{-1}]
q_s	saturation specific humidity [kg kg^{-1}]
Q_c	vertically averaged heating rate [K kg s^{-5}]
R	gas constant for dry air [$\text{J kg}^{-1} \text{K}^{-1}$]
R_v	gas constant for water vapor [$\text{J kg}^{-1} \text{K}^{-1}$]
r_m	vertically averaged relative humidity
ρ	correlation function for observed and model variables
σ	vertical coordinate following terrain
$\dot{\sigma}$	vertical motion in terrain-following coordinate [mb h^{-1}]
ζ	mass-weighted vorticity [$\text{kg m}^{-1} \text{s}^{-3}$]
T	temperature [K]
T^*	mean temperature varying only in vertical [K]
t	time coordinate [s]
Δt	integration time interval [s]
τ	wind stress [$\text{kg m}^{-1} \text{s}^{-2}$]
τ_s	surface wind stress [$\text{kg m}^{-1} \text{s}^{-2}$]
θ	potential temperature [K]

u	east-west horizontal component of wind [m s^{-1}]
u_g	east-west geostrophic wind component [m s^{-1}]
v	north-south horizontal component of wind [m s^{-1}]
v_g	north-south geostrophic wind component [m s^{-1}]
\vec{V}	velocity vector [m s^{-1}]
μ	fixed non-dimensional diffusion coefficient
v	analysis iteration
x	east-west spatial coordinate [m]
Δx	grid interval distance in x-coordinate [m]
χ	velocity potential [kg m s^{-3}]
y	north-south spatial coordinate [m]
Δy	grid interval distance in y-coordinate [m]
Ψ	streamfunction [kg m s^{-3}]

FOUR-DIMENSIONAL DATA ASSIMILATION OF GALE DATA USING A MULTIVARIATE ANALYSIS SCHEME AND A MESOSCALE MODEL WITH DIABATIC INITIALIZATION

1. INTRODUCTION

Four-dimensional data assimilation, in the context of numerical weather prediction, is the process of specifying initial conditions for the integration of a numerical forecast model. In this process, new observational data are merged, using some analysis procedure, with the ongoing integration of the prediction model. Data analysis and model prediction, along with model initialization, make up the major components of the data-assimilation process. A short-range model forecast serves as a first guess for the subsequent analysis.

The overall purpose of this research is to develop a method of data assimilation, which includes a cost-effective multivariate analysis scheme, accounts for diabatic effects in the model initialization, and uses a fine-resolution mesoscale model, in order to produce improved analyses of mesoscale circulations and then more reliable forecasts of coastal frontogenesis/cyclogenesis and associated precipitation. The goal here is also to investigate the impact of assimilating high-frequency observational data using a mesoscale model. To achieve this goal, the following objectives were required: 1) develop and test a computationally efficient, multivariate objective analysis scheme, 2) shorten model spinup by including diabatic heating in the initialization procedure, and 3) combine these components with a mesoscale numerical model to form an intermittent data-assimilation system and then evaluate the results.

Four-dimensional data-assimilation methods, along with the most commonly used objective analysis and initialization techniques, are examined from a historical perspective in Chapter 2. Operational techniques, including intermittent data assimilation and Newtonian nudging, and next-generation methods (Kalman-Bucy filtering and the adjoint method) are briefly described. Several methods are compared, with primary emphasis

being placed on recent papers dealing with the operational assimilation techniques. Ongoing and future research is outlined, and some important implications of this research are discussed. Following this extensive literature review, the NRL/NCSU Limited-Area Numerical Weather Prediction Model (referred to hereafter as the NRL/NCSU mesoscale model) is described in Chapter 3. This model, which was developed jointly by the U.S. Naval Research Laboratory (NRL) and North Carolina State University (NCSU), is used throughout the course of this research. The description includes the model's dynamics, numerics, physics, and vertical mode initialization procedure.

In Chapter 4, the successive correction scheme of Bratseth (1986) is applied for the multivariate analysis of data collected during the Genesis of Atlantic Lows Experiment (GALE), which was conducted over the southeastern U.S. during the winter of 1986. The newly-developed multivariate analysis interpolation procedure is described in detail, and the utility of the analysis scheme is measured. After univariate analyses of the mass and wind fields are produced, the coupling of these fields is achieved through additional iterations of the geopotential, utilizing improved estimates of the geostrophic wind to extrapolate the geopotential to the grid points. The wind analysis is then corrected for the new geostrophic wind. This study revealed that the objective analysis scheme successfully resolved mesoscale structures and significantly improved the absolute vorticity and vertical velocity fields.

Diabatic forcing from convective heating, as applied in the model initialization procedure, is discussed in Chapter 5. Latent-heating profiles are computed from 'spun-up' model-generated and observed rainfall. The latent heating is distributed in the vertical according to the cumulus convective parameterization scheme (Kuo scheme) of the model. Compatibility between the specified heating during initialization and the heating during early model integration is retained by merging the model integrated rainfall and

heating rates with those rates from the initialization. The inclusion of convective heating in the model initialization substantially reduced the spinup of model rainfall.

In Chapter 6, the multivariate, successive correction analysis and the diabatic initialization components are combined with a mesoscale numerical weather prediction model to form an intermittent data-assimilation system. A thorough evaluation of the assimilation system was performed using GALE data. Finally, a summary and major conclusions are presented in Chapter 7.

2. LITERATURE REVIEW OF DATA ASSIMILATION

2.1 Introduction

Two major motivations for using data assimilation exist: as an analysis/diagnostic/research tool and for operational weather forecasting. Data assimilation has been applied not only in meteorology (air pollution and planetary boundary layer studies, forecast case studies, quantitative assessment of new observing systems, among others), but also in oceanography for describing ocean currents (Ghil 1989; Robinson 1986). To summarize all relevant work pertaining to data assimilation is indeed a difficult task because the contents are spread so widely. The purpose of this review is only to provide an overview of four-dimensional data assimilation with primary emphasis on assimilation methods currently useful for operational weather forecasting. To make this review more complete, attention has also been given to the state-of-the-art or "next-generation" techniques, but to a lesser extent. Excellent reviews covering the early days of data assimilation research in both simulation and real-data studies are available in the literature. The interested reader is referred to Bengtsson (1975a), McPherson (1975), Hollingsworth (1986), and Bourke et al. (1985). Plus, a comprehensive history of data analysis and assimilation is given by Daley (1991), whereas a more abbreviated examination of data assimilation techniques is rendered by Harms et al. (1992b).

Numerical weather prediction (NWP) has classically been viewed as an initial-value problem where the governing equations of geophysical fluid dynamics are integrated forward in time from a set of initial values. The quality of NWP is strongly dependent on the accuracy of specifying these initial conditions and on the ability to model mathematically the dynamics and physical processes of the atmosphere. In a

pioneering paper, Charney et al. (1969) suggested combining past and current data in a numerical model such that the model's equations provide time continuity and dynamic coupling among the atmospheric fields. This concept, which has merged objective numerical analysis and numerical weather prediction, has become known as four-dimensional data assimilation (FDDA) and has proven to be a major advance in NWP during the past 20 years.

What inspired this major advance, or in other words, what spurred this development of data assimilation? The advent of meteorological satellites in the 1960s raised the possibility that nearly continuous atmospheric temperature observations would be available on a global basis. However, these space-based observing systems measure only radiance (or temperature) distributed in space and time, rather than at fixed locations and times. In order to fully utilize this new source of data, the numerical weather prediction techniques had to be adjusted. Beginning with Charney et al. (1969), Smagorinsky et al. (1970), Rutherford (1972), and Morel and Talagrand (1974), research progressed in reconstructing unobserved variables from the observed variables through the numerical model's dynamical coupling between those variables. By combining information about the state of the atmosphere, earlier observations are carried forward to provide an independent source of information to be added to the newly acquired observations.

Morel (1981) further illustrated why data assimilation is essential in NWP by listing five key reasons: 1) the inadequate distribution (spatial gaps) of the twice-daily upper-air sounding data, 2) the discrepancy between the conventional observations as point measurements and the true volume averages required by numerical models, 3) the inherently asynoptic character of remote observations obtained from sunsynchronous orbiting satellites, 4) the inadequate vertical resolution of remote observations of cloud motions from geostationary satellites, and 5) the significant random and systematic

errors involved in the data processing required for reconstructing atmospheric fields from remotely measured physical quantities. He concluded that any weather prediction model must be initialized by merging the new observations with the currently estimated meteorological fields, computed on the basis of earlier observations, while taking into account the dynamical constraints between successive model states, specified by the governing dynamical equations.

This process of merging new observational data with the ongoing integration of a numerical forecasting model is known as "data assimilation" or, equivalently, "four-dimensional data assimilation" in consideration of the time-space distribution of the data base. Then, as stated by Warner (1987), "the overall objective of the assimilation process is to provide the best possible initial state from which to begin a forecast, where the term "best" implies an appropriate balance as well as reflects optimal use of four-dimensional data (synoptic as well as asynoptic) to define the structures on all scales at the initial time."

In the past 20 years, many techniques have been developed to insert data into dynamic models. However, the first data-assimilation experiments were simplistic and of limited success. The observation simply replaced the model forecast value at the model grid point nearest the observation location (Jastrow and Halem 1970). This technique, known as direct insertion, is inadequate from the initialization point of view (Bengtsson 1975b). Direct insertion shocks the system and generates large-amplitude waves, or gravitational oscillations. For example, if observations of the mass field are inserted into a primitive equation model, an imbalance is created between the mass and wind fields. When the model integration is resumed, this imbalance is manifested as large-amplitude gravitational oscillations; this is the model's attempt to restore the dynamic balance which was disrupted by the data insertion. Techniques such as damping time integration schemes and time filters were developed to dampen these non-meteorological waves.

However, this damping must be rather strong and can be harmful to the meteorological modes. Bengtsson (1975b) stated that the shock effect will be reduced if locally analyzed data (interpolating the observation to several nearby grid points) are inserted into the model instead of observations only (indirect insertion). For example, applying a local multivariate analysis, or correspondingly, relating wind and geopotential by the geostrophic relation and inserting both height and winds simultaneously proved successful by speeding the updating considerably (see Fig. 2.1). The multivariate procedure mentioned here produces a simultaneous weighting of mass and motion observations, subject to the constraint of geostrophy (Petersen 1968; Eddy 1973; Daley and Puri 1980).

Of the several FDDA methods that have been investigated over the last two decades, some have been implemented operationally while others have not yet been used or are in the developmental stage. In the 1970s, regional/mesoscale weather forecasting models were developed, normal mode initialization was introduced, and global data assimilation became operational. With the advent of mesoscale modeling, FDDA applications are also geared toward the mesoscale, with the emphasis shifting from applications on the global scale.

In operational numerical prediction systems, FDDA can be categorized into two broad areas: continuous methods and intermittent (analysis-forecast cycle) methods. The former refers to the insertion of data into a model as it is received, in a temporally continuous fashion. The analysis-forecast cycle clearly illustrates the four components of data assimilation: quality control, objective analysis, initialization, and an initial guess from a short-range forecast. With this method, the data are assimilated intermittently at specified intervals. So-called next-generation data-assimilation methods are being researched today, with the two most prevalent being the adjoint method based on the variations of calculus and the Kalman-Bucy filter technique.

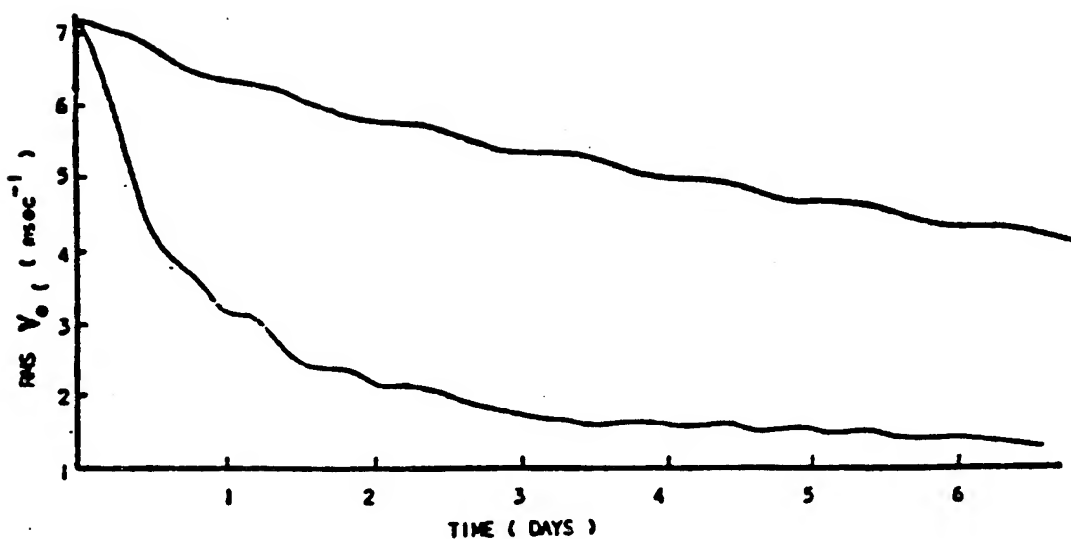


Figure 2.1. Successive reduction of wind error using a direct insertion (upper curve) of height data in a barotropic model. Corresponding results using height as well as from the derived geostrophic winds (lower curve) (McPherson 1975).

Since quality control, objective analysis, and initialization are intricate parts of data assimilation, it is appropriate to consider each of these components in the present discussion. Quality-control methods and the most commonly used objective analysis and initialization techniques are overviewed, followed by a discussion of various data-assimilation methods. Then, two studies, comparing operational data-assimilation techniques, are reviewed, and some important implications of FDDA and ongoing and future research in data assimilation are outlined.

2.2 Quality Control

Quality control is an integral part of a data-assimilation system. Quality-control algorithms are designed to modify or reject erroneous meteorological data. Following Daley (1991), observational data errors can be classified into two groups: natural error and gross (or rough) error. The natural error includes instrument error and error of representativeness. The data describe the behavior of the instrument itself, not the behavior of the meteorological parameter it is intended to measure. Every instrument is approximate by its very nature. Errors of representativeness are deviations caused by small-scale perturbations and are also referred to as micrometeorological errors. Gross errors originate from improperly calibrated or malfunctioning instruments, incorrect registration of observations, incorrect coding of observations, and telecommunication errors. These errors (natural and gross) can be either random or spatially or temporally correlated, and there can be systematic biases. The systematic errors can result from improper calibration of an instrument or from the influence of some persistent factor that is not accounted for or is accounted for inaccurately.

Several quality-control techniques are used routinely to screen bad data. These techniques can be divided into four major categories (following Gandin 1988). The first

two, plausibility check and check for contradictions, are used to identify gross errors based on the physical reasonableness of the data. Plausibility checks are the most widely used quality-control methods. These checks analyze each datum independently of other data. A simple plausibility check is one that rejects data values that can never occur in reality--for example, positive temperatures ($^{\circ}\text{C}$) at 300 mb. Other versions compare the datum with the climatological mean or with a background field (numerical forecast). If the deviation is too large, the datum may be rejected. The check for contradictions is based on an analysis of two or more parameters at the same point. An example is the occurrence of rain in the absence of clouds.

The remaining quality-control procedures include checks that rely on some common information and redundancy between observations. The spatial continuity (or consistency) check compares a datum with data at adjacent locations. This method, also known as the buddy check, demands spatial consistency among the data. A temporal continuity check can also be made in which temporal continuity is required with past observations. Finally, checks using dynamic relations such as the geostrophic or hydrostatic relation can be used to check geopotential height with temperature and mass with wind. These checks require the data to obey the dynamic relation at least approximately, otherwise the data are suspected or rejected.

The necessity for including automated quality control in operational NWP was recognized during the early era of NWP. Significant advances have been made in quality control, including the development of methods using optimum interpolation (Rutherford 1976; Lorenc et al. 1977; Lorenc 1981). Recent advances include the complex quality-control method of Gandin (1988) and the Bayesian approach of Lorenc and Hammon (1988). Reviews on various quality control methods have been authored by Belousov et al. (1968), Gustavsson (1981), and Lorenc (1985).

2.3 Objective Analysis Techniques

Objective analysis (the second major component of FDDA) and quality control have become intertwined and, as a result, the data-assimilation process is more internally consistent. Excellent reviews on objective analysis have been presented by McPherson (1976) and Gustavsson (1981). The present discussion contains a synopsis of selected topics from these two reviews. According to McPherson (1976), objective analysis is a process in which meteorological observations distributed in space and time are combined with forecasts from previous analyses and perhaps with climatology to form a numerical representation of the state of the atmosphere. This representation takes the form of values of the meteorological variables at regularly spaced grid points subject to various mathematical and physical constraints.

The objective analysis process consists of three subprocesses which are essential for the overall success or effectiveness of the FDDA system: 1) filtering of small amplitude random and systematic errors; 2) interpolation to a regular network of grid points or, in the case of spectral analysis, integration of the representing mathematical space functions over the irregularly spaced observations; and 3) forced adjustment of the meteorological variables using dynamic relationships among these variables.

Within a relatively short period of time, objective (numerical) analysis schemes were independently developed by several meteorologists. Panofsky (1949) devised the first objective analysis method--polynomial interpolation, or the so-called surface-fitting type. An extension of this method was developed by Gilchrist and Cressman (1954) and became the first operational objective analysis. In this technique, mathematical (polynomial) functions are adjusted to observed data in the close vicinity of the grid point, for which analyzed values are required. The adjustment or fit is obtained by a least squares technique. The polynomial method is nonlinear since nonlinear functions are

used to approximate the variation of the analyzed variable. However, the resulting analyzed value at the grid point is a linear function of the observed data and, in this respect, this method is similar to the other analysis methods that will be described.

Bergthorsson and Döös (1955) introduced the successive correction method, and a similar method was devised by Cressman (1959). Cressman's successive correction technique essentially replaced the polynomial interpolation method because the latter produced unreasonable analyses at the edge of data-rich and data-sparse areas. In the successive correction technique, a forecast model provides the preliminary estimate (first guess) of the field to be analyzed. The basic idea of the method is to correct this preliminary field iteratively during several analysis "scans"; the results of one scan become the first guess for the next scan. The estimate is modified by a combination of corrections computed for each grid point. The corrections, which are proportional to the difference between the observed and first guess values, are weighted empirically with observations nearest the grid point weighted the most heavily.

By using a short-range forecast based on a previous analysis as the first guess, the effect of past data is allowed to influence the analysis and thereby contributes to the temporal continuity and spatial coherence of the analysis. For many years, successive correction methods were most widely used in operational forecast centers.

This early dominance of the successive correction methods was taken over during the last decade by statistical (optimal) interpolation schemes, which were originally introduced by Eliassen (1954) and Gandin (1963). Statistical interpolation was also studied extensively by Alaka and Elvander (1972) and Phillips (1976). This analysis technique is based on statistical linear regression and provides a systematic framework for blending observations of differing error characteristics with recent predictions or climatology. More accurate data receive more weight in the analysis. As in the successive correction method, the analyzed value at the grid point is the sum of the first

guess and a linear combination of corrections, which are proportional to the difference between observational and first guess values. The weighting coefficients are determined from the condition that the mean-square-error of the analyzed values be minimum, and they depend on the spatial covariances among the analyzed variables. This method is, in principle, spatially coherent and, like its counterpart of successive correction, incorporates temporal continuity through the use of a short-range forecast from the preceding analysis as a first guess.

The polynomial interpolation method mentioned earlier reappeared in the British Meteorological Office analysis (Dixon et al. 1972) and in the spectral analysis method devised by Flattery (1971). In the spectral analysis technique, mathematical functions are globally adjusted to fit observed data. One additional analysis method that has been utilized in the FDDA context (see discussion in section 5) is the variational technique introduced by Sasaki (1958). This method is a post-analysis adjustment technique based on the calculus of variations and is very effective in making the analyzed fields compatible with a forecast model. A functional is used, which minimizes the analyzed-minus-observed difference, filters undesirable high-frequency and high-wavenumber features, and employs dynamical constraints. These constraints may be strong (satisfied exactly) or weak (satisfied approximately).

Over the past 30 years, numerous variations of these different objective-analysis methods have been developed. Some versions are hybrids belonging to more than one of the aforementioned techniques.

According to McPherson (1976), objective analysis methods used in operational meteorology can be divided into two basic categories. The first represents an analyzed field as a series expansion (spectral analysis):

$$Z_g = a_1 f_1 + a_2 f_2 + \dots + a_m f_m \quad 2.1$$

where Z_g represents the departure of the field from its mean value. The f_i represents a set of orthogonal functions--for example, a cosine series. The analysis procedure involves determining the time-dependent coefficients a_i which make the series expansion best fit the observed data by, for example, a least-squares technique. Analysis methods of this type are in operational use at the National Meteorological Center (NMC) (Flattery 1971; Hayden 1976) and the United Kingdom Meteorological Office (UKMO) (Dixon 1976).

The second basic method, called the "gridpoint" method, includes statistical interpolation and successive correction techniques. Here, the analyzed value Z_g^a at a discrete point g is given by a linear combination of observations that are nearby in time and space:

$$Z_g^a = a_1 Z_1^o + a_2 Z_2^o + \dots + a_n Z_n^o \quad 2.2$$

where Z^o represents observed values at the several stations within some predetermined influence radius of point g , and the coefficients a_i determine the influence of each observation on the analyzed value. In this case, the analysis involves determining the coefficients a_i in the linear combination for each point of the analysis grid.

Two forms of representation are associated with these two basic methods of analysis: the discrete form and the spectral form. In the former, the analysis is a set of values at discrete points in space and time; in the latter, the analysis is represented by a series expansion such as Eq. 2.1. The spectral form has been used primarily for global and hemispheric applications. The discrete form has been extensively used for limited-area applications in mesoscale meteorology.

2.4 Initialization Techniques

The objective-analysis methods described in the previous section generally do not provide balanced mass and wind fields to initiate a forecast. Uncompensated errors in wind and pressure-temperature observations, interpolation of observations to model grids, and the numerical model's inability to exactly describe the atmosphere are the primary sources of this dynamical inconsistency. The dynamical imbalances in the initial data lead to the generation of spurious inertia-gravity-wave oscillations, or "meteorological noise." Primitive equation models, unlike geostrophic models, admit these higher-frequency gravity-wave solutions that can have amplitudes much greater than their counterpart in the real atmosphere. These gravity wave oscillations can obscure the lower-frequency Rossby-mode component of the model, which constitutes the meteorological signal. Early numerical modelers called attention to the need to eliminate the spurious high-frequency oscillations, which can compromise the forecast procedure. First of all, these fast-moving gravity waves require short computational time steps; second, they can seriously interfere with very short-range forecasts (<12 h); and third, they can impair vertical motion and, hence, precipitation forecasts (Daley 1981). Therefore, a long-standing approach has been to eliminate or effectively reduce the amplitude of these fast-moving inertia-gravity waves at initial forecast time. This process is known as model initialization. Charney (from unpublished letter to Phillip Thompson, 12 February 1947) provided insight for rectifying this initialization problem by suggesting that one should modify the initial state or modify the governing equations; that is, use filtered models.

The first and simplest approach was to exclude any possibility of the high-frequency oscillations by using a "filtered system" such as the balance equations which simply reduce the model dynamics to the quasi-geostrophic response. However, this

approach severely restricts the model dynamics, which results in very poor forecasts beyond 24 hours. The so-called primitive equations account for more atmospheric dynamics and can yield much better forecasts, so they are generally used. However, the primitive equations do allow the amplification of fast-moving gravity waves which requires some modification of the initial conditions to achieve the desired dynamical balance.

Over the years, many initialization methods have been developed. A summary of the more widely used techniques are presented here. For a more detailed review, the reader is referred to Daley (1991). In static initialization, the data are adjusted at a single time level to conform to some dynamical constraints. That is, certain time derivatives are identified as vanishing in order to eliminate or reduce the generation of inertia-gravity wave noise. In the conventional static initialization, a standard practice is to first analyze the geopotential field using pressure-height data and use wind observations to estimate the gradient of the geopotential using the geostrophic relation. The analyzed geopotential fields on pressure surfaces are then used in the mass balance equation to obtain the streamfunction of the nondivergent wind, from which the rotational wind component can be computed. A major limitation in using the balance equation to determine a rotational wind for initializing a primitive equation model is that the lack of a divergent wind component insures the presence of gravitational modes (Haltiner and Williams 1980).

The most common approach of initialization in intermittent FDDA is normal mode initialization, which achieves dynamical balance using the normal modes of the linearized dynamical equations. The direct use of normal modes was introduced by Dickinson and Williamson (1972). They proposed that the amplitudes of the unwanted, fast-moving modes be set to zero. Their method was effective in suppressing the spurious noise in linear models, but failed in the nonlinear case. A nonlinear normal mode scheme was independently developed by Machenhauer (1977) and Baer (1977). In nonlinear normal

mode initialization, the tendency of the unwanted modes are set to zero, versus setting the amplitude of these modes to zero. The solution of the nonlinear equation requires an iterative process. Unfortunately, this nonlinear scheme, without the inclusion of diabatic effects, suppressed the meridional circulation in the tropics. Puri and Bourke (1982) used the idea that the tropical divergent circulations driven by convection influence mainly the low frequency gravity modes. Therefore, they excluded these low frequency modes from the initialization using a frequency cutoff. Wergen (1982) introduced another method in which average diabatic heating is obtained by integrating the model for a few time steps prior to initialization. This model-produced diabatic heating is then included in the nonlinear forcing in the iterative process.

In global models, (Andersen 1977; Daley 1979; Temperton and Williamson 1981; for example), after the normal modes of the model are computed, the high-frequency inertia-gravity waves can be removed by projecting the inertial wind and mass fields onto these normal modes. However, in limited-area models it is not possible to define the horizontal structure of the normal modes.

Bourke and McGregor (1983) introduced a method of initializing a limited-area model without explicitly computing horizontal normal modes. In this technique, termed vertical mode initialization, the free modes of oscillation of the prediction model are identified by linearizing the equations about a basic state of rest. This linearization permits a simple decomposing of the three-dimensional eigenvalue problem into a series of two dimensional problems. The vertical decomposing leads to a number of characteristic vertical modes, one corresponding to each discrete level in the model. Balance conditions on the horizontal structure equations are then derived for each vertical mode. Filtering conditions, in which the tendencies of divergence and ageostrophic vorticity are set to zero, are applied to derive linear diagnostic equations for the mass and divergence fields. In Fig. 2.2, from Bourke and McGregor (1983), graphs of surface

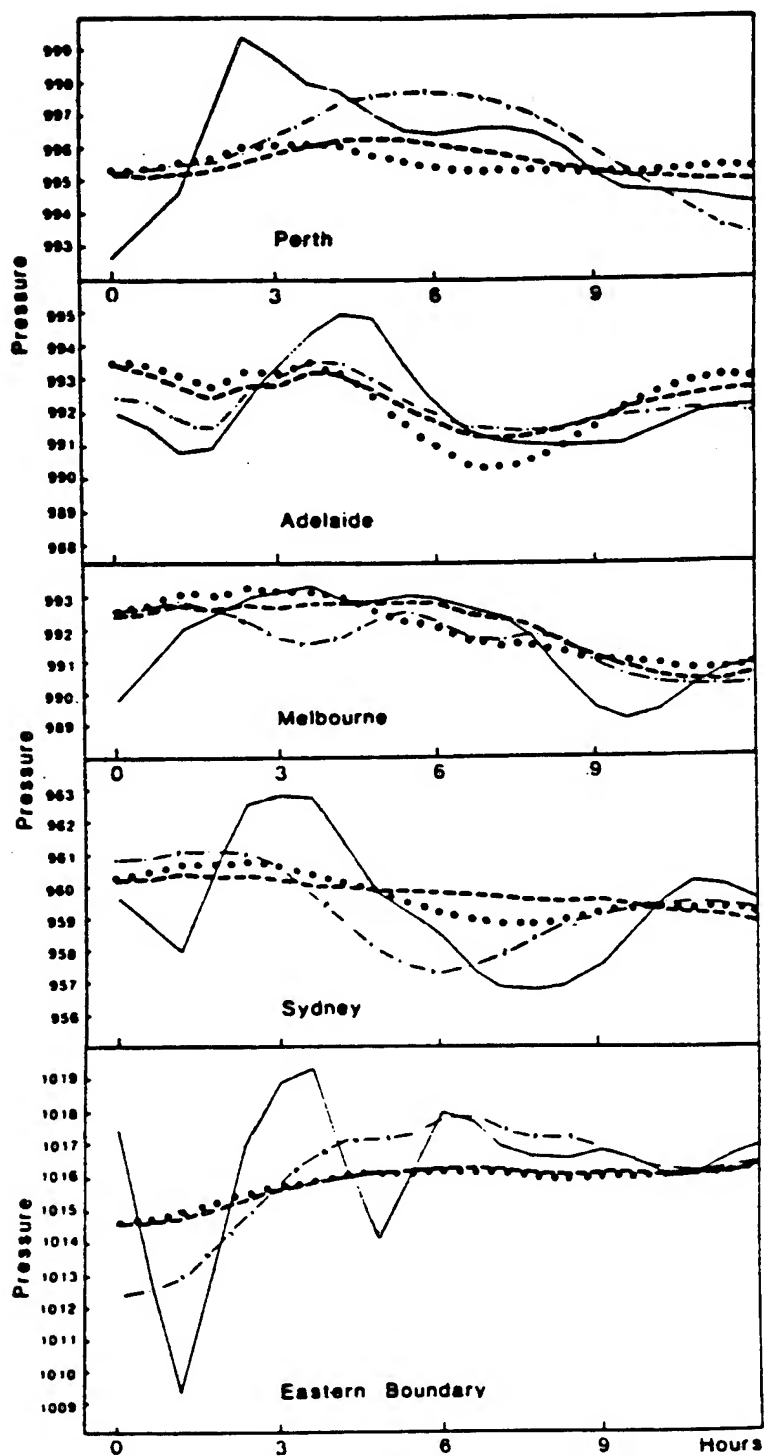


Figure 2.2. Surface pressures (mb) for individual grid points for the first 12 h of prognosis using an uninitialed analysis (solid curves), after initializing two vertical modes (dot-dash), and after initializing two vertical modes (dashes--using Dirichlet boundary conditions and dots--using Neumann boundary conditions) (Bourke and McGregor 1983).

pressure before and after initialization using the Australian regional primitive equation model are shown. It is obvious that the initialization procedure successfully removed noise from the integrations.

Temperton (1988) devised a method of applying Machenhauer's criterion without requiring the computation of the coefficients of the individual modes. Figure 2.3 (from Temperton 1988) shows graphs of 500-mb geopotential before and after the application of Temperton's implicit normal mode initialization for the Canadian finite-element model. This method is also successful in removing the high-frequency noise.

Although appropriate for intermittent FDDA, the normal mode initialization is a distinct, separate step from the objective analysis and usually leads to changes in model parameters. As a result, the initialized analysis may no longer fit the observations as closely as desired. An alternative, known as dynamic initialization, has the advantage of avoiding the complications of computing normal modes. In this method, which was introduced by Miyakoda and Moyer (1968), observations are inserted (intermittently or continuously) over a period of time. The method has the added advantage of simplicity and can balance physical processes as well as the mass and wind fields. In dynamic initialization, the model equations were integrated forward and backward through time under controls that encourage time derivatives to become small compared to spatial derivatives, which in turn selectively dampened the high-frequency components of the solutions. Early versions of this technique required several repetitions of the integration cycle to successfully reduce the gravity-wave oscillations and, as a result, these schemes were computationally expensive. Another disadvantage was that the slow modes of the model were dampened.

More recently, researchers including Bratseth (1982), Sugi (1986), and Satomura (1988) have developed schemes which are more computationally efficient and have more selective damping properties. Figure 2.4 (from Sugi 1986) depicts graphs of the gravity-

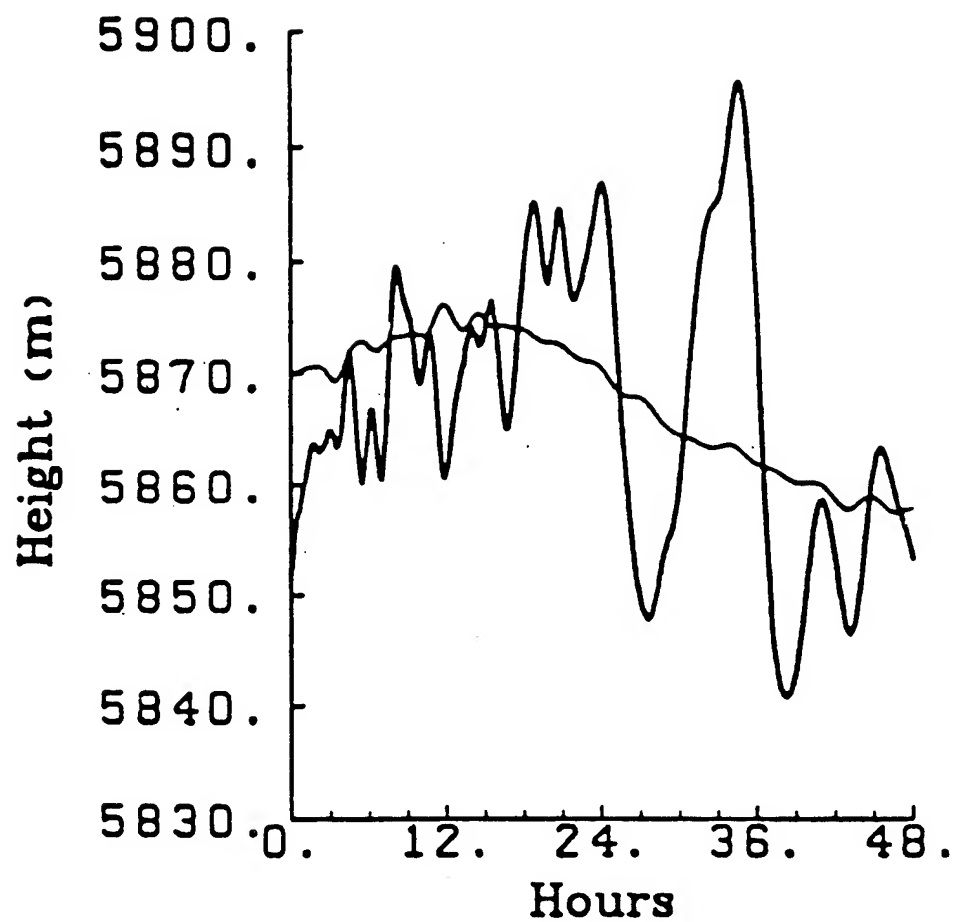


Figure 2.3. Time trace of height field. Heavy line: no initialization. Light line: after two iterations of the implicit nonlinear normal mode initialization scheme (Temperton 1988).

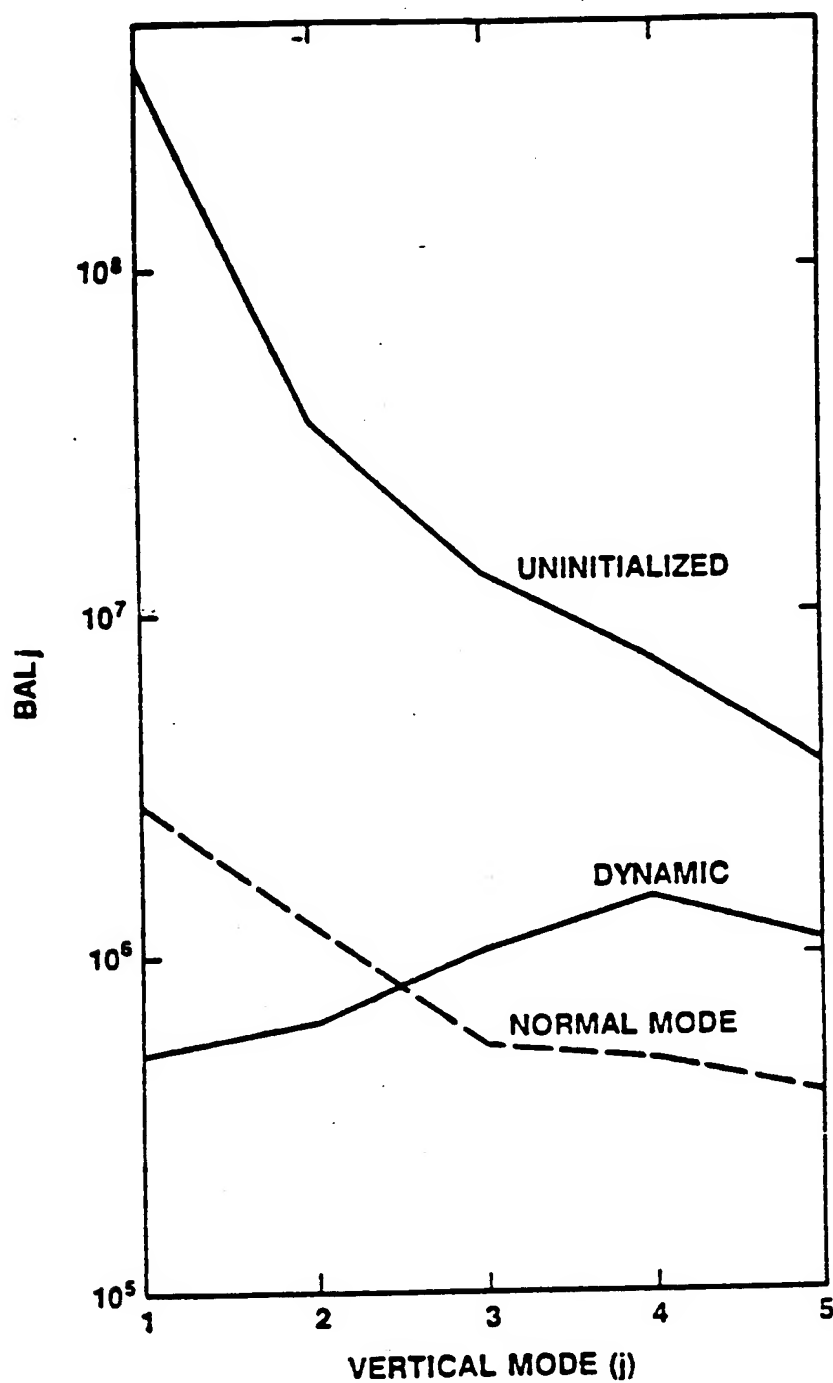


Figure 2.4. Gravity-wave activity (before and after initialization) for five vertical modes of a baroclinic model (Sugi 1986).

wave activity (before and after initialization) for five vertical modes of a baroclinic model. The gravity-wave noise is dramatically reduced, particularly for the modes of large equivalent depths. Dynamic initialization, as well as the Laplace transform and bounded derivative methods (described below), is well suited for initializing data on a limited domain.

Lynch (1985a) developed an effective method of initialization based on a filtering scheme which uses a modified inverse Laplace transform. This technique is equivalent to the nonlinear normal mode initialization method, but it has the advantage of not requiring a transformation of the model equations into normal mode space. Therefore, the Laplace transform method is well suited for initializing limited-area models with complex boundary conditions. Lynch (1985b) used his method to initialize data for a barotropic limited-area model, successfully removing high-frequency gravity wave oscillations during the model integration. This technique has also been applied in a filtering integration scheme for continuous data assimilation.

Another technique, which has been used to initialize models of limited domain, is the bounded derivative method. Kreiss (1979) developed the methodology of controlling the amplitudes of the high-frequency inertia-gravity waves by requiring the derivatives of the model's dependent variables with respect to time to be bounded, i.e., of order unity, at the initial time. First, the equations of motion are nondimensionalized so that certain terms are multiplied by a small parameter, ϵ . Then, if the first derivatives are bounded, the equations can only be satisfied if the model atmospheric flow is geostrophic and nondivergent to order ϵ . If the second-order time derivatives are bounded, the resulting diagnostic relationships are the quasi-geostrophic omega equation and the nonlinear balance equation.

2.5 Various Data-Assimilation Methods

An assimilation method extensively used in operational meteorology is the analysis-forecast cycle technique, commonly referred to simply as intermittent data assimilation (see Fig. 2.5). This process consists of four steps which are repeated at each assimilation cycle (typically every 3-12 h). After the data have been checked (quality controlled), a static three-dimensional objective analysis (typically successive correction or optimal interpolation) is performed using observations and a background field. The background or "first guess" is usually a prior model forecast valid at the analysis time, or can simply be climatology or a combination of both. Then, the analyzed fields are adjusted, or initialized, to conform to some dynamical constraint(s) in order to reduce or eliminate inertia-gravity-wave noise. The final step consists of a short-range numerical forecast to obtain first-guess fields for the analysis at the next assimilation cycle. Thus, the new estimates (analyzed fields) are clearly based on the past observations, being carried forward in time by the model forecast, and on the current observations. The intermittent updating process is entirely appropriate as long as most available data are taken at the same time, for example, at synoptic times. This technique is currently used at most of the world's major operational forecasting centers, including the NMC (DiMego 1988), the Norwegian Meteorological Institute (Gronas and Midtbo 1986), and the European Centre for Medium-Range Weather Forecasts (ECMWF) (Hollingsworth 1986).

The extensive operational use of intermittent data assimilation is primarily due to its computational efficiency. In addition, this method normally includes a normal mode initialization scheme that produces a balanced mass/wind initial state. A disadvantage of this method is that it is not totally suited for asynoptic data types; that is, it can not

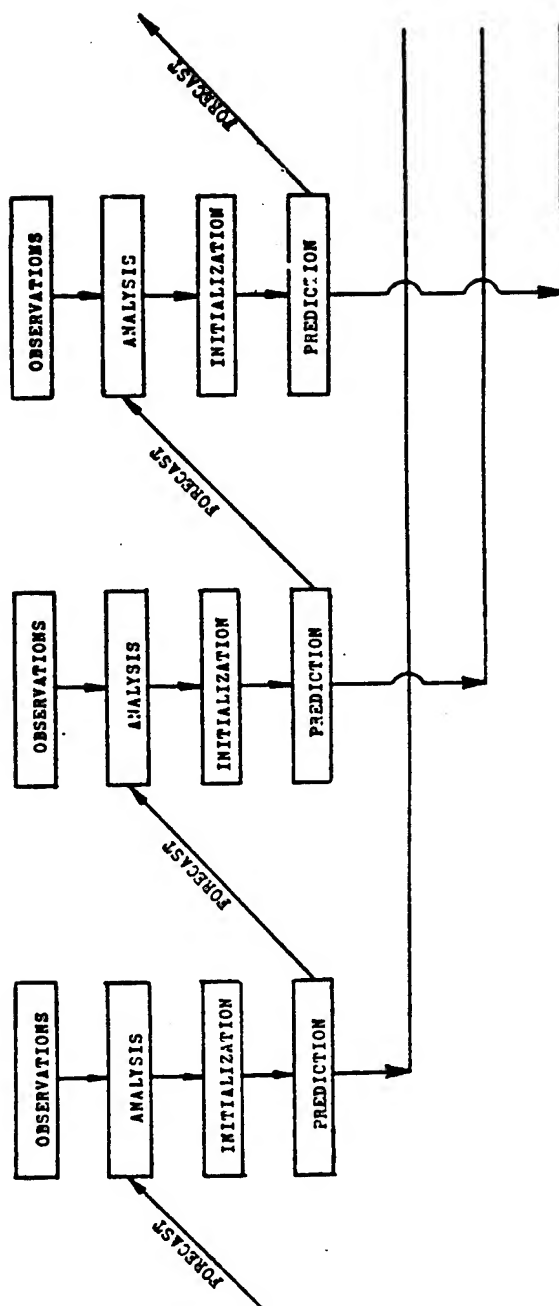


Figure 2.5. Intermittent data assimilation using an analysis-forecast cycle (Bengtsson 1975a).

assimilate data continuously. However, updates on the order of every 2 to 3 h can be made, allowing some asynoptic data into the assimilation.

Two other mathematically elegant methods, Kalman-Bucy filtering and the adjoint method using variational techniques, have emerged as state-of-the-art methodology in FDDA. The latter is briefly reviewed first. For a more rigorous and complete discussion of the general theory of these two techniques, the reader is referred to Daley (1991).

Variational assimilation, based on the calculus of variations, involves the incorporation of dynamical constraints in a variational treatment and has been pursued by Sasaki (1969), Stephens (1970), and others for several years. In variational calculus, stationary points (extrema) of integral expressions known as functionals are determined. J is a functional of the function $q(t)$ in the interval (t_m, t_n) , if it depends on all the values $q(t)$ for $t_m \leq t \leq t_n$. In this approach, successive analyses are mutually adjusted to effectively increase the database at each time step by using information at other analysis times through the forecast equations. The objective is to produce initialized values of q subject to certain constraints such as the hydrostatic relation, the continuity equation, the geostrophic relation, or the nonlinear balance equation. The approach is designed to keep the initialized fields close to the observations while satisfying the constraint (Daley 1991).

Lewis (1972) developed a variational scheme using a thermal wind relationship and the hydrostatic equation as constraints. A more recent variational approach, known as the adjoint method (Lewis and Derber 1985), uses a complete dynamic model as a strong constraint. This method fits a model to observational data distributed over a finite period by computing derivatives of model output. An iterative method minimizes the weighted squared difference between the original analyses at several times and the coincident solutions to the model (constraint) for a given output variable. The final analyses are constrained to satisfy the model forecast from a set of initial conditions. The functional, J , is minimized by finding the gradient of J with respect to the initial conditions.

The output of any model depends upon a set of input variables: initial conditions, boundary conditions, and even modeling parameters of physical processes. Because of this dependence, the "adjoint" can be used to determine the sensitivity of the model output to any input parameter, i.e., initial conditions. Neglecting forecast errors over the assimilation period (time period spanning the observations), this technique can produce the optimal initial state (end of the assimilation period) such that the model best fits the observations through the entire period.

The alternate "next-generation" FDDA method is called Kalman-Bucy (K-B) filtering. The K-B method can be thought of as a continuous dynamic FDDA where the weighting factors are optimally determined by explicitly calculating the error covariance of the analysis. In 1960, Kalman developed the basic theory for the linear, unbiased data assimilation scheme known as the Kalman filter (Kalman 1960).

The K-B filter (Kalman and Bucy 1961; Ghil et al. 1979 and 1981), which is the time-continuous counterpart to Kalman's original scheme, uses the forecast model itself to predict the background error statistics. The goal of this method is to obtain the most accurate analysis value for all time during the assimilation period using only present and past observations. The weight given to the current observations is inversely proportional to their variance, and the accuracy of the analysis is the sum of the accuracies of the forecast, based on the past observations, and of the current observations. The K-B filter minimizes the analysis error variance not only at every time step, but over the entire assimilation interval in which data are provided (Ghil 1989). Through an application of Bayesian ideas in a dynamical sense (Kalman 1960; Lorenc 1986), the filter is able to extract all useful information from the observational increment/residual at each time step, thus, allowing observations to be discarded as soon as they are assimilated. As a result, the method is sequential.

The K-B filter and the adjoint method are very promising assimilation techniques. Both methods have been shown to produce improved assimilated states for model forecast integration as compared to those from the operational techniques. However, these "next-generation" data assimilation methods are of limited practicality at the present because of their complexity and extensive computational requirements. Therefore, operational implementation is still several years away (Stauffer and Seaman 1990). However, Lorenc (1988) has pursued approximations to the adjoint technique in a quest to make it operational in numerical weather prediction.

Most research has been directed toward the less elegant but more practical method of dynamic assimilation, in which the numerical prediction model serves as an integrator of observations distributed in time and space. In this approach, which has become known simply as "nudging" or Newtonian relaxation, the model integration is interrupted periodically and the current model state is updated with the new observations. During the assimilation cycle, or preforecast integration period, the model variables are gradually driven, or nudged, toward the observations by extra forcing terms in the equations (Anthes 1974; Kistler 1974; Hoke and Anthes 1976; Davies and Turner 1977). As a result, the model fields are gradually corrected and no further dynamic balancing through initialization is required. The general form of the predictive equation of variable S is:

$$\frac{\partial S}{\partial t} = F(S, \tilde{x}, t) + G \cdot W (S_0 - S) . \quad 2.3$$

All of the model's physical forcing terms (Coriolis, advection, etc.) are represented by F , where S represents a model dependent variable, S_0 represents observations of S , \tilde{x} is the independent spatial variable, and t is time. The second term on the right is the nudging term, where G is the nudging constant (generally 10^{-3} to 10^{-4}) and W represents a four-

dimensional weighting function. The data to be nudged can be either derived or measured, analyzed to a grid for assimilation into the model, or inserted as individual observations.

This technique, which has been successful in bringing the data and the model in harmony and providing a relatively noise-free start for the forecast, has been widely used on the global scale (Lyne et al. 1982; Krishnamurti et al. 1988) and on the regional scale in limited-area models (Anthes 1974; Hoke and Anthes 1977). Of late, several researchers have developed a new interest in this technique (Stauffer et al. 1985; Bell 1986; Ramamurthy and Carr 1987; Kao and Yamada 1988; Wang and Warner 1988; Kuo and Guo 1989; Stauffer and Seaman 1987, 1990). It is currently used operationally at the UKMO for both global (Lyne et al. 1982) and regional (Bell 1986) data assimilation.

The nudging technique mentioned above does possess a few desirable attributes; these were summarized by N. L. Seaman (from his lecture notes presented at the 1990 Summer Colloquium on Mesoscale Data Assimilation, Boulder, Colorado): 1) The assimilating model is complete, so irreversible processes are included without difficulty. 2) Any data type that can be represented as a tendency of a prognostic variable can be assimilated. 3) Observation-nudging can easily assimilate asynoptic and single-level data. 4) Analysis-nudging requires that the analyses be performed only once prior to model integration, i.e., it is economical. 5) Nudging does not require a separate balancing/initialization step. 6) Nudging is conceptually and computationally simple. On the other hand, this method has a few disadvantages: 1) The nudging constant is generally assigned in an application-dependent semi-arbitrary manner. 2) Observation-nudging is based on "continuous analysis" during model integration and can become computationally expensive. 3) Analysis nudging is not well-suited for asynoptic data types. 4) Use of accurate data in observation-nudging may cause assimilation of local or unrepresentative components, e.g., microscale observations spread over a large area.

2.6 Comparisons of Operational Assimilation Techniques

Two papers from the recent literature (Ramamurthy and Carr 1987; Kuo and Guo 1989) compared different data-assimilation methods. Unlike the purpose of the present discussion, both of the aforementioned articles advocated Newtonian nudging. The sole purpose here is to offer a short review of the available comparative studies.

Ramamurthy and Carr (1987) studied the applicability of several assimilation techniques currently being employed in operational models. A prime scientific objective was to determine the "best" way to assimilate asynoptic observations in limited-area models. A sequence of ten assimilation experiments was conducted using different update procedures. In each experiment, their limited-area model was initialized with ECMWF FGGE level III-b data, and then 12-h assimilations were performed using level II-b data from the 1979 Summer Monsoon Experiment (SMONEX). Forecasts were then made from these assimilated states. The first experiment served as the control run since no assimilation was performed. Figure 2.6 is a schematic of the overall assimilation-forecast strategy; four types of data assimilation were compared: 1) In the static assimilation, the model was updated only once at the end of the preforecast (assimilation) period. An initialization step was then taken to suppress the noise associated with the external inertia-gravity mode; the internal modes were not initialized. 2) The intermittent data-assimilation experiment was similar to the static case, except the model was updated twice during the assimilation period. 3) Four experiments were conducted using continuous indirect data assimilation in which the model was updated whenever new observations became available. 4) Newtonian relaxation was used in the last three experiments; the model state was nudged toward analyses produced from the observations. The reader should see Ramamurthy and Carr (1987) for a detailed description of the experiments.

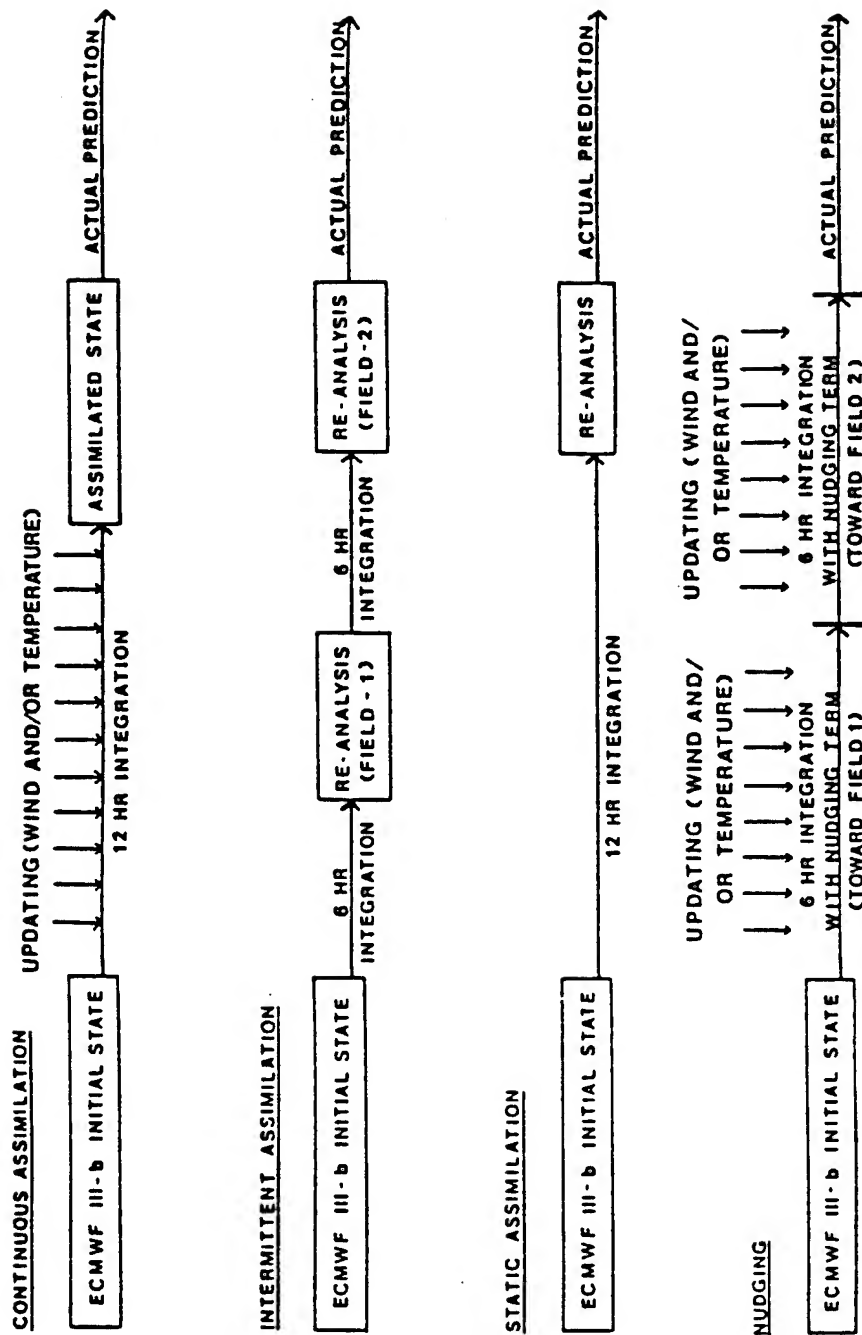


Figure 2.6. A schematic of the assimilation-forecast cycle for various experiments (Ramamurthy and Carr 1987).

Comparisons among these differing techniques were made by examining assimilated states (analyses obtained at the end of the 12-h assimilation period). Newtonian nudging produced better assimilated states than did the continuous assimilations via indirect insertion. Also, the continuous assimilation experiments produced noisy assimilated fields due to insertion shocks.

From each of the assimilated states, 24-h forecasts were made and the results were compared against each other and with the observations. The continuous assimilation (via indirect insertion) continued to suffer from the ill effects of the insertion shock. However, the forecasts from the nudging experiments had a minimal amount of noise.

The degree of spinup was examined in terms of the development of precipitation. The excessive shocking associated with continuous insertion was detrimental to the spinup process and consequently to the rainfall predictions. The rotational nudging experiment (only the rotational component of the wind was nudged) produced the most accurate rainfall predictions. The lack of divergence-related shock in this approach aided in the evolution of the physical processes.

The predicted tracks of the cyclone in the SMONEX case study were compared. During the first 12 h (assimilation period), the cyclone's movement was erratic in all of the experiments due to the rapid mutual adjustment between the mass and wind fields that occurred in the early stages of integration. In the static and intermittent assimilation experiments in which the fields were replaced completely at the end of the assimilation period, this problem extended into the forecast stage for another 12 h. Overall, the nudging experiments predicted more accurate tracks than the other experiments.

In another comparative study, Kuo and Guo (1989) examined different data-assimilation strategies. They conducted a series of observing-system simulation experiments (OSSEs) to test a Newtonian nudging technique for continuous assimilation of observations from a hypothetical network of profilers. Twenty experiments were

described in their paper. Similar to the work of Ramamurthy and Carr, they investigated static initialization, intermittent assimilation, and Newtonian nudging.

Comparisons of the three assimilation techniques were made by obtaining time series of wind and temperature errors during the assimilation period. With nudging, the errors decreased gradually during the period. The intermittent assimilation produced a stepwise decrease in the errors and the results after four assimilation cycles were considerably better than in the static assimilation case. This reveals that intermittent data assimilation was also effective in producing an improved initial state for the model forecast.

When considering model noise generated during the preforecast period, a strong difference emerged between continuous nudging and the intermittent assimilation. In the nudging experiment, the model noise gradually decreased during the assimilation period. In contrast, the intermittent data assimilation produced model noise with large spikes immediately after each reanalysis of the wind field. However, this noise could have been reduced substantially if a normal mode initialization procedure had been incorporated.

The two papers reviewed above suggest that Newtonian nudging is the best assimilation method among those compared. However, the investigators' findings may be scientifically inconclusive due to their incomplete tests (notably, their failure to include an effective normal mode initialization procedure in the intermittent data assimilation experiments). Furthermore, their comparisons were limited to operational data assimilation techniques. The next-generation methods will produce more optimal assimilated states for initiating a numerical weather prediction model. But as stated previously, these methods are still in the developmental research stage and computationally efficient versions are not currently available for operational use.

2.7 FDDA Research: Implications and the Future

FDDA has been developed tremendously during the past 15 years and is now an essential component of numerical analysis and prediction systems in both research and operations. The improving performance of medium-range global and hemispheric prediction and the rapid development of limited-area and mesoscale models at centers such as the NMC, ECMWF, and UKMO clearly illustrate the practical benefits of research in data assimilation.

The systematic development of data assimilation methods has made possible the use of unconventional and asynoptic observations from satellites, aircraft, drifting buoys, and soon from wind profilers and doppler radars. As a result, the accuracy of short-range forecasts has significantly improved, although only minor changes have occurred in the global observing system since the Global Weather Experiment in 1979 (Bengtsson and Shukla 1988). According to Lange and Hellsten (1986), the 3-day rms forecast error for the Northern Hemisphere dropped by more than 35% between 1979 and 1986. During the same period, medium-range weather prediction has been usefully extended in the time scale from 3 - 4 days to about 7 days in the Northern Hemisphere and to 4 days in the Southern Hemisphere (Bengtsson 1985; Bourke et al. 1985). The largest improvement has occurred at middle and high latitudes of the Northern Hemisphere. Weather prediction in the tropics has not improved nearly as much, due to insufficient observations and deficiencies in the formulation of critical physical processes.

Lorenz (1982) addressed the limit of medium-range predictability and concluded that it is possible to predict instantaneous weather patterns with better accuracy than guesswork nearly two weeks in advance. Such extensions in predictability will depend on the ability to improve current data-assimilation systems as well as the numerical prediction models themselves.

Research is ongoing to find ways to improve data assimilation methods. A number of research centers are investigating higher-resolution models, better numerical techniques, improved physical parameterizations, and improved models of auto- and cross-correlation functions for prediction error. Another area of interest is in specifying the diabatic heating at the initial forecast time. A detailed specification is necessary in order to correctly analyze and forecast the divergent wind field over the tropics. A few universities are making major strides in developing the next-generation FDDA techniques and enhancing existing methods. For example, adjoint methods are being intensely investigated at the University of Oklahoma; K-B filtering at McGill University, Montreal, Canada; and Newtonian relaxation at the Pennsylvania State University.

Several other critical research topics need attention during the 1990s. They include: assimilation of moisture processes (rainfall data and integrated liquid water), lateral boundary conditions and mesoscale predictability (predictive skill of limited-area models is strongly controlled by the lateral boundary conditions), assimilation of surface conditions/characteristics, and quality control, which will continue to be a priority as new data types are applied in FDDA. Data assimilation is relatively new on the meso-alpha and sub-alpha scales and needs considerable research with improved datasets. Existing first-generation assimilation systems must be improved to effectively forecast on these small scales.

During the next decade, FDDA will play a role in solving or alleviating important environmental issues such as air pollution and climate control (increasing CO₂ and the ozone hole). Recent clean-air legislation requiring the use of low-sulfur fuels and extremely expensive equipment will make accurate numerical models of atmospheric-chemistry transport and removal more important than ever. FDDA can be used to obtain accurate meteorological fields for input to complex air-chemistry models. Bengtsson and Shukla (1988) have suggested that a comprehensive analysis of global observations

based on an FDDA system with a realistic physical model should be used to produce internally consistent, homogeneous datasets for the earth's climate system. These global observations will include many new environmental variables such as external forcing variables, concentrations of radiatively and chemically important rare species, and land surface and oceanic variables. New remote-sensing systems such as EOS (Earth Observing System) will monitor these variables.

With these environmental issues in mind, Daley (1991) elaborated on a possible vision of the future of data assimilation:

"Firstly, data assimilation will no longer be entirely or even primarily concerned with short (or medium) range weather forecasting. Secondly, the data base will become incredibly diverse in both variables measured and type of observing system. Thirdly, assimilating models will be much more comprehensive, involving ocean, land surface and stratospheric components. Finally, there will be considerably more emphasis on the long term stability of algorithms to facilitate climate change signal detection."

3. NRL/NCSU MESOSCALE MODEL

The forecast model used throughout this data-assimilation research study was developed at the Naval Research Laboratory and North Carolina State University and is described in detail by Madala et al. (1987), Holt et al. (1990), and Sashegyi and Madala (1990, 1992b). The use of the full model is based in the philosophy that no compromise should be made in any components of the assimilation system. The model generates forecast of temperature, wind, surface pressure, humidity, geopotential height, vorticity, vertical velocity, and precipitation.

3.1 Dynamics of the Model

The prediction model is based on the primitive equations. The horizontal momentum equations, thermodynamic energy equation, moisture conservation equation, and pressure tendency equation make up the set of prognostic equations. The hydrostatic and continuity equations are used as diagnostic equations for geopotential height and vertical motion. The prognostic equations include forcing terms, diabatic heating terms, and sink/source terms, which are regarded as physical processes and are treated separately. The primitive equations can be written in flux form in the sigma coordinates as

$$\begin{aligned} \frac{\partial(p_s u)}{\partial t} + \frac{1}{h_x h_y} \left[\frac{\partial}{\partial x} (p_s u h_y u) + \frac{\partial}{\partial y} (p_s v h_x u) \right] + \frac{\partial}{\partial \sigma} (p_s \sigma u) - f p_s v \\ = - \frac{p_s}{h_x} \frac{\partial \phi}{\partial x} - \frac{R T}{h_x} \frac{\partial p_s}{\partial x} + p_s F_u \end{aligned} \quad 3.1$$

$$\begin{aligned}
\frac{\partial(p_s v)}{\partial t} + \frac{1}{h_x h_y} \left[\frac{\partial}{\partial x} (p_s u h_y v) + \frac{\partial}{\partial y} (p_s v h_x v) \right] + \frac{\partial}{\partial \sigma} (p_s \dot{\sigma} v) + f p_s u \\
= -\frac{p_s}{h_y} \frac{\partial \phi}{\partial y} - \frac{R T}{h_y} \frac{\partial p_s}{\partial y} + p_s F_v
\end{aligned}
\quad 3.2$$

$$\begin{aligned}
\frac{\partial(p_s T)}{\partial t} + \frac{1}{h_x h_y} \left[\frac{\partial}{\partial x} (p_s u h_y T) + \frac{\partial}{\partial y} (p_s v h_x T) \right] + \left[\frac{p}{p_0} \right]^{\kappa} \frac{\partial}{\partial \sigma} (p_s \dot{\sigma} \theta) \\
- \frac{R T}{c_p} \left[-\tilde{D} - \frac{u}{h_x} \frac{\partial p_s}{\partial x} - \frac{v}{h_y} \frac{\partial p_s}{\partial y} \right] = p_s F_T
\end{aligned}
\quad 3.3$$

$$\frac{\partial(p_s q)}{\partial t} + \frac{1}{h_x h_y} \left[\frac{\partial}{\partial x} (p_s u h_y q) + \frac{\partial}{\partial y} (p_s v h_x q) \right] + \frac{\partial}{\partial \sigma} (p_s \dot{\sigma} q) = p_s F_q
\quad 3.4$$

$$\frac{\partial p_s}{\partial t} = -\tilde{D}
\quad 3.5$$

with the hydrostatic and continuity equations given by

$$\frac{\partial \phi}{\partial \sigma} = -\frac{R T}{\sigma}
\quad 3.6$$

$$\frac{\partial(p_s \dot{\sigma})}{\partial \sigma} = \tilde{D} - D
\quad 3.7$$

where the horizontal components of the wind u and v , the temperature T , specific humidity q , and the surface pressure p_s are the model prognostic variables. The geopotential, potential temperature, and vertical motion in sigma coordinates are represented by ϕ , θ , and σ , respectively. The vertical sigma coordinate (σ) is defined by the ratio of the pressure p to the surface pressure p_s (Phillips 1957), h_x and h_y are the map factors for the horizontal x and y coordinates, and p_0 is a standard reference level of 1000 mb. κ is given by the ratio of R , the gas constant for dry air, to c_p , the specific heat at constant pressure for dry air. The mass divergence D is defined by

$$D = \nabla \cdot (p_s \vec{V}) = \frac{1}{h_x h_y} \left[\frac{\partial}{\partial x} (p_s u h_y) + \frac{\partial}{\partial y} (p_s v h_x) \right] \quad 3.8$$

and \tilde{D} is the vertically integrated mass divergence given by

$$\tilde{D} = \int_0^1 \nabla \cdot (p_s \vec{V}) d\sigma \quad 3.9$$

The terms F_u , F_v , F_T , and F_q on the right-hand side (RHS) are forcing terms and represent physical processes such as friction, diffusion, heating and moistening due to cumulus convection and large-scale precipitation, among others. The boundary condition at the model top ($\sigma = 0$) and bottom ($\sigma = 1$) is $\dot{\sigma} = 0$.

The model dynamical equations in flux form can then be written in finite difference and vector notation. Details of the vector and matrix elements can be found in the report by Madala et al. (1987).

3.2 Numerics of the Model

This hydrostatic, primitive equation model uses a terrain-following coordinate system and has a one-way interacting nested grid network. The domains of the fine and coarse grids, with the smoothed model topography used on each, are shown in Fig. 3.1. The coarse grid domain includes the continental United States and extends from 40°W to 140°W and 10°N to 70°N with a horizontal resolution of 2° longitude (170 km at 40°N) by 1.5° latitude (166.5 km). The GALE (inner or fine) grid covers a smaller domain including the eastern half of the United States and extending out over the Gulf Stream from 58°W to 102°W and 23.5°N to 56.5°N with a finer horizontal resolution of 2/3° longitude (56.7 km at 40°N) by 0.5° latitude (55.5 km). With this grid resolution, the integration time step used is 180 seconds on the coarse grid and 60 seconds on the fine grid. The continuous governing equations are written in flux form and the finite difference scheme is a second-order quadratic conserving scheme. The Arakawa C-grid (Arakawa and Lamb 1977) in spherical coordinates is used for horizontal differencing. Lateral boundary conditions suggested by Davies (1976, 1983) are emphasized in the present version of the model at each grid boundary.

In the vertical, both grids use 10 equally spaced sigma levels. The vertical layers and the horizontal staggered C-grid are illustrated in Fig. 3.2 for the simple case of only two model levels. In the vertical, the layers are of varying thickness $\Delta\sigma_k$ with the prognostic variables u , v , T , and q , and the geopotential ϕ defined at sigma levels σ_k . The vertical motion σ in the sigma coordinate is staggered in the vertical, being defined at sigma levels $\sigma_k + \Delta\sigma_k/2$ at the boundaries between the vertical layers.

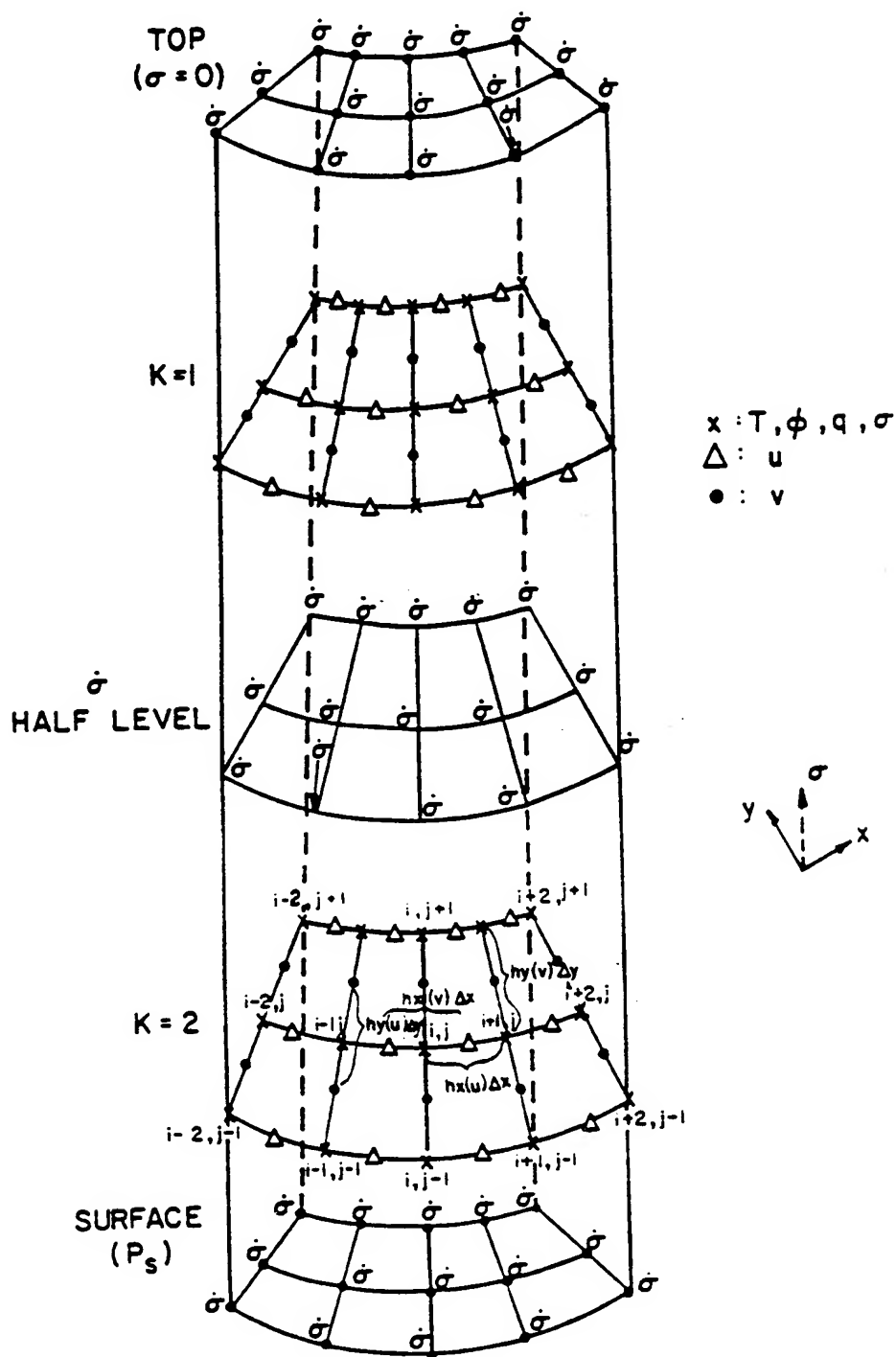


Figure 3.2. Horizontal staggered C-grid and vertical grid network utilized in the model for the simple case of two model sigma levels ($K=2$).

3.2.1 Split-Explicit Time Integration

The model's time integration scheme is the split-explicit method which allows larger time steps by effectively separating various terms in the prognostic equations into parts governing the slow-moving Rossby modes and fast-moving gravity modes. In applying the split-explicit scheme of Madala (1981) to the nested model, the time step on each grid satisfies the non-linear CFL condition with centered differencing for the phase speed of the fourth internal vertical gravity mode of the model. Initial estimates of the tendencies of the model variables for all the terms are computed with a large time step Δt . These explicit first estimates of the tendencies of the mass (surface pressure p_s and temperature T) and wind components (u and v) are then corrected for the motion of the higher frequency gravity modes (external and first two internal modes).

These corrections to the mass and momentum tendencies are computed by integrating, at shorter time steps, the amplitudes of the deviations of the divergence and generalized geopotential from their values at time t , for each of the first three vertical modes. Time steps of $\Delta t/8$, $\Delta t/4$, and $\Delta t/2$ are used for the external modes and first two internal vertical modes, respectively. The average of these deviations, over the interval of twice the large time step, is then used to correct the initial estimate of the variables, with the non-linear forcing held constant. Madala's split-explicit scheme is extremely cost-effective, requiring only 20-25% of the computer time expended by explicit methods. Plus, Sashegyi and Madala (1990) showed that this technique reduces the amplitude of the freely-propagating higher-frequency gravity waves.

3.2.2 Lateral Boundary Conditions

To update the flow at the horizontal boundaries of each grid during the integration of the NRL/NCSU mesoscale model, boundary conditions are required for the horizontal components of the wind field and for the mass and humidity fields. Surface pressure p_s , temperature T , and specific humidity q are defined at the lateral boundary. The wind components are staggered in the C grid, which allows the tangential wind to be defined at the boundary and the normal wind to be staggered half a grid point in from the boundary. Idealized boundary values and tendencies for the coarse grid are derived from 12-hourly NMC 2.5° hemispheric analyses. The fine-grid boundary values are obtained from the coarse grid integration.

Computed model variables are relaxed to the boundary values in a boundary zone of six points using the Davies scheme (1976, 1983). The model variables are adjusted at each time step according to:

$$a = (1 - \alpha) a_m + \alpha a_b \quad 3.10$$

where 'a' is the independent model variable $p_s u$, $p_s v$, p_s , $p_s T$, or $p_s q$, and is a linear combination of the model computed value a_m and the prescribed boundary value a_b . Following Gronas et al. (1987), α is defined as a quadratic function of the distance (n) from the lateral boundary in units of the grid spacing:

$$\alpha = \begin{cases} 1 & \text{for } n = 0 \\ \left[\frac{6.5 - n}{6} \right]^2 & \text{for } 1 \leq n \leq 5 \\ 0 & \text{for } n \geq 6 \end{cases} \quad 3.11$$

Coarse-grid boundary values are computed at each time step by a linear interpolation in time from the 12-hourly NMC analyses. At each time step, model variables on the coarse grid are linearly interpolated to the six points in the boundary zone

of the fine mesh. Then these values are linearly interpolated in time to the intermediate time steps for the fine grid.

3.3 Physics of the Model

Physical parameterizations suitable for simulating extratropical cyclones are used. These model physics are described below.

3.3.1 Planetary Boundary Layer

The planetary boundary layer is parameterized using a single layer with the fluxes of heat, momentum, and humidity computed using a generalized similarity theory, in which the drag coefficients are stability dependent (Chang 1981). The exchange of momentum, moisture, and sensible heat between the surface and the lowest model layer is proportional to the differences in the wind velocity, humidity, and temperature between those two levels and is given by:

$$\frac{\partial p_s V}{\partial t} = -g \frac{\partial \tau}{\partial \sigma} = -\frac{g \tau_s}{\Delta \sigma} \quad 3.12$$

$$\frac{\partial p_s T}{\partial t} = g \frac{\partial H}{\partial \sigma} = \frac{g H_s}{\Delta \sigma} \quad 3.13$$

where τ is the stress, H is the sensible heat flux, and τ_s and H_s are the respective surface values. A similar relationship holds between the specific humidity q and the moisture flux E . The magnitudes of the surface stress and surface fluxes of sensible heat and humidity are related to the values of the wind, potential temperature, and specific

humidity in the lowest model layer. In this parameterization, only positive heat and moisture fluxes are computed. Heat and moisture loss to the ocean surface is not considered.

3.3.2 Horizontal Diffusion

The model has horizontal diffusion to control noise accumulation during integration. The diffusion is of second order and is applied directly on the horizontal sigma surfaces using a forward time differencing scheme. The model variables for the flux form of the equations are smoothed by application of the two dimensional diffusion operator $\nabla \cdot K_H \nabla$. The operator is applied directly to the wind components $p_s u$ and $p_s v$, while for the temperature $p_s T$, specific humidity $p_s q$, and surface pressure p_s , the operator is applied on the deviations from values computed at the same sigma levels for the U.S. standard atmosphere. The diffusion coefficient varies with latitude as the square of the longitudinal map factor h_x , so that the coefficient of diffusion decreases as the longitudinal grid distance decreases with increasing latitude. We define the diffusion coefficient K_H as

$$K_H = \frac{[h_x \Delta x]^2 \mu}{2 \Delta t} \quad 3.14$$

where μ is a fixed non-dimensional diffusion coefficient, Δx and Δt are the latitudinal grid spacing and time step, respectively. A value of $\mu = 0.005$ was found to provide sufficient smoothing, without excessively damping the synoptic scale waves on the coarse grid. On the fine grid, a value of $\mu = 0.006$ is used to provide a little more damping of the small scale features.

3.3.3 Cumulus Convection

Convective heating, precipitation, and moistening of the environment are parameterized using the method developed by Kuo (1974) and modified by Anthes (1977). Convective heating is released in an atmospheric column when there is conditionally unstable stratification and moisture convergence. Kuo assumed that deep convection occurs in a conditionally unstable environment where there is large-scale convergence at low levels in the troposphere. It is further assumed that the deep clouds dissipate and mix horizontally with the environmental air, releasing heat and moisture. The total moisture used to form the clouds in a given area is given by the total horizontal convergence of moisture into that area. The converged moisture is partitioned into moistening and heating parts where the ratio is determined by the vertically averaged relative humidity of the column. The vertical heating profile is determined by the difference between the predicted temperature sounding and the moist adiabat constructed from the boundary layer temperature and humidity.

First, the horizontal moisture convergence M is computed for all model layers using

$$M = \nabla \cdot (p_s \vec{V} q) = \frac{1}{h_x h_y} \left[\frac{\partial}{\partial x} (p_s u h_y q) + \frac{\partial}{\partial y} (p_s v h_x q) \right] \quad 3.15$$

The total horizontal moisture convergence M_t is computed by summing over all the layers except the top layer, where M_t is given by

$$M_t = -\frac{p_s}{g} \int_{\sigma}^1 \nabla \cdot (p_s \vec{V} q) d\sigma \quad 3.16$$

The moisture convergence in the top layer is computed separately, since it is assumed that clouds do not penetrate into the top layer. The air column is tested for convectively

unstable lapse rates if the total moisture convergence M_t exceeds a critical value. The total moisture used in cloud formation is dependent on the vertically averaged relative humidity r_m in the environment. This moisture can be partitioned into a fraction $(1-b) M_t$, which is condensed and precipitated out in the cloud, and a fraction $b M_t$ which moistens the cloud (or condenses and re-evaporates at the same level), where the fraction is defined as $b = 1-r_m$. Assuming the cloud dissipates and mixes with the environmental air, then the moistening and heating rates of the environment can be easily computed. The vertically averaged heating rate Q_c and moistening rate D_c satisfy

$$(1-b) M_t = \frac{c_p Q_c}{g L_c} \quad 3.17$$

$$b M_t = \frac{D_c}{g} \quad 3.18$$

where L_c is the latent heat of condensation. The precipitation P_c from cumulus clouds follows from

$$P_c = (1-b) g M_t \quad 3.19$$

3.3.4 Large-Scale Precipitation

The parameterization of large-scale or non-convective precipitation/heating follows Manabe et al. (1965); that is, the excess moisture in a supersaturated layer within a stably stratified environment is condensed out isobarically, leaving the layer saturated. The evaporation of precipitation in unsaturated layers below the cloud base is also accounted for.

Following the outline in Haltiner and Williams (1980), if q and T are the initial values of the specific humidity and temperature of the supersaturated layer, then the resulting saturation specific humidity q_s is given by

$$q + \Delta q = q_s(T + \Delta T) \cong q_s(T) + \left[\frac{\partial q_s}{\partial T} \right]_p \Delta T \quad 3.20$$

where Δq and ΔT are the changes (assumed small) in the specific humidity and temperature of the layer. Using the Clausius-Clapeyron equation to define the saturation vapor pressure as a function of the temperature and rearranging, the change in the specific humidity is given by:

$$\Delta q = \frac{q - q_s}{1 + L_c^2 q_s / c_p R_v T^2} \quad 3.21$$

where R_v is the gas constant for water vapor. Δq is reduced at each model level by a factor to account for that fraction which re-evaporates in the next layer below. The corresponding ΔT at each level is given by $c_p \Delta T = -L_c \Delta q$, and the total large-scale non-convective precipitation P_L is given by:

$$P_L = -\frac{p_s}{g} \int_0^1 \nabla q \, d\sigma \quad 3.22$$

3.3.5 Dry Convective Adjustment

Also following Manabe et al. (1965), a dry convective adjustment is applied to remove any absolutely unstable lapse rates in the model atmosphere. In the real atmosphere, unstable lapse rates, which can develop due to large surface fluxes of sensible heat for example, are removed through dry convection (plumes, rolls, etc). In the model, these mechanisms are sub-grid scale. However, such unstable lapse rates will produce unrealistically large vertical velocities in the model. To resolve this problem, the

vertical column at each grid point in the model domain is tested for any absolutely unstable lapse rates. Then, for each sequence of unstable layers in the vertical, the sub-grid scale vertical mixing is parameterized in the model following Manabe et al. (1965). It is assumed that parcels in unstable layers are lifted adiabatically to the next layer, exchanging their heat at constant pressure, while conserving the total enthalpy. The exchange of heat takes place until the temperatures of the unstable layer and the first stable layer above the unstable layers are adjusted to a neutral lapse rate.

3.3.6 Surface Parameters

At the earth's surface, weekly-averaged sea surface temperatures (SST) of 0.5° resolution, taken from the GALE datasets, are interpolated to the model's fine grid. Climatological SSTs for the months of January and February of one degree resolution, taken from Reynolds (1982), are interpolated temporally to obtain a weekly mean and interpolated spatially to the coarse grid of the model. A sea/ice boundary is derived from the U.S. Navy's climatological sea/ice boundaries for month of January. Model topography for both grid domains is obtained from Navy 10-minute global topographical data.

3.4 Model Initialization

The vertical mode initialization scheme of Bourke and McGregor (1983), as applied by Sashegyi and Madala (1990, 1992a) and Harms et al. (1992a), is used to reduce the undesirable gravity wave oscillations in numerical integrations of the NRL/NCSU mesoscale model. The scheme applies a correction to the Rossby modes by averaging a separate integration for those gravity modes whose phase speeds are much

larger than meteorological systems. In this scheme, filtering conditions for the inertia-gravity waves are applied to the model dynamical equations to derive linear diagnostic equations for the mass and divergence fields for the first few vertical modes of the limited-area model. The process sets time derivatives of the gravity-wave oscillations resulting from imbalances between the initial mass and momentum fields to zero by decomposing the total model tendencies into normal modes. With suitable boundary conditions, the equations are then solved iteratively for the first three vertical modes of the numerical model to remove the high frequency gravity waves from the initial conditions. The scheme has been shown to be an application of the normal mode initialization scheme, developed by Machenhauer (1977) and Baer (1977) and used in global models (for example Andersen 1977; Daley 1979; Williamson and Temperton 1981), without the horizontal structure of the normal modes having to be computed (Juvanon du Vachat 1986; Temperton 1988).

As in Bourke and McGregor (1983), the mass field remains fixed at the lateral boundaries of the model. Bourke and McGregor assumed that the divergence does not change at the boundary. To provide a more realistic boundary condition, an approximate mass divergence is computed inside the lateral boundary using the thermodynamic equation. In the present scheme, the resulting changes to the tangential and normal wind are computed assuming no change in the stream function and velocity potential along the lateral boundaries of the model domain. By using the C grid and defining the tangential wind at the lateral boundary and the normal wind staggered half a grid point inside the lateral boundary, the changes in the wind field along the boundary are then naturally consistent with the changes in the integrated vorticity and mass divergence over the model domain.

Following Temperton and Williamson (1981), the vertical structure of the model's normal modes is obtained by separating the linear and non-linear terms of the

governing equations and then linearizing about a basic state at rest with a mean temperature $T^*(\sigma)$, which varies only in the vertical. A generalized geopotential is defined whose derivative gives the horizontal pressure gradient in the horizontal equations of motion and whose time tendency is related to the divergence. A separation of the vertical structure of the model variables is then possible. The model dynamical equations are expressed as time tendencies of mass-weighted vorticity ζ , mass divergence D , and generalized geopotential Φ . The equations with the β term included with the non-linear terms on the RHS are written as:

$$\frac{\partial \zeta}{\partial t} + f D = A_{\zeta} \quad 3.23$$

$$\frac{\partial D}{\partial t} + \nabla^2 \Phi - f \zeta = A_D \quad 3.24$$

$$\frac{\partial \Phi}{\partial t} + \lambda_k D = A_{\Phi} \quad 3.25$$

The freely-propagating inertia-gravity waves in the model are solutions to these linearized equations with the forcing terms on the RHS of the equations equal to zero. Here, f is the Coriolis parameter, D is the mass divergence, u and v are the horizontal wind components, and Φ is the generalized geopotential, defined as:

$$\Phi = p_s \left[\phi - \phi_s + R T^* - \phi^* \right] \quad 3.26$$

where p_s is the surface pressure, ϕ is the geopotential, ϕ_s is the surface geopotential, R is the gas constant for dry air, and ϕ^* is the average geopotential on the sigma surface of the model. Equations 3.23 - 3.25 describe the shallow water equations, where the phase speed of the free gravity modes is given by $\lambda_k^{1/2}$, where λ_k (which can be represented as

an equivalent depth multiplied by the acceleration due to gravity) is the eigenvalue for the k^{th} mode.

The filtering conditions of Bourke and McGregor,

$$\frac{\partial D}{\partial t} = \frac{\partial}{\partial t} [f\zeta - \nabla^2 \Phi] = 0 \quad 3.27$$

on the divergence D and the ageostrophic "vorticity" $f\zeta - \nabla^2 \Phi$, need to be applied to Eqs. 3.23 - 3.25 for only the first three vertical modes, whose phase speeds of the gravity modes are much larger than about 25 m s^{-1} . Since the terms on the RHS of Eqs. 3.23 - 3.25 depend on the vorticity, divergence, and geopotential, the resulting set of equations is solved iteratively (Bourke and McGregor 1983).

The resulting changes to the horizontal wind field are computed from the changes in the mass divergence and mass weighted vorticity by solving the following Poisson's equations:

$$\nabla^2 \Delta\chi = \Delta D \quad 3.28$$

$$\nabla^2 \Delta\Psi = \Delta\zeta \quad 3.29$$

for the changes in the velocity potential $\Delta\chi$ and the stream function $\Delta\Psi$ for each sigma level of the model. Then changes to the mass weighted wind follow from:

$$\Delta(\overline{p_s}u) = \delta_x \Delta\chi - \delta_y \Delta\Psi \quad 3.30$$

$$\Delta(\overline{p_s}v) = \delta_y \Delta\chi + \delta_x \Delta\Psi \quad 3.31$$

Finally, following Temperton (1984), the changes in the surface pressure p_s and the temperature T can be derived directly from changes in the generalized geopotential.

4. APPLICATION OF THE BRATSETH SCHEME FOR THE ANALYSIS OF GALE DATA

The mesoscale weather prediction model described in Chapter 3 provides a short-range forecast which serves as the background field, or first guess, for our numerical analysis. Following a brief introduction of various analysis techniques, an in-depth description of the NRL/NCSU objective analysis scheme, which was developed and tested during the course of this research, is given.

4.1 Introduction

During the 1960s and 70s, the most widely used objective analysis technique in operational data assimilation and forecast systems was the method of successive correction. This type of analysis was first introduced by Bergthorsson and Döös (1955), and a number of versions have been developed by Cressman (1959), Barnes (1973), and others. It is still widely used for the analysis of mesoscale systems in the research community (Koch et al. 1983; Benjamin and Seaman 1985; for example). However, these successive correction schemes possess a couple of undesirable attributes. First, the analysis converges to the data, and if a first guess is used, then too much attention is paid to the observations relative to the first guess. Second, observations in regions of high data density are given excessive weight relative to observations in areas of low data density.

In the 1980s, emphasis shifted in operational community toward the more mathematically complex and computationally expensive method of statistical

interpolation, or better known as optimal interpolation. With optimal interpolation, analysis errors are minimized with respect to the spatial structure of observational and forecast errors. A concise review of objective analysis can be found in the paper by Schlatter (1988). Recently the method of optimum interpolation has been applied with success to operational limited-area modelling systems (DiMego 1988; Benjamin 1989; Mills and Seaman 1990).

A paper by Bratseth (1986) has caused a recent resurgence of the successive correction method. He introduced a successive correction scheme, in which the solution converges toward the solution obtained by optimal interpolation. His technique alleviates the aforementioned shortcomings of previous successive correction methods by utilizing the forecast error covariance to define weights which are reduced in regions of higher data density by use of a normalizing factor. Additionally, the Bratseth method requires much less computational expense than does optimal interpolation methods. Therefore, it is very attractive for use for a limited-area forecast system when only limited resources are available. This approach to successive correction methodology is currently being used operationally in a multivariate analysis for the limited-area forecast system at the Norwegian Meteorological Institute (Gronas and Midtbo 1986). An algorithm similar to the Bratseth scheme has been applied at the U.K. Meteorological Office to directly insert data into both the global and regional models (Lorenc et al. 1991). With each iteration of the scheme, the mass and wind variables are updated in a sequential fashion. To maintain balance in their models, changes to the geostrophic component of the wind are derived from any mass changes; the wind changes are non-divergent and the divergence during integration is damped.

A simplified multivariate, successive correction objective analysis scheme using the Bratseth method has been developed at the U.S. Naval Research Laboratory (NRL) and North Carolina State University (NCSU) to analyze data collected during the Genesis

of Atlantic Lows Experiment. During intensive observing periods, more frequent upper air soundings were taken at selected National Weather Service (NWS) sites over the region of the eastern U.S., supplemented by additional sites along the coast, dropsondes deployed from aircraft offshore, and a denser set of surface observations (Dirks et al. 1988; Raman and Riordan 1988). As has been the practice with limited-area forecast systems using optimal interpolation, the length scales of the correlation functions in the Bratseth scheme are reduced from those used with global models to provide more detail at the smaller scales (DiMego 1988). After a number of iterations of the scheme, the length scale of the correlation functions is further reduced for subsequent iterations to speed the convergence of the scheme (Gronas and Midtbo 1986; Seaman 1988). A prior forecast generated by the NRL/NCSU mesoscale model is used, as in the operational limited-area models, to provide a first guess for the analysis scheme. With the coarse resolution of the upper-air network, it is only by using such a mesoscale model to generate a first guess, is there any hope that any realistic mesoscale features generated by the model will be preserved or even enhanced by the analysis. The analysis of the deviations of the data from the first guess covers a region similar to the model's fine grid but at a lower resolution of 1.5° in latitude and longitude. The grid spacing used is consistent with the average upper air station spacing of about 350 km over the eastern U.S. To remove bad data or data inconsistent with the scales resolved by the numerical model, an efficient quality control procedure was implemented in a manner similar to DiMego (1988).

In this chapter, a general description of our objective analysis method is given and a qualitative evaluation of the scheme is provided. Experiments with the analysis scheme are described. The vertical mode initialization scheme of Bourke and McGregor (1983) is used to diagnose the divergent circulations associated with the analyzed mesoscale features and upper-level jet streaks. The interaction of these secondary circulations in the jet streaks can be important for cyclone development (see Uccellini et al. 1984; Uccellini

and Kocin 1987; for example). The impact of these mesoscale circulations produced by the analysis on subsequent forecasts is tested and precipitation forecasts are compared to observed values.

4.2 The NRL/NCSU Objective Analysis Scheme

A simplified application of the Bratseth (1986) scheme has been developed, as compared to the full multivariate implementation used at the Norwegian Meteorological Institute by Gronas and Midtbo (1986). In our scheme, univariate analyses of the mass and wind fields are first performed using the successive correction approach of Bratseth. The deviations from our first-guess field, which is derived from a prior 12-h forecast valid at the analysis time, are analyzed. To provide the coupling between the wind and mass fields, the analyzed wind is used as an initial estimate of the geostrophic wind in a further iteration on the geopotential. The geostrophic wind is used to extrapolate the geopotential to the grid point locations in a fashion similar to Cressman (1959), but consistent with the Bratseth scheme. In each subsequent iteration, an improved geostrophic wind estimate is then defined by the new geopotential gradient, and not by the original wind as is widely used with the Cressman scheme. The wind analysis is then corrected for the new geostrophic wind as in Kistler and McPherson (1975). A further analysis of the wind is performed to improve the larger scales of the ageostrophic wind. The temperature is then corrected with the new geopotential thicknesses. The resulting analysis corrections are interpolated to the model sigma coordinates to update the first-guess forecast, so as to not destroy any balance or small mesoscale features generated by the model.

A set of upper-air soundings, which were interpolated to 10-mb levels from the surface up to 100 mb, and surface data for the second Intensive Observing Period (IOP)

of GALE were obtained from the GALE Data Center (GDC) at Drexel University (Mercer 1987). The data domain included the eastern U.S. and western North Atlantic from 115°W to 45°W in longitude and from 10°N to 60°N in latitude. A higher density of upper-air soundings and surface data is found in the inner GALE region covering the Carolinas and southern Virginia from the Gulf Stream to the Appalachians. An analysis grid covered the data domain with a resolution of 1.5° in latitude and longitude extending from 116°W to 44°W in longitude and from 9°N to 61.5°N in latitude. To correct the model forecast first guess in areas with no data over the ocean and around the lateral boundaries of the analysis grid, bogus data derived from the NMC analysis are used. After the analysis is complete, the resulting corrections are merged with corrections to the first guess derived from the NMC analysis in a zone along the lateral boundaries of the analysis grid. The corrections are then bicubically interpolated to the model fine grid and added to the original first guess on the pressure surfaces to provide a final analysis. The corrections themselves are also interpolated in the vertical to the sigma surfaces of the model to correct the original first-guess model forecast. By applying the vertical mode initialization scheme, both the divergent and the ageostrophic wind are derived from the analysis.

A further important part of any analysis scheme of real data is the quality control of the data prior to the analysis. Data, which are inconsistent with the first guess or with neighboring observations or are of a scale too small to be resolved by the analysis scheme, must be removed to prevent aliasing into the larger scales in the analysis.

4.2.1 Data Preparation and Quality Control

An efficient quality control procedure has been developed for use with the analysis scheme, similar to those at operational weather centers. The soundings are first

checked for hydrostatic consistency and smoothed, retaining data at 50-mb levels, to be more representative of our 10-layer model vertical resolution. Similar procedures to those used at NMC in the regional analysis (DiMego 1988) are followed by performing a "gross" check in which observations with large deviations from the first-guess values and any missing data are removed. In a simplified "buddy" check, observations not agreeing with neighboring observations are removed. Close observations are replaced by an average "super" observation and any remaining isolated observations are eliminated. To smoothly merge with the NMC analysis at that synoptic hour, bogus data derived from the NMC analysis at that time are added in data void regions such as over the ocean or at the lateral boundary of the analysis domain. Over the ocean, the NMC analysis acts as a test of our scheme. A further advantage of the quality control is that by removing bad and missing data prior to the analysis our analysis code is able to be vectorized to run rapidly on a supercomputer. Using these procedures, the influence of any data errors and biases is reduced. The details of each of the components of the data preparation and quality control follow.

a) Hydrostatic check and smoothing

After being checked for hydrostatic consistency, the soundings are smoothed in the vertical. The temperatures and the u and v wind components were averaged over 20-mb intervals weighted by the log of pressure for the temperatures and by the mass for the u and v wind components. The humidities, which were more noisy (Kreitzberg, personal communication), were smoothed by averaging over 50-mb intervals using the mixing ratios weighted by the mass. Consistent geopotentials were then recomputed and variables retained only for levels every 50 mb. For each sounding, a "daily average" surface temperature is computed by linear extrapolation from levels above the boundary

layer. The sea level pressure is computed by extrapolation of the average surface temperature to sea level, and a plateau correction is added (Saucier 1955). To extrapolate heights to pressure levels below ground level, an average of the surface temperature and the daily average is used. For efficiency, the soundings are sorted into 5° latitude/longitude boxes for each pressure level, at 50-mb increments from sea level to 100 mb.

b) Gross errors

At each pressure level, data are checked for gross errors, as compared to the first-guess analysis, which has been interpolated to the pressure surfaces from the earlier 12-h model forecast. In this gross check, those upper-air observations that differ in magnitude by more than four standard deviations from the first guess are rejected. Any missing data specified in the sounding are also removed. For the sea-level pressure, those values that differ in magnitude by more than two and a half times the standard deviation are rejected. Estimates of the standard deviation of the observations from the first-guess forecast are obtained by adding a forecast error growth to the observational error. The values used are slight modifications to those used at operational centers (DiMego 1988; Shaw et al. 1987). For sea-level pressure, an observational error of 1.5 mb is used with forecast error growth of 1.0 mb in 6 h to give a first-guess error of 3.5 mb for a 12-h forecast using our limited-area model. For the upper-air variables, the values used for the observational error and the forecast error growth are listed in Table 4.1. For the remaining quality-control procedures and the analysis, only the deviations of the data from the first guess are retained.

TABLE 4.1. Standard deviation of the observational errors and forecast error growth for a six-hour forecast period in parentheses. These are the input error statistics for the objective analysis.

Pressure (mb)	Height (m)	Temperature (°C)	Rel humidity (%)	u,v Wind (m s ⁻¹)
100	20 (17)	2.0 (0.7)	----	3.5 (1.3)
150	18 (18)	1.8 (0.6)	----	4.0 (1.4)
200	15 (18)	1.8 (0.5)	----	4.0 (1.5)
250	14 (18)	1.5 (0.6)	----	4.0 (1.6)
300	14 (18)	1.0 (0.6)	17 (4)	4.0 (1.6)
350	14 (17)	1.0 (0.5)	15 (4)	4.0 (1.7)
400	12 (16)	1.0 (0.5)	13 (4)	3.5 (1.7)
450	10 (14)	1.0 (0.4)	13 (4)	3.5 (1.6)
500	9 (12)	1.0 (0.3)	13 (4)	3.0 (1.6)
550	8 (10)	1.0 (0.3)	13 (3)	3.0 (1.5)
600	7 (9)	1.0 (0.3)	12 (3)	3.0 (1.4)
650	6 (8)	1.2 (0.3)	12 (3)	3.0 (1.3)
700	6 (8)	1.3 (0.3)	12 (2)	2.5 (1.2)
750	6 (8)	1.4 (0.3)	12 (2)	2.5 (1.2)
800	6 (8)	1.5 (0.4)	13 (2)	2.5 (1.1)
850	6 (8)	1.5 (0.5)	13 (2)	2.5 (1.1)
900	5 (8)	1.8 (0.5)	13 (2)	2.5 (1.1)
950	5 (8)	1.8 (0.6)	13 (2)	2.5 (1.1)
1000	5 (8)	1.8 (0.6)	13 (2)	2.5 (1.1)

c) Buddy check

A simplified buddy check procedure is used, in which deviations of the observations from the first guess are compared with the deviations from all neighboring observations including itself. Each observation is compared with itself and all the others, within a maximum distance of 833 km (equal to 7.5° of latitude). The maximum allowed deviations for a pair of observations is a linear function of the cartesian distance between the observations, and is equal to one standard deviation at zero distance and increases to 3.5 times the standard deviation at the maximum distance.

d) Average close observations and eliminate isolated observations

To speed the convergence of the iterative analysis scheme, observations in close geographical proximity are combined into a single "super" observation. Each 5° box is divided into smaller boxes of 1.25° longitude by 1° latitude, and an average of all the data within each smaller box is computed, assigning the average latitude and longitude for the position. To further prevent isolated data from adversely affecting the analysis (generating circular corrections), any remaining isolated data are removed. For each data box with less than two of the surrounding eight boxes having any data, the data in that box are removed.

e) Merge with NMC analysis

In regions of no data over the ocean, additional "bogus" soundings, derived from the difference between the first-guess forecast and the NMC 2.5° hemispheric analysis, are used to merge our analysis smoothly with the NMC analysis over the ocean at

synoptic hours. At off-synoptic times, no bogus soundings are added and the analysis returns to the background in regions of no data. To match the resolution of the NMC analysis, two bogus soundings spaced $5/3^\circ$ apart in latitude and longitude are used in each empty interior box requiring bogus data, and one sounding is used at the center of each boundary box requiring bogus data. The requirement for adding bogus data to an empty box depends on the availability of data in the neighboring boxes. In this case, additional bogus soundings have been added over the Gulf of Mexico and off the east coast of the U.S. An example for 1200 UTC January 25 in Fig. 4.1a shows the locations of the geopotential height data at 500 mb after the quality control. Very few upper-air real observations (shown by the crosses) are found over the oceans, where NMC "bogus" data (shown by stars) have been added. For the sea-level pressure, shown in Fig. 4.1b, many more observations were available over the ocean, many of which are superobs.

4.2.2 Analysis Interpolation

The attractive features of the Bratseth successive correction scheme (1986) for the interpolation of the observations to the analysis grid are: 1) the weights are dependent on the covariance between observations and, therefore, are dependent on the accuracy of the observations, 2) the weights are reduced in regions of higher-data density, and 3) the scheme converges to that obtained by optimal interpolation. As has been done in the operational implementation of this scheme in Norway by Gronas and Midtbo (1986), the width of the modelled covariance function is reduced after three or four iterations to speed the convergence of the scheme at the smaller scales. Further passes of the analysis scheme on a smaller grid can be easily added in regions of higher observational density, such as in regions of drifting buoys or dropwindsondes. This was applied to the case of

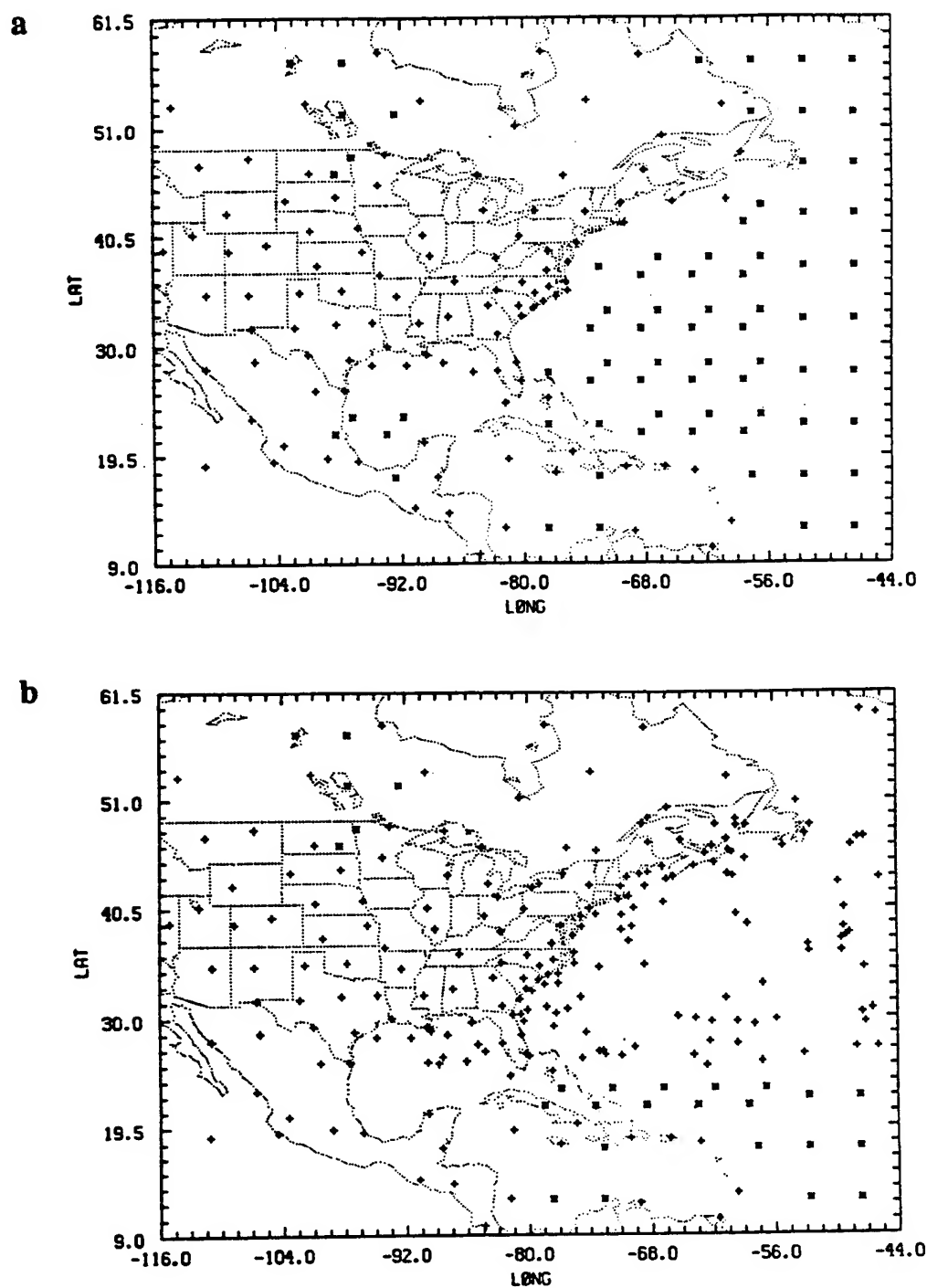


Figure 4.1. The location of the data for (a) the geopotential height at 500 mb and (b) the sea level pressure after quality control. The observations are indicated by the '+', while bogus values are indicated by '*'. The analysis grid is indicated by the tick marks along the domain boundary.

a hurricane with an earlier version of the analysis based on the Barnes scheme by Shi et al. (1991). The steps are further described below.

a) Univariate analysis of the mass and wind field

In the first step of the analysis scheme, univariate analyses of sea-level pressure, geopotential, temperature, and humidity corrections to the first guess are successively adjusted at each iteration. In the Bratseth scheme, estimates of both the interpolated correction and the observation correction are computed using the iterative formulas. For the geopotential corrections ϕ to the first-guess values of geopotential provided by an earlier 12-h forecast, the interpolated value at the grid point "x" is given by:

$$\phi_x^{(v+1)} = \phi_x^{(v)} + \sum_{j=1}^n \alpha_{xj} \left[\phi_j^o - \phi_j^{(v)} \right] \quad 4.1$$

and the estimate of the value of observation correction is given by:

$$\phi_i^{(v+1)} = \phi_i^{(v)} + \sum_{j=1}^n \alpha_{ij} \left[\phi_j^o - \phi_j^{(v)} \right] \quad 4.2$$

where ϕ_j^o is the value of the observation, and $\phi_x^{(v)}$ and $\phi_j^{(v)}$ are the interpolated values at the grid point and the estimate of the observation value, respectively, for the v^{th} iteration.

The starting corrections $\phi_x^{(1)}$ and $\phi_j^{(1)}$ are zero. The weights, which are dependent on the covariance of the corrections for the first guess, are in each case given by:

$$\alpha_{xj} = \frac{\overline{\phi_x^{(1)} \phi_j^{(1)}}}{m_j \sigma^2} = \frac{\rho_{xj}}{m_j} \quad 4.3$$

$$\alpha_{ij} = \frac{\overline{\phi_i \phi_j}}{m_j \sigma^2} = \frac{\rho_{ij} + \epsilon^2 \delta_{ij}}{m_j} \quad 4.4$$

where the covariances are defined in terms of a correlation function ρ for the true values ϕ^t , and ϵ^2 is the ratio of the observation error variance σ_ϵ^2 to the first-guess (forecast) error variance σ^2 . For the forecast error variance, we use the same variance used in the quality control for the variance of the observations from the first-guess forecast listed in Table 4.1. A "local data density" m_j is defined at the observation location by

$$m_j = \frac{1}{\sigma^2} \sum_{k=1}^n \overline{\phi_j \phi_k} = \sum_{k=1}^n [\rho_{jk} + \epsilon^2 \delta_{jk}] \quad 4.5$$

The correlation function $\rho(r)$ for the geopotential corrections ϕ is modeled as a Gaussian,

$$\rho(r) = e^{-(r/d)^2} \quad 4.6$$

which is a function of the distance r between observations. The correlation length scale "d" is defined by 500 km for the first 3 or 4 iterations and by 275 km for one additional iteration. Since our mesoscale model can resolve smaller scale mesoscale features than can operational regional models, a somewhat smaller length scale is used, as compared to that used at NMC (577 km) by DiMego (1988). After the first pass of our analysis scheme, the data are again checked for inconsistency with the first-pass analysis itself. Any inconsistent data, which differ more than 2.5 times (1.5 times for sea-level pressure) the standard deviation from the first pass, are removed and the first pass is repeated. The same correlation function is used for the univariate analysis of sea-level pressure, temperature, and relative humidity. With observation errors included, the estimate of observation is not equal to the analyzed value interpolated to the observation location, but

it converges rapidly to the value of the observation itself (Bratseth 1986). For a fixed length scale of 500 km, the convergence of the observation estimate and the convergence of the analyzed value at the observation location are shown in Fig. 4.2. The convergence is measured with respect to the number of analysis iterations. When the length scale is reduced after just 3 or 4 iterations, the resulting rms differences for both the observation estimate and analyzed value are substantially reduced, as depicted in Fig. 4.2. It can be noted however, that if there was no observation error, they would be the same.

For the univariate analysis of wind corrections to the first-guess wind field, different correlation functions are used. The correlation functions for the wind components can be derived from the correlation function $\rho(r)$ for the geopotential (Gronas and Midtbo 1986). The functional form of the correlation functions ρ_u and ρ_v for the components of the wind field are given by

$$\rho_u = \left[1 - \frac{(y-y_j)^2}{d_u^2} \right] \rho(r) \quad 4.7$$

$$\rho_v = \left[1 - \frac{(x-x_j)^2}{d_u^2} \right] \rho(r) \quad 4.8$$

where $\rho(r)$ is the correlation function for the geopotential, (x,y) and (x_j,y_j) are the cartesian positions of two observations. These correlations effectively give smaller weights across the direction of the wind than along it without having to compute wind direction as in Benjamin and Seaman (1985). A modified length scale " d_u " is used which is different from the length scale " d " used for $\rho(r)$. A value of 700 km is assigned for d_u , whereas the length scale for $\rho(r)$ is 500 km. This value of d_u fits the length scale found by Hollingsworth and Lonnberg (1986), where the transverse correlations in the

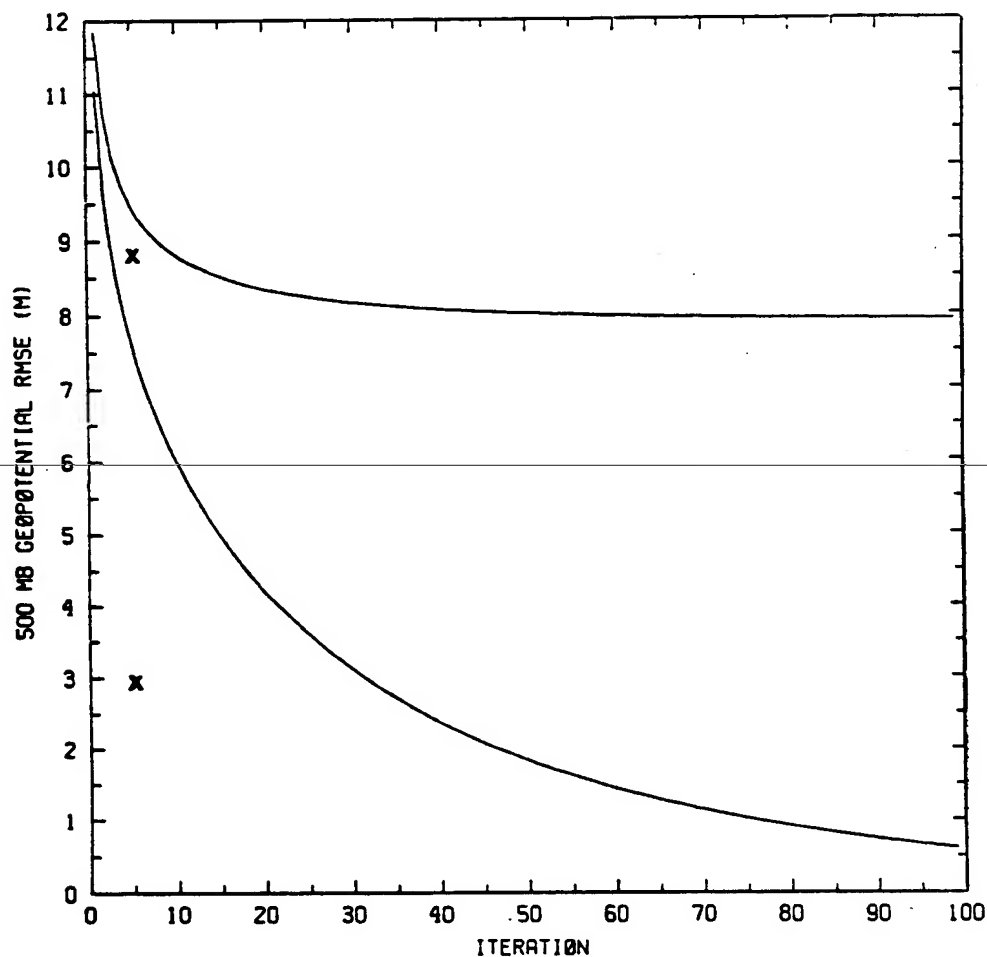


Figure 4.2. The root mean square (rms) of the difference between the observation estimate and the observation value for the geopotential at 500 mb (lower curve) as a function of the iteration number. The upper curve shows the rms of the difference between the analysis value interpolated to the observation point and the observation value. The rms values obtained after four iterations followed by a further iteration with a reduced length scale are indicated by the X's.

wind reach zero. After 3 to 4 iterations, the length scales, d_u and d_v , are reduced to 380 km and 275 km, respectively, for one more iteration to again speed convergence.

b) Geostrophic enhancement of the geopotential

A further four iterations are used for the geopotential correction, using improving estimates of the geostrophic wind at each iteration to extrapolate the geopotential correction to the grid points. An initial estimate of geostrophic wind is obtained from the previous univariate u , v wind corrections by linear interpolation. The interpolated value $\phi_x^{(v+1)}$ at the grid point is now given after the v^{th} iteration by

$$\phi_x^{(v+1)} = \phi_x^{(v)} + \sum_{j=1}^n \alpha_{xj} \left[\begin{aligned} &\phi_j^o - \phi_j^{(v)} - c_j (y - y_j) f_j \left\{ u_g^{(v)} - u_g^{(v-1)} \right\}_j \\ &+ c_j (x - x_j) f_j \left\{ v_g^{(v)} - v_g^{(v-1)} \right\}_j \end{aligned} \right] \quad 4.9$$

and the observation estimate $\phi_i^{(v+1)}$ is

$$\phi_i^{(v+1)} = \phi_i^{(v)} + \sum_{j=1}^n \alpha_{ij} \left[\begin{aligned} &\phi_j^o - \phi_j^{(v)} - c_j (y_i - y_j) f_j \left\{ u_g^{(v)} - u_g^{(v-1)} \right\}_j \\ &+ c_j (x_i - x_j) f_j \left\{ v_g^{(v)} - v_g^{(v-1)} \right\}_j \end{aligned} \right] \quad 4.10$$

where ϕ_j^o is the value of the observation and $u_{g,j}^{(v)}$ is an estimate of the geostrophic wind correction at the observation point for the v^{th} iteration. $\phi_j^{(v)}$ and $u_{g,j}^{(v-1)}$ are the prior estimates of the value of the observation of geopotential and the geostrophic wind, respectively, at the observation point. For the next iteration, an improved estimate of the geostrophic wind correction $(u_{g,j}^{(v+1)}, v_{g,j}^{(v+1)})$ is obtained at the observation point by linear

interpolation of grid point values computed from the interpolated values of the geopotential at the grid points.

$$u_{g,x}^{(v+1)} = - \frac{\frac{-y}{c} \delta_y \phi_x^{(v+1)}}{f^* \Delta y} \quad 4.11$$

$$v_{g,x}^{(v+1)} = - \frac{c \delta_x \phi_x^{(v+1)}}{f^* \Delta x} \quad 4.12$$

$u_{g,x}^{(v)}$ is the value of the geostrophic wind at the grid point, derived from the geopotential $\phi_x^{(v)}$, and $u_{g,j}^{(v)}$ is the value at the observation point obtained by bilinear interpolation from $u_{g,x}^{(v)}$, for the v th iteration. "f" is the Coriolis parameter, and $f^* = \max(f(15^\circ N), |f|) \text{sign}(f)$. "c" is a geostrophy factor depending on the latitude θ in degrees as

$$c = \begin{cases} 1 & \text{for } |\theta| > 30^\circ \\ 0.5 [1 + \cos(12\theta)] & \text{for } 15^\circ \leq |\theta| \leq 30^\circ \\ 0 & \text{for } |\theta| < 15^\circ \end{cases} \quad 4.13$$

The four iterations use a single correlation scale "d" of 500 km. Only the larger scales are corrected, without changing the smaller scales which are not as geostrophic. In a 9-point zone along the boundary of our analysis grid, the analyzed values are merged with values interpolated from the NMC analysis. The analyzed values in the first six points closest to the boundary are replaced by the NMC values, while a linear weighting of (.25,.75), (.5,.5), (.75,.25) is used to merge the analyzed values with the NMC values.

c) Enhancements to the wind field and temperature gradients

Following Kistler and McPherson (1975), the geostrophic part of the corrections to the wind field is adjusted to match the new corrections for the geopotential. That is, the univariate wind corrections are modified by adding the difference in the geostrophic wind between the geostrophic and univariate analysis of the geopotential. Four additional passes of the univariate wind analysis are then performed to enhance the corrections of the ageostrophic wind. A similar merging with wind derived from the NMC analysis is performed in the 9-point boundary zone as was done with the geopotential. After the corrections have been computed at all analysis pressure levels of the analysis, the univariate temperature corrections are adjusted to match the computed thickness corrections. The final corrections are then bicubically interpolated to the model horizontal grid and added to the first guess on the pressure surfaces.

The analysis deviations are interpolated in the vertical to the model sigma levels and the model background forecast is updated. Before interpolating in the vertical, an initial estimate of new surface pressure is computed from the analyzed full fields on the p levels. The surface pressure of the background forecast is similarly computed from the fields of temperature and geopotential height on the pressure levels. The difference in surface pressure between the two is then added to the original surface pressure of the background forecast to obtain the corrected surface pressure. The analysis deviations are then linearly interpolated in the vertical to the model sigma levels and added to the first-guess model forecast. The thermodynamic variables (temperature, humidity) are interpolated to the model sigma levels, assuming they are linear in the log of pressure, while the wind components are interpolated assuming they are linear in the pressure.

4.3 Testing the Analysis Scheme

The utility of an analysis scheme may be judged in several ways, including its ability to: 1) define accurately the amplitude and phase of meteorological waves, 2) fit data within the accuracy of observations, 3) distinguish between accurate and erroneous data, and 4) provide initial conditions for numerical weather prediction models such that forecast error is minimized. In section 4.2, it was shown that our analysis scheme fits the data to a desirable limit. Here, we will concentrate on items 1) and 4) from a qualitative viewpoint by comparing our analyses and subsequent model forecasts based on these fields with the mesoscale analyses of Bosart (1988) and Doyle and Warner (1990) and the NMC 2.5°-resolution hemispheric analyses, and forecasts produced from these NMC fields by our limited-area model. Application of the vertical mode initialization scheme on both the NMC and our analyses is used to compare the mesoscale vertical motion and ageostrophic wind derived from the NRL and NMC analyses. Model forecast precipitation is compared in each case to observed values. Analyses of GALE raingauge data from GDC (Mercer 1987) on a polar stereographic grid of about 84 km resolution were interpolated to a 0.5° latitude/longitude grid. To provide values outside of the region of the GDC precipitation analyses, precipitation estimates on a 1°-resolution grid derived from satellite by Martin et al. (1988) at the Cooperative Institute for Meteorological Satellite Studies at the University of Wisconsin were also interpolated to the 0.5° grid. These rainfall estimates were derived from digital infrared images of the GOES-6 satellite using the Global Precipitation Index technique of Arkin (1983). This technique assumes that rainfall (R in mm) is linearly related to the fractional cloud cover (f):

$$R = k \times f \quad 4.14$$

where the coefficient k has a value of 72 mm/day.

4.3.1 Experimental Design

A number of cases were performed to test the effectiveness of the NRL/NCSU objective analysis scheme; these are outlined in Table 4.2. The analyses were made using surface and atmospheric sounding data collected during IOP 2 of GALE. Twelve-hourly NMC 2.5° hemispheric analyses for the period 0000 UTC 25 January to 1200 UTC 26 January 1986 (25/00Z to 26/12Z) were used for the initial conditions to generate the first-guess 12-h forecasts and for comparison to our analyses. Six model variables were analyzed: sea level pressure, geopotential height, u- and v- wind components, temperature, and relative humidity. Analyses were performed at 19 vertical levels from 1000 mb to 100 mb at 50-mb increments on a horizontal grid with a resolution of 1.5° latitude by 1.5° longitude. These analyses produced from the NRL/NCSU objective analysis scheme are referred to as simply NRL analyses.

In case 4.1, the model is initialized from the 25/00Z NMC analysis. The 12-h forecast serves as the background, or first guess, for univariate (case 4.2) and multivariate (case 4.3) analyses using the NRL/NCSU scheme. For each case, 24-h forecasts are then produced. The 25/12Z NMC analysis and a 24-h subsequent forecast (case 4.4) serve as a baseline for comparison. Cases 4.5 and 4.6 are identical to cases 4.3 and 4.4, except the analyses are valid at 26/00Z and the 12-h forecast from case 4.4 serves as the first guess for the NRL analysis in case 4.5. The analyses in cases 4.7 and 4.8 are valid 12 h later at 26/12Z. These 8 cases essentially serve as 3 separate experiments: 1) 25/12Z analyses and subsequent forecasts, 2) 26/00Z analyses and forecasts, and 3) those at 26/12Z.

TABLE 4.2. Analysis and Forecast Test Cases

Case	
4.1	25/00Z NMC analysis and 12-h model integration
4.2	25/12Z univariate analysis with 12-h forecast from case 4.1 as first guess and 24-h integration
4.3	25/12Z multivariate analysis with 12-h forecast from case 4.1 as first guess and 24-h integration
4.4	25/12Z NMC analysis and 24-h integration
4.5	26/00Z multivariate analysis with 12-h forecast from case 4.4 as first guess and 24-h integration
4.6	26/00Z NMC analysis and 24-h integration
4.7	26/12Z multivariate analysis with 12-h forecast from case 4.6 as first guess and 24-h integration
4.8	26/12Z NMC analysis and 24-h integration

4.3.2 The Synoptic Situation

During the period 25/00Z to 27/12Z, coastal frontogenesis and cyclogenesis took place along the eastern seaboard. Riordan (1990) and Doyle and Warner (1990) describe the initial stages of the coastal frontogenesis from 24 January. At 25/00Z, coastal frontogenesis had begun offshore along the Carolina coast in an onshore easterly flow regime and by 25/12Z a 1000-km long coastal front paralleled the coastline. Cold air damming east of the Appalachians and warming of the easterly air over the Gulf Stream were the major factors contributing to the strong thermal gradient along the coast. The easterly flow regime can be seen in the coarse NMC 1000-mb analysis in Fig. 4.3a, which is however unable to resolve the strong thermal gradient along the coast. In the upper levels of the atmosphere, a broad, long-wave trough was present over the central U. S. (Fig. 4.3b). An associated 250-mb jet with maximum winds of $55\text{--}60\text{ m s}^{-1}$ extended from northeast Texas across the Ohio River Valley. During the next 24 h, the trough moved eastward and deepened rapidly due to a second short wave digging southward in the large-scale trough. By 26/00Z, the coastal front extended from Georgia to southern New England and a weak low moved up the coast along the front, reaching the Chesapeake Bay by 26/12Z (Fig. 4.3c). In the next 12 h, the coastal low merged with a weak trough seen in Fig. 4.3c moving eastwards from the Great Lakes.

The disturbance which ultimately became the first of the major cyclones of GALE was present as a minor frontal wave in extreme southeast Texas at 25/12Z. The surface disturbance remained weak as it advanced along the Gulf coast and on 26 January the surface wave weakened further as it moved across Georgia. In response to the strong upper-level short wave reaching the east coast, a new center formed off Cape Hatteras and deepened rapidly as it moved north and combined with the pre-existing waves associated with the northward-moving coastal low and eastward moving trough. By

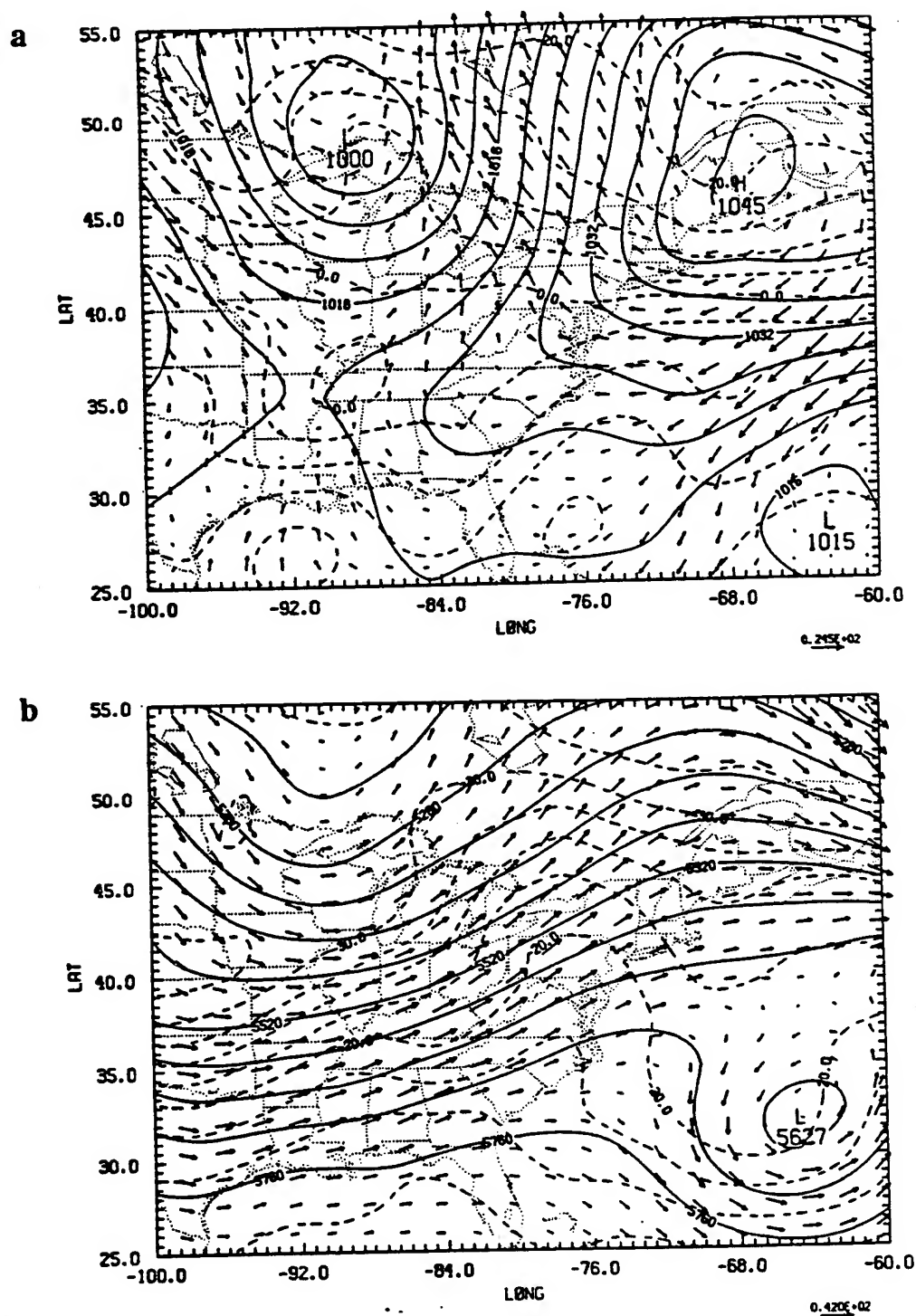


Figure 4.3. (a) Sea-level pressure (mb) and temperature ($^{\circ}\text{C}$) and winds at 1000 mb, and (b) geopotential height (m), temperature ($^{\circ}\text{C}$) and winds at 500 mb for the NMC analysis on 25/12Z. (c) and (d) as in (a) except for 26/12Z and 27/12Z, respectively. Contours of sea-level pressure and temperature at 1000 mb are 4 mb and 5°C , respectively. Maximum wind vector indicated by labelled arrow in m s^{-1} .

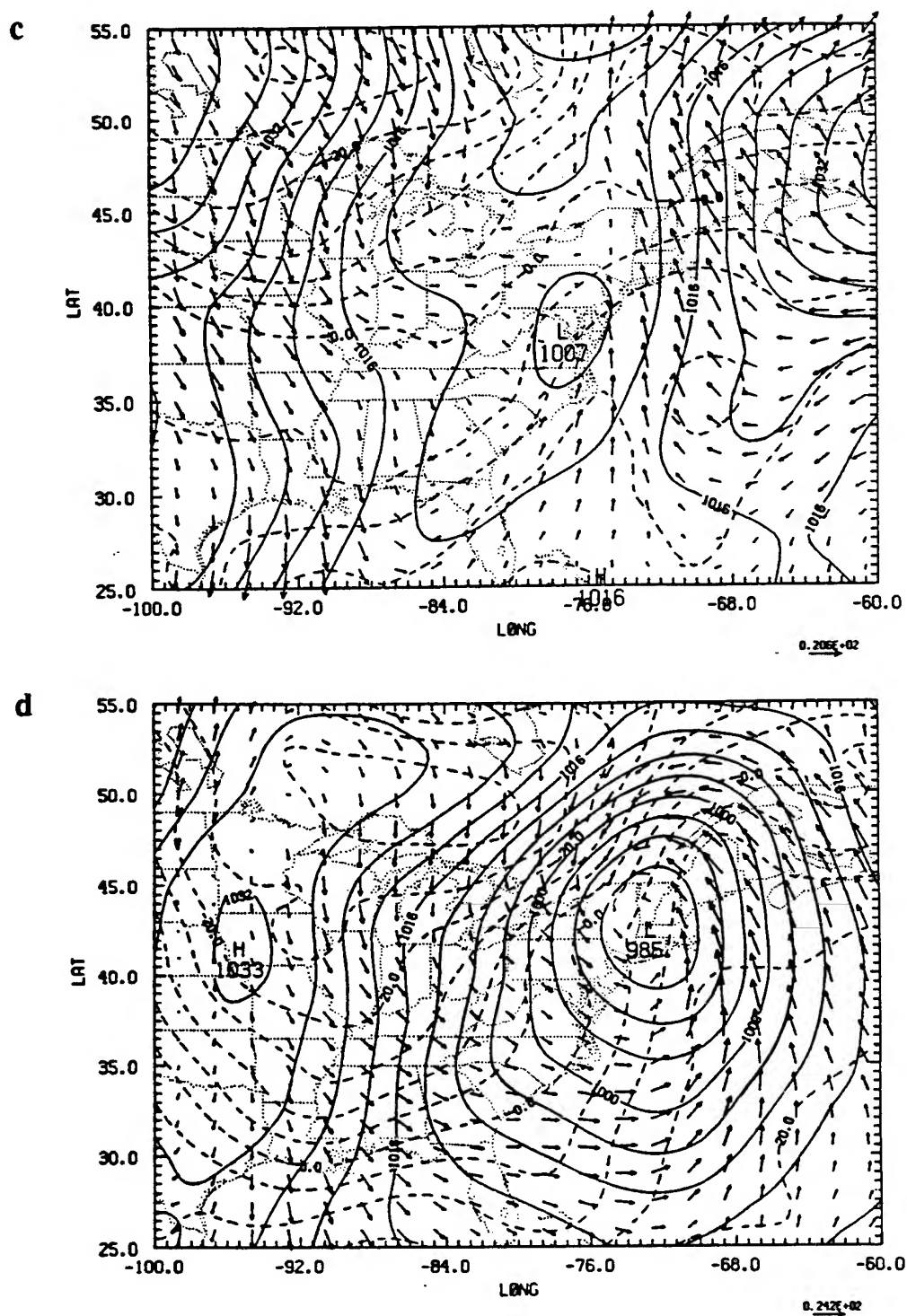


Figure 4.3. Continued.

27/12Z, the well-developed low pressure center crossed the New England coast, as shown in Fig. 4.3d.

4.4 Results

Comparisons between first-guess forecast fields, univariate analyses, multivariate analyses, NMC analyses, and Bosart's detailed hand analyses are made at 25/12Z and 26/00Z. Also, model forecasts resulting from these analyses are compared with each other and with the Bosart analyses valid at specific forecast times.

4.4.1 Comparison of 25/12Z Analyses

Sea-level pressure, surface temperature, and 1000-mb winds for the first guess (12-h forecast from case 4.1), and the NRL analysis at 25/12Z are shown in Figs. 4.4a and b. The first guess, shown in Fig. 4.4a, had the cold air damming with strong ridging east of the Appalachians. The presence of a strong temperature gradient along the Carolina coast signified the existence of a coastal front. The NRL analysis shown in Fig. 4.4b retained these features, suggesting that they were present in the data. The 25/12Z analysis of Doyle and Warner (1990) verifies that the coastal front and the cold air damming were present (see Fig 2b. of Doyle and Warner). Note that the coarse NMC analysis shown in Fig. 4.3a is unable to resolve the tight thermal gradient along the coast. The NRL analyses also retained the strong onshore flow from the first guess and which is readily apparent in Doyle and Warner's analysis along the Carolina coast. The overall pressure pattern from the NRL analysis matched Doyle and Warner's analysis much better than the coarse NMC analysis was able to do. Note the position and magnitude of the "low" of 1000 mb over Lake Superior and the "high" of 1046 mb over the Gulf of

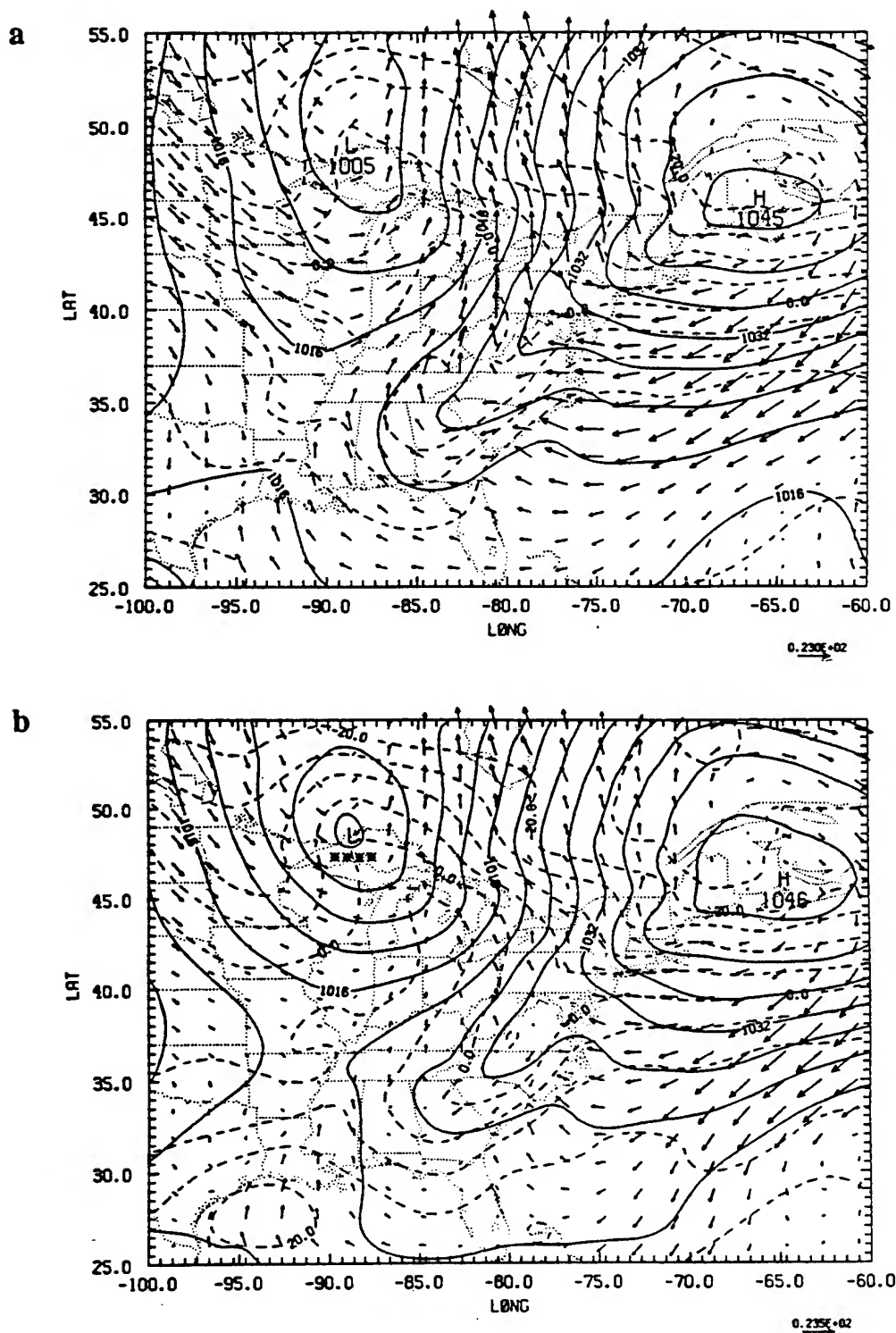


Figure 4.4. Sea-level pressure (mb) and 1000-mb temperature ($^{\circ}\text{C}$) and winds at 25/12Z for (a) the first guess, a 12-h forecast from case 4.1 and (b) NRL analysis. (c) and (d) as in (a) and (b) but for the geopotential height (m), temperature ($^{\circ}\text{C}$), and winds at 500 mb. Contours of geopotential and temperature at 500 mb are 60 m and 2.5°C , respectively.

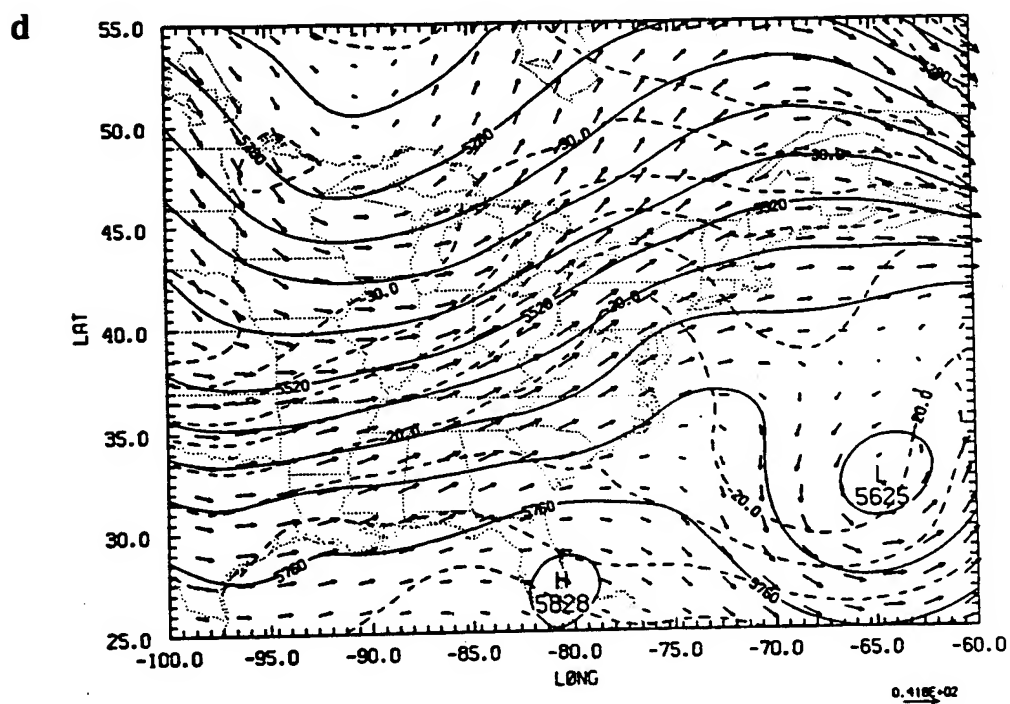
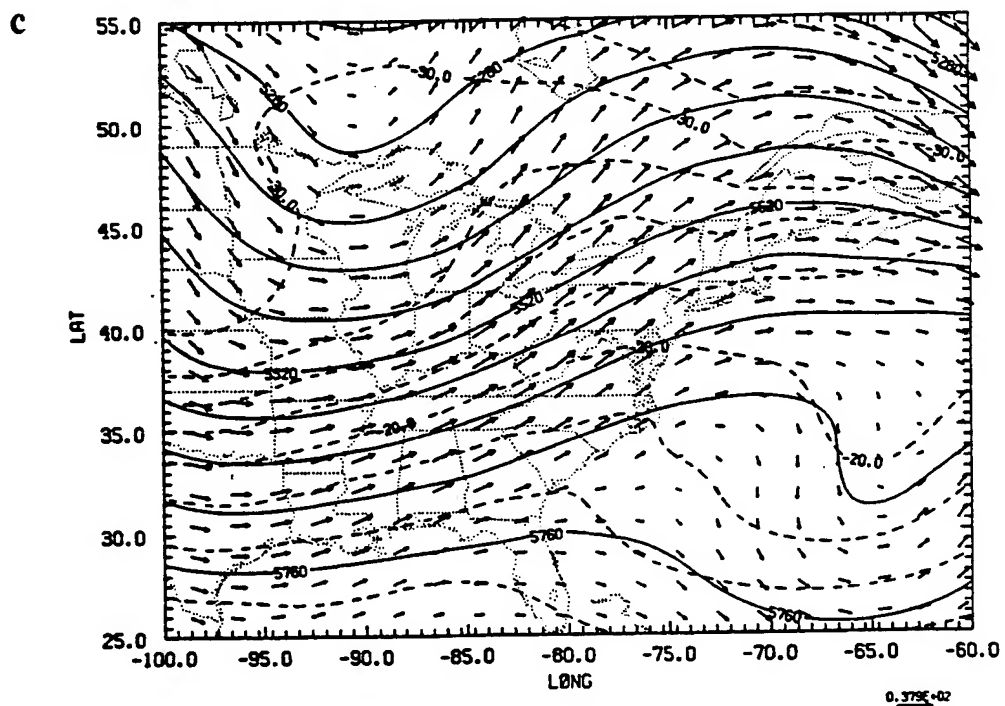


Figure 4.4. Continued.

St. Lawrence. The first-guess "low" was in error by 5 mb and was corrected totally by the NRL analysis.

The analysis of 500-mb geopotential height, temperature and winds are compared to the first guess in Figs. 4.4c and d. The NMC 500-mb analysis shown in Fig. 4.3b shows a cutoff low of 5627 m over the western Atlantic. The first-guess field provided by the model forecast failed to deepen the low significantly, and only a weak trough is present. The univariate NRL analysis (not shown) does capture this feature, but the low is not quite deep enough (5634 m). The multivariate analysis (Fig. 4.4d) is able to deepen the low even more to 5625 m by extrapolating geopotential heights using wind information, and the associated winds are somewhat stronger. It is worth noting that the data used in the NRL analysis in the vicinity of the cutoff low are in fact bogus values derived from the NMC analysis (see Fig. 4.1a). The NRL multivariate analysis, as noted above, reproduced the NMC analysis for the cutoff low with remarkable accuracy, considering the coarse resolution of the bogus data supplied to the analysis. The first-guess 500-mb temperature field is out of phase in the Great Lakes region. The -30°C isotherm in the NMC analysis is over Lake Michigan, whereas the first-guess forecast has it lagging too far to the west over Minnesota. Some improvement is gained with the NRL univariate analysis, but the phase error is totally corrected by the multivariate analysis.

The NRL analysis is successful in pushing the first-guess 500-mb relative humidity field toward the NMC analysis (not shown). In particular, a high moisture tongue off the Carolina coast was absent in the first-guess field. The NRL analysis was successful in moistening the model environment to the appropriate level. The 250-mb jet associated with the upper-level long wave trough is depicted in Fig. 4.5. The jet from the first guess is too weak and broad with a jet maximum of about 50 m s^{-1} , compared to the NMC analysis which has a jet maximum of 55 m s^{-1} . Both the univariate and

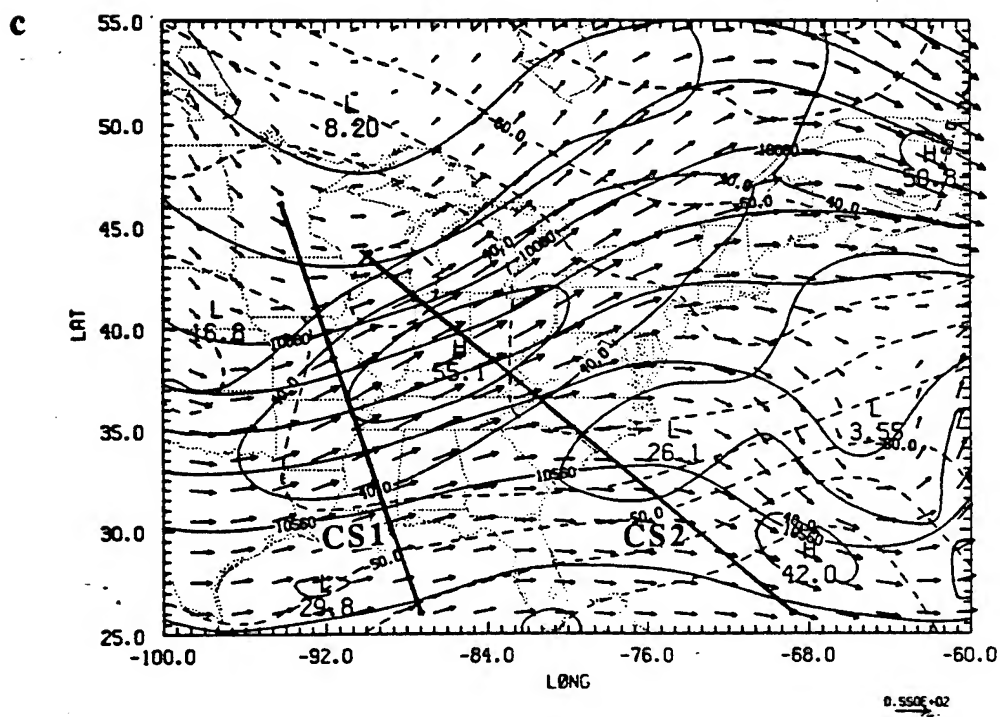


Figure 4.5. Continued.

multivariate analyses corrected the wind speeds and sharpened the jet, with the multivariate analysis having a slightly smaller maximum than the univariate analysis. Actually the analyzed jet maximum in the multivariate case is still 2 m s^{-1} stronger than that in the NMC analysis. However, this is not alarming since our analysis is on a finer scale than the NMC analysis.

The first-guess second-order fields of absolute vorticity and the vertical motion are significantly improved by the NRL objective analysis. The 500-mb absolute vorticity and vertical motion fields for the first guess and NRL analysis are shown in Fig. 4.6. For comparison, the vorticity and vertical motion derived from the NMC analysis are shown in Fig. 4.7. The vertical motion from the analyses is derived by application of the vertical mode initialization procedure. The NRL multivariate analysis greatly improved the overall pattern, including the gradients of vorticity, when compared to the first-guess field. The vorticity maxima for the multivariate analysis are close in value to those in the NMC analysis. In the first-guess vertical motion field, the subsidence west of the cutoff low is strengthened by the NRL analysis and is in close agreement with that derived for the NMC analysis. However, the rising motion associated with the developing coastal front in the first-guess field is retained in the NRL analysis. The rising motion, associated with the surface cyclone located on the southeast Texas coast and a secondary circulation of the upper-level jet's entrance region, is evident over eastern Texas and northern Mississippi. These two centers of ascending motion are better defined in the NRL analysis than either the first guess or the NMC analysis.

Cross sections were produced to further investigate the secondary ageostrophic circulations, associated with the upper-level jet and the coastal front. The locations of the cross sections are displayed in Fig. 4.5c. Cross section CS1 (94°W , 46°N to 87.3°W , 26°N), which extends from Minnesota to the central Gulf of Mexico, cuts across the entrance region of the upper-level polar jet. The second cross section (CS2 from 90°W ,

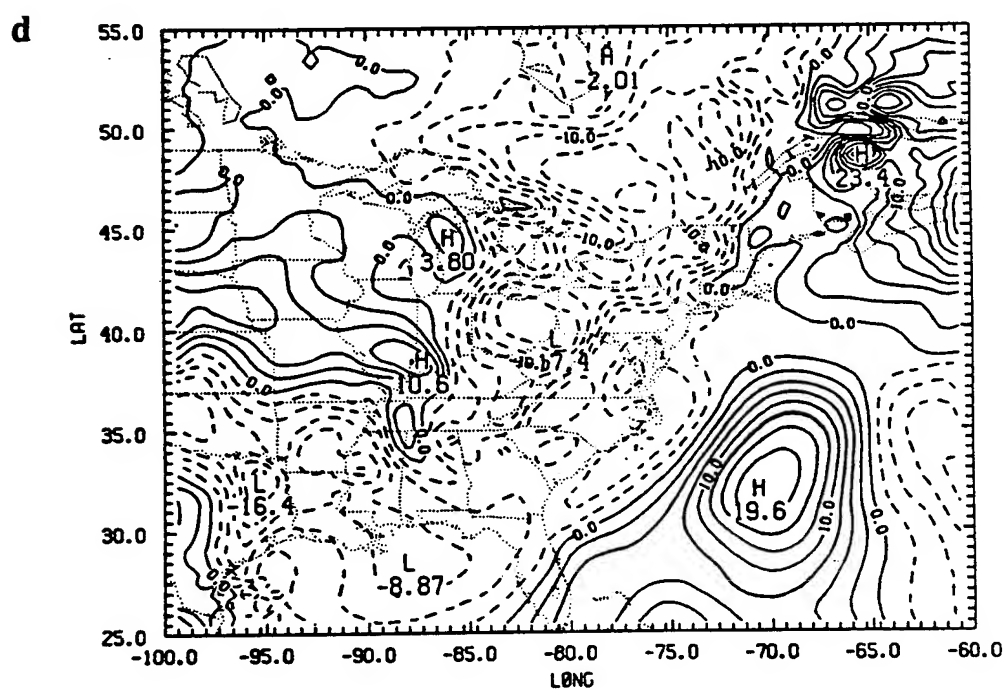
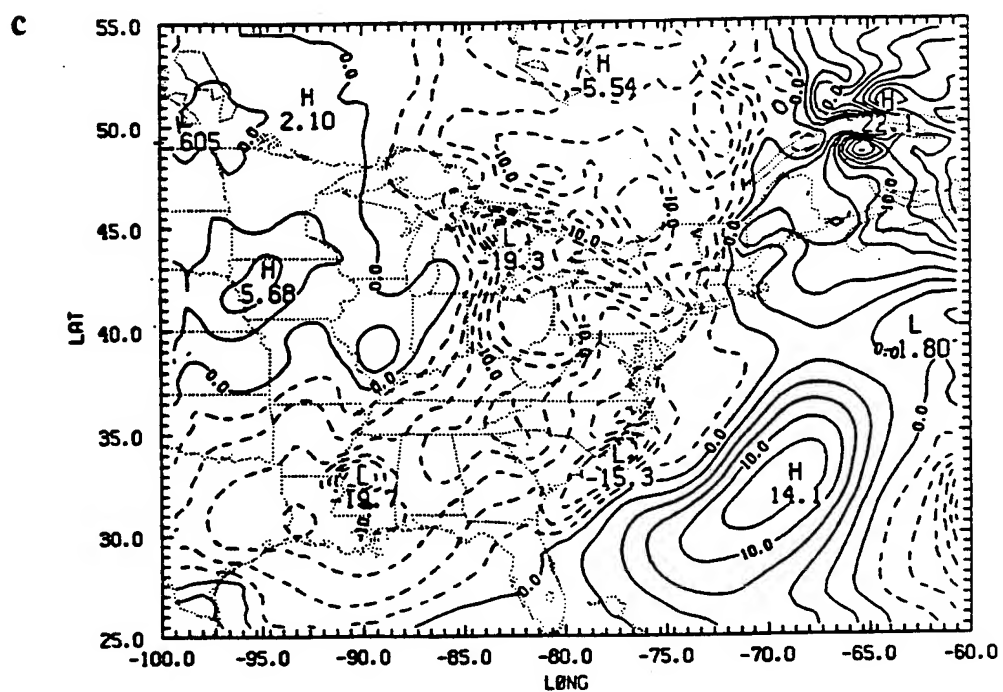


Figure 4.6. Continued.

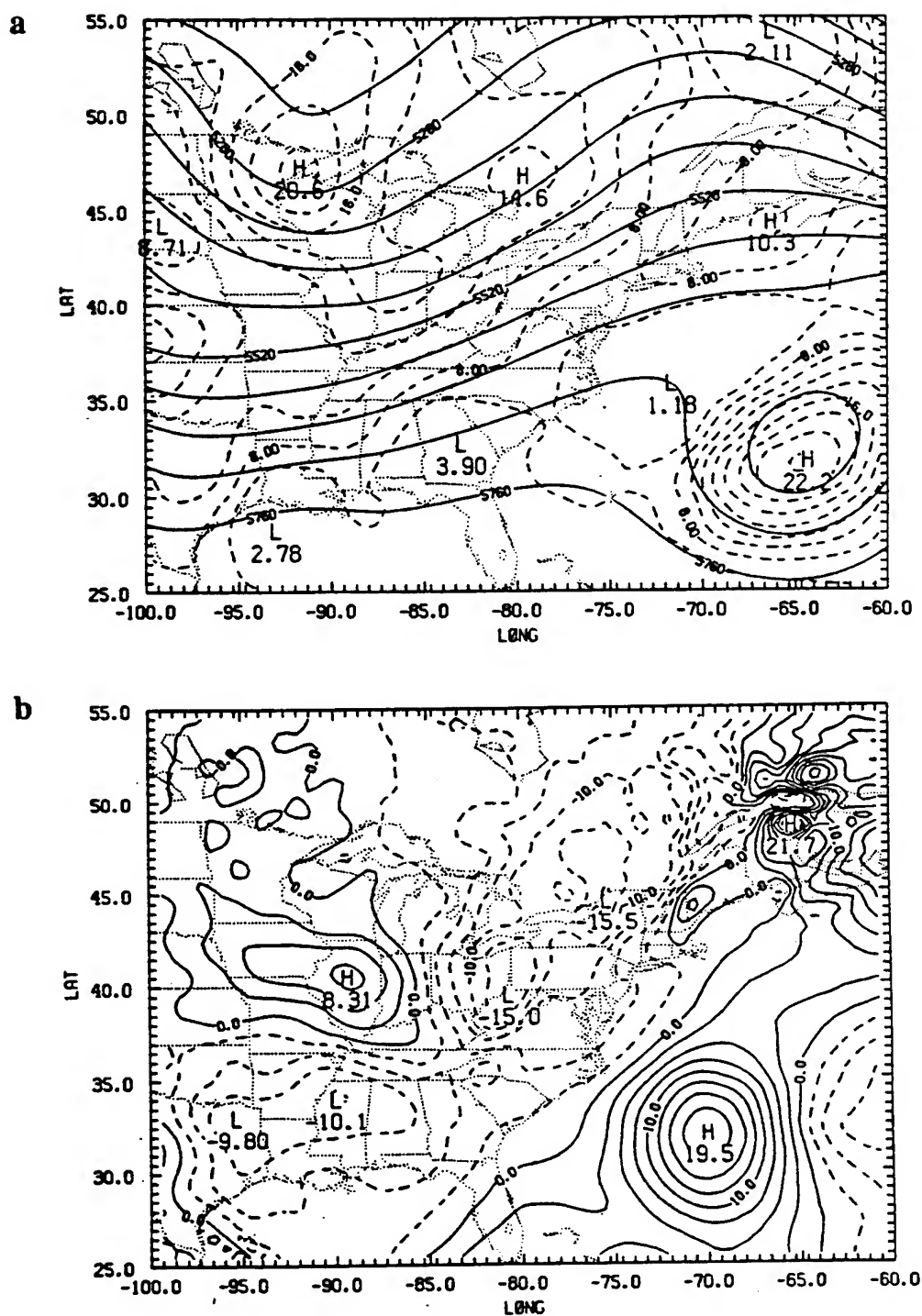


Figure 4.7. (a) Absolute vorticity (in units of 10^{-5} s^{-1}) with geopotential height (m) and (b) the vertical velocity in mb h^{-1} at 500 mb on 25/12Z for the NMC analysis. Vertical motion of magnitudes -20 mb h^{-1} or greater are contoured every 2.5 mb h^{-1} .

43.5°N to 68.7°W, 26°N) is perpendicular to the Carolina coast. In all figures displaying cross sections, the positions of the grid points every 0.5° in latitude are denoted by the inner tick marks for facilitation in locating meteorological features of interest. The wind speed normal to each cross section is shown in Fig. 4.8. In the cross section across the Gulf of Mexico, the NMC analysis at 25/12Z (Fig. 4.9b) shows a broad region of ascending motion in the right rear flank of the polar jet. The NRL analysis (Fig. 4.9a) has enhanced the secondary circulation in this region. The maximum vertical velocity is 40% greater than in the NMC analysis (-14 mb h^{-1} vs. -10 mb h^{-1}). Also, more evident in the NRL analysis is the ascent associated with the subtropical jet stream to the south. Figure 4.10 depicts the cross section perpendicular to the Carolina coast for both the NRL and NMC analyses. As shown in Fig. 4.10a, the NRL analysis is successful in maintaining the shallow ascent associated with the coastal front, which was generated in the first-guess forecast. Note the maximum ascent of -18.3 mb h^{-1} about 15000 km from the northernmost end (left side of cross section) in Fig. 4.10a. This circulation is much stronger and more well-defined than the corresponding circulation from the NMC analysis (Fig. 4.10b). The subsidence west of the cutoff low in the subtropical jet stream and ascent east of the approaching upper-level trough (see Fig. 4.6) are also seen in both cases. Increased humidities at low levels offshore and over the coastal front, with dryer values behind the front, are seen in Fig. 4.10c for the NRL analysis. A narrower tongue of high humidity is also found at mid-levels.

4.4.2 Comparison of Model Forecasts (25/12Z-26/12Z)

Forecasts using the different analyses to derive the initial conditions are compared in cases 4.3 and 4.4. After 6 h of model integration (at 25/18Z), the forecast based on the NMC analysis (case 4.4) still contained a relatively weak thermal gradient in the

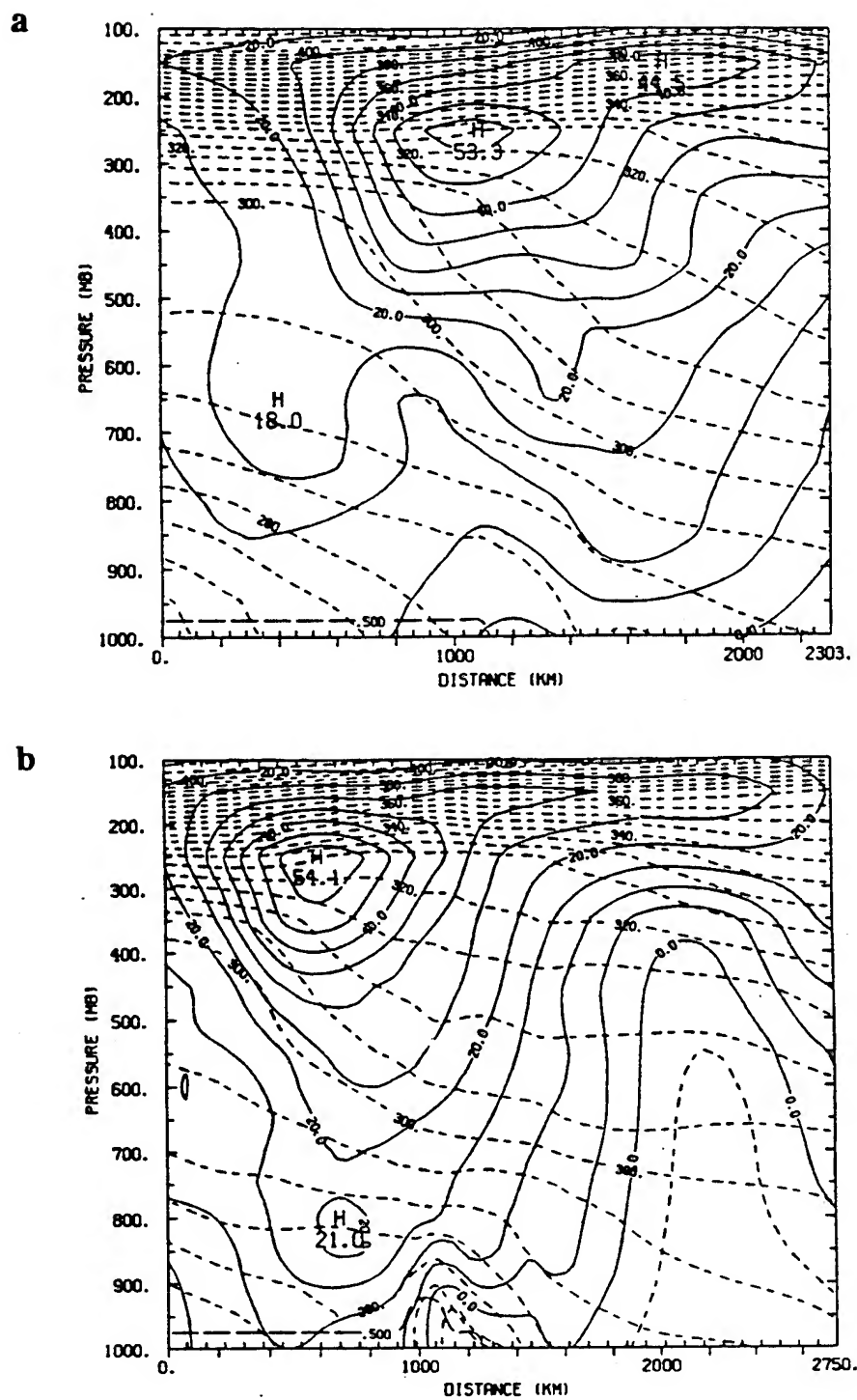


Figure 4.8. Magnitude of the wind normal to the plane of cross sections (a) CS1 and (b) CS2 at 25/12Z for the NRL analysis (see Fig. 4.5c). Contours every 5 m s^{-1} . Potential temperature ($^{\circ}\text{K}$) is also shown by the dashed contours every 5°K in the troposphere. The position of the grid points every 0.5° in latitude are shown by the inner tick marks.

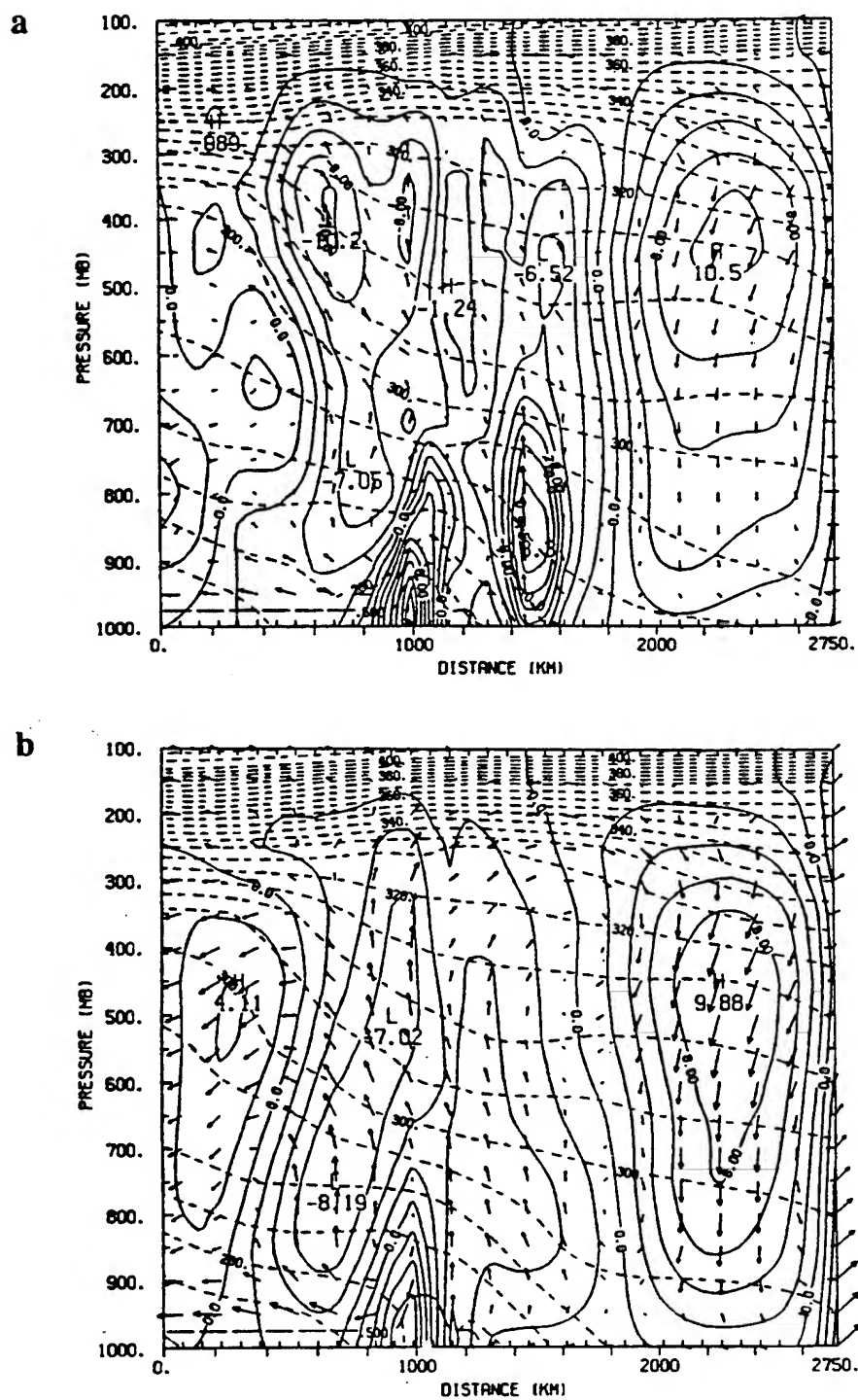


Figure 4.10. The vertical motion and ageostrophic wind in the plane of cross section CS2 at 25/12Z for (a) the NRL analysis and (b) for the NMC analysis. (c) and (d) as in (a) and (b) but for the relative humidity, contoured every 10% for 30% and above. Contours of vertical motion as in Fig. 4.9. See Fig. 4.5c for location of CS2.

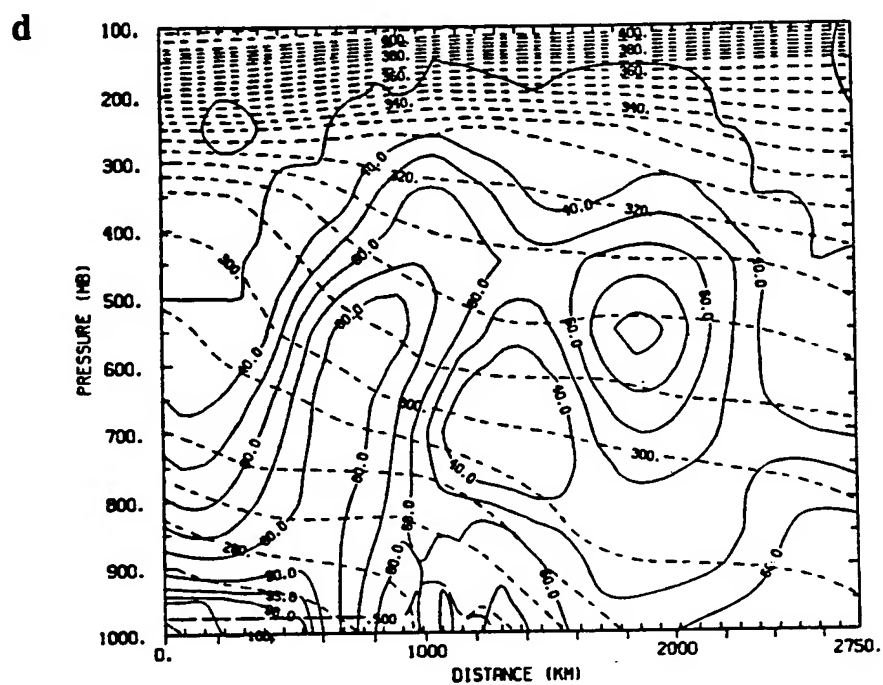
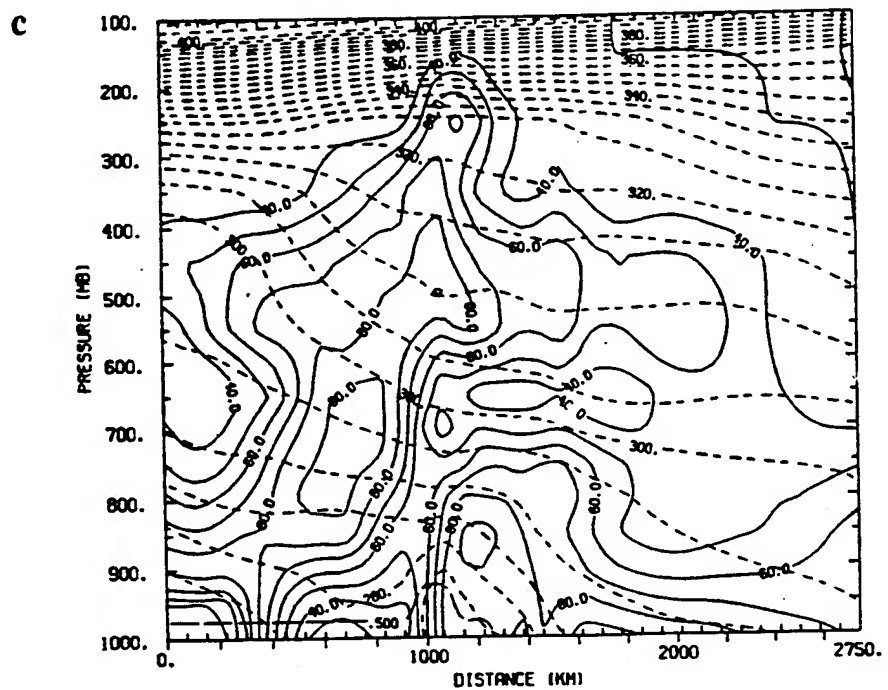


Figure 4.10. Continued.

vicinity of the coastal front (shown in Fig. 4.11a), since the model was still in a spin-up mode. An inverted surface trough is present near Jacksonville, Florida in Fig. 4.11b in the case using the NRL analysis (case 4.3). This feature is weaker and further east in the NMC case. Bosart's analysis (Fig. 4.12) verifies the presence of the trough with the genesis of a cyclonic circulation. A weak surface low is also indicated just north of New Orleans in better agreement with the Bosart analysis, than the NMC case. The weak coastal circulation, which forms a low pressure center that moves northeast along the coast, is handled better in the NRL case compared to that using the NMC analysis.

The 500-mb mass and wind fields are very similar from both cases at 25/18Z. However, differences do exist in the 500-mb vertical motion (Fig. 4.13) and moisture fields (not shown). In the NRL case 4.3, a significant upward vertical motion had developed off the Carolina coast. These vertical velocities are missing in the NMC case 4.4. As a result, no precipitation was forecast along the coastal front during the first 6 h of integration in the case originating from the NMC analysis. Case 4.3 also produced stronger vertical motions over the Mississippi Gulf coast associated with the secondary jet circulation and an area of positive vorticity advection at 500 mb. Both 25/12Z analyses, NMC and NRL, had a strong 500-mb moisture tongue off the Carolina coast. Unlike that of the NMC case, the stronger coastal front circulation from the NRL case had pushed the moisture tongue inland by 25/18Z.

At 26/00Z, the coastal front has developed from Georgia to southern New England in an onshore easterly flow regime. Figure 4.14a illustrates that NRL case still retains a stronger thermal gradient associated with the front than does the NMC case 4.4 (Fig. 4.14b). The inverted surface trough of low pressure remains more pronounced in the NRL case as compared to the NMC case. In both cases, the surface low along the Alabama coast is in good agreement with the analyses of Bosart and Doyle and Warner for position and intensity.

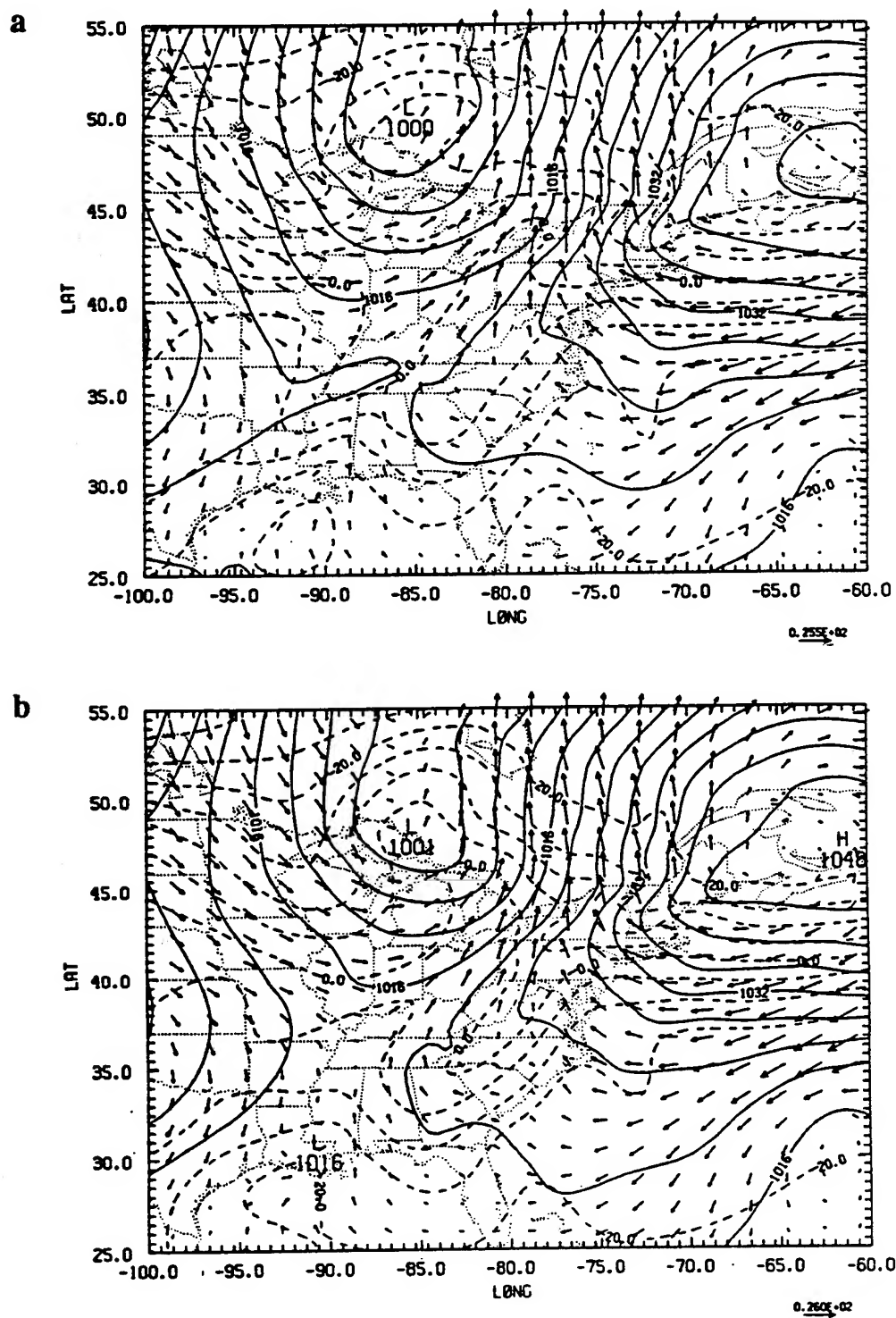


Figure 4.11. Six-hour forecast of sea-level pressure (mb), surface air temperature ($^{\circ}\text{C}$), and 1000 mb winds valid at 25/18Z for (a) case 4.4 from the NMC analysis and (b) case 4.3 from the NRL analysis. Contours as in Fig. 4.3.

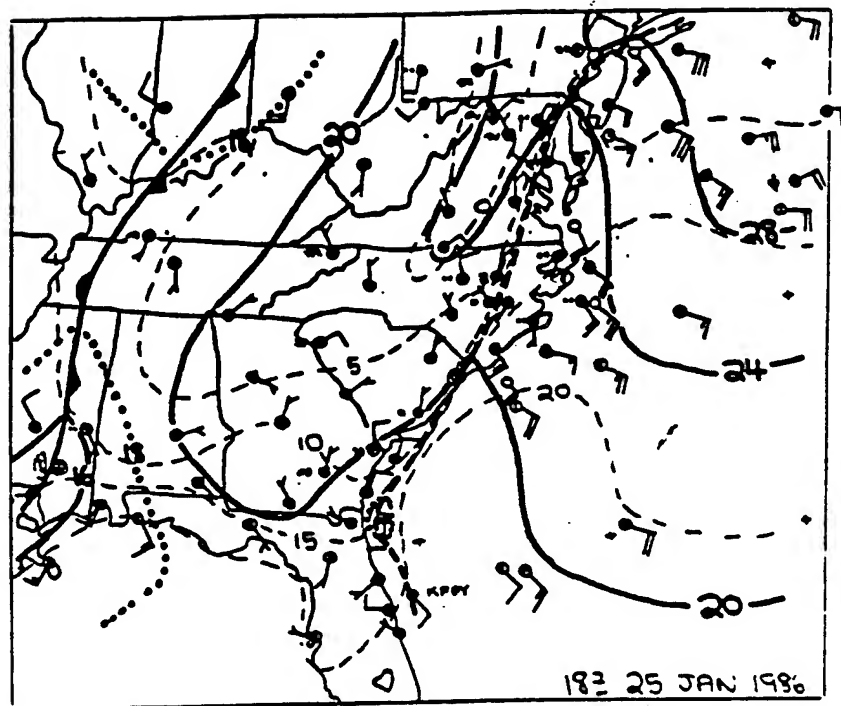


Figure 4.12. GALE analysis of sea-level pressure deviation (from 1000 mb), surface temperature ($^{\circ}\text{C}$) and wind for 25/18Z by Bosart (1988). Surface temperature contours every 5°C .

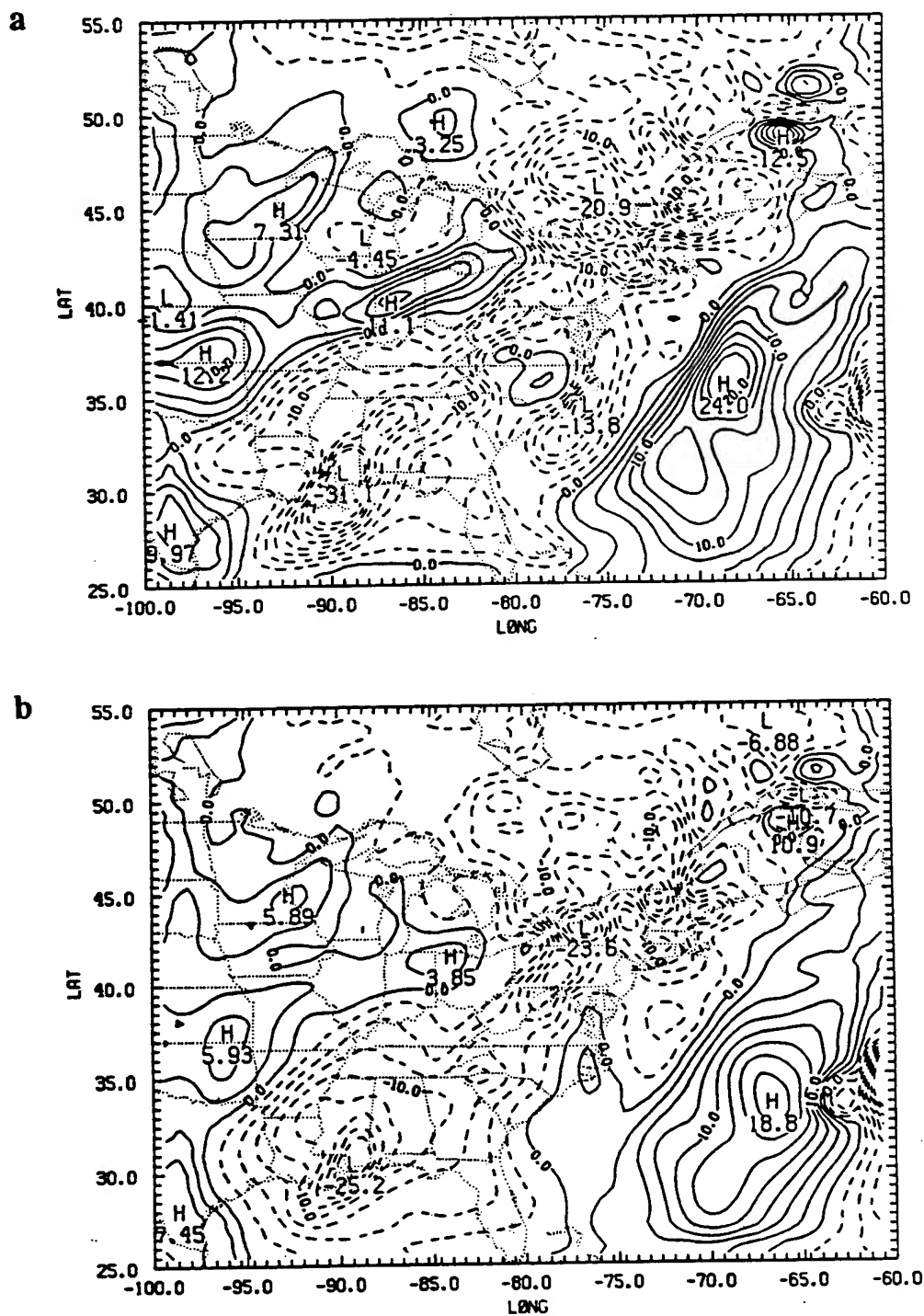


Figure 4.13. Six-hour forecast of vertical velocity (mb h^{-1}) at 500 mb valid at 25/18Z for (a) case 4.3 from the NRL analysis and (b) case 4.4 from the NMC analysis. Contours of vertical motion as in Fig. 4.7.

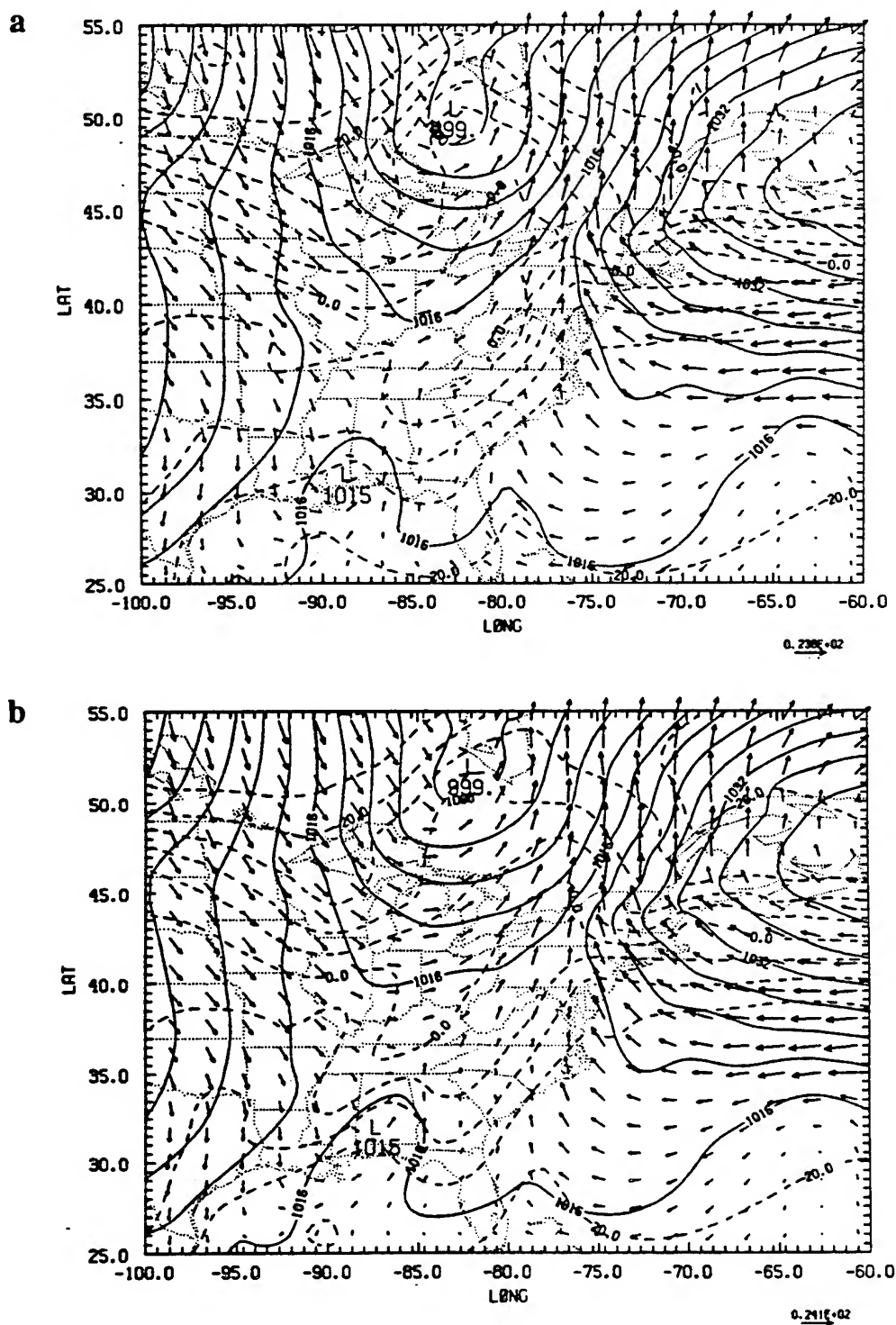


Figure 4.14. Twelve-hour forecast of sea-level pressure (mb), temperature ($^{\circ}\text{C}$) and winds at 1000 mb valid at 26/00Z for (a) case 4.3 from the NRL analysis and (b) case 4.4 from the NMC analysis. (c) and (d) as in (a) and (b) but for the forecast of six-hour accumulated precipitation (25/18Z- 26/00Z) in cm. Contours of precipitation at 0.25 and every 0.5 cm for 0.5 and above.

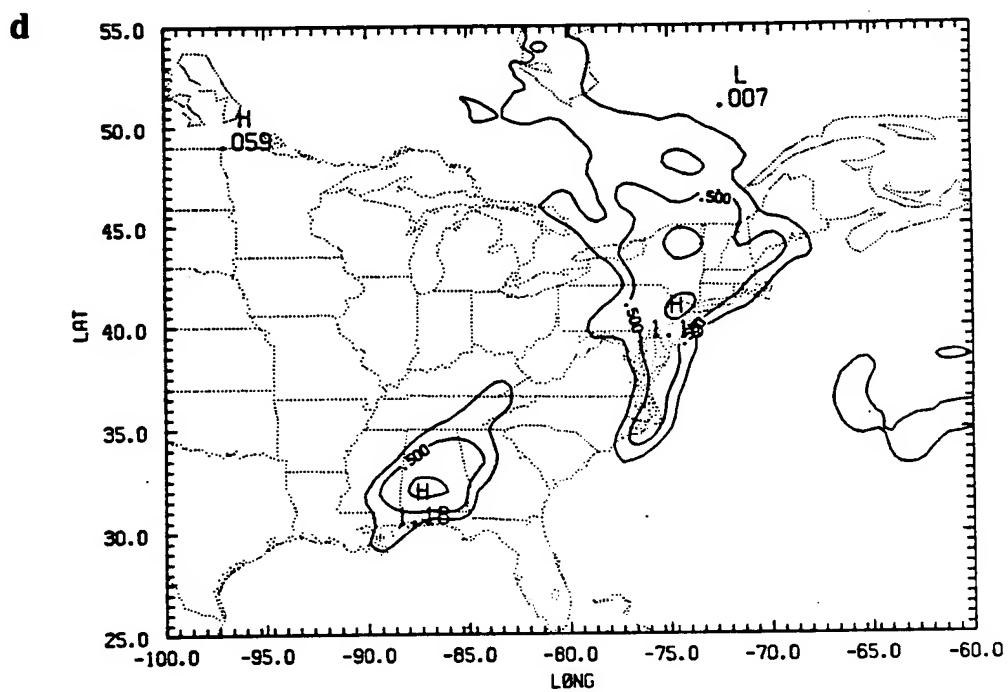
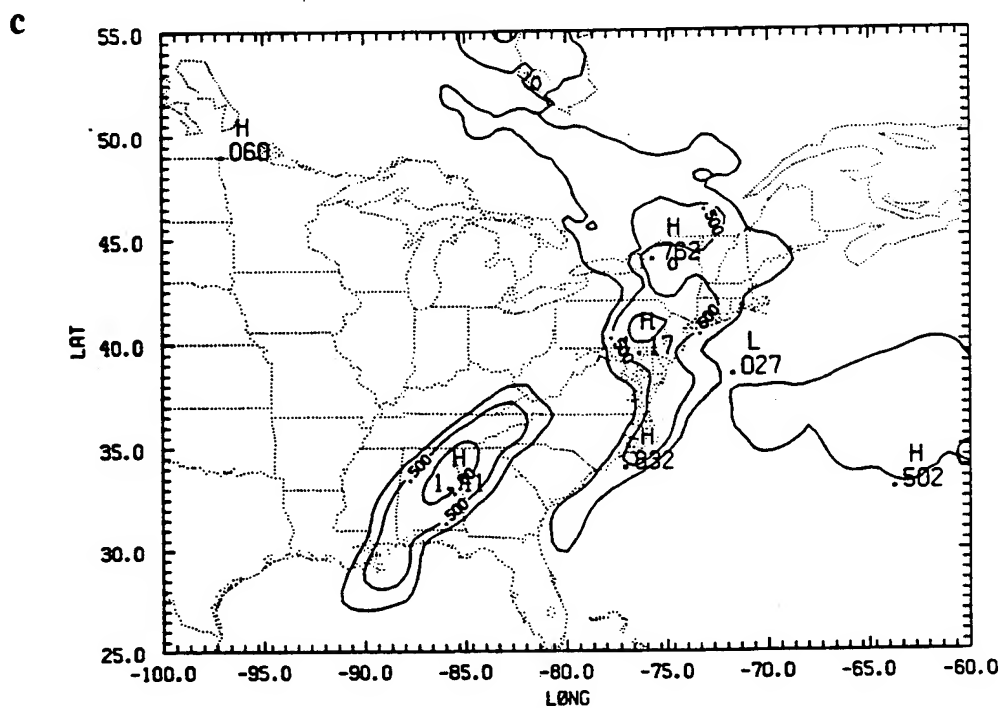


Figure 4.14. Continued.

The 500-mb relative humidity fields are now very similar; after 12 h of integration, model spinup in the NMC case is essentially complete. Still, the 500-mb absolute vorticity in the NRL case over Georgia associated with the surface cyclone along the central Gulf coast is much stronger than that in the NMC case. In addition, the upward vertical motion associated with the inverted surface trough, i.e. the southern extent of the coastal front, over the Georgia coast is much better developed in the forecast originating from the NRL multivariate analysis. Figures 4.14c and d depict the accumulated 6-h rainfall ending at 26/00Z for the NRL and NMC cases. The key difference is again that the NRL case is able to produce precipitation due to mesoscale circulations associated with the coastal front along the Georgia and South Carolina coasts; whereas, the NMC case fails to develop any rainfall in this region. The NRL case is in more agreement with the observed precipitation shown in Fig. 4.15, which does show rainfall associated with the coastal front and with the low along the Gulf coast.

The effects of starting with stronger secondary circulations in the entrance region to the jet and in the coastal front are illustrated in cross sections of the ageostrophic flow and the relative humidity across the Carolina coast in Fig. 4.16. The main difference is the stronger secondary circulation associated with the jet entrance region in the NRL case. In the NRL case (Fig. 4.16a), the coastal circulation is clearly captured by the jet's circulation, which also intensifies the subsidence in the cutoff low offshore and the ageostrophic flow across the coastal front. Higher low-level humidities are also advected over the front in the NRL case (Fig. 4.16b) to produce the forecast precipitation.

The cyclonic circulation which formed near Jacksonville, Florida continues up the coast as a weak low. By 26/06Z, it is located near Wilmington, North Carolina. The low along the central Gulf coast is just a few miles southeast of Pensacola, Florida. The positions of these circulations from the NRL case are in excellent agreement with Bosart's analysis (not shown). Once again, the 500-mb ascending vertical velocities

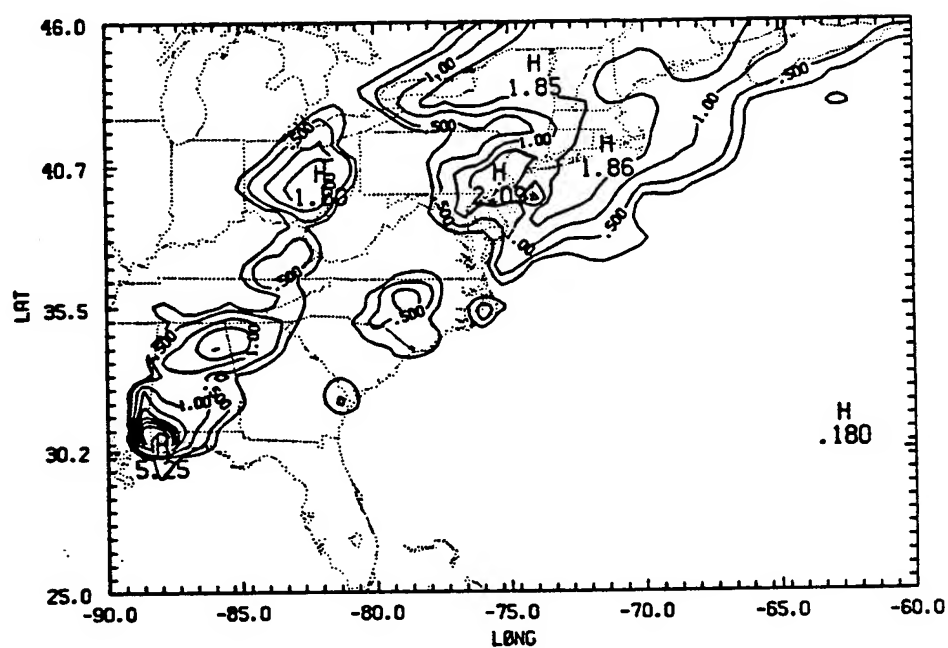


Figure 4.15. Six-hour accumulation of observed precipitation in cm for the same period as in Fig. 14 c and d. Contours of precipitation as in Fig. 4.14.

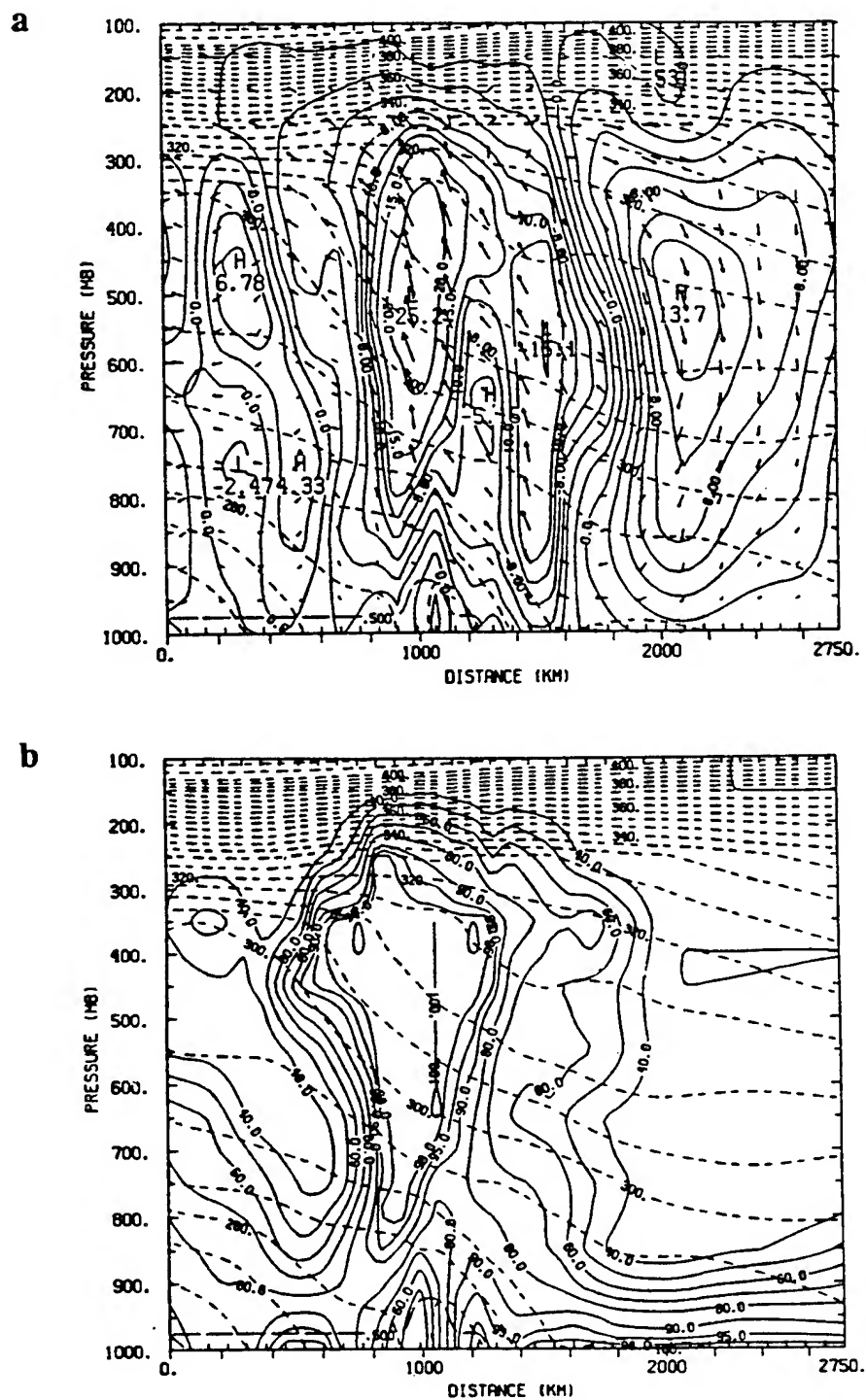


Figure 4.16. Twelve-hour forecast of (a) the vertical motion (mb h^{-1}) and ageostrophic wind (m s^{-1}) and (b) relative humidity (%) in the plane of cross section CS2 valid at 26/00Z for case 4.3 from the NRL analysis. (c) and (d) as in (a) and (b) but for case 4.4 from the NMC analysis. See Fig. 4.5c for location of CS2.

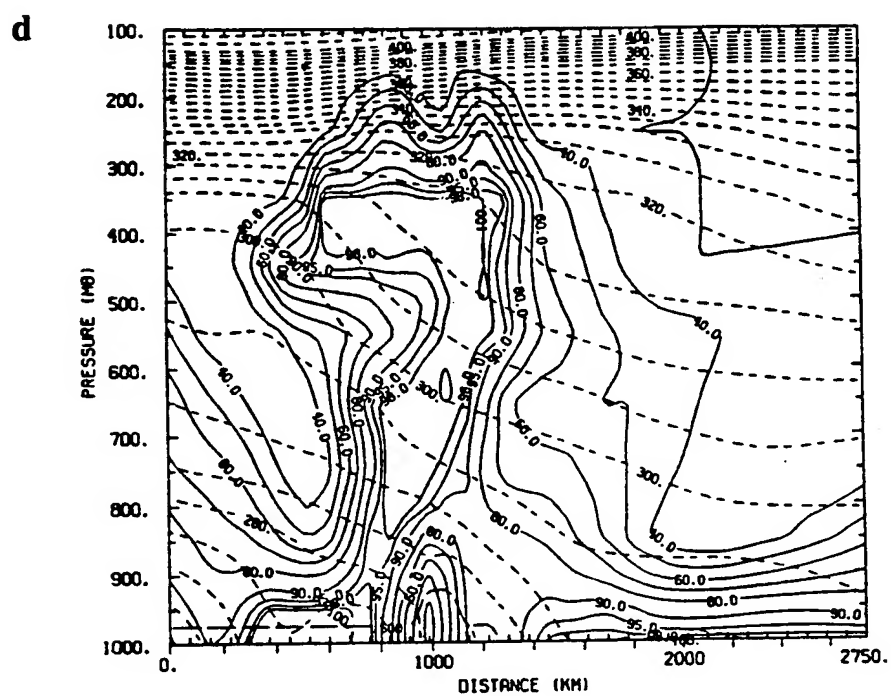
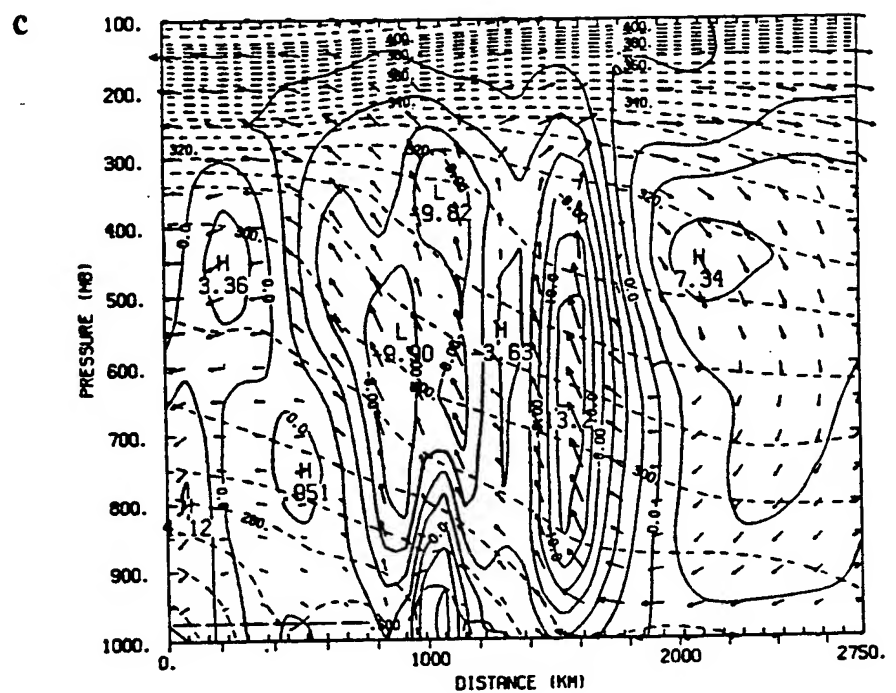


Figure 4.16. Continued.

along the coastal front and associated with the surface wave over the Florida panhandle are about 25% greater in the NRL case versus the NMC case.

4.4.3 Comparisons using 26/00Z and 26/12Z Cases

The analyses for 26/00Z and the subsequent forecasts are compared in cases 4.5 and 4.6. At 26/00Z, the NRL analysis once again produced a much tighter thermal gradient across the coastal front than shown by the coarser NMC analysis. In this case however, the NRL analysis was able to significantly sharpen the first-guess temperature gradient across the Carolina coast. The cold air damming is missing in the first-guess field (Fig. 4.17a) and NMC analysis (not shown), but is still evident in the NRL analysis (Fig. 4.17b). The NRL/NCSU analysis scheme was able to use the observational data to enhance the background's weaker gradient generated by our mesoscale model.

At 500 mb, the NRL analysis in case 4.5, like in case 4.3, is successful in correcting the background fields. The phase of the temperature field is again adjusted and the cutoff low has been deepened by 48 m and is within 6 m of the NMC analyzed value. The strong vorticity maximum at the base of the large-scale trough at 500 mb is of the same magnitude in both cases. A weak vorticity maximum is present over Georgia in the NRL analysis (Fig 4.17d) which is not discernible in the NMC analysis (Fig 4.17c). This is a reflection of the stronger secondary circulation in the entrance region of the jet over the eastern U.S. as it interacts with the coastal low. At 250 mb, this jet is also stronger and sharper in the NRL analysis (not shown). As the short wave over the Great Lakes moves eastward, it produces confluence of the flow into the jet thereby strengthening it. The secondary circulation in the entrance region of the jet has begun to absorb and deepen the coastal front's ageostrophic circulation as shown in the cross sections (CS2) in Fig. 4.18. However, the coastal front circulation is still a distinct

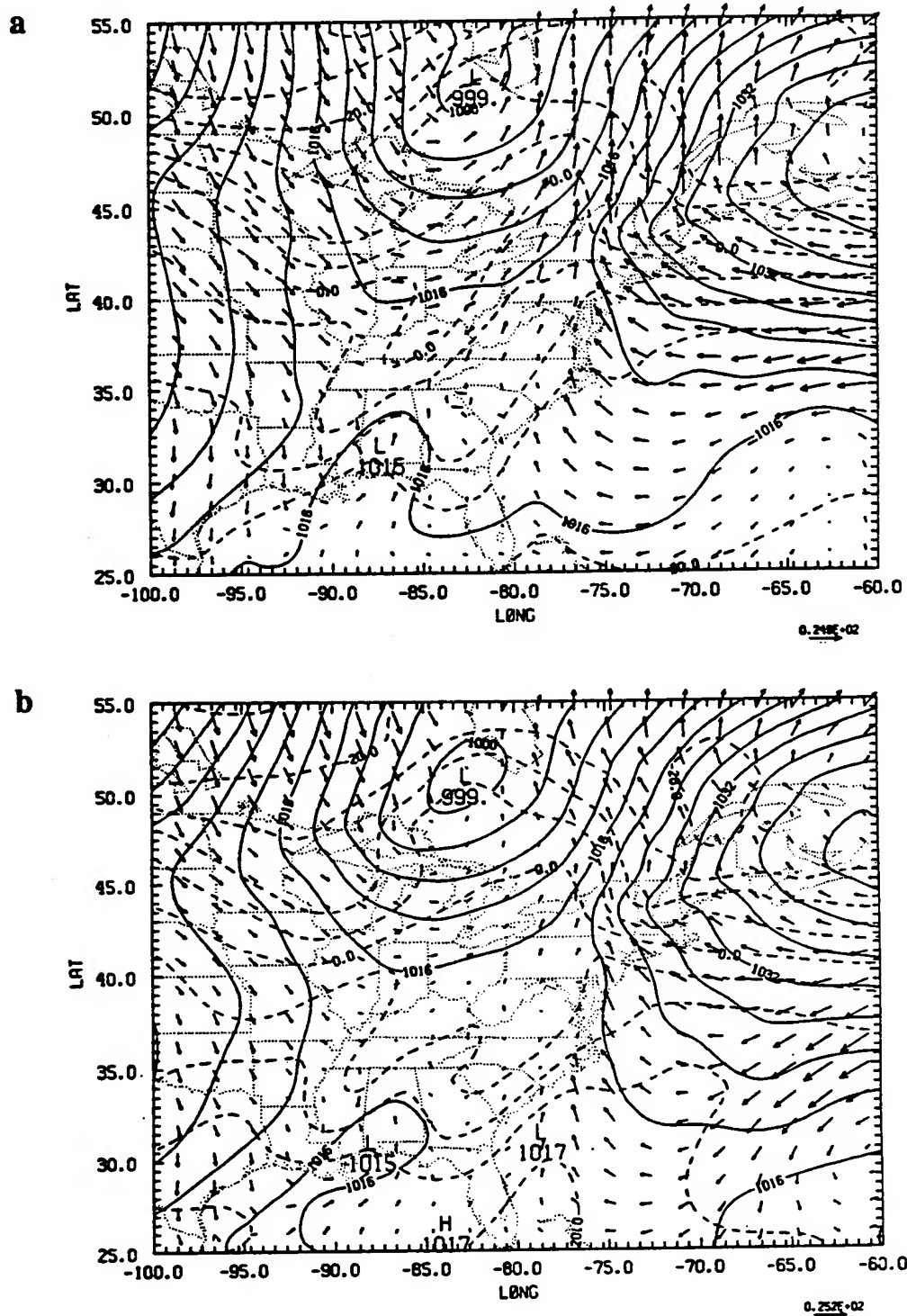


Figure 4.17. Sea-level pressure (mb) and 1000-mb temperature ($^{\circ}\text{C}$) and winds at 26/00Z for (a) the first guess, a 12-h forecast from case 4.4 and (b) the NRL analysis. Absolute vorticity (in units of 10^{-5} s^{-1}) with geopotential height (m) at 500 mb at the same time for (c) the NMC analysis and (d) the NRL analysis.

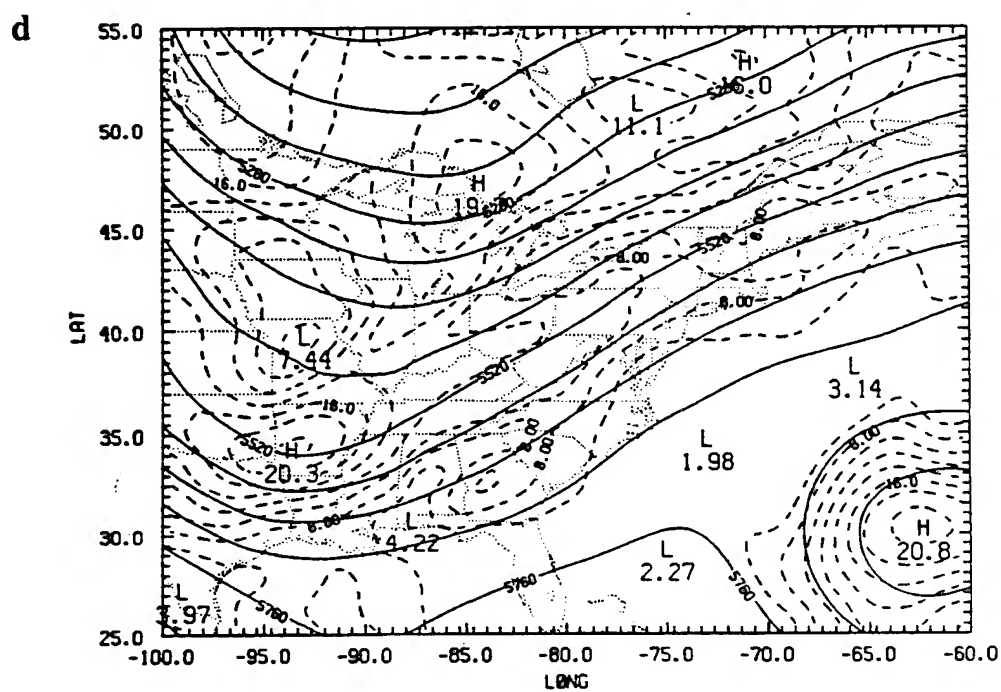
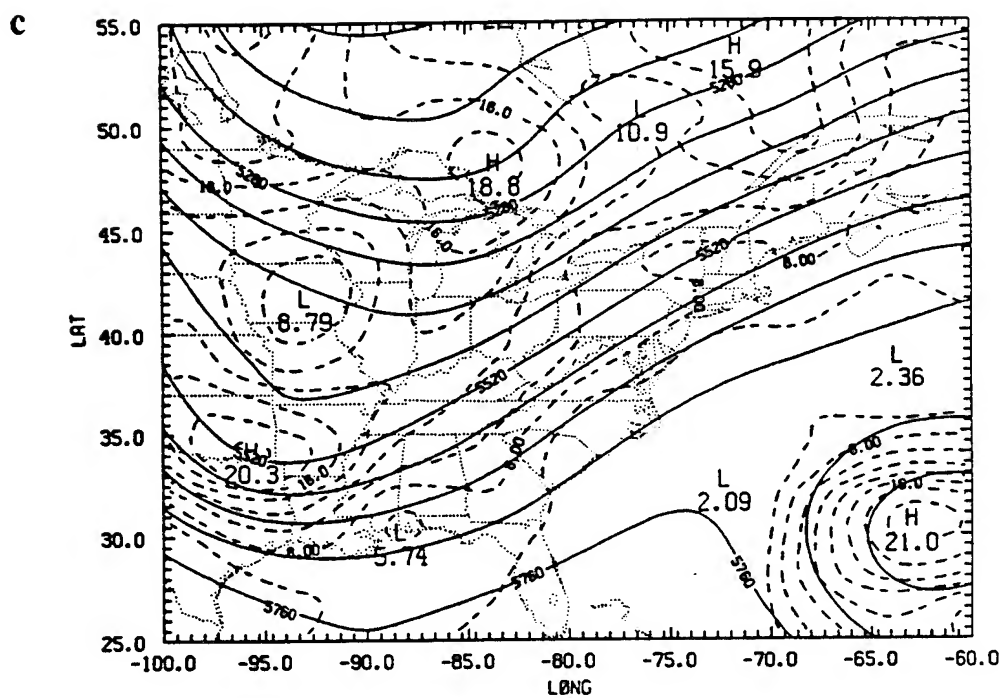


Figure 4.17. Continued.

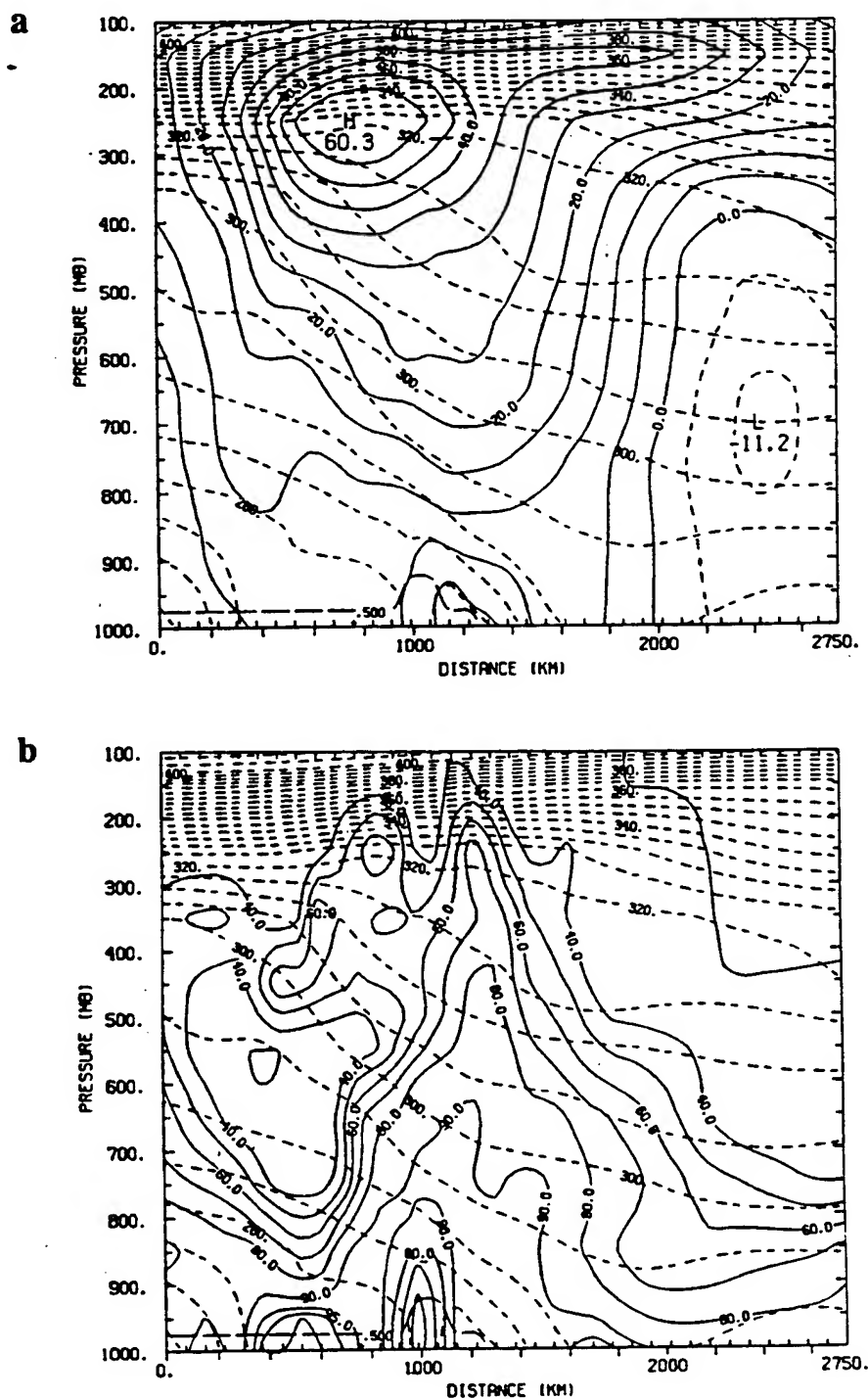


Figure 4.18. The magnitude of (a) the wind (m s^{-1}) normal to the plane of the cross section and (b) the relative humidity (%) in the cross section CS2 for the NRL analysis at 26/00Z. The vertical motion and ageostrophic wind in the plane of cross section CS2 at 26/00Z for (c) the NRL analysis and (d) for the NMC analysis.

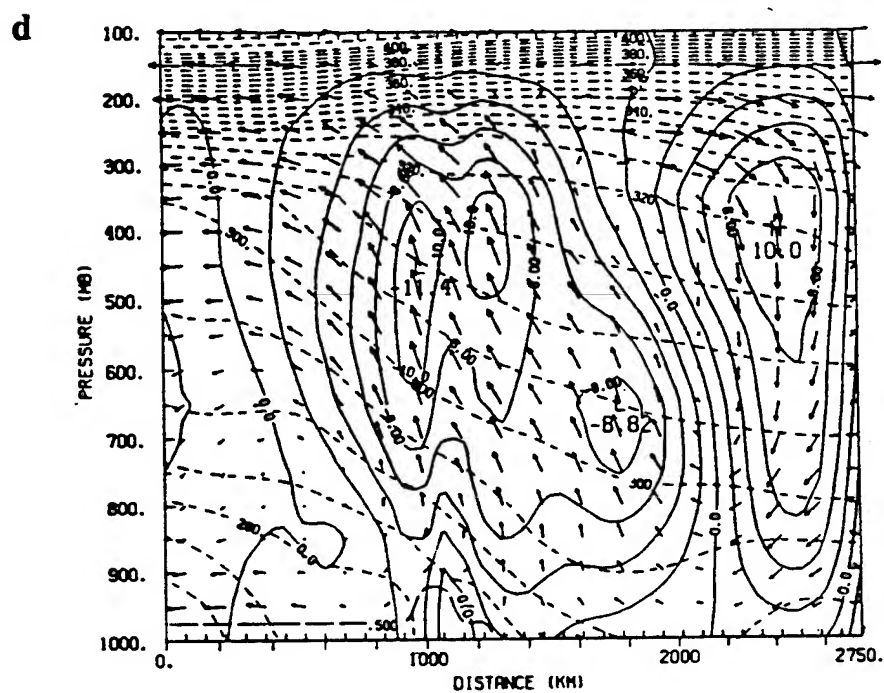
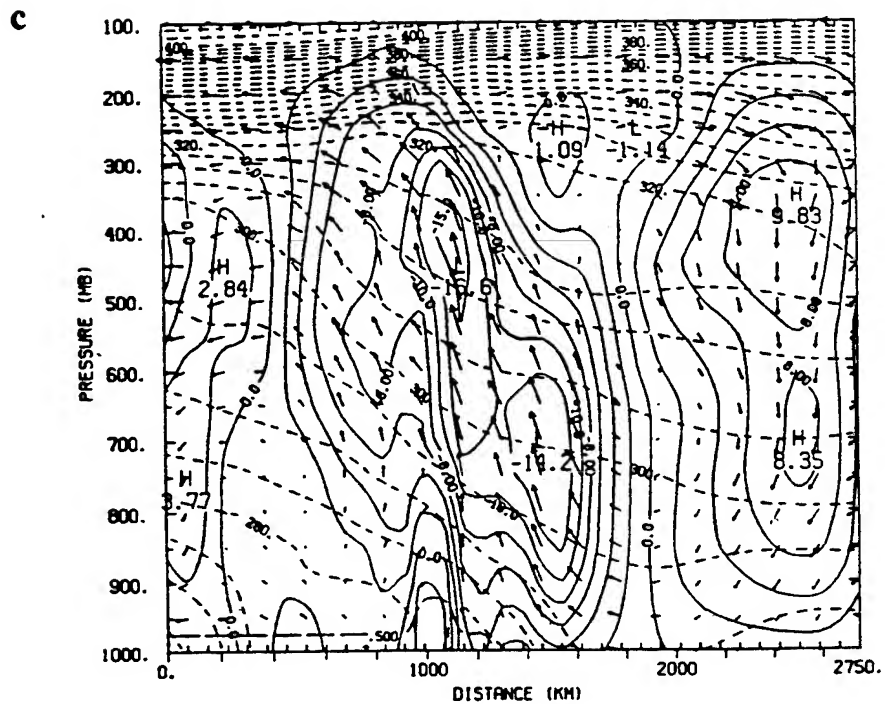


Figure 4.18. Continued.

feature in the cross section, particularly for the NRL analysis shown in Fig. 4.18c. The ageostrophic circulation due to the coastal front remains stronger and sharper in the NRL analysis as compared to the NMC analysis in Fig. 4.18d. Higher humidities are also found over the region of the coastal front in the NRL analysis (Fig. 4.18b). The mesoscale circulation derived from our analysis is also consistent with the 12-h forecast produced in case 4.3, giving confidence in our diagnosed secondary circulations. Also, the horizontal temperature gradient in the lowest 100 mb of the atmosphere in the vicinity of the front (1200 - 1600 km from northernmost end of CS2) is much greater in case 4.3.

By 26/06Z, the forecast from the NRL case 4.5 possessed stronger 500-mb vorticity and vertical velocities along the east coast than in the NMC case 4.6. The resulting 6-h precipitation pattern is much better in case 4.5 (Fig. 4.19a). With a fine-resolution model forecast serving as the first guess, the NRL analysis has the advantage of possessing the strong mesoscale circulations and higher initial humidities which help to force the precipitation. Whereas, the forecast in case 4.6 (Fig. 4.19b) originates from the coarse NMC analysis, which fails to capture these features and leads to a substantial model spin-up which is readily apparent in the precipitation pattern, when compared to the observed rainfall in Fig. 4.19c.

After 12 h of model integration, the surface temperature gradient in the coastal trough is still markedly stronger, and heavier precipitation is generated in the lee of the Appalachians in the forecast originating from the NRL analysis (Fig. 4.20). However, by this time, the upper-level features in the two cases 4.5 and 4.6 are very similar. A cross section (CS3 from 84°W, 43.5°N to 62°W, 27.5°N) across the coast in the region of the coastal low shows a strong vertical circulation in the coastal low merged with the secondary circulation in the jet entrance region (Fig. 4.21a and b). A cross section (CS4 from 70°W, 53°N to 80°W, 28°N) along the coastline cutting through this jet and the one at the base of the large-scale trough is shown in Fig. 4.21c and d. The coastal low

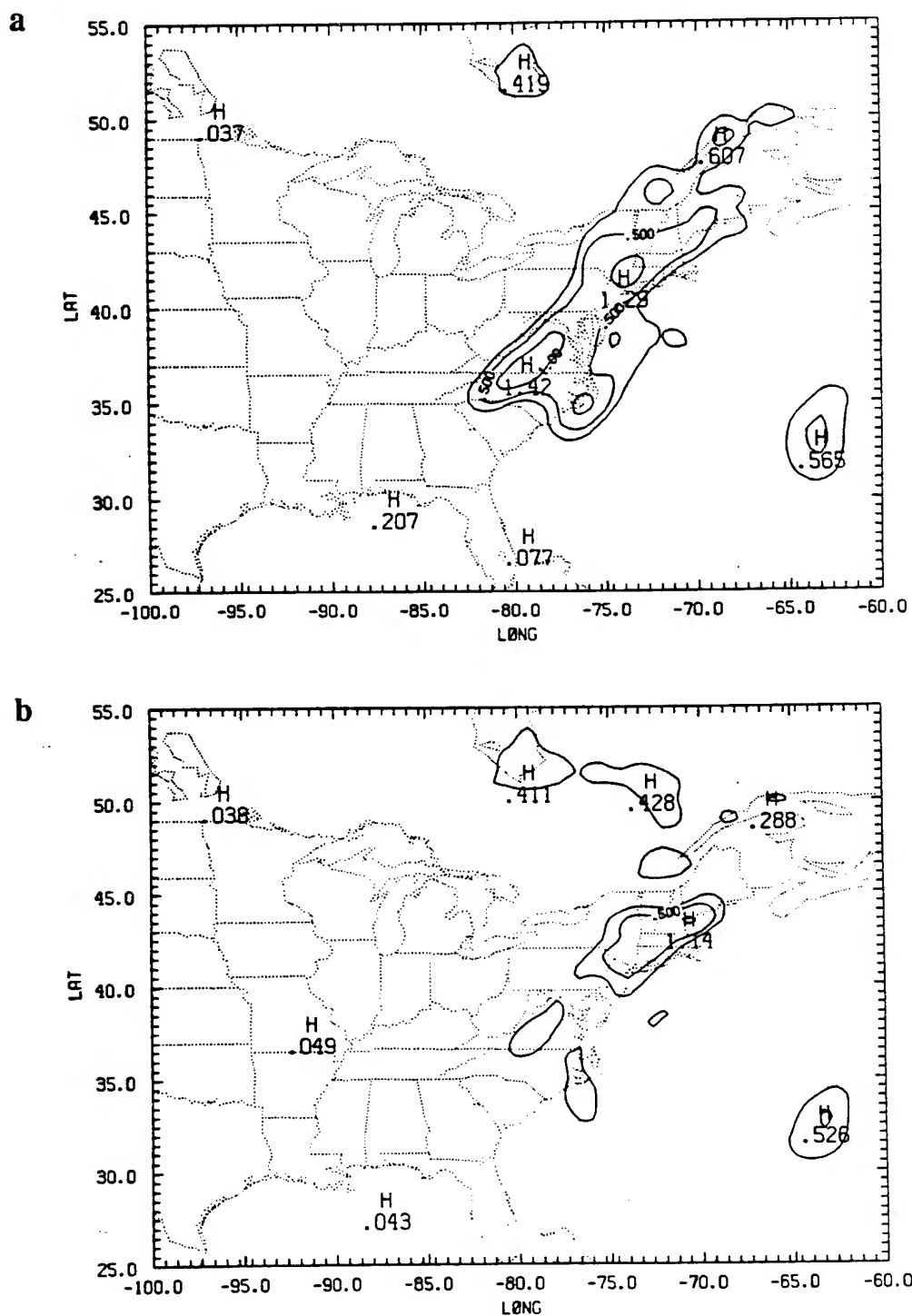


Figure 4.19. Forecast of accumulated total precipitation (26/00Z- 26/06Z) in cm for (a) case 4.5 from the NRL analysis and (b) case 4.6 from the NMC analysis. (c) Six-hour accumulation of observed precipitation (26/00Z- 26/06Z) in cm.

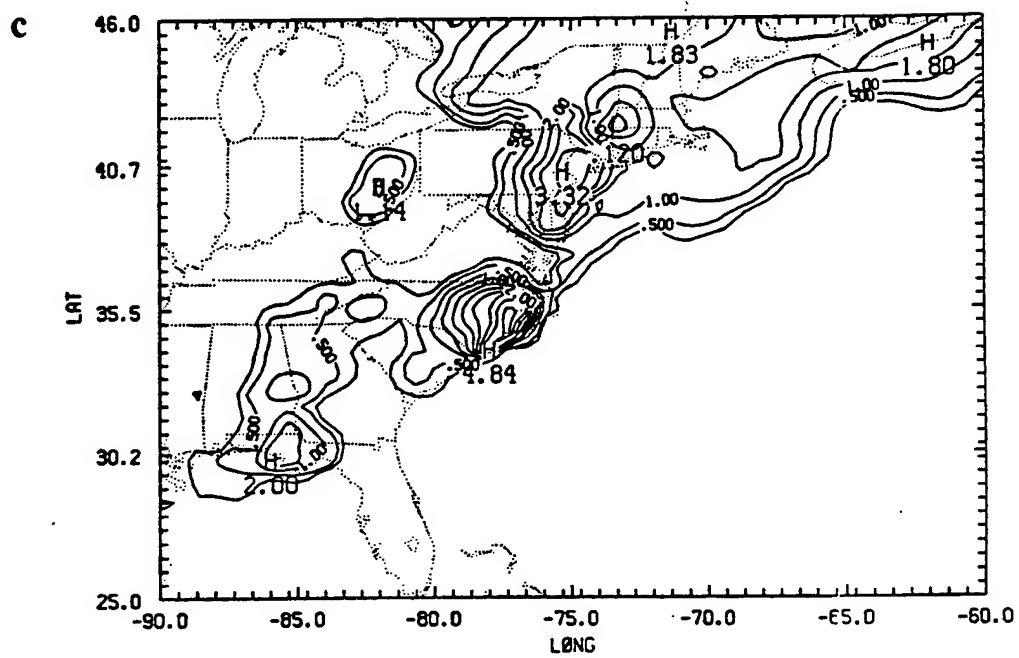


Figure 4.19. Continued.

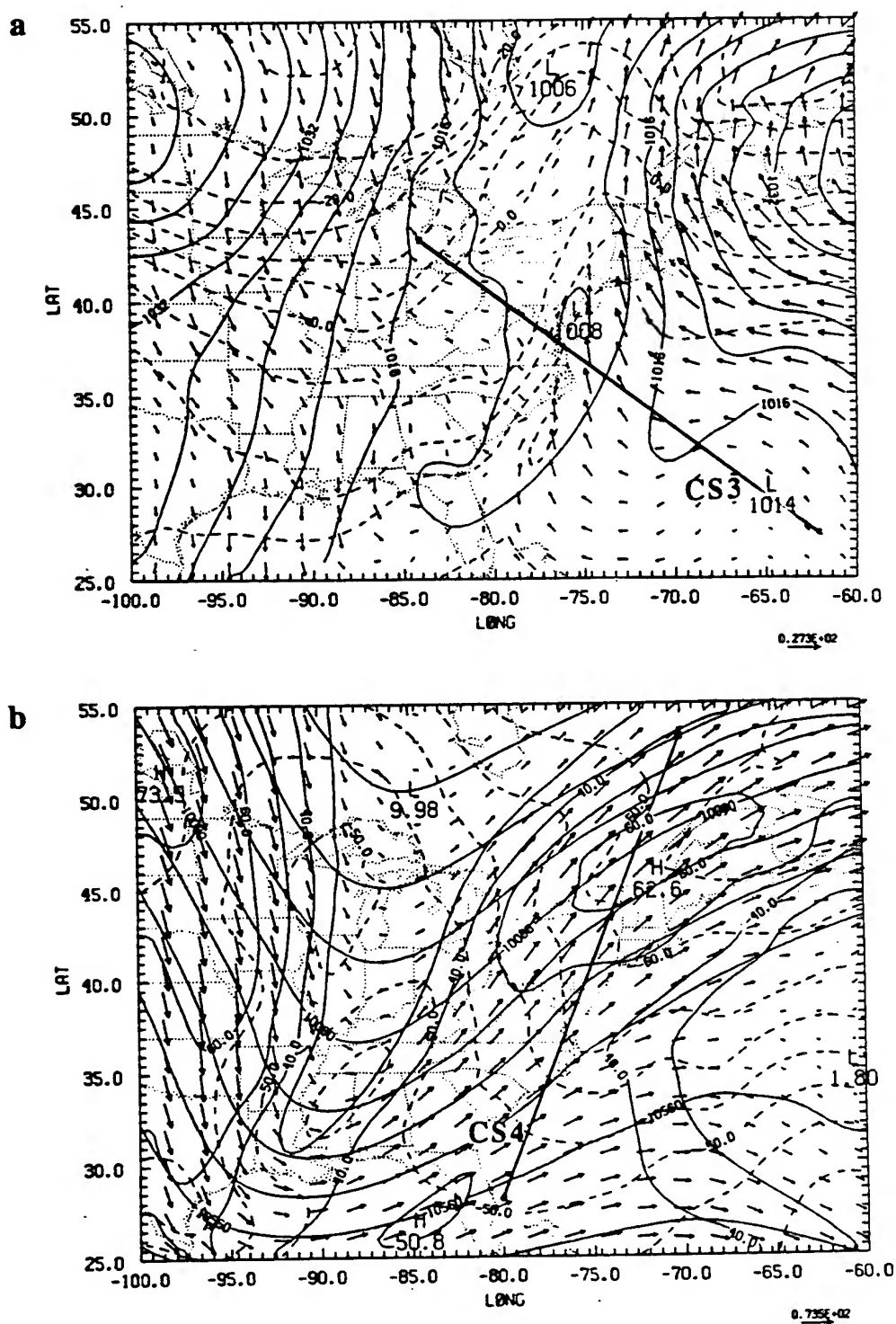


Figure 4.20. Twelve-hour forecast of (a) sea-level pressure (mb) and 1000-mb temperature (°C) and winds and (b) the geopotential height (m), temperature (°C), and winds at 250 mb valid at 26/12Z for case 4.5 from the NRL analysis at 26/12Z. The forecast 6-h accumulated precipitation in cm, valid at 26/12Z for (c) case 4.5 from the NRL analysis and (d) case 4.6 from the NMC analysis.

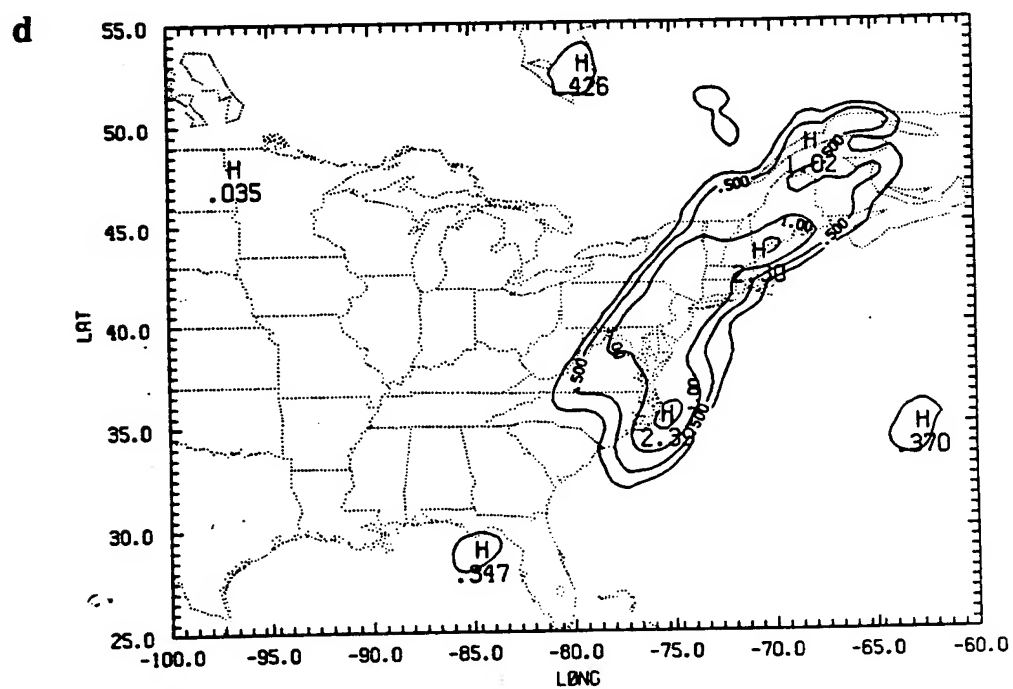
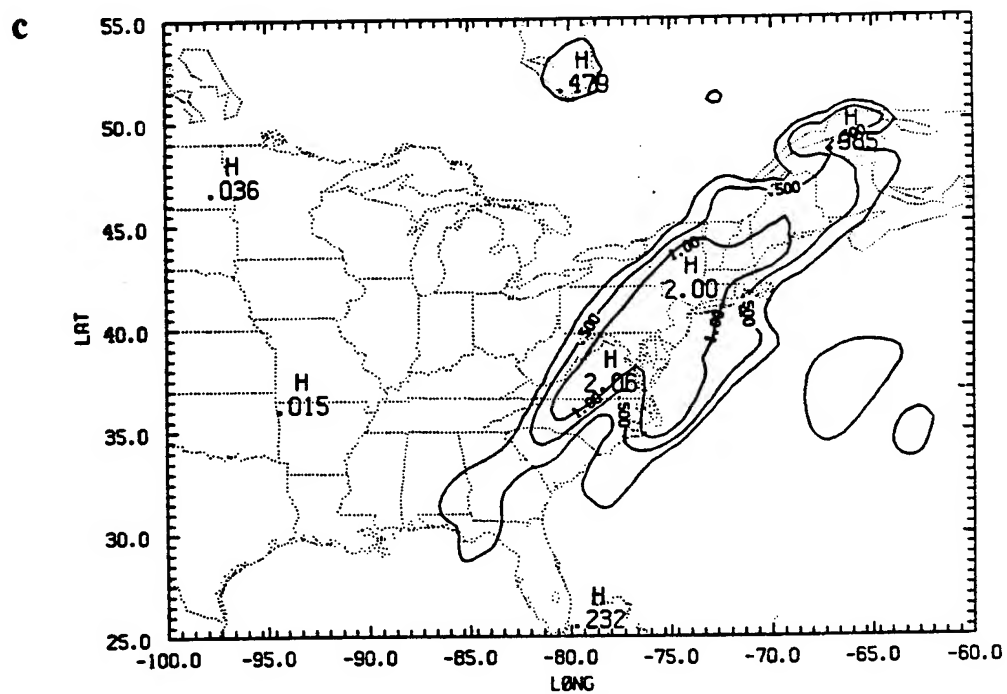


Figure 4.20. Continued.

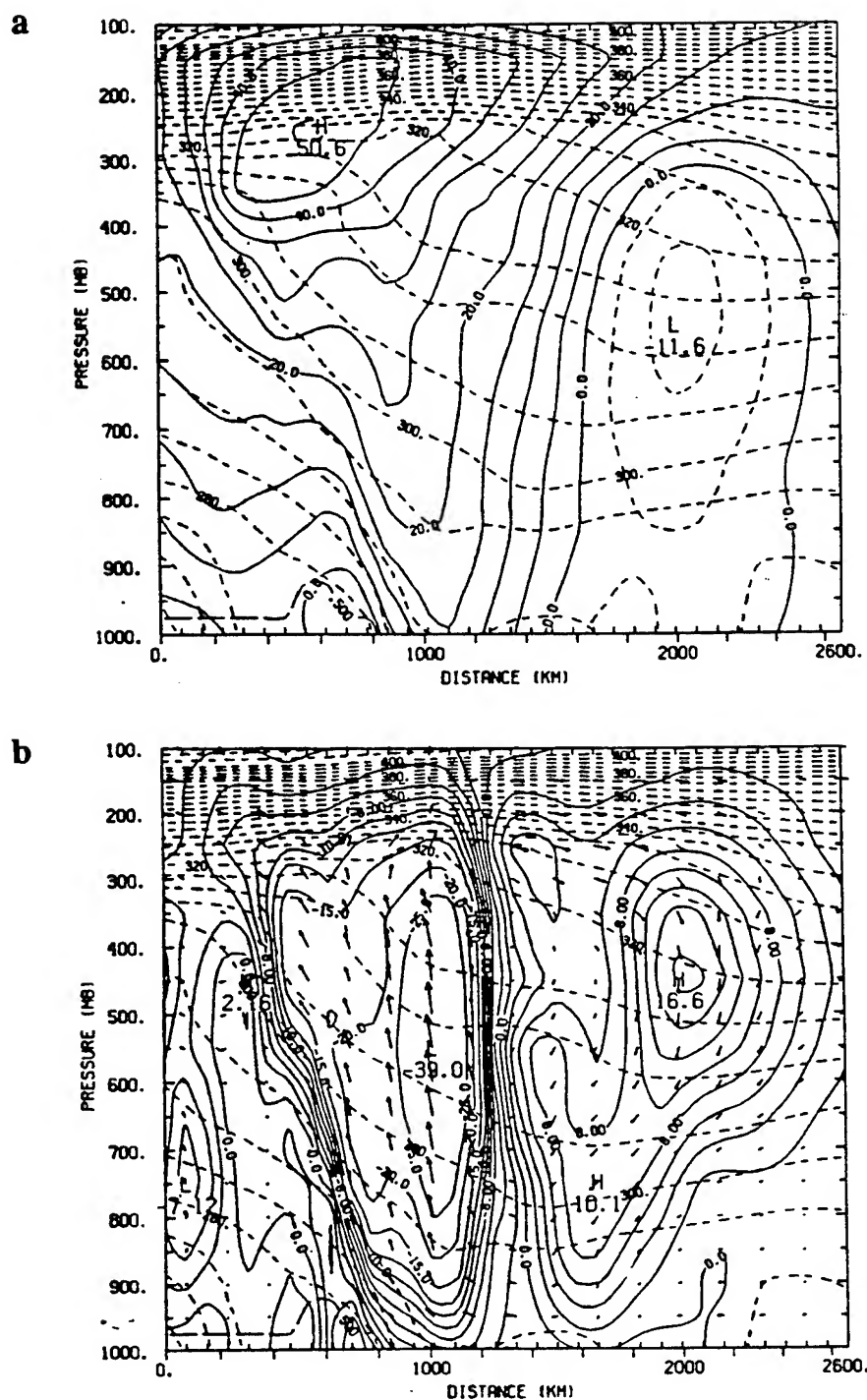


Figure 4.21. Twelve-hour forecast for case 4.5 of the (a) wind (m s^{-1}) normal to cross section CS3 (see Fig. 4.20a) and (b) the vertical motion (mb h^{-1}) and ageostrophic wind (m s^{-1}) in the plane of CS3, valid at 26/12Z. (c) and (d) as in (a) and (b) but for the cross section CS4 (see Fig. 4.20b).

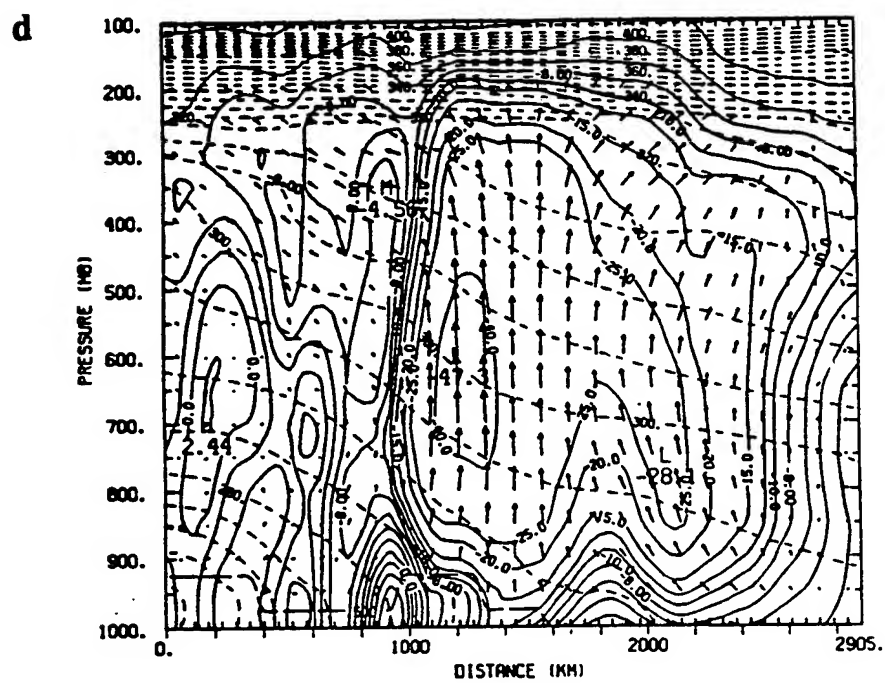
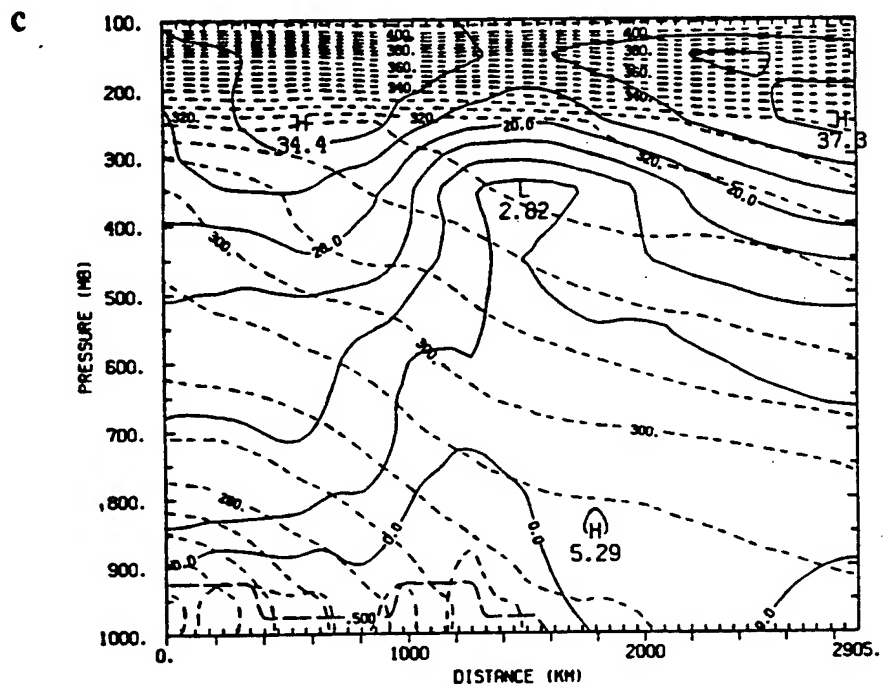


Figure 4.21. Continued.

circulation is shown to the rear of the strengthening direct secondary circulation in the entrance region of the northern jet. Ascent to the south, which is stronger in the forecast from the NRL analysis, is associated with the exit region of the jet at the base of the large-scale trough. This ascent leads to the increased precipitation over western Georgia, which is confirmed by the observed precipitation.

The analyses shown in Fig. 4.22 at 26/12Z confirm the large scale of the developing surface low pressure and upper-air trough, as the strong short wave reaches its base and the northern jet is strengthened by the short wave from the Great Lakes. Due to this large scale, the differences between the NRL and NMC analyses are less apparent. The merging of the circulations associated with the entrance region of the northern jet and the coastal low is still better resolved however by the NRL analysis. Cross sections along (CS4) and across (CS3) the coastline in Fig. 4.23 show the merging of the two circulations. Two circulations can be clearly seen in the cross section across the coast in the region of maximum ascent in the coastal low. As a result of the larger scale of the new developing system, the subsequent forecasts from the NRL (case 4.7) and NMC (case 4.8) analyses reveal less differences than previously. The 12- and 24-h surface forecasts for the NRL case 4.7 (Fig. 4.24) show the development of a new low off Hatteras, which moves northward and deepens rapidly to overshadow the earlier coastal low. In Fig 4.25, cross sections (CS5 from 70°W, 50.5°N to 76°W, 28°N and CS6 from 68.7°W, 55.5°N to 76.7°W, 25.5°N; see Fig. 4.24) along the coast show the secondary circulation in the exit region of the southern jet catching up with the circulation in the entrance region of the northern jet, so that they cooperate in strengthening the ascent in the rapidly developing low. Such has been found in other cases analyzed by Uccellini and Kocin (1987).

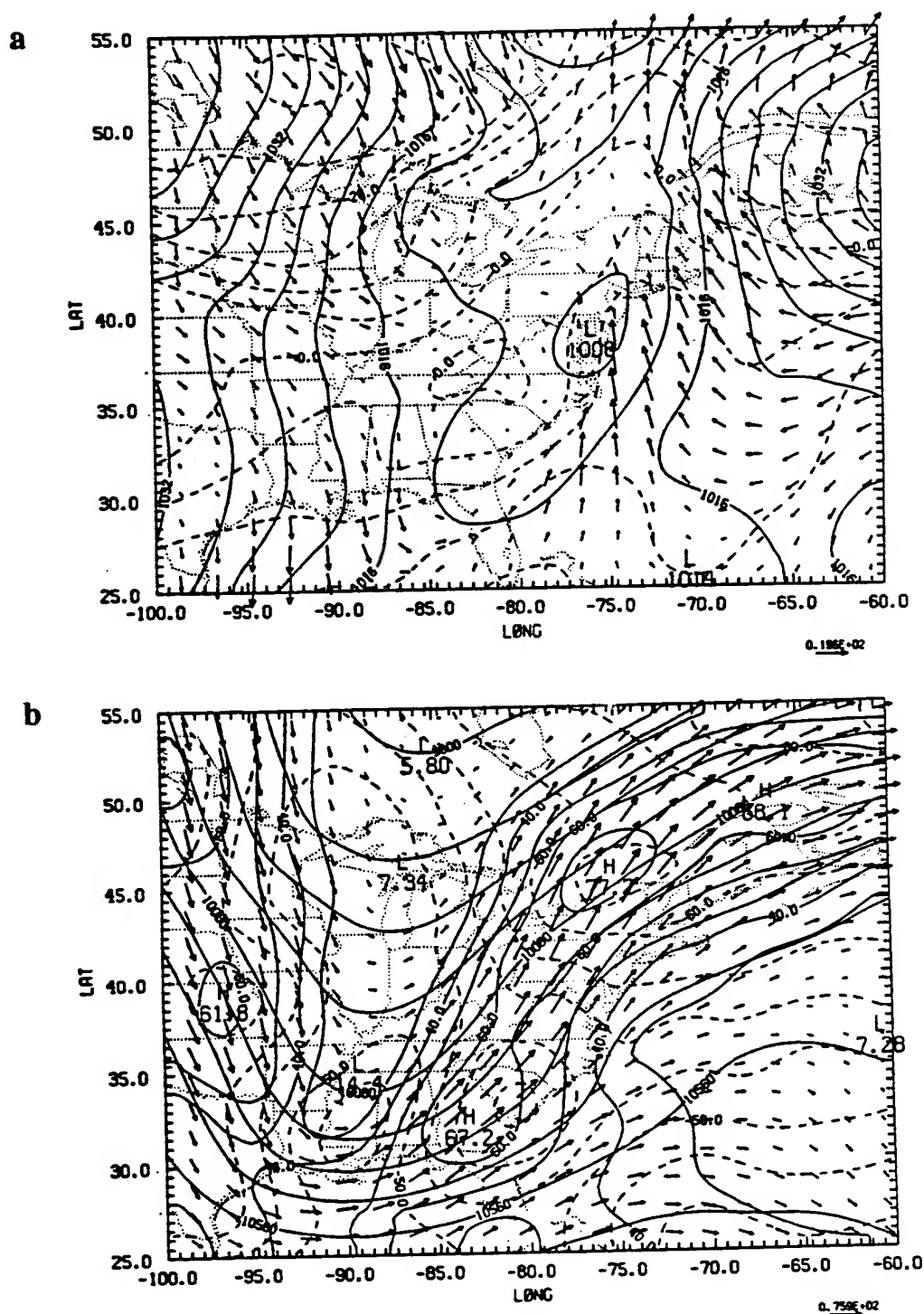


Figure 4.22. (a) Sea-level pressure (mb) and 1000-mb temperature ($^{\circ}\text{C}$) and winds, (b) the geopotential height (m), temperature ($^{\circ}\text{C}$), and winds at 250 mb, (c) absolute vorticity (in units of 10^{-5} s^{-1}) with geopotential height (m) at 500 mb, and (d) the vertical velocity in mb h^{-1} at 500 mb for the NRL analysis at 26/12Z.

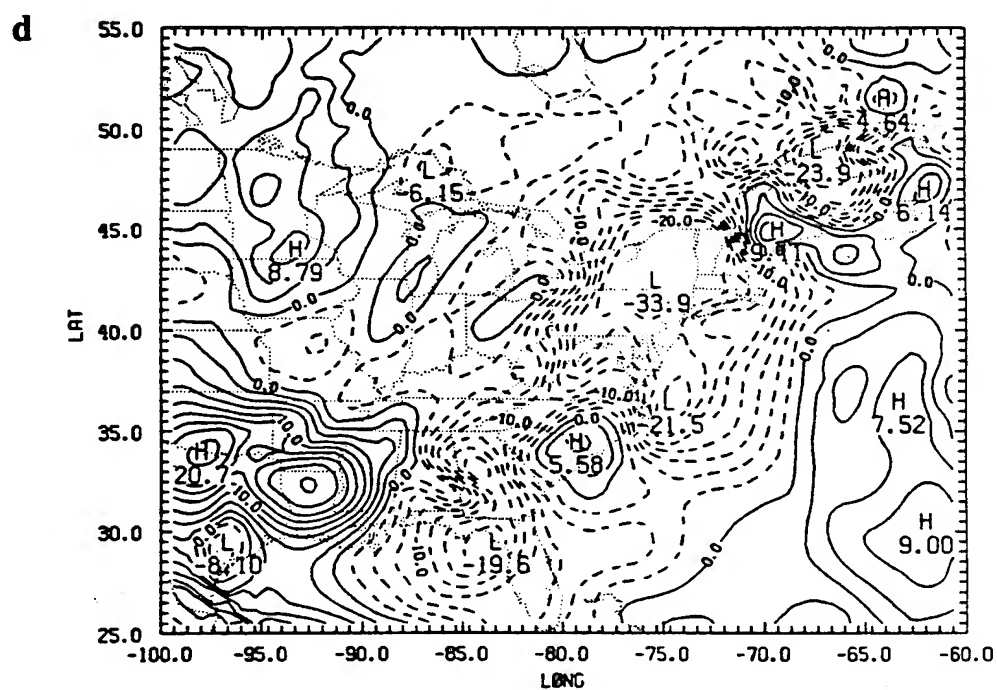
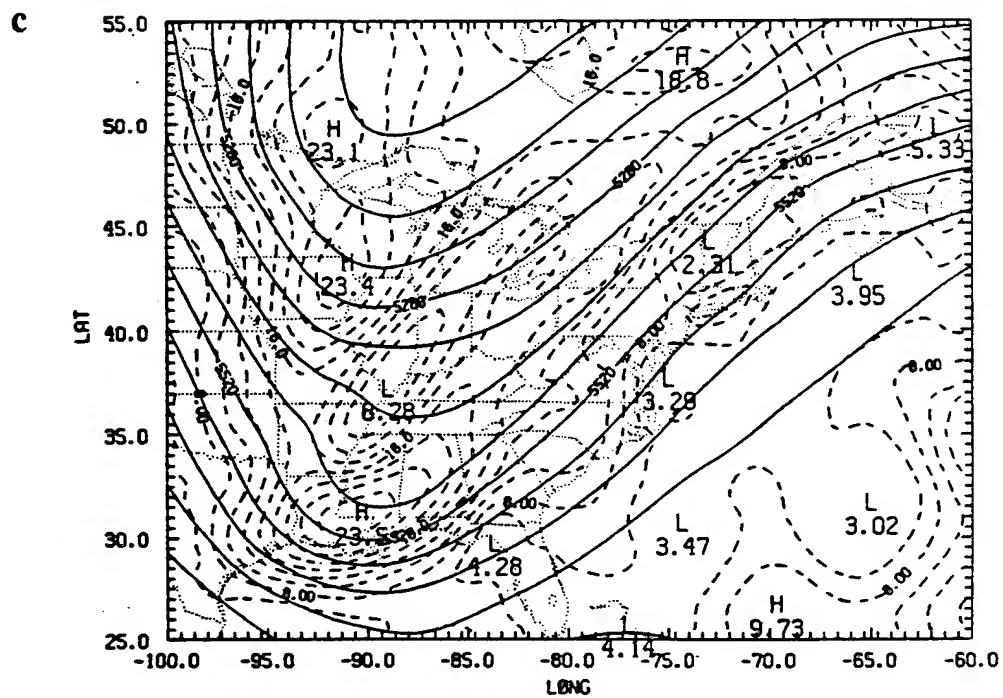


Figure 4.22. Continued.

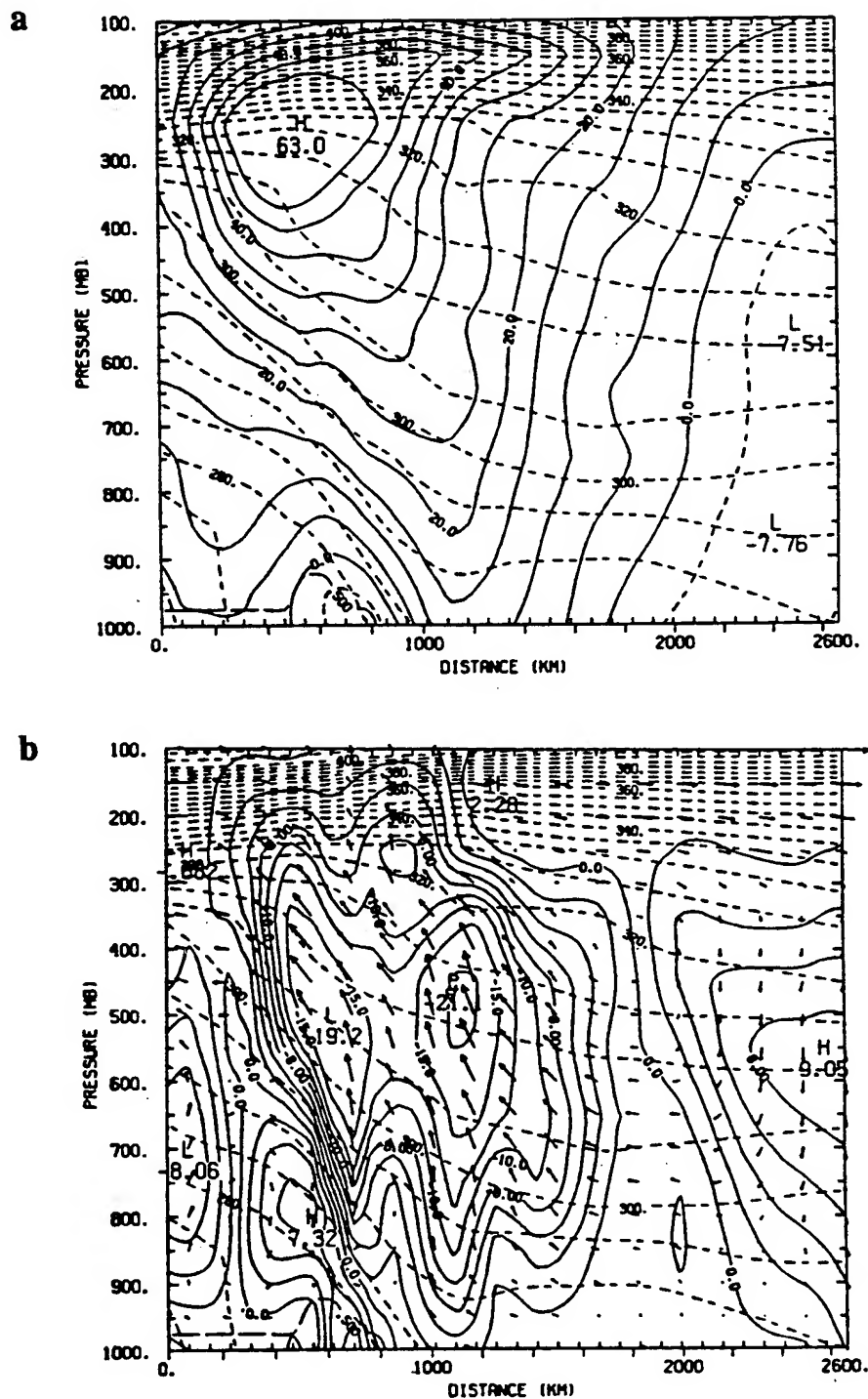


Figure 4.23. (a) The wind (m s^{-1}) normal to the cross section CS3 and (b) the vertical motion (mb h^{-1}) and ageostrophic wind (m s^{-1}) in the plane of CS3 for the NRL analysis valid at 26/12Z. (c) and (d) as in (a) and (b) but for the cross section CS4.

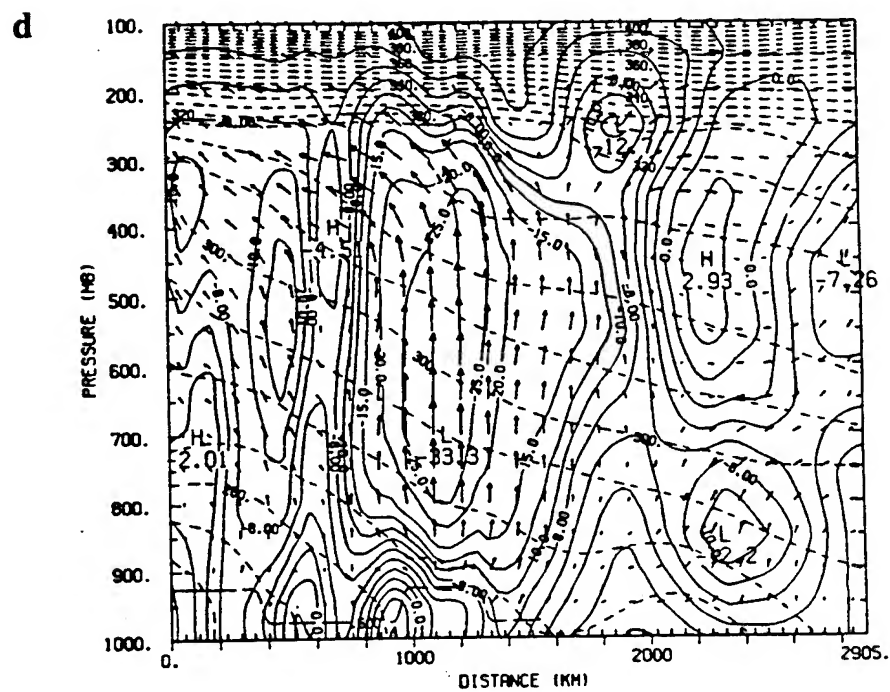
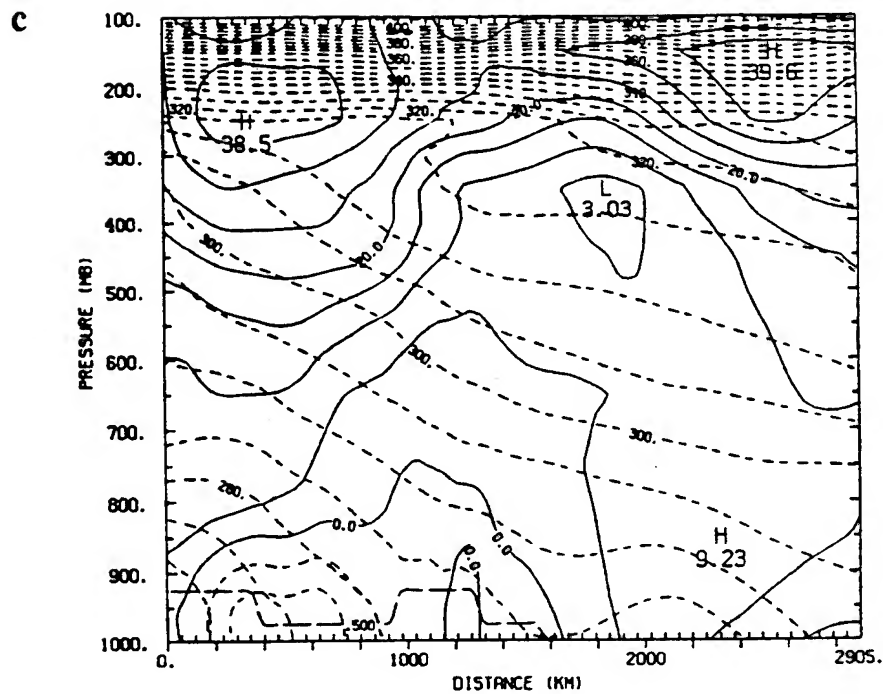


Figure 4.23. Continued.

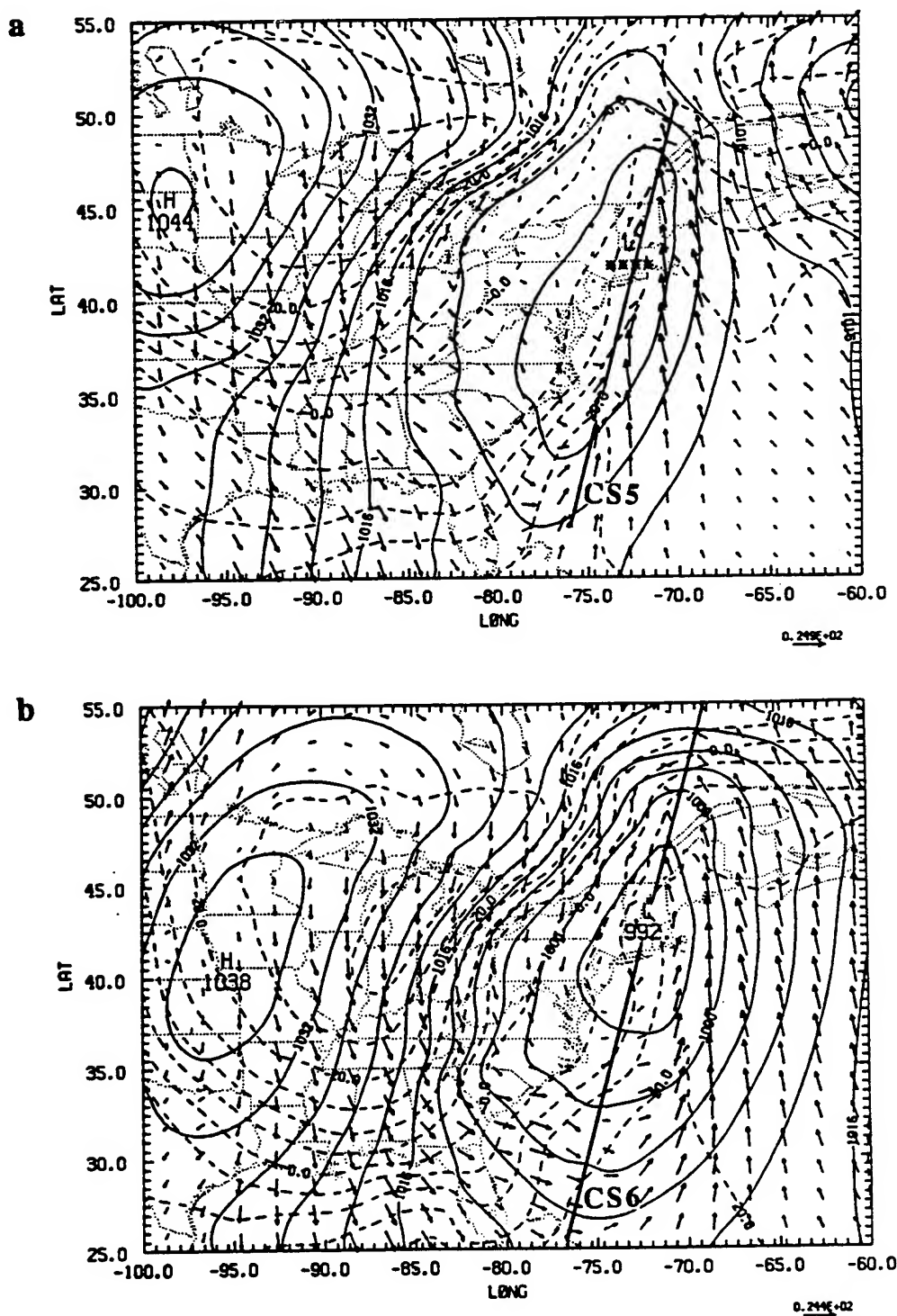


Figure 4.24. (a) Sea-level pressure (mb) and 1000-mb temperature ($^{\circ}\text{C}$) and winds for (a) a 12-h forecast valid at 27/00Z and (b) a 24-h forecast valid at 27/12Z for case 4.7 integrated from the NRL analysis at 26/12Z.

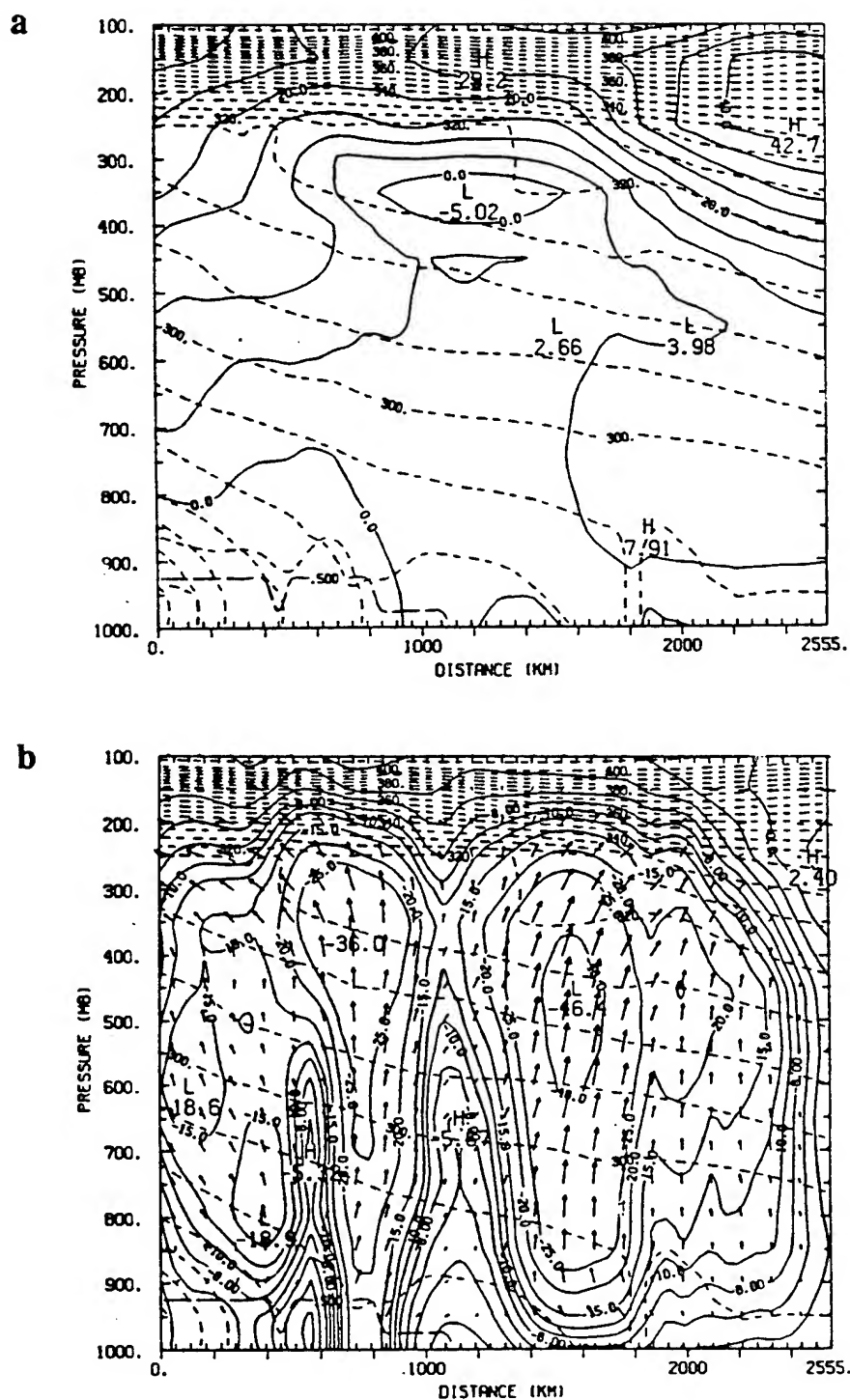


Figure 4.25. Twelve-hour forecast for case 4.7 of the (a) wind (m s^{-1}) normal to cross section CS5 (see Fig. 4.24a) and (b) the vertical motion (mb h^{-1}) and ageostrophic wind (m s^{-1}) in the plane of the same cross section valid at 27/00Z. (c) and (d) the same as (a) and (b) but for a 24-h forecast for cross section CS6 (see Fig. 4.24b) valid at 27/12Z.

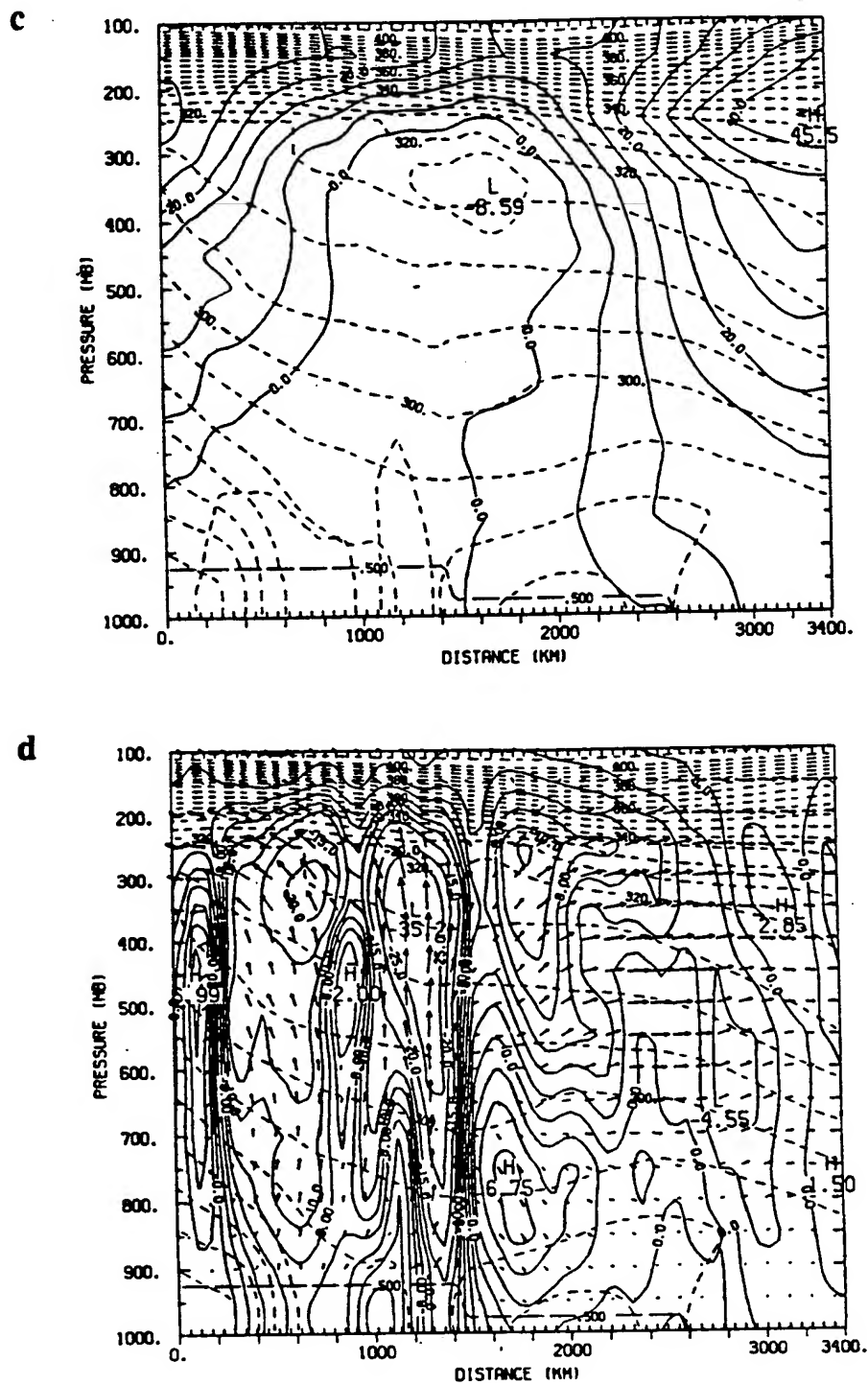


Figure 4.25. Continued.

4.5 Summary

During the last decade, optimal interpolation replaced successive correction methods as the dominant objective analysis technique in operational weather forecasting systems. However, with the advent of Bratseth's (1986) analysis scheme, which converges to the optimal interpolation solution, the less expensive approach of successive correction has become a powerful and attractive alternative analysis method. The objective analysis scheme developed for use with the NRL/NCSU mesoscale model utilizes the Bratseth scheme, in which the data weights are dependent on the covariance between observations, are reduced in regions of higher data density, and include observational errors.

A computationally inexpensive multivariate methodology for linking the mass and momentum fields has been devised and is different from earlier methods reported in the literature. The key element is obtaining the gradient of the geopotential change from the change in u - and v - through the geostrophic relation at each iteration of the analysis process.

A qualitative evaluation of the NRL/NCSU objective analysis scheme has been accomplished. Several tests were conducted using a GALE IOP 2 data set. NRL analyses verified well against Bosart's hand analyses. The multivariate analysis was successful in deepening the cutoff low over the western Atlantic. The univariate analysis showed some improvement, but as expected, the multivariate analysis proved to be superior by using wind information to achieve gradients of geopotential through the geostrophic relationship. The NRL multivariate analysis was also successful in bringing the first-guess temperature pattern into proper phase.

A very encouraging finding was that the second-order fields of absolute vorticity and vertical motion were significantly improved by the objective analysis. Gradients and

maxima and minima were pushed toward those found in the NMC analyses. In addition, the upper-level jet from the background field was strengthened and tightened.

In the cases where the forecast originated from an NRL analysis, the forecast fields maintained the mesoscale features better than those originating from an NMC analysis. The first-guess fields from a prior model forecast already contains those finer scale features. The objective analysis was not only successful in retaining those finer scale features, but also was able to correct their phases and magnitudes. The mesoscale circulations associated with the coastal front on 25-26 January 1986 were forecast more accurately when the NRL multivariate analysis was incorporated.

5. DIABATIC INITIALIZATION EXPERIMENTS WITH CONVECTIVE HEATING

The analyses presented in the previous chapter were initialized adiabatically for model integration. That is, the vertical mode initialization procedure did not include forcing due to diabatic heating. Here, convective heating is accounted for in the model initialization.

5.1 Introduction

The dominant forcing in the troposphere within areas of precipitation is diabatic heating (convective and radiative heating and large-scale condensation). The present study deals strictly with diabatic heating from cumulus convection. A convective heating term is incorporated in the balance condition for the high frequency normal modes (Bengtsson 1981; Errico and Rasch 1988; Kitade 1983; Wergen 1983). With the inclusion of heating corresponding to observed rainfall data in the diabatic forcing term, the initialization can force the model state toward the real atmospheric state. As a result, the diabatic initialization corrects the model's forecast fields. Possibly the primary benefit of initialization with diabatic forcing is that the spinup problem (the extent that the initial amplitude of the divergent part of the wind and the precipitation are in error) can be minimized. That is, diabatic vertical mode initialization (DVMI), also referred to as diabatic nonlinear normal mode initialization, produces an initial model state which already includes convective heating.

Model spinup appears in all numerical forecast systems both in midlatitudes and tropics (Kasahara et al. 1988). It is one of the most serious problems in numerical

weather prediction and has been documented in research and operational models. Girard and Jarraud (1982) and Heckley (1985) documented spinup in the operational models used by the European Centre for Medium Range Weather Forecasts. Whereas, Miyakoda et al. (1978) and Donner (1988) illustrated different aspects of the spinup phenomena in research models at the Geophysical Fluid Dynamics Laboratory and National Center for Atmospheric Research, respectively.

Inadequate physical parameterizations and incorrect initial specifications of divergence, moisture and thermal fields are the primary causes of spinup (Mohanty et al. 1986). Until recently, most normal mode initialization methods were adiabatic in nature; that is, the existing latent heating at the initial model time was excluded leaving out a significant heat source which affected the adjustment between the mass and momentum fields. Lejenas (1980) found that adiabatic normal mode initialization, while providing improved vertical velocity profiles, does not alleviate the spinup problem. Data-assimilation techniques which incorporate a spun-up background field in the analysis of observed data have been developed. At the start of each update cycle of the assimilation, the background forecast field is corrected using the observed mass and momentum fields. During this process, the divergent part of the wind is lost primarily because the divergence has the same order of magnitude as the errors in the wind field. This divergent circulation associated with upward vertical motion can be regained if the analysis at each cycle of the assimilation is initialized with a diabatic initialization procedure. Turpeinen et al. (1990) concluded that the inclusion of observed low-level latent heat sources with a consistent and higher-resolution moisture analysis are critical components in reducing the underestimation of initial divergence, and hence precipitation rates.

Throughout the 1980s, NWP models incorporating initial latent heating based on rain rates have been developed. Turpeinen et al. (1990) summarized the main features of some of these models. Mohanty et al. (1986) investigated the inclusion of diabatic

heating in the vertical mode initialization (VMI) and found that the divergent circulation was rapidly destroyed by the integrated model heating if it differed too much from the observed heating. In the present study, we have merged the model-produced heating, during the first few hours of integration, with the heating used in the initialization.

The major thrust here is to incorporate the latent-heat forcing into the vertical mode initialization of the NRL/NCSU mesoscale model in an effort to shorten the spinup time. The goal is also to demonstrate that VMI with diabatic forcing provides improved initialized fields over adiabatic VMI. A diabatic heating term, derived from 'spunup' model convective rainfall and observed rainfall, has been included in the vertical mode initialization to better define the initial conditions for model integration. Several model runs (test cases) are made to test the effectiveness of DVMI as compared to initialization excluding the heating term, or adiabatic VMI (AVMI). The procedure for computing the diabatic heating for the initialization is described, followed by the experimental design and results.

5.2 Diabatic Heating in Model Initialization

Until recently the NRL/NCSU model was initialized exclusively using an adiabatic vertical mode initialization. The procedure is detailed by Sashegyi and Madala (1990, 1992a) and is discussed briefly in Chapter 3 of this document. In their VMI only the first three modes, the external mode and first two internal modes of the model, are initialized. Sashegyi and Madala (1990) showed that the first two modes require only two iterations of the scheme to converge. The third mode converged after five iterations. The phase speeds of these modes are much faster than typical meteorological systems, which move at speeds less than 20 m s^{-1} .

Adiabatic VMI has proven to be extremely effective in controlling spurious large-amplitude gravity wave oscillations due to initial imbalances between the mass and wind fields in primitive equation models (Puri and Miller 1990; Sashegyi and Madala 1990). However, the use of AVMI leads to a drastic depletion of the divergent circulation.

Wergen (1983 and 1987) introduced a procedure to overcome this problem, in which average diabatic heating is obtained by integrating the model for a few time steps prior to the initialization. The average heating is then included in the nonlinear forcing of the iterative initialization process. The fixed diabatic heating is determined as the time-mean heating generated by model physics (cumulus parameterization and large-scale heating) during the short integration. Unfortunately, most forecast models do not produce realistic heating rates during the first few hours, leading to the spinup problem. Therefore, for present experiments, the choice was made to integrate the model for 9 h before accumulating the model latent heating and convective rainfall from which our time-mean heating and rainfall rates were derived. The diabatic VMI (DVMI) used in this study is similar to Wergen's, but it is original in that 'spun-up' model heating is applied in the initialization, rather than the heating from the first few hours of integration as is usually done. The procedure involves the following steps:

- The model is integrated for 12 h from adiabatically initialized fields. Convective rainfall, from which the diabatic heating is derived, is accumulated from 9-12 h of this initial integration (control run), allowing ample time for model spinup.

- Time average convective rainfall rates over the 3-h period are derived for all grid points.

- The average rain rates are converted into vertical profiles of heating using a reverse Kuo cumulus parameterization. This vertical distribution of the latent heating is based on the cumulus convective scheme of the model. Thus, no simplifying hypotheses are needed. The advantage of the present approach is an improved consistency obtained

with the physical parameterization scheme of the model. In future studies, observed rainfall will be combined with our model rainfall rates in this procedure to obtain more objectivity.

-- This three-dimensional diabatic heating field is then added as a forcing term in the VMI thermodynamic energy balance equation as the implicit DVMI is performed. As a result, diabatic effects are implicitly included in the specification of the heating field.

The diabatic initialization described above is primarily for heating associated with convective precipitation. The heating is nearly zero in the lower troposphere and varies significantly from case to case in the upper troposphere. The first three modes of the model account for 40 to 50% of the convective heating in the upper troposphere. Therefore, we assume that the method described here accounts for a significant part of the divergence field.

The conversion of rainfall rates into vertical profiles of convective heating depends on the stability of the environment as determined by the cumulus parameterization. If convective instability occurs, a heating function is computed using the reverse Kuo scheme. This heating function is then used to distribute the diabatic heating, derived from the average rainfall rates, in the vertical direction. If the environment is convectively stable, the diabatic heating associated with the two-dimensional rainfall distribution will be taken as zero. Therefore, non-convective precipitation does not contribute to the diabatic heating in the present initialization scheme.

The persistence of balance achieved by DVMI during the early stages of the model integration depends heavily on the compatibility between the specified heating during initialization and the model-produced heating during integration (Puri and Miller 1990). Puri (1987) suggested that one possible way of retaining this compatibility in the heating rates would be to adjust the moisture field until the model-produced heating rates determined by the convective parameterization in the model are similar to those used

during DVMI. Here, two procedures are used to retain this desired compatibility in heating rates. First, the model rainfall and heating rates produced during the first 3 h of integration are merged with the corresponding rates from the initialization. A nonlinear weighting factor (α) is employed where $\alpha=1$ at $t=0$ h and $\alpha=0$ at $t=3$ h. The relation is given by:

$$R_m = \alpha R_i + (1-\alpha) R_c \quad 5.1$$

where R_i is the convective rainfall rate used in the diabatic VMI, R_c is the model-produced convective rainfall rate, R_m is the merged rain rate, and α is given by:

$$\alpha = 1 - \frac{[1 + \sin(\pi t / 3 - \pi / 2)]}{2} \quad 5.2$$

The above relations allow the influence of the initialized heating and rain rates to approach zero in a smoother manner than a simple linear relationship would allow. Merging is applicable only for DVMI cases since AVMI, by definition, does not include a diabatic heating term in its balance equation.

The second method involves adjusting the humidity fields prior to initialization. The importance of moisture adjustment in diabatic initialization was emphasized by Wolcott and Warner (1981). They argued that if the environment is not humid enough, the upward motion associated with the initialized divergence field will not be sustained by latent heat release. In the present study, specific humidity is enhanced only at grid points where convective rainfall is occurring and the relative humidity is less than 95%. At those points, the specific humidity is increased to 95% of the saturation specific humidity at the three lowest model levels. However, our findings indicated that the changes in the humidity fields were small, and, as a result, the adjustment had minimal affect on the convective rainfall. Since the modeled large-scale condensation occurs only upon

supersaturation, not at 95% relative humidity, this moisture adjustment would have little affect on non-convective precipitation.

5.3 Experimental Design

Initially, three test cases (model runs) were performed to determine improvements (if any) in the model initial state and subsequent forecasts using DVMI versus AVMI. The first is a control run (case 5.1) in which the model is initialized at 1200 UTC 26 January 1986 (26/12Z) using the NMC analyzed data. These data of 2.5° resolution are first interpolated to the model grid and then initialized with the AVMI for the first three vertical normal modes of the model. The model is then integrated for 24 h. The 12-h forecast from the control run serves as the initial fields for cases 5.2 and 5.3. In case 5.2, the model is initialized using DVMI on the forecast fields from case 5.1 valid at 27/00Z. Model-generated rainfall (26/21Z to 27/00Z of the control) is used to compute heating rates at each vertical level of the model for the DVMI. The model is then integrated for 12 h, with heat/rain merging. The initialization for the next case (case 5.3) is simply an AVMI on the control run's 12-h forecast.

For this study, the control run is considered the "truth" for comparison against the other two cases. From 26/12Z to 27/00Z of the control run, the model should have sufficient time to spin up, or in other words, develop the divergent part of the wind. By using model-generated rainfall rates in the DVMI (case 5.2), one would expect a negligible spinup during the subsequent forecast. Also, one might expect little change due to the initialization using model rain since the model heating function is consistent with other model parameters. By comparing the initialized and subsequent forecast fields from case 5.2 with the corresponding fields from the control, one can determine if the

model-generated rainfall, which is a two-dimensional (2-D) distribution, can re-create the 3-D distribution of vertical heating rates accurately.

5.4 Results

The following results were obtained by making qualitative comparisons of meteorological fields from the different model initializations and forecasts of the three test cases. The differences between cases 5.2 and 5.3 of their respective initialized fields of 1000 mb, 500 mb, and 250 mb geopotential height, temperature, and winds are extremely small. As expected, the first-order analysis fields (12-h forecast from the control run) changed little with each initialization in these test cases and, as a result, the forecasts (valid at 27/12Z) of these variables from these two runs are almost identical and agree well with the control run forecast.

5.4.1 Comparison of Initialized Vertical Velocity

Since vertical velocity or omega (dp/dt) is directly related to diabatic heating, we can expect noticeable differences between the initial states of omega from cases 5.2 and 5.3. Furthermore, the effectiveness of diabatic heating in inducing divergent circulations can be seen by comparing omega fields from DVMI and those resulting from AVMI. As expected, in geographic areas absent of precipitation, vertical velocity patterns in cases 5.2 (DVMI) and 5.3 (AVMI) are approximately the same and very close to the "truth" (Fig. 5.1). Off the east coast, an area of strong ascent stretches along the eastern seaboard and is associated with the old frontal boundary and the developing cyclone off the North Carolina coast. In this region where the control run ("truth") predicts heavy rain at initialization time (27/00Z), the initialized state for case 5.2 is very close to the

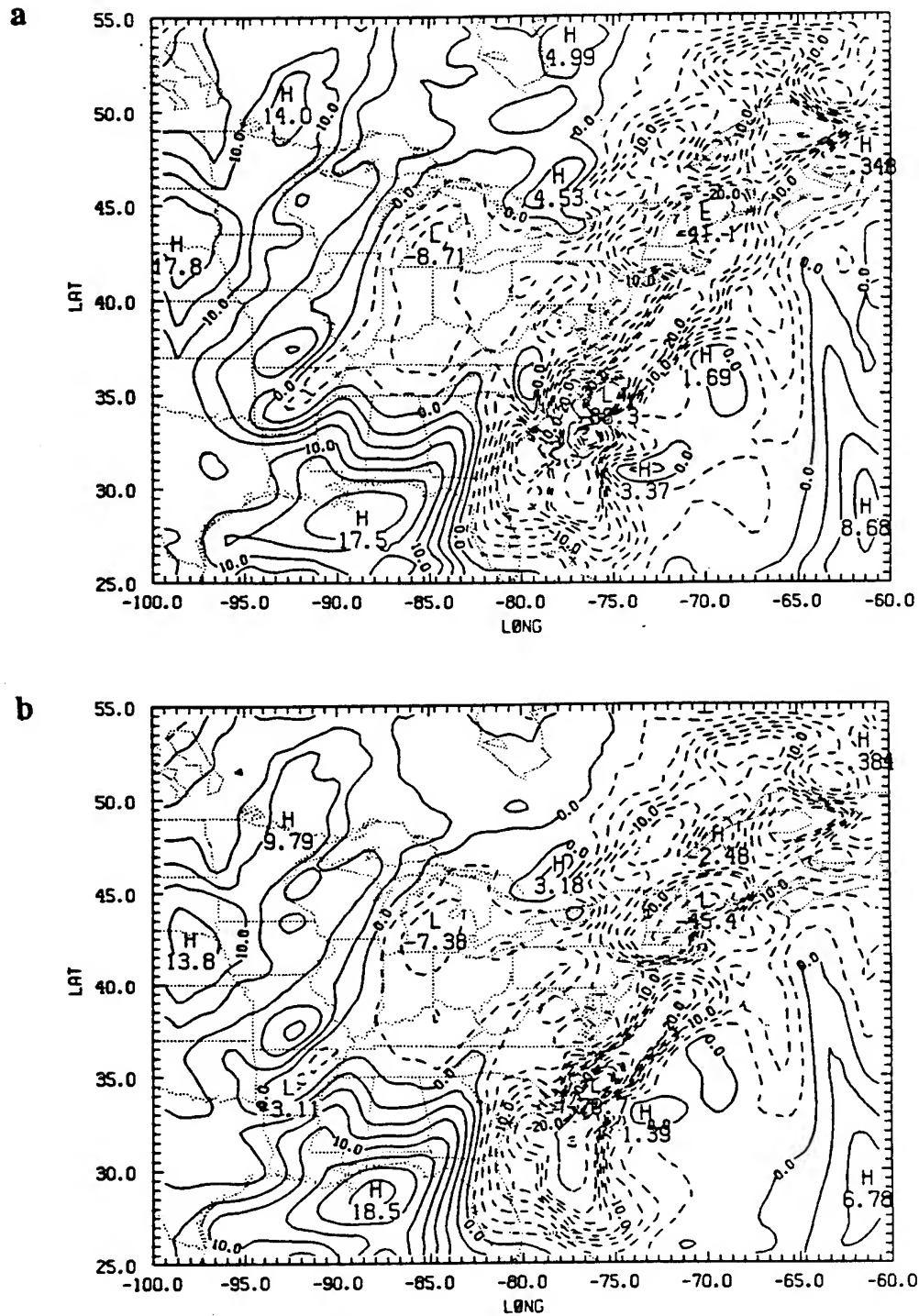


Figure 5.1. 500-mb vertical motion fields valid at 27/00Z: (a) from 12-h forecast of the control (case 5.1), (b) after DVMI (case 5.2), and (c) after AVMI (case 5.3). Vertical motion of magnitude of -20 mb h^{-1} or more are contoured every 2.5 mb h^{-1} .

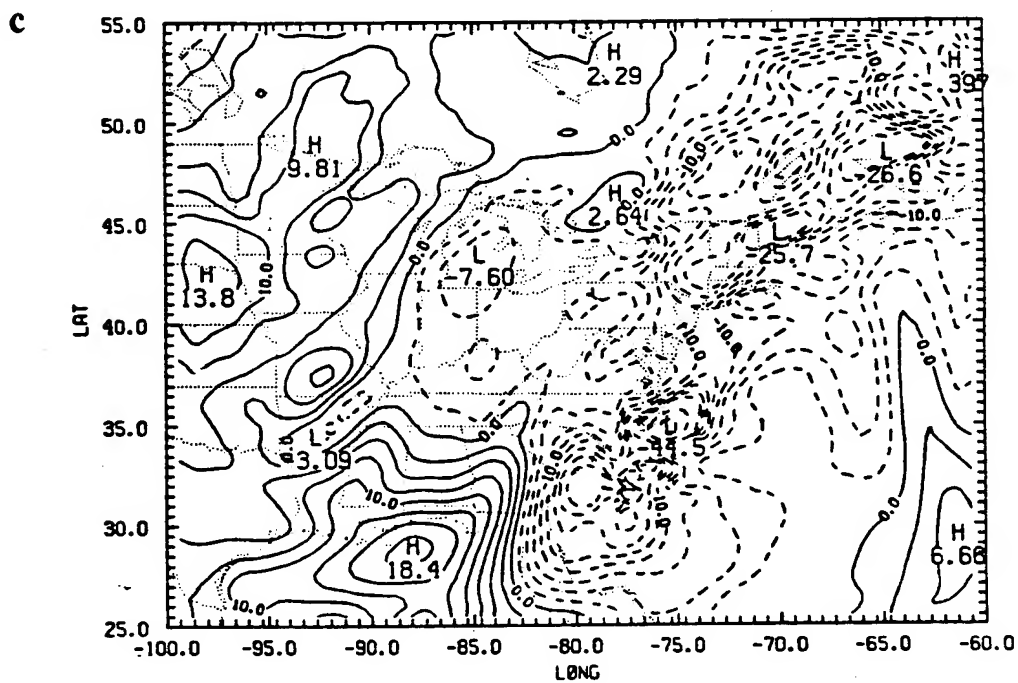


Figure 5.1. Continued.

"truth." The pattern and positions of maxima and minima in the omega field show little change from the control run, suggesting the 3-D structure of model convective heating can be re-created from a 2-D rain distribution. A further comparison between case 5.2 and case 5.3 reveals the deficiency of AVMI. In the vicinity of the developing cyclone off Cape Hatteras, the magnitude of omega has changed substantially using AVMI; the maximum upward velocity is only about 60% of that resulting from DVMI. Since a significant amount of the divergence (and hence vertical motions) associated with heavy precipitation events may be forced by latent heat release, and since the nonlinear step in the AVMI does not include this diabatic forcing, the divergence due to this forcing will be removed as if it were associated with unwanted gravity waves. As a result, the vertical velocities are underestimated.

5.4.2 Forecast Precipitation Comparisons

The patterns of 12-h (27/00Z - 27/12Z) convective rainfall in cases 5.2 and 5.3 are very similar to each other and to the control in areal coverage and accumulation. The 12-h convective rainfall forecast from the adiabatically initialized fields is just as good as the forecast originating from the diabatically initialized fields. Since the physics and dynamics of the nonlinear normal mode procedure are internally consistent with the numerical model (which provided the analysis fields), the initialization procedure, whether with or without diabatic heating, changes the model forecast fields only a small amount. As a result, the subsequent forecasts are essentially the same. Therefore, additional model experiments were performed in which GALE 3-hourly surface and upper-air data were analyzed using a multivariate, successive correction objective analysis scheme (Sashegyi et al. 1992). Model forecast fields served as the first guess for the analyses. Adiabatic (AVMI) and diabatic (DVMI) initializations were performed on the

analysis fields. In the latter case, observed rain data was combined with the model-produced rainfall for computation of the 3-dimensional heating function in the model initialization procedure.

Figure 5.2 shows 6-h observed rainfall and accumulated forecast rainfall valid 26/00Z - 26/06Z. The forecast in Fig. 5.2a was initialized with DVMI at 26/00Z. The rainfall pattern is similar to the observed; in particular, over Alabama and along the central Gulf coast region, the model was able to predict the precipitation during this short-range forecast. However, the forecast originating from AVMI (Fig. 5.2b) fails to capture any rainfall over the Gulf coast associated with the developing short wave. The absence of diabatic heating from the VMI has caused a spinup problem in this case. RMS differences between these forecasts and observed rainfall were computed. The differences were computed only at gridpoints in which at least 0.01 cm of either forecast or observed rainfall accumulated during the 6-h period. When initializing with AVMI and DVMI, the rms differences were 0.9 cm and 0.7 cm, respectively. The larger rms difference in the AVMI case is due to model spinup. The disparity between these two cases would be even greater, if only the accumulated rainfall from the first 3 h of model integration was compared. A complete description of these experiments and discussion of results within the context of four-dimensional data assimilation is given by Harms et al. (1992c)

5.5 Summary

In this study, the viewpoint taken was that the "best" initialized states were those which were least altered by initialization. From comparisons of vertical velocity fields, we found that DVMI with model rain produced an initial state very similar to the "truth" and, thus, successfully re-created the 3-D distribution of convective heating from the 2-D model rain distribution. The AVMI (case 5.3) changed the "true" analysis significantly

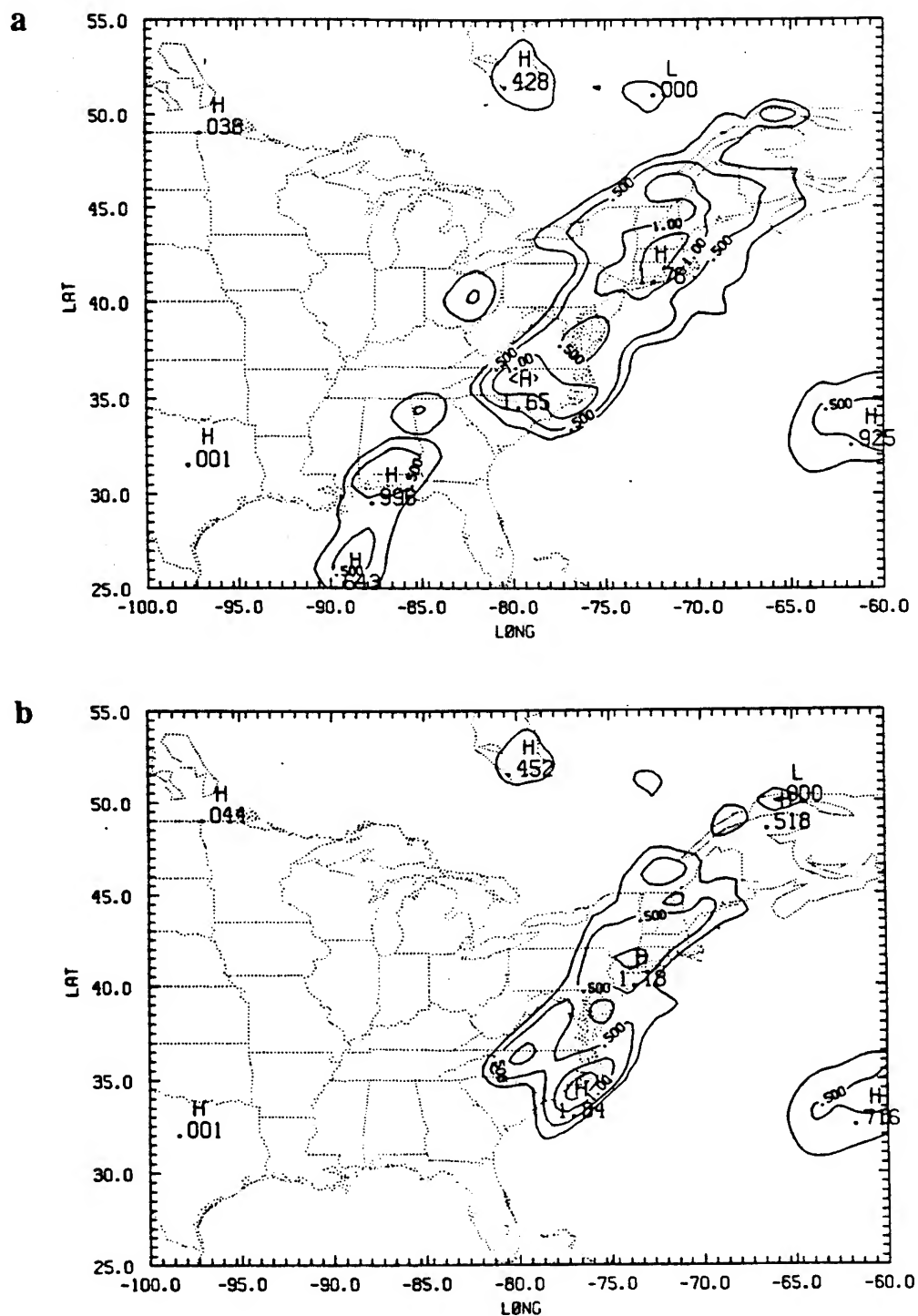


Figure 5.2. Forecasts of accumulated total precipitation in cm (26/00Z - 26/06Z) originating from (a) DVMI and (b) AVMI. (c) Observed precipitation in cm for the same period. Contours at 0.25 cm and every 0.5 cm for 0.5 and above.

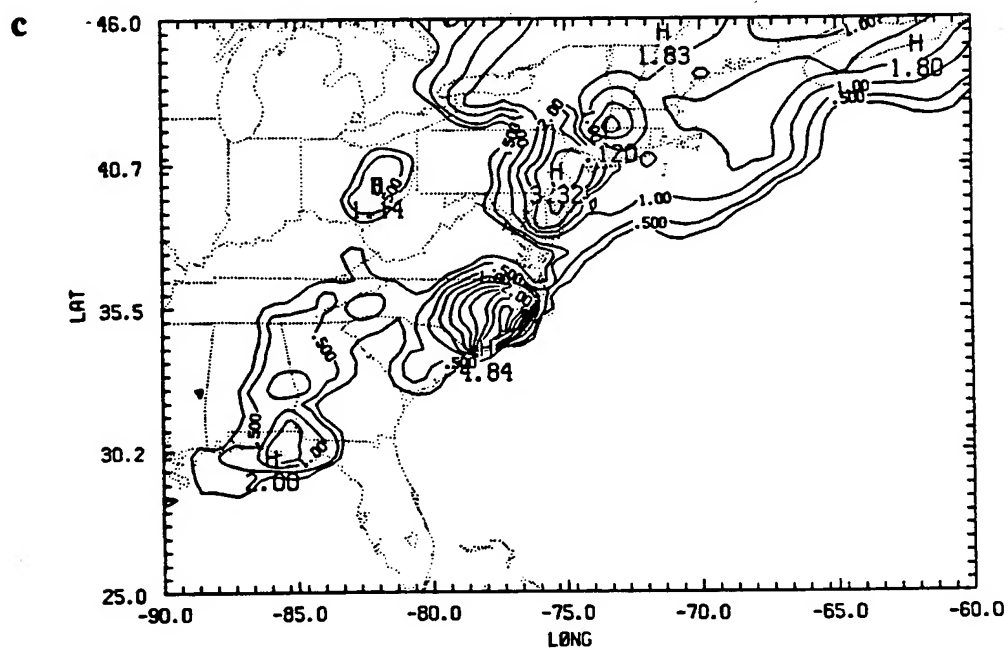


Figure 5.2. Continued.

by reducing the maximum vertical velocities to about 60% of that resulting from DVMI. With the diabatic heating term which forces, to a large degree, convective precipitation, the DVMI (unlike the AVMI) retains the divergence (or vertical motion) associated with the convection.

When DVMI is performed on the analysis fields, model spinup time is reduced. The pre-forecast integration of the model ensures that the analyses are spunup and that the circulations in these analyses are consistent with the model resolution and external parameters such as topography. The initializations and forecasts were performed in this study for the midlatitudes, which dictates a relatively short spinup. In the data-sparse tropics, spinup can be expected to be much greater. In the tropical case, DVMI with merging will be critical in reducing spinup time.

6. IMPACT OF ASSIMILATING 3-HOURLY GALE DATA

The discussion to this point has dealt with the major components of data assimilation: objective analysis, initialization, and model forecast. In the following discussion, these components are linked together to form a four-dimensional data-assimilation system.

6.1 Introduction

A limited-area intermittent data-assimilation system is used to assimilate 3-hourly data collected during the Genesis of Atlantic Lows Experiment (GALE), which was conducted over the southeastern U.S. during the winter of 1986. The system, developed jointly by NRL and NCSU, is used to generate initial conditions for the NRL/NCSU mesoscale model. The NRL/NCSU data-assimilation system consists of a multivariate, successive correction objective analysis, a diabatic vertical mode initialization (VMI), and a mesoscale numerical forecast. The development of four-dimensional data-assimilation systems for limited areas is being driven by a need to optimally utilize data from the new observing systems of the 1990s (e.g., Next Generation Radar [NEXRAD], Special Sensor Microwave/ Imager [SSM/I], and Wind Profilers) in mesoscale models. Until these new observing systems become operational, other data sources must be used to test assimilation techniques.

During intensive observing periods (IOPs) of GALE, 3-hourly upper-air soundings were taken at selected National Weather Service (NWS) sites over the eastern U.S., supplemented by more frequent and higher density soundings taken at sites along the east coast and by dropsondes deployed offshore by aircraft (Dirks et al. 1988). These

3-hourly asynoptic upper-air observations from the GALE experiment are ideal for testing the impact of assimilating high-frequency observations in a mesoscale model.

The influence of GALE data on the regional analyses and assimilation system at the National Meteorological Center (NMC) has been investigated by Rodgers et al. (1990) and DiMego et al. (1989). Using the higher density GALE soundings along the east coast at the synoptic hours of 0000 and 1200 UTC only, Rodgers et al. (1990) found only a minimal impact on the NMC operational regional analyses and the subsequent forecasts which were rerun for IOPs 1 and 2. Some noise and bias problems were found however in the geopotential in the mid-troposphere in the supplemental soundings along the east coast, which may have contributed to the negative result. Also, at the time of their study, a 6-h forecast from the global spectral model was being used as the first guess for the operational regional analyses (Hoke et al. 1989) and no feedback between the regional model and the analysis could take place. To test an intermittent assimilation for use with future high-frequency wind profiler data, DiMego et al. (1989) used a 3-h update cycle, with the regional model providing the first guess, to assimilate the 3-hourly GALE asynoptic data from a single 12-h period during IOP 1. For their single case, an improvement in the analysis at the end of the 12-h period of assimilation was demonstrated. A stronger jet with stronger horizontal and vertical shears in the final analysis led to a better definition of the indirect circulation in the exit region of the jet in the initialized field. They also asserted that the low-level cyclogenesis was improved in the first 12 h of the subsequent forecast. Even assimilating the winds alone improved the final analysis when compared to the operational analysis which did not use the GALE asynoptic data.

In the present paper, a finer-resolution mesoscale model is used in the assimilation experiments with the GALE asynoptic data, and the model and analysis domains are centered on the GALE region. The horizontal resolution of the fine grid in the

NRL/NCSU model is about 50 km at 45°N, whereas the fine mesh of NMC's nested grid model used by DiMego et al. (1990) had at that time a resolution of about 85 km at the same latitude (Hoke et al. 1989). In the present case, the data assimilation is extended for a full 2 1/2-day period for the second IOP of GALE, during which time a substantial number of asynoptic observations were available. During this time, several upper troposphere jets propagated across the region of the GALE data, and a cyclone developed in the region along the east coast. Since the ultimate test of any data-assimilation system's usefulness is the quality of the forecast produced from the assimilated states, focus is placed heavily on comparisons of subsequent forecasts as well as on the analyses from which they were initialized.

As noted by Kanamitsu (1989), a number of advantages are realized when using a four-dimensional data assimilation system (such as the one described in this paper) for specifying the initial state for a numerical forecast: 1) Using a comprehensive assimilation model with full physics as the assimilation model provides the most accurate first guess for the following objective analysis. This allows optimum use of model feedback in regions where data are sparse in time and space. Plus, it ensures that the initial state specification possesses a resolution compatible with the high-resolution forecast model. 2) Using the model forecast as the first guess for the next analysis enables information from earlier observations to be carried forward to provide an independent source of information to be added to the newly-acquired data. That is, the background forecast feeds information forward to the next forecast. 3) Using a multivariate objective analysis ensures a degree of balance between the mass and momentum fields, which helps minimize changes due to the initialization. 4) A multivariate analysis scheme also enables one model variable to be updated from observations of another variable.

The primary purpose here is three-fold: 1) to describe our data assimilation system, 2) to evaluate the effectiveness of the system, and 3) to assess what impact the high-density 3-hourly GALE data have on the NRL analyses and forecasts. More specifically, the analysis performance is addressed both by data-fitting statistics and by comparison with operational analyses. Also, precipitation forecasts are compared using predictions originating from NMC operational analyses, from assimilated fields excluding the 3-hourly data, and from assimilated analyses including the GALE asynoptic data.

6.2 The Data-Assimilation System

The NRL/NCSU four-dimensional data-assimilation system uses the intermittent data-assimilation method (or analysis/forecast cycle) in which a model forecast serves as the background field, or first guess, for the analysis of new data. The assimilation system analyzes asynoptic GALE surface and upper-air data every 3, 6, or 12 h using the NRL/NCSU multivariate, successive correction scheme. The analyzed mass and momentum fields are balanced by an initialization procedure. A short-range forecast is then made to serve as the first guess for the next analysis. The NRL/NCSU mesoscale model is used as the assimilation model to generate the background fields for the analysis at each cycle of the assimilation. The same model is used to produce subsequent forecasts from the assimilated states, thus ensuring compatibility of model resolution and physical processes between assimilated and forecast states. In addition, Bell (1986) documented that model spinup time can be substantially reduced if the forecast model being initialized is also the assimilation vehicle. He recognized that the analyzed fields from the assimilation must contain detail compatible with the resolution of the forecast model grid; otherwise, the model will require time to generate the small scale circulations. Furthermore, with a fine grid resolution of approximately 50 km, the NRL/NCSU

mesoscale model is designed to capture and retain the mesoscale information from the GALE data network.

The NRL/NCSU data-assimilation system is also fully diabatic incorporating 3-hourly observed and model-generated precipitation rates in its vertical mode initialization. The initialization scheme is used to correct the divergent part of the wind produced by the analysis and to provide initial conditions for model integration at the next assimilation cycle.

At the start of each update cycle of the assimilation, the analysis procedure corrects the background forecast field using the observed mass and momentum fields. During this process, the divergent part of the wind is lost primarily because the divergence has the same order of magnitude as does the errors in the wind field. This divergent circulation can be regained if the analysis at each cycle of the assimilation is initialized with a diabatic initialization procedure. In the present assimilation system, the interpolated analyses are initialized separately on both coarse and fine grids for the first three vertical modes of the numerical model using the vertical mode scheme of Bourke and McGregor (1983), as applied to the NRL/NCSU model by Sashegyi and Madala (1992a) and Harms et al. (1992a). This scheme generates a balanced divergent part of the wind field, while producing only small changes to the geopotential and vorticity.

Harms et al. (1992a) discussed the importance of including diabatic forcing in the model initialization. With the inclusion of heating corresponding to observed rainfall in the diabatic forcing term of the thermodynamic balance equation, the initialization can force the model state toward the real atmospheric state and substantially reduce model spinup. In our diabatic vertical mode initialization procedure, diabatic heating rates are computed from a merged field of observed and model-produced rainfall.

Model convective rainfall is accumulated during the integration of the previous assimilation cycle from 3 h before the current initialization time to 3 h past that initial

time. In other words, the model convective precipitation is accumulated for 6 h centered around the beginning of the current assimilation cycle. As a result, the model integration for each assimilation cycle is 3 h longer than the cycle duration (period between updates). For cycle durations of 3, 6, and 12 h, the model is integrated for 0, 3, and 9 h, respectively, before the rainfall accumulation begins. Therefore, in the latter two assimilation cases, the model is spunup prior to collecting the model convective rain. During the vertical mode initialization, this model-produced rainfall is combined with analyzed 6-h observed rainfall (satellite-derived and GALE 3-hourly raingauge data, described in the next section) valid for the same period, a time frame extending to 3 h beyond the current analysis time. This procedure requires the assimilation to occur at least 3 h after real time. However, in this sense, diabatic heating rates used in the initialization are derived from rainfall accumulations which are time-centered at the appropriate time (valid at initialization) and, therefore, are temporally representative rates. The observed values are used where available over the model grid; otherwise, the model values are used.

This 6-h combined rainfall field is converted into time-average rainfall rates for all grid points. The average rain rates are converted into vertical profiles of heating using a reverse Kuo cumulus parameterization. This vertical distribution of the latent heating is based on the cumulus convective scheme of the model. Thus, no simplifying hypotheses are needed. The advantage of the present approach is an improved consistency obtained with the physical parameterization scheme of the model. This three-dimensional diabatic heating field is then added as a fixed forcing term in the thermodynamic energy balance equation as each iteration of the vertical mode initialization is performed.

During the first 3 h of model integration of each assimilation cycle, the model-produced convective rainfall and heating rates are merged with the corresponding rates used in the previous initialization, thus ensuring the desired compatibility with the heating

rates at initialization. As mentioned earlier, the heating rates used in the initialization are derived from a 6-h accumulation of rainfall centered on the initialization time. Therefore, this 6-h amount includes rainfall accumulated for 3 h beyond the valid time of the initialization, that is, the same 3 h of subsequent model integration in which the merging of heat/rain rates occurs. Thus, these heating rates used in the initialization and first 3 h of subsequent "assimilation" model integration are representative of "observed" heating rates for this period. Thus, the merging process forces the subsequent model heating toward the "observed" heating.

6.3 Experimental Design

The system was tested using data collected over a 2 1/2-day period from 1200 UTC 25 January to 0000 UTC 28 January 1986 (25/12Z to 28/00Z). This data included a set of upper air soundings, which were interpolated to 10-mb levels from the surface up to 100 mb, and surface observations for IOP 2 of GALE. These datasets were obtained from the GALE Data Center (GDC) at Drexel University (Mercer 1987). The data domain included the eastern U.S. and western North Atlantic from 115°W to 45°W in longitude and from 10°N to 60°N in latitude. A higher density of upper-air and surface data is found in the inner GALE region covering the Carolinas and southern Virginia from the Gulf Stream to the Appalachians. The sounding network for GALE consisted of 39 National Weather Service (NWS) sites which made launches at 3-h intervals when weather events dictated. These observing sites were supplemented by seven Cross-chain LORAN-C Atmospheric Sounding System (CLASS) sites, which made launches as often as every 90 minutes, in North Carolina and South Carolina. Plus, numerous dropwindsondes were deployed over the Atlantic Ocean and the Gulf of Mexico during IOP 2, as well as observing systems aboard two ships in Atlantic coastal waters (Mercer

and Kreitzberg 1986). The GALE datasets included upper-air observations (primarily synoptic) from several other NWS sites, the Canadian Weather Service sites, and a few sites in Mexico. The GALE observations were grouped into data windows of 3 h centered on the analysis times of 0000, 0300, 0600, 0900, 1200, 1500, 1800, and 2100 UTC.

As mentioned in Chapter 4, in regions of no data over the ocean, bogus data, derived from the difference between the first guess forecast and the NMC 2.5° hemispheric analysis, are used to merge the analysis smoothly with the NMC analysis over the data-sparse ocean regions at synoptic hours. At off-synoptic times, no bogus soundings are added and the analysis returns to the background in regions of no data. As an example, Fig. 6.1 shows the locations of surface and upper-air data at 26/00Z and 26/03Z after the quality control. Very few upper-air real observations (shown by the crosses) are found over the oceans, where NMC "bogus" data (shown by stars) have been added at the synoptic hours (Figs. 6.1a and c). At the asynoptic hours (Figs. 6.1b and d), the number and aerial coverage of the data is much less than at the synoptic times as noted above. Table 6.1 shows the average number of surface and upper-air observations, before and after quality control, available at each analysis time, with the number of bogus data shown in parentheses. As was also clear in Fig. 6.1, there is considerable variation. At the asynoptic times, only a limited number of sounding data is available with these being solely from the GALE network. The actual number of data analyzed is less than the number of real GALE observations, particularly in the case of surface data. In the quality control procedures, gross error checks and buddy checks eliminate a few data. Data in close proximity of each other or observations from the same location within a given 3-h data window are averaged to create super observations.

Three-hour observed rainfall amounts from IOP 2 of GALE are used in the diabatic vertical mode initialization. The raingauge data obtained from the GALE Data Center at

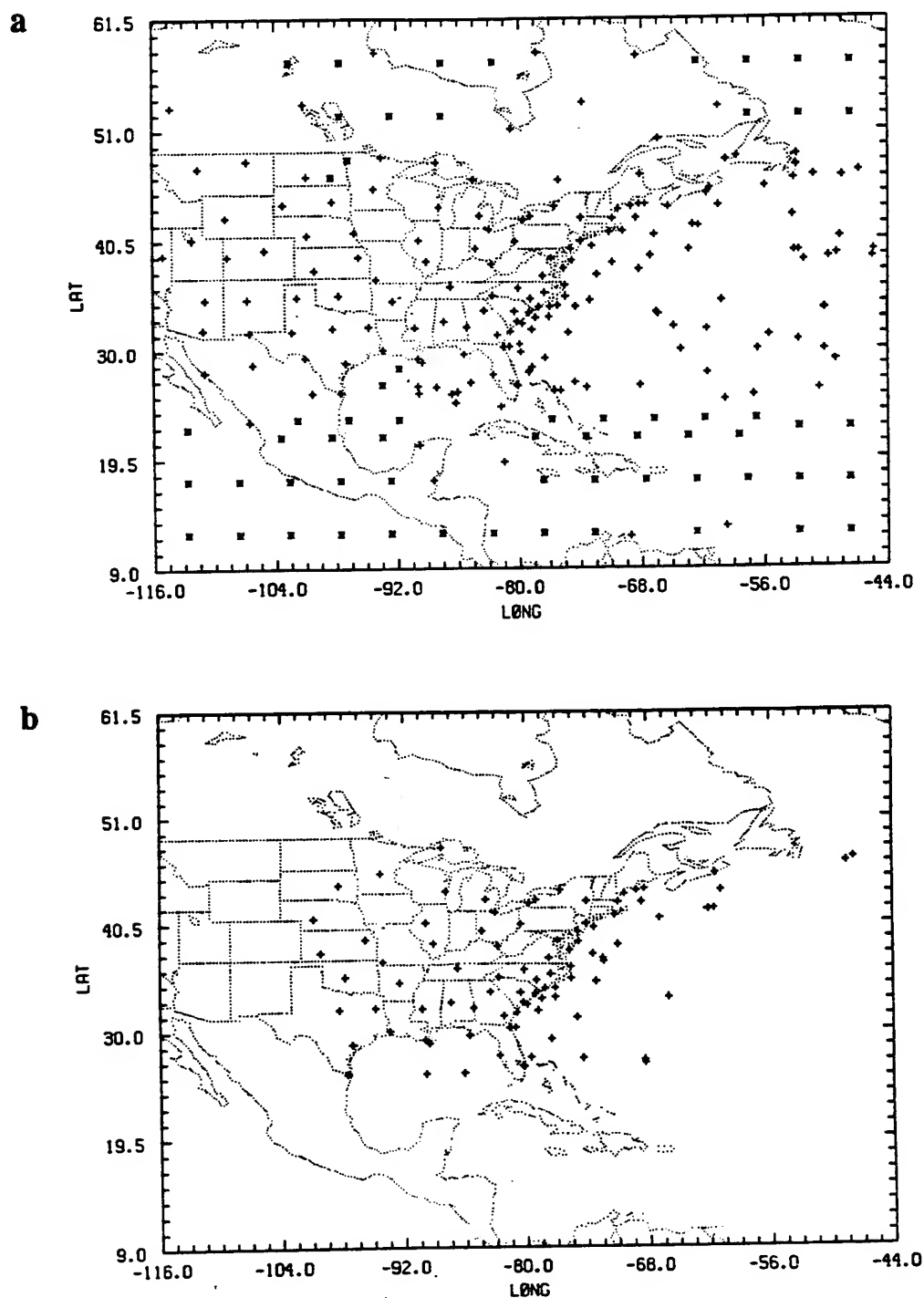


Figure 6.1. The locations of surface (a and b) and upper-air (c and d) data at 26/00Z and 26/03Z, respectively. The observations are indicated by the '+', while bogus values are indicated by '*'. The analysis grid is indicated by the tick marks along the domain boundary.

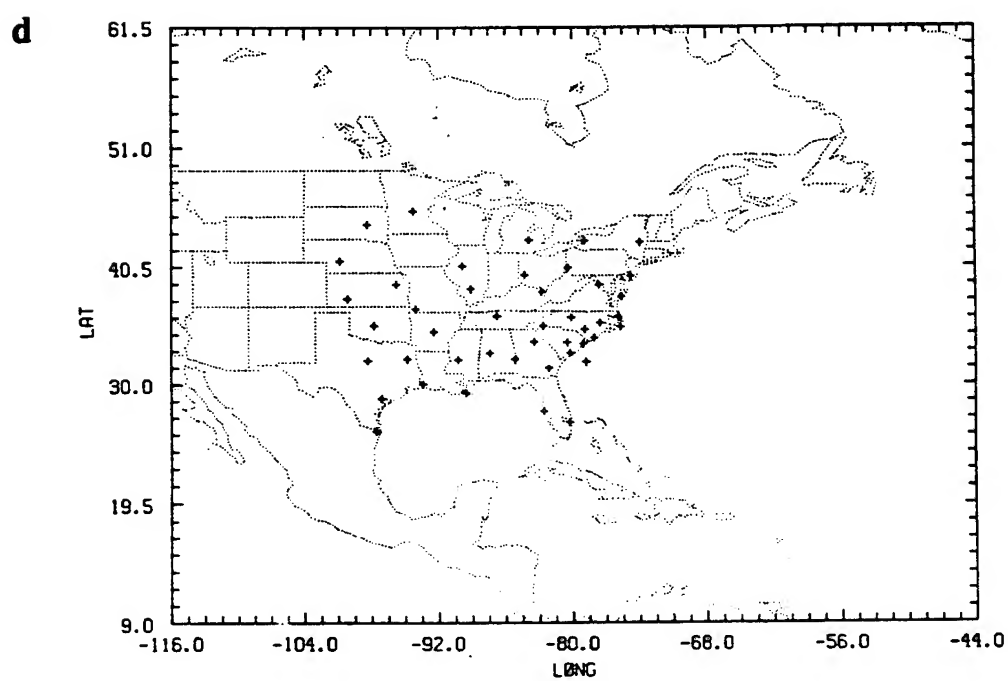
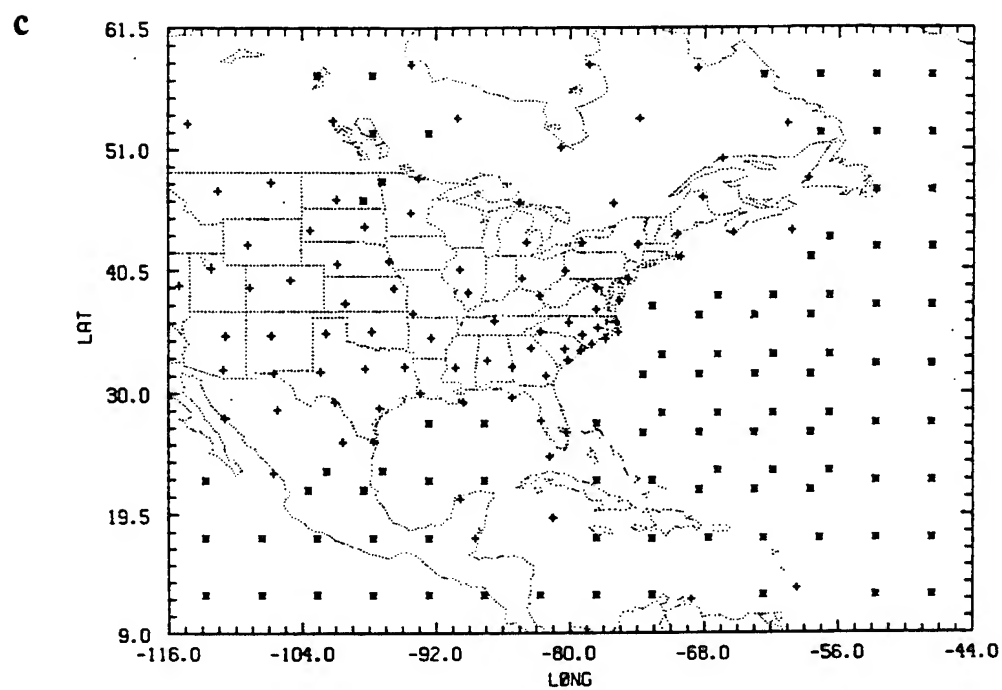


Figure 6.1. Continued.

TABLE 6.1. Average number of observations, before and after quality control and creation of super observations, in each analysis time window. Average number of bogus observations is in parentheses

<u>Analysis Time</u>	<u>Upper-air</u>			<u>Surface</u>		
0000 UTC	101	89	(93)	337	170	(64)
0300 UTC	49	42		226	85	
0600 UTC	51	44		277	120	
0900 UTC	48	42		232	87	
1200 UTC	113	103	(76)	376	198	(42)
1500 UTC	47	40		232	87	
1800 UTC	49	42		308	138	
2100 UTC	41	35		225	81	

Drexel University were bilinearly interpolated to the fine grid of the NRL/NCSU model. Values for the coarse grid were then obtained by computing a 9-point average using fine grid values. These raingauge data were supplemented, or merged, with the satellite-derived rainfall analyses provided by the University of Wisconsin (Martin et al. 1988). These satellite-derived rainfall values were available as 6-h accumulations on a one degree latitude by one degree longitude grid which extended from approximately 25°N to 46°N and 60°W to 85°W. The 6-h derived amounts were temporally interpolated to obtain 3-h accumulations, which were then bilinearly interpolated to the model grids. These interpolated fields of satellite-derived rainfall were merged with the GALE raingauge data to produce our "observed" 3-h rainfall data. When and where available, the raingauge values were kept; otherwise, the merged values were represented by the satellite-derived rainfall.

To test the effectiveness of the NRL/NCSU data-assimilation system and to assess the impact, if any, of the 3-hourly GALE data on the assimilation and subsequent forecasts initialized from our assimilated states, five experimental cases were performed, as outlined in Table 6.2. In experiment 1, 12-hourly National Meteorological Center 2.5° hemispheric analyses (NMC analyses) for the period 25/12Z to 28/00Z are used. No re-analysis was performed to incorporate the high-density GALE data; therefore, these NMC analyses represent our "no assimilation" case and serve as the control experiment for comparison with analyses from the assimilation experiments. Differences in the assimilated analyses from the control analyses are attributable to both the assimilation of the 3-hourly data and the use of the high horizontal resolution NRL/NCSU mesoscale model in the assimilation process.

The 25/00Z NMC analysis was used to cold start the remaining experiments. The first analysis of GALE data occurs at 25/12Z in these assimilation runs. The 25/00Z NMC analysis was initialized and then the model was integrated for 12 h. The 12-h

TABLE 6.2. Data Assimilation Experiments.

Experiment	Assimilation Cycle	Initialization Type	Remarks
1 - Control	N / A	*AVMI	No assimilation--uses NMC analyses
2 - 12DI	12 Hours	*DVMI	Assimilation without asynoptic GALE data
3 - 06DI	6 Hours	DVMI	Assimilation with 6-hourly GALE data
4 - 03DI	3 Hours	DVMI	Assimilation with 3-hourly GALE data
5 - 06AI	6 Hours	AVMI	Assimilation with 6-hourly GALE data; no diabatic heating in model initialization

*AVMI -- Adiabatic vertical mode initialization

*DVMI -- Diabatic vertical mode initialization

forecast served as the first-guess field for the initial analysis in the assimilation sequences. In experiment 2, the intermittent data assimilation was performed from 25/12Z to 28/00Z with a 12-h update cycle, where only synoptic data entered into the analyses. An update cycle of 6 h was used in experiment 3. GALE data valid at 00, 06, 12, and 18Z were incorporated. Like experiment 2, the assimilation is performed for a 2 1/2-day period. Due to extremely limited sounding data at 25/15Z and 25/21Z, the assimilation run in experiment 4 began at 26/00Z, using the 26/00Z analysis from experiment 3 as its initial assimilated state. The update cycle here is 3 h to use all 3-hourly GALE data from 26/00Z to 28/00Z. Diabatic vertical mode initialization was used in experiments 2, 3, and 4. Experiment 5 was identical to experiment 3 with a 6-h update cycle, except diabatic heating was excluded from the vertical mode initialization. The assimilated states (analyses at each update cycle) from experiments 2 - 5 were saved for post-processing, i.e. inter-comparisons and comparisons with the NMC analyses. For all experiments, a 3-h data window centered on the analysis time was used.

From the assimilated fields valid at 26/00Z and 26/12Z of each experiment, 24-h forecasts were produced using the same model that was used in the assimilation. Prior to model integration, these assimilated analyses were initialized using the vertical mode initialization procedure. The model initialization using analyses from experiments 2, 3, and 4 included forcing due to diabatic heating. But for the sake of fairness, the diabatic heating was derived from only rainfall occurring prior to forecast start time (a 3-h accumulation), versus a 6-h accumulation centered on the analysis/initialization time as done in the assimilation runs.

6.4 Results

Evaluation of the experiments is performed by means of data-fitting statistics, where rms differences between observations and analyses and between observations and background forecast fields are compared. The evaluation also includes a more subjective comparison of synoptic-scale and mesoscale patterns, amplitudes, and positions of specific features from the analyses (assimilated states) and the subsequent 24-h forecasts.

6.4.1 Statistical Evaluation and Discussion

Root-mean-square errors for the fit of background forecasts and analyses to the observations at each cycle of the assimilation experiments were compiled. The data used here are those passed by the data checking procedures in the analysis scheme. The bogus data are not included in this statistical evaluation. These statistics were computed for each analysis variable (geopotential, u- and v- wind components, temperature, and relative humidity) at each of the 19 analysis levels from 1000 mb to 100 mb. Figure 6.2 shows the average analysis and average background forecast rms errors in geopotential for the assimilation analyses and forecasts valid at 0000 and 1200 UTC from experiments 2, 3, and 4 which had update cycles of 12, 6, and 3 h, respectively. By extracting the statistics at only the synoptic hours (cycles), the comparison is more equitable than if including statistics from all hours of experiments 3 and 4. In Fig. 6.2b, the rms error in the background geopotential at the synoptic hours was greatest at all levels when using the 12-h update cycle. In the upper troposphere and at the surface, the 3-h update cycle led to the least error with about 5 - 10 m less error than with the 12-h cycle. These results show that a positive impact is made on the first guess field of geopotential at the synoptic hours when 3-hourly GALE data are included. However, in the mid- and lower

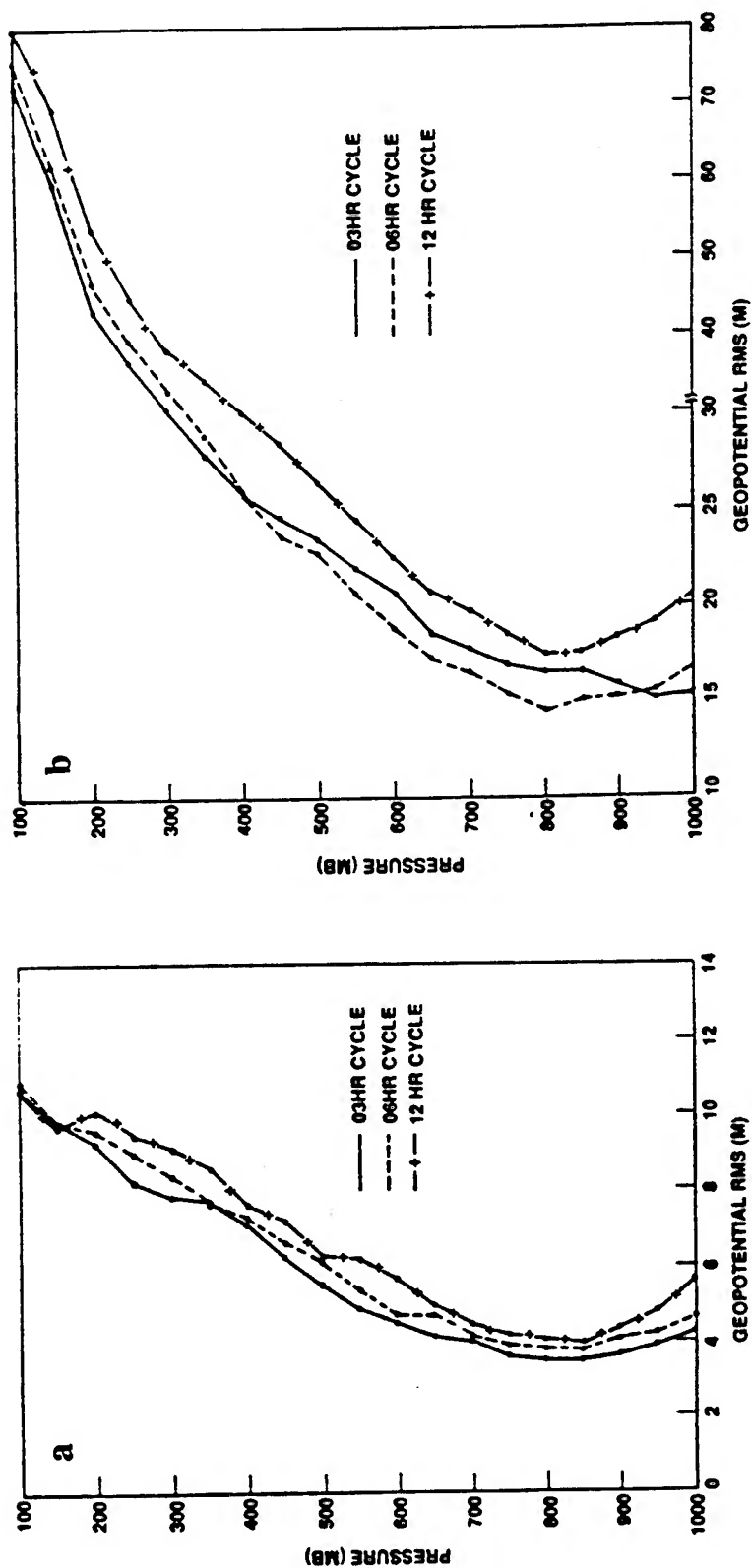


Figure 6.2. (a) Average analysis rms errors and (b) average background forecast rms errors for geopotential (m) from the 0000 and 1200 UTC update cycles of experiments 2 (12DI), 3 (06DI), and 4 (03DI).

troposphere, the 6-h update cycle gave slightly better results than when updating every 3 h. A possible explanation could be that the 3-h cycle may not allow sufficient time for model spinup in regions not updated by the 3-hourly asynoptic data. The corresponding average analysis rms errors at the synoptic hours, displayed in Fig. 6.2a, are significantly less, as expected, than the background errors. Here, the inclusion of the 3-hourly data led to a decrease in analysis errors throughout the troposphere, with the assimilation using the 3-h update cycle being better than the 6-h update cycle.

Error statistics were also compiled at the asynoptic hours of 0600 and 1800 UTC from experiments 3 and 4. As shown in Fig. 6.3, the background and analysis errors in geopotential decreased at all levels as additional 3-hourly data were assimilated; that is, the assimilation with an update cycle of 3 h showed an improvement over the case with a 6-h cycle. Clearly at the asynoptic hours, the improved background fields from the high-resolution forecast model are successful in carrying information from earlier asynoptic observations forward in time, leading to an improved analysis which then results in a better background forecast for the next update cycle of the assimilation.

Figures 6.4 - 6.6 illustrate the average rms statistics of u -, v -, and relative humidity from experiments 2 - 4 for the synoptic update cycles. Even though the analysis error in the wind and humidity fields remained essentially unchanged as the assimilation cycle decreased, the subsequent forecasts improved at all levels with the decreasing cycle length.

Average root-mean-square errors for geopotential from experiments 3 and 5 (all cycles included) are plotted in Fig. 6.7. Assimilation with diabatic heating included in the initialization procedure (06DI) resulted in background errors within the lower troposphere of about 1 m less than in the assimilation excluding the convective heating (06AI), but little or no improvement at higher levels. The analysis errors from these two experiments were almost identical. Similar results were found for the wind components and relative

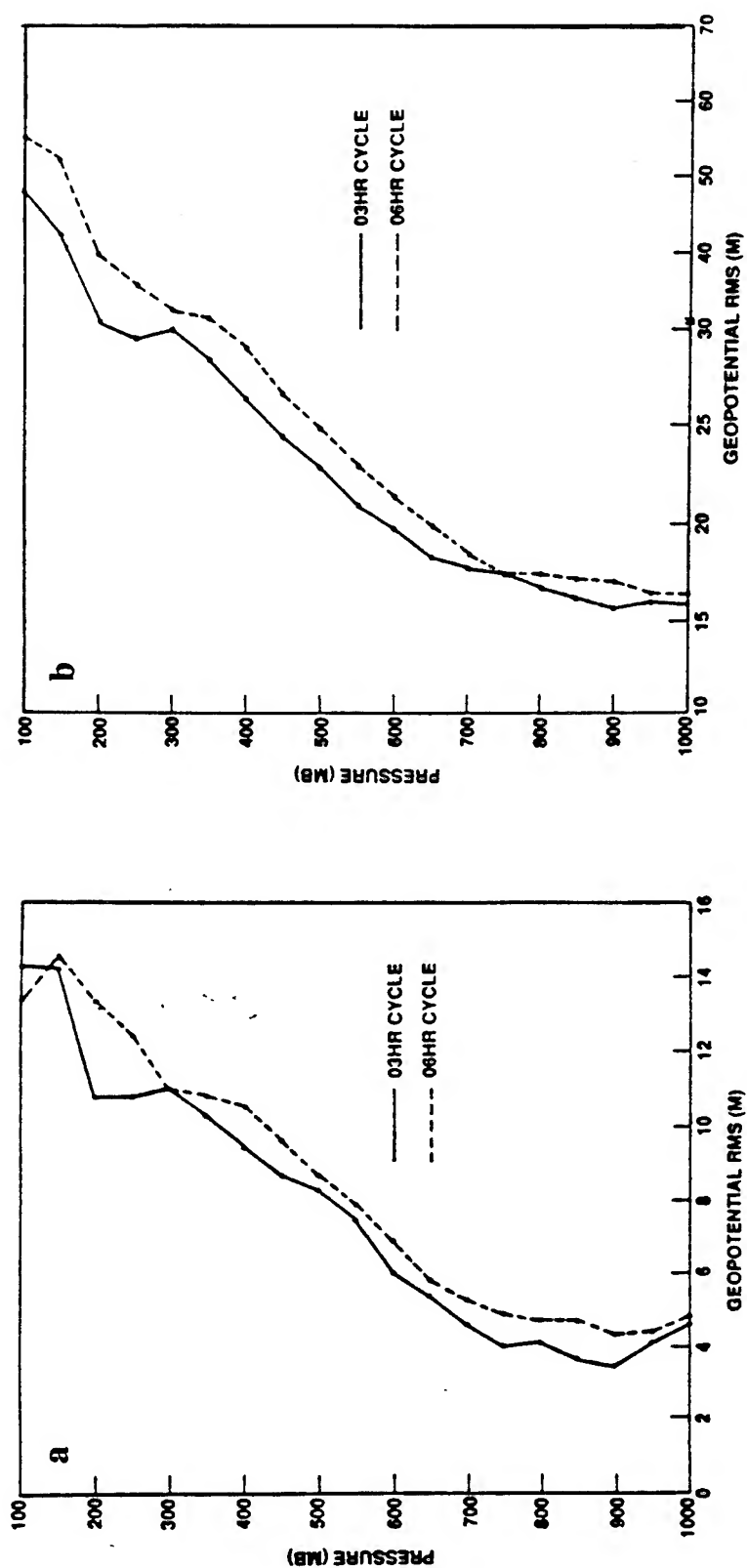


Figure 6.3. (a) Average analysis rms errors and (b) average background forecast rms errors for geopotential (m) from the 0600 and 1800 UTC update cycles of experiments 3 (06DI) and 4 (03DI).

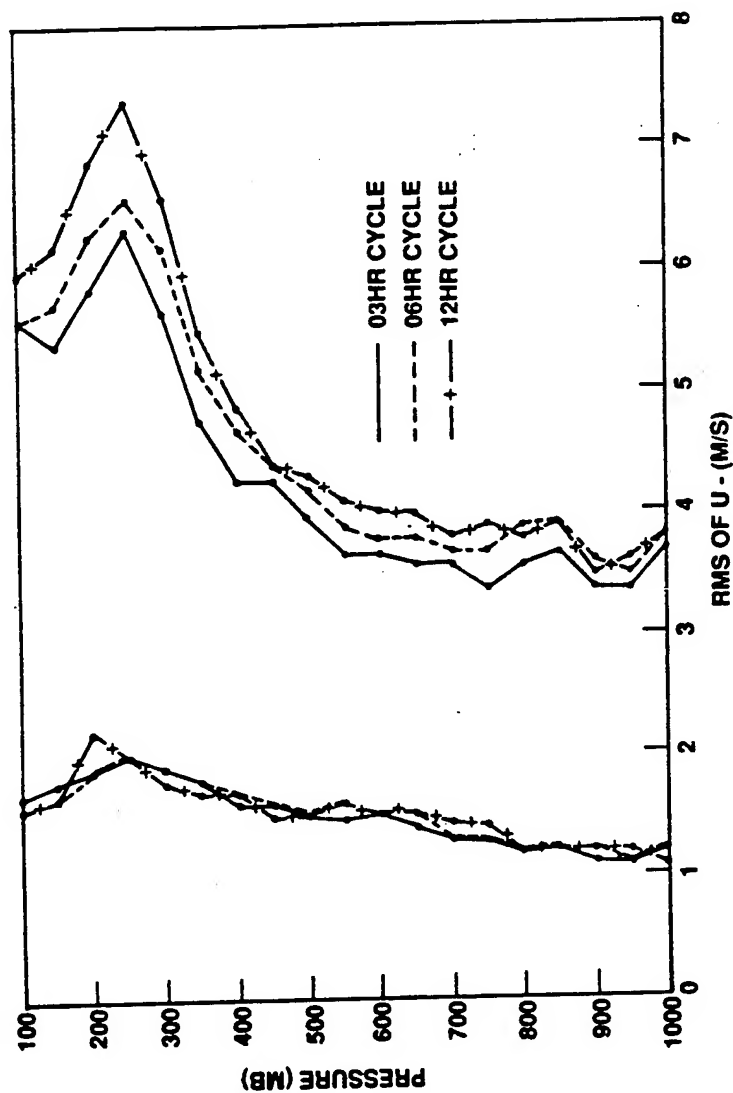


Figure 6.4. Average analysis and background forecast rms errors for the u- wind component (m s^{-1}) from the 0000 and 1200 UTC update cycles of experiments 2 (12DI), 3 (06DI), and 4 (03DI). Analysis error plots are on the left side of the figure.

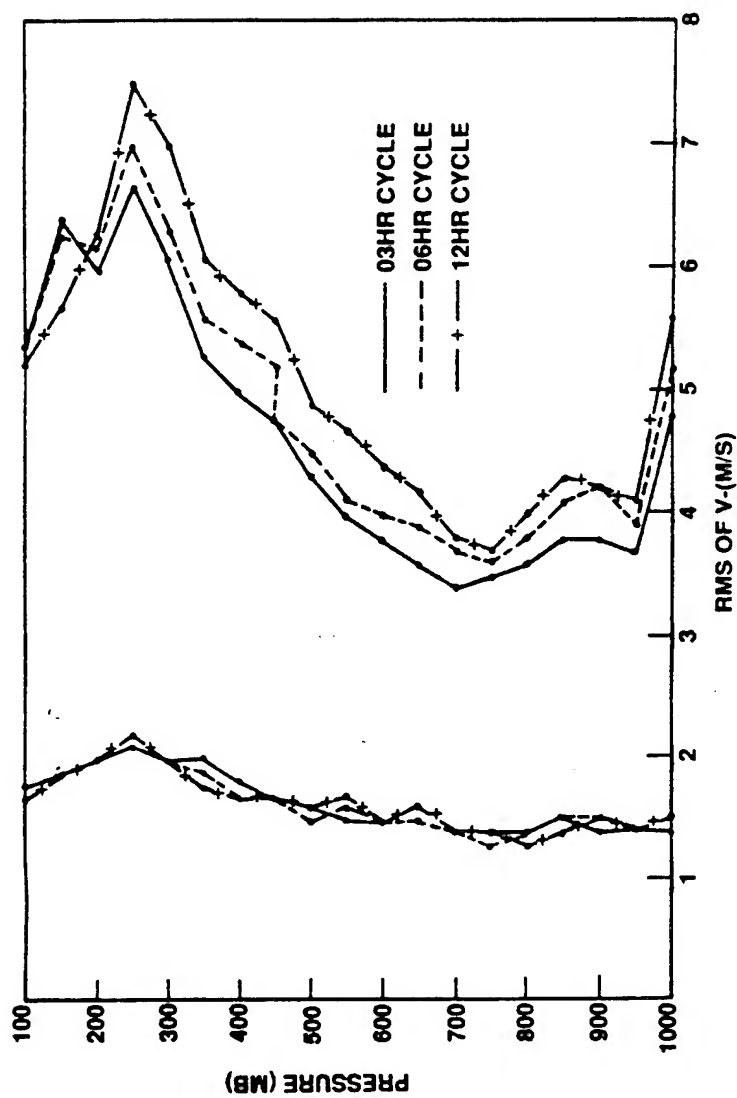


Figure 6.5. Average analysis and background forecast rms errors for the v- wind component (m s^{-1}) from the 0000 and 1200 UTC update cycles of experiments 2 (12DI), 3 (06DI), and 4 (03DI). Analysis error plots are on the left side of the figure.

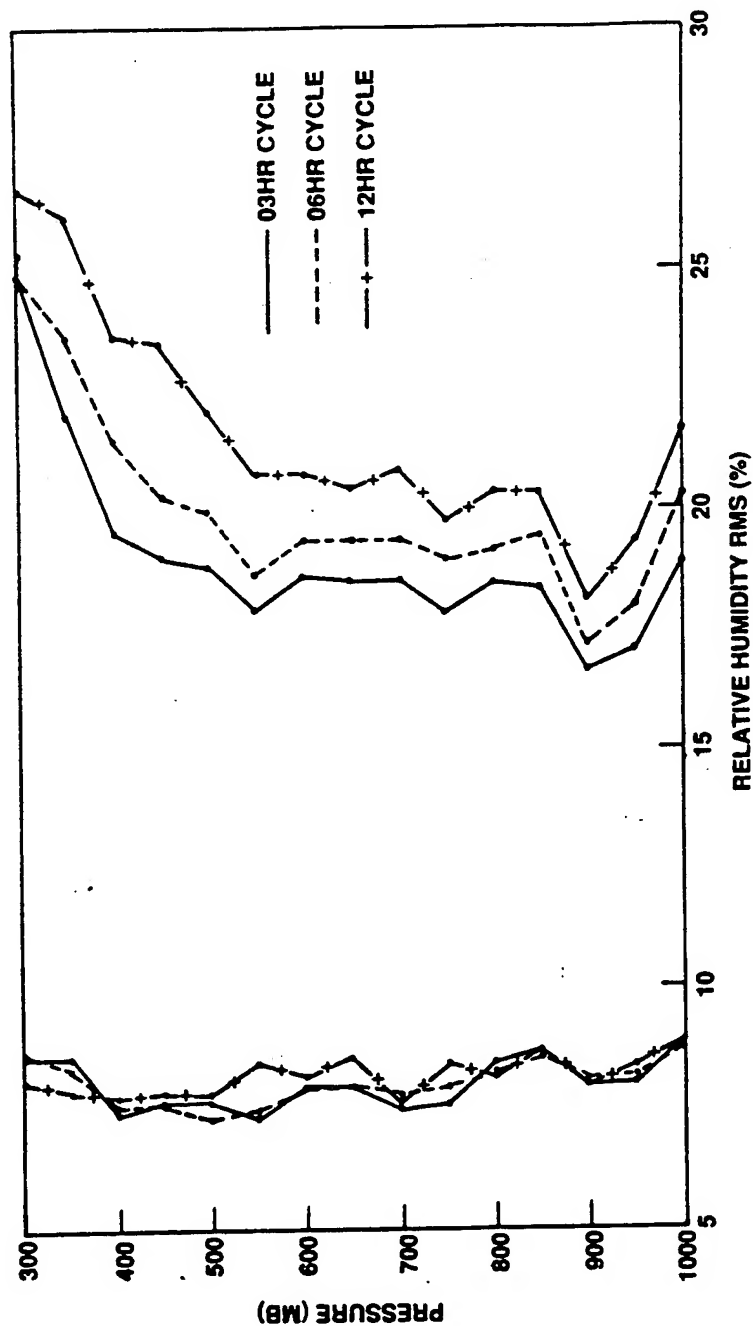


Figure 6.6. Average analysis and background forecast rms errors for relative humidity (%) from the 0000 and 1200 UTC update cycles of experiments 2 (12DI), 3 (06DI), and 4 (03DI). Analysis error plots are on the left side of the figure.

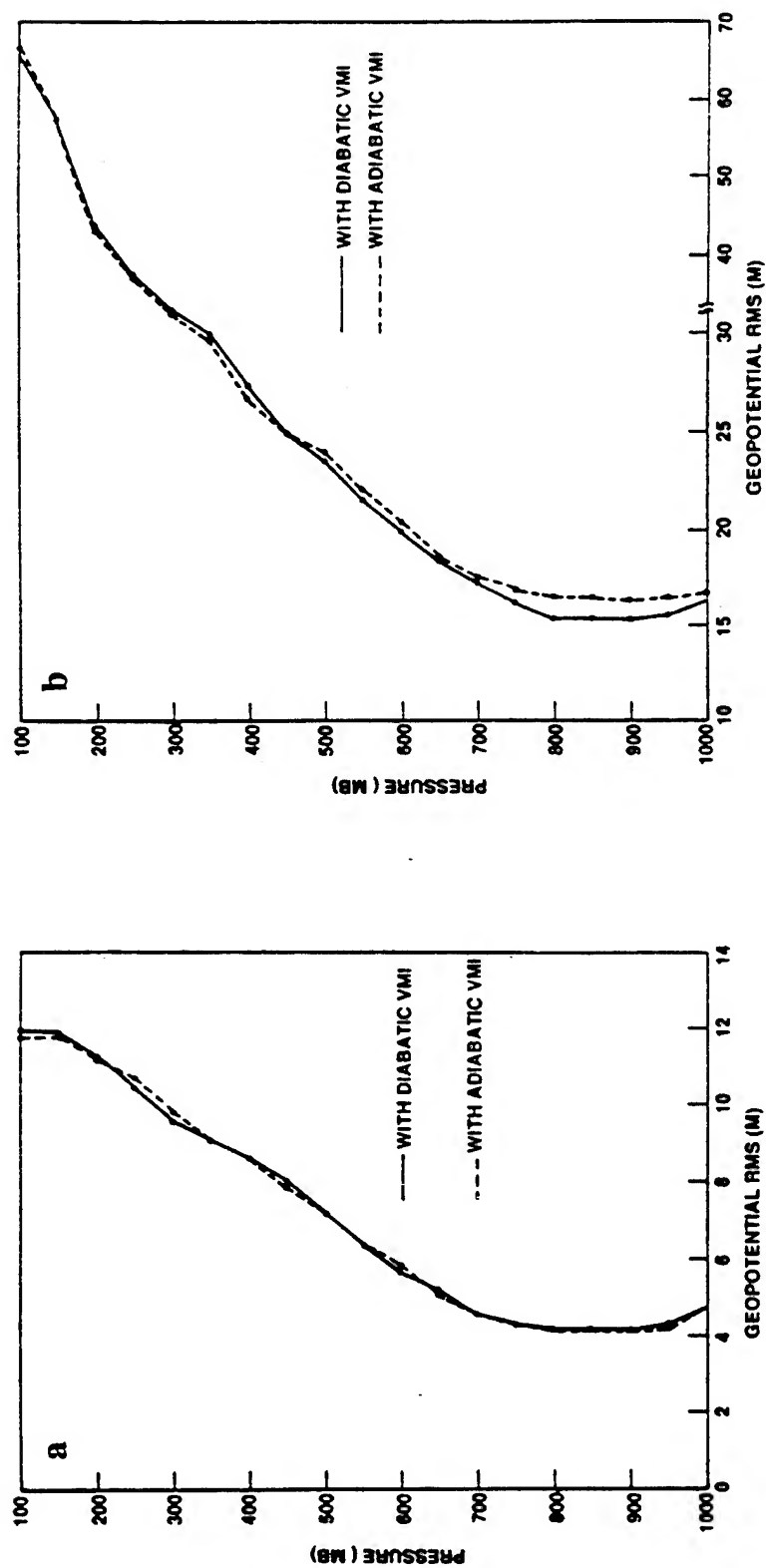


Figure 6.7. (a) Average analysis rms errors and (b) average background forecast rms errors for geopotential (m) from all update cycles of experiments 3 (06DI) and 5 (06AI).

humidity. These results suggest that the inclusion or exclusion of the diabatic forcing in the assimilation model initialization has minimal impact on the assimilation of these first order variables.

Generally, the background forecast errors at all levels (as shown in Figs. 6.2 - 6.7) are in good agreement with and verify our estimates of the standard deviations of the observations from the first guess forecasts (refer to Table 6.3). These estimates are a sum of the input observational error and a linear forecast growth error. With further testing, we can utilize statistics compiled over a longer period to further adjust these input error statistics for use in the analysis.

Further insight can be gained by investigating the time variation of the statistics in the case of the assimilation with update cycle of 3 h (experiment 4). Figure 6.8a shows plots of average rms analysis errors for the geopotential at 0300 and 1500 UTC, 0600 and 1800 UTC, 0900 and 2100 UTC, and 1200 and 0000 UTC from experiment 4. The analysis error (differences between analysis and observations) is less at the synoptic hours of 0000 and 1200 UTC than at the asynoptic hours. The larger errors noted by Rodgers et al. (1990) in the geopotential data from the supplemental GALE soundings along the east coast may have contributed to the higher rms errors at the asynoptic hours. At the synoptic hours, more data were used covering the whole analysis domain (see Fig. 6.1), and the average analysis error would be less. The average rms background errors for geopotential are shown in Fig. 6.8b. In general, the background fields for the 0000 and 1200 UTC analyses had the largest rms error, while those for the 0300 and 1500 UTC analyses possessed the least error. From the smaller analysis error and the larger data coverage at the synoptic hours, one would expect a more accurate background forecast for the 0300 and 1500 UTC analyses. At synoptic hours, the background in regions outside of the influence of the asynoptic data would be less accurate and the comparison with synoptic data would lead to larger errors. However, at 0600 and 1800

TABLE 6.3. Standard deviation of the observational errors and updated forecast error growth for a 6-h forecast period in parentheses. These are the input error statistics for the objective analysis.

Pressure (mb)	Height (m)	Temperature (°C)	Rel humidity (%)	u,v Wind (m s ⁻¹)
100	20 (25)	2.0 (0.7)	----	3.5 (1.3)
150	18 (25)	1.8 (0.6)	----	4.0 (1.4)
200	15 (20)	1.8 (0.5)	----	4.0 (1.5)
250	14 (18)	1.5 (0.6)	----	4.0 (1.6)
300	14 (16)	1.0 (0.6)	17 (4)	4.0 (1.6)
350	14 (14)	1.0 (0.5)	15 (4)	4.0 (1.7)
400	12 (12)	1.0 (0.5)	13 (4)	3.5 (1.7)
450	10 (11)	1.0 (0.4)	13 (4)	3.5 (1.6)
500	9 (10)	1.0 (0.3)	13 (4)	3.0 (1.6)
550	8 (10)	1.0 (0.3)	13 (3)	3.0 (1.5)
600	7 (9)	1.0 (0.3)	12 (3)	3.0 (1.4)
650	6 (8)	1.2 (0.3)	12 (3)	3.0 (1.3)
700	6 (8)	1.3 (0.3)	12 (2)	2.5 (1.2)
750	6 (8)	1.4 (0.3)	12 (2)	2.5 (1.2)
800	6 (8)	1.5 (0.4)	13 (2)	2.5 (1.1)
850	6 (8)	1.5 (0.5)	13 (2)	2.5 (1.1)
900	5 (8)	1.8 (0.5)	13 (2)	2.5 (1.1)
950	5 (8)	1.8 (0.6)	13 (2)	2.5 (1.1)
1000	5 (8)	1.8 (0.6)	13 (2)	2.5 (1.1)

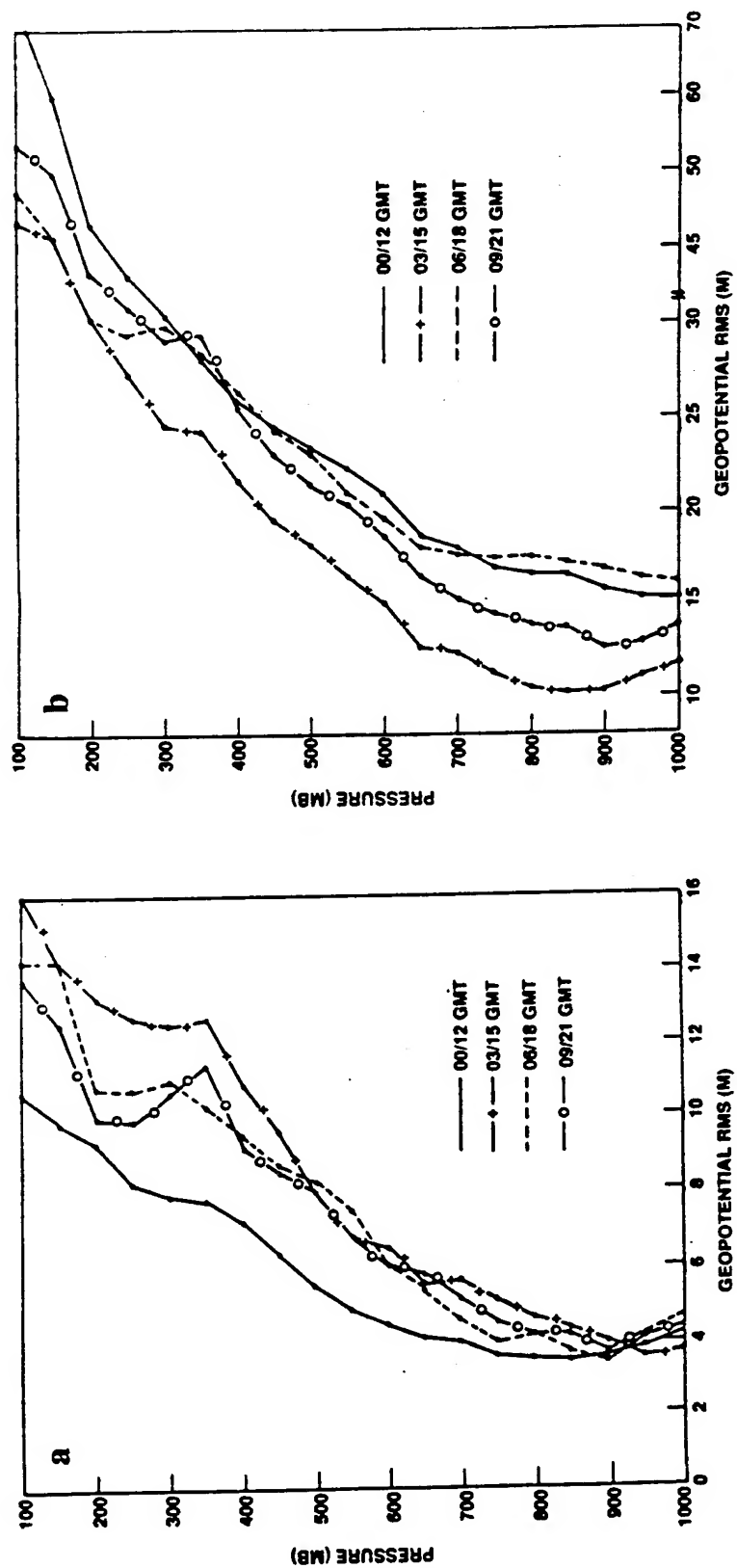


Figure 6.8. (a) Average analysis rms errors and (b) average background forecast rms errors for geopotential (m) from experiment 4 (03DI) at the 0300 / 1500 UTC, 0600 / 1800 UTC, 0900 / 2100 UTC, and 1200 / 0000 UTC update cycles.

UTC, the errors in the background fields were larger than the errors in the first-guess fields valid at 0900 and 2100 UTC.

Similar statistics were compiled from experiment 4 for the u- and v- wind components and relative humidity (not shown). However, the results are not as clear cut as in the case of geopotential. The background error at the 0300 and 1500 UTC cycles was generally less than that at the synoptic cycles, and likewise the analysis error at the 0300 and 1500 UTC cycles was generally larger than that at the 0000 and 1200 UTC update cycles. But the errors of the two sets of intermediate cycles (0600/1800 UTC and 0900/2100 UTC) were very random, with values not always falling between the errors from the 0300/1500 cycles and the synoptic cycles as in the case with geopotential.

These results can be useful in adjusting the input background forecast error growth rate used in the objective analysis scheme. Currently, the analysis error and the error growth are fixed values for all cycles within a given assimilation sequence. When considering the above results, it may be prudent in the future to adjust the analysis error and the forecast error growth, particularly for geopotential, in a fashion that allows the input background error to be largest at the 0000 and 1200 UTC update cycles and least at the 0300 and 1500 UTC cycles.

6.4.2 Subjective Evaluation and Discussion

Some synoptic analysis of the results is beneficial for understanding the impact of four-dimensional data assimilation on synoptic and mesoscale features, i.e. in the present study, the impact of assimilating the 3-hourly GALE observations. Here, emphasis is placed on a few significant events in the surface and 500-mb analyses and the forecast precipitation fields. Precipitation forecasts are verified against our observed precipitation (raingauge / satellite-derived rainfall). Precipitation verification is especially valuable

since rainfall is the result of many complex physical processes and is usually characterized by considerable small-scale variability. Since rainfall is dependent on divergence and vertical motion, it is also a good indicator of the accuracy of the model's dynamic balance and intervariable consistency.

a) Analysis aspects

Sea-level pressure and 1000-mb wind and temperature analysis fields from the "no assimilation" case and the assimilation with a 12-h update cycle (12DI) at 25/12Z are shown in Fig. 6.9. The 12DI analysis, shown in Fig. 6.9b, captured the strong temperature gradient associated with the coastal front along the Carolina coast and also the cold air damming with strong ridging east of the Appalachians. The 25/12Z Bosart surface analysis (Fig. 6.10) verifies the existence of these mesoscale features. However, the "no assimilation" analysis, shown in Fig. 6.9a, has a weaker thermal gradient along the coast. Strong onshore flow, which is readily apparent in Bosart's analysis, was also present in the assimilated analysis. Figure 6.11 shows the 1000-mb specific humidity fields from experiments 1 and 2. The low-level moisture gradients at the coastal front and with the short wave over the western Gulf of Mexico are much greater in the 12DI analysis than in the "no assimilation" analysis.

At 26/00Z, surface and 500-mb analyses from experiments 1, 2, 3, and 5 were examined. Compared to the "no assimilation" analyses, the assimilated surface fields possessed much stronger thermal and low-level moisture gradients across the coastal front, with little distinction between the three assimilations of varying update cycles (not shown). The 500-mb relative humidity analyses, shown in Fig. 6.12, reveal a better distinction. While rain was falling over central North Carolina at 26/00Z, an upper-level moisture maxima was present there in the assimilated fields. However, the analysis from

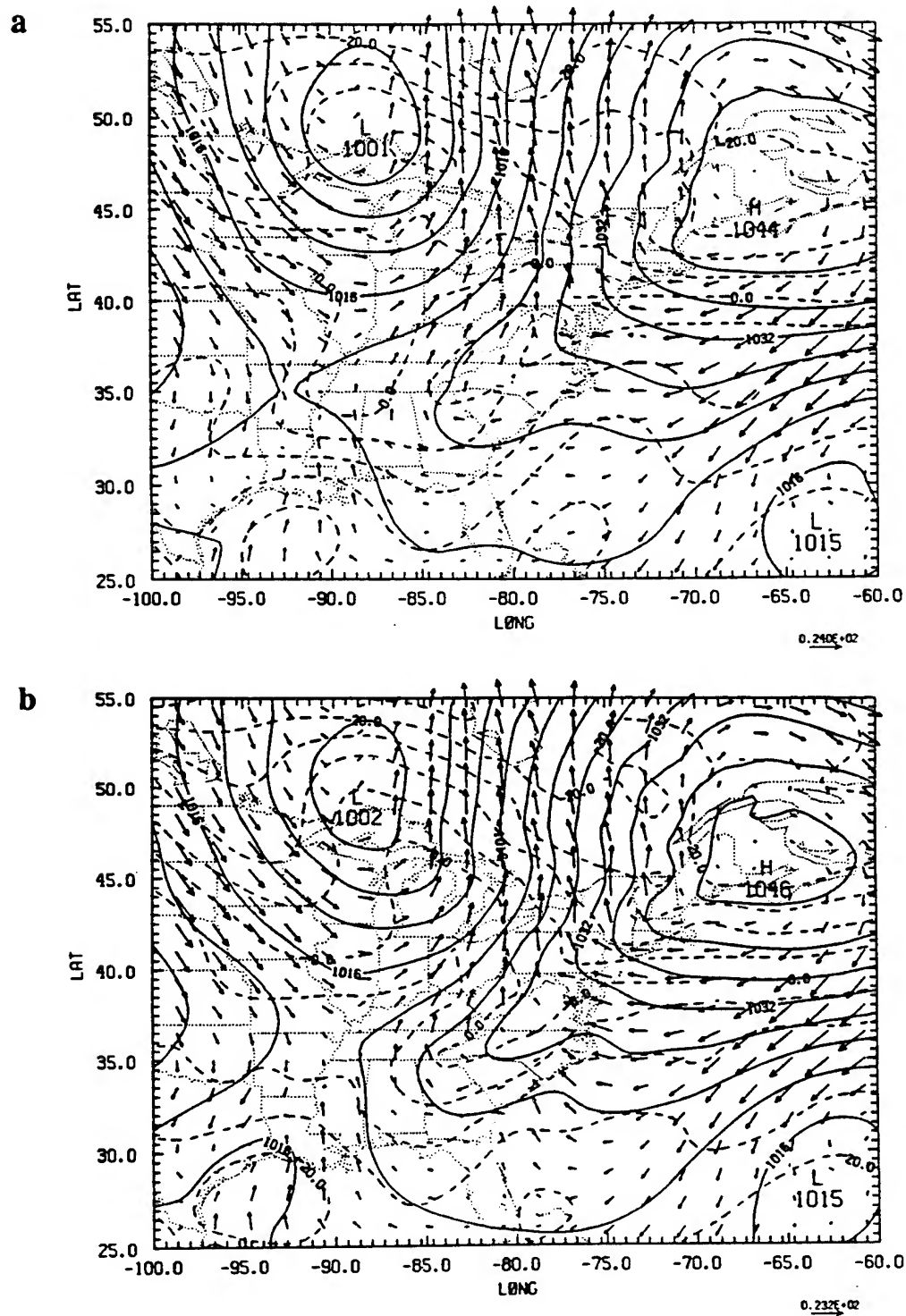


Figure 6.9. Sea-level pressure (mb), 1000-mb temperature ($^{\circ}\text{C}$) and wind analyses at 25/12Z from (a) experiment 1 (no assimilation) and (b) experiment 2 (12DI). Contours of sea level pressure and temperature at 1000 mb are 4 mb and 5°C , respectively.

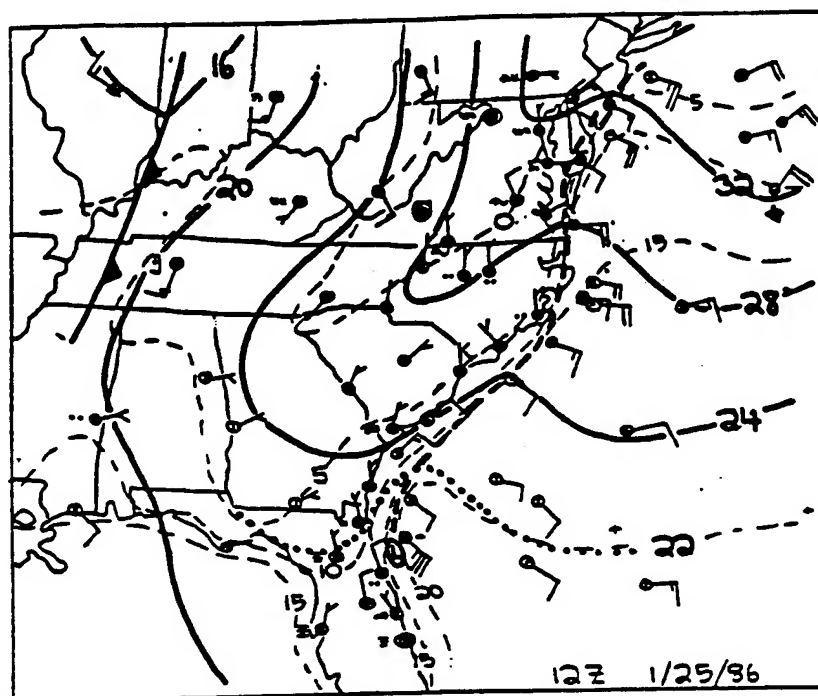


Figure 6.10. GALE analysis of sea-level pressure deviation (from 1000 mb), surface temperature ($^{\circ}\text{C}$) and wind for 25/12Z by Bosart (1988). Surface temperature contours every 5°C .

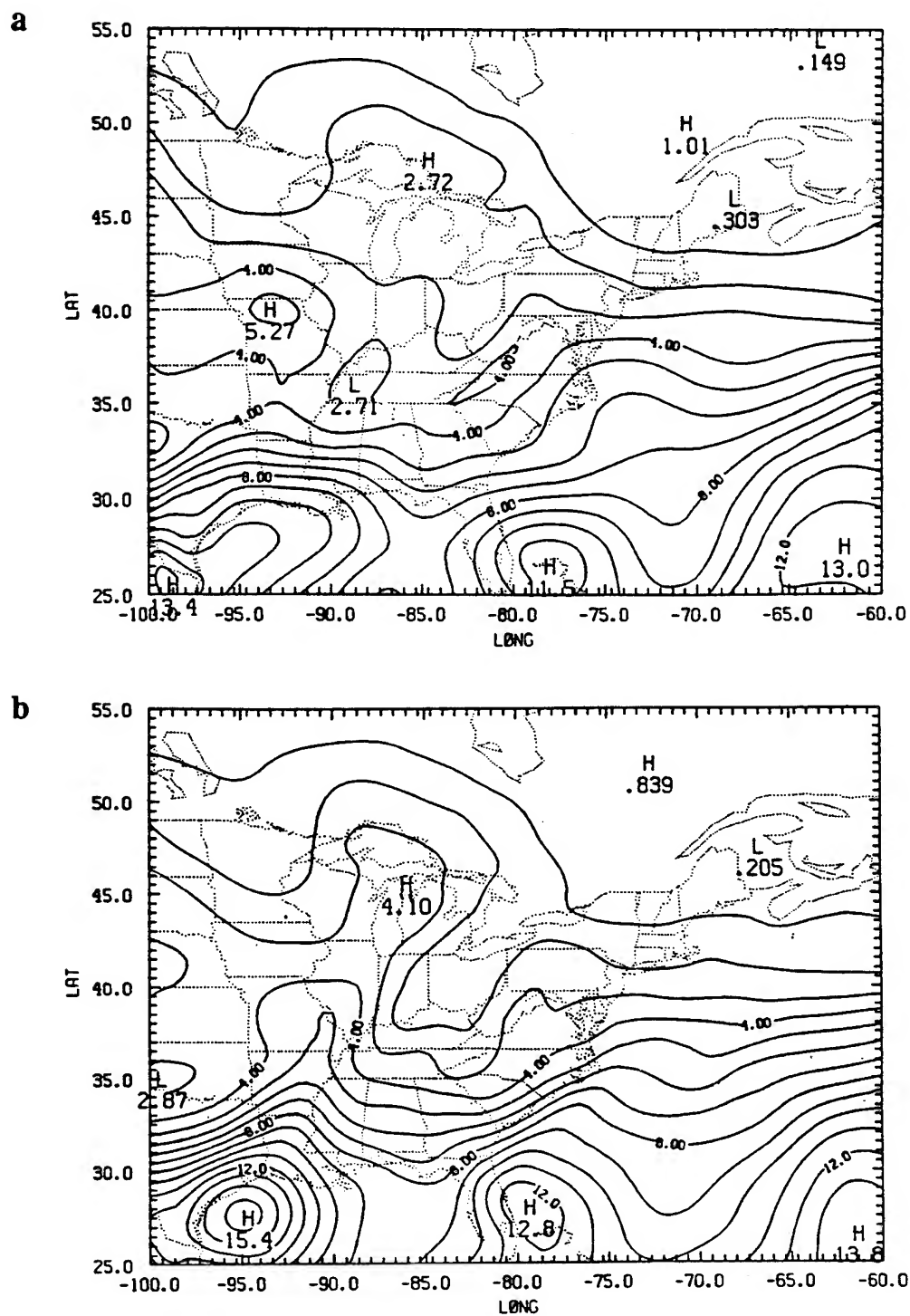


Figure 6.11. 1000-mb specific humidity (g kg^{-1}) analyses at 25/12Z from (a) experiment 1 (no assimilation) and (b) experiment 2 (12DI). Contours are every 1 g kg^{-1} .

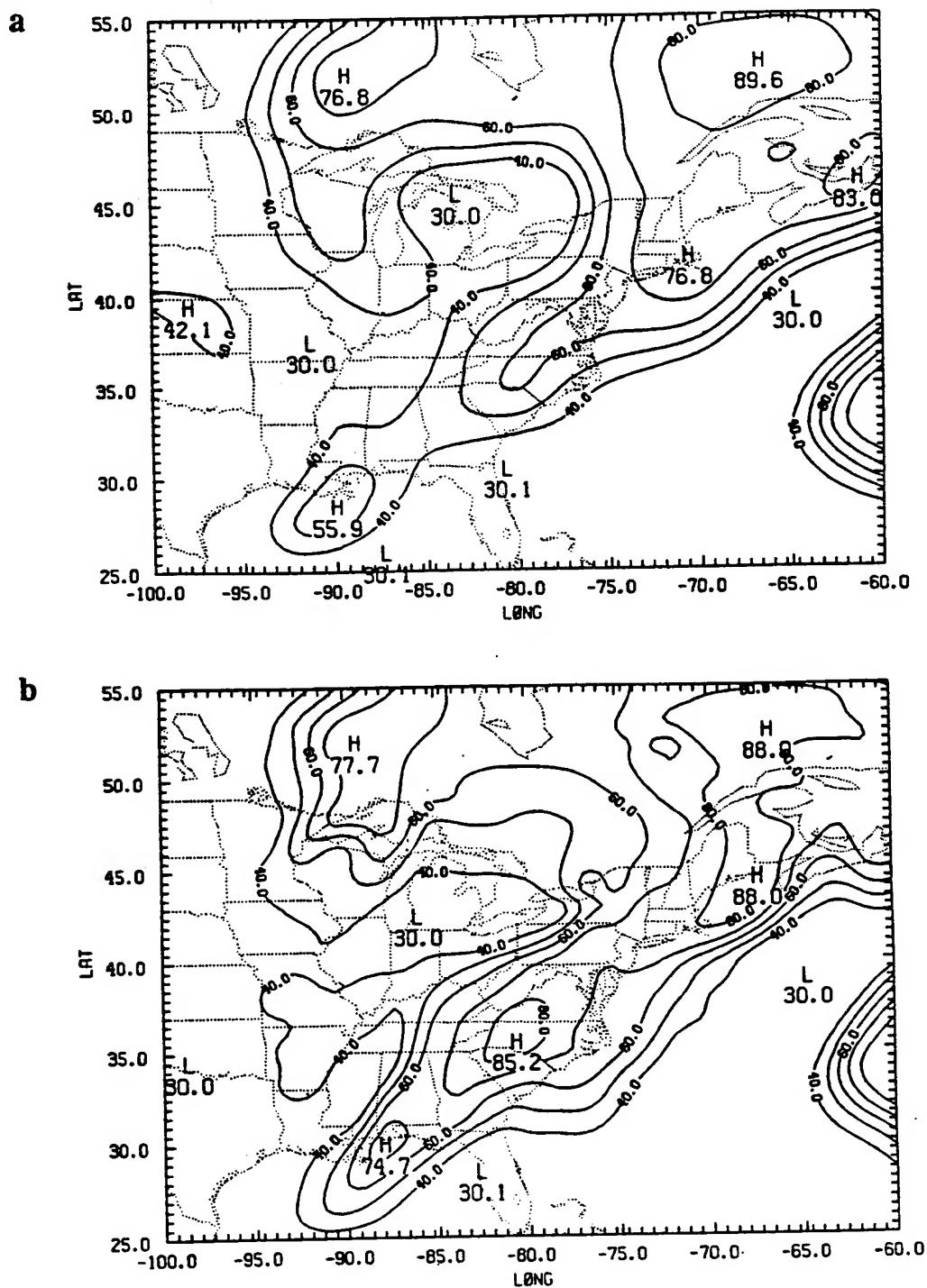


Figure 6.12. 500-mb relative humidity (%) analyses at 26/00Z from (a) experiment 1 (no assimilation), (b) experiment 2 (12DI), (c) experiment 3 (06DI), and (d) experiment 5 (06AI). Contours are every 10%.

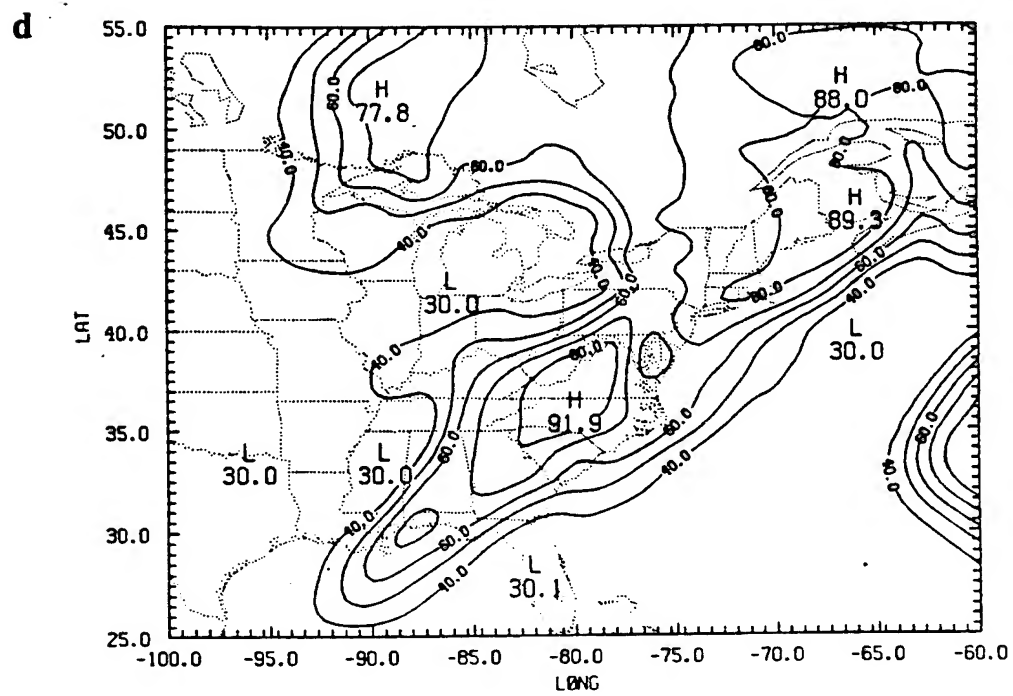
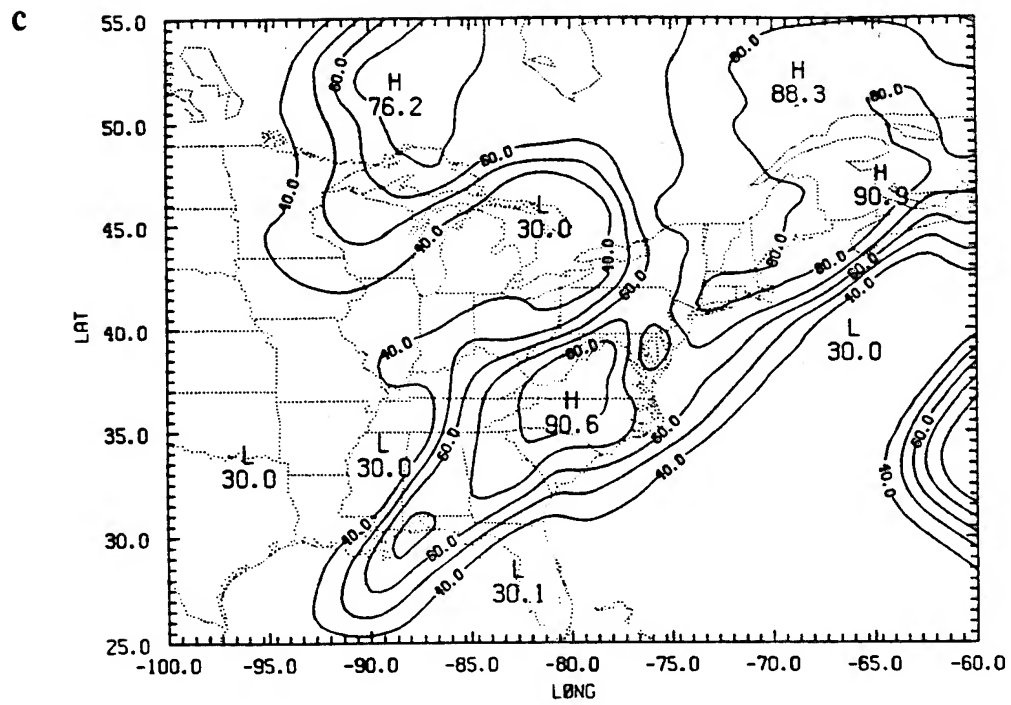


Figure 6.12. Continued.

the 6-h update cycle had the greatest value showing that asynoptic GALE data, in this case, led to an improvement over the assimilation with 12-h updates. Over the central Gulf coast, all three assimilations produced a moisture tongue (with relative humidity over 70%) associated with an eastward-moving short-wave disturbance. The "no assimilation" analysis showed a maxima of only 56% in this region where rainfall was occurring. The overall upper-level moisture pattern from the 06AI assimilation (i.e., VMI without diabatic heating) was very close to the other assimilated states. As noted in the previous section, the inclusion of diabatic heating in the vertical mode initialization led to little change in the first order field. This is not necessarily true in the case of vertical motion, which is related directly to diabatic heating. From the vertical velocity fields, shown in Fig. 6.13, a clear distinction between the experiment with diabatic VMI (experiment 3) and that with adiabatic VMI (experiment 5) can be seen. The assimilation with diabatic heating included in VMI shows a stronger vertical circulation at the coastal front at 26/00Z. The vertical motion along the east coast from the assimilated experiments was much stronger and had much more detail than that from the "no assimilation" case, with the 06DI assimilation producing slightly greater vertical motions at the coastal front than did the assimilation with a 12-h update cycle. Also, stronger vertical velocities are present over the central Gulf coast associated with the developing wave in all the assimilated states as compared to the "no assimilation" analysis.

Cross sections were produced to further investigate the ageostrophic circulation associated with the coastal front and an advancing upper-level jet. Cross section 2 (CS2 from 90°W, 43.5°N to 68.7°W, 26°N) cuts across the entrance region of the jet over the southeast U.S. and extends across the Carolina coast (see Fig. 4.5c). Figure 6.14 shows the magnitude of the wind speed normal to the cross section from the "no assimilation" case and the 12DI assimilation for 26/00Z. The ageostrophic circulations in the plane of CS2 for these two cases are depicted in Fig. 6.15. The mesoscale circulation of the

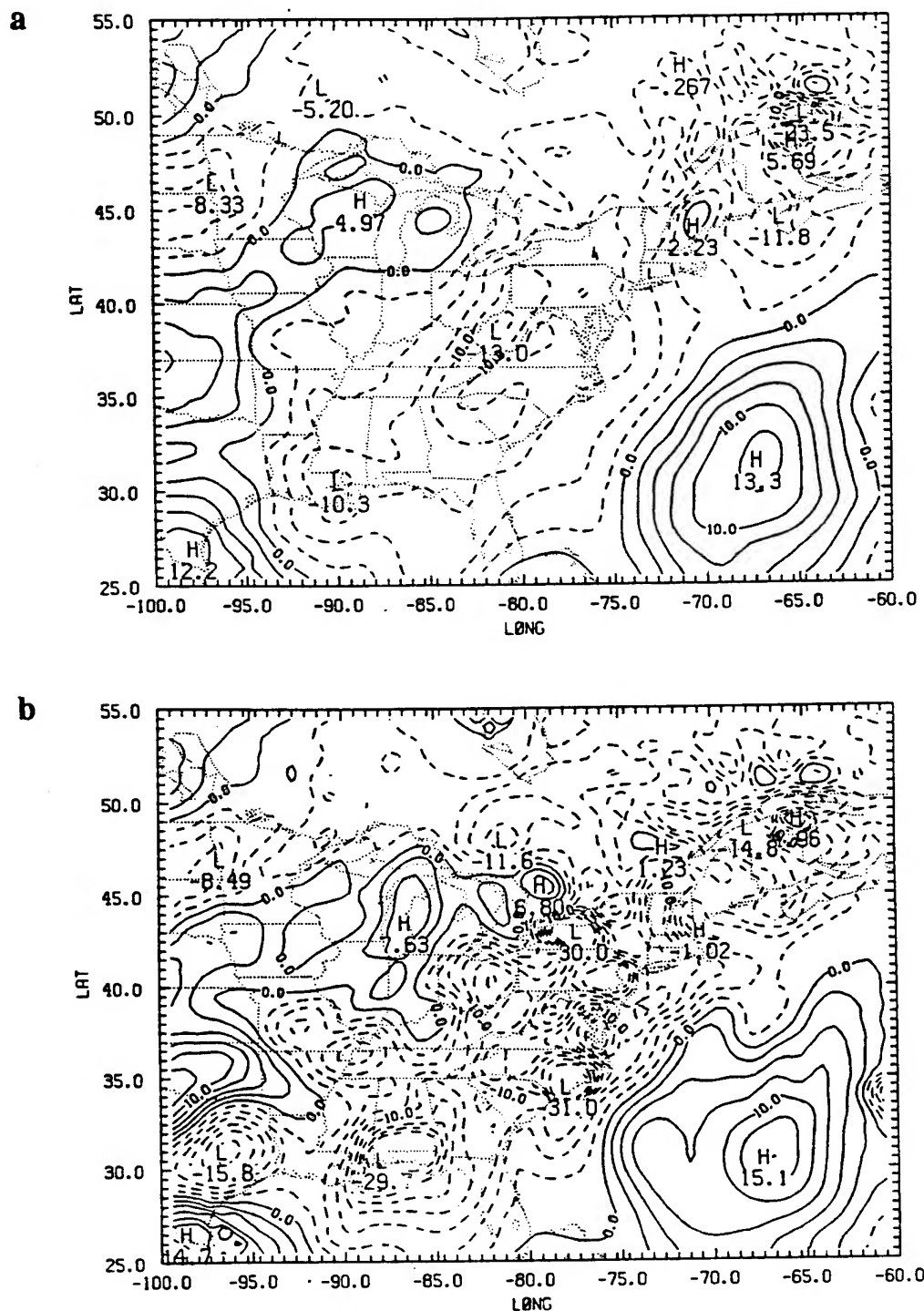


Figure 6.13. 500-mb vertical velocity (mb h⁻¹) analyses at 26/00Z from (a) experiment 1 (no assimilation), (b) experiment 2 (12DI), (c) experiment 3 (06DI), and (d) experiment 5 (06AI). Vertical motion of magnitude of -20 mb h⁻¹ or more are contoured every 2.5 mb h⁻¹.

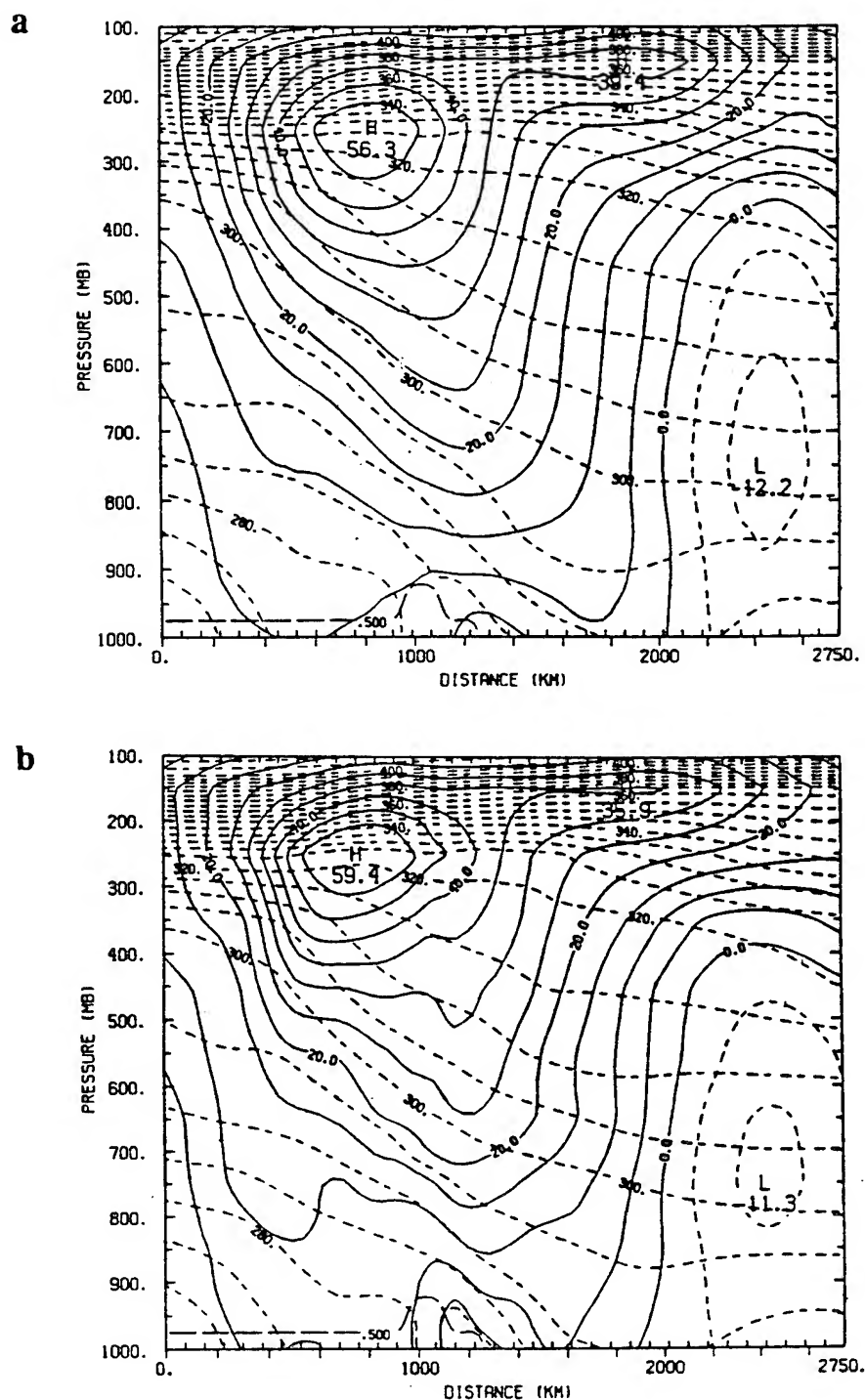


Figure 6.14. Wind speed (m s^{-1}) normal to the plane of CS2 at 26/00Z from (a) experiment 1 (no assimilation) and (b) experiment 2 (12DI). Contours are every 5 m s^{-1} . The potential temperature ($^{\circ}\text{K}$) is also shown by the dashed contours every 5°K .

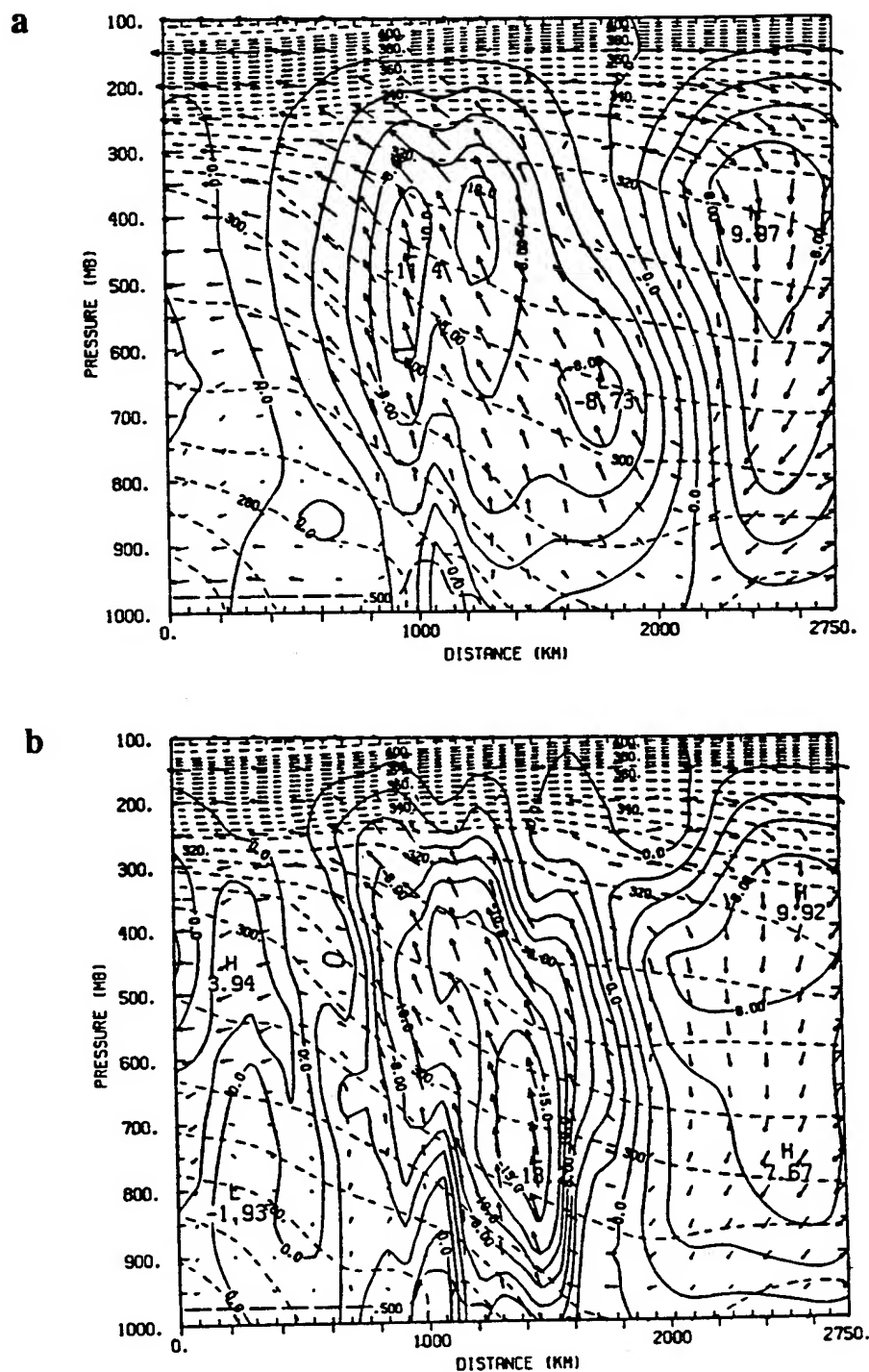


Figure 6.15. Vertical motion (mb h^{-1}) and ageostrophic wind (m s^{-1}) in the plane of CS2 at 26/00Z from (a) experiment 1 (no assimilation) and (b) experiment 2 (12DI). The magnitude of the vertical motion is represented by the solid contours at -40, -25, -20, -15, -12.5 and every 2 mb h^{-1} for -10 and above.

coastal front is still a distinct feature within the 12DI analysis. However, the jet's secondary circulation has begun to absorb and deepen the coastal front's ageostrophic circulation as shown in the cross section. The ageostrophic circulation at 26/00Z due to the coastal front is much stronger and sharper in the 12DI as compared to the control analysis, with maximum ascents of -18.2 and -8.7 mb h^{-1} at the coastal front, respectively. The 06DI assimilation (cross section not shown) strengthened the ageostrophic circulation, but only by a small amount (-19.1 mb h^{-1} vs. -18.2 mb h^{-1}).

At 26/12Z, there is little difference in the surface temperature, wind, and pressure fields from the various assimilations sequences. In the 1000-mb specific humidity fields, the moisture gradient along the front on the east coast was sharpest in the 3-h cycle assimilation, followed by 06DI, then 12DI, with the "no assimilation" analysis having the weakest gradient. The 500-mb relative humidity analyses from experiments 1 - 4 again depicted the tongue of upper-level moisture extending over the eastern U.S. from Georgia to Maine. As in the lower troposphere, the 03DI assimilation generated the sharpest gradient and largest maxima and the "no assimilation" case produced the weakest. Little difference was found in the vertical motion fields resulting from the assimilation runs, with all displaying much greater maxima and detail than in the "no assimilation" experiment.

At 27/00Z and 27/12Z, the assimilated fields from experiments 2, 3, and 4 are very similar. The influence of the 3-hourly GALE data seems to be impacting the assimilation primarily when mesoscale circulations are predominant, i.e., there is a positive impact in the small-scale. When the synoptic-scale circulation became stronger and essentially engulfed the coastal front, less impact was noted. However, each of the assimilations still produced analyses which were noticeably different from the "no assimilation" case. One surface feature worth noting at 27/00Z is the positions of the low pressure centers from each experiment. By 27/00Z the disturbance, which had moved from the northern

Gulf of Mexico across southern Georgia, again appeared as a closed surface low in the assimilation analyses; rapid cyclogenesis had just begun (Fig. 6.16a). The low pressure center which was earlier associated with the coastal front had moved north and would soon merge with a weak northern low, associated with a short-wave trough which had advanced eastward from the Great Lakes region into New England. However, the "no assimilation" analysis does not distinguish those circulations, instead only the deepening low pressure center is depicted in a position farther up the east coast (Fig. 6.16b). By 27/03Z, the 03DI assimilation had deepened the cyclone's central pressure by 3 mb (Fig. 6.16c) and moved it just off the Delaware coast in close proximity with the "no assimilation" position at 27/00Z. This would seem to suggest that only a slight timing error in the development of the strengthening cyclone differentiates the "no assimilation" analysis from the assimilation case. However, investigation of the ageostrophic circulations along the east coast proves otherwise. As in other cases of rapid cyclogenesis (Uccellini and Kocin 1987, for example), the rapid development is being aided by the indirect circulations of an exiting upper-level jet to the north and an approaching jet located south of the low. In this case, the northern jet has also been strengthened by the short-wave trough from the Great Lakes. These jets are evident in Fig. 6.17a which is a cross section (CS7, see Fig. 6.16a) along the east coast (69.3°W , 49.5°N to 80.0°W , 26.5°N) of the normal wind speed at 27/00Z. Figures 6.17b and 6.17c are cross sections of the ageostrophic circulations from the 03DI and "no assimilation" cases. The 03DI analysis shows the ascending motion associated with the northern low (point A of Fig. 6.17b), still retains the mesoscale circulation associated with the decaying coastal low (point B), and depicts the strong vertical circulation of the developing low at point C. The secondary circulation of the coastal low is being absorbed by the indirect circulation of the entrance region of the northern jet. The ageostrophic circulation from the "no assimilation" analysis (Fig. 6.17c) fails to capture

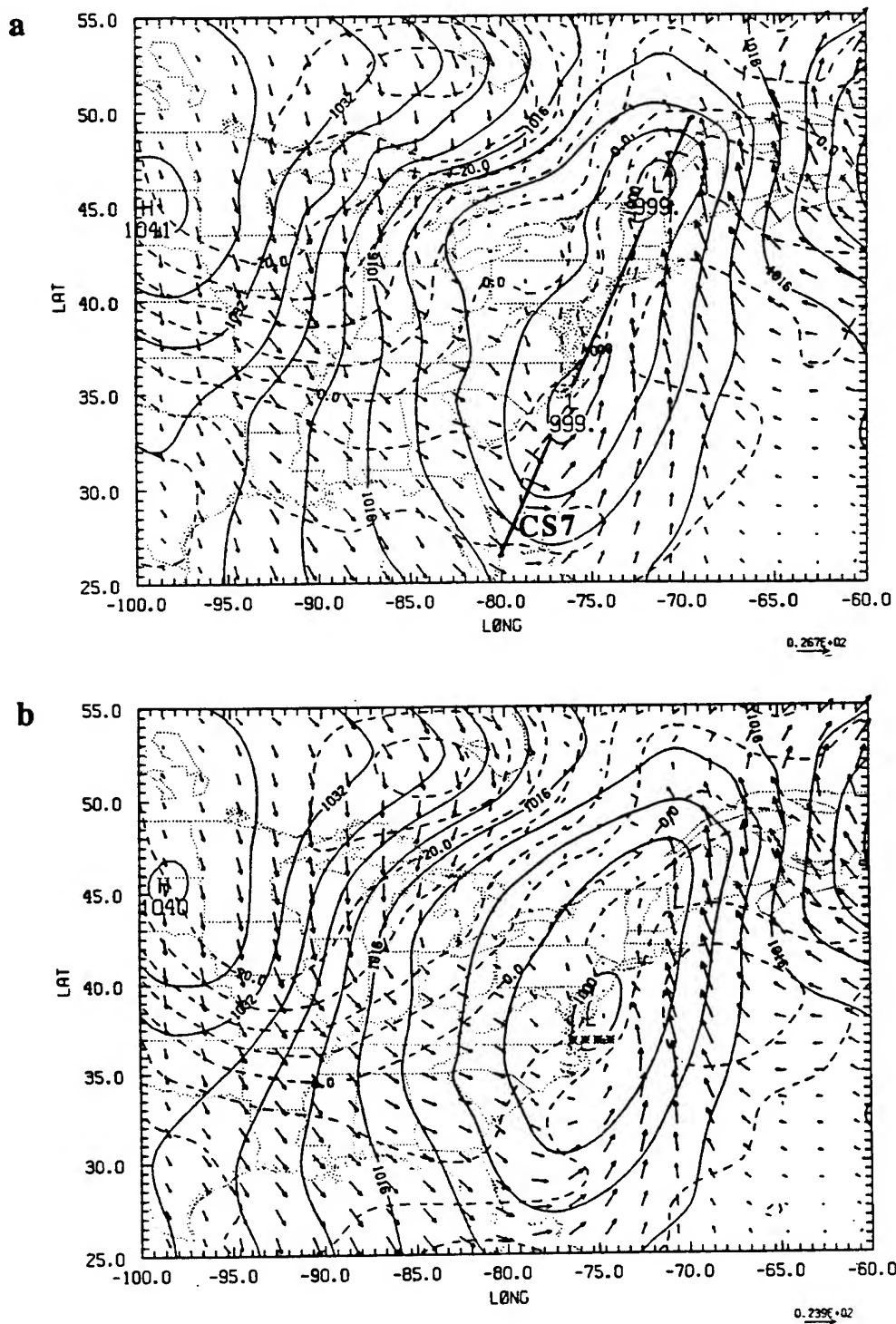


Figure 6.16. Sea-level pressure (mb), 1000-mb temperature ($^{\circ}\text{C}$) and wind analyses at 27/00Z from (a) experiment 4 (03DI) and (b) experiment 1 (no assimilation), and at 27/03Z from (c) experiment 4 (03DI). Contours as in Fig. 6.9.

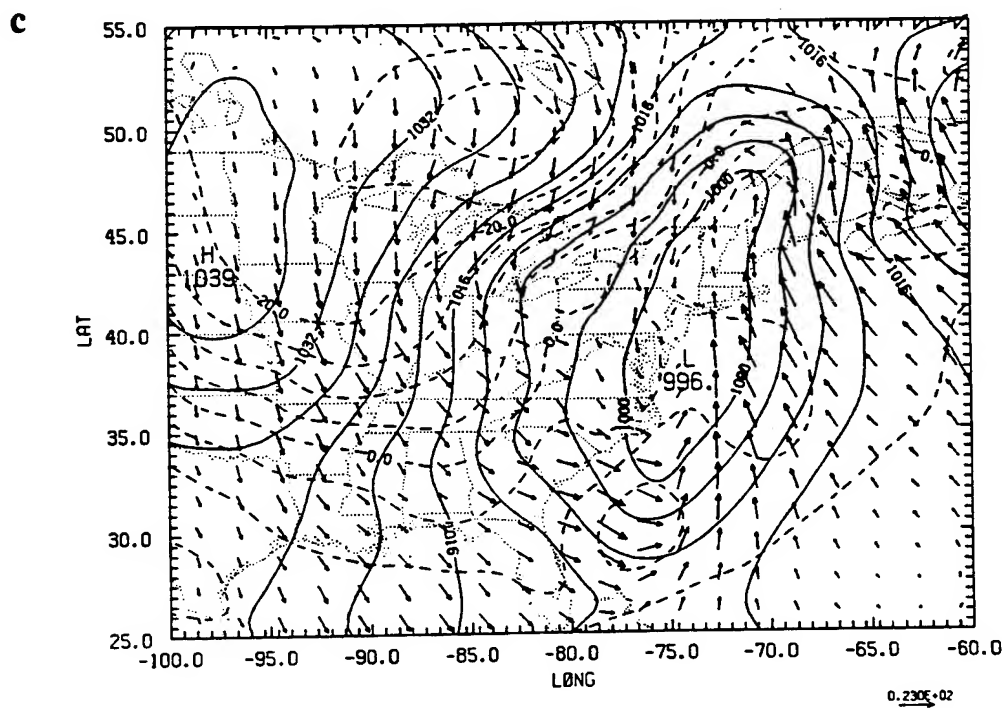


Figure 6.16. Continued.



• • • • •

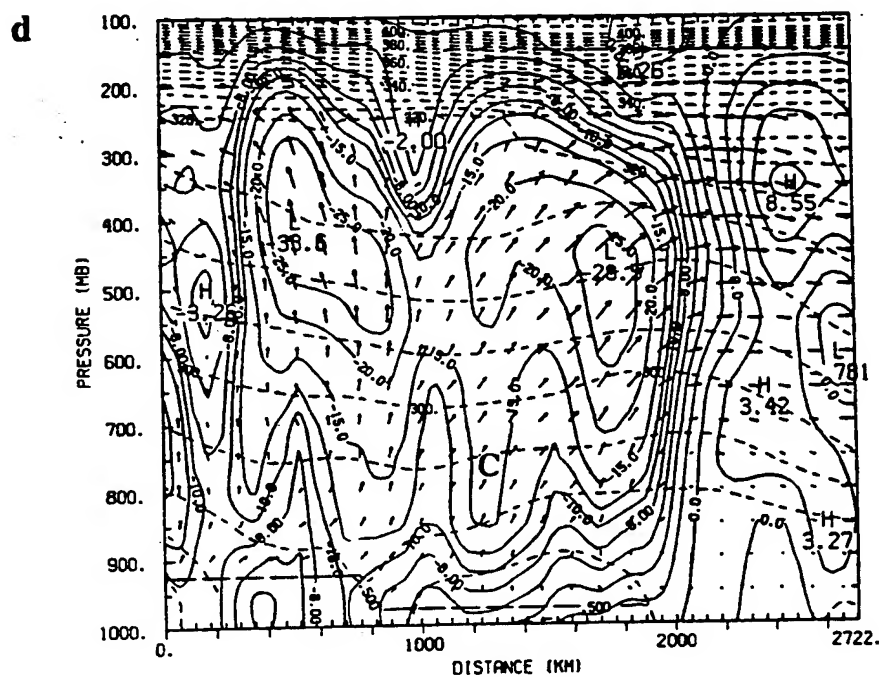
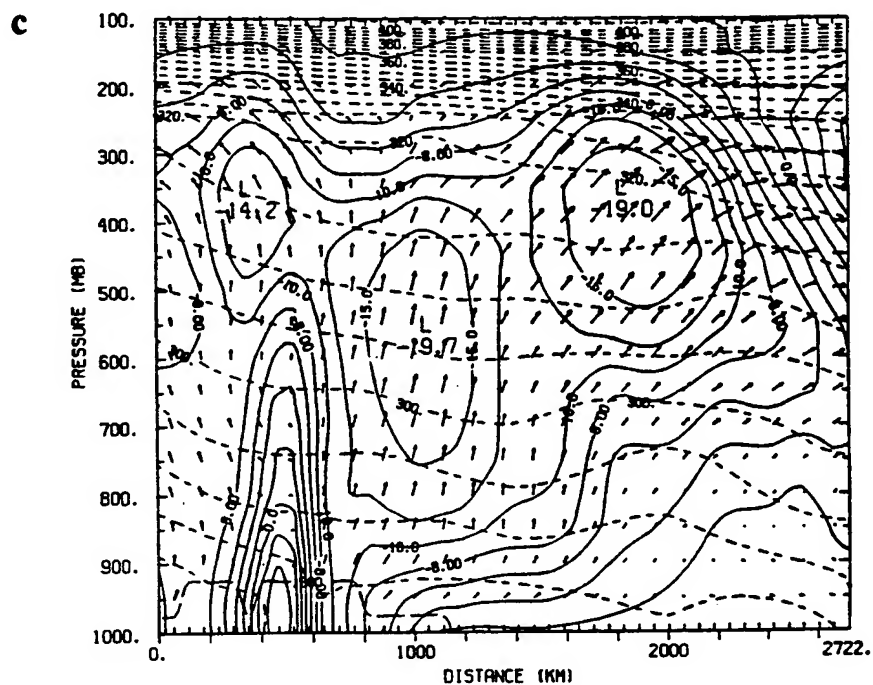


Figure 6.17. Continued.

these various features. It simply depicts the strong vertical motion of the deepening low, being supported by the indirect circulations of the two jets. Figure 6.17d shows the 03DI ageostrophic circulation at 27/03Z. By this time, the analyzed deepening low had moved a little farther north (point C). The circulations associated with the northern low and coastal low are merging and continue to be engulfed by the jet's secondary circulation.

By 27/12Z, the rapidly deepening cyclone had tracked northeast to New England in both the "no assimilation" and 03DI cases (Figs. 6.18a and 6.18b). With the support of the secondary circulations of the two jets, the low had deepened by 15 mb in the "no assimilation" analysis and 17 mb in the 03DI analysis. The synoptic scale circulation of the cyclone was now totally dominant, with the mesoscale circulation of the coastal low being completely absorbed in the large-scale circulation. As a result, the pattern of the ageostrophic circulation along CS6 (68.7°W, 55.5°N to 76.7°W, 25.5°N; see Fig. 4.24b) from the 03DI assimilation (Fig. 6.19b) is very similar to that from the "no assimilation" case (Fig. 6.19a). But the cyclone's vertical motion from the assimilation case is much stronger, with a maximum of -45 mb h^{-1} versus -26.2 mb h^{-1} .

b) Subsequent forecast aspects

The true test of the goodness of any data assimilation designed for the purpose of providing initial conditions for a numerical weather prediction model is the accuracy of the forecasts produced from the assimilated states. Twenty-four-hour forecasts starting at 26/00Z were generated from analyses in experiments 1 (no assimilation), 2 (12DI), 3 (06DI), and 5 (06AI). Comparisons among these forecasts were made and are now discussed.

Six-hour forecasts, valid at 26/06Z, of sea-level pressure, surface air temperature and winds are shown in Fig. 6.20. The forecasts originating from the assimilated fields

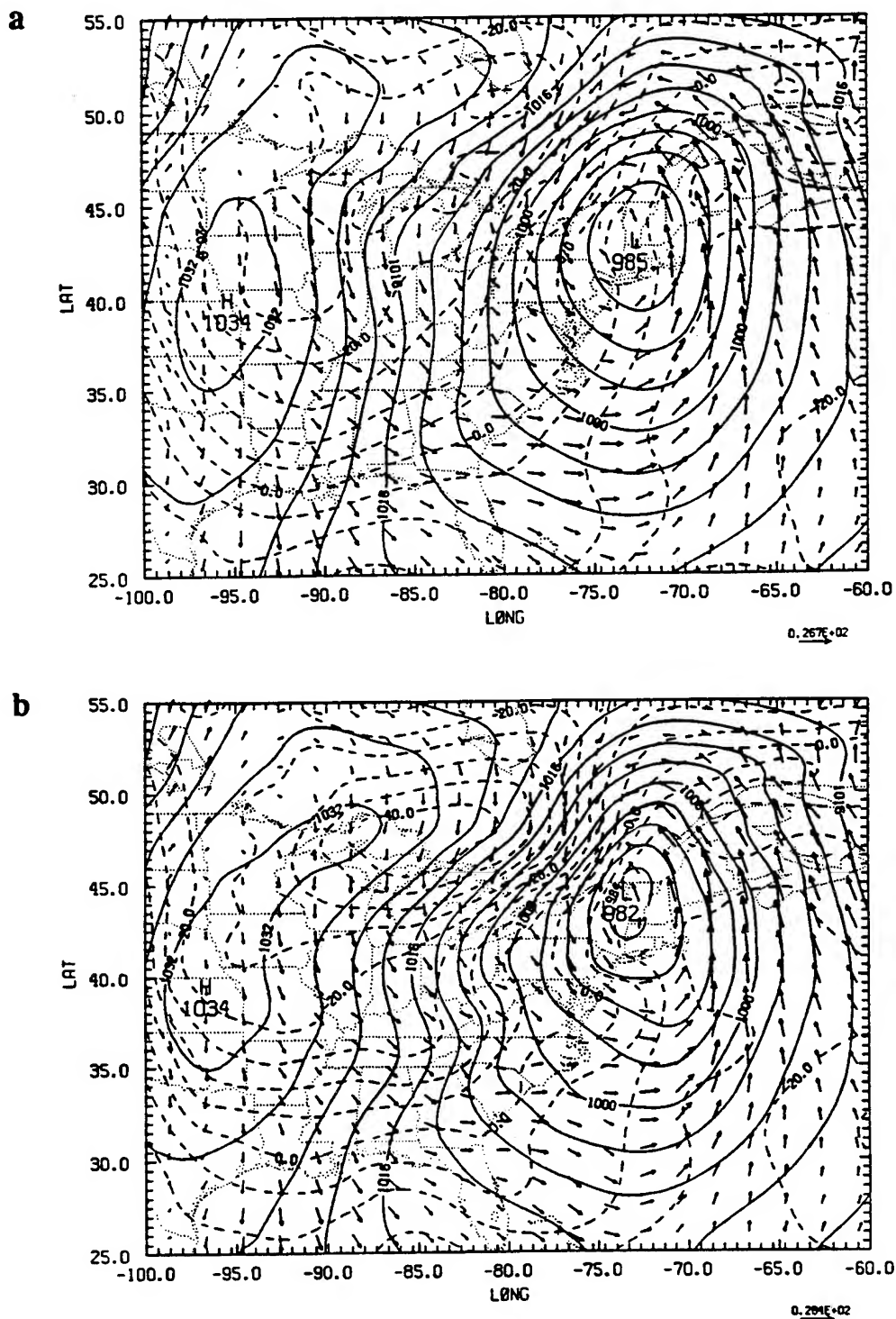


Figure 6.18. Sea-level pressure (mb), 1000-mb temperature ($^{\circ}$ C) and wind analyses at 27/12Z from (a) experiment 1 (no assimilation) and (b) experiment 4 (03DI). Contours as in Fig. 6.9.

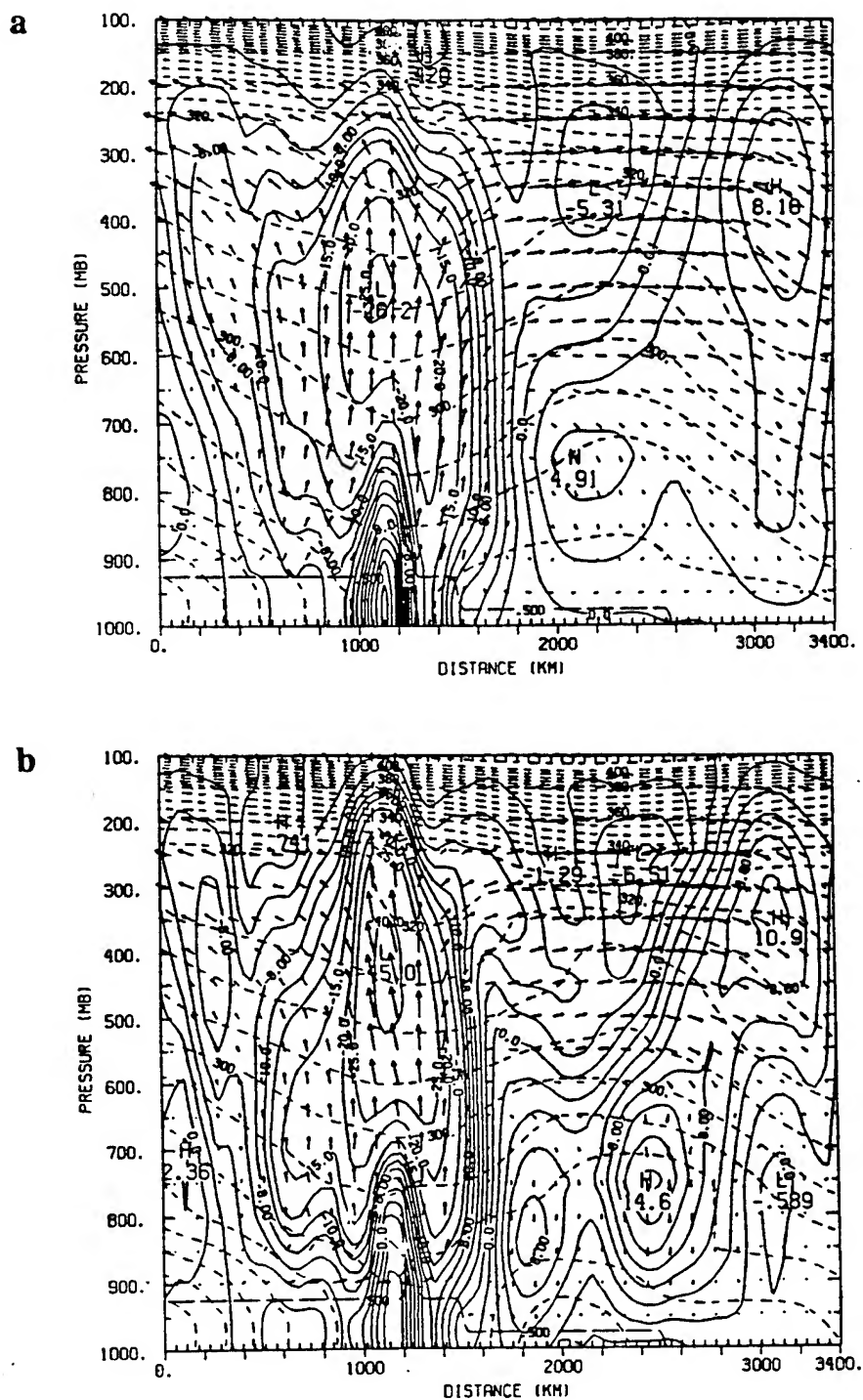


Figure 6.19. Cross sections (CS6) of the ageostrophic circulation at 27/12Z from (a) experiment 1 (no assimilation) and (b) experiment 4 (03DI). Contours as in Fig. 6.15.

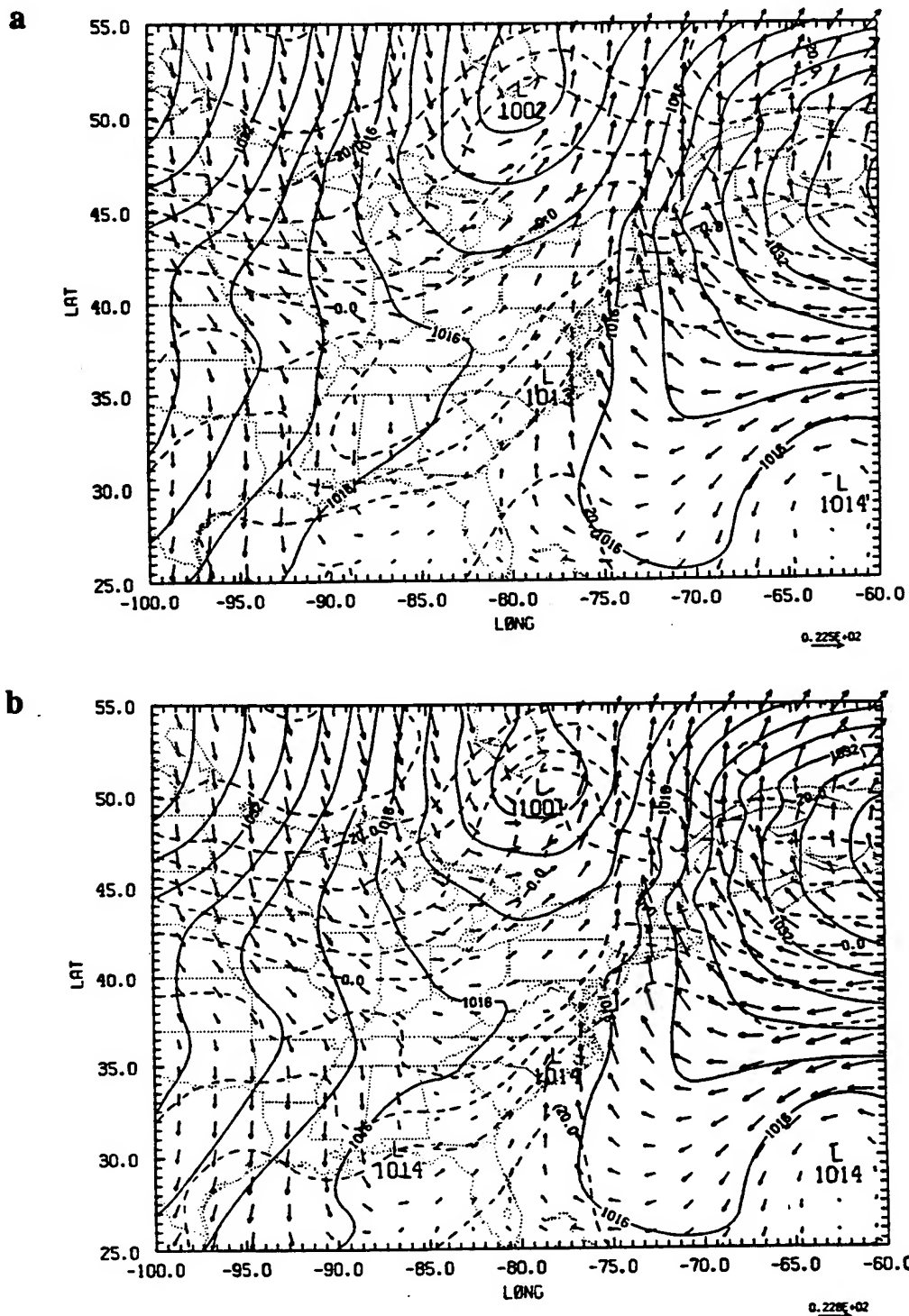


Figure 6.20. Six-hour forecasts of sea-level pressure (mb), surface air temperature ($^{\circ}\text{C}$), and 1000-mb winds valid at 26/06Z from (a) experiment 1 (no assimilation), (b) experiment 2 (12DI), and (c) experiment 3 (06DI). Contours and in Fig. 6.9.

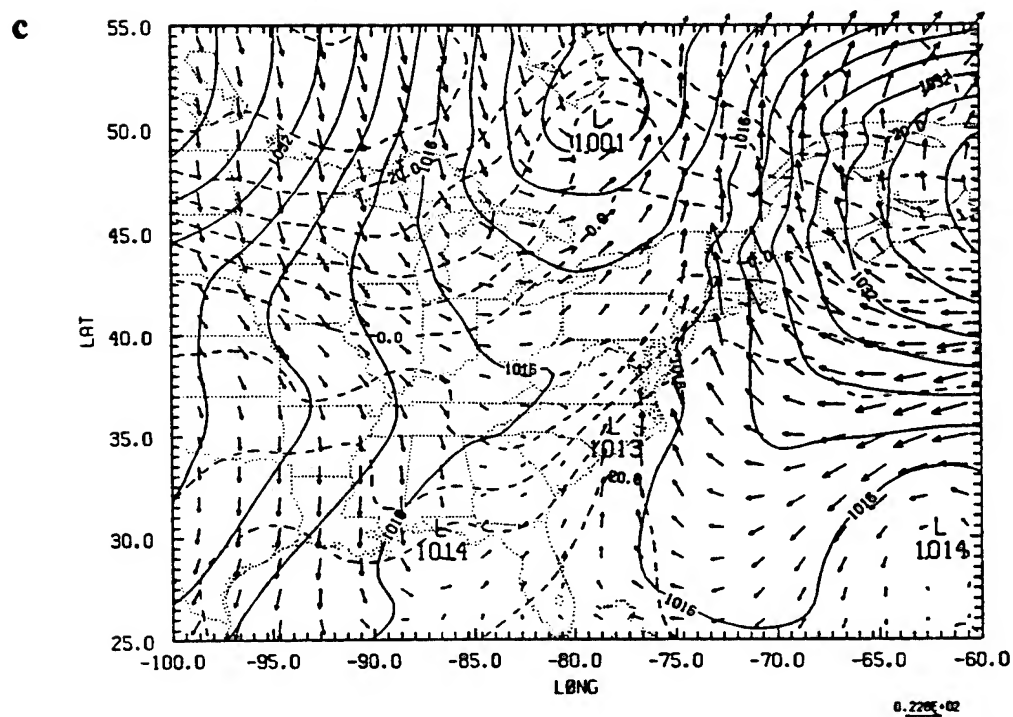


Figure 6.20. Continued.

have much tighter temperature gradients along the Carolina coast in the vicinity of the coastal front than does the forecast from the "no assimilation" case. The frontal temperature gradients resulting from experiments 2 and 3 are in very good agreement with the Bosart hand analysis (Fig. 6.21) with a temperature contrast of approximately 15°C from Charlotte, North Carolina to a position just off the South Carolina coast. Bosart's analysis shows a low of 1012 mb on the Florida panhandle and a low of less than 1012 mb which had formed on the southern end of the coastal front. In reference to these low pressure centers, the 12DI forecast verifies the best in regards to central pressure, but the 06DI forecast predicts the positions more accurately. As in the case of the analyses, the forecasts from the assimilated states produce a much tighter low level moisture gradient at the coastal front than does the "no assimilation" forecast (not shown).

Six-hour observed rainfall and accumulated forecast rainfall (26/00Z - 26/06Z) for experiments 1, 3, and 5 are shown in Fig. 6.22. The forecasts from the assimilated cases, 06DI (Fig. 6.22b) and 12DI (not shown), match the observed precipitation pattern (Fig. 6.22d) reasonably well and show much more rapid spinup of rainfall than does the "no assimilation" forecast. Here, the disadvantage of not having a mesoscale assimilation model to generate and maintain small-scale features is evident. The "no assimilation" forecast must spinup these circulations and, as a result, gives a poor short-range rainfall prediction. The forecast from experiment 5 (06AI in Fig. 6.22c) fails to capture any rainfall over the Gulf coast associated with the developing short wave. The absence of diabatic heating from the VMI has caused a spinup problem in this case.

The 12-h surface and low-level moisture forecasts (valid at 26/12Z) from the various assimilations are very similar and, like the 6-h forecasts, have much stronger gradients along the east coast of the U.S. than does the "no assimilation" forecast. Figure 6.23 depicts the 6-h accumulated rainfall ending at 26/12Z. The forecasts from

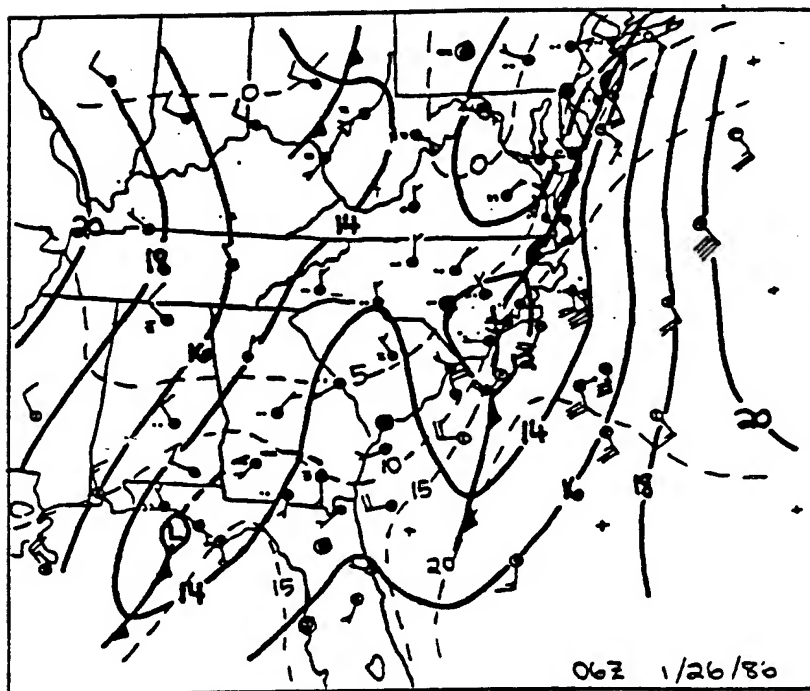


Figure 6.21. GALE analysis of sea-level pressure deviation (from 1000 mb), surface temperature ($^{\circ}\text{C}$) and wind for 26/06Z by Bosart (1988). Surface temperature contours every 5°C .

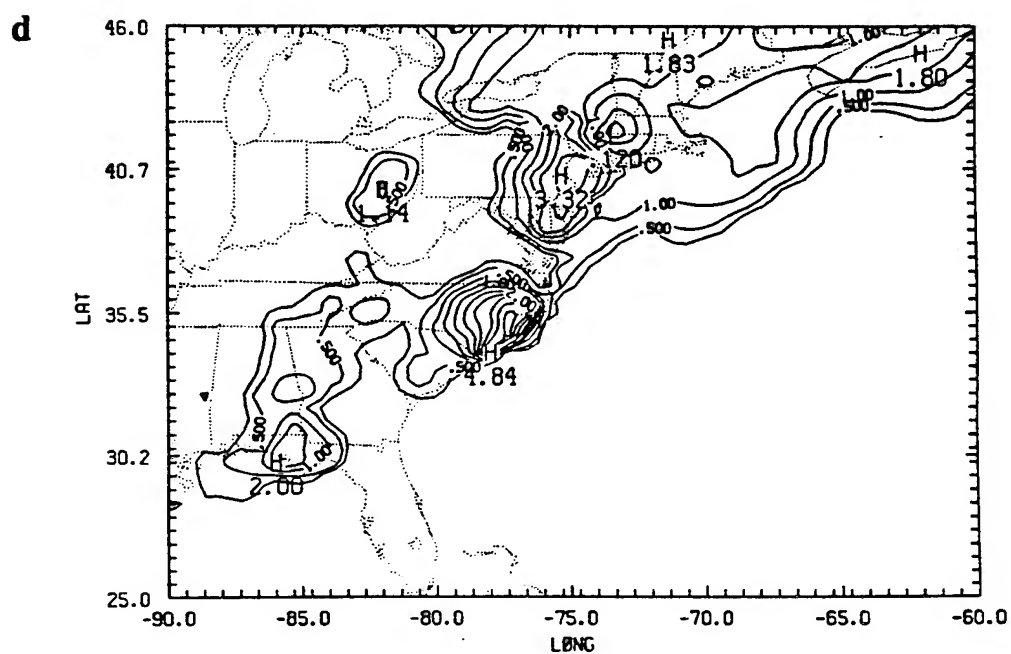
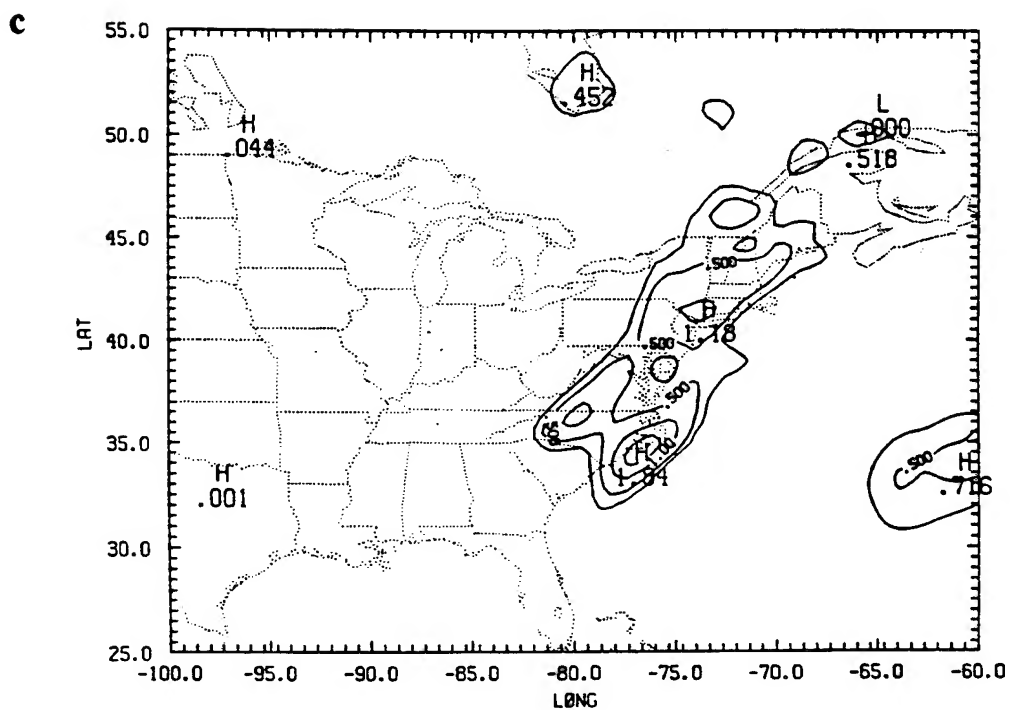


Figure 6.22. Continued.

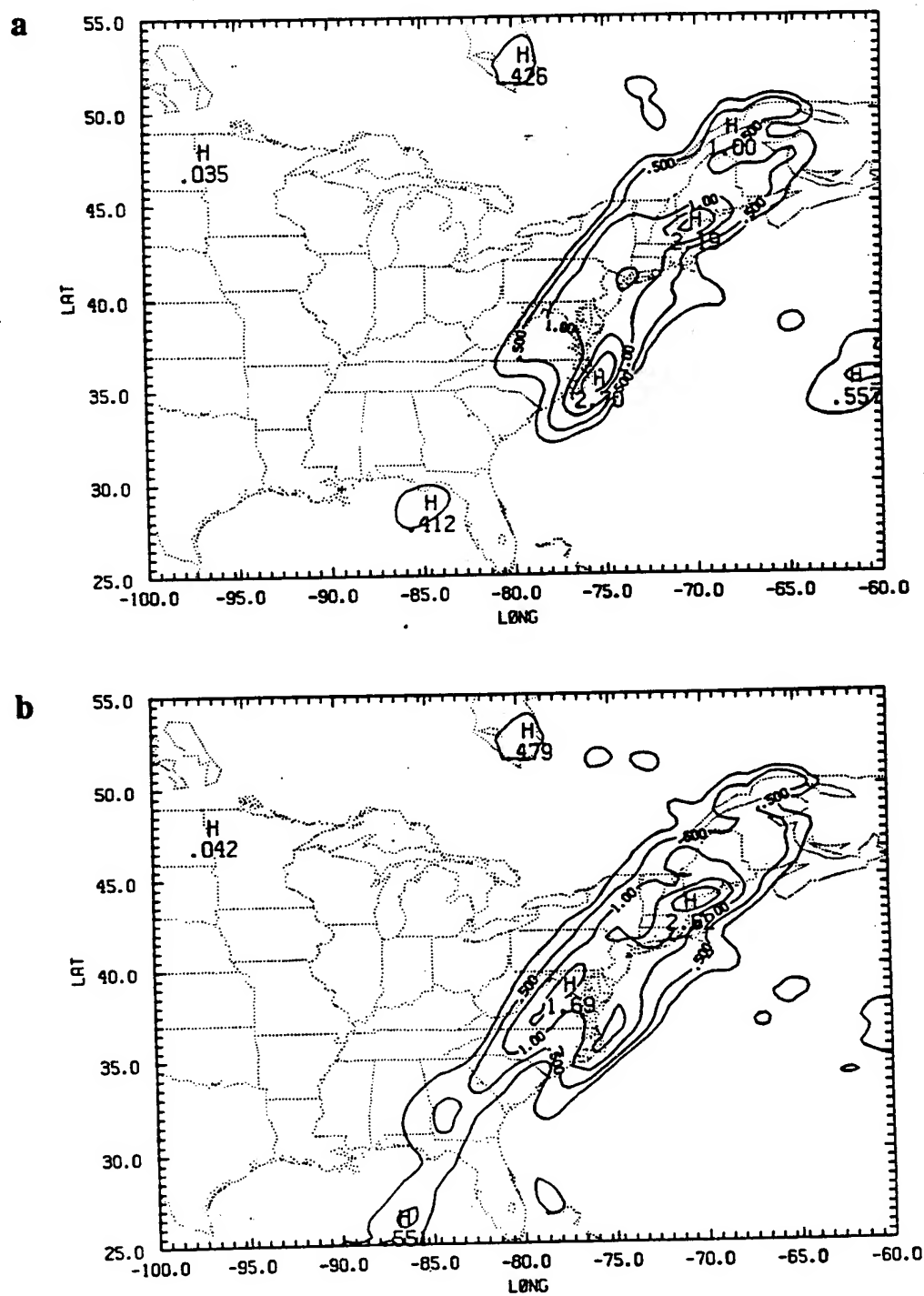


Figure 6.23. Forecasts of accumulated total precipitation in cm (26/06Z - 26/12Z) from (a) experiment 1 (no assimilation), (b) experiment 2 (12DI), and (c) experiment 3 (06DI). (d) Observed precipitation in cm (26/06Z - 26/12Z). Contours same as in Fig. 6.22.

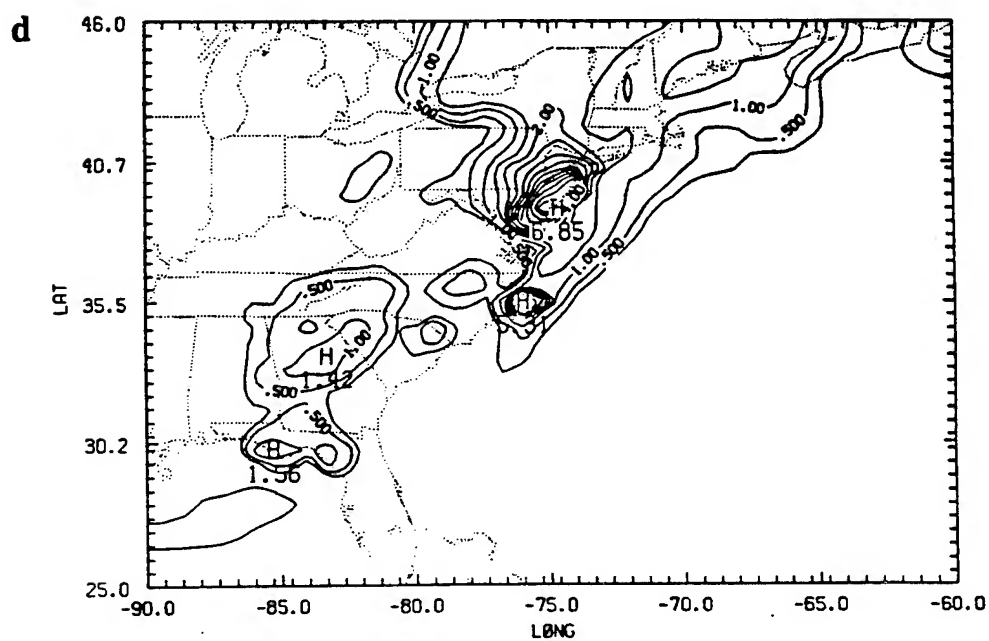
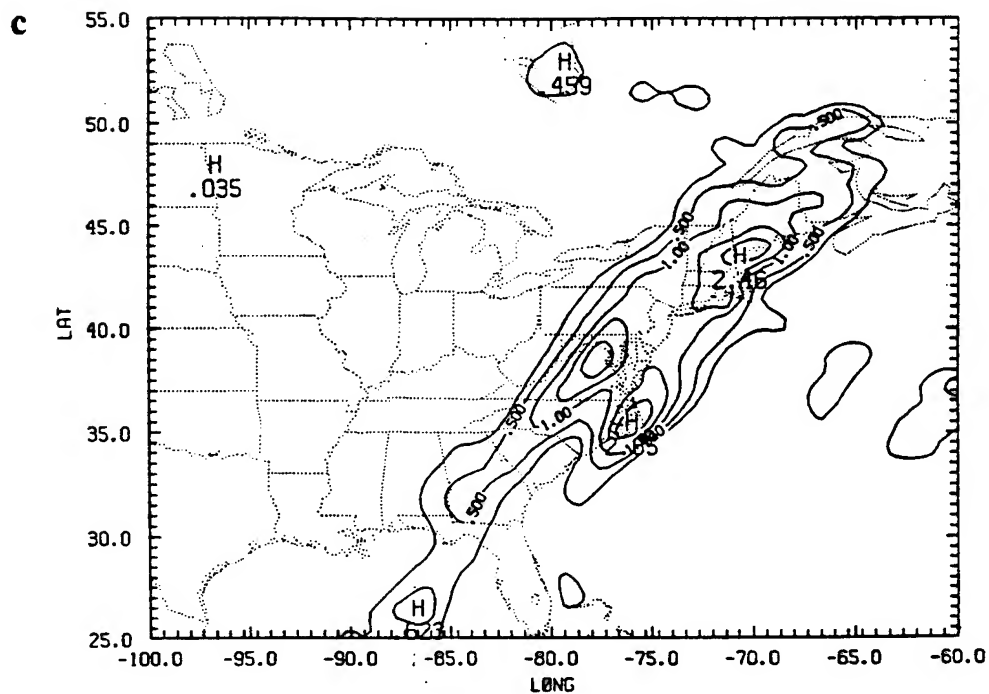


Figure 6.23. Continued.

06DI and 12DI are much better than that from the "no assimilation" case and verify reasonably well with the observed rainfall. However, the forecast from 12DI produced a maximum of only 1.5 cm near Cape Hatteras, whereas the 06DI forecast maximum was nearly 3 cm, a value much closer to the observed maximum of 5.31 cm. The rainfall forecast from experiment 5 (06AI) continued to be too weak on the southern extent of the precipitation area and the "no assimilation" case almost totally missed this feature. The forecasts from all the experiments completely missed the maximum of 6.85 cm in New Jersey as depicted in Fig. 6.23d. The horizontal resolution of even our fine-resolution mesoscale model is insufficient to resolve individual convective cells. The model's cumulus parameterization can not be expected to duplicate the observed precipitation maxima resulting from these sub-grid scale convective storms.

By 26/18Z the accumulated 6-h precipitation forecasts (Fig. 6.24) had become more similar with each extending the rainfall area across central Florida. However, the 06DI and 12DI forecasts did extent the precipitation area over most of North Carolina and South Carolina in agreement with the observed pattern, whereas the "no assimilation" forecast had moved all precipitation offshore for latitudes south of Virginia.

A second set of forecasts with an initiation time of 26/12Z were produced from experiments 1 - 4. Figure 6.25 depicts 6-h forecasts of sea-level pressure and 1000-mb temperature and wind fields; these forecasts, including the one from the "no assimilation" analysis, are very similar. Note similarities in temperature gradients along the east coast of U.S. and the locations of the coastal low defined by the center of the low pressure over southeast New York state. The coastal low is seen merging with a trough of low pressure to the northwest. The new cyclone center is forming near Cape Hatteras in the extended trough along the coast. The low-level moisture fields (not shown) are equally similar, particularly the sharp gradient associated with the frontal system along the east coast. The 6-h accumulated rainfall forecasts ending at 26/18Z originating from the

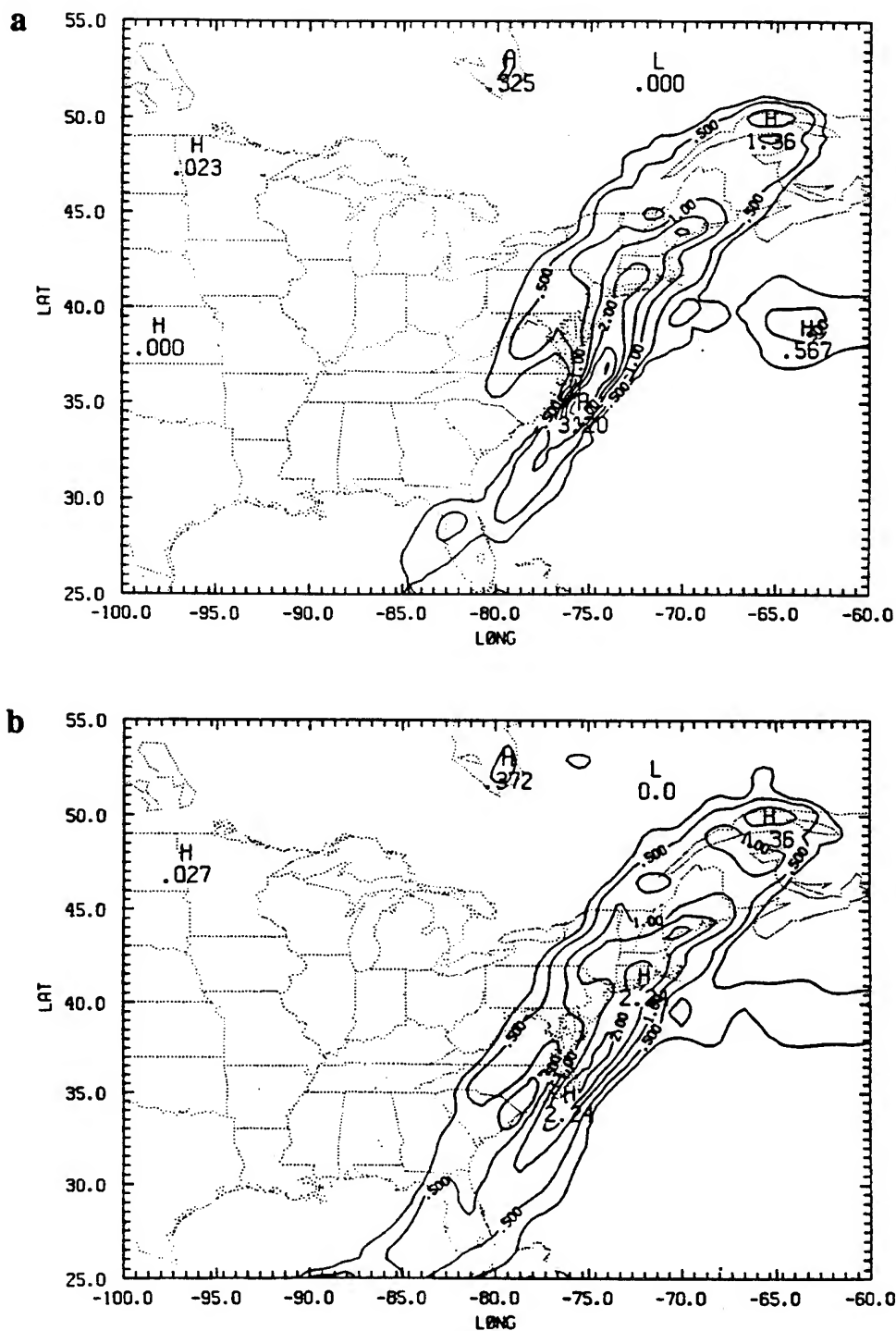
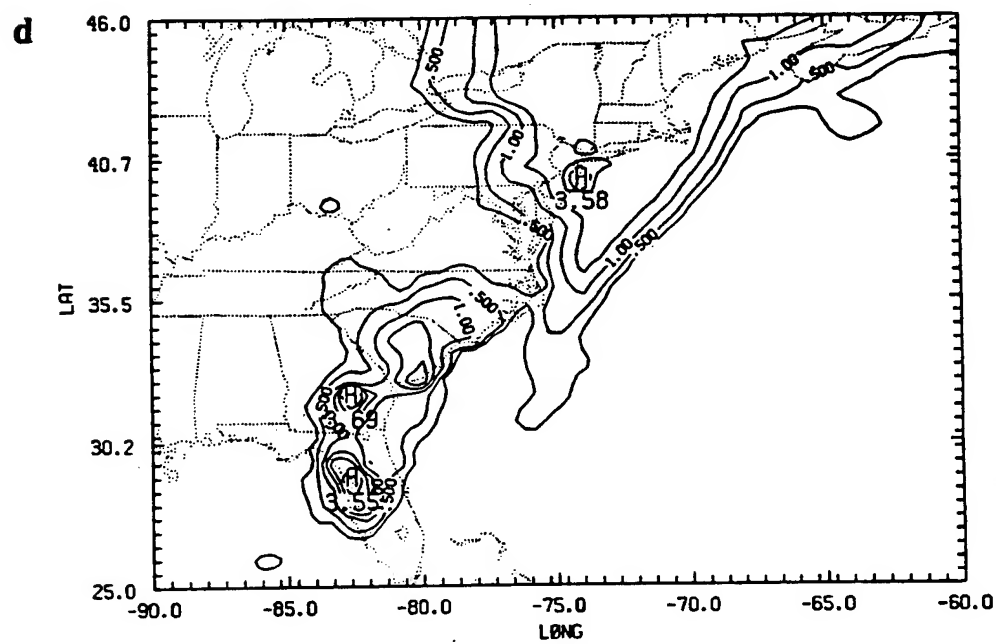
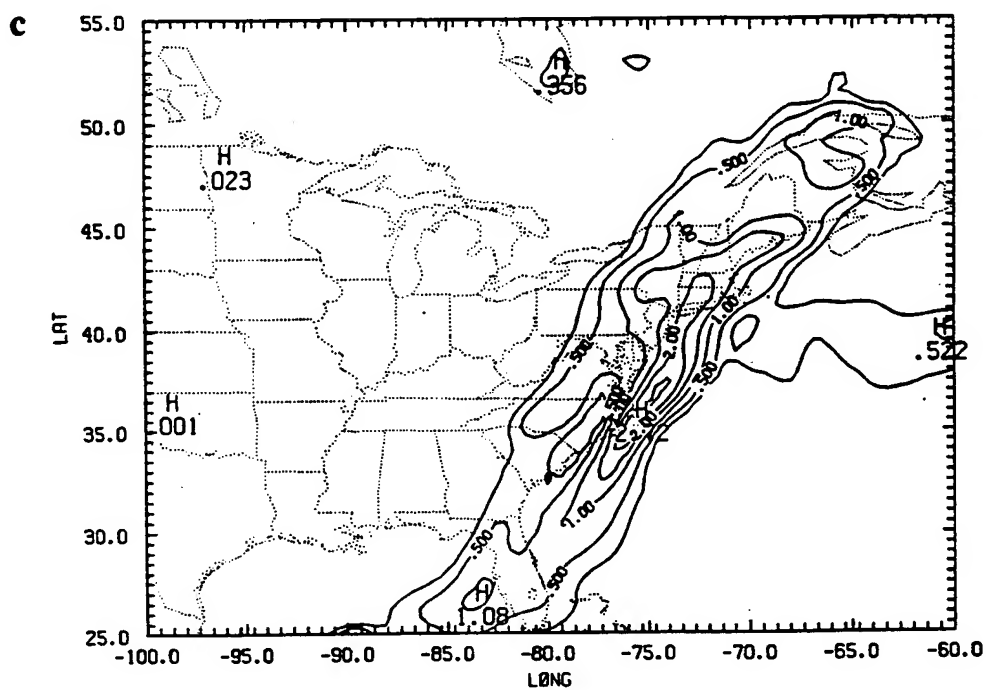


Figure 6.24. Forecasts of accumulated total precipitation in cm (26/12Z - 26/18Z) from (a) experiment 1 (no assimilation), (b) experiment 2 (12DI), and (c) experiment 3 (06DI). (d) Observed precipitation in cm (26/12Z - 26/18Z). Contours same as in Fig. 6.22.



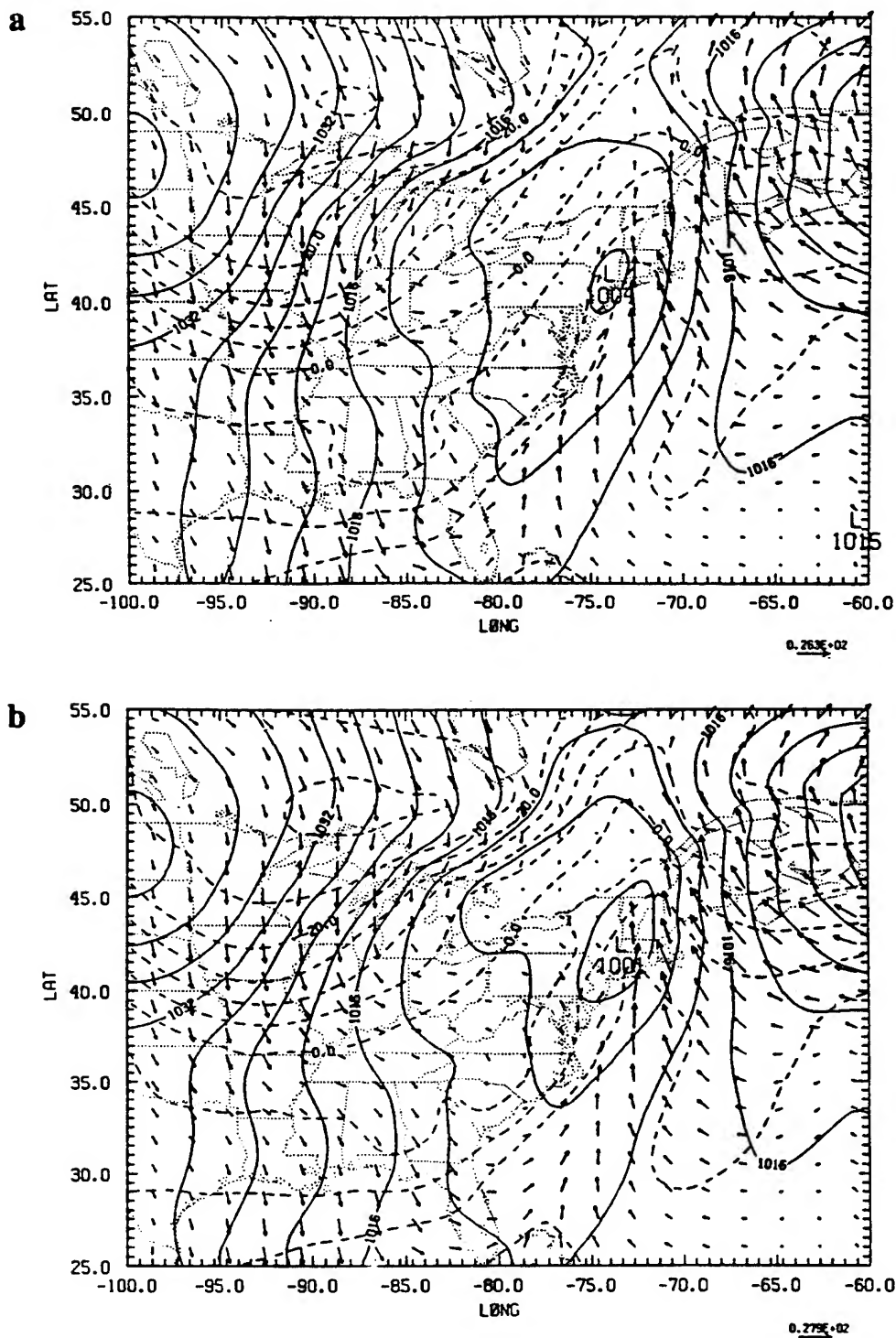


Figure 6.25. Six-hour forecasts of sea-level pressure (mb) and 1000-mb temperature (°C) and wind valid at 26/18Z from (a) experiment 1 (no assimilation), (b) experiment 2 (12DI), (c) experiment 3 (06DI), and (d) experiment 4 (03DI).

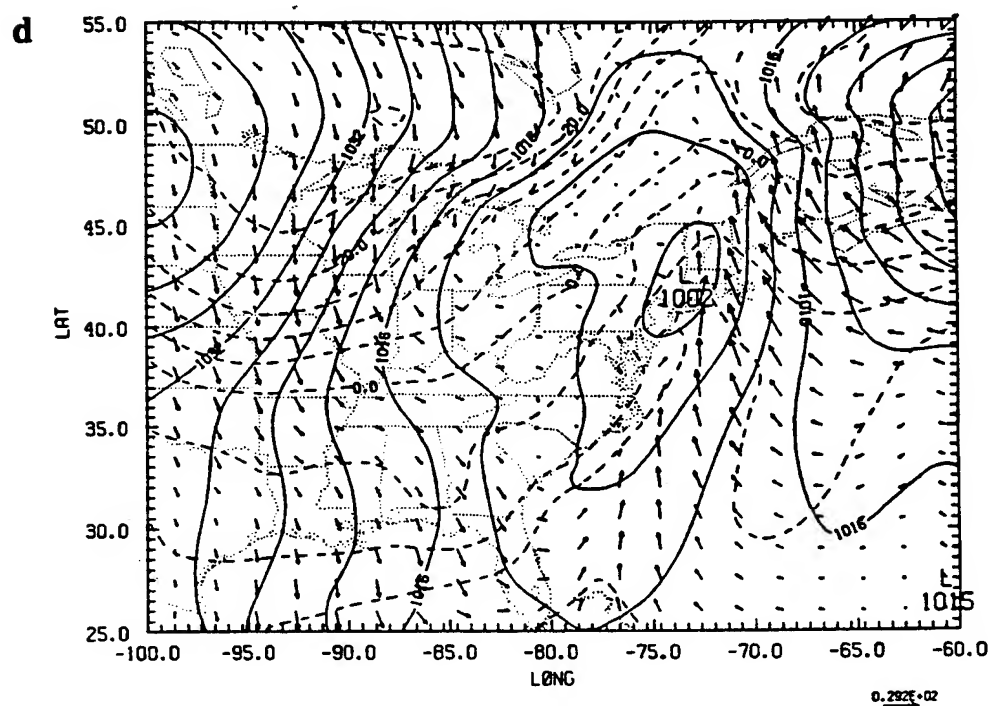
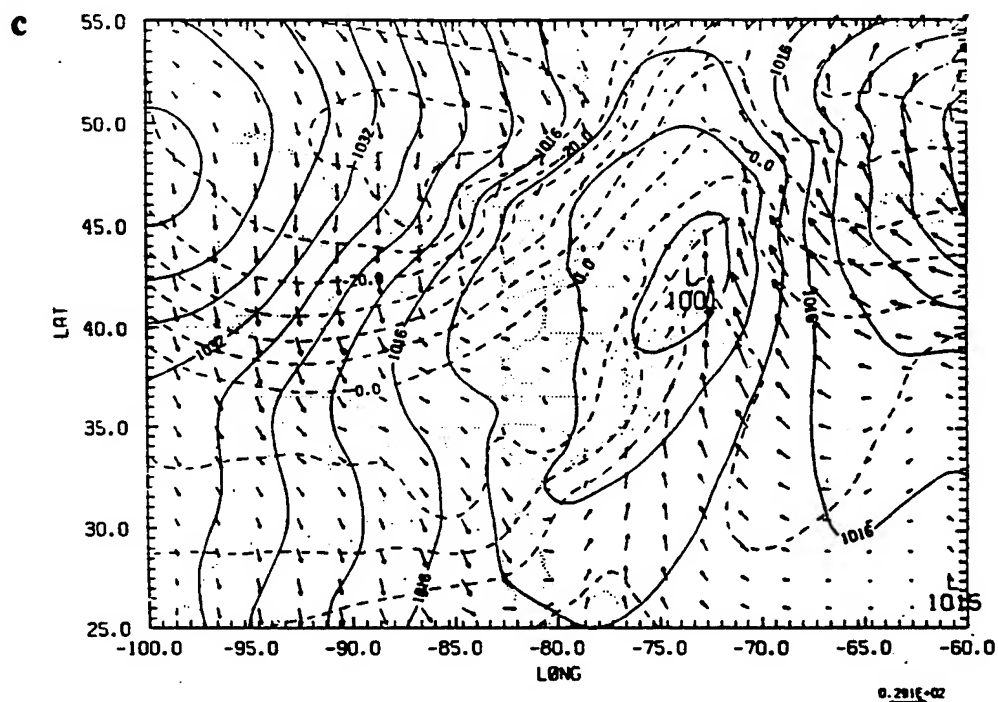


Figure 6.25. Continued.

assimilated fields are much better than the forecast originating from the "no assimilation" analysis, with the forecasts from the 3-h (03DI, not shown) and 6-h (06DI) cycle assimilations being the closest to and in good agreement with the observed rainfall pattern (Fig. 6.26). In other words, the assimilation process had an impact: there is a definite improvement over the "no assimilation" case, and the assimilation of asynoptic 3-hourly GALE data had at least a minor impact in the rainfall since the assimilations with the 3-h and 6-h cycles led to slightly better forecast precipitation fields than the case from the 12-h cycle assimilation.

During the remainder of the prediction period, the synoptic-scale circulation of this developing east coast cyclone was dominant and the forecast patterns from the different experiments were quite similar. The 12- and 24-h forecast precipitation fields from each case, including the "no assimilation" experiment, were similar and in reasonable agreement with the observed precipitation. By 27/00Z, a low pressure center appeared off the North Carolina coast and deepened rapidly as it moved along the coast (Fig. 6.27). In the 12-h forecasts (valid at 27/00Z) from the assimilated fields, the region of low pressure extends farther north and indicates two different northern centers (Fig. 6.27b), which compare more favorably with the assimilated analysis shown in Fig. 6.16a. The 24-h surface forecasts from the control and 03DI cases are shown in Figs. 6.27c and d. These forecasts are very similar, except that the center of the low has a better position in the assimilated case when compared with the analysis in Fig. 6.18b. It seems that the assimilation of the GALE data had less impact particularly in the precipitation during the latter part of the forecast period. The rainfall was being forced primarily by the large synoptic-scale circulation of the developing east coast cyclone, enabling the control forecast to produce adequate results. However, the 12- and 24-h surface pressure forecasts, with the assimilation of the GALE data, show more

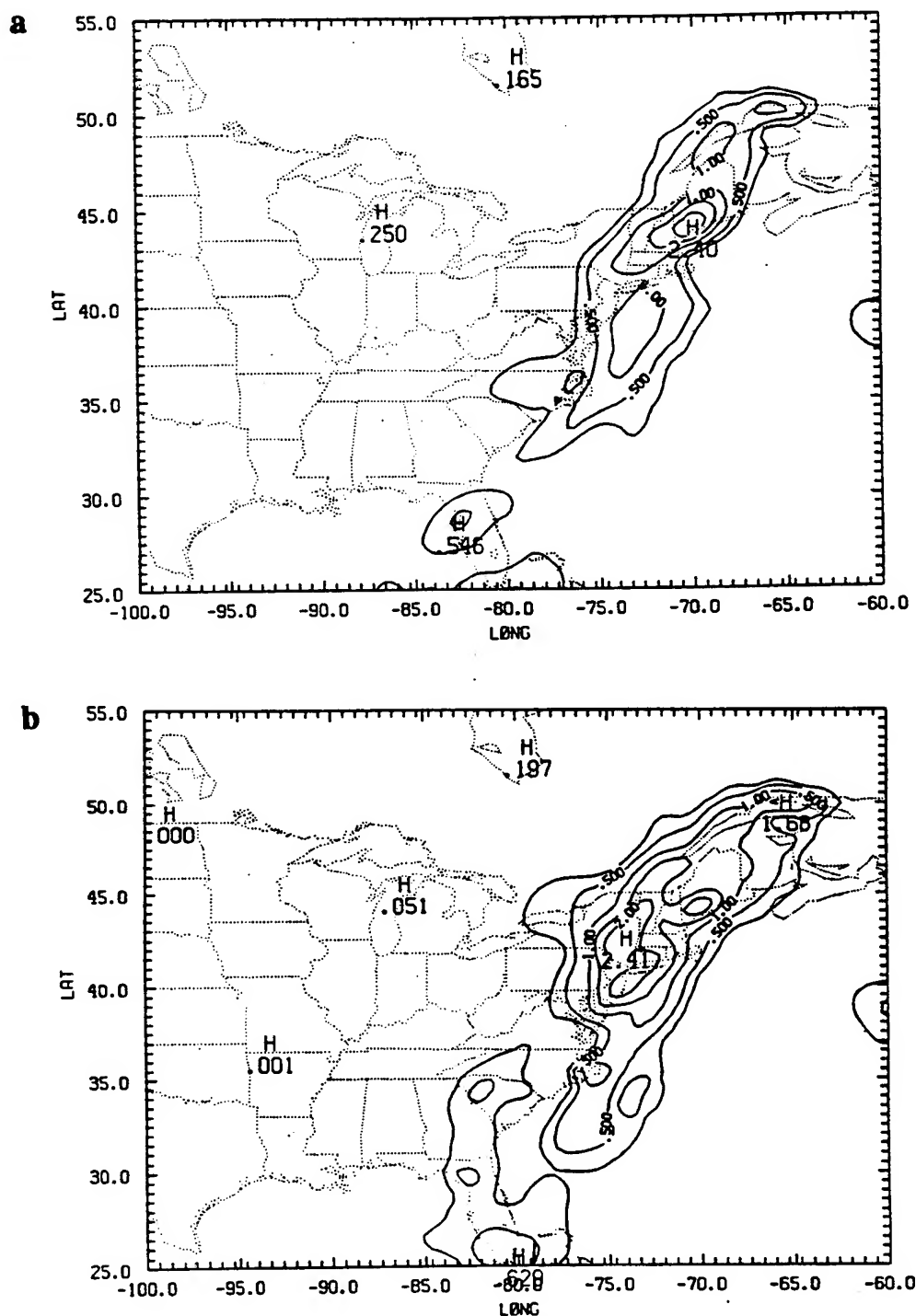


Figure 6.26. Forecasts of accumulated total precipitation in cm (26/12Z - 26/18Z) from (a) experiment 1 (no assimilation), (b) experiment 2 (12DI), and (c) experiment 3 (06DI), with forecast start time of 26/12Z. (d) Observed precipitation in cm (26/12Z - 26/18Z). Contours same as in Fig. 6.22.

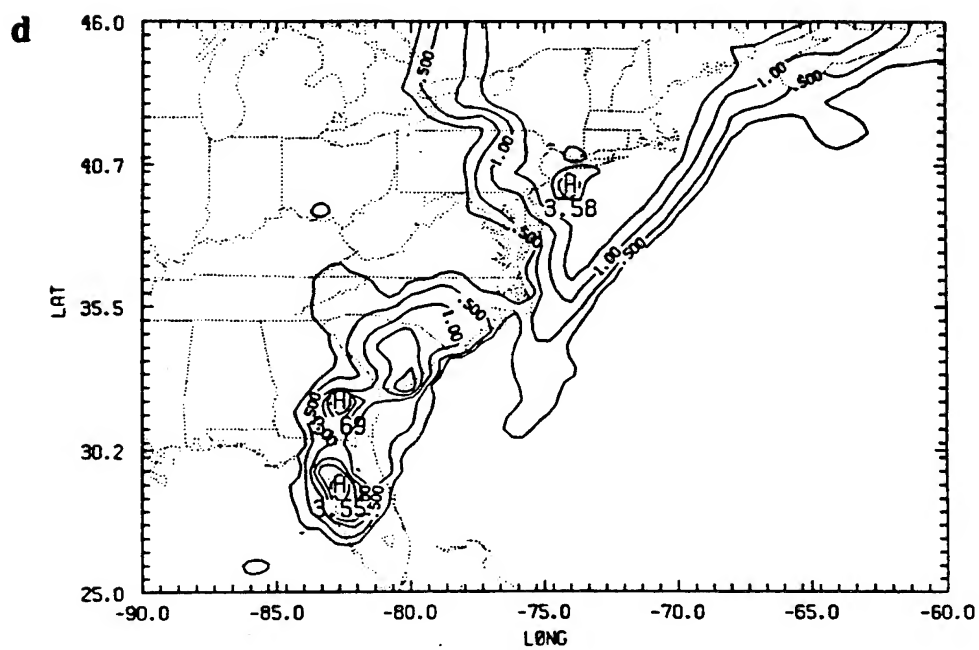
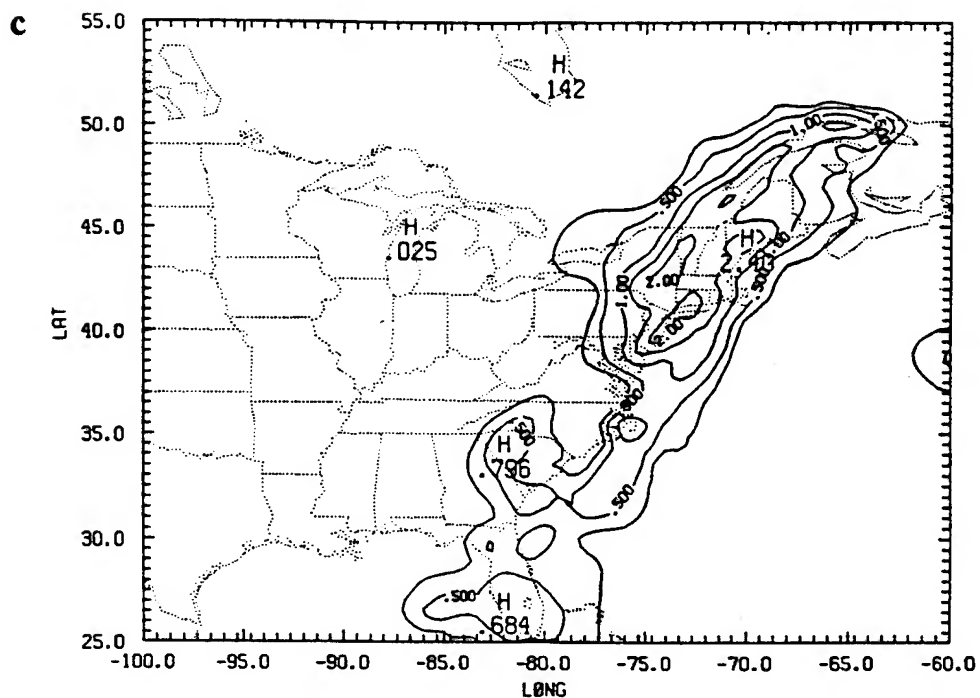


Figure 6.26. Continued.

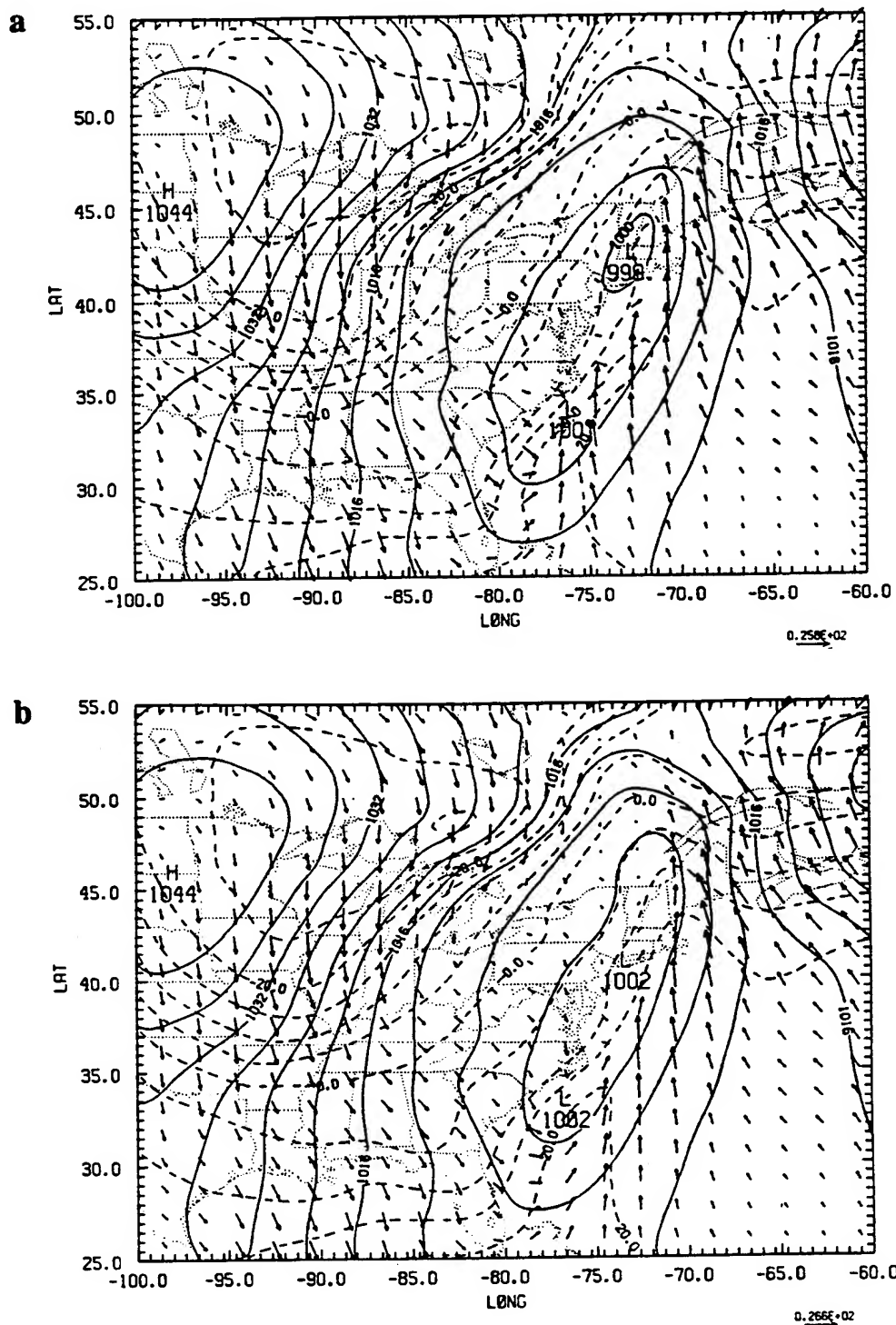


Figure 6.27. 12-h forecasts of sea-level pressure (mb) and 1000-mb temperature (°C) and wind valid at 27/00Z from (a) experiment 1 (no assimilation) and (b) experiment 4 (03DI), and 24-h forecasts valid at 27/12Z from (c) experiment 1 (no assimilation) and (d) experiment 4 (03DI).

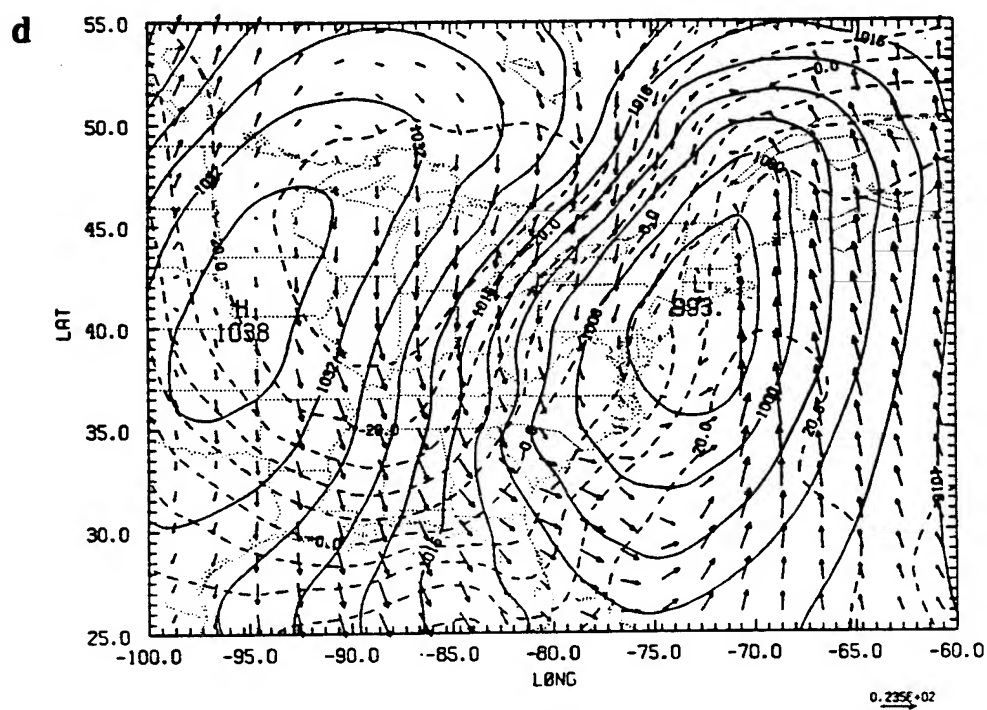
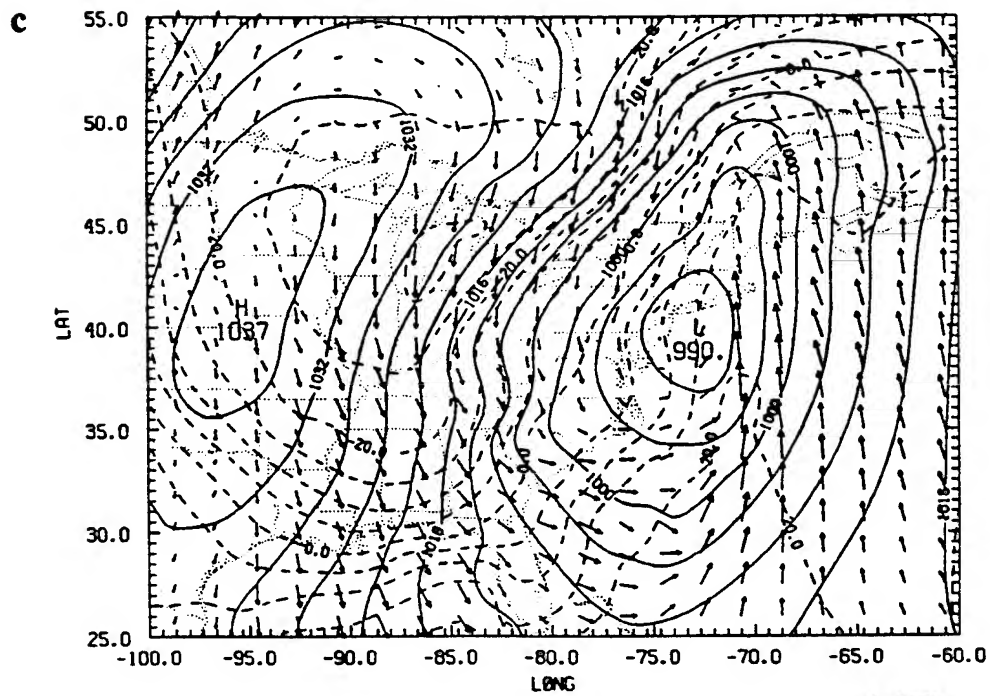


Figure 6.27. Continued.

consistency with the assimilated analyses than the control forecasts do with the NMC analyses.

7. CONCLUSIONS

Four-dimensional data-assimilation methodology has been applied to high-frequency observational data using a multivariate, successive correction objective analysis scheme, a diabatic vertical mode initialization procedure, and a fine-resolution mesoscale numerical weather prediction model. With only a limited number of iterations, the NRL/NCSU objective analysis scheme, based on Bratseth weighting functions, converges to the optimal interpolation solution. This scheme produces accurate analysis fields by using wind information to achieve gradients of geopotential through the geostrophic relationship. It is also successful in correcting the phase of the first-guess temperature field, improving the second-order fields of absolute vorticity and vertical motion, strengthening the first-guess upper-level jet, and resolving mesoscale circulations.

When diabatic vertical mode initialization is performed on these analysis fields, model spinup is reduced. With the inclusion of diabatic heating, which forces convective precipitation, the VMI retains the divergence, and therefore vertical motion, associated with the convection. This diabatic initialization procedure is used to initialize the background forecasts at each cycle of the assimilation process. Observed rainfall, coupled with "spunup" model rainfall, is used to derive three-dimensional heating fields. The method ensures temporal consistency of the diabatic heating rates by using rainfall rates which are time-centered (-3H to +3H) on the analysis/initialization valid time. This procedure also ensures that the heating rates in the initial integration of the subsequent assimilated background forecast are representative of the "observed" heating.

The performance of the assimilation system was evaluated by means of data-fitting statistics and subjective comparisons of assimilated states and subsequent forecasts. The

assimilated background forecast rms error for all analysis variables decreased significantly as the length of the update cycle shortened, i.e. as additional asynoptic, high-density GALE data were assimilated. The same was true for the analysis error of geopotential. This decrease in background and analysis error clearly shows that the inclusion of the 3-hourly GALE data had a positive impact on the assimilation. The analysis errors of the wind components and relative humidity varied little between the different experiments, due most likely to relatively large observational error in the wind and humidity. The background and analysis rms errors changed little when diabatic heating was included in the vertical mode initialization, suggesting that the inclusion or exclusion has minimal impact on the assimilation of these first-order variables. The assimilation with a 3-h update cycle revealed that the background forecast error generally increases as the period from the previous synoptic update to the current analysis/forecast cycle increases. With only small insertions of data at the asynoptic cycles (as compared to complete datasets at the synoptic hours), the effectual background forecast duration of successive update cycles increases between synoptic updates for geopotential.

A subjective evaluation of the assimilation system was conducted by comparing surface and 500-mb analyses and forecast fields. The analyses and subsequent forecasts from each of the assimilation experiments were consistently better than the "no assimilation" analyses (NMC analyses) and subsequent forecasts. A temporal consistency was achieved between the assimilated analyses and forecasts, which was not achieved without assimilation. Stronger thermal and moisture gradients and vertical motions were evident at the coastal front in the assimilated fields. There was less difference between the various assimilations which included the diabatic VMI. The surface analyses of pressure, wind, and temperature and vertical motion fields were generally very similar. However, the 03DI and 06DI lower- and upper-level moisture analyses showed some improvement over the 12DI analyses. Here, the inclusion of the

3-hourly GALE data made a positive impact on the moisture analyses. Excluding diabatic heating from the VMI (06AI) led to no noticeable detriment in the analyses of first order variables, but did result in weaker vertical velocities associated with the mesoscale circulation of the coastal front and upper-level jet streaks. This result is reasonable since vertical motion is directly related to diabatic heating.

A subjective verification of forecast 6-h accumulated precipitation was conducted. Precipitation verification is a valuable measure of the forecast "goodness" since rainfall is dependent on many complex physical processes; as a result, it is much more difficult to predict accurately than the other modelled variables. The forecast originating from the assimilated states verified reasonably well with the observed rainfall and were much better than the "no assimilation" forecasts, showing much faster spinup of forecast precipitation than did the control case. The assimilations with shorter update cycles (included asynoptic GALE data) led to slightly improved precipitation forecast as compared to the 12DI forecasts.

The results of this study show that the assimilation of GALE data in a mesoscale model is successful in producing significantly improved analyses and subsequent forecasts which are more consistent in time. The results also indicate that a small area of higher temporal data resolution can, when assimilated with high-resolution mesoscale prediction model, lead to improved assimilated states and better forecasts. However, the impact of the GALE data on the forecasts was generally greater when mesoscale circulations were important, such as in the interaction of the coastal front and the upper-level jet during the period prior to rapid cyclogenesis. When the large-scale synoptic system became dominant, the 3-hourly data had less impact in the subsequent forecasts.

In the present study, only diabatic heating associated with convective precipitation is considered. Future work should include the investigation of latent heating resulting from large-scale, non-convective rainfall. Also, forecast precipitation totals in areas of

strong convection were sometimes far from the observed amounts even when the 3-hourly GALE data were assimilated. The extremely small scale of the convective activity precluded our model from resolving these features. Work has begun to increase the model's horizontal and vertical resolutions and to include vertical accelerations. That is, the NRL/NCSU model will be converted to a 16-layer, non-hydrostatic model with horizontal grid spacing on the order of 5 to 10 km. Significant improvement in rainfall forecasts should result.

8. LIST OF REFERENCES

- Alaka, M. A., and R. C. Elvander, 1972: Optimum interpolation from observations of mixed quality. *Mon. Wea. Rev.*, **100**, 612-624.
- Andersen, J. H., 1977: A routine for normal mode initialization with non-linear correction for a multi-level spectral model with triangular truncation. ECMWF Internal Report No. 15, European Centre for Medium Range Weather Forecasts, Bracknell, U. K., 41 pp.
- Anthes, R. A., 1974: Data assimilation and initialization of hurricane prediction models. *J. Atmos. Sci.*, **31**, 702-719.
- , 1977: A cumulus parameterization scheme utilizing a one-dimensional cloud model. *Mon. Wea. Rev.*, **105**, 270-286.
- Arakawa, A., and V. R. Lamb, 1977: Computational design of the basic dynamical processes of the UCLA general circulation model. *Methods in Computational Physics*, Vol 17, General Circulation Models of the Atmosphere, J. Chang, Ed., Academic Press, New York, 173-265.
- Arkin, P. A., 1983: A diagnostic precipitation index from infrared satellite imagery. *Tropical Ocean - Atmosphere Newsletter*, **17**, 5-7. (Available from JISAO, U. of Washington, AK-40, Seattle, WA 98105).
- Baer, F., 1977: Adjustments of initial conditions required to suppress gravity oscillations in non-linear flows. *Beitr. Phys. Atmos.*, **50**, 350-366.
- Barnes, S.L., 1973: Mesoscale objective map analysis using weighted time- series observations. NOAA Technical Memorandum, ERL NSSL-62, Norman, OK, 60 pp.
- Bell, R. S., 1986: The Meteorological Office fine-mesh data assimilation scheme. *Meteor. Mag.*, **115**, 161-177.
- Belousov, S. L., L. S. Gandin, and S. A. Mashkovich, 1968: Computer processing of current meteorological data. *Hydrometeoizdat* [Meteor. Trans. No. 18, 1972. Canada Dept. of the Environment, Atmospheric Environment Service, Downsview, Ontario], 227 pp. (in Russian).
- Bengtsson, L., 1975a: Four-dimensional data assimilation of meteorological observations. GARP Publ. Ser., No. 15, WMO/ICSU, Geneva, 76 pp.
- , 1975b: Problems in four-dimensional data assimilation. *Seminars of Scientific Foundation of Medium Range Weather Forecasts, Part I*, Reading, September 1975, 113-138.

- , 1981: Current problems in four-dimensional data assimilation. *Data Assimilation Methods. ECMWF Seminar 1980*, 195-217. (Available from the European Centre for Medium Range Weather Forecasts, Shinfield Park, Reading RG29AX, England.)
- , 1985: Medium range forecasting at the ECMWF. *Adv. Geophys.*, **28B**, 3-56.
- , and J. Shukla, 1988: Integration of space and in situ observations to study global climate change. *Bull. Amer. Meteor. Soc.*, **69**, 1130-1143.
- Benjamin, S.G., 1989: An isentropic meso-scale analysis system and its sensitivity to aircraft and surface observations. *Mon. Wea. Rev.*, **117**, 1586-1603.
- , and N.L. Seaman, 1985: A simple scheme for objective analysis in curved flow. *Mon. Wea. Rev.*, **113**, 1184-1198.
- Bergthorsson, P., and B. R. Döös, 1955: Numerical weather map analysis. *Tellus*, **7**, 329-340.
- Bosart, L. F., 1988: Coastal frontogenesis and cyclogenesis during GALE IOP #2. Preliminary Reports, GALE/CASP Workshop, November 2-6 1987, Virginia Beach, VA, 75-93 (available from GALE Project Office, PO Box 3000, Boulder CO 80807).
- Bourke, W., and J. L. McGregor, 1983: A nonlinear vertical mode initialization scheme for a limited area prediction model. *Mon. Wea. Rev.*, **111**, 2285-2297.
- , R. Seaman, and K. Puri, 1985: Data assimilation. *Adv. Geophys.*, **28B**, 124-149.
- Bratseth, A. M., 1982: A simple and efficient approach to the initialization of weather prediction models. *Tellus*, **34**, 352-357.
- , 1986: Statistical interpolation by means of successive corrections. *Tellus*, **38A**, 439-447.
- Chang, S. W., 1981: Test of a planetary boundary-layer parameterization based on a generalized similarity theory in tropical cyclone models. *Mon. Wea. Rev.*, **109**, 843-853.
- , K. Brehme, R. Madala, and K. Sashegyi, 1989: A numerical study of the East Coast snow storm of February 10-12, 1983. *Mon. Wea. Rev.*, **117**, 1768-1778.
- Charney, J., M. Halem, and R. Jastrow, 1969: Use of incomplete historical data to infer the present state of the atmosphere. *J. Atmos. Sci.*, **26**, 1160-1163.
- Cressman, G., 1959: An operational objective analysis system. *Mon. Wea. Rev.*, **87**, 367-374.

- Daley, R., 1979: The application of non-linear normal mode initialization to an operational forecast model. *Atmos. Ocean*, **17**, 97-124.
- , 1981: Predictability experiments with a baroclinic model. *Atmos. Ocean*, **19**, 77-109.
- , 1991: *Atmospheric Data Analysis*. Cambridge University Press, Cambridge, 457 pp.
- , and K. Puri, 1980: Four dimensional data assimilation and the slow manifold. *Mon. Wea. Rev.*, **108**, 85-99.
- Davies, H. C., 1976: A lateral boundary formulation for multi-level prediction models. *Quart. J. Roy. Meteor. Soc.*, **102**, 405-418.
- , 1983: Limitations of some common lateral boundary schemes used in regional NWP models. *Mon. Wea. Mon.*, **111**, 1002-1012.
- , and R. E. Turner, 1977: Updating prediction models by dynamical relaxation: An examination of the technique. *Quart. J. Roy. Meteor. Soc.*, **103**, 225-245.
- Dickinson, R. E., and D. L. Williamson, 1972: Free oscillations of a discrete stratified fluid with application to numerical weather prediction. *J. Atmos. Sci.*, **29**, 623-640.
- DiMego, G. J., 1988: The National Meteorological Center regional analysis system. *Mon. Wea. Rev.*, **116**, 977-1000.
- , J. P. Gerrity, R. A. Petersen, and E. Rogers, 1989: Intermittent assimilation of emulated wind profiler data with the NMC Regional Data Assimilation System (RDAS). Preprints, 12th Conference on Weather Analysis and Forecasting, Amer. Meteor. Soc., Monterey, CA, October 2-6, 1989.
- Dirks, R. A., J. P. Kuettner, and J. A. Moore, 1988: Genesis of Atlantic Lows Experiment (GALE): An overview. *Bull. Amer. Meteor. Soc.*, **69**, 148-160.
- Dixon, R., 1976: An objective analysis system using orthogonal polynomials. GARP WGNE Report No. 11, 73-85. [Available from WMO, Geneva].
- , E. Spackman, I. Jones, and A. Francis, 1972: The global analysis of meteorological data using orthogonal polynomial base functions. *J. Atmos. Sci.*, **29**, 609-622.
- Donner, L. J., 1988: An initialization for cumulus convection in numerical weather prediction models. *Mon. Wea. Rev.*, **116**, 377-385.
- Doyle, J. D., and T. T. Warner, 1990: Mesoscale coastal processes during GALE IOP 2. *Mon. Wea. Rev.*, **118**, 283-308.
- Eddy, A., 1973: The objective analysis of atmospheric structure. *J. Meteor. Soc. Jpn.*, **51**, 450-457.

- Eliassen, A., 1954: Provisional report on calculation of spatial covariance and autocorrelation of the pressure field. Rept. No. 5, Institute of Weather and Climate Res., Academy of Science Oslo, 11 pp., (reprinted in *Dynamic Meteorology: Data Assimilation Methods*, L. Bengtsson, M. Ghil, and E. Kallen, Eds., Springer-Verlag, New York, 319-330).
- Errico, R. M., and P. J. Rasch, 1988: A comparison of various normal-mode initialization schemes and the inclusion of diabatic processes. *Tellus*, 40A, 1-25.
- Flattery, T., 1971: Spectral models for global analysis and forecasting. *Proc. Sixth AWS Technical Exchange Conf.*, Air Weather Service Technical Report No. 242, 42-54.
- Gandin, L. S., 1963: Objective analysis of meteorological fields. *Hydrometeoizdat* (in Russian), English translation by Israel Program for Scientific Translations, Jerusalem, 1965, 242 pp. [Available from NTIS, as N66-18047].
- , 1988: Complex quality control of meteorological observations. *Mon. Wea. Rev.*, 116, 1137-1156.
- Ghil, M., 1989: Meteorological data assimilation for oceanographers, Part I: Description and theoretical framework. *Dyn. of Atmos. and Oceans*, 13, 171-218.
- , S. Cohn, J. Tavantzis, K. Bube, and E. Issacson, 1981: Applications of estimation theory to numerical weather prediction. *Dynamic Meteorology: Data Assimilation Methods*, L. Bengtsson, M. Ghil, and E. Kallen, Eds., Springer-Verlag, New York, 139-224.
- , M. Halem, and R. Atlas, 1979: Time-continuous assimilation of remote-sounding data and its effect on weather forecasting. *Mon. Wea. Rev.*, 107, 140-171.
- Gilchrist, B., and G. P. Cressman, 1954: An experiment in objective analysis. *Tellus*, 6, 97-101.
- Girard, C., and M. Jarraud, 1982: Short and medium range forecast differences between a spectral and grid point model: An extensive quasi-operational comparison. Tech. Rep. No. 32, European Centre for Medium Range Weather Forecasts, 176 pp. (Available from ECMWF, Shinfield Park, Reading, England).
- Gronas, S., A. Foss, and M. Lystad, 1987: Numerical simulations of polar lows in the Norwegian Sea. *Tellus*, 39A, 334-353.
- , and K. H. Midtbo, 1986: Operational multivariate analyses by successive corrections. Collection of papers presented at WMO/IUGG numerical weather prediction symposium, Tokyo, 4-8 August 1986. *J. Meteor. Soc. Jpn.*, 61-74.
- Gustavsson, N., 1981: A review of methods for objective analysis. *Dynamic Meteorology: Data Assimilation Methods*, L. Bengtsson, M. Ghil, and E. Kallen, Eds., Springer-Verlag, New York, 17-76.

- Haltiner, G. J., and R. T. Williams, 1980: *Numerical Prediction and Dynamic Meteorology*. Second ed., John Wiley and Sons, New York, 477 pp.
- Harms, D. E., R. V. Madala, S. Raman, and K. D. Sashegyi, 1992a: Diabatic initialization experiments with convective heating. Submitted to *Meteor. and Atmos. Phys.*
- , S. Raman, and R. V. Madala, 1992b: An examination of four-dimensional data-assimilation techniques for numerical weather prediction. *Bull. Amer. Meteor. Soc.*, **73**, 425-440.
- , K. D. Sashegyi, R. V. Madala, and S. Raman, 1992c: Impact of assimilating 3-hourly GALE data using a mesoscale weather prediction model. Submitted to *Mon. Wea. Rev.*
- Hayden, C. M., 1976: Satellite reference level experiments with VTRR and the NMC global spectral analyses. GARP WGNE Report No. 11, 57-72. [Available from WMO, Geneva].
- Heckley, W. A., 1985: Systematic errors of the ECMWF operational forecasting model in tropical regions. *Quart. J. Roy. Meteor. Soc.*, **111**, 709-738.
- Hoke, J. E., and R. A. Anthes, 1976: The initialization of numerical models by a dynamical initialization technique. *Mon. Wea. Rev.*, **104**, 1551-1556.
- , and -----, 1977: Dynamic initialization of a three-dimensional primitive-equation model of Hurricane Alma of 1962. *Mon. Wea. Rev.*, **105**, 1266-1280.
- , N. A. Phillips, G. J. DiMego, J. J. Tuccillo, and J. G. Sela, 1989: The Regional Analysis and Forecast System of the National Meteorological Center. *Weather and Forecasting*, **4**, 323-334.
- Hollingsworth, A., 1986: Objective analysis for numerical weather prediction. *Short and Medium-Range Weather Prediction, Proc. WMO/IUGG NWP Symposium*, Tokyo, 11-59.
- , and P. Lonnberg, 1986: The statistical structure of short-range forecast errors as determined from radiosonde data. Part I: The wind field. *Tellus*, **38A**, 111-136.
- Holt, T., S. Chang, and S. Raman, 1990: A numerical study of the coastal cyclogenesis in GALE IOP 2: Sensitivity to PBL parameterizations. *Mon. Wea. Rev.*, **118**, 234-257.
- Jastrow, R., and M. Halem, 1970: Simulation studies related to GARP. *Bull. Amer. Meteor. Soc.*, **51**, 490-513.
- Juvanon du Vachat, R., 1986: A general formulation of normal modes for limited-area models: Application to initialization. *Mon. Wea. Rev.*, **114**, 2478-2487.
- Kalman, R. E., 1960: A new approach to linear filtering and prediction problems. *Trans. ASME, J. Basic Eng.*, **82D**, 35-45.

- , and R. S. Bucy, 1961: New results in linear filtering and prediction theory. *Trans. ASME, J. Basic Eng.*, **83D**, 95-108.
- Kanamitsu, M., 1989: Description of the NMC global data assimilation and forecast system. *Weather and Forecasting*, **4**, 335-342.
- Kao, C.-Y. J., and T. Yamada, 1988: Use of the CAPTEX data for evaluations of a long-range transport numerical model with a four-dimensional data assimilation technique. *Mon. Wea. Rev.*, **116**, 293-306.
- Kasahara, A., R. C. Balgovind, and B. B. Katz, 1988: Use of satellite radiometric imagery data for improvement in the analysis of divergent wind in the tropics. *Mon. Wea. Rev.*, **116**, 866-883.
- Kistler, R. E., 1974: A study of data assimilation techniques in an autobarotropic primitive equation channel model. M. S. thesis, The Pennsylvania State University, 84 pp.
- , and R. D. McPherson, 1975: On the use of a local wind correction technique in four-dimensional data assimilation. *Mon. Wea. Rev.*, **103**, 445-449.
- Kitade, T., 1983: Nonlinear normal mode initialization with physics. *Mon. Wea. Rev.*, **111**, 2194-2213.
- Koch, S. E., M. DesJardins, and P. J. Kocin, 1983: An interactive Barnes objective map analysis scheme for use with satellite and conventional data. *J. Clim. Appl. Meteor.*, **22**, 1487-1503.
- Kreiss, H.-O., 1979: Problems with different time scales for ordinary differential equations. *SIAM J. Num. Anal.*, **16**, 980-998.
- Krishnamurti, T. N., H. S. Bedi, W. Heckley, and K. Ingles, 1988: Reduction of the spinup time for evaporation and precipitation in a spectral model. *Mon. Wea. Rev.*, **116**, 907-920.
- Kuo, H.-L., 1974: Further studies of the influence of cumulus convection on large-scale flow. *J. Atmos. Sci.*, **31**, 1232-1240.
- Kuo, Y.-H., and Y.-R. Guo, 1989: Dynamic initialization using observations from a network of profilers. *Mon. Wea. Rev.*, **117**, 1975-1998.
- Lange, A., and E. Hellsten, 1986: Results of the WMO/CAS NWP data study and intercomparison project for forecasts for the Northern Hemisphere in 1981-82. WMO Short- and Medium-Range Weather Prediction Research, Publication Series No. 2, WMO, Geneva.
- Lejenas, H., 1980: On the influence of the technique of nonlinear normal mode initialization on the nonconvective precipitation rate. *Mon. Wea. Rev.*, **108**, 1465-1468.

- Lewis, J. M., 1972: An operational upper air analysis using the variational method. *Tellus*, **24**, 514-530.
- , and J. C. Derber, 1985: The use of adjoint equations to solve a variational adjustment problem with advective constraints. *Tellus*, **37A**, 309-322.
- Lorenc, A., 1981: A global three-dimensional multivariate statistical interpolation scheme. *Mon. Wea. Rev.*, **109**, 701-721.
- , 1985: Analysis methods for the quality control of observations. *Workshop on the Use and Quality Control of Meteorological Observations*, Reading, U. K., European Centre for Medium Range Weather Forecasts, 397-428.
- , 1986: Analysis methods for numerical weather prediction. *Quart. J. Roy. Meteor. Soc.*, **112**, 1177-1194.
- , 1988: A practical approximation to optimal four-dimensional objective analysis. *Mon. Wea. Rev.*, **116**, 730-745.
- , R. S. Bell, and B. MacPherson, 1991: The Meteorological Office analysis correction data assimilation scheme. *Quart. J. Roy. Meteor. Soc.*, **117**, 59-89.
- , and O. Hammon, 1988: Objective quality control of observations using Bayesian methods. Theory and a practical implementation. *Quart. J. Roy. Meteor. Soc.*, **114**, 515-543.
- , I. Rutherford, and G. Larsen, 1977: The ECMWF analysis and data assimilation scheme--Analysis of mass and wind fields. European Centre for Medium-Range Weather Forecasts, Reading, Berkshire, U. K., Tech. Rep. No. 6.
- Lorenz, E. N., 1982: Atmospheric predictability experiments with a large numerical model. *Tellus*, **34**, 505-513.
- Lynch, P., 1985a: Initialization using Laplace transforms. *Quart. J. Roy. Meteor. Soc.*, **111**, 243-258.
- , 1985b: Initialization of a barotropic limited-area model using the Laplace transform technique. *Mon. Wea. Rev.*, **113**, 1338-1344.
- , 1991: Filtering integration schemes based on the Laplace and Z- transforms. *Mon. Wea. Rev.*, **119**, 653-666.
- Lyne, W. H., R. Swinbank, and N. T. Birch, 1982: A data assimilation experiment and the global circulation during the FGGE special observing periods. *Quart. J. Roy. Meteor. Soc.*, **108**, 575-594.
- Machenhauer, B., 1977: On the dynamics of gravity oscillations in a shallow water model with applications to normal mode initialization. *Beitr. Phys. Atmos.*, **50**, 253-271.

- Madala, R. V., 1981: Efficient time integration schemes for atmosphere and ocean models. *Finite Difference Techniques for Vectorized Fluid Dynamic Calculations*, Chpt. 4, Springer Verlag, pp 56-74.
- , S. W. Chang, U. C. Mohanty, S. C. Madan, R. K. Paliwal, V. B. Sarin, T. Holt, and S. Raman, 1987: Description of the Naval Research Laboratory Limited Area Dynamical Weather Prediction Model. NRL Memorandum Report, No. 5992, Naval Research Laboratory, Washington, D.C., 131 pp.
- Manabe, S., J. Smagorinsky, and R.F. Strickler, 1965: Simulated climatology of a general circulation model with a hydrologic cycle. *Mon. Wea. Rev.*, **93**, 769-798.
- Martin, D. W., B. Auvine, and B. Hinton, 1988: Atlantic Ocean Rain Maps for GALE. Report on Contract NAG5-742, Space Science and Engineering Center, Madison, WI 53706, 98 pp.
- McPherson, R. D., 1975: Progress, problems, and prospects in meteorological data assimilation. *Bull. Amer. Meteor. Soc.*, **56**, 1154-1166.
- , 1976: Operational objective analysis techniques and potential applications for mesoscale meteorology. *Mesoscale Meteorology and Forecasting*, P. S. Ray, Ed., Amer. Meteor. Soc., Boston, 151-172.
- Mercer, T. J., 1987: Genesis of Atlantic Lows Experiment (GALE): Data Users Guide. Available from GALE Data Center, Department of Physics and Atmospheric Science, Drexel University, Philadelphia, PA, 19104.
- , T. J., and C. W. Kreitzberg, 1986: Genesis of Atlantic Lows Experiment (GALE): Field Program Summary. Available from GALE Data Center, Department of Physics and Atmospheric Science, Drexel University, Philadelphia, PA, 19104.
- Mills, G. A., and R. S. Seaman, 1990: The BMRC regional data assimilation system. *Mon. Wea. Rev.*, **118**, 1217-1237.
- Miyakoda, K., and R. Moyer, 1968: A method of initialization for dynamical weather forecasting. *Tellus*, **20**, 115-128.
- , R. F. Stricker, and J. Chludinsky, 1978: Initialization with the data assimilation method. *Tellus*, **30**, 32-54.
- Mohanty, U. C., A. Kasahara, and R. Errico, 1986: The impact of diabatic heating on the initialization of a global forecast model. *J. Meteor. Soc. Jpn.*, **64**, 805-817.
- Morel, P., 1981: An overview of meteorological data assimilation. *Dynamic Meteorology: Data Assimilation Methods*, L. Bengtsson, M. Ghil, and E. Kallen, Eds., Springer-Verlag, New York, 5-16.
- , and O. Talagrand, 1974: Dynamic approach to meteorological data assimilation. *Tellus*, **26**, 334-344.

- Panofsky, H., 1949: Objective weather map analysis. *J. Meteor.*, **6**, 386-392.
- Petersen, D. P., 1968: On the concept and implementation of sequential analysis for linear random fields. *Tellus*, **20**, 673-686.
- Phillips, N. A., 1957: A coordinate system having some special advantages for numerical forecasting. *J. of Meteor.*, **14**, 184-185.
- , 1976: The impact of synoptic observing and analysis systems on flow pattern forecasts. *Bull. Amer. Meteor. Soc.*, **57**, 1225-1250.
- Puri, K., 1987: Some experiments on the use of tropical diabatic heating information for initial state specification. *Mon. Wea. Rev.*, **115**, 1394-1406.
- , and W. Bourke, 1982: A scheme to retain the Hadley circulation during nonlinear normal mode initialization. *Mon. Wea. Rev.*, **110**, 327-335.
- , and M. J. Miller, 1990: The use of satellite data in the specification of convective heating for diabatic initialization and moisture adjustment in numerical weather prediction models. *Mon. Wea. Rev.*, **118**, 67-93.
- Ramamurthy, M. K., and F. H. Carr, 1987: Four-dimensional data assimilation in the monsoon region, Part I: Experiments with wind data. *Mon. Wea. Rev.*, **115**, 1678-1706.
- Raman, S., and A.J. Riordan, 1988: Genesis of Atlantic Lows Experiment: The Planetary-Boundary-layer subprogram of GALE. *Bull. Amer. Meteor. Soc.*, **69**, 161-172.
- Reynolds, R.W., 1982: A monthly averaged climatology of sea surface temperatures. NOAA Technical Report, NWS-31, Climate Analysis Center, National Weather Service, Washington, D.C., 35pp.
- Riordan, A. J., 1990: Examination of the mesoscale features of the GALE coastal front of 25-26 January 1986. *Mon. Wea. Rev.*, **118**, 258-282.
- Robinson, A. R., 1986: Data assimilation, mesoscale dynamics and dynamical forecasting. *Advanced Physical Oceanographic Numerical Modelling*, J. J. O'Brien, Ed., D. Reidel Pub. Co., 465-483.
- Rodgers, E., G. J. DiMego, J. P. Gerrity, R. A. Petersen, B. D. Schmidt, and D. M. Kann, 1990: Preliminary experiments using GALE observations at the National Meteorological Center. *Bull. Amer. Meteor. Soc.*, **71**, 319-333.
- Rutherford, I. D., 1972: Data assimilation by statistical interpolation of forecast error fields. *J. Atmos. Sci.*, **29**, 809-815.
- , 1976: An operational three-dimensional multivariate objective analysis scheme. *Proc. GARP Conf. on Four Dimensional Data Assimilation*, Paris, GARP WGNE Rep. No. 11, 98-121.

- Sasaki, Y., 1958: An objective analysis based on the variational method. *J. Meteor. Soc. Jpn.*, **36**, 77-88.
- , 1969: Proposed inclusion of time variation terms, observational in numerical variational objective analysis. *J. Meteor. Soc. Jpn.*, **47**, 115-124.
- Sashegyi, K. D., D. E. Harms, R. V. Madala, and S. Raman, 1992: Application of the Bratseth scheme for the analysis of GALE data using a mesoscale model. Conditionally accepted for publication in *Mon. Wea. Rev.*
- , and R. V. Madala, 1990: Tests of initialization procedures with the NRL limited area numerical weather prediction model. NRL Memorandum Report 6648, Washington, D. C., 88 pp.
- , and -----, 1992a: Application of vertical mode initialization to a limited area model in flux form. *Mon. Wea. Rev.* (in press).
- , and -----, 1992b: Test of a nested mesoscale model for the case of the development of an extratropical cyclone during GALE. Technical Memorandum Report, Naval Research Laboratory, Washington D.C.
- Satomura, I., 1988: Dynamic normal mode initialization of a limited-area model. *J. Meteor. Soc. Jpn.*, **66**, 261-276.
- Saucier, W. J.; 1955: Principles of Meteorological Analysis. The University of Chicago Press. Chicago, 438 pp. (p 56-59).
- Schlatter, T. W., 1988: Past and present trends in the objective analysis of meteorological data for nowcasting and numerical forecasting. Preprints, 8th Conference on Numerical Weather Prediction, Amer. Meteor. Soc., Feb 22-26, Baltimore, MD, J9-J25.
- Seaman, R. S., 1988: Some real data tests of the interpolation accuracy of Bratseth's successive correction method. *Tellus*, **40A**, 173-176.
- Shaw, D. B., P. Lonnberg, A. Hollingsworth, and P. Uden, 1987: Data assimilation: The 1984/85 revisions of the ECMWF mass and wind analysis. *Quart. J. Roy. Meteor. Soc.*, **113**, 533-566.
- Shi, J. J., S. Chang, K. Sashegyi, and S. Raman, 1991: Enhancement of objective analysis of hurricane Florence (1988) with dropsonde data. Preprints, 19th Conference on Hurricanes and Tropical Meteorology, Amer. Meteor. Soc., May 6-10, Miami, FL, 335-337.
- Smagorinsky, J., K. Miyakoda, and R. Strickler, 1970: The relative importance of variables in initial conditions for dynamical weather prediction. *Tellus*, **22**, 141-157.

- Stauffer, D. R., and N. L. Seaman, 1987: A real-data numerical study and four-dimensional data assimilation application for mesobeta-scale flow in complex terrain. *Proc. Symp. Mesoscale Analysis and Forecasting*, Vancouver, ESA, 533-538.
- , and -----, 1990: Use of four-dimensional data assimilation in a limited-area mesoscale model, Part I: Experiments with synoptic-scale data. *Mon. Wea. Rev.*, **118**, 1250-1277.
- , T. T. Warner, and N. L. Seaman, 1985: A Newtonian "nudging" approach in four-dimensional data assimilation: Use of SESAME-IV data in a mesoscale model. *Preprints, Seventh Conf. on Numerical Weather Prediction*, Montreal, Amer. Meteor. Soc., 77-82.
- Stephens, J., 1970: Variational initialization of the balance equation. *J. Appl. Meteor.*, **9**, 732-739.
- Sugi, M., 1986: Dynamic normal mode initialization. *J. Meteor. Soc. Jpn.*, **64**, 623-632.
- Temperton, C., 1984: Orthogonal vertical modes for a multilevel model. *Mon. Wea. Rev.*, **112**, 503-509.
- , 1988: Implicit normal mode initialization. *Mon. Wea. Rev.*, **116**, 1013-1031.
- , and D. L. Williamson, 1981: Normal mode initialization for a multilevel grid-point model, Part I: Linear aspects. *Mon. Wea. Rev.*, **109**, 729-743.
- Turpeinen, O. M., L. Garand, R. Benoit, and M. Roch, 1990: Diabatic initialization of the Canadian Regional Finite-Element (RFE) model using satellite data. Part I: Methodology and application to a winter storm. *Mon. Wea. Rev.*, **118**, 1381-1395.
- Uccellini, L. W., and P. J. Kocin, 1987: The interaction of jet streak circulations during heavy snow events along the east coast of the United States. *Weather and Forecasting*, **2**, 289-308.
- , -----, R.A. Petersen, C. H. Wash, and K. F. Brill, 1984: The Presidents' Day cyclone of 18-19 February 1979: Synoptic overview and analysis of the subtropical jet streak influencing the pre-cyclogenetic period. *Mon. Wea. Rev.*, **112**, 31-55.
- Wang, W., and T. T. Warner, 1988: Use of four-dimensional data assimilation by Newtonian relaxation and latent heat forcing to improve a mesoscale-model precipitation forecast, a case study. *Mon. Wea. Rev.*, **116**, 2593-2613.
- Warner, T. T., 1987: Four-dimensional initialization of mesoscale models. *Proc. Symp. Mesoscale Analysis and Forecasting*, Vancouver, Canada, 17-19 August 1987, ESA SP-282, pp. 663-665.

- Wergen, W., 1982: Incorporation of diabatic effects in non-linear normal mode initialization. In *The GARP Programme on Numerical Experimentation*, Rep. No. 3, GARP/WCRP, WMO/ICSU, Geneva, pp. 2.8-2.10.
- , 1983: Initialization. Interpretation of Numerical Weather Prediction Products, ECMWF Seminar/Workshop 1982, 31-57. (Available from the European Centre for Medium Range Weather Forecasts; Shinfield Park, England RG29AX, England.)
- , 1987: Diabatic nonlinear normal mode initialization for a spectral model with a hybrid vertical coordinate. ECMWF Technical Report No. 59, ECMWF, 83 pp.
- Williamson, D. L., and C. Temperton, 1981: Normal mode initialization for a multilevel grid-point model. Part II: Nonlinear aspects. *Mon. Wea. Rev.*, **109**, 744-757.
- Wolcott, S. W., and T. T. Warner, 1981: A humidity initialization utilizing surface and satellite data. *Mon. Wea. Rev.*, **109**, 1989-1998.
- Yamada, T., 1976: On the similarity functions A, B and C of the planetary boundary layer. *Mon. Wea. Rev.*, **33**, 781-793.
- , 1979: PBL similarity profiles determined from a level-2 turbulence-closure model. *Bound. Layer Meteor.*, **17**, 333-351.

Appendix C

Diabatic Initialization Test Using the Naval Research Laboratory Limited-Area Numerical Weather Prediction Model

Reprinted from MONTHLY WEATHER REVIEW, Vol. 121, No. 11, November 1993
American Meteorological Society

**Diabatic Initialization Tests Using the Naval Research Laboratory Limited-Area
Numerical Weather Prediction Model**

DEWEY E. HARMS

RANGARAO V. MADALA

SETHU RAMAN

KEITH D. SASHEGYI

NOTES AND CORRESPONDENCE

Diabatic Initialization Tests Using the Naval Research Laboratory Limited-Area Numerical Weather Prediction Model

DEWEY E. HARMS

Department of Marine, Earth and Atmospheric Sciences, North Carolina State University, Raleigh, North Carolina

RANGARAO V. MADALA

Naval Research Laboratory, Washington, D.C.

SETHU RAMAN

Department of Marine, Earth and Atmospheric Sciences, North Carolina State University, Raleigh, North Carolina

KEITH D. SASHEGYI

Naval Research Laboratory, Washington, D.C.

22 June 1992 and 9 April 1993

ABSTRACT

Diabatic forcing has been incorporated into a nonlinear normal-mode initialization scheme to provide more realistic initial conditions and to alleviate the problem of the spinup time of the Naval Research Laboratory Limited-Area Numerical Weather Prediction Model. Latent heating profiles are computed from the observed rainfall and from the model-generated convective rainfall at locations where there were no observations. The latent heating is distributed in the vertical according to the cumulus convective parameterization scheme (Kuo scheme) of the model. The results of a case study from the Genesis of Atlantic Lows Experiment indicated that model spinup of forecast rainfall can be reduced when diabatic initialization with merging of heat and/or rain is used.

1. Introduction

The dominant forcing in the troposphere within areas of large precipitation is diabatic heating (convective and radiative heating, and large-scale condensation). The present study deals strictly with diabatic heating from cumulus convection. A convective heating term is incorporated in the balance condition for the high-frequency normal modes (Bengtsson 1981; Errico and Rasch 1988; Kitade 1983; Wergen 1983). With the inclusion of heating corresponding to observed rainfall data in the diabatic forcing term, the initialization can force the model state toward the real atmospheric state. As a result, the diabatic initialization can improve the model's forecast fields. Possibly, the primary benefit of initialization with diabatic forcing and moisture initialization is that the spinup problem can be reduced. That is, diabatic nonlinear normal-

mode initialization (DNNMI) produces an initial model state that already includes realistic heating.

Model spinup appears in all numerical forecast systems both in midlatitudes and tropics (Kasahara et al. 1988). It is one of the most serious problems in numerical weather prediction (NWP), and has been documented in research and operational models. Girard and Jarraud (1982) and Heckley (1985) documented spinup in the operational models used by the European Centre for Medium-Range Weather Forecasts, whereas Miyakoda et al. (1978) and Donner (1988) illustrated different aspects of the spinup phenomena in research models at the Geophysical Fluid Dynamics Laboratory and National Center for Atmospheric Research, respectively.

Inadequate physical parameterizations and incorrect initial specifications of divergence, moisture, and thermal fields are the primary causes of spinup (Mohanty et al. 1986). Most normal-mode initialization methods have been adiabatic in nature; that is, the existing latent heating at the initial model time was excluded, leaving out a significant heat source that affected the adjustment between the mass and momentum fields. Lejenas

Corresponding author address: Prof. Sethu Raman, Department of Marine, Earth and Atmospheric Sciences, College of Physical and Mathematical Sciences, North Carolina State University, Box 8208, Raleigh, NC 27695-8208.

(1980) found that adiabatic normal-mode initialization, while providing improved vertical velocity profiles, does not alleviate the spinup problem. Data assimilation techniques that incorporate a more realistic background field in the analysis of observed data have been developed (Lejenas 1980). At the start of each update cycle of the assimilation, the background forecast field is corrected using the observations of mass, momentum, and humidity. During this process, the divergent part of the wind is not represented properly, because the divergence has the same order of magnitude as the errors in the wind field. A consistent diabatic circulation can be generated if the analysis at each cycle of the assimilation is initialized with a diabatic initialization procedure. Turpeinen et al. (1990) concluded that the inclusion of observed low-level latent heat sources with a consistent and higher-resolution moisture analysis are critical components in reducing the underestimation of initial divergence and, hence, precipitation rates.

Throughout the 1980s, NWP models incorporating initial latent heating based on rain rates have been developed. Turpeinen et al. (1990) summarized the main features of some of these models. Mohanty et al. (1986) investigated the inclusion of diabatic heating in the normal-mode initialization (NMI) and found that the divergent circulation was rapidly destroyed by the integrated model heating if it differed too much from the observed heating. In the present study, we have merged the model-produced heating, during the first few hours of integration, with the heating used in the initialization.

The major thrust of this paper is to incorporate the latent heat forcing released due to convective precipitation estimated from the conventional and satellite observations into the normal-mode initialization of the Naval Research Laboratory (NRL) Limited-Area Numerical Weather Prediction Model in an effort to shorten the spinup time. Our goal is also to demonstrate that NMI with diabatic forcing provides improved initialized fields over adiabatic NMI. We have included a diabatic heating term, derived from "spunup" model convective rainfall and observed rainfall, in our nonlinear normal-mode initialization (NNMI) to better define the initial conditions for model integration.

Several model runs (test cases) are made to test the effectiveness of DNNMI as compared to initialization excluding the heating term, or adiabatic NNMI (ANNMI). The NRL mesoscale model is briefly described in the next section. The procedure for computing the diabatic heating for the initialization is then described, followed by the experimental design and results.

2. Model description

The model used in the present study was developed at the Naval Research Laboratory, and is detailed in Holt et al. (1990) and in NRL memorandum reports

by Madala et al. (1987) and Sashegyi and Madala (1992). This is a primitive equation model in terrain-following coordinates having a one-way interacting nested grid network. The coarse grid covers a domain including the continental United States from 10° to 70° N and 40° to 140° W, with a horizontal resolution of 2° longitude (170 km at 40° N) \times 1.5° latitude (166.5 km). The Genesis of Atlantic Lows Experiment (GALE) (inner or fine) grid covers a smaller domain including the eastern half of the United States and extending out over the Gulf Stream from 23.5° to 56.5° N and 58° to 102° W with a finer horizontal resolution of 0.67° longitude (56.7 km at 40° N) \times 0.5° latitude (55.5 km). In the vertical, both grids use 10 equally spaced sigma levels. Model topography for both grid domains is obtained from navy 10-min global topographical data. Even though this paper addresses latent heat release due to convective precipitation, there are two reasons for selecting this extratropical case. One is the availability of a comprehensive GALE dataset. The other is the existence of mesoscale convection over the ocean and the coastal areas due to strong boundary-layer baroclinicity.

The continuous governing equations are written in flux form, and the model's time integration scheme is the split-explicit method that allows larger time steps by effectively separating various terms in the prognostic equations into parts governing the slow-moving Rossby modes and fast-moving gravity modes. A staggered grid network (Arakawa's C grid) is used for horizontal differencing. Lateral boundary conditions suggested by Davies (1976, 1983) are employed in the present version of the model. Monin-Obukhov similarity theory (Yamada 1979) is used to determine the surface transfer of momentum, sensible heat, and latent heat. The cumulus convective parameterization scheme used in this model is the one suggested by Kuo (1974) and modified by Anthes (1977). The parameterization of large-scale or nonconvective precipitation follows Haltiner and Williams (1980); that is, the excess moisture in a supersaturated layer is condensed out isobarically.

3. Diabatic heating in model initialization

Until recently, the NRL model was initialized exclusively using an adiabatic nonlinear normal-mode initialization. The procedure is detailed by Sashegyi and Madala (1990, 1993). In their NNMI, only the first three modes—the external mode and first two internal modes of the model—are initialized. Sashegyi and Madala (1990) showed that the first two modes require only two iterations of the scheme to converge. The third mode converged after five iterations.

Adiabatic NNMI has proven to be extremely effective in controlling spurious large-amplitude gravity-wave oscillations due to initial imbalances between the mass and wind fields in primitive equation models (Puri and Miller 1990; Sashegyi and Madala 1990).

However, the use of adiabatic NNMI (ANNMI) leads to a drastic depletion of the divergent circulation.

Wergen (1983, 1987) introduced a procedure to overcome this problem, in which average diabatic heating is obtained by integrating the model for a few time steps prior to the initialization. The average heating is then included in the nonlinear forcing of the iterative initialization process. The fixed diabatic heating is determined as the time-mean heating generated by model physics (cumulus parameterization and large-scale heating) during the short integration. Unfortunately, most forecast models do not produce realistic heating rates during the first few hours. Therefore, in our experiments we chose to integrate the model for 9 h before accumulating the model latent heating and convective rainfall from which our time-mean heating and rainfall rates were derived. The diabatic NNMI (DNNMI) used in this study is similar to Wergen's, but it is original in that spunup model heating is applied in the initialization rather than the heating from the first few hours of integration, as is usually done. The procedure involves the following steps.

- 1) The model is integrated for 12 h from adiabatically initialized fields. Convective rainfall, from which the diabatic heating is derived, is accumulated from 9 to 12 h of this initial integration (control run), allowing ample time for model spinup.

- 2) Time average convective rainfall rates over the 3-h period are derived for all grid points using conventional and satellite-derived observations. Model rainfall was used for locations over the coastal ocean, since satellite rainfall data were unreliable.

- 3) The model is tested for convective instability at the observed rainfall locations. The average rain rates are converted into vertical profiles of heating using a reverse Kuo cumulus parameterization only at the locations where the atmosphere is convectively unstable. Inversion of the Kuo scheme is essentially straightforward and is done only when the atmosphere is convectively unstable at a location (Harms et al. 1992). This vertical distribution of the latent heating is based on the cumulus convective scheme of the model. Thus, no simplifying hypotheses are needed. The advantage of the present approach is an improved consistency obtained with the physical parameterization scheme of the model.

- 4) This three-dimensional diabatic heating field is then added as a forcing term in the NNMI thermodynamic energy balance equation as the DNNMI is performed. As a result, diabatic effects are explicitly included in the specification of the heating field.

The aforementioned diabatic initialization is primarily for heating associated with convective precipitation. The heating is nearly zero in the lower troposphere and varies significantly from case to case in the upper troposphere. The first three modes of the model account for 40%–50% of the convective heating in the upper troposphere. Therefore, we assume that the

method described here accounts for a significant part of the divergence field. The iterative scheme used in the DNNMI does not converge to a solution with the inclusion of the fourth mode, although it may contribute significantly to convection.

The conversion of rainfall rates into vertical profiles of convective heating depends on the stability of the environment as determined by the cumulus parameterization. If convective instability occurs, a heating function is computed using the reverse Kuo scheme. This heating function is then used to distribute the diabatic heating, derived from the average rainfall rates, in the vertical direction. If the environment is convectively stable, the diabatic heating associated with the two-dimensional rainfall distribution will be taken as zero. Therefore, nonconvective precipitation does not contribute to the diabatic heating in the present initialization scheme.

The persistence of balance achieved by DNNMI during the early stages of the model integration depends heavily on the compatibility between the specified heating during initialization and the model-produced heating during integration (Puri and Miller 1990). Puri (1987) suggested that one possible way of retaining this compatibility in the heating rates would be to adjust the moisture field until the model-produced heating rates determined by the convective parameterization in the model are similar to those used during DNNMI. Here, two procedures are used to retain this desired compatibility in heating rates. First, the model rainfall and heating rates produced during the first 3 h of integration are merged with the corresponding rates from the initialization. A nonlinear weighting factor α is employed where $\alpha = 1$ at $t = 0$ h and $\alpha = 0$ at $t = 3$ h. The relation is given by

$$R_m = \alpha R_i + (1 - \alpha) R_c, \quad (1)$$

where R_i is the convective rainfall rate (from the control) used in DNNMI, R_c is the model-produced convective rainfall rate, R_m is the merged rain rate, and α is given by

$$\alpha = 1 - \frac{[1 + \sin(\pi t/3 - \pi/2)]}{2}. \quad (2)$$

The foregoing relations allow the influence of the initialized heating and rain rates to approach zero in a smoother manner than a simple linear relationship would allow. Merging is applicable only for DNNMI cases, since ANNMI, by definition, does not include a diabatic heating term in its balance equation.

The second method involves adjusting the humidity fields prior to initialization. The importance of moisture adjustment in diabatic initialization was emphasized by Wolcott and Warner (1981). They argued that if the environment is not humid enough, the upward motion associated with the initialized divergence field will not be sustained by latent heat release. In the pres-

ent study, specific humidity is enhanced only at grid points where convective rainfall is occurring and the relative humidity is less than 95%. At those points, the specific humidity is increased to 95% of the saturation specific humidity at the three lowest model levels. However, we found that the changes in the humidity fields were small and, as a result, the adjustment had minimal effect on the convective rainfall. Since the modeled large-scale condensation occurs only upon supersaturation, not at 95% relative humidity, this moisture adjustment would have little effect on non-convective precipitation.

4. Experimental design

Before the experiments are described, the synoptic situation for our study is given.

a. Synoptic setting

During the period 0000 UTC 25 January–0000 UTC 27 January 1986, coastal frontogenesis and cyclogenesis took place along the eastern seaboard. At 0000 UTC 26 January, the coastal front extended from Georgia to southern New England. Cold-air damming and warming of the air over the Gulf Stream led to the strong thermal gradient along the coast. By 1200 UTC 26 January 1986, a weak surface disturbance was located across the Carolinas and Georgia. This disturbance would strengthen over the next 12 h due to cold-air advection aloft approaching from the northwest in association with a cold front in the Ohio River valley. The surface cyclone center became evident off the Carolina coast around 0000 UTC 27 January 1986.

By 1200 UTC 27 January 1986, a developing low pressure system was found off the New Jersey coast, replacing the coastal front wave that had moved northward into New England and disappeared. Behind the developing cyclone, cold air associated with a midtropospheric vortex continued southeastward. This influx of cold air over the warm waters of the Gulf Stream fueled coastal frontogenesis south of the developing cyclone.

b. Description of the model experiments

Initially, three test cases (model runs) were performed to determine improvements (if any) in the model initial state and subsequent forecasts using DNNMI versus ANNMI. The first is a control run in which the model is initialized at 1200 UTC 26 January 1986 using the NMC analyzed data. These fields of 2.5° resolution are first interpolated to the model grid and then initialized with the ANNMI for the first three vertical normal modes of the model. The model is then integrated for 24 h. The 12-h forecast from the control run serves as the initial fields for experiments 2 and 3. In case 2, the model is initialized using DNNMI on the forecast fields from case 1 valid at 0000 UTC 27

January 1986. The analyzed rainfall that includes the observations and the model rainfall in data-void areas (2100 UTC 26 January–0000 UTC 27 January 1986 of the control) is used to compute heating rates at each vertical level of the model for the DNNMI. The model is then integrated for 12 h, with heat and/or rain merging. The initialization for the next case (run 3) is simply an ANNMI on the control run's 12-h forecast.

For this study, the control run is compared against the other two cases; from 1200 UTC 26 January to 0000 UTC 27 January 1986 of the control run, the model should have developed the divergent part of the wind reasonably well. By using model-generated rainfall rates in the DNNMI (case 2), one would expect a negligible spinup during the subsequent forecast. Also, one might expect little change due to the initialization using model rain since the model heating function is consistent with other model parameters. By comparing the initialized and subsequent forecast fields from case 2 with the corresponding fields from the control, one can determine if the model-generated rainfall, which is a 2D distribution, can re-create the 3D distribution of vertical heating rates accurately.

5. Results

The results obtained by making qualitative comparisons of meteorological fields from the different model initializations and forecasts of the three test cases indicate that the differences between cases 2 and 3 of their respective initialized fields of 1000-, 500-, and 250-mb geopotential height, temperature, and winds are extremely small. As expected, the first-order analysis fields (12-h forecast of run 1) changed little with each initialization in these test cases, and as a result, the forecasts (valid at 1200 UTC 27 January 1986) of these variables from these two runs are almost identical and agree well with the control run forecast.

a. Comparison of initialized vertical velocity

Since vertical velocity or ω (dp/dt) is directly related to diabatic heating, we can expect noticeable differences between the initial states of omega from cases 2 and 3. Furthermore, the effectiveness of diabatic heating in inducing divergent circulations can be seen by comparing omega fields from DNNMI and those resulting from ANNMI. As expected, in geographic areas absent of precipitation, vertical velocity patterns in cases 2 (DNNMI) and 3 (ANNMI) are approximately the same and very close to the "control simulation" (Fig. 1). Off the East Coast, an area of strong ascent stretches along the eastern seaboard, and is associated with the old frontal boundary and the developing cyclone off the North Carolina coast. In this region, where the control run ("truth") predicts heavy rain at initialization time (0000 UTC 27 January 1986), the initialized state for run 2 is very close to the control simulation. The pattern and positions of maxima and minima in

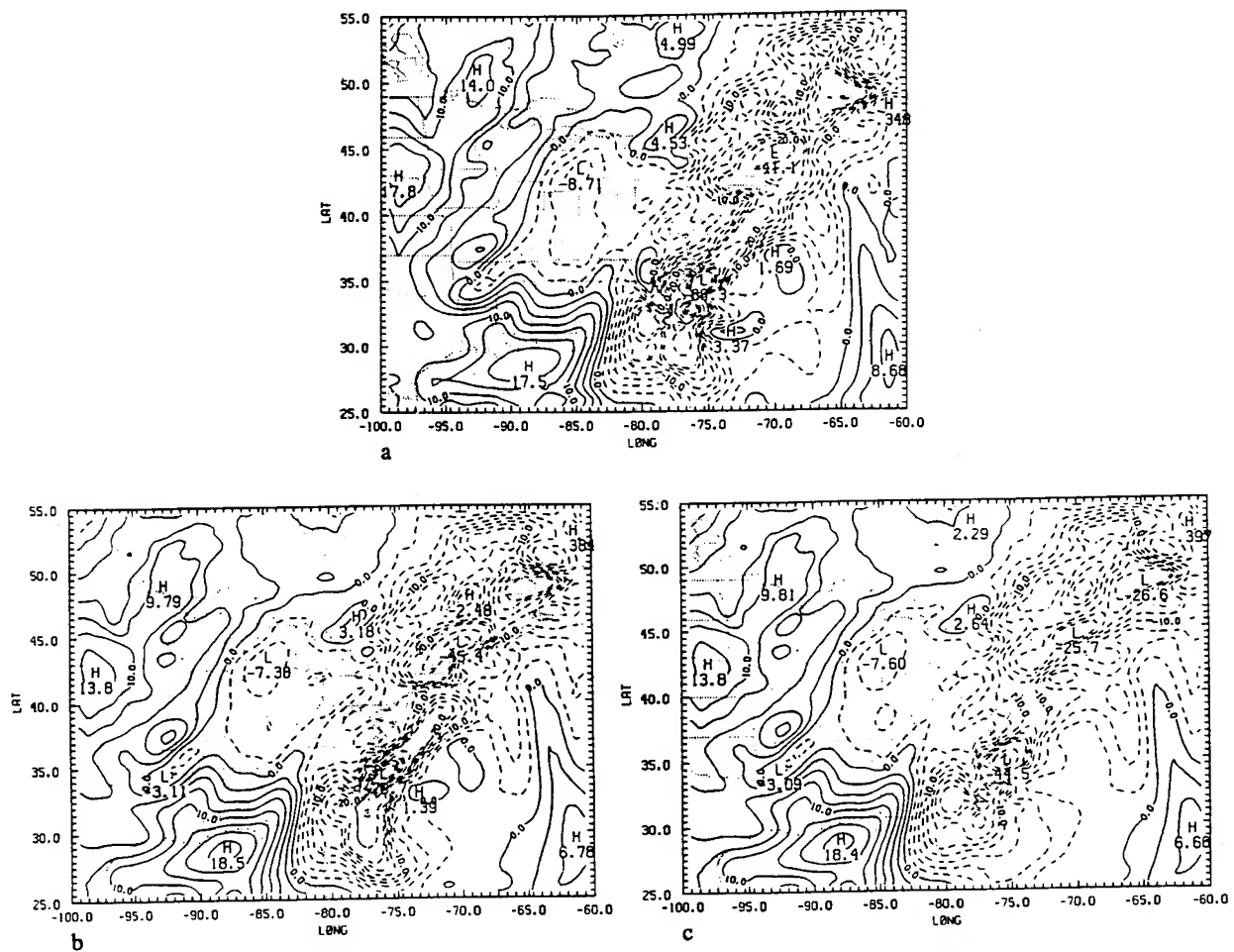


FIG. 1. Vertical-motion fields (mb h^{-1}) for 500 mb valid at 0000 UTC 27 January 1986: (a) from 12-h forecast of the control run, (b) after DNNMI (case 2), and (c) after ANNMI (case 3).

the omega field show little change from the control run, suggesting the 3D structure of model convective heating can be re-created from a 2D rain distribution. A further comparison between case 2 and case 3 reveals the deficiency of ANNMI. In the vicinity of the developing cyclone, the magnitude of ω has changed substantially using ANNMI; the maximum upward velocity is only about 60% of that resulting from DNNMI. Since a significant amount of the divergence (and hence vertical motions) associated with heavy precipitation events may be forced by latent heat release, and since the nonlinear step in the ANNMI does not include this diabatic forcing, the divergence due to this forcing will be removed as if it were associated with unwanted gravity waves. As a result, the vertical velocities are underestimated.

b. Forecast precipitation comparisons

The patterns of 12-h (0000–1200 UTC 27 January 1986) rainfall in runs 2 and 3 are very similar to each other and to the control (run 1) in areal coverage and

accumulation. The 12-h rainfall forecast from the adiabatically initialized fields is just as good as the forecast originating from the diabatically initialized fields. Since the physics and dynamics of the nonlinear normal-mode procedure are internally consistent with the numerical model (which provided the analysis fields), the initialization procedure, whether with or without diabatic heating, changes the model forecast fields only a small amount. As a result, the subsequent forecasts are essentially the same. Therefore, additional model experiments were performed in which GALE 3-h surface and upper-air data at 0000 UTC 27 January 1986 were analyzed using a multivariate, successive correction objective analysis scheme (Sashegyi et al. 1993). Model forecast fields served as the first guess for the analyses. Adiabatic (ANNMI) and diabatic (DNNMI) initializations were performed on the analysis fields. In the latter case, rain data from conventional raingages over land and from satellite-based observations over water were combined with the model-produced rainfall for computation of the 3D heating function in the model initialization procedure.

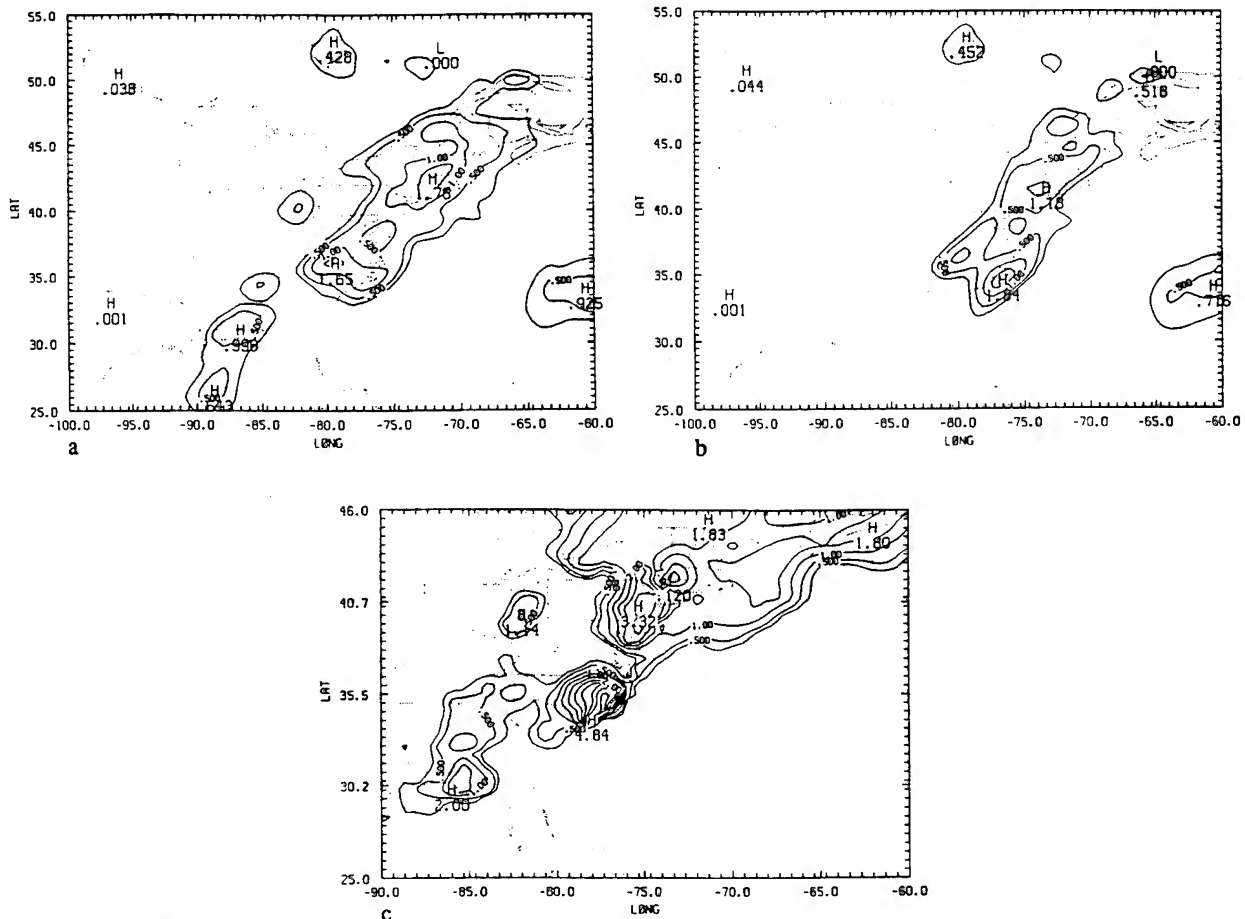


FIG. 2. Forecasts of accumulated total precipitation (cm) (0000–0600 UTC 26 January 1986) originating from (a) DNNMI and (b) ANNMI. (c) Observed precipitation (cm) for the same period.

Figure 2 shows 6-h observed rainfall and accumulated forecast rainfall valid 0000–0600 UTC 26 January 1986. The observations over the GALE area were obtained using raingages and were averaged over 6 h. Over the open ocean away from coastal regions and over the land west of 90°W and north of 45°N , where conventional rainfall data were not available, data were obtained from the University of Wisconsin and consisted of rainfall rates derived from the outgoing long-wave radiation (OLR) sensor aboard *GOES-6* with 1° resolution. Near the coastal ocean where OLR data is not reliable, model-produced rainfall rates are used. These three datasets are blended in a way to ensure smooth transition. Forecast and observed rainfalls in this figure include both convective and nonconvective precipitation. Since this version of the model is the same as the NORAPS (Navy Operational Regional Analysis Prediction System) used by Liou et al. (1990), the breakdown of the convective versus stratiform precipitation is essentially similar to their results. The forecast in Fig. 2a was initialized with DNNMI at 0000 UTC 26 January. The rainfall pattern is similar to the observed: in particular, over Alabama and along the central Gulf coast region, the model was able to predict

the precipitation during this short-range forecast. However, the forecast originating from ANNMI (Fig. 2b) fails to capture any rainfall over the Gulf coast associated with the developing short wave. The absence of diabatic heating from the NNMI has caused a spinup problem in this case. Root-mean-square differences between these forecasts and observed rainfall were computed. The differences were computed only at grid points in which at least 0.01 cm of either forecast or observed rainfall accumulated during the 6-h period. When initializing with ANNMI and DNNMI, the rms differences were 0.9 and 0.7 cm, respectively. The larger rms difference in the ANNMI case is due to model spinup. The disparity between these two cases would be even greater, if only the accumulated rainfall from the first 3 h of model integration was compared.

6. Summary and conclusions

In this study, we took the viewpoint that the “best” initialized states were those that were least altered by initialization. From comparisons of vertical velocity fields, we found that DNNMI with the analyzed rain produced an initial state very similar to the control

simulation and, thus, successfully re-created the 3D distribution of convective heating from the 2D model rain distribution. The ANNMI (case 3) changed the analysis significantly by reducing the maximum vertical velocities to about 60% of that resulting from DNNMI. With the diabatic heating term that forces (to a large degree) convective precipitation, the DNNMI (unlike the ANNMI) retains the divergence (or vertical motion) associated with the convection.

When DNNMI is performed on the analysis fields, model spinup time is reduced. The preforecast integration of the model ensures that the analyses are spun up and that the circulations in these analyses are consistent with the model resolution and external parameters such as topography. The initializations and forecasts were performed in this study for the midlatitudes, which dictates a relatively short spinup. In the data-sparse tropics, spinup can be expected to be much greater. In the tropical case, DNNMI with merging will be critical in reducing spinup time.

In the present study, we considered only diabatic heating associated with convective precipitation. We plan to investigate the latent heating resulting from large-scale, nonconvective rainfall in the near future. The spunup model heating approach will again be incorporated and tested.

Acknowledgments. This research was supported by NRL's basic research program, by SPAWAR, and by the U.S. Air Force. Part of the computer time was provided by the North Carolina Super Computing Center, Research Triangle Park.

REFERENCES

- Anthes, R. A., 1977: A cumulus parameterization scheme utilizing a one-dimensional cloud model. *Mon. Wea. Rev.*, **105**, 270–286.
- Bengtsson, L., 1981: Current problems in four-dimensional data assimilation. *Data Assimilation Methods. ECMWF Seminar 1980*, ECMWF, 195–217. [Available from the European Centre for Medium-Range Weather Forecasts, Shinfield Park, Reading RG29AX, England.]
- Davies, H. C., 1976: A lateral boundary formulation for multi-level prediction models. *Quart. J. Roy. Meteor. Soc.*, **102**, 405–418.
- , 1983: Limitations of some common lateral boundary schemes used in regional NWP models. *Mon. Wea. Mon.*, **111**, 1002–1012.
- Donner, L. J., 1988: An initialization for cumulus convection in numerical weather prediction models. *Mon. Wea. Rev.*, **116**, 377–385.
- Errico, R. M., and P. J. Rasch, 1988: A comparison of various normal-mode initialization schemes and the inclusion of diabatic processes. *Tellus*, **40A**, 1–25.
- Girard, C., and M. Jarraud, 1982: Short and medium range forecast differences between a spectral and grid point model: An extensive quasi-operational comparison. Tech. Rep. No. 32, European Centre for Medium-Range Weather Forecasts, 176 pp. [Available from ECMWF, Shinfield Park, Reading, England.]
- Haltiner, G. J., and R. T. Williams, 1980: *Numerical Prediction and Dynamic Meteorology*. 2d ed. John Wiley and Sons, 477 pp.
- Harms, D. E., K. D. Sashegyi, R. V. Madala, and S. Raman, 1992: Four dimensional data assimilation of GALE data using a multivariate analysis scheme and a mesoscale model with diabatic initialization. Tech. Rep. NRL/MR/4223-92-7147, 219 pp. [Available from Naval Research Laboratory, Washington, DC 20375-5320.]
- Heckley, W. A., 1985: Systematic errors of the ECMWF operational forecasting model in tropical regions. *Quart. J. Roy. Meteor. Soc.*, **111**, 709–738.
- Holt, T., S. Chang, and S. Raman, 1990: A numerical study of the coastal cyclogenesis in GALE IOP 2: Sensitivity to PBL parameterizations. *Mon. Wea. Rev.*, **118**, 234–257.
- Kasahara, A., R. C. Balgovind, and B. B. Katz, 1988: Use of satellite radiometric imagery data for improvement in the analysis of divergent wind in the tropics. *Mon. Wea. Rev.*, **116**, 866–883.
- Kitade, T., 1983: Nonlinear normal mode initialization with physics. *Mon. Wea. Rev.*, **111**, 2194–2213.
- Kuo, H.-L., 1974: Further studies of the influence of cumulus convection on large-scale flow. *J. Atmos. Sci.*, **31**, 1232–1240.
- Lejenas, H., 1980: On the influence of the technique of nonlinear normal mode initialization on the nonconvective precipitation rate. *Mon. Wea. Rev.*, **108**, 1465–1468.
- Madala, R. V., S. W. Chang, U. C. Mohanty, S. C. Madan, R. K. Paliwal, V. B. Sarin, T. Holt, and S. Raman, 1987: Description of the Naval Research Laboratory Limited Area Dynamical Weather Prediction Model. NRL Memo. 5992, Naval Research Laboratory, Washington, D.C., 131 pp.
- Miyakoda, K., R. F. Stricker, and J. Chludinsky, 1978: Initialization with the data assimilation method. *Tellus*, **30**, 32–54.
- Mohanty, U. C., A. Kasahara, and R. Errico, 1986: The impact of diabatic heating on the initialization of a global forecast model. *J. Meteor. Soc. Japan*, **64**, 805–817.
- Puri, K., 1987: Some experiments on the use of tropical diabatic heating information for initial state specification. *Mon. Wea. Rev.*, **115**, 1394–1406.
- , and M. J. Miller, 1990: The use of satellite data in the specification of convective heating for diabatic initialization and moisture adjustment in numerical weather prediction models. *Mon. Wea. Rev.*, **118**, 67–93.
- Sashegyi, K. D., and R. V. Madala, 1990: Tests of initialization procedures with the NRL limited area numerical weather prediction model. NRL Memo. 6648, Washington, D.C., 88 pp.
- , and —, 1992: Test of a nested mesoscale model for the case of the development of an extratropical cyclone during GALE. Tech. Memo., Naval Research Laboratory, Washington, D.C.
- , and —, 1993: Application of vertical mode initialization to a limited area model in flux form. *Mon. Wea. Rev.*, **121**, 207–220.
- , D. E. Harms, R. V. Madala, and S. Raman, 1993: Application of the Bratseth scheme for the analysis of GALE data using a mesoscale model. *Mon. Wea. Rev.*, **121**, 2331–2350.
- Turpeinen, O. M., L. Garand, R. Benoit, and M. Roch, 1990: Diabatic initialization of the Canadian regional finite-element (RFE) model using satellite data. Part I: Methodology and application to a winter storm. *Mon. Wea. Rev.*, **118**, 1381–1395.
- Wergen, W., 1983: Initialization. Interpretation of Numerical Weather Prediction Products, *ECMWF Seminar/Workshop 1982*, ECMWF, 31–57. [Available from the European Centre for Medium-Range Weather Forecasts: Shinfield Park, England RG29AX, England.]
- , 1987: Diabatic nonlinear normal mode initialization for a spectral model with a hybrid vertical coordinate. ECMWF Tech. Rep. No. 59, ECMWF, 83 pp.
- Wolcott, S. W., and T. T. Warner, 1981: A humidity initialization utilizing surface and satellite data. *Mon. Wea. Rev.*, **109**, 1989–1998.
- Yamada, T., 1979: PBL similarity profiles determined from a level-2 turbulence-closure model. *Bound.-Layer Meteor.*, **17**, 333–351.

Appendix D

Tests of Initialization Procedures With the NRL Limited Area Numerical Weather Prediction Model



NRL Memorandum Report 6648

Tests of Initialization Procedures With the NRL Limited Area Numerical Weather Prediction Model

K. D. SASHEGYI* AND R. V. MADALA

*Atmospheric Physics Branch
Space Science Division*

**Science Applications International Corporation
P.O. Box 1303, McLean, VA 22102*

June 29, 1990

REPORT DOCUMENTATION PAGE			Form Approved OMB No. 0704-0188	
Public reporting burden for this collection of information is estimated to average 1 hour per response, including the time for reviewing instructions, searching existing data sources, gathering and maintaining the data needed, and completing and reviewing the collection of information. Send comments regarding this burden estimate or any other aspect of this collection of information, including suggestions for reducing this burden, to Washington Headquarters Services, Directorate for Information Operations and Reports, 1215 Jefferson Davis Highway, Suite 1204, Arlington, VA 22202-4302, and to the Office of Management and Budget, Paperwork Reduction Project (0704-0188), Washington, DC 20503.				
1. AGENCY USE ONLY (Leave blank)	2. REPORT DATE 1990 June 29	3. REPORT TYPE AND DATES COVERED Interim		
4. TITLE AND SUBTITLE Tests of Initialization Procedures with the NRL Limited Area Numerical Weather Prediction Model		5. FUNDING NUMBERS PE - 61153N PR - RR033-034A WU - DN156046		
6. AUTHOR(S) R. V. Madala and K. D. Sashegyi				
7. PERFORMING ORGANIZATION NAME(S) AND ADDRESS(ES) Naval Research Laboratory Washington, DC 20375-5000		8. PERFORMING ORGANIZATION REPORT NUMBER NRL Memorandum Report 6648		
9. SPONSORING/MONITORING AGENCY NAME(S) AND ADDRESS(ES) Office of Naval Research Arlington, VA 22217		10. SPONSORING/MONITORING AGENCY REPORT NUMBER		
11. SUPPLEMENTARY NOTES *Science Applications International Corporation P.O. Box 1303, McLean, VA 22102				
12a. DISTRIBUTION/AVAILABILITY STATEMENT Approved for public release; distribution unlimited.		12b. DISTRIBUTION CODE		
13. ABSTRACT (Maximum 200 words) Several methods are tested to reduce the undesirable gravity wave oscillations in numerical integrations of the Naval Research Laboratory's Limited Area Weather Prediction model. The split-explicit temporal integration scheme used in the model is shown by itself to reduce the amplitude of the external gravity wave oscillations in the first six hours of integration. In a static non-linear initialization procedure, a diagnostic relation is derived for the geopotential on the sigma surfaces of the model. The procedure provides a balanced initial state, except for an initial adjustment of the vertical motion in the first five hours of integration. A vertical mode initialization procedure, following Bourke and McGregor (1983) is also developed for the model. The scheme is tested on two grids, of differing domain size and grid resolution. Convergence of the scheme is shown to be faster for the case of smoother topography along the lateral boundaries. Integrations with two different lateral boundary treatments are compared. The procedure is shown to prevent gravity wave oscillations without producing a mean drift in the surface pressure, to provide a balanced mass divergence, and to produce smaller changes to the initial mass and wind fields, compared to the static initialization.				
14. SUBJECT TERMS Initial conditions, initialization, filtering gravity waves Limited area numerical weather prediction model, static non-linear mass balance, vertical mode initialization			15. NUMBER OF PAGES 91	
			16. PRICE CODE	
17. SECURITY CLASSIFICATION OF REPORT UNCLASSIFIED	18. SECURITY CLASSIFICATION OF THIS PAGE UNCLASSIFIED	19. SECURITY CLASSIFICATION OF ABSTRACT UNCLASSIFIED	20. LIMITATION OF ABSTRACT UL	

CONTENTS

1. Introduction	1
2. Model Description	5
2.1 Vertical modes of the model	6
2.2 Split-explicit time integration	11
2.3 Lateral boundary conditions	12
3. Static Initialization	15
3.1 Non-divergent wind on pressure surfaces	15
3.2 Static non-linear mass balance	17
3.3 Application of static initialization	19
4. Implicit Normal Mode Initialization	21
4.1 Inertia- gravity wave modes	21
4.2 Vertical mode initialization	23
4.2.1 Filtering equations	23
4.2.2 Iterative procedure	26
4.2.3 Changes to the horizontal wind, temperature and surface pressure	28
4.3 Convergence of the vertical mode scheme	30
4.3.1 Using the low resolution US grid	30
4.3.2 Using the high resolution GALE grid	33
5. Model Integrations with Static Initialization	37
5.1 Damping by split-explicit scheme	38
5.2 Non-divergent and statically balanced initial fields	39
6. Model Integrations with Vertical Mode Initialization	41
6.1 Integrations on the US domain	42
6.2 Integrations on the GALE domain	43
7. Summary and Conclusions	46
Acknowledgements	49
Appendix: Split-explicit scheme	51
References	55

TESTS OF INITIALIZATION PROCEDURES WITH THE NRL LIMITED AREA NUMERICAL WEATHER PREDICTION MODEL

1. INTRODUCTION

Various initialization procedures have been tested for use with the Naval Research Laboratory's (NRL) Limited Area Weather Prediction system. The system has been developed to study the development of extratropical cyclones, which occurred along or off the East coast of the U.S. during the Genesis of Atlantic Lows Experiment (GALE) and the Experiment on Rapidly Intensifying Cyclones over the Atlantic (ERICA). Errors in the analysis (which can be due to observational errors and unresolvable scales of motion) and inaccuracies in the model physics give rise to inertia-gravity wave oscillations in numerical integrations of the model. Such errors are reflected as unbalanced deviations in the wind and mass fields, which generate freely propagating inertia-gravity waves. For the external and first few internal vertical modes of the numerical model, the phase speeds of these free inertia-gravity waves are much larger than the speeds of meteorological systems. The resulting high frequency oscillations can be seen in the surface pressure for example, with amplitudes as large as 5 to 10 mb.

Over the years, various methods have been used to reduce these high frequency oscillations in integrations of numerical weather prediction models. Among these, initial conditions used for integrations of the model are sometimes modified or initialized by application of various filtering equations. In the conventional static initialization performed on pressure surfaces, horizontal scaling arguments are used to derive the non-linear mass balance equation, which relates the geopotential and the stream function of the non-divergent wind for the larger scale atmospheric motions (see Haltiner and Williams, 1980, for example). In midlatitudes it has been customary to use the observed geopotential heights to compute a statically balanced wind field, assuming the wind is geostrophic at the lateral boundaries of the model (see Bengtsson, 1975, for example). On the other hand in the tropics, the non-divergent wind is used to derive a statically balanced temperature from the geopotential (see Krishnamurti, 1979, for example). Since most numerical weather prediction models use vertical coordinates different from the pressure, these statically balanced mass and wind fields must be then

interpolated to the model vertical coordinates, introducing some noise in the initial conditions. Sundqvist (1975) used horizontal scaling arguments to derive the non-linear mass balance equation directly on the vertical sigma levels of his numerical model. In the normal mode initialization, used in global numerical weather prediction models (Andersen, 1977, Daley, 1979, Temperton and Williamson, 1981, Williamson and Temperton, 1981, for example), the normal modes of the numerical model are computed and by projecting the initial wind and mass fields (which have been interpolated to the model coordinates) onto these normal modes, the high frequency inertia-gravity waves can then be removed. However in limited area models, it is not possible to define the horizontal structure of the normal modes. In the vertical mode initialization scheme of Bourke and McGregor (1983), filtering conditions for the inertia-gravity waves are applied to the model dynamical equations to derive linear diagnostic equations for the mass divergence and generalized geopotential for the first few vertical modes of the model. With the further condition that the linearized potential vorticity is unchanged by the procedure, the equations can be solved iteratively for the amplitude of the high frequency gravity waves in the initial conditions. The scheme has been shown to be an application of the normal mode initialization scheme used in global models, without the horizontal structure of the normal modes having to be computed (Juvanon du Vachat, 1986; Temperton, 1988).

To reduce the amplitude of these high frequency gravity wave oscillations in the NRL model, several basic types of initialization procedures have been used. A static initialization procedure, which had been developed for the NRL model, is tested. With the future implementation of a wind profiling network in the U.S., there is renewed interest in deriving geopotential heights from the wind field in the midlatitudes. In the NRL scheme then, the non-divergent wind is first computed from the analyzed winds on the pressure surfaces. The computed non-divergent wind and the analyzed temperatures are then interpolated to the model vertical coordinates. A diagnostic relation for the geopotential on the sigma surfaces of the numerical model is derived, by setting the tendency of mass divergence to zero and ignoring vertical advection and friction in the divergence equation. For the boundary condition on the geopotential, we generalized the conventional geostrophic relationship,

deriving diagnostic conditions for the normal derivatives of the geopotential by ignoring the tendencies of momentum in the momentum equations.

A second type of initialization procedure, based on the vertical mode initialization scheme of Bourke and McGregor (1983), has also been developed for the NRL model. As is customary, we keep the geopotential, temperature and pressure fixed at the lateral boundaries of the model. To provide a boundary condition for the mass divergence however, an approximate mass divergence is computed along the lateral boundary using the thermodynamic equation. In our scheme, changes in the tangential wind along the lateral boundaries are consistent with the changes in the vorticity and divergence computed by the scheme.

The effect of the split-explicit scheme, which is used for integration in time in the NRL model, and the non-linear initialization procedures in reducing gravity wave oscillations in integrations of the NRL model are investigated. The influence of two different lateral boundary treatments and two different grids of differing resolution and domain size are investigated. In these integrations, idealized boundary conditions are obtained by interpolation from operational analyses. To minimize the impact of noise from the boundaries influencing the interior, the boundary conditions are derived from initialized fields for the cases of integrations starting from initialized fields.

The numerical model, the vertical modes, the split-explicit integration scheme and the two different lateral boundary treatments are described in section 2. In section 3, the static initialization procedure is described and illustrated. The vertical mode scheme is then described in section 3. The convergence of the scheme is also shown for the two different grids. A low resolution grid with a resolution of 2° in longitude by 1.5° in latitude, covers the continental U.S., and a high resolution grid of 0.5° resolution in latitude and longitude covers the eastern U.S. In section 5, integrations with the split-explicit scheme for time integration are compared with a centered difference scheme on the high resolution grid, for uninitialized initial conditions. Integrations with the split-explicit scheme are then compared for varying degrees of static initialization. In section 6, integrations with

initial conditions, initialized with the vertical mode scheme, are compared to integrations with uninitialized fields for both the low and high resolution grids. Differences due to the different lateral boundary treatments are compared. The results are summarized and discussed in section 7.

2. MODEL DESCRIPTION

The Naval Research Laboratory's primitive equations model (Madala et al., 1987) uses sigma coordinates in the vertical and incorporates topography and physical parameterizations of the boundary layer and precipitation processes. The model is integrated in time using the efficient split-explicit method (Madala, 1981). In the horizontal, an Arakawa C grid (Arakawa and Lamb, 1977) is used with a latitude and longitude grid. The finite difference scheme is a second order quadratic conserving scheme. The model has been used for example to study the east coast snow storm of 10-12 February, 1983 (Chang et al., 1989). For experiments in this paper, ten layers of equal thickness (with $\Delta\sigma = 0.1$) are used in the vertical sigma (σ) coordinate from the surface ($\sigma = 1$) to the model top ($\sigma = 0$). The model includes large scale precipitation and a cumulus parameterization using a modified Kuo scheme. Unstable lapse rates are removed by a dry convective adjustment scheme following Manabe et al. (1965). The boundary layer is parameterized using a drag coefficient formulation, and second order horizontal diffusion is included.

Two different model grids are used for the model. A low resolution grid (called the US grid), with a resolution of 2° longitude by 1.5° latitude, covers the continental U.S. in a domain from 140.0°W to 40.0°W and 10.0°N to 70.0°N . The other grid (called the GALE grid) is a high resolution grid of 0.5° resolution in latitude and longitude, covering the eastern U.S. from 102.5°W to 57.5°W and 22.5°N to 47.5°N . Analyses at 14 standard pressure levels (from 50 to 1000 mb) on a 2.5° hemispheric grid from the National Meteorological Center (NMC) provide the initial conditions and idealized boundary conditions for model integrations in this paper. The NMC 2.5° resolution hemispheric analysis is interpolated to the horizontal model grid using Lagrangian cubic polynomial interpolation. The thermodynamic variables are interpolated in the vertical to the model sigma levels assuming they are linear in the log of the pressure, while the wind components are interpolated assuming they are linear in the pressure. An enveloped topography is derived for each model grid from the U.S. Navy's global 10 minute elevation data, by computing the average height for each model grid square and adding one standard deviation. On each model grid, the enveloped topography is then filtered by using the two-dimensional triangular smoother-desmoother of

Shapiro (1970), to filter out any wavelengths in the topography of twice the grid distance. For use with the vertical mode initialization scheme, the model topography is further smoothed by using one pass of the two-dimensional nine point triangular smoother (Shapiro, 1970). Climatological mean sea surface temperatures for the month of January of one degree resolution, taken from Reynolds (1982), are interpolated to the model grids.

2.1 Vertical Modes of the Model

In order to solve for the vertical modes of our numerical model, we linearize about a basic state at rest with a mean temperature T^* , which is a function of sigma only, and separate the linear and non-linear terms in the model dynamical equations. The model dynamical equations in flux form can then be written in matrix notation as

$$\frac{\partial \bar{p}_s^x u}{\partial t} + \delta_x \Phi = A_u \quad (2.1)$$

$$\frac{\partial \bar{p}_s^y v}{\partial t} + \delta_y \Phi = A_v \quad (2.2)$$

$$\frac{\partial \bar{p}_s T}{\partial t} + M_2 D = A_T \quad (2.3)$$

$$\frac{\partial \bar{p}_s}{\partial t} + N_2^T D = 0 \quad (2.4)$$

and the hydrostatic relation and continuity equation are written

$$\phi - \phi_s = M_1 T \quad (2.5)$$

$$p_s \dot{\sigma} = N_1 D \quad (2.6)$$

where column vectors are in bold type, M_1 , M_2 , N_1 are matrices, and N_2^T represents the transpose of vector N_2 . The vertical sigma coordinate (σ) is defined by the ratio of the pressure p to the surface pressure p_s (Phillips, 1957). The dynamical variables are in vector form, where the elements of the vectors represent the values of the variables at each of the ten model sigma

levels for a single horizontal grid point. The vectors u , v represent the horizontal wind, T the temperature and ϕ the geopotential, at each of the model sigma levels, which are defined at the middle of each of the sigma layers in the vertical. ϕ_s is the surface geopotential (at $\sigma = 1$). The generalized geopotential Φ is defined as

$$\Phi = p_s[\phi - \phi_s + RT^* - \phi^*] \quad (2.7)$$

where the average geopotential ϕ^* on the sigma surface is related to the mean temperature T^* through the hydrostatic relation $\phi^* = M_1 T^*$. The vertical motion σ in the sigma coordinate (σ) is staggered in the vertical, being defined at sigma levels at the boundaries between the vertical layers. Subscripts representing the horizontal grid points on the C grid (see also grid mesh in Fig. 2 in section 2.3) have been omitted for clarity. The x and y coordinates are defined by multiplying the longitude and latitude in radians by the average radius of the earth. The mass divergence D on the sigma surfaces is defined on the C grid in our spherical coordinates by

$$D = \frac{1}{h_y} \delta_x (h_y \overline{p_s^x} u) + \frac{1}{h_x} \delta_y (\overline{h_x^y} \overline{p_s^y} v) \quad (2.8)$$

Here the difference operator δ is defined in the x direction, using the generalized geopotential Φ as an example, by

$$\delta_x \Phi = \frac{\Phi(x+\Delta x/2) - \Phi(x-\Delta x/2)}{h_x \Delta x} \quad (2.9)$$

where Δx is the grid spacing for the x coordinate and h_x (equal to the cosine of the latitude for our coordinate) is the map factor for the x coordinate. A similar difference operator is defined for the y coordinate, where the map factor is $h_y = 1$ in our case. An averaging operator is also defined in the x -direction, using the surface pressure as an example, by

$$\overline{p_s^x} = \frac{p_s(x+\Delta x/2) + p_s(x-\Delta x/2)}{2} \quad (2.10)$$

A similar averaging operator is defined for the y -coordinate and a two dimensional averaging can be defined as

$$\overline{p_s^{xy}} = \overline{p_s^{xy}} = \overline{p_s^{yx}} \quad (2.11)$$

Elements of the matrices M_1 , M_2 , N_1 and the vector N_2 are functions of sigma only. The vectors on the right hand side (RHS) of Eqs. (2.1), (2.2) and (2.3) include Coriolis, friction, non-linear advection and diabatic terms. Details of the vector and matrix elements can be found in the report by Madala et al. (1987).

Solutions to the homogeneous equations (in which terms on the RHS of Eqs. (2.1), (2.2), (2.3) and (2.4) are zero) are freely propagating gravity waves. Now eliminating all variables in the homogeneous equations except Φ , we obtain

$$\frac{\partial^2 \Phi}{\partial t^2} - M_3 \nabla^2 \Phi = 0 \quad (2.12)$$

where the matrix M_3 is defined as $M_3 = M_1 M_2 + (RT^* - \phi^*) N_2^T$ and whose elements are only functions of the vertical sigma coordinate and do not depend on the x and y coordinates. In our x and y spherical coordinates, the two dimensional Laplacian ∇^2 is defined by

$$\nabla^2 \Phi = \frac{1}{h_y} \delta_x (h_y \delta_x \Phi) + \frac{1}{h_x} \delta_y (h_x \delta_y \Phi) \quad (2.13)$$

Similarly, we can show that the mass divergence D satisfies the same equation (2.12), while the vorticity of the background flow is not affected by gravity wave motions. The equation (2.12) is separable and by separating the vertical structure, a set of vertical eigenmodes and corresponding eigenvalues can be obtained (see also Kasahara and Puri, 1981, for example). In terms of our matrix notation, the eigenvectors ϵ_k and corresponding eigenvalues λ_k are found by solving the matrix equation

$$M_3 \epsilon_k = \lambda_k \epsilon_k. \quad (2.14)$$

If E represents the eigenvector matrix (with each column representing an eigenvector ϵ_k) of matrix M_3 , and Λ is the diagonal matrix with the diagonal elements given by the eigenvalues λ_k , then we can write

$$M_3 E = \Lambda E. \quad (2.15)$$

and by multiplying Eq. (2.12) by the inverse of E we have

$$\frac{\partial^2 e}{\partial t^2} - \Lambda \nabla^2 e = 0 \quad (2.16)$$

where $e = E^{-1} \Phi$, and we have used the property of the eigenvector matrix that $E^{-1} M_3 E = \Lambda$, which can be easily verified by comparing the elements of matrices $M_3 E$ and $E \Lambda$ (see Strang, 1988, p254, for example). For each vertical mode we have

$$\frac{\partial^2 e_k}{\partial t^2} - \lambda_k \nabla^2 e_k = 0 \quad (2.17)$$

where e_k is the amplitude of the generalized geopotential and λ_k is the

TABLE 1: Mean temperatures for 12Z January 23, 1986, on sigma surfaces of 10 layer model for GALE grid.

Model Level	Sigma Level	Temperature (°K)
1	0.05	205.9
2	0.15	214.0
3	0.25	222.1
4	0.35	236.1
5	0.45	249.4
6	0.55	259.4
7	0.65	266.6
8	0.75	271.9
9	0.85	275.9
10	0.95	278.4

TABLE 2: The equivalent depths and the phase speeds for the vertical modes of a ten layer model for the mean temperature profile defined in Table 1.

Mode No.	Equiv. Depth (meters)	Phase Speed (meters s ⁻¹)
1	9,399.0	303.5
2	1,508.0	121.6
3	226.6	47.1
4	85.7	29.0
5	30.3	17.2
6	13.7	11.6
7	6.4	7.9
8	2.7	5.1
9	0.9	3.0
10	0.2	1.3

eigenvalue for the k^{th} mode. Eq. (2.17) is a wave equation describing the propagation of the free gravity mode whose phase speed c_k is given by $\sqrt{\lambda_k}$. In the linearization used here to obtain the gravity modes, the Coriolis term is combined with the non-linear terms, and as such the gravity modes are applicable only for high frequencies or small time periods compared to the period of inertial oscillations. However it can be noted that the vertical structure of the modes derived in this case is unchanged even if the Coriolis terms are included with the linear terms on the left hand side of Eqs. (2.1) and (2.2). In this case the linearization defines the inertia-gravity modes (see section 4.1).

As an example the eigenmodes are computed for the ten layer model using a temperature profile taken from the NMC 2.5° hemispheric analysis for 12Z January 23, 1986 during the second Intensive Observing Period (IOP) of GALE.

The temperatures are interpolated to the model grid and averaged on the sigma surfaces over the GALE grid covering the eastern U.S. The average temperatures on the model sigma levels at the middle of each layer are shown in Table 1. The eigenvalues and the phase speeds for each of the ten vertical modes computed are shown in Table 2. The eigenvalues are given in terms of equivalent depths defined by λ_k/g , where g is the acceleration due to gravity. The corresponding vertical structure for each of the modes is shown in Fig. 1. The number of zero crossings in the vertical structure of each mode is given by the mode number minus one. The phase speeds of the modes vary from 303.5 m s^{-1} for the external (first) mode to 1.3 m s^{-1} for the tenth mode. For the first three modes, the external mode and first two internal modes, the phase speeds are much faster than typical meteorological systems, which are typically less than 20 m s^{-1} . Then to integrate a model with a centered difference scheme in time and a grid spacing Δx , the time step $2 \Delta t$ must be small enough to satisfy the CFL condition $2 \Delta t (U+c) / \Delta x \leq 1$, for the external gravity mode which has the fastest phase speed c , and where U is a maximum advecting wind speed (see for example Mesinger and Arakawa, 1976, p51). To allow the NRL model to be integrated more efficiently at a larger time step, more appropriate for meteorological systems, the split-explicit scheme was developed.

2.2 Split-Explicit Time Integration

In the split-explicit method of Madala (1981), a centered difference scheme is used with a large time step to compute initial estimates of the tendencies of the model variables for all the terms, except for diffusion which uses forward differencing. The time step satisfies the CFL condition for the phase speed of the 4th gravity mode. To step the model variables at time $t - \Delta t$ forward in time by $2 \Delta t$, using the centered difference scheme, the non-linear terms and forces are computed at time t . These first estimates of the tendencies of the mass (surface pressure p_s , temperature T) and wind fields (u, v) are then corrected for the motion of the higher frequency gravity modes, assuming that the computed non-linear, Coriolis, diabatic and friction forcing terms are constant during the time step of $2 \Delta t$. The specific humidity q is not corrected. To obtain the corrections, the amplitudes of the deviations of the divergence $D - D(t)$ and the generalized geopotential

$\Phi - \Phi(t)$ are integrated over the interval of $2 \Delta t$ at smaller time steps, for each of the first three vertical modes. For the external mode a time step of $\Delta t/8$ is used, while for the first two internal vertical modes time steps of $\Delta t/4$ and $\Delta t/2$, respectively, are used. The average of these deviations, over the interval of twice the large time step $2 \Delta t$, is then used to correct the initial explicit estimate of the variables. Further details can be found in the Appendix. For the integration of the deviations of the divergence a lateral boundary condition is also required for the generalized geopotential. A boundary value for $\Phi - \Phi(t)$ is computed by a linear interpolation from the boundary values at $t - \Delta t$ and t . Further pragmatic boundary conditions are provided by reducing the amplitude and phase of the deviations of the divergence and generalized geopotential in a boundary zone (see the Appendix). Besides providing a 4 to 5 times saving in computer time over explicit methods, the averaging of the lower gravity wave eigenmodes can be expected to reduce the amplitude of the freely propagating higher frequency gravity waves.

2.3 Lateral Boundary Conditions

To update the large scale flow at the horizontal boundaries during the integration of the NRL model, externally prescribed boundary conditions are required for both the u and v components of the wind field and the mass and humidity fields. In the model, the mass and humidity variables of surface pressure p_s , temperature T , geopotential ϕ (or generalized geopotential Φ), and specific humidity q are defined at the lateral boundary. The wind components are staggered in the C grid and as applied to the NRL model, the tangential wind is defined at the boundary, while the normal wind is staggered half a grid point in from the boundary (see Fig. 2). In this paper two different lateral boundary treatments, the tendency relaxation scheme of Perkey and Kreitzberg (1976) and the Davies (1976, 1983) relaxation scheme, are used and compared for use with various initialization procedures. To provide the model boundary conditions in our experiments, idealized boundary values and tendencies are derived from the NMC 2.5 degree hemispheric analyses, interpolated to the model grid.

(a) Perkey Kreitzberg scheme.

In the Perkey Kreitzberg scheme, model computed tendencies for each of the dependent variables are blended with specified boundary tendencies in a

boundary zone of 5 points. After each time step, the model tendencies for each of the independent model variables are adjusted according to

$$\frac{\partial a}{\partial t} = (1-\alpha) \left[\frac{\partial a}{\partial t} \right]_m + \alpha \left[\frac{\partial a}{\partial t} \right]_b \quad (2.18)$$

where a is the independent model variable $\bar{p}_s^x u$, $\bar{p}_s^y v$, p_s , $p_s T$, or $p_s q$, subscript m represents the model computed value, and subscript b the prescribed boundary value. α is a linear function of the minimum distance (n) from the lateral boundary, in units of the grid spacing. As in Chang et al. (1989), we use for the mass and humidity variables (that is, for p_s , $p_s T$, $p_s q$)

$$\alpha = \begin{cases} 1 - \frac{n}{5} & \text{for } n \leq 5 \\ 0 & \text{for } n > 5 \end{cases} \quad (2.19)$$

while for the wind components $\bar{p}_s^x u$, $\bar{p}_s^y v$, which are staggered on the grid mesh, we use

$$\alpha_u = \begin{cases} 1 & \text{for } n \leq 0.5 \\ \bar{a}^x & \text{for } n \geq 1 \end{cases} \quad (2.20)$$

$$\alpha_v = \begin{cases} 1 & \text{for } n \leq 0.5 \\ \bar{a}^y & \text{for } n \geq 1 \end{cases} \quad (2.21)$$

The boundary tendencies, derived from the twelve hourly NMC analyses, are updated every twelve hours of model integration.

(b) Davies scheme.

In the Davies scheme, computed model variables are relaxed to the boundary values themselves at each time step in a boundary zone of 6 points. In this case, the model variables are adjusted at each time step according to

$$a = (1-\alpha) a_m + \alpha a_b \quad (2.22)$$

where, following Grønås et al. (1987), we define α as a quadratic function of the minimum distance (n) from the lateral boundary, in units of the grid spacing. For the mass variables we use

$$a = \begin{cases} 1 & \text{for } n = 0 \\ \left[\frac{6.5 - n}{6} \right]^2 & \text{for } 1 \leq n \leq 5 \\ 0 & \text{for } n \geq 6 \end{cases} \quad (2.23)$$

The functions a_u and a_v for the u and v components of the wind field are defined similarly as in Eqs. (2.20) and (2.21), using the averaging operators in the x and y coordinate directions, respectively. At each time step, the boundary values are computed by a linear interpolation in time from the 12 hourly NMC analyses.

3. STATIC INITIALIZATION

In the static initialization procedure used at NRL, a diagnostic relationship is derived for the geopotential on the sigma surfaces of the model. The non-divergent wind is first computed for the analyzed winds on the pressure surfaces. The NRL model differs from many other limited area models in that the tangential wind is specified at the lateral boundary of the model, instead of the normal wind. To compute the non-divergent wind then we solve for the stream function, assuming that the tangential wind along the lateral boundary is purely non-divergent. The non-divergent wind and the analyzed temperatures are then interpolated to the sigma coordinates of the model. A diagnostic relation is then derived for the geopotential on the sigma surfaces of the numerical model, by ignoring the tendency of divergence, vertical advection and friction. The initial non-divergent wind and analyzed temperatures, interpolated to the sigma surfaces, are used to compute the non-linear forcing terms. Boundary conditions for the normal derivatives of the geopotential are obtained by ignoring the tendencies in the momentum equations.

3.1 Non-Divergent Wind on Pressure Surfaces

For large scale atmospheric motions, the divergence of the velocity field is an order of magnitude smaller than the vorticity. To a first approximation then, the flow can be considered non-divergent on surfaces of constant pressure. On pressure surfaces, the vorticity ζ_p and divergence D_p are defined on the model horizontal grid as

$$\zeta_p = \frac{1}{h_y} \delta_x (h_y v) - \frac{1}{h_x} \delta_y (h_x u) \quad (3.1)$$

$$D_p = \frac{1}{h_y} \delta_x (h_y u) + \frac{1}{h_x} \delta_y (h_x v) \quad (3.2)$$

where u and v are the analyzed wind components on a pressure surface, interpolated to the horizontal grid of the model. The non-divergent flow can

then be described by introducing a stream function ψ , so that the non-divergent wind components u_ψ and v_ψ at that pressure level are given by

$$\begin{aligned} u_\psi &= -\delta_y \psi \\ v_\psi &= \delta_x \psi \end{aligned} \quad (3.3)$$

By computing the vorticity on the pressure surface, we can solve Poisson's equation,

$$\nabla^2 \psi = \zeta_p \quad (3.4)$$

for the stream function ψ , and whence for the non-divergent wind. To provide boundary conditions for the stream function, we assume that the analyzed tangential wind along the boundary of our model domain is purely non-divergent. Then we obtain the Neumann boundary conditions for the stream function

$$\begin{aligned} \delta_y \psi &= -u \quad \text{at } y = y_0, y_1 \\ \delta_x \psi &= v \quad \text{at } x = x_0, x_1 \end{aligned} \quad (3.5)$$

where y_0, y_1 give the southern and northern lateral boundaries and x_0, x_1 give the western and eastern boundaries. In this case the stream function is not unique, since adding a constant value to the solution of the stream function is also a solution. As described in the report of Sashegyi and Madala (1989), to obtain a unique solution for the stream function, we prescribe a value for the stream function $\psi = 0$ at a single arbitrary point on the boundary and use the elliptic equations solver of Madala (1978, 1981). Choice of a zero value as a first guess of the solution of the stream function then leads to the efficient convergence of Madala's elliptic equations solver.

As eloquently described by Lynch (1989), the partitioning of the wind into the divergent and non-divergent parts is not unique in a limited area domain. The choice of using the tangential wind on the boundary to describe the normal gradient of the stream function, minimizes the kinetic energy in the divergent wind and does not lead to a mixed divergent and non-divergent term in the kinetic energy balance. It can be noted that choice of defining the normal wind at the boundary in some models, instead of the tangential wind used in the NRL model, leads to solving Poisson's equation

$$\nabla^2 \chi = D_p \quad (3.6)$$

for a velocity potential χ , which defines the divergent component of the wind. The non-divergent wind is then computed by subtracting the divergent component from the original wind field. For the boundary conditions in this case, it is

assumed that $\chi = 0$ at the lateral boundaries, that is, it is assumed that the divergent component of the wind is zero on the boundary.

3.2 Static Non-Linear Mass Balance

For large scale atmospheric motions, the time tendency of the divergence is small compared to the other terms in the divergence equation. A diagnostic equation for the geopotential on the sigma surfaces of the model can then be derived by ignoring this term. We can rewrite the model momentum equations (2.1) and (2.2) in the form

$$\frac{\partial \bar{p}_s^x u}{\partial t} + \bar{p}_s^x \delta_x \phi + R \bar{T}^x \delta_x p_s = N_u \quad (3.7)$$

$$\frac{\partial \bar{p}_s^y v}{\partial t} + \bar{p}_s^y \delta_y \phi + R \bar{T}^y \delta_y p_s = N_v \quad (3.8)$$

where we have included the non-linear advection of momentum, the Coriolis force and friction in the terms on the RHS. The equation for the mass divergence on the sigma surfaces is then obtained by taking δ_x of h_y times Eq. (3.7) and adding δ_y of h_x times Eq. (3.8) giving

$$\frac{\partial D}{\partial t} + \nabla \cdot [p_s \nabla (\phi - \phi_s)] = N_D - \nabla \cdot [RT \nabla p_s + p_s \nabla \phi_s] \quad (3.9)$$

where the horizontal geopotential gradient is given by $\nabla \phi = (\delta_x \phi, \delta_y \phi)$ and we have utilized the two dimensional divergence operator ∇ to define

$$N_D = \nabla \cdot N_V = \frac{1}{h_y} \delta_x (h_y N_u) + \frac{1}{h_x} \delta_y (h_x N_v) \quad (3.10)$$

$$\nabla \cdot (p_s \nabla \phi) = \frac{1}{h_y} \delta_x (h_y \bar{p}_s^x \delta_x \phi) + \frac{1}{h_x} \delta_y (h_x \bar{p}_s^y \delta_y \phi) \quad (3.11)$$

Here we have also defined the vector N_V by $N_V = (N_u, N_v)$. Since the time tendency of the divergence is assumed small compared to the other terms in the

mass divergence equation (3.9), we can ignore this term. That is, setting the tendency of the mass divergence zero in Eq. (3.9), we have

$$\nabla \cdot [p_s \nabla (\phi - \phi_s)] = N_D - \nabla \cdot [RT \nabla p_s + p_s \nabla \phi_s] \quad (3.12)$$

To compute the term N_D , we first compute the non-divergent wind on the pressure surfaces, as described in section 3.1. The non-divergent wind and the analyzed temperatures are then interpolated to the sigma surfaces of the model (see the beginning of section 2 on the model description). The non-divergent wind is then used to compute the terms on the RHS of Eqs. (3.7) and (3.8) ignoring vertical advection and friction (leaving horizontal advection and Coriolis forces). The analyzed temperatures and a surface pressure computed on the model topography by interpolation are used to compute the remaining forcing terms on the RHS of Eq. (3.12).

To solve Eq. (3.12), boundary conditions are required for the geopotential. To obtain the boundary conditions we ignore the tendencies of the u and v momentum in Eqs. (3.7) and (3.8) to obtain the Neumann boundary conditions for the geopotential

$$\overline{p_s^x} \delta_x (\phi - \phi_s) = N_u - R \overline{T^x} \delta_x p_s - \overline{p_s^x} \delta_x \phi_s \quad (3.13)$$

at $x = x_0 + \frac{\Delta x}{2}$, $x_1 - \frac{\Delta x}{2}$ and

$$\overline{p_s^y} \delta_y (\phi - \phi_s) = N_v - R \overline{T^y} \delta_y p_s - \overline{p_s^y} \delta_y \phi_s \quad (3.14)$$

at $y = y_0 + \frac{\Delta y}{2}$, $y_1 - \frac{\Delta y}{2}$,

where $y = y_0, y_1$ give the southern and northern lateral boundaries and $x = x_0, x_1$ give the western and eastern boundaries. In Fig. 2, our boundary conditions for the geopotential gradient are defined along the lines given by the shorter dashes, half a grid point in from the lateral boundary. Essentially, we have generalized the conventional geostrophic boundary condition relating the gradient of the geopotential to the geostrophic wind, by using the non-divergent wind and including the non-linear horizontal advection term. The

elliptic equation (3.12) can now be solved for the geopotential using the Neumann boundary conditions (3.13) and (3.14) with an elliptic equations solver, such as the Stabilized Error Vector Propagation (SEVP) solver (see Madala, 1978; Sashegyi and Madala, 1989). For the SEVP solver, the initial geopotential derived from the observed temperatures is used to provide the prescribed value at a point on the lateral boundary (to give a unique solution) and to provide the first guess for the solver.

The balanced temperatures on the sigma surfaces are then found from the balanced geopotential, by inverting the hydrostatic equation. Use of the hydrostatic equation to compute the temperature introduces a $2 \Delta\sigma$ saw tooth wave structure in the vertical temperature profile. To remove this buckling, deviations of the temperatures T' from the mean temperature T^* are computed at sigma levels at the boundaries of the vertical layers (half way between the model sigma levels).

$$T' = \overline{T}^{\sigma} - \overline{T^*}^{\sigma} \quad (3.15)$$

The corrected temperatures are then obtained by adding the deviations (interpolated back to the model sigma levels) to the mean temperature and removing the mean of the deviations, so that the mean is unchanged.

$$T = T^* + \overline{T'}^{\sigma} - \langle \overline{T'}^{\sigma} \rangle \quad (3.16)$$

where $\langle \rangle$ is the horizontal average over the model domain on the sigma surface.

3.3 Application of Static Initialization

As an illustration of the scheme, the analyzed winds and temperatures, taken from the NMC analysis for 12Z January 23, 1986, are first interpolated to the model horizontal GALE grid for each of the 14 standard pressure levels from 50 to 1000 mb in a domain covering the eastern U.S. The horizontal resolution of the GALE grid is 0.5° in latitude and longitude in a domain 102.5°W to 57.5°W and 22.5°N to 47.5°N . The non-divergent wind is then computed as outlined above in section 3.1. In Fig. 3a we show the root-mean-square (rms) changes that result in the u-component of the wind field after

computing the non-divergent wind. Changes in the v-component of the wind field are similar. We see that average changes in the wind field are 2 m s^{-1} in the upper troposphere and 1.0 to 1.5 m s^{-1} in the middle and lower troposphere. The non-divergent wind and analyzed temperatures on the 14 standard pressure levels are then interpolated in the vertical to the ten model sigma levels. Our diagnostic equation for the geopotential is then used to compute a balanced geopotential on the sigma surfaces. In Fig. 3b we show the rms changes in the temperature at each of the model sigma levels resulting from solving for the non-linear mass balance. Changes in the temperature in the upper troposphere of 1°C reduce to 0.5°C in the middle troposphere. However in the lower troposphere large changes of 4.0°C are found. For comparison, the actual analyzed winds and temperatures are interpolated to the model sigma levels. In Figure 4, we compare the wind and temperature fields for the analyzed fields and the statically initialized fields, after having interpolated them back to 500 and 1000 mb pressure levels for display. At the 500 mb level, the temperature changes are small although the small trough is weaker as a result of the non-linear mass balance. At the 1000 mb level however the strength of the front is greatly weakened by the scheme, as is reflected in the large rms change in temperature seen in Fig. 3b.

4. IMPLICIT NORMAL MODE INITIALIZATION

We follow the vertical mode initialization scheme of Bourke and McGregor (1983) by using the model dynamical equations to filter out the high frequency inertia-gravity waves. Filtering conditions are applied to the model dynamical equations to derive linear diagnostic equations for the mass divergence and generalized geopotential, which are solved iteratively for the first three vertical modes of the numerical model. The further condition that the linearized potential vorticity is unchanged by the procedure is required to compute the vorticity. Boundary conditions on the generalized geopotential and mass divergence are required. As is customary, we keep the geopotential, temperature and pressure fixed at the lateral boundaries. To provide a boundary condition for the divergence, an approximate divergence is computed using the thermodynamic equation. In our scheme, changes in the tangential wind along the lateral boundaries are consistent with the changes in the vorticity and divergence computed by the scheme.

4.1 Inertia- Gravity Wave Modes

We express the dynamical equations in terms of the time tendencies of mass weighted vorticity, divergence and generalized geopotential, linearized about the basic state at rest with mean temperature T^* . The equations, with the β term included with the non-linear terms on the RHS, are

$$\frac{\partial \zeta}{\partial t} + f D = A_{\zeta} \quad (4.1)$$

$$\frac{\partial D}{\partial t} + \nabla^2 \Phi - f \zeta = A_D \quad (4.2)$$

$$\frac{\partial \Phi}{\partial t} + M_3 D = A_{\Phi} \quad (4.3)$$

Here f is the Coriolis parameter, which is a function of latitude and we have further defined the mass weighted vorticity ζ on the sigma surfaces as

$$\zeta = \frac{1}{h_y} \delta_x (h_y \overline{p_s^y} v) - \frac{1}{h_x} \delta_y (h_x \overline{p_s^x} u) \quad (4.4)$$

In the equations we have ignored the staggering of the vorticity and mass divergence relative to the generalized geopotential.

The freely propagating inertia-gravity waves in the model are solutions to the linearized equations (4.1), (4.2) and (4.3) with the forcing terms on the RHS of the equations equal to zero. Taking the time derivative of Eq. (4.2) and eliminating the tendencies of the generalized geopotential and the vorticity using Eqs. (4.3) and (4.1) with the terms on the RHS zero, we find that the mass divergence satisfies the equation

$$\frac{\partial^2 D}{\partial t^2} + \left[f^2 - M_3 \nabla^2 \right] D = 0 \quad (4.5)$$

In this case, the vertical modes, which are again found by solving for the eigenmodes of matrix M_3 , have the same vertical structure as that computed for the gravity wave modes in section 2.1. The "ageostrophic deviations" $f\zeta - \nabla^2\Phi$, which is f times the ageostrophic vorticity, can also be shown to satisfy the same equation. Eliminating D from the homogeneous form of Eqs. (4.1) and (4.3), an expression for the tendency of the linearized potential vorticity Q is obtained

$$\frac{\partial}{\partial t} (M_3 \zeta - f \Phi) = 0 \quad (4.6)$$

where the linearized potential vorticity Q is defined as

$$Q \equiv (\zeta - f M_3^{-1} \Phi) \quad (4.7)$$

That is, the linearized potential vorticity Q is unchanged by the inertia-gravity wave motions (see also Errico, 1986).

Now in terms of the amplitude of the mass divergence for each vertical mode, we have

$$\frac{\partial^2 d_k}{\partial t^2} + \left[f^2 - \lambda_k \nabla^2 \right] d_k = 0 \quad (4.8)$$

By including the Coriolis parameter in the linearization, we have introduced a low frequency cutoff for the inertia-gravity wave modes (see also Gill, 1982, for example). Assuming that the latitudinal wavelength of the modes are small compared to the change in the Coriolis parameter f with latitude, Eq. (4.8) is a wave equation with the phase speed of the plane wave modes given by

$$c_k^2 = \lambda_k \left[1 + \left[\frac{1}{\kappa R_d} \right]^2 \right] \quad (4.9)$$

where R_d is the Rossby radius of deformation defined by

$$R_d = \frac{\sqrt{\lambda_k}}{f} \quad (4.10)$$

and $\kappa = (\kappa_x, \kappa_y)$ is the horizontal wavenumber with $\kappa^2 = \kappa_x^2 + \kappa_y^2$. At the higher frequencies (that is, for wavelengths small compared to $2\pi R_d$), the phase speeds of the modes can be approximately given by $\sqrt{\lambda_k}$ and the modes are essentially the gravity wave modes computed in section 2.1. For our ten layer model and our limited area domains, the gravity waves for the first two modes are largely of high frequencies, since the Rossby radius of deformation is large (7,256 km and 2,907 km at 35°N for example, for the first and second modes, respectively), compared to the size of the model domain. However, for the higher modes, the Rossby radius of deformation becomes comparable or smaller than the domain size (1,126 km and 693 km for the third and fourth modes at 35°N , for example), and the gravity waves are of lower frequency.

4.2 Vertical Mode Initialization

4.2.1 Filtering Equations. We want to reduce the initial amplitude and tendency of the high frequency inertia-gravity waves so that their amplitude remains small during the integration of the numerical model. By requiring that initially the first and second derivatives of the mass divergence are zero, the amplitudes of the high frequency inertia-gravity waves will be kept small during integration of the model. Taking the time derivative of Eq. (4.2) and substituting for the tendencies of the generalized geopotential and vorticity

from Eqs. (4.1) and (4.3), an expression for the second derivative of the mass divergence with respect to time is obtained,

$$\frac{\partial^2 D}{\partial t^2} - M_3 \nabla^2 D + f^2 D = \frac{\partial A_D}{\partial t} - \nabla^2 A_\phi + f A_\zeta \quad (4.11)$$

The terms on RHS of Eqs. (4.1), (4.2), (4.3), which include the beta and non-linear terms, vary slowly with time compared to the time scale for high frequency gravity waves. Therefore we can ignore the time tendency of A_D in Eq. (4.11). Then applying our filtering conditions

$$\frac{\partial D}{\partial t} = \frac{\partial^2 D}{\partial t^2} = 0 \quad (4.12)$$

to Eqs. (4.2) and (4.11) respectively, we obtain

$$\nabla^2 \phi - f \zeta = A_D \quad (4.13)$$

$$M_3 \nabla^2 D - f^2 D = \nabla^2 A_\phi - f A_\zeta \quad (4.14)$$

To complete the set of equations a further condition is required. Assuming that the changes to our initial fields due to our filtering procedure will be small, then the changes to our fields represent that part of the fields due to the freely propagating inertia-gravity waves. If they are small, their motion can be described by the linearized equations (4.1), (4.2) and (4.3) with the terms on the RHS equal to zero. We can therefore require that the linearized potential vorticity be unchanged by our initialization procedure. Our filtering conditions are now

$$M_3 \nabla^2 \phi - f^2 \phi = M_3 (A_D + f Q_0) \quad (4.15)$$

$$M_3 \nabla^2 D - f^2 D = \nabla^2 A_\phi - f A_\zeta \quad (4.16)$$

$$\zeta - f M_3^{-1} \phi = Q_0, \text{ a constant} \quad (4.17)$$

We only need to filter the high frequency gravity waves, whose phase speeds are much larger than the typical speeds of weather systems. Therefore our

filtering conditions need only be applied for those vertical modes whose phase speeds are larger than about 25 m s⁻¹. For the ten layer model example shown in Table 2, filtering the first three modes is sufficient. Using the same vertical structure we defined earlier we can express our variables in terms of amplitudes for each of the vertical modes, where

$$e = E^{-1}\Phi, d = E^{-1}D, v = E^{-1}\zeta, \eta = E^{-1}Q.$$

Then our filtering conditions for the first three modes $k = 1, 2, 3$ can be written

$$\nabla^2 e_k - \frac{f^2}{\lambda_k} e_k = a_k \quad (4.18)$$

$$\nabla^2 d_k - \frac{f^2}{\lambda_k} d_k = \frac{1}{\lambda_k} b_k \quad (4.19)$$

$$v_k = \frac{f}{\lambda_k} \overline{e_k^{xy}} + \eta_0 \quad (4.20)$$

where the forcing functions a_k and b_k are the k^{th} elements of the vectors

$$a = E^{-1} (A_D + f \overline{Q_0^{xy}}) \quad (4.21)$$

$$b = E^{-1} (\nabla^2 A_\Phi - f \overline{A_\zeta^{xy}}) \quad (4.22)$$

Here we have reintroduced the averaging operators to take into account the staggering of the variables on our model grid. Since the forcing functions on the RHS of Eqs. (4.18) and (4.19) depend on the vorticity, divergence and geopotential, the set of equations is solved iteratively. With a first estimate for the variables given by the uninitialized fields, the forcing functions for the Helmholtz equations can be computed by integrating the model to obtain the non-linear terms A_D , A_Φ , A_ζ , and the initial potential vorticity Q_0 computed. By solving the Helmholtz equations for the amplitudes of generalized geopotential and divergence, new values of the variables can be computed. By recomputing the forcing functions the process can be repeated.

We require boundary conditions for the amplitudes of the generalized geopotential and the mass divergence to solve the Helmholtz equations at each iteration of our initialization procedure. We choose to keep Φ fixed at the boundary, so that at the boundary ϕ , T and p_s are unchanged by the

initialization procedure. It has been customary to set the amplitude of the mass divergence in the first three modes to zero along the boundary and adjusting the integrated divergence over the model domain. However for a domain with substantial topographic features along the boundary, this is too restrictive. We choose to estimate the divergence at the first mass point in from the boundary using the thermodynamic equation and neglecting the tendency of the generalized geopotential. In terms of the amplitudes of the vertical modes we have, using thermodynamic equation (4.3) with $\frac{\partial e}{\partial t} = 0$,

$$d_k = \frac{\{E^{-1}A_\phi\}_k}{\lambda_k} \quad (4.23)$$

4.2.2 Iterative Procedure. By defining incremental changes to the amplitudes of mass divergence, generalized geopotential and vorticity for each iteration i

$$d_k^i = d_k^{i-1} + \Delta d_k^i, \quad e_k^i = e_k^{i-1} + \Delta e_k^i, \quad v_k^i = v_k^{i-1} + \Delta v_k^i \quad (4.24)$$

an equivalent scheme can be derived for the incremental changes. For the i th iteration of the amplitudes of the generalized geopotential, mass divergence and vorticity, we have for the k th mode

$$\nabla^2 e_k^i - \frac{f^2}{\lambda_k} e_k^i = a_k^{i-1} \quad (4.25)$$

$$\nabla^2 d_k^i - \frac{f^2}{\lambda_k} d_k^i = \frac{1}{\lambda_k} b_k^{i-1} \quad (4.26)$$

$$\lambda_k v_k^i - f \overline{e_k^{i-1} xy} = \lambda_k v_k^{i-1} - f \overline{e_k^{i-1} xy} \quad (4.27)$$

We can use Eqs. (4.2) and (4.11) to compute the residuals which remained after the previous $(i-1)$ th iteration. Using Eq. (4.17) to substitute for the vorticity in the equation for the mass divergence Eq. (4.2) and multiplying by E^{-1} , we find that

$$\nabla^2 e_k^{i-1} - \frac{f^2}{\lambda_k} e_k^{i-1} = a_k^{i-1} - \frac{\partial d_k^{i-1}}{\partial t} \quad (4.28)$$

That is, the residual remaining after the $(i-1)^{th}$ iteration for the equation of the amplitude of the generalized geopotential is given by the tendency of the mass divergence. A similar residual can be computed for equation for the amplitude of the mass divergence. Taking the time derivative of Eq. (4.2) and substituting for the second time derivative of the mass divergence in Eq. (4.11) and then multiplying by E^{-1} , we find

$$\nabla^2 d_k^{i-1} - \frac{f^2}{\lambda_k} d_k^{i-1} = \frac{1}{\lambda_k} b_k^{i-1} - \frac{1}{\lambda_k} \frac{\partial}{\partial t} \left[\nabla^2 e_k^{i-1} - f \overline{v_k^{i-1}xy} \right] \quad (4.29)$$

That is, the residual remaining after the $(i-1)^{th}$ iteration is given by the tendency of the amplitude of the ageostrophic deviation $f\zeta - \nabla^2\phi$. Then by subtraction, we find that the incremental changes are forced by

$$\nabla^2 \Delta e_k^i - \frac{f^2}{\lambda_k} \Delta e_k^i = \frac{\partial d_k^{i-1}}{\partial t} \quad (4.30)$$

$$\nabla^2 \Delta d_k^i - \frac{f^2}{\lambda_k} \Delta d_k^i = \frac{1}{\lambda_k} \left[\nabla^2 \frac{\partial e_k^{i-1}}{\partial t} - f \frac{\partial \overline{v_k^{i-1}xy}}{\partial t} \right] \quad (4.31)$$

$$\Delta v_k^i = \frac{f}{\lambda_k} \Delta e_k^{i*xy} \quad (4.32)$$

where the terms on the RHS of Eqs. (4.30), (4.31) are now the residuals from the previous iteration. To compute the residuals on the RHS, we integrate the model one time step to compute adiabatic tendencies without friction, diabatic heating, or updating of the values of the model variables at the lateral boundaries. The residuals are then computed from

$$\frac{\partial d}{\partial t} = E^{-1} \frac{\partial D}{\partial t} = E^{-1} \left[\delta_x \left[\frac{\partial \overline{p_s^x u}}{\partial t} \right] + \frac{1}{h_x} \delta_y \left[\overline{h_x^y} \frac{\partial \overline{p_s^y v}}{\partial t} \right] \right] \quad (4.33)$$

$$\frac{\partial v}{\partial t} = E^{-1} \frac{\partial \zeta}{\partial t} = E^{-1} \left[\delta_x \left[\frac{\partial \overline{p_s^y v}}{\partial t} \right] - \frac{1}{h_x^y} \delta_y \left[h_x \frac{\partial \overline{p_s^x u}}{\partial t} \right] \right] \quad (4.34)$$

$$\frac{\partial e}{\partial t} = E^{-1} \frac{\partial \phi}{\partial t} = E^{-1} \left[M_1 \left[\frac{\partial \overline{p_s^T}}{\partial t} \right] + \left[R^T - \phi^* \right] \left[\frac{\partial \overline{p_s}}{\partial t} \right] \right] \quad (4.35)$$

In terms of the changes to the amplitude of the generalized geopotential our boundary condition on changes to e becomes

$$\Delta e_k = 0. \quad (4.36)$$

In terms of changes to the amplitude of the divergence the boundary condition becomes

$$\Delta d_k = \frac{1}{\lambda_k} \frac{\partial e_k}{\partial t} \quad (4.37)$$

4.2.3 Changes to the Horizontal Wind, Temperature and Surface Pressure.

The resulting changes to the horizontal wind field can then be computed from the changes in the divergence and vorticity by solving for the changes in the velocity potential and the stream function. The grid stencil for the divergence (and velocity potential) and the vorticity (and stream function) is shown in Fig. 5. That is, given the change in the divergence $\Delta D = E \Delta d$ we solve a Poisson's equation

$$\nabla^2 \Delta \chi = \Delta D \quad (4.38)$$

for the change $\Delta \chi$ in the velocity potential χ at the interior mass (generalized geopotential Φ) points (see Fig. 5) for each sigma level of the model. The boundary condition on $\Delta \chi$ is

$$\Delta \chi = 0 \quad (4.39)$$

at the model lateral boundaries. This produces no change in the tangential wind along the model boundaries, but only change to the divergent wind in the interior. Now given the change in the vorticity $\Delta \zeta = E \Delta v$ we solve a Poisson's equation

$$\nabla^2 \Delta \psi = \Delta \zeta \quad (4.40)$$

for the change $\Delta \psi$ in the stream function ψ for each sigma level of the model. The vorticity changes calculated from Eq. (4.32) are specified at interior points staggered half a grid distance from the mass and wind points. Since the integrated vorticity over the domain may change, the integrated tangential wind along our model boundary may change. We therefore prescribe a boundary condition of no change in the stream function

$$\Delta \psi = 0 \quad (4.41)$$

at fictitious boundary staggered half a grid point outside our model boundary, implying that the non-divergent wind does not change there. However the non-divergent wind and hence the tangential wind does change along the model

boundary. The gradients of the changes of the stream function and the velocity potential at each sigma level of the model then define the changes to the mass weighted wind,

$$\Delta(\overline{p_s^x} u) = \delta_x \Delta\chi - \delta_y \Delta\psi \quad (4.42)$$

$$\Delta(\overline{p_s^y} v) = \delta_y \Delta\chi + \delta_x \Delta\psi \quad (4.43)$$

With the changes to the wind field defined in this way, the changes to the wind field along the lateral boundaries of the model are consistent with the changes in the vorticity and mass divergence over the model domain.

Following Temperton (1984), the changes in the surface pressure p_s , and the temperature T can be derived directly from changes in the generalized geopotential Φ . We consider the linearized equations for the motion of the freely propagating gravity waves

$$\frac{\partial \Phi}{\partial t} = -M_3 D \quad (4.44)$$

$$\frac{\partial p_s T}{\partial t} = -M_2 D \quad (4.45)$$

Now eliminating D we can relate the tendencies of surface pressure and temperature to that of the generalized geopotential for gravity wave motions, so that

$$\frac{\partial p_s}{\partial t} = -N_2^T D = N_2^T M_3^{-1} \frac{\partial \Phi}{\partial t} \quad (4.46)$$

$$\frac{\partial p_s T}{\partial t} = M_2 M_3^{-1} \frac{\partial \Phi}{\partial t} \quad (4.47)$$

Since the changes derived from our initialization procedure represent the gravity wave part of the flow, we can assume a wave solution for the changes. The changes to the surface pressure and temperature are then related to the changes in the generalized geopotential by

$$\Delta p_s = N_2^T M_3^{-1} \Delta \Phi = N_2^T M_3^{-1} E \Delta e \quad (4.48)$$

$$\Delta(p_s T) = M_2 M_3^{-1} \Delta \Phi = M_2 M_3^{-1} E \Delta e \quad (4.49)$$

4.3 Convergence of the Vertical Mode Scheme

To test our vertical mode initialization procedure, we use the 12 hourly NMC 2.5° hemispheric analyses for the period 12Z January 23 to 12Z January 29, 1986, for the period of the second Intensive Observing Period (IOP) of GALE. The initial synoptic situation, showing a cold front moving off the east coast of the U.S. and a low in the Gulf of Alaska, is shown in Figs. 4 and 8. During this IOP, a coastal front develops along the east coast of the U.S. and subsequently, a cyclone develops offshore when the low system from the Gulf of Alaska reaches the east coast. The thirteen analyses for the period are interpolated to the model coordinates for the two different horizontal grids with differing domain size and resolution and then initialized with the vertical mode scheme for the first three vertical modes only. The US grid covers a domain including the continental U.S.A. with a horizontal resolution of 2° longitude by 1.5° latitude. The GALE grid covers a smaller domain including the eastern half of the U.S.A. and extending out over the Atlantic to 52.5°W with a finer horizontal resolution of 0.5° in longitude and latitude. In the vertical, both grids use ten equally spaced sigma levels. The smoothed model topography used for each grid is shown in Fig. 6a and b. For the GALE grid, a case with smoother topography along the lateral boundary, shown in Fig. 6c, is also generated by merging the courser topography from the US grid (Fig. 6a) with the GALE topography (Fig. 6b) in a boundary zone with a width of five degrees in latitude and longitude. The merging is carried out by linearly interpolating the courser topography from the US grid to the GALE grid, and replacing the GALE topography at the first seven points in from the boundary. At the eight to tenth points, a linear combination is used with weights given by (0.75, 0.25), (0.5, 0.5) and (0.25, 0.75) for the course topography and GALE topography, respectively.

4.3.1 Using the low resolution US grid. At the analysis times, the initial amplitudes for the mass divergence and vorticity are computed on the US grid for each of the vertical modes, prior to initialization. The mean amplitudes of the mass divergence and vorticity for each of the vertical modes are averaged over the US domain and in time over the period of interest for the thirteen analyses and shown in Table 3. The mean amplitude of the vorticity decreases with increasing mode number, while the mean amplitude of

TABLE 3: The mean mass divergence and vorticity on the sigma surfaces of the model for the US grid, averaged for the week of 12Z January 23 to 12Z January 29, 1986.

Mode No.	Mass Divergence (dynes cm ⁻² s ⁻¹)	Vorticity (dynes cm ⁻² s ⁻¹)
1	7.68	82.04
2	7.54	36.28
3	12.63	36.98
4	9.08	32.86
5	7.63	17.53
6	6.32	11.82
7	4.81	8.14
8	3.81	5.56
9	2.92	4.41
10	1.82	2.65

the mass divergence maximizes at the third mode. As expected, the amplitudes of the divergence are an order of magnitude smaller than the amplitude of vorticity for the external mode. The analyses, interpolated to the model sigma coordinates for the US grid, are initialized with the vertical mode scheme for the first three vertical modes only. After each iteration of our vertical mode initialization procedure, the resulting root-mean-square (rms) changes in the amplitudes of the mass divergence, vorticity, generalized geopotential and surface pressure were computed. In Fig. 7 we show these rms changes, averaged for all the analysis times, at each iteration of the initialization procedure. For each of the first three vertical modes initialized, it can be noted that the mean rms changes in the amplitudes of the divergence at the first iteration of the procedure are as large as the initial amplitudes themselves, while the changes in the amplitude of the vorticity are very small compared to

their initial values. For the first two modes, the changes in the amplitude of the mass divergence decrease rapidly with increasing iterations, with the changes being very small after just two iterations. For the third mode, the changes in amplitudes of the mass divergence do not decrease as rapidly. The mean rms changes in the surface pressure, shown in Fig. 7d are less than a mb for each iteration.

To demonstrate the effect of the number of modes initialized on the changes in the amplitude of the mass divergence with each iteration, the number of modes initialized is varied from one to six modes for the case of one analysis on 12Z January 23, 1986. In Fig. 7e we show the changes in the mass divergence for the highest mode number initialized for each of the cases. The rate of decrease in the mass divergence changes increases as the higher order modes are initialized, and in fact increases with iteration for the sixth mode initialized. For the first two modes, the gravity waves are essentially of high frequency, since the Rossby radius of deformation is so large for these modes (see section 4.1). As the mode number increases however, the Rossby radius of deformation decreases and the frequency of the inertia-gravity mode decreases for the same wavelengths. The tendencies of the mass divergence for the gravity modes are then much less for the higher order modes, and convergence of the scheme would be expected to be slower.

As an illustration, we demonstrate the result of the vertical mode initialization using the NMC analysis for 12Z January 23, 1986. The initial analyzed sea-level pressure and wind field at the sigma level $\sigma = 0.25$ are shown in Figs. 8a and 8b. A deep surface low of 987 mb lies west of Greenland and high pressure dominates the eastern U.S. Aloft at the jet level, strong jet maxima of about 55 and 48 m s^{-1} straddle a trough over the eastern U.S., with a further jet maximum upstream, entering the domain from the Gulf of Alaska. The surface pressure change resulting from the vertical mode initialization is shown in Fig. 8c. The surface pressure adjustments due to initialization are small, with an rms change in this case of 0.9 mb and at most several mb in places. After the initialization, the vertical motion $\dot{\sigma}$ in the middle troposphere at a sigma level $\sigma = 0.45$, is shown in Figure 8d. Upward motion relative to the sigma surface (negative values of the vertical motion) is found on the south side of the jet off the coast of North America

and also ahead of the exit region of the jet streak. Sinking motion is found in the region of the high surface pressure over the eastern U.S. In sigma coordinates, the sigma surfaces follow the sloping topography, with the result that westerly flow in the lee of mountains gives rise to strong upward motions on the sigma surface. Such strong topographic signatures are seen in the lee of the Rockies and the Appalachian mountains. In Fig. 9 we compare the contributions to the vertical motion from the first three modes (Fig. 9a), which are initialized, and from the remaining modes (Fig. 9b), which are unchanged by the initialization procedure. The strong signal due to the mountains clearly dominates the vertical motion computed for the first three modes, while smaller synoptic scale magnitudes are apparent in the remaining modes.

The vertical mode initialization scheme removes that portion of the initial wind and mass fields that describe the inertia-gravity waves (for modes 1 to 3). Such structures then should be seen in the changes made to the analyzed fields resulting from the initialization. In Fig. 10a we show the wind and geopotential height changes at the jet level $\sigma = 0.25$. At the jet level, we see that the geopotential changes reach 30 to 40 gpm in places. The wind field shows flow of several m s^{-1} crossing the contours of geopotential height, indicative of inertia-gravity wave structures (see Matsuno, 1966, for example). At the same level the changes in temperature and the u and v components of the wind are shown in Fig. 10b, c and d. The changes in the temperature are at most a degree, while changes in the wind components are at most several m s^{-1} . Typical vertical profiles of the rms changes in the u component and the temperature are shown in Fig. 11. The resulting changes in the mean temperature, shown in Table 4, are very small and at most 0.15°C in the upper troposphere.

4.3.2 Using the high resolution GALE grid. For the smaller GALE grid with 0.5 degree resolution, the mean amplitudes for the vorticity and mass divergence are shown in Table 5, for each of the vertical modes. For each iteration of our vertical mode initialization scheme, the mean rms changes in the amplitudes of the divergence and the vorticity are shown in Fig. 12, for the first three modes initialized. In this case, the amplitude changes for the geopotential (or equivalently vorticity) decrease very rapidly for all the

TABLE 4: The root-mean-square changes in the mean temperature on the US grid for 12Z January 23, 1986, resulting from vertical mode initialization.

Model Level	Sigma Level	ΔT^* (°K)
1	0.05	0.052
2	0.15	0.143
3	0.25	0.098
4	0.35	0.048
5	0.45	0.022
6	0.55	0.018
7	0.65	0.014
8	0.75	0.069
9	0.85	-0.001
10	0.95	-0.011

three modes. However, the amplitude changes for the mass divergence in the case of the third mode do not decrease as rapidly and in fact do not reduce to zero. On the GALE grid, smaller scale topographic features of appreciable amplitude are present (see Fig. 6b), compared to the US grid (see Fig. 6a). For the third mode, the gravity modes at these smaller scales are of high frequency and of shorter vertical scale. Non-linear effects of the gravity waves interacting with the topography can become significant. Also in the boundary zone, where there was no special smoothing of the topography, the divergence forced by the topography for these modes can get quite large. Then the errors in the computed boundary divergence can be large also. To test the latter, the initialization is repeated for two cases with the topography on the GALE grid smoothed in a five degree boundary zone, as outlined in the beginning of section 4d (see Fig. 6c). In Fig. 12c we compare the changes in the amplitude of the mass divergence when the unsmoothed (Fig. 6b) and the

smoothed topography (Fig. 6c) are used for a typical example (such as for the analysis on 12Z January 23, 1986) and for an extreme example with much larger changes at higher iterations (for 12Z January 24). In both cases, the changes in the mass divergence decrease much more rapidly when the topography is smoothed in a five degree boundary zone.

For the smaller GALE grid, the initial sea level pressure and wind field in the upper troposphere at sigma level $\sigma = 0.25$ for 12Z January 23, 1986 is shown in Fig. 13a and b. A front is shown moving off the east coast of the U.S. with high pressure dominating the eastern half of the U.S. A strong jet streak is leaving the domain at the north-east corner of the domain and a minor short wave trough with its associated jet maximum is located on the Gulf of Mexico. The surface pressure changes, shown in Fig. 13c are small, being at

TABLE 5: The mean mass divergence and vorticity on the sigma surfaces of the model for the GALE grid, averaged for the week of 12Z January 23 to 12Z January 29, 1986.

Mode No.	Mass Divergence (dynes cm ⁻² s ⁻¹)	Vorticity (dynes cm ⁻² s ⁻¹)
1	7.53	92.17
2	8.12	39.21
3	15.11	42.80
4	10.05	37.65
5	9.17	19.48
6	6.73	12.05
7	4.79	7.96
8	3.84	5.72
9	2.74	4.32
10	1.72	2.51

most a mb. In this GALE domain, the western boundary is at about 1 km, sloping down to 500 to 250 meters within 5 degrees in from the boundary (Fig. 6b). The topographic features in the domain produce a strong signal in the vertical motion field shown in Fig. 13d. The increasing westerly shear with height at the western boundary and in the lee of the Appalachians, produces strong rising motion in sigma coordinates. Away from the influences of sloping sigma surfaces over the topography, sinking motion is observed in the high pressure along the Mississippi river valley and rising motion on the south side of the jet axis off the east coast. Qualitative agreement is found with the vertical motion field produced for the larger US domain. When the smoother topography in the boundary zone (see Fig. 6c) is used, the large noisy values in the vertical motion along the northern boundary and south-west corner (seen in Fig. 13d) are removed, while the interior remains unchanged (see Fig. 13e). The strong signal remaining in the vertical motion field along the western boundary, due to the high gradients in the topography there, demonstrates the importance of the specification of accurate boundary conditions used for the solution of the divergence changes in the initialization procedure. For this case the resulting changes in the geopotential and wind and temperature changes at $\sigma = 0.25$ are shown in Fig 14. In the upper troposphere, the resulting rms changes in the wind components are about 1 m s^{-1} , while the rms temperature changes are about 0.5°C . In the vertical, the variation of the rms changes in the wind components and temperature with each iteration is similar to that shown for the US grid in Fig. 11, decreasing with increasing number of iterations. Three iterations are sufficient for the changes in the wind and temperature to be very small.

5. MODEL INTEGRATIONS WITH STATIC INITIALIZATION

To test the effect of the split-explicit time integration scheme in smoothing the unwanted high frequency oscillations in the NRL model, the model is integrated on the GALE grid with uninitialized data both with the split-explicit scheme described in section 2.2 and with an explicit time integration scheme of smaller time steps. Integrations with varying degrees of static initialization are then compared in three other experiments. Time series of the surface pressure and the vertical motion $\dot{\sigma}$ in sigma coordinates at selected points on the GALE grid were compared in the five experiments, which are listed in Table 6. The NMC 2.5 degree hemispheric analysis for 12Z January 23, 1986 is used to start the integrations for each of the experiments. This is a case of a cold-air damming and coastal front event, which occurred from January 23-25, 1986, during GALE. The GALE grid covers a domain from 22.5°S to 47.5°N in latitude and 102.5°W to 57.5°W in longitude, with 0.5 degree horizontal resolution.

For the experiments here, the Perkey Kreitzberg lateral boundary formulation, described in section 2.3a is used. To provide the boundary tendencies for each of the experiments, the non-divergent wind is computed for

TABLE 6: Experiments with Static Initialization on GALE grid.

- 1A Explicit Integration with uninitialized initial state using leapfrog scheme with a $2 \Delta t$ time step of 60 secs.
- 1B Split-Explicit Integration with uninitialized initial state, using a $2 \Delta t$ time step of 300 secs.
- 1C Split-Explicit integration with Non-divergent Initial State, using a $2 \Delta t$ time step of 300 secs.
- 1D Split-Explicit integration with Static Non-linear Mass Balance, using a $2 \Delta t$ time step of 300 secs.

Supplementary experiment:

- 1C' Same as 1C, but with boundary tendencies computed from non-divergent wind and observed temperatures.

each of the 12 hourly NMC analyses, the fields interpolated to the sigma coordinates of the model and a statically balanced temperature computed as outlined in section 3.2. Initial boundary values and 12 hour tendencies are then extracted for the 5 point boundary zone, defined in section 2.3a. To provide the same boundary values in each of the experiments, the initial fields for each experiment are merged with the statically balanced fields in the boundary zone, using the linear function α defined by Eq. (2.19). That is, we multiply the initial fields by $(1-\alpha)$ and add α times the statically balanced fields in the boundary zone.

5.1 Damping by Split-Explicit Scheme

In expt 1A, the model is integrated in time with a conventional leapfrog scheme for 12 hours with a $2 \Delta t$ time step of 60 s starting from uninitialized data. Oscillations of surface pressure of as much as 5 to 8 mb of amplitude and periods of 1 to 2 hours are observed in the first 12 hours of integration. Curve A in Fig. 15a shows these typical oscillations in the surface pressure at a grid point at 90°W and 35°N in the western half of the domain. Curve A in Fig. 15b shows the vertical motion $\dot{\sigma}$ interpolated to a sigma level at $\sigma = 0.5$, for the same grid point. The curve A shows a typical rapid adjustment (increase in this figure) in the first 6 of the integration with smaller oscillations of periods of 2 to 4 hours superimposed. The higher frequency oscillations in surface pressure are largely due to the barotropic external gravity mode while the adjustment and oscillations in the vertical motion in the middle troposphere are largely due to the internal gravity modes.

In expt 1B, the model is integrated for 48 hours with the split-explicit scheme using a $2 \Delta t$ time step of 300 s starting again from the same uninitialized data. For the first hour or so the oscillations in the surface pressure (Curve B in Fig. 15a) are the same as in the explicit integration. However the oscillations are strongly damped in the next three hours of integration. Little difference is noticed in Fig. 15b in the variation of $\dot{\sigma}$ at $\sigma = 0.5$ between the explicit (Curve A) and split-explicit (Curve B) integrations. One can conclude that the split-explicit integration scheme acts to reduce the amplitude of the unwanted external gravity waves in the first three to four hours of integration.

5.2 Non-Divergent and Statically Balanced Initial Fields

As outlined in section 3.1, the analyzed vorticity on pressure surfaces is used to first calculate the non-divergent component of the wind. A first guess of the surface pressure and temperature is found by interpolation to the model topography. The non-divergent wind, analyzed temperature and humidity are then interpolated to the model sigma levels. The initial and non-divergent wind fields at 1000 mb and 500 mb were compared in Fig. 4. In expt 1C, a 48 hour integration using the split-explicit scheme is then performed with this data. As shown by Curve C in Figure 16a, the amplitude of the initial oscillations of the surface pressure are reduced to 2 to 3 mb and are largely damped out after 3 hours. Oscillations in the surface pressure of a mb can be still seen at a grid point at 83°W and 35°N (not shown) over the Appalachian mountains. Curve C in Figure 16b shows that the strong adjustment (increase) in the vertical motion $\dot{\sigma}$ is still present in the first 6 hours and the superimposed higher frequency oscillations are only slightly reduced in amplitude. By removing the divergent component of the wind from the analyzed data the initial value of the vertical motion is also reduced. On sigma surfaces over sloping topography, a vertical shear of the non-divergent wind will introduce divergence on the sigma surfaces, as will errors caused by vertical interpolation. By largely removing the horizontal divergence we have essentially removed the external gravity mode after three hours of integration.

In a supplementary experiment 1C', boundary tendencies are computed from analyzed temperatures and the non-divergent winds on pressure surfaces, instead of from statically balanced temperatures. For initial conditions, the analyzed temperatures and winds are interpolated to the sigma coordinates without merging the statically balanced temperatures in the boundary zone. The integrations in this case were largely indistinguishable from those expt 1C. Since in the PK scheme, we damp only the tendencies in the boundary zone, initial differences in the boundary zone in the two cases are damped, leading to similar integrations. Little difference was also found in the integrations if the mass divergence is removed from the initial fields on the sigma surfaces instead of on the pressure surfaces.

A static initialization of the mass field is performed using the non-linear mass balance equation in sigma coordinates, as outlined in section 3.2. The non-linear balance equation is used to derive a balanced geopotential and temperature field from the non-divergent wind field. In Fig. 4 we showed the initial and balanced temperature fields interpolated to the 1000 mb pressure level. As mentioned in section 3.3, the balanced temperature field is much smoother than the initial field, due to the smoothing of the Laplacian operator. In expt 1D, a 48 hour integration was carried out starting from this statically initialized data. The oscillations in the surface pressure, shown in Curve D of Figure 16a, are of the same amplitude as in the non-divergent case (Curve C in Fig. 16a), being damped after 3 hours of integration. However, a small mean drift of about a mb is seen to develop in the surface pressure (curve D) during the 12 hours of integration. Again oscillations of surface pressure of a mb still remain over the Appalachian mountains. The vertical motion shown in curve D of Figure 16b still shows the rapid adjustment (increase) during the first 5 hours, but the higher frequency oscillations are much reduced in amplitude and mostly eliminated after 4 hours of integration. The non-linear balance of the mass field essentially removes the internal gravity waves except for the initial adjustment in the first 4 hours.

When using the split-explicit scheme and starting from uninitialized or initialized data, the 12 to 48 hour forecasts are very similar. Even in expt 1D, where the static initialization had smoothed out the initial temperature gradient along the front (see Fig. 4), the model regenerates the temperature gradient and intensifies it further in the first 12 hours. As an example, we show in Fig. 17, the variation of the surface pressure and the vertical motion at a grid point in the second twelve hours of integration for expts 1B, 1C and 1D. In the case of expts 1B and 1C, the variation in the surface pressure is much the same. Since the same boundary values and tendencies were used in the three expts (expts 1B, 1C and 1D), we see that the drift in the surface pressure, produced by the static initialization, is eliminated in the second twelve hours. Only in the case of expt 1A, with a 12 hour explicit time integration with uninitialized data, are high frequency oscillations in the surface pressure and vertical motion still substantial after 12 hours of integration, producing more noticeable differences in the 12 hour forecast.

6. MODEL INTEGRATIONS WITH VERTICAL MODE INITIALIZATION

To assess the effect of the vertical mode initialization procedure in removing the high frequency gravity wave oscillations, the NRL model is integrated starting from initialized and uninitialized data, for the two different US and GALE grids of differing domain size and horizontal resolution. The influence of two different lateral boundary treatments, namely the tendency relaxation scheme of Perkey and Kreitzberg (PK) and the Davies relaxation scheme, is also investigated. The experiments are summarized in Table 7. As described in section 2.3, model computed tendencies are relaxed to specified boundary tendencies in a boundary zone of 5 points at each time step in the PK scheme. The 12 hourly boundary tendencies, derived from the NMC hemispheric analyses interpolated to the model grid. In the Davies scheme, large scale boundary values are computed by linear interpolation from 12 hourly values, derived from NMC analyses, which have been interpolated to the model grid. The computed model variables are then relaxed to the boundary

TABLE 7: Experiments with Vertical Mode Initialization.

US GRID (with a $2 \Delta t$ time step of 400 secs):

- 2B 24 Hour integration with uninitialized initial state, using PK lateral boundary scheme.
- 2C 24 Hour integration with initialized initial state, using PK lateral boundary scheme.
- 2E 24 Hour integration with initialized initial state, using Davies lateral boundary scheme.

GALE GRID (with a $2 \Delta t$ time step of 100 secs):

- 3B 12 Hour integration with uninitialized initial state, using PK lateral boundary scheme.
- 3C 12 Hour integration with initialized initial state, using PK lateral boundary scheme.
- 3D 12 Hour integration with uninitialized initial state, using Davies lateral boundary scheme.
- 3E 12 Hour integration with initialized initial state, using Davies lateral boundary scheme.

values themselves at each time step in a boundary zone of 6 points. For integrations with initialized fields, the analyzed fields interpolated to the model grid are also initialized to provide balanced boundary values and tendencies. In this way we prevent a lot of noise propagating from the boundary into the interior of the model domain, which could contaminate the results. On the two grids, the smoothed topography, as shown in Fig. 6 is used for the integrations.

6.1 Integrations on the US grid

In the first three experiments listed in Table 7, we compare 24 hour integrations with initialized and uninitialized initial conditions on the US grid, using the two different lateral boundary treatments. The split-explicit integration scheme is used in each case with a $2 \Delta t$ time step of 400 seconds. In expt 2B, the PK tendency relaxation scheme is used for the lateral boundary treatment with uninitialized initial conditions. The 12 hourly boundary tendencies are derived from the uninitialized analyzed fields. Initial oscillations of nearly 8 mb in the surface pressure, caused by the uninitialized initial conditions, are damped by the split-explicit scheme in the first 6 hours or so, as was shown in section 5.1. As an example, curve B in Figs. 18a and b shows the variation of the surface pressure with time at a grid point at 90°W and 35°N on the US grid. In expt 2C, initialized initial conditions are used with the PK lateral boundary scheme. The boundary tendencies in this case are derived from initialized NMC analysis fields. With initialized initial conditions, the high frequency oscillations are almost completely removed, even over high topography such as the Rocky Mountains. An example with the surface pressure can be seen with curve C in Figs. 18a and b. Large high frequency oscillations in the vertical motion are also eliminated for the interior grid points, as can be seen in Figs. 18c and d. Even though both expts 2B and 2C used somewhat different boundary conditions (uninitialized values versus initialized values) no mean drift was produced. In the boundary zone, the difference seen between the results in expt 2B and that in expt 2C, is due to gravity waves, which are damped in time by the PK scheme.

In expt 2E, the Davies scheme is used with initialized initial conditions. As can be seen by Curve E in Fig. 18, use of the Davies scheme produces a similarly smooth integration of the surface pressure and the same variation in the vertical motion. However, the variation of the surface pressure with time in this case does differ somewhat after 4 hours from that found with the PK tendency relaxation scheme. The PK scheme produced some artificially larger vertical motions at the first grid point inside the boundary. The time variation of the surface pressure and vertical motion at a grid point in the boundary zone, at a distance of three times the grid spacing in from the boundary, is shown in Fig. 19. A linear variation of the surface pressure is seen with time in the boundary zone when the Davies scheme is used. With the PK scheme oscillations of long period of about 12 hours can be seen in the surface pressure and the vertical motion. The variation of the vertical motion is small for the Davies scheme at this point. This noise, generated by the PK scheme in the boundary zone, may have propagated into the interior to cause the differences seen in the integrations after 4 hours. The difference can be seen (in Fig. 18b for example) as a low amplitude oscillation of long period at 12 to 24 hours integration. However little overall differences can be seen in the 12 and 24 hour forecast fields between each of the experiments.

6.2 Integrations on the GALE grid

A series of four integrations are conducted on the GALE grid with uninitialized and initialized initial conditions with the two lateral boundary schemes (see last four experiments listed in Table 7). In each case, the split-explicit scheme is used for time integration with a $2 \Delta t$ time step of 200 seconds. For the cases with initialized initial conditions, 12 hourly boundary values and tendencies are computed from the NMC analyzes, interpolated to the model grid and then initialized. The integrations with initialized initial conditions, expts 3C and 3E, essentially remove the high frequency oscillations. As an example in Fig. 20, we show the variation of surface pressure and the vertical motion in the middle troposphere at two grid points on the GALE grid for the different integrations with initialized and uninitialized initial conditions. The grid point at 90°W and 35°N is in the western half of the domain, while the grid point at 83°W and 35°N lies on the top of the Appalachian Mountains. With the PK lateral boundary scheme,

oscillations of a mb or so are seen during the integration period when uninitialized initial conditions are used (Curve B). With initialized initial conditions obtained with the vertical mode scheme, the oscillations are removed except for an initial hump of 0.5 mb in the surface pressure seen after the first two hours of integration (Curve C). With the Davies scheme and initialized initial conditions, a smoother variation of the surface pressure is seen (Curve E). The rapid initial adjustment in the vertical motion has been largely removed, leaving a slower increase in the vertical motion with time.

In expt 3D, the Davies scheme for the lateral boundary treatment is used with uninitialized initial conditions. A different response is produced in the surface pressure, while the response in the vertical motion field is similar to the PK scheme for grid points in the interior of the domain. In Fig. 21, we compare the surface pressure variation and vertical motion in the middle troposphere at our two grid points for initialized and uninitialized initial conditions, when the Davies scheme is used. In the case of the Davies scheme with uninitialized initial conditions, an initial shock of large amplitude is seen in the surface pressure (curve D in Figs. 21a and b), which is rapidly damped in the first 4 hours or so. The scheme acts to damp any gravity waves that propagate into the boundary zone from the interior. Using initialized initial conditions, this initial shock is eliminated (curve E in Figs. 21a and b). With time, the integrations in the first 12 hours differ by as much as a mb or so in expts 3D and 3E (see Fig. 21). The difference is explained by the fact that in expt 3D, we force uninitialized boundary values in the boundary zone, and the model solution in the interior is forced to adjust in the first three of four hours of integration.

In the boundary zone large differences are found when using the different boundary treatments. In Figs. 22a and b, we show the variation of the surface pressure at two grid points in the boundary zone for the different lateral boundary treatments. The grid point at 59°W and 40°N lies a distance of three grid lengths from the lateral boundary (at 57.5°W), while the grid point at 58°W and 40°N is a distance of one grid length. With the Davies scheme, the boundary values are strongly forced in the boundary zone, which is reflected in the linear variation in the surface pressure in the boundary zone (see

curve E in Figs. 22a and b, for example). With the PK scheme, oscillations in the surface pressure, with an amplitude of one to two mb and period of about twelve hours, can be seen in the boundary zone (see curve C in Fig. 22a and b). The two schemes also differ in their response in the vertical motion in the boundary zone. With the PK scheme, the vertical motion piles up at the first grid point in from the boundary, while with the Davies scheme, larger vertical motions are found in the zone between the interior region and the boundary zone. The variation of the vertical motion at the two grid points in the boundary zone is shown in Figs. 22c and d. Using the Davies scheme, curve E in Fig. 22c shows a slow increase of the vertical motion to $20 \times 10^{-3} \text{ hr}^{-1}$, for the grid point which is a distance of three grid lengths in from the lateral boundary. In Fig. 22d, curve E shows a slower linear variation of the vertical motion, increasing to $10 \times 10^{-3} \text{ hr}^{-1}$, at the grid point one grid length from the boundary. With the PK scheme low amplitude changes in the vertical motion occur at the boundary between the boundary zone and the interior (see curve C in Fig. 22c), while unrealistically large values of $30 \times 10^{-3} \text{ hr}^{-1}$ are reached in the vertical motion at the grid point lying a distance of one grid length in from the lateral boundary (see curve C in Fig. 22d). In Fig. 23, we compare the surface pressure variation and vertical motion in the middle troposphere at our two grid points in the boundary zone for initialized and uninitialized initial conditions, when the Davies scheme is used. The boundary values are again strongly forced in the boundary zone in both cases. The initial shock in the surface pressure variation in curve D, in Fig. 23a, is eliminated by the initialization (curve E).

7. SUMMARY AND CONCLUSIONS

To remove the high frequency gravity wave oscillations, various initialization procedures have been tested for use with the Naval Research Laboratory limited area numerical weather prediction model. Operational analyses obtained from the National Meteorological Center (NMC) for the period of the second intensive observing period of the GALE experiment are used to test the procedures and provide initial and boundary conditions for model integrations. The model is integrated with initial conditions with varying degrees and type of initialization on two different model grids, one a low resolution grid of 2° longitude by 1.5° latitude covering the continental U.S. (US grid) and the other a higher resolution grid of 0.5° in latitude and longitude covering the eastern U.S. (GALE grid). The influence of two different lateral boundary treatments, namely the tendency relaxation scheme of Perkey and Kreitzberg (PK) and the Davies relaxation scheme, are compared. For integrations with initialized fields, the NMC analyzed fields interpolated to the model grid are also initialized to provide balanced boundary values and tendencies. This reduces noise in the boundary zone, which can propagate into the interior of the domain and contaminate our test.

In the static initialization procedure, the non-divergent wind is first computed for the analyzed winds on the pressure surfaces, by solving for the streamfunction. The non-divergent wind and the analyzed temperatures are then interpolated to the sigma coordinates of the model. A diagnostic relation is then derived for the geopotential on the sigma surfaces of the numerical model, by ignoring the tendency of divergence, non-linear vertical advection and friction. The initial non-divergent wind and analyzed temperatures, interpolated to the sigma surfaces are used to compute the non-linear forcing terms. With the tangential wind defined along the model lateral boundary with the C grid, consistent boundary conditions for the normal derivatives of the geopotential are easily obtained by ignoring the tendencies in the momentum equations.

The NRL model uses the split-explicit scheme to integrate in time. The scheme is compared to a centered difference scheme by integrating the model on the GALE grid. The split-explicit scheme has been shown to reduce the

amplitude of the unwanted external gravity wave oscillations in the first three to four hours of integration. However, a typical rapid adjustment with superimposed oscillations occurs in the mid-troposphere vertical motion in the first 4 to 6 hours of integration. The new static initialization procedure is also tested on the GALE grid. By interpolating the non-divergent wind and analyzed temperature to the model sigma surfaces, the amplitude of the initial oscillations of the surface pressure are reduced to 2 to 3 mb and are largely damped out after 3 hours. Using the non-divergent wind and performing a static non-linear balance of the mass field, provides a balanced initial state, except for a smooth initial adjustment of the vertical motion in the first five hours or less of integration and a small mean drift in the surface pressure. For the varying degrees of static initialization, similar 12 to 48 hour forecasts are produced when the split-explicit scheme for time integration was used.

A vertical mode initialization scheme following that of Bourke and McGregor (1983) has been developed for use with the NRL model. Filtering conditions are applied to the model dynamical equations to derive to linear diagnostic equations for the mass divergence and geopotential, which are solved iteratively for the first three vertical modes of the numerical model. These modes have phase speeds which are much faster than those of meteorological systems. The further condition that the linearized potential vorticity is unchanged by the procedure is required to compute the vorticity. The observed wind and temperature is first interpolated to the sigma surfaces of the model. The iterative procedure is then used to compute incremental changes to the generalized geopotential, mass divergence and vorticity for the first three vertical modes of the numerical model. As is customary, we keep the geopotential, temperature and pressure fixed at the lateral boundaries in the scheme. To provide a boundary condition for the divergence however, an approximate divergence at the boundary is computed using the thermodynamic equation. In our scheme, changes in the tangential wind along the lateral boundaries are consistent with the changes in the vorticity and mass divergence computed. The procedure provides a balanced vertical motion field and produces smaller changes to the initial mass and wind fields, compared to the static initialization. The scheme is tested on two grids, of differing domain size and grid resolution. Convergence of the scheme is rapid with the

lower resolution US grid, with three iterations of the scheme being sufficient for convergence. With the smaller GALE grid of higher resolution and sloping topography along two boundaries, the convergence of the scheme is slower and in fact the mass divergence didn't converge for the third mode. However, by smoothing the topography in a boundary zone of five degrees, the convergence of the scheme is much improved. In both cases, changes in the mass and wind fields are still small after three iterations.

Integrations with initial conditions, initialized with the vertical mode initialization procedure, prevent gravity wave oscillations, without producing a mean drift in the surface pressure, and provide a balanced vertical motion field. On the coarse US grid, little difference is found between integrations using either of the lateral boundary treatments. However, some low amplitude oscillations in the surface pressure of long period remain in the interior of the domain and some noise is generated in the vertical motion at the lateral boundaries when the Perkey Kreitzberg scheme is used. On the smaller GALE grid, some noise is produced in the vertical motion in the boundary zone by both schemes. In the interior, the Davies scheme produces a smoother variation of the surface pressure. When the Davies scheme is used with integrations starting from uninitialized data and boundary values, an initial shock in the surface pressure is damped in the first four hours. However a small drift in the surface pressure is produced. This indicates that the boundary values used with the Davies scheme should be as balanced as possible for the numerical model, being initialized or derived from integrations on a larger grid or with another model. Similar 12 to 48 hour forecasts are again produced with the various experiments.

For grids of high resolution such as our GALE grid, and especially when fine scale topography is used along the boundary, it is recommended that no more than three iterations of the vertical mode scheme should be used in practice. For grids of even higher resolution, only the first two modes may be able to be initialized, with possibly no more than three iterations used with the scheme. Some improvement however, can be expected by smoothing the topography in the boundary zone or using a nested model to provide more accurate boundary values for the mass divergence for the inner nested grids.

ACKNOWLEDGEMENTS

The first author was supported under contract number N00014-86-C-2365 with NRL and the second author was supported by SPAWAR and NRL's basic research program. Preliminary results were described by Sashegyi et al. (1987) in the Proceedings of the IAMAP Symposium on Mesoscale Analysis and Forecasting, held 17-19 August 1987 in Vancouver, Canada and by Sashegyi and Madala (1988) in the preprints volume of the Eight Conference on Numerical Weather Prediction, which was held 22-26 February 1988 in Baltimore, Maryland.

APPENDIX: SPLIT-EXPLICIT SCHEME

The model equations in matrix notation can be written

$$\frac{\partial \bar{p}_s^x u}{\partial t} + \delta_x \bar{\Phi} = A_u \quad (A1)$$

$$\frac{\partial \bar{p}_s^y v}{\partial t} + \delta_y \bar{\Phi} = A_v \quad (A2)$$

$$\frac{\partial p_s T}{\partial t} + M_2 D = A_T \quad (A3)$$

$$\frac{\partial p_s}{\partial t} + N_2^T D = 0 \quad (A4)$$

$$\frac{\partial p_s q}{\partial t} = A_q \quad (A5)$$

$$\phi - \phi_s = M_1 T \quad (A6)$$

where the variables are defined in section 2.1, and the non-linear, Coriolis, friction and diabatic terms are included in the terms on the right hand sides of the equations. Integrating (A1), (A2), (A3), (A4) and (A5) over a time step $2 \Delta t$ we obtain

$$\bar{p}_s^x u(t+\Delta t) - \bar{p}_s^x u(t-\Delta t) + 2\Delta t \delta_x \bar{\Phi} = 2\Delta t \bar{A}_u \quad (A7)$$

$$\bar{p}_s^y v(t+\Delta t) - \bar{p}_s^y v(t-\Delta t) + 2\Delta t \delta_y \bar{\Phi} = 2\Delta t \bar{A}_v \quad (A8)$$

$$p_s T(t+\Delta t) - p_s T(t-\Delta t) + 2\Delta t M_2 \bar{D} = 2\Delta t \bar{A}_T \quad (A9)$$

$$p_s(t+\Delta t) - p_s(t-\Delta t) + 2\Delta t N_2^T \bar{D} = 0 \quad (A10)$$

$$p_s q(t+\Delta t) - p_s q(t-\Delta t) = 2\Delta t \bar{A}_q \quad (A11)$$

$$\text{where the averages } \bar{a} = \frac{1}{2 \Delta t} \int_{t-\Delta t}^{t+\Delta t} a \, dt \quad (A12)$$

and \bar{p}_s^x and \bar{p}_s^y represent grid point averages as defined in section 2.1. The non-linear and Coriolis terms on the right hand sides are slowly varying so that $\bar{A}_u = A_u(t)$, $\bar{A}_v = A_v(t)$, $\bar{A}_T = A_T(t)$. For an explicit time step choosing

$\bar{\Phi} \approx \Phi(t)$, $\bar{D} \approx D(t)$, gives the conventional centered difference scheme for time integration. We use this explicit difference scheme to compute first estimates of the variables at time $t+\Delta t$, giving

$$\bar{p}_s^x u^{ex}(t+\Delta t) - \bar{p}_s^x u(t-\Delta t) + 2\Delta t \delta_x \bar{\Phi}(t) = 2\Delta t A_u(t) \quad (A13)$$

$$\bar{p}_s^y v^{ex}(t+\Delta t) - \bar{p}_s^y v(t-\Delta t) + 2\Delta t \delta_y \bar{\Phi}(t) = 2\Delta t A_v(t) \quad (A14)$$

$$p_s T^{ex}(t+\Delta t) - p_s T(t-\Delta t) + 2\Delta t M_2 D(t) = 2\Delta t A_T(t) \quad (A15)$$

$$p_s^{ex}(t+\Delta t) - p_s(t-\Delta t) + 2\Delta t N_2^T D(t) = 0 \quad (A16)$$

$$p_s q^{ex}(t+\Delta t) - p_s q(t-\Delta t) = 2\Delta t A_q(t) \quad (A17)$$

Subtracting these equations from Eqs. (A7), (A8), (A9), (A10) and (A11), we can then write for the corrected variables

$$\bar{p}_s^x u(t+\Delta t) + 2\Delta t \delta_x [\bar{\Phi} - \Phi(t)] = \bar{p}_s^x u^{ex}(t+\Delta t) \quad (A18)$$

$$\bar{p}_s^y v(t+\Delta t) + 2\Delta t \delta_y [\bar{\Phi} - \Phi(t)] = \bar{p}_s^y v^{ex}(t+\Delta t) \quad (A19)$$

$$p_s T(t+\Delta t) + 2\Delta t M_2 [\bar{D} - D(t)] = p_s T^{ex}(t+\Delta t) \quad (A20)$$

$$p_s(t+\Delta t) + 2\Delta t N_2^T [\bar{D} - D(t)] = p_s^{ex}(t+\Delta t) \quad (A21)$$

$$p_s q(t+\Delta t) = p_s q^{ex}(t+\Delta t) \quad (A22)$$

where the terms on the right-hand side are the explicit computations of the variables. We only need to compute the corrections $\bar{\Phi} - \Phi(t)$, $\bar{D} - D(t)$ for those vertical modes whose phase speeds relative to the ground $U + \sqrt{\lambda_k}$ are greater than $\Delta x/(2\Delta t)$, where U is the maximum background flow speed. It can also be noted that the specific humidity q need not be corrected. To obtain the corrections for these modes, the amplitudes of the deviations $\bar{\Phi} - \Phi(t)$, $\bar{D} - D(t)$ are integrated at smaller time steps, over the interval of twice the large time step.

To integrate the deviations we require equations for the tendencies of mass divergence and generalized geopotential. By taking δ_x of h_y times Eq. (A1) and adding δ_y of h_x times Eq. (A2) we obtain the equation for the divergence. By taking M_1 times Eq. (A3) and adding $(RT^* + \phi^*)$ times Eq. (A4) an equation for the generalized geopotential is obtained. That is

$$\frac{\partial D}{\partial t} + \nabla^2 \Phi = A_m \quad (A23)$$

$$\frac{\partial \Phi}{\partial t} + M_3 D = M_1 A_T \quad (A24)$$

$$\text{where } A_m = \frac{1}{h_y} \delta_x (h_y A_u) + \frac{1}{h_x} \delta_y (\overline{h_x^y} A_v) \quad (A25)$$

and the two dimensional Laplacian ∇^2 is defined by Eq. (2.13) in section 2.1. In terms of our vertical modes, the amplitudes of the mass divergence and generalized geopotential are $d = E^{-1}D$, $e = E^{-1}\Phi$. The amplitudes of the deviations of the divergence $d_k^n - d_k(t)$, and the generalized geopotential $e_k^n - e_k(t)$ are integrated with smaller time steps given by $\Delta\tau_k = \Delta t/m_k$. For the ten layer model, the deviations are computed for the first three modes with m_k given by 8, 4 and 2 respectively. Now integrating over smaller time steps we have

$$d_k^{n+1} - d_k^{n-1} + 2 \Delta\tau_k \nabla^2 e_k^n = 2 \Delta\tau_k \{ E^{-1} A_m(t) \}_k \quad (A26)$$

$$e_k^{n+1} - e_k^{n-1} + 2 \Delta\tau_k \lambda_k d_k^n = 2 \Delta\tau_k \{ E^{-1} M_1 A_T(t) \}_k \quad (A27)$$

For our explicit time step, applying the centered difference scheme with time step $2 \Delta t$ to Eqs. (A23) and (A24), or from Eqs. (A13), (A14), (A15), (A16) directly, we obtain

$$d_k^{\text{ex}}(t+\Delta t) - d_k(t-\Delta t) + 2 \Delta t \nabla^2 e_k(t) = 2 \Delta t \{ E^{-1} A_m(t) \}_k \quad (A28)$$

$$e_k^{\text{ex}}(t+\Delta t) - e_k(t-\Delta t) + 2 \Delta t \lambda_k d_k(t) = 2 \Delta t \{ E^{-1} M_1 A_T(t) \}_k \quad (A29)$$

By subtraction we obtain the equations for integrating the deviations $d_k^n - d_k(t)$, $e_k^n - e_k(t)$,

$$\begin{aligned}
[d_k^{n+1} - d_k(t)] - [d_k^{n-1} - d_k(t)] &+ 2\Delta\tau_k \nabla^2 (e_k^n - e_k(t)) \\
&= \frac{1}{m_k} [d_k^{\text{ex}}(t+\Delta t) - d_k(t-\Delta t)]
\end{aligned} \tag{A30}$$

$$\begin{aligned}
[e_k^{n+1} - e_k(t)] - [e_k^{n-1} - e_k(t)] &+ 2\Delta\tau_k \lambda_k (d_k^n - d_k(t)) \\
&= \frac{1}{m_k} [e_k^{\text{ex}}(t+\Delta t) - e_k(t-\Delta t)]
\end{aligned} \tag{A31}$$

where $d_k^{\text{ex}}(t+\Delta t) = \{E^{-1}D^{\text{ex}}(t+\Delta t)\}_k = \{E^{-1}[\delta_x(\bar{p}_s^x u^{\text{ex}}) + \frac{1}{h_x} \delta_y(\bar{h}_x^y \bar{p}_s^y v^{\text{ex}})]\}_k$

and $e_k^{\text{ex}}(t+\Delta t) = \{E^{-1}\Phi^{\text{ex}}(t+\Delta t)\}_k$

The required corrections are then given by

$$\bar{d}_k - d_k(t) = \frac{1}{m_k} \sum_{n=1}^{m_k} (d_k^n - d_k(t)) \tag{A32}$$

$$\bar{e}_k - e_k(t) = \frac{1}{m_k} \sum_{n=1}^{m_k} (e_k^n - e_k(t)) \tag{A33}$$

For the integration of the deviations of the divergence, a lateral boundary condition is required for the generalized geopotential. The boundary value for $e_k - e_k(t)$ is computed by linear interpolation from the values at $t - \Delta t$ and t . Further pragmatic boundary conditions are provided by reducing the amplitude and phase speed of the deviations of the divergence and generalized geopotential in the boundary zone by the factor $1-a$, where a is defined in section 2.3, for the two different lateral boundary formulations. That is to reduce the phase speed c_k in the boundary zone, we multiply λ_k in Eq. (A31) and the ∇^2 term in Eq. (A30) by $(1-a)$. The amplitudes are reduced in the boundary zone by multiplying the correction terms in Eqs. (A20) and (A21) by $(1-a)$ and those in Eqs (A18) and (A19) by $(1-a_u)$ and $(1-a_v)$, respectively.

REFERENCES

- Andersen, J.H., 1977: A routine for normal mode initialization with non-linear correction for a multi-level spectral model with triangular truncation. ECMWF Internal Report No. 15, European Centre for Medium Range Weather Forecasts, Bracknell, U.K., 41 pp.
- Arakawa, A., and V.R. Lamb, 1977: Computational design of the basic dynamical processes of the UCLA general circulation model. Methods in Computational Physics, Vol. 17, General Circulation Models of the Atmosphere, J. Chang, Ed., Academic Press, New York, 173-265.
- Bengtsson, L., 1975: Four-dimensional assimilation of meteorological observations. GARP Publication Series, No. 15, World Meteorological Organization, Geneva, Switzerland, 57-69.
- Bourke, W., and J.L. McGregor, 1983: A nonlinear vertical mode initialization scheme for a limited area prediction model. Mon. Wea. Rev., 111, 2285-2297.
- Chang, S., K. Brehme, R. Madala, K. Sashegyi, 1989: A numerical study of the east coast snowstorm of 10-12 February 1983. Mon. Wea. Rev., 117, 1768-1778.
- Daley, R., 1979: The application of non-linear normal mode initialization to an operational forecast model. Atmosphere-Ocean, 17, 97-124.
- Davies, H.C., 1976: A lateral boundary formulation for multi-level prediction models. Quart. J. Roy. Meteor. Soc., 102, 405-418.
- Davies, H.C., 1983: Limitations of some common lateral boundary schemes used in regional NWP models. Mon. Wea. Rev., 111, 1002-1012.
- Errico, R.M., 1986: Initialization of the PSU/NCAR mesoscale model. NCAR Technical Note, NCAR/TN-270+IA, National Center for Atmospheric Research, Boulder, CO., 120pp.
- Gill, A.E., 1982: Atmosphere-Ocean Dynamics. Academic Press, New York, 662pp.
- Grønås, S., A. Foss and M. Lystad, 1987: Numerical simulations of polar lows in the Norwegian Sea. Tellus, 39A, 334-353.
- Haltiner, G.J., and R.T. Williams, 1980: Numerical Prediction and Dynamic Meteorology. Second ed., John Wiley and Sons, New York, 477pp.
- Juwanon du Vachat, R., 1986: A general formulation of normal modes for limited-area models: Application to initialization. Mon. Wea. Rev., 114, 2478-2487.
- Kasahara, A., and K. Puri, 1981: Spectral representation of three-dimensional global data by expansion in normal mode functions. Mon. Wea. Rev., 109, 37-51.

- Krishnamurti, T.N., 1979: Tropical Meteorology. Compendium of Meteorology for use by Class I and Class II meteorological personnel, Vol. 2, Part 4, A. Wiin-Nielsen, Ed. WMO Technical Publication, No. 364, World Meteorological Organization, Geneva, Switzerland, 428pp.
- Lynch, P., 1988: Deducing the wind from vorticity and divergence. Mon. Wea. Rev., 116, 86-93.
- Madala, R.V., 1978: An efficient direct solver for separable and non-separable elliptic equations. Mon. Wea. Rev., 106, 1735-1741.
- Madala, R.V., 1981: Efficient time integration schemes for atmosphere and ocean models. Finite Difference Techniques for Vectorized Fluid Dynamic Calculations, D.L. Book, Ed., Chap. 4, Springer-Verlag, New York, 56-74.
- Madala, R.V., 1981: Solution of elliptic equations. Finite Difference Techniques for Vectorized Fluid Dynamic Calculations, D.L. Book, Ed., Chap. 7, Springer-Verlag, New York, 117-134.
- Madala, R.V., S.W. Chang, U.C. Mohanty, S.C. Madan, R.K. Paliwal, V.B. Sarin, T. Holt and S. Raman, 1987: Description of the Naval Research Laboratory Limited Area Dynamical Weather Prediction Model. NRL Memorandum Report, No. 5992, Naval Research Laboratory, Washington, D.C., 131pp.
- Manabe, S., J. Smagorinsky, and R.F. Strickler, 1965: Simulated climatology of a general circulation model with a hydrologic cycle. Mon. Wea. Rev., 93, 769-798.
- Matsuno, T., 1966: Quasi-geostrophic motions in the equatorial area. Jour. Meteor. Soc. Japan, Series II, 44, 25-43.
- Mesinger, F., and A. Arakawa, 1976: Numerical Methods used in Atmospheric Models. GARP Publication Series, No. 17, Vol. 1, World Meteorological Organization, Geneva, Switzerland, 64pp.
- Perkey, D.J., and C.W. Kreitzberg, 1976: A time-dependent lateral boundary scheme for limited-area primitive equation models. Mon. Wea. Rev., 104, 744-755.
- Phillips, N.A., 1957: A coordinate system having some special advantages for numerical forecasting. Jour. of Meteor., 14, 184-185.
- Reynolds, R.W., 1982: A monthly averaged climatology of sea surface temperatures. NOAA Technical Report, NWS-31, Climate Analysis Center, National Weather Service, Washington, D.C., 35pp.
- Sashegyi, K.D., S.W. Chang and R.V. Madala, 1987: Preliminary results from real data experiments with the NRL mesoscale numerical model. Proceedings, Symposium on Mesoscale Analysis and Forecasting, Incorporating Nowcasting, IAMAP, Aug 17-19, Vancouver, Canada, ESA SP-282, 497-500.
- Sashegyi, K.D., and R.V. Madala, 1988: Initialization experiments with the NRL mesoscale numerical model. Preprints, 8th Conference on Numerical Weather Prediction, Amer. Meteor. Soc., Feb 22-26, Baltimore, MD, 778-781.

- Sashegyi, K.D., and R.V. Madala, 1989: A user's guide to the SEVP solver: An efficient direct solver for elliptic partial differential equations. NRL Memorandum Report, No. 6450, Naval Research Laboratory, Washington, D.C., 38pp.
- Shapiro, R., 1970: Smoothing, filtering and boundary effects. Rev. Geophys. Space Phys., 8, 359-387.
- Strang, G., 1988: Linear Algebra and its Applications. Third ed., Harcourt Brace Jovanovich, San Diego, CA., 505pp.
- Sundqvist, H., 1975: Initialization for models using sigma as the vertical coordinate. Jour. Appl. Meteor., 14, 153-158.
- Temperton, C., 1984: Orthogonal vertical modes for a multilevel model. Mon. Wea. Rev., 112, 503-509.
- Temperton, C., 1988: Implicit normal mode initialization. Mon. Wea. Rev., 116, 1013-1031.
- Temperton, C., and D.L. Williamson, 1981: Normal mode initialization for a multilevel grid-point model. Part I: Linear aspects. Mon. Wea. Rev., 109, 729-743.
- Williamson, D.L., and C. Temperton, 1981: Normal mode initialization for a multilevel grid-point model. Part II: Nonlinear aspects. Mon. Wea. Rev., 109, 744-757.

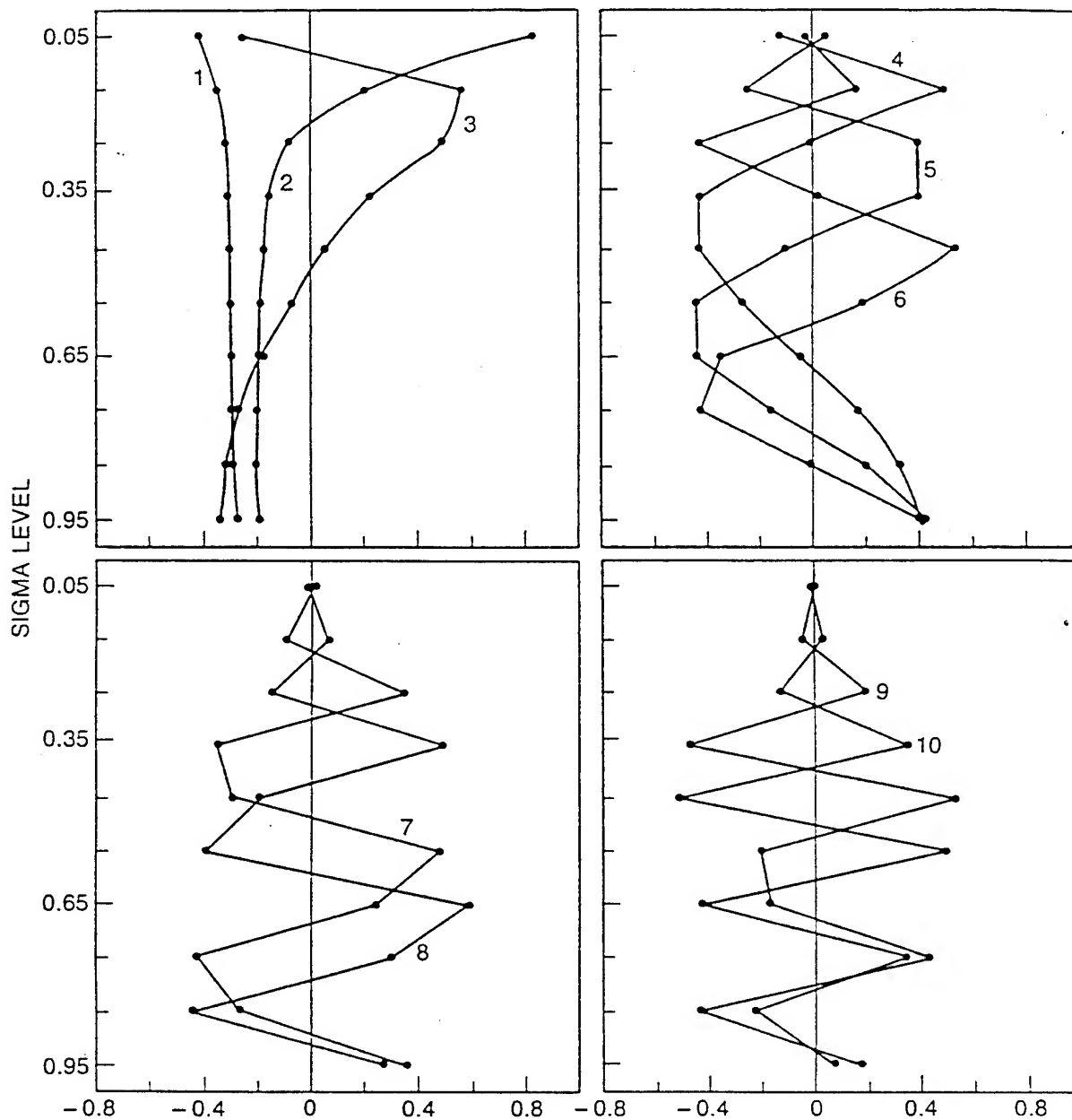


FIG. 1. The vertical structure of the modes versus sigma level in a ten layer model for the case of a basic state at rest with the mean temperature profile defined in Table 1.

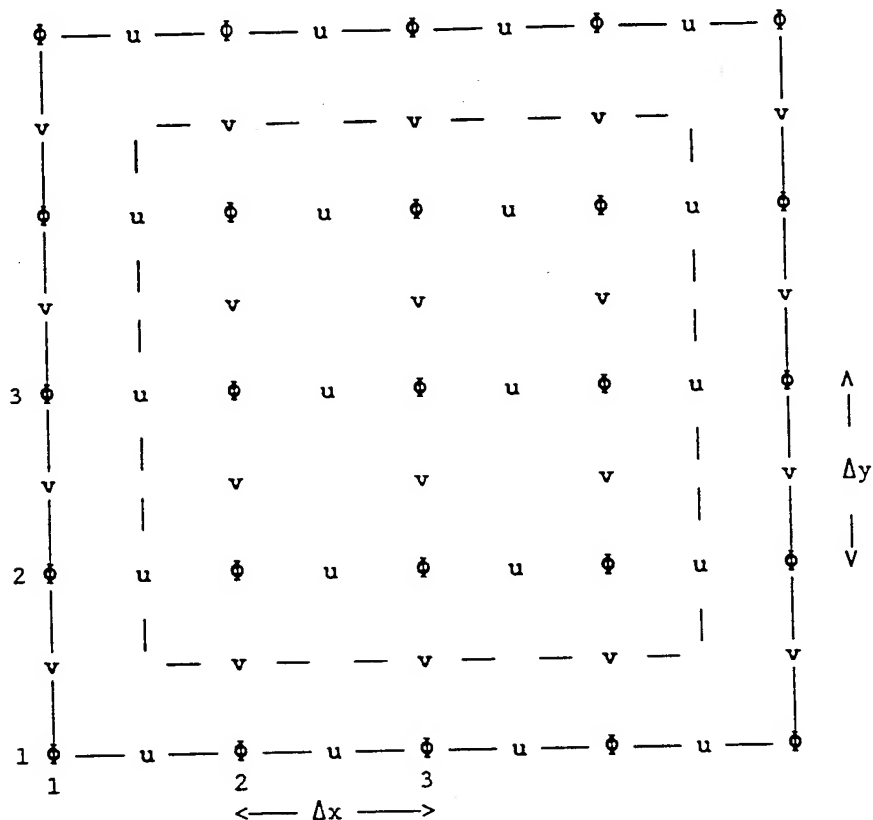


FIG. 2. The horizontal grid stencil for the Arakawa C grid as applied to the NRL model, showing the lateral boundary grid points. u and v represent the horizontal wind components. The surface pressure p_s , the temperature T , the geopotential ϕ , specific humidity q , the mass divergence D and vertical motion σ are defined at the same horizontal grid point as the generalized geopotential ϕ .

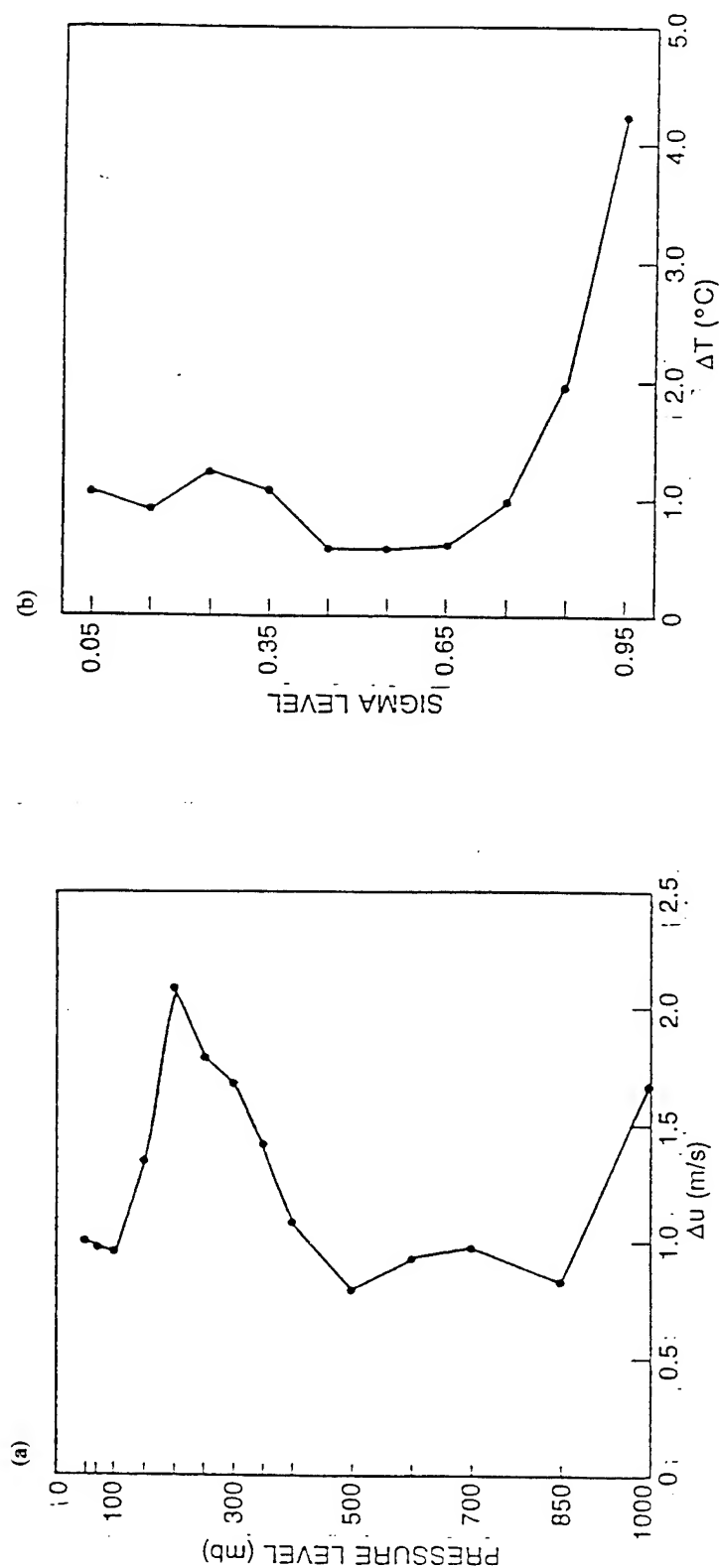


FIG. 3. The root-mean-square changes for 122 January 23, 1986 on the GALE grid in (a) the u-component of the analyzed wind as a result of computing the non-divergent wind and (b) the root-mean-square changes in the analyzed temperature after the non-linear mass balance equation is used to replace the temperature.

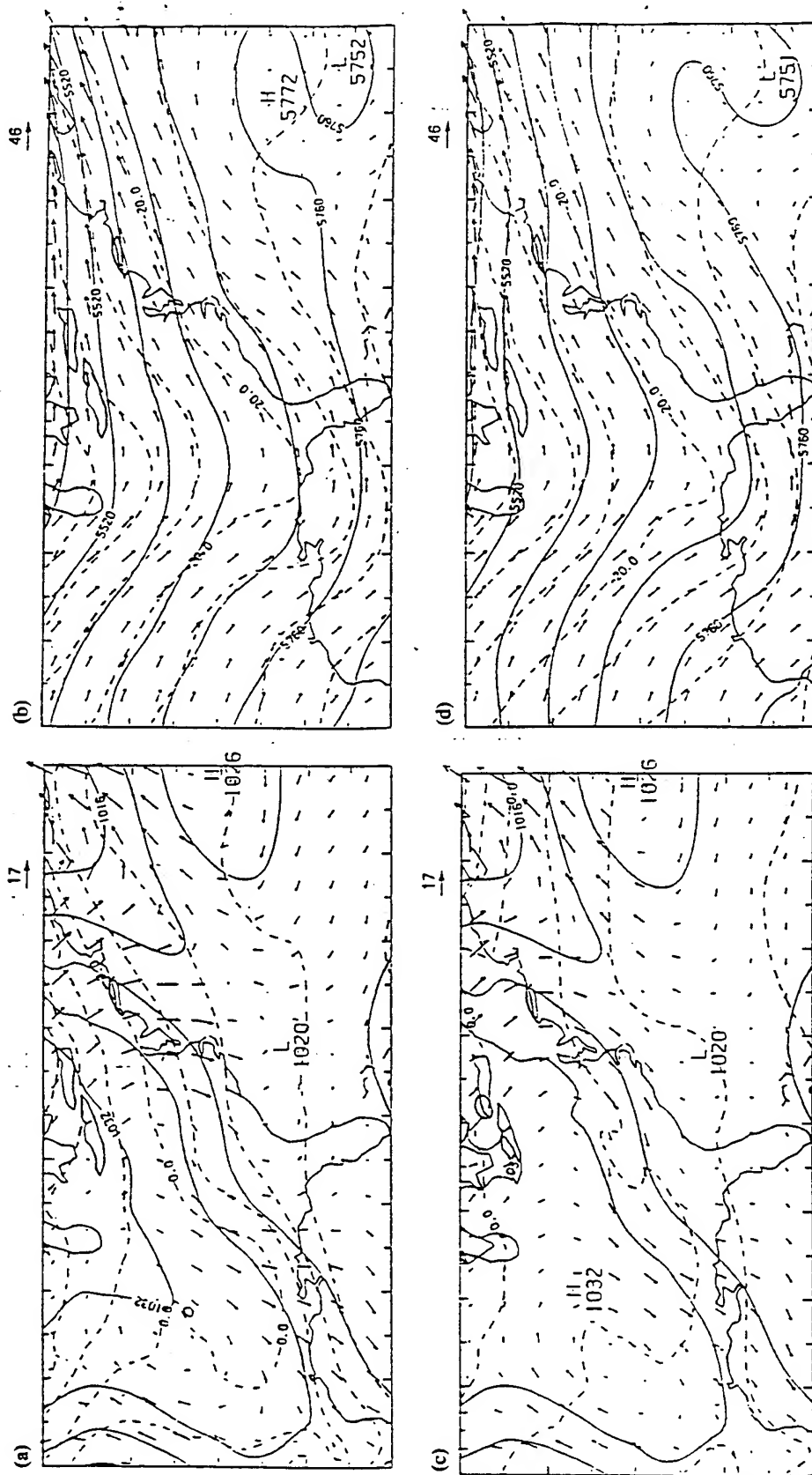


FIG. 4. (a) The analyzed sea-level pressure, wind and temperature at 1000 mb on the GALE grid for 122 January 23, 1986. The contours of sea-level pressure are every 4 mb and every 5°C for the temperature. The maximum wind vector is 17 m s⁻¹. (b) The analyzed geopotential, wind and temperature at 500 mb on the GALE grid for 122 January 23, 1986. The contours of geopotential are every 60 gpm and every 2.5°C for the temperature. The maximum wind vector is 46 m s⁻¹. The 1000 mb and 500 mb fields after static initialization are shown in (c) and (d).

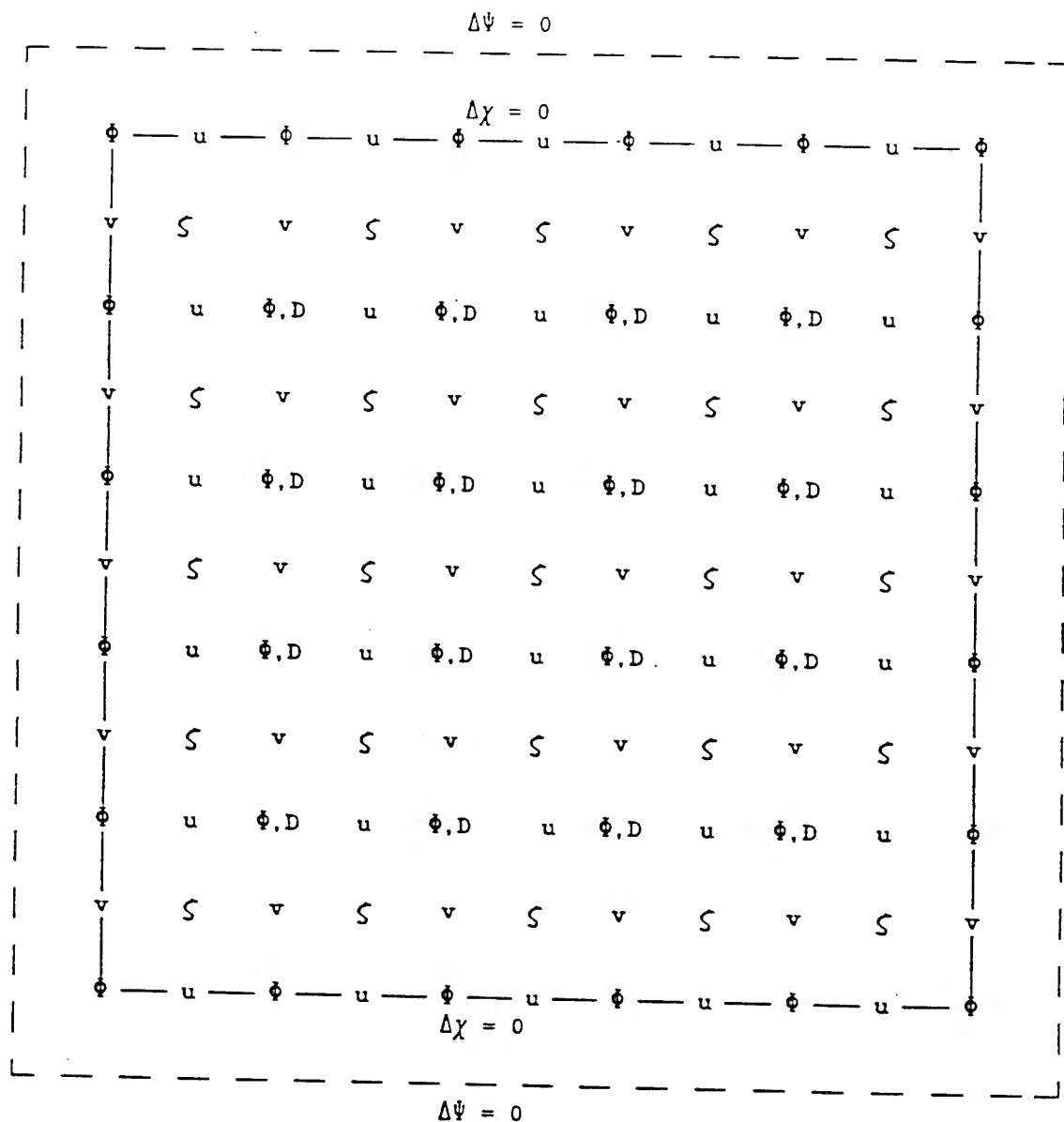


FIG. 5. The horizontal grid stencil used to compute the changes in the wind field, given the changes in the mass divergence and vorticity. The stream function change $\Delta\Psi$ is defined in the interior at the same grid point as the vorticity S , while the velocity potential change $\Delta\chi$ is defined at the same grid point as the mass divergence D . The lateral boundary conditions for $\Delta\chi$ and $\Delta\Psi$ are indicated.

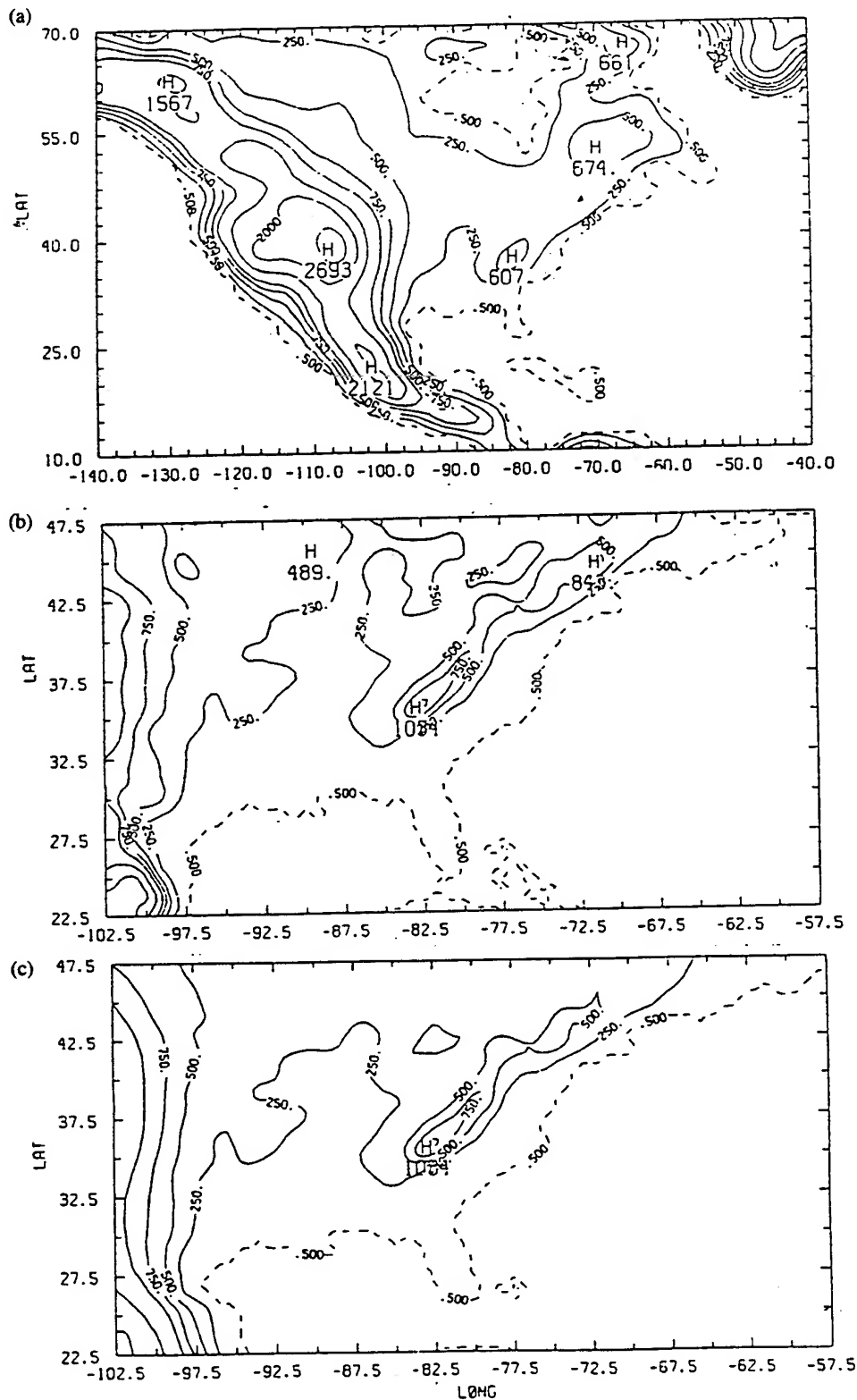


FIG. 6. The smoothed model topography for (a) the US grid, (b) for the GALE grid and (c) for the GALE grid with the topography further smoothed in a five degree zone around the lateral boundary. The horizontal resolution is 2° longitude by 1.5° latitude for the US grid and 0.5° in latitude and longitude for the GALE grid. The contour intervals are 500 m for elevations above 1000 m, and 250 m for those below 1000 m.

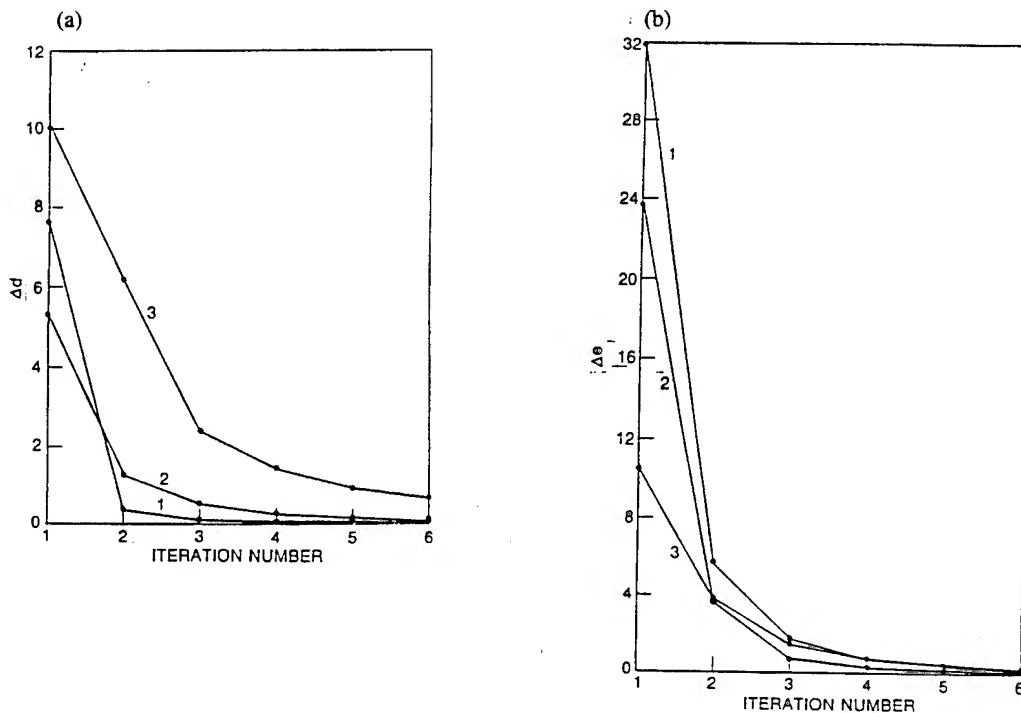


FIG. 7. The root-mean-square (rms) changes in the amplitudes on the US grid of (a) the mass divergence Δd in dynes $\text{cm}^{-2} \text{s}^{-1}$, (b) the generalized geopotential Δe in units of $10^{11} \text{ dynes s}^{-2}$, and (c) the vorticity Δv in dynes $\text{cm}^{-2} \text{s}^{-1}$, versus the iteration number in the vertical mode initialization scheme, for each of the first three vertical modes. In (d) is shown the rms change Δp_s in the surface pressure in mb versus the iteration number. The rms values are averaged for all the analyses of the week of 12Z January 23 to 12Z January 29, 1986. (e) The rms change in the amplitude of the mass divergence Δd in dynes $\text{cm}^{-2} \text{s}^{-1}$ versus iteration number for the highest mode initialized, as the number of modes initialized is varied from one to six modes for the analysis on 12Z January 23, 1986 only.

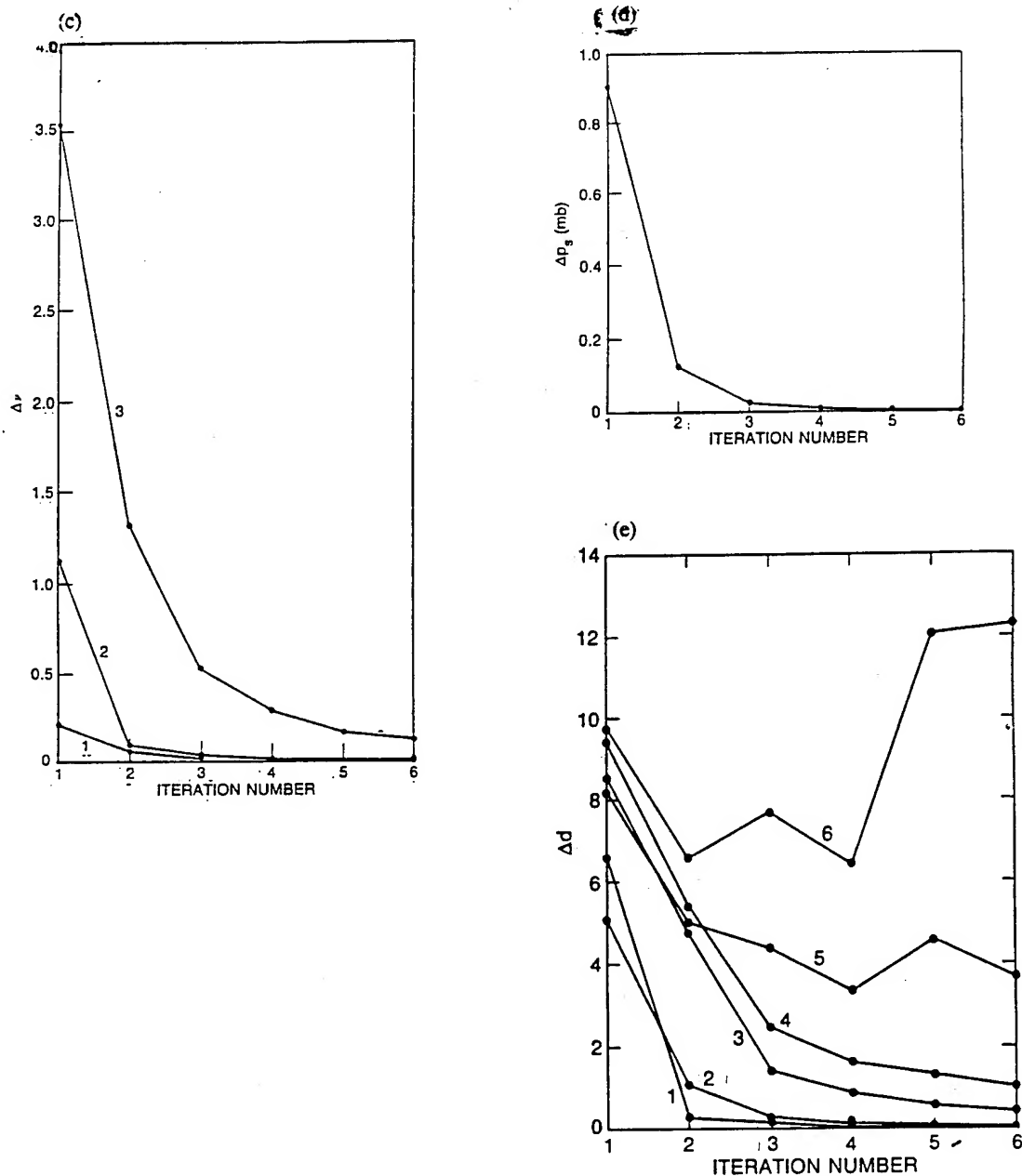


FIG. 7. The root-mean-square (rms) changes in the amplitudes on the US grid of (a) the mass divergence Δd in dynes $\text{cm}^{-2} \text{s}^{-1}$, (b) the generalized geopotential $\Delta \phi$ in units of 10^{11} dynes s^{-2} , and (c) the vorticity Δv in dynes $\text{cm}^{-2} \text{s}^{-1}$, versus the iteration number in the vertical mode initialization scheme, for each of the first three vertical modes. In (d) is shown the rms change Δp_s in the surface pressure in mb versus the iteration number. The rms values are averaged for all the analyses of the week of 122 January 23 to 122 January 29, 1986. (e) The rms change in the amplitude of the mass divergence Δd in dynes $\text{cm}^{-2} \text{s}^{-1}$ versus iteration number for the highest mode initialized, as the number of modes initialized is varied from one to six modes for the analysis on 122 January 23, 1986 only.

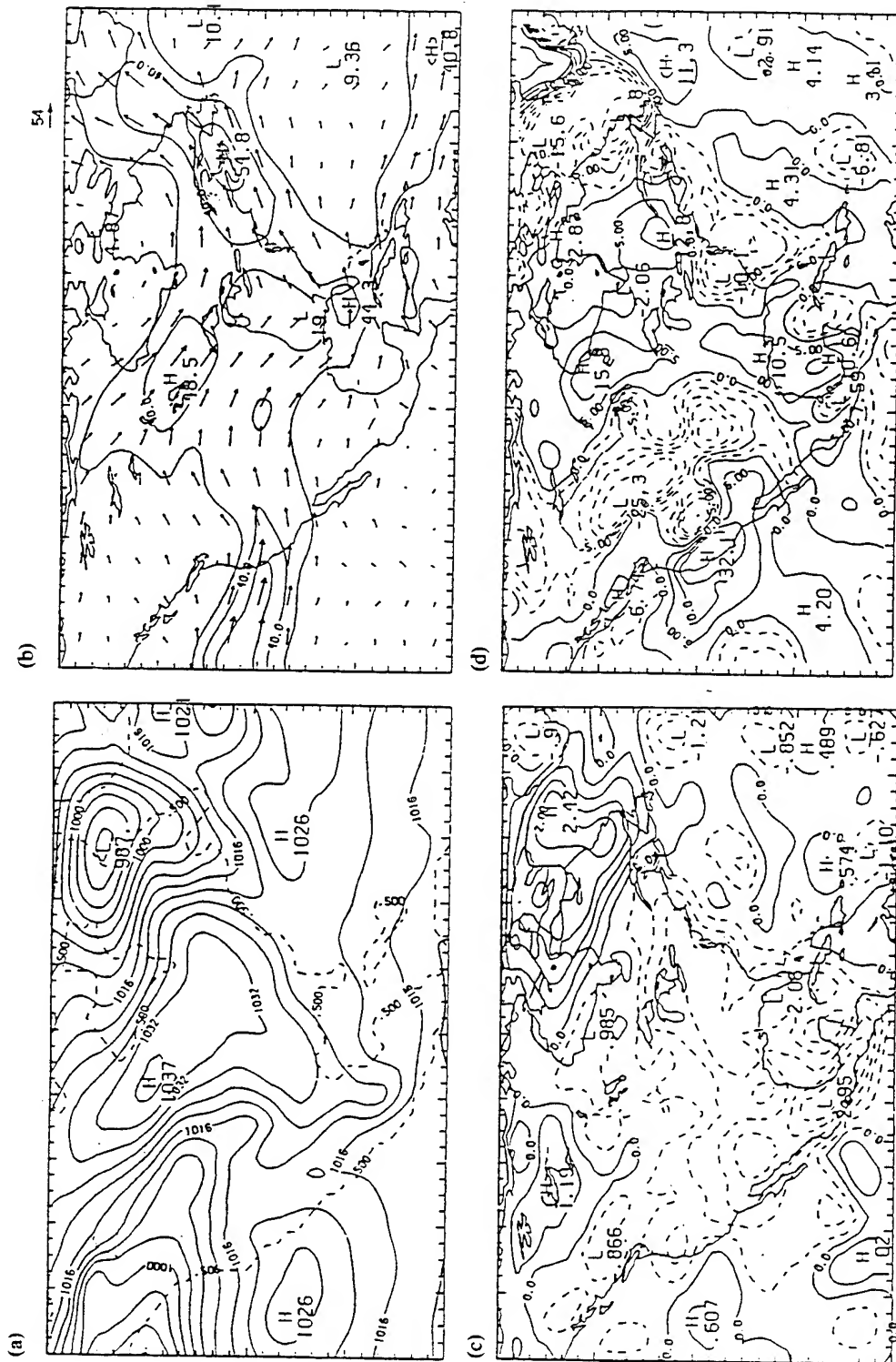


FIG. 8. The analyzed (a) sea-level pressure and (b) wind field on the US grid at model sigma level $\sigma = 0.25$ for 122 January 23, 1986. The contours of sea-level pressure are every 4 mb and the isotachs are every 10 m s⁻¹, increasing from 30 m s⁻¹. The maximum wind vector shown is 54 m s⁻¹. (c) The surface pressure change and (d) the vertical motion field in units of 10⁻³ hr⁻¹ in the middle troposphere at a sigma level $\sigma = 0.45$, after the vertical mode initialization. Contours of surface pressure change are every 0.5 mb. Contours for the vertical motion are every 2.5×10^{-3} hr⁻¹ for magnitudes above 10×10^{-3} hr⁻¹ and every 15×10^{-3} hr⁻¹ otherwise.

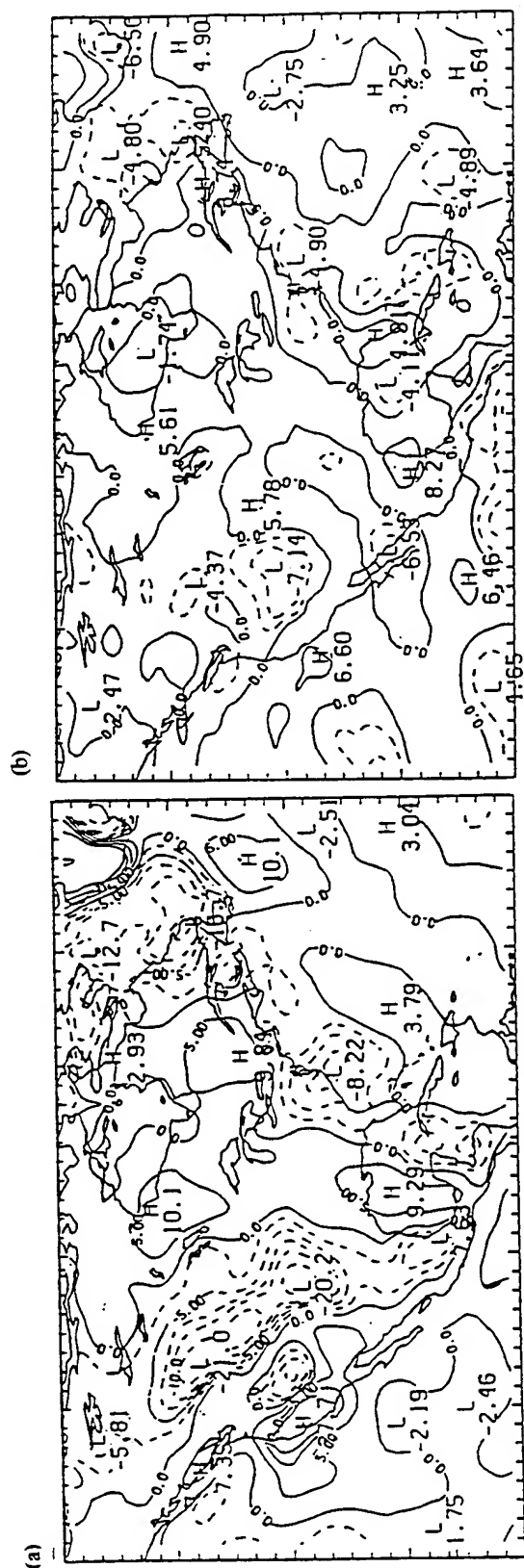


FIG. 9. The contribution to the vertical motion at sigma level $\sigma = 0.45$ in (a) the first three vertical modes, and (b) in the remaining modes. Contours of vertical motion are as in Fig. 8d.

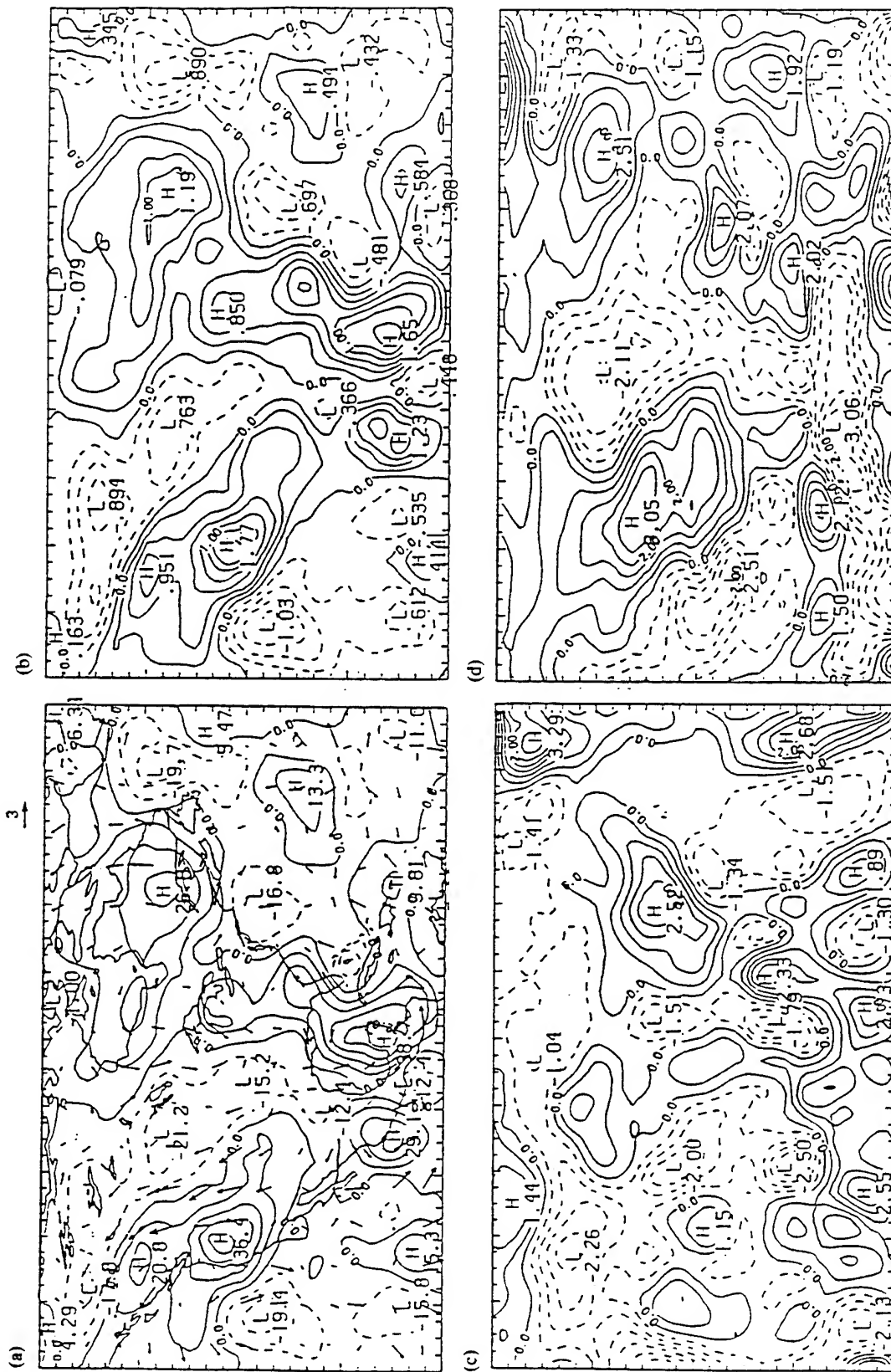


FIG. 10. The changes on the US grid in (a) the geopotential height and the wind field, (b) the temperature, (c) the u-component of the wind and (d) the v-component of the wind at the sigma level of $\sigma = 0.25$ for 12Z January 23, 1986. The contours of geopotential change are every 8 gpm and the maximum vector is 3 m s^{-1} . Contours of the wind components are 0.5 m s^{-1} , and 0.25°C for the temperature changes.

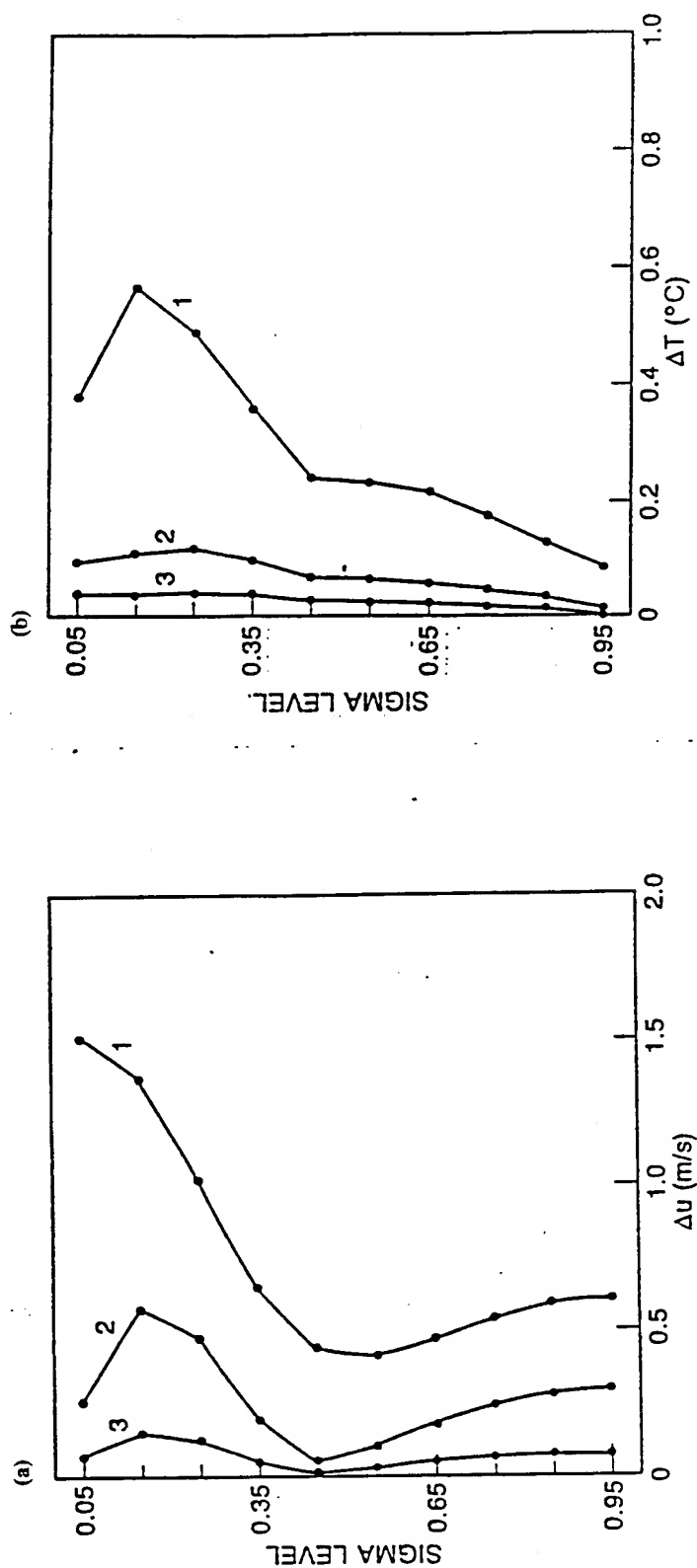


FIG. 11. The root-mean-square changes on the US grid in (a) the u-component of the wind in m s^{-1} and (b) the temperature in $^{\circ}\text{C}$, versus sigma level for the first three iterations of the vertical mode initialization scheme, for 122 January 23, 1986.

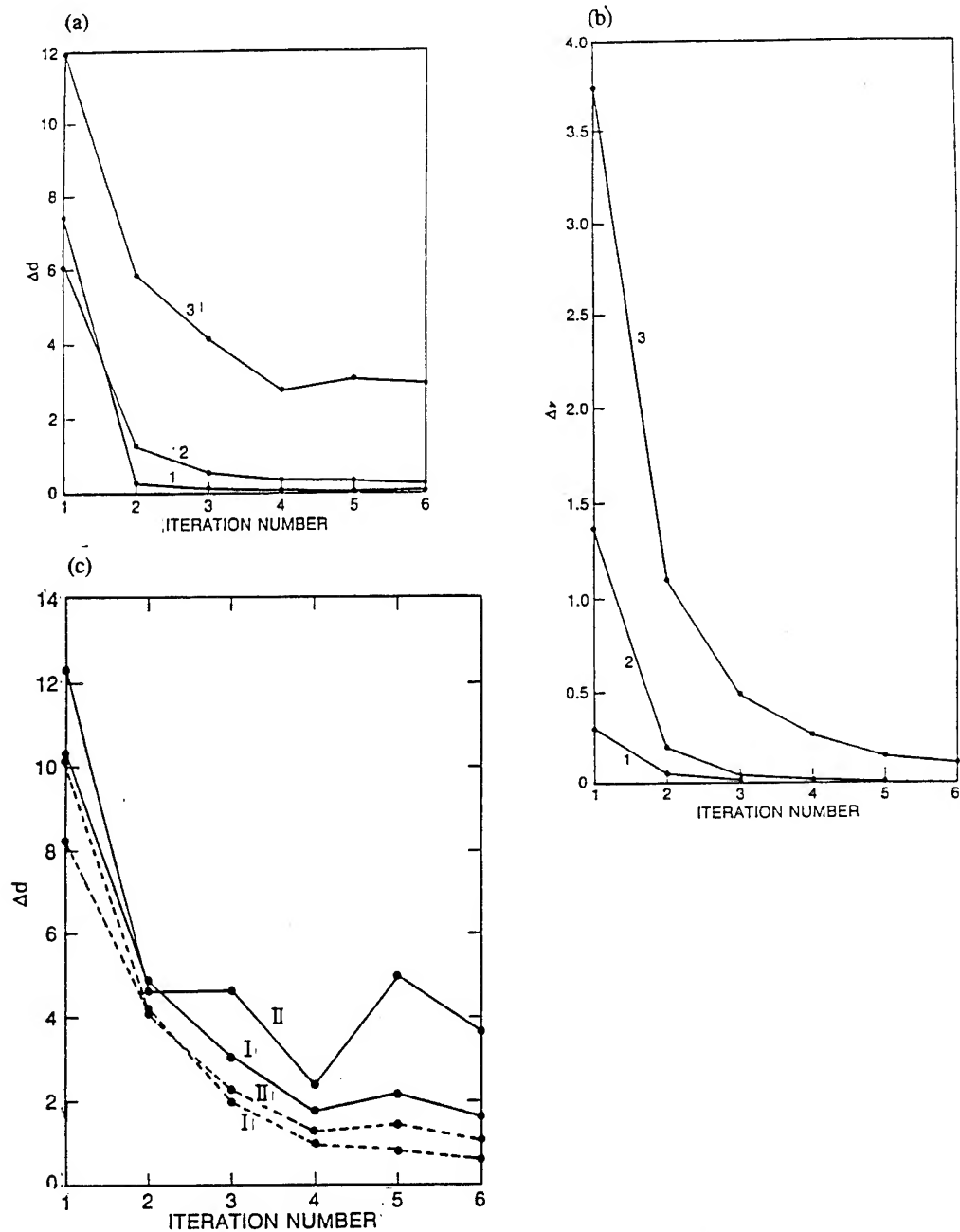


FIG. 12. The root-mean-square (rms) changes on the GALE grid in the amplitudes of (a) the mass divergence, and (b) the vorticity versus iteration number in the vertical mode initialization scheme for each of the first three vertical modes, averaged for all the analyses for the week of 122 January 23 to 122 January 29, 1986. (c) Comparing the rms changes in the amplitude of the mass divergence when the GALE topography (see Fig. 6b) is used (solid lines) to that when the GALE topography, which has been further smoothed (see Fig. 6c) in a five degree zone around the lateral boundary, is used (dashed lines). The analyses only on 122 January 23 (labelled I) and 122 January 24, 1986 (labelled II) are used.

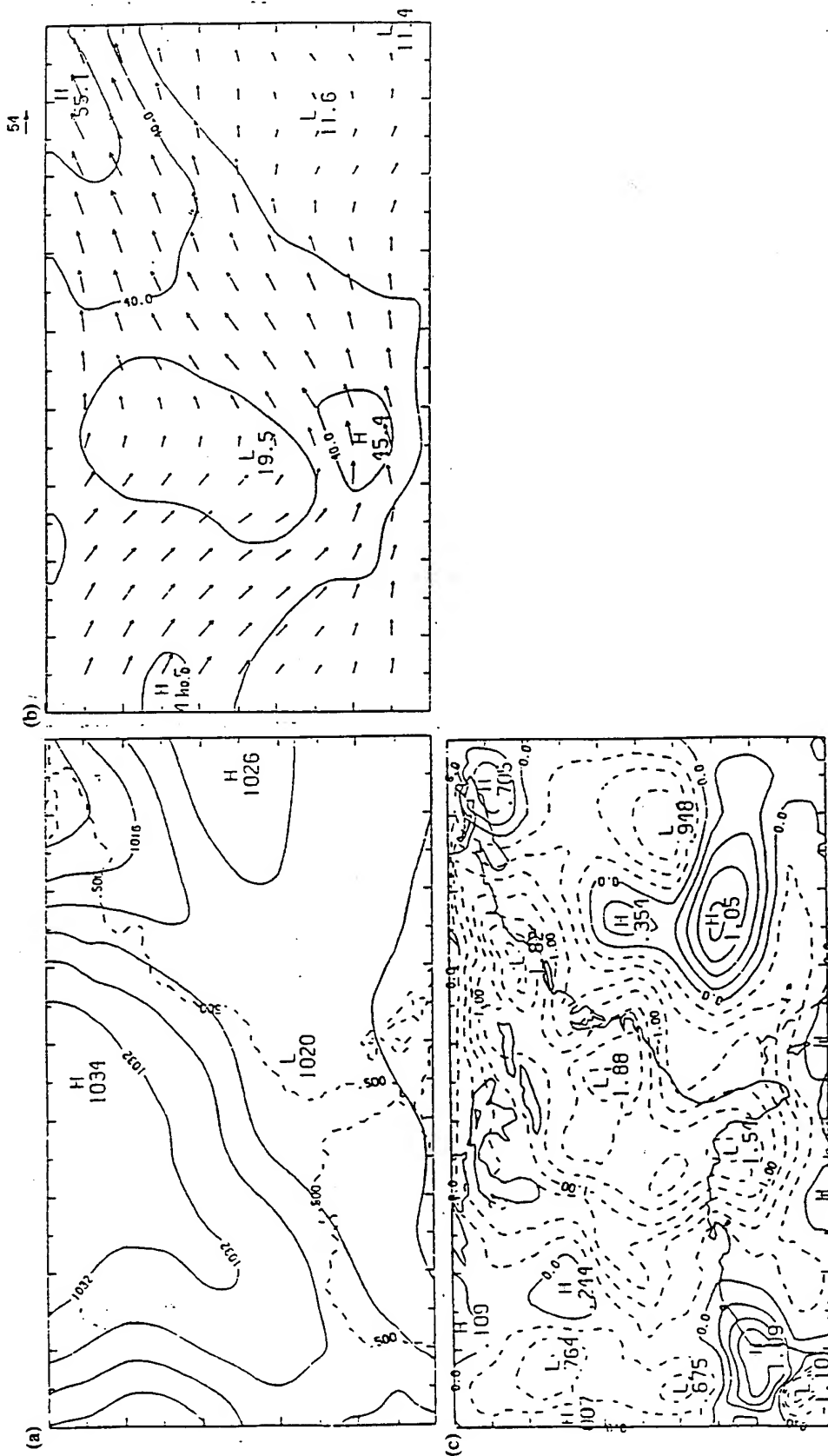


FIG. 13. The analyzed (a) sea-level pressure and (b) wind field on the GALE grid at the model sigma level $\sigma = 0.25$ for 122 January 23, 1986. The contours are as in Fig. 8a and b. The maximum wind vector shown is 54 m s^{-1} . (c) The surface pressure change in mb, after the vertical mode initialization. Contours of surface pressure change are every 0.25 mb .

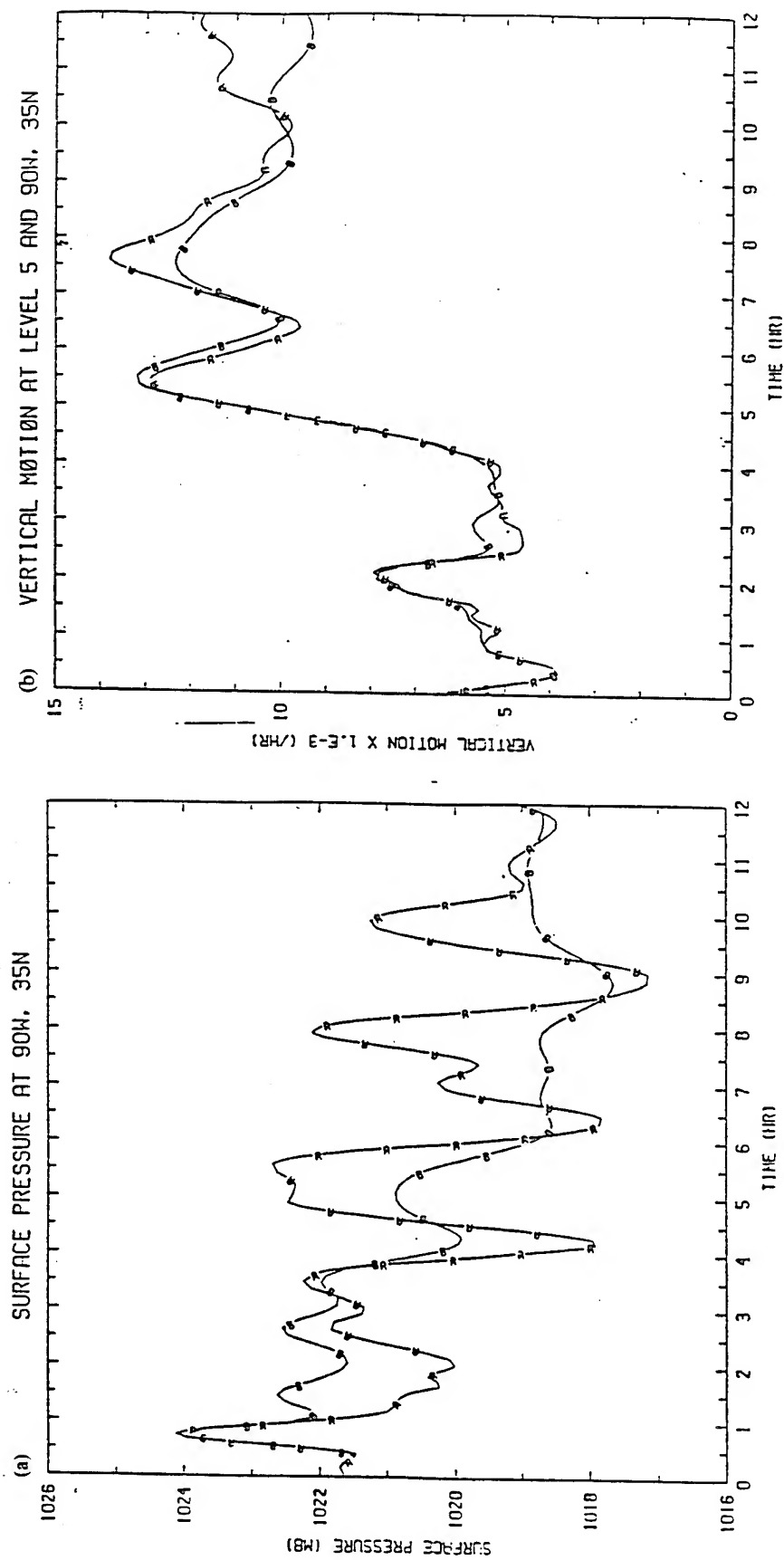


FIG. 15. Time series of (a) surface pressure in mb and (b) the vertical motion (in sigma coordinates) in hour⁻¹ at sigma level $\sigma = 0.5$, at a grid point on the GALE grid at 90°W and 35°N, during the first 12 hours of integration. Curves are for uninitialized initial conditions for an explicit integration in time (Curve A) and a split-explicit integration (Curve B).

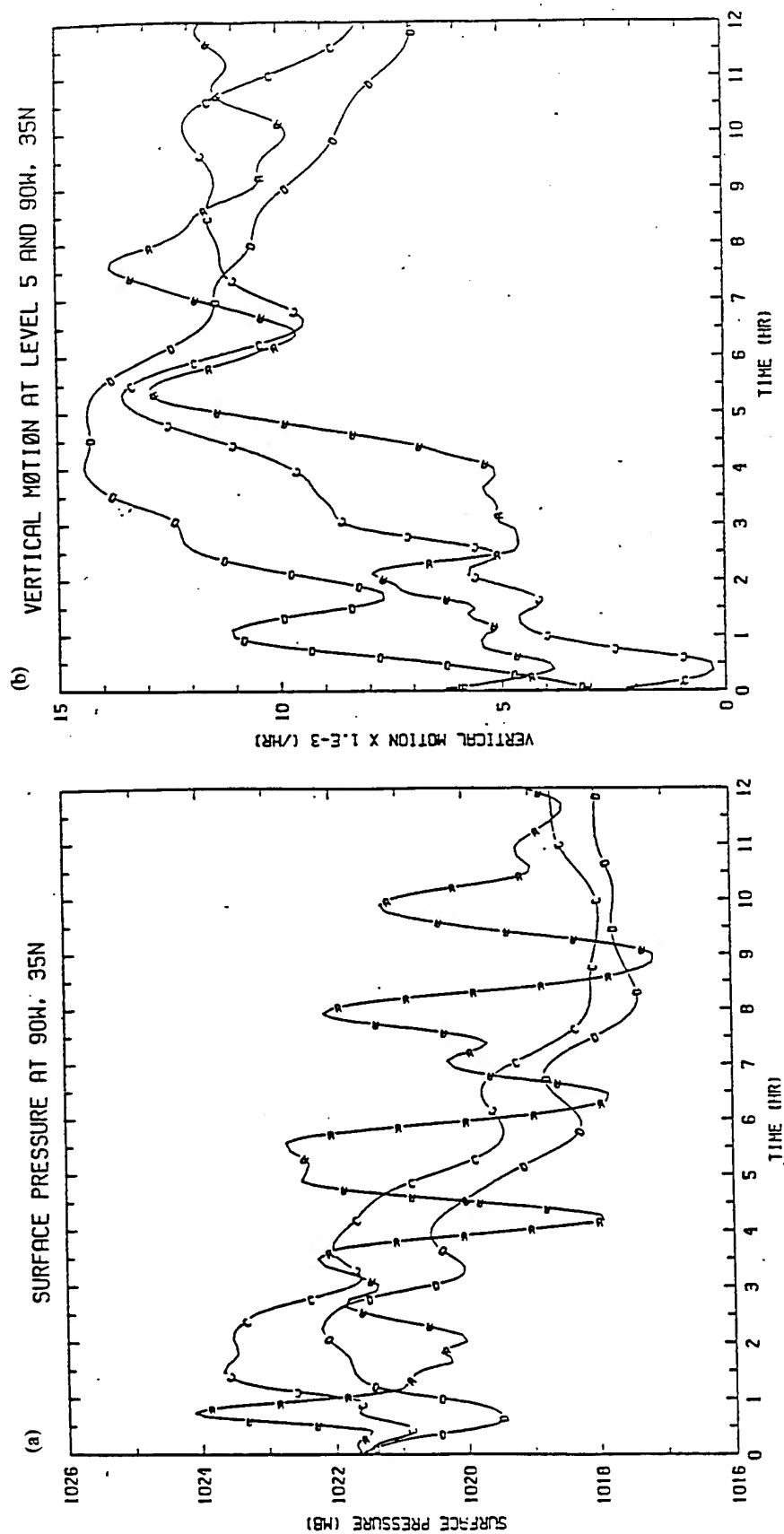


FIG. 16. Time series of (a) surface pressure in mb and (b) the vertical motion (in sigma coordinates) in hour⁻¹ at sigma level $\sigma = 0.5$, at a grid point on the GALE grid at 90°W and 35°N, during the first 12 hours of integration. Curves are for uninitialized initial conditions for an explicit integration in time (Curve A); for a split-explicit integration with a non-divergent initial condition (Curve C) and for split-explicit integrations with a non-linear mass balance (Curve D).

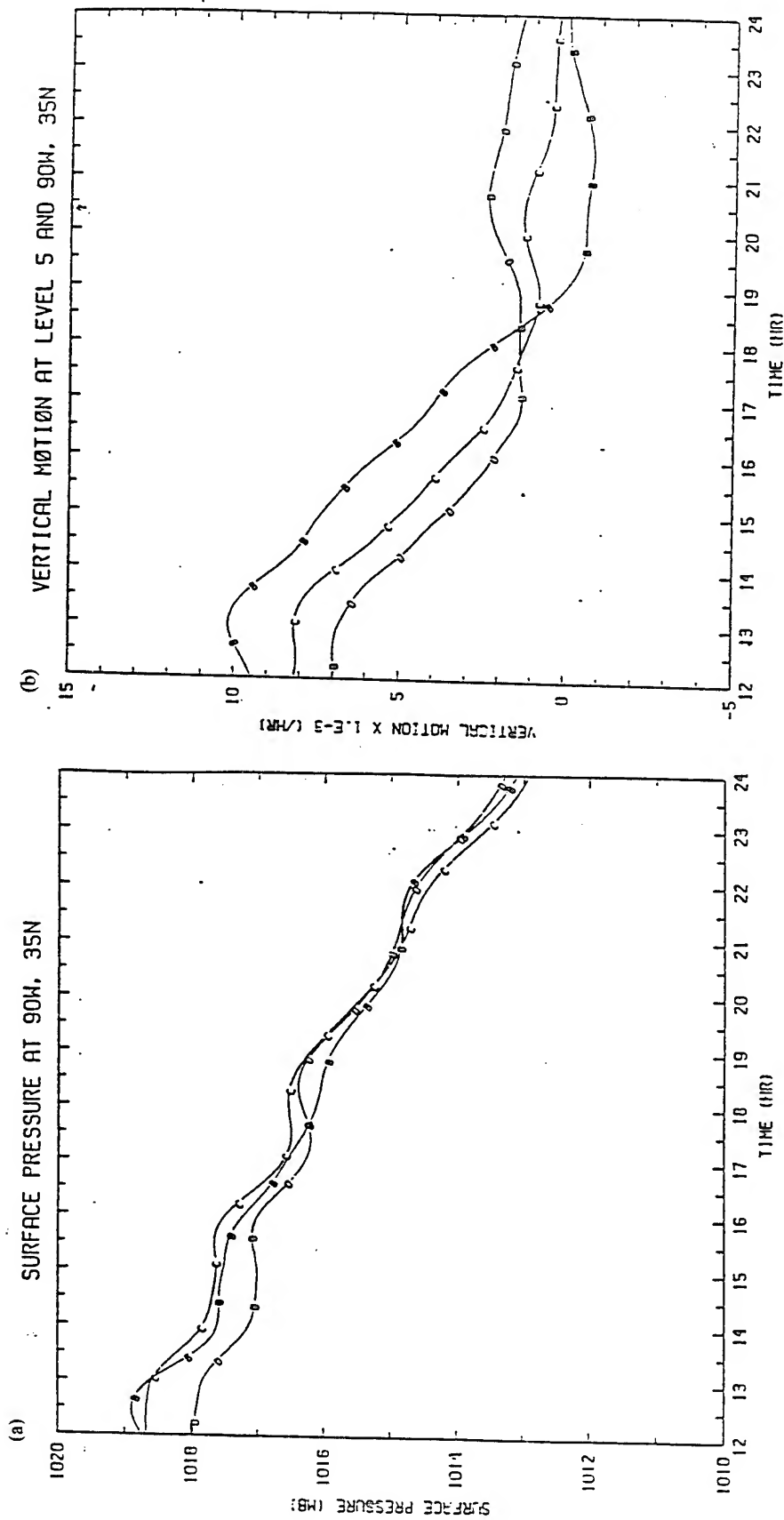


FIG. 17. Time series of (a) surface pressure in mb and (b) the vertical motion (in sigma coordinates) in hour⁻¹ at sigma level $\sigma = 0.5$, at a grid point on the GALE grid at 90°W and 35°N, during the second 12 hours of integration. Curves are for uninitialized initial conditions for a split-explicit integration (Curve B); for a split-explicit integration with a non-divergent initial condition (Curve C) and for split-explicit integrations with a non-linear mass balance (Curve D).

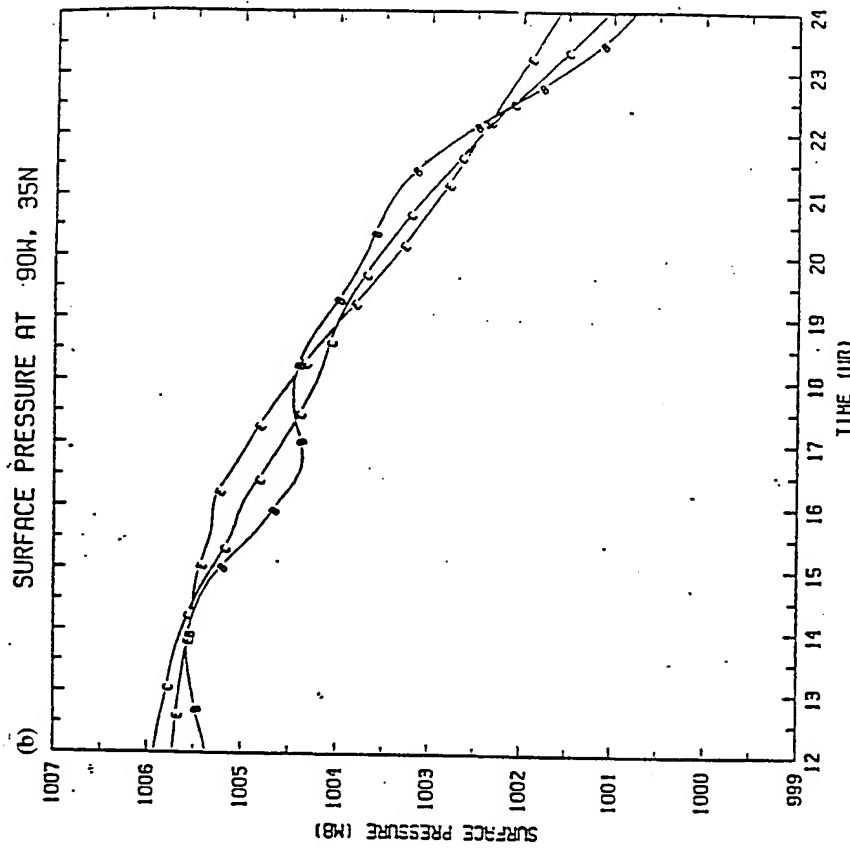
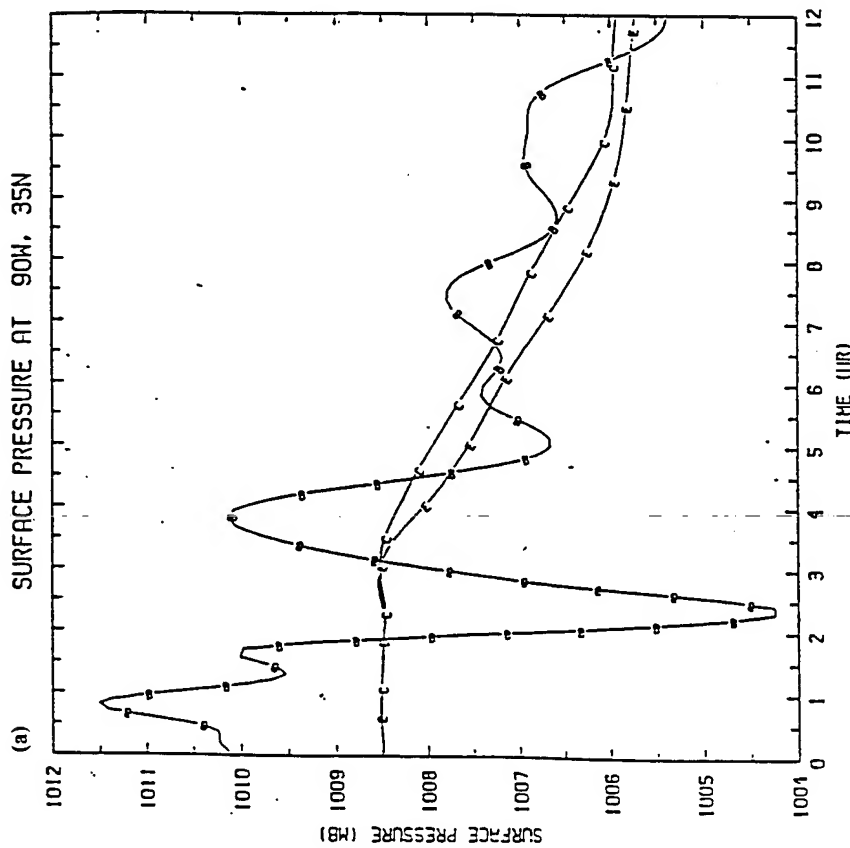


FIG. 18. Time series of surface pressure in mb and the vertical motion (in sigma coordinates) at $\sigma = 0.5$, at a grid point at 90°W and 35°N on the US grid. (a) shows the surface pressure during the first 12 hours of integration and (b) the second 12 hours of integration. (c) shows the vertical motion in hour^{-1} during the first 12 hours of integration and (d) the second 12 hours of integration. Curves are for uninitialized initial conditions (Curve B) and for initialized initial conditions (Curve C), using the Perkey Kreitzberg lateral boundary scheme. Curve E is for initialized initial conditions with the Davies lateral boundary scheme.

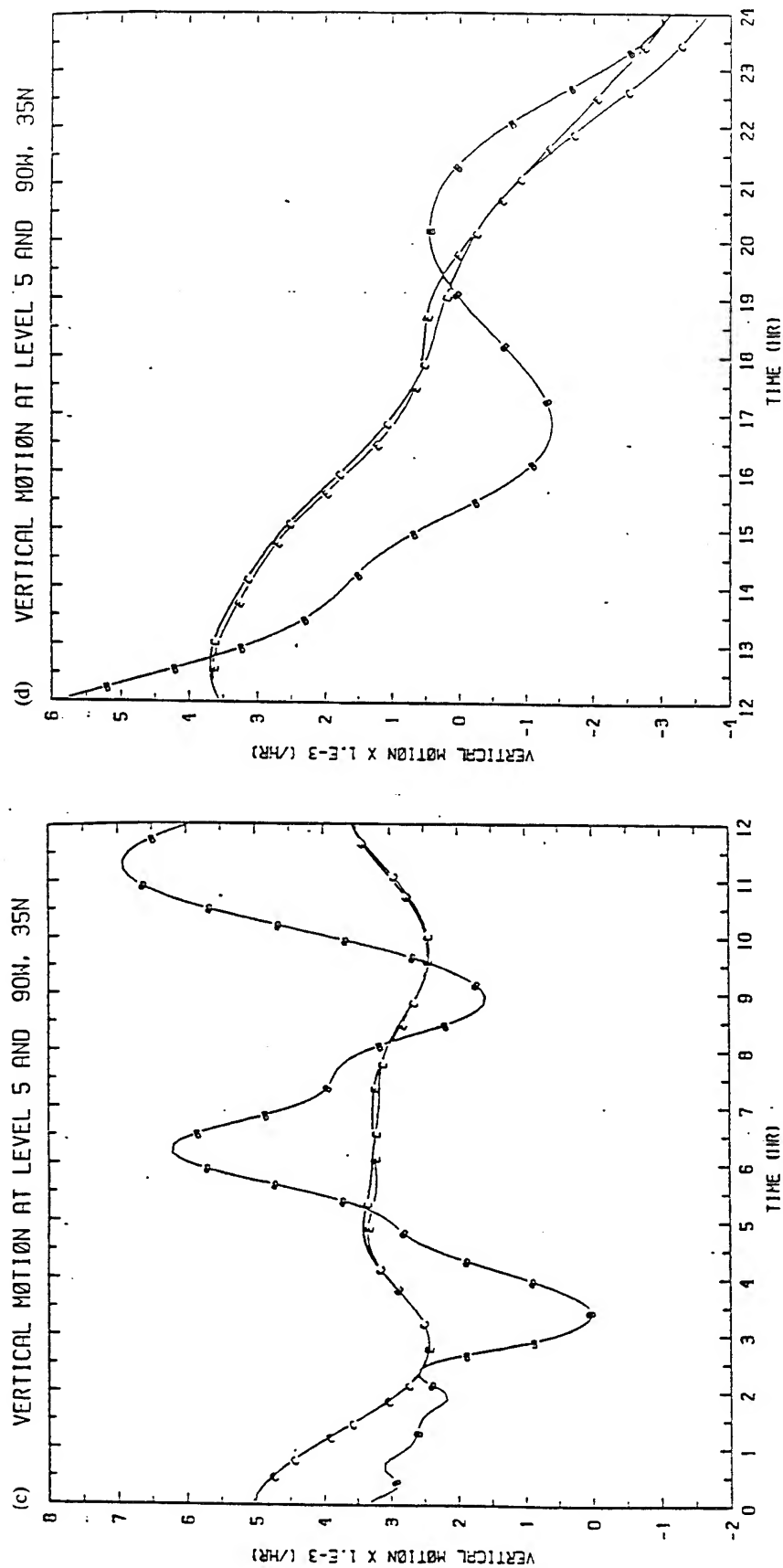


FIG. 18. Time series of surface pressure in mb and the vertical motion (in sigma coordinates) at $\sigma = 0.5$, at a grid point at 90°W and 35°N on the US grid. (a) shows the surface pressure during the first 12 hours of integration and (b) the second 12 hours of integration. (c) shows the vertical motion in hour⁻¹ during the first 12 hours of integration and (d) the second 12 hours of integration. Curves are for uninitialized initial conditions (Curve B) and for initialized initial conditions (Curve C), using the Perkey Kreitzberg lateral boundary scheme. Curve E is for initialized initial conditions with the Davies lateral boundary scheme.

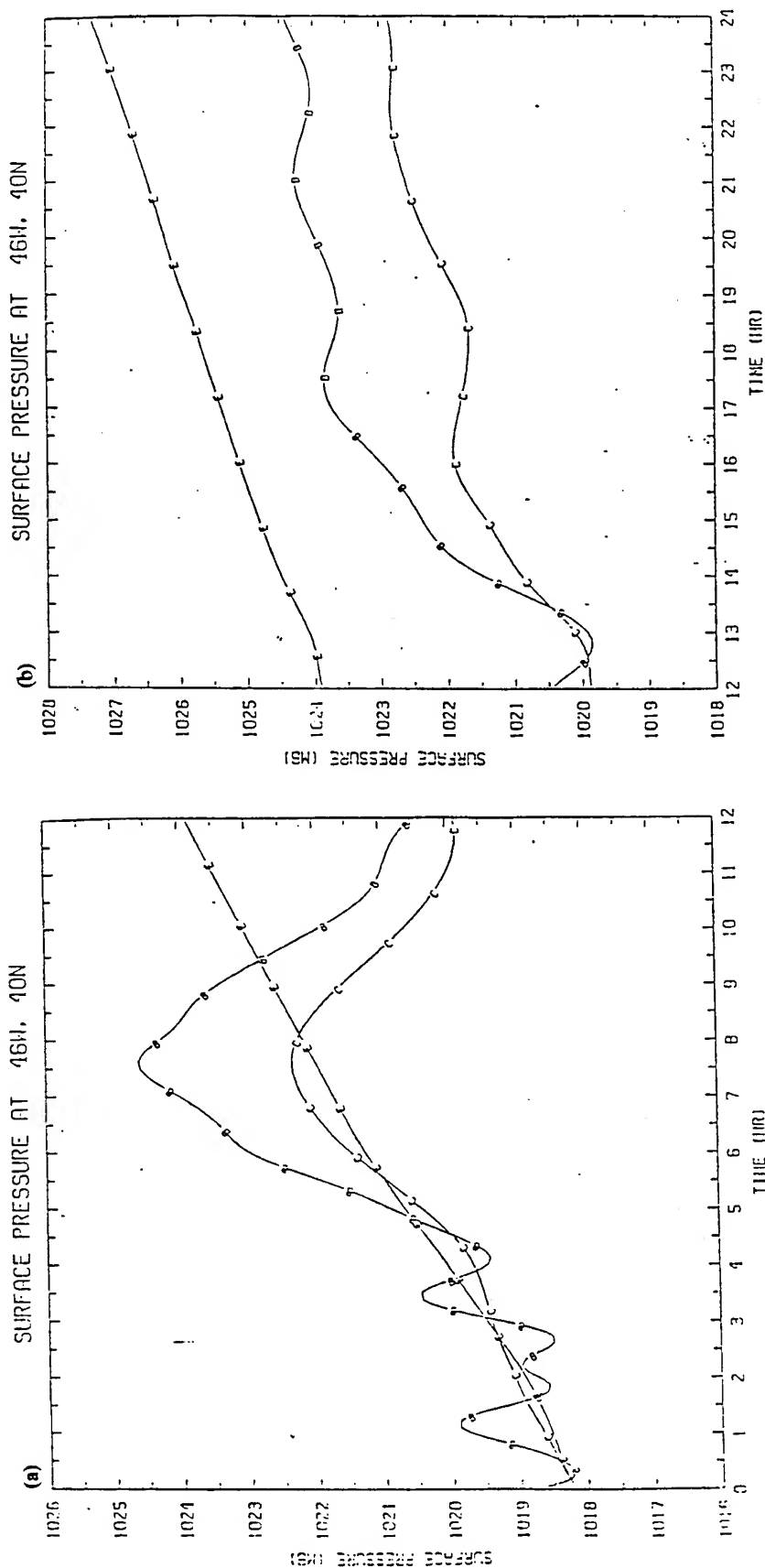


FIG. 19. Time series of surface pressure in mb and the vertical motion (in sigma coordinates) in hour⁻¹ at $\sigma = 0.5$, at a grid point in the boundary zone on the US grid at 46°W and 40°N. (a) shows the surface pressure in mb during the first 12 hours of integration and (b) the second 12 hours of integration. (c) shows the vertical motion during the first 12 hours of integration and (d) the second 12 hours of integration. Curves are as in Fig. 18.

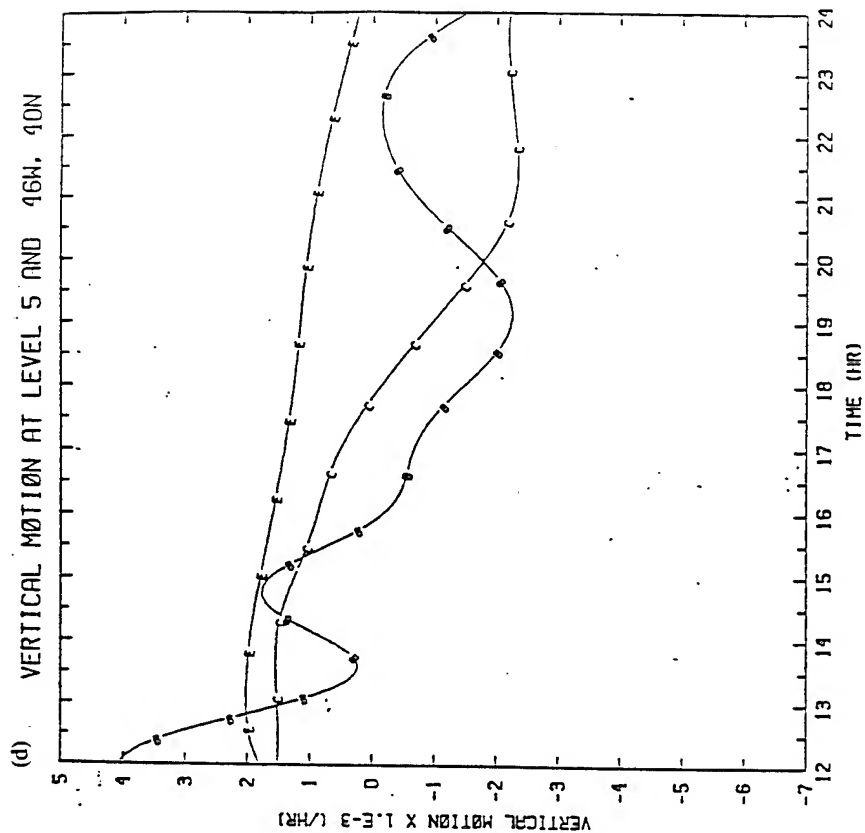
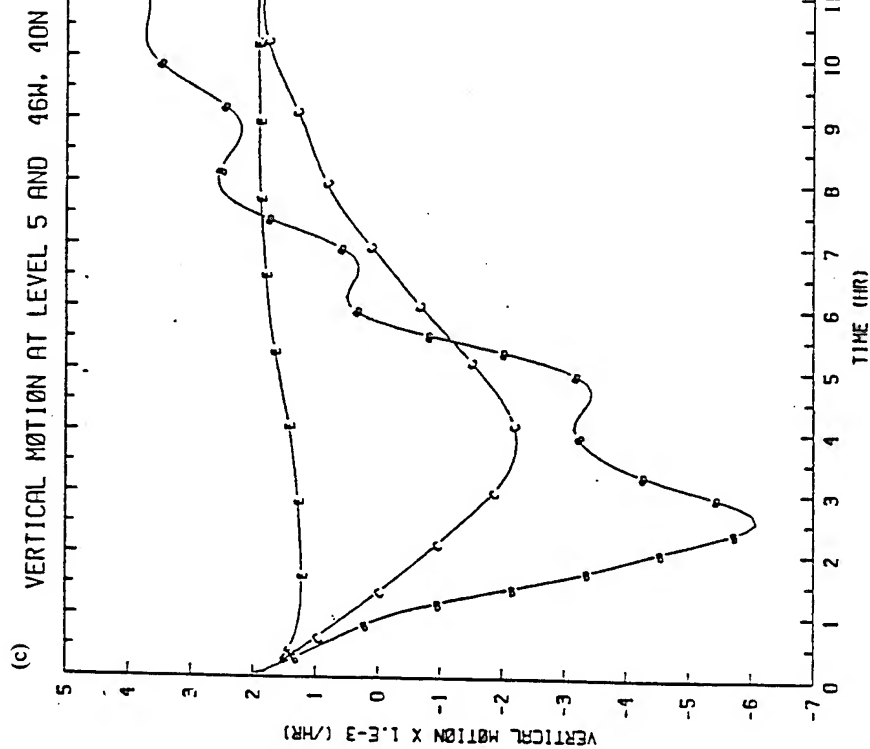


FIG. 19. Time series of surface pressure in mb and the vertical motion (in sigma coordinates) in hour^{-1} at $\sigma = 0.5$, at a grid point in the boundary zone on the US grid at 46°W and 40°N . (a) shows the surface pressure in mb during the first 12 hours of integration and (b) the second 12 hours of integration. (c) shows the vertical motion during the first 12 hours of integration and (d) the second 12 hours of integration. Curves are as in Fig. 18.

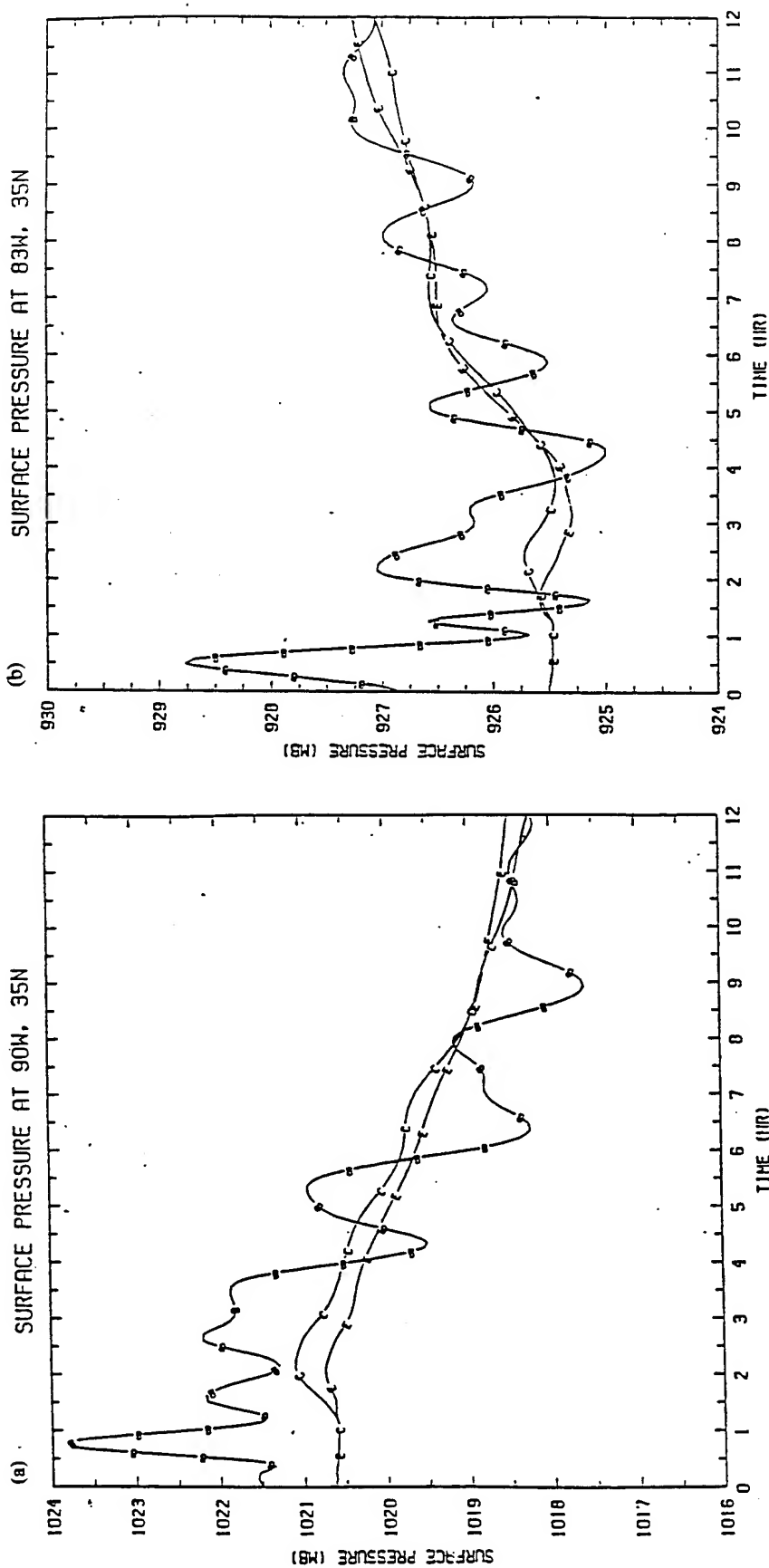


FIG. 20. Time series of surface pressure and the vertical motion (in sigma coordinates) at $\sigma = 0.5$ at two grid points on the GALE grid during the 12 hours of integration. (a) shows the surface pressure in mb at 90°W and 35°N and (b) at 83°W and 35°N. (c) shows the vertical motion in hour⁻¹ at 90°W and 35°N and (d) at 83°W and 35°N. Curves are for uninitialized initial conditions (Curve B) and for initialized initial conditions (Curve C), using the Perkey Kreitzberg lateral boundary scheme. Curve E is for initialized initial conditions with the Davies lateral boundary scheme.

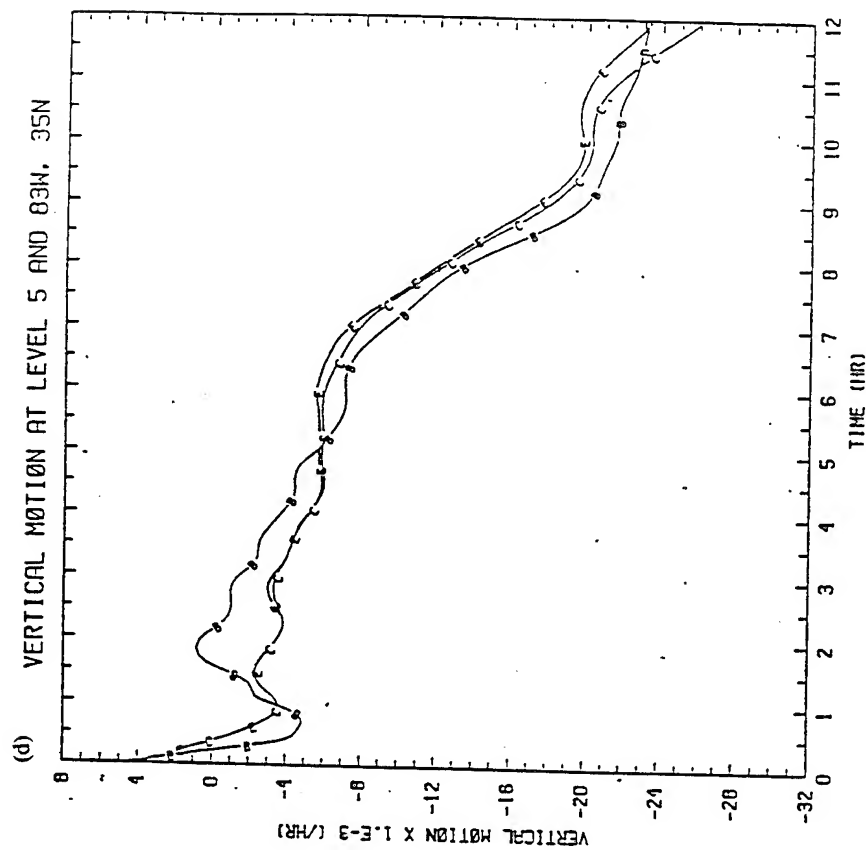
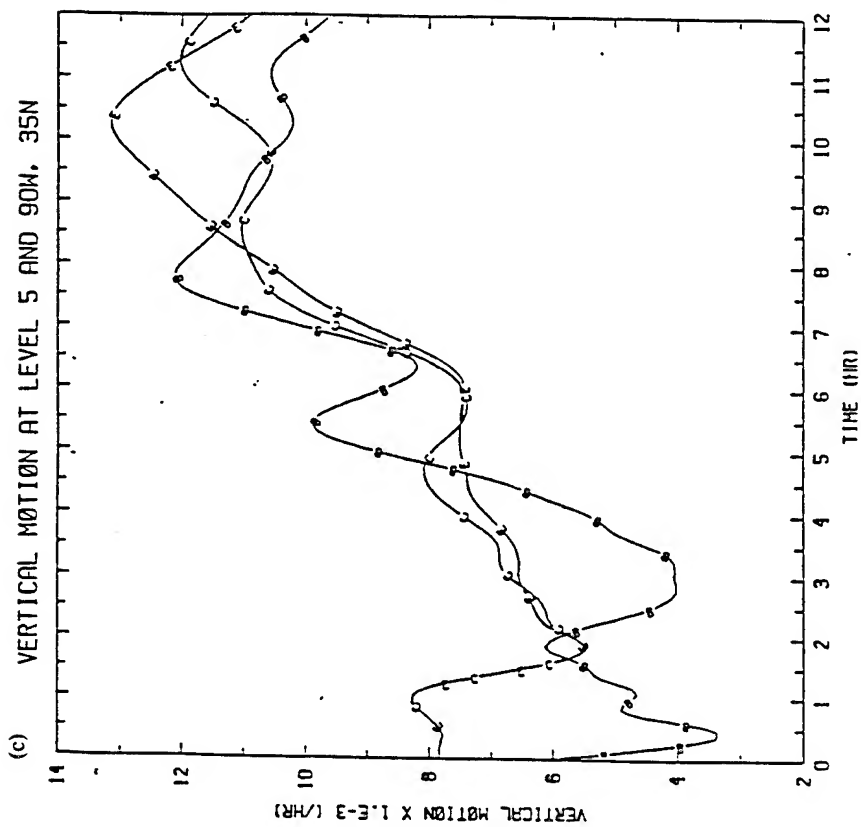


FIG. 20. Time series of surface pressure and the vertical motion (in sigma coordinates) at $\sigma = 0.5$ at two grid points on the GALE grid during the 12 hours of integration. (a) shows the surface pressure in mb at 90°W and 35°N and (b) at 83°W and 35°N . (c) shows the vertical motion in hour^{-1} at 90°W and 35°N and (d) at 83°W and 35°N . Curves are for uninitialized initial conditions (Curve B) and for initialized initial conditions (Curve C), using the Perkey Kreitzberg lateral boundary scheme. Curve E is for initialized initial conditions with the Davies lateral boundary scheme.

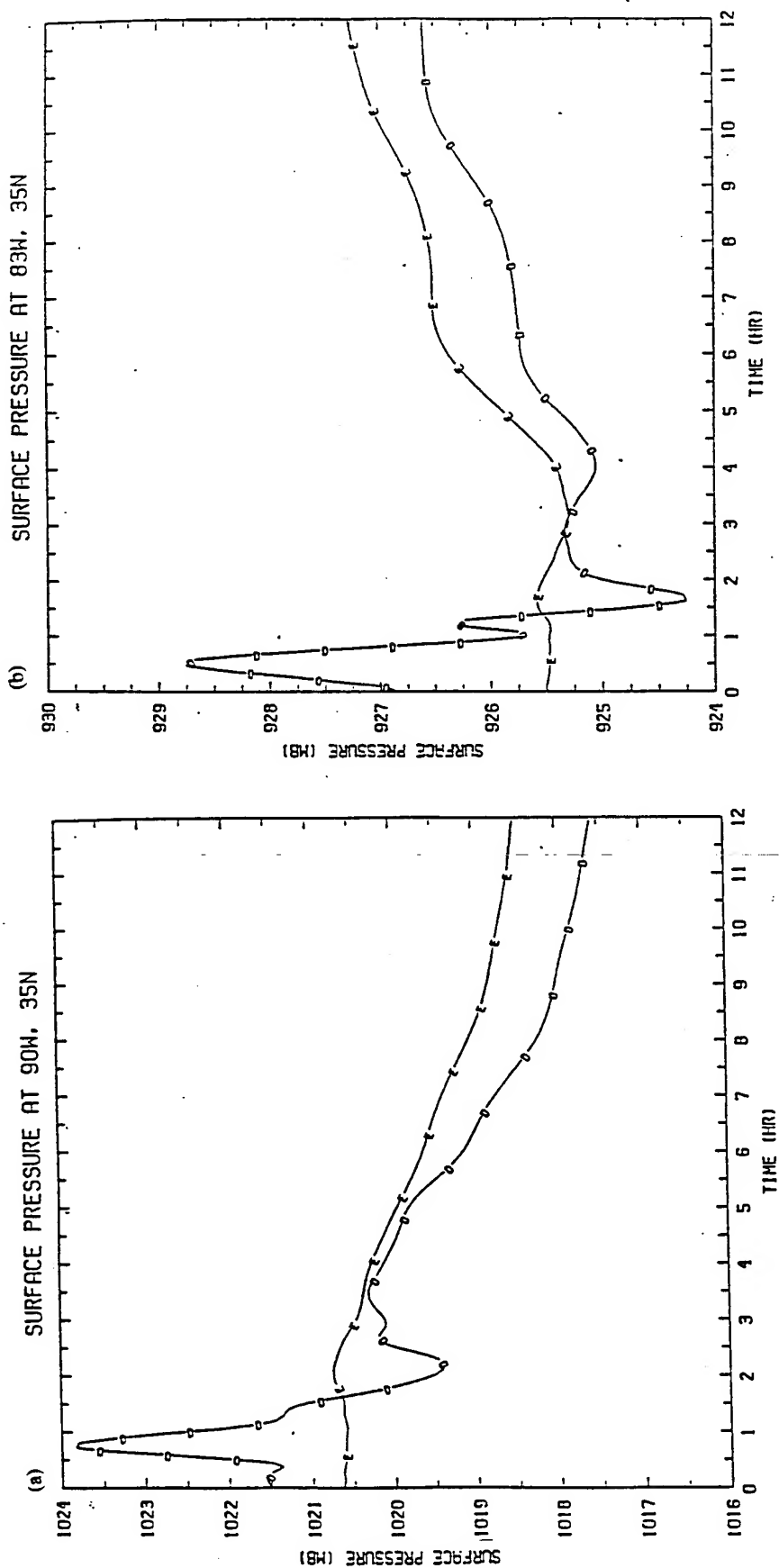


FIG. 21. Time series of surface pressure and the vertical motion (in sigma coordinates) at $\sigma = 0.5$ at two grid points on the GALE grid during the 12 hours of integration. (a) shows the surface pressure in mb at 90°W and 35°N and (b) at 83°W and 35°N. (c) shows the vertical motion in hour⁻¹ at 90°W and 35°N and (b) at 83°W and 35°N. Curves are for uninitialized initial conditions (Curve D) and for initialized initial conditions (Curve E), using the Davies lateral boundary scheme.

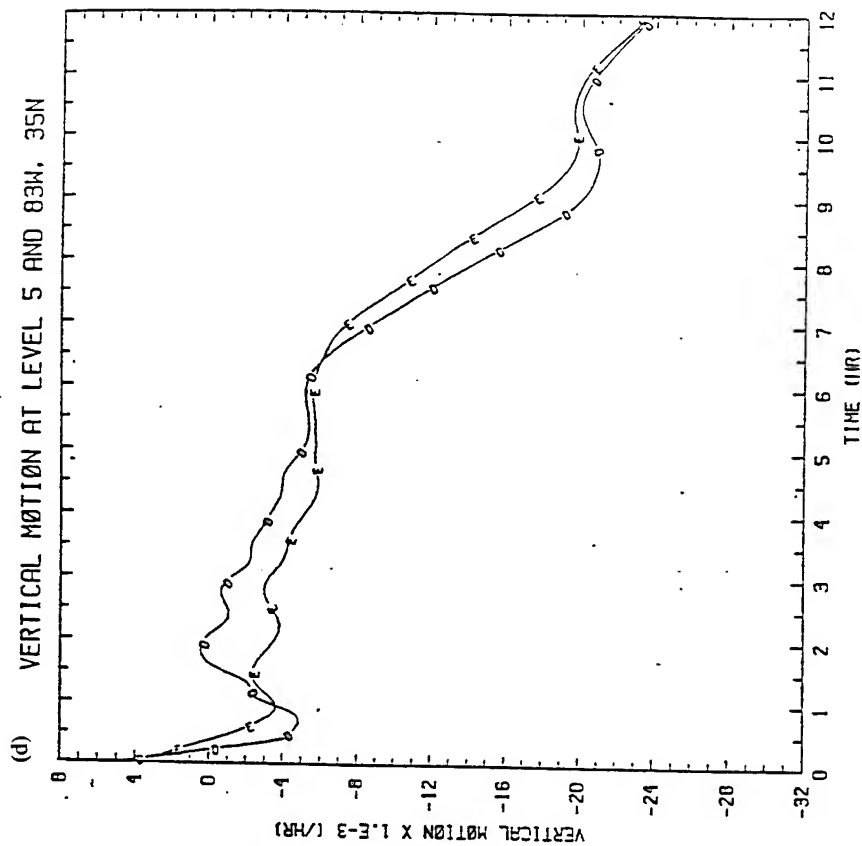
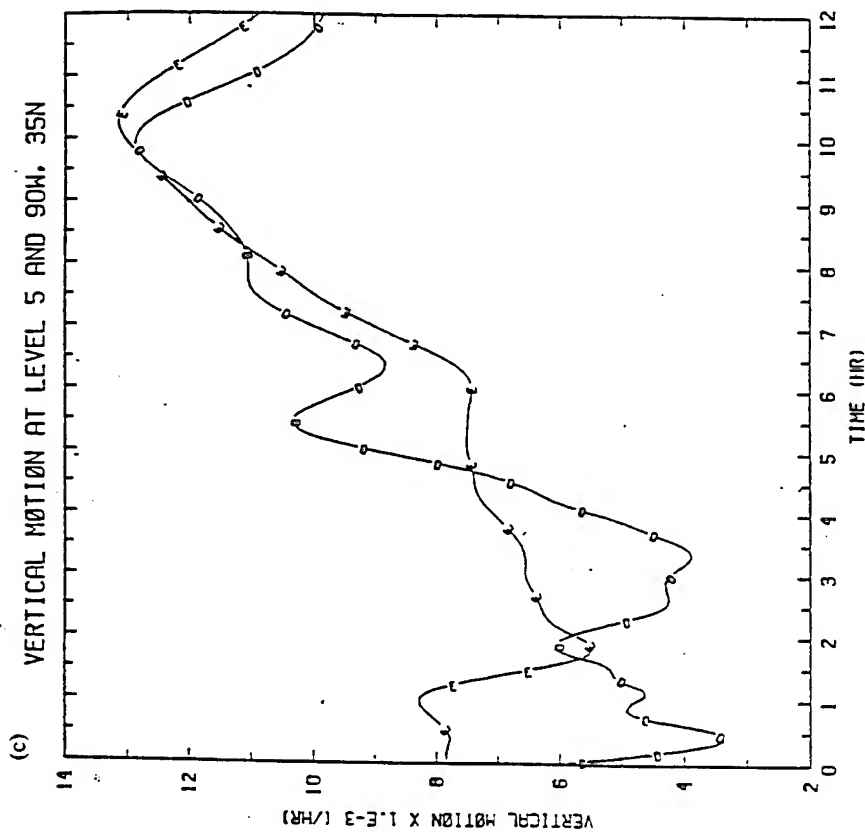


FIG. 21. Time series of surface pressure and the vertical motion (in sigma coordinates) at $\sigma = 0.5$ at two grid points on the GALE grid during the 12 hours of integration. (a) shows the surface pressure in mb at 90°W and 35°N and (b) at 83°W and 35°N. (c) shows the vertical motion in hour⁻¹ at 90°W and 35°N and (d) at 83°W and 35°N. Curves are for uninitialized initial conditions (Curve D) and for initialized initial conditions (Curve E), using the Davies lateral boundary scheme.

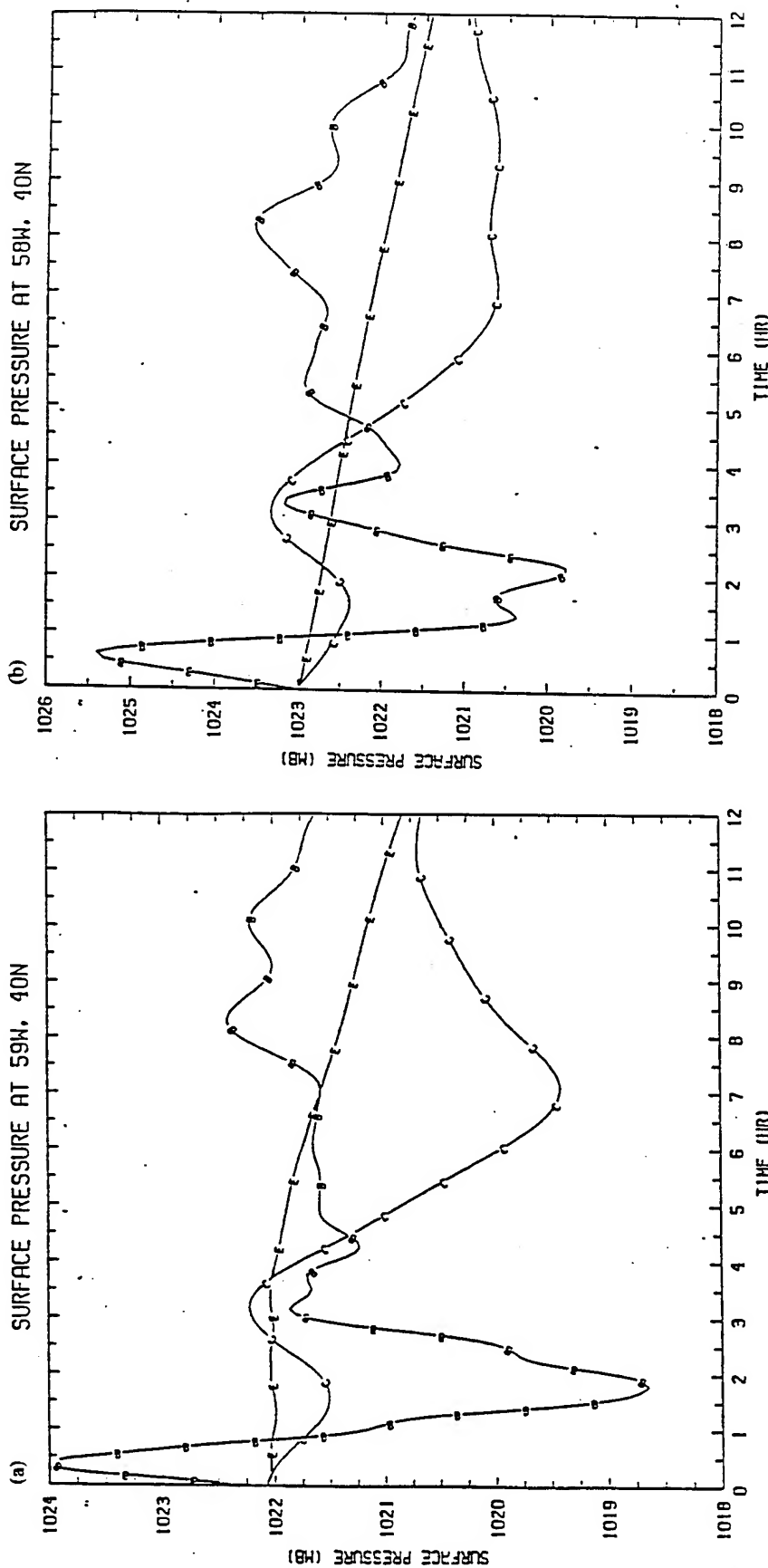


FIG. 22. Time series of surface pressure and the vertical motion (in sigma coordinates) at $\sigma = 0.5$ at two grid points in the boundary zone on the GALE grid during the 12 hours of integration. (a) shows the surface pressure in mb at 59°W and 40°N and (b) at 58°W and 40°N. (c) shows the vertical motion in hour⁻¹ at 59°W and 40°N and (d) at 58°W and 40°N. Curves are for uninitialized initial conditions (Curve B) and for initialized initial conditions (Curve C), using the Perkey Kreitzberg lateral boundary scheme. Curve E is for uninitialized initial conditions with the Davies lateral boundary scheme.

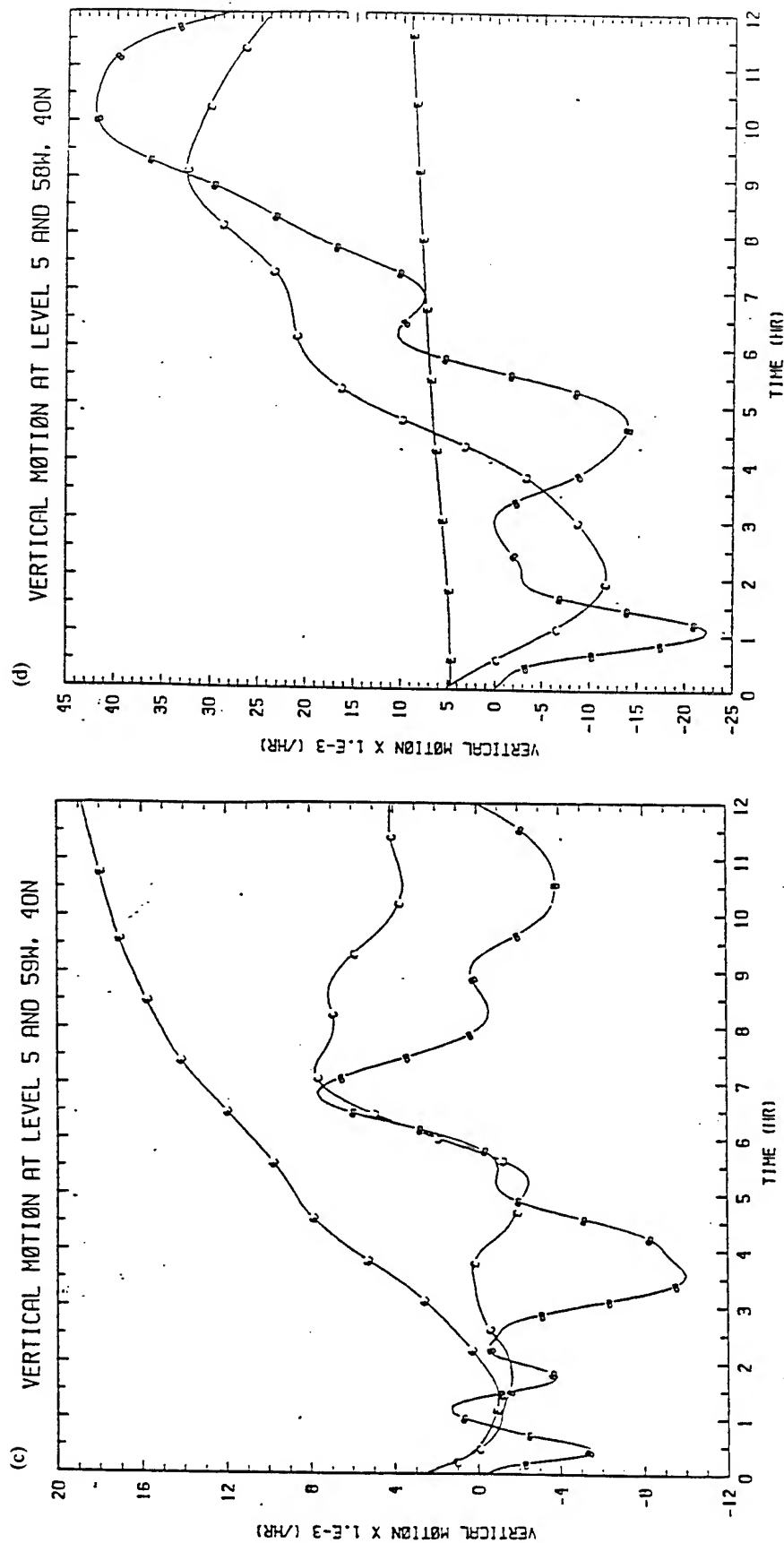


FIG. 22. Time series of surface pressure and the vertical motion (in sigma coordinates) at $\sigma = 0.5$ at two grid points in the boundary zone on the GALE grid during the 12 hours of integration. (a) shows the surface pressure in mb at 59°W and 40°N and (b) at 58°W and 40°N. (c) shows the vertical motion in hour⁻¹ at 59°W and 40°N and (d) at 58°W and 40°N. Curves are for uninitialized initial conditions (Curve B) and for initialized initial conditions (Curve C), using the Perkey Kreitzberg lateral boundary scheme. Curve E is for uninitialized initial conditions with the Davies lateral boundary scheme.

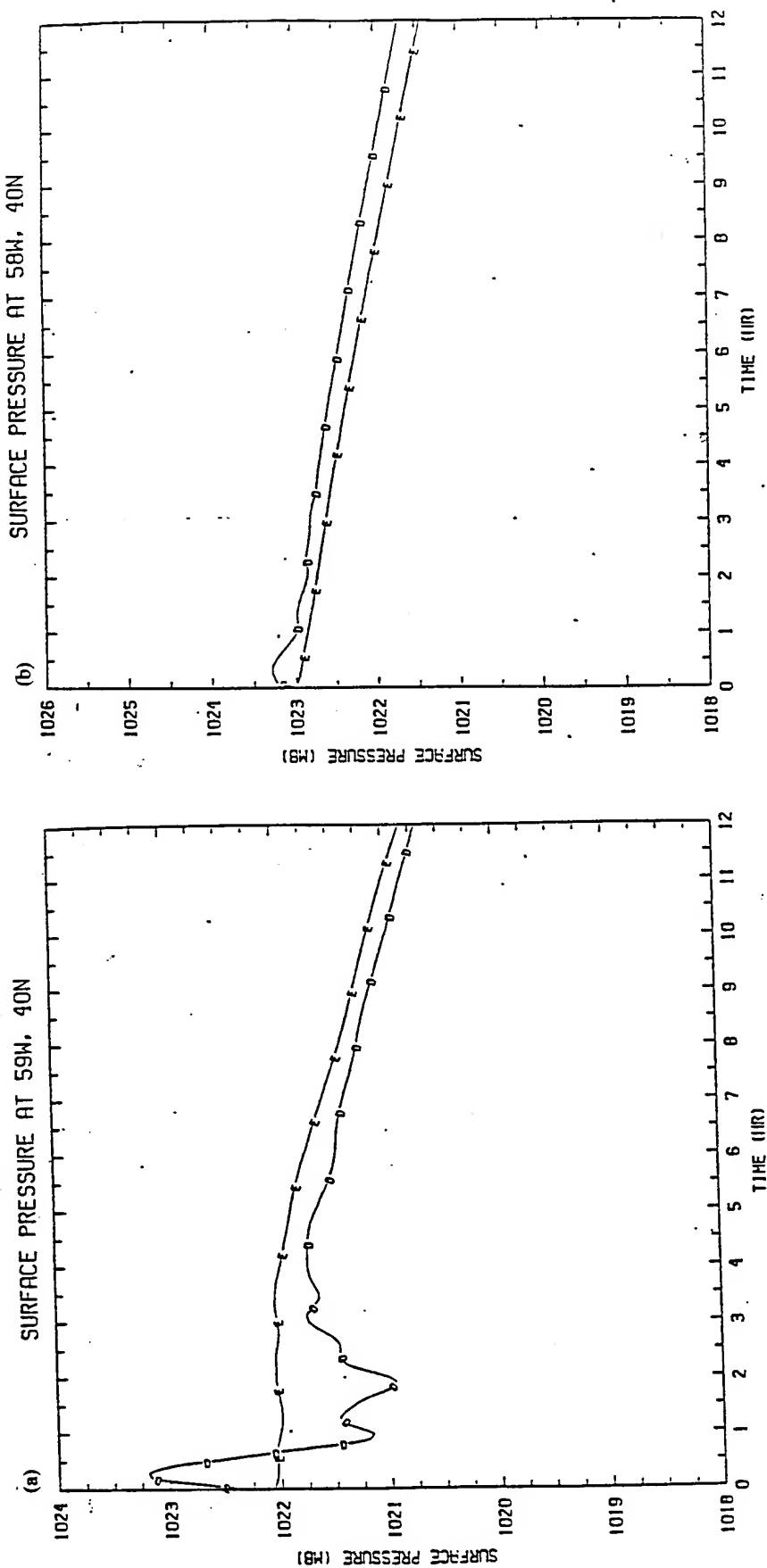


FIG. 23. Time series of surface pressure and the vertical motion (in sigma coordinates) at $\sigma = 0.5$ at two grid points in the boundary zone on the GALE grid during the 12 hours of integration. (a) shows the surface pressure in mb at 59°W and 40°N and (b) at 58°W and 40°N . (c) shows the vertical motion in hour^{-1} at 59°W and 40°N and (d) at 58°W and 40°N . Curves are for uninitialized initial conditions (Curve D) and for initialized initial conditions (Curve E), using the Davies lateral boundary scheme.

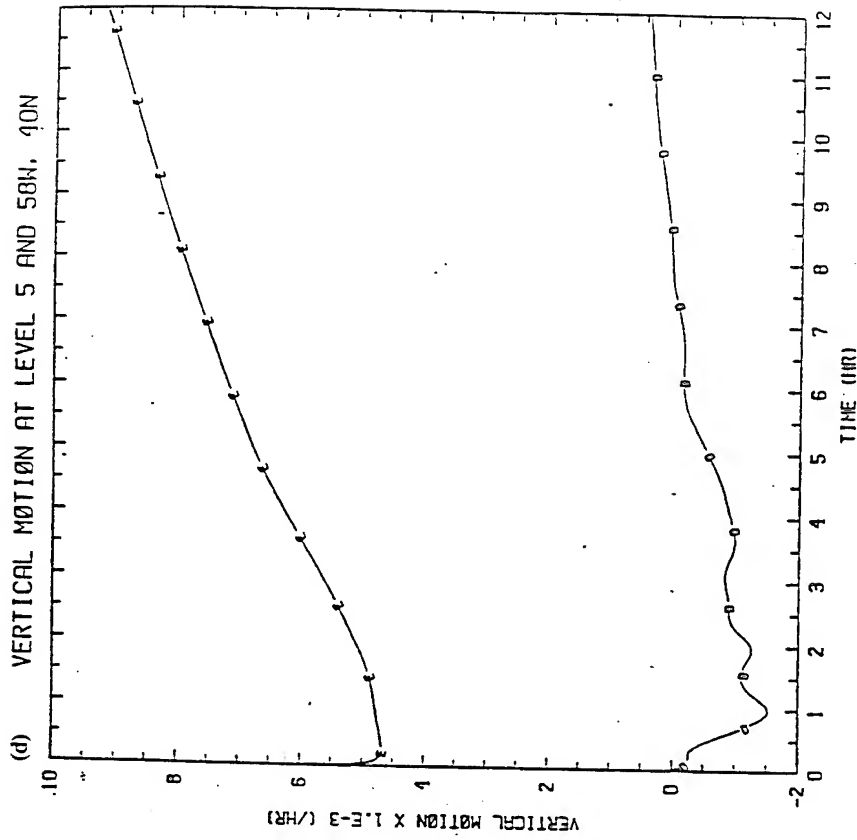
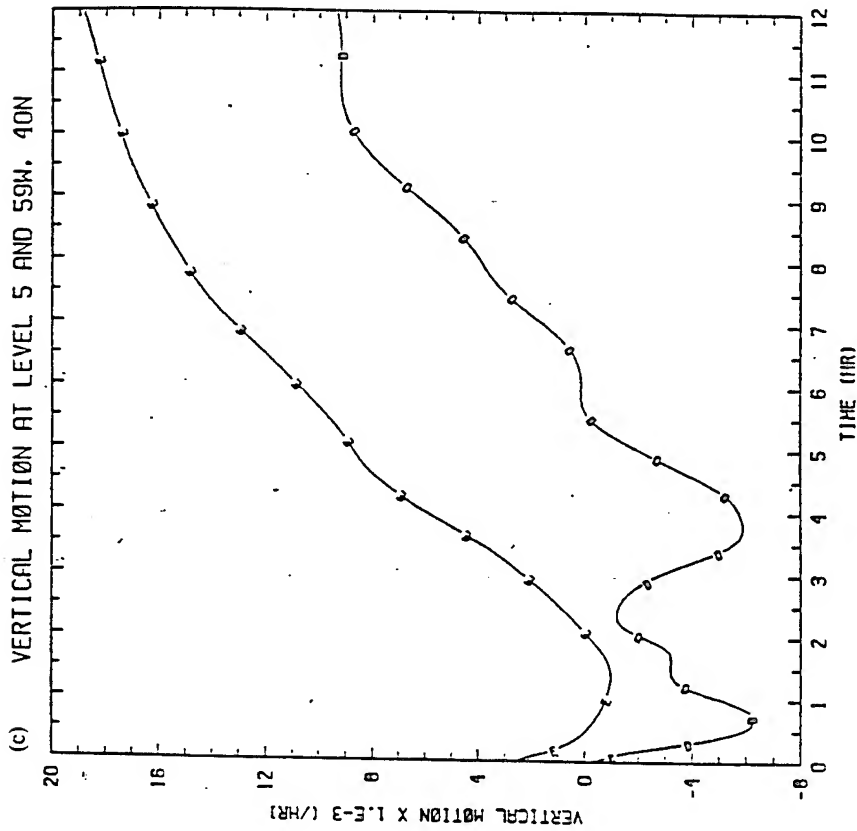


FIG. 23. Time series of surface pressure and the vertical motion (in sigma coordinates) at $\sigma = 0.5$ at two grid points in the boundary zone on the GALE grid during the 12 hours of integration. (a) shows the surface pressure in mb at 59°W and 40°N and (b) at 58°W and 40°N . (c) shows the vertical motion in hour^{-1} at 59°W and 40°N and (d) at 58°W and 40°N . Curves are for uninitialized initial conditions (Curve D) and for initialized initial conditions (Curve E), using the Davies lateral boundary scheme.

Appendix E

Application of Vertical-Mode Initialization to a Limited-Area Model in Flux Form

Application of Vertical-Mode Initialization to a Limited-Area Model in Flux Form

KEITH D. SASHEGYI*

Science Applications International Corporation, McLean, Virginia

RANGARAO V. MADALA

Naval Research Laboratory, Washington, D.C.

(Manuscript received 16 June 1991, in final form 15 May 1992)

ABSTRACT

The vertical-mode initialization procedure of Bourke and McGregor is applied to a limited-area weather prediction model that is formulated in flux form and is shown to be successful in reducing the undesirable gravity-wave oscillations in integrations of the numerical model. Alternative boundary conditions are developed for the scheme so that the changes to the wind at the lateral boundaries of the model are consistent with the changes in the integrated mass divergence and vorticity over the domain. The convergence of the modified scheme is shown to be rapid for two different grids. For a grid with significant topography along the lateral boundaries, use of increased diffusion in the boundary zone is shown to negatively impact the convergence of the scheme. Model integrations are performed to show the effectiveness of the scheme with improved boundary conditions in removing the gravity-wave oscillations. The results are compared with the damping of the gravity waves in the boundary zone by the time-integration scheme and by different lateral boundary treatments. The influence of noisy boundary values is also tested.

1. Introduction

Normal-mode initialization, which was developed by Machenhauer (1977) and Baer (1977), has been very successful in removing the high-frequency gravity-wave oscillations from integrations of global numerical weather prediction models (see review by Daley 1981). Briere (1982) applied nonlinear normal-mode initialization to a limited-area model, computing the normal modes for an f -plane linearization in which the map factors were constant and where the values of the model variables were assumed constant at the lateral boundaries. The vertical-mode initialization scheme of Bourke and McGregor (1983) introduced filtering conditions for inertia-gravity waves that can be applied to the dynamical equations of a limited-area model and that were shown to be related to the application of nonlinear normal-mode initialization for an f -plane linearization. Juvanon du Vachat (1986) and Temperton (1988) eloquently describe this equivalence of the application of Bourke and McGregor's filtering conditions in physical space to nonlinear normal-mode initialization, without the horizontal structure of the

normal modes having to be computed. Temperton shows in fact that the normal-mode scheme can be "implicitly" implemented in the physical space of the vertical modes of the model without any knowledge required of the normal modes themselves. The approach is extended by Temperton (1988) to include the β term in the linearization and to use higher-order time derivatives for the filtering conditions. In the vertical-mode scheme, the filtering conditions are applied to those vertical modes of the model for which the phase speeds of the freely propagating gravity modes are larger than the typical speeds of weather systems. These schemes, however, do preclude using a frequency cutoff, as can be applied to each individual normal mode in the normal-mode initialization. This can be a disadvantage for limited-area models of large domain size, since the larger global-scale gravity modes of lower frequency will also be filtered (Temperton 1988). In this case, a horizontal-scale filter would need to be applied to correct the problem.

In this paper, the vertical-mode initialization scheme B of Bourke and McGregor (1983) is applied to a limited-area weather prediction model formulated in flux form and using an alternative approach to the boundary conditions for the scheme. The linearization of the flux form of the equations is not as straightforward as with the usual advective form of the equations used by Bourke and McGregor. In these vertical-mode initialization schemes, diagnostic equations are derived for the mass and divergence fields of the limited-area model

* Present affiliation: Center for Advanced Space Sensing, Naval Research Laboratory, Washington, D.C.

Corresponding author address: Dr. Keith D. Sashegyi, Atmosphere/Ocean Sensing Branch, Naval Research Laboratory, Code 4220, Washington, DC 20375-5000.

and then, with suitable boundary conditions, solved iteratively for the first three vertical modes of the numerical model. As in Bourke and McGregor, we keep the mass field fixed at the lateral boundaries of the model. To provide a boundary condition for the mass divergence, however, we use an approximate mass divergence computed inside the lateral boundary by using the thermodynamic equation instead of assuming that the divergence does not change at the boundary as in Bourke and McGregor. In our scheme, the resulting changes to the tangential and normal wind are computed assuming no change in the streamfunction and velocity potential along the lateral boundaries of the model domain. With careful choice of the grid arrangement, the changes in the wind field along the boundary are consistent with the changes in the integrated vorticity and mass divergence over the model domain. Such consistency has not been achieved in applications of the scheme in other models.

The numerical model, the derivation of the vertical modes, and the application of the vertical-mode scheme for our model difference equations in flux form are briefly summarized in section 2. The convergence of the modified scheme for two different grids of differing resolution and domain size is shown in section 3. For uninitialized initial conditions, the influence of the treatment of the lateral boundaries and use of the split-explicit scheme for time integration in damping the high-frequency gravity waves in the boundary zone is shown for different lateral boundary treatments. The results are compared with integrations starting with initialized fields and using idealized boundary values derived from operational analyses that have been further initialized on the model grid. The effect of using boundary values derived from the uninitialized fields is also tested. The results are summarized in section 4.

2. Model description

The Naval Research Laboratory's (NRL) primitive equations model (Madala et al. 1987) is formulated in flux form; it uses sigma coordinates in the vertical and incorporates topography and physical parameterizations of the boundary-layer and precipitation processes. In the horizontal, the mass and momentum variables are staggered on a C grid (Arakawa and Lamb 1977) for spherical coordinates. In the vertical, the atmosphere is divided into a number of layers. All the dependent variables except the vertical velocity are defined at the middle of the layers, while the vertical velocity is defined at the levels separating the layers. The finite-difference scheme in flux form is second-order accurate, and, in the absence of sources and sinks, conserves total mass, momentum, and energy. The model uses horizontal diffusion of the second order and includes large-scale precipitation and a cumulus parameterization using a modified Kuo (1974) scheme. For testing the initialization scheme, ten equally spaced

layers are used, and the boundary layer is parameterized by using a drag-coefficient formulation. The time-integration scheme is a split-explicit method with time steps varying with the vertical modes (Madala 1981). In the scheme, we choose a large time step Δt , which satisfies the CFL condition for the third internal vertical gravity mode of the numerical model, and we integrate the model forward one time step. Corrections for the "faster" vertical modes are then integrated at smaller time steps of $\Delta t/8$, $\Delta t/4$, $\Delta t/2$ for the external, first internal, and second internal vertical modes, respectively, with boundary conditions specified for the mass variables at the lateral boundaries of the model. The slowly varying terms, such as the nonlinear, frictional, Coriolis, and heating terms, are computed once for every large time step.

After each large time step, boundary values for the mass and wind fields are required at the lateral boundaries of the model. At the lateral boundaries, the mass variables and the tangential wind are specified at the outer lateral boundary of the model in our case, while the normal wind is specified at grid points staggered half a grid distance into the interior. In this paper, both the tendency damping scheme of Perkey and Kreitzberg (1976) and the relaxation scheme of Davies (1976, 1983) are used to update the boundary values in a zone along the lateral boundary. Due to the overspecification of the model variables at the lateral boundary by using either of the above pragmatic schemes, the mass variables and tangential wind at the boundaries are essentially ignored by the model dynamics during integration, leaving the normal wind along the boundary to influence the interior solution. To prevent any unrealistic buildup of mass in the model domain by errors in the specified normal wind at the boundary (particularly when using uninitialized initial conditions or boundary values), the normal winds are further altered at the boundary after each time step to eliminate any change in the total mass in the model domain. Most other limited-area models that use the C grid define the normal wind at the outer lateral boundary of the model domain so that the specified tangential wind along the boundary influences the interior solution through the model dynamics. In that case, unrealistic buildup of mass should be less severe. In our case, however, by using initialized initial conditions and boundary values during integration of the model, the correction to the normal winds at the lateral boundary is very small and even unnecessary. Further, as we will see, our arrangement does facilitate solving for the streamfunction and velocity potential on the model grid during the initialization of the initial fields.

a. Vertical modes of the model

To solve for the vertical structure of the normal modes of our gridpoint model, we follow Temperton and Williamson (1981) and linearize about a basic state at rest with a mean temperature, which is a function

of the sigma coordinate only, separating the linear and nonlinear terms in the finite-difference form of the model governing equations. As they show, a generalized geopotential is defined whose derivative gives the horizontal pressure gradient in the horizontal equations of motion and whose time tendency is related to the divergence. A separation of the vertical structure of the model variables is then possible. An outline of the procedure follows for our model equations in flux form. The linearization of the pressure-gradient term in the flux form of the equations is not as straightforward as in the advective case treated by Temperton and Williamson (1981). The momentum equation for the u component of the wind in flux form in sigma coordinates is, for example,

$$\begin{aligned} \frac{\partial(p_s u)}{\partial t} + \frac{1}{h_x h_y} \left[\frac{\partial}{\partial x} (p_s u h_y u) + \frac{\partial}{\partial y} (p_s v h_x u) \right] \\ + \frac{\partial}{\partial \sigma} (p_s \sigma u) - f p_s v \\ = - \frac{p_s}{h_x} \frac{\partial \phi}{\partial x} - \frac{RT}{h_x} \frac{\partial p_s}{\partial x} + p_s F_u, \quad (1) \end{aligned}$$

where u and v are the horizontal wind components, T the temperature, ϕ the geopotential, p_s the surface pressure, and σ the vertical motion in the sigma coordinate. The map factors are h_x and h_y , f is the Coriolis parameter, and R is the gas constant for dry air. Friction and diffusion are represented by F_u . The pressure-gradient term can be written

$$\begin{aligned} - \frac{p_s}{h_x} \frac{\partial \phi}{\partial x} - \frac{RT}{h_x} \frac{\partial p_s}{\partial x} \\ = - \frac{1}{h_x} \left[\frac{\partial}{\partial x} (p_s \phi) + (RT - \phi) \frac{\partial p_s}{\partial x} \right], \end{aligned}$$

which when writing the temperature T in terms of a mean T^* plus a deviation T' becomes

$$\begin{aligned} - \frac{1}{h_x} \left[\frac{\partial}{\partial x} (p_s \phi) + (RT^* - \phi^*) \frac{\partial p_s}{\partial x} + (RT' - \phi') \frac{\partial p_s}{\partial x} \right] \\ = - \frac{1}{h_x} \left[\frac{\partial}{\partial x} p_s (\phi - \phi_s + RT^* - \phi^*) \right. \\ \left. + \frac{\partial}{\partial x} (p_s \phi_s) + (RT' - \phi') \frac{\partial p_s}{\partial x} \right]. \quad (2) \end{aligned}$$

A generalized geopotential Φ is defined by

$$\Phi = p_s (\phi - \phi_s + RT^* - \phi^*), \quad (3)$$

where ϕ_s is the geopotential at the surface and $\phi = \phi^* + \phi'$. To allow for the tendency of the generalized geopotential to be later related to the mass divergence, it is necessary to remove the surface geopotential in the definition. This is not necessary when linearizing the advective form of the equations. Also, the extra middle

term depending on the surface geopotential must be combined with the nonlinear terms. Since, however, topographic effects are treated as nonlinear corrections in the linearization anyway, the added term is not considered a problem. The finite-difference form of the governing equations in flux form can now be written as

$$\frac{\partial \bar{p}_s^x u}{\partial t} - \bar{p}_s f \bar{v}^y x + \delta_x \Phi = A_u, \quad (4)$$

$$\frac{\partial \bar{p}_s^y v}{\partial t} + \bar{p}_s f \bar{u}^x y + \delta_y \Phi = A_v, \quad (5)$$

$$\frac{\partial p_s T}{\partial t} + \mathbf{M}_2 \mathbf{D} = A_T, \quad (6)$$

$$\frac{\partial p_s}{\partial t} + \mathbf{N}_2^T \mathbf{D} = 0, \quad (7)$$

and further the hydrostatic relation and continuity equations are written

$$\phi - \phi_s = \mathbf{M}_1 \mathbf{T}, \quad (8)$$

$$p_s \sigma = \mathbf{N}_1 \mathbf{D}, \quad (9)$$

where u , v , Φ , A , T , and \mathbf{D} are column vectors, \mathbf{M}_1 , \mathbf{M}_2 , \mathbf{N}_1 are matrices, and \mathbf{N}_2^T represents the transpose of vector \mathbf{N}_2 . The dynamical variables are in vector form, where the elements of the vectors u , v , T , ϕ , and Φ represent the values of the horizontal wind components, temperature, geopotential, and generalized geopotential at each of the model sigma levels for a single horizontal grid point. Here, \mathbf{D} is the mass-weighted divergence on the sigma surfaces. The average geopotential ϕ^* on the sigma surface is related to the mean temperature T^* through the hydrostatic relation $\phi^* = \mathbf{M}_1 \mathbf{T}^*$. The vertical motion σ in the sigma coordinate σ is defined for sigma levels at the boundaries between the vertical layers. Subscripts representing the horizontal grid points on the C grid have been omitted for clarity. Here, the difference and averaging operators δ and " $\bar{\cdot}$ " are defined in the x direction, for example, by

$$\delta_x \phi = \frac{\phi(x + \Delta x/2) - \phi(x - \Delta x/2)}{h_x \Delta x},$$

$$\bar{p}_s^x = \frac{p_s(x + \Delta x/2) + p_s(x - \Delta x/2)}{2},$$

where Δx is the grid spacing for the x coordinate. Elements of the matrices \mathbf{M}_1 , \mathbf{M}_2 , \mathbf{N}_1 , and the vector \mathbf{N}_2 are functions of sigma only. The vectors on the right-hand side (rhs) of Eqs. (4), (5), and (6) include friction, nonlinear advection, diabatic terms, and the extra term due to the surface geopotential. Details of the vector and matrix elements can be found in the report by Madala et al. (1987).

By using the definition of Φ in Eq. (3) and combining Eqs. (6) and (7), we obtain for the time tendency of Φ ,

$$\frac{\partial \Phi}{\partial t} + \mathbf{M}_3 \mathbf{D} = \mathbf{A}_\Phi, \quad (10)$$

where the matrix \mathbf{M}_3 is defined as $\mathbf{M}_3 = \mathbf{M}_1 \mathbf{M}_2 + (\mathbf{RT}^* - \phi^*) \mathbf{N}_2^T$ and whose elements are only functions of the vertical sigma coordinate, while $\mathbf{A}_\Phi = \mathbf{M}_1 \mathbf{A}_T$. Solutions to the homogeneous form of Eqs. (4), (5), and (10) (with the terms on the rhs equal to zero) are the freely propagating normal modes of the numerical model. To obtain the vertical structure of the normal modes, the eigenvectors and corresponding eigenvalues are found for the matrix \mathbf{M}_3 . If \mathbf{E} represents the eigenvector matrix (with each column representing an eigenvector) of matrix \mathbf{M}_3 , then the resulting diagonalization is

$$\mathbf{E}^{-1} \mathbf{M}_3 \mathbf{E} = \mathbf{\Lambda},$$

where $\mathbf{\Lambda}$ is a diagonal matrix with the diagonal elements given by the eigenvalues. For the ten-layer model used in this paper, there are ten vertical modes. The first vertical mode with the largest eigenvalue is the external (barotropic) mode with nearly constant amplitude in the vertical direction and a phase speed of about 300 m s⁻¹. With decreasing magnitude of the eigenvalue, the vertical structure of the mode has more nodes (zero crossings) in the vertical ($k - 1$ nodes for the k th vertical mode), and the phase speed of the vertical mode decreases, reducing to about 1 m s⁻¹ for the tenth vertical mode (slowest phase speed).

b. Vertical-mode initialization

To suppress the high-frequency inertia-gravity-wave oscillations in integrations of the numerical model, scheme B of Bourke and McGregor is used. The scheme requires that, initially, the time tendencies of the divergence and the ageostrophic vorticity are zero and that the linearized potential vorticity does not change for the first few vertical modes of the numerical model. In fact, the amplitude of each gravity mode depends only on the projection of the divergence and the ageostrophic vorticity onto the horizontal structure of that normal mode (Leith 1980). It is not surprising that for the f -plane linearization, Bourke and McGregor showed that their scheme B is the equivalent in physical space to Machenhauer's condition on the amplitudes of the normal modes, which requires that the tendencies of the amplitudes of the fast gravity modes be zero at the start of the integration (see also Juvanon du Vachat 1986 and Temperton 1988). Further, the result of applying Machenhauer's scheme in normal-mode initialization is that the required change Δc_n to each of the initial complex coefficients of the fast gravity modes is related to the tendency of each fast mode

computed by integrating the model forward one time step, as

$$\Delta c_n = \frac{i}{\nu_n} \frac{\partial c_n}{\partial t},$$

where ν_n is the frequency for that normal mode. When this is implemented in the physical space of the vertical modes of the model, the resulting set of linear equations relate the changes in the vorticity, divergence, and mass for the first few vertical modes to the tendencies of vorticity, divergence, and mass for the gravity modes alone (Temperton 1988).

An outline of the scheme of Bourke and McGregor with different boundary conditions follows as applied to the flux form of our equations. Details can be found in the report by Sashegyi and Madala (1990). The momentum equations (4) and (5) can be expressed alternatively in terms of the time tendencies of the mass-weighted vorticity ζ and the mass divergence \mathbf{D} as

$$\frac{\partial \bar{\zeta}^{xy}}{\partial t} + f \mathbf{D} = \bar{\mathbf{A}}_\zeta^{xy}, \quad (11)$$

$$\frac{\partial \mathbf{D}}{\partial t} + \nabla^2 \Phi - f \bar{\zeta}^{xy} = \mathbf{A}_D, \quad (12)$$

where the mass-weighted vorticity ζ and the mass divergence \mathbf{D} are defined on the sigma surfaces by

$$\zeta = \frac{1}{h_y} \delta_x (h_y \bar{p}_s^y v) - \frac{1}{h_x} \delta_y (h_x \bar{p}_s^x u),$$

$$\mathbf{D} = \frac{1}{h_y} \delta_x (h_y \bar{p}_s^x u) + \frac{1}{h_x} \delta_y (h_x \bar{p}_s^y v),$$

and the two-dimensional Laplacian of the generalized geopotential Φ is defined by

$$\nabla^2 \Phi = \frac{1}{h_y} \delta_x (h_y \delta_x \Phi) + \frac{1}{h_x} \delta_y (h_x \delta_y \Phi).$$

We use here the mass-weighted vorticity and the mass divergence to be consistent with the flux form of our model equations instead of using the kinematic vorticity and divergence as in Bourke and McGregor. In this linearization, the β terms are included with the nonlinear terms on the rhs of Eqs. (11) and (12), as is our extra term due to removing the surface geopotential from the pressure-gradient term.

We can express our variables in terms of amplitudes for each of the vertical modes, where

$$\xi = \mathbf{E}^{-1} \zeta,$$

$$\mathbf{d} = \mathbf{E}^{-1} \mathbf{D},$$

$$\eta = \mathbf{E}^{-1} \Phi,$$

$$\mathbf{a}_\zeta = \mathbf{E}^{-1} \bar{\mathbf{A}}_\zeta,$$

$$\mathbf{a}_D = \mathbf{E}^{-1} \mathbf{A}_D,$$

$$\mathbf{a}_\Phi = \mathbf{E}^{-1} \mathbf{A}_\Phi.$$

Multiplying Eqs. (11), (12), and (10) by \mathbf{E}^{-1} , we obtain for each vertical mode k ,

$$\frac{\partial \bar{\xi}_k^{xy}}{\partial t} + f d_k = \bar{a}_{r,k}^{xy}, \quad (13)$$

$$\frac{\partial d_k}{\partial t} + \nabla^2 \eta_k - f \bar{\xi}_k^{xy} = a_{D,k}, \quad (14)$$

$$\frac{\partial \eta_k}{\partial t} + \lambda_k d_k = a_{\Phi,k}, \quad (15)$$

where, for example, ξ_k , the k th element of the vector ξ , describes the amplitude of the dynamic vorticity for the k th vertical mode. The equations describe the shallow-water equations, where the phase speed of the free gravity modes is given by $\sqrt{\lambda_k}$, where λ_k (which can be interpreted as an equivalent depth multiplied by the acceleration of gravity) is the eigenvalue for the k th mode. If the terms on the rhs of Eqs. (13), (14), and (15) are zero, then it can be shown that the linearized potential vorticity v_k , which is defined here in flux form as

$$v_k \equiv \bar{\xi}_k^{xy} - f \lambda_k^{-1} \eta_k,$$

is unchanged by the freely propagating gravity-wave motions (Temperton 1988).

The filtering conditions of Bourke and McGregor

$$\frac{\partial d_k}{\partial t} = \frac{\partial}{\partial t} (f \xi_k - \nabla^2 \eta_k) = 0 \quad (16)$$

on the divergence d_k and the ageostrophic vorticity $f \xi_k - \nabla^2 \eta_k$ need only be applied to Eqs. (13), (14), and (15) for the first three vertical modes whose phase speeds of the gravity modes are much larger than about 25 m s^{-1} . Since the terms on the rhs of Eqs. (13), (14), and (15) depend on the geopotential, divergence, and vorticity, the resulting set of equations is solved iteratively (Bourke and McGregor 1983). Then, by applying the filtering conditions for the first three vertical modes and by requiring that the linearized potential vorticity be unchanged by the initialization procedure, we obtain for the changes $\Delta \eta_k$, Δd_k , $\Delta \xi_k$ at each iteration

$$\nabla^2 \Delta \eta_k - \frac{f^2}{\lambda_k} \Delta \eta_k = \frac{\partial d_k}{\partial t}, \quad (17)$$

$$\nabla^2 \Delta d_k - \frac{f^2}{\lambda_k} \Delta d_k = \frac{1}{\lambda_k} \frac{\partial}{\partial t} (\nabla^2 \eta_k - f \bar{\xi}_k^{xy}), \quad (18)$$

$$\Delta \xi_k = \frac{f}{\lambda_k} \Delta \eta_k^{xy}, \quad (19)$$

for $k = 1, 2, 3$, where the residuals on the rhs of Eqs. (17) and (18) are given by the tendencies of the mass divergence and the ageostrophic vorticity. These equations are in the same form as Eqs. (35), (46), and (37) given in Bourke and McGregor, except that we have

used the mass-weighted values, and our generalized geopotential uses the surface as the reference level instead of sea level. To compute these tendencies, we integrate the model one time step adiabatically without friction, diabatic heating, or updating the values of the model variables at the lateral boundaries. The tendencies of the mass divergence and ageostrophic vorticity follow from the tendencies of the u and v components of the momentum in Eqs. (4) and (5).

To solve Eqs. (17), (18), and (19), boundary conditions for the amplitudes of the generalized geopotential and the mass divergence are required. As in Bourke and McGregor, we keep Φ (that is, the geopotential ϕ , temperature T , and surface pressure p_s) unchanged at the lateral boundaries by the initialization procedure. However, we estimate the divergence at the first grid point in from the boundary by using the thermodynamic Eq. (15) and by applying the condition that the tendency of the generalized geopotential is zero (scheme A of Bourke and McGregor) only at the lateral boundary. In this way, actual boundary changes to the mass divergence are not required, as in Bourke and McGregor, who assumed no change in the divergence along the boundary. For the changes to the amplitude of the divergence, the boundary condition is then found to be

$$\Delta d_k = \frac{1}{\lambda_k} \frac{\partial \eta_k}{\partial t}.$$

Equations (17)–(19) are then solved for the changes of the amplitudes of the generalized geopotential, mass divergence, and mass-weighted vorticity for each of the three modes. Note that the amplitude of the divergence is solved over a somewhat smaller domain. The resulting changes are then converted back to physical space.

The resulting changes to the horizontal wind field are computed from the changes in the mass divergence and mass-weighted vorticity by solving

$$\nabla^2 \Delta \chi = \Delta D,$$

$$\nabla^2 \Delta \Psi = \Delta \zeta,$$

for the changes $\Delta \chi$ and $\Delta \Psi$, where the elements of these vectors are the changes in the velocity potential and streamfunction, respectively, at each model vertical level. The gradients of streamfunction and the velocity potential define the nondivergent and divergent components of the momentum field, respectively, so that changes to the mass-weighted wind follow from

$$\Delta(\bar{p}_s^x u) = \delta_x \Delta \chi - \delta_y \Delta \Psi,$$

$$\Delta(\bar{p}_s^y v) = \delta_y \Delta \chi + \delta_x \Delta \Psi.$$

For the boundary conditions in our case, we use no change in the velocity potential $\Delta \chi = 0$ at the model lateral boundaries, so that there is no change in the divergent component of the tangential wind defined

along the model lateral boundaries. We allow, then, the normal wind to change along the lateral boundary consistent with the change in the integrated mass divergence over the model domain. By specifying no change in the streamfunction $\Delta\Psi = 0$ at fictitious points outside of the model C grid, we allow the non-divergent component of the tangential wind to change along the lateral boundary consistent with the change in the integrated vorticity over the model domain.

With their choice of defining the normal wind at the outer model boundary for their C grid, Bourke and McGregor also have to pragmatically impose unaltered normal velocities at the lateral boundary during the initialization, if they use the same boundary conditions on the change in the streamfunction and velocity potential. Alternatively, they used Neumann boundary conditions for the velocity potential for zero change in the normal velocities along the boundaries. This, however, imposed no change in the total divergence over the domain, and the area averaged of the divergence change had to be removed before computing the divergent wind. By our choice of defining the tangential wind at the lateral boundary and the normal wind staggered half a grid point inside the lateral boundary, our scheme avoids these problems.

As in Bourke and McGregor, we use the linearized Eqs. (6), (7), and (10) with rhs equal to zero to relate the tendencies of surface pressure and temperature to that of the generalized geopotential for the gravity-wave modes, so that

$$\frac{\partial p_s}{\partial t} = -\mathbf{N}_2^T \mathbf{D} = \mathbf{N}_2^T \mathbf{M}_3^{-1} \frac{\partial \Phi}{\partial t},$$

$$\frac{\partial p_s T}{\partial t} = \mathbf{M}_2 \mathbf{M}_3^{-1} \frac{\partial \Phi}{\partial t}.$$

The changes to the surface pressure and temperature caused by the gravity modes then follow from the changes in the generalized geopotential as

$$\Delta p_s = \mathbf{N}_2^T \mathbf{M}_3^{-1} \Delta \Phi,$$

$$\Delta(p_s T) = \mathbf{M}_2 \mathbf{M}_3^{-1} \Delta \Phi.$$

3. Testing of the vertical-mode scheme

To test the vertical-mode initialization procedure of Bourke and McGregor in the flux form for the modified boundary conditions with a 10-layer version of our model, we use 12-h analyses obtained from the National Meteorological Center (NMC) on a 2.5° hemispheric grid for the period 1200 UTC 23 January–1200 UTC 29 January 1986. This period covered the second intensive observing period (IOP) of the Genesis of Atlantic Lows Experiment (GALE), during which a coastal front develops along the east coast of the United States, and subsequently, a cyclone develops offshore

when a short wave from the Gulf of Alaska reaches the East Coast. During the coastal-front development, shorter synoptic waves propagate eastward in a generally zonal westerly flow without much development. During the latter part of the IOP, the short waves deepen a large-scale trough, which is developing over the eastern United States. These cases provide typical examples of winter circulations for testing the initialization scheme.

The 13 analyses for the period are interpolated to the ten model sigma levels for two different horizontal grids of differing domain size and resolution and then initialized on each grid with the vertical-mode scheme for the first three vertical modes only. A low-resolution grid (called the U.S. grid), with a resolution of 2° longitude \times 1.5° latitude covers the continental United States in a domain from 10° to 70° N and 140° to 40° W. The other grid (called the GALE grid) is a higher-resolution grid of 0.5° resolution in latitude and longitude covering the eastern United States from 102.5° to 57.5° W and 22.5° to 47.5° N. The model topography used for each grid is shown in Figs. 1a and 1b. For the GALE grid, the significant topographic features along the western and northern boundaries of the domain provide a good test of our particular linearization used.

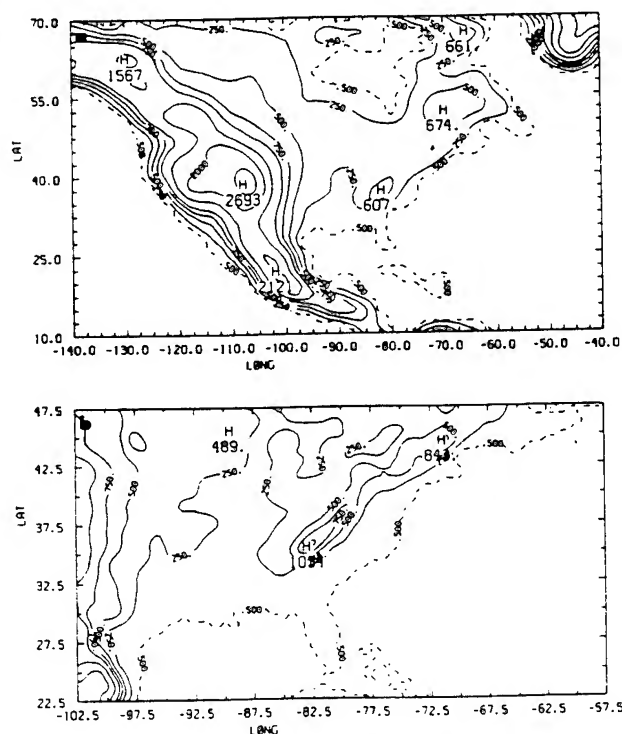


FIG. 1. The model topography on (a) the U.S. grid and (b) the GALE grid. The contour intervals are 500 m for elevations above 1000 m, and 250 m for those below 1000 m. The model continental outline is indicated by the dashed line.

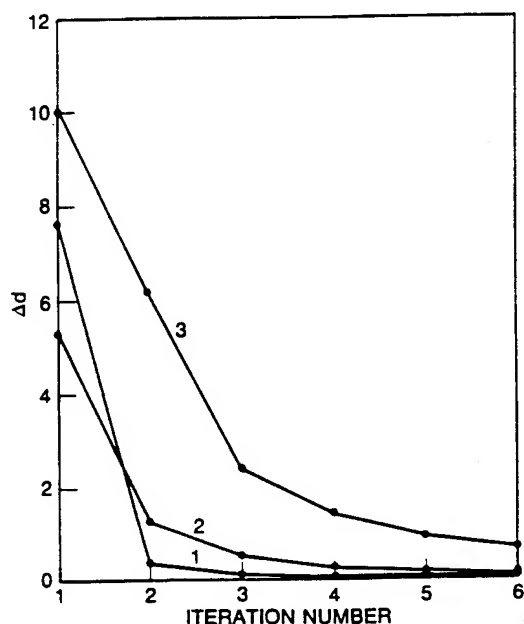


FIG. 2. The root-mean-square (rms) changes in the amplitude of the mass divergence Δd ($\text{dyn cm}^{-2} \text{s}^{-1}$) for each of the first three vertical modes on the U.S. grid versus the iteration number in the vertical-mode initialization scheme.

a. Influence of grid resolution and topography on the convergence

To measure the convergence of the scheme with our modified boundary conditions, root-mean-square (rms) changes for the first three vertical modes of the mass divergence, vorticity, and generalized geopotential

were computed after each iteration of the scheme for each of the 13 analysis times on each of the U.S. and GALE grids. On both grids, the rms changes of generalized geopotential and vorticity decrease rapidly with increasing iteration for each of the three modes. The changes of the divergence for each mode decrease in magnitude somewhat less rapidly. For all 13 analyses on the U.S. grid, the average of the rms values of the change in the mass divergence Δd over the grid for each of the first three modes is shown in Fig. 2 for each of the six iterations. As can be seen in the figure, the changes Δd do not decrease as rapidly for the third mode, as compared to the first two vertical modes. While three iterations are sufficient for the changes in the wind and temperature to become small, six iterations are required for changes in the vertical motion (or divergence) to become negligible. As in Bourke and McGregor, the resulting rms changes in the temperature and wind components in the upper troposphere after initialization are at most a degree and a couple of meters per second, respectively, and decrease with increasing pressure in the lower troposphere. The rms changes in our case also decrease rapidly with increasing iteration. To illustrate, the rms changes in the u component of the wind and the temperature over the U.S. grid are shown for one case in Fig. 3 as a function of the sigma level for each of the first three iterations. The magnitude of the changes in the wind are found to decrease rapidly with increasing iteration, even at individual grid points in strong wind regimes where problems have arisen in other normal-mode initialization schemes. We attribute this to our consistent choice of boundary conditions for the streamfunction and velocity potential.

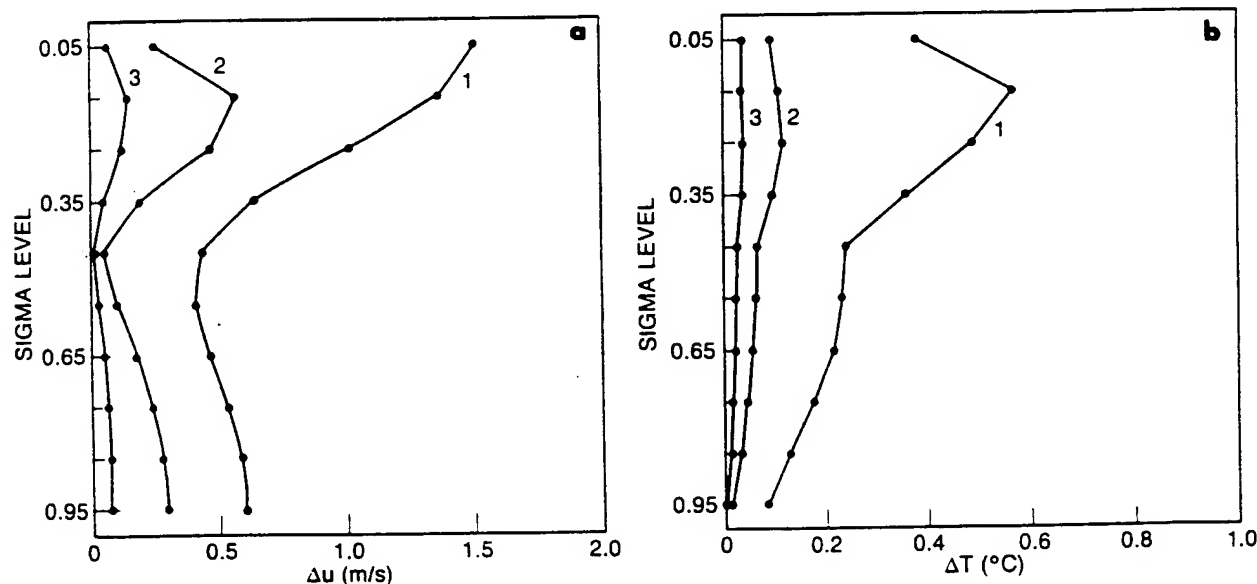


FIG. 3. The rms changes in (a) the u component of the wind (m s^{-1}) and (b) the temperature ($^{\circ}\text{C}$) on the U.S. grid versus sigma level for the first three iterations of the vertical-mode initialization scheme for 1200 UTC 23 January 1986.

In our case, even on the smaller GALE grid with 0.5° resolution and significant topographic features along the western and northern boundaries, the rms changes were similar to those on the U.S. grid. In many limited-area models, the diffusion is increased in a sponge zone around the lateral boundaries to remove noise produced by some formulations of the boundary conditions, particularly in the presence of topography. In our model, the edge of a sponge zone was defined by an ellipse centered in the domain, a distance of 15 grid points from the middle of the eastern and western boundaries and 10 grid points from the middle of the northern and southern boundaries. In the sponge zone, the diffusion was increased linearly from an interior value of $4 \times 10^8 \text{ cm}^2 \text{ s}^{-1}$ to five times this value at the middle of a boundary and to ten times at the corners of the domain. Computing the tendencies in the vertical-mode scheme with such strong diffusion in a boundary zone can have adverse effects on the convergence of the vertical-mode scheme when there is topography near the boundaries. With vertical shear of the wind, the horizontal gradient of the wind on the sigma surface can be large over topographic features and be diffused over the sigma surfaces by the strong

diffusion. The effect of a sponge zone in our model is illustrated for one case on the GALE grid in Fig. 4. The figure shows the rms changes of the divergence Δd for the second and third vertical modes versus each iteration of our vertical-mode scheme with and without use of the sponge zone. With the sponge zone, the amplitude changes for the mass divergence do not decrease to zero in the case of the third mode. The effect on the second mode is much less and even less on the first mode (not shown). As shown by Rasch (1985), including the parameterization of precipitation processes in the initialization for a global spectral model produces high-frequency forcing that causes the Machenhauer scheme to diverge. The divergence of the scheme is more severe for the shallower modes. Here, including the sponge zone of strong diffusion in the initialization produces a similar result for our mesoscale model. Use of a better iterative scheme in the initialization could remove this problem (Rasch 1985).

For several cases, we also used Bourke and McGregor's boundary condition of no change in the divergence along the model lateral boundary and solved for the changes in the amplitudes of the mass divergence. For the case illustrated in Fig. 4, the results are shown for the third mode by the "x" at each iteration. No difference is found for the first and second modes. Essentially, little difference is seen in the convergence of their scheme, and the resulting changes in the mass and wind fields were the same. Only very small differences were seen in the vertical motion produced by their boundary condition on the mass divergence when compared to ours.

To illustrate the results of the vertical-mode initialization, Figs. 5 and 6 show the result for the National Meteorological Center (NMC) analysis interpolated to the two grids for 1200 UTC 23 January 1986. The initial analyzed sea level pressure and the wind field at the sigma level $\sigma = 0.25$ are shown on the U.S. grid in Figs. 5a and 5b. A deep surface low of 987 mb lies west of Greenland with a trailing front moving off the east coast of the United States and high pressure dominating the eastern half of the United States. Aloft at the jet level, strong jet maxima of about 55 and 48 m s^{-1} straddle a trough over the eastern United States, with a further jet maximum upstream entering the domain from the Gulf of Alaska. After the initialization, the change in the u component of the wind at the jet level and the resulting vertical motion $\omega = dp/dt$ in the middle troposphere are shown in Figs. 5c and 5d. Both fields are very smooth even to the boundary. Upward motion is associated with the low and trailing front and ahead of a weak short-wave trough over the southeastern United States. Sinking motion is found in the region of the high surface pressure over the eastern United States. Larger changes in the u component of the wind are seen in the normal wind along the western and eastern boundaries when compared to the tangential wind along the northern and southern boundaries;

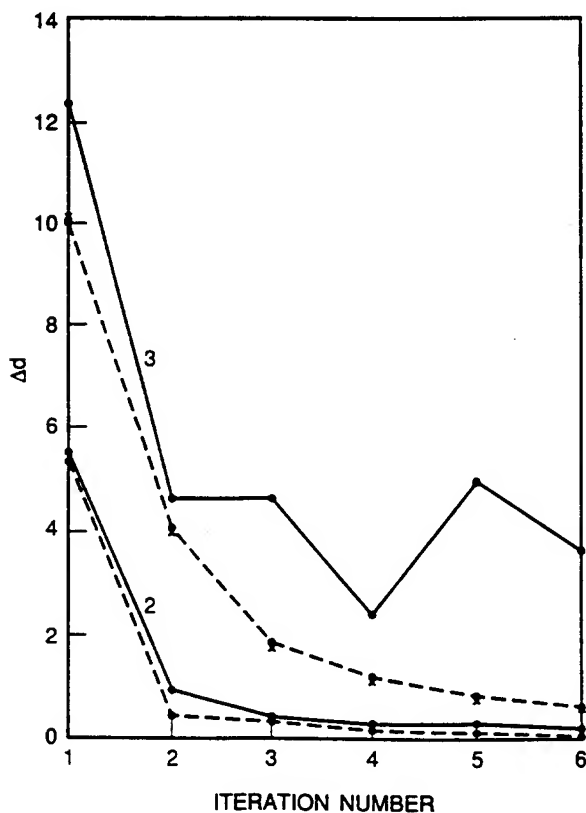


FIG. 4. The rms changes in the amplitude of the mass divergence for the second and third vertical modes on the GALE grid when the increased diffusion is used in the sponge zone (solid lines) and when no sponge zone is used (dashed lines) for 1200 UTC 24 January 1986.

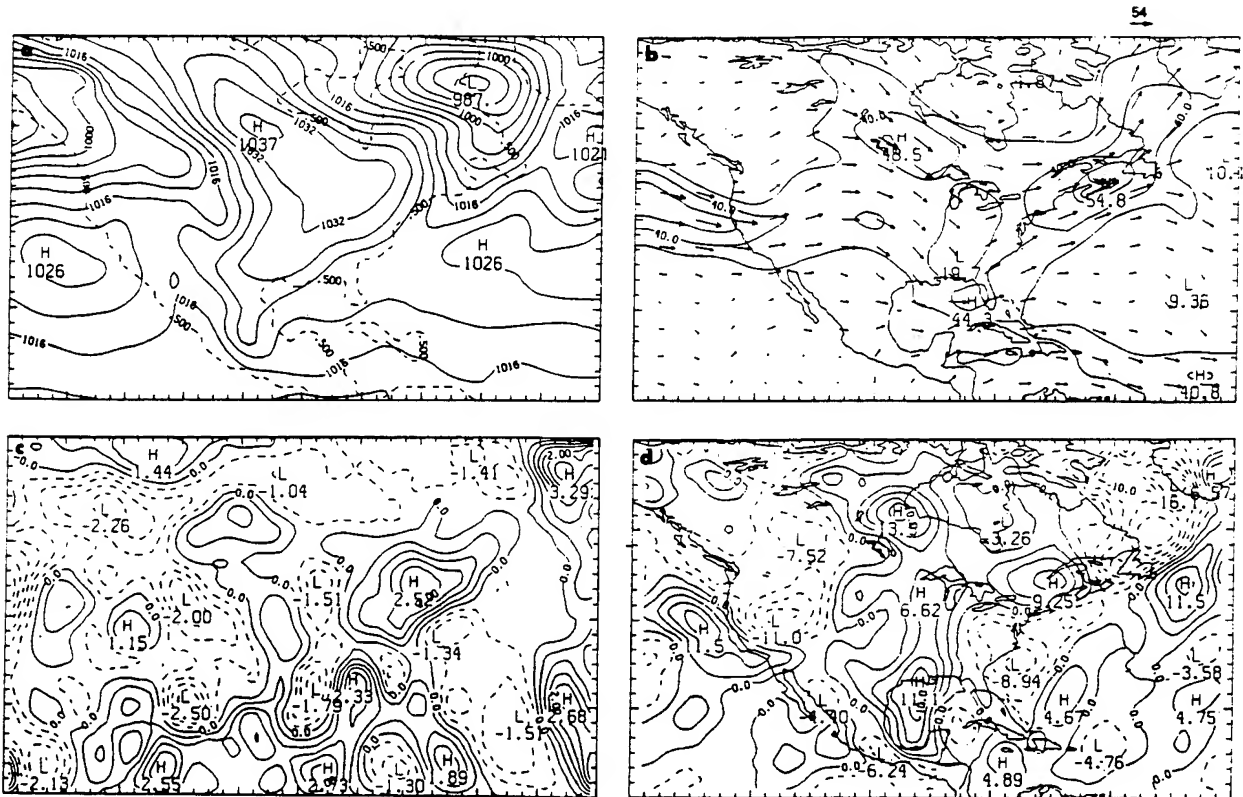


FIG. 5. The analyzed (a) sea level pressure and (b) wind field at sigma level $\sigma = 0.25$ on the U.S. grid for 1200 UTC 23 January 1986. (c) The change in the u component of the wind at sigma level $\sigma = 0.25$ and (d) the vertical motion (mb h^{-1}) at sigma level $\sigma = 0.45$, after initialization for the same grid and time. The contours of sea level pressure are every 4 mb, the isotachs of the wind are every 10 m s^{-1} , increasing from 30 m s^{-1} (maximum wind vector shown is 54 m s^{-1}), and the contours of the change in the u component of the wind are 0.5 m s^{-1} . Contours for the vertical motion are every 2.5 mb h^{-1} .

this is caused by the larger changes in the mass divergence produced by the scheme when compared to the vorticity.

For the smaller GALE grid, the results are shown in Fig. 6. Good correspondence between the changes in the u component of the wind are found when comparing both grids. Similar magnitudes and patterns are observed for the rising motion off the East Coast along the front and over the Appalachians and for the sinking motion in the high pressure along the Mississippi River valley. Along the northern and southwestern boundary of the GALE grid, the topographic features in the domain produce a strong, noisy signal in the vertical-motion field when the sponge zone is used (Fig. 6d), which is not present when the sponge zone is not used (Fig. 6c).

b. Model integrations and influence of lateral boundaries

For a limited-area model, the lateral boundary conditions can also act to damp gravity-wave oscillations in the region of the boundary, and thereby, in time, remove those in the interior as they propagate away into the boundary region. In this way, many limited-

area models have been used with simple initialization procedures, such as removing the divergent wind component from the initial data. The split-explicit scheme used for time integration in the NRL model may also act to damp the gravity waves (Sashegyi and Madala 1988). To demonstrate the effect of the vertical-mode initialization procedure in removing the high-frequency gravity-wave oscillations, the NRL model is integrated on the U.S. grid for 24 h starting from initialized and uninitialized data. The impact of the initialization in the limited-area model is compared with the damping of the gravity waves by different lateral boundary treatments and the split-explicit scheme. Results are compared by using the tendency-relaxation scheme of Perkey and Kreitzberg (1976), the relaxation scheme of Davies (1976, 1983), and constant boundary values. Integrations with the split-explicit scheme are compared to those using an explicit leapfrog (centered difference) scheme. The integrations illustrated in the following figures for the U.S. grid are listed in Table 1. In the first integration A, a centered-difference scheme is used in time with a time step of 40 s. In the remaining integrations, the split-explicit integration scheme is used with a time step of 200 s.

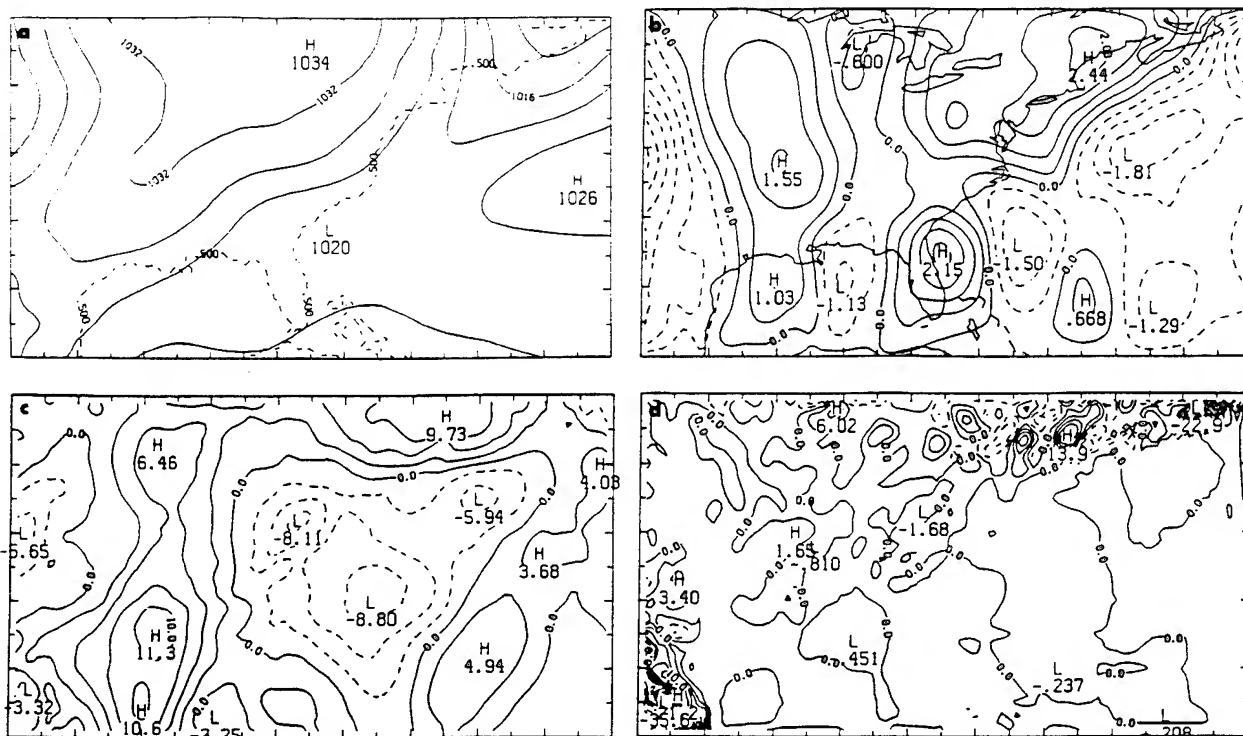


FIG. 6. (a) The analyzed sea level pressure, (b) the change in the u component of the wind field at sigma level $\sigma = 0.25$, (c) the vertical motion (mb h^{-1}) at sigma level $\sigma = 0.45$ after initialization, and (d) the change in the vertical motion when the sponge zone with increased diffusion is used, for the GALE grid on 1200 UTC 23 January 1986. The contours are as in Fig. 5.

In the Perkey and Kreitzberg (PK) scheme, model-computed tendencies are relaxed at each time step to specified boundary tendencies in a boundary zone of five points. In the boundary zone, the PK scheme reduces the advection speed of the deviation of the interior solution from the boundary solution, with the advection speed decreasing to zero at the boundary (Davies 1983). The phase speed of the gravity waves is similarly reduced in the boundary zone. The result is that gravity waves can be removed from the interior of the domain, piling up in the boundary zone. In the Davies scheme, computed model variables are relaxed at each time step to the boundary values in a boundary zone of six points. With the Davies scheme, the amplitude of the interior solution deviation (and that of the gravity waves) is damped in the boundary zone, with the damping increasing closer to the boundary (Davies 1983). Idealized boundary values and tendencies for the model grid are derived from the 12-h NMC hemispheric analyses interpolated to the model grid. For the Davies scheme, the boundary values are further linearly interpolated in time to each time step of the model. To minimize the impact of noise from the boundaries influencing the interior, the boundary conditions are derived from initialized fields for the cases A–E and A' in Table 1.

In Fig. 7, we illustrate the effect of the vertical-mode initialization, comparing the damping of the gravity

waves for the different boundary treatments for the integrations A–E and A'. The figure shows the variation with time of the surface pressure and the vertical motion (in sigma coordinates) in the middle troposphere

TABLE 1. Model integrations on U.S. grid.

A	24-h explicit integration (time step of 40 s) for uninitialized initial conditions, using PK lateral boundary scheme.
B	24-h split-explicit integration (time step of 200 s) for uninitialized initial conditions, using PK lateral boundary scheme.
C	24-h split-explicit integration (time step of 200 s) for initialized initial conditions, using PK lateral boundary scheme.
D	24-h split-explicit integration (time step of 200 s) for uninitialized initial conditions, using Davies lateral boundary scheme.
E	24-h split-explicit integration (time step of 200 s) for initialized initial conditions, using Davies lateral boundary scheme.
Supplementary integrations with split-explicit scheme	
A'	24-h integration for uninitialized initial conditions, using constant boundary values.
B'	24-h integration for uninitialized initial conditions, using PK lateral boundary scheme with analyzed boundary values.
D'	24-h integration for uninitialized initial conditions, using Davies lateral boundary scheme with analyzed boundary values.

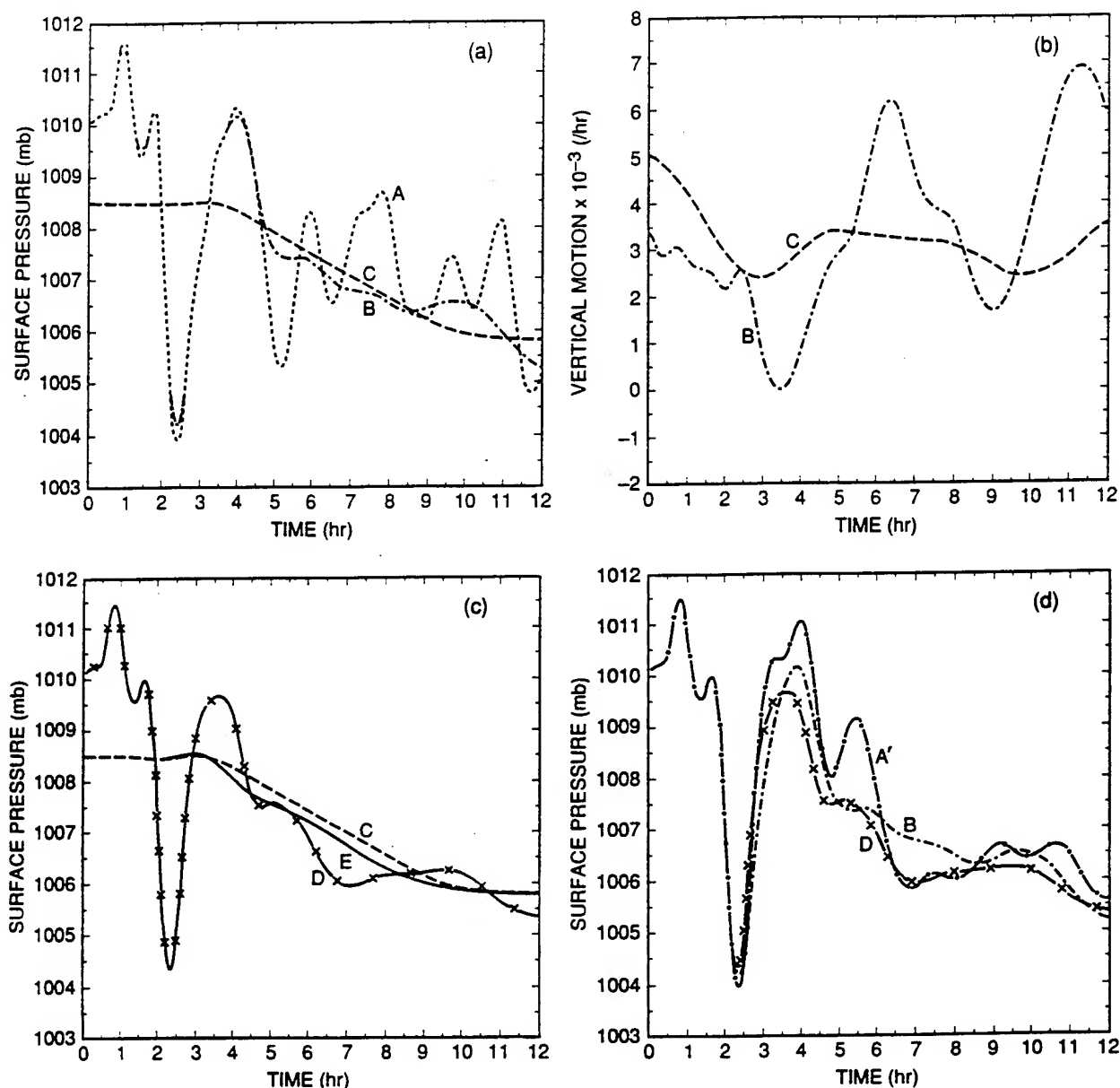


FIG. 7. Time series of surface pressure (mb) and the vertical motion (in sigma coordinates per hour) at $\sigma = 0.5$, at a grid point at 35°N , 90°W on the U.S. grid during the first 12 h of integration. Here, (a) and (c) show the surface pressure for each of the integrations A–E in Table 1, (b) shows the vertical motion for integrations B and C, and (d) compares integration A' for constant boundary values to integrations B and D.

at a sigma level $\sigma = 0.5$ at a grid point at 35°N , 90°W in the interior of the U.S. grid. In the first two integrations, we compare integrations with explicit (A) and split-explicit integration schemes (B) for uninitialized initial conditions on the U.S. grid when using the PK lateral boundary treatment. Large initial oscillations in the interior of nearly 8 mb in the surface pressure in curve A in Fig. 7a caused by the uninitialized initial conditions are damped somewhat by the action of the PK scheme in the lateral boundary zone after 4 h or so of integration, after allowing time for the external

gravity waves to reach the western boundary. Stronger damping is found after 4 h for the surface pressure in curve B when the PK scheme is combined with the split-explicit scheme. When using the Davies scheme with uninitialized initial conditions in integration D, the oscillations in the surface pressure (curve D in Fig. 7c) are similar to that in integration B. In fact, the result is the same for the surface pressure independent of whether an explicit or split-explicit scheme is used for time integration. For the constant boundary conditions used with the split-explicit scheme in integration

A', larger oscillations are found in Fig. 7d when compared to using the PK scheme (curve B) and Davies scheme (curve D). We can conclude that both the PK and Davies schemes are damping the gravity waves in the boundary zone, as expected. Note that the surface-pressure oscillations in integration A' are smaller after 4 h when compared with using the leapfrog scheme, a result similar to that found with integrations A and B. In integrations C and E, initialized initial conditions are used with the PK and Davies lateral boundary schemes, respectively. With initialized initial conditions, the high-frequency oscillations are almost completely removed in the surface pressure in both cases (curves C and D in Fig. 7c), even over high topography such as the Rocky Mountains (not shown). A bigger impact of the initialization scheme, however, is shown in the vertical-motion field. With uninitialized initial conditions the exact same large oscillations are produced in the vertical motion for integrations A, A', B, and D (only curve B shown in Fig. 7b). These large oscillations in the vertical motion are also eliminated for the interior grid points, as can be seen by curve C in Fig. 7b, where integration E produces the exact same trace in the vertical motion.

In Fig. 8, we compare the effect of using boundary values derived from the NMC analyses without initialization for integrations B' and D' with the split-explicit scheme starting from initialized initial conditions with the PK and Davies lateral boundary schemes. Not surprisingly, the effect is minimal when using the PK scheme, since only boundary tendencies are adjusted by the scheme. With the Davies scheme, a small shock, which settles down in a few hours, is seen in curve D' in the surface pressure trace in Fig. 8a. Small oscillations, however, remain in the vertical motion (Fig. 8b).

Larger differences are seen in the boundary zone with the different boundary treatments. The time variation of the surface pressure and vertical motion at a grid point in the boundary zone at a distance of three times the grid spacing in from the boundary is shown in Fig. 9. A similar linear variation of the surface pressure in time largely equal to the linear trend forced by the external boundary values is seen in Fig. 9a, when the Davies scheme is used for uninitialized (curve D) or initialized initial conditions (curve E). The variation of the vertical motion in time is small in Fig. 9b for the Davies scheme at this point for both integrations D and E, with some noise for integration D for uninitialized initial conditions. By using the PK scheme for uninitialized initial conditions, the typical pileup of mass followed by a decrease can be seen in the surface pressure in Fig. 9a for both integrations A and B in Table 1, although it is less for the split-explicit scheme (curve B). The exact same oscillation of the vertical motion is produced in Fig. 9b for the split-explicit integration B (shown) as for the explicit integration A (not shown). Even with initialized initial conditions,

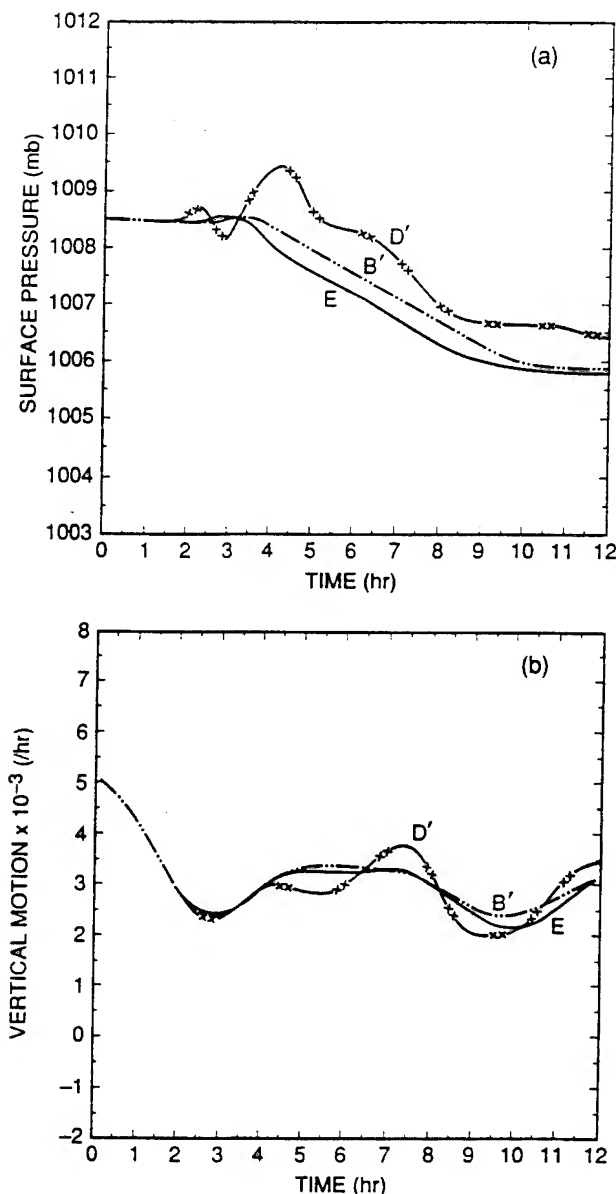


FIG. 8. Time series of (a) surface pressure (mb) and (b) the vertical motion (in sigma coordinates per hour) at $\sigma = 0.5$ at the same grid point and period as Fig. 7, but comparing the effect of on integrations B' and D' using analyzed boundary values.

the PK scheme produces a significant difference in the surface pressure (curve C) after 7 h or so when compared with the Davies scheme in integration E. This difference, generated by the PK scheme in the boundary zone and propagating into the interior, causes some small differences in the integrations even after 12 h (not shown), when comparing with the integrations with Davies scheme.

4. Summary

The vertical-mode initialization scheme of Bourke and McGregor (1983) has been applied to a limited-

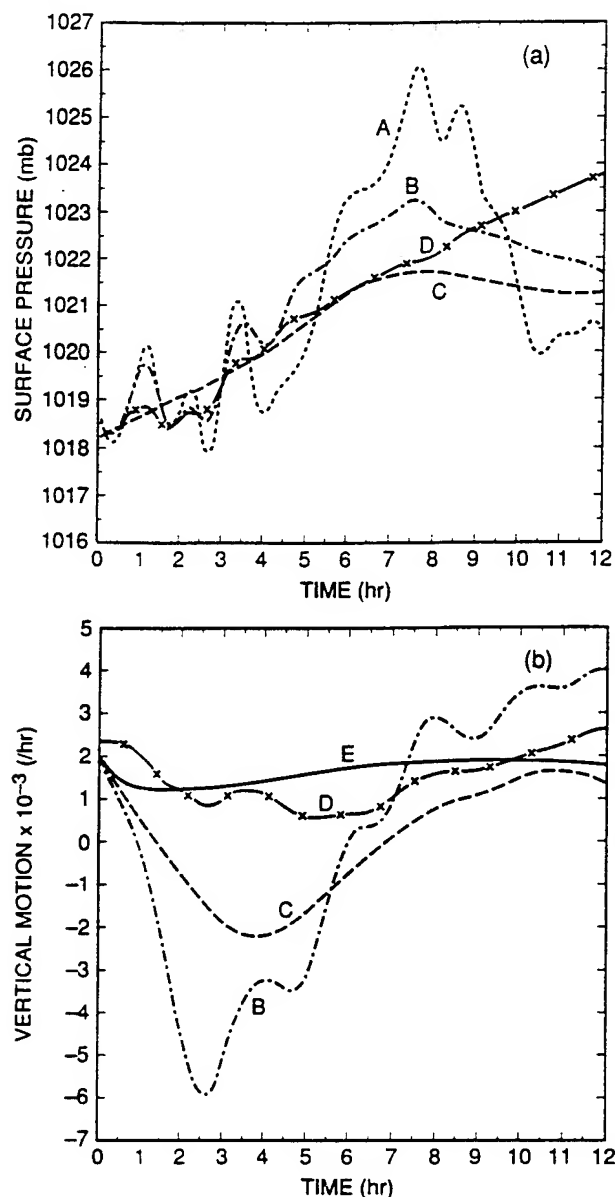


FIG. 9. Time series of (a) surface pressure (mb) and (b) the vertical motion (in sigma coordinates per hour) at $\sigma = 0.5$ at a grid point in the boundary zone on the U.S. grid at 40°N , 46°W during the first 12 h of integration. Curves are labeled as listed in Table 1.

area model in flux form with different boundary conditions. Filtering conditions for the fast gravity modes are applied to the model dynamical equations to derive diagnostic equations for the mass divergence and generalized geopotential, which are solved iteratively for the first three vertical modes of the numerical model. As is Bourke and McGregor, we keep the geopotential, temperature, and pressure fixed at the lateral boundaries in the scheme. To provide a boundary condition for the mass divergence, however, an approximate mass divergence is computed at the lateral boundary by using

the thermodynamic equation. Also, by careful choice of the grid arrangement at the boundary and by using boundary conditions of no change in the streamfunction and velocity potential, the changes to the tangential and normal wind at the boundaries of the model domain are maintained consistent with the changes in the integrated vorticity and mass divergence over the model domain.

The modified scheme is tested on two grids of differing domain size and grid resolution. With our boundary conditions, the convergence of the scheme is rapid for both grids. The improvement due to the consistent set of boundary conditions used for the scheme has been demonstrated. Our boundary condition on the mass divergence is, however, shown to give essentially the same result as that of no change in the mass divergence used by Bourke and McGregor. When significant topography exists along the boundaries of the model domain, use of strong diffusion in the boundary region for the computation of the tendencies is shown to slow the convergence of the scheme for the third vertical mode. This demonstrates that care must be taken when using a numerical model to compute the tendencies required by the initialization scheme if the convergence of the scheme is not to be slowed. The model is integrated starting with uninitialized and initialized data by using different lateral boundary treatments, namely, the tendency relaxation scheme of Perkey and Kreitzberg (1976), the Davies (1976, 1983) relaxation scheme, and constant boundary values. Starting from uninitialized initial conditions, damping by the Davies scheme is stronger, while use of the split-explicit scheme improves the damping of the Perkey-Kreitzberg scheme. Starting from initialized fields on the coarse U.S. grid, little difference is found in the interior between integrations by using either of the lateral boundary treatments of Perkey and Kreitzberg or Davies. Use of externally prescribed boundary values, which are themselves not balanced, is shown to negatively impact the integration somewhat when the Davies scheme is used. Even with initialized initial conditions and boundary values, however, errors were produced in the boundary zone by the Perkey-Kreitzberg scheme.

Acknowledgments. The first author was supported under Contract N00014-86-C-2365 with NRL and the second author was supported by NRL's basic research program and the U.S. Navy's SPAWAR program. The constructive comments and helpful insights on the application of the initialization scheme provided by the reviewers of this paper and an earlier manuscript were much appreciated by the authors.

REFERENCES

- Arakawa, A., and V. R. Lamb. 1977: Computational design of the basic dynamical processes of the UCLA general circulation model. *Methods in Computational Physics*, Vol. 17, General

- Circulation Models of the Atmosphere*. J. Chang, Ed., Academic Press, 173-265.
- Baer, F., 1977: Adjustment of initial conditions required to suppress gravity oscillations in nonlinear flows. *Contrib. Atmos. Phys.*, **50**, 350-366.
- Bourke, W., and J. L. McGregor, 1983: A nonlinear vertical mode initialization scheme for a limited area prediction model. *Mon. Wea. Rev.*, **111**, 2285-2297.
- Briere, S., 1982: Nonlinear normal mode initialization of a limited area model. *Mon. Wea. Rev.*, **110**, 1166-1186.
- Daley, R., 1981: Normal mode initialization. *Rev. Geophys. Space Phys.*, **19**, 450-468.
- Davies, H. C., 1976: A lateral boundary formulation for multi-level prediction models. *Quart. J. Roy. Meteor. Soc.*, **102**, 405-418.
- , 1983: Limitations of some common lateral boundary schemes used in regional NWP models. *Mon. Wea. Rev.*, **111**, 1002-1012.
- Juvanon du Vachat, R., 1986: A general formulation of normal modes for limited-area models: Application to initialization. *Mon. Wea. Rev.*, **114**, 2478-2487.
- Kuo, H. L., 1974: Further studies of the parameterization of the influence of cumulus convection on large-scale flow. *J. Atmos. Sci.*, **31**, 1232-1240.
- Leith, C., 1980: Nonlinear normal mode initialization and quasi-geostrophic theory. *J. Atmos. Sci.*, **37**, 958-968.
- Machenhauer, B., 1977: On the dynamics of gravity oscillations in a shallow water model, with applications to normal mode initialization. *Contrib. Atmos. Phys.*, **50**, 253-271.
- Madala, R. V., 1981: Efficient time integration schemes for atmosphere and ocean models. *Finite Difference Techniques for Vectorized Fluid Dynamic Calculations*, D. L. Book, Ed., Springer-Verlag, 56-74.
- , S. W. Chang, U. C. Mohanty, S. C. Madan, R. K. Paliwal, V. B. Sarin, T. Holt, and S. Raman, 1987: Description of the Naval Research Laboratory Limited Area Dynamical Weather Prediction Model. Naval Research Laboratory Memorandum Rep., No. 5992, 131 pp. [NTIS A182780.]
- Perkey, D. J., and C. W. Kreitzberg, 1976: A time-dependent lateral boundary scheme for limited-area primitive equation models. *Mon. Wea. Rev.*, **104**, 744-755.
- Rasch, P. J., 1985: Developments in normal mode initialization. Part II: A new method and its comparison with currently used schemes. *Mon. Wea. Rev.*, **113**, 1753-1770.
- Sashegyi, K. D., and R. V. Madala, 1988: Initialization experiments with the NRL mesoscale numerical model. Preprints, *Eighth Conf. on Numerical Weather Prediction*, Baltimore, Amer. Meteor. Soc., 778-781.
- , and —, 1990: Tests of initialization procedures with the NRL limited area numerical weather prediction model. Naval Research Laboratory Memorandum Rep., No. 6648, 70 pp. [NTIS A223549.]
- Temperton, C., 1988: Implicit normal mode initialization. *Mon. Wea. Rev.*, **116**, 1013-1031.
- , and D. L. Williamson, 1981: Normal mode initialization for a multilevel grid-point model. Part I: Linear aspects. *Mon. Wea. Rev.*, **109**, 729-743.

Appendix F

An Examination of Four Dimensional Data-Assimilation Techniques for Numerical Weather Prediction

An Examination of Four-Dimensional Data-Assimilation Techniques for Numerical Weather Prediction

Dewey E. Harms*,
Sethu Raman*, and
Rangarao V. Madala*

Abstract

Four-dimensional data-assimilation methods, along with the most commonly used objective analysis and initialization techniques, are examined from a historical perspective. Operational techniques, including intermittent data assimilation and Newtonian nudging, and next-generation methods (Kalman-Bucy filtering and the adjoint method) are briefly described. Several methods are compared, with primary emphasis being placed on recent papers dealing with the operational assimilation techniques. Ongoing and future research is outlined, and some important implications of this research are discussed.

1. Introduction

Two major motivations for using data assimilation exist: as an analysis/diagnostic/research tool and for operational weather forecasting. Data assimilation has been applied not only in meteorology (air pollution and planetary boundary-layer studies, forecast case studies, quantitative assessment of new observing systems, among others), but also in oceanography for describing ocean currents (Ghil 1989; Robinson 1986). To summarize all relevant work pertaining to data assimilation is indeed a difficult task, because the contents are spread so widely. The purpose of the present paper is only to provide an overview of four-dimensional data assimilation with primary emphasis on assimilation methods currently useful for operational weather forecasting. To make this review more complete, attention has also been given to the state-of-the-art or "next-generation" techniques, but to a lesser extent. Excellent reviews covering the early days of data-assimilation research in both simulation and real-data studies are available in the literature. The interested reader is referred to Bengtsson (1975a), McPherson (1975), Hollingsworth (1986), and Bourke et al. (1985). Plus, a comprehensive history of data analysis and assimilation is given by Daley (1991).

Numerical weather prediction (NWP) has classi-

cally been viewed as an initial-value problem where the governing equations of geophysical fluid dynamics are integrated forward in time from a set of initial values. The quality of NWP is strongly dependent on the accuracy of specifying these initial conditions and on the ability to model mathematically the dynamics and physical processes of the atmosphere. In a pioneering paper, Charney et al. (1969) suggested combining past and current data in a numerical model such that the model's equations provide time continuity and dynamic coupling among the atmospheric fields. This concept, which has merged objective numerical analysis and numerical weather prediction, has become known as four-dimensional data assimilation (FDDA) and has proven to be a major advance in NWP during the past 20 years.

What inspired this major advance, or in other words, what spurred this development of data assimilation? The advent of meteorological satellites in the 1960s raised the possibility that nearly continuous atmospheric temperature observations would be available on a global basis. However, these space-based observing systems measure only radiance (or temperature) distributed in space and time, rather than at fixed locations and times. In order to fully utilize this new source of data, the numerical weather prediction techniques had to be adjusted. Beginning with Charney et al. (1969), Smagorinsky et al. (1970), Rutherford (1972), and Morel and Talagrand (1974), research progressed in reconstructing unobserved variables from the observed variables through the numerical model's dynamical coupling between those variables. By combining information about the state of the atmosphere, earlier observations are carried forward to provide an independent source of information to be added to the newly acquired observations.

Morel (1981) further illustrated why data assimilation is essential in NWP by listing five key reasons: 1) the inadequate distribution (spatial gaps) of the twice-daily upper-air sounding data, 2) the discrepancy between the conventional observations as point measurements and the true volume averages required by numerical models, 3) the inherently asynoptic character of remote observations obtained from sunsynch-

*Department of Marine, Earth and Atmospheric Sciences, North Carolina State University, Raleigh, NC 27695-8208

*Naval Research Laboratory, Washington, D.C. 20375

©1992 American Meteorological Society

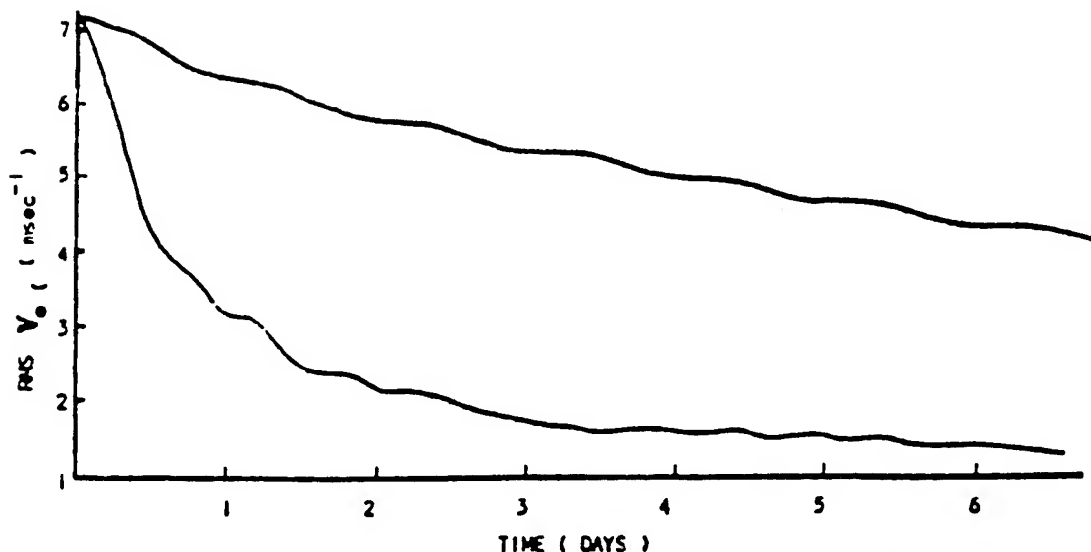


FIG. 1. Successive reduction of wind error using a direct insertion (upper curve) of height data in a barotropic model. Corresponding results using height as well as from the derived geostrophic winds (lower curve) (McPherson 1975).

ronous orbiting satellites, 4) the inadequate vertical resolution of remote observations of cloud motions from geostationary satellites, and 5) the significant random and systematic errors involved in the data processing required for reconstructing atmospheric fields from remotely measured physical quantities. He concluded that any weather prediction model must be initialized by merging the new observations with the currently estimated meteorological fields, computed on the basis of earlier observations, while taking into account the dynamical constraints between successive model states, specified by the governing dynamical equations.

This process of merging new observational data with the ongoing integration of a numerical forecasting model is known as "data assimilation" or, equivalently, "four-dimensional data assimilation," in consideration of the time-space distribution of the database. Then, as stated by Warner (1987), "the overall objective of the assimilation process is to provide the best possible initial state from which to begin a forecast, where the term 'best' implies an appropriate balance and reflects optimal use of four-dimensional data (synoptic as well as asynoptic) to define the structures on all scales at the initial time."

In the past 20 years, many techniques have been developed to insert data into dynamic models. However, the first data-assimilation experiments were simplistic and of limited success. The observation simply replaced the model forecast value at the model grid point nearest the observation location (Jastrow and Halem 1970). This technique, known as direct insertion, is inadequate from the initialization point of view (Bengtsson 1975b). Direct insertion gives a shock

to the system and generates high-amplitude waves, or gravitational oscillations. For example, if observations of the mass field are inserted into a primitive equation model, an imbalance is created between the mass and wind fields. When the model integration is resumed, this imbalance is manifested as high-amplitude gravitational oscillations; this is the model's attempt to restore the dynamic balance, which was disrupted by the data insertion. Techniques such as damping time-integration schemes and time filters were developed to dampen these nonmeteorological waves. However, this damping must be rather strong and can be harmful to the meteorological modes. Bengtsson (1975b) stated that the shock effect will be reduced if locally analyzed data (interpolating the observation to several nearby grid points) are inserted into the model instead of observations only (indirect insertion). For example, applying a local multivariate analysis, or, correspondingly, relating wind and geopotential by the geostrophic relation and inserting both height and winds simultaneously proved successful by speeding the updating considerably (Fig. 1). The multivariate procedure mentioned here produces a simultaneous weighting of mass and motion observations, subject to the constraint of geostrophicity (Petersen 1968; Eddy 1973; Daley and Puri 1980).

Of the several FDDA methods that have been investigated over the last two decades, some have been implemented operationally while others have not yet been used or are in the developmental stage. In the 1970s, regional/mesoscale weather forecasting models were developed, normal mode initialization was introduced, and global data assimilation became operational. With the advent of mesoscale modeling,

FDDA applications are also geared toward the mesoscale, with the emphasis shifting from applications on the global scale.

In operational numerical prediction systems, FDDA can be categorized into two broad areas: continuous method and intermittent (analysis–forecast cycle) method. The former refers to the insertion of data into a model as it is received, in a temporally continuous fashion. The analysis–forecast cycle clearly illustrates the four components of data assimilation: quality control, objective analysis, initialization, and an initial guess from a short-range forecast. With this method, the data are assimilated intermittently at specified intervals. So-called next-generation data-assimilation methods are being researched today, with the two most prevalent being the adjoint method based on the variations of calculus and the Kalman–Bucy filter technique.

Since quality control, objective analysis, and initialization are intricate parts of data assimilation, it is appropriate to consider each of these components in the present paper. Quality control methods are outlined in section 2. The most commonly used objective analysis and initialization techniques are overviewed in sections 3 and 4, respectively, followed by a discussion of various data-assimilation methods in section 5. Then, in section 6, two studies, comparing operational data-assimilation techniques, are reviewed. Section 7 outlines some implications of FDDA and highlights ongoing and future research in data assimilation. Finally, a summary is given in section 8.

2. Quality control

Quality control is an integral part of a data-assimilation system. Quality-control algorithms are designed to modify or reject erroneous meteorological data. Following Daley (1991), observational data errors can be classified into two groups: natural error and gross (or rough) error. The natural error includes instrument error and error of representativeness. The data describe the behavior of the instrument itself, not the behavior of the meteorological parameter it is intended to measure. Every instrument is approximate by its very nature. Errors of representativeness are deviations caused by small-scale perturbations and are also referred to as micrometeorological errors. Gross errors originate from improperly calibrated or malfunctioning instruments, incorrect registration of observations, incorrect coding of observations, and telecommunication errors. These errors (natural and gross) can be either random or spatially or temporally correlated, and there can be systematic biases. The systematic errors can result from improper calibration

of an instrument or from the influence of some persistent factor that is not accounted for or is accounted for inaccurately.

Several quality-control techniques are used routinely to screen bad data. These techniques can be divided into four major categories (following Gandin 1988). The first two, plausibility check and check for contradictions, are used to identify gross errors based on the physical reasonableness of the data. Plausibility checks are the most widely used quality-control methods. These checks analyze each datum independently of other data. A simple plausibility check is one that rejects data values that can never occur in reality—for example, positive temperatures ($^{\circ}\text{C}$) at 300 mb. Other versions compare the datum with the climatological mean or with a background field (numerical forecast). If the deviation is too large, the datum may be rejected. The check for contradictions is based on an analysis of two or more parameters at the same point. An example is the occurrence of rain in the absence of clouds.

Quality control is an integral part of a data-assimilation system. Quality-control algorithms are designed to modify or reject erroneous meteorological data.

The remaining quality-control procedures include checks that rely on some common information and redundancy between observations. The spatial continuity (or consistency) check compares a datum with data at adjacent locations. This method, also known as the buddy check, demands spatial consistency among the data. A temporal continuity check can also be made in which temporal continuity is required with past observations. Finally, checks using dynamic relations such as the geostrophic or hydrostatic relation can be used to check geopotential height with temperature and mass with wind. These checks require the data to obey the dynamic relation at least approximately, otherwise the data are suspected or rejected.

The necessity for including automated quality control in operational NWP was recognized during the early era of NWP. Significant advances have been made in quality control, including the development of methods using optimum interpolation (Rutherford 1976; Lorenc et al. 1977; Lorenc 1981). Recent advances include the complex quality-control method of Gandin (1988) and the Bayesian approach of Lorenc and Hammon (1988). Reviews on various quality control methods have been authored by Belousov et al. (1968), Gustavsson (1981), and Lorenc (1985).

3. Objective analysis techniques

Objective analysis (the second major component of FDDA) and quality control have become intertwined and, as a result, the data-assimilation process is more internally consistent. Excellent reviews on objective analysis have been presented by McPherson (1976) and Gustavsson (1981). The present discussion contains a synopsis of selected topics from these two reviews. According to McPherson (1976), objective analysis is a process in which meteorological observations distributed in space and time are combined with forecasts from previous analyses and perhaps with climatology to form a numerical representation of the state of the atmosphere. This representation takes the form of values of the meteorological variables at regularly spaced grid points subject to various mathematical and physical constraints.

The objective analysis process consists of three subprocesses that are essential for the overall success or effectiveness of the FDDA system: 1) filtering of small-amplitude random and systematic errors; 2) interpolation to a regular network of grid points or, in the case of spectral analysis, integration of the representing mathematical space functions over the irregularly spaced observations; and 3) forced adjustment of the meteorological variables using dynamic relationships among these variables.

Within a relatively short period of time, objective (numerical) analysis schemes were independently developed by several meteorologists. Panofsky (1949) devised the first objective analysis method—polynomial interpolation, or the so-called surface-fitting type. An extension of this method was developed by Gilchrist and Cressman (1954) and became the first operational objective analysis. In this technique, mathematical (polynomial) functions are adjusted to observed data in the close vicinity of the grid point, for which analyzed values are required. The adjustment or fit is obtained by a least squares technique. The polynomial method is nonlinear since nonlinear functions are used to approximate the variation of the analyzed variable. However, the resulting analyzed value at the grid point is a linear function of the observed data and, in this respect, this method is similar to the other analysis methods that will be described.

Bergthorsson and Döös (1955) introduced the successive correction method, and a similar method was devised by Cressman (1959). Cressman's successive correction technique essentially replaced the polynomial interpolation method because the latter produced unreasonable analyses at the edge of data-rich and data-sparse areas. In the successive corrective technique, a forecast model provides the preliminary estimate (first guess) of the field to be analyzed. The basic

idea of the method is to correct this preliminary field iteratively during several analysis "scans"; the results of one scan become the first guess for the next scan. The estimate is modified by a combination of corrections computed for each grid point. The corrections, which are proportional to the difference between the observed and first-guess values, are weighted empirically, with observations nearest the grid point weighted the most heavily.

By using a short-range forecast based on a previous analysis as the first guess, the effect of past data is allowed to influence the analysis and thereby contributes to the temporal continuity and spatial coherence of the analysis. For many years, successive correction methods were most widely used in operational forecast centers.

By using a short-range forecast based on a previous analysis as the first guess, the effect of past data is allowed to influence the analysis and thereby contributes to the temporal continuity and spatial coherence of the analysis. For many years, successive correction methods were most widely used in operational forecast centers.

This early dominance of the successive correction methods was taken over during the last decade by statistical (optimal) interpolation schemes, which were originally introduced by Eliassen (1954) and Gandin (1963). Statistical interpolation was also studied extensively by Alaka and Elvander (1972) and Phillips (1976). This analysis technique is based on statistical linear regression and provides a systematic framework for blending observations of differing error characteristics with recent predictions or climatology. More accurate data receive more weight in the analysis. As in the successive correction method, the analyzed value at the grid point is the sum of the first guess and a linear combination of corrections, which are proportional to the difference between observational and first-guess values. The weighting coefficients are determined from the condition that the mean-square-error of the analyzed values be minimum, and they depend on the spatial covariances among the analyzed variables. This method is, in principle, spatially coherent and, like its counterpart of successive correction, incorporates temporal continuity through the use of a short-range forecast from the preceding analysis as a first guess.

The polynomial interpolation method mentioned earlier reappeared in the British Meteorological Office analysis (Dixon et al. 1972) and in the spectral analysis method devised by Flattery (1971). In the spectral analysis technique, mathematical functions are globally adjusted to fit observed data. One additional analysis method that has been utilized in the FDDA context (see discussion in section 5) is the variational technique introduced by Sasaki (1958). This method is a post-analysis adjustment technique based on the calculus of variations and is very effective in making the analyzed fields compatible with a forecast model. A functional is used, which minimizes the analyzed-minus-observed difference, filters undesirable high-frequency and high-wavenumber features, and employs dynamical constraints. These constraints may be strong (satisfied exactly) or weak (satisfied approximately).

Over the past 30 years, numerous variations of these different objective-analysis methods have been developed. Some versions are hybrids belonging to more than one of the aforementioned techniques.

According to McPherson (1976), objective-analysis methods used in operational meteorology can be divided into two basic categories. The first represents an analyzed field as a series expansion (spectral analysis):

$$Z_g = a_1 f_1 + a_2 f_2 + \dots + a_m f_m, \quad (3.1)$$

where Z_g represents the departure of the field from its mean value. The f_i represents a set of orthogonal functions—for example, a cosine series. The analysis procedure involves the determination of the time-dependent coefficients a_i , which make the series expansion best fit the observed data by, for example, a least-squares technique. Analysis methods of this type are in operational use at the National Meteorological Center (NMC) (Flattery 1971; Hayden 1976) and the United Kingdom Meteorological Office (UKMO) (Dixon 1976).

The second basic method, called the “gridpoint” method, includes statistical interpolation and successive correction techniques. Here, the analyzed value Z_g^a at a discrete point g is given by a linear combination of observations that are nearby in time and space:

$$Z_g^a = a_1 Z_1^o + a_2 Z_2^o + \dots + a_n Z_n^o, \quad (3.2)$$

where Z^o represents observed values at the several stations within some predetermined influence radius of point g , and the coefficients a_i determine the influence of each observation on the analyzed value. In this case, the analysis involves determining the coefficients a_i in the linear combination for each point of the analysis grid.

Two forms of representation are associated with these two basic methods of analysis: the discrete form and the spectral form. In the former, the analysis is a set of values at discrete points in space and time; in the latter, the analysis is represented by a series expansion such as (3.1). The spectral form has been used primarily for global and hemispheric applications. The discrete form has been extensively used for limited-area applications in mesoscale meteorology.

4. Initialization techniques

The objective-analysis methods described in the previous section generally do not provide balanced mass and wind fields to initiate a forecast. Uncompensated errors in wind and pressure–temperature observations, interpolation of observations to model grids, and the numerical model’s inability to exactly describe the atmosphere are the primary sources of this dynamical inconsistency. The dynamical imbalances in the initial data lead to the generation of spurious inertia–gravity-wave oscillations, or “meteorological noise.” Primitive equation models, unlike geostrophic models, admit these higher-frequency gravity-wave solutions that can have amplitudes much greater than their counterpart in the real atmosphere. These gravity-wave oscillations can obscure the lower-frequency Rossby-mode component of the model, which constitutes the meteorological signal. Early numerical modelers called attention to the need to eliminate the spurious high-frequency oscillations, which can compromise the forecast procedure. First of all, these fast-moving gravity waves require short computational time steps; second, they can seriously interfere with very short-range forecasts (<12 h); and third, they can impair vertical motion and, hence, precipitation forecasts (Daley 1981). Therefore, a long-standing approach has been to eliminate or effectively reduce these fast-moving inertia–gravity waves at initial forecast time. This process is known as model initialization. Charney (from unpublished letter to Phillip Thompson, 12 February 1947) provided insight for rectifying this initialization problem by suggesting that one should modify the initial state or modify the governing equations; that is, use filtered models.

The first and simplest approach was to exclude any possibility of the high-frequency oscillations by using a “filtered system” such as the balance equations, which simply reduce the model dynamics to the quasigeostrophic response. However, this approach severely restricts the model dynamics, which results in very poor forecasts beyond 24 hours. The so-called primitive equations account for more atmospheric

dynamics and can yield much better forecasts, so they are generally used. However, the primitive equations do allow the amplification of fast-moving gravity waves, which requires some modification of the initial conditions to achieve the desired dynamical balance.

Over the years, many initialization methods have been developed. A summary of the more widely used techniques is presented here. For a more detailed review, the reader is referred to Daley (1991). In static initialization, the data are adjusted at a single time level to conform to some dynamical constraints. That is, certain time derivatives are identified as vanishing, in order to eliminate or reduce the generation of inertia-gravity-wave noise. In the conventional static initialization, a standard practice is to first analyze the geopotential field using pressure-height data and use wind observations to estimate the gradient of the geopotential using the geostrophic relation. The analyzed geopotential fields on pressure surfaces are

The most common approach of initialization in intermittent FDDA is normal mode initialization, which achieves dynamical balance using the normal modes of the linearized dynamical equations.

then used in the mass balance equation to obtain the streamfunction of the nondivergent wind, from which the rotational wind component can be computed. A major limitation in using the balance equation to determine a rotational wind for initializing a primitive equation model is that the lack of a divergent wind component insures the presence of gravitational modes (Haltiner and Williams 1980).

The most common approach of initialization in intermittent FDDA is normal mode initialization, which achieves dynamical balance using the normal modes of the linearized dynamical equations. The direct use of normal modes was introduced by Dickinson and Williamson (1972). They proposed that the amplitudes of the unwanted, fast-moving modes be set to zero. Their method was effective in suppressing the spurious noise in linear models, but failed in the nonlinear case. A nonlinear normal mode scheme was independently developed by Machenhauer (1977) and Baer (1977). In nonlinear normal mode initialization, the tendency of the unwanted modes are set to zero, versus setting the amplitude of these modes to zero. The solution of the nonlinear equation requires an iterative process. Unfortunately, this nonlinear scheme, without the inclusion of diabatic effects, suppressed the meridional circulation in the tropics. Puri and

Bourke (1982) used the idea that the tropical divergent circulations driven by convection mainly influence the low-frequency gravity modes. Therefore, they excluded these low-frequency modes from the initialization using a frequency cutoff. Wergen (1982) introduced another method in which average diabatic heating is obtained by integrating the model for a few time steps prior to initialization. This model-produced diabatic heating is then included in the nonlinear forcing in the iterative process.

In global models (Andersen 1977; Daley 1979; Temperton and Williamson 1981; for example), after the normal modes of the model are computed, the high-frequency inertia-gravity waves can be removed by projecting the inertial wind and mass fields onto these normal modes. However, in limited-area models it is not possible to define the horizontal structure of the normal modes.

Bourke and McGregor (1983) introduced a method of initializing a limited area model without explicitly computing horizontal normal modes. In this technique, termed *vertical mode initialization*, the free modes of oscillation of the prediction model are identified by linearizing the equations about a basic state of rest. This linearization permits a simple decomposing of the three-dimensional eigenvalue problem into a series of two-dimensional problems. The vertical decomposing leads to a number of characteristic vertical modes, one corresponding to each discrete level in the model. Balance conditions on the horizontal structure equations are then derived for each vertical mode. Filtering conditions, in which the tendencies of divergence and ageostrophic vorticity are set to zero, are applied to derive linear diagnostic equations for the mass and divergency fields. In Fig. 2, from Bourke and McGregor (1983), graphs of surface pressure before and after initialization using the Australian regional primitive equation model are shown. It is obvious that the initialization procedure successfully removed noise from the integrations.

Temperton (1988) devised a method of applying Machenhauer's criterion without requiring the computation of the coefficients of the individual modes. Figure 3 (from Temperton 1988) shows graphs of 500-mb geopotential before and after the application of Temperton's implicit normal-mode initialization for the Canadian finite-element model. This method is also successful in removing the high-frequency noise.

Although appropriate for intermittent FDDA, the normal-mode initialization is a distinct, separate step from the objective analysis and usually leads to changes in model parameters. As a result, the initialized analysis may no longer fit the observations as closely as desired. An alternative, known as dynamic initializa-

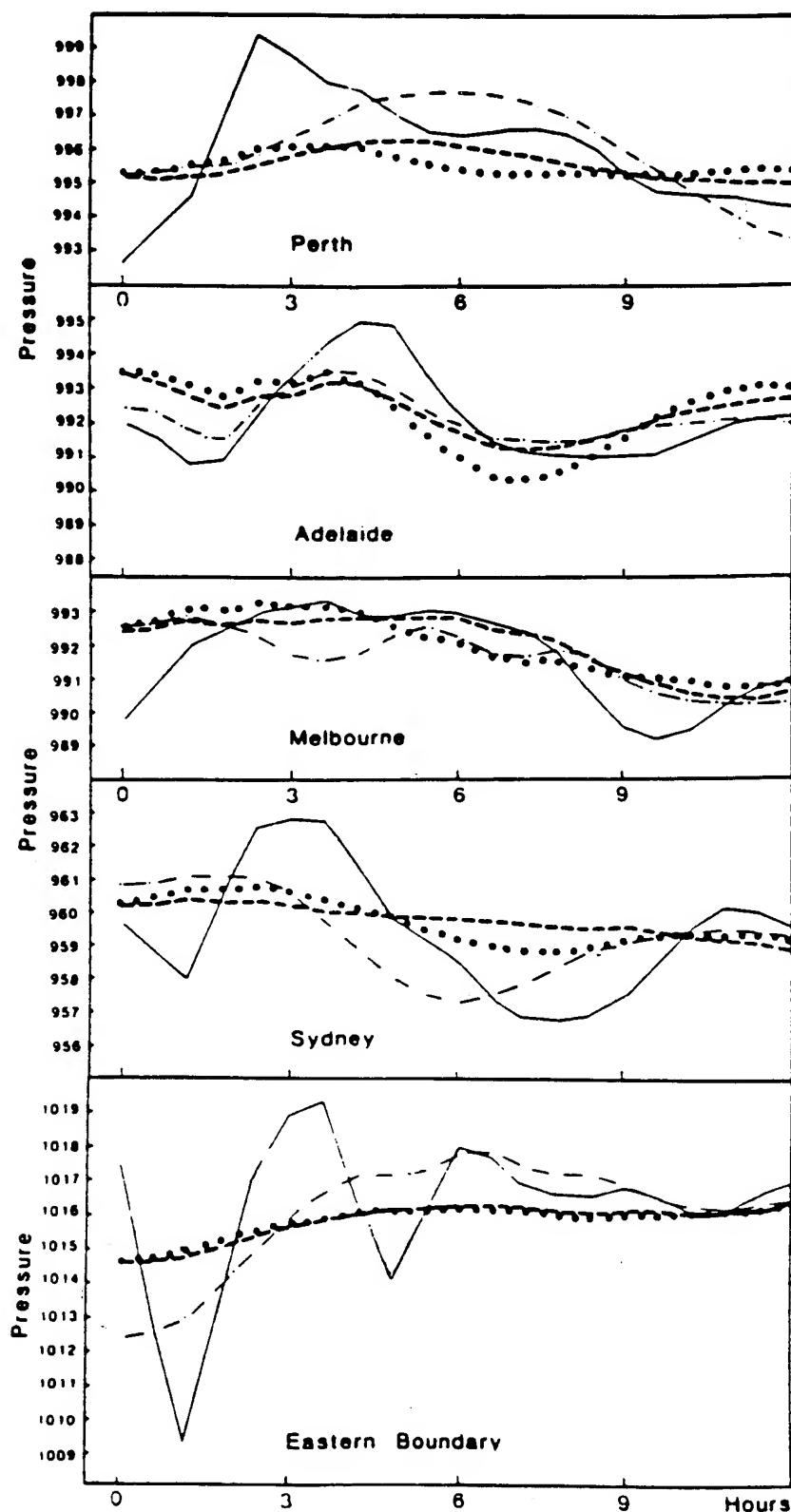


FIG. 2. Surface pressures in millibars for individual grid points for the first 12 h of prognosis using an uninitialized analysis (solid curves), after initializing two vertical modes (dot-dash), and after initializing two vertical modes (dashes—using Dirichlet boundary conditions; and dots—using Neumann boundary conditions) (Bourke and McGregor 1983).

tion, has the advantage of avoiding the complications of computing normal modes. In this method, which was introduced by Miyakoda and Moyer (1968), observations are inserted (intermittently or continuously) over a period of time. The method has the added advantage of simplicity and can balance physical processes as well as the mass and wind fields. In dynamic initialization, the model equations were integrated forward and backward through time under controls that encourage time derivatives to become small compared to spatial derivatives, which in turn selectively dampened the high-frequency components of the solutions. Early versions of this technique required several repetitions of the integration cycle to successfully reduce the gravity-wave oscillations and, as a result, these schemes were computationally expensive. Another disadvantage was that the slow modes of the model were dampened.

More recently, researchers including Bratseth (1982), Sugi (1986), and Satomura (1988) have developed schemes that are more computationally efficient and have more selective damping properties. Figure 4 (from Sugi 1986) depicts graphs of the gravity-wave activity (before and after initialization) for five vertical modes of a baroclinic model. The gravity-wave noise is dramatically reduced, particularly for the modes of large equivalent depths. Dynamic initialization, as well as the Laplace transform and bounded derivative methods (described below), is well suited for initializing data on a limited domain.

Lynch (1985a) developed an effective method of initialization based on a filtering scheme that uses a modified inverse Laplace transform. This technique is equivalent to the nonlinear normal-mode initialization method, but it has the advantage of not requiring a transformation of the model equations into normal mode space. Therefore, the Laplace trans-

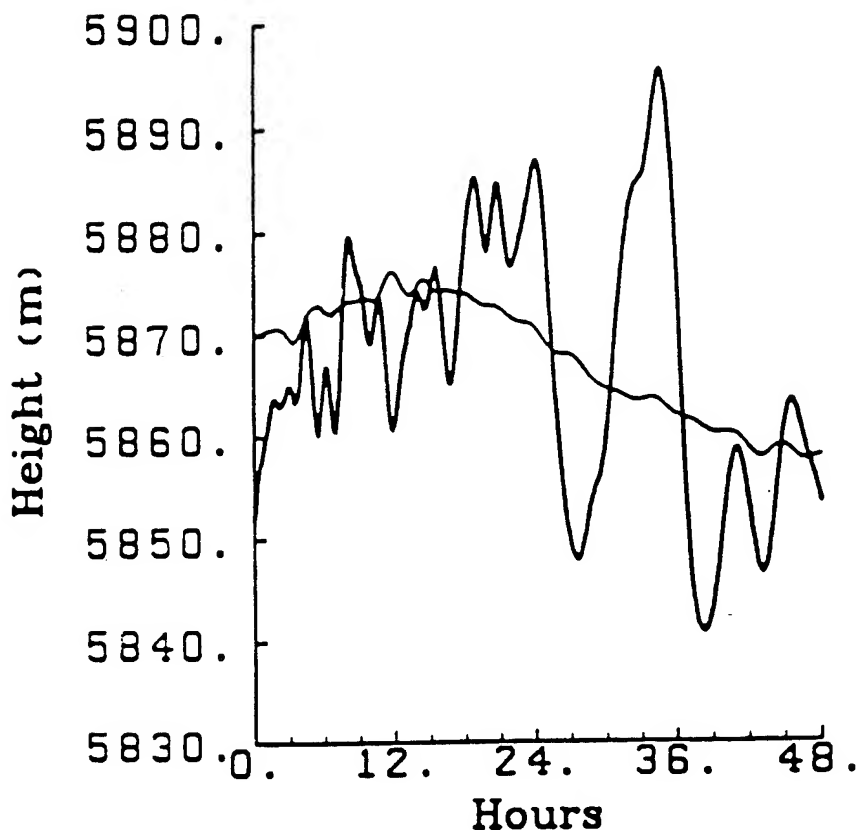


FIG. 3. Time trace of height field. Heavy line: no initialization. Light line: after two iterations of the implicit nonlinear normal-mode initialization scheme (Temperton 1988).

form method is well suited for initializing limited-area models with complex boundary conditions. Lynch (1985b) used his method to initialize data for a barotropic limited-area model, successfully removing high-frequency gravity-wave oscillations during the model integration. This technique has also been applied in a filtering integration scheme for continuous data assimilation.

Another technique, which has been used to initialize models of limited domain, is the bounded derivative method. Kreiss (1979) developed the methodology of controlling the amplitudes of the high-frequency inertia-gravity waves by requiring the derivatives of the model's dependent variables with respect to time to be bounded, i.e., of order unity, as the initial time. First, the equations of motion are nondimensionalized so that certain terms are multiplied by a small parameter, ε . Then, if the first derivatives are bounded, the equations can only be satisfied if the model atmospheric flow is geostrophic and nondivergent to the order ε . If the second-order time derivatives are bounded, the resulting diagnostic relationships are the quasi-geostrophic omega equation and the nonlinear balance equation.

to obtain first-guess fields for the analysis at the next assimilation cycle. Thus, the new estimates (analyzed fields) are clearly based on the past observations, being carried forward in time by the model forecast, and on the current observations. The intermittent updating process is entirely appropriate as long as most available data are taken at the same time, for example, at synoptic times. This technique is currently used at most of the world's major operational forecasting centers, including the NMC, (DiMego 1988); the Norwegian Meteorological Institute (Gronas and Midtbo 1986); and the European Centre for Medium-Range Weather Forecasts (ECMWF) (Hollingsworth 1986).

The extensive operational use of intermittent data assimilation is primarily due to its computational efficiency. In addition, this method normally includes a normal-mode initialization scheme that produces a balanced mass/wind initial state. A disadvantage of this method is that it is not totally suited for asynoptic data types; that is, it can not assimilate data continuously. However, updates on the order of every 2 to 3 h can be made, allowing some asynoptic data into the assimilation.

Two other mathematically elegant methods,

5. Various data-assimilation methods

An assimilation method extensively used in operational meteorology is the analysis-forecast cycle technique, commonly referred to simply as intermittent data assimilation (see Fig. 5). This process consists of four steps, which are repeated at each assimilation cycle (typically every 3–12 h). After the data have been checked (quality controlled), a static three-dimensional objective analysis (typically successive correction or optimal interpolation) is performed using observations and a background field. The background or "first guess" is usually a prior model forecast valid at the analysis time, or it can simply be climatology or a combination of both. Then, the analyzed fields are adjusted, or initialized, to conform to some dynamical constraint(s) in order to reduce or eliminate inertia-gravity-wave noise. The final step consists of a short-range numerical forecast

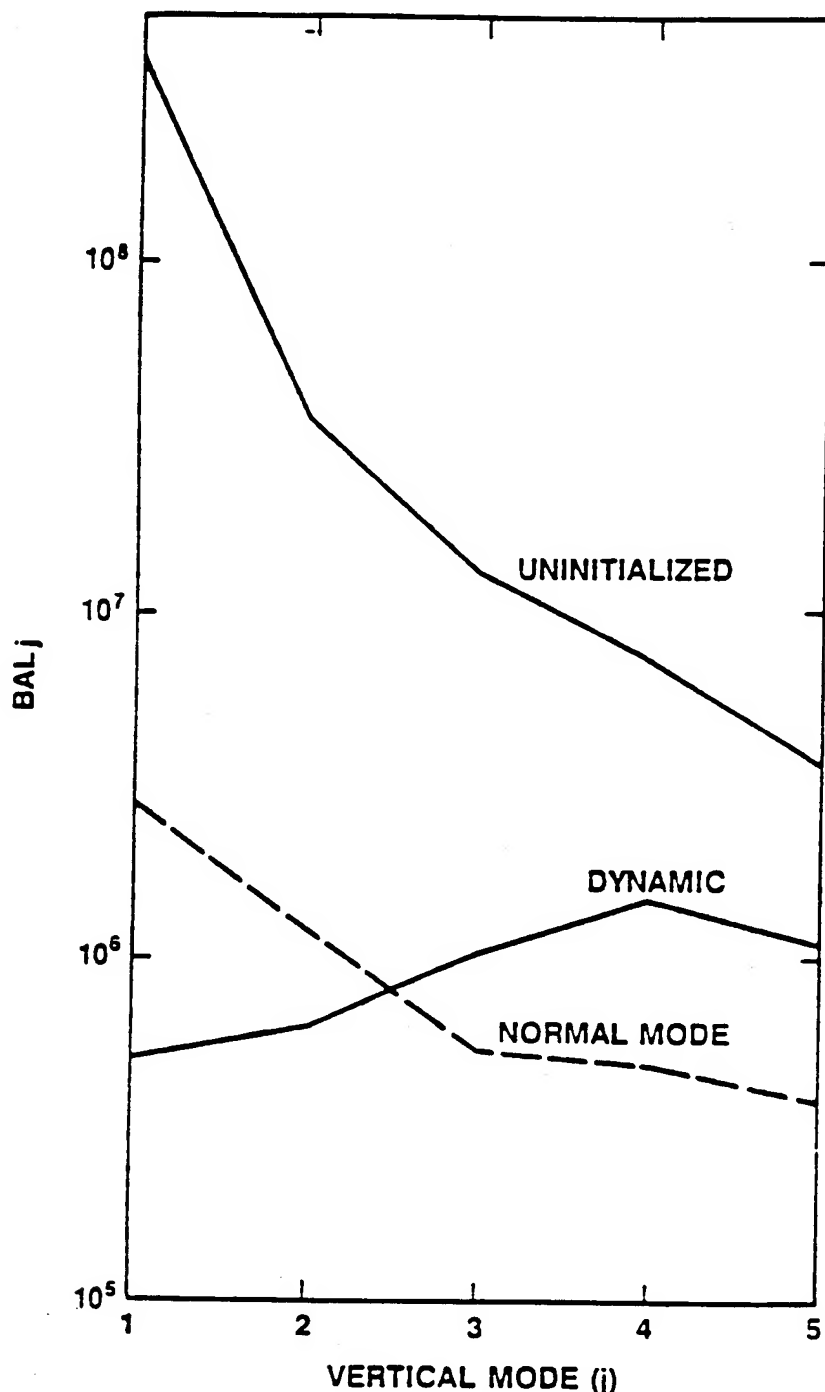


FIG. 4. Gravity-wave activity (before and after initialization) for five vertical modes of a baroclinic model (Sugi 1986).

Kalman-Bucy filtering and the adjoint method using variational techniques, have emerged as state-of-the-art methodology in FDDA. The latter is briefly reviewed first. For a more rigorous and complete discussion of the general theory of these two techniques, the reader is referred to Daley (1991).

Variational assimilation, based on the calculus of variations, involves the incorporation of dynamical

to the initial conditions.

The output of any model depends upon a set of input variables: initial conditions, boundary conditions, and even modeling parameters of physical processes. Because of this dependence, the "adjoint" can be used to determine the sensitivity of the model output to any input parameter, i.e., initial conditions. Neglecting forecast errors over the assimilation period

constraints in a variational treatment and has been pursued by Sasaki (1969), Stephens (1970), and others for several years. In variational calculus, stationary points (extrema) of integral expressions known as functionals are determined. J is a functional of the function $q(t)$ in the interval (t_m, t_n) , if it depends on all the values $q(t)$ for $t_m \leq t \leq t_n$. In this approach, successive analyses are mutually adjusted to effectively increase the database at each time step by using information at other analysis times through the forecast equations. The objective is to produce initialized values of q subject to certain constraints, such as the hydrostatic relation, the continuity equation, the geostrophic relation, or the nonlinear balance equation. The approach is designed to keep the initialized fields close to the observations while satisfying the constraint (Daley 1991).

Lewis (1972) developed a variational scheme using a thermal wind relationship and the hydrostatic equation as constraints. A more recent variational approach, known as the adjoint method (Lewis and Derber 1985), uses a complete dynamic model as a strong constraint. This method fits a model to observational data distributed over a finite period by computing derivatives of model output. An iterative method minimizes the weighted squared difference between the original analyses at several times and the coincident solutions to the model (constraint) for a given output variable. The final analyses are constrained to satisfy the model forecast from a set of initial conditions. The functional, J , is minimized by finding the gradient of J with respect

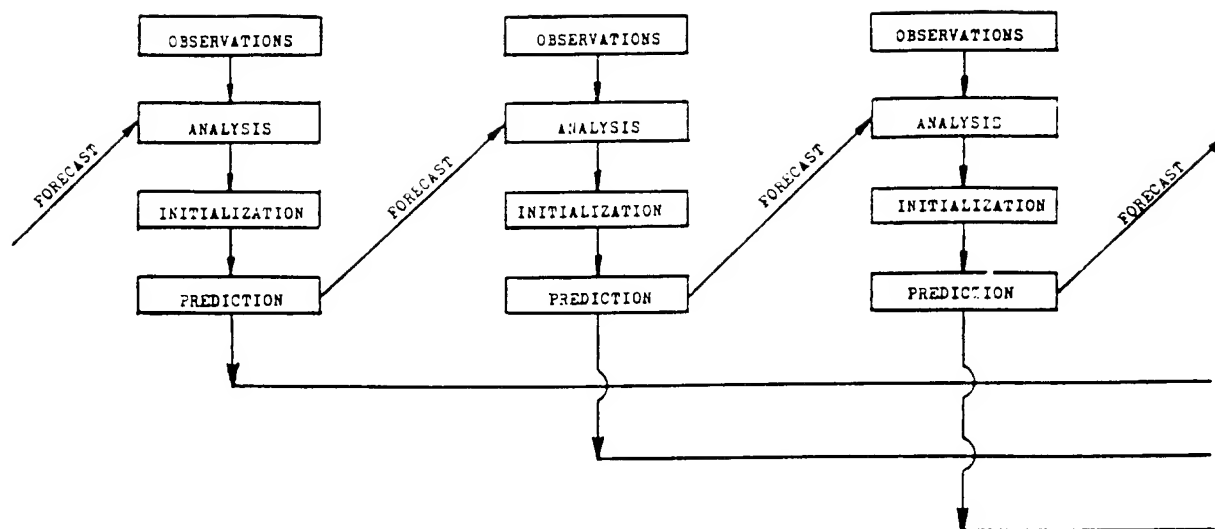


Fig. 5. Intermittent data assimilation using an analysis-forecast cycle (Bengtsson 1975).

(time period spanning the observations), this technique can produce the optimal initial state (end of the assimilation period) such that the model best fits the observations through the entire period.

The alternate "next-generation" FDDA method is called Kalman-Bucy (K-B) filtering. The K-B method can be thought of as a continuous dynamic FDDA where the weighting factors are optimally determined by explicitly calculating the error covariance of the analysis. In 1960, Kalman developed the basic theory for the linear, unbiased data-assimilation scheme known as the Kalman filter (Kalman 1960).

The K-B filter (Kalman and Bucy 1961; Ghil et al. 1979, 1981), which is the time-continuous counterpart to Kalman's original scheme, uses the forecast model itself to predict the background error statistics. The goal of this method is to obtain the most accurate analysis value for all time during the assimilation period using only present and past observations. The weight given to the current observations is inversely proportional to their variance, and the accuracy of the analysis is the sum of the accuracies of the forecast, based on the past observations, and of the current observations. The K-B filter minimizes the analysis error variance not only at every time step, but over the entire assimilation interval in which data are provided (Ghil 1989). Through an application of Bayesian ideas in a dynamical sense (Kalman 1960; Lorenc 1986), the filter is able to extract all useful information from the observational increment/residual at each time step, thus allowing observations to be discarded as soon as they are assimilated. As a result, the method is sequential.

The K-B filter and the adjoint method are very promising assimilation techniques. Both methods have

been shown to produce improved assimilated states for model forecast integration as compared to those from the operational techniques. However, these "next-generation" data-assimilation methods are of limited practicality at the present because of their complexity and extensive computational requirements. Therefore, operational implementation is still several years away (Stauffer and Seaman 1990). However, Lorenc (1988) has pursued approximations to the adjoint technique in a quest to make it operational in numerical weather prediction.

Most research has been directed toward the less elegant but more practical method of dynamic assimilation, in which the numerical prediction model serves as an integrator of observations distributed in time and space. In this approach, which has become known simply as "nudging" or Newtonian relaxation, the model integration is interrupted periodically and the current model state is updated with the new observations. During the assimilation cycle, or preforecast integration period, the model variables are gradually driven, or nudged, toward the observations by extra forcing terms in the equations (Anthes 1974; Kistler 1974; Hoke and Anthes 1976; Davies and Turner 1977). As a result, the model fields are gradually corrected and no further dynamic balancing through initialization is required. The general form of the predictive equation of variable S is:

$$\frac{\partial S}{\partial t} = F(S, \bar{x}, t) + G W (S_o - S). \quad (5.1)$$

All of the model's physical forcing terms (Coriolis, advection, etc.) are represented by F , where S is a model-dependent variable, S_o represents observations of S , \bar{x} is the independent spatial variable, and t

is time. The second term on the right is the nudging term, where G is the nudging constant (generally 10^{-3} to 10^{-4}) and W represents a four-dimensional weighting function. The data to be nudged can be either derived or measured, analyzed to a grid for assimilation into the model, or inserted as individual observations.

This technique, which has been successful in bringing the data and the model in harmony and providing a relatively noise-free start for the forecast, has been widely used on the global scale (Lyne et al. 1982; Krishnamurti et al. 1988) and on the regional scale in limited-area models (Anthes 1974; Hoke and Anthes 1977). Of late, several researchers have developed a new interest in the technique (Stauffer et al. 1985; Bell 1986; Ramamurthy and Carr 1987; Kao and Yamada 1988; Wang and Warner 1988; Kuo and Guo 1989; Stauffer and Seaman 1987, 1990). It is currently used operationally at the UKMO for both global (Lyne et al. 1982) and regional (Bell 1986) data assimilation.

The nudging technique mentioned above does possess a few desirable attributes; these were summarized by N. L. Seaman (from his lecture notes presented at the 1990 Summer Colloquium on Mesoscale Data Assimilation, Boulder, Colorado): 1) The assimilating model is complete, so irreversible processes are included without difficulty. 2) Any data type that can be represented as a tendency of a prognostic variable can be assimilated. 3) Observation nudging can easily assimilate synoptic and single-level data. 4) Analysis nudging requires that the analyses be performed only once prior to model integration; i.e., it is economical. 5) Nudging does not require a separate balancing/initialization step. 6) Nudging is conceptually and computationally simple.

On the other hand, this method has a few disadvantages: 1) The nudging constant is generally assigned in an application-dependent semiarbitrary manner. 2) Observation nudging is based on "continuous analysis" during model integration and can become computationally expensive. 3) Analysis nudging is not well suited for synoptic data types. 4) Use of accurate data in observation nudging may cause assimilation of local or unrepresentative components (e.g., microscale observations spread over a large area).

6. Comparisons of operational assimilation techniques

Two papers from the recent literature (Ramamurthy and Carr 1987; Kuo and Guo 1989) compared different data-assimilation methods. Unlike the purpose of the present paper, both of the aforementioned articles advocated Newtonian nudging. The sole purpose

here is to offer a short review of the available comparative studies.

Ramamurthy and Carr (1987) studied the applicability of several assimilation techniques currently being employed in operational models. A prime scientific objective was to determine the "best" way to assimilate synoptic observations in limited-area models. A sequence of ten assimilation experiments were conducted using different update procedures. In each experiment, their limited-area model was initialized with ECMWF FGGE level III-b data, and then 12-h assimilations were performed using level II-b data from the 1979 Summer Monsoon Experiment (SMONEX). Forecasts were then made from these assimilated states. The first experiment served as the control run, since no assimilation was performed. Figure 6 is a schematic of the overall assimilation-forecast strategy; four types of data assimilation were compared: 1) In the static assimilation, the model was updated only once at the end of the preforecast (assimilation) period. An initialization step was then taken to suppress the noise associated with the external inertia-gravity mode; the internal modes were not initialized. 2) The intermittent data-assimilation experiment was similar to the static case, except the model was updated twice during the assimilation period. 3) Four experiments were conducted using continuous indirect data assimilation in which the model was updated whenever new observations became available. 4) Newtonian relaxation was used in the last three experiments; the model state was nudged toward analyses produced from the observations. The reader should see Ramamurthy and Carr (1987) for a detailed description of the experiments.

Comparisons among these differing techniques were made by examining assimilated states (analyses obtained at the end of the 12-h assimilation period). Newtonian nudging produced better assimilated states than did the continuous assimilations via indirect insertion. Also, the continuous assimilation experiments produced noisy assimilated fields due to insertion shocks.

From each of the assimilated states, 24-h forecasts were made and the results were compared against each other and with the observations. The continuous assimilation (via indirect insertion) continued to suffer from the ill effects of the insertion shock. However, the forecasts from the nudging experiments had a minimal amount of noise.

The degree of spinup was examined in terms of the development of precipitation. The excessive shocking associated with continuous insertion was detrimental to the spinup process and consequently to the rainfall predictions. The rotational nudging experiment (only the rotational component of the wind was nudged)

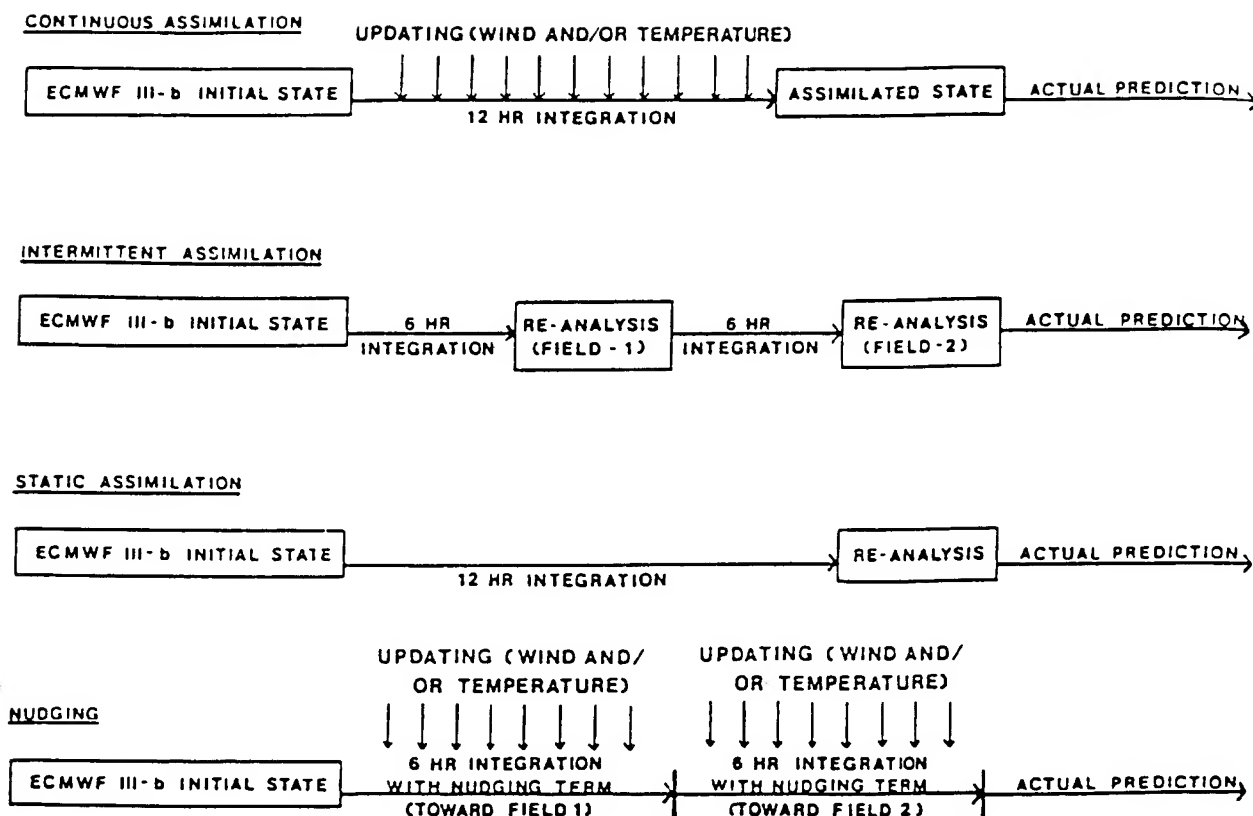


Fig. 6. A schematic of the assimilation-forecast cycle for various experiments (Ramamurthy and Carr 1987).

produced the most accurate rainfall predictions. The lack of divergence-related shock in this approach aided in the evolution of the physical processes.

The predicted tracks of the cyclone in the SMONEX case study were compared. During the first 12 h (assimilation period), the cyclone's movement was erratic in all of the experiments due to the rapid mutual adjustment between the mass and wind fields that occurred in the early stages of integration. In the static and intermittent assimilation experiments in which the fields were replaced completely at the end of the assimilation period, this problem extended into the forecast stage for another 12 h. Overall, the nudging experiments predicted more accurate tracks than the other experiments.

In another comparative study, Kuo and Guo (1989) examined different data-assimilation strategies. They conducted a series of observing-system simulation experiments (OSSEs) to test a Newtonian nudging technique for continuous assimilation of observations from a hypothetical network of profilers. Twenty experiments were described in their paper. Similar to the work of Ramamurthy and Carr, they investigated static initialization, intermittent assimilation, and Newtonian nudging.

Comparisons of the three assimilation techniques

were made by obtaining time series of wind and temperature errors during the assimilation period. With nudging, the errors decreased gradually during the period. The intermittent assimilation produced a stepwise decrease in the errors and the results after four assimilation cycles were considerably better than in the static assimilation case. This reveals that intermittent data assimilation was also effective in producing an improved initial state for the model forecast.

When considering model noise generated during the preforecast period, a strong difference emerged between continuous nudging and the intermittent assimilation. In the nudging experiment, the model noise gradually decreased during the assimilation period. In contrast, the intermittent data assimilation produced model noise with large spikes immediately after each reanalysis of the wind field. However, this noise could have been reduced substantially if a normal-mode initialization procedure had been incorporated.

The two papers reviewed above suggest that Newtonian nudging is the best assimilation method among those compared. However, the investigators' findings may be scientifically inconclusive due to their incomplete tests (notably, their failure to include an effective normal-mode initialization procedure in the intermittent data-assimilation experiments). Further-

more, their comparisons were limited to operational data-assimilation techniques. The next-generation methods will produce more optimal assimilated states for initiating a numerical weather prediction model. But as stated previously, these methods are still in the developmental research stage and computationally efficient versions are not currently available for operational use.

7. FDDA research: Implications and the future

FDDA has been developed tremendously during the past 15 years and is now an essential component of numerical analysis and prediction systems in both research and operations. The improving performance of medium-range global and hemispheric prediction and the rapid development of limited-area and mesoscale models at centers such as the NMC, ECMWF, and UKMO clearly illustrate the practical benefits of research in data assimilation.

The systematic development of data-assimilation methods has made possible the use of unconventional and synoptic observations from satellites, aircraft, drifting buoys, and soon from wind profilers and doppler radars. As a result, the accuracy of short-range forecasts has significantly improved, although only minor changes have occurred in the global observing system since the Global Weather Experiment in 1979 (Bengtsson and Shukla 1988). According to Lange and Hellsten (1986), the 3-day rms forecast error for the Northern Hemisphere dropped by more than 35% between 1979 and 1986. During the same period, medium-range weather prediction has been usefully extended in the time scale from 3–4 days to about 7 days in the Northern Hemisphere and to 4 days in the Southern Hemisphere (Bengtsson 1985; Bourke et al. 1985). The largest improvement has occurred at middle and high latitudes of the Northern Hemisphere. Weather prediction in the tropics has not improved nearly as much, due to insufficient observations and deficiencies in the formulation of critical physical processes.

Lorenz (1982) addressed the limit of medium-range predictability and concluded that it is possible to predict instantaneous weather patterns with better accuracy than guesswork nearly two weeks in advance. Such extensions in predictability will depend on the ability to improve current data-assimilation systems as well as the numerical prediction models themselves.

Research is ongoing to find ways to improve data-assimilation methods. A number of research centers are investigating higher-resolution models, better numerical techniques, improved physical parameter-

izations, and improved models of auto- and cross-correlation functions for prediction error. Another area of interest is in specifying the diabatic heating at the initial forecast time. A detailed specification is necessary in order to correctly analyze and forecast the divergent wind field over the tropics. A few universities are making major strides in developing the next-generation FDDA techniques and enhancing existing methods. For example, adjoint methods are being intensely investigated at the University of Oklahoma; K–B filtering at McGill University, Montreal, Canada; and Newtonian relaxation at the Pennsylvania State University.

Several other critical research topics need attention during the 1990s. They include: assimilation of moisture processes (rainfall data and integrated liquid water), lateral boundary conditions and mesoscale predictability (predictive skill of limited-area models is strongly controlled by the lateral boundary conditions), assimilation of surface conditions/characteristics, and

During the next decade, FDDA will play a role in solving or alleviating important environmental issues such as air pollution and climate control (increasing CO₂ and the ozone hole). Recent clean-air legislation requiring the use of low-sulfur fuels and extremely expensive equipment will make accurate numerical models of atmospheric-chemistry transport and removal more important than ever.

quality control, which will continue to be a priority as new data types are applied in FDDA. Data assimilation is relatively new on the meso-alpha and sub-alpha scales and needs considerable research with improved datasets. Existing first-generation assimilation systems must be improved to effectively forecast on these small scales.

During the next decade, FDDA will play a role in solving or alleviating important environmental issues such as air pollution and climate control (increasing CO₂ and the ozone hole). Recent clean-air legislation requiring the use of low-sulfur fuels and extremely expensive equipment will make accurate numerical models of atmospheric-chemistry transport and removal more important than ever. FDDA can be used to obtain accurate meteorological fields for input to complex air-chemistry models. Bengtsson and Shukla (1988) have suggested that a comprehensive analysis of global observations based on an FDDA system with

a realistic physical model should be used to produce internally consistent, homogeneous datasets for the earth's climate system. These global observations will include many new environmental variables such as external forcing variables, concentrations of radiatively and chemically important rare species, and land surface and oceanic variables. New remote-sensing systems such as EOS (Earth Observing System) will monitor these variables.

With these environmental issues in mind, Daley (1991) elaborated on a possible vision of the future of data assimilation:

Firstly, data assimilation will no longer be entirely or even primarily concerned with short (or medium) range weather forecasting. Secondly, the data base will become incredibly diverse in both variables measured and type of observing system. Thirdly, assimilating models will be much more comprehensive, involving ocean, land surface and stratospheric components. Finally, there will be considerably more emphasis on the long term stability of algorithms to facilitate climate change signal detection.

8. Summary

In this paper, an attempt has been made to offer a review of four-dimensional data assimilation from a historical perspective with emphasis on two of the major components of data assimilation: objective analysis and initialization. Major objective analysis methods were reviewed by McPherson (1976) and Gustavsson (1981) and have been summarized here. These include polynomial interpolation, successive correction, optimal interpolation, spectral analysis, and variational techniques. Several model-initialization methods have been highlighted; among these are static initialization, nonlinear normal-mode initialization, vertical-mode initialization, implicit normal-mode initialization, dynamic initialization, Laplace transform, bounded derivative technique, and the variational method.

Several data-assimilation methods have been reviewed, including the two leading next-generation FDDA techniques: the adjoint method and the Kalman-Bucy filtering. Newtonian relaxation and the analysis-forecast cycle (intermittent data assimilation) were identified as the two major types of FDDA used today in operational numerical weather prediction, and they will likely be needed to meet the challenges imposed by new observing systems at least into the mid-1990s. These two methods, along with continuous assimilation via indirect insertion and static assimilation, were compared.

Finally, some important implications of FDDA research have been given. FDDA has undoubtedly led to

significant improvements in short- and medium-range weather forecasting and may provide the much-needed edge in coping with the pressing environmental issues (air pollution and climate control) of the nineties.

Acknowledgments. The authors extend their appreciation to the Naval Research Laboratory and the U.S. Air Force for supporting this work.

References

- Alaka, M. A., and R. C. Elvander, 1972: Optimum interpolation from observations of mixed quality. *Mon. Wea. Rev.*, **100**, 612–624.
- Andersen, J. H., 1977: A routine for normal mode initialization with non-linear correction for a multi-level spectral model with triangular truncation. ECMWF Internal Report No. 15, European Centre for Medium-Range Weather Forecasts, Bracknell, U.K., 41 pp.
- Anthes, R. A., 1974: Data assimilation and initialization of hurricane prediction models. *J. Atmos. Sci.*, **31**, 702–719.
- Baer, F., 1977: Adjustments of initial conditions required to suppress gravity oscillations in non-linear flows. *Beitr. Phys. Atmos.*, **50**, 350–366.
- Bell, R. S., 1986: The Meteorological Office fine-mesh data assimilation scheme. *Meteor. Mag.*, **115**, 161–177.
- Belousov, S. L., L. S. Gandin, and S. A. Mashkovich, 1968: Computer processing of current meteorological data. *Hydrometeoizdat* [Meteor. Trans. No. 18, 1972. Canada Dept. of the Environment, Atmospheric Environment Service, Downsview, Ontario], 227 pp. (in Russian).
- Bengtsson, L., 1975a: Four-dimensional data assimilation of meteorological observations. GARP Publ. Ser., No. 15, WMO/ICSU, Geneva, 76 pp.
- , 1975b: Problems in four-dimensional data assimilation. *Seminars of Scientific Foundation of Medium Range Weather Forecasts. Part I*, Reading, 113–138.
- , 1985: Medium range forecasting at the ECMWF. *Adv. Geophys.*, **28B**, 3–56.
- , and J. Shukla, 1988: Integration of space and in situ observations to study global climate change. *Bull. Amer. Meteor. Soc.*, **69**, 1130–1143.
- Bergthorsson, P., and B. R. Döös, 1955: Numerical weather map analysis. *Tellus*, **7**, 329–340.
- Bourke, W., and J. L. McGregor, 1983: A nonlinear vertical mode initialization scheme for a limited area prediction model. *Mon. Wea. Rev.*, **111**, 2285–2297.
- , R. Seaman, and K. Puri, 1985: Data assimilation. *Adv. Geophys.*, **28B**, 124–149.
- Bratseth, A. M., 1982: A simple and efficient approach to the initialization of weather prediction models. *Tellus*, **34**, 352–357.
- Charney, J., M. Halem, and R. Jastrow, 1969: Use of incomplete historical data to infer the present state of the atmosphere. *J. Atmos. Sci.*, **26**, 1160–1163.
- Cressman, G., 1959: An operational objective analysis system. *Mon. Wea. Rev.*, **87**, 367–374.
- Daley, R., 1979: The application of non-linear normal mode initialization to an operational forecast model. *Atmos. Ocean*, **17**, 97–124.
- , 1981: Predictability experiments with a baroclinic model. *Atmos. Ocean*, **19**, 77–109.
- , 1991: *Atmospheric Data Analysis*. Cambridge University Press, 457 pp.

- , and K. Puri, 1980: Four dimensional data assimilation and the slow manifold. *Mon. Wea. Rev.*, **108**, 85–99.
- Davies, H. C., and R. E. Turner, 1977: Updating prediction models by dynamical relaxation: An examination of the technique. *Quart. J. Roy. Meteor. Soc.*, **103**, 225–245.
- Dickinson, R. E., and D. L. Williamson, 1972: Free oscillations of a discrete stratified fluid with application to numerical weather prediction. *J. Atmos. Sci.*, **29**, 623–640.
- DiMego, G. J., 1988: The National Meteorological Center regional analysis system. *Mon. Wea. Rev.*, **116**, 977–1000.
- Dixon, R., 1976: An objective analysis system using orthogonal polynomials. GARP WGNE Report No. 11, 73–85. [Available from World Meteorological Organization, Geneva.]
- , E. Spackman, I. Jones, and A. Francis, 1972: The global analysis of meteorological data using orthogonal polynomial base functions. *J. Atmos. Sci.*, **29**, 609–622.
- Eddy, A., 1973: The objective analysis of atmospheric structure. *J. Meteor. Soc. Jpn.*, **51**, 450–457.
- Eliassen, A., 1954: Provisional report on calculation of spatial covariance and autocorrelation of the pressure field. Rept. No. 5, Institute of Weather and Climate Res., Academy of Science Oslo, 11 pp. (reprinted in *Dynamic Meteorology: Data Assimilation Methods*, L. Bengtsson, M. Ghil, and E. Kallen, Eds., Springer-Verlag, 319–330).
- Flattery, T., 1971: Spectral models for global analysis and forecasting. *Proc. Sixth AWS Technical Exchange Conf.*, Air Weather Service Technical Report No. 242, 42–54.
- Gandin, L. S., 1963: Objective analysis of meteorological fields. *Hydrometeoizdat* (in Russian), English translation by Israel Program for Scientific Translations, Jerusalem, 1965, 242 pp. (available from NTIS, as N66-18047).
- , 1988: Complex quality control of meteorological observations. *Mon. Wea. Rev.*, **116**, 1137–1156.
- Ghil, M., 1989: Meteorological data assimilation for oceanographers. Part I: Description and theoretical framework. *Dyn. Atmos. and Oceans*, **13**, 171–218.
- , M. Halem, and R. Atlas, 1979: Time-continuous assimilation of remote-sounding data and its effect on weather forecasting. *Mon. Wea. Rev.*, **107**, 140–171.
- , S. Cohn, J. Tavantzis, K. Bube, and E. Issacson, 1981: Applications of estimation theory to numerical weather prediction. *Dynamic Meteorology: Data Assimilation Methods*, L. Bengtsson, M. Ghil, and E. Kallen, Eds., Springer-Verlag, 139–224.
- Gilchrist, B., and G. P. Cressman, 1954: An experiment in objective analysis. *Tellus*, **6**, 97–101.
- Gronas, S., and K. H. Midtbo, 1986: Four dimensional data assimilation at the Norwegian Meteorological Institute. Tech. Report 66, Research Dept., The Norwegian Meteorological Institute, Oslo, Norway, 66 pp.
- Gustavsson, N., 1981: A review of methods for objective analysis. *Dynamic Meteorology: Data Assimilation Methods*, L. Bengtsson, M. Ghil, and E. Kallen, Eds., Springer-Verlag, 17–76.
- Haltiner, G. J., and R. T. Williams, 1980: *Numerical Prediction and Dynamic Meteorology*. Second ed., John Wiley and Sons, 477 pp.
- Hayden, C. M., 1976: Satellite reference level experiments with VTRR and the NMC global spectral analyses. GARP WGNE Report No. 11, 57–72. [Available from World Meteorological Organization, Geneva.]
- Hoke, J. E., and R. A. Anthes, 1976: The initialization of numerical models by a dynamical initialization technique. *Mon. Wea. Rev.*, **104**, 1551–1556.
- , and R. A. Anthes, 1977: Dynamic initialization of a three-dimensional primitive-equation model of Hurricane Alma of 1962. *Mon. Wea. Rev.*, **105**, 1266–1280.
- Hollingsworth, A., 1986: Objective analysis for numerical weather prediction. *Short and Medium-Range Weather Prediction, Proc. WMO/IUGG NWP Symposium*, Tokyo, 11–59.
- Jastrow, R., and M. Halem, 1970: Simulation studies related to GARP. *Bull. Amer. Meteor. Soc.*, **51**, 490–513.
- Kalman, R. E., 1960: A new approach to linear filtering and prediction problems. *Trans. ASME. J. Basic Eng.*, **82D**, 35–45.
- , and R. S. Bucy, 1961: New results in linear filtering and prediction theory. *Trans. ASME. J. Basic Eng.*, **83D**, 95–108.
- Kao, C.-Y. J., and T. Yamada, 1988: Use of the CAPTEX data for evaluations of a long-range transport numerical model with a four-dimensional data assimilation technique. *Mon. Wea. Rev.*, **116**, 293–306.
- Kistler, R. E., 1974: A study of data assimilation techniques in an autobarotropic primitive equation channel model. M.S. thesis, The Pennsylvania State University, 84 pp.
- Kreiss, H.-O., 1979: Problems with different time scales for ordinary differential equations. *SIAM J. Num. Anal.*, **16**, 980–998.
- Krishnamurti, T. N., H. S. Bedi, W. Heckley, and K. Ingles, 1988: Reduction of the spinup time for evaporation and precipitation in a spectral model. *Mon. Wea. Rev.*, **116**, 907–920.
- Kuo, Y.-H., and Y.-R. Guo, 1989: Dynamic initialization using observations from a network of profilers. *Mon. Wea. Rev.*, **117**, 1975–1998.
- Lange, A., and E. Hellsten, 1986: Results of the WMO/CAS NWP data study and intercomparison project for forecasts for the Northern Hemisphere in 1981–82. WMO Short- and Medium-Range Weather Prediction Research, Publication Series No. 2, WMO, Geneva.
- Lewis, J. M., 1972: An operational upper air analysis using the variational method. *Tellus*, **24**, 514–530.
- , and J. C. Derber, 1985: The use of adjoint equations to solve a variational adjustment problem with advective constraints. *Tellus*, **37A**, 309–322.
- Lorenc, A., 1981: A global three-dimensional multivariate statistical interpolation scheme. *Mon. Wea. Rev.*, **109**, 701–721.
- , 1985: Analysis methods for the quality control of observations. *Workshop on the Use and Quality Control of Meteorological Observations*, Reading, U.K., European Centre for Medium-Range Weather Forecasts, 397–428.
- , 1986: Analysis methods for numerical weather prediction. *Quart. J. Roy. Meteor. Soc.*, **112**, 1177–1194.
- , 1988: A practical approximation to optimal four-dimensional objective analysis. *Mon. Wea. Rev.*, **116**, 730–745.
- , and O. Hammon, 1988: Objective quality control of observations using Bayesian methods: Theory and a practical implementation. *Quart. J. Roy. Meteor. Soc.*, **114**, 515–543.
- , I. Rutherford, and G. Larsen, 1977: The ECMWF analysis and data assimilation scheme—Analysis of mass and wind fields. European Centre for Medium-Range Weather Forecasts, Reading, Berkshire, Tech. Rep. No. 6.
- Lorenz, E. N., 1982: Atmospheric predictability experiments with a large numerical model. *Tellus*, **34**, 505–513.
- Lynch, P., 1985a: Initialization using Laplace transforms. *Quart. J. Roy. Meteor. Soc.*, **111**, 243–258.
- , 1985b: Initialization of a barotropic limited-area model using the Laplace transform technique. *Mon. Wea. Rev.*, **113**, 1338–1344.
- , 1991: Filtering integration schemes based on the Laplace and Z transforms. *Mon. Wea. Rev.*, **119**, 653–666.
- Lyne, W. H., R. Swinbank, and N. T. Birch, 1982: A data assimilation experiment and the global circulation during the FGGE special observing periods. *Quart. J. Roy. Meteor. Soc.*, **108**, 575–594.
- Machenhauer, B., 1977: On the dynamics of gravity oscillations in a shallow water model with applications to normal mode initialization. *Beitr. Phys. Atmos.*, **50**, 253–271.

- McPherson, R. D., 1975: Progress, problems, and prospects in meteorological data assimilation. *Bull. Amer. Meteor. Soc.*, **56**, 1154–1166.
- , 1976: Operational objective analysis techniques and potential applications for mesoscale meteorology. *Mesoscale Meteorology and Forecasting*, P. S. Ray, Ed., Amer. Meteor. Soc., 151–172.
- Miyakoda, K., and R. Moyer, 1968: A method of initialization for dynamical weather forecasting. *Tellus*, **20**, 115–128.
- Morel, P., 1981: An overview of meteorological data assimilation. *Dynamic Meteorology: Data Assimilation Methods*, L. Bengtsson, M. Ghil, and E. Kallen, Eds., Springer-Verlag, 5–16.
- , and O. Talagrand, 1974: Dynamic approach to meteorological data assimilation. *Tellus*, **26**, 334–344.
- Panofsky, H., 1949: Objective weather map analysis. *J. Meteor.*, **6**, 386–392.
- Petersen, D. P., 1968: On the concept and implementation of sequential analysis for linear random fields. *Tellus*, **20**, 673–686.
- Phillips, N. A., 1976: The impact of synoptic observing and analysis systems on flow pattern forecasts. *Bull. Amer. Meteor. Soc.*, **57**, 1225–1250.
- Puri, K., and W. Bourke, 1982: A scheme to retain the Hadley circulation during nonlinear normal mode initialization. *Mon. Wea. Rev.*, **110**, 327–335.
- Ramamurthy, M. K., and F. H. Carr, 1987: Four-dimensional data assimilation in the monsoon region. Part I: Experiments with wind data. *Mon. Wea. Rev.*, **115**, 1678–1706.
- Robinson, A. R., 1986: Data assimilation, mesoscale dynamics and dynamical forecasting. *Advanced Physical Oceanographic Numerical Modelling*, J. J. O'Brien, Ed., D. Reidel Pub. Co., 465–483.
- Rutherford, I. D., 1972: Data assimilation by statistical interpolation of forecast error fields. *J. Atmos. Sci.*, **29**, 809–815.
- , 1976: An operational three-dimensional multivariate objective analysis scheme. *Proc. GARP Conf. on Four Dimensional Data Assimilation*, Paris, GARP WGNE Rep. No. 11, 98–121.
- Sasaki, Y., 1958: An objective analysis based on the variational method. *J. Meteor. Soc. Jpn.*, **36**, 77–88.
- , 1969: Proposed inclusion of time variation terms, observational in numerical variational objective analysis. *J. Meteor. Soc. Jpn.*, **47**, 115–124.
- Satomura, I., 1988: Dynamic normal mode initialization of a limited-area model. *J. Meteor. Soc. Jpn.*, **66**, 261–276.
- Smagorinsky, J., K. Miyakoda, and R. Strickler, 1970: The relative importance of variables in initial conditions for dynamical weather prediction. *Tellus*, **22**, 141–157.
- Stauffer, D. R., and N. L. Seaman, 1987: A real-data numerical study and four-dimensional data assimilation application for mesobeta-scale flow in complex terrain. *Proc. Symp. Mesoscale Analysis and Forecasting*, Vancouver, ESA, 533–538.
- , and —, 1990: Use of four-dimensional data assimilation in a limited-area mesoscale model. Part I: Experiments with synoptic-scale data. *Mon. Wea. Rev.*, **118**, 1250–1277.
- , T. T. Warner, and N. L. Seaman, 1985: A Newtonian "nudging" approach in four-dimensional data assimilation: Use of SESAME-IV data in a mesoscale model. Preprints, *Seventh Conf. on Numerical Weather Prediction*, Montreal, Amer. Meteor. Soc., 77–82.
- Stephens, J., 1970: Variational initialization of the balance equation. *J. Appl. Meteor.*, **9**, 732–739.
- Sugi, M., 1986: Dynamic normal mode initialization. *J. Meteor. Soc. Jpn.*, **64**, 623–632.
- Temperton, C., 1988: Implicit normal mode initialization. *Mon. Wea. Rev.*, **116**, 1013–1031.
- , and D. L. Williamson, 1981: Normal mode initialization for a multilevel grid-point model, Part I: Linear aspects. *Mon. Wea. Rev.*, **109**, 729–743.
- Wang, W., and T. T. Warner, 1988: Use of four-dimensional data assimilation by Newtonian relaxation and latent heat forcing to improve a mesoscale-model precipitation forecast, a case study. *Mon. Wea. Rev.*, **116**, 2593–2613.
- Warner, T. T., 1987: Four-dimensional initialization of mesoscale models. In *Proc. Symp. Mesoscale Analysis and Forecasting*, Vancouver, Canada, ESA SP-282, 663–665.
- Wergen, W., 1982: Incorporation of diabatic effects in non-linear normal mode initialization. *The GARP Programme on Numerical Experimentation*, Rep. No. 3, GARP/WCRP, WMO/ICSU, Geneva, 2.8–2.10.

Appendix G

SSM/I Observations of ERICA IOP 4 Marine Cyclone: A Comparison with In Situ Observations and Model Simulation

SSM/I Observations of ERICA IOP 4 Marine Cyclone: A Comparison with In Situ Observations and Model Simulation

SIMON W. CHANG

Naval Research Laboratory, Washington, D.C.

RANDALL J. ALLISS AND SETHU RAMAN

Department of Marine, Earth and Atmospheric Sciences, North Carolina State University, Raleigh, North Carolina

JAINN-JONG SHI

Science Applications International Corporation, McLean, Virginia

(Manuscript received 6 October 1992, in final form 3 March 1993)

ABSTRACT

Fields of rainfall rates, integrated water vapor (IWV), and marine surface wind speeds retrieved by the Special Sensor Microwave/Imager (SSM/I) during the intensive observational period 4 on 4 January 1989 of the Experiment on Rapidly Intensifying Cyclones over the Atlantic (ERICA) were analyzed. Subjectively analyzed and model-simulated frontal structures were used to examine the spatial relationship of the SSM/I observed fields to the rapidly intensifying storm and the associated fronts. Qualitative and quantitative comparisons of SSM/I retrievals with GOES imagery, conventional observations, and results produced from the Naval Research Laboratory's (NRL) limited-area numerical model were also made.

SSM/I rainfall was found along the cold and warm fronts, with heavy precipitation within frontal bands. The spatial pattern and characteristics of SSM/I precipitation closely resembled those simulated by the model. Both the warm and the cold front were found to be located near the area of the strongest gradient in IWV. In the warm sector, areas of IWV greater than 40 mm were found, an amount supported by model simulations. Both SSM/I rain rate and IWV distribution were found to be useful in locating the cold and warm fronts. There was good agreement on the relationship of frontal locations to the precipitation patterns and IWV gradients. Most of the high-wind area near the storm center was obscured by clouds for marine surface wind retrieval. SSM/I-retrieved marine surface winds outside the cloud shield (flag 0) were compared to ship- and buoy-reported winds. It was found that the retrieved wind estimates were within $0\text{--}3\text{ m s}^{-1}$ of in situ observation over areas of slow wind shifts. The errors became larger in regions of rapid wind shifts.

1. Introduction

Since first deployed in earth orbit in the 1960s, meteorological satellites have been beneficial in tracking the course and development of maritime extratropical cyclones. Visible and infrared satellite imageries have aided forecasters in the analysis of these storms over the data-sparse oceans.

Over the past 15 years, sensors responsive to the upwelling microwave radiation have been launched aboard polar orbiting satellites. Microwave remote sensing has provided significant improvements in quantitative measurements of atmospheric variables such as integrated water vapor, rainfall rates, and marine surface wind speeds. Because the ocean has a relatively low and uniform emissivity compared with land

in the microwave region, the ocean becomes an excellent background for measuring these parameters that are associated with extratropical cyclones. Meteorological parameters have been successfully obtained from the Scanning Multichannel Microwave Radiometer (SMMR) aboard the Seasat and *Nimbus-7* satellites, and the Electrically Scanning Microwave Radiometer (ESMR) aboard the *Nimbus-6* and *-7* satellites, and have been useful in the research of tropical and extratropical cyclones (Rodgers and Adler 1981; McMurdie and Katsaros 1985; Katsaros and Lewis 1986; McMurdie et al. 1987).

More recently, microwave remote sensing of tropical and extratropical systems has been improved via data collected from the Special Sensor Microwave/Imager (SSM/I) that flies aboard the Defense Meteorological Satellite Program (DMSP) satellites. Compared to the SMMR and ESMR sensors, the polar orbiting SSM/I operates continuously, providing much better sampling of marine cyclones. The SSM/I swath width is ap-

Corresponding author address: Dr. Simon W. Chang, Naval Research Laboratory, Code 7220, Washington, DC 20375-5000.

proximately 1400 km, which is nearly double that of SMMR. Relatively high-resolution (~ 25 km) products are routinely being provided by SSM/I. Good resolution is required when studying the intense mesoscale precipitation patterns that are observed in marine cyclones.

This paper presents an analysis of SSM/I-observed fields of an explosive midlatitude cyclone that developed on 4 January 1989 during the intensive observational period (IOP) 4 of the Experiment on Rapidly Intensifying Cyclones over the Atlantic (ERICA). SSM/I-derived rainfall rates, integrated water vapor (IWV), and marine surface wind speeds are all used to study the storm structure. Comparisons of SSM/I-retrieved marine surface winds with in situ ship and buoy reports will also be presented. Quantitative comparison of SSM/I-retrieved rain rates and IWV with independent observations is difficult; therefore, they will be compared with realistically simulated results produced by a limited-area model initialized with the National Meteorological Center Regional Analysis and Forecast System (NMCRAFS) analysis. Comparison of SSM/I-retrieved and model-generated fields has been conducted before, mainly for verification of numerical prediction models (e.g., Raustein et al. 1991; Pudykiewicz et al. 1992). In this study, ERICA IOP 4 frontal positions based on SSM/I retrieval and model results will be compared with subjectively analyzed positions of Neiman and Shapiro (1993). The motivation of this work is 1) to analyze ERICA IOP 4 marine cyclones based on SSM/I observations, 2) to provide a mutual validation of the SSM/I-observed quantities and independently obtained, realistic numerical

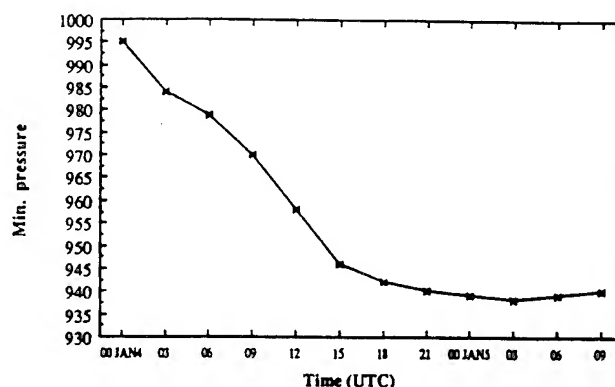


FIG. 2. Central pressure (mb) evolution from 0000 UTC 4 January to 0000 UTC 5 January. A deepening rate of $24 \text{ mb } (6 \text{ h})^{-1}$ was estimated to have occurred between 0900 and 1500 UTC.

model simulations, and 3) to prepare for the eventual use of SSM/I data in initializing numerical models in order to improve the forecast of intense cyclones over data-sparse oceans.

2. Synoptic overview of ERICA IOP-4

ERICA field summary, NMC surface analysis, and surface analyses by Sanders (1993, personal communication), Neiman and Shapiro (1993), and Neiman et al. (1993), as well as airborne radar observations of Wakimoto et al. (1992), indicated that a cyclone developed rapidly and tracked east and northeast over the western North Atlantic Ocean during ERICA IOP 4. Figure 1 shows the storm track from the ERICA field summary. The initial stages of development were characterized by an incipient marine cyclone off Cape Hatteras, North Carolina. A coastal trough and front extended southwestward from the cyclone center, separating warm, moist air over the Gulf Stream from cooler and drier continental air situated over the coastal plain.

The low developed in response to a vigorous upper-level short wave that crossed the United States east coast at approximately 0000 UTC 4 January. Cyclogenesis commenced beneath diffluent frontolytic 500-mb flow and strong 700-mb ascent with vertical velocities greater than 6 cm s^{-1} after the approaching upper-level jet streak became vertically in phase with the surface cyclone (Neiman et al. 1993). Over the next 24 h the cyclone deepened from 996 mb at 0000 UTC 4 January to 938 mb at 0000 UTC 5 January (Fig. 2, ERICA field summary). The end of the rapid deepening phase occurred around 1800 UTC 4 January when a central pressure of 942 mb was analyzed. The storm produced a line of intense thunderstorms in advance of the cold front. A strong northwesterly flow of cold air to the rear of the storm produced the dramatic cloud street pattern seen in the imagery. The tight cloud band that nearly encompassed a small "eye" feature marked the location of lowest pressure at this time.

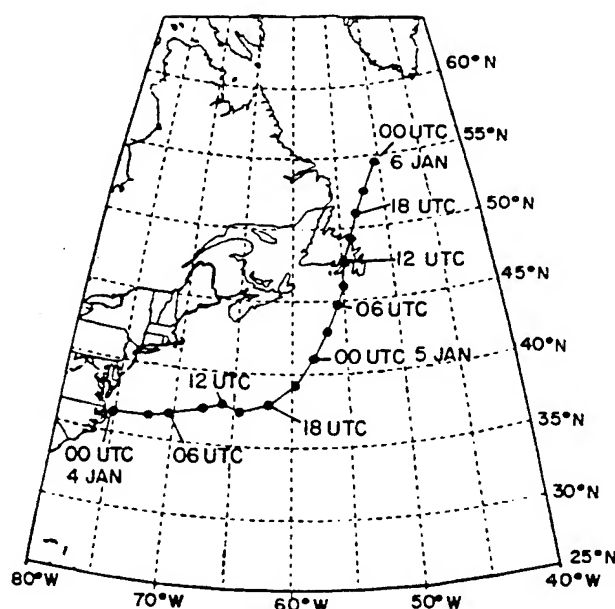


FIG. 1. The 3-h storm track of ERICA IOP 4 cyclone. Times are labeled every 6 h from 0000 UTC 4 January to 0000 UTC 6 January 1989.

This eyelike feature may have been the result of strong mesoscale convection near the center of the storm during the period of rapid intensification. For additional detailed synoptic analyses, GOES imagery, and airborne radar observations of the ERICA IOP 4 cyclone, readers are referred to Wakimoto et al. (1992), Neiman and Shapiro (1993), Neiman et al. (1993), Sanders (1989), and Sanders (1993, personal communication).

SSM/I-retrieved fields and model-simulated fields will be analyzed in relationship to the unique frontal structure of the ERICA IOP 4 storm in this study. The frontal positions at 0000, 0600, 1200, and 1800 UTC on 4 January and 0000 UTC on 5 January are plotted in Fig. 3. During the period of interest between 0000 UTC 4 January and 0000 UTC 5 January, DMSP F-8 with SSM/I flew over the ERICA IOP 4 storm at 0000, 0930, and 2200 UTC 4 January. To facilitate the comparison with synoptic analysis, the frontal positions of Neiman et al. (1993) were linearly interpolated in time to produce the front structure at 0930 and 2200 UTC (Fig. 4). We should note that these frontal positions are based on eyeball interpolation of Neiman et al. and are not supported by any observations.

3. SSM/I: Sensor and algorithm

The microwave sensor SSM/I, from which observations were made for this study, was launched in June 1987. This radiometer has seven channels at 19.35, 22.235, 37.0, and 85.5 GHz, all with both vertical and horizontal polarizations except for the 22.235-GHz channel, which has only vertical polarization. The SSM/I measures upwelling microwave radiation at spatial intervals from 12.5 km at 85.5 GHz to 25 km at the three lower frequencies. The sensor footprints

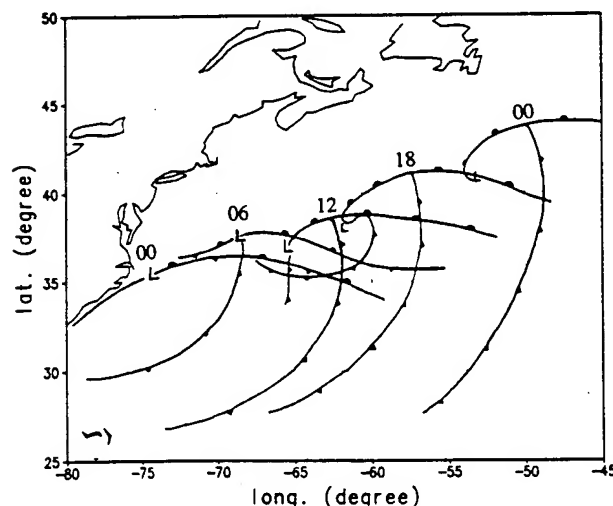


FIG. 3. (a) Surface frontal positions at 0000, 0600, 1200, and 1800 UTC 4 January and 0000 UTC 5 January 1989, based on Neiman et al. (1993). The times are written over the triple point, where the cold front intersects the warm front.

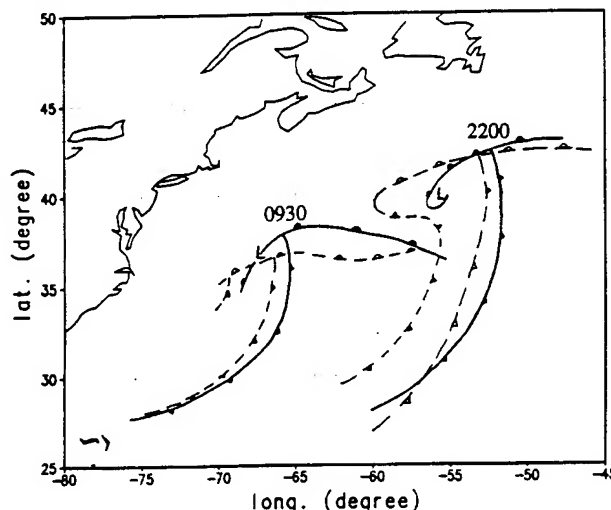


FIG. 4. Frontal positions at 0930 and 2200 UTC 4 January by a linear interpolation in time of Neiman et al. (solid lines). Numerical model-simulated frontal positions valid at 0930 and 2200 UTC are plotted in dashed lines.

range in diameter from 55 km at 19 GHz to 15 km at 85.5 GHz. More detailed SSM/I sensor description can be found in Hollinger (1989, 1991).

Several SSM/I rain-rate algorithms have been developed (Adler et al. 1991; Kummerow et al. 1989). The rain-rate algorithm used in this study was described by Olson (1989) and Hollinger (1991). Since the 85-GHz (V) channel was deemed unstable during ERICA, an alternative algorithm was applied using the 85-GHz (H) channel, as well as the 22-GHz (V), 37-GHz (V), and (H) channels and the 19-GHz (V) and (H) channels. Pixels within ± 100 km of the coast were not processed, because of possible ambiguity, although additional algorithms for the land-sea interface are now being developed (Adler 1992, personal communication). The recommended alternate algorithm (Hollinger 1991) is used:

$$R = \exp(-0.42383 - 0.0082985T_{85h} + 0.01496T_{19v} + 0.00583T_{19h}) - 4.0 \text{ mm h}^{-1}, \quad (1)$$

over the ocean, and

$$R = \exp(1.32526 - 0.08150T_{37v} + 0.01638T_{37h} + 0.03561T_{22v} + 0.05079T_{19v} - 0.01875T_{19h}) - 8.0 \text{ mm h}^{-1}, \quad (2)$$

over land, where R is the rainfall rate and T_{37v} , T_{37h} , T_{19v} , T_{19h} , T_{22v} , and T_{85h} are the brightness temperatures (BT) of the 37-GHz (V), 37-GHz (H), 19-GHz (V), 19-GHz (H), 22-GHz (V), and 85-GHz (H) channels, respectively.

The SSM/I wind speed algorithm was designed to retrieve wind speeds over the oceans and to be valid

at 19.5 m above the ocean surface. The magnitude of microwave energy being emitted from the ocean surface is a function of the wave structure and foam coverage, which in turn are influenced by the wind speed. Therefore, by measuring the ocean surface microwave emission, the SSM/I is able to infer marine surface wind speeds. The 19-GHz (V) and 37-GHz (H) polarized channels are most sensitive to the ocean roughness and foam (Goodberlet et al. 1989). Two other channels, the 22 GHz (V) and 37 GHz (V), are also used to subtract from atmospheric effects in estimating a surface wind speed. The 22-GHz (V) channel is used to address atmospheric water vapor effects, while the difference between the 37-GHz (V) and 37-GHz (H) channels ($37V - 37H$) are used to detect cloud and liquid water scattering (Goodberlet et al. 1989). The recommended algorithm for wind speed in meters per second (WS) (Hollinger 1991) is

$$WS = 147.90 + 1.0969T_{19v} - 0.4555T_{22v} - 1.7600T_{37v} + 0.7860T_{37h}, \quad (3)$$

where T_{22v} are the BTs of the 22-GHz (V) polarized channel and the other variables are as before.

Upwelling microwave energy at the SSM/I frequencies emitting from the ocean surface is masked by rain and hail in the atmosphere. Additionally, the effective resolution of the algorithm is limited by the resolving power of the SSM/I antenna at 19, 22, and 37 GHz. Furthermore, the naturally presented high spatial variabilities in wind speed are smoothed, resulting effectively in a reduction of resolution. Therefore, wind speed retrieval is quite sensitive to atmospheric conditions, and "rain flags" have been established to estimate the degree of uncertainty of each calculated wind speed due to the presence of intervening water vapor, cloud water, rain, or hail (Goodberlet et al. 1989). For the least contaminated wind retrieval, flag 0, the expected error is 1 m s^{-1} . The errors for flags 1 and 2 are, respectively, $2\text{--}5 \text{ m s}^{-1}$ and greater than 5 m s^{-1} (Hollinger 1991; Alliss et al. 1993). These latter errors are too large for meaningful analysis of the IOP 4 storm; therefore, to be conservative, the comparison in our study will be carried out only for flag 0 retrievals.

The SSM/I is also capable of measuring the amount of water vapor present between the ocean's surface and the top of the atmosphere. The IWV content of the atmosphere is important because it can provide valuable information on the location of surface fronts. Similar to the rain rate, many SSM/I water vapor algorithms have been developed (e.g., Alishouse et al. 1990). The algorithm used in this study is described in more detail in Hollinger (1991); however, it uses a nonlinear combination of the BTs from the 19-, 22-, and 37-GHz channels. The algorithm was validated by large quantities of radiosonde measurements of water vapor, and can provide IWV values from 0 to 80 kg m^{-2} (or 8-cm equivalent depth of water).

SSM/I observations of the ERICA IOP 4 cyclone were available at 0000, 0930, and 2200 UTC 4 January during the period between 0000 UTC 4 January and 0000 UTC 5 January. Brightness temperatures were sampled at a resolution of 25 km in longitude and latitude for the precipitation and approximately 50 km for both the IWV and marine wind speeds. All retrieved fields are then bilinearly interpolated to a grid with 0.25° resolution in latitude and longitude, covering the same domain as the Naval Research Laboratory (NRL) numerical model. Missing pixels within the swath were given values equal to the average value of surrounding pixels. A five-point running average was performed on most of the SSM/I fields, which will be discussed, unless specified otherwise. Because the cyclogenesis of the IOP 4 storm occurred almost entirely over the ocean, and the greater uncertainties of retrieval over land, only observations over the ocean in SSM/I swaths are discussed.

4. Numerical model

The model used for this study is the NRL limited-area numerical weather prediction system. The system contains an objective analysis scheme, initialization, the numerical model, and the output-diagnostics package. The numerical model is a three-dimensional, hydrostatic, primitive equation system that includes planetary boundary layer (PBL), cumulus, and radiation parameterizations. The formulation of the model is described in Madala et al. (1987), Chang et al. (1989), and Holt et al. (1990).

The version of the model that generated the result for the comparison in this study is identical to the one in Chang and Holt (1993) and Chang et al. (1993). The model contains 136×141 horizontal grid points with a horizontal resolution of 0.33° in longitude and 0.25° in latitude. The horizontal resolution is designed to have nearly the same effective resolution of the SSM/I measurements. The model domain covers the east coast of the United States and the western North Atlantic from 20° to 55°N and 85° to 40°W . This version of the model has 16 sigma layers in the vertical.

The PBL parameterization is based on the budget equations of the turbulent kinetic energy (TKE) and dissipation rate. A soil slab model is used to forecast the land surface temperature. The ERICA data center's 50-km resolution sea surface temperature dataset is used to describe the sea surface temperature. The 50-km dataset is used because it shows a strong gradient between the Gulf Stream and the continental shelf/slope water. A modified Kuo cumulus parameterization is used. The model uses the NMC RAFS 2.5° analysis at 0000 UTC 4 January as the initial conditions for the integrations. The RAFS analysis is not enhanced by the SSM/I observations. Therefore, the simulated storm behavior and structures can be considered independent of the SSM/I-observed fields.

The simulated fronts at SSM/I overpasses of 0930 and 2200 UTC, subjectively determined based on simulated mass and momentum fields, are depicted in Fig. 4. As shown in Chang and Holt (1993), the model-simulated minimum sea level pressure (SLP) of the ERICA IOP 4 storm starts from 998 mb at 0000 UTC 4 January and deepens to 952 mb in 24 h, an underprediction of the intensification by 15 mb. However, it is not the purpose of this study to reproduce the remarkable intensification of the IOP 4 cyclone. Model-simulated results are used in this study to mainly fill in the gap in time and space between the SSM/I overpasses at 0930 and 2200 UTC 4 January. The model produces high resolution (compared to available conventional observations) and dynamically consistent mass and momentum fields that give a more complete view of the cyclone and associated fronts than may be possible using the relative narrow SSM/I swath of 1400 km. Also, model-simulated IWV and precipitation rates provide reasonable comparisons with SSM/I retrievals that are not available from conventional observations. As will be discussed, the model-simulated storm track is approximately 1° – 2° latitude south of the analyzed track. Therefore, when model results are compared with observations and SSM/I retrievals, it is constructive to discuss the simulated fields relative to the simulated cyclone and frontal positions.

5. 0000 UTC 4 January

a. Rain rate

At 0000 UTC 4 January, a weak surface disturbance started to organize off the East Coast as two upper-level short-wave troughs were merging. The cold front structure and convective activities were not yet prominent, as indicated by the *GOES-7* IR image (Fig. 5). The SSM/I pass at 0000 UTC showed an area of light precipitation from the coastal waters off southern Vir-

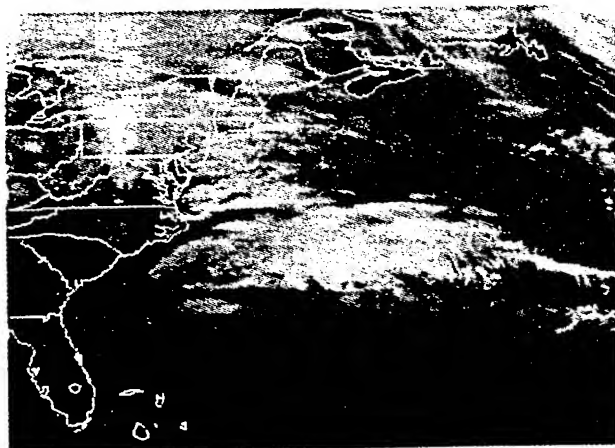


FIG. 5. *GOES-7* enhanced IR image at 0000 UTC 4 January.

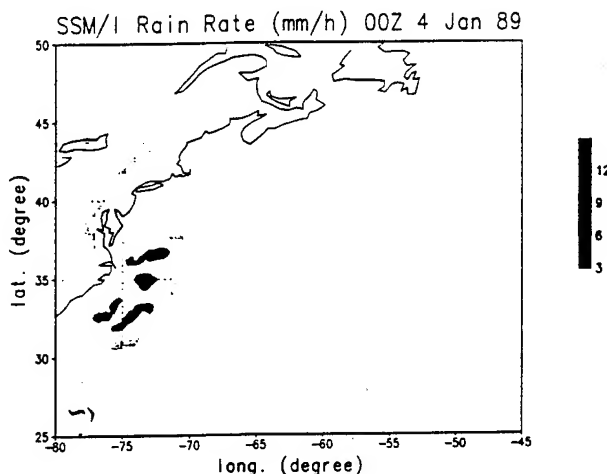


FIG. 6. SSM/I rainfall rates (mm h^{-1}) at 0000 UTC 4 January. The intensity of precipitation for all rain-rate figures is indicated by the gray scales on the right.

ginia and south along the North and South Carolina coastlines (Fig. 6). The areas of heavier precipitation were oriented northeast–southwest along the Gulf Stream, with maximum rainfall rates of 9 mm h^{-1} . Although there was little organization of the precipitation pattern with respect to the developing cyclone at 0000 UTC as the storm was in its initial stage, the SSM/I-observed heavier precipitation bands are parallel to the front analyzed by Neiman et al. (1992), as was the *GOES* imagery (Fig. 5). The orientation of the bands also appears to be parallel to the coast and to the sea surface temperature, suggesting that the air–sea–land interaction may have affected the organization of the convections at the early stage of the cyclogenesis. The gap in the convective activity along the front was evident in both the IR and SSM/I images.

b. IWV

Figure 7 shows the SSM/I IWV pattern at 0000 UTC 4 January, with the surface stationary front as analyzed by Neiman and Shapiro (1993) superimposed. The strongest IWV gradient was found in the cold-air sector of the storm. The sharpest gradient of SSM/I IWV occurred along the Carolina coast, probably due to the sea–land contrast and the Gulf Stream. Some considerable gradient also existed to the north of the analyzed front east of the Virginia shoreline, also likely to be modulated by the sea surface temperature (SST) distribution there. In a study of North Pacific winter cyclones using microwave data from the *Nimbus-7* satellite, Katsaros and Lewis (1986) found that a strong gradient in integrated atmospheric water vapor was a good indicator for locations of surface fronts. These results were further supported by similar studies described in Katsaros et al. (1989) and McMurdie and Katsaros (1985). Here, the surface cold and warm

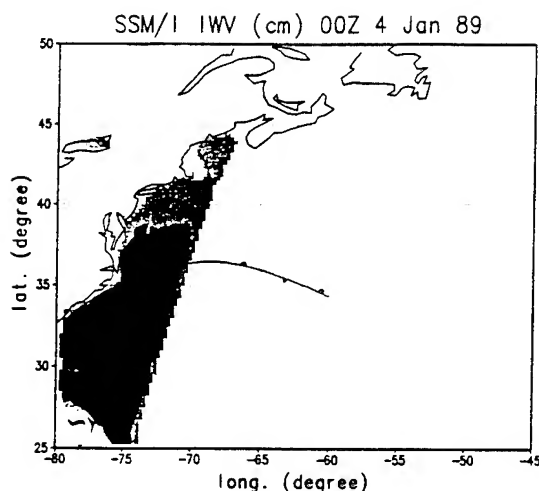


FIG. 7. SSM/I-retrieved integrated water vapor (cm) equivalent water depth at 0000 UTC 4 January with analyzed front. Front analyzed by Neiman et al. is superimposed.

fronts were located just west and north, respectively, of the maximum IWV. Values greater than 32 mm were common in the warm sector, with maximums greater than or equal to 40 mm occurring near the Gulf Stream. In contrast to the Neiman and Shapiro analysis (Fig. 7), the NMC surface analysis (not shown) placed the cold front west of the low center in a concave curvature, more in agreement with the IWV gradients.

c. Surface wind speed

Figure 8 shows the SSM/I-retrieved marine surface wind speeds at 0000 UTC 4 January, plotted as isotachs at a 3 m s^{-1} interval. Only wind retrievals with flag = 0 were plotted. Unfortunately, areas of high wind near the center of the low pressure center were under cloud cover (Figs. 5 and 6), rendering wind speed retrievals highly unreliable near the low center. Several ship- and buoy-reported wind bars taken from Sanders surface analysis were also plotted for comparison. The three reports north of 37°N seemed to agree well with the SSM/I retrievals. The report just offshore of 2.5 m s^{-1} wind was located in a region where SSM/I retrievals showed $0\text{--}3 \text{ m s}^{-1}$. The two other reports of 5 m s^{-1} were in an area where SSM/I retrieved $3\text{--}6 \text{ m s}^{-1}$.

In the small region just offshore of North Carolina, the SSM/I-retrieved wind speeds of more than 12 m s^{-1} were supported by the 17.5 m s^{-1} wind reported by a nearby ship *WRGL*, although it could not be ascertained whether the ship was within the area of higher retrieval uncertainties (i.e., flag greater than zero). The two reports of 10 and 12.5 m s^{-1} south of 30°N seemed to be $1\text{--}2 \text{ m s}^{-1}$ higher than the SSM/I retrievals. These errors are within the expected range of the SSM/I calibration and validation (Hollinger 1991).

6. 0930 UTC 4 January

a. Rain rate

At 0930 UTC 4 January, the IOP 4 cyclone was well developed, with a minimum SLP of 970 mb (Sanders analysis). The *GOES-7* enhanced IR image (Fig. 9) showed a well-developed comma-shaped cloud pattern with very cold cloud tops near 40°N , 65°W , just northeast of the analyzed triple point (the intersection of the warm and cold front). High clouds were also evident along the tail of the comma-shaped cloud pattern. These high cloud tops were located mostly east of 65°W , well to the east of the analyzed cold front. The frontal system (Fig. 4) showed an occluded warm front (Neiman et al. 1993) with a "T-bone" shape structure (Shapiro and Keyser 1990). Figure 10a shows the SSM/I-retrieved precipitation-rate pattern at 0930 UTC with the interpolated frontal position [Neiman and Shapiro (1993) analysis]. This overpass captured only a portion of the storm's precipitation field and missed the low center. Significant retrieved rainfall occurred in association with both the interpolated cold and warm fronts and primarily in the warm sector, with the heaviest precipitation (rates greater than 12 mm h^{-1}) located just to the east of the triple point. The SSM/I precipitation was mostly prefrontal near the interpolated cold front. Along the warm front, the heavy precipitation shifted from prefrontal near the triple point to postfrontal toward the east. This shifting was also recognizable from Fig. 2 of Wakimoto et al. (1992); it showed the *GOES* infrared imagery and frontal positions at 0600 UTC.

Figure 10b shows the NRL model-simulated sea level pressure (SLP) and precipitation-rate fields at 9.5 h, valid for 0930 UTC 4 January. Superimposed on Fig. 10b was the model-produced fronts based on simulated

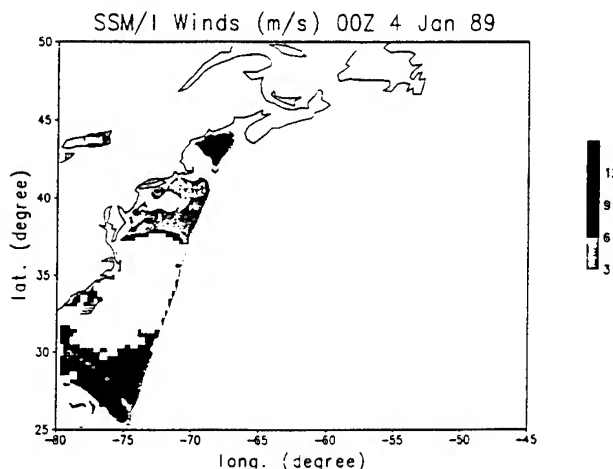


FIG. 8. SSM/I-retrieved marine surface wind speeds with flag 0. Ship and buoy reports are superimposed with half-bars of 2.5 m s^{-1} , bars of 5 m s^{-1} , and flags of 25 m s^{-1} .

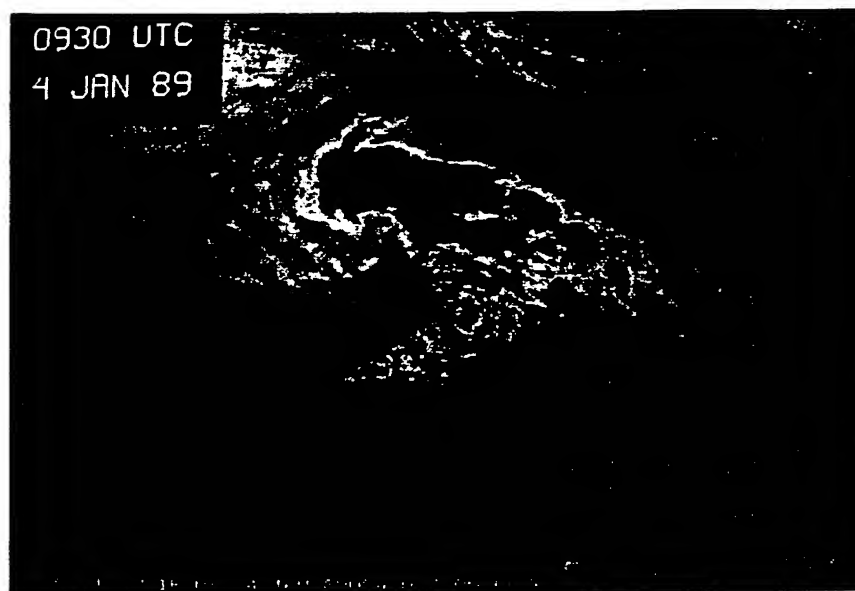


FIG. 9. GOES-7 enhanced IR image at 0900 UTC 4 January.

mass and momentum fields. [More detailed discussion of the model cyclone and frontal structure will be reported in Chang et al. (1993).] Model-simulated precipitation over the cyclone scale had already developed a comma-shaped pattern, but there was very little precipitation at the low pressure center. Model-produced heaviest precipitations concentrated mostly along the warm front. A maximum rainfall rate of 17 mm h^{-1} was predicted just to the north of the low center, where there was a hook-shaped convective pattern, as observed at 0600 UTC (Figs. 1 and 2 in Wakimoto et al.). To the east of the triple point, the precipitation shifted to the south of the warm front, similar to the

relative position of the SSM/I precipitation and the analyzed (interpolated) fronts of Neiman and Shapiro. Unfortunately, because the SSM/I swath at 0930 UTC just missed the low center, a comparison of the precipitation patterns near the center could not be made. The model-produced warm front, lying to the west of the triple point, started to bend back toward the south at this time due to the strong cross-frontal shear. This was coincident with the westward development of the low pressure center along the occluded warm front. Along the cold front there was a band of light precipitation. Around the western tip of the low center, a secondary push of cold air was evident in the rainfall-

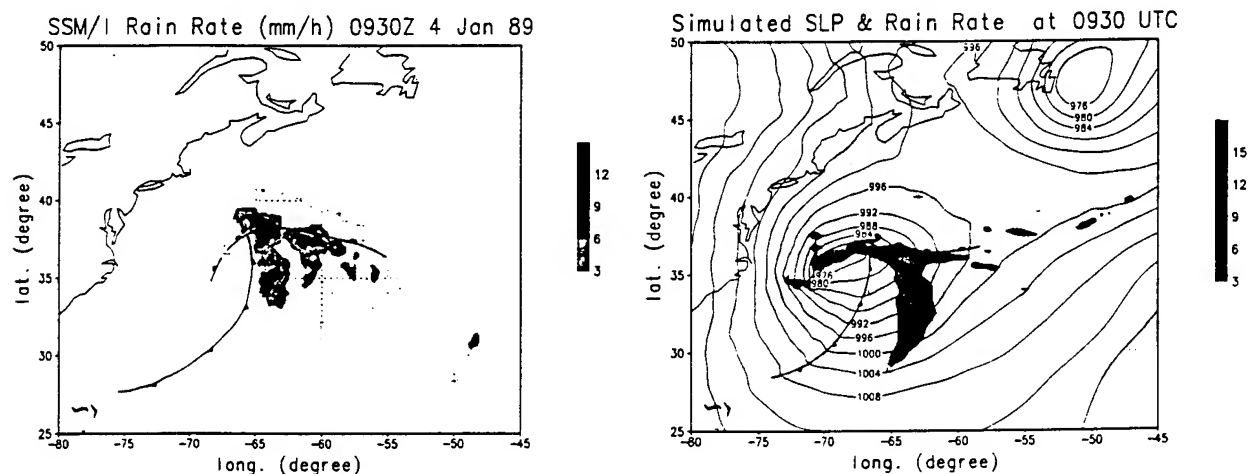


FIG. 10. (a) SSM/I rainfall rates at 0930 UTC, with the interpolated analyzed frontal position superimposed. (b) Model-simulated SLP (mb, isobars in solid lines, 4-mb intervals) and rainfall rate (mm h^{-1} , in shades) at 9.5 h, valid for 0930 UTC 4 January, with simulated frontal position superimposed.

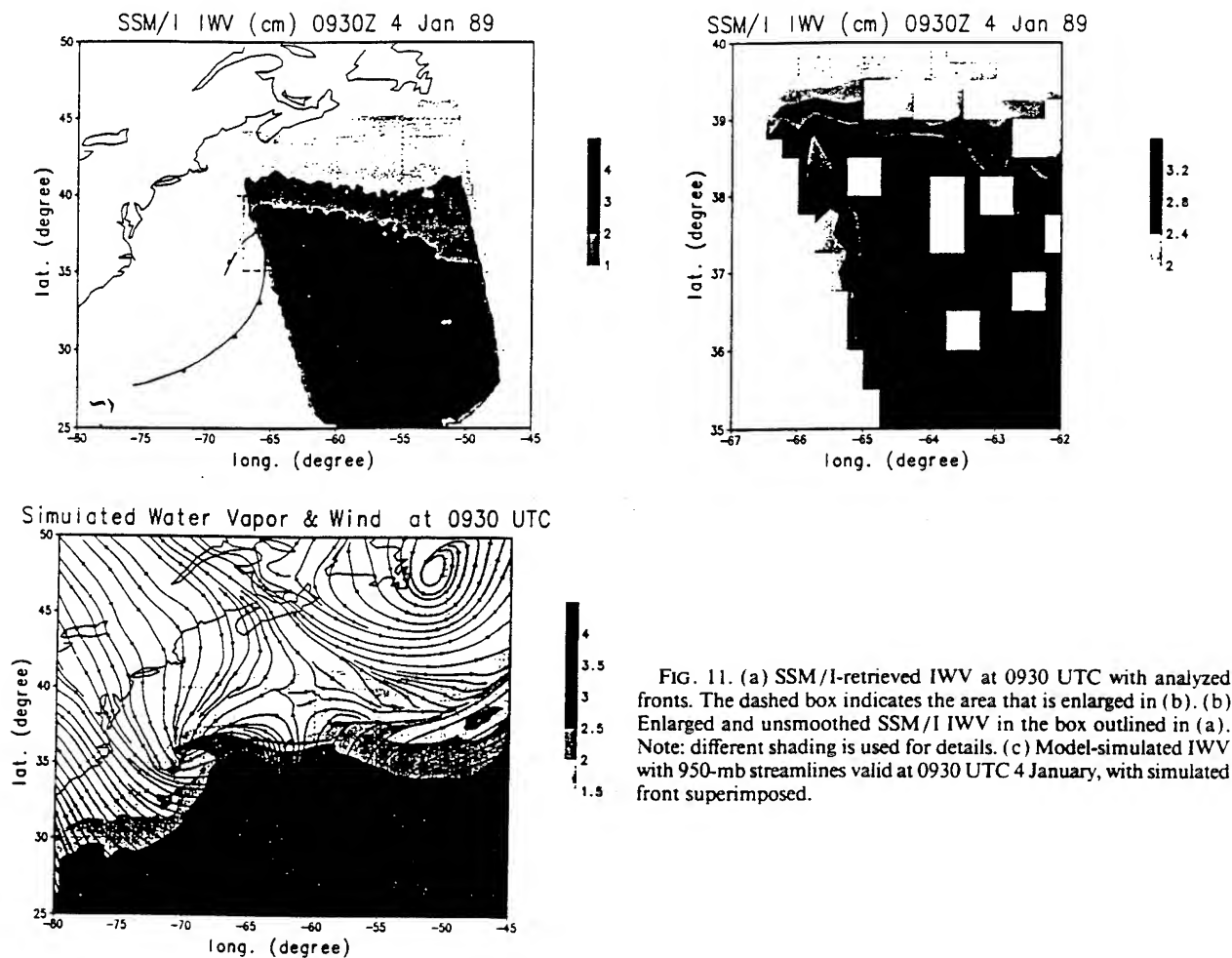


FIG. 11. (a) SSM/I-retrieved IWPV at 0930 UTC with analyzed fronts. The dashed box indicates the area that is enlarged in (b). (b) Enlarged and unsmoothed SSM/I IWPV in the box outlined in (a). Note: different shading is used for details. (c) Model-simulated IWPV with 950-mb streamlines valid at 0930 UTC 4 January, with simulated front superimposed.

rate pattern and in the IWPV, which is discussed in the following. The north-south-oriented precipitation along 63°W was displaced several hundred kilometers east of the cold front. The IR imagery at 0600 (see Wakimoto et al. 1992) and 0930 UTC in Fig. 9 also suggested a strong convection band well east of the cold front. In all, the SSM/I-retrieved precipitation pattern seemed to agree with the model-produced pattern within the SSM/I swath. However, the model produced heavier (lighter) precipitation along the warm (cold) front compared to the retrieval.

b. IWPV

Figure 11a shows the SSM/I-retrieved IWPV pattern at 0930 UTC along with the interpolated Neiman et al. frontal analysis. The pattern showed high IWPV values (>3 cm) in the warm sector, with a band of extremely high moisture (IWPV >4 cm) located just to the east of the cold front. Strong IWPV gradients existed to the north of the warm front. The interpolated warm front nearly coincided with the 3-cm contour, giving credence to the assertion of Katsaros and Lewis (1986)

that the strong IWPV gradient was a good indicator of the surface front. To the southeast and away from the IOP 4 cyclone, there was another high IWPV between 30°N , 50°W and 25°N , 55°W .

Because the low center was located just outside of the SSM/I swath, and the triple point just inside, the box encircled by the dashed lines in Fig. 11a between 35° – 40°N and 67° – 62°W deserved an enlargement for a detailed view. The enlarged SSM/I-retrieved IWPV field shown in Fig. 11b was not smoothed, and missing pixels (white squares in the swath) were not filled in. In Fig. 11b, the warm front was clearly located along the 3-cm IWPV contour between 38° and 39°N . There was no discernible discontinuity of IWPV on the north side of the warm front at the triple point, characteristic of a warm front occlusion. The cold front was also along the 3-cm contour just west of 65°W . West of the advancing cold front there was a notch of dry air along the western edge of the swath where the IWPV decreased to 2 cm, most noticeable at 37.5°N , 65.5°W . This was an indication of the wraparound of cold and dry air, transported by the southwesterly flow behind the cold front. The intrusion of the cold and dry air to the south

and east of the low center was also evident from the model-simulated IWV field (Fig. 11c). The westward extension of the high IWV north of the low center and the eastward extension of the low IWV south of the low center depicted the circulation around the occluded warm front. Strong IWV gradients were located to the north of the warm front and to the west of the cold front. Compared to the SSM/I IWV, the model-produced IWV was approximately 0.5 cm lower. Along the warm front, the 2.5-cm contour was north of the warm front west of the triple point but gradually shifted to south of the warm front farther east, consistent with the simulated precipitation pattern (Fig. 10b). The warm sector had high IWV values with two very high IWV bands extended from the tropics at 70° and 60°W, outlining the conveyor belts of moisture supply from low latitudes into the marine cyclone. In general, SSM/I-retrieved and model-produced IWV fields agreed very well relative to their respective (analyzed and simulated) frontal positions.

c. Surface wind speed

The SSM/I-retrieved surface winds at 0930 UTC are depicted in Fig. 12. Again, the high wind area near the low center and frontal regions were excluded due to high uncertainties (flag numbers greater than zero). For comparison, selected ship reports at 0600 (denoted by black dots) and 1200 (denoted by open circles) UTC outside the cloud shields were plotted. There was a rapid wind shift north of 40°N due to the departure of a previous cyclone and the approaching of the IOP 4 storm (Fig. 10b). In this region, SSM/I-retrieved wind speeds seemed to be consistently 1–4 m s⁻¹ lower than the ship reports. Counting clockwise from the report near 40°N, 50°W, the ship-reported and -retrieved wind speeds were 15 versus 12–15 m s⁻¹, 12.5 versus

9–12 m s⁻¹, 10 versus 6–9 m s⁻¹, 5 versus 6–9 m s⁻¹, 10 versus 6–9 m s⁻¹, 5 versus 3–6 m s⁻¹, and, finally, 10 versus 3–6 m s⁻¹. To the south of the cloud shield in the warm sector where the southwesterly winds were steady the agreement between the SSM/I retrieval and ship reports was very good. This suggests that the steadiness of marine boundary layer winds and ocean surface wave characteristics must be taken into consideration in designing a surface wind algorithm in the future to achieve higher accuracy.

7. 2200 UTC 4 January

a. Rain rate

At 2200 UTC, the IOP 4 cyclone had experienced the most rapid intensifying stage, reaching a central SLP of about 940 mb, close to the lowest SLP of the system. The cyclone was almost in the middle of the Atlantic Ocean, and the comma-shaped cloud seemed to occupy much of the basin. The GOES enhanced IR (Fig. 13) showed a convectively active band extended from the north of the low center, arcing around the east and south perimeter. High clouds extended into the Gulf of St. Lawrence. The cold and drier air had intruded near the low center as indicated by the partial clearing near the center. Disorganized shallow convections dominated in the cold air mass behind the cold front along 35°N and between 70° and 55°W where significant air-sea heat transfers occurred (Atlas et al. 1986). The system would deepen only a few millibars more, and the overall convective activity started to weaken. The SSM/I swath encompassed most of the cold front (Fig. 14). There was almost no heavy precipitation around the low center. The rain rate showed that there were many mesoscale active convections, with a rain rate greater than 12 mm h⁻¹ embedded along the cold front, as evident in the IR imagery (Fig. 13) and radar observations (Wakimoto et al. 1992). One particular interesting feature in Fig. 14 was that the heavier precipitation was displaced to the east along the northern portion of the cold front but was consistent with the southern portion of the cold front. This was similar to what Wakimoto et al. had found at 1800 UTC (Fig. 7c of their paper), although the convection-front intersection point at 2200 UTC was closer to the warm front than at 1800 UTC. This could mean 1) that the Neiman et al. analyzed cold front was misplaced, or 2) that the displacement between the convection and cold front existed throughout the evolution of the cyclone.

The 22-h model-simulated rainfall rate, valid for 2200 UTC, was shown in Fig. 14b. The low pressure center was now almost devoid of precipitation. The precipitation pattern near the center obtained an eye-wall-like shape, similar to the IR image (Fig. 13). Major precipitation occurred along the warm front and extended from the triple point at approximately 41°N

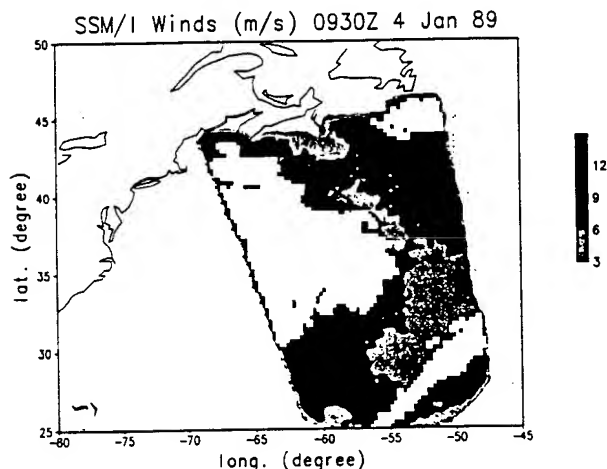


FIG. 12. Same as Fig. 8—SSM/I-retrieved marine surface winds with flag 0 except at 0930 UTC. The ship reports with black dots are at 0600 UTC—with open circles, at 1200 UTC.

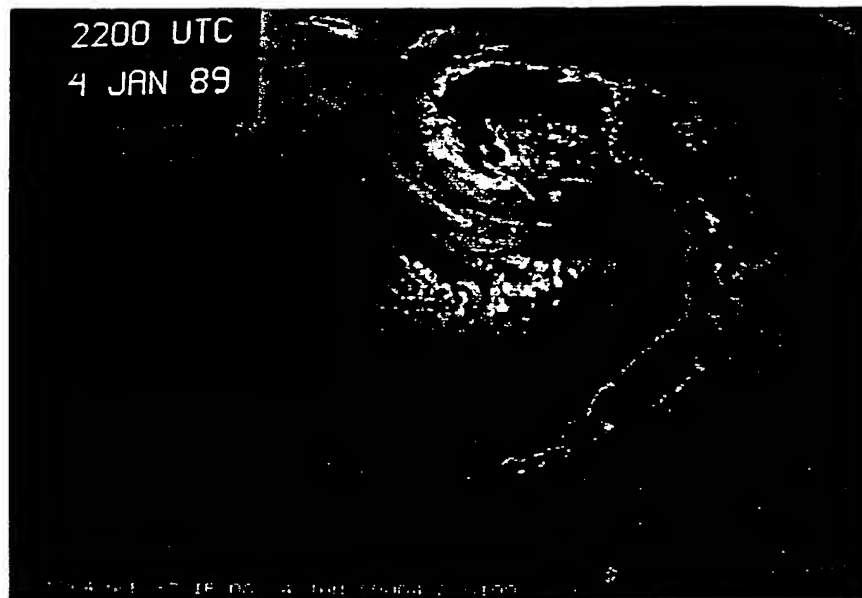


FIG. 13. GOES-7 IR imagery at 2200 UTC 4 January.

along the cold front to 25°N . The simulated rain-rate distribution clearly depicted the right-angled intersection of the cold front to the warm front. Simulated mass and momentum fields seemed to support the existence of the secondary cold front analyzed by Sanders and Neiman et al. The model-simulated temperature gradient was situated behind the secondary cold front. The primary cold front had little temperature gradient associated with it. In fact, there was warm advection across the primary cold front. Between the primary "cold" front and the secondary cold front there was a relatively cloud-free zone. To the west of the secondary cold front and in the cold air there were scattered and disorganized convection, consistent with the GOES IR

image (Fig. 13). (A more detailed description of model results will be reported in Chang et al. 1993.) Compared to the SSM/I-retrieved rain rates, the model produced heavier precipitation along the warm front, with a maximum rate of 20 mm h^{-1} , and lighter precipitation along the cold front, with a maximum rate of 3 mm h^{-1} . The squall-line feature east of the primary cold front was evident in the model simulation, enhanced IR, and SSM/I retrieval.

b. IWV

SSM/I-measured IWV at 2200 UTC is shown with an interpolated front in Fig. 15a. The area with more

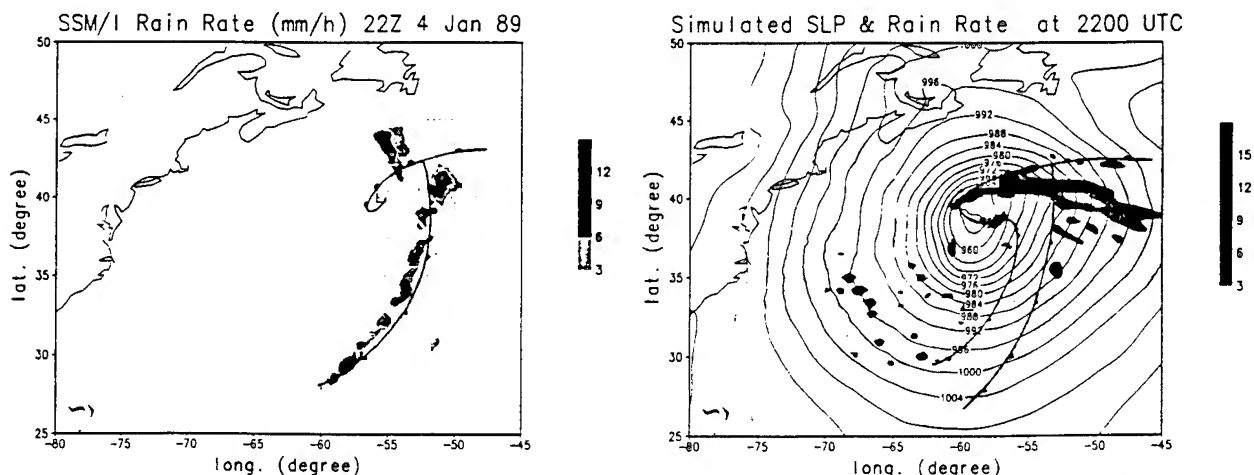


FIG. 14. (a) Same as Fig. 10a except for 2200 UTC 4 January. (b) Same as Fig. 10b except for 2200 UTC 4 January.

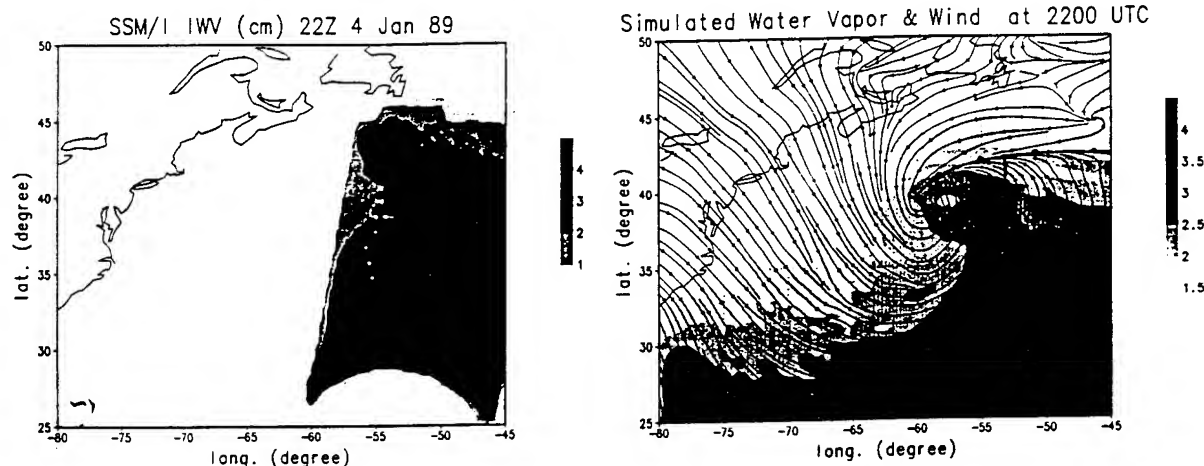


FIG. 15. (a) Same as Fig. 11a except for 2200 UTC 4 January. (b) Same as Fig. 11c except for 2200 UTC 4 January.

than 3 cm of IWV had extended farther north together with the warm sector compared to 0930 UTC (Fig. 11a). The interpolated cold front now was located mostly to the east of the 3–4-cm contour in agreement with the location of the SSM/I-observed precipitation west of the cold front. There was an isolated area with $IWV > 3$ cm north of the occluded warm front, collocated with the heavy precipitation there (Fig. 14).

Figure 15b shows the model-simulated IWV and 950-mb streamlines valid for 2200 UTC. Similar to the IWV field at 0930 UTC (Fig. 11c), the high IWV values were found mostly in the warm sector. A moist tongue extended from the tropics just ahead of the primary cold front to the high latitudes and to the east of the storm. In the cold air, IWV decreased rapidly toward the west, in spite of the long fetch over warm ocean. Strong gradients again were located along the warm and cold fronts. The model-simulated primary cold front was more associated with IWV gradients than with temperature gradients (see section 6a). Distribution of IWV near the center still reflected the effect of horizontal advection by the frontal and cyclonic circulations. The circular area with relative low IWV at 39°N , 57°W was collocated with the precipitation-free area between the two eyewall-like regions of convection. The high IWV band east of the cold front in the simulation was in agreement with the aforementioned squall-line feature. Overall, the model-simulated IWV values were less than the SSM/I retrieved by no more than 0.5 cm.

c. Surface wind speed

Cloud cover and high wind speeds at this time rendered most wind retrievals unreliable (flag greater than zero) over most of the swath (Fig. 16). The comparison of the retrieved with the two ship reports near the storm center with 30 and 40 m s^{-1} wind was not meaningful due to the uncertainty of the locations. One report of 12.5 m s^{-1} within the swath east of 50°W was in an

area of $6\text{--}9\text{ m s}^{-1}$ retrieved speed. This showed the limitation of the SSM/I marine surface wind retrieval. Continuous vigorous validation with wind speeds over 12 m s^{-1} can perhaps improve the confidence level of flag 1 retrievals. We found that for this particular storm, the area cover by high flags (>0) coincides approximately with the gale force wind region. The boundary of the high flag region may well be used for gale-force warning; however, the generalization to other cases cannot be made.

8. Conclusions

Patterns of rainfall rates, integrated water vapor and marine surface wind speeds were derived from SSM/I brightness temperatures. These fields were used to analyze the explosive midlatitude cyclone that developed during ERICA IOP 4. In addition, the SSM/I fields were compared to in situ ship and buoy

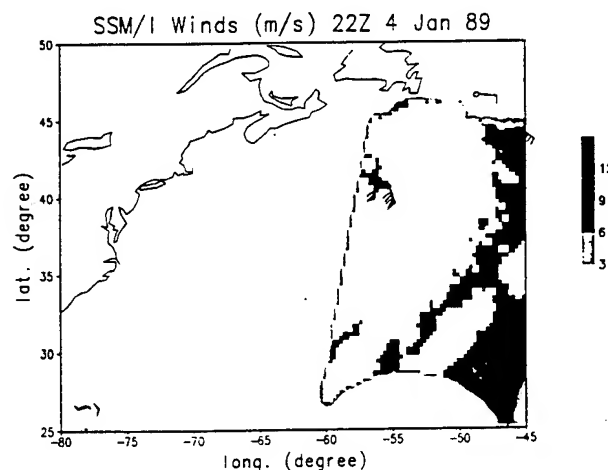


FIG. 16. Same as Fig. 12 except at 2200 UTC 4 January. Black dots denote reports made at 1800 UTC 4 January—open circles at 0000 UTC 5 January.

reports and to results produced by the NRL limited-area model.

This study has determined that SSM/I-derived rainfall rates were found along and ahead of the cold and warm fronts during the mature stage of the storm. These results also supported those shown by the model simulations. The active warm front and the warm-front occlusion (the "T-bone" fronts) in the Neiman and Shapiro (1993) surface analysis were evident in the SSM/I-observed precipitation patterns. Mesoscale areas of convection observed by SSM/I along the cold front supported the precipitation field observed by airborne radar (Wakimoto 1992). Additionally, the increase in areal coverage and intensity of SSM/I rainfall rates was consistent with the observed intensification of the storm. Quantitative comparison with model simulated rainfall rates was made. In general, the model simulated rainfall rates along the warm front were higher by a maximum of 5 mm h^{-1} , and rainfall rates along the cold front were lower by a maximum of $3\text{--}5 \text{ mm h}^{-1}$.

Patterns of SSM/I-derived IWV were viewed. It was found that the IWV had the strongest gradients along fronts, and the highest IWV values lay ahead of the cold front in the warm sector of the storm. Values in excess of 40 mm were not uncommon within the warm sector of this storm. The IWV patterns can provide additional information for frontal analysis, especially over regions where conventional data are sparse or a cirrus shield is particularly dense. The pattern of the SSM/I-retrieved IWV fields on the cyclone scale and frontal scale were further supported by NRL limited-area model forecasts. SSM/I-retrieved IWV values were generally 5 mm higher than model-simulated values.

Compared with ship reports, the SSM/I-retrieved marine surface wind speeds were slightly lower by $1\text{--}3 \text{ m s}^{-1}$. However, in regions of rapid wind shifts, as we found in the case of 0930 UTC overpass, the difference was larger. The IOP 4 storm, because of its location (over the ocean), size, and intensity, provided an excellent opportunity to apply the SSM/I wind speed algorithm in determining the boundary of near-gale force winds (15 m s^{-1}).

The potential usefulness of the SSM/I instrument in the analysis of midlatitude cyclones has been addressed. Because of its better resolution, SSM/I-retrieved IWV and precipitation patterns are very useful in supplementing conventional data in subjective analyses, especially for weather systems over data-sparse oceans. The rainfall rate, IWV, and marine surface wind speeds can also be very beneficial in objective analysis and numerical weather predictions. Marine surface wind speeds are being used in global data assimilations at NMC (Yu and Deaven 1991) and Fleet Numerical Ocean Center (Goerss and Phoebus 1992). Chang and Holt (1993) discussed the methodology and demonstrated the potential benefit of assimilation of SSM/I rainfall rates in a limited-area numerical model.

The rainfall rate can be used in dynamic initializations as well as in forecast models as forcing functions. The IWV can be used in moisture analysis or can provide surface latent heat fluxes (Miller and Katsaros 1992). Further exploitation and applications of SSM/I-retrieved fields are being conducted at NRL.

Acknowledgments. We thank Dr. James Hollinger, Mr. Glenn Sandlin, and Mr. David Spangler of the Naval Research Laboratory for providing the SSM/I data. We thank Dr. Paul Neiman for sending us his yet unpublished manuscripts on the ERICA IOP 4 cyclone. We also thank Prof. Fred Sanders for sending us his surface analysis. His interest and comments, and those from four anonymous reviewers, have greatly improved the presentation of our paper. The research was supported by an NRL basic research fund and an ONR Grant N00014 92 AF002.

REFERENCES

- Adler, R. F., H.-Y. M. Yeh, N. Prasad, W.-K. Tao, and J. Simpson, 1991: Microwave simulation of a tropical rainfall system with a three-dimensional cloud model. *J. Appl. Meteor.*, **30**, 924–953.
- Alishouse, J., S. Snyder, J. Vongsathorn, and R. Ferraro, 1990: Determinations of oceanic total precipitable water from the SSM/I. *IEEE Trans. Geosci. Remote Sens.*, **28**, 811–816.
- Alliss, R. A., S. Raman, and S. W. Chang, 1992: Special Sensor Microwave/Imager (SSM/I) observations of Hurricane Hugo (1989). *Mon. Wea. Rev.*, **120**, 2723–2737.
- , S. W. Chang, and S. Raman, 1993: Applications of SSM/I data in the analysis of Hurricane Florence (1988). *J. Appl. Meteor.*, **32**, in press.
- Atlas, D., B. Walter, S. Chou, and P. J. Sheu, 1986: The structure of the unstable Marine boundary layer viewed by lidar and aircraft observations. *J. Atmos. Sci.*, **43**, 1301–1308.
- Chang, S. W., and T. R. Holt, 1993: Impact of SSM/I rainfall rates on numerical predictions of winter cyclones. *Mon. Wea. Rev.*, **121**, in press.
- , K. D. Sashegyi, and T. R. Holt, 1991: Important physical processes in the evolution of mesoscale frontal structure of the ERICA IOP-4 cyclone. *Proc., Ninth Conf. on Numerical Weather Prediction*, Denver, CO, 760–761.
- , T. R. Holt, and K. D. Sashegyi, 1993: A numerical study of the frontal structure of the ERICA IOP 4 marine cyclone. *Mon. Wea. Rev.*, **121**, in press.
- , K. Brehme, R. V. Madala, and K. D. Sashegyi, 1989: A numerical study of the East Coast snowstorm of 10–12 February 1983. *Mon. Wea. Rev.*, **117**, 1768–1778.
- Goerss, J. S., and P. A. Phoebus, 1992: The navy's operational atmospheric analysis. *Wea. Forecasting*, **7**, 232–249.
- Goodberlet, M. A., C. T. Swift, and J. C. Wilkerson, 1989: Remote sensing of ocean surface winds with the Special Sensor Microwave/Imager. *J. Geophys. Res.*, **94**, 547–555.
- Hollinger, J. P., 1989: DMSP Special Sensor Microwave/Imager calibration/validation. Final Report Vol. I. [Available from the author at Naval Research Laboratory, Washington, D.C. 20375.]
- , 1991: DMSP Special Sensor Microwave/Imager calibration/validation. Final Report Vol. II. [Available from the author at Naval Research Laboratory, Washington, D.C. 20375.]
- Holt, T., S. W. Chang, and S. Raman, 1990: A numerical study of the coastal cyclogenesis in GALE IOP 2: Sensitivity to PBL parameterization. *Mon. Wea. Rev.*, **118**, 234–257.
- Katsaros, K. B., and R. Lewis, 1986: Mesoscale and synoptic scale features of North Pacific weather systems observed with the

- scanning multichannel microwave radiometer on *Nimbus 7*. *J. Geophys. Sci.*, **91**, 2321–2330.
- , I. Bhatti, L. A. McMurdie, and G. W. Petty, 1989: Identification of atmospheric fronts over the ocean with microwave measurements of water vapor and rain. *Wea. Forecasting*, **4**, 449–460.
- Kummerow, C., R. A. Mack, and I. M. Hakkarinen, 1989: A self-consistency approach to improve microwave rainfall rate estimation from space. *J. Appl. Meteor.*, **28**, 869–884.
- McMurdie, L. A., and K. B. Katsaros, 1985: Atmospheric water distribution in a mid-latitude cyclone observed by the Seasat scanning multichannel microwave radiometer. *Mon. Wea. Rev.*, **113**, 584–598.
- , and K. Katsaros, 1992: Satellite derived integrated water vapor and rain intensity patterns: Indicators of rapid cyclogenesis. *Proc. Sixth Conf. on Satellite Meteorology and Oceanography*, Atlanta, GA, Amer. Meteor. Soc., J11–J114.
- , G. Levy, and K. Katsaros, 1987: On the relationship between scatterometer-derived convergences and atmospheric moisture. *Mon. Wea. Rev.*, **115**, 1281–1294.
- Madala, R. V., S. W. Chang, U. C. Mohanty, S. C. Madan, R. K. Paliwal, V. B. Sarin, T. Holt, and S. Raman, 1987: Description of Naval Research Laboratory limited area dynamical weather prediction model. NRL Tech. Rep. 5992, Washington, D.C., 131 pp.
- Miller, D. K., and K. B. Katsaros, 1992: Satellite-derived surface latent heat fluxes in a rapidly intensifying marine cyclone. *Mon. Wea. Rev.*, **120**, 1093–1107.
- Neiman, P. J., and M. A. Shapiro, 1993: The life cycle of an extratropical marine cyclone. Part I: Frontal-cyclone evolution and thermodynamic air–sea interaction. *Mon. Wea. Rev.*, **121**, 2153–2176.
- , —, and L. S. Fedor, 1993: The life cycle of an extratropical marine cyclone. Part II: Mesoscale structure and diagnostics. *Mon. Wea. Rev.*, **121**, 2177–2199.
- Olson, W. S., 1989: Physical retrieval of rainfall rates over the ocean by multispectral microwave radiometry-application to tropical cyclones. *J. Geophys. Res.*, **94**, 2267–2280.
- Pudykiewicz, J., R. Beniot, and J. Mailhot, 1992: Inclusion and verification of a predictive cloud-water scheme in a regional numerical weather prediction model. *Mon. Wea. Rev.*, **120**, 612–626.
- Raustein, E., H. Sundqvist, and K. B. Katsaros, 1991: Quantitative comparison between simulated cloudiness and clouds objectively derived from satellite data. *Tellus*, **43A**, 306–320.
- Rodgers, E. B., and R. F. Adler, 1981: Tropical cyclone rainfall characteristics as determined from a satellite passive microwave radiometer. *Mon. Wea. Rev.*, **109**, 506–521.
- Sanders, F., 1989: *Surface Analyses during ERICA*. [Available from ERICA Data Center, Drexel University, Philadelphia, PA 19104.]
- Wakimoto, R. M., W. Blier, and C. Liu, 1992: The frontal structure of an explosive oceanic cyclone: Airborne radar observations of ERICA IOP 4. *Mon. Wea. Rev.*, **120**, 1135–1155.
- Yu, T.-W., and D. G. Deaven, 1991: Use of SSM/I wind speed in NMC's GDAS. *Proc. 9th Conf. Numerical Weather Predictions*, Denver, CO, Amer. Meteor. Soc., 416–417.

Appendix H

Applications of SSM/I Data in the Analysis of Hurricane Florence (1988)

Applications of SSM/I Data in the Analysis of Hurricane Florence (1988)

RANDALL J. ALLISS

Department of Marine, Earth and Atmospheric Sciences, North Carolina State University, Raleigh, North Carolina

GLENN D. SANDLIN AND SIMON W. CHANG

Naval Research Laboratory, Washington, D.C.

SETHU RAMAN

Department of Marine, Earth and Atmospheric Sciences, North Carolina State University, Raleigh, North Carolina

(Manuscript received 10 June 1992, in final form 23 March 1993)

ABSTRACT

Data from the Special Sensor Microwave/Imager (SSM/I) on board a Defense Meteorological Satellite Program satellite are used to study the precipitation patterns and wind fields associated with Hurricane Florence (1988). SSM/I estimates indicate that the intensification of Florence was coincident with the increase in total latent heat release. Additionally, an increase in the concentration and areal coverage of heavier rain rates near the center is observed. SSM/I marine surface winds of Florence are examined and compared to in situ data, and to an enhanced objective isotach analysis over the Gulf of Mexico. Results indicate that the SSM/I winds are weaker than those depicted in the enhanced objective analysis and slightly stronger than in situ observations. Finally, center positions of Florence are estimated using the 85-GHz brightness-temperature imagery. Much improved estimates are achieved using this imagery compared to using GOES infrared imagery. These results concur with previous studies that applications of SSM/I data could be valuable in augmenting current methods of tropical cyclone analysis.

1. Introduction

The advent of the meteorological satellite in the 1960s has significantly improved tropical cyclone detection, analysis, and prediction. The geostationary satellites provide imagery (e.g., every half-hour) in the visible (VS), infrared (IR), and water vapor channels on a routine basis. Sensors flown aboard polar-orbiting satellites, like the Advanced Very High Resolution Radiometer (AVHRR), which has higher IR resolution than the geostationary satellites, have been beneficial to the forecaster in observing tropical cyclones. In June of 1987, the first Special Sensor Microwave/Imager (SSM/I) was launched aboard a Defense Meteorological Satellite Program (DMSP) satellite. The polar-orbiting SSM/I provides data in seven microwave channels for both land and atmospheric remote sensing.

SSM/I algorithms that relate polarized microwave brightness temperatures (BT) to certain atmospheric parameters, including rain rates and wind speeds, can be used to study tropical cyclones (Rodgers and Adler 1981). Emitted microwave radiation at 85.5 GHz can

penetrate the overlying cirrus clouds, commonly associated with hurricanes, with limited attenuation, revealing the low-level center, which can be inferred from the convective organization. With a resolution of approximately 12.5 km, the center position of developed tropical cyclones without visible eyes can be better estimated using 85-GHz imagery than by using conventional visible and infrared imagery alone (Velden et al. 1989).

The objective of this article is to present SSM/I rainfall rates and other precipitation parameters during various stages of Atlantic Hurricane Florence's (1988) development. Comparisons are made between the precipitation patterns of Florence and those of devastating Hurricane Hugo (1989). During Florence's short life, it went through episodes of rapidly changing convective activity (Rodgers et al. 1991). Because Florence only reached minimal hurricane strength, its intensity may have been greatly modulated by the convection. Florence was captured in SSM/I imagery every 12 h during a 3-day period. In addition to the SSM/I precipitation rates, SSM/I near-surface wind speeds were retrieved to determine the extent of near tropical storm-force winds ($\geq 15 \text{ m s}^{-1}$). These SSM/I wind speeds are compared to in situ data and to an enhanced objective isotach analysis that includes dropsonde data (Shi et

Corresponding author address: Dr. Simon W. Chang, Naval Research Laboratory, Code 7225, Department of the Navy, Washington, DC 20375-5000.

al. 1991). Finally, SSM/I estimates of storm location are compared to the National Hurricane Center (NHC) best-track data.

2. Special Sensor Microwave/Imager (SSM/I)

The SSM/I is a passive radiometric system that measures the upwelling radiation from the surface of the earth and atmosphere. The SSM/I is aboard a DMSP polar-orbiting satellite that orbits the earth in a near sun-synchronous mode at an altitude of 833 km, and with an orbital period of 102 min. The SSM/I completes 32 scans per minute over a swath of 1400 km, and measures upwelling radiation at 19.3, 22.2, 37.0, and 85.5 GHz. By initial design, all but the 22-GHz channel provide BT for the vertical (V) and horizontal polarizations (H). The 22-GHz channel measures only V polarized radiation. Each channel has a different-sized footprint. See Hollinger et al. (1991) for more detailed information on the graphic description of the footprint geometry. The 85-GHz channel has the smallest footprint (15 km × 13 km) while the 19-GHz channel has the largest (69 km × 43 km). The imager senses an average emission from each footprint. Although the footprint sizes of each channel are different, a 25-km resolution is representative of the combined channels used in the algorithms and is thus selected for the resolution of the precipitation and wind data.

a. Rainfall-rate algorithm

The rain-rate algorithm used in this study is described by Olson (1989) and Hollinger (1991). Since the 85-GHz V channel was unavailable during September 1988, an alternative algorithm is applied using the 85-GHz H channel, as well as the 22-GHz V, 37-GHz V and H channels, and the 19-GHz V and H channels. Pixels within ±100 km of the coast were not processed because of possible ambiguity, although additional algorithms for the land-sea interface are now being developed (Adler 1992, personal communication). The recommended alternate algorithm (Hollinger 1991) is used.

Over ocean:

$$R = \exp(-0.42383 - 0.0082985T_{85h} + 0.01496T_{19v} + 0.00583T_{19h}) - 4.0 \text{ mm h}^{-1}, \text{ and } (1)$$

over land:

$$R = \exp(1.32526 - 0.08150T_{37v} + 0.01638T_{37h} + 0.03561T_{22v} + 0.05079T_{19v} - 0.01875T_{19h}) - 8.0 \text{ mm h}^{-1}, (2)$$

where R is the rainfall rate and T_{37v} , T_{37h} , T_{19v} , T_{19h} , T_{22v} , and T_{85h} are the BTs of the 37-GHz V, 37-GHz H, 19-GHz V, 19-GHz H, 22-GHz V, and 85-GHz H channels, respectively. If the formulas produced a

rainfall rate less than zero, then the rain rate value was set equal to zero.

SSM/I-derived rainfall rates using this algorithm have been statistically validated by comparisons with radar estimates (Olson 1989). The rainfall-rate validation was conducted by obtaining ground truth from radars at both the Marshall Islands, Kwajalein, and Darwin, Australia. Additionally, seven radars in the United Kingdom and one located at Cape Canaveral, Florida, were used in the validation. SSM/I rainfall rates were found to have a standard deviation of 5 mm h⁻¹ over the rainfall rate range of 0–25 mm h⁻¹.

b. Wind speed algorithm

The SSM/I wind speed algorithm was designed to retrieve wind speeds over the oceans and to be valid at 19.5 m above the ocean surface. The magnitude of microwave energy being emitted from the ocean surface is dependent on the wave structure and foam coverage, which in turn are influenced by the wind speed. Therefore, by measuring the ocean surface microwave emission, the SSM/I is able to infer the ocean surface wind speed. The 19-GHz V and 37-GHz H polarized channels are most sensitive to the ocean roughness and foam (Goodberlet et al. 1989). The wind algorithm utilizes two other channels: the 22-GHz V and 37-GHz V channels, to account for atmospheric attenuation effects. The 22-GHz V channel is used to address atmospheric water vapor effects, while the difference between the 37-GHz V and 37-GHz H channels (37V – 37H) is used to detect cloud and liquid water scattering (Goodberlet et al. 1989). The algorithm for wind speed (WS) used in this study (Hollinger 1991) is:

$$WS = 147.90 + 1.0969T_{19v} - 0.4555T_{22v} - 1.7600T_{37v} + 0.7860T_{37h}, (3)$$

where T_{22v} is the BT of the 22-GHz V polarized channel and the other variables are as given previously.

Currently, there are two fundamental limitations to the accuracy of SSM/I wind speed retrievals: the resolution of the instrument and the presence of cloud water, rain, and hail in the atmosphere. Upwelling microwave energy at the SSM/I frequencies, which is coming from the ocean surface, can be masked by the emission and attenuation characteristics of rain and hail in the earth's atmosphere. Therefore, "rain flags" have been established to estimate the degree of uncertainty of each calculated wind speed due to the presence of intervening water vapor, cloud water, rain, or hail (Goodberlet et al. 1989). The SSM/I wind speed uncertainties for the respective rain flags are listed in Table 1. Additionally, the effective resolution of the algorithm is limited by the resolving power of the SSM/I antenna at 19, 22, and 37 GHz, which can act to smooth the high spatial gradients in wind speed present in nature.

SSM/I wind speeds have been validated by comparisons with NOAA buoys, and found to have an ac-

TABLE 1. SSM/I rain flags and their standard deviations (after Goodberlet et al. 1989).

Rain flag	Standard deviations of wind speed (m s^{-1})
0	<2
1	2–5
2 and 3	>5

curacy of $\pm 2 \text{ m s}^{-1}$ between 3 and 25 m s^{-1} , within which 85% of the retrievals occurred. For the remaining 15% of the retrievals, winds are flagged, and are progressively uncertain with increasing flag numbers as atmospheric attenuation increases (Goodberlet et al. 1989). Wind speeds above 25 m s^{-1} have not been validated.

3. Hurricane Florence

The circulation that eventually became Hurricane Florence developed within an area of disturbed weather located in the south-central Gulf of Mexico on 7 September 1988. This area of convection had previously been associated with a cold front that had entered the Gulf of Mexico from the north several days earlier. This system subsequently strengthened and became Tropical Storm Florence. According to NHC best-track data, Florence tracked eastward and then northward on 8 September. On 9 September, Florence began to accelerate toward the north and intensify. By 1800 UTC 9 September, Florence had become a hurricane just south of New Orleans. An air force reconnaissance aircraft reported maximum sustained winds of 33 m s^{-1} at this time and estimated a minimum central pressure of 985 mb. Florence made landfall in southeastern Louisiana at 0200 UTC 10 September. After landfall, Florence rapidly weakened as it moved northwest and dissipated over eastern Texas on 11 September (Lawrence and Gross 1989). Figure 1 shows the track of Florence.

4. SSM/I precipitation patterns of Florence

Six SSM/I images of Florence were obtained at approximately 12-h intervals from tropical depression stage through final landfall. Rainfall rates from each pass beginning 1200 UTC 7 September through 0000 UTC 10 September were compiled and interpolated onto a grid with a horizontal resolution of 0.25° in longitude and latitude. Figure 2a reveals the SSM/I precipitation rates at 1200 UTC 7 September. At this time, Florence was classified as a tropical depression by NHC. Maximum sustained winds were estimated to be 15 m s^{-1} . The rain-rate imagery shows a small pocket of rain rates greater than 20 mm h^{-1} embedded within a larger area of lighter rainfall just to the northwest of the Yucatan Peninsula. The area of relatively

heavier precipitation of greater than 20 mm h^{-1} at this time is placed to the south of the center.

Twelve hours later at 0000 UTC 8 September, SSM/I rain-rate imagery reveals that the precipitation field has expanded with a larger area of rain rates greater than 20 mm h^{-1} (Fig. 2b). Additionally, a cyclonic curvature is now evident in the overall precipitation pattern. Florence was upgraded to a tropical storm by NHC at this time when maximum sustained winds were estimated to be 23 m s^{-1} . The SSM/I image at this time showed a weak north-south-oriented rainband present to the north of the main area of convection. The low-level center, as indicated by the best-track data during this time, was still to the north of the deep convective region.

The pass at 1200 UTC 8 September reveals two areas of heavy precipitation (Fig. 2c). The first, along the northwest coast of the Yucatan Peninsula, is associated with Florence. The second area is located over the northeastern Gulf of Mexico and is associated with a stalled frontal system that extends from the northeast Gulf of Mexico to the southeast coast of the United States. The area of precipitation associated with Tropical Storm Florence with rain rates greater than 20 mm h^{-1} have grown considerably during this time.

The two SSM/I images of Florence on 9 September capture the rapid intensification of the precipitation patterns on this day. The areal coverage of intense precipitation at 0000 UTC (Fig. 2d) associated with Florence is considerably less than the previous SSM/I pass. The intensity decreased slightly over this 12-h period with a 2-mb central pressure increase. Over the next 12 h, however, two areas of convection developed

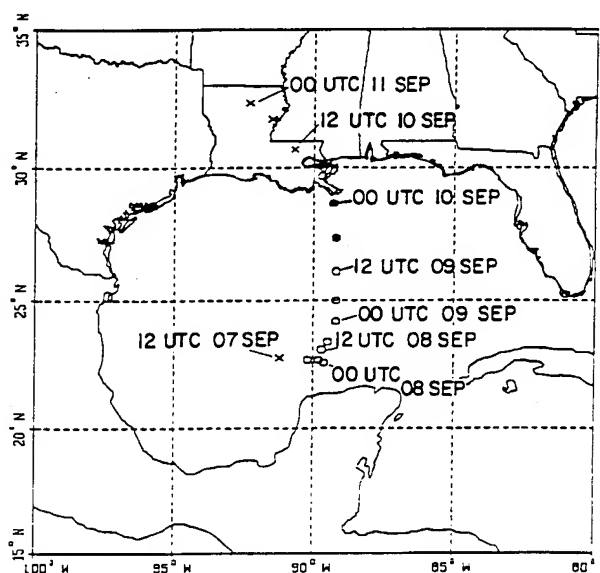


FIG. 1. Track of Hurricane Florence every 6 h from depression stage through final landfall: x—tropical depression stage, o—tropical storm stage, and ●—hurricane stage. Times and dates are indicated at 0000 and 1200 UTC each day.

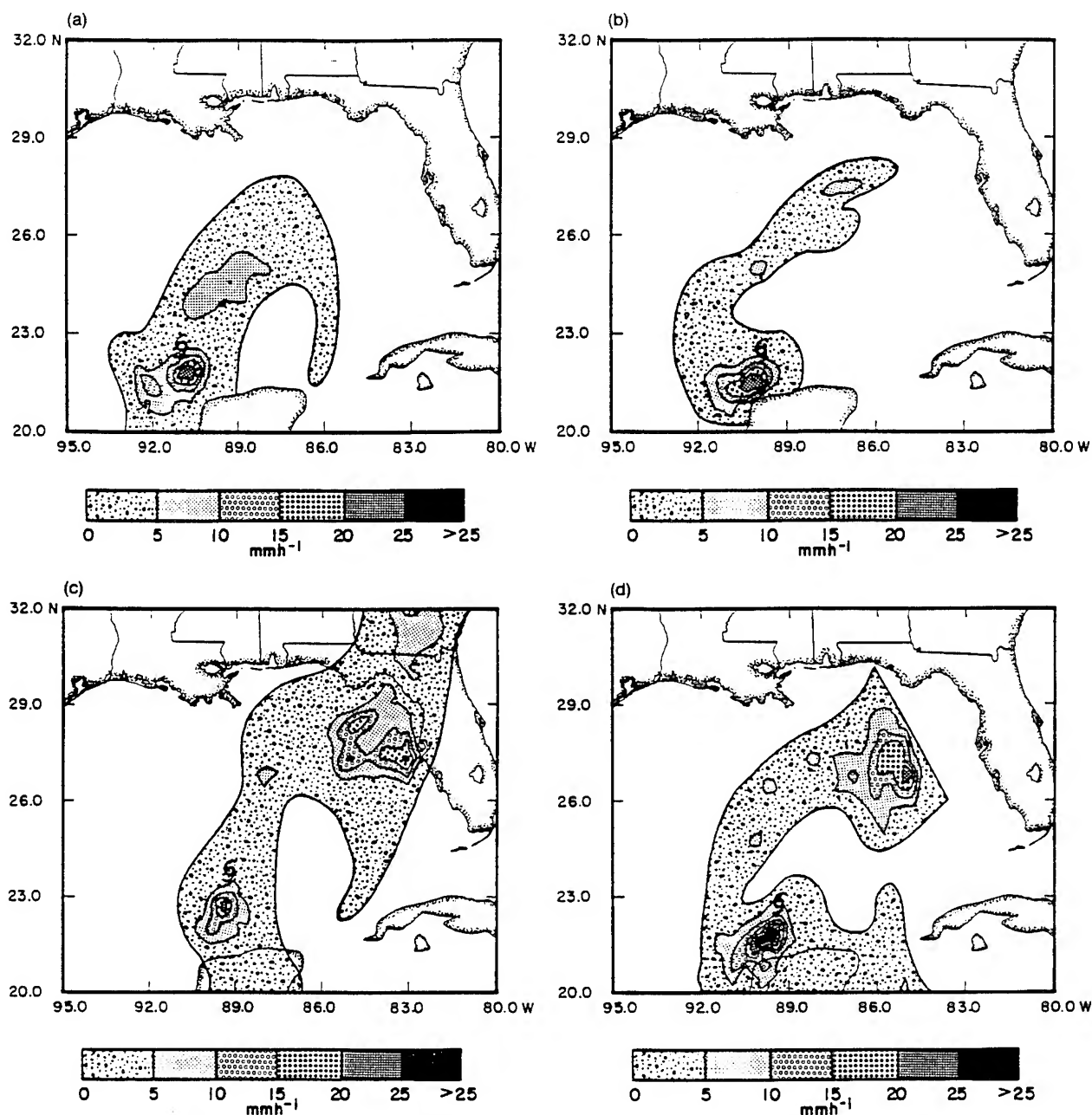


FIG. 2. (a) SSM/I rainfall rates at 1200 UTC 7 September 1988. The legend for all rain rate displays is indicated on the figure: (b) same as (a) except for 0000 UTC 8 September 1988; (c) same as (a) except for 1200 UTC 8 September; (d) same as (a) except for 0000 UTC 9 September; (e) same as (a) except for 1200 UTC 9 September; and (f) same as (a) except for 0000 UTC 10 September. The tropical storm symbol on each figure indicates the center of Florence during that pass.

around the center of Florence (Fig. 2e). The SSM/I image at 1200 UTC 9 September shows the explosive increase in the areal coverage of Florence's precipitation pattern. Rain rates greater than 25 mm h^{-1} are present to the northwest and southeast of the low-level center. These areas of heavy precipitation, as expected, are exactly coincident with the deeply convective regions seen in the GOES infrared imagery at 1200 UTC (Fig. 4 of Rodgers et al. 1991). The low-level center of Flor-

ence at this time is marked by a minimum in SSM/I rainfall rates. A large rainband is also observed in the precipitation field emanating from the northernmost convective region and extending south along the east coast of the Yucatan.

Figure 3 reveals a west-to-east cross section of rainfall rates through the center of Florence at 1200 UTC 9 September. The presence of two maxima in rainfall on either side of the center is evident. Rainfall rates of 19

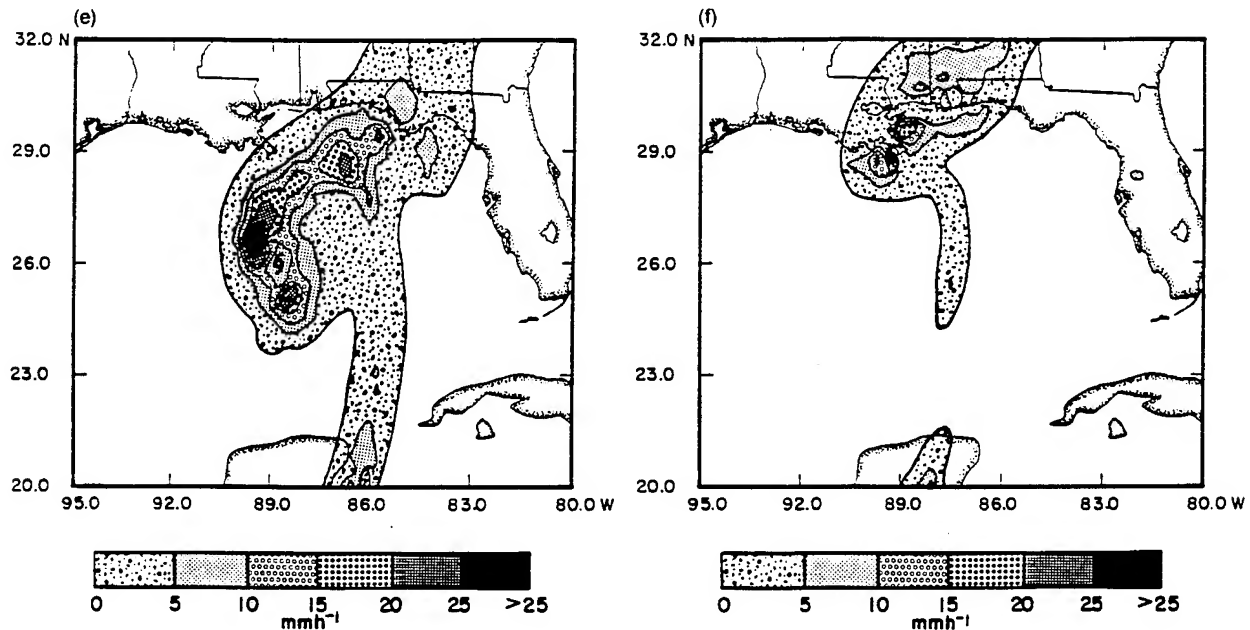


FIG. 2. (Continued)

and 12 mm h^{-1} are evident on the west and east sides of the center, respectively, with a minimum of 2.5 mm h^{-1} in the center. A small secondary maximum is also noted 330 km to the east of the center, associated with the rainband shown in Fig. 2e.

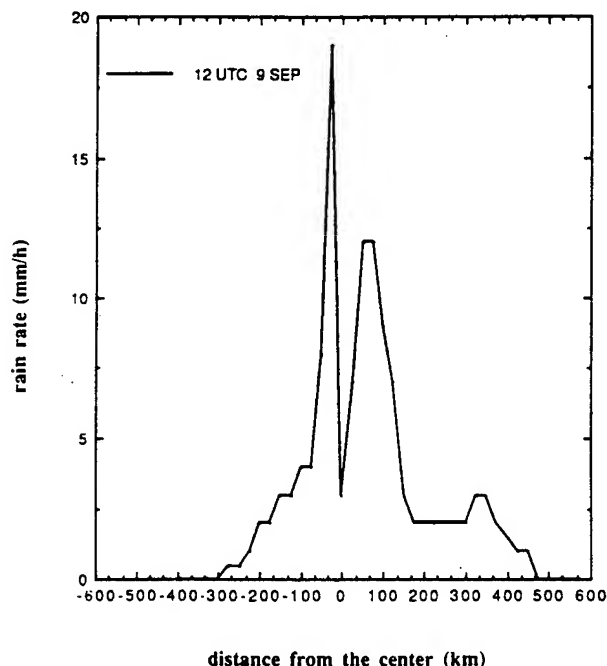


FIG. 3. West-to-east cross section of rain rates through the center of Florence at 1200 UTC 9 September. Refer to Fig. 2f for the location of the cross section. Maximum rainfall rates of 19 and 11 mm h^{-1} are evident on the west and east sides of the eyewall, respectively. A minimum value of 2.5 mm h^{-1} is observed in the eye region.

Several hours prior to the SSM/I overpass at 0000 UTC 10 September, Florence had reached its maximum intensity. The center of circulation determined by NHC was located just south of the Mississippi delta. SSM/I 85-GHz imagery revealed an intrusion of dry air into the circulation from the west and southwest (not shown). As a result, the convection had become weak and disorganized. SSM/I rain rates at 0000 UTC confirm this weakening (Fig. 2f). Although precipitation is evident, all heavy precipitation has diminished with no rain rates greater than 10 mm h^{-1} found near the center. The decrease in rain rates at this time is in agreement with the radar reflectivities of the NWS WSR-57 at Slidell, Mississippi (Hollinger 1989).

5. Other rainfall characteristics

a. SSM/I-derived parameters

The average rain rates within radii of 111, 222, and 444 km of the center are computed and evaluated for each SSM/I pass. Figure 4 shows the 111-km average rain rate (mm h^{-1}) versus the minimum central pressure as a function of time. Calculations are made over a 2-day period during which Florence strengthened from a tropical depression to a strong tropical storm. The SSM/I data just prior to landfall were excluded from the calculation due to the land contamination. Figure 4 reveals that the average rain rate within the 111-km radius is highly correlated with the central sea level pressure. The increase in rainfall is especially notable between the 0000 UTC 9 September and 1200 UTC 9 September passes in which the average rain rate increases from 3.0 to more than 13 mm h^{-1} . During the same period, the minimum central pressure drops

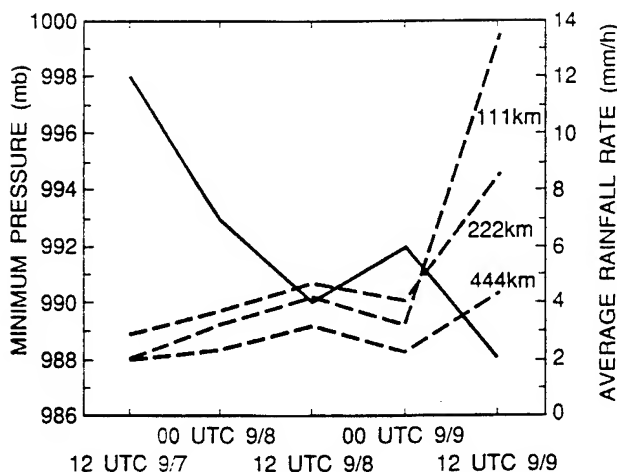


FIG. 4. The average rain rate (mm h^{-1} , dashed lines) within an 111-, 222-, and 444-km radius of the center versus minimum central pressure (mb, solid line) as a function of time. A decrease in central pressure corresponds to an increase in the average rain rate.

from 992 to 988 mb. The average rain rates within the 222- and 444-km radii also show the same correlation with Florence's intensity. The average rain rate within the 222-km radius is larger than that of the 111 km between 1200 UTC 7 September and 0000 UTC 9 September, indicating that the heavier precipitation is located off the storm center. A standard Student's *t*-test is conducted to determine the correlation between the average rain rate (111-km radius) and minimum pressure. A correlation coefficient of -0.93 was found significant at the 2% level. This suggests that there is a strong association between the increase or decrease in SSM/I rain rates and the intensity of Florence. Similar results were obtained for Hurricane Hugo of 1989 (Alliss et al. 1992).

The total latent heat release (TLHR) for five SSM/I observations is evaluated for a circular area with a radius of 444 km from the center. The center for all passes was determined by an analysis of the 85-GHz imagery. The TLHR over an area is given by

$$\text{TLHR} = L\rho \int_A R da, \quad (4)$$

where ρ is the density of rainwater assumed to be $1.0 \times 10^3 \text{ kg m}^{-3}$, L , the latent heat of condensation ($2.5 \times 10^6 \text{ J kg}^{-1}$), da , the incremental area (27 km^2), R , the rainfall rate at each grid point, and A , the area of integration.

The time-averaged TLHR within 444 km of the center of Florence is calculated to be $11.5 \times 10^{14} \text{ W}$. This estimate results from five passes over a 48-h period during which time Florence's intensity was mostly below hurricane strength. By comparison, Alliss et al. (1992) found for eight SSM/I observations of Hurricane Hugo of 1989 an average TLHR of $16.6 \times 10^{14} \text{ W}$. At Hugo and Florence's peak intensities the maximum TLHR within 444 km radius of the center and

the corresponding pressures were $20.5 \times 10^{14} \text{ W}$ and 918 mb and $17.5 \times 10^{14} \text{ W}$ and 988 mb, respectively. Hurricane Hugo was a much larger hurricane than Florence, having a well-developed and intense inner-core region. The inner core of Florence, however, was much smaller and less defined, thus the large differences calculated in the TLHR are consistent with the respective intensities.

Figure 5 reveals the trend of the computed TLHR, maximum winds, and minimum pressure from the NHC best-track data for each SSM/I time over a 48-h period. In the 24-h period beginning at 1200 UTC 7 September until 1200 UTC 8 September the TLHR increases nearly 60% from 7.6×10^{14} to $13.0 \times 10^{14} \text{ W}$. The minimum central pressure of Florence decreases 8 mb during this 24-h period. The 4-mb intensification of Florence observed on 9 September is also coincident with an increase in the TLHR. In the next 12-h period between 0000 and 1200 UTC 9 September, the TLHR increases 55% from 9.5×10^{14} to $17.5 \times 10^{14} \text{ W}$, whereas the central pressure decreases by only 4 mb. Similar results were obtained for smaller radii calculations of TLHR. Unfortunately, Florence starts to be influenced by land shortly after 1200 UTC 9 September, a long persistent trend, and the lag between precipitation and intensity in a relatively uniform environment cannot be observed.

b. Spatial variations of rainfall rates

The contributions of rainfall within specified rain-rate categories and the areal coverage of these rain rates were examined during Florence's intensification episode on 9 September. Figures 6a and 6b show the percent areal coverage of rainfall and the percent contribution of rainfall for four rain-rate categories within 200 km of the center. Figure 6a reveals the distribution

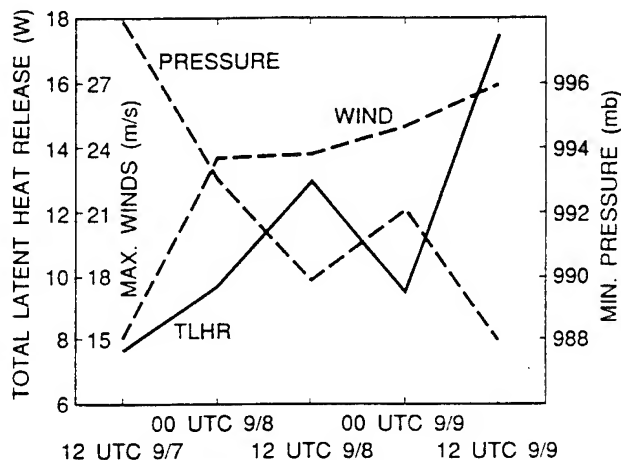


FIG. 5. Total latent heat release ($\times 10^{14} \text{ W}$) within a 444-km radius of the center as a function of time for Florence. Minimum pressure (mb) and maximum winds (m s^{-1}) are also shown for each SSM/I pass. All wind and pressure data was obtained from the NHC best-track data.

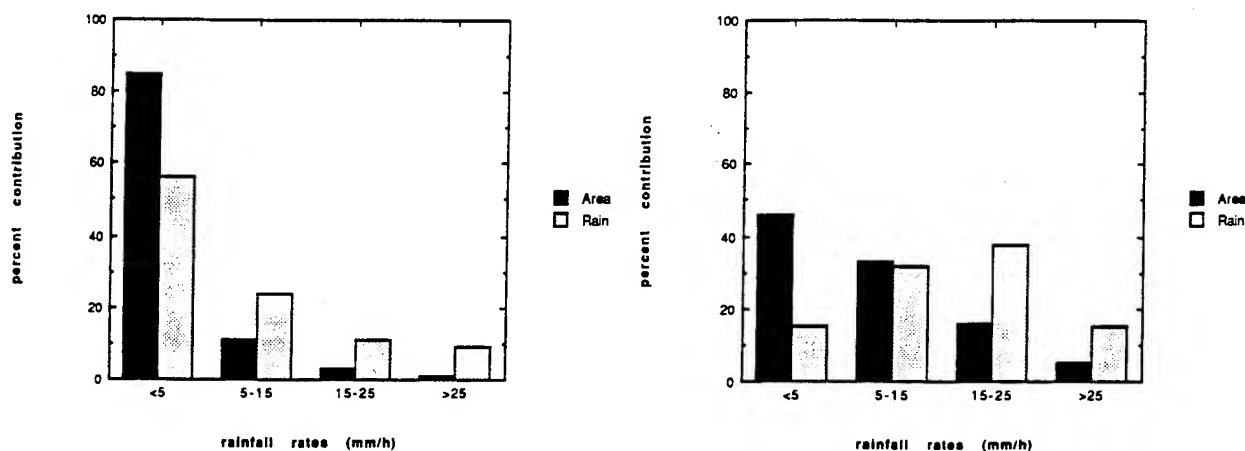


FIG. 6. Percent areal coverage (black shade) and percent contribution (dotted shade) of rainfall by four rain-rate categories within a radius of 200 km from the center for (a) 0000 UTC 9 September and (b) 1200 UTC 9 September.

at 0000 UTC 9 September when a minimum pressure of 992 mb was estimated. Rain rates less than 5 mm h^{-1} occur in 85% of the area and contribute to 56% of the total precipitation. Rates greater than 15 mm h^{-1} occur in only 4% of the area and contribute to only 20% of the total rainfall. Due to the absence of deep convection, high rain rates were not the dominant feature in Florence during this pass.

As the storm intensified over the next 12 h, the intensity and coverage of the rainfall also increased. A major shift in the rain-rate distribution is noted during the SSM/I observation at 12 UTC 9 September. Figure 6b indicates that rates less than 5 mm h^{-1} now occur in only 46% of the area and contribute to less than 15% of the total rainfall. Rates between 15 and 25 mm h^{-1} occur in 16% of the area and contribute to nearly 40% of the total rainfall. The increasingly important contribution of heavier rainfall becomes evident during this pass. Percentage areal coverage and percentage amount contribution (in brackets) of rates greater than 25 mm h^{-1} increase from 1% (9%) at 0000 UTC to 5% (15%) at 1200 UTC. It appears that as Florence intensified, both the areal and amount contribution of heavier precipitation within the 200-km radius increase. These observations concur with those results obtained for Hurricane Hugo (1989). The overall magnitude of the percent areal coverage and the percent contribution of rainfall greater than or equal to 15 mm h^{-1} in Florence is 40% of what is observed for the same category in Hugo. This difference is probably due to the large contrast in intensity.

The azimuthally averaged spatial distribution of rainfall as a function of distance from the center is computed for the two SSM/I overpasses on 9 September. Figure 7 shows the average rainfall rate for each 20-km radius from the center during the intensification episode. As Florence intensifies, the maximum average rain rate within each radius also increases. More importantly, the maximum rainfall moves closer to the center from 0000 to 1200 UTC, suggesting the devel-

opment of inner-core convection. At 0000 UTC, the maximum average rain rate is 5 mm h^{-1} at 130 km from the center. Twelve hours later, a maximum value of 16 mm h^{-1} is reached 70 km from the center. During this period, the minimum sea level pressure of Florence decreases from 992 to 988 mb. In the case of Hugo (1988), it is also found that the maximum precipitation shifts toward the center as Hugo intensifies (Fig. 13 in Alliss et al. 1992). There, the maximum precipitation rates are between 15 and 20 mm h^{-1} , reflecting the much stronger intensity compared to Florence. Furthermore, the double eyewall observed in Hugo, which may have contributed to its intensity changes, is not apparent in Florence.

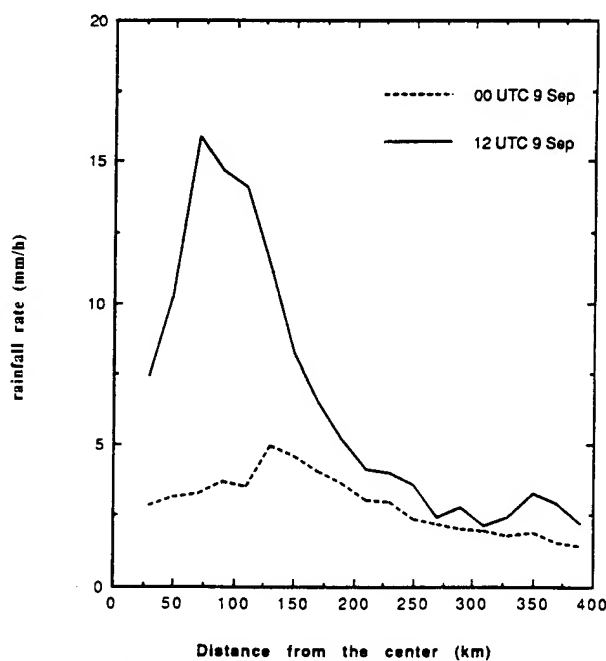


FIG. 7. Average rainfall rate as a function of distance from the storm center for 0000 and 1200 UTC 9 September.

6. SSM/I wind speed observations

Surface wind measurements over the open oceans are sparse and mainly limited to buoys and ships of opportunity. The majority of these reports originate in shipping lanes and along coastlines, most of which lie outside the tropics. These platforms do not provide a complete description of the horizontal distribution of surface wind speeds. Moreover, ships that do report winds avoid regions of stormy weather. In this section, we evaluate the usefulness of SSM/I-derived winds in the Florence case.

Fifty-one Omega dropwindsondes (ODWs) were deployed by the Atlantic Oceanographic and Meteorological Laboratories/Hurricane Research Division (AOML/HRD) during a synoptic flow experiment centered on Hurricane Florence on 8–9 September 1988. The data collected were employed to enhance a regional analysis and forecast system analysis of Florence's surface wind field at 0000 UTC 9 September (Shi et al. 1991). The enhanced analysis is used for comparison with SSM/I-derived wind speeds here. The ODW data used in the analysis were collected between 2100 UTC 8 September and 0300 UTC 9 September and assumed valid at 0000 UTC.

A second validation of SSM/I-derived wind speed observations is presented. In this case, a set of ship and buoy observations at 1200 UTC 9 September are compared with the SSM/I winds.

As discussed in section 2b, a set of rain flags is devised to indicate the reliability of the retrieval because the SSM/I marine surface wind retrieval is easily affected by atmospheric attenuations. In the following discussion, the retrieved wind speed will be presented along with the rain flags, indicating the quality of the retrieval.

a. SSM/I winds at 0000 UTC 9 September

Figure 8a shows SSM/I wind speeds (rain flag 0) rounded to the nearest meter per second at 0000 UTC 9 September. At this time, the center of Florence was near 24.2°N, 89.2°W. These wind speed estimates occur where the atmospheric attenuation is quite small, and thus represent the highest reliability. The majority of the rain flag 0 wind speed estimates within this swath are less than 15 m s⁻¹ and occur outside the precipitation of Florence's inner region and the coastal front (see Fig. 2d). Furthermore, only 40% of the SSM/I wind retrievals during this pass in the Gulf of Mexico are of rain flag 0 quality.

In this SSM/I overpass, more than 30% of the SSM/I wind speeds are of rain flag 1 quality. Here a method is devised to include wind speed retrieval with flag 1 so that more retrieved winds can be used and displayed. The method uses the probability that a rain flag 1-derived wind speed yields an actual wind of at least 15 m s⁻¹. The 15 m s⁻¹ threshold is chosen because it is close to the gale-force wind. We assume that there is a Gaussian distribution in the probability of actual wind speeds for a given retrieved wind speed. According to

Table 1, the wind speeds with flag 1 quality have a standard deviation of no larger than 5 m s⁻¹. Therefore, for example, if the algorithm yields a 20 m s⁻¹ wind speed it will have at least an 84% chance that the actual wind speed is at least 15 m s⁻¹ and a 16% probability that the actual wind is less than 15 m s⁻¹. Table 2 shows the probability of tropical storm winds based on rain flag 1 wind speeds.

Figures 8a and 9 display the area with different probabilities of occurrence of wind speeds greater than or equal to 15 m s⁻¹. The few large asterisks in Fig. 8a denote where there is at least a 84% probability of wind speeds larger than 15 m s⁻¹. The small crosses in Fig. 8a indicate a range of 50%–84% likelihood of such occurrence and the very small dots indicate a less than 50% probability. Only a small area east of the center suggests the actual winds may be as high as 15 m s⁻¹. The majority of the area in the flag 1 region outside the precipitation is experiencing less than 15 m s⁻¹ winds at 0000 UTC. The large dots in Fig. 8a indicate rain flags 2 and 3, where attenuation due to heavy precipitation results in unreliable SSM/I wind speeds (refer to Table 1).

Figure 8b shows the ODW-enhanced 1000-mb-level isotach analysis at 0000 UTC 9 September of Shi et al. (1991) superimposed on the SSM/I-derived wind speeds valid at the same time. The integers in Fig. 8b represent both rain flag 0 and 1 wind speeds. Throughout the entire region covered by Florence, the SSM/I wind speeds are, in general, underestimated compared to the enhanced analysis. The isotach analysis shows that winds greater than 15 m s⁻¹ are present in areas to the east and west of Florence's center. Furthermore, large gradients in the wind field are present over the same region in the isotach analysis, which is not well resolved by the SSM/I. In the ODW data, winds below the 950-mb level are normally not reported. Therefore, winds below the lowest reporting levels in the enhanced analysis of Shi et al. are assumed to be the same as those at the lowest reporting levels. This may lead to an overestimate of the 1000-mb winds in the analysis.

b. SSM/I winds at 1200 UTC 9 September

The SSM/I wind estimates for 1200 UTC 9 September are shown in Fig. 9. At this time, the center of Florence was located at 26.1°N, 89.2°W. For rain flag 0 wind speeds, maximum winds obtained from the algorithm are no greater than 16 m s⁻¹. Since the precipitation shield associated with Florence has expanded by this time, the majority of the area is dominated by rain flags greater than zero. The high likelihood, however, that winds equal or exceed tropical storm force is apparent near the western and eastern periphery of the storm's inner-core region. As mentioned in the above, the presence of precipitation greatly affects the SSM/I wind reliability. This is evident in Fig. 9 as the spatial pattern of rain flags 2 and 3 are highly repre-

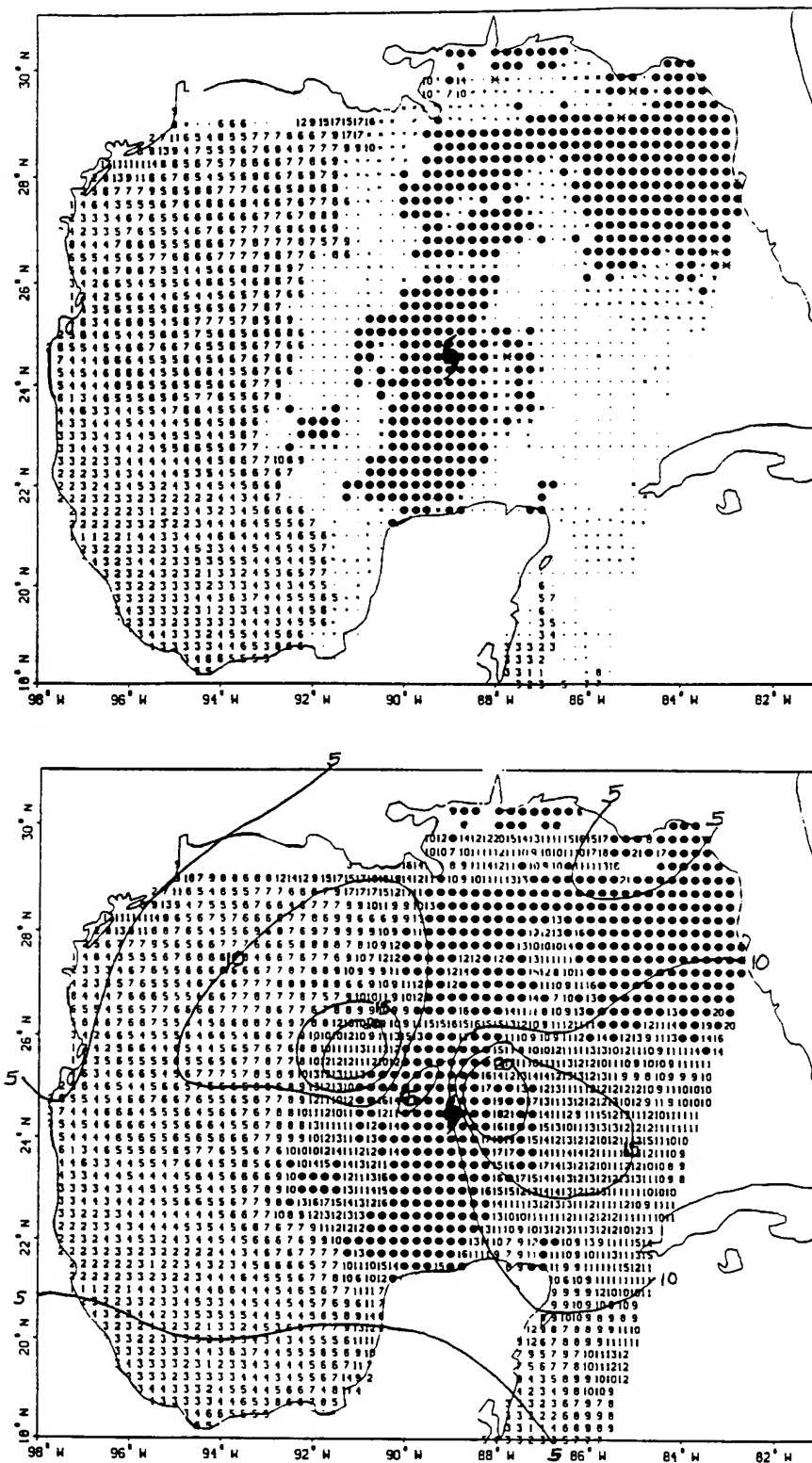


FIG. 8. (a) SSM/I-derived winds at 0000 UTC 9 September. All values indicate rain flag 0 wind speeds (m s^{-1}). Asterisks, crosses, and solid dots indicate the range of probabilities for winds of at least 15 m s^{-1} as indicated in Table 2. Blank areas indicate missing data. Large dots indicate rain flag 2 and 3 wind speeds. The hurricane symbol denotes the location of the low pressure center. (b) Isotach analysis based on ODW observations with a 5 m s^{-1} isotach interval superimposed on the SSM/I wind speed estimates at 0000 UTC 9 September. SSM/I wind speeds with flag 0 and 1 are in meters per second.

TABLE 2. The probability that an SSM/I-derived wind speed with a rain flag of 1 is at least 15 m s^{-1} . The method assumes a Gaussian distribution of the estimated wind speed.

Estimated rain flag 1 wind speed (m s^{-1})	Probability of 15 m s^{-1} wind
≥ 20	$>84\%$
15–20	50%–84%
<15	$<50\%$

sentative of the extensive precipitation field observed by SSM/I (Fig. 2e).

For comparison, reported buoy and coastal station winds in the Gulf of Mexico region at 1200 UTC are listed in Table 3. The latitude, longitude, and observed wind speed are shown, along with the nearest SSM/I wind speed and its corresponding rain flag. Three of the seven comparisons were for rain flag 0 wind speeds, all of which are within 2 m s^{-1} of the observed ship and buoy wind speeds. For the remaining four comparisons, which are for rain flag 1 wind speeds, all but one fall within 3 m s^{-1} . In our sample, all of the SSM/I wind speeds less than 15 m s^{-1} fall within the $\pm 2 \text{ m s}^{-1}$ specification. For SSM/I wind speeds of at least 15 m s^{-1} , two out of three of the samples are within $\pm 3 \text{ m s}^{-1}$ of comparative ship and buoy observations. Overall, the SSM/I winds have a 1.28 m s^{-1} high bias with a standard deviation of 2.03 m s^{-1} .

For 23 overpasses of tropical cyclones, Holliday and Waters (1989) determined that the occurrences of SSM/I wind speeds less than 15 m s^{-1} lay within the

$\pm 2 \text{ m s}^{-1}$ ground-truth specification for 70% of the samples. For SSM/I winds greater than or equal to 15 m s^{-1} , 82% were within $\pm 3 \text{ m s}^{-1}$ of comparative ship and buoy observations. Our samples here agree with the above assessment.

7. SSM/I center fixing estimations

The Florence case provided an excellent opportunity to test the utility of the higher-resolution (12.5 km) 85-GHz BT in estimating the center location of Florence. Velden et al. (1989) and Alliss et al. (1992) have both shown the value of using SSM/I data to determine tropical cyclone center locations. Because Florence was not a well-developed tropical cyclone, deep convective clouds were not organized near the center of circulation. This makes estimations of the center location using GOES IR and visible imagery somewhat difficult. SSM/I 85-GHz imagery, however, provided information on the low-level circulation characterized by a cyclonic twist of low clouds inward toward a center point.

Subjective SSM/I estimation of the center position has been conducted by determining the location of the low-level center as defined by the spiral-shaped signature in the 85-GHz channel near the storm center. Comparisons to NHC best-track data are made between 1) GOES IR estimates, made subjectively in non-real time without looping or aircraft reconnaissance data, and 2) SSM/I fixes. Because all of the SSM/I passes are either at 0000 or 1200 UTC, GOES visible imagery

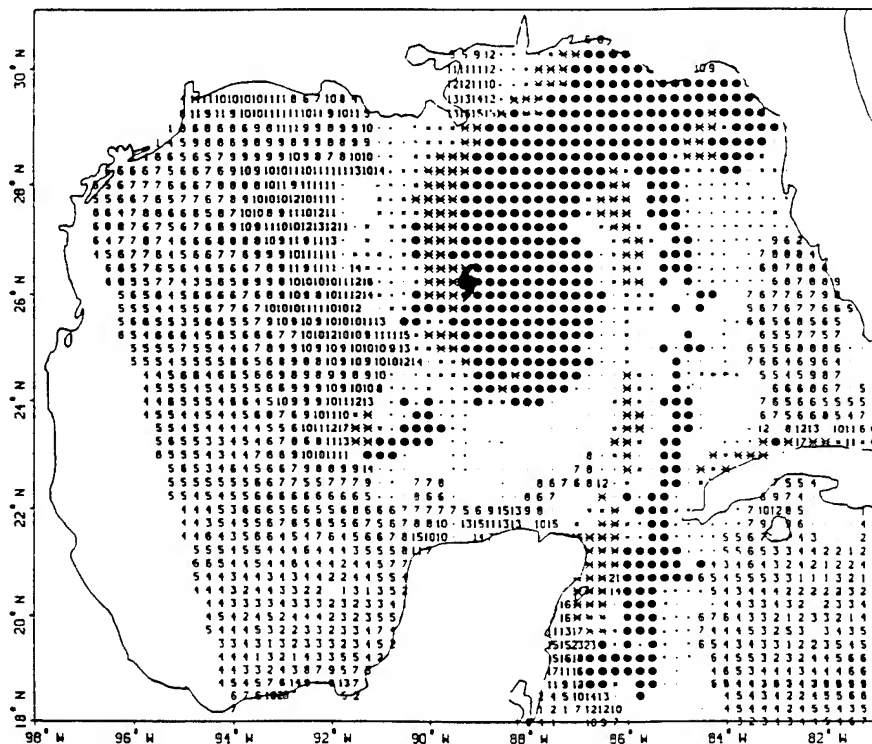


FIG. 9. Same as Fig. 8a except valid at 1200 UTC 9 September.

are not available for the comparison, only GOES IR imagery is used for the estimate. The results of the comparisons are presented Table 4. For the six passes, the average error, standard deviation σ , best case, and worst case are shown. The comparison shows that for the entire sample the average SSM/I estimate is much improved over the GOES IR estimate. In all cases, estimates made when using SSM/I are closer to NHC best-track data than when using GOES IR imagery. The mean errors of 65 km using the GOES IR imagery is improved to 19 km using the SSM/I 85-GHz imagery. It should be noted that there are only six fixes in this comparison and it is imperative that a larger sample of cases be examined to further assess in a statistically meaningful way the accuracy of using the 85-GHz imagery for center fixing. The 85-GHz imagery from the second and third SSM/I in orbit should also be used for comparison with GOES visible imagery for more recent cases.

8. Conclusions

SSM/I observations of rainfall have been used to analyze the precipitation patterns associated with Hurricane Florence of 1988. Based upon SSM/I precipitation estimates, the intensification of Florence is found to be accompanied by increases in the average rainfall, the relative contribution of heavier rainfall, and the total latent heat release. Unfortunately, the lag between the maximum TLHR and minimum pressure cannot be determined from these SSM/I observations due to Florence making landfall. SSM/I observations of Florence's precipitation field and its trend during intensification support those seen in the much larger and more intense Hurricane Hugo.

The surface wind field associated with Florence is analyzed using SSM/I marine surface wind speed data. SSM/I estimates that winds at 0000 UTC 9 September are generally lighter than an ODW-enhanced wind analysis valid for the approximately 950-mb level. On the other hand, SSM/I-derived wind speeds at 1200 UTC 9 September are slightly stronger than in situ observations over the Gulf of Mexico but the errors

TABLE 3. Latitude and longitude of available surface wind observations from Gulf of Mexico buoys and coastal stations at 1200 UTC 9 September 1988. SSM/I-estimated winds and rain flags (in parentheses) are also shown.

Collocated wind observations (m s^{-1})			
Latitude (°N)	Longitude (°W)	Ship and buoy	SSM/I
26.0	93.5	8	6 (0)
26.0	86.0	15	17 (1)
28.8	89.2	16	19 (1)
24.5	82.0	8	9 (0)
27.2	82.5	4	5 (1)
29.3	94.8	3	4 (0)
26.0	89.7	20	24 (1)

TABLE 4. The average error, standard deviation (σ), best case, and worst case between NHC best-track positions and 1) GOES IR estimations. 2) SSM/I estimations. All values are in kilometers.

	GOES	SSM/I
Average error	65	19
Standard deviation	44	6
Best case	30	10
Worst case	162	26

are well within specifications of algorithm validation. Due to the presence of heavy precipitation and cloud liquid water near the inner-core region, accurate maximum wind estimates from SSM/I are unavailable.

The ability of SSM/I 85-GHz imagery to provide much improved estimates of the location of Florence's center was clearly shown. Center position estimates using SSM/I imagery compared much better to the NHC best-track data than GOES IR imagery estimates.

Acknowledgments. We thank Mr. Jainn-Jong Shi of North Carolina State University (NCSU) for providing the enhanced dropsonde wind analysis and Mr. Kevin Schrab, also of NCSU, for assistance in the statistical analysis. The research was supported by SPAWAR (6370 X-1596-0932), NRL (basic research program), and ONR (N00014 92 AF002).

REFERENCES

- Alliss, R. A., S. W. Chang, and S. Raman, 1992: Special Sensor Microwave/Imager (SSM/I) observations of Hurricane Hugo (1989). *Mon. Wea. Rev.*, **120**, 2723–2737.
- Goodberlet, M. A., C. T. Swift, and J. C. Wilkerson, 1989: Remote sensing of ocean surface winds with the Special Sensor Microwave/Imager. *J. Geophys. Res.*, **94**, 547–555.
- Holliday, C. R., and K. R. Waters, 1989: SSM/I observations of tropical cyclone gale force vicinity winds. *Proc., Fourth Conf. on Satellite Meteor. and Oceanography*, Amer. Meteor. Soc., San Diego, 267–270.
- Hollinger, J. P., 1989: DMSP Special Sensor Microwave/Imager Calibration Validation, Final Report Vol. II. [Available from Simon Chang, Naval Research Laboratory, Washington, D.C. 20375.]
- Lawrence, M. B., and J. M. Gross, 1989: Annual summaries: Atlantic hurricane season of 1988. *Mon. Wea. Rev.*, **117**, 2248–2259.
- Olson, W. S., 1989: Physical retrieval of rainfall rates over the ocean by multispectral microwave radiometry—Application to tropical cyclones. *J. Geophys. Res.*, **94**, 2267–2280.
- Rodgers, E. B., and R. F. Adler, 1981: Tropical cyclone rainfall characteristics as determined from a satellite passive microwave radiometer. *Mon. Wea. Rev.*, **109**, 506–521.
- , S. Chang, J. Stout, J. Steranka, and J. J. Shi, 1991: Satellite observations of variations in tropical cyclone convection caused by upper-tropospheric troughs. *J. Appl. Meteor.*, **30**, 1163–1184.
- Shi, J.-J., S. Chang, K. Sashegyi, and S. Raman, 1991: Enhancement of objective analysis of Hurricane Florence (1988) with dropsonde data. *Proc. 19th Conf. of Hurricanes and Tropical Meteorology*, Amer. Meteor. Soc., Miami, FL, 335–337.
- Velden, C. S., W. S. Olson, and B. A. Roth, 1989: Tropical cyclone center-fixing using SSM/I data. *Proc., Fourth Conf. on Satellite Meteor. and Oceanography*, San Diego, 36–39.

Appendix I

Numerical Investigation of the Interaction Between Hurricane Florence (1988) and Its Upper-Level Environment

**NUMERICAL INVESTIGATION OF THE INTERACTION BETWEEN
HURRICANE FLORENCE (1988) AND ITS UPPER-LEVEL
ENVIRONMENT**

by

JAINN JONG SHI

A dissertation submitted to the Graduate Faculty of
North Carolina State University
in partial fulfillment of the
requirements for the Degree of
Doctor of Philosophy

MARINE, EARTH AND ATMOSPHERIC SCIENCES

Raleigh

1993

Approved By:

W. E. Rouse

J. D. Watson

A. W. Clay

Mark DeMaria

Ed Hamon

Chair of Advisory Committee

SHI, JAINN JONG. Numerical Investigation of the Interaction between Hurricane Florence (1988) and Its Upper-Level Environment. (Under the direction of Dr. Sethu Raman)

Omega-Dropwindsonde (ODW) data were used to enhance the National Meteorological Center/Regional Analysis and Forecast System (NMC/RAFS) 2.5⁰ analysis at 0000 UTC 9 September 1988 with a nested three-pass Barnes objective analysis scheme. Results revealed that the minimum sea surface pressure (SLP) was analyzed to be 994 mb, improved from 1004 mb in the NMC/RAFS 2.5⁰ analysis. The Naval Research Laboratory limited-area tropical cyclone model was employed to simulate Hurricane Florence with the NMC/RAFS 2.5⁰ analysis (the control experiment) and an analysis enhanced by the ODW data. The simulation results demonstrated that the analysis enhanced by the ODW data drastically improved the simulation in both intensity and storm track. The 24 hour storm track was improved by about 75%, while the forecast error of the intensity was reduced by about 10 mb.

The Special Sensor Microwave/Imager (SSM/I) retrieved rain rates at 0000 UTC and 1200 UTC on 9 September 1988 were assimilated into the model during the model integration. Results revealed that the forecast error of the landfall location in the control experiment was reduced by about 50% (from 2.95⁰ to 1.55⁰ latitude), and the landfall time error by 7 hours (from 9 hours to 2

DEDICATION

I dedicate this dissertation to my wife, Amy and my three lovely children, Katherine, Vincent and Edward. Without their strong support and encouragement, it would not be possible for me to complete this dissertation.

ACKNOWLEDGMENTS

I desire to express my deepest appreciation to Dr. Sethu Raman, the chairman of the advisory Committee and Dr. Simon Chang, one of my committee members, for their guidance in this research. They also provided many helpful suggestions for the completion of this dissertation. Particular thanks is given to Dr. Mark DeMaria, one of my committee members, for patiently sharing his time to review this dissertation and providing numerous important suggestions. Appreciation is also extended to the other committee members, Dr. Gerald F. Watson for giving me valuable suggestions and Dr. Woodrow E. Robbins for his suggestions in Computer Graphics.

I am very grateful for the time I was able to spend with Drs. Rao Madala and Keith Sashegyi of the Naval Research Laboratory. They gave me many technical and scientific assistances in utilizing the Naval Research Laboratory's Forecasting and Analysis System for this research. I thank Mr. Randy Alliss, who is my fellow graduate student, for processing the SSM/I retrieved rain rates for me. I also thank Dr. Edward Rodgers of the Goddard Space Flight Center of NASA for providing some help for this research.

Finally, I wish to thank my parents, wife, Amy and lovely children --- Katherine, Vincent and Edward, for their support during this work.

This research was supported by the Naval Research Laboratory, Washington, D.C..

TABLE OF CONTENTS

	Page
LIST OF TABLES.....	viii
LIST OF FIGURES.....	x
LIST OF SYMBOLS.....	xxi
1. INTRODUCTION.....	1
1.1 Background.....	1
1.2 Literature Review.....	3
1.2.1 General Characteristics of the Outflow Layer of Tropical Cyclones.....	3
1.2.2 Influence of the Upper-Tropospheric Environmental Flow on the Outflow layer and the Intensification of a Tropical Cyclone.....	8
1.2.3 Eddy Angular Momentum Flux.....	13
1.3 Research Objectives.....	15
2. DATA SOURCES.....	17
2.1 NMC/RAFS 2.5 Degree Analyses.....	17
2.2 Omega-Dropwindsonde (ODW) Data.....	18
2.3 Special Sensor Microwave/Imager (SSM/I) Data.....	21
3. SYNOPTIC REVIEW OF HURRICANE FLORENCE (1988).....	23
3.1 Breif Life History.....	23
3.2 Evolution of Florence's Convection.....	25
3.3 Upper-Tropospheric Environment of Florence and Its Possible Influences on Florence's Outflow.....	35

4.	NRL REGIONAL ANALYSIS AND FORECAST SYSTEM.....	46
4.1	Data Analysis System.....	46
4.1.1	Quality Control on the Sounding Data.....	47
4.1.2	Barnes Objective Analysis.....	49
4.2	Three-dimensional Prediction Model.....	55
4.2.1	Governing Equations.....	56
4.2.2	Grid Structure.....	59
4.2.3	Numerical Scheme.....	61
4.2.4	Boundary Conditions.....	66
4.3	Physics of the Model.....	67
4.3.1	Horizontal Diffusion.....	67
4.3.2	Cumulus Convection.....	68
4.3.3	Large Scale precipitation.....	70
4.3.4	Dry Convective Adjustment.....	73
4.3.5	Planetary Boundary Layer.....	73
4.4	Vertical Mode Initialization.....	74
5.	OBJECTIVE ANALYSIS AND INITIALIZATION OF FLORENCE.....	77
5.1	Analyses of Florence.....	77
5.1.1	Result With Two-Pass, Single-Grid Barnes Scheme.....	77
5.1.2	Result With Three-Pass, Nested-Grid Barnes Scheme.....	86
5.1.3	Summary.....	94
5.2	Initialization of Florence.....	95
6.	SIMULATION OF HURRICANE FLORENCE (1988).....	100
6.1	Control Experiment with NMC/RAFS 2.5 Degree Analyses.....	100
6.2	Integrations from the the ODW1 and ODW2	

Enhanced Analyses.....	106
6.3 Comparison of Simulated Rain Rates and SSM/I Imageries.....	118
6.4 Summary.....	124
7. ASSIMILATION OF SSM/I RAINFALL RATE DATA.....	128
7.1 Control Experiment with the Assimilation of the SSM/I Rain Rates.....	131
7.2 ODW2 Experiment with the Assimilation of the SSM/I Rain Rates.....	139
7.3 Summary.....	143
8. STRUCTURE OF OUTFLOW LAYER AND JET AS REVEALED BY MODEL SIMULATIONS.....	148
8.1 General Structure.....	148
8.2 Cross-Sections of the Model Outflow Jet.....	155
8.3 Angular Momentum Budget.....	162
9. UPPER-TROPOSPHERIC ENVIRONMENTAL INFLUENCES ON FLORENCE.....	167
10. SUMMARIES.....	186
10.1 Conclusions.....	186
10.2 Future Research.....	194
11. LIST OF REFERENCES.....	196

LIST OF TABLES

Table	Page
3.1 Preliminary Best Track of Hurricane Florence, obtained from National Hurricane Center (NHC) in Miami, Florida.....	26
5.1. Minimum SLPs, minimum 1000 mb heights, maximum 1000 mb wind speeds from the best track record, NMC/RAFS 2.5 ⁰ Analysis and three different ODW enhanced analyses. The minimum 1000 mb height was not available from the best track record.....	82
6.1. Minimum SLP (mb), maximum wind speed (ms^{-1}) and location of storm center from the best track record, the control experiment, Exp. ODW1 and ODW2.....	105
6.2 Landfall times and locations from the best track record, the control experiment, Exp. ODW1 and ODW2. The landfall locations relative to the location shown in the best track record are also listed.....	125
7.1. Minimum SLP (mb), maximum wind speed (ms^{-1}) and location of storm center from the best track record,	

	Exp. Control+SSMI and ODW2+SSMI.....	132
7.2	Landfall times and locations from the best track record, the control experiment, Exp. Control+SSMI, ODW2 and ODW2+SSMI. The landfall locations relative to the location shown in the best track record are also listed.....	146
8.1	Model and empirical angular momentum budget in the outflow layer of tropical cyclone. Units are in 10^{22} g cm ⁻² s ⁻² . The values for mean storms are adopted from Anthes (1974).....	165
9.1.	Minimum SLP (mb), maximum wind speed (ms ⁻¹) and location of storm center from the best track record, Exp. ODW2 and ODW2+WTR.....	172
9.2	Model angular momentum budget in the outflow layer of tropical cyclone. Units are in 10^{22} g cm ⁻² s ⁻²	185

LIST OF FIGURES

Figure		Page
1.1	Upper-tropospheric outflow layer Analysis for Hurricane Camile, 1969. Values of isotaches are in ms^{-1} . The principle outflow channel is north of the cyclone center. Circle is at radius of 6° latitude (666 km). Figure adapted from Black and Anthes (1971).....	5
1.2	Same as Figure 1.1 except for Hurricane Irene, 1981. The outflow channel is located to the northeast of the cyclone center. Figure adapted from Smith (1975).....	5
1.3	Outflow channel schematic from Sadler (1976). Note that the cyclone is located to the right rear of the wind speed maximum in the outflow channel.....	10
2.1	Location and time (UTC) of the Omega-Dropwindsonde data collected during Synoptic Flow Experiment on 8-9 September 1988.....	20
3.1	Position and Intensity (maximum winds in meters per second) of Hurricane Florence (7-10 September 1988)	

	at every 6 hour. Crosses locate Florence's position at 0000 UTC each day. Figure adapted from Rodgers et al. (1991).....	24
3.2	SSM/I retrieved rain rates at 1200 UTC 7 September 1988.....	27
3.3	Same as Fig. 3.2 except for 0000 UTC 8 September 1988.....	29
3.4	Same as Fig. 3.2 except for 1200 UTC 8 September 1988.....	30
3.5	Same as Fig. 3.2 except for 0000 UTC 9 September 1988.....	31
3.6	Same as Fig. 3.2 except for 1200 UTC 9 September 1988.....	33
3.7	Same as Fig. 3.2 except for 0000 UTC 10 September 1988.....	34
3.8	GOES VISSR infrared (11.5 μ m) image of Hurricane Florence between 0200 UTC and 1200 UTC 9 September 1988 at 2 hour interval. The white contours depict the	

	warmest VISSR infrared water vapor ($6.7\ \mu\text{m}$) brightness temperature between 258 and 264 degree K at 2 degree K interval. The star depicts Florence's center. Figure adapted from Rodgers et al. (1991).....	36
3.9	Same as Fig. 3.8 except for the time between 1000 UTC and 1500 UTC 9 September 1988 at 1 hour interval.....	37
3.10	Geopotential heights (m) and wind vectors at 250 mb of the NMC/RAFS 2.5 ⁰ analysis at 1200 UTC 8 September 1988.....	38
3.11	Same as Fig. 3.10 except for 0000 UTC 9 September 1988.....	40
3.12	Same as Fig. 3.10 except for the isotaches (ms^{-1}) at 0000 UTC 9 September 1988.....	41
3.13	Same as Fig. 3.10 except for 1200 UTC 9 September 1988.....	42
3.14	Same as Fig. 3.10 except for the isotaches (ms^{-1}) at 1200 UTC 9 September 1988.....	43
3.15	Cirrus-level winds (ms^{-1}) and streamline analysis for	

	Hurricane Florence at 1200 UTC 8 September, 0000 UTC and 1200 UTC 9 September 1988. Shaded area represents wind speeds $\geq 25 \text{ ms}^{-1}$. Hurricane symbol depicts the center of Florence. Dashed line represents the upper-level tropospheric trough's axis. Full wind barb represents 10 ms^{-1} . Figure adapted from Rodgers et al. 1991.....	44
4.1	Analysis domain for the nested three-pass objective analysis. Shaded area is for the first and second pass. Plain area inside the shaded area is for the third pass. The hurricane symbol depict the location of Florence's center at 0000 UTC 9 September 1988.....	54
4.2	Horizontal and vertical grid network utilized in the model for the simple case $K = 2$	60
4.3	Model's σ -coordinate structure for this study	62
4.4	Division of time interval $2\Delta t$ into m -subintervals used in the split-explicit time integration scheme.....	65
5.1a	Sea level pressures (mb) and surface temperatures (degree C) of the NMC 2.5 ⁰ analysis at 0000 UTC 9 September 1988.....	78

5.1b	Same as Fig. 5.1a except for the 1000 mb geopotential heights (m) and wind vectors (ms^{-1}).....	79
5.1c	Same as Fig. 5.1a except for the 1000 mb isotaches.....	81
5.2a	Sea level pressures (mb) and surface temperatures (degree C) of the ODW1 enhanced analysis by the single-grid two-pass Barnes scheme.....	83
5.2b	Same as Fig. 5.2a except for the 1000 mb geopotential heights (m) and wind vectors (ms^{-1}).....	84
5.2c	Same as Fig. 5.2a except for the 1000 mb isotaches.....	85
5.3a	Sea level pressures (mb) and surface temperatures (degree C) of the ODW1 enhanced analysis by the nested three-pass Barnes scheme.....	87
5.3b	Same as Fig. 5.3a except for the 1000 mb geopotential heights (m) and mb wind vectors (ms^{-1}).....	88
5.3c	Same as Fig. 5.3a except for the 1000 mb isotaches.....	90
5.4a	Sea level pressures (mb) and surface temperatures	

	(degree C) of the ODW2 enhanced analysis by the nested three-pass Barnes scheme.....	91
5.4b	Same as Fig. 5.4a except for the 1000 mb geopotential heights (m) and wind vectors (ms^{-1}).....	92
5.4c	Same as Fig. 5.4a except for the 1000 mb isotaches.....	93
5.5	1000 mb temperatures of the NMC 2.5 ⁰ analysis at 0000 UTC 9 September 1988.....	97
5.6	Sea level pressures (mb) and surface temperatures (degree C) of the ODW2 enhanced analysis by the nested three-pass Barnes scheme after intialized by the Vertical Mode Initialization (VMI).....	98
5.7	Same as Fig. 5.6 except for 1000 mb isotaches.....	99
6.1a	Sea level pressures (mb) and surface temperatures (degree C) of the control experiment at 12 hour.....	102
6.1b	Same as Fig. 6.1a except for 18 hour.....	103
6.1c	Same as Fig. 6.1a except for 24 hour.....	104

6.2a	Sea level pressures (mb) and surface temperatures (degree C) of Exp. ODW1 at 12 hour.....	107
6.2b	Same as Fig. 6.2a except for 18 hour.....	108
6.2c	Same as Fig. 6.2a except for 24 hour.....	109
6.3a	Sea level pressures (mb) and surface temperatures (degree C) of Exp. ODW2 at 12 hour.....	110
6.3b	Same as Fig. 6.3a except for 18 hour.....	111
6.3c	Same as Fig. 6.3a except for 24 hour.....	112
6.4	Tracks of Florence in the best track record, the control experiment, Exp. ODW1 and ODW2.....	114
6.5	Evolution of minimum SLP of Florence with time in the best track record, the control experiment, Exp. ODW1 and ODW2.....	117
6.6	Simulated rain rate (mm h^{-1}) of the control experiment at 12 hour.....	119
6.7	Same as Fig. 6.6 except for 24 hour.....	120

6.8	Simulated rain rate (mm h^{-1}) of Exp. ODW2 at 12 hour.....	122
6.9	Same as Fig. 6.8 except for 24 hour.....	123
7.1a	Sea level pressures (mb) and surface temperatures (degree C) of Exp. Control+SSMI at 12 hour.....	133
7.1b	Same as Fig. 7.1a except for 18 hour.....	134
7.1c	Same as Fig. 7.1a except for 24 hour.....	135
7.2	Tracks of Florence in the best track record, control experiment, Exp. Control+SSMI, ODW2 and ODW2+SSMI....	137
7.3	Simulated rain rates of Exp. Control+SSMI at 24 hour.....	138
7.4a	Sea level pressures (mb) and surface temperatures (degree C) of Exp. ODW2+SSMI at 12 hour.....	140
7.4b	Same as Fig. 7.4a except for 18 hour.....	141
7.4c	Same as Fig. 7.4a except for 24 hour.....	142

7.5	Simulated rain rates of Exp. ODW2+SSMI at 24 hour.....	144
7.6	Evolution of minimum SLP of Florence with time in the best track record, the control experiment, Exp. Control+SSMI, ODW2 and ODW2+SSMI.....	145
8.1	200 mb geopotential heights (m) and wind vectors (ms^{-1}) of Exp. ODW2+SSMI at 12 hour.....	149
8.2	Same as Fig. 8.1 except for the 200 mb isotaches.....	151
8.3	same as Fig. 8.2 except for 24 hour.....	152
8.4	Same as 8.1 except for the 200 mb relative humidities.	154
8.5	Location of cross-sections. 7 cross-sections are in the entrance region of the outflow jet --- A1 to A7, and 6 cross-sections are in the exit region --- B1 to B6. Contours are the 200 mb isotaches. Shaded area represents the area with wind speed greater than 30 ms^{-1}	156
8.6	Composite cross-section in the entrance region of the outflow jet of Exp. ODW2+SSMI at 24 hour. Contours are the wind component (ms^{-1}) normal to the	

	cross-section (positive means blowing into the paper). Vectors are the combination of the vertical velocity (mb h^{-1}) and the wind component (ms^{-1}) tangential to the cross-section. Shaded area are the relative humidity.....	157
8.7	Same as Fig. 8.6 except for the composite cross-section in the exit region of the outflow jet.....	159
8.8	Same as Fig. 8.6 except that the shaded areas are the horizontal potential temperature (degree C) deviation...	161
9.1	Sea level pressures (mb) and 1000 mb wind vectors (ms^{-1}) of the ODW2+WTR analysis after initialized by the VMI.....	169
9.2	200 mb isotaches of the ODW2 analysis after initialized by the VMI.....	170
9.3	Same as Fig. 9.2 except for the ODW2+WTR analysis after initialized by the VMI.....	171
9.4	200 mb isotaches of Exp. ODW2+WTR at 12 hour.....	174
9.5	Same as Fig. 9.4 except for Exp. ODW2.....	175

9.6	Mean convective rain rates of Exp. ODW2 and ODW2+WTR inside a $2^0 \times 2^0$ box centered at the storm center. Dashed box contains mean convective rain rates between 10 and 15 hour.....	176
9.7	200 mb relative humidities of Exp. ODW2+WTR at 12 hour.....	178
9.8	Same as Fig. 9.7 except for Exp. ODW2.....	179
9.9	Same as Fig. 8.6 except for Exp. ODW2+WTR.....	180
9.10	Same as Fig. 8.7 except for Exp. ODW2+WTR.....	181
9.11	Same as Fig. 8.6 except for Exp. ODW2.....	182
9.12	Same as Fig. 8.7 except for Exp. ODW2.....	183
10.1	Sea level pressure (mb), 950 mb wind vectors (ms^{-1}) and integrated water vapor (cm) of Exp. ODW2 at 12 hour.....	192

LIST OF SYMBOLS

b	$=r_m$, partitioning parameter
d_{gp}	grid-point distance between the grid point (i,j) and the center of the model domain
d_i	radius of influence
d_n	distance between two grid points
e_0	correction value at observation location in the first correction pass
e_1	correction value at observation location in the second correction pass
e_s	saturation water vapor pressure at a given temperature
f	Coriolis parameter
g	acceleration due to gravity
g_0	estimated value at observation location for the first correction pass
h	height
h_x	map factor in the x-direction
h_y	map factor in the y-direction
i	grid point index in the x-direction
i_c	x-direction grid point value of the center of the model
j_c	y-direction grid point value of the center of the model
j	grid point index in the y-direction
m	$=rv$, relative angular momentum
q	specific humidity

q_c	specific humidity of cloud
q_e	specific humidity of the environment
q_s	saturation specific humidity at a given temperature
r	radius
r_0	radius of the maximum tangential wind
r_m	vertically averaged relative humidity
t	time coordinate
u	velocity component in the x-direction; radial wind component in the cylindrical coordinates
v	velocity component in the y-direction; tangential wind component in the cylindrical coordinates
w	velocity component in the z-direction
w_n	weighting function
C_p	specific heat for dry air at constant pressure
D	mass divergence
D_n	average minimum station spacing
\tilde{D}	surface pressure tendency
F	any dependent variable of the model
F_u	the friction force in the x-direction
F_v	the friction force in the y-direction
F_T	source or sink of heat
F_q	source or sink of moisture
G_0	correction value at grid point in the first correction pass
G_1	correction value at grid point in the second correction pass
H	total amount of water vapor needed to create a cloud over

	an unit area
K	= R/C_P ; index
K_H	horizontal diffusion coefficient
L	latent heat of condensation
M	total angular momentum in a certain volume; the total number of grid points in the x-direction; horizontal moisture convergence per unit area
M_t	total moisture convergence per unit column
N	the total number of grid points in the y-direction; northern hemisphere
P	pressure
P_b	pressure of the bottom of a cumulus cloud
P_s	surface pressure
P_t	pressure of the top of a cumulus cloud
R	gas constant for dry air; rain rate
R_c	critical radius
R_v	gas constant for water vapor
T	temperature
T_c	cloud temperature
T_e	environmental temperature
\vec{V}	velocity
W	western hemisphere
X	any dependent variable of the model
X_0	NMC/RAFS 2.5 ⁰ analysis
δx	finite difference operator in the x coordinate

δy	finite difference operator in the y coordinate
$\delta \sigma$	finite difference operator in the σ coordinate
Δx	half degree longitude distance at equator
Δy	half degree latitude distance at equator
Δt	time interval
α	weighting parameter
ϕ	geopotential; latitude
γ	numerical convergence parameter; relaxation parameter
η	factor to represent the nonmeasurable subgrid scale supply of moisture
κ	weight parameter; $=R/C_p$
θ	potential temperature; latitude
ρ	air density
ρ_w	air density of water
σ	$= P/P_s$, vertical coordinate in the model
$\dot{\sigma}$	$= d\sigma/dt$, vertical velocity in the σ coordinate
σ_0	$= 1000/P_s$
σ_t	value of σ at the cloud top
$\Delta \sigma$	vertical depth of each layer in the model
$\Delta \tau$	subdivided time interval of Δt
ω	$= -dp/dt$, vertical velocity in P-coordinate
∇	mathematical gradient operator

1. INTRODUCTION.

1.1 Background.

Mature hurricanes or typhoons are among the most destructive of all natural disasters and produce tremendous annual losses in lives and properties. With the gale force wind and torrential rainfall, they are capable of completely destroying coastal towns and killing hundreds of thousands of people in many countries around the globe (Anthes, 1982).

A tropical storm is generally defined as a warm core, low pressure system in which the maximum sustained surface wind is 35 knots (17 ms^{-1}) or greater. Tropical storms with a maximum sustained surface wind equal or exceeding 65 knots (33 ms^{-1}) are defined as tropical cyclones (over the Indian Ocean), hurricanes (over the Atlantic Ocean and the Eastern Pacific Ocean) or typhoons (over the Western Pacific Ocean).

Numerous observational and numerical modeling studies during the past 40 years have tremendously increased our understanding of these destructive storms. The adoption of satellite data also helps forecasters and scientists to track the movement and intensity of tropical cyclones. However, as compared to the understanding of mid-latitude weather systems, most of the structure and behavior

of tropical cyclones are still not fully understood, mainly because of the insufficient observational data over the vast tropical ocean.

Past studies (Black and Anthes, 1971; Sadler, 1976 and 1978; Frank, 1977b; Tyleya and Kurihara, 1981; Pfeffer and Challa, 1981; Merrill, 1984; Holland and Merrill, 1984; Chen and Gray, 1984; Ooyama, 1987; Merrill, 1988 a and b; Molinari and Vollaro, 1989 and 1990; Kaplan and Franklin, 1991; Shi et al., 1990; Rodgers et al., 1991; DeMaria et al., 1993) have demonstrated that the movement and growth of tropical cyclones are affected by the interaction between the upper layer of tropical cyclones and its environmental flows. For example, Holland and Merrill (1984) pointed out that the strong cyclonic vorticity in the lower and middle troposphere in an intense tropical cyclone becomes more stable and likely more resistant to environmental forcing, whereas the upper tropospheric anticyclonic, asymmetric outflow is not as stable inertially (Black and Anthes, 1971), and therefore may be less resistant to the environmental forcing. Thus, the movement and intensity of an intense tropical cyclone would probably respond more rapidly to upper tropospheric forcings. Therefore, an improved understanding of the structure of the outflow layer of tropical cyclone is important in predicting tropical cyclone intensification and motion.

Real data analysis of the outflow layer of the tropical cyclone is almost impossible because of the sparsity of the observational

data over the tropical ocean. Even when some observational data are available, the studies still suffer from not enough resolution in the time domain. Much of our knowledge has come from composite studies (Black and Anthes, 1971; Sadler, 1976 and 1978; McBride, 1981; Chen and Gray, 1984; Merrill, 1988 a and b; DeMaria et al., 1993), a few case studies (Molinari and Vollaro, 1989 and 1990; Kaplan and Franklin, 1990; Rodgers et al., 1991) or some idealized model studies (Tyleya and Kurihara, 1981; Pfeffer and Challa, 1981; Ooyama, 1987; Shi et. al, 1990).

As will be discussed in Chapter 3, observational evidence suggests that the upper tropospheric, environmental forcing was a key factor for the intensification of Hurricane Florence (1988). Therefore, this storm will be further investigated using a three-dimensional, primitive equation, tropical cyclone model initialized with conventional synoptic data enhanced by high spatial resolution observational data. It is assumed that Florence's convection system and its outflow structure and dynamics can be realistically simulated so that high resolution data in the time domain will be obtained. The numerical model can then be used as a tool to study the environmental flow influence on the outflow of Florence.

1.2 Literature Review.

1.2.1 General Characteristics of the Outflow Layer of

Tropical Cyclones.

The outflow layer of the tropical cyclone is generally anticyclonic and divergent on the synoptic scale. It is considerably more asymmetric than the middle and lower layers (Alaka, 1961, 1962; Miller, 1963). Black and Anthes (1971) noted that the outflow circulation is highly asymmetric, especially beyond 400 km from the storm center where the standard deviation of the radial and tangential wind components exceed the mean value. In their study, the asymmetric part of the circulation is obtained by subtracting the axisymmetric part of the circulation from the total flow. The resultant circulation, defined as the asymmetric wind, reveals that two eddies dominate the outflow structure. It is suggested that these eddies are organized by the environmental flow streaming around the divergent outflow field.

The outflow layer of the tropical cyclone is comparatively shallow, generally confined between 100 and 300 mb (Frank, 1977a). The asymmetric outflow of the tropical cyclone is characterized by outflow jets. Merrill (1984) mentioned that the outflow from a hurricane appears to be concentrated into one or two outflow maxima or channels. The wind maximum in the outflow layer can normally be found to the north or northwest of the storm center. Figs. 1.1 and 1.2 show this concept. Chen and Gray (1984) speculated that the outflow jets help to remove mass from the

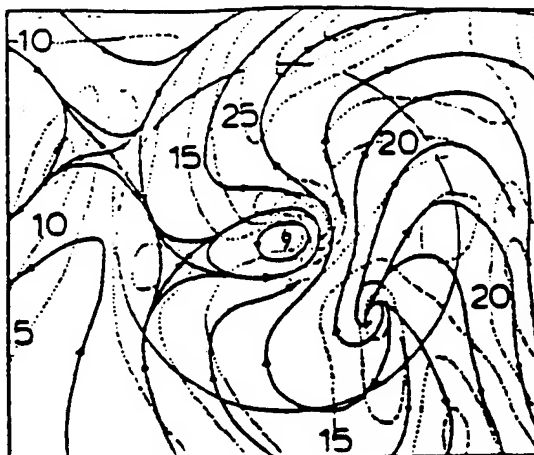


Figure 1.1 Upper-tropospheric outflow layer Analysis for Hurricane Camile, 1969. Values of isotaches are in ms^{-1} . The principle outflow channel is north of the cyclone center. Circle is at radius of 6° latitude (666 km). Figure adapted from Black and Anthes (1971) .

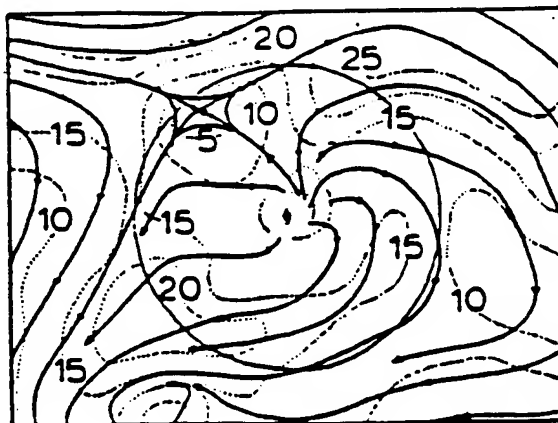


Figure 1.2 Same as Figure 1.1 except for Hurricane Irene, 1981. The outflow channel is located to the northeast of the cyclone center. Figure adapted from Smith (1975).

central region and transport the warm and dry air to outer regions, maintaining the convective instability near the eye.

Merrill (1984) noted that the appearance of outflow channels is similar to that of the "jet streaks" which are commonly observed in association with the mid-latitude troughs. He also speculated that the upper-tropospheric, baroclinic processes may be important in the hurricane outflow jet streak. He speculated that there may be a possible secondary circulation around the outflow layer, similar to the jet streak in mid-latitudes. In the classical jet streak theory (Palmen and Newton, 1969), confluence of the synoptic scale flow into the entrance region results in a stronger temperature gradient and the development of a thermally direct secondary circulation with ascending motion occurring to the warm side of the upper-tropospheric temperature gradient. This circulation acts to reduce the temperature gradient and decrease the vertical shear to keep the flow in thermal-wind balance. Therefore the jet streak would increase the upper-tropospheric vertical motion within the convective region of the cyclone. This would then enhance deep convection, and shift the net convective heating upward. The outgoing flux of warm air from the cyclone center acts to further increase the temperature gradient, and thus, results in a positive feedback.

Merrill (1984) also noticed that there exists a secondary

maximum inflow layer at approximately 400 mb level, which could be the return branch of the secondary circulation. The existence of jet streaks and the secondary circulations may also explain the existence of cirrus lines oriented radially outward from the cyclone which are sometimes observed in intensifying cyclones.

Ooyama (1987) was able to generate the asymmetric outflow in various environmental flows in a simple two dimensional (in the x- and y- directions) model of the outflow layer using shallow water equations with a prescribed upwelling mass flux. In his model study, two well-defined outflow channels in opposite directions were generated in a horizontally sheared environmental flow with easterly to the south and westerly to the north, while only one well-defined channel was generated in a horizontally sheared environmental flow with only westerlies. He also found that the cyclonic vorticity only exists within a radius of 250 km in his model.

The numerical study by Shi et al. (1990) demonstrated that the existence of a circum-jet secondary circulation at the entrance region of the outflow jet. They found that the circum-jet secondary circulation at the entrance region of the outflow jet is thermally induced with the ascending branch located on the anticyclonic shear side of the outflow jet, and the descending branch located at the cyclonic shear side of the outflow jet. Monilari and Vollaro (1989)

also speculated that the upward motion constantly occurs at radii inside of the outflow maximum.

In his composite study, Merrill (1988a) found that the upper-tropospheric circulation associated with a hurricane is clearly visible on the synoptic scale with a substantial asymmetric component of both radial and tangential winds. However, he also stated that the outward branch of the hurricane's secondary circulation found in the outflow layer between 100-300 mb, which was demonstrated in his previous result, is somewhat misleading, since the flows in the upper troposphere are obviously not all coming out from the hurricane, although these flows may interact with each other in some important ways.

1.2.2 Influence of the Environment on the Outflow layer and the Intensification of a Tropical Cyclone.

In the past two decades, there are many observational studies (e.g. Sadler, 1976 and 1978; Steranka et al., 1986; Rodgers et al., 1987; Merrill, 1988 a and b; Molinari and Vollaro, 1989 and 1990; Shi et al., 1990; Rodgers et al., 1991) which link the behavior of tropical cyclones to the strength and position of upper tropospheric troughs (UTTs). Sadler showed that in general as an UTT aligns vertically with the underlying tropical cyclone, the tropical cyclone weakens. If a tropical cyclone is aligned with an upper tropospheric

ridge, the cyclone generally intensifies. However, the relationship between the UTTs and a tropical cyclone is not simple and straightforward. For example, Chen and Gray (1984) suggested that the outflow jets are formed by the coupling of the storm's outflow with upper- and mid-tropospheric troughs. Rodgers et al. (1987) also observed this phenomenon.

In spite of the evident relationship between UTTs and the intensity of tropical cyclones, the mechanisms of the intensification still are not fully understood. But, an outflow channel to the westerlies has long been recognized as a requirement for tropical storm development. Sadler (1976) suggested that the multi-directional outflow channels to the large scale circulation of the upper troposphere serve to remove the excess heat in the tropical cyclone's central region. Fig. 1.3 is a schematic illustrating the relationship between the tropical storm outflow and some common large circulation patterns. In Fig. 1.3a, the storm's northern outflow is suppressed when it is located in a region of upper-tropospheric northeasterly. In Fig. 1.3b, the eastern side of deep troughs in the westerlies is the principal outflow channel for the cyclone. In Fig. 1.3c, there is an outflow channel to the east of an UTT into the large-scale westerlies and an outflow into the equatorial easterlies south of the sub-equatorial ridge. This configuration permits vigorous outflow for efficient removal of mass and heat from the tropical cyclone, and is, therefore, most

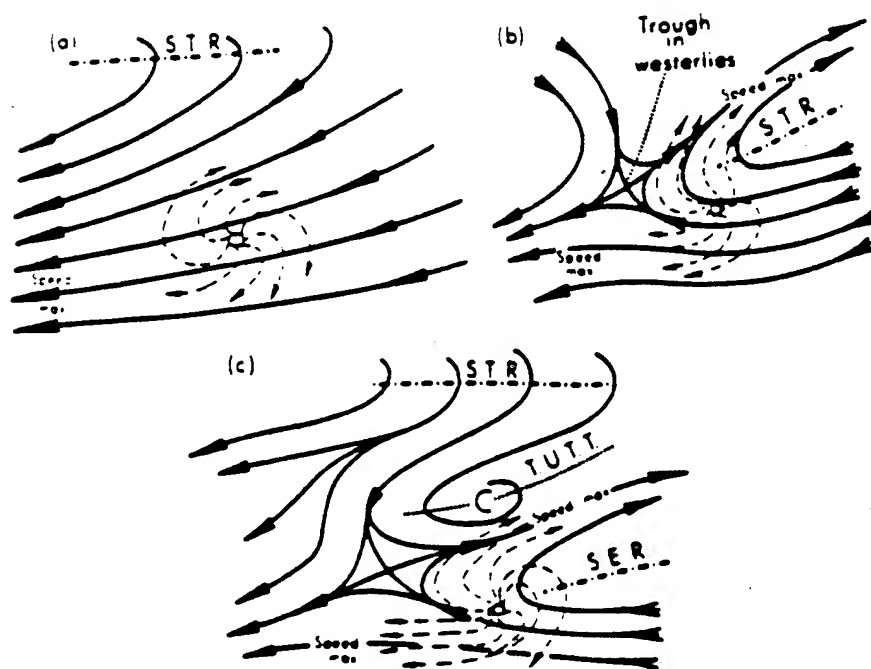


Figure 1.3 Outflow channel schematic from Sadler (1976). Note that the cyclone is located to the right rear of the wind speed maximum in the outflow channel.

favorable for intensification.

According to Sadler(1976), a tropical cyclone is likely to intensify if it is surrounded by concentrated air currents to the east of an upper-tropospheric trough in the upper troposphere or by a strong equatorial outflow channel (see Fig. 1.3). Sadler (1978) further elaborated that the strengthening of an outflow channel can extend inward towards the storm center and act as an outflow link to the cyclone's inner region of deep convection.

Holland and Merrill (1984) used observations in the Australian southwest Pacific region with the help of a axisymmetric diagnostic model to study the dynamics of tropical cyclone structural changes. They found that a poleward outflow jet is formed by a coupling between the tropical cyclone and passing disturbances in the subtropical westerlies. They further elaborated that a dominant feature of the interaction is the strong poleward outflow into the divergent region ahead of an approaching westerly trough. Their research provided an important conclusion that upper tropospheric interactions between tropical cyclones and their environments can directly affect intensity change.

Recent study of satellite-measured total ozone amount by Rodgers et al. (1987) suggested that the enhancement of the inner core convection of a tropical cyclone can be related to the upper-

tropospheric environment forcing. They found that an increase in the inner core convection in Hurricane Irene (1980) was preceded by the formation of an outflow channel. When the strength of the outflow channel decreased, the inner core convection weakened abruptly. They also found that there was a 33 hour lag between the changes in the inner core convection and Irene's intensity changes.

Based on the satellite derived tracers (e.g., cirrus clouds, water vapor, and ozone), Rodgers et al. (1991) suggested that the intensification of Hurricane Florence (1988) was caused by the approaching of the upper-tropospheric trough from the west. They also indicated that the development of the second convective cell north of the Florence's center may have been initiated by the ascending branch of the circum-jet secondary circulation at entrance region of the outflow jet of Florence enhanced by an approaching westerly UTT. The numerical experiments by Shi et al. (1990) also showed that an accelerated outflow jet, which may be accelerated by an approaching westerly UTT, helps to increase the mass divergence in the outflow layer.

Most of the above results suggest that interactions with an UTT or upper-level westerly trough is favorable for intensification. In contrast to these results, Merrill (1988b) argued that the environmental interactions with mature tropical cyclones must, in general, contribute negatively to intensity change because real

tropical cyclones seldom attain the intensity allowable under theoretical constraints as described in Emanuel (1986). He stated that interaction with an upper-level westerly trough which stimulates intensification is not apparent, because such cases often end with the hurricane coming under increasing westerly shear and filling.

1.2.3 Eddy Angular Momentum Flux.

Pfeffer (1958) proposed that cyclonic angular momentum is transferred into the cyclonic core of the hurricane through the "horizontal-eddy" process. Black and Anthes (1971) found an anticyclonic eddy to the right and a cyclonic eddy to the left of the storm motion. These eddies also transport a significant amount of negative relative angular momentum outward. Anthes (1974) further stated that the outflow layer of actual storms exhibits a great degree of asymmetry as indicated by a sizable horizontal eddy angular momentum flux. He also noted that a large import of angular momentum is required to offset frictional loss to the sea.

Intense, well organized inward eddy angular momentum flux is found in developing Atlantic hurricanes and weak, poorly organized flux is found in non-developing disturbances (Pfeffer and Challa, 1981). In their model study, Pfeffer and Challa (1981) also stated that without the observed eddy flux convergence of momentum, a

weak disturbance is not capable of developing into a hurricane through only the Ekman pumping and cooperative instability in the model. Holland (1983), in his composite study, found that the azimuthal eddy transport of angular momentum is effective at large radii in the upper outflow layer for a developed cyclone, while the mean transverse circulation dominates the inner region.

Using a 5-year composite of Atlantic hurricanes, Merrill (1988a) found sizable eddy import of angular momentum in the outflow layer. However, he also quickly pointed out that there is no clear relationship between eddy angular momentum flux and intensity changes of hurricanes (Merrill, 1988b). He speculated that any benefits to the hurricane from the eddy angular momentum flux will be offset by the increasing vertical shear. Molinari and Vollaro (1989) analyzed the outflow layer winds of Hurricane Elena (1985) during its life cycle at 12 hour intervals for six days. They found that the azimuthal eddy angular momentum flux at large radii is important to the intensification of Elena. They also suggested that operational forecasts of tropical cyclones could benefit from the calculations of eddy momentum flux because they measure the integrated effect in the storm environment, regardless of the complexity of the interactions.

DeMaria et al. (1993) calculated the eddy flux convergence (EFC) of relative angular momentum for the named tropical cyclones

during 1989-1991 Atlantic hurricane seasons. They found that a period of enhanced EFC within 1500 km of the storm center occurred about every 5 days due to the interaction with upper-level troughs. They also stated that the storm intensified just after the period of enhanced EFC in about one-third of the cases.

1.3 Research Objective

The primary objectives of this study are: (1) to reveal the detail structures of the outflow layer and jet of Florence; (2) to investigate the interactions between Florence and its upper level environmental forcings.

The ODW data will be used to enhance the NMC/RAFS 2.5⁰ analyses using the three-pass, nested Barnes scheme. The enhanced data will be initialized by a vertical mode initialization (VMI) scheme and then used as the initial condition for the numerical model simulations. The SSM/I rainfall rates will be first used as the observational evidence of the evolution of Florence's convection and later be assimilated into the tropical cyclone model to increase the accuracy of the estimation of the moisture convergence in the cumulus parameterization. The structure of the outflow of the simulated Hurricane Florence, especially the outflow channel (or jet), will be carefully analyzed. The mass divergence, potential vorticity, upper-tropospheric relative humidity (RH), and angular

momentum budget will be calculated and discussed. The vertical structure of the outflow jet of the model Florence will also be analyzed. In addition, the sensitivity of the outflow layer and the intensity of Florence to an UTT will be examined by additional numerical experiments.

In Chapter 2, the sources of the data used for this study will be reviewed. In Chapter 3, the history and structure of Hurricane Florence will be discussed. Some observational evidence of Hurricane Florence regarding the convection and the influence of the UTT on the outflow and the intensity of Hurricane Florence will also be discussed in Chapter 3. In Chapter 4, the analysis and forecast system used in this study will be reviewed. The data enhanced by the ODW data using the objective analysis scheme will be presented in Chapter 5. In Chapter 6, the result of the numerical model simulations will be presented. The result of the SSM/I data assimilation into the numerical model for the simulation of Hurricane Florence will be shown in Chapter 7. In Chapter 8, the structure of the outflow jet and its cross-section will be analyzed. The sensitivity of the outflow and the intensity of Florence will be carried out in Chapter 9. Finally, the summaries and conclusions will be discussed in Chapter 10.

2. DATA SOURCES.

The data used for this numerical study were acquired from three different sources. The first data source is the 2.5° analyses of the Regional Analysis and Forecasting System (RAFS) of the National Meteorological Center (NMC). The second source is the Omega-Dropwindsonde (ODW) data acquired from the Hurricane Research Division of the Atlantic Oceanographic and Meteorological Laboratory (AOML/HRD) of the National Oceanic and Atmospheric Administration (NOAA). The third source is the Special Sensor Microwave/Imager (SSM/I) data acquired from the Remote Sensing Division of the Naval Research Laboratory (NRL). The NMC/RAFS 2.5° analyses were used as the first guess (background data) in the nested-grid analysis scheme which will be discussed in Chapter 4. The ODWs were used to enhance the NMC/RAFS 2.5° analyses. The SSM/I rain rates were assimilated into the numerical model as an observational rain rate in one of the model simulations. The SSM/I data were also used as the observational evidence and verification for the model generated rain rates.

2.1 NMC/RAFS 2.5 Degree Analyses.

The Regional Analysis and Forecasting System (RAFS) of the National Meteorological Center (NMC) was implemented operationally on 27 March, 1985. The purpose of the system is to provide the

improved short term numerical guidance up to 48 hours to forecasters throughout the United States (DiMego, 1988; Hoke et al., 1989). The principal emphasis is on improved prediction of quantitative precipitation and significant weather events.

The system consists of three components: the regional optimum interpolation analysis, the nonlinear normal initialization and the nested forecast model. The analysis is performed on a lat-long grid with a basic resolution of 2° longitude by 1.5° latitude. The data produced by the system are later archived with a resolution of 2.5° in both longitude and latitude direction at the Data Support Section of the National Center for Atmospheric Research (NCAR). The NMC/RAFS 2.5° Analyses at 00 UTC 9 September 1988 were obtained from NCAR for this numerical study.

2.2 Omega-Dropwindsonde (ODW) Data.

Since 1982, Synoptic Flow Experiments have been conducted by the Hurricane Research Division of the Atlantic Oceanographic and Meteorological Laboratory (AOML/HRD). The experiments are designed to determine the three-dimensional structure of tropical cyclones below ~400 mb within roughly 1000 km of the storm's center (Kaplan and Franklin 1991; Franklin and DeMaria 1992). During each Synoptic Flow Experiment, the experiment collected a set of Omega-Dropwindsonde (ODW) data which were deployed from NOAA WP-3D aircrafts flying near 400 mb surrounding the targeted

tropical storm.

Franklin and DeMaria (1992) demonstrated that the ODWs collected during the 1982-1989 Synoptic Flow Experiments resulted in highly consistent reductions in track forecast errors. In addition, they demonstrate the ability of utilizing all the data available with a scale-controlled objective analysis described by Ooyama (1987). Their results also suggest that the collection of the ODWs in the hurricane environment can be a viable, cost-effective means of improving operational hurricane forecasts. Furthermore, Franklin et al. (1993) used the ODWs in a nested objective analysis scheme following Ooyama (1987) and DeMaria et al. (1992) to determine the kinematic structure of Hurricane Gloria (1985). They mentioned that the nested analyses of Hurricane Gloria, based on the ODWs and Doppler radar data, are the most complete kinematic analyses of a single hurricane constructed to date.

A total of 51 ODWs were deployed from two NOAA WP-3D aircrafts flying near 400 mb during a Synoptic Flow Experiment on 8-9 September 1988. This makes more realistic description of the initial conditions for the numerical simulation of Florence possible. Fig. 2.1 shows the two flight routes, and the locations and release times of the ODWs. The release times ranged from 1817 UTC on 8 September 1988 to 0247 UTC on 9 September 1988. Each ODW consists of the time and date of launch, location of launch (longitude

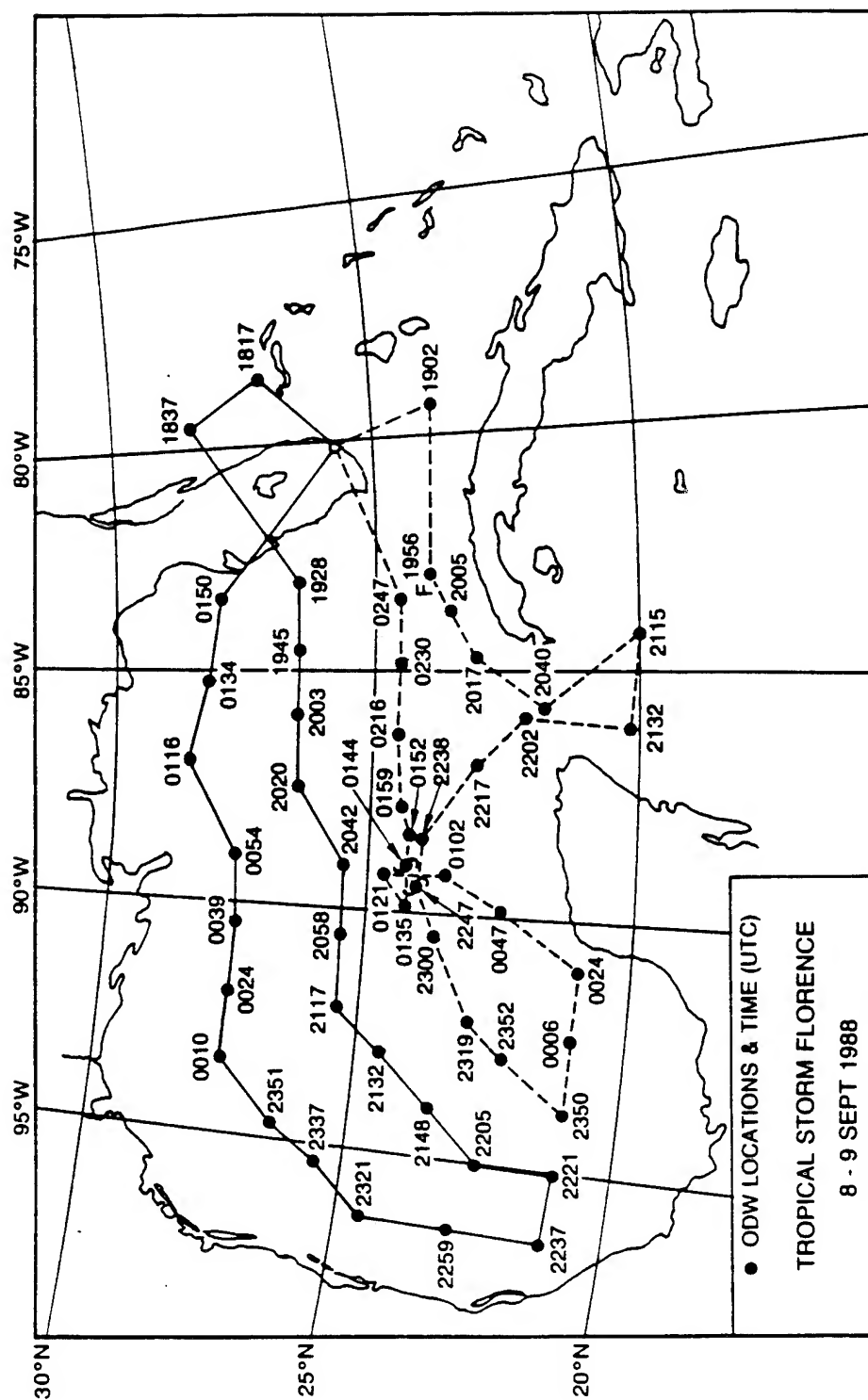


Figure 2.1 Location and time (UTC) of the Omega-Dropwindsonde data collected during Synoptic Flow Experiment on 8-9 September 1988.

and latitude) and the sounding data recorded at every 10 mb down from the flight level (ranged from 374 to 528 mb) to surface. The sounding data included pressure, temperature, relative humidity, geopotential height, wind direction, wind speed and wind uncertainty. The wind data were missing at lowest few levels near surface in every ODW record.

2.3 Special Sensor Microwave/Imager (SSM/I) Data.

The SSM/I is a seven-channel, four-frequency, linearly-polarized, passive radiometric system which measures atmospheric, ocean, and terrain microwave brightness temperatures (BT) at 19.3, 22.0, 37.0, and 85.5 GHz. According to Hollinger (1989 and 1991) the first Special Sensor Microwave/Imager (SSM/I) was launched on 19 June 1987 aboard a Defense Meteorological Satellite Program (DMSP) satellite. The DMSP satellite is a polar-orbiting satellite which orbits the earth in a near sun-synchronous mode at an altitude of 833 km, and with an orbit period of 102 minutes. The SSM/I data are processed to obtain near real-time global maps of cloud water, rain rates, integrated water vapor over ocean, marine wind speed and etc. Recent studies (Velden et al., 1989; Alliss et al., 1992 and 1993; Chang et al. 1993; Chang and Holt, 1993) have validated the usefulness of the meteorological parameters derived from the SSM/I brightness temperature data for observational or numerical studies.

By design, the seven channels consist of the vertical (V) and horizontal polarization (H) channels for 19, 37 and 85 GHz, and only the vertical polarization channel for 22 GHz. The 85 GHz (V) was deemed unusable during September 1988. In this study, a rain rate algorithm described by Hollinger (1991) was opted to convert the BT data to rain rates for six different times every 12 hours between 12 UTC 7 September to 00 UTC 10 September 1988, roughly covering the life span of Hurricane Florence until just before it made the landfall in New Orleans area. Following Hollinger (1991), the rain rate algorithm is

Over ocean:

$$R = \exp [-0.42383 - 0.0082985T_{85H} + 0.01496T_{19V} + 0.00583T_{19H}] - 4.0 \text{ mm h}^{-1} \quad (2.1)$$

Over land:

$$R = \exp [1.32526 - 0.8150T_{37V} + 0.01638T_{37H} + 0.03561T_{22V} + 0.05079T_{19V} - 0.01875T_{19H}] - 8.0 \text{ mm h}^{-1} \quad (2.2)$$

where R = rain rate and T_{37V} , T_{37H} , T_{19V} , T_{19H} , T_{22V} , and T_{85H} are the BT's of the 37 GHz (V) and 37 GHz (H), 19 GHz (V), 19 GHz (H), 22 GHz (V) and 85 GHz (H) channels, respectively. If the formulas produce a rain rate less than zero, the rain rate is set equal to zero.

3. Synoptic Review of Hurricane Florence (1988).

3.1 Brief Life History.

Fig. 3.1, adapted from Rodgers et al. (1991), shows Florence's position and intensity (maximum wind in ms^{-1}) every 6 hours between 0600 UTC on September 7 and 1200 UTC on September 10. Hurricane Florence's circulation started to form from a quasi-stationary frontal cloud band in the south-central Gulf of Mexico on September 7, 1988. The frontal cloud band had previously been associated with a cold front which entered the Gulf of Mexico from the northeast several days earlier. Florence was classified as a tropical depression with a maximum wind speed of 25 knot and a central pressure at 1000 mb at 0000 UTC September 7. The circulation quickly intensified into a tropical storm with a maximum wind speed of 40 knot and a central pressure of 998 mb at 1800 UTC September 7. It moved eastward in the first 24 hours and then turned northward on September 8. It moved toward the northern Gulf Coast and became a category-1 hurricane with a maximum wind speed of 65 knot and a central pressure of 985 mb at 1800 UTC on September 9. Florence made landfall over southeastern Louisiana at 0200 UTC on September 10, and quickly weakened as it moved over the New Orleans area and dissipated on the 11th in east Texas (Lawrence and Gross, 1989). The life span of Florence's circulation only lasted for about 4 days. There was one casualty that resulted

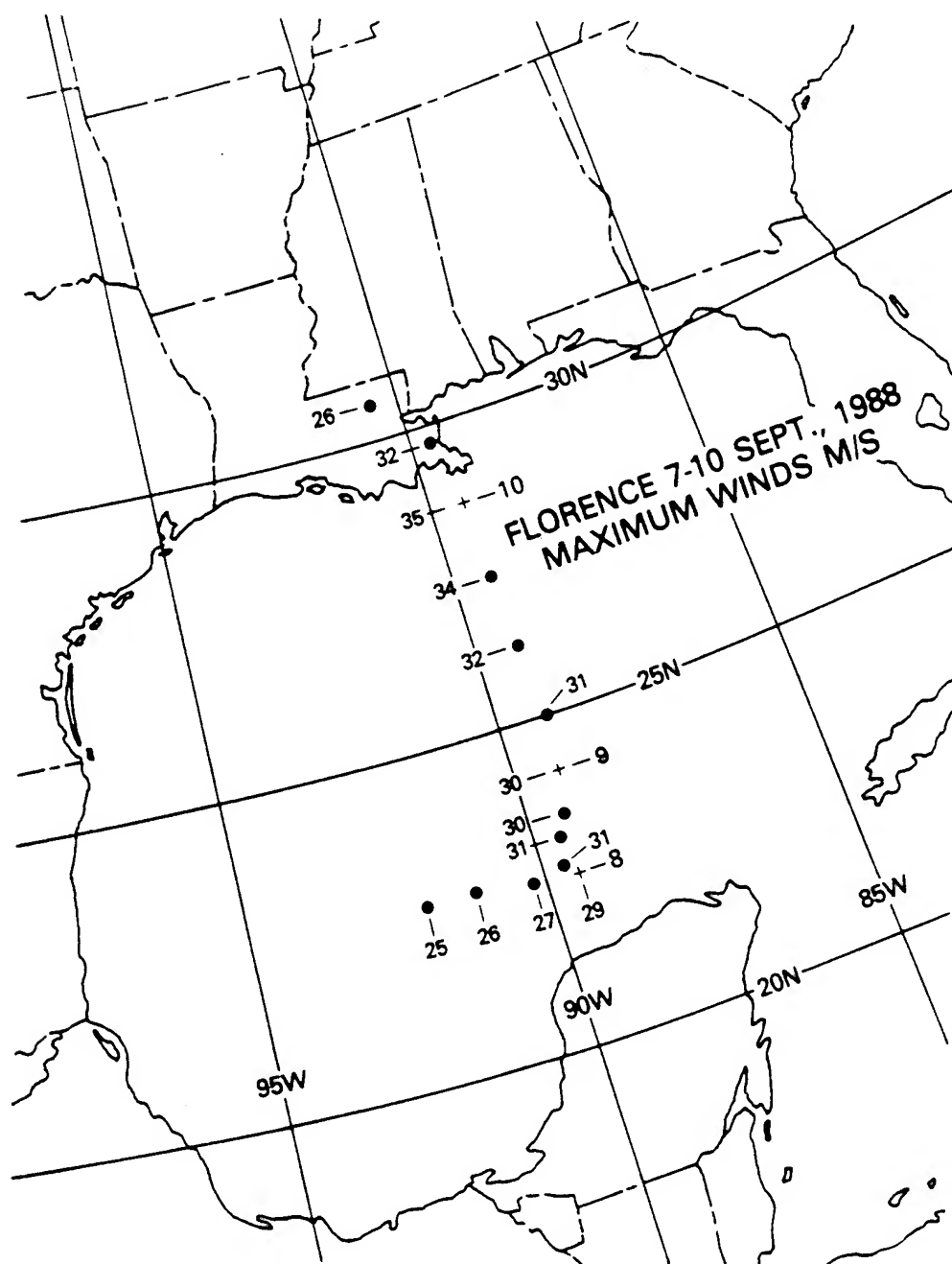


Figure 3.1 Position and Intensity (maximum winds in meters per second) of Hurricane Florence (7-10 September 1988) at every 6 hour. Crosses locate Florence's position at 0000 UTC each day. Figure adapted from Rodgers et al. (1991).

from Florence. One man died while trying to secure his boat. The damage total estimated at around 2.5 million dollars, primarily in southeastern Louisiana.

According to the best track data from the National Hurricane Center (NHC), Florence was a hurricane force for only 12 hours inside the time window from 1200 UTC on 9 September to 0600 UTC on 10 September (Table 3.1). Air Forces reconnaissance estimated that the highest sustained surface wind was 36 ms^{-1} and the lowest surface pressure was 982 mb occurring at 2300 UTC on September 9, just 3 hours before landfall. Rainfall totals of up to 100 mm were observed along the path of the storm (Lawrence and Gross, 1989). Florence caused the water level to rise from 1 to 2 m above normal along the southeast Louisiana and Mississippi coast just east of where the center moved ashore.

3.2 Evolution of Florence's Precipitation and Convection.

As mentioned in the previous chapter, SSM/I retrieved precipitation rate data for Florence were obtained at approximately 12 hour intervals from 1200 UTC September 7 to 0000 UTC September 10. Fig. 3.2 shows the SSM/I precipitation rate at 0000 UTC September 7 which was the time Florence was classified as a tropical depression by NHC. The area with relatively heavy rainfall of $>20 \text{ mm h}^{-1}$ at this time is located to the south of the center. At

DATE	TIME (UTC)	POSITION LATITUDE(N) LONGITUDE(W)	PRESSURE (mb)	WIND (ms ⁻¹)	STAGE
9/07	0600	22.8	92.0	1000	12.9 Tropical Depression
"	1200	22.8	91.2	998	15.4 "
"	1800	22.7	90.2	996	20.6 Tropical Storm
9/08	0000	22.6	89.6	993	23.1 "
"	0600	22.7	89.8	990	23.1 "
"	1200	23.1	89.7	990	23.1 "
"	1800	23.4	89.5	992	23.1 "
9/09	0000	24.2	89.2	992	25.7 "
"	0600	25.0	89.2	991	25.7 "
"	1200	26.1	89.2	988	28.3 "
"	1800	27.4	89.2	985	33.4 Hurricane
9/10	0000	28.7	89.3	983	36.0 "
"	0600	29.7	89.7	988	30.9 Tropical Storm
"	1200	30.7	90.7	998	15.4 Tropical Depression
"	1800	31.8	91.5	1003	10.3 "
9/11	0000	32.4	92.3	1007	7.7 "
"	0600	32.7	93.3	1009	7.7 "
"	1200	33.0	94.5	1010	7.7 "
9/09	2300	28.5	89.3	982	36.0 Minimum Pressure
9/10	0200	29.1	89.3	984	36.0 Landfall

Table 3.1. Preliminary Best Track of Hurricane Florence, obtained from the National Hurricane Center in Miami, Florida.

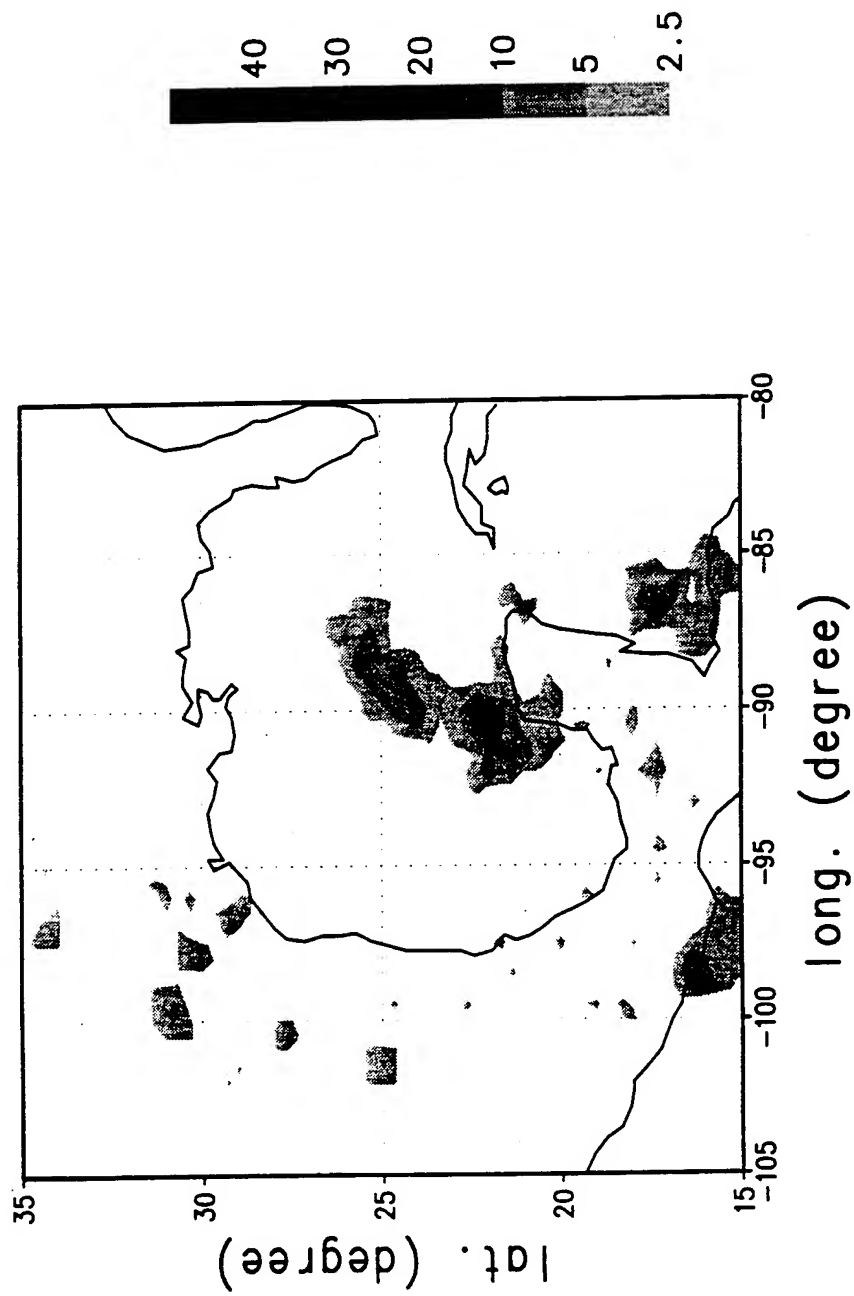


Figure 3.2 SSM/I retrieved rain rates at 1200 UTC 7 September 1988.

0000 UTC September 8, the SSM/I precipitation rate (Fig. 3.3) shows that the area of heavy rainfall of $>20 \text{ mm h}^{-1}$ had expanded slightly. Florence had become a tropical storm by this time with a maximum sustained wind estimated to be 23.1 ms^{-1} (see Table 3.1). As the storm center moved eastward for about 1.6° longitude, the convective region also moved eastward. At this time, the storm center was still north of the convective region. At around 0000 UTC September 8, Florence started to moved northward.

Twelve hours later at 1200 UTC September 8, the SSM/I retrieved precipitation rate (Fig. 3.4) revealed two areas of convective region. The first convective region, associated with Florence, was located along the northern coast of the Yucatan Peninsula and was south of the low-level center. The second region was located off the west coast of Florida over the northeastern Gulf of Mexico. The second area had weaker convection and was an extension of the stationary frontal system that extended to the North Carolina coast. The intensity of the precipitation rate associated with Florence had increased from $>20 \text{ ms}^{-1}$ to $> 25 \text{ ms}^{-1}$. At this time, Florence was 0.6° north of its previous location.

At 0000 UTC September 9, the SSM/I derived precipitation rate (Fig. 3.5) showed no sign of intensification while the maximum sustained wind increased slightly to 25.7 ms^{-1} (see Table 3.1). In fact, the convective area seemed to have weakened. The convection

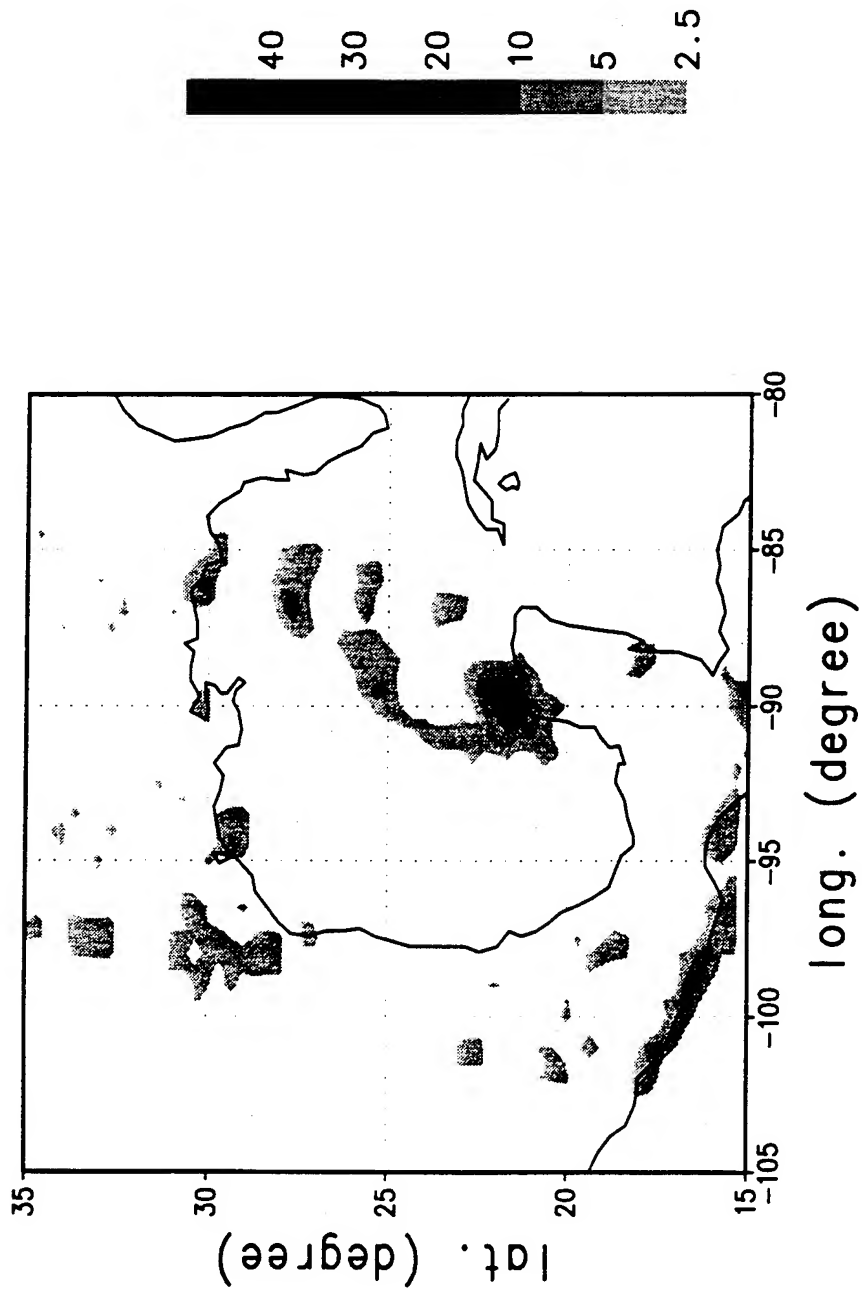


Figure 3.3 Same as Fig. 3.2 except for 0000 UTC 8 September 1988.

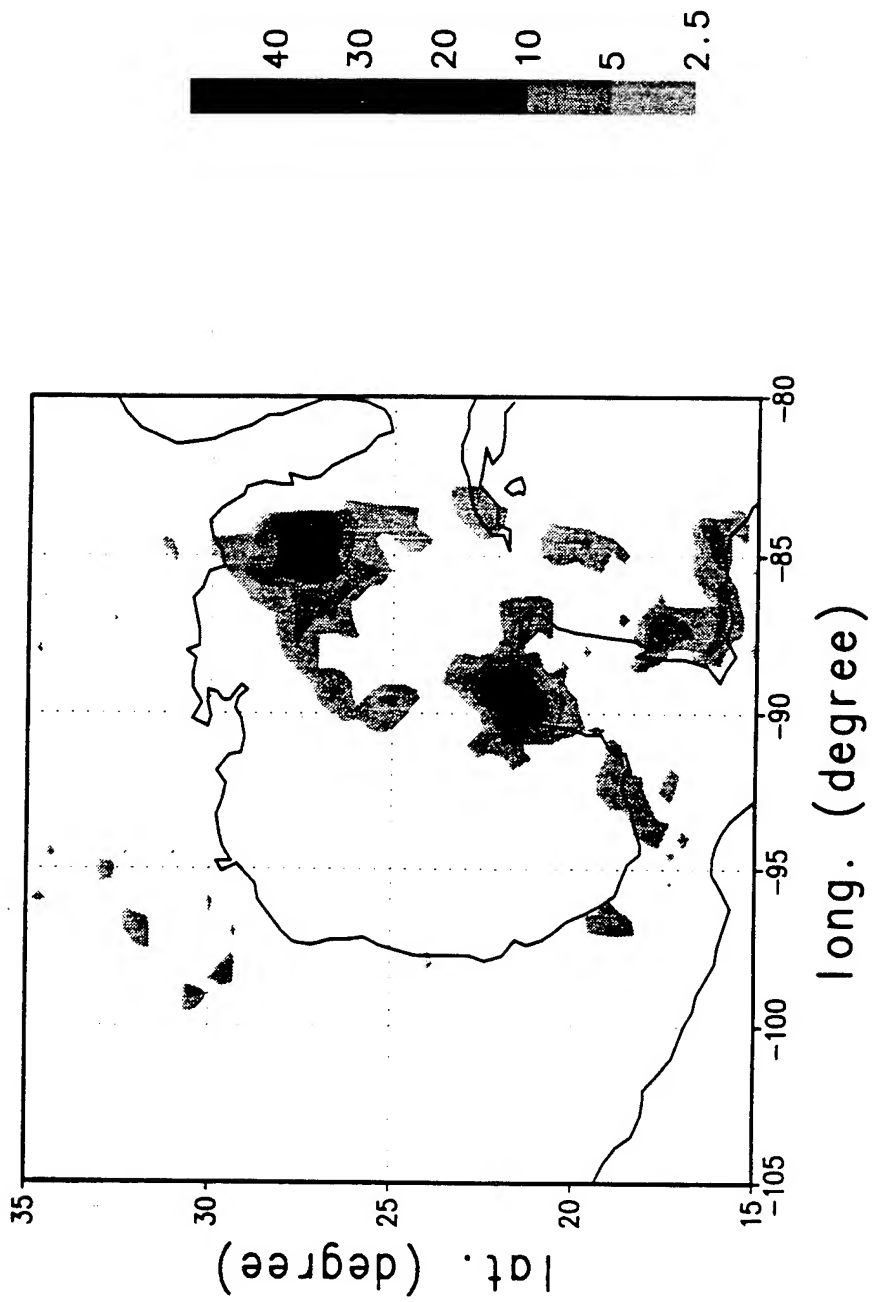


Figure 3.4 Same as Fig. 3.2 except for 1200 UTC 8 September 1988.

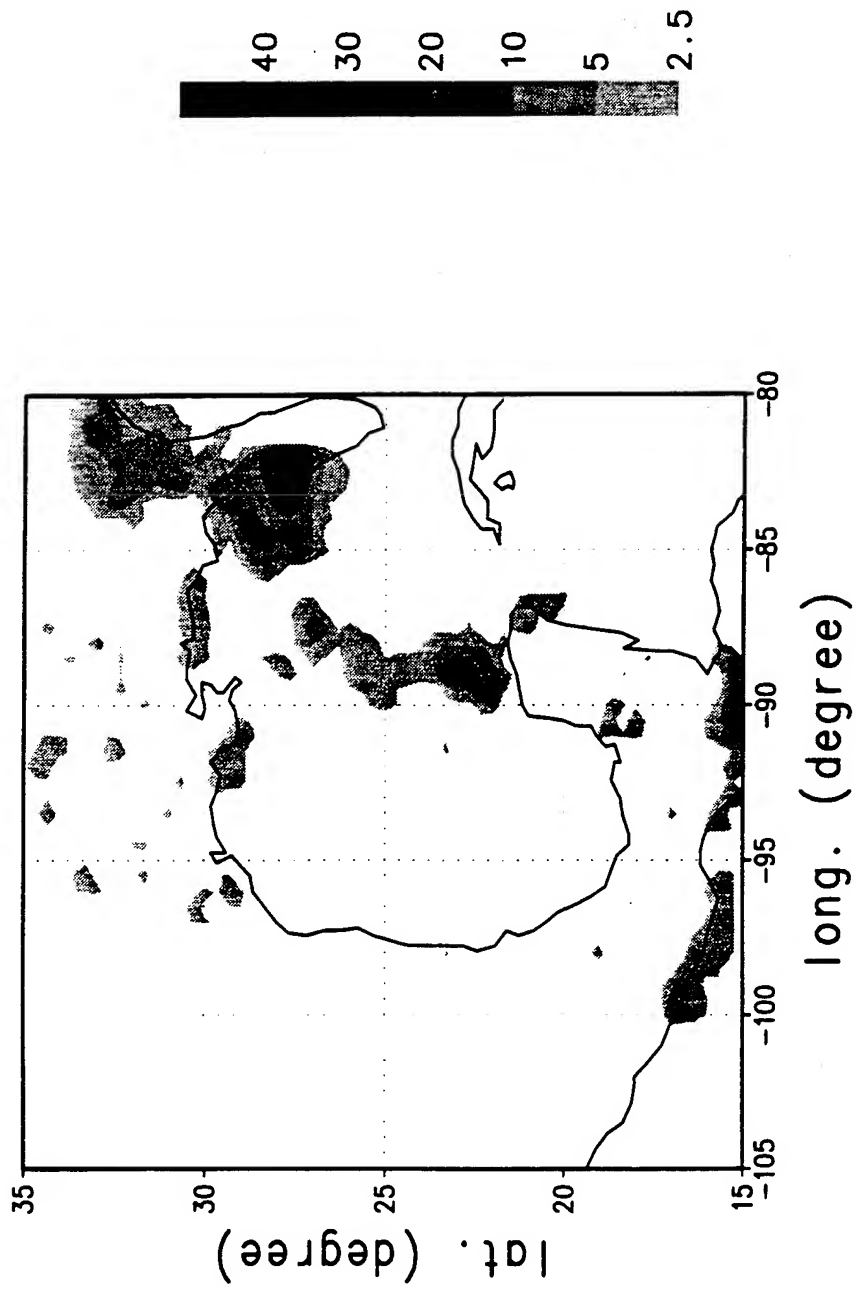


Figure 3.5 Same as Fig. 3.2 except for 0000 UTC 9 September 1988.

only could be seen south of the low-level center of Florence, which continued its course moving northward. During the next 12 hours from 0000 UTC to 1200 UTC September 9, the deep convection intensified rapidly. As shown in Fig. 3.6, the SSM/I precipitation rate showed that a new convective cell north of center had develop during this 12-hour period. This was confirmed by a GOES infrared imagery which will be discussed later. A deep convective region with $>25 \text{ mm h}^{-1}$ was located southeast of the low-level center while a deeper convective region with $>30 \text{ mm h}^{-1}$ was located north of the low-level center. The convective region north of the low-level center was extended and curled northeastward for about 5° long. This is sometimes an indication of forming of the outflow channel at upper levels.

While Florence continued to move northward, it also continued intensifying. It reached its maximum intensity with a maximum sustained wind of 36 ms^{-1} and a central pressure of 982 mb (Table 3.1). Florence was upgraded to a hurricane at 1800 UTC September 9. Fig. 3.7 reveals the SSM/I precipitation rate at 0000 UTC September 10. The deep convective region was north of New Orleans near the coast of Louisiana with a rain rate around 15 mm h^{-1} . However, Florence still maintained its hurricane force at this time. Two hours later at 0200 UTC September 10, Florence made landfall.

Rodgers et al. (1991) presented GOES infrared imageries (Fig.

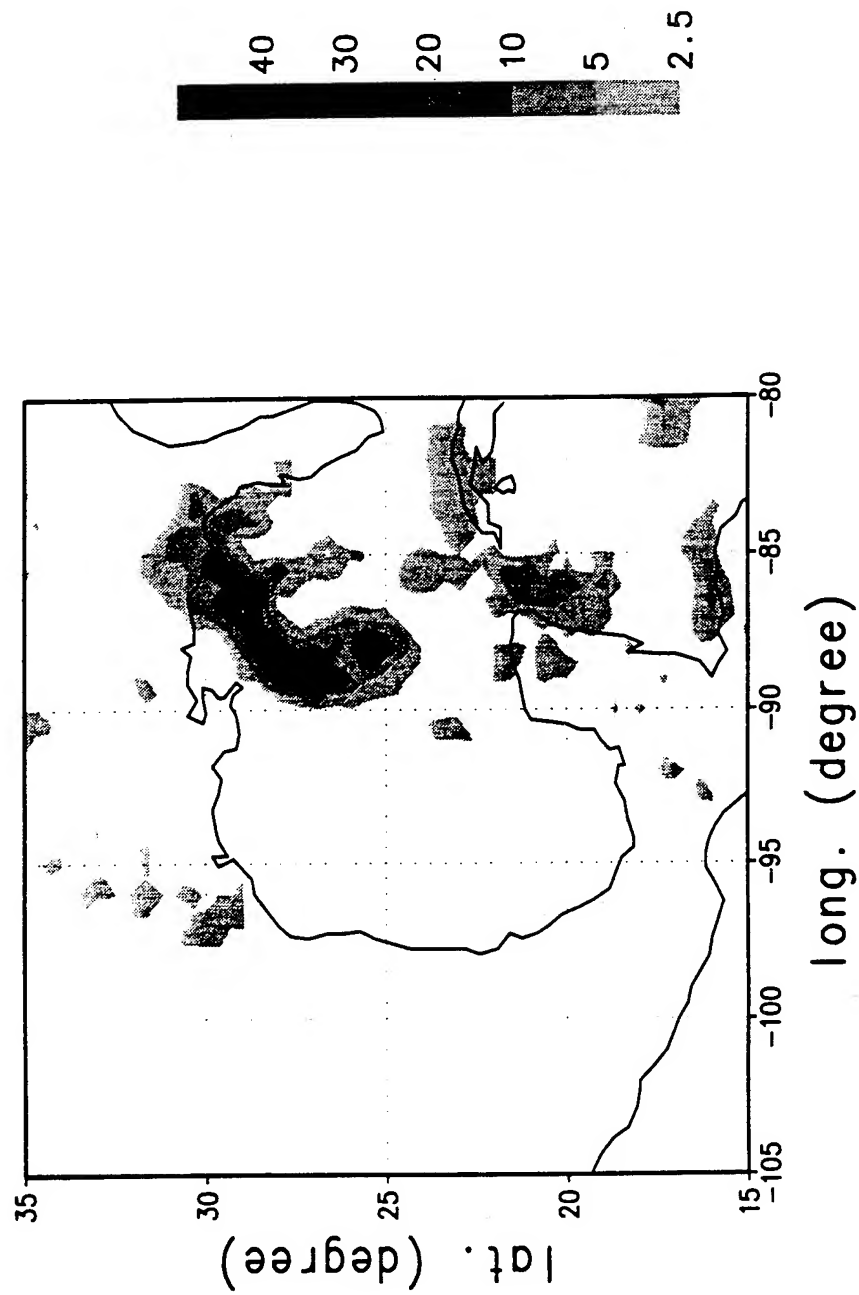


Figure 3.6 Same as Fig. 3.2 except for 1200 UTC 9 September 1988.

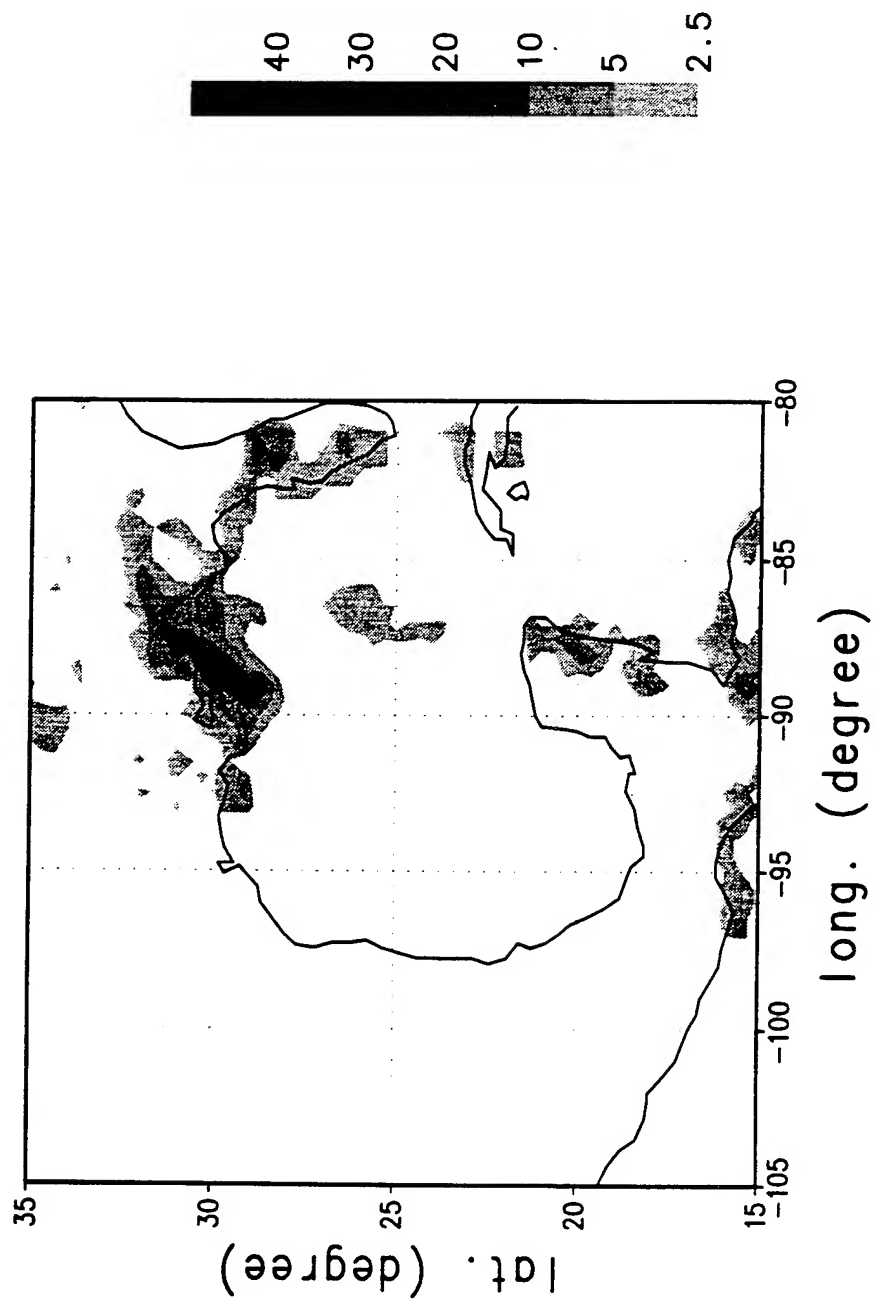
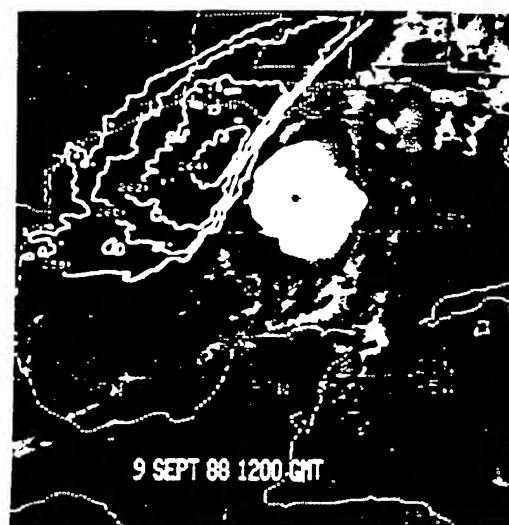
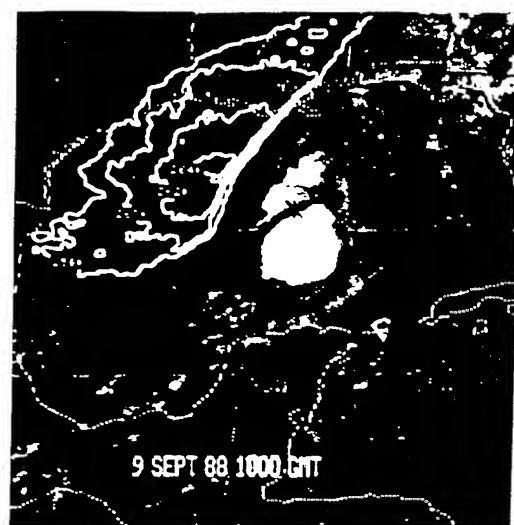
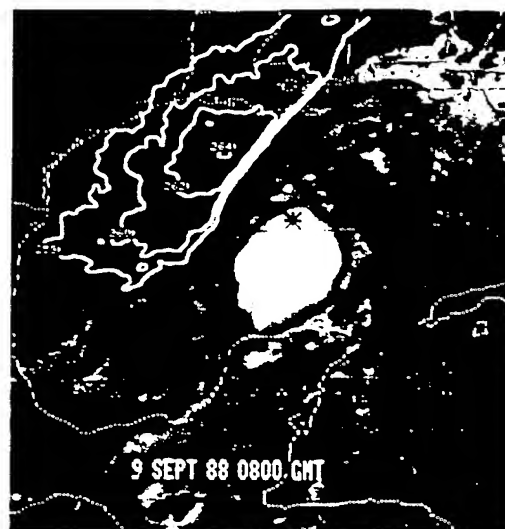
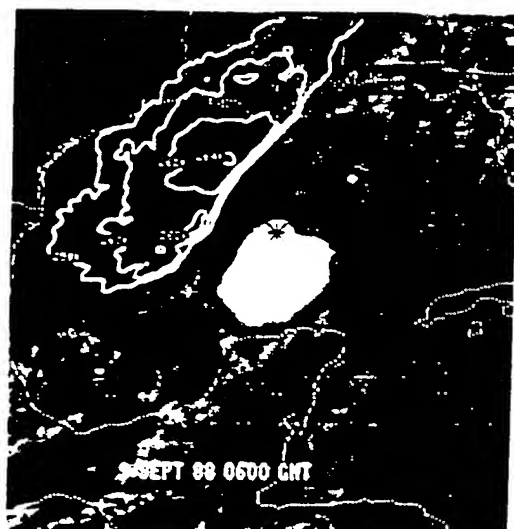
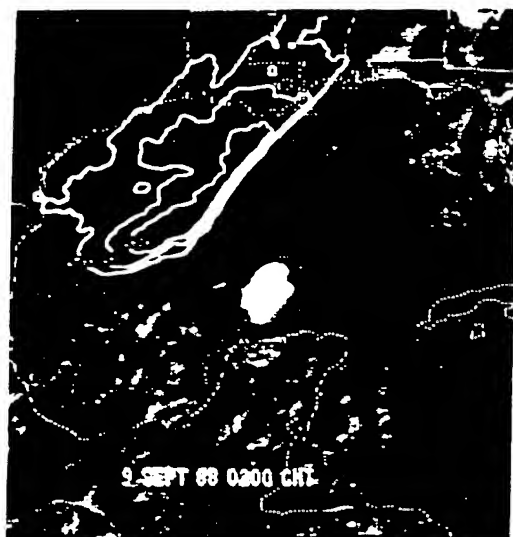


Figure 3.7 Same as Fig. 3.2 except for 0000 UTC 10 September 1988.

3.8) which confirmed the development of the second deep convective cell north of the low-level center at 1200 UTC September 9 shown in the SSM/I precipitation rate at the same time (Fig. 3.6). Fig 3.8 shows the GOES infrared imagery at every two hours from 0200 UTC to 1200 UTC September 9. As shown in Fig. 3.8, the second deep convective cell appeared at 0800 UTC and then expeditiously expanded and intensified. At 1200 UTC, the newly developed second deep convective cell had reached a size larger than its counterpart southeast of the low-level center. GOES infrared imageries also confirmed the existence of a large rain band that stretched from the convective region to the area off east coast of the Yucatan Peninsula. The second convective cell eventually merged with the convective region southeast of the low-level center and the combined convective region moved northward toward New Orleans as seen in Fig. 3.9.

3.3 Upper-Tropospheric Environment of Florence and Its Possible Influences on Florence's Outflow.

Before Florence became a hurricane on September 9, there was an UTT approaching from the west as shown in the NMC/RAFS 2.5⁰ analysis at 1200 UTC September 8 (Fig. 3.10). The trough extended from the southern part of Illinois into the eastern part of Texas. Twelve hours later at 0000 UTC September 9, the UTT moved eastward into the northern Gulf of Mexico originating from





9 SEPT 88 1000 GMT



9 SEPT 88 1100 GMT



9 SEPT 88 1200 GMT



9 SEPT 88 1300 GMT



9 SEPT 88 1400 GMT



9 SEPT 88 1500 GMT

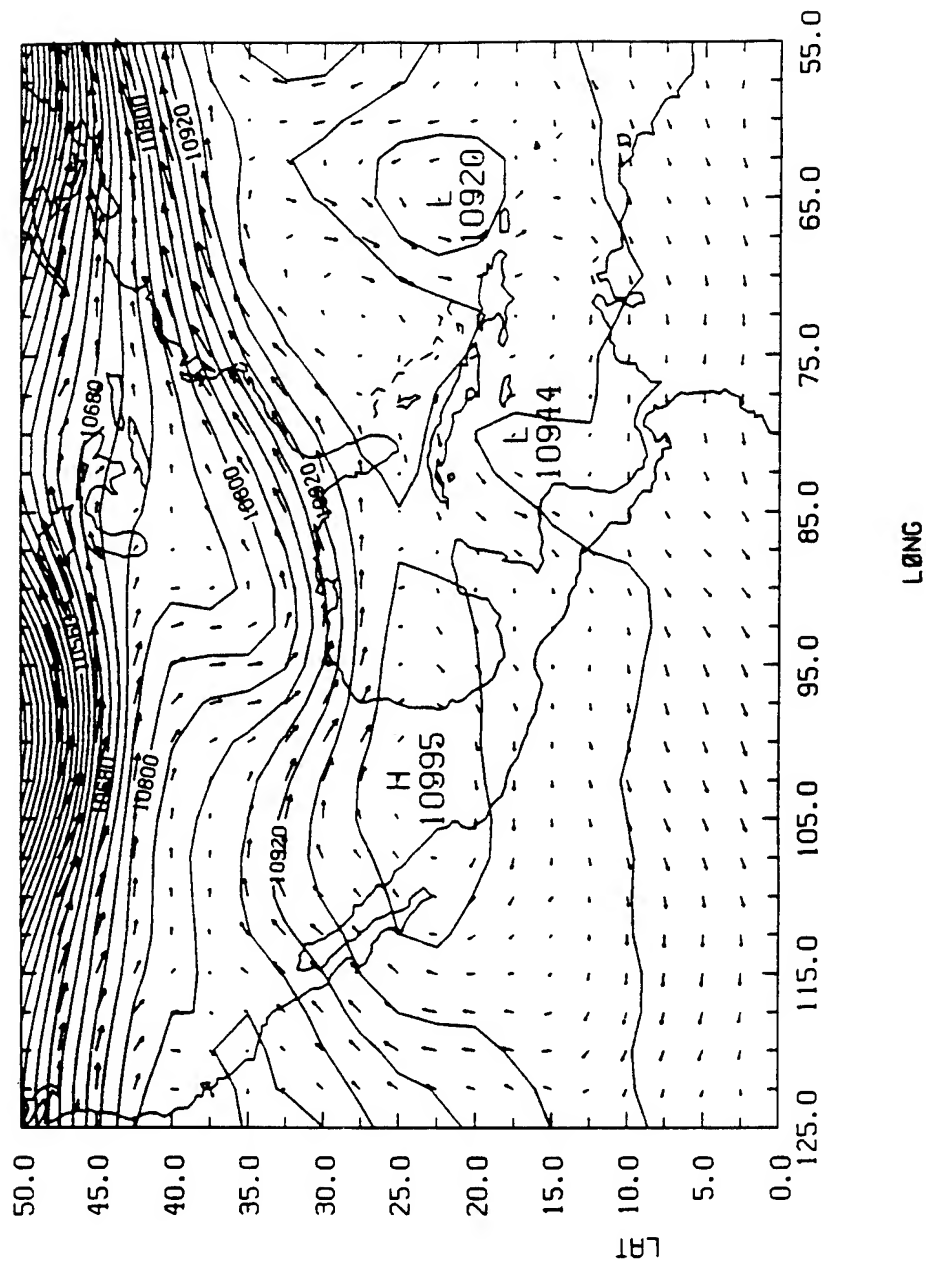


Figure 3.10 Geopotential heights (m) and wind vectors at 250 mb of the NMC/RAFS 2.5° analysis at 1200 UTC 8 September 1988.

Tennessee (Fig. 3.11). At this time, the westerly jet (Fig. 3.12) might have provided a channel for the forming of the outflow jet of Florence and initiated the development of the second convective cell north of Florence's center a few hours later, as described in the previous section. At 1200 UTC September 9, the UTT (Fig. 3.13 and 3.14) moved slightly eastward and was apparently weakening as compared to the UTT in Fig. 3.11 and 3.12.

Rodgers et al. (1991) used the satellite derived cirrus-level wind and ozone data to show the approaching of the UTT from the west. Fig. 3.15 shows the cirrus-level streamline analyses and wind speed (shaded area means $\geq 25 \text{ ms}^{-1}$) at 12 hours interval from 1200 UTC September 8 to 1200 UTC September 9. At 1200 UTC September 8 (Fig. 15a), there was a minor UTT in the northwestern Gulf of Mexico just northwest of Florence's center. Twelve hours later (Fig. 3.15b), the UTT became deeper and stronger and extended further south. At this time, the UTT was west of the Florence's center resulting from the northward movement of Florence. Fig 3.15c shows the existence of the outflow jet located north of the Florence center at 1200 UTC September 9. Rodgers et al. (1991) speculated that the combination of the observed evolution of Florence's outflow (Fig. 3.15) and the convection (Fig. 3.8 and 3.9) provides some evidence that the outflow jet-induced secondary circulation might enhance the convective growth in the entrance region of the outflow jet. The above mechanism was also illustrated in the numerical study of Shi

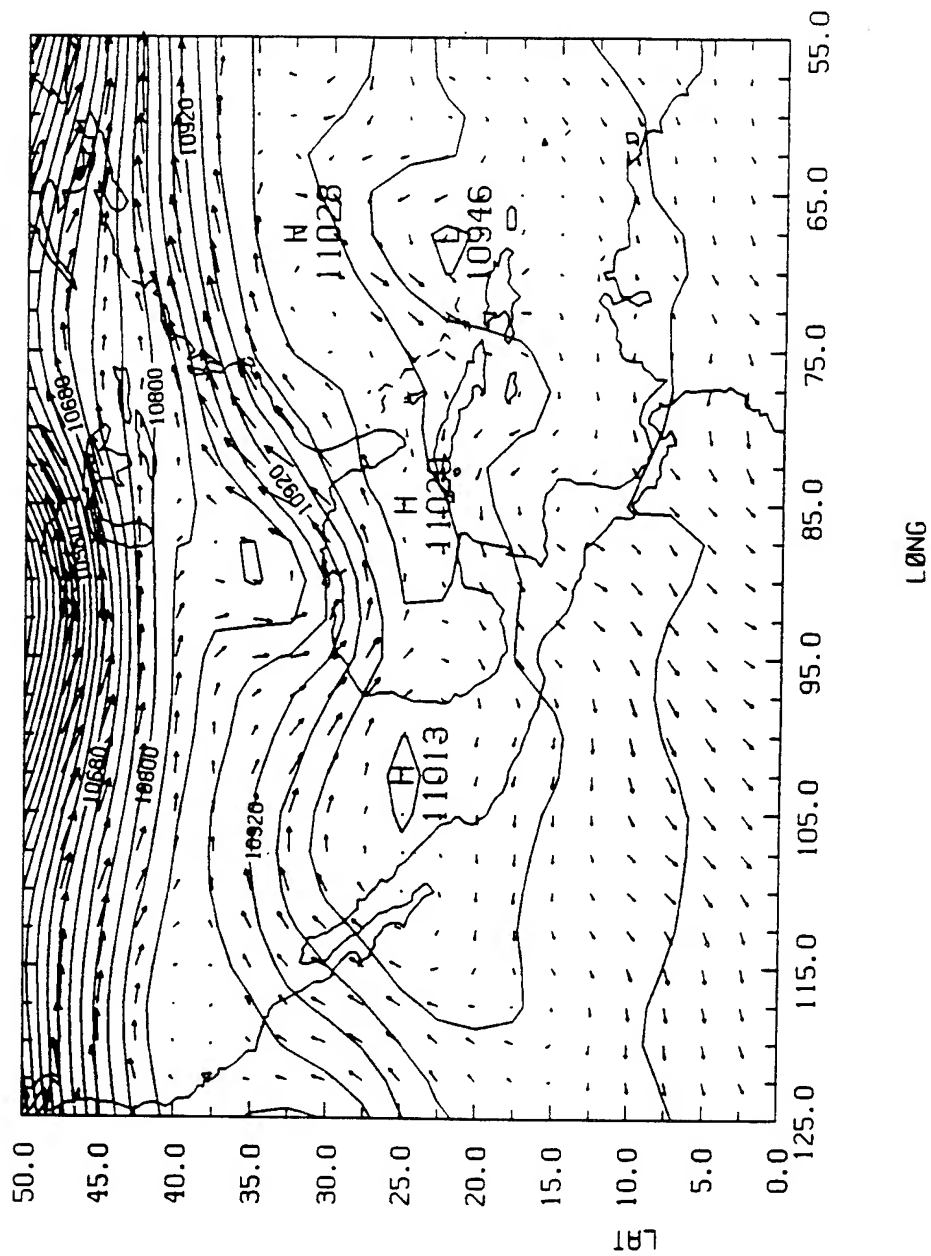


Figure 3.11 Same as Fig. 3.10 except for the time at 0000 UTC 9 September 1988.

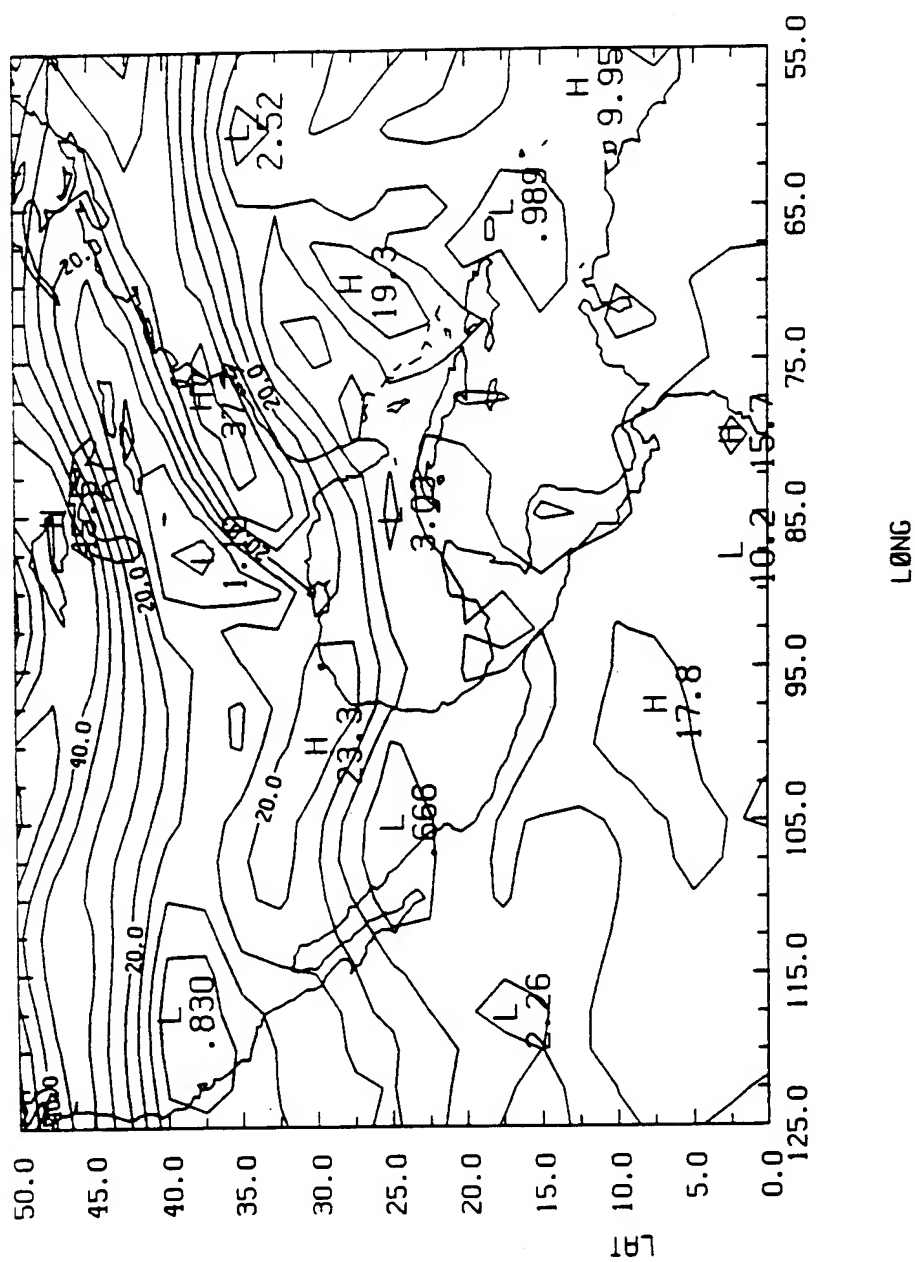


Figure 3.12 Same as Fig. 3.10 except for the isotaches (ms⁻¹) at 0000 UTC 9 September 1988.

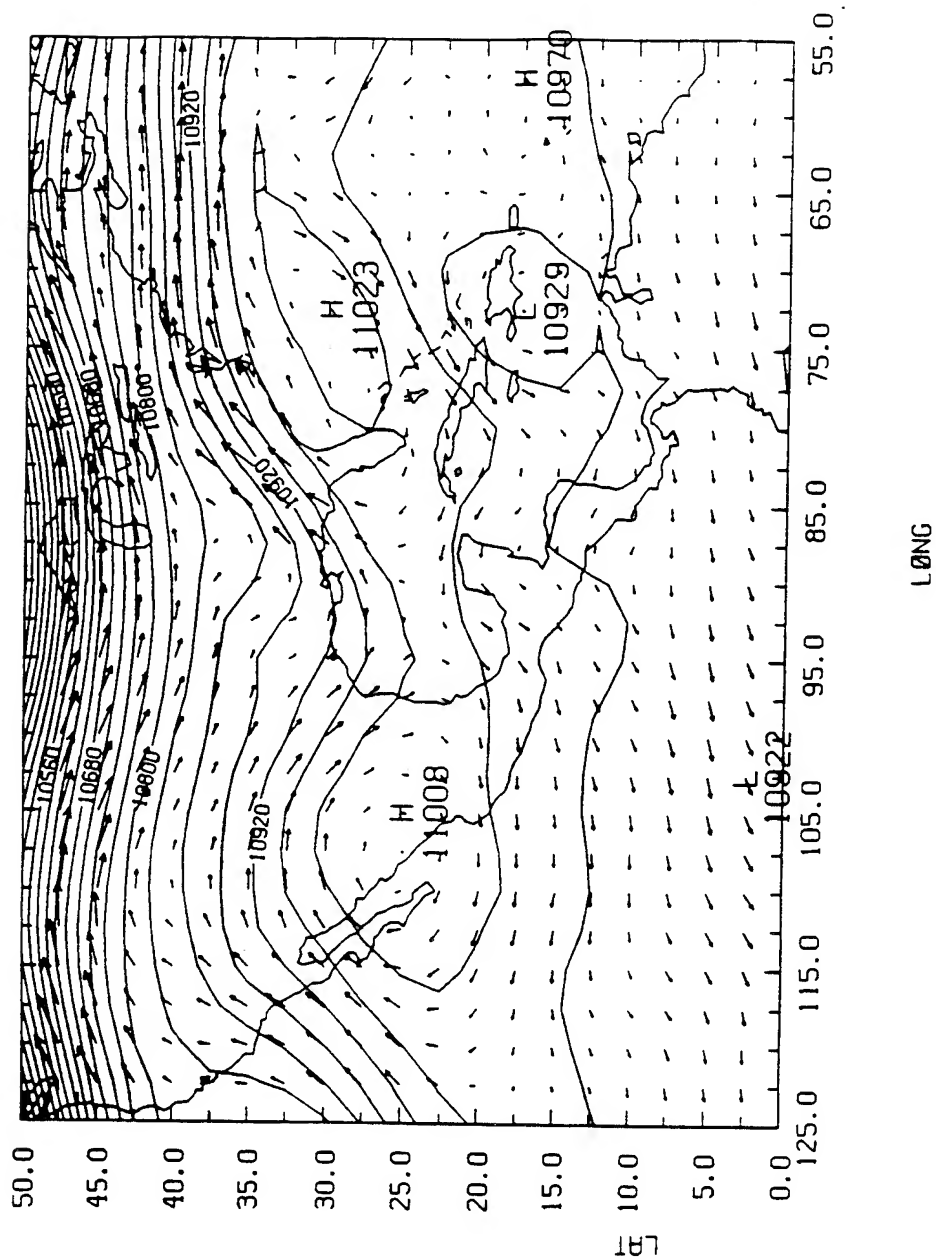


Figure 3.13 Same as Fig. 3.10 except for the time at 1200 UTC 9 September 1988.

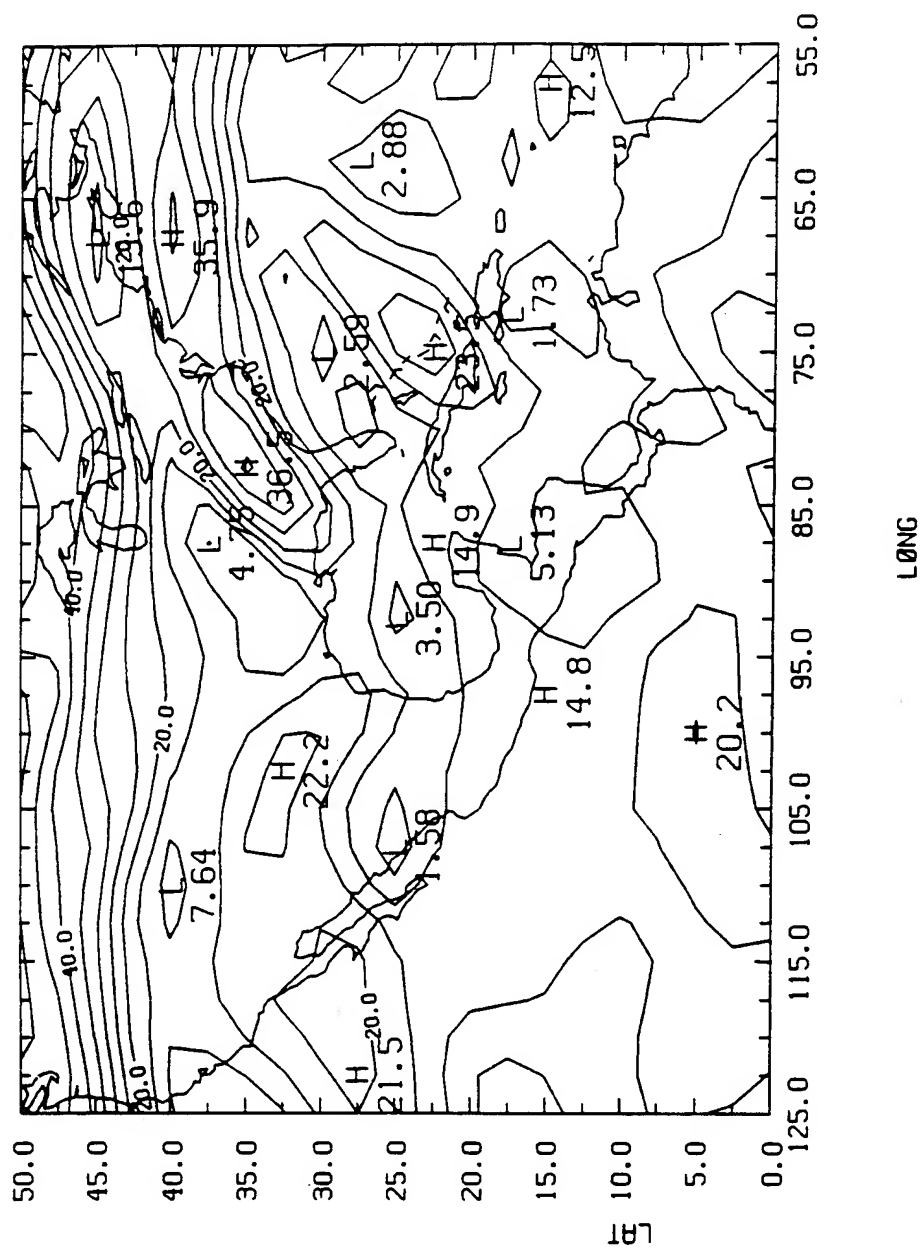


Figure 3.14 Same as Fig. 3.10 except for the isotaches (ms^{-1}) at 1200 UTC 9 September 1988.

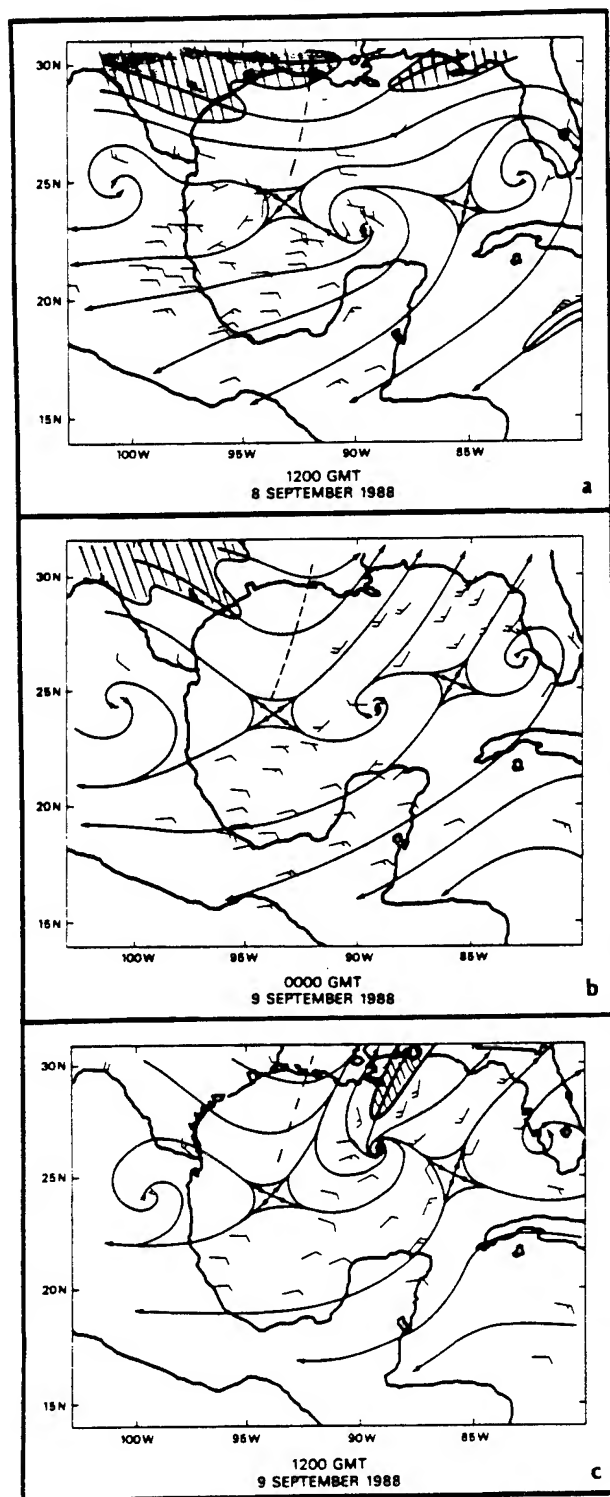


Figure 3.15 Cirrus-level winds (ms^{-1}) and streamline analysis for Hurricane Florence at 1200 UTC 8 September, 0000 UTC and 1200 UTC 9 September 1988. Shaded area represents wind speeds $\geq 25 \text{ ms}^{-1}$. Hurricane symbol depicts the center of Florence. Dashed line represents the upper-level tropospheric trough's axis. Full wind barb represents 10 ms^{-1} . Figure adapted from Rodgers et al. 1988..

et al (1990) using an idealized tropical cyclone outflow. Fig. 3.15c suggests that Florence's northern outflow became channeled and enhanced as the system interacted with the UTT.

4. NRL Regional ANALYSIS AND FORECAST SYSTEM.

The current conventional observation networks and assimilation scheme cannot routinely define tropical cyclone structure and reliable steering flows (Bender et al. 1991; Lord 1991; Davidson and Puri 1992). The accurate description of the initial conditions in numerical simulations of the tropical cyclone always suffers from two main difficulties. The first is the lack of observational data over tropical oceans. This is an important factor limiting the improvement of numerical model simulations and hurricane track forecast accuracy (Neumann, 1981). The second is the inability to utilize all the data in the analysis, when it is available. Anthes (1982) has stated that a reasonably good density and accuracy of observations are required to initialize hurricane models. He also enunciated that an accurate wind analysis is of prime importance in initializing hurricane models. In this study, the limited-area prediction of Naval Research Laboratory (NRL), which includes a data assimilation system, a non-linear normal model initialization scheme and a limited-area numerical model, will be used.

4.1 Data Assimilation System.

The objective analysis system in NRL includes two steps. The first step is the data quality control and consistency check. The

second step is the Barnes objective analysis scheme with either a two-pass successive-correction procedure for a single-grid or a three-pass procedure for a nested-grid. These two steps will be described separately in Section 4.1.1 and 4.1.2. The result of the analysis will be discussed in the next chapter.

4.1.1 Data Preparation and Quality Control.

Data preparation and quality control is an integral part of the NRL data assimilation system. It is designed to modify or reject the erroneous and unreliable meteorological data. In the NRL data assimilation system, observations will first be checked for the hydrostatic consistency. If not, geopotential height of that observation is recomputed according to the temperature and the surface pressure at the same location. In this step, ODW observations are checked. The data are also smoothed in the vertical direction to filter out noises of the scales smaller than the model's vertical resolution. In this step, if the surface pressure of the data is less than 1000 mb, the 1000 mb level data is obtained by extrapolation from the lowest two levels data available.

There are two quality control checks which are implemented in a manner similar to DiMego (1988). The first one is a "gross" check to examine the magnitude of the observed data and to reject any report which is non-meteorological. For example, a sea level surface

pressure of 700 mb or 1300 mb will be rejected. The second one is a "buddy" check which detects any observation datum which is inconsistent with those from surrounding stations and may result in an unrealistic analysis. Both of gross checks and buddy checks are performed for all reports. At each reporting location, the observation have to agree meteorologically with at least half of the reports within certain radius. Observed data that failed in the buddy check are deleted from the data set for the next step. The choice of the radius of the buddy check depends on the data resolution and the nature of the weather phenomena which the prediction model intends to include. In this study, a radius of 3° latitude is selected. The details of the quality control in NRL data assimilation system are documented in Harms et. al (1992) and Sashegyi et al. (1993).

Two more tasks are done in this step to speed up the Barnes scheme in the next step. The first is to create in the data rich areas "super observations" which are generated by taking averages of the data values and the data locations. This will reduce the computation required in the Barnes scheme. The second is to put bogus data reports with perfect analysis in the area which has no data report. This will help to vectorize the codes of the Barnes scheme. In this step, the average minimum station spacing D_n and critical radius R_c (or cutoff radius) used in the Barnes scheme, are also computed. The area coverage and density of the ODWs shown in Fig. 2.1 has also

been used to set up the analysis domain and the resolution of the Barnes scheme. For the available ODWs, the average minimum station spacing D_n is 135.0 km for the first two passes and 67.5 km for the third pass. The critical radii R_c (or cutoff radius) are 864.0 km for the first two passes and 432.0 km for the third pass, respectively. The calculations of D_n and R_c are based on Koch et al. (1981). Details about D_n and R_c will be discussed in the next section.

4.1.2 The Nested Barnes Scheme.

A Barnes objective analysis scheme is a two-pass successive correction scheme following Barnes (1964 and 1973), Koch et al. (1981), Koch et al. (1983) and Harms (1985). In this section, we will first briefly discuss the two-pass Barnes scheme and then the reason for adding the third pass with a nested grid

For each grid point, the Barnes scheme uses a Gaussian weighted-averaging method to assign a non-zero weight to the observations within a cutoff radius R_c according to the distance between the grid point and each observation. All the observations beyond R_c from the grid point are assigned a zero weight. Let d_n represent the distance between the (i,j) grid point and an observed datum $f(x_n, y_n)$. Let κ be the weight parameter for each pass. The weight function $w_n(i,j)$ is expressed as

$$w_n(i, j) = \exp\left(-\frac{d_n(i, j)^2}{\kappa}\right) \quad (4.1)$$

From (4.1), a radius of influence d_i can be determined by letting $w_n(i, j) = e^{-1}$. Consequently,

$$\frac{d_i^2}{\kappa} = 1 \quad (4.2)$$

or,

$$d_i = \kappa^{0.5} \quad (4.3)$$

The parameter κ is decreased from its first pass value κ_0 to its second pass value of

$$\kappa_1 = \gamma \kappa_0 \quad (4.4)$$

where γ ($=0.3$ in our study) is a "numerical convergence parameter" that forces a high degree of convergence (agreement) between the observation value $f(x, y)$ and the interpolated value $g(x, y)$ at each observation location. The cutoff radius R_c is determined by

$$R_c = (20\kappa)^{0.5} \cong 4.5\kappa^{0.5} = 4.5d_i \quad (4.5)$$

Where d_i is the radius of influence at which $w_n(i, j) = e^{-1}$. Based on Koch et al.(1983), κ_0 is acquired by

$$\kappa_0 = 5.052 \left(\frac{2D_n}{\pi} \right) \quad (4.6)$$

Where D_n is the average minimum station spacing. The weight parameter is fixed by the data spacing to give maximum response of e^{-1} at the $2D_n$ scale. Before starting the objective analysis, a bi-linear interpolation is applied to interpolate the background data (2.5° analyses of NMC/RAFS) from the grid points to the data locations and then compute the corrections $e_0(x,y)$ by subtracting the background data from the observed data $f(x,y)$. In the NRL data assimilation system, the Barnes scheme is actually performed on the correction field e_0 . Near the boundary, the result of the correction field analysis is merged with the background data to gain the final analysis field. For the first correction pass, the correction field e_0 is interpolated to the grid point by using

$$G_0(i, j) = \frac{\sum_{n=1}^N w_n(i, j) e_0(x_n, y_n)}{\sum_{n=1}^N w_n(i, j)} \quad (4.7)$$

Then, $G_0(i,j)$, the correction field at the grid points after first pass, are bi-linearly interpolated back to the observation data locations to gain the first correction pass estimated value g_0 . The first pass error can then be determined by

$$e_1(x_n, y_n) = e_0(x_n, y_n) - g_0(x_n, y_n) \quad (4.8)$$

For the second pass, the weight function is

$$w'_n(i, j) = \exp \left(-\frac{d_n(i, j)^2}{\kappa_1} \right) \quad (4.9)$$

where $\kappa_1 = \gamma\kappa_0$ as in (4.4). The first pass error e_1 is interpolated to the grid points based on the weight function $w'_n(i, j)$. The second correction pass grid point value $G_1(i, j)$ is computed by

$$G_1(i, j) = G_0(i, j) + \frac{\sum_{n=1}^N w'_n(i, j) e_1(x_n, y_n)}{\sum_{n=1}^N w'_n(i, j)} \quad (4.10)$$

Of course, more correction passes can be performed iteratively. Koch et al. (1983) has proven that when the value of convergence parameter γ is chosen small enough, no real benefit can be gained in making more than one correction pass. This means that the Barnes analysis scheme with two passes is sufficient. More details about the Barnes analysis scheme were documented in Koch et al (1983), Harms et al. (1992) and Sashegyi et al. (1993). As mentioned before, D_n and R_c are 135 and 864 km respectively in our study based on the distribution of the ODWs.

After the analysis is done, the correction field analysis which

are on the grid points will be added to the background data to get the enhanced field. The domain of the analysis grid is from 78° to 99° W and from 18° to 32° N, which covers all the ODW drop locations. As will be shown in the next chapter, the analyses obtained with the first two passes failed to reproduce the details of Florence's structure resolved by the ODWs. A third pass is therefore added to the Barnes objective analysis scheme. Fig. 4.1 shows the analysis domain for all three passes of the Barnes scheme. The horizontal resolutions are one half degree in both x- and y-direction for the first two passes including the area outside the domain of analysis grid and are one-sixth degree for the third pass.

As will be shown in the next chapter, the buddy check deleted the data with extreme values (e.g., lowest surface pressure, lowest geopotential height and strongest wind) near the center in the conventional single-grid two-pass Barnes analysis. Because the scale of the storm center is small, the buddy check is performed to prevent data near the storm center from affecting a large area away from the center. Otherwise, the analysis would result in a weaker pressure gradient and an unrealistic circulation pattern. It is also obvious from Fig. 2.1 that the ODW data resolution near the hurricane center is about twice the resolution away from the center. The average station spacing near the center is about 0.7° while it is about 1.5° away from the center. To resolve the small scale feature near the center afforded by the high ODW data

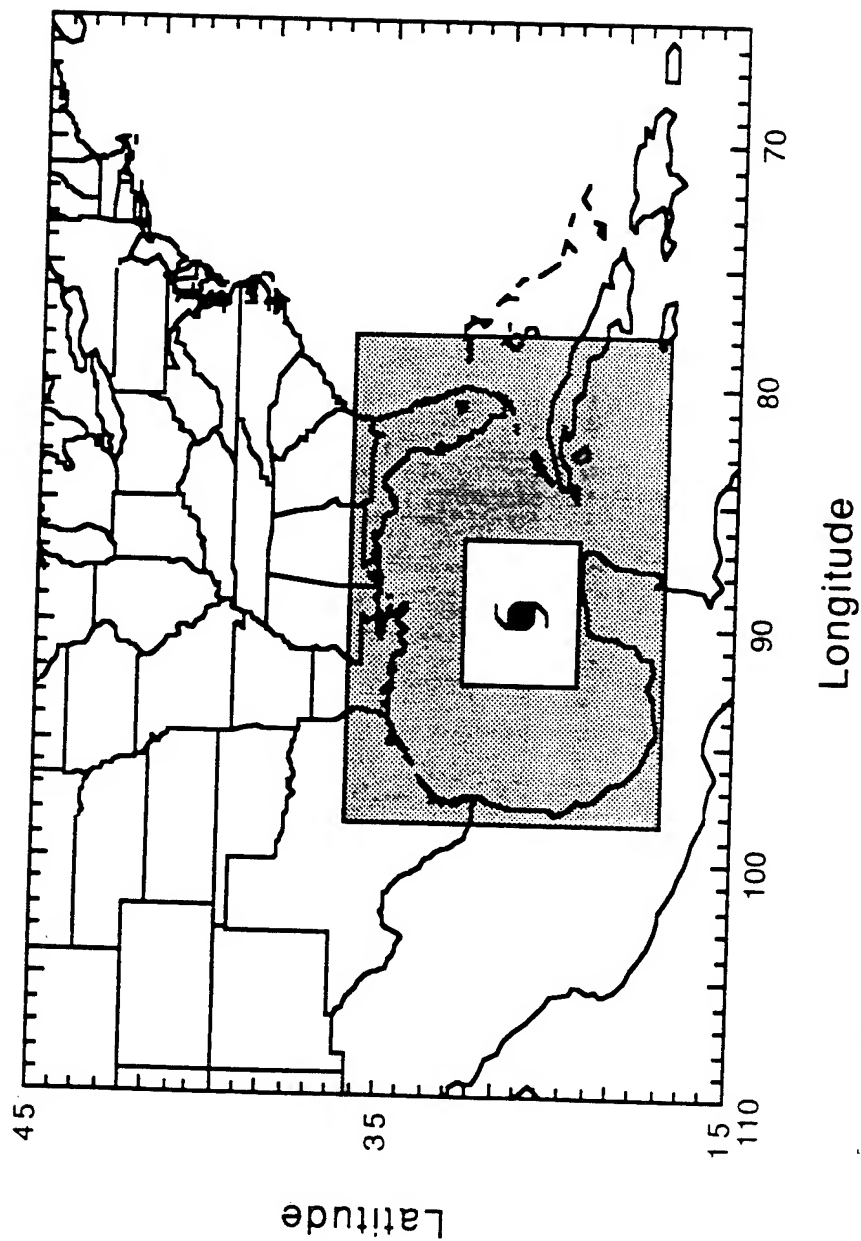


Figure 4.1 Analysis domain for the nested three-pass objective analysis. Shaded area is for the first and second pass. Plain area inside the shaded area is for the third pass. The hurricane symbol depict the location of Florence's center at 0000 UTC 9 September 1988.

resolution there, a nested-grid three-pass Barnes scheme with the third pass is employed. The inner-most grid covers a domain of 5° by 6° with a resolution of $1/6$ degree centered around Florence (Fig. 4.1), and with a smaller value of D_n and R_c than their counterparts in the first two passes for the coarser grids. As was shown in Section 4.1.1, D_n used in the third pass is 67.5 km, half the value (135 km) in the first two passes. For the third pass, the analyses after the first two passes will be used as the background data. The ODWs without the buddy check will be used to enhance the background data. The result after the proposed nested-grid three-pass Barnes scheme will be discussed in the next chapter.

4.2 Naval Research Laboratory's Tropical Cyclone Model.

The Naval Research Laboratory's (NRL) tropical cyclone model is a three-dimensional, hydrostatic, primitive equation model incorporating a split-explicit time integration scheme along with cumulus and boundary layer parameterizations. The tropical cyclone model used in this real case simulation study is basically the same as the one-grid version of NRL limited area numerical model described in Madala et al. (1987), Chang et al. (1989) and Holt et al. (1990) except that there are 23 layers in this version of the model. The model utilizes a sigma vertical coordinate and time dependent boundary conditions. In the following sections more details about this model will be presented.

4.2.1 Governing Equations.

The governing primitive equations incorporated in the model are formulated in the flux forms, i.e., $P_S u$, $P_S v$, etc. The system of seven equations (five prognostic and two diagnostic) form a closed system for the seven dependent variables: u , v , T , q , P_S , ϕ and $\dot{\sigma}$, where u and v are the velocity components in the x - and y -direction, respectively. T is the temperature, q is the specific humidity, P_S is the surface pressure, ϕ the geopotential height and $\dot{\sigma}(=d\sigma/dt)$ is the vertical velocity. The equations given below describe the motion of a mesoscale, hydrostatic, baroclinic atmosphere in a system with $\sigma(=P/P_S)$ as the vertical coordinate. The equations are expressed in x , y , σ and t coordinates using the generalized expression for curvilinear distance.

1. The momentum equation in x -direction (east-west):

$$\begin{aligned} \frac{\partial P_S u}{\partial t} + \frac{1}{h_x h_y} \left(\frac{\partial (P_S u h_y u)}{\partial x} + \frac{\partial (P_S v h_x u)}{\partial y} \right) + \frac{\partial (P_S \dot{\sigma} u)}{\partial \sigma} - f P_S v \\ + P_S \frac{uv}{h_x h_y} \frac{\partial h_x}{\partial y} = - \frac{P_S}{h_x} \frac{\partial \phi}{\partial x} - \frac{RT}{h_x} \frac{\partial P_S}{\partial x} + P_S F_u \end{aligned} \quad (4.11)$$

where F_u is the frictional force and h_x and h_y are the map factors in the x - and y - direction, respectively. R is the gas constant for dry air and f is the Coriolis parameter.

2. The momentum equation in y direction (north-south):

$$\begin{aligned} \frac{\partial P_s v}{\partial t} + \frac{1}{h_x h_y} \left(\frac{\partial (P_s u h_y v)}{\partial x} + \frac{\partial (P_s v h_x v)}{\partial y} \right) + \frac{\partial (P_s \dot{\sigma} v)}{\partial \sigma} + f P_s u \\ - P_s \frac{u^2}{h_x h_y} \frac{\partial h_x}{\partial y} = - \frac{P_s}{h_y} \frac{\partial \phi}{\partial y} - \frac{RT}{h_y} \frac{\partial P_s}{\partial y} + P_s F_v \end{aligned} \quad (4.12)$$

where F_v is the frictional force.

3. The thermodynamic equation:

$$\begin{aligned} \frac{\partial P_s T}{\partial t} + \frac{1}{h_x h_y} \left(\frac{\partial (P_s u h_y T)}{\partial x} + \frac{\partial (P_s v h_x T)}{\partial y} \right) + \left(\frac{\sigma}{\sigma_0} \right)^\kappa \frac{\partial (P_s \dot{\sigma} \theta)}{\partial \sigma} - \frac{RT}{C_p} \tilde{D} \\ - \frac{RT}{C_p} \left(\frac{u}{h_x} \frac{\partial P_s}{\partial x} + \frac{v}{h_y} \frac{\partial P_s}{\partial y} \right) = P_s F_T \end{aligned} \quad (4.13)$$

where F_T is the source or sink of heat, such as sensible heat and release of latent heat from moisture, $\sigma_0 = 1000/P_s$, $\kappa = R/C_p$ and θ is the potential temperature. C_p is the specific heat of dry air at constant pressure.

4. The moisture continuity equation:

$$\frac{\partial P_s q}{\partial t} + \frac{1}{h_x h_y} \left(\frac{\partial (P_s u h_y q)}{\partial x} + \frac{\partial (P_s v h_x q)}{\partial y} \right) + \frac{\partial (P_s \dot{\sigma} q)}{\partial \sigma} = P_s F_q \quad (4.14)$$

where F_q is the source or sink of moisture, such as condensation and evaporation.

5. The hydrostatic equation:

$$\frac{\partial \phi}{\partial \sigma} = - \frac{RT}{\sigma} \quad (4.15)$$

6. The continuity equation:

$$\frac{\partial P_s \dot{\sigma}}{\partial \sigma} = \tilde{D} - D \quad (4.16)$$

7. The surface pressure tendency equation:

$$\frac{\partial P_s}{\partial t} = - \tilde{D} \quad (4.17)$$

where

$$\tilde{D} = \int_0^1 \nabla \cdot (P_s \vec{V}) d\sigma \quad (4.18)$$

and mass divergence

$$D = \nabla \cdot (P_s \vec{V}) = \frac{1}{h_x h_y} \left(\frac{\partial (h_y P_s u)}{\partial x} + \frac{\partial (h_x P_s v)}{\partial y} \right) \quad (4.19)$$

All the variables have their conventional meteorological meaning and are defined in the list of symbols. Equations 4.11 to

4.17 form a closed set of equations if the functional form of the last terms representing the source or sink in Equations 4.11 to 4.17 (i.e., F_u , F_v , F_T and F_q) are known.

4.2.2 Grid Structure.

The number of grid points of this model is $(M \times N \times KK)$, where M , N and KK are maximum grid points in the x -, y - and σ - directions. The vertical depth of each layer is defined as $\Delta\sigma(k)$, where $K = 1$ to KK . The horizontal intervals between each two grid points are one half of a degree longitude and one-third of a degree latitude distance in the x - and y - direction, respectively. While the horizontal coordinates are curvilinear with horizontal grid spacing, the actual horizontal interval are $h_x\Delta x$ and $h_y\Delta y$, where h_x and h_y are map scale factors, and Δx and Δy are one half of a degree longitude and one-third of a degree latitude distances at the equator. In this study, h_x and h_y are equal to $\cos(\theta)$ and 1, respectively, where θ is the latitude.

The horizontal grid network is fully staggered in Arakawa's C grid (see Figure 4.2) because of its accuracy in simulating the geostrophic adjustment process. Surface pressure (P_s), temperature (T), geopotential height (ϕ) and specific humidity (q) are computed at mass points (i,j) , while the east-west velocity component u is defined at the midpoint of mass points along the x -direction and the

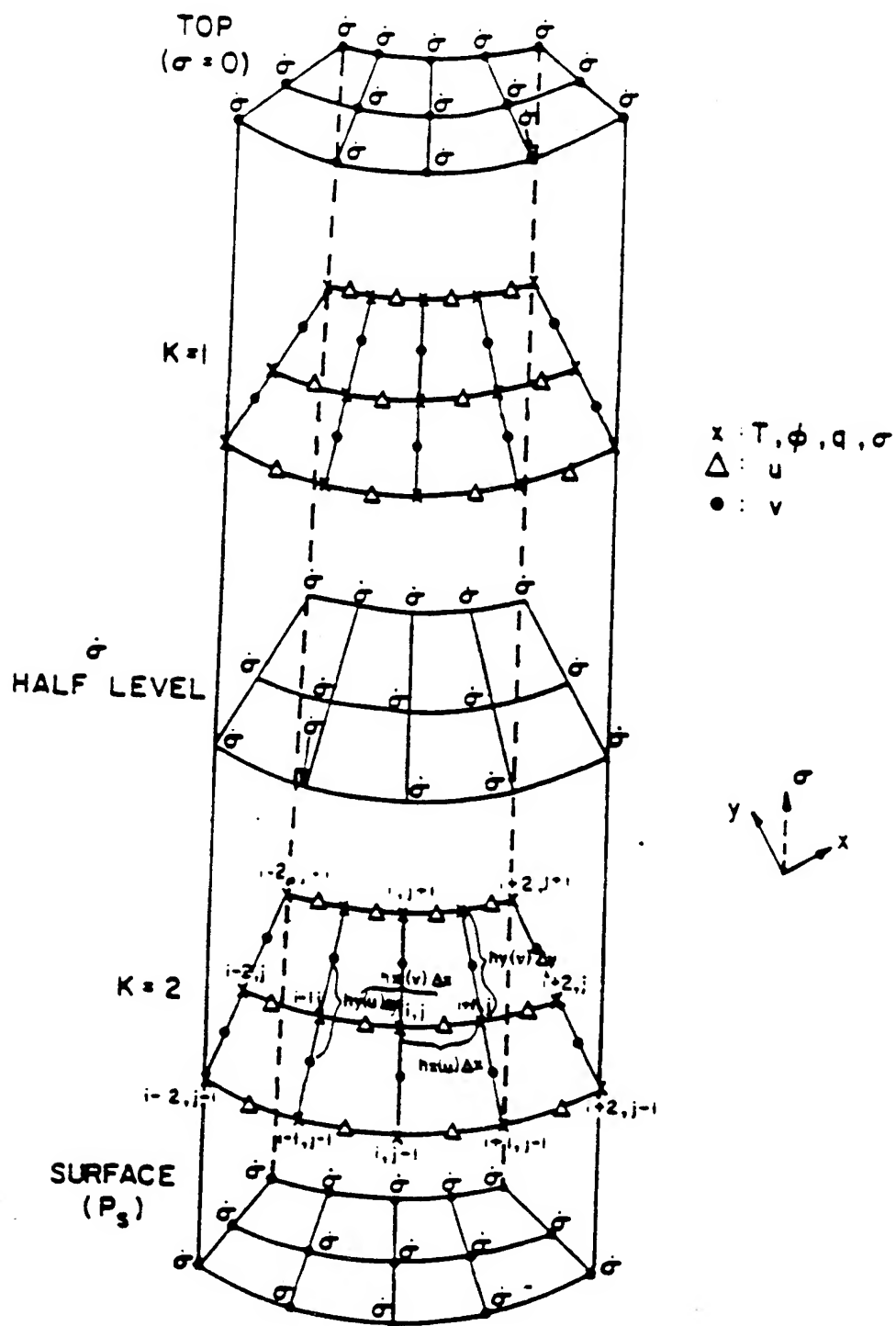


Figure 4.2 Horizontal and vertical grid network utilized in the model for the simple case $K = 2$.

north-south velocity component v is computed at the midpoint along the y -direction.

By definition, σ is equal to unity at the surface and zero at the top of the model. The vertical velocity $\dot{\sigma}$, defined as $d\sigma/dt$, is evaluated at the $(K + 1/2)$ levels for $K = 0$ to $KK-1$ (see Figure 4.3), where KK is the total number of layers. Vertical velocity is equal to zero at surface ($K = KK + 1/2$, and $\sigma = 1$) and at the top ($K = 0$ and $\sigma = 0$) of the model.

For this study, the grid system has $91 \times 91 \times 23$ points (in the x , y and σ direction). The model horizontal domain is from 110°W to 65°W and 15°N and 45°N . As shown in Fig. 4.3, the vertical resolution is higher in the planetary boundary layer for the multi-layer turbulent kinetic energy closure scheme of the boundary layer parameterization which will be described later in this chapter.

4.2.3 Numerical Scheme.

a. Spatial Differencing scheme.

The spatial finite differencing of the governing equations are second order accurate, quadratic conserving. Let the parameter $F_{i,j}^k$ represent the value F (any dependent variable in the model) at the (i,j) th horizontal grid point on the K -th level. Then, δ_x , δ_y and δ_σ

K =		σ	
0.5	1	$\Delta\sigma = 0.05$	0.00
1.5	2	0.05	0.025
	3	0.05	0.075
	4	0.05	
	5	0.05	
	6	0.05	
	7	0.05	
	8	0.05	
	9	0.05	
	10	0.05	
	11	0.05	
	12	0.05	
	13	0.05	
	14	0.05	
	15	0.05	
	16	0.05	
	17	0.05	0.825
	18	0.05	0.875
	19	0.04	0.92
	20	0.03	0.955
	21	0.015	0.9775
21.5	22	0.01	0.99
22.5	23	0.005	0.9975
23.5			1.00

Figure 4.3 Model's σ -coordinate structure for this study.

represent the finite differencing operators in the horizontal and the vertical such that:

$$\delta_x F_{i,j}^k = \frac{(F_{i+\frac{1}{2},j}^k - F_{i-\frac{1}{2},j}^k)}{h_x(i,j) \Delta x} \quad (4.20)$$

$$\delta_y F_{i,j}^k = \frac{(F_{i,j+\frac{1}{2}}^k - F_{i,j-\frac{1}{2}}^k)}{h_y(i,j) \Delta y} \quad (4.21)$$

$$\delta_\sigma F_{i,j}^k = \frac{(F_{i,j}^{k+\frac{1}{2}} - F_{i,j}^{k-\frac{1}{2}})}{\Delta \sigma(k)} \quad (4.22)$$

where Δx and Δy are half degree longitude and one-third degree latitude distance at equator, $h_x(i,j)$ and $h_y(i,j)$ are the map factors in the x- and y-direction at the (i,j)th grid point for F, respectively.

b. Time Integration Scheme.

The time integration scheme in this model is the split-explicit method with the Leapfrog scheme (central differencing scheme). The split-explicit method (Madala, 1981) is utilized to allow for a larger time step by separately integrating vertical normal modes of the linearized version of prognostic equations.

The meteorologically relevant Rossby modes move much slower than the gravity modes, especially the external gravity mode.

In the split-explicit method, one uses the linearized equations of motion, which can be splitted into n vertical modes for the model with n layers. The nonlinear terms are then treated as a source for the gravity modes. For example, in the 23 layer model used in this study, the external and the first four internal gravity modes have characteristic wave speeds roughly of 300, 100, 30 and 15 ms^{-1} , respectively. In real atmosphere, Rossby mode moves roughly at 20 ms^{-1} . The external and first internal modes, moving much faster than the Rossby mode, require a much smaller time step, as restricted by CFL (Courant-Friedrichs-Levy) condition for explicit temporal integration. Therefore, one simply integrates the faster modes with a sufficiently small time steps, and then integrates the slower modes equations with a larger Rossby time step.

In the split-explicit method, the time interval Δt is subdivided into m subintervals of length $\Delta \tau$ (see Fig. 4.4). Within these subintervals, the time integration is carried out by the leap frog scheme. The numerical scheme in the tropical cyclone model subdivides the time interval t into 8, 4 and 2 subintervals for the external, first and second internal gravity modes, respectively. All the other modes move slowly enough to be incorporated into the large Rossby time step, Δt .

For the first time step of integration of the subinterval $\Delta \tau$, the Euler-forward time integration method is used to march from

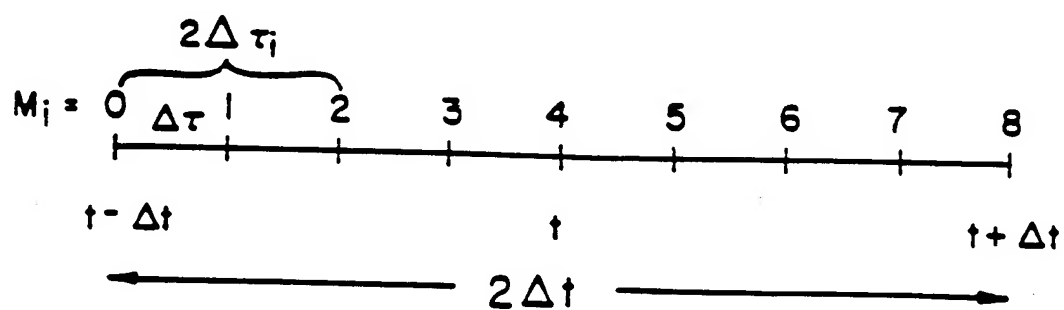


Figure 4.4 Division of time interval $2\Delta t$ into m -subintervals used in the split-explicit time integration scheme.

time $t - \Delta t$ (i.e., $M_i = 0$ in Fig. 4.4) to $t - \Delta t + \Delta \tau$ (i.e., $M_i = 1$ in Fig. 4.4). Then the Leapfrog scheme is used to march each successive time step $\Delta \tau$ until time $t + \Delta t$. For this study, Δt is equal to 60 seconds.

4.2.4 Lateral Boundary Conditions.

Proper specification of the lateral boundary condition is of vital importance to accurate limited-area model forecasts. Improper handling of lateral boundary conditions can often offset any advantages gained by increased horizontal resolution. Following Chang et al. (1989), a relaxation, lateral boundary treatment with a tendency damping suggested by Perkey and Kreitzberg (1976) is used. The relaxation scheme, in which values within five grid points from the lateral boundary were nudged toward the NMC/RAFS 2.5⁰ analyses, is used here:

$$\frac{\delta X}{\delta t} = (1 - \alpha) \left(\frac{\delta X}{\delta t} \right)_m + \gamma (X_0 - X) \quad (4.23)$$

where X represents the dependent variables in the model, $(\delta X / \delta t)_m$ represents model computed tendencies, γ is the relaxation parameter (= Coriolis parameter f), α is the weighting parameter with value varying between 0 and 1 and is a linear function of grid-point distance from the lateral boundaries, and X_0 represents the NMC/RAFS 2.5⁰ analysis. Values of X_0 are updated every 12 hours

using the NMC/RAFS 2.5⁰ analysis. For example, the integration between 0 and 12 hour, the values from the NMC/RAFS 2.5⁰ analysis valid at 12 hour are used, and between 12 and 24 hour, the values valid at 24 hour are used.

4.3 Physics of the Model.

4.3.1 Horizontal Diffusion.

In the tropical cyclone model, the model variables in the flux form are horizontally smoothed by a two-dimensional diffusion operator $\nabla \cdot K_H \nabla$, where K_H is the horizontal diffusion coefficient. K_H is of the order of $4 \times 10^8 \text{ cm}^2 \text{ s}^{-1}$, which is the value used in the model.

A circular (in terms of grid point) sponge zone is setup near the model's boundaries. Value of K_H is increased outside a circular central region of the model domain. Assuming that (i_c, j_c) is the center of the model domain, it is defined that

$$d_{gp} = \sqrt{(i - i_c)^2 + (j - j_c)^2} \quad (4.24)$$

where d_{gp} is the grid-point distance between the grid point (i,j) and the center of the model domain. The value of K_H is defined as

$$K_H = 1.2 \times 10^8 (d_{gp} - 30) + 4.0 \times 10^8 \text{ cm}^2 \text{ s}^{-1} \quad \text{for } d_{gp} > 30 \quad (4.25)$$

and

$$K_H = 4 \times 10^8 \text{ cm}^2 \text{ s}^{-1} \quad \text{for } d_{gp} \leq 30 \quad (4.26)$$

4.3.2 Cumulus Convection.

The model uses a modified Kuo scheme for parameterizing the effect of cumulus convection. The scheme was introduced by Kuo (1974) and later modified by Anthes (1977), and is based on the theory of the conditional instability of the second kind (CISK) (Charney and Eliassen, 1964). According to CISK, the convection occurs when there is a low-level moisture convergence in a conditionally unstable environment. It is also assumed that the cloud base is at the Lifting Condensation Level (LCL) and the cloud top is at the level where the temperature of the moist adiabat equals that of the environment. The temperature and humidity profile of the cloud is given by the moist adiabat.

The horizontal moisture convergence M per unit area is first computed for all the layers by

$$M = \nabla \cdot (P_s \vec{V}q) = \frac{1}{h_x h_y} \left(\frac{\partial (h_y P_s u q)}{\partial x} + \frac{\partial (h_x P_s v q)}{\partial y} \right) \quad (4.27)$$

The total moisture convergence M_t per unit column is then computed by

$$M_t = -\frac{P_s}{g} \int_{\sigma_t}^1 M d\sigma \quad (4.28)$$

where σ_t is the σ value at the cloud top.

The total amount of water vapor (H) needed to form a cloud over an unit area is computed as a function of the difference between the cloud temperature T_c and the environmental temperature T_e and the difference between the cloud humidity q_c and the environmental humidity q_e . H is then defined by

$$H = g^{-1} \int_{\sigma_t}^{\sigma_b} \left[\frac{C_p}{L} (T_c - T_e) + (q_c - q_e) \right] d\sigma \quad (4.29)$$

where σ_b and σ_t are the σ values at the bottom and top of the cloud and L is the latent heat of condensation. Conditional instability is assumed to exist when $H > 0$. The total moisture convergence M_t can be partitioned into a heating part bM_t which is condensed and precipitated out and a moistening part $(1-b)M_t$ which moistens the cloud. As suggested by Anthes (1977), the fraction is defined as $b=r_m$, where r_m is the vertically averaged relative humidity in the environment. The moistening rate and heating rate can then be

calculated, so do the new temperature and humidity values for the next time step.

In this study, we also further modify Kuo's scheme by adding a nonmeasurable subgrid scale moisture supply following Krishnamurti et al. (1983). The total moisture convergence M_t per unit area as in Equation (4.28) is multiplied by a factor of $(1+\eta)$ to form

$$M_c = M_t (1 + \eta) \quad (4.30)$$

where $M_t\eta$ represent the nonmeasurable subgrid scale supply of moisture. M_t is replaced by M_c in the partition process of the cumulus parameterization scheme used in the tropical cyclone model. Krishnamurti et al. (1983) used GATE observations to estimate the value of η with a multiple regression search of large scale parameters via least square minimization of errors. They found that η ranges from 0.0 to 0.8. In this study, with the help of some supplemental numerical experiments, we find that a value of 0.3 is the most suitable for the Florence simulation. Equation (4.30) is only applied inside a 5° by 5° box centered around Florence.

4.3.3 Large Scale precipitation.

The large scale precipitation is parameterized by the method

first introduced by Manabe et. al. (1965), and later described in Haltiner and Williams (1980). After the temperature and humidity have been updated at each time step, if there is any supersaturated layer in the model, the excess moisture is condensed out isobarically with the released latent heat warming the air, leaving the layer saturated. Following Haltiner and Williams (1980), the temperature and humidity adjustment δT and δq , must bring T and q of the supersaturated air to a saturated state in accordance with the equations

$$-L \delta q = C_p \delta T \quad (4.31)$$

and

$$q + \delta q = q_s(T + \delta T, P) \quad (4.32)$$

where q_s is the saturation specific humidity. In order to solve the system numerically, Equation (4.32) can be approximated into

$$q + \Delta q = q_s(T + \Delta T) \cong q_s(T) + \left(\frac{\partial q_s}{\partial T} \right)_p \Delta T \quad (4.33)$$

where Δq is the excess moisture needed to be condensed out. Next,

$$q_s \cong 0.622 \frac{e_s}{P} \quad (4.34)$$

where e_s is the saturation water vapor pressure at a given temperature. Then, for small changes dq_s in the saturation vapor pressure, we have

$$Pdq_s \approx 0.622 de_s \quad (4.35)$$

Furthermore, from the Clausius-Clapeyron equation

$$de_s = \left(\frac{Le_s}{R_v T^2} \right) dT \quad (4.36)$$

where R_v is the gas constant for water vapor and L is the latent heat of condensation or evaporation. Substitute Equation (4.34) and (4.35) into (4.36) to give

$$dq_s = 0.622 \left(\frac{Le_s}{R_v P T^2} \right) dT = \left(\frac{Lq_s}{R_v T^2} \right) dT \quad (4.37)$$

This result can be substituted into Equation (4.33) and rearranged to get

$$\Delta q = \frac{q_s - q}{1 + L^2 q_s / C_p R_v T^2} \quad (4.38)$$

assuming

$$-L\Delta q = C_p \Delta T \quad (4.39)$$

After Δq is calculated, ΔT can be calculated from Equation (4.39). Δq is reduced at each model level by an empirical determined fraction to account for the fraction which re-evaporates in the next level below. The corresponding ΔT is also given by Equation (4.39).

4.3.4 Dry Convective Adjustment.

During a model integration, if the lapse rate becomes unstable, unrealistically large vertical velocities will be produced. However, persistent unstable lapse rates are not characteristic of the atmosphere and tend to be removed by convection. The vertical column at each grid point in the model domain is tested for any unstable lapse rate, layer by layer. For unstable vertical layers, it is assumed in the model that parcels in the layer are lifted adiabatically to the next layer, exchanging their heat at constant pressure. The exchange takes place until the temperature of the unstable layers are adjusted to a neutral lapse rate. It is apparent that the adjustment of one layer may create an unstable lapse rate in the adjacent layers. The dry convection is carried out iteratively until the column is stable or neutral throughout the whole column.

4.3.5 Planetary Boundary Layer.

The planetary boundary layer of the tropical cyclone model is similar to the one used in Holt et al. (1990). It is parameterized by

the turbulent kinetic energy (TKE) E - ϵ closure with the constants of Detering and Etling (1985). The eddy viscosity in this parameterization is taken as

$$K_m = \frac{C_2 E^2}{\epsilon} \quad (4.40)$$

where K_m is the eddy viscosity, E is the TKE, ϵ is the energy dissipation and C_2 is a constant of 0.026 (Detering and Etling, 1985). Prognostic equations for turbulent kinetic energy (E) and energy dissipation (ϵ) are documented in Holt et al. (1990). The surface layer is parameterized by the Monin-Obukhov similarity relations (Businger et al., 1971). The model temperature at the lowest model layer ($\sigma=9.9975$) is also used as the ground temperature.

The sea surface temperature is obtained from the multi-channel sea surface temperature (MCSST) data derived from AVHRR (Advanced Very High Resolution Radiometer) imageries by University of Miami. This MCSST product is a weekly composite for the global SST at approximately 18 km. Topography used in this model is derived from the United States Navy global 10-minute elevation data,.

4.4 Vertical Mode Initialization.

Errors in the analysis, which can be due to observational

errors and unresolvable scales of motion and inaccuracies in the model physics, may generate freely propagating, inertial-gravity wave oscillations during the numerical integration of models. Such errors are reflecting the unbalance among the wind, mass and temperature fields. For the external and first few vertical modes of the numerical model, the phase speeds of these free propagating, inertial-gravity waves are much larger than the speeds of meteorological systems. The resulting high frequency oscillations can be easily seen in the surface pressure with amplitude as large as 5 to 10 mb (Sashegyi and Madala, 1993).

To reduce the amplitude of these high frequency oscillations inertial-gravity, a Vertical Mode Initialization (VMI) scheme (Sashegyi and Madala, 1990 and 1993) has been developed in NRL following Bourke and McGregor (1983) to filter out the high frequency inertial-gravity waves. The divergence is not assumed to be equal to zero as in the static initialization scheme. Instead, the filtering condition in the VMI is to assume that the first and second derivative of divergence with time is equal to zero. This is based on the fact that the divergence does exist in the real atmosphere. So, the divergence should not be completely removed from the analysis. A second condition, that the linearized potential vorticity is unchanged by the procedure, is required to compute the vorticity. Filtering conditions are applied to the model dynamically equations to derive linear diagnostic equations for the mass divergence,

vorticity and generalized geopotential, which are solved iteratively for the first three vertical modes of the numerical model. Details of the VMI were documented in Sashegyi and Madala (1993). The VMI scheme of the NRL produces a balanced vertical motion field and produces smaller changes to the initial mass and wind fields than the static initialization scheme. The result and discussion after the VMI will be given in the next chapter.

5. OBJECTIVE ANALYSIS AND INITIALIZATION OF FLORENCE.

As mentioned above, the ODWs were used to enhanced the first guess, which are the NMC/RAFS 2.5^0 analyses at 0000 UTC on 09/09/88 bi-cubically interpolated onto a grid of 0.5^0 resolution in longitude and latitude to match the average spacing of the ODWs. Two different ODW data sets were used in this study. In both set, the ODW data were assumed to be valid at 0000 UTC September 9. The first set (ODW1) used all 51 ODW data. The second set (ODW2) is a subset of ODW1 except that a time domain of six-hour from 2100 UTC on September 8 to 0300 UTC September 9 is imposed to filter out the ODW data outside this time domain. A total of 13 ODWs were excluded from ODW1 to form ODW2. The choice of a six-hour time domain centered at 0000 UTC on September 9 was simply based on a 3 hour data cutoff time commonly used in many operation forecasting centers.

5.1 Analyses of Florence.

5.1.1 Result with Two-Pass, Single-Grid Barnes Scheme.

Fig. 5.1a shows the sea level pressures and surface temperatures, and Fig. 5.1b shows the 1000 mb geopotential heights and wind vectors of the NMC/RAFS 2.5^0 analysis at 0000 UTC on September 9. At this time, there is a weak low pressure system in the Gulf of Mexico with a minimum sea level pressure (SLP) of 1004

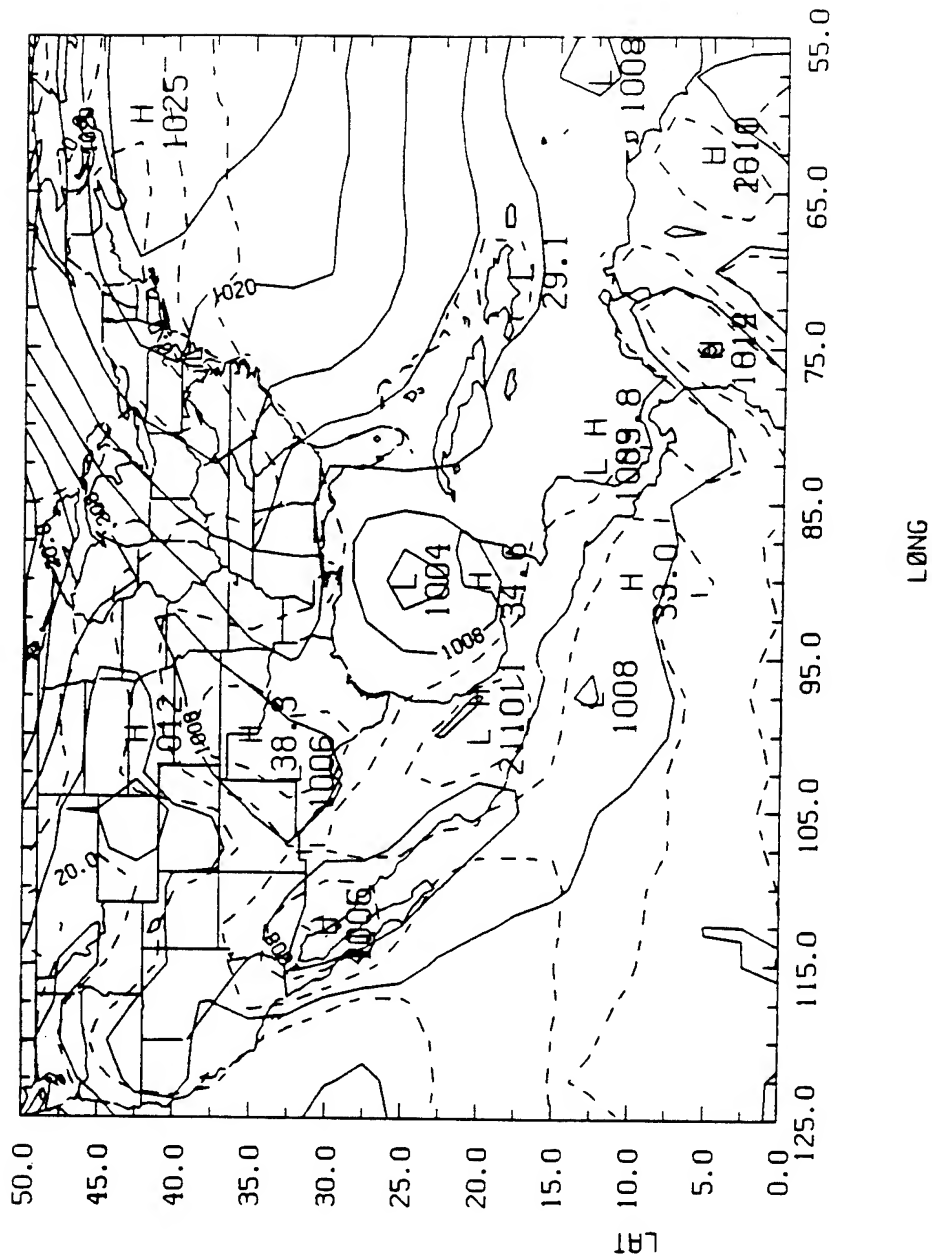


Figure 5.1a Sea level pressures (mb) and surface temperatures (degree C) of the NMC 2.5° analysis at 0000 UTC 9 September 1988.

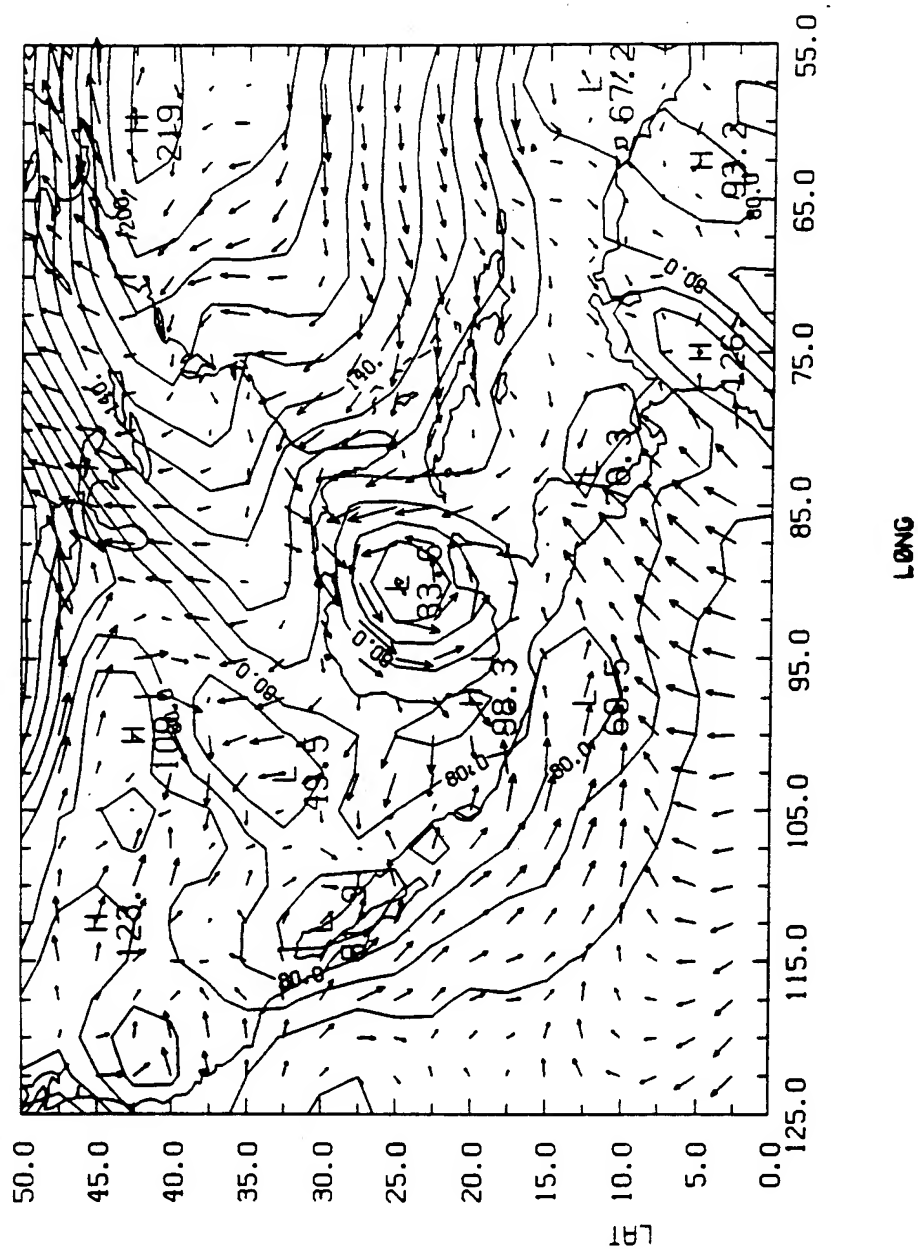


Figure 5.1b Same as Figure 5.1a except for the 1000 mb geopotential heights (m) and wind vectors (ms^{-1}).

mb and a central 1000 mb geopotential height of 33.6 m. The 1000 mb wind vectors in the Gulf of Mexico reveal a weak cyclonic circulation with a maximum wind speed of 13.8 ms^{-1} (in Fig. 5.1c). The best track record (Table 3.1) indicates that the central SLP and the maximum surface wind were 992 mb and 30 ms^{-1} at 0000 UTC on September 9, respectively. It is clear that the NMC/RAFS 2.5⁰ analysis does not fully reproduce Florence's intensity and structure at 0000 UTC on September 9. For easy comparison, Table 5.1 lists the minimum SLP, minimum 1000 mb height and 1000 mb maximum wind speed from the best track record, NMC/RAFS 2.5⁰ analysis and three different ODW enhanced analyses.

Fig. 5.2a and 5.2b show the SLPs and the 1000 mb geopotential heights and wind vectors from the enhanced analyses with the ODW1 data set analyzed by the single-grid Barnes scheme in which only two passes were used. The enhanced analysis shows a better organized tropical storm in the Gulf of Mexico as compared to the NMC/RAFS 2.5⁰ analysis in Fig. 5.1. Comparing both analyses, the central SLP of the two pass analysis with ODW1 is analyzed to be 4 mb deeper than the NMC/RAFS 2.5⁰ analysis. Correspondingly, the 1000 mb geopotential height is analyzed to be 3.6 m instead of 33.6 m. Fig. 5.2c shows the enhanced 1000 mb isotaches. The maximum 1000 mb wind speed near Florence changes from 13.8 ms^{-1} (in Fig. 5.1c) to 16.5 ms^{-1} (in Fig. 5.2c). A relatively calm region near Florence's center is also apparent in Fig. 5.2c but not in Fig. 5.1c. The

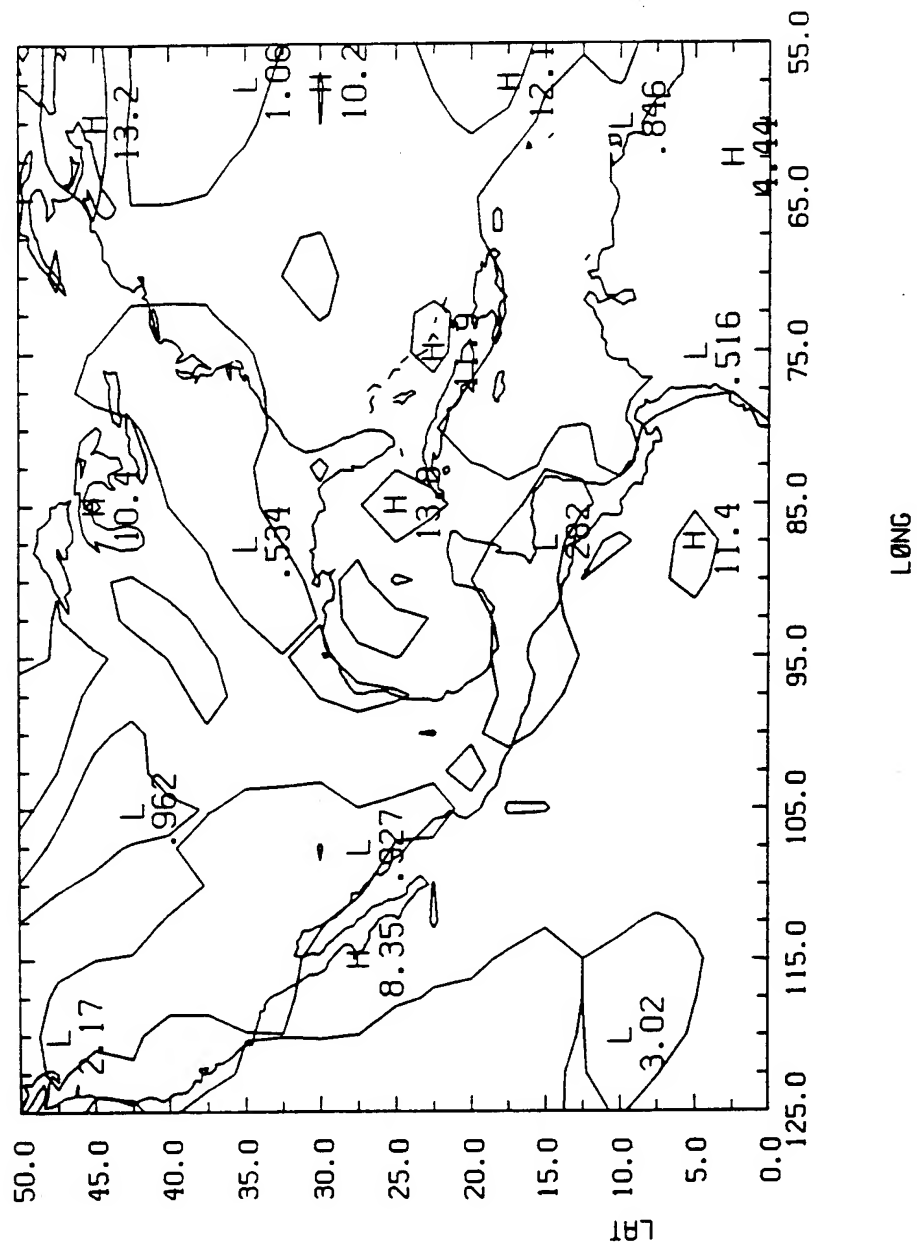


Figure 5.1c Same as Figure 5.1a except for the 1000 mb isotaches.

	Minimum SLP (mb)	Minimum 1000 mb height (m)	Maximum 1000 mb wind speed (m s ⁻¹)
Best track record	992	-----	25.7
NMC/RAFS 2.5° Analysis	1004	33.6	13.8
ODW1 enhanced analysis with single-grid two-pass	1000	3.57	16.5
ODW1 enhanced analysis with nested three-pass	994	-53.2	26.5
ODW2 enhanced analysis with nested three-pass	994	-52.0	30.4

Table 5.1. Minimum SLPs, minimum 1000 mb heights, maximum 1000 mb wind speeds from the best track record, NMC/RAFS 2.5° Analysis and three different ODW enhanced analyses. The minimum 1000 mb height was not available from the best track record.

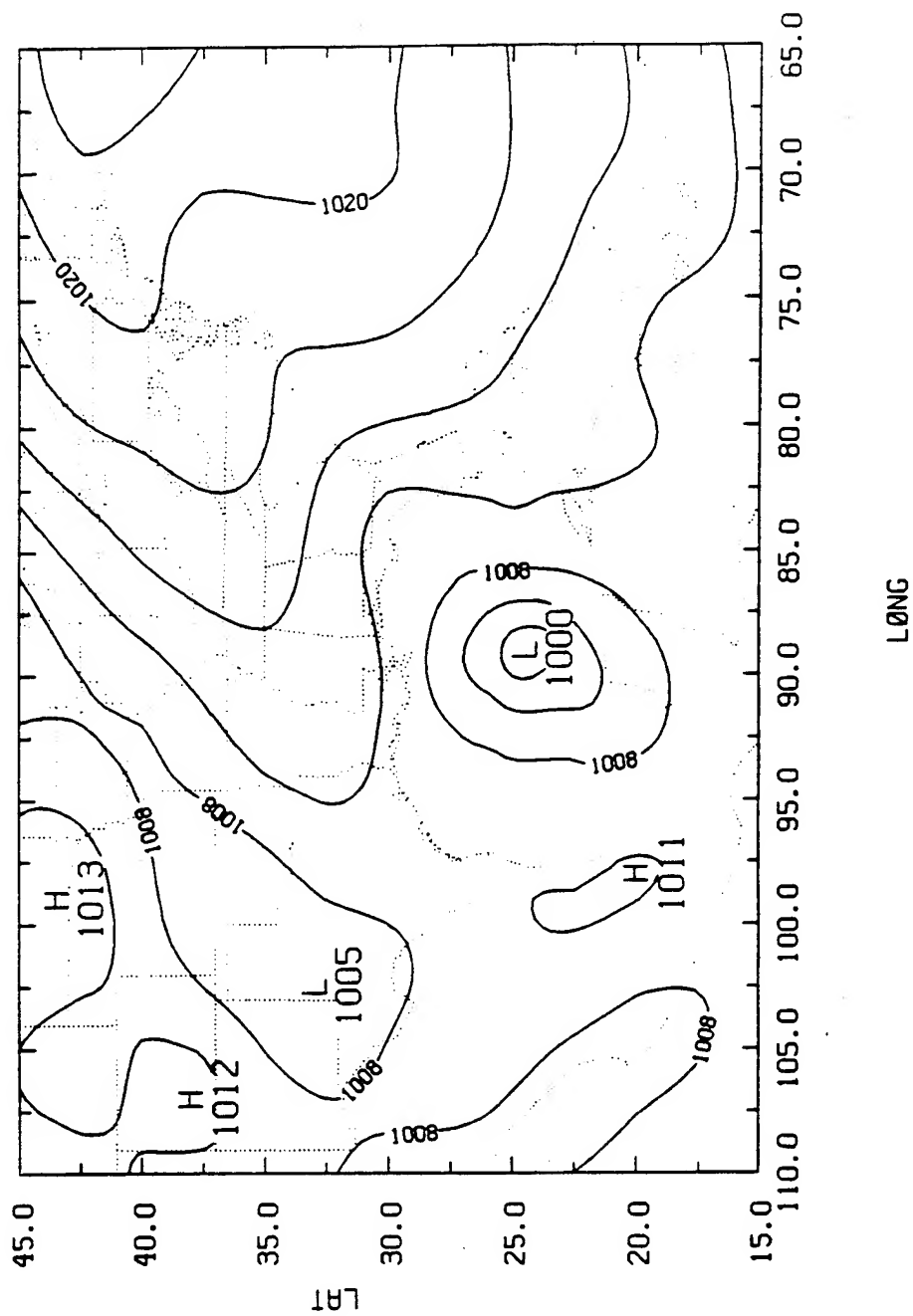


Figure 5.2a Sea level pressures (mb) and surface temperatures (degree C) of the ODW1 enhanced analysis by the single-grid two-pass Barnes scheme.

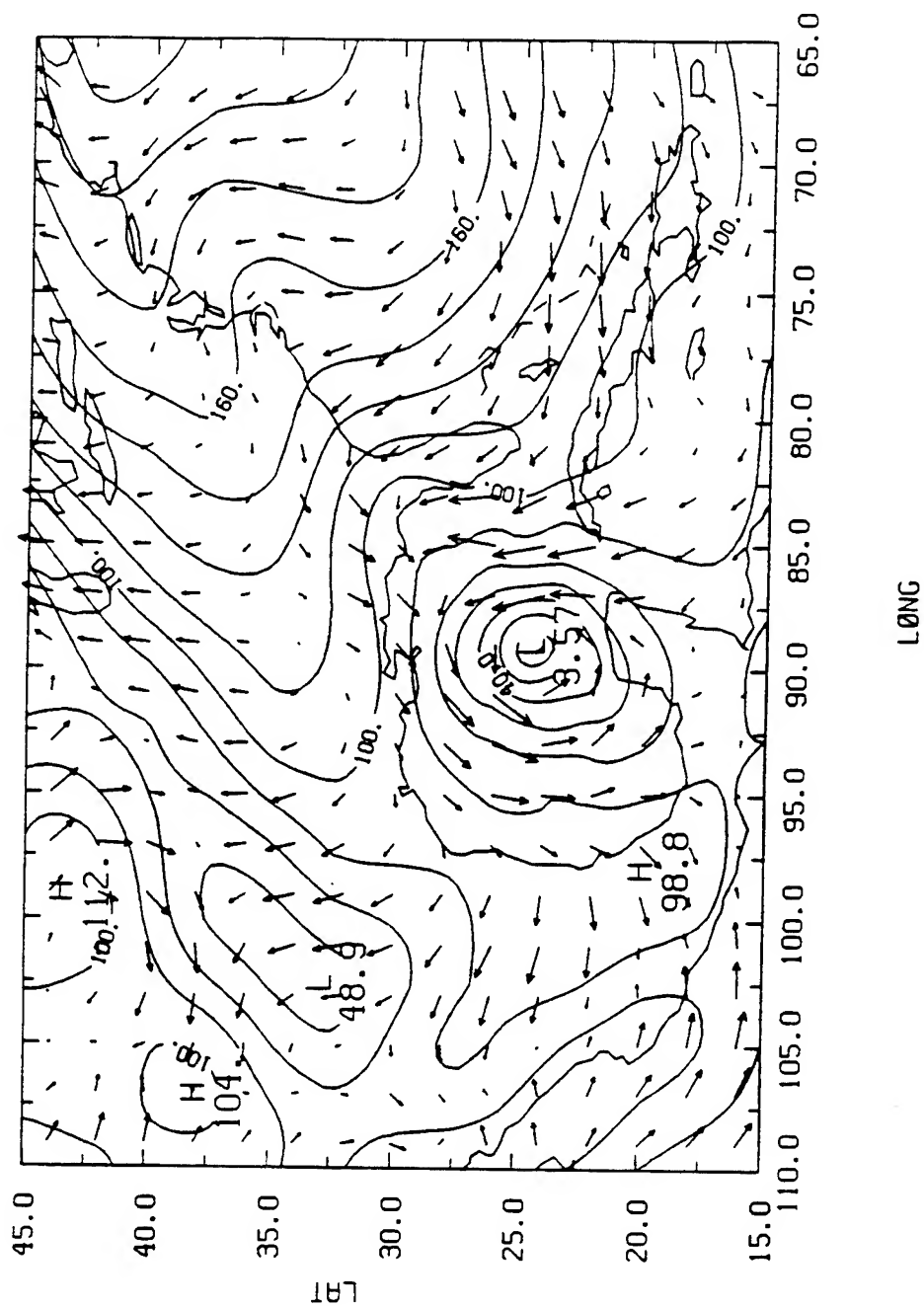


Figure 5.2b Same as Figure 5.2a except for the 1000 mb geopotential heights (m) and wind vectors (ms^{-1}).

single-grid two-pass enhanced analysis with ODW1 have shown the hurricane in more detail and provide better analysis. The two-pass enhanced analysis with the ODW2 data were also performed. Results are not shown here because the analysis is similar to the analysis enhanced by ODW1.

5.1.2 Result with Three-Pass, Nested-Grid Barnes Scheme.

A detailed examination of the ODW1 data reveals that SLP of 992 mb and 1000 mb geopotential heights of -65 m were recorded at some locations near the hurricane center. It is apparent that a more realistic analysis can still be extracted from the ODW data. As mentioned in the previous chapter, the analysis after the first two passes are used as the background data. The ODW1 inside the third pass domain without "buddy" checks are used in the analysis. Because the third pass is carried out over a smaller region covering only the hurricane inner core region, this should ensure that the analysis is confined within the region near the inner core of Florence and result in a better representation of Florence's structure in the inner region. The same analysis procedure is also performed with ODW2.

Fig. 5.3a shows the SLPs and Fig. 5.3b shows the 1000 mb geopotential heights and wind vectors enhanced by the ODW1 with

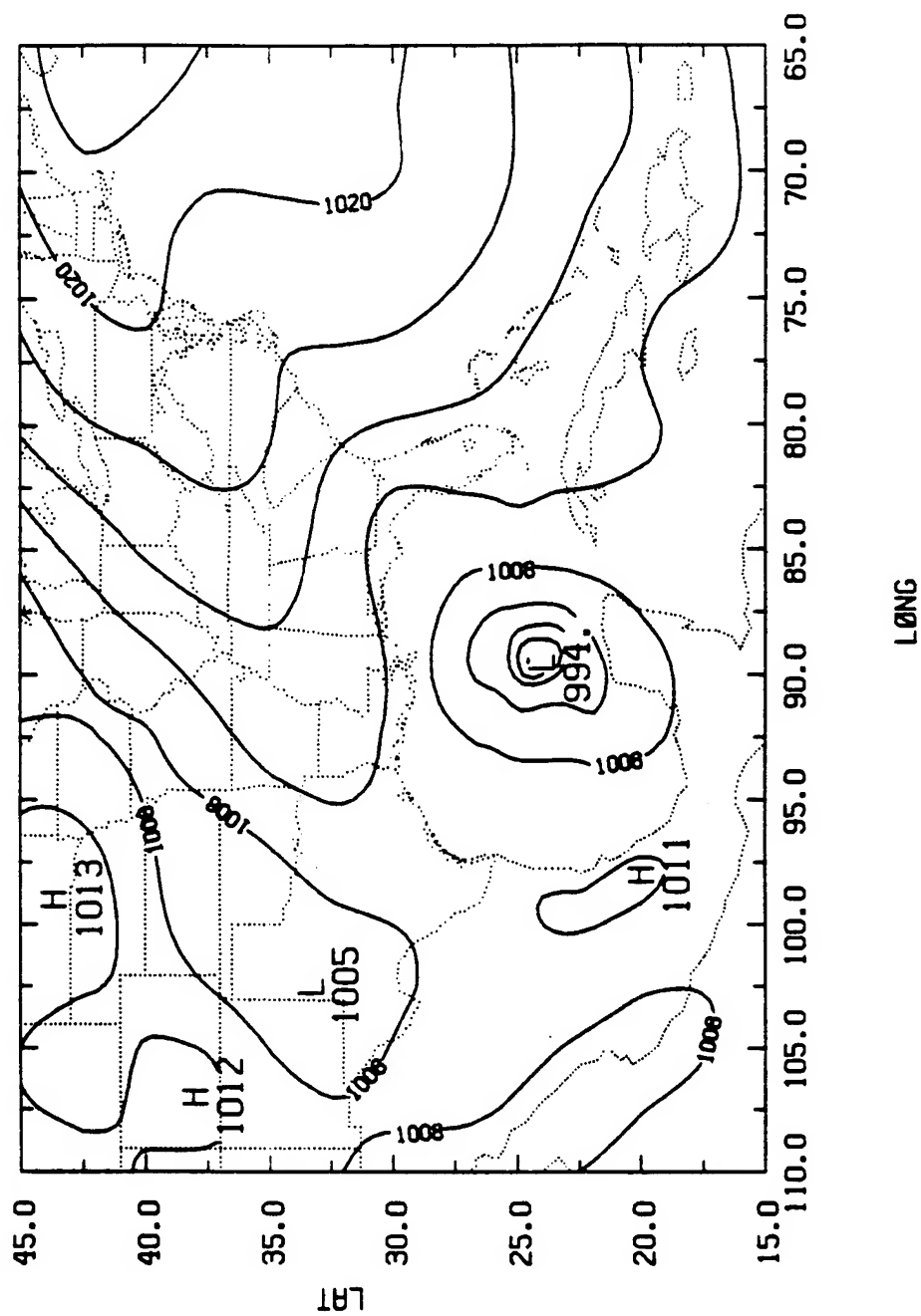


Figure 5.3a Sea level pressures (mb) and surface temperatures (degree C) of the ODW1 enhanced analysis by the nested three-pass Barnes scheme.

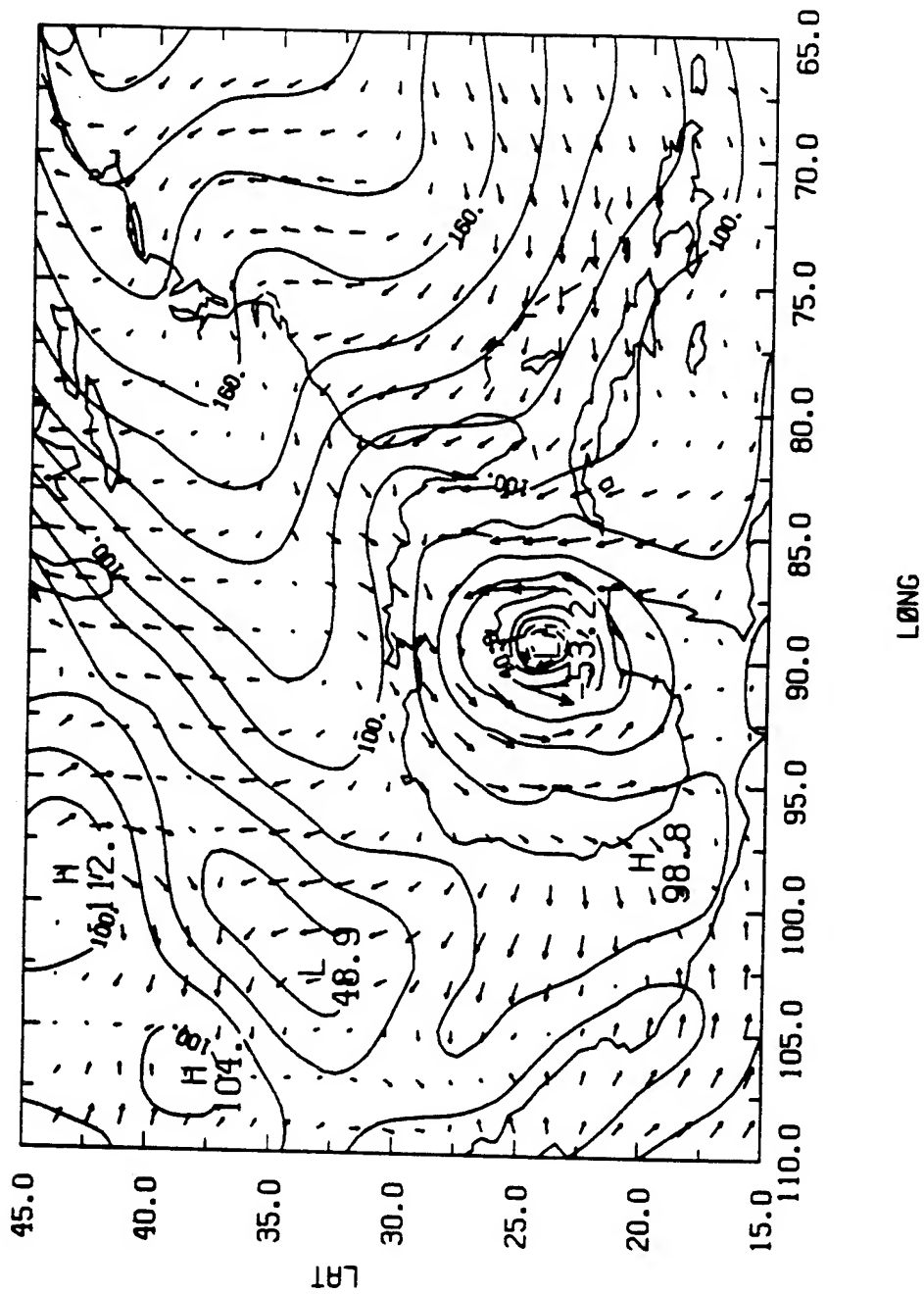


Figure 5.3b Same as Figure 5.3a except for the 1000 mb geopotential heights (m) and mb wind vectors (ms^{-1}).

the nested three-pass Barnes scheme. Comparing Figs. 5.2 to Figs. 5.2, it is clear that the central pressure and the 1000 mb geopotential height are reduced from 1000 mb and 3.57 m with two passes to 994 mb and -53.20 m with three passes, respectively. Fig. 5.3a and 5.3b show more tightly packed contours near the center which are typical for a tropical cyclone. Fig. 5.3c shows the 1000 mb isotaches with a maximum wind speed of 26.5 ms^{-1} , increased from 16.5 ms^{-1} from the two-pass single-grid analysis (Fig. 5.2c). The nested third pass also results in an increase of the wind speed in the northwest and northeast quadrants near the center (Fig. 5.3c).

It is clear that the general patterns and the environments of Florence in the two objective analyses (Fig. 5.2 and Fig. 5.3) are basically the same except for the intensity and the structure near the storm center. It is apparent that the analysis obtained with the nested three-pass analysis scheme has a stronger intensity, which is closer to the best track record (Table 3.1). The additional pass resolves the structure of the center better than the analysis obtained with the single-grid two-pass analysis scheme.

ODW2 was also used to enhance the same first guess which were used with the ODW1. This was done because some ODW data dropped before 2100 UTC September 8 and after 0300 UTC September 9 may not be suitable to represent the synoptic conditions at 0000 UTC September 9. Fig. 5.4a, 5.4b and 5.4c show

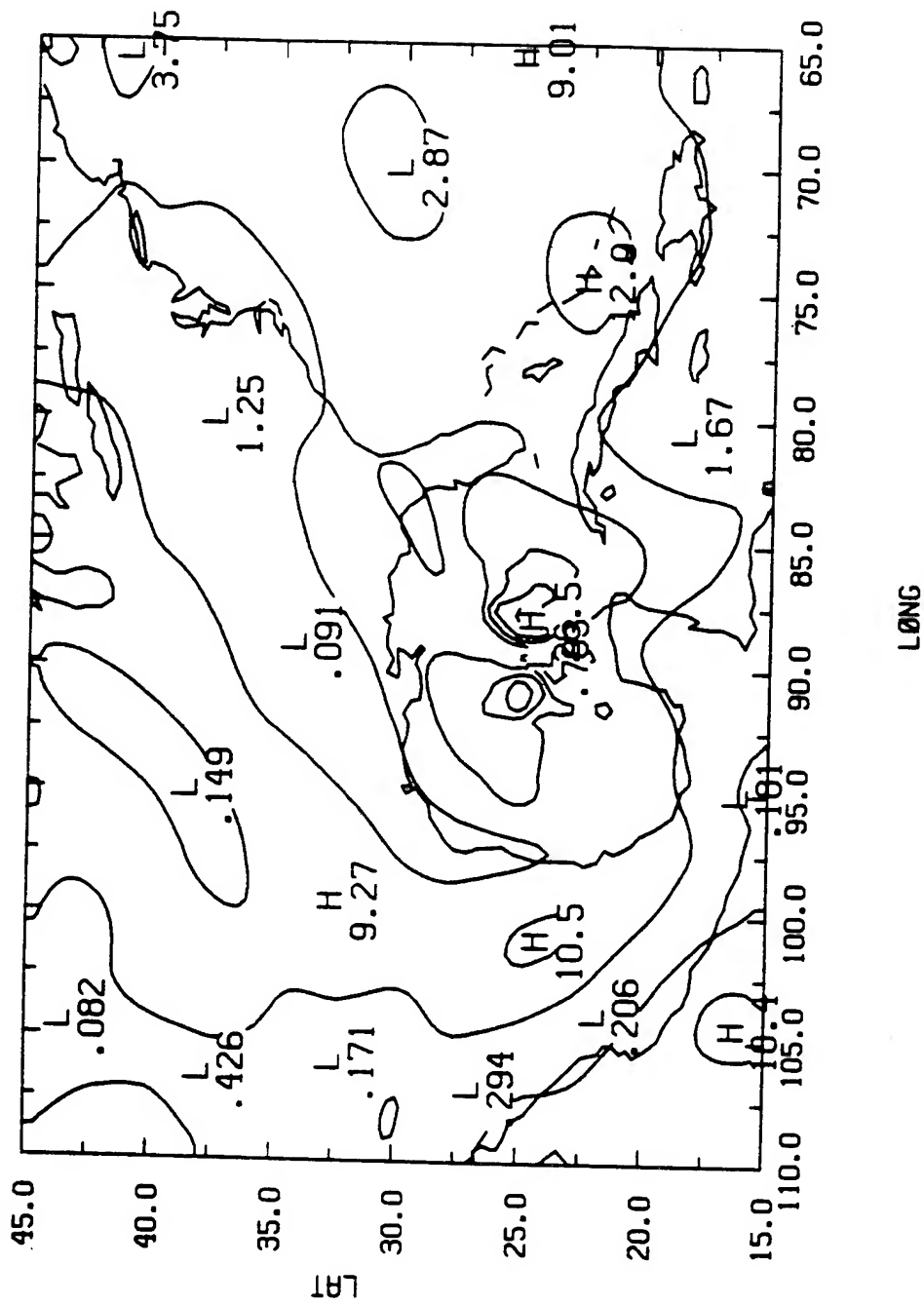


Figure 5.3c Same as Figure 5.3a except for the 1000 mb isotaches.

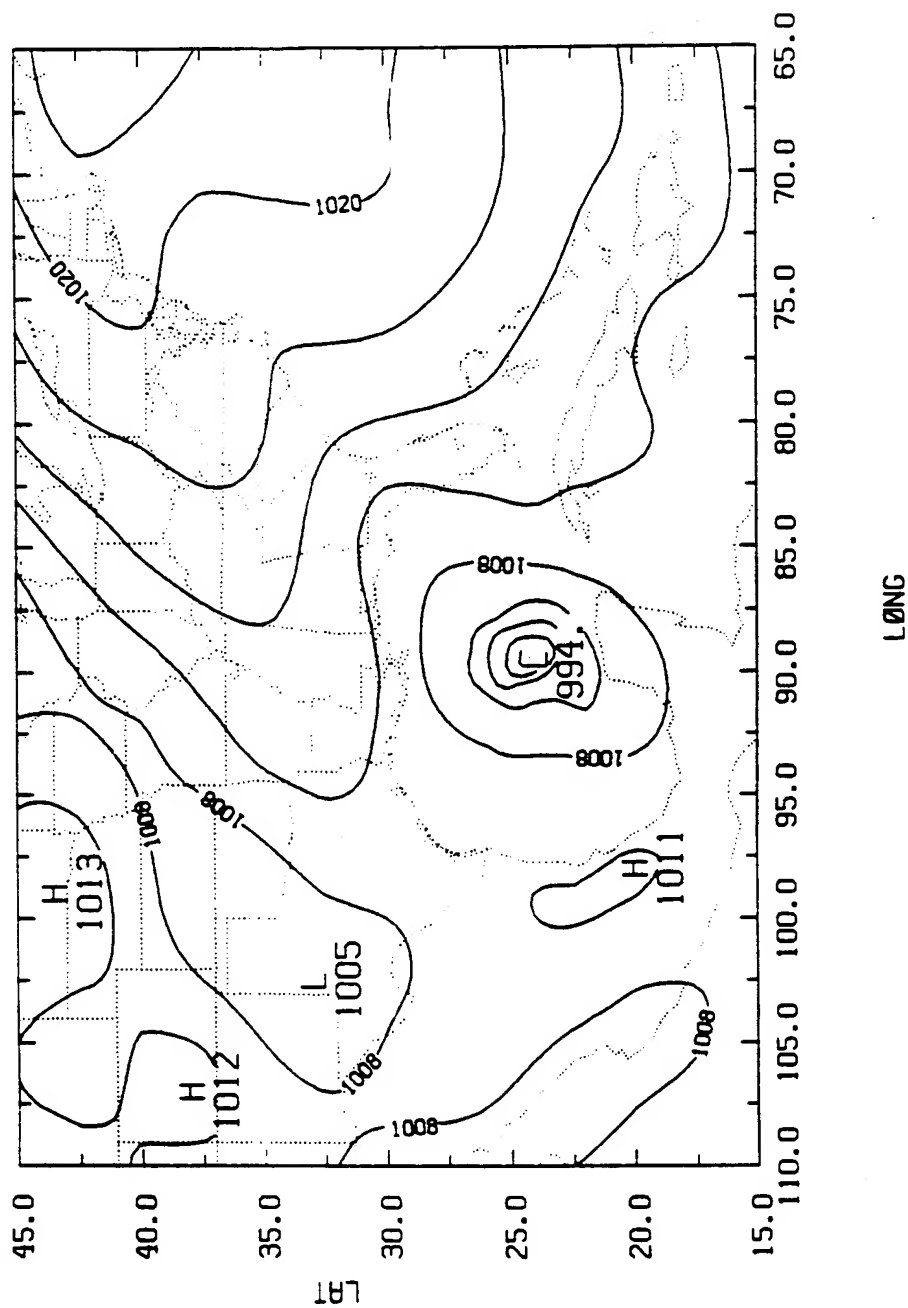


Figure 5.4a Sea level pressures (mb) and surface temperatures (degree C) of the ODW2 enhanced analysis by the nested three-pass Barnes scheme.

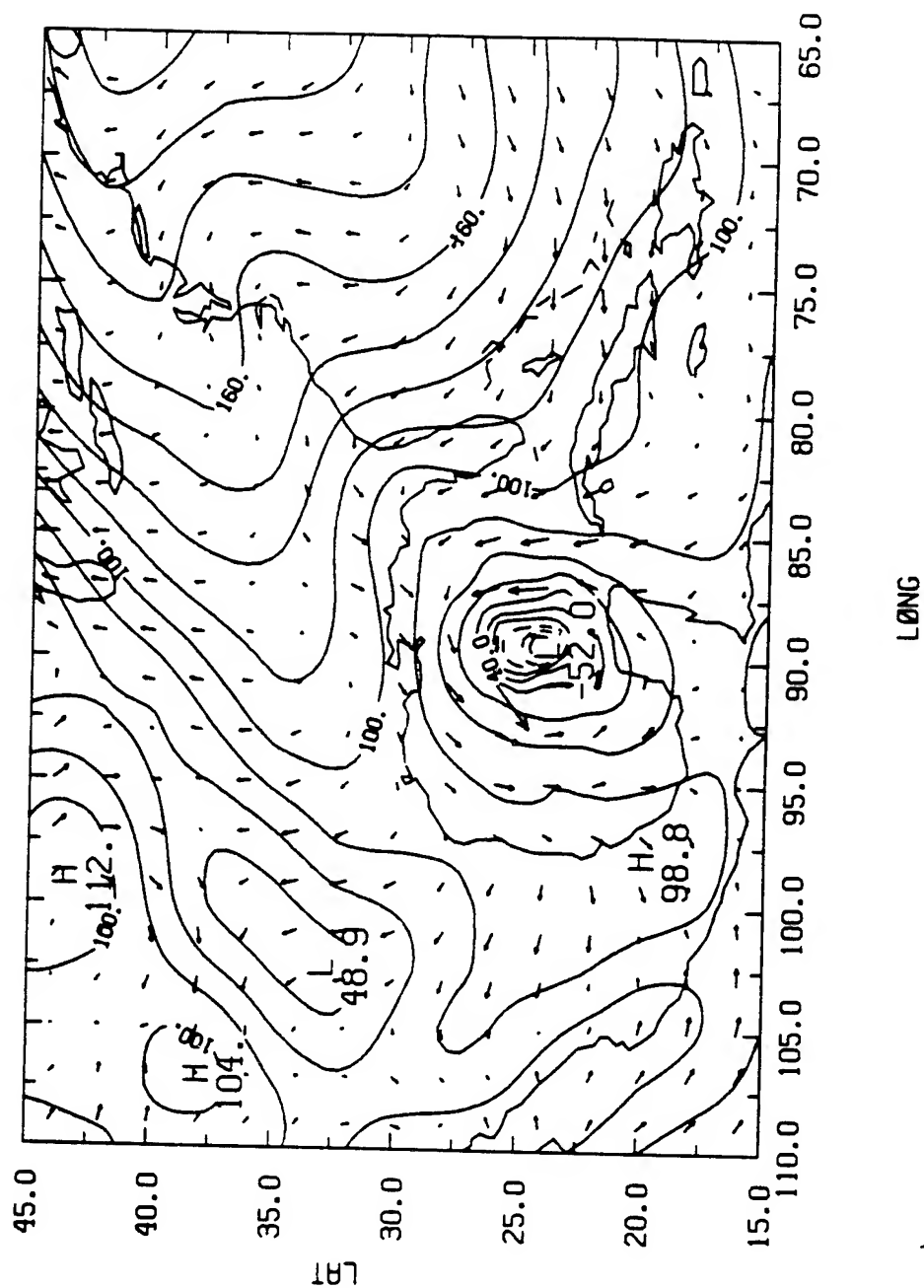


Figure 5.4b Same as Figure 5.4a except for the 1000 mb geopotential heights (m) and wind vectors (ms^{-1}).

the SLPs, the 1000 mb geopotential heights and wind vectors and the 1000 mb isotaches enhanced by ODW2 with the nested three-pass Barnes scheme. The SLP pattern and the minimum SLP remain almost unchanged from the enhanced analysis with ODW1 (Fig. 5.3a). The 1000 mb geopotential height was also nearly identical except that the minimum height was increased from -53.2 m (Fig. 5.3b) to -52.0 m (Fig. 5.4b). However, comparing Fig. 5.4c and Fig. 5.3c, the maximum wind speed was increased from 26.5 m (Fig. 5.3c) to 30.4 m (Fig. 5.4c) and the location of the maximum wind speed was shifted from northeast of Florence to northwest in the analysis with ODW2. This shift is because most of the ODW data that were dropped from the original data set to form ODW2 covered mainly the western and northern portion of Florence (see Fig. 2.1).

5.1.3 Summary.

The two-pass Barnes scheme with an uniform grid is incapable of fully utilizing the ODW data collected during the Synoptic Flow Experiment on 8-9 September 1988. A nested three-pass, Barnes scheme was then applied to accommodate the relatively higher resolution of the ODWs near the center of Florence. In addition, a six-hour time window (three hours before and after 0000 UTC, 9 September 1988) was used to filter out the ODWs that were collected outside the time window. The primary result shows the ODW data are useful in enhancing the NMC/RAFS 2.5⁰ analyses to

produce a well organized tropical cyclone, even with just the two-pass Barnes scheme. The result also shows that the analyses with the nested three-pass Barnes scheme enhance the NMC/RAFS 2.5⁰ analyses much better than the analyses with the two-pass, single-grid Barnes scheme. In Table 5.1, the minimum SLP was changed from 1004 mb in the NMC/RAFS 2.5⁰ analysis to 1000 mb in the ODW1 analysis with the two-pass, single-grid analysis and to 994 mb in both the ODW1 and ODW2 analysis with the nested three-pass analysis (Table 5.1), while it is 992 mb in the best track record at 0000 UTC on September 9.

After a close examination of the objective analyses, it is difficult to determine the superiority between the ODW1 and ODW2 enhanced analyses. The tropical cyclone model was then integrated with the NMC/RAFS 2.5⁰ analyses and the two different enhanced objective analysis data sets as the initial conditions to study the importance of an accurate objective analysis to the numerical simulation. The result will be shown in Chapter 6.

5.2 Initialization.

As mentioned in Chapter 4, the VMI were used to initialize the analyses in order to minimize the high frequency inertial-gravity wave oscillations. The NMC/RAFS 2.5⁰ analyses (Control) and the three-pass enhanced analysis data by ODW1 and ODW2 were all

initialized by the VMI before being used as the initial condition of the tropical cyclone model. Before the initialization process, the 1000 mb temperature field was recomputed hydrostatically from the 850 mb temperature based on a moist adiabatic lapse rate. The reason for recomputing the 1000 mb temperature field is that the 1000 mb temperature field of the NMC/RAFS 2.5⁰ analyses has unrealistic high values east of the Rocky Mountain (Fig. 5.5).

Fig 5.6 shows the initialized SLPs and the 1000 mb wind vectors of the ODW2 enhanced analyses with three passes while Fig. 5.7 shows the initialized 1000 mb isotaches of the ODW2 enhanced analyses with three passes. Comparing with Fig. 5.4a and 5.4c, it is apparent that the VMI weakened the minimum SLP of Florence by about 9 mb while the 1000 mb maximum wind speed was decreased only by 1.3 ms^{-1} . The same effect was also revealed in the minimum SLP and 1000 mb maximum wind speed of Florence with the ODW1 enhanced analyses (not shown here).

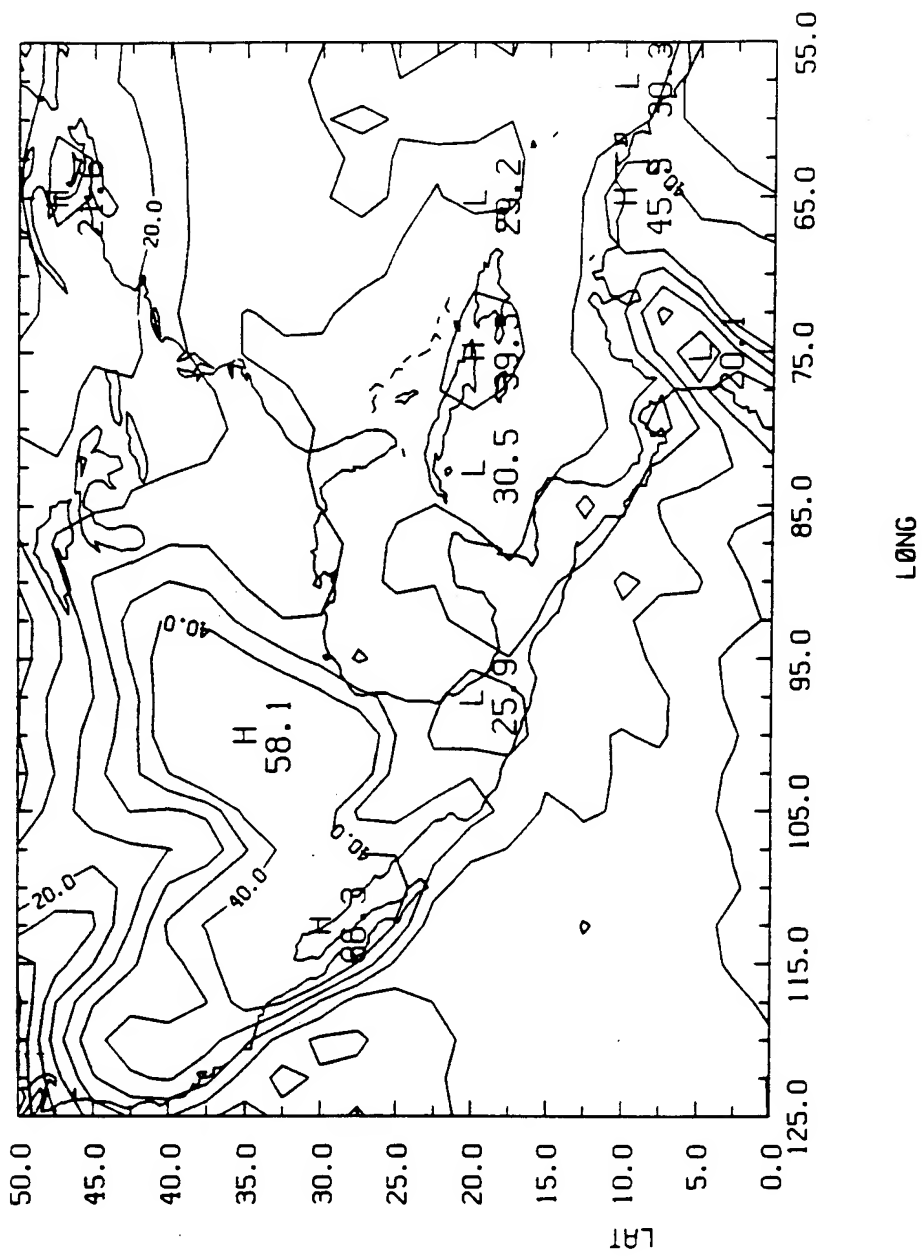
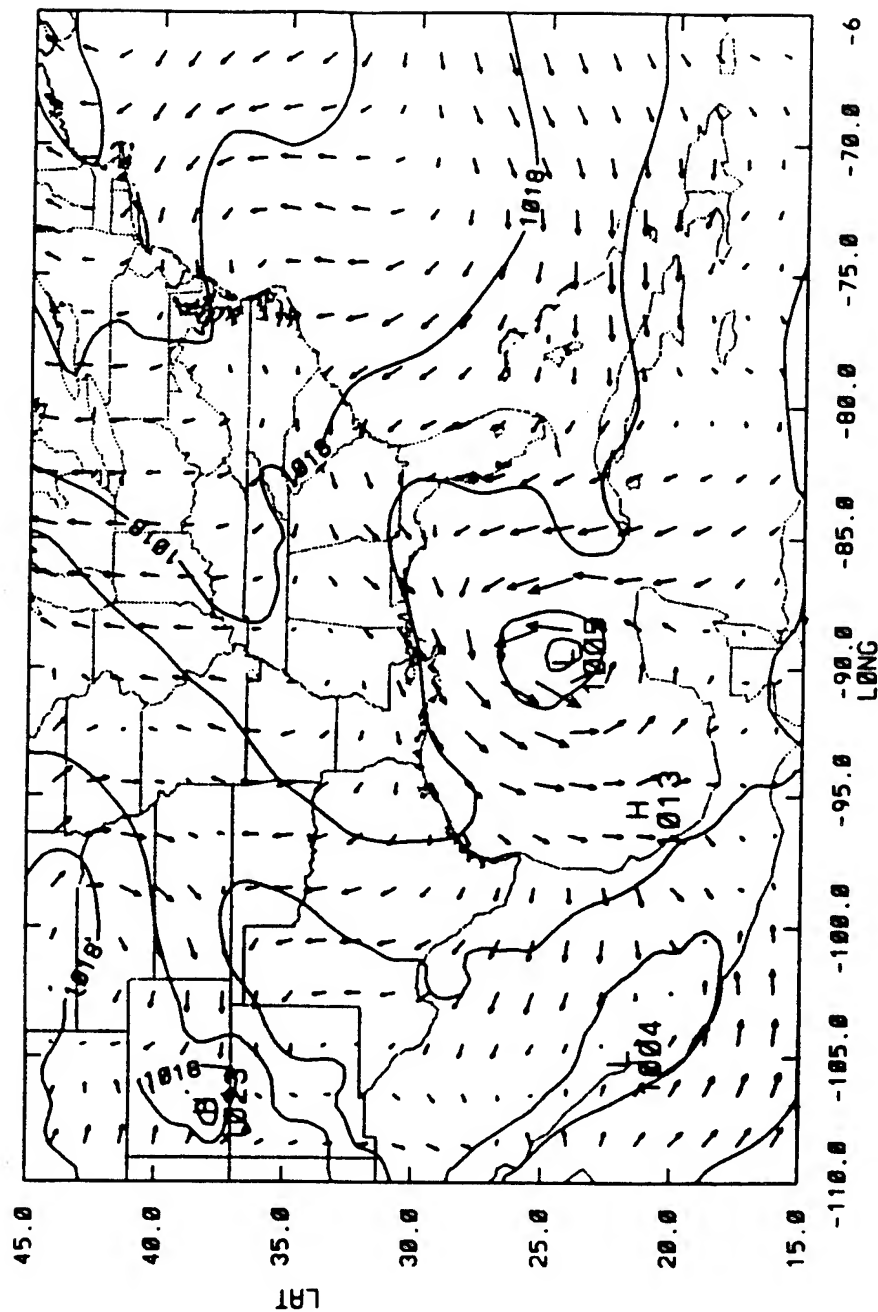


Figure 5.5 1000 mb temperatures of the NMC 2.5° analysis at 0000 UTC 9 September 1988.



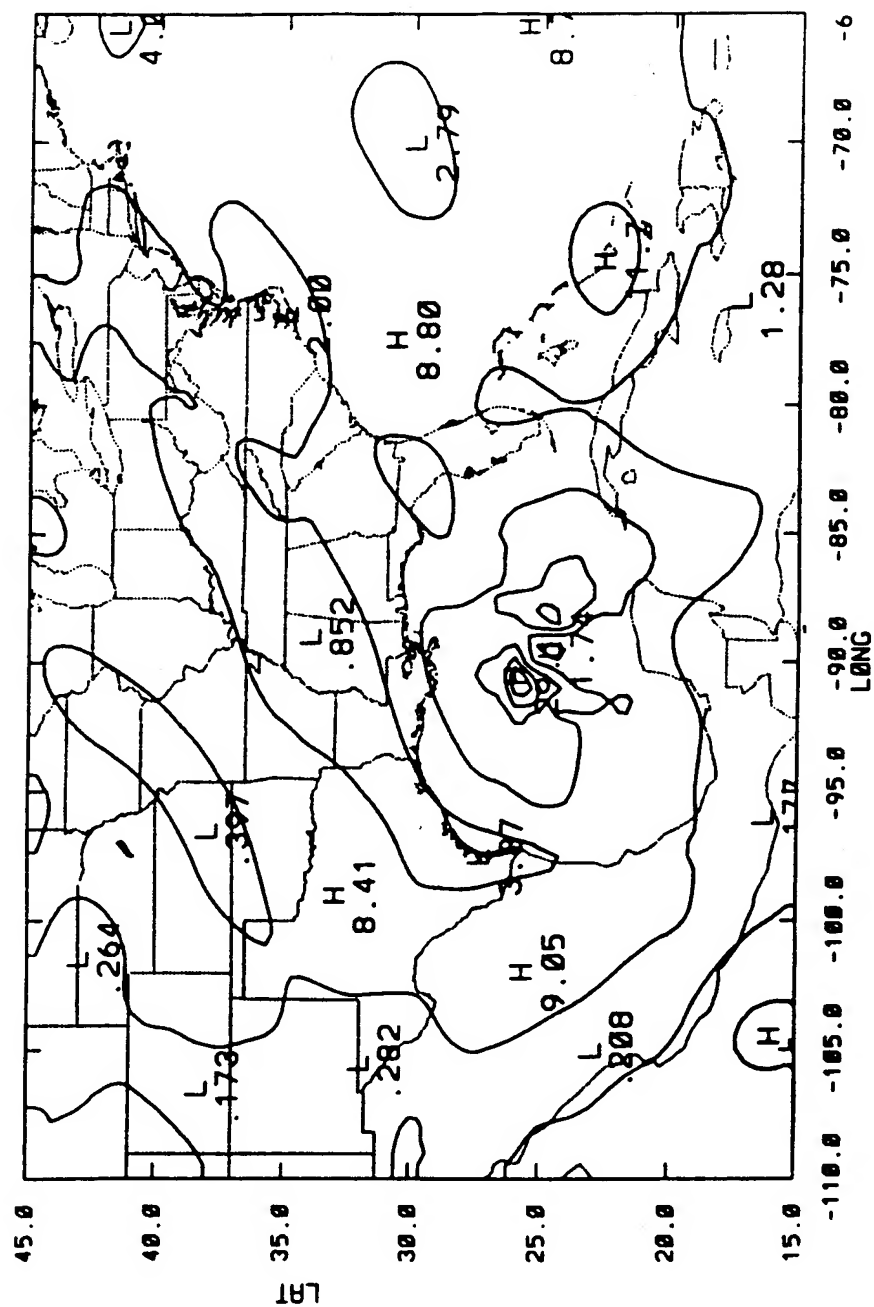


Figure 5.7 Same as Figure 5.6 except for 1000 mb isotaches.

6. SIMULATION OF HURRICANE FLORENCE (1988).

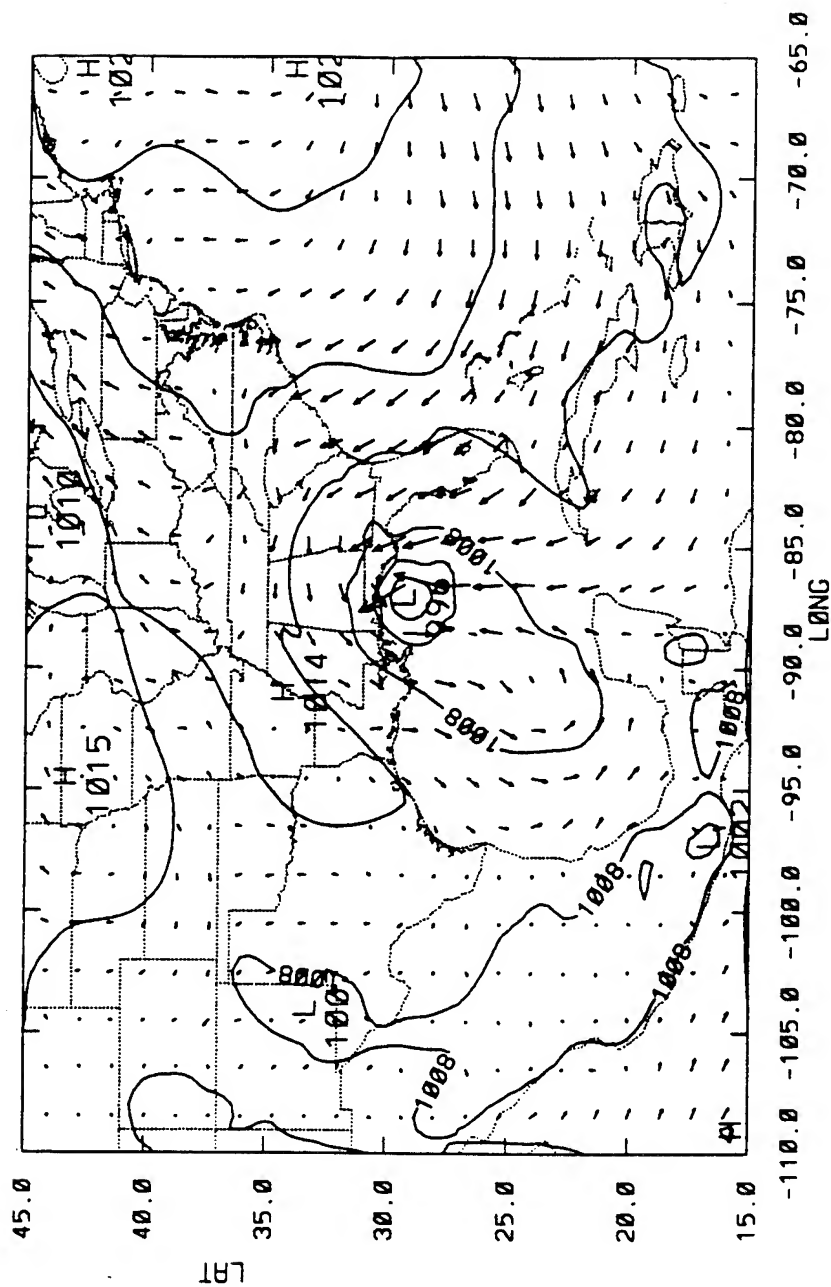
In order to assess the impact of the ODWs and the SSM/I rain rate data on the numerical simulation and to analyze the outflow structures of Florence (1988), five different model integrations with different initial data have been conducted. All the model runs were started at 0000 UTC 9/9/88 and integrated for 48 hours. The first numerical simulation (the control experiment) used the NMC/RAFS 2.5⁰ analyses at 0000 UTC 9/9/88 as the initial data. The second numerical simulation (Exp. ODW1) used the ODW1 enhanced analysis as the initial data. The third one (Exp. ODW2) was the same as the second except it used the ODW2 enhanced analyses as the initial data. The fourth (Exp. Control+SSMI) and fifth ones (Exp. ODW2+SSMI) used the NMC/RAFS 2.5⁰ analyses at 0000 UTC 9/9/88 and the ODW2 enhanced analyses, respectively, with the SSM/I rain rate data assimilated into the model during the integration. The last two experiments were designed to study the impact of the SSM/I rain rate data on the numerical simulation. The details of the SSM/I rain rate assimilation in Exps. Control+SSMI and ODW2+SSMI will be described in Chapter 7. In addition, a detailed diagnosis of the simulated structure of the outflow of Florence will be presented in Chapter 8. In this chapter, the storm intensity, track and rain rates in the control, ODW1 and ODW2 experiments are discussed.

6.1 Control Experiment with NMC/RAFS 2.5 Degree

Analyses.

Fig. 6.1 shows the SLPs and the 1000 mb wind vectors at 12, 18 and 24 hour from the control experiment. The minimum SLPs of the control experiment are 996, 995 and 997 mb at 12, 18 and 24 hour respectively. The locations of the control storm center are at (87.1W, 29.1N), (86.8W, 30.7N) and (86.7W, 32.1N) at 12, 18 and 24 hour respectively. Compared with the best track record shown in Table 3.1, the simulated storm in the control experiment is weaker than the best track record by an average of 10 mb and moves northward faster than the best track record. At 24 hour, the control storm is 3.4° north and 2.6° east of Florence in the best track record. The maximum surface wind speeds are 33.6, 28.6 and 22.2 ms^{-1} at 12, 18 and 24 hour respectively. The maximum wind speed at 24 hour is much weaker than the best track record because the control storm has made landfall at 17 hour, while the best track record shows that Florence was actually still over the ocean at 0000 UTC September 10.

The comparison of the minimum SLPs, the maximum wind speeds and the locations of the storm center from the best track record and the three simulation experiments: the control experiment, Exp. ODW1 and ODW2, are listed in Table 6.1. It is clear that the control experiment started with NMC/RAFS 2.5° analysis does not reproduce the intensity and the track of the Florence well. The storm



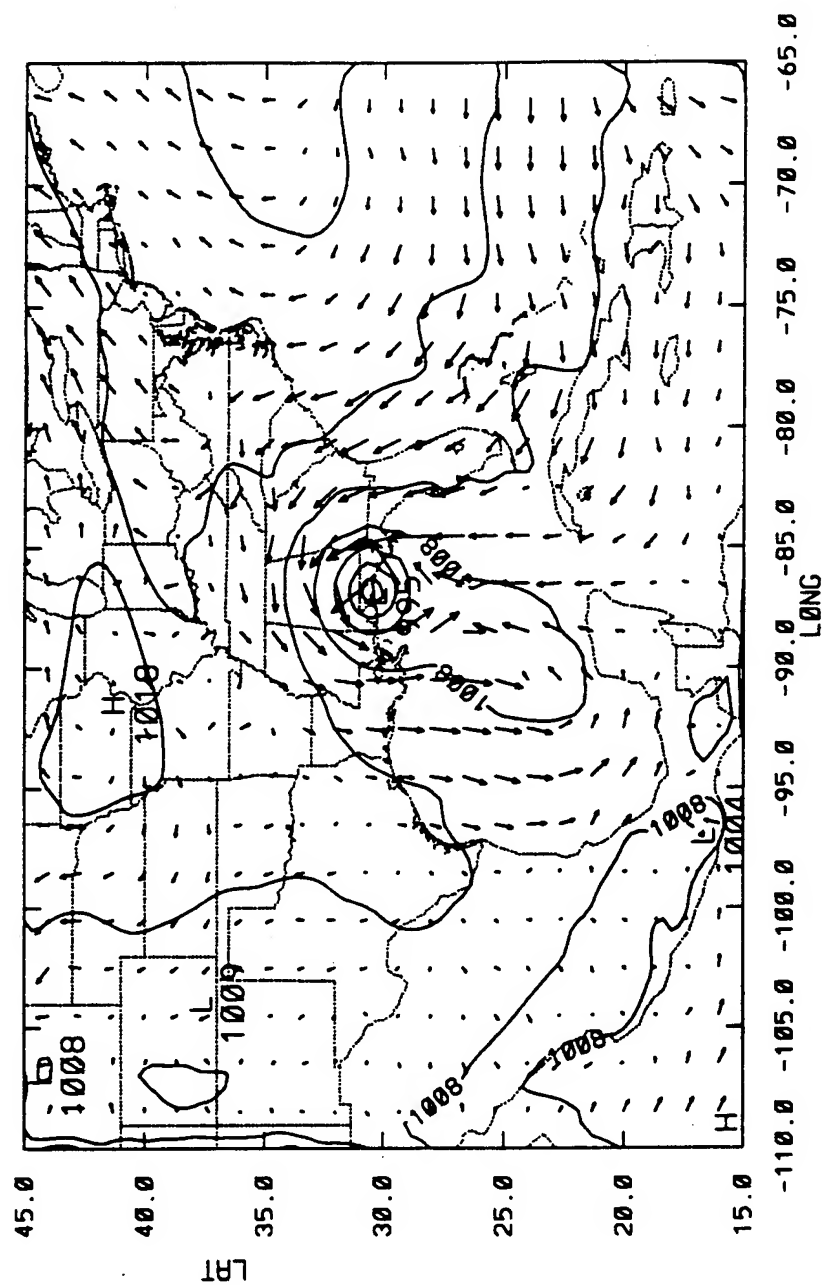


Figure 6.1b Same as Figure 6.1a except for 18 hour.

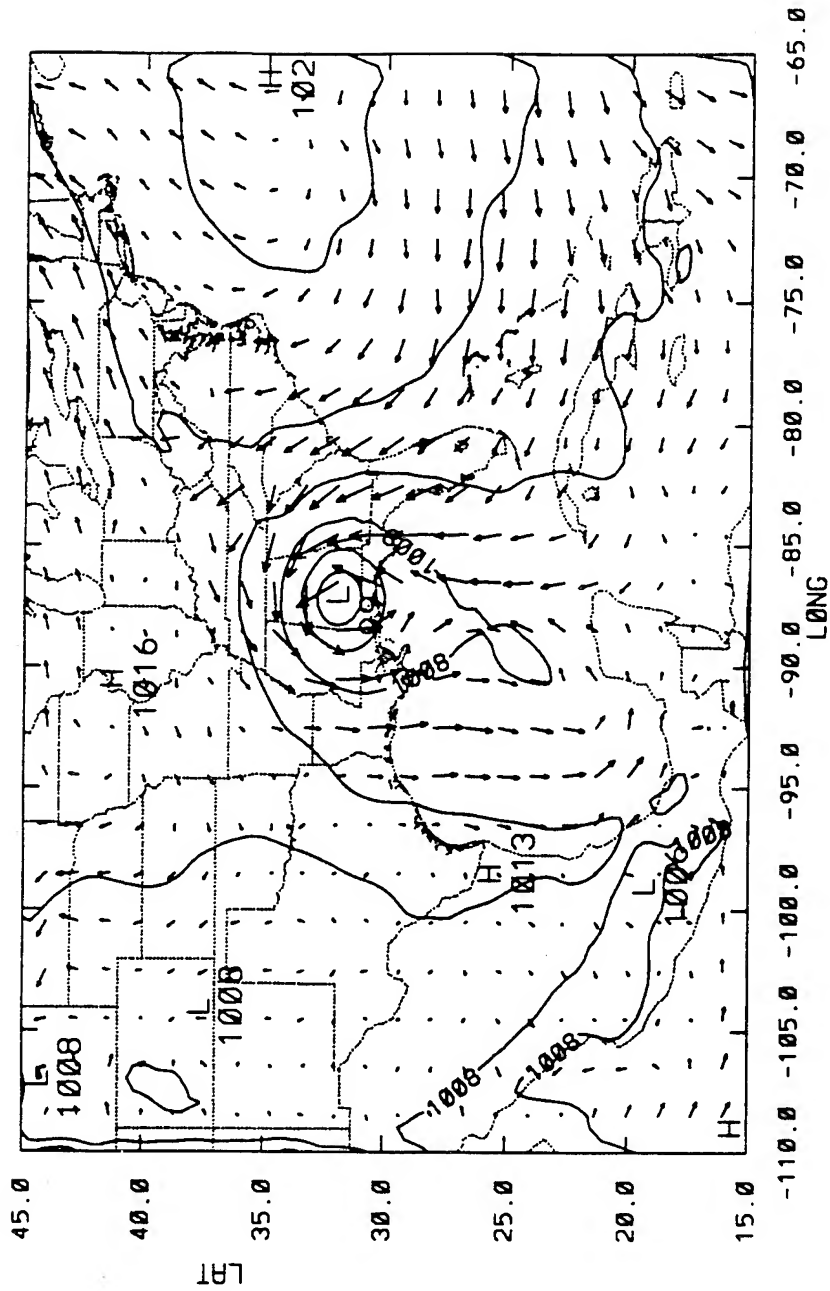


Figure 6.1c Same as Figure 6.1a except for 24 hour.

Minimum Sea Level Pressure (mb)					
	0 h	6 h	12 h	18 h	24 h
Best Track Record	992	991	988	985	983
Control	1006	1003	996	995	997
ODW1	1003	999	996	985	980
ODW2	1005	1001	997	988	987

Maximum Surface Wind Speed (ms^{-1})					
	0 h	6 h	12 h	18 h	24 h
Best Track Record	25.7	25.7	28.3	33.4	36.0
Control	14.1	23.7	33.6	28.6	22.2
ODW1	22.1	24.2	31.4	35.9	46.8
ODW2	28.4	24.4	30.4	35.8	38.8

Location of Storm Center					
	0 h	6 h	12 h	18 h	24 h
Best Track Record	89.2W 24.2N	89.2W 25.2N	89.2W 26.1N	89.2W 27.4N	89.3W 28.7N
Control	89.9W 24.9N	87.1W 27.3N	87.1W 29.1N	86.8W 30.7N	86.7W 32.1N
ODW1	89.4W 24.2N	88.9W 25.3N	88.7W 27.3N	89.2W 28.3N	89.4W 29.6N
ODW2	89.4W 24.3N	88.6W 25.6N	88.8W 27.1N	89.1W 28.5N	89.3W 29.6N

Table 6.1. Minimum SLP (mb), maximum wind speed (ms^{-1}) and location of storm center from the best track record, the control experiment, Exp. ODW1 and ODW2.

in the control experiment makes landfall at about 17 hour, valid for 1700 UTC September 9, which is 9 hours earlier than the actual landfall. The location of the landfall in the control experiment is in northwestern Florida and is about 3 degree northeast of the location of the actual landfall in the best track record. The intensity of the storm in the control experiment is much weaker than the best track record because the faster northward moving speed in the simulated storm may have prevented it from acquiring the moisture needed for intensification. In Fig. 6.1, there is a warm front stretched from northern Florida to North Carolina. This is verified by the surface analysis (not shown here) issued by National Weather Service (NWS).

6.2 Integrations from the ODW1 and ODW2 Enhanced Analyses.

The second and third model simulations are Exp. ODW1 and ODW2 which were integrated from the ODW1 and ODW2 enhanced analysis, respectively. Fig. 6.2 shows the SLPs and the 1000 mb wind vectors at 12, 18 and 24 hour of Exp. ODW1. The minimum SLPs of the simulated storm in Exp. ODW1 are 996, 985 and 980 mb at 12, 18 and 24 hour respectively. The locations of the simulated storm center are (88.7W, 27.29N), (89.2W, 28.3N) and (89.4W, 29.6N). The maximum surface wind speeds of the simulated storm are 31.4, 35.9 and 46.8 ms^{-1} at 12, 18 and 24 hour respectively as shown in Table 6.1. For Exp. ODW2, Fig. 6.3 shows the SLPs and the 1000 mb wind

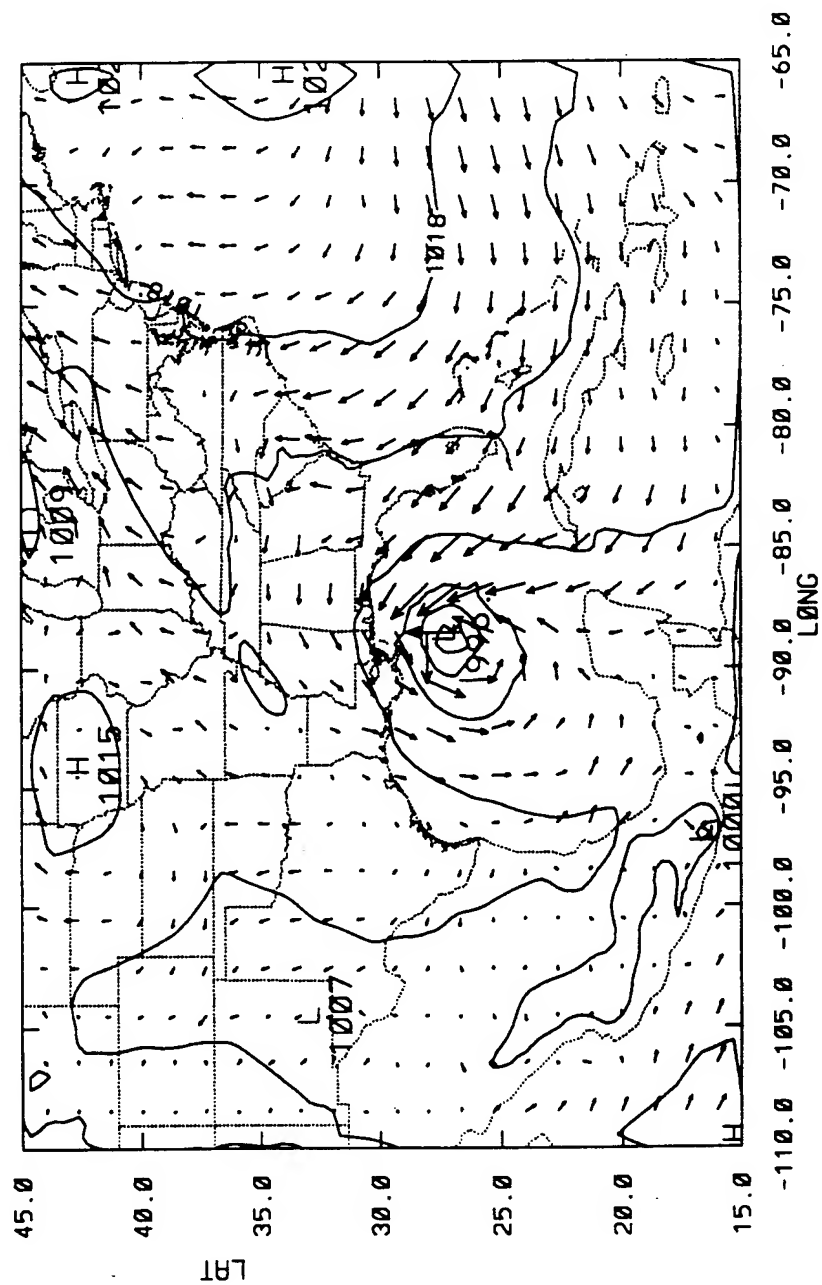


Figure 6.2a Sea level pressures (mb) and surface temperatures (degree C) of Exp. ODW1 at 12 hour.

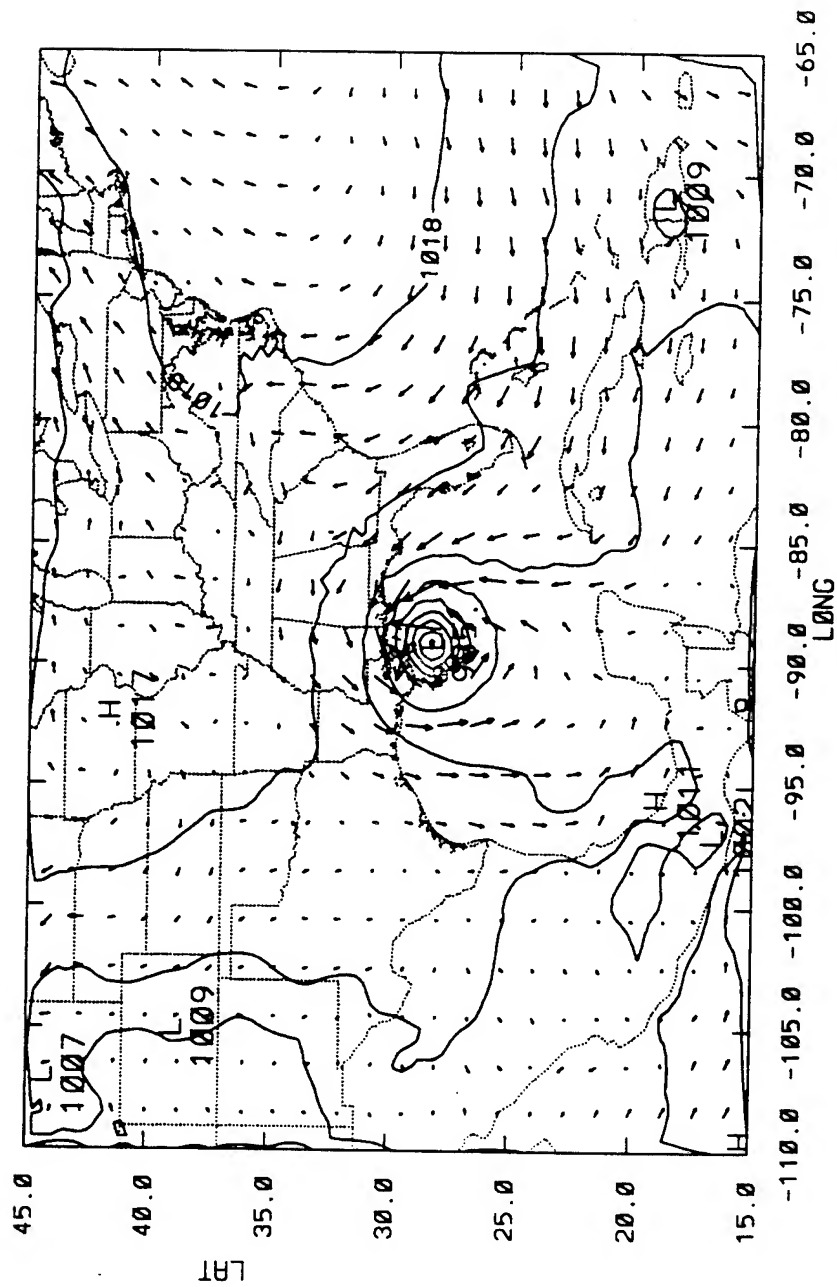


Figure 6.2b Same as Figure 6.2a except for 18 hour.

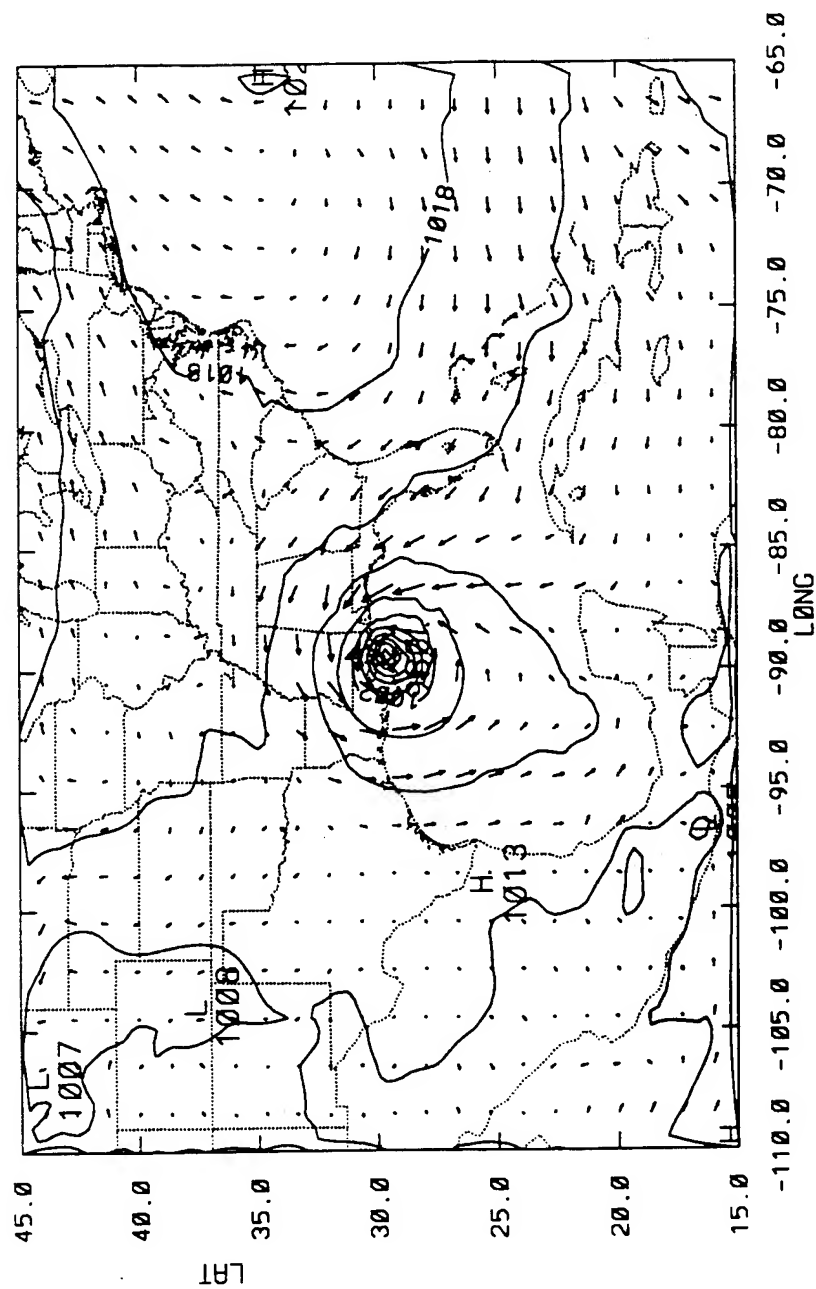


Figure 6.2c Same as Figure 6.2a except for 24 hour.

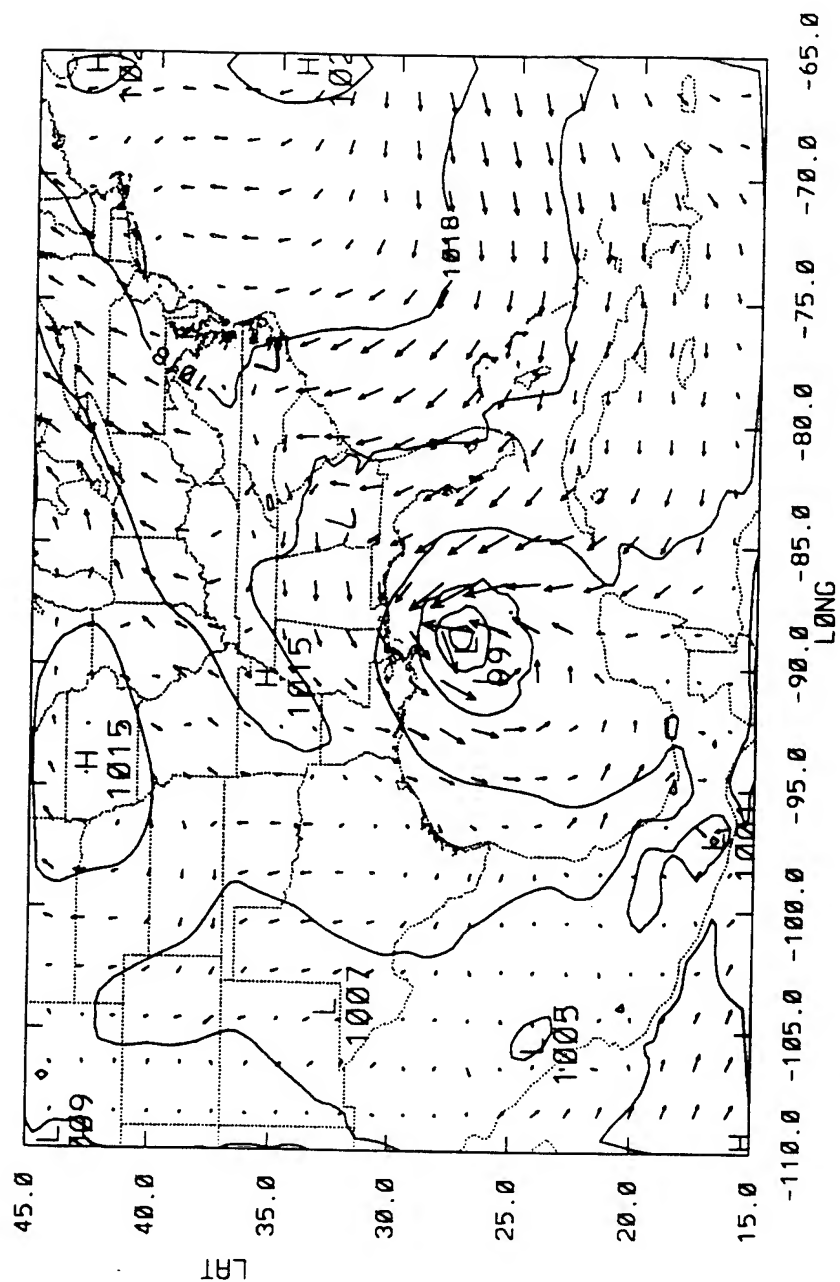


Figure 6.3a Sea level pressures (mb) and surface temperatures (degree C) of Exp. ODW2 at 12 hour.

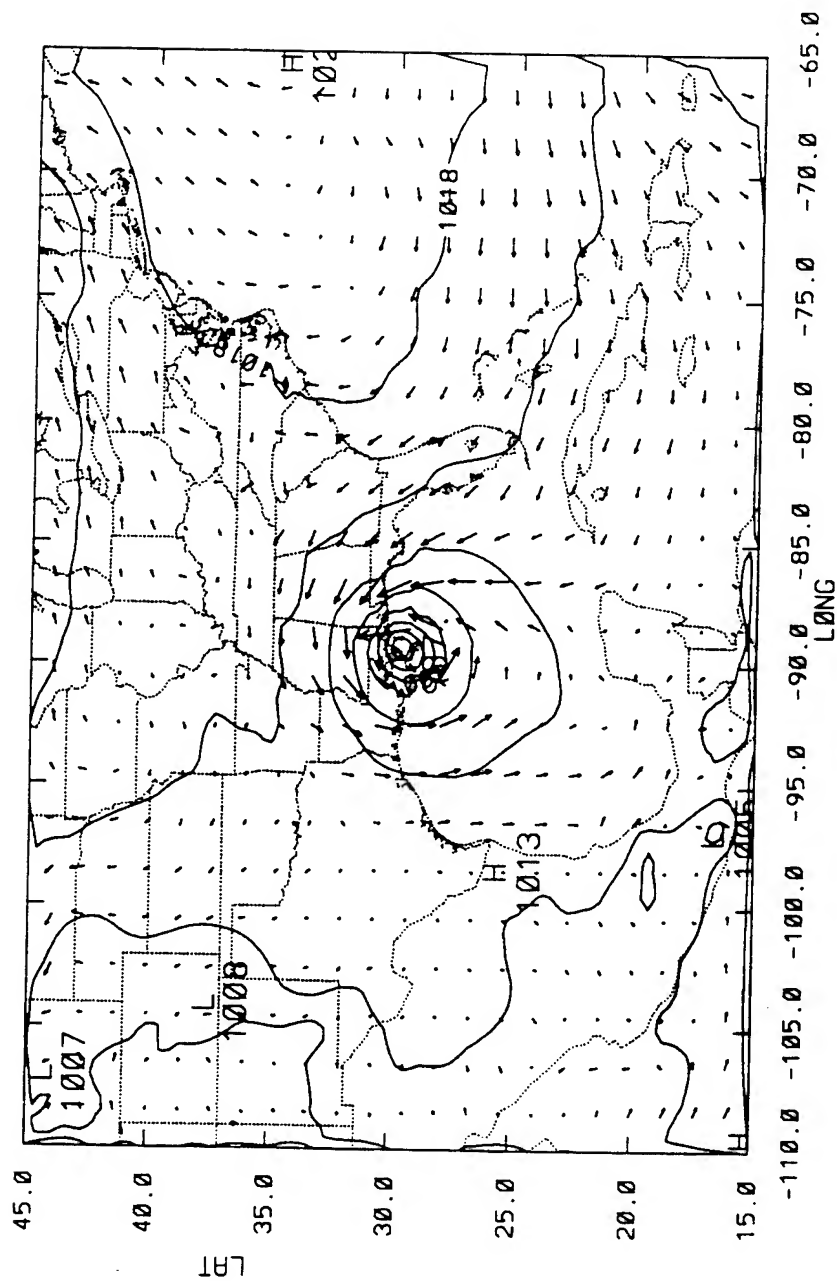


Figure 6.3c Same as Figure 6.3a except for 24 hour.

vectors of the simulated storm in Exp. ODW2 at 12, 18 and 24 hour. The minimum SLPs of the storm in Exp. ODW2 are 997, 988 and 987 mb at 12, 18 and 24 hour respectively, while the locations of the storm center are (88.8W, 27.1N), (89.1, 28.5N) and (89.3W, 29.6N). The maximum surface wind speeds of the simulated storm in Exp. ODW2 are 30.4, 35.8 and 38.8 ms^{-1} at 12, 18 and 24 hour, respectively. As compared to the best track record (Table 6.1), it is clear that the intensity of the simulated storm in Exp. ODW1 is stronger than the best track record, while the intensity of the one in Exp. ODW2 is closer to the best record in terms of the maximum wind speeds. As shown in Fig. 6.2 and 6.3, the storms in Exp. ODW1 and ODW2 are much better organized than the storm in the control experiment (Fig. 6.1). The warm front that stretched from northern Florida to North Carolina is also shown in both numerical experiments.

Fig. 6.4 shows Florence's track based on the best track record, the control experiment, Exp. ODW1 and ODW2. As mentioned above, the track from the control experiment is roughly 2° - 2.5° east of the best track and this simulated storm moves faster than Florence in the best track record. The center of Florence in the control experiment is about 4.1 degree northeast of the actual position in the best track record at 24 hour. On the other hand, Florence tracks in both numerical experiments with the ODW enhanced analyses are very close to the best track of Florence. At 24 hour, the center of

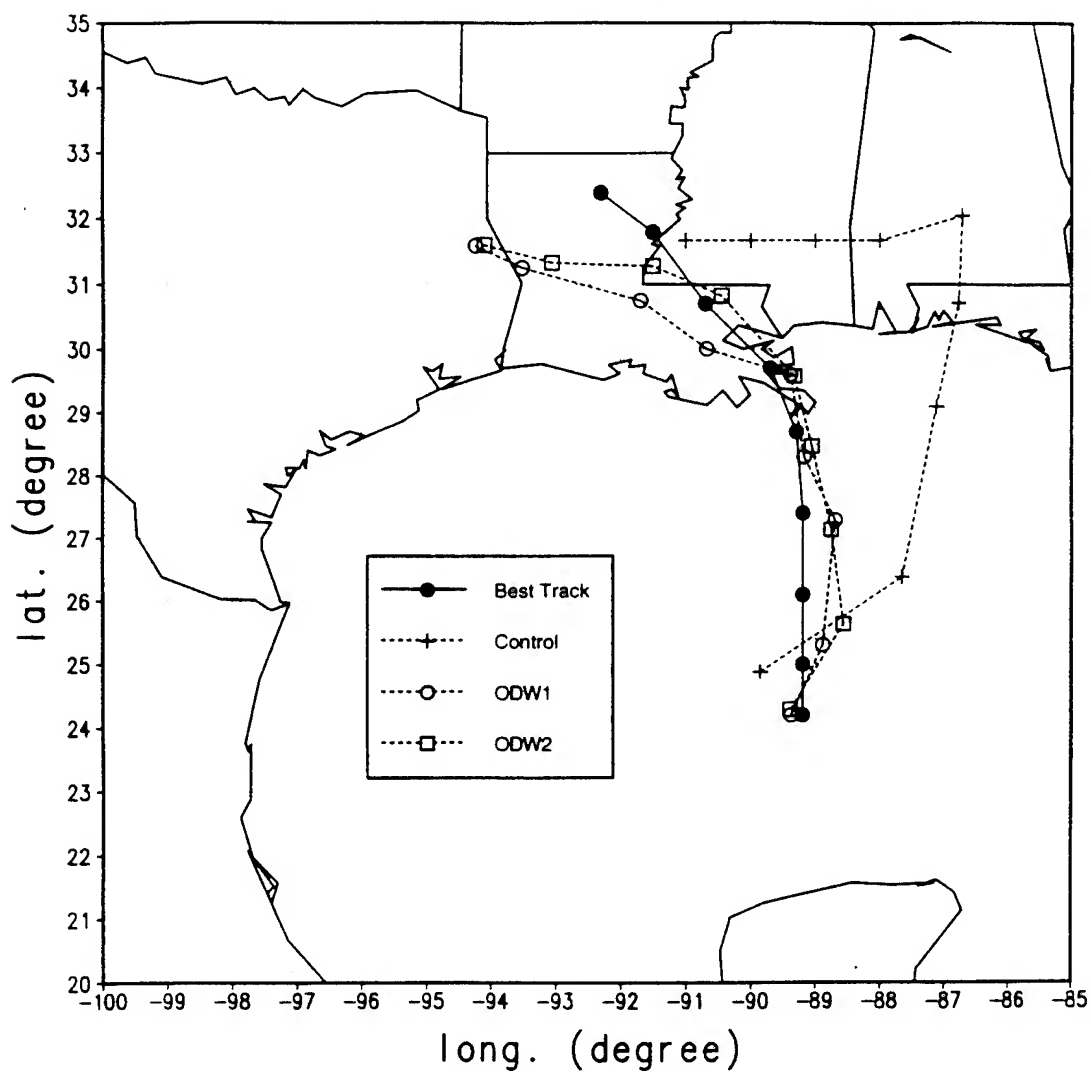


Figure 6.4 Tracks of Florence in the best track record, the control experiment, Exp. ODW1 and ODW2.

Florence in Exp. ODW1 is 0.1 degree west and 0.9 degree north of the best track position, while the center of Florence in Exp. ODW2 is 0.9 degree north of the best track position. Both numerical experiments with the ODW enhanced analyses have improved the prediction of location of the Florence's center at 24 hour by 75%. The simulated storms in both numerical experiments with the ODW enhanced analyses make landfall at 24 hour which is two hours earlier than the actual landfall shown in the best track record , while the storm in the control experiment make landfall 9 hours earlier as discussed earlier. In Fig. 6.4, the simulated storms in both numerical experiments with the ODW enhanced analyses move northeastward in early hours of the integration, while the best track record shows that Florence moved straightway northward between 0000 UTC 9 September and 0000 UTC 10 September. The track in both Exps. ODW1 and ODW2, however, are very close to the best track record after 12 hour. The initial northeast motion may be partially because of the spin-up process of the tropical cyclone model in the early hours of the integration. As shown in Table 6.1, the maximum surface wind speed of Exp. ODW2 at 6 hour is weaker than the initial maximum surface wind speed due to the sudden onset of the frictional force, which is also part of the spin-up.

The result shown in Table 6.1 suggests that both numerical experiments with the ODW enhanced analysis have produced tropical cyclones with the intensities comparable to the best track record.

Another important parameter is the evolution of minimum SLPs, which can serve as an indicator of the quality of the simulation. Fig. 6.5 shows the evolution of the minimum SLPs in the best track record, the control experiment, Exps. ODW1 and ODW2. In the first 12 hours, the storm in the control experiment intensifies quicker than both experiments with the ODW enhanced analyses. Because of its fast motion, the Control storm starts to weaken after it makes landfall at around 17 hour.

For Exp. ODW1, the intensity of the simulated storm is stronger than the best track record after 19 hour. Both Exps. ODW1 and ODW2 reach their lowest minimum SLPs at 22 and 23 hour, respectively, with the minimum SLPs of 978.7 mb and 986.3 mb for Exp. ODW1 and ODW2, respectively. The best track record shows that Florence reached its maximum intensity at 23 hour with the minimum SLP of 982 mb. Therefore, the storm in Exp. ODW1 reaches the lowest minimum SLP one hour earlier than the best track record, while the storm in Exp. ODW2 reaches the lowest minimum SLP at the same time as the best record track. Both experiments with the ODW enhanced analyses make landfall at around 0000 UTC September 10, two hours earlier than what the best track record shows. It is also clear that Exp. ODW2 produces the best minimum SLP as compared to the best track record among the three experiments (see Fig. 6.5). This suggests that ODW2 analysis may represent the actual field better.

Minimum Sea Level Pressure

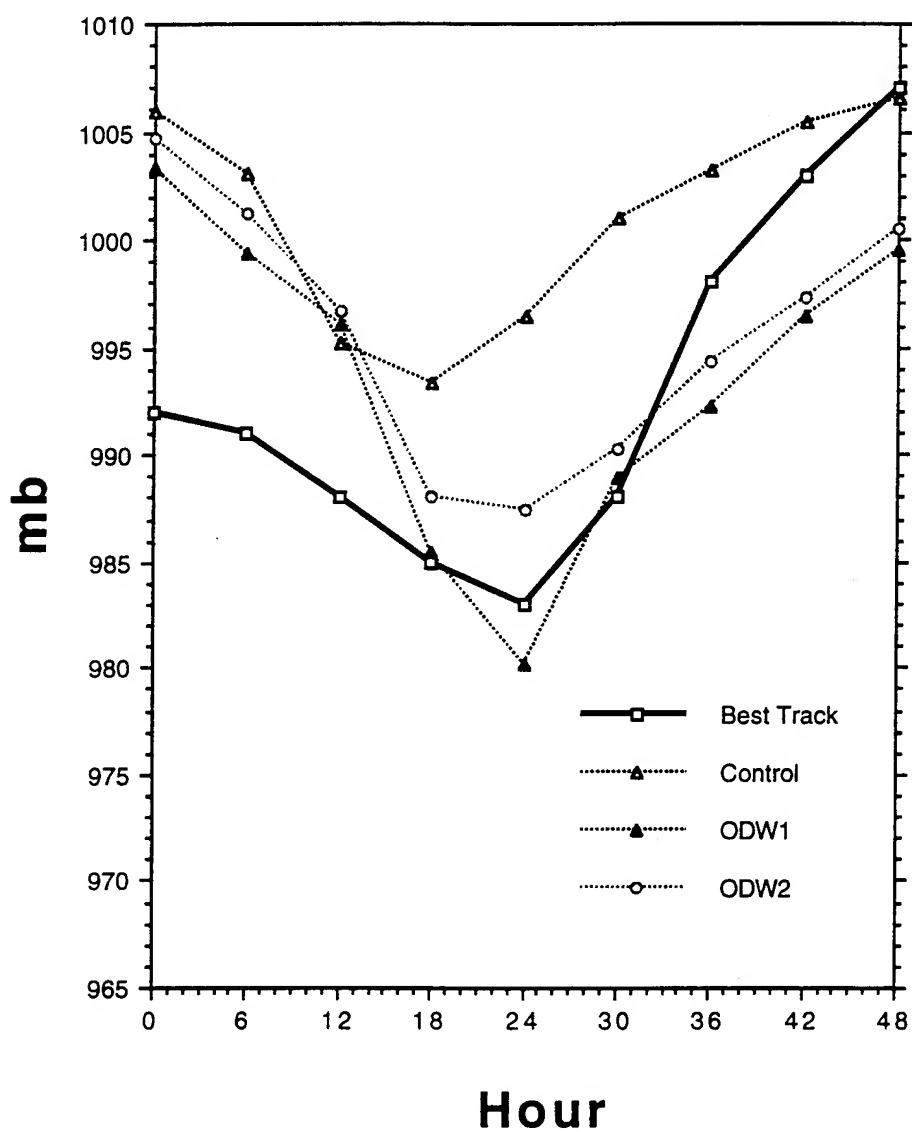


Figure 6.5 Evolution of minimum SLP of Florence with time in the best track record, the control experiment, Exp. ODW1 and ODW2.

The simulated storms in both numerical experiments with the ODW analysis move west-northwestward in the next 24 hours of integration (Fig. 6.4), while the best track record shows that Florence moved northwestward during this time span. Fig. 6.5 shows that the weakening rates of the simulated storms from both numerical experiments with the ODW analysis are slower than the best track record between 24 and 48 hour. This result indicates that the effect of the better initial analysis gradually diminishes with time. This might also be due to the PBL and cumulus parameterizations.

6.3. Comparison of Simulated Rain Rates and SSM/I Imageries.

As mentioned in Chapter 2, SSM/I retrieved rain rate data will be used to compare with the model simulated rain rates of Florence. Fig 6.6 and 6.7 shows the rain rates from the control experiment at 12 and 24 hour. At 12 hour in the control experiment, the heaviest rain rates ($> 40 \text{ mm h}^{-1}$) are located in the northeastern Gulf of Mexico off the northwestern Florida coast and at the state border of Florida, Georgia and Alabama. Relatively heavy SSM/I rain rates ($> 30 \text{ mm h}^{-1}$) at this same time are located in the north center of the Gulf of Mexico (Fig. 3.6). At 24 hour (Fig. 6.7), the heaviest rain rates ($> 20 \text{ mm h}^{-1}$) in the control experiment are located far in-land

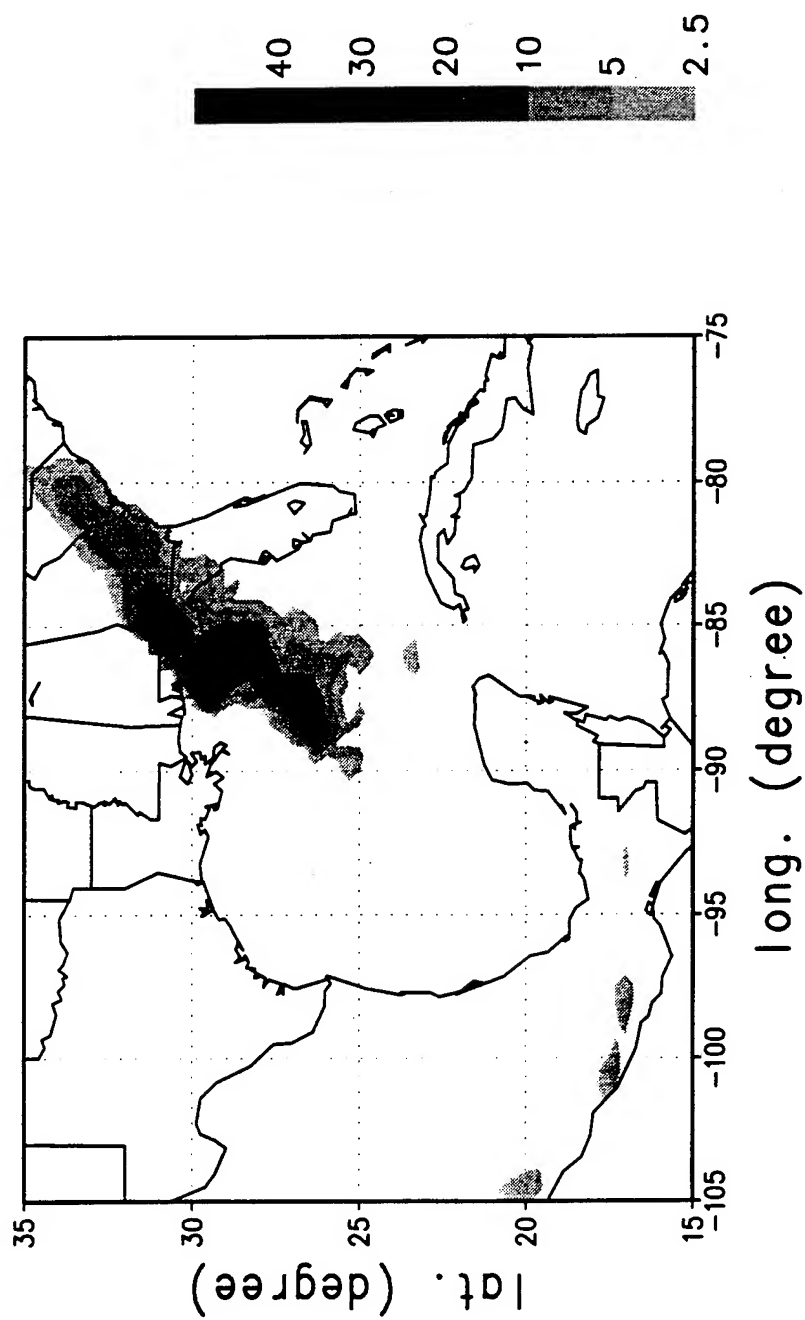


Figure 6.6 Simulated rain rate (mm h⁻¹) of the control experiment at 12 hour.

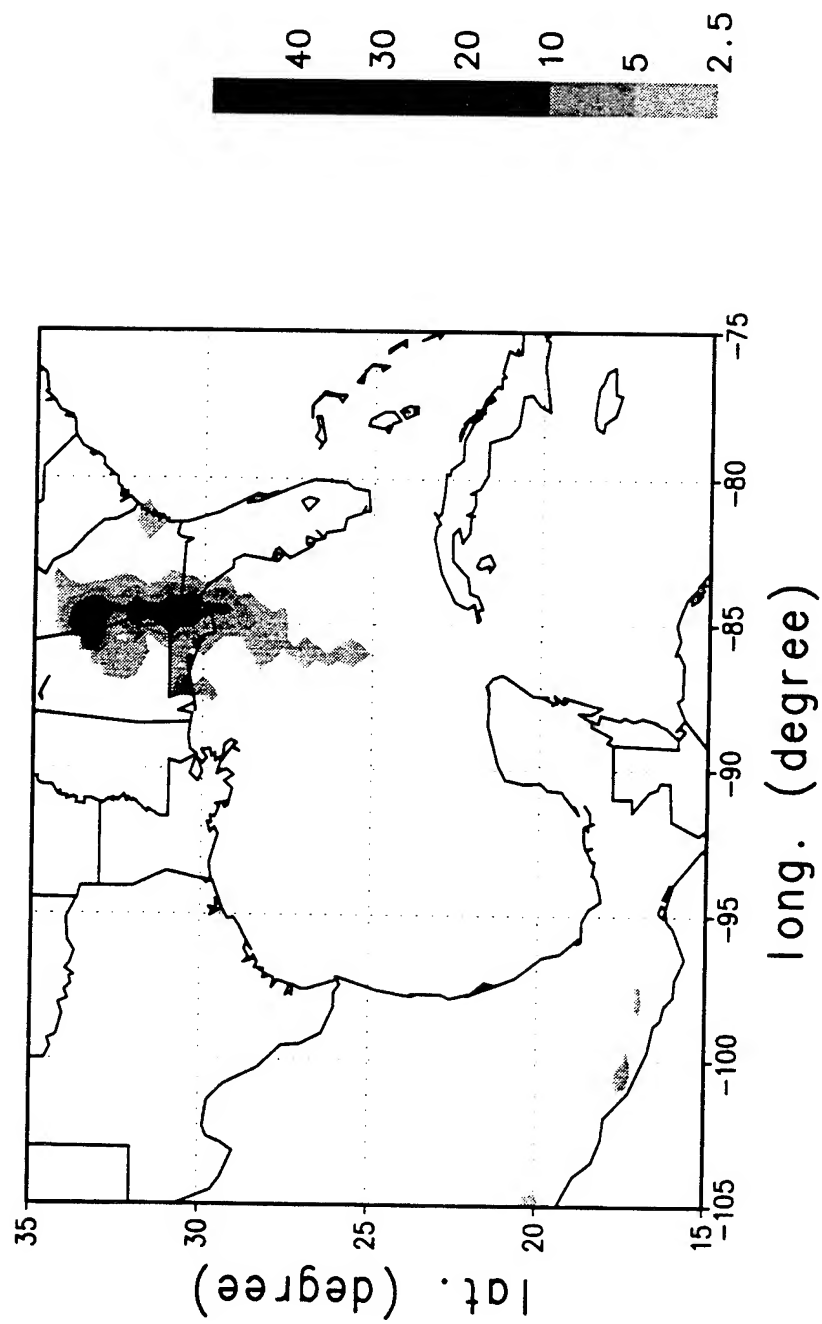


Figure 6.7 Same as Figure 6.6 except for 24 hour.

in Georgia with the heavy rain rate region stretching southward into the Gulf of Mexico, while the heaviest SSM/I rain rates ($> 15 \text{ mm h}^{-1}$) are located near New Orleans (see Fig. 3.7). It is apparent that the control experiment did not reproduce the SSM/I retrieved the rain rates of Florence mainly because of a bad track forecast.

Next, the model simulated rain rates from Exp. ODW2 are examined. Fig. 6.8 and 6.9 show the rain rates from Exp. ODW2 at 12 and 24 hour. The heaviest rain rates ($> 40 \text{ mm h}^{-1}$) at 12 hour are located at around 88.5° W and 27.5° N , which is about 0.7 degree northwest of the heaviest rain rates ($> 30 \text{ mm h}^{-1}$) of the SSM/I retrieval (Fig. 3.6). The model simulated rain rates in Exp. ODW2 also show the same general northeastern and southeastern extension of the strong convection region as shown in Fig. 3.6. The model simulated rain rates in Exp. ODW2 have two secondary convective region northeast ($> 15 \text{ mm h}^{-1}$) and southeast ($> 10 \text{ mm h}^{-1}$) of the primary convective region, similar to the SSM/I rain rates at the same time. The simulated rain rates in Exp. ODW1 were also examined. Because the result is similar to the result in Exp. ODW2, the result in Exp. 1 is not shown here.

At 24 hour, the heaviest model simulated rainfall ($> 40 \text{ mm h}^{-1}$) in Exp. ODW2 is located just off the coast of Mississippi in a northeast-southwest oriented rain band. The heavy rain rate region starts at the border of Alabama and Georgia and extents

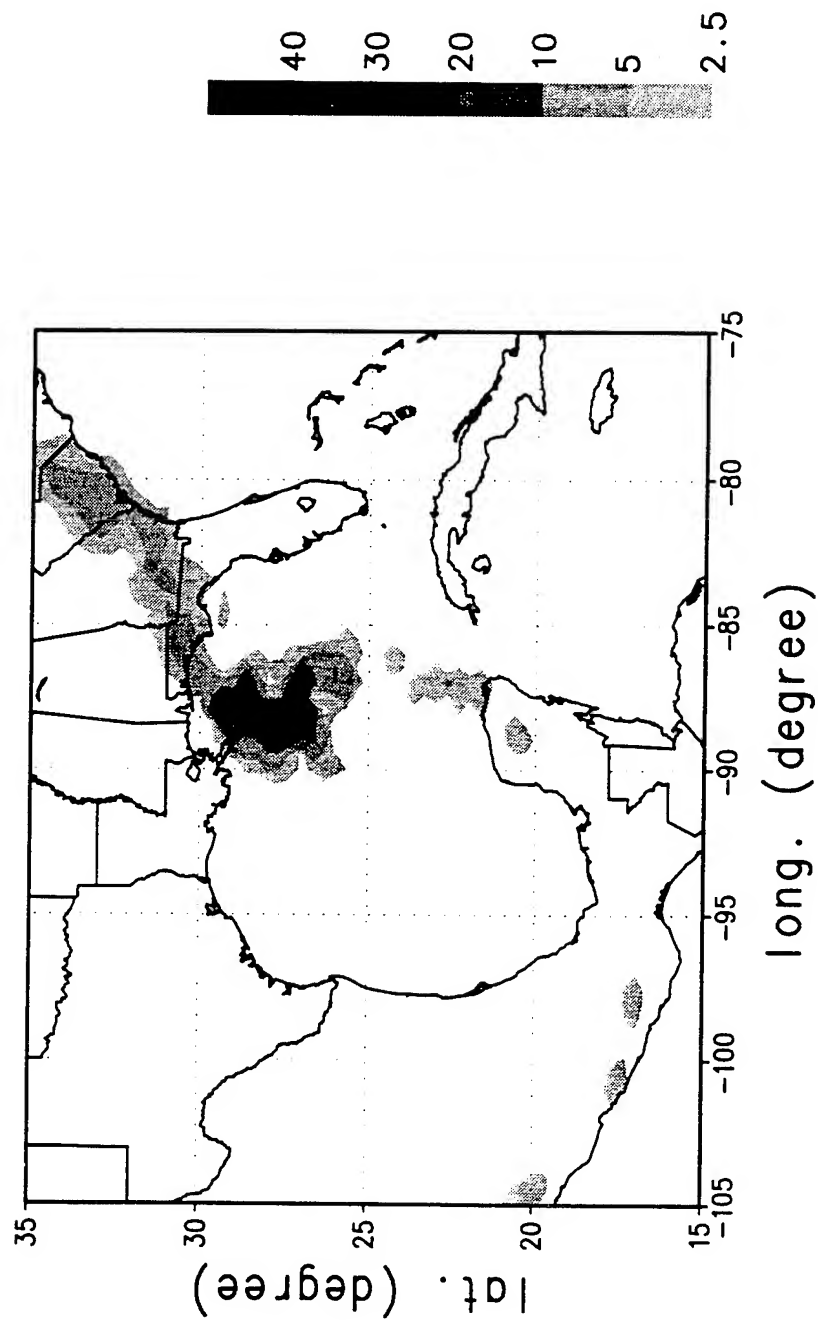


Figure 6.8 Simulated rain rate (mm h^{-1}) of Exp. ODW2 at 12 hour.

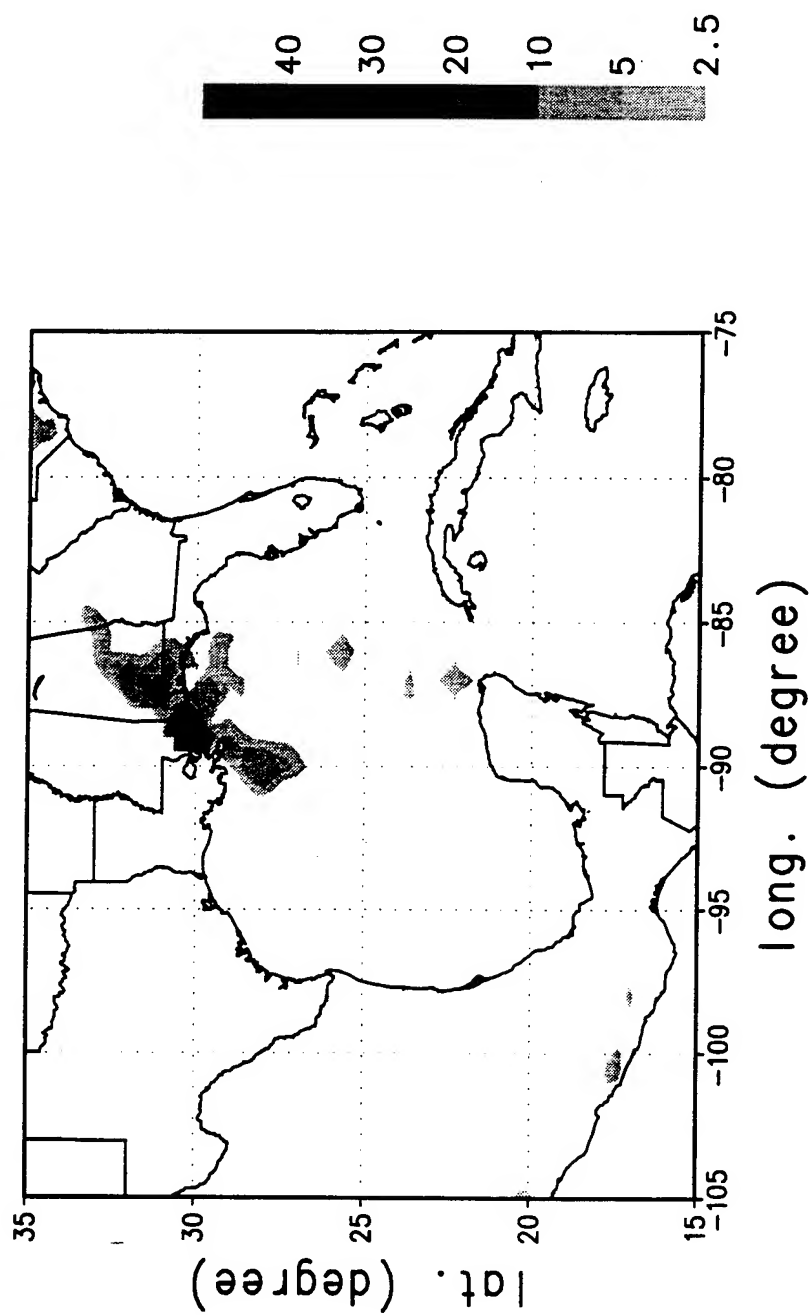


Figure 6.9 Same as Figure 6.8 except for 24 hour.

southwestward into the Gulf of Mexico off the Louisiana Coast. As compared to the SSM/I rain rates at 0000 UTC 10 September 1988, the rainfall pattern in Exp. ODW2 has the same northeast to southwest orientation as in the SSM/I rain rates (Fig. 3.7), except the SSM/I retrieval has a lighter maximum rain rate ($> 15 \text{ mm h}^{-1}$). Although the simulated rain rates at 12 hour have mostly reproduced the SSM/I rain rates in location and intensity, it is obvious, locationwise, that the model simulated rain rates in Exp. ODW2 at 24 hour is closer to the SSM/I rain rates than the ones at 12 hour. This may be because the early hour spin-up process has partially affected the simulation at 12 hour as mentioned previously and the simulated storm center location in Exp. ODW2 at 24 hour is closer to the best track location than the one at 12 hour (Fig. 6.4).

6.4 Summary.

Three experiments are performed to study the impact of the ODW data on the model simulation of Florence. Result shows that the numerical experiment with either the ODW1 or ODW2 analysis greatly improves the simulation over the control experiment initialized with NMC/RAFS 2.5⁰ analysis. These simulations also show that the numerical experiment started with the ODW2 data set is slightly better than the one started with the ODW1 data set. This suggests that the choice of a six-hour time window (from 2100 UTC 8 September to 0300 UTC 9 September) is appropriate. Table 6.2

	Landfall time	Landfall location	
		Long. and Lat.	relative location to best track
Best Track Record	0200 UTC 9/10/93	89.3W 29.1N	
Control Experiment	1700 UTC 9/ 9/93	86.7W 30.5N	2.95 degree northeast
Exp. ODW1	0000 UTC 9/10/93	89.4W 29.6N	0.51 degree north
Exp. ODW2	0000 UTC 9/10/93	89.3W 29.6N	0.50 degree north

Table 6.2 Landfall times and locations from the best track record, the control experiment, Exp. ODW1 and ODW2. The landfall locations relative to the location shown in the best track record are also listed.

shows the time of landfall and locations from the best track record, the control experiment, Exp. ODW1 and Exp. ODW2. It is clear in Table 6.2 that both numerical experiments with the ODW data reduce the forecast error of the time of landfall in the control experiment by 7 hours (down from 9 hours to 2 hours) and the error of the landfall location in the control experiment by about 2.5 degree (down from roughly 3.0 degree to about 0.5 degree). This is an improvement of more than 80%. Figs. 6.4 and 6.5 reveal that the impact of the ODW data is more pronounced in the first 24 hours integration. After first 24 hours, the impact of the ODW data gradually decreased.

The comparison of the rain rates in Exp. ODW2 and SSM/I imageries shows that the heaviest rain rates ($> 40 \text{ mm h}^{-1}$) in Exp. ODW2 at 12 hour are roughly 33% greater than the SSM/I rain rates ($> 30 \text{ mm h}^{-1}$) and the heaviest rain rates ($> 40 \text{ mm h}^{-1}$) in Exp. ODW2 at 24 hour are more than twice of the SSM/I rain rates ($> 15 \text{ mm h}^{-1}$). Nevertheless, the rainfall patterns in Exp. ODW2 at 12 and 24 hour agree well with the SSM/I rainfall pattern. Previous studies (Rodgers et al., 1991; Alliss et al. 1992 and 1993) have shown that the rain rates retrieved from the SSM/I imageries are good observational means for hurricane and mid-latitude marine cyclone studies. However, the rain rate patterns derived from the SSM/I imageries are more accurate than the values of the retrieved rain rates due to retrieval uncertainties (Chang and Holt, 1993). This study has shown that the rain patterns in Exp. ODW2 agree well with

the SSM/I rain rates at 12 and 24 hour, while the intensities of the simulated rain rates compare fairly well only at 12 hour. The SSM/I rain rates at 0000 and 1200 UTC 9 September are assimilated into the model simulations initialized with the NMC/RAFS 2.5⁰ as well as the ODW2 analysis. Results from these simulations will be discussed in the next chapter.

7. Assimilation of SSM/I Rainfall Rate Data

Despite numerous research efforts, an accurate description of the temporal and spatial distribution of latent heating in numerical models is still one of the major obstacles in numerical weather prediction. The accurate description of the distribution of the latent heating is particularly important in the numerical simulation or prediction of hurricanes, which rely on the release of latent heating as a major energy source. As mentioned in the previous chapter, it is suspected that the simulated rain rates in Exp. ODW2 at 12 hour were affected by the model spin-up. Davidson and Puri (1992) have stated that diabatic heat sources, which includes the latent heat sources, are generally poor-defined in the initial conditions, especially for tropical cyclones. They also stated that the model forecasted diabatic heating may not be in the right place or occur at the right time if the latent heat sources are poorly defined in the initial conditions.

Efforts have been made to assimilate the observed or satellite-retrieved rain rates into numerical models in the past. Molinari (1982) successfully assimilated a relatively small area of radar-observed rain rates into numerical model to improve the simulation of a hurricane. Idealized rain rates were incorporated into a mesoscale hurricane model by using dynamic initialization (Fiorino and Warner, 1981). Chang and Holt (1993) assimilated the

SSM/I rain rates into the NRL model to simulate a rapidly moving and intensifying extra-tropical marine cyclone. Their results showed that the assimilation of the SSM/I rain rates cuts the intensity forecast error by 50%. These studies demonstrated that the assimilation of the latent heating rates has a positive impact on the simulation of hurricanes and rapidly intensifying extra-tropical cyclones.

After the flight of the first SSM/I aboard a DMSP satellite in 1987, more directly measured and accurate rain rates with near global coverage became available on a daily basis. In this study, the SSM/I retrieved rain rate data are assimilated into the model during the integration to study the effectiveness in improving the simulation of Florence.

As described in Chapter 4, a modified Kuo scheme is used in this tropical cyclone model to parameterize the cumulus convection. Following Chang and Holt (1993), the convective latent heating at a grid point is

$$\frac{dT}{dt} = \frac{b g L M_t (T_c - T)}{C_p P_s \int_{\sigma} (T_c - T) d\sigma} \quad (7.1)$$

where b is a partitioning parameter set equal to the vertical mean relative humidity; T_c , the cloud temperature; L , the specific latent

heat; C_p , the specific heat at constant pressure of air; P_s , the surface pressure. M_t in (7.1) is the total moisture convergence and is defined as

$$M_t = \frac{P_s}{g} \int_{\sigma} -\nabla \cdot \vec{V} q \, d\sigma \quad (7.2)$$

where q is the specific humidity. The rain rate ($\delta R / \delta t$) in terms of centimeters per second in the model is then defined at each grid point as

$$\frac{\delta R}{\delta t} = \frac{P_s C_p}{g \rho_w L} \int_{\sigma} \frac{\delta T}{\delta t} \, d\sigma \quad (7.3)$$

where ρ_w is the density of liquid water. In this assimilation experiment, the left-hand side term of (7.3) is replaced by the SSM/I retrieved rain rates in the area inside the SSM/I swath. The SSM/I rain rates at 0000 UTC 9 September 1988 are assimilated into the tropical cyclone model at 0-3 hour, while the SSM/I rain rates at 1200 UTC 9 September 1988 are assimilated at 9-15 hour integration. To study the impact of the assimilation of the SSM/I rain rates, both the NMC/RAFS 2.5⁰ (Exp. Control+SSMI) and ODW2 (Exp. ODW2+SSMI) analyses are used as the initial condition of the model integrations. Both assimilation experiments are integrated for 48 hours.

7.1 Control Experiment with the Assimilation of the SSM/I Rain Rates.

Table 7.1 lists the minimum SLP, the maximum surface wind speed and the location of the storm center of the best track record, Exp. Control+SSMI and ODW2+SSMI. Fig. 7.1 shows the SLPs and the 1000 mb wind vectors in Exp. Control+SSMI at 12, 18 and 24 hour. It is clear that the intensity of the simulated storm is stronger than the one in the control experiment. At 24 hour, the minimum SLP is 990 mb in Table 7.1, compared to 997 mb in Table 6.1. Fig. 7.1 also shows that there is a warm front stretching from northern Florida to North Carolina at 12 hour, which also appears in all the other experiments. The simulated storm in this experiment makes landfall at (88.9W, 30.6N) in Mississippi at 24 hour (0000 UTC September 10), while Florence made landfall at (89.3W, 29.1N) at 0200 UTC September 10 (Table 3.1). The location of the landfall of the simulated storm is about 1.55 degree north-northeast of the location shown in the best track record. This is an improvement to the landfall in the control experiment, which is about 3 degree northeast of the best track landfall location. Also, in the control experiment, landfall occurs at 17 hour, 9 hours too early. The landfall occurs at 24 hour in Exp. Control+SSMI, which is a great improvement.

The minimum SLP of the simulated storm in Exp. Control+SSMI

Minimum Sea Level Pressure (mb)					
	0 h	6 h	12 h	18 h	24 h
Best track record	992	991	988	985	983
Control+SSMI	1006	1004	1002	999	992
ODW2+SSMI	1005	1003	999	992	985

Maximum Surface Wind Speed (ms ⁻¹)					
	0 h	6 h	12 h	18 h	24 h
Best track record	25.7	25.7	28.3	33.4	36.0
Control+SSMI	14.1	20.3	23.1	29.3	32.3
ODW2+SSMI	28.4	20.0	24.2	34.5	38.3

Location of Storm Center					
	0 h	6 h	12 h	18 h	24 h
Best track record	89.2W 24.2N	89.2W 25.2N	89.2W 26.1N	89.2W 27.4N	89.3W 28.7N
Control+SSMI	89.9W 24.9N	89.0W 25.3N	89.1W 25.9N	88.5W 27.4N	88.9W 30.6N
ODW2+SSMI	89.4W 24.3N	89.1W 25.5N	89.4W 26.5N	89.2W 27.5N	89.6W 29.0N

Table 7.1. Minimum SLP (mb), maximum wind speed (ms^{-1}) and location of storm center from the best track record, Exp. Control+SSMI and ODW2+SSMI.

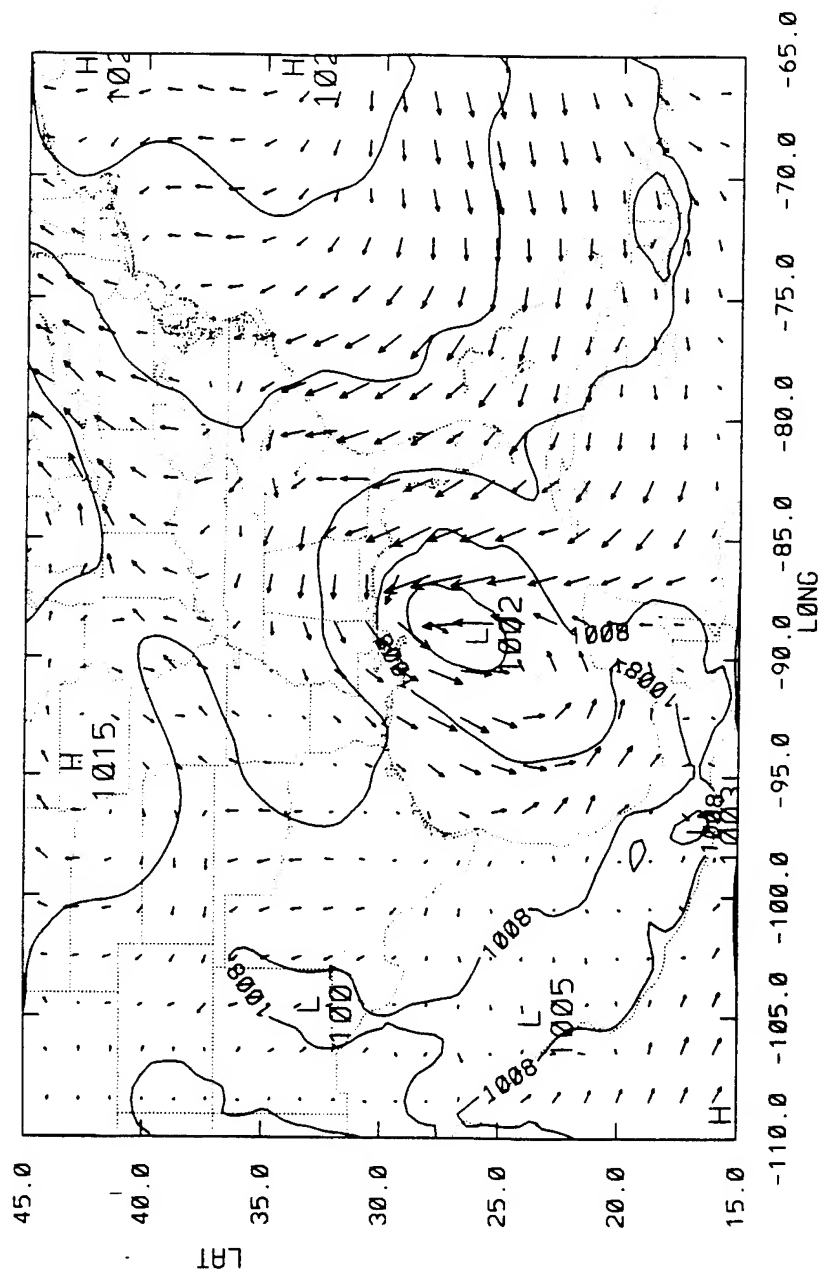


Figure 7.1a Sea level pressures (mb) and surface temperatures (degree C) of Exp. Control+SSM1 at 12 hour.

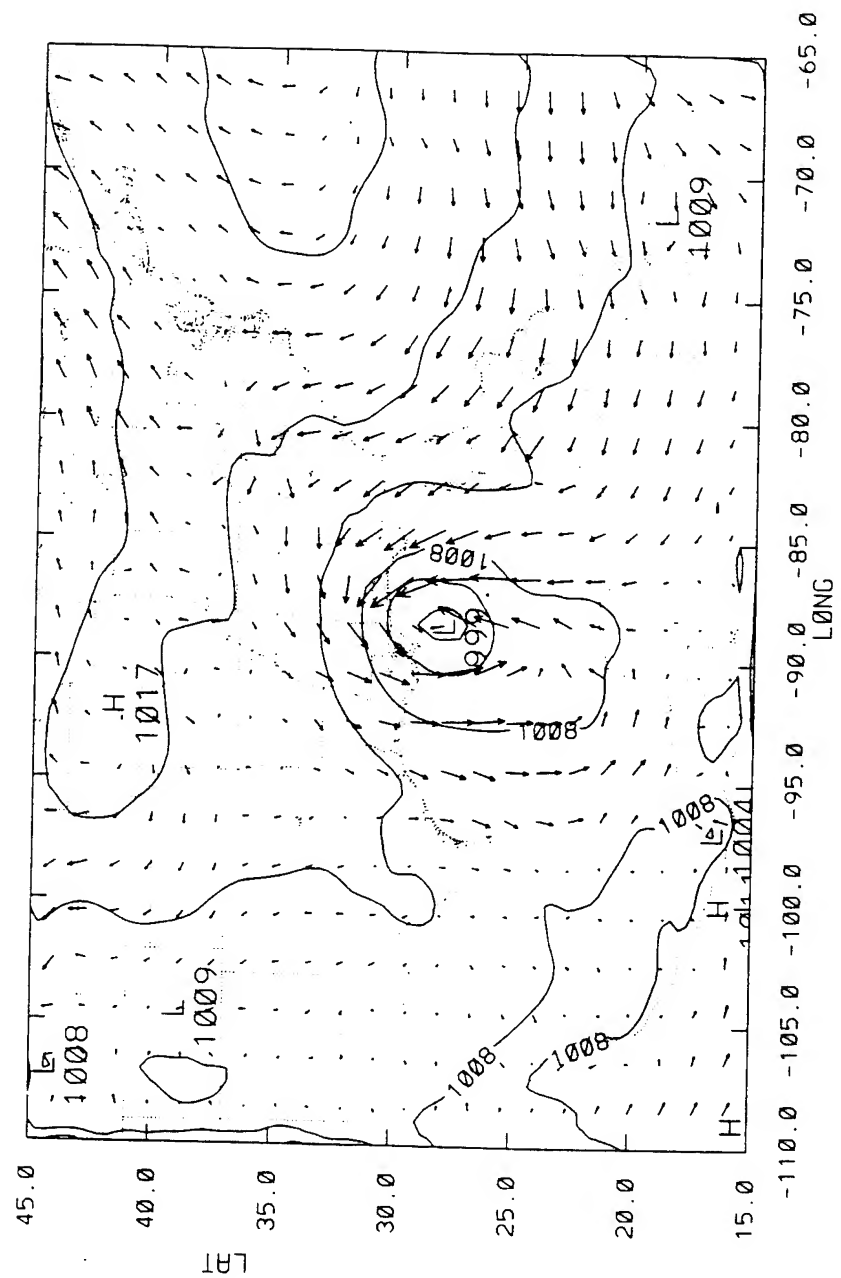


Figure 7.1b Same as Figure 7.1a except for 18 hour.

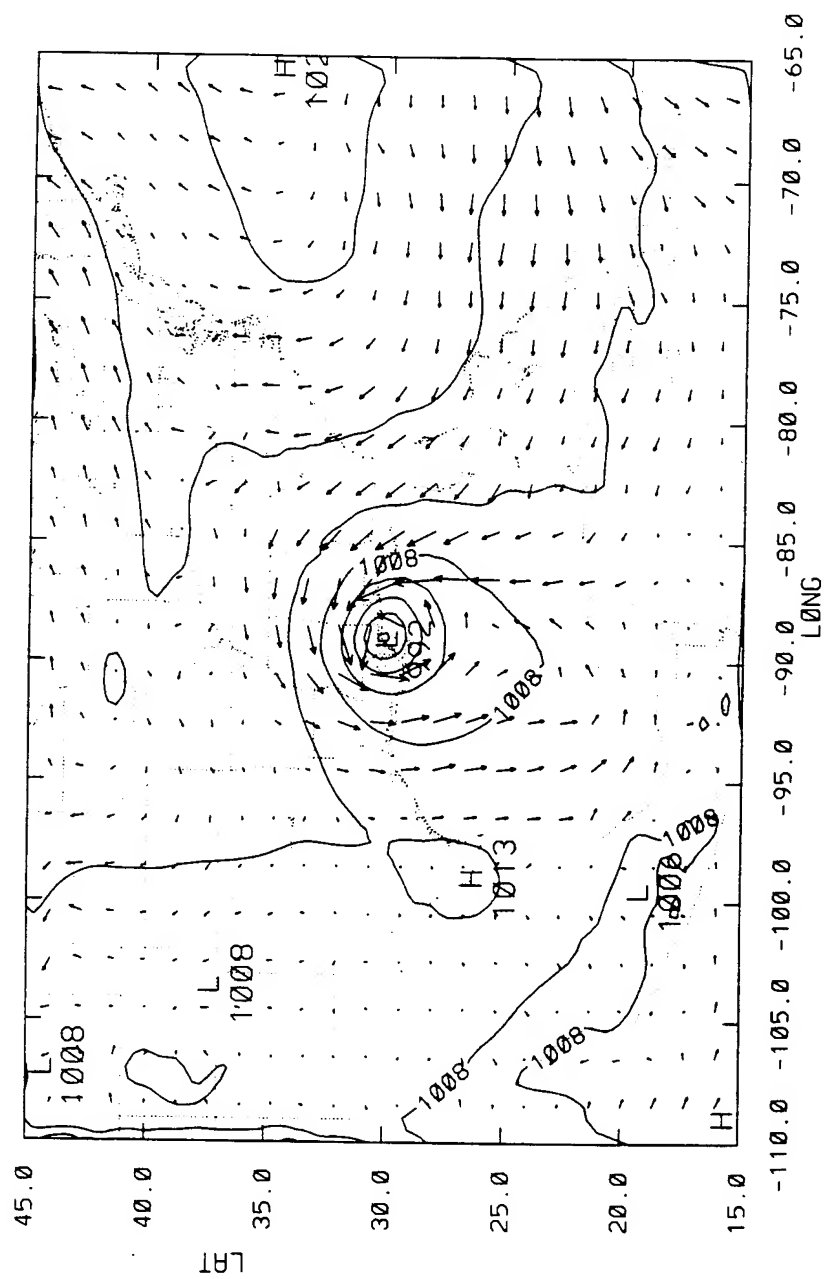


Figure 7.1c Same as Figure 7.1a except for 24 hour.

are 1002, 999 and 990 mb at 12, 18 and 24 hour, respectively (Table 7.1). Comparing with the result from the control experiment (Table 6.1), Exp. Control+SSMI reduces the forecast error of the minimum SLP by 7 mb (from 14 to 7 mb) at 24 hour. The maximum surface wind speed from Exp. Control+SSMI at 12, 18 and 24 hour are 23.1, 29.3 and 32.3 ms^{-1} , respectively. The result also shows that the maximum surface wind speed prediction at 24 hour is improved from 22.2 ms^{-1} in the control experiment (Table 6.1) to 32.3 ms^{-1} in this experiment. The maximum wind speed forecast error is reduced from 13.8 to 3.7 ms^{-1} . The predicted location of the storm center at 24 hour is 1.9 degree north-northeast of the best track location (Table 6.1 and Fig. 7.2). The location forecast error is improved by more than 50% from 4.1 degree to 1.9 degree. Fig. 7.2 shows that the predicted track from Exp. Control+SSMI is greatly improved from the control experiment.

The simulated rain rates in Exp. Control+SSMI (Fig. 7.3) at 24 hour are compared with the SSM/I rain rates (Fig. 3.7) and their counterpart in the control experiment (Fig. 6.7). Fig 7.3 shows that the heaviest rain rates ($> 40 \text{ mm h}^{-1}$) in Exp. Control+SSMI is located at the state border of Alabama and Louisiana near the coast and the region of heavy rain rates extends from central Alabama into the Gulf of Mexico. Comparing Figs. 3.7 and 7.3, the simulated rain rates don't agree well with the SSM/I rain rates in pattern and intensity. The simulated rain rates at 12 hour are not shown here because the

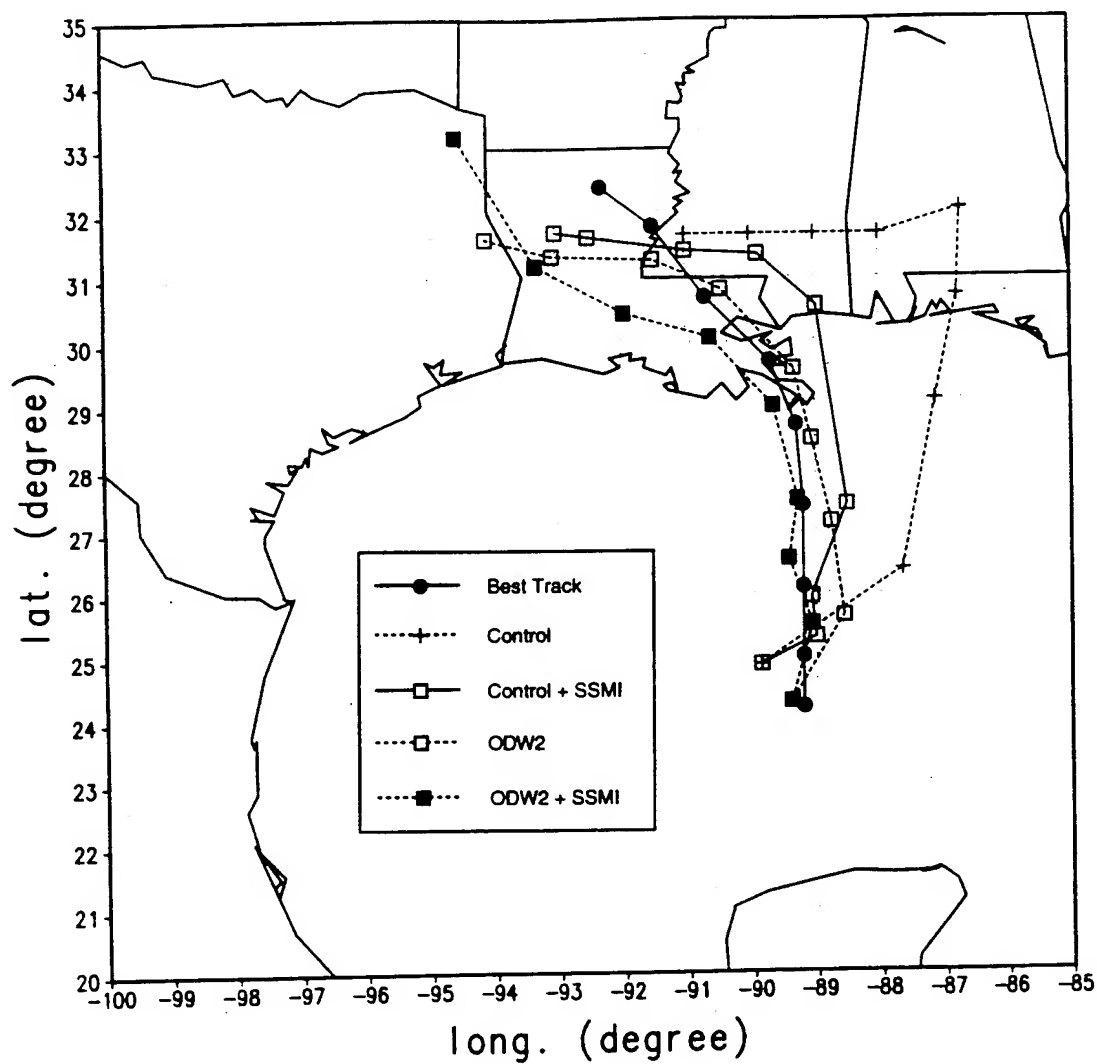


Figure 7.2 Tracks of Florence in the best track record, control experiment, Exp. Control+SSMI, ODW2 and ODW2+SSMI.

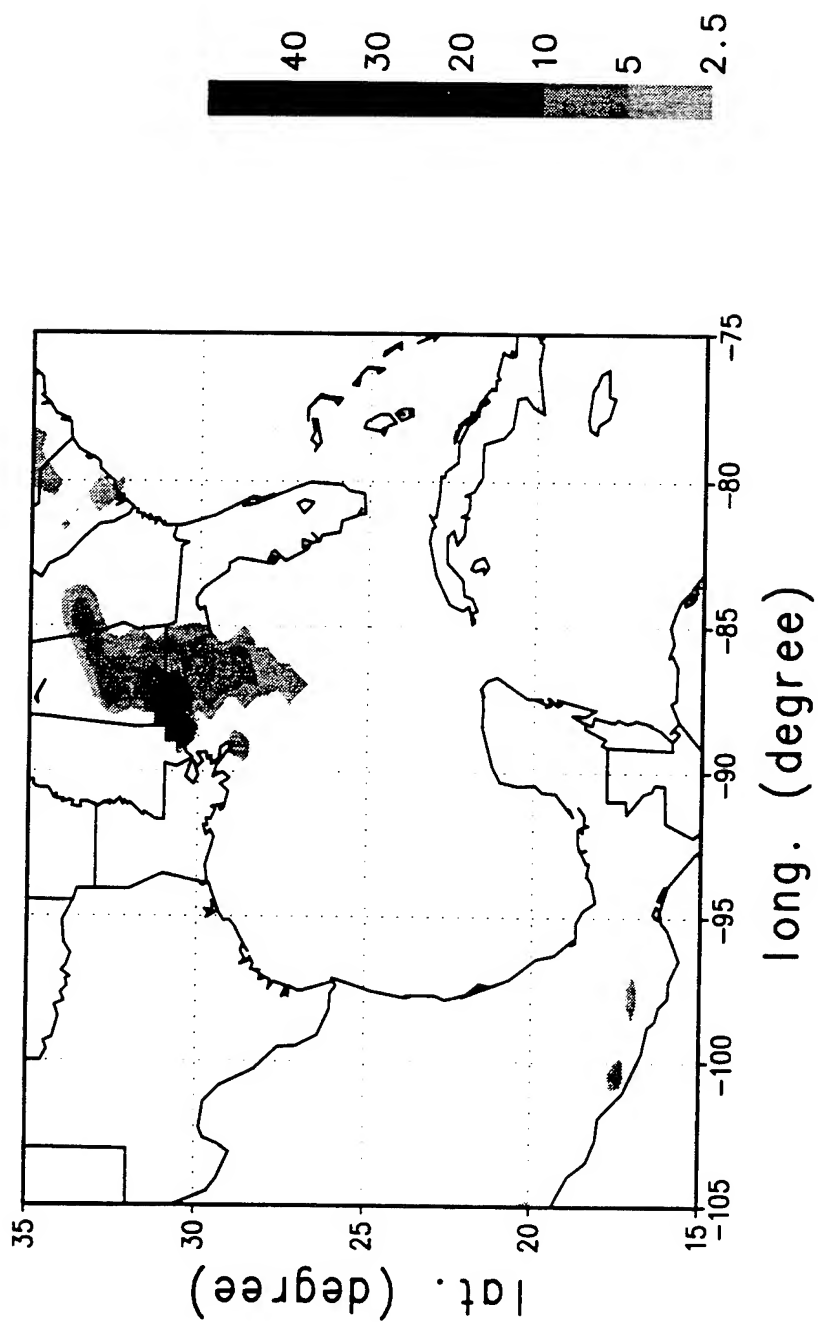


Figure 7.3 Simulated rain rates of Exp. Control+SSM/I at 24 hour.

12 hour is in the time window of the assimilation of the SSM/I retrieved rain rates at 1200 UTC September 9.

7.2 ODW2 Experiment with the Assimilation of the SSM/I Rain Rates.

The SSM/I rain rates at 0000 UTC and 1200 UTC September 9 are assimilated into the model integration with the ODW2 analysis as the initial condition in Exp. ODW2+SSMI using the same procedure mentioned above. Fig. 7.4 shows the SLPs and the 1000 mb wind vectors in Exp. ODW2+SSMI at 12, 18 and 24 hour. The minimum SLPs at 12, 18 and 24 hour are 999, 992 and 987 mb (Table 7.1), respectively. The corresponding maximum wind speeds are 24.2, 34.5 and 38.3 ms^{-1} , respectively. Comparing the results from Exp. ODW2 and ODW2+SSMI (Tables 6.1 and 7.1) with the best track record, Exp. ODW2+SSMI improves the prediction of the minimum SLP by 2 mb (down from 987 mb in ODW2 experiment to 985 mb), and the maximum wind speed by 0.5 ms^{-1} . Furthermore, comparing the tracks in Exp. ODW2 and ODW2+SSMI with the best track record (Fig. 7.2), the track in Exp. ODW2+SSMI at 24 hour is closer to the best track record than the one in Exp. ODW2. The location of the storm center in Exp. ODW2+SSMI at 24 hour is roughly 0.4 degree northwest of the best track location. For comparison, the storm center in Exp. ODW2 at 24 hour is 0.9 degree north of the best track location.

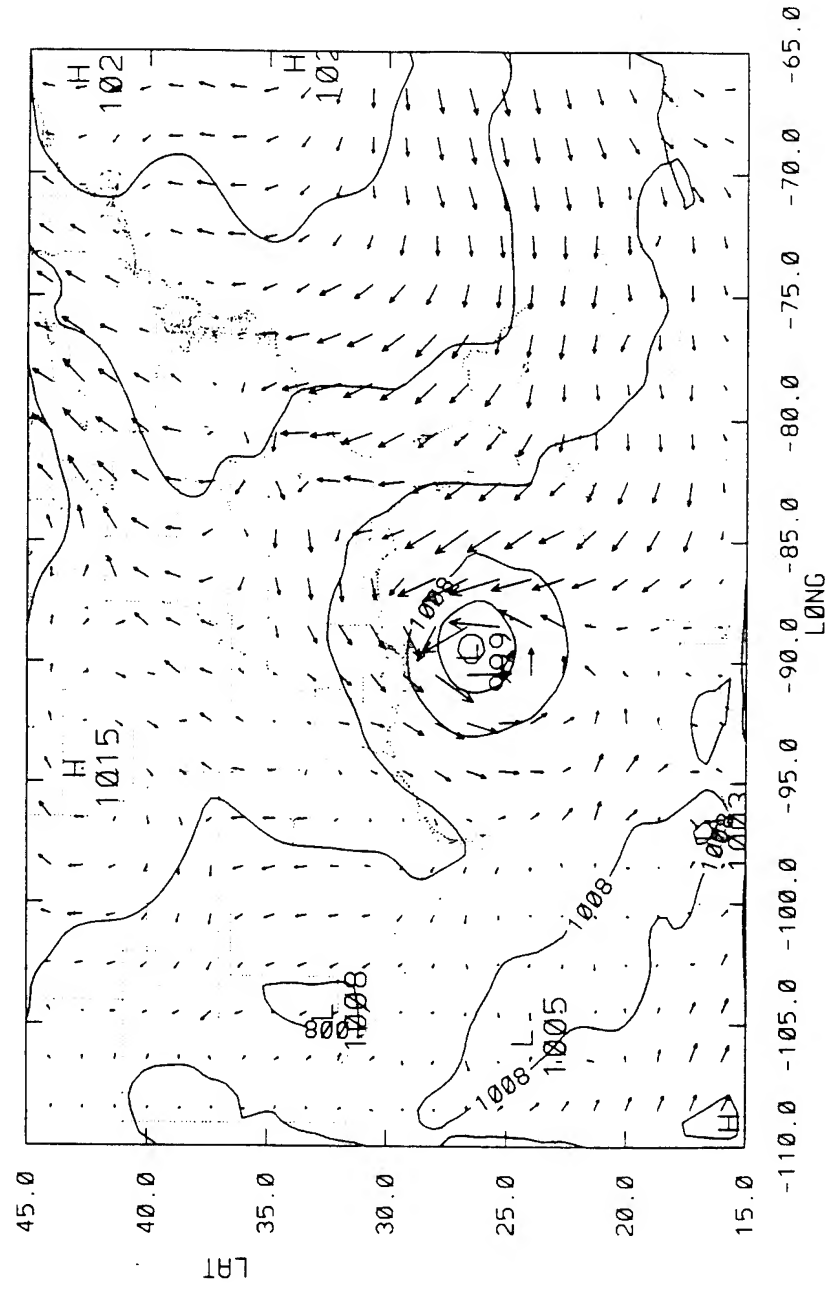


Figure 7.4a Sea level pressures (mb) and surface temperatures (degree C) of Exp. ODW2+SSM1 at 12 hour.

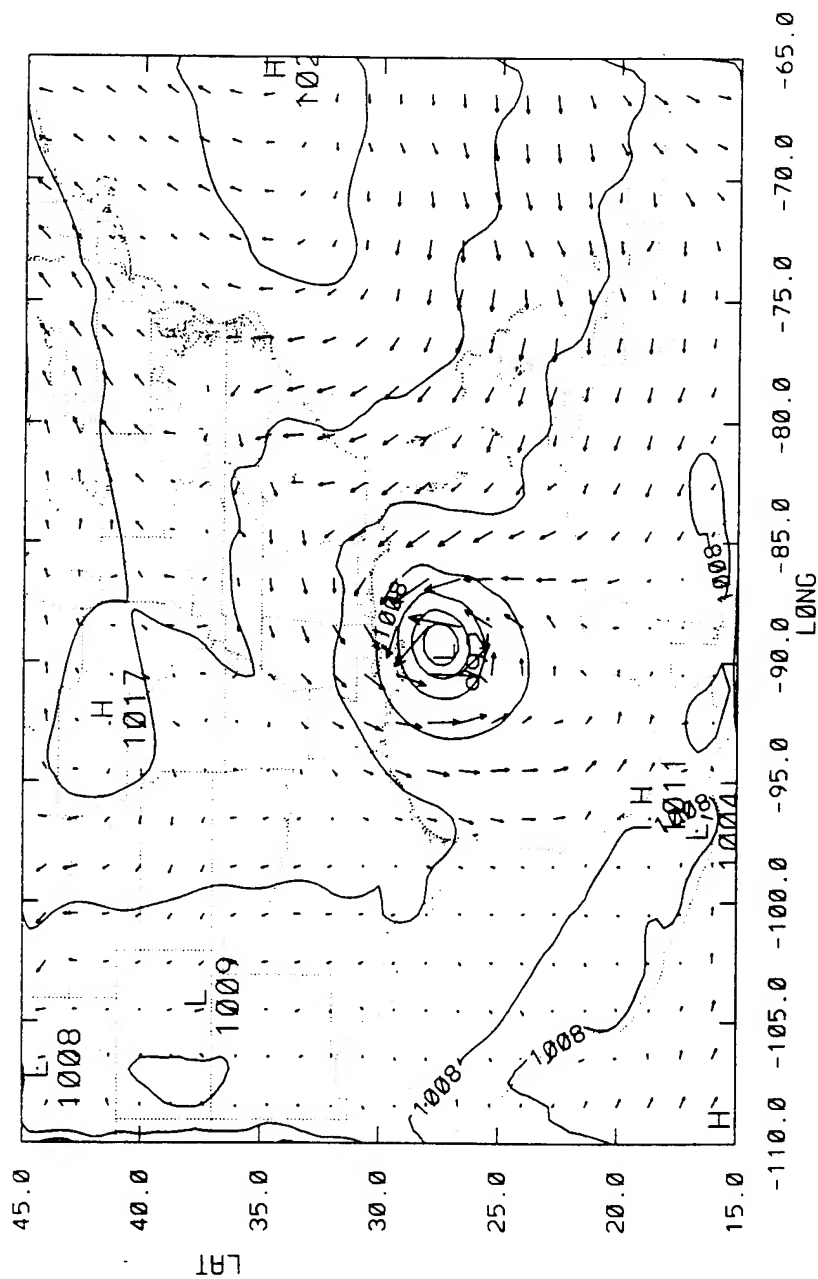


Figure 7.4b Same as Figure 7.4a except for 18 hour.

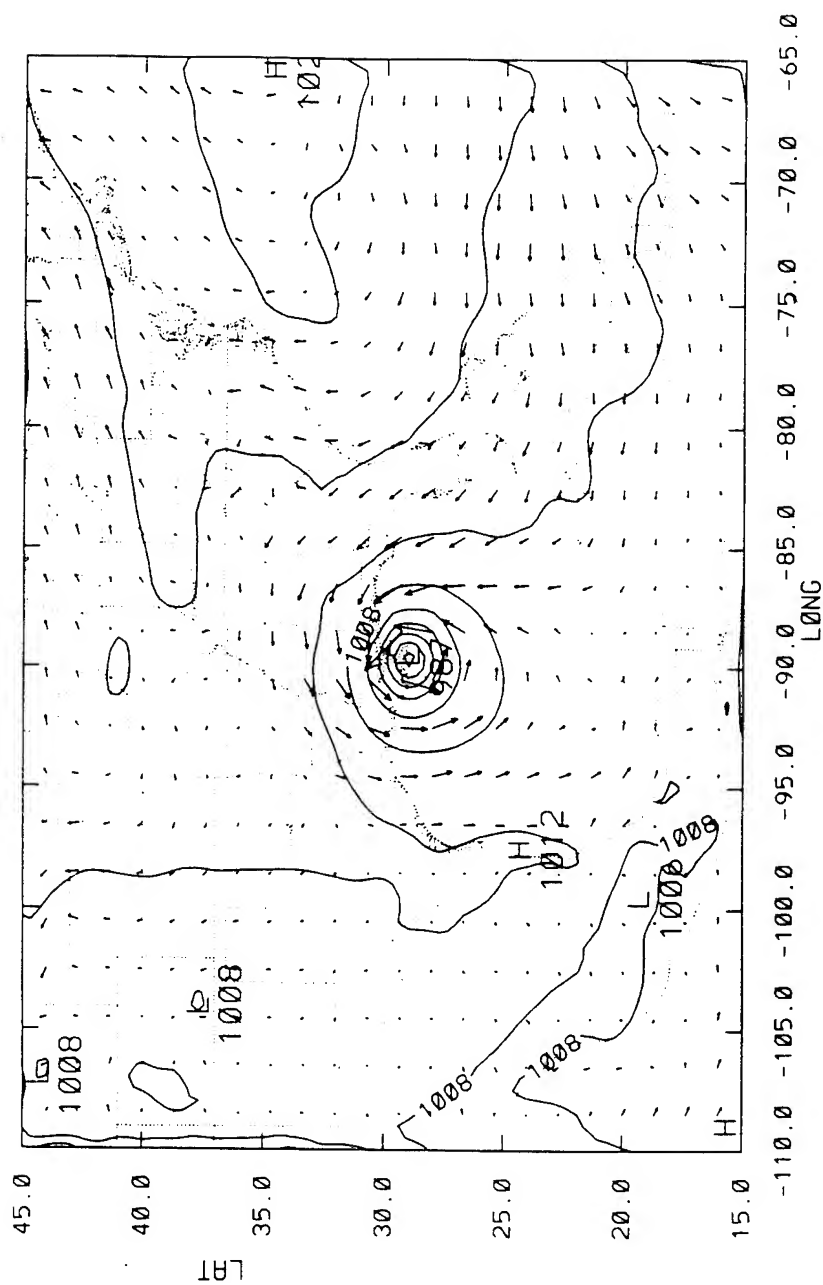


Figure 7.4c Same as Figure 7.4a except for 24 hour.

The simulated rain rates from Exp. ODW2+SSM/I at 24 hour (Fig. 7.5) are also compared with the one in Exp. ODW2 (Fig. 6.9) and the SSM/I retrieval (Fig. 3.7). Fig 7.5 shows that the heaviest rain rates ($> 30 \text{ mm h}^{-1}$) are located just east of New Orleans and north of the Mississippi River Delta. The pattern of the rain rates in this experiment is similar to Exp. ODW2 and the SSM/I retrieved rain rates. The intensity of the simulated rain rates in this experiment is weaker than the one ($>40 \text{ mm h}^{-1}$) in Exp. ODW2, but stronger than the SSM/I rain rates ($>15 \text{ mm h}^{-1}$).

7.3 Summary.

Results from Exp. Control+SSM/I show that the assimilation of the SSM/I rain rates greatly improve the model forecast of Florence when the NMC/RAFS 2.5⁰ analysis is used as the initial condition. The improvement is made in intensity, track and landfall time and location. Results from Exp. ODW2+SSM/I only show a moderate improvement over Exp. ODW2 because Exp. ODW2 has already achieved some improvement over the control experiment due to the utilization of the ODW data.

Fig. 7.6 shows the variation of the minimum SLP with time. Combining the result shown in Figs. 7.2 and 7.6, the model predicts the track and minimum SLP well after 24 hour in all experiments, although Exp. ODW2+SSM/I has the best track prediction. Table 7.2

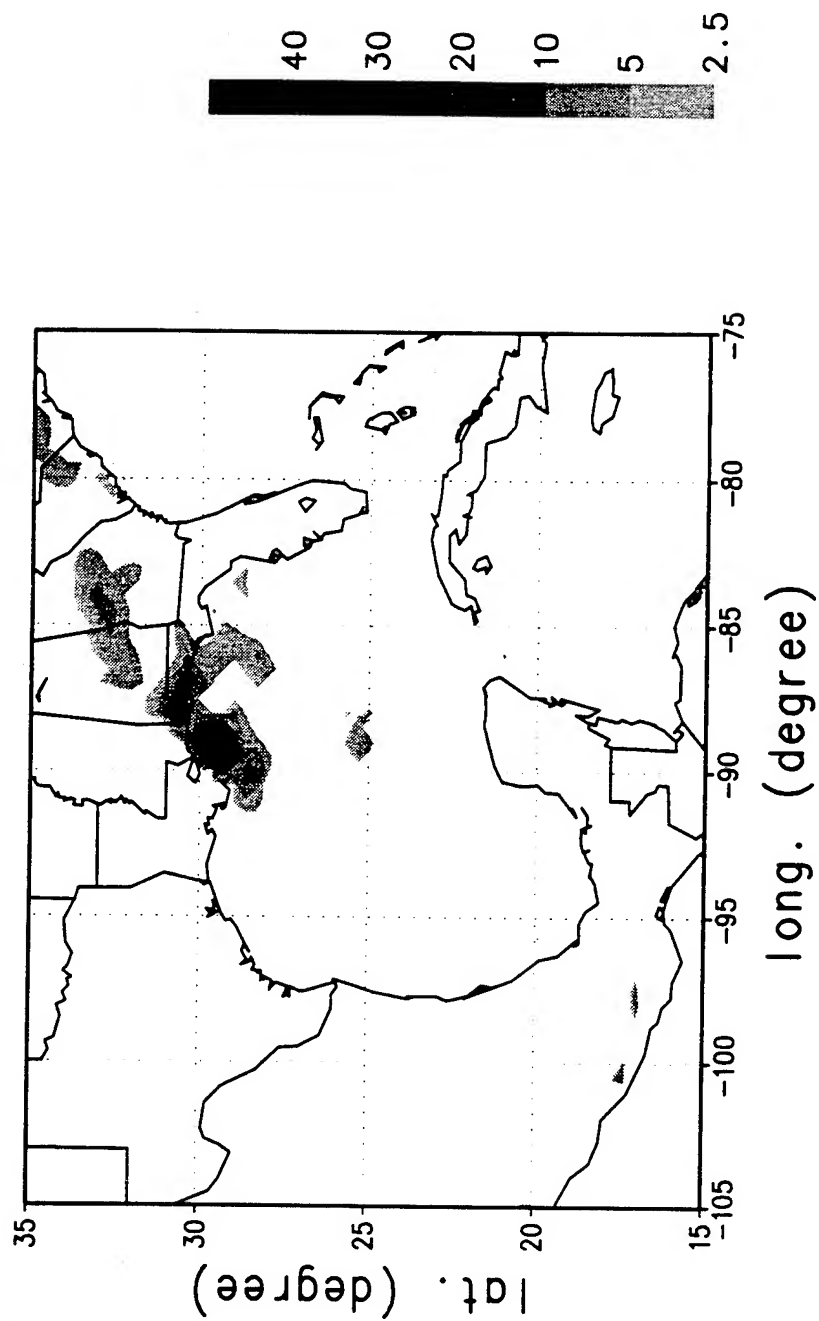


Figure 7.5 Simulated rain rates of Exp. ODW2+SSM/I at 24 hour.

Minimum Sea Level Pressure

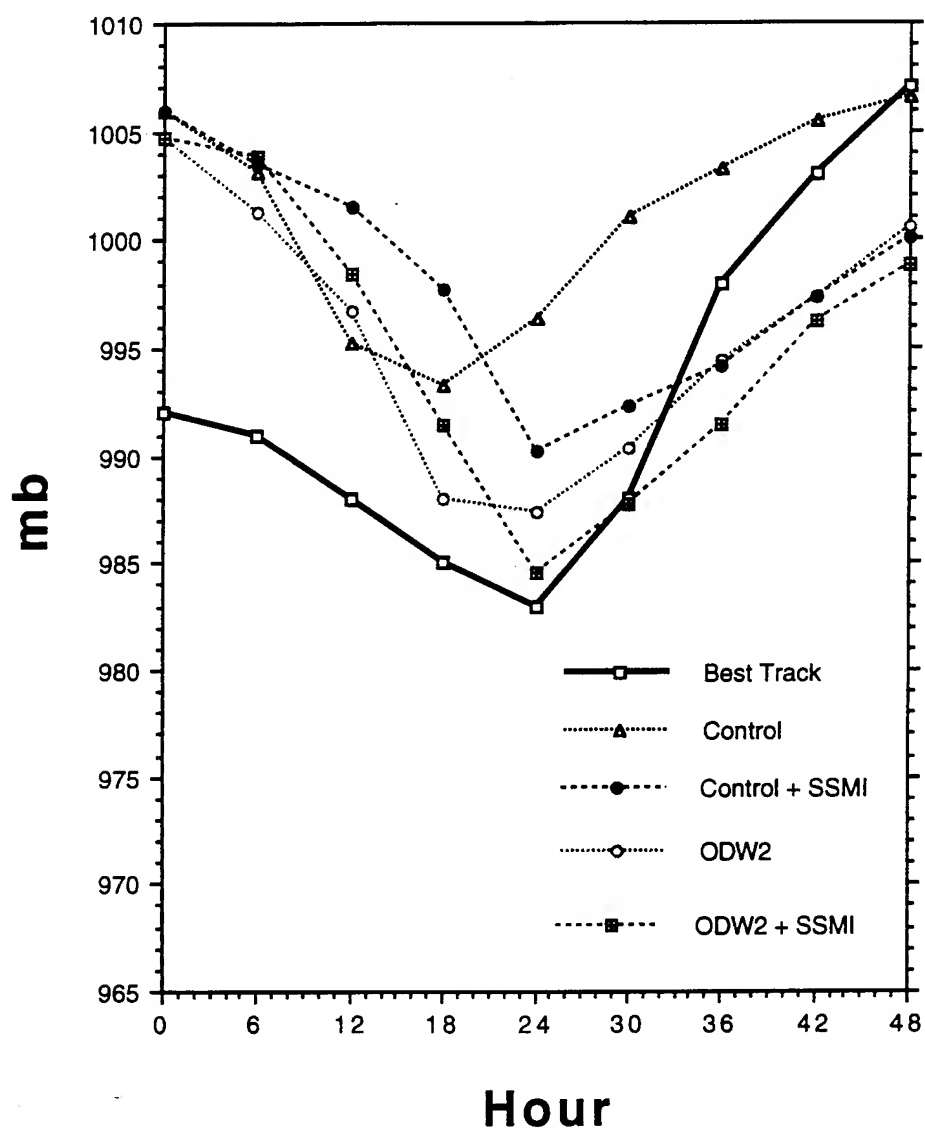


Figure 7.6 Evolution of minimum SLP of Florence with time in the best track record, the control experiment, Exp. Control+SSMI, ODW2 and ODW2+SSMI.

	Landfall Time	Long. and Lat.	Landfall Location relative location to best track
Best Track Record	0200 UTC 9/10/93	89.3W 29.1N	
Control Experiment	1700 UTC 9/ 9/93	86.7W 30.5N	2.95 degree northeast
Exp. Control+SSMI	0000 UTC 9/10/93	88.9W 30.6N	1.55 degree north
Exp. ODW2	0000 UTC 9/10/93	89.3W 29.6N	0.50 degree north
Exp. ODW2+SSMI	0200 UTC 9/10/93	89.9W 29.4N	0.67 degree northwest

Table 7.2 Landfall times and locations from the best track record, the control experiment, Exp. Control+SSMI, ODW2 and ODW2+SSMI. The landfall locations relative to the location shown in the best track record are also listed.

lists the landfall time and location of the control experiment, Exps. Control+SSM/I, ODW2 and ODW2+SSM/I and the best track record. It shows that the landfall time of the simulated storm from Exp. ODW2+SSM/I is the same as the best track record (26 hour). Exp. Control+SSM/I reduces the forecast error of the landfall location in the control experiment by about 50% (down from 2.95 degree in Control experiment to 1.55 degree) while the landfall time error is improved by 7 hours (down from 9 hours in the control experiment to 2 hours).

This sequence of numerical experiments, in which SSM/I retrieved rain rates are assimilated, reveals that the assimilation of the SSM/I rain rates improves the track forecast error by about 50% when the NMC/RAFS 2.5⁰ analysis is used as the initial condition. The impact of the SSM/I rain rates on the numerical prediction is reduced when the ODW data are available and used as the initial condition. Nevertheless, it is apparent that the combination of the ODW and SSM/I retrieved data provides the best simulation among all the experiments in this study. This result is consistent with the estimate of the impact of the SSM/I rain rates on the numerical simulation in Chang and Holt (1993).

8. STRUCTURE OF OUTFLOW LAYER AND JET AS REVEALED BY MODEL SIMULATIONS.

As discussed in Chapter 1, the outflow layer is generally anticyclonic and divergent on the synoptic scale. It is also generally confined between 100 and 300 mb (Frank 1977a). Black and Anthes (1971) noted that the outflow circulation is highly asymmetric, especially beyond 400 km from the storm center where the standard deviation of the radial and tangential wind components exceed the mean value. In this study, the result of Exp. ODW2+SSMI is analyzed to reveal the structure of the outflow layer and outflow jet of Florence. As revealed by the cross-section diagnosis (will be discussed later), the strongest model simulated outflow occurs between 100 and 250 mb. The general structure of Florence's outflow layer at 200 mb will be discussed in Section 8.1. Cross-sections of the outflow jet will be presented in Section 8.2. The angular momentum budget will be described in Section 8.3.

8.1 General Structure.

Fig. 8.1 shows the simulated 200 mb geopotential heights and wind vectors of Exp. ODW2+SSMI. A trough at 200 mb extends from eastern Tennessee into the northern Gulf of Mexico, agreeing with the NMC/RAFS 2.5⁰ analysis at 1200 UTC September 9 (Fig. 3.13). There is an upper-level high pressure located near the center of the

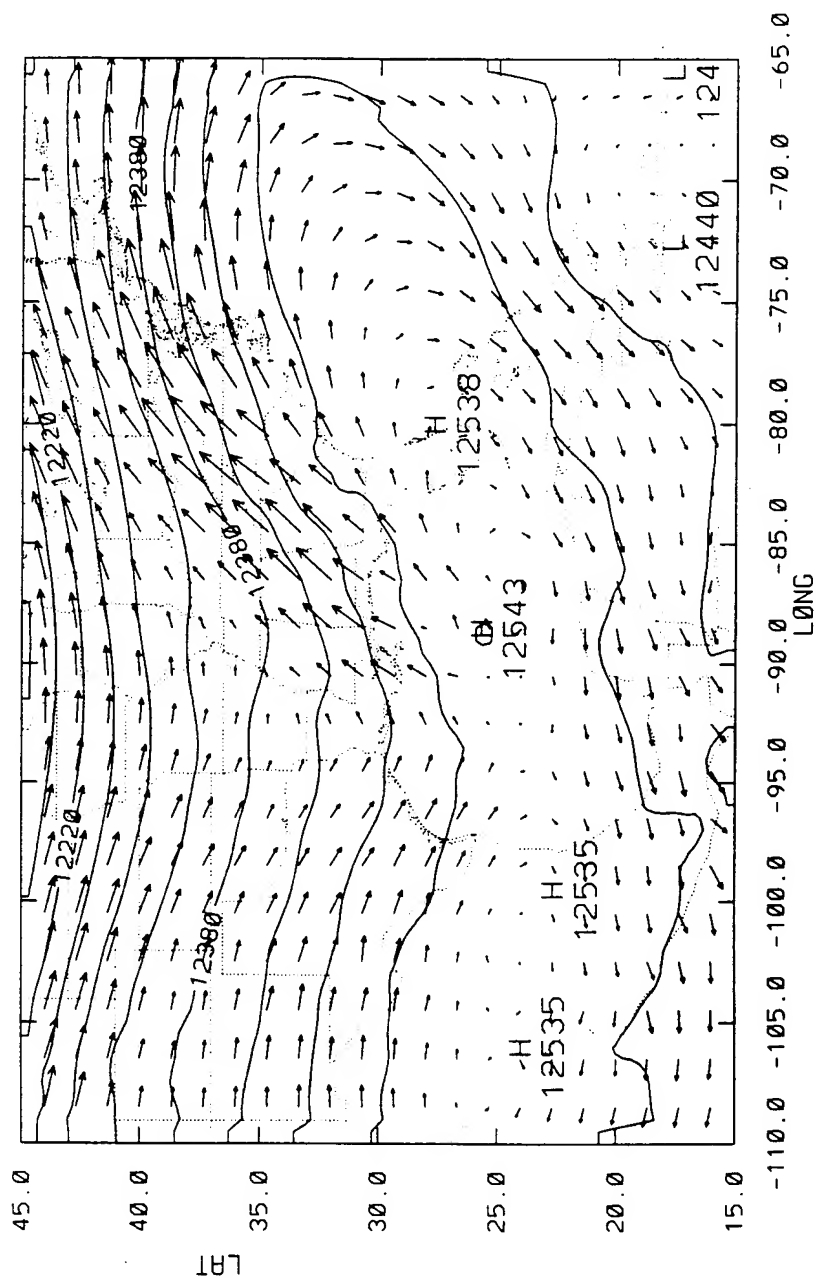


Figure 8.1 200 mb geopotential heights (m) and wind vectors (ms^{-1}) of Exp. ODW2+SSM1 at 12 hour.

Gulf of Mexico, corresponding to the low level center of Florence. Fig. 8.2 shows the simulated 200 mb isotachs of Exp. ODW2+SSMI at 12 hour. The outflow layer is highly asymmetric, especially beyond three degrees radius with an outflow channel or jet starting from about three degrees north of the center, extending northeastward into Atlantic Ocean. The outflow jet is elongated with a length of roughly 2500 km and a width of 500 km judging from the 30 ms^{-1} isotach (Fig. 8.2). The location of the outflow jet also agrees with NMC/RAFS 2.5° analysis at 1200 UTC September 9 (Fig. 3.14), except the simulated jet is stronger because of the higher horizontal resolution included in the model. The outflow jet has a maximum wind speed of 42.4 ms^{-1} , 5.8 ms^{-1} stronger the NMC/RAFS 2.5° analysis. The outflow has anticyclonic curvature except near the storm center where the wind is relatively calm. As shown in Figs. 8.1 and 8.2, at the entrance region (near southern portion of Louisiana, Mississippi and Alabama) of the jet, there is a strong anticyclonic shear along the jet core facing the storm center and a strong cyclonic shear away from the storm center in the direction perpendicular to the outflow jet. Downstream at the exit region, the jet becomes diffused with diminishing horizontal shears at both sides of the jet. This structure is similar to that in the idealized model study by Shi et al. (1991). At 24 hour, the 200 mb isotachs (Fig. 8.3) show that the westerly jet has moved northeastward away from Hurricane Florence and is located over Virginia. At this time, Florence was about to make landfall.

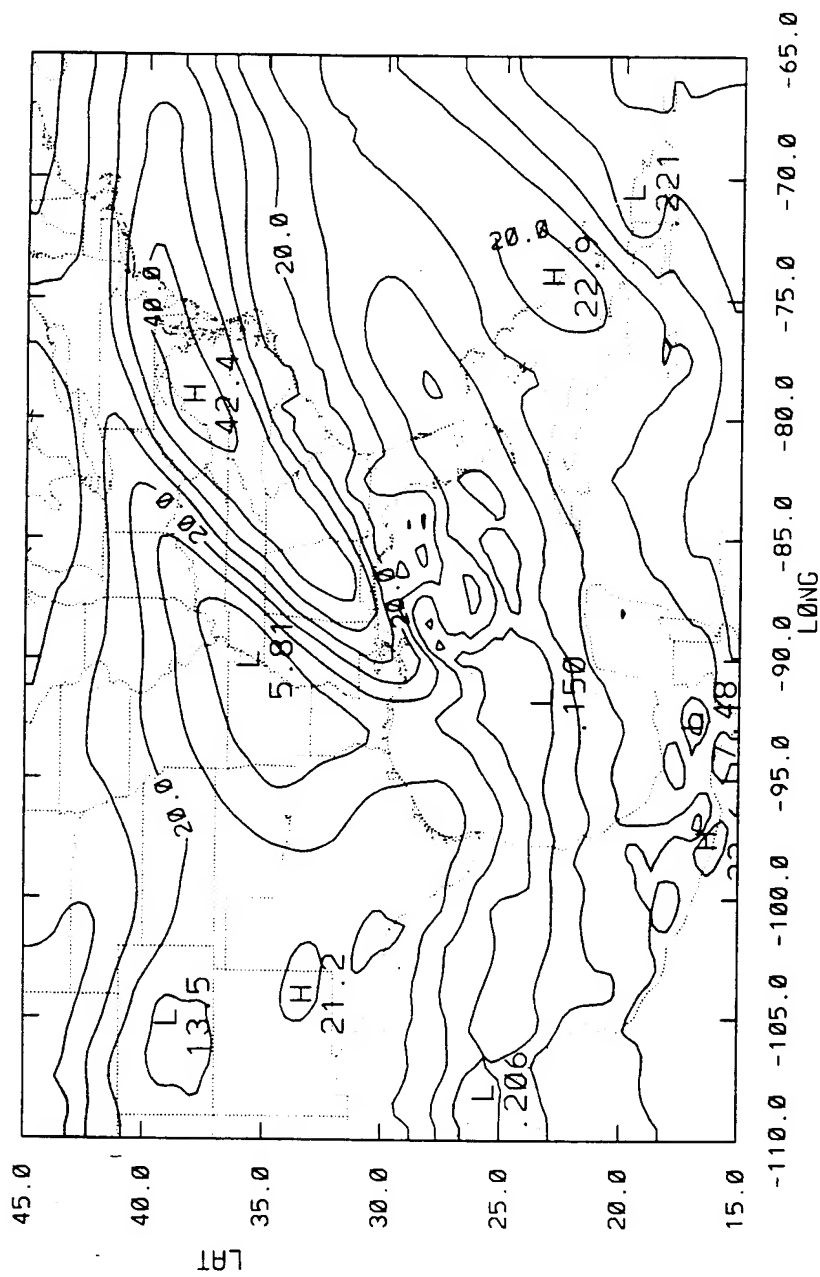


Figure 8.2 Same as Figure 8.1 except for the 200 mb isotaches.

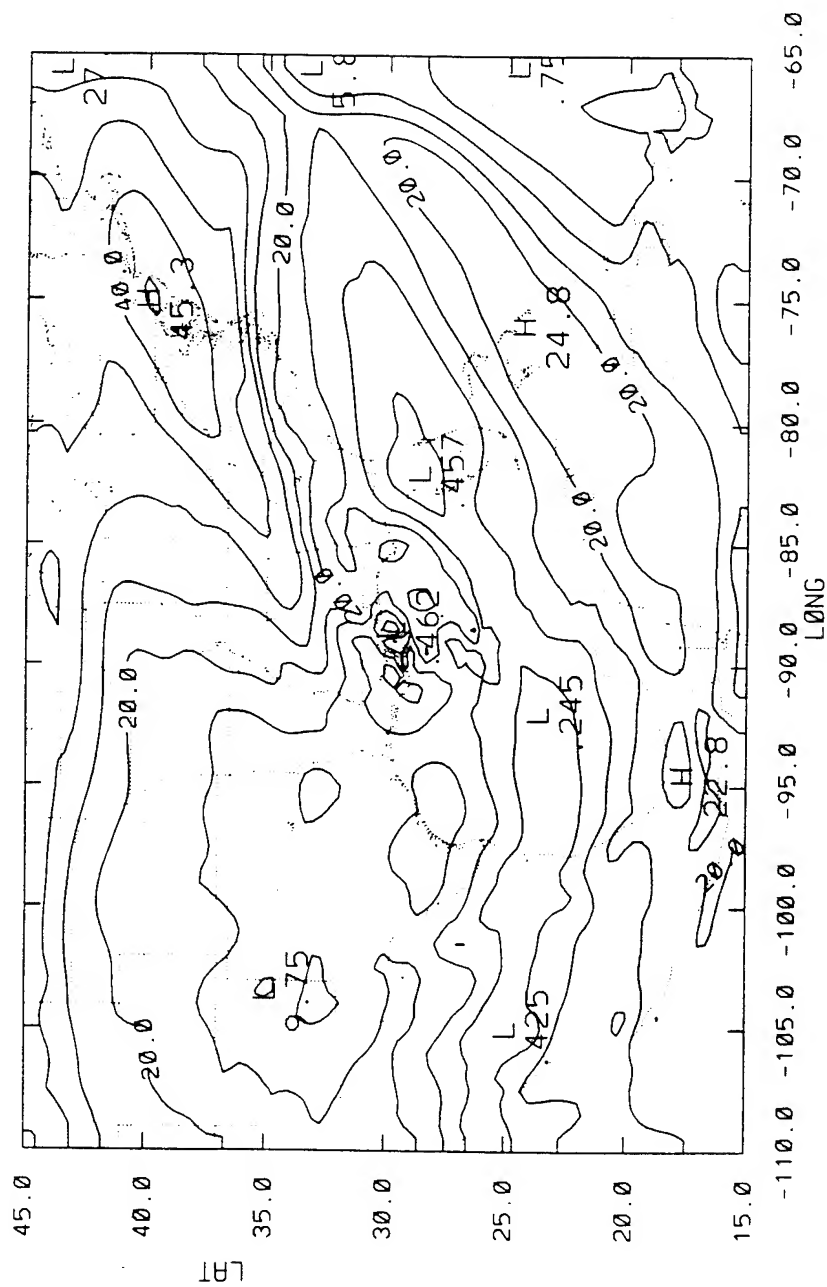


Figure 8.3 same as Figure 8.2 except for 24 hour.

The structure of the relative humidity (RH) field is usually determined by the transport process in the outflow layer, reflecting the important features of the outflow momentum field. Fig. 8.4 shows the relative humidity (RH) in the outflow layer at 12 hour. There is a wet canopy with $RH > 80\%$ over the storm center. This wet canopy also extends northeastward along the anticyclonic shear side of the outflow jet. A very sharp RH gradient exists in the direction perpendicular to the outflow jet. RH is greater than 80% on the anticyclonic side of the entrance region of the outflow jet. On the cyclonic shear side of the entrance region, it is much drier with $RH < 40\%$. The RH pattern in the outflow layer is similar to the SSM/I rain rate pattern in Fig. 3.6 and is also an indication of the existence of the circum-jet secondary circulation (Shi et al., 1990). The particular RH distribution suggests that there is a circum-jet secondary circulation with ascending motion on the anticyclonic shear side and descending motion on the cyclonic shear side. The high RH ($> 80\%$) region in the anticyclonic shear side is coinciding with the ascending branch of the circum-jet secondary circulation, while the drier ($< 40\%$) region in the cyclonic shear side coinciding with the descending branch (will be shown in the next section). At the exit region of the outflow jet (over Virginia and Maryland), a wet canopy with $RH > 80\%$ occurs downwind of the cyclonic shear side, while there is a dry tongue ($RH < 60\%$) on the anticyclonic shear side. This structure is an indication of the reverse of the circum-jet

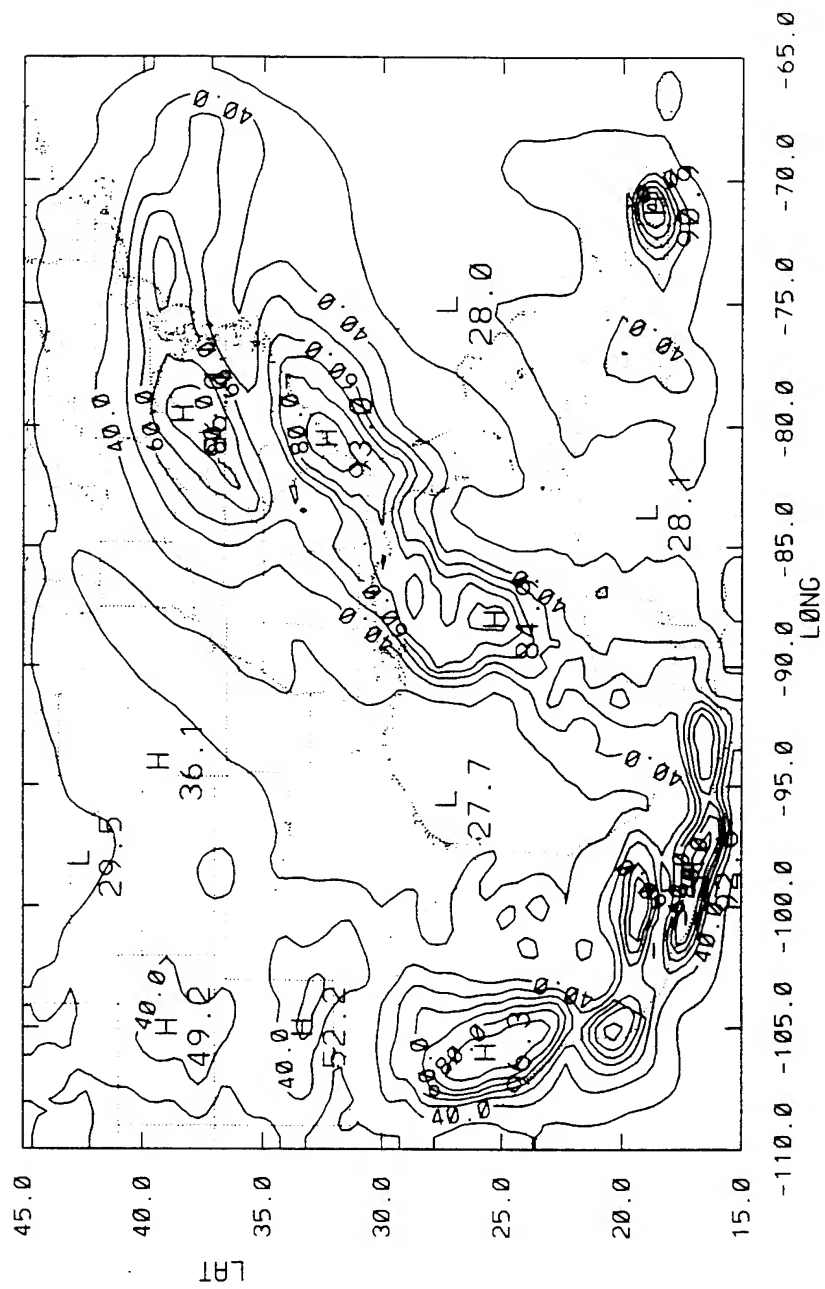


Figure 8.4 Same as 8.1 except for the 200 mb relative humidities.

secondary circulation. These results re-confirm the configuration of the secondary circulation and the tropical cyclone outflow jet proposed by Shi et al. (1990) based on the structure of an idealized tropical cyclone.

8.2 Cross-Sections of the Model Outflow Jet.

A composite cross-sectional structure of the wind and RH field are obtained by averaging the values of the cross-sections of the outflow jet. The composite cross-section in the entrance region of the outflow jet is an average of values of Cross-sections A1 thru A7 and the one in the exit region is B1 thru B6 (Fig. 8.5).

Fig. 8.6 shows the composite cross-section of the wind and RH field in the entrance region at 12 hour. The vectors are formed by the vertical velocity (mb h^{-1}) and horizontal wind components (ms^{-1}) tangential to the cross-section. The isotaches are the horizontal wind component (ms^{-1}) normal to the cross-section with positive values for the southwesterly wind (into the cross-section) and negative values for the northeasterly wind (out of the cross-section). The cross-section is roughly 10° latitude wide. The number on the x-coordinate only means the number of intervals. The 0-value end is the northwest end of the cross-section, while the 40-value end is the southeast end. The shaded areas represent the magnitude of the relative humidity. Fig 8.6 again shows that the high RH ($> 90\%$)

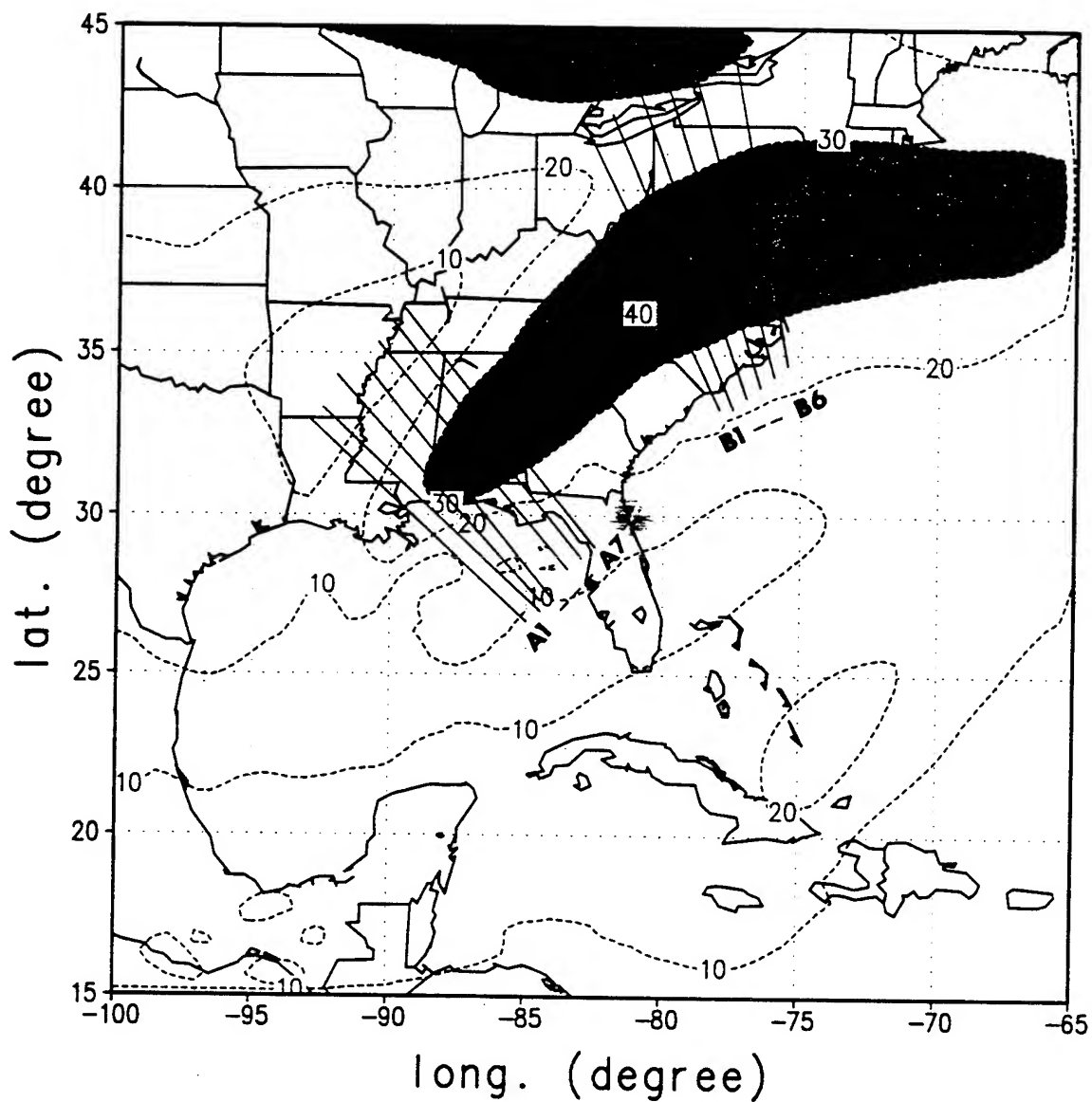


Figure 8.5 Location of cross-sections. 7 cross-sections are in the entrance region of the outflow jet --- A1 to A7, and 6 cross-sections are in the exit region --- B1 to B6. Contours are the 200 mb isotaches. Shaded area represents the area with wind speed greater than 30 ms^{-1} .

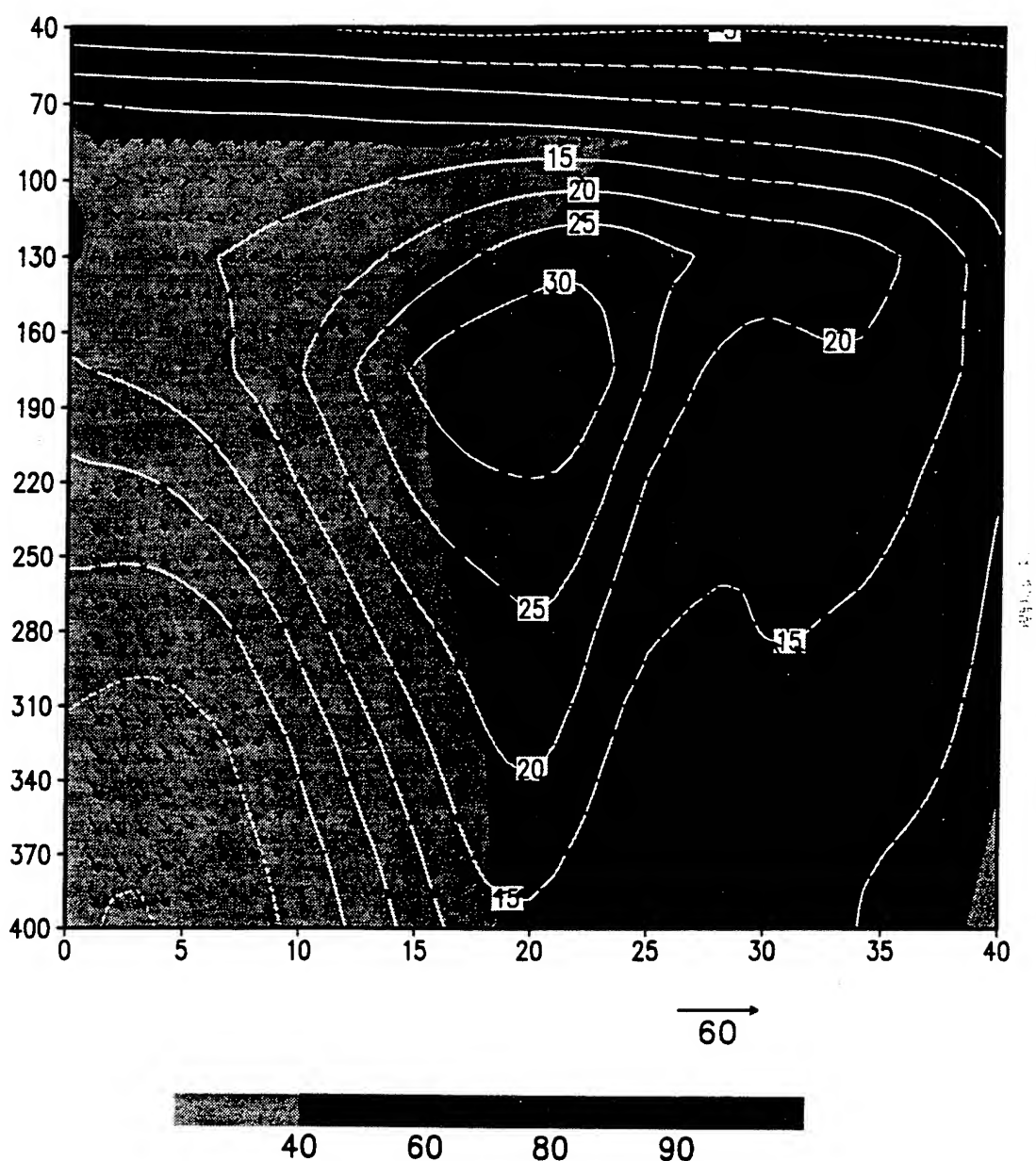


Figure 8.6 Composite cross-section in the entrance region of the outflow jet of Exp. ODW2+SSM1 at 24 hour. Contours are the wind component (ms^{-1}) normal to the cross-section (positive means blowing into the paper). Vectors are the combination of the vertical velocity (mb h^{-1}) and the wind component (ms^{-1}) tangential to the cross-section. Shaded area are the relative humidity.

is located on the anticyclonic shear side of the outflow jet, coinciding with a strong ascending motion, while the low RH ($< 40\%$) is on the cyclonic shear side coinciding with a weak descending motion. There is also an outward (from the anticyclonic to cyclonic shear side of the outflow jet), cross-jet motion between 130 and 250 mb. Merrill (1984) and Shi et al. (1990) suggested that the circum-jet secondary circulation has an outward branch above the jet, an inward branch below the jet (near 400 mb), an ascending branch on the anticyclonic shear side and a descending branch on the cyclonic shear side of the outflow jet. The result revealed here also indicates the existence of the circum-jet secondary circulation in the outflow layer. However, the inward branch below the outflow jet in the entrance region is less apparent in this study, probably because of the presence of the coastal warm front and other synoptic features. It is difficult to separate the circulations caused by the outflow jet and by the warm front, especially since the ascending branch of the secondary circulation is in close proximity of the warm front.

Fig. 8.7 shows the composite cross-section in the exit region. This figure reveals that the dry region upwind on the cyclonic shear side in the entrance region has become more humid, and the anticyclonic shear side has become less humid ($< 60\%$) between 100 and 190 mb. Comparing Figs. 8.6 and 8.7, the high RH moves outward and upward through downstream transport and a reversal of the

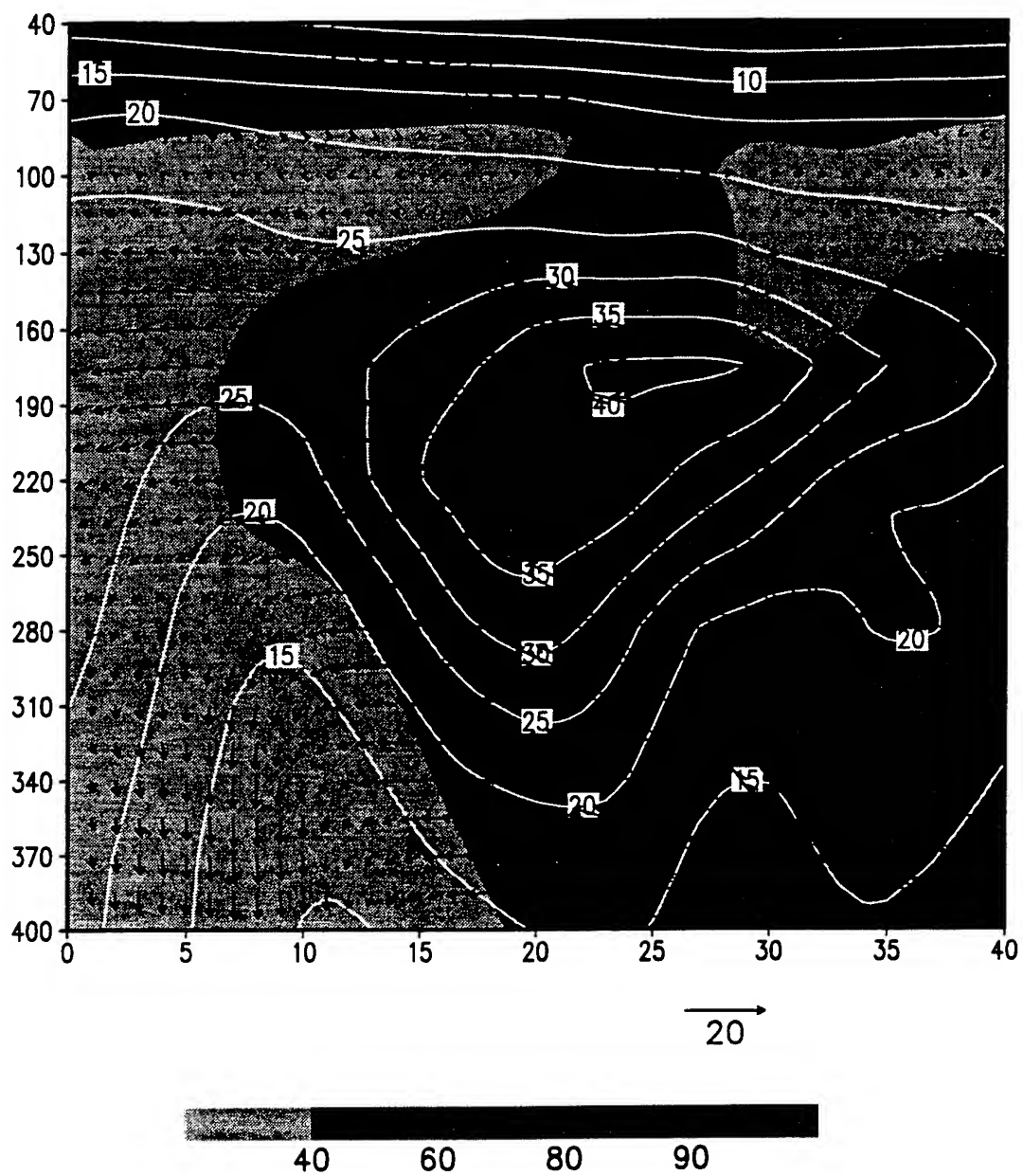


Figure 8.7 Same as Figure 8.6 except for the composite cross-section in the exit region of the outflow jet.

secondary circulation. As shown in Fig. 8.7, there is a relative well-defined thermally indirect secondary circulation between 100 and 190 mb with an ascending motion on the cyclonic shear side and a descending motion on the anticyclonic shear side. The drier region on the anticyclonic shear side coincides with the descending branch of the secondary circulation. The outward branch moves through the jet core, and the inward branch is situated just above the jet. The secondary circulation is more apparent on the composite for the exit region than for the entrance region.

The composite potential temperature deviations for the entrance region are calculated by subtracting the along-the-cross-section mean. The 12 hour potential temperature deviations for the entrance region (Fig. 8.8) shows the anticyclonic shear side is warmer than the cyclonic shear side of the outflow jet below 160 mb, which indicates that the circum-jet secondary circulation is thermally directed. This result agrees with Shi et al. (1990) and confirms the hypothesis of Merrill (1984). For extratropical upper-level jets, the confluence of the synoptic scale flow into the entrance region of the jet results in a stronger temperature gradient and a thermally direct circum-jet secondary circulation (Palmen and Newton, 1969; Uccellini et al., 1984). Comparing Fig. 8.6 and 8.8, it is apparent that the secondary circulation acts to reduce the horizontal temperature gradient in the outflow layer. At mean time, the efflux of the warm air from the storm center through the

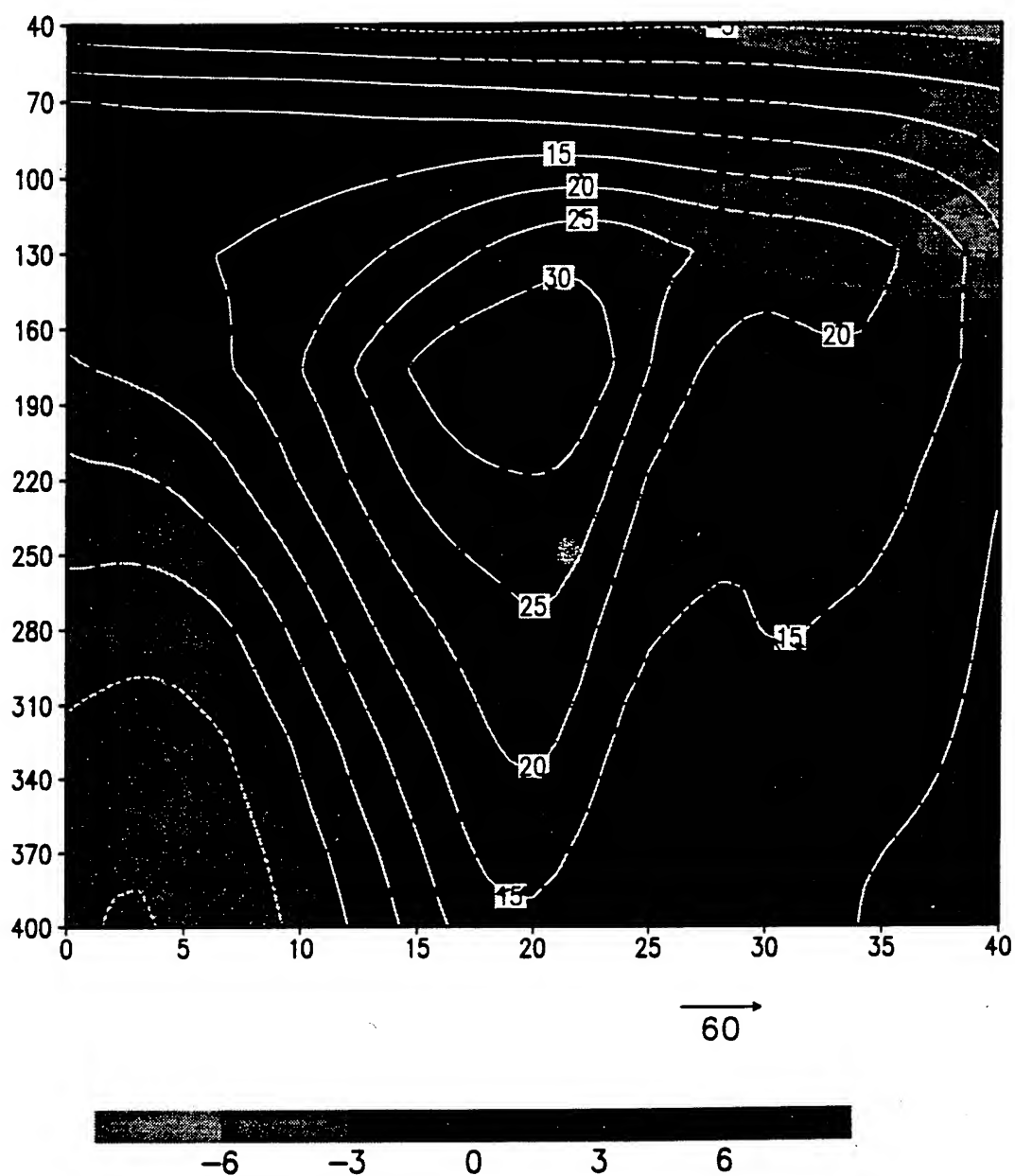


Figure 8.8 Same as Figure 8.6 except that the shaded areas are the horizontal potential temperature (degree C) deviation.

outflow jet acts to further increase the temperature gradient in the outflow layer and to maintain the strength of the circum-jet secondary circulation. Fig. 8.6 suggests that the secondary circulation may also cause enhanced convection at the ascending branch which would transport moisture upward and help to maintain the temperature gradient through latent heat release.

8.3 Angular Momentum Budget.

Previous studies (Black and Anthes, 1971; Holland 1983; Molinari and Vollaro, 1989) showed that the inward azimuthal eddy cyclonic angular momentum flux (AMF) is important to the intensification of tropical cyclones. Challa and Pfeffer (1990) claimed that the characteristic difference between the developing and non-developing disturbances is the presence (in the developing disturbances) of the well-developed influx of cyclonic eddy angular momentum at outer radii in the upper troposphere. Molinari and Vollaro (1989) suggested that operational forecasts of tropical cyclone could benefit from the analysis of AMF, because AMF measures the integrated effects of the interactions between the tropical cyclones and their environments, regardless of the complexity of the interactions.

The budget of the angular momentum of the outflow layer is calculated to study the importance of the eddy AMF. Following

Anthes (1974) and Shi et al. (1990), the angular momentum budget equation in a cylindrical coordinate system is defined as

$$\frac{\partial M}{\partial t} = -2\pi \int_{h_1}^{h_2} \int_{r_0}^{r_1} r^2 \rho(z) (\langle f \rangle \langle u \rangle + \langle f' u' \rangle) dr dz$$

(1) (2)

$$- 2\pi \int_{h_1}^{h_2} [r_1 \rho(z) \langle \langle m \rangle \langle u \rangle \rangle_{r_1} - r_0 \rho(z) \langle \langle m \rangle \langle u \rangle \rangle_{r_0}] dz$$

(3)

$$- 2\pi \int_{h_1}^{h_2} [r_1 \rho(z) \langle \langle m' u' \rangle \rangle_{r_1} - r_0 \rho(z) \langle \langle m' u' \rangle \rangle_{r_0}] dz$$

(4)

$$- 2\pi \int_{r_0}^{r_1} r [(\rho \langle w \rangle \langle m \rangle)_{h_2} - (\rho \langle w \rangle \langle m \rangle)_{h_1}] dr$$

(5)

$$- 2\pi \int_{r_0}^{r_1} r [(\rho \langle m' w' \rangle)_{h_2} - (\rho \langle m' w' \rangle)_{h_1}] dr$$

(6)

(8.1)

and

$$M = \int_{h_1}^{h_2} \int_{r_0}^{r_1} \int_0^{2\pi} r \rho m d\lambda dr dz \quad (8.2)$$

where $m=rv$ (relative angular momentum), and u and v are the radial and tangential velocities in cylindrical coordinates, r is the radius from the storm center as determined by the SLP. In (8.1), the symbol $\langle \rangle$ represents an azimuthal mean and $(\)'$ denotes a deviation from the mean. Vertical integrations are carried out between the geopotential heights of $h_1=11000$ gpm and $h_2=17000$ gpm, containing most of the outflow. The first and second term on the RHS in (8.1) denote the mean and eddy Coriolis torque, the third and fourth terms denote the horizontal convergence of mean and eddy angular momentum fluxes, respectively. Finally, the fifth and sixth terms represent the vertical convergence of mean and eddy angular momentum fluxes, respectively. To evaluate the values of these terms, model results are linearly interpolated to the cylindrical-height coordinates. Because of the size of this model storm, the outer region is defined from 300 to 700 km, instead of the 300 to 1000 km used by Shi et al. (1990). The values of each term in (8.1) calculated from the Exp. ODW2's result at 12 hour are listed in Table 8.1. For comparison, values from the idealized model tropical cyclone in Shi et al. (1990) and observed values for mean tropical storms in Palmen and Riehl (1957) and Pfeffer (1958) are also listed.

	Radius (km)	Coriolis torque	Horizontal flux		Vertical flux	
			Mean	Eddy	Mean	Eddy
Mean storm (Palmen and Riehl, 1957)	0-333	-48.0	-20.0	8.0	40.0	20.0
	333-666	-143.0	76.0	23.0	- - -	44.0
Mean storm (Pfeffer, 1958)	222-444	-54.0	46.0	20.0	5.0	- - -
	444-666	-78.0	-11.0	13.0	-4.0	- - -
Model storm (Shi et al., 1991)	0-300	-4.3	3.5	-0.7	-0.3	- - -
	300-1000	-47.6	13.4	35.1	1.1	-0.4
Model Florence (1988) from Exp. ODW2	0-300	-40.1	30.6	-17.1	-14.9	-8.7
	300-700	-403.9	172.5	158.4	1.5	-0.9

Table. 8.1 Model and empirical angular momentum budget in the outflow layer of tropical cyclone. Units are in $10^{22} \text{ g cm}^2 \text{ s}^{-2}$. The values for mean storms are adopted from Anthes (1974).

Table 8.1 shows that the values of various terms in (8.1) evaluated from the modeled tropical cyclones compare reasonably with those of the observational studies and the previous model study. The values from Shi et al. (1990) are smaller because the vertical integration depth is only 1000 gpm (from 13700 to 14700 gpm). The vertical momentum fluxes in Palmen and Riehl (1957) contain unaccounted-for residuals. The angular momentum balance in both the simulated and the observed tropical cyclones is basically maintained by the Coriolis torque and horizontal transports. Both the model results of this study and previous study by Shi et al. (1990) show that the contribution by the horizontal eddy AMF convergence is similar to the mean momentum flux convergence in the outer region. This study reveals that the mean horizontal AMF dominates in the inner region while the eddy horizontal AMF is roughly equal to the contribution from the mean in the outer region, agreeing with the observational study of Molinari and Vollaro (1989). All four results indicate the importance of the eddy horizontal AMF. Both model results show a negative contribution of the horizontal eddy AMF indicating the cyclonic motion near the storm center in the outflow layer. The importance of the eddy term again underscores the dominance of the outflow jet in the outflow layer and the highly asymmetric nature of the outflow layer of tropical cyclones.

9. UPPER-TROPOSPHERIC ENVIRONMENTAL INFLUENCES ON FLORENCE

Despite many observational and model studies in the past two decades as mentioned in Chapter 1, the interactions between the outflow of tropical cyclones and their upper level environments are still not fully understood. Sadler (1976) found that the position of an UTT relative to the center of a tropical cyclone was crucial for the intensification of a tropical cyclone. Holland and Merrill (1984) elaborated that an approaching upper level westerly trough provides a divergent region for the outflow of tropical cyclones. Molinari and Vollaro (1989) documented that Hurricane Elena (1985) experienced a major second intensification associated with a large inward eddy momentum flux in the outflow layer caused by the passage of a mid-latitude trough north of the hurricane. They also stated that the enhanced anticyclonic outflow from the storm's initial deepening sufficiently reduced the inertial stability of the outflow layer. This reduction of the inertial stability allowed the environmental forcing (e.g., the upper level westerly trough) to interact with the outflow layer, resulting in the second intensification of Hurricane Elena (1985).

The cause-effect relationship between environmental forcings and tropical cyclone intensity changes is however still not fully and quantitatively documented. In order to investigate the interaction

between the environmental forcings and the outflow layer of Hurricane Florence (1988), a numerical experiment (Exp. ODW2+WTR) is conducted for this study. For this experiment, the ODW2 analysis is re-processed to reduce the cyclonic curvature of the upper level westerly trough at 0000 UTC September 9. This is done to determine the impact of the weakened westerly jet on the outflow layer of Florence. In the re-processing of the ODW2 analysis, the north-south component of the wind is set to zero in the layer between 100 and 500 mb and in the region between 30° and 45° N. To further weaken the temperature gradient associated with the westerly jet, the temperature at each grid point is set to the zonal mean temperature.

After the re-process, the new analysis ODW2+WTR is then initialized by the VMI. Fig. 9.1 shows the SLPs and the 1000 mb wind vectors of the ODW2+WTR analysis after initialized by the VMI. Comparing Figs. 9.1 and 5.6, the SLPs and wind pattern surrounding the storm are almost unchanged while the upper level westerly jet has been weakened by about 6.9 ms^{-1} from 34.5 ms^{-1} (Fig. 9.2) to 29.6 ms^{-1} (Fig. 9.3). The tropical cyclone model is then integrated for 48 hours to investigate the impact of the weakened westerly jet on the structure changes of Florence.

As shown in Table 9.1, the minimum SLP of Exp. ODW2+WTR at 24 hour is 2 mb weaker than the one of Exp. ODW2 and the maximum

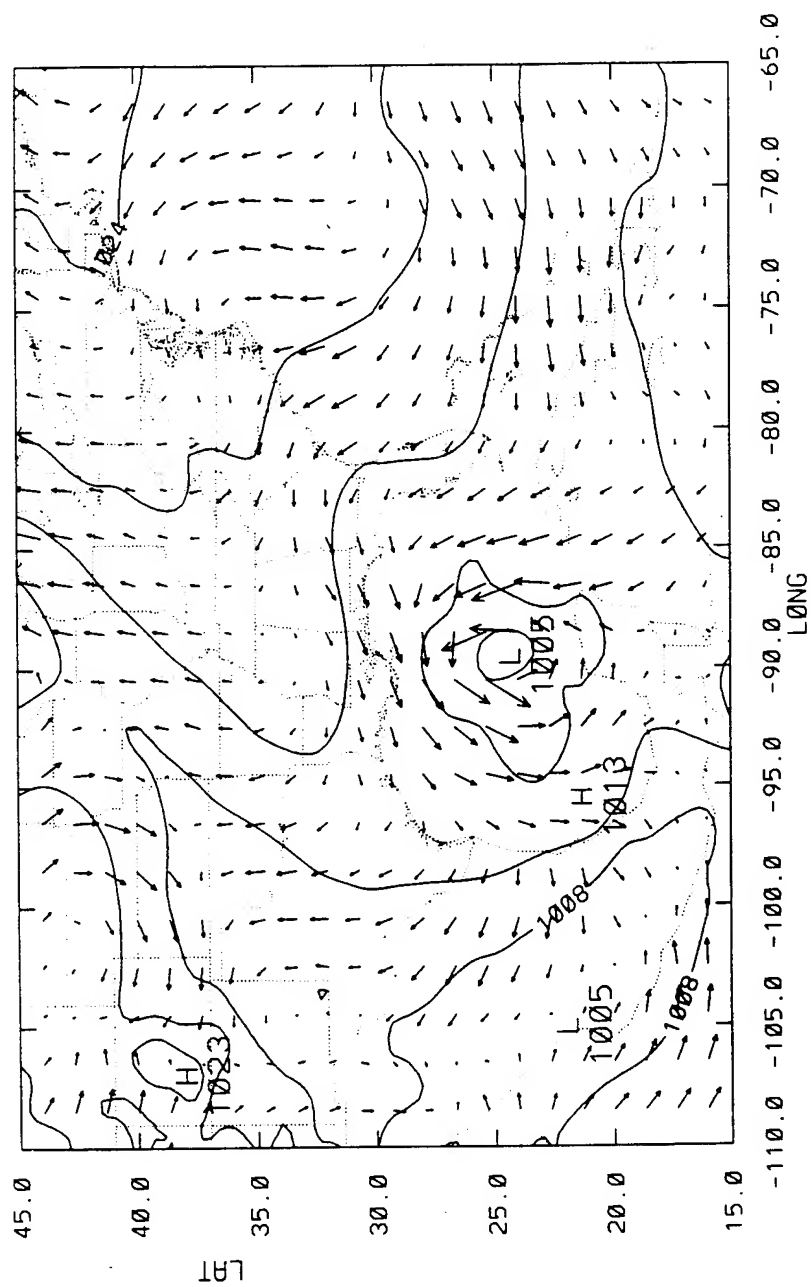


Figure 9.1 Sea level pressures (mb) and 1000 mb wind vectors (ms⁻¹) of the ODW2+WTR analysis after initialized by the VMI.

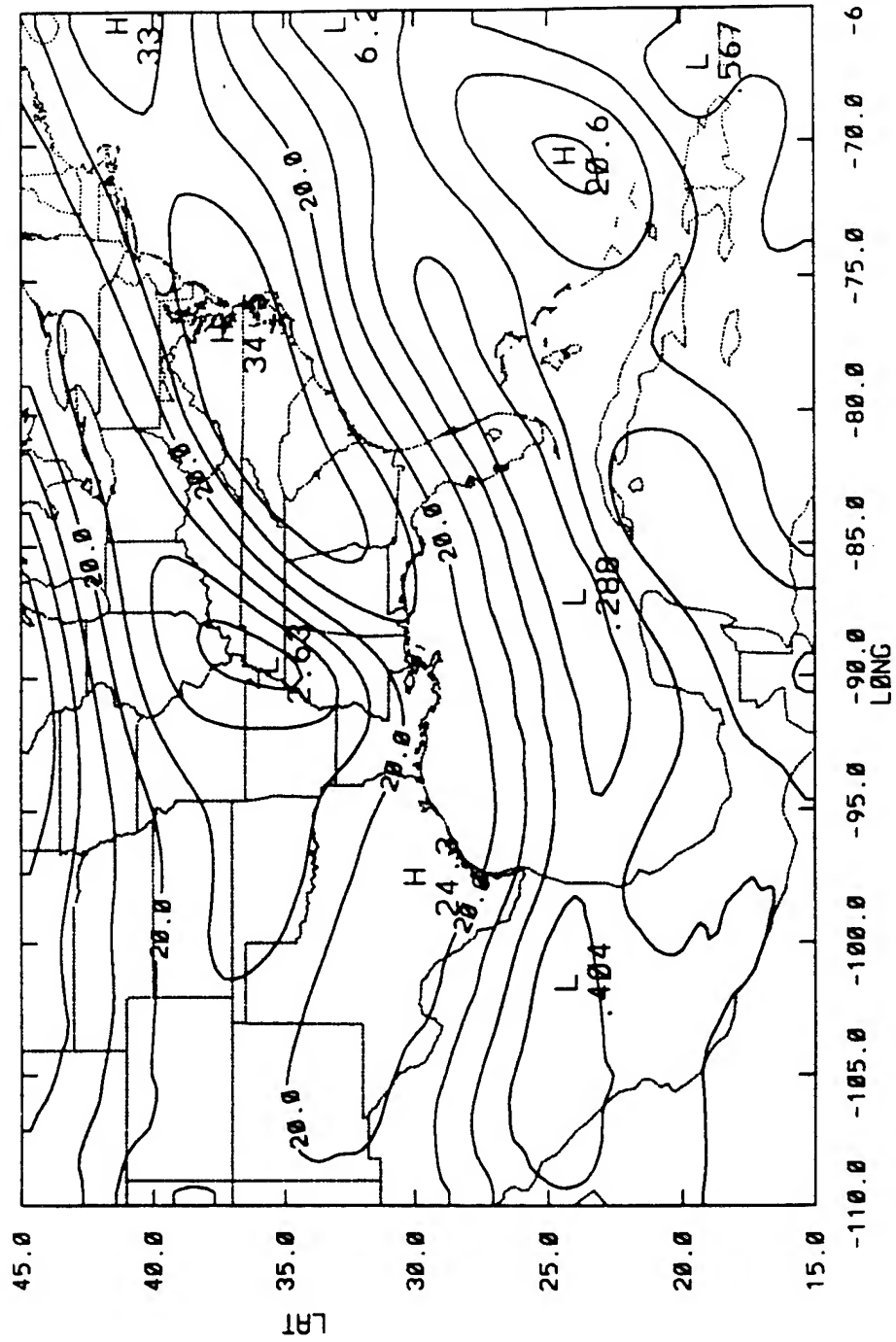


Figure 9.2 200 mb isotaches of the ODW2 analysis after initialized by the VMI.

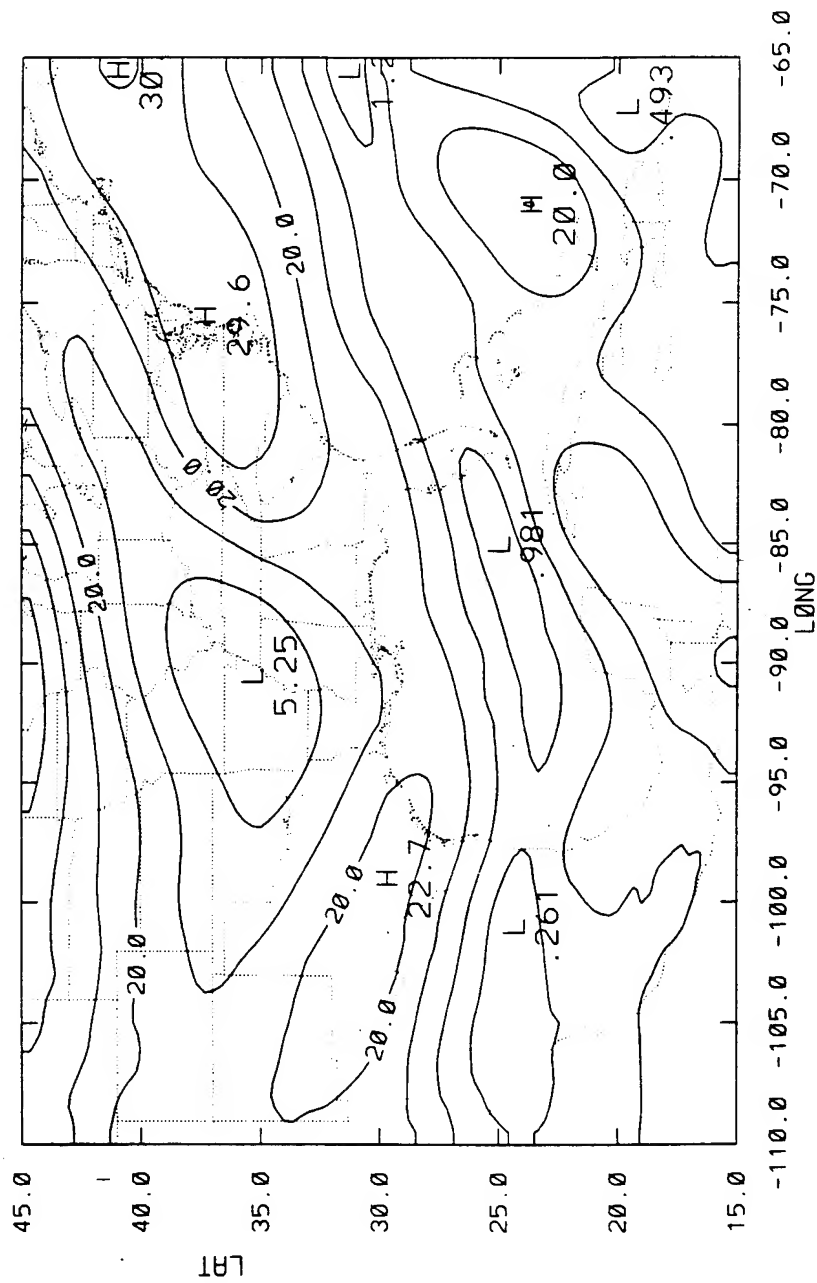


Figure 9.3 Same as Figure 9.2 except for the ODW2+WTR analysis after initialized by the VMI.

Minimum Sea Level Pressure (mb)					
	0 h	6 h	12 h	18 h	24 h
Best Track Record	992	991	988	985	983
ODW2	1005	1001	997	988	987
ODW2+WTR	1005	1001	997	990	989

Maximum Surface Wind Speed (ms ⁻¹)					
	0 h	6 h	12 h	18 h	24 h
Best Track Record	25.7	25.7	28.3	33.4	36.0
ODW2	28.4	24.4	30.4	35.8	38.8
ODW2+WTR	28.7	26.0	29.7	35.3	33.8

Location of Storm Center					
	0 h	6 h	12 h	18 h	24 h
Best Track Record	89.2W 24.2N	89.2W 25.2N	89.2W 26.1N	89.2W 27.4N	89.3W 28.7N
ODW2	89.4W 24.3N	88.6W 25.6N	88.8W 27.1N	89.1W 28.5N	89.3W 29.6N
ODW2+WTR	89.4W 24.3N	89.5W 25.7N	89.1W 27.1N	89.6W 28.7N	89.9W 30.0N

Table 9.1. Minimum SLP (mb), maximum wind speed (ms⁻¹) and location of storm center from the best track record, Exp. ODW2 and ODW2+WTR.

surface wind of Exp. ODW2+WTR is 5.0 ms^{-1} or 15% weaker than that of Exp. ODW2. Fig. 9.4 shows the 200 mb isotaches of Exp. ODW2 at 12 hour and Fig. 9.5 shows Exp. ODW2+WTR at 12 hour. It is apparent that the maximum wind in the outflow jet of Exp. ODW2+WTR is 7.1 ms^{-1} weaker than its counterpart of Exp. ODW2. The result here suggests that the strength of an approaching westerly jet is partially responsible to the intensification of Florence.

Previous studies (Holland and Merrill, 1984; Shi et al., 1990) suggested that the existence of the outflow jet provides a channel to remove the warm air from the core of tropical cyclones. Holland and Merrill (1984) further speculated that the enhanced outflow may further increase the convection in the core region. Fig. 9.6 shows that the mean convective precipitations of Exp. ODW2+WTR inside a $2^{\circ} \times 2^{\circ}$ box centered at the storm center are reduced by about an average of 15-20% between 10 and 15 hour, coinciding with the 15% reduction of the maximum wind in the outflow jet. The weaker convection in the core region between 10 and 15 hour eventually results in a weaker hurricane at 24 hour. These result are consistent with Holland and Merrill (1984) and Shi et al. (1990). Fig. 9.6 also shows that the inner core convection of Exp. ODW2 and ODW2+WTR reach their maximum at 13 hour while the intensities of both storms reach their maximum at 23 hour. This result suggests that Florence's intensity responds to the intensification of the inner core convection which occurred 10 hours earlier.

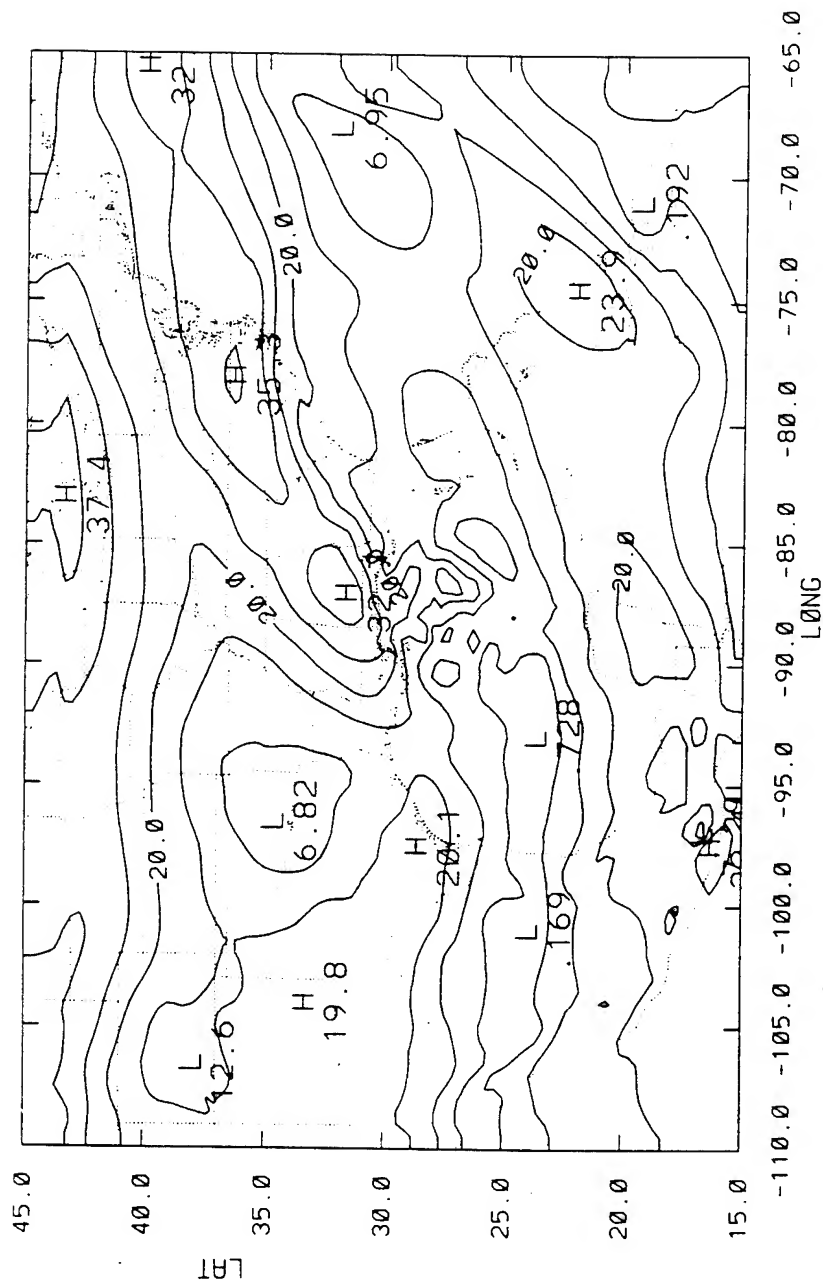


Figure 9.4 200 mb isotaches of Exp. ODW2+WTR at 12 hour.

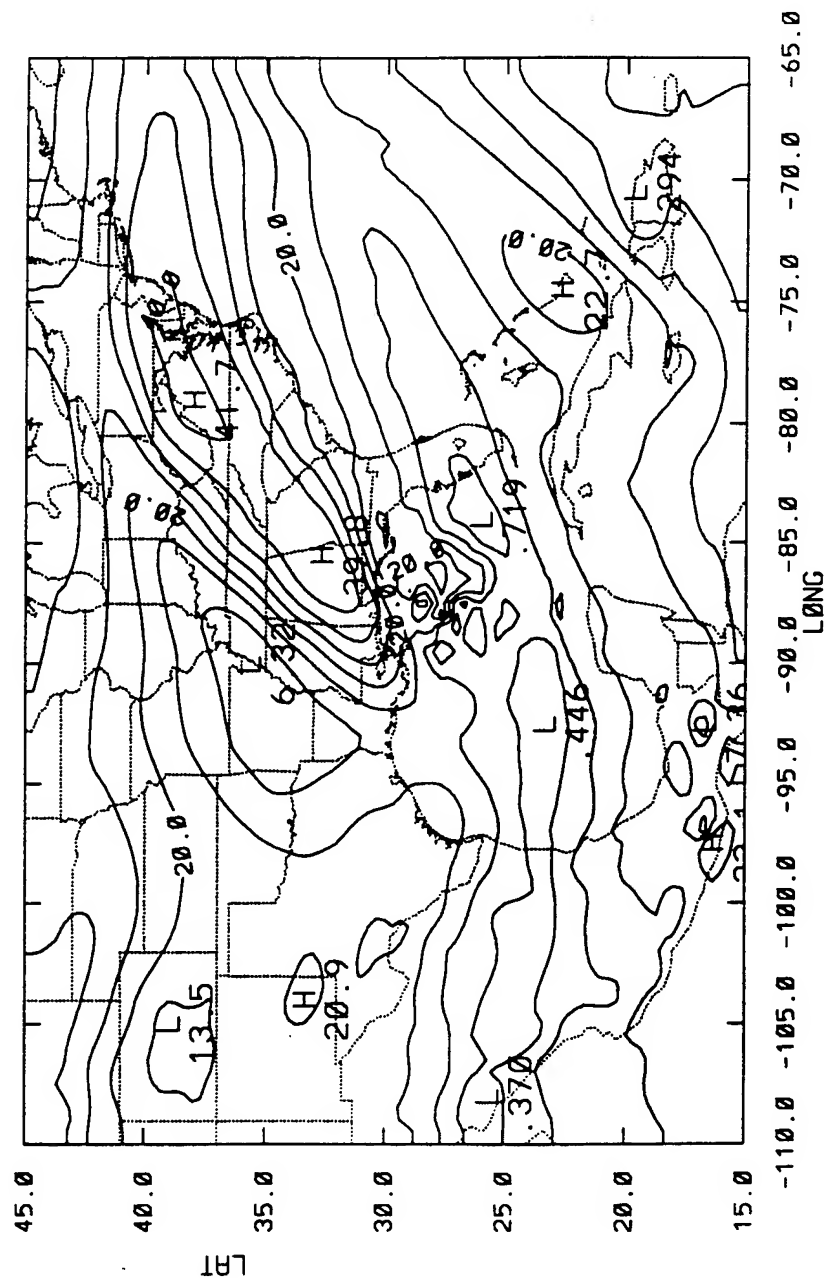


Figure 9.5 Same as Figure 9.4 except for Exp. ODW2.

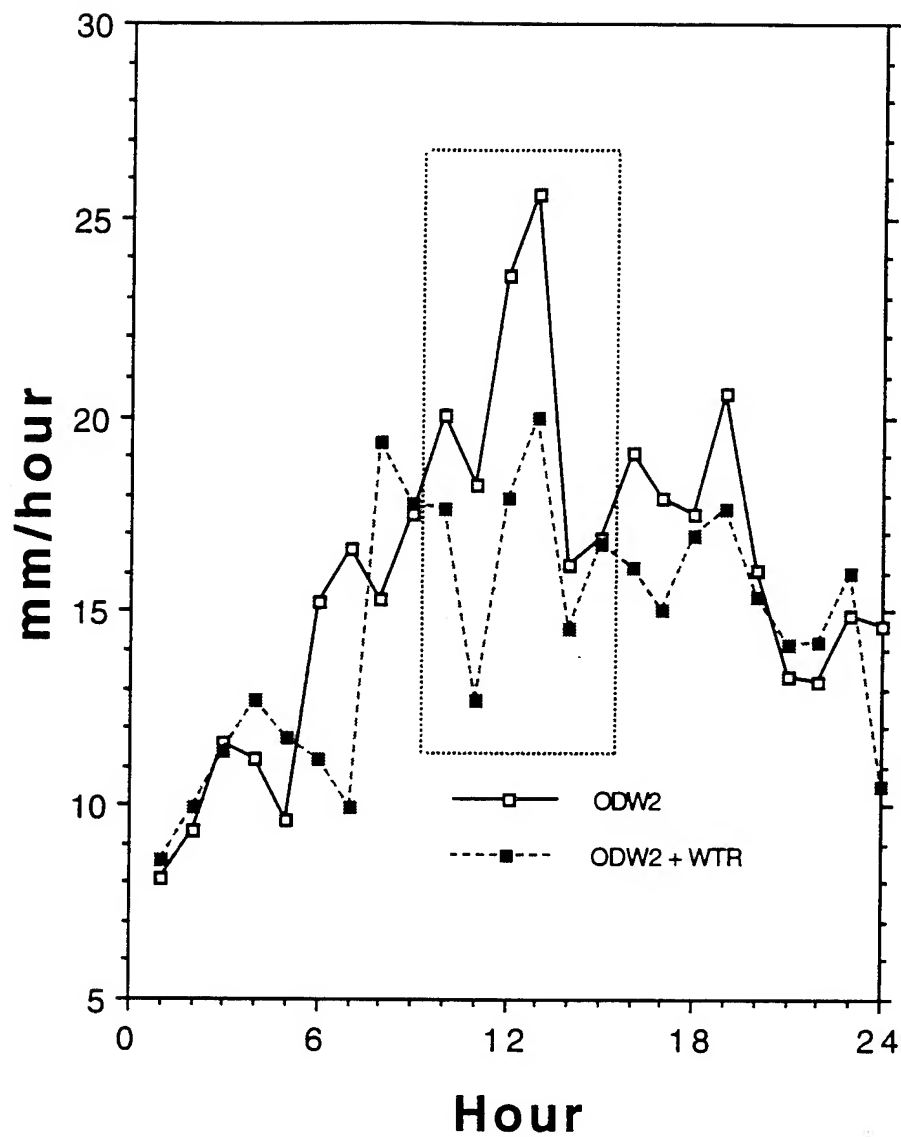


Figure 9.6 Mean convective rain rates of Exp. ODW2 and ODW2+WTR inside a $2^0 \times 2^0$ box centered at the storm center. Dashed box contains mean convective rain rates between 10 and 15 hour.

Fig. 9.7 shows the 12 hour 200 mb RH field of Exp. ODW2+WTR. Comparing with the 12 hour 200 mb RH contours of Exp. ODW2 (Fig. 9.8), the wet canopy (RH > 70%, also shown in Fig. 8.3) in Fig. 9.8 over Virginia and West Virginia, embedded in the cyclonic shear side of the exit region of the outflow jet of Exp. ODW2, is absent in Exp. ODW2+WTR. The dry tongue on the anticyclonic shear side of the outflow jet in the exit region of Exp. ODW2 also vanishes. As discussed in previous chapter, the wet canopy on the anticyclonic shear side of the outflow jet in the exit region may result from the downwind transport of moisture in the outflow jet. Fig. 9.7 indicates that the weaker outflow jet may also result in a weaker downwind transport of moisture.

More evidences of a weaker secondary circulation in Exp. ODW2+WTR can be provided by the cross-section diagnosis. Figs. 9.9 and 9.10 show the composite cross-sections of wind and RH in the entrance and exit regions of Exp. ODW2+WTR at 12 hour. For comparison, the composite cross-sections of wind and RH in the entrance (Fig. 9.11) and exit regions (Fig. 9.12) of Exp. ODW2 at 12 hour are also shown here. The cross-sectional analyses are produced by the same method used for Fig. 8.6 and 8.7 and from the same locations as Fig. 8.6 and 8.7. Comparing Exp. ODW2+WTR (Fig. 9.9) and Exp. ODW2 (Fig. 9.11), the area on the anticyclonic shear side of the entrance region of Exp. ODW2+WTR is drier (>80 %) than that (> 90%)

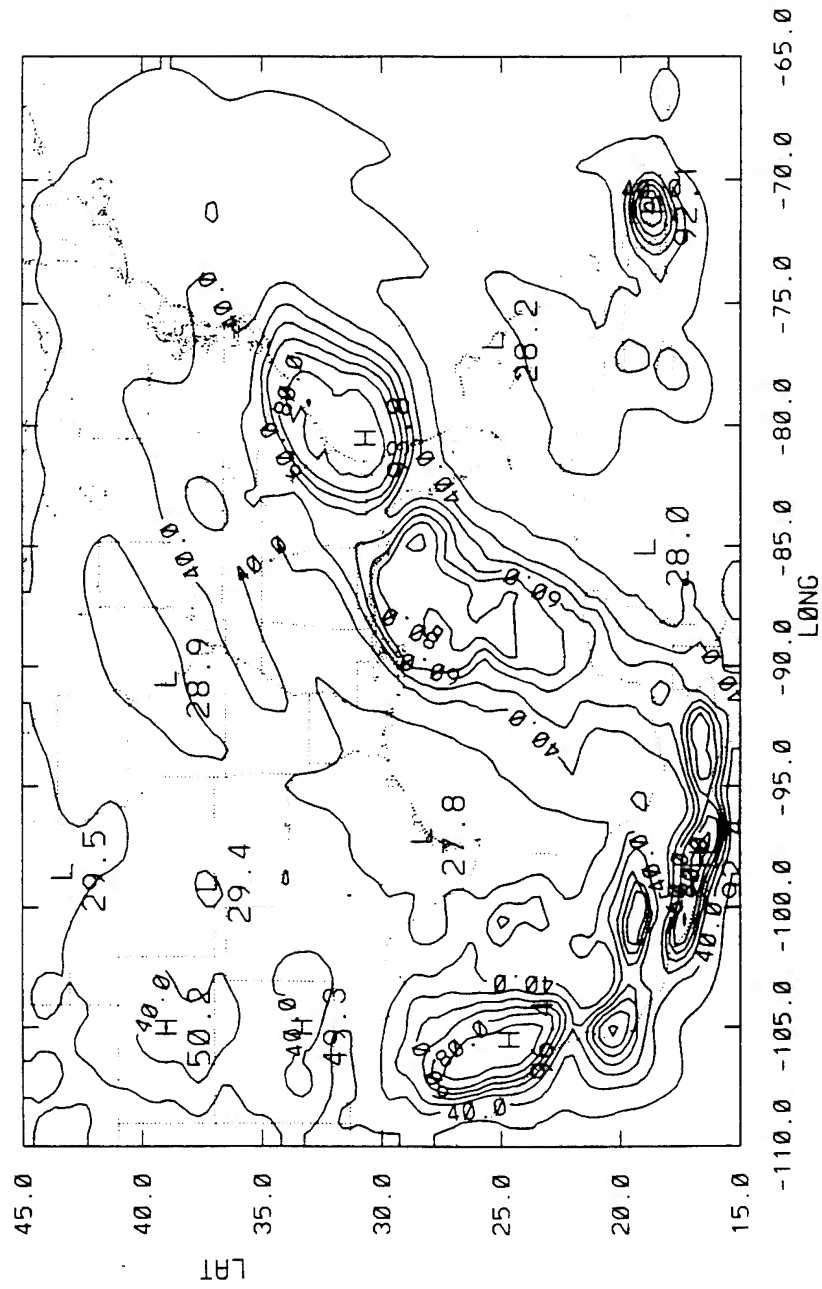


Figure 9.7 200 mb relative humidities of Exp. ODW2+WTR at 12 hour.

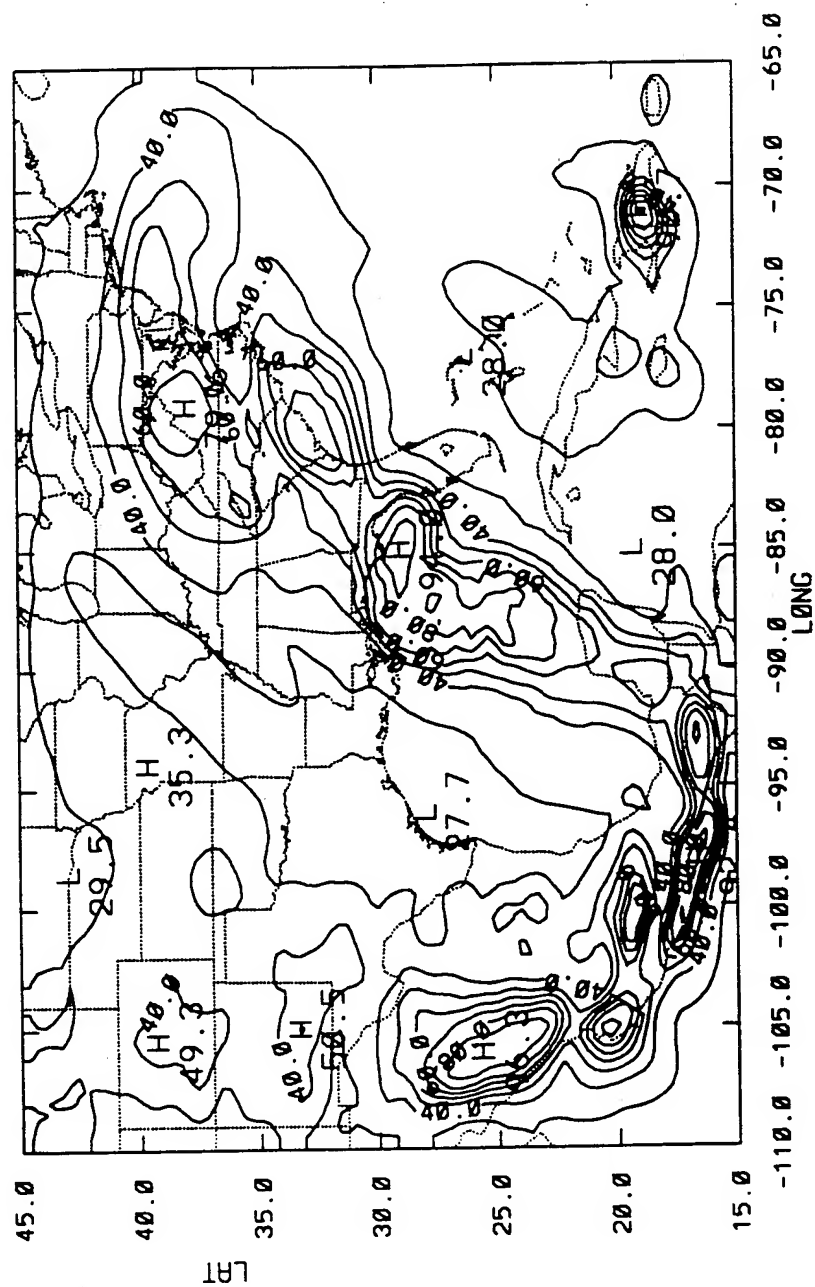


Figure 9.8 Same as Figure 9.7 except for Exp. ODW2.

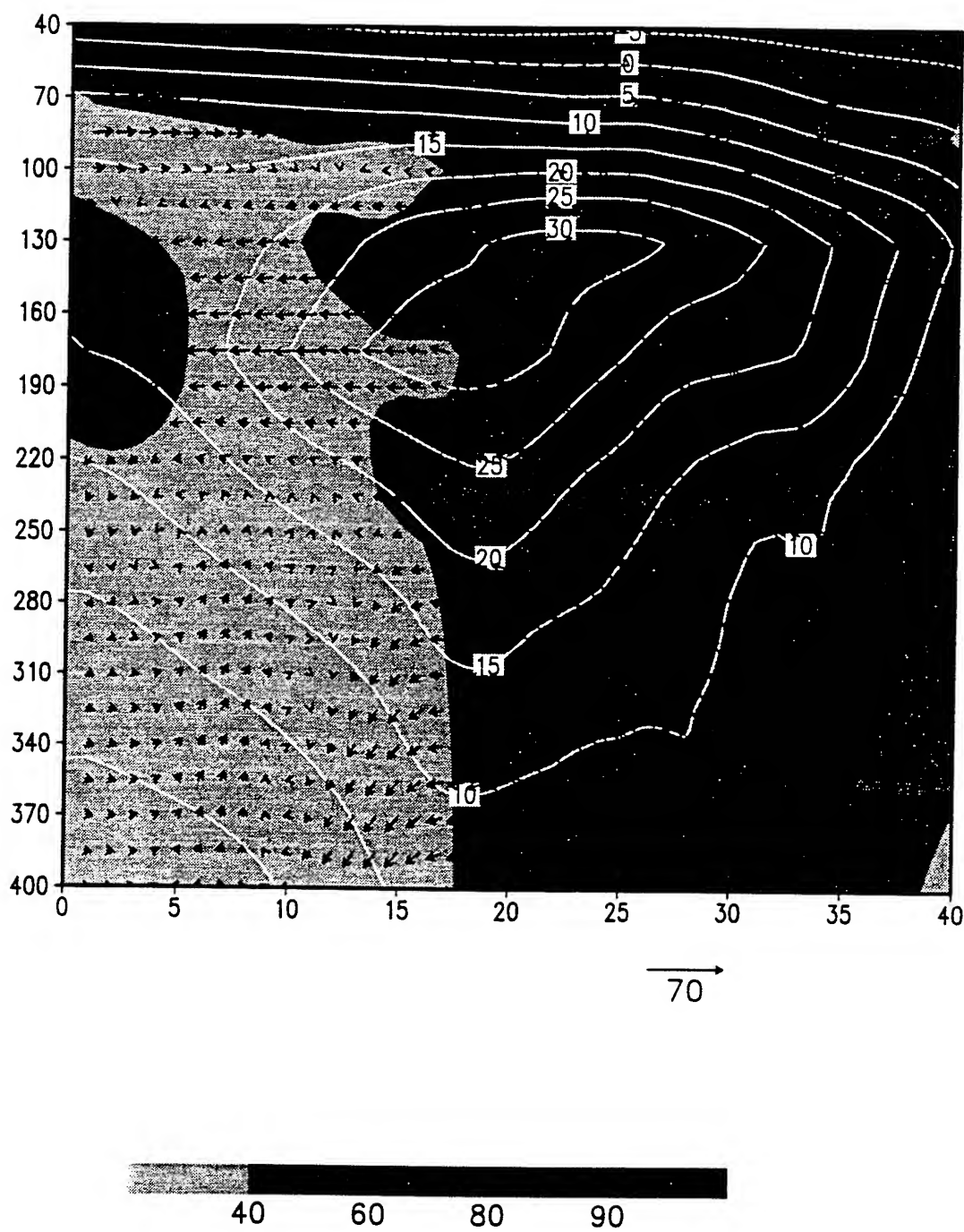


Figure 9.9 Same as Figure 8.6 except for Exp. ODW2+WTR.

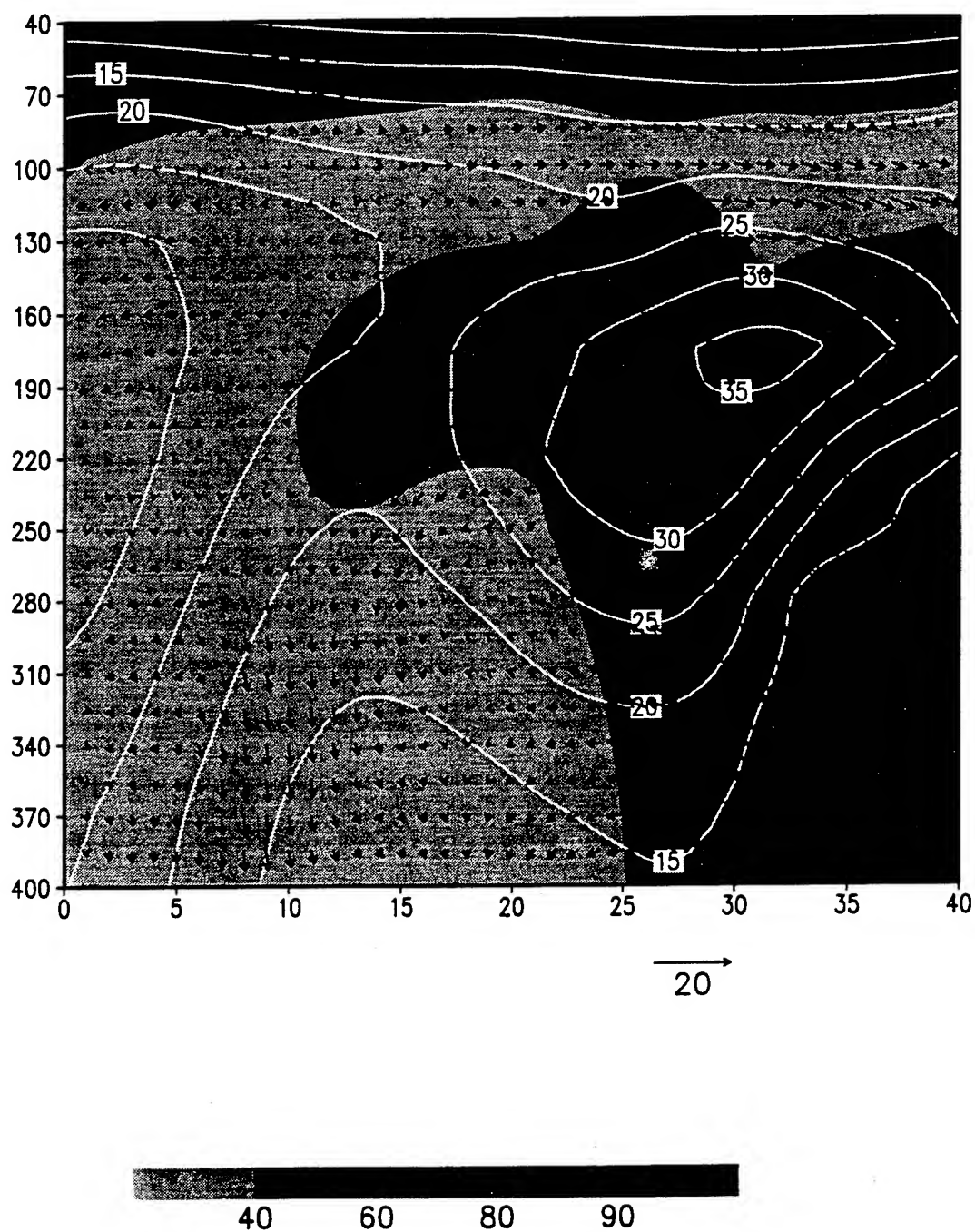


Figure 9.10 Same as Figure 8.7 except for Exp. ODW2+WTR.

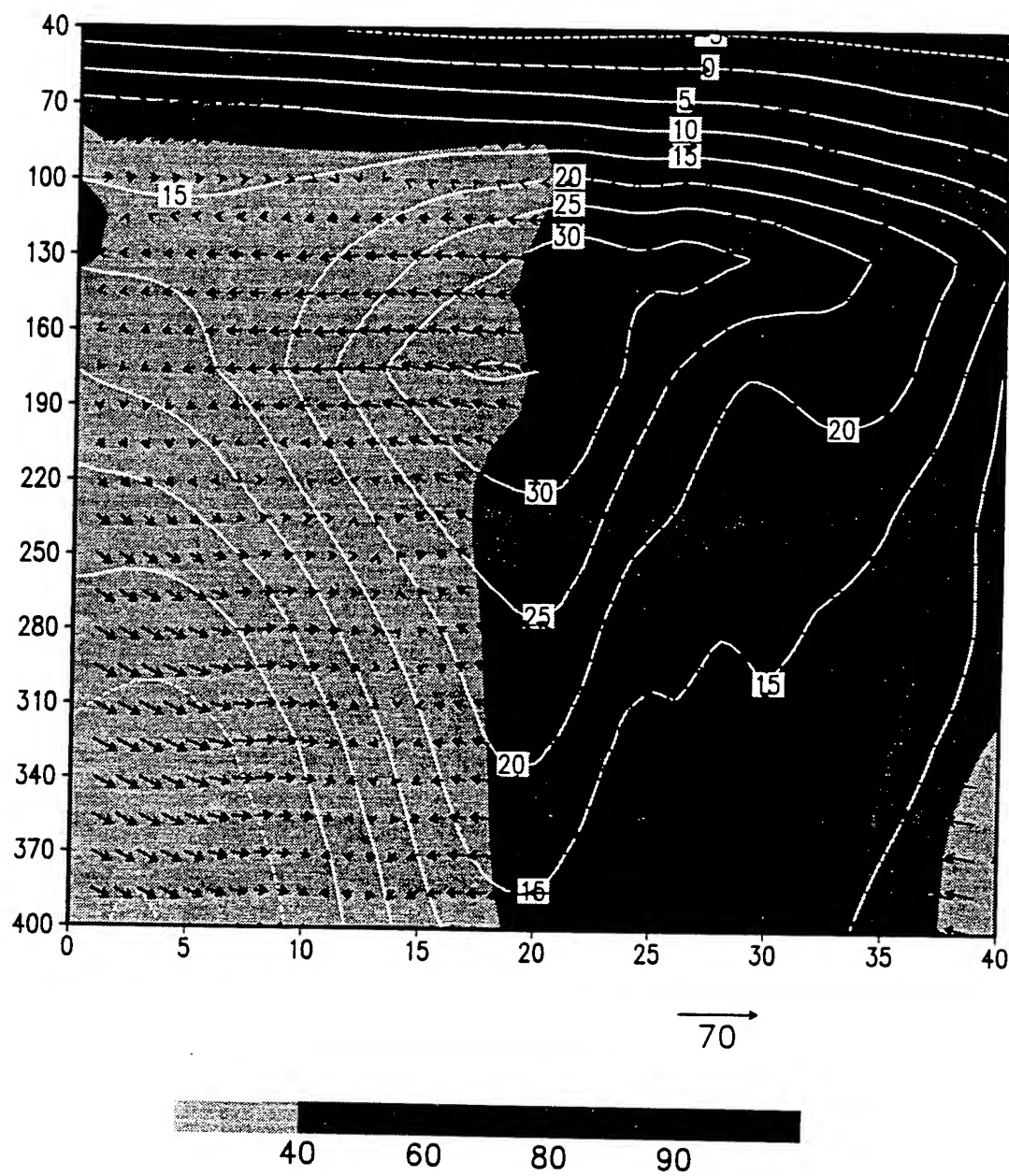


Figure 9.11 Same as Figure 8.6 except for Exp. ODW2.

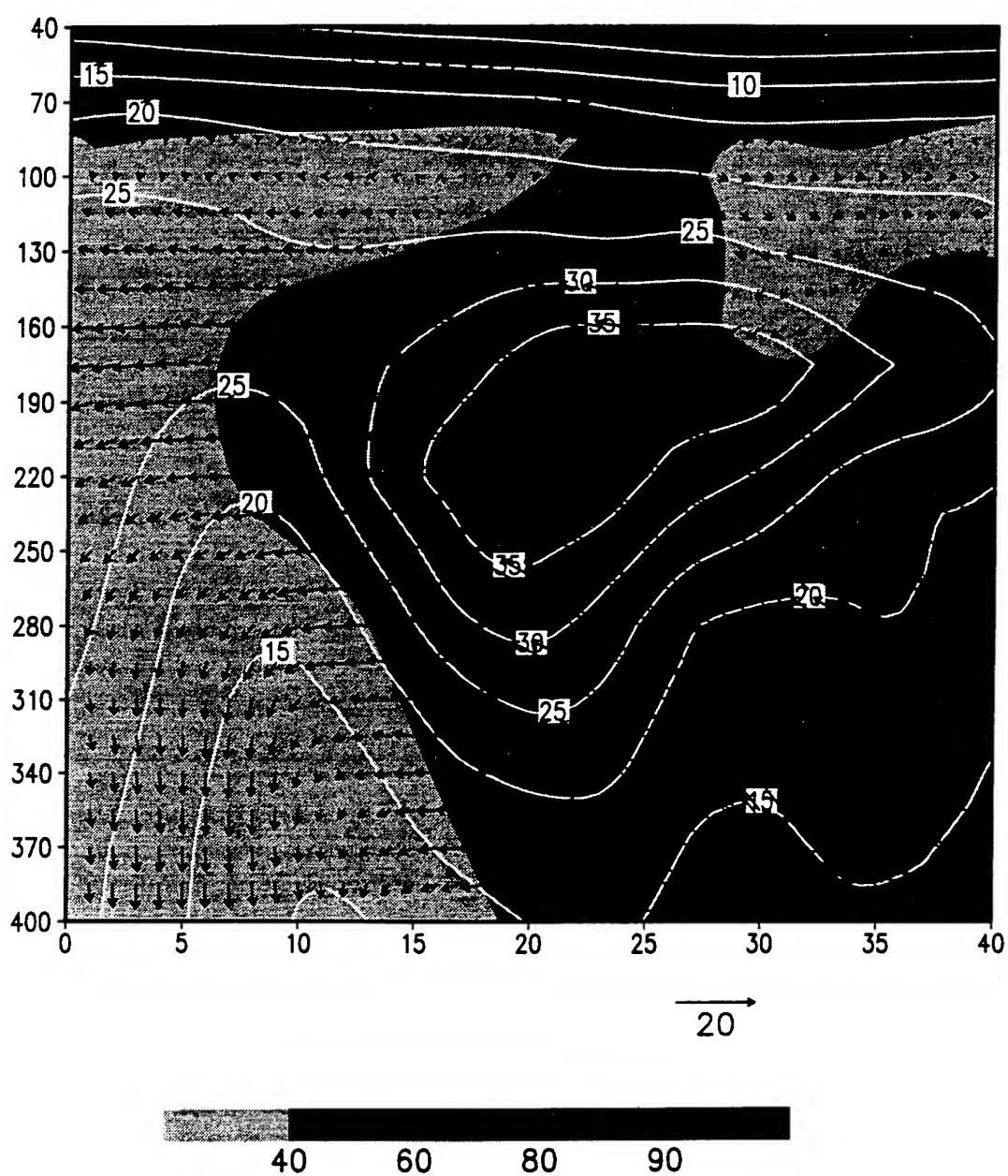


Figure 9.12 Same as Figure 8.7 except for Exp. ODW2.

in Fig. 9.11 ($> 90\%$). Although it is difficult to separate the circulations caused by the outflow jet, inner core convection and the warm front, this suggests that the ascending branch of the secondary circulation is weaker in Exp. ODW2+WTR, because of a weaker outflow jet. In Fig. 9.10, the reversed circum-jet secondary circulation is still evident, but the area on the cyclonic shear side is also drier ($> 40\%$) as compared to the RH field ($> 60\%$) in Exp. ODW2 shown in Fig. 9.12. This indicates a weaker reversed secondary circulation.

Molinari and Vollaro (1989) found that there is a high correlation between the azimuthal eddy cyclonic AMF at large radii and central pressure changes at later hours. DeMaria et al. (1993) also stated that the upper level eddy angular momentum flux convergence is an important factor for the intensification of tropical cyclones. Table 9.2 lists the angular momentum budgets calculated from the results of Exp. ODW2 and ODW2+WTR at 12 hour using equation (8.1). The results show a larger net horizontal import of the eddy cyclonic angular momentum ($158.4 \text{ g cm}^{-2} \text{ s}^{-2}$) corresponding to a stronger outflow jet of Exp. ODW2 as compared to a smaller net horizontal import ($98.1 \text{ g cm}^{-2} \text{ s}^{-2}$) in Exp. ODW2+WTR. This result indicates that the outflow jet can be accelerated by an approaching westerly trough and the enhanced outflow jet increases the inward eddy transport of cyclonic angular momentum. This result is also consistent with Challa and Pfeffer (1990).

	Radius (km)	Coriolis torque	Horizontal flux		Vertical flux	
			Mean	Eddy	Mean	Eddy
Model Florence (1988) from Exp. ODW2	0-300	-40.1	30.6	-17.1	-14.9	-8.7
	300-700	-403.9	172.5	158.4	1.5	-0.9
Model Florence (1988) from Exp. ODW2 + WTR	0-300	-44.7	29.2	-6.7	-18.3	-7.2
	300-700	-402.8	198.5	98.1	3.9	-5.5

Table. 9.2 Model angular momentum budget in the outflow layer of tropical cyclone. Units are in $10^{22} \text{ g cm}^{-2} \text{ s}^{-2}$.

10. SUMMARIES

10.1 Conclusions.

Many computations and numerical simulations were performed in this study. A nested three-pass Barnes scheme was developed to accommodate the resolution of the ODWs near the center of Hurricane Florence (1988). The enhanced NMC/RAFS 2.5⁰ analysis by the ODWs was then used as the initial condition for the numerical simulation of Florence. Next, the SSM/I retrieved rain rates were assimilated into the tropical cyclone model to study their impact on the numerical simulation of Florence. The model results were analyzed to reveal the detailed structure of the outflow layer and outflow jet of Florence. Finally, a numerical experiment was performed to study the interactions between the outflow layer of Florence and the upper level westerlies.

The two-pass Barnes scheme with an uniform grid was incapable of fully utilizing the potential of the ODWs for Hurricane Florence, collected during the Synoptic Flow Experiment on 8-9 September 1988. A nested three-pass Barnes scheme was then developed and used to enhance the NMC/RAFS 2.5⁰ analysis. A ± 3 -hour time window (centered around 0000 UTC 9 September 1988) was imposed to filter out the ODWs outside the time domain. Even with the two-pass Barnes scheme, the results showed the

usefulness of the ODWs for enhancing the NMC/RAFS 2.5⁰ analysis. The enhanced analysis produced a more organized and detailed representation of Florence than the NMC/RAFS 2.5⁰ analysis. The results also showed that both the ODW1 (without time window) analysis and ODW2 (with time window) analysis with the nested three-pass Barnes scheme enhanced the NMC/RAFS 2.5⁰ analysis much better than the ODW1 analysis with the two-pass Barnes scheme with an uniform grid. The analyzed minimum SLP at 0000 UTC September 9 was changed from 1004 mb in the NMC/RAFS 2.5⁰ analysis to 1000 mb in the ODW1 analysis with the two-pass analysis. With the nested three-pass analysis, however, the minimum SLP was analyzed to be 994 mb in both ODW1 and ODW2 analyses, only two mb higher than that in the best track record.

After an examination of the objective analysis results, it was difficult to distinguish the superiority between the ODW1 and ODW2 analyses. Therefore, the NRL limited-area tropical cyclone model was employed to simulate Hurricane Florence with three different initial data sets, which were the NMC/RAFS 2.5⁰ analysis (the control experiment), the ODW1 analysis (Exp. ODW1) and the ODW2 analysis (Exp. ODW2). Both the ODW1 and ODW2 analyses drastically improved the simulation in both intensity and storm track. The storm track was improved by about 75% (from 4.1⁰ to 1.0⁰ forecast error) at 24 hour, while the forecast error of the intensity was improved by about 10 mb (from 17 mb to 4 mb) in Exp. ODW2. The

storm in Exp. ODW1 over-intensified by 3.0 mb at 24 hour, while the storm in Exp. ODW2 under-intensified by 4 mb. In Exp. ODW2, the evolution of the minimum SLP was more similar to the best track record than the one in Exp. ODW1 (Fig. 6.5). The forecast error of the maximum surface wind speed in Exp. ODW2 was only 2.8 ms^{-1} (Table 6.1), as compared to 10.8 ms^{-1} in Exp. ODW1. These results suggested that the ODW2 analysis was more effective as the initial condition in simulating Florence than the ODW1 analysis. However, this did not mean that the ODWs collected outside the time window and away from the Florence's inner core region were not useful. It was only that these ODWs were not suitable to represent the actual atmospheric condition at 0000 UTC September 9. In addition, the simulated precipitation of Exp. ODW2 compared well with the SSM/I retrieved rain rates at 1200 UTC 9 September 1988 and 0000 UTC 10 September 1988.

These simulations demonstrated the usefulness of the ODW data on the simulation of Hurricane Florence. The result is in agreement with Franklin and DeMaria (1992), in which a barotropic, nested, spectral hurricane track forecasting model was used to determine the impact of the ODW data. The advantage of using a three-dimensional primitive equation model, as in this study, is that the model can simulate the hurricane structure in more detail and physical processes are more faithfully simulated. DeMaria et al. (1992) also mentioned that the prediction of the surrounding

synoptic-scale flow clearly requires the inclusion of baroclinic and physical processes.

The rainfall rates retrieved from Special Sensor Microwave/Imager (SSM/I) imageries at 0000 UTC and 1200 UTC 9 September 1988 were assimilated into the tropical model, with the NMC/RAFS 2.5° analysis (Exp. Control+SSMI) and the ODW enhanced analysis (Exp. ODW2+SSMI). Results revealed that Exp. Control+SSMI reduced the forecast error of the landfall location in the control experiment by about 50% (from 2.95° to 1.55°), and the landfall time error by 7 hours (from 9 hours to 2 hours). This study suggested that the assimilation of SSM/I rain rates can improve the forecast, especially in the operational analysis when the ODW data are not available. The impact of the assimilation of SSM/I rain rates on the numerical prediction of Florence was reduced when the simultaneous ODW data were assimilated into the initial condition. Nevertheless, it was apparent that the combination of the ODW and SSM/I retrieved data provided the best simulation among all the experiments in this study. This result of Exp. Control+SSMI and ODW2+SSMI in general agreed with the assessment of Chang and Holt (1993) for an extra-tropical marine cyclone. This study suggested that operational forecasts can benefit from the assimilation of the ODW and SSM/I data into the numerical model in the prediction of the tropical cyclone's intensity and track.

Diagnosis of the 200 mb level structure of Exp. ODW2+SSMI at 12 hour showed that the outflow layer was highly asymmetric, especially beyond three degrees radius, with an outflow jet originating at approximately three degrees north of the storm center (Figs 8.1 and 8.2). The outflow jet was elongated with a length of roughly 2500 km and a width of 500 km. Further diagnosis of the 12 hour wind, RH and horizontal potential temperature deviations in the outflow jet at the entrance and exit regions of the outflow showed that there was a thermally-direct, circum-jet secondary circulation in the entrance region (Fig. 8.6) and a thermally indirect one in a reversed direction in the exit region (Fig. 8.7). The secondary circulation had an outward branch above the jet, an inward branch below the jet (near 400 mb), an ascending branch in the anticyclonic shear side and a descending branch in the cyclonic shear side of the outflow jet. However, the inward branch below the outflow jet in the entrance region of the outflow jet was less apparent in this study than the one shown in Shi et al. (1990) because of the complexity due to the existence of the warm front along the East Coast. It was difficult to isolate the circulations purely caused by the outflow jet from other effects. In general, the structure of the outflow layer and jet of the simulated Florence were similar to the ones shown in the idealized model study by Shi et al. (1990). At 24 hour, the westerly jet moved northeastward and was located over Virginia and far away from Hurricane Florence (Fig. 8.3). This resulted in the cutoff of the outflow and consequently the

weakening of the intensity of Florence. At mean time, the cold and dry air intrusion from southwest might also have negatively contributed to the further intensification of Florence (see Fig. 10.1). At 24 hour, Florence was also about to make landfall. This result is similar to the case described by Holland and Merrill (1984) where Hurricane Kerry began to decay after the cutoff of the poleward outflow channel.

Calculation of the angular momentum budget at 12 hour (Table 8.1) demonstrated that the angular momentum balance was primarily maintained by the Coriolis torque and horizontal transports. Table 8.1 revealed that the contribution by the horizontal eddy cyclonic AMF convergence was the dominant feature at large radii. This feature was in agreement with the observational study by Molinari and Vollaro (1989). This result again underscored the dominance of the outflow jet in the outflow layer and the highly asymmetric nature of the outflow layer of tropical cyclones (Black and Anthes, 1971).

To investigate the interactions between Hurricane Florence (1988) and its environments, a numerical experiment with a weakened westerly trough (Exp. ODW2+WTR) was proposed in Shi et al. (1990) and conducted here. In this numerical experiment, the ODW2 analysis was re-processed to weaken the upper level westerly trough and then used as the initial condition of the numerical

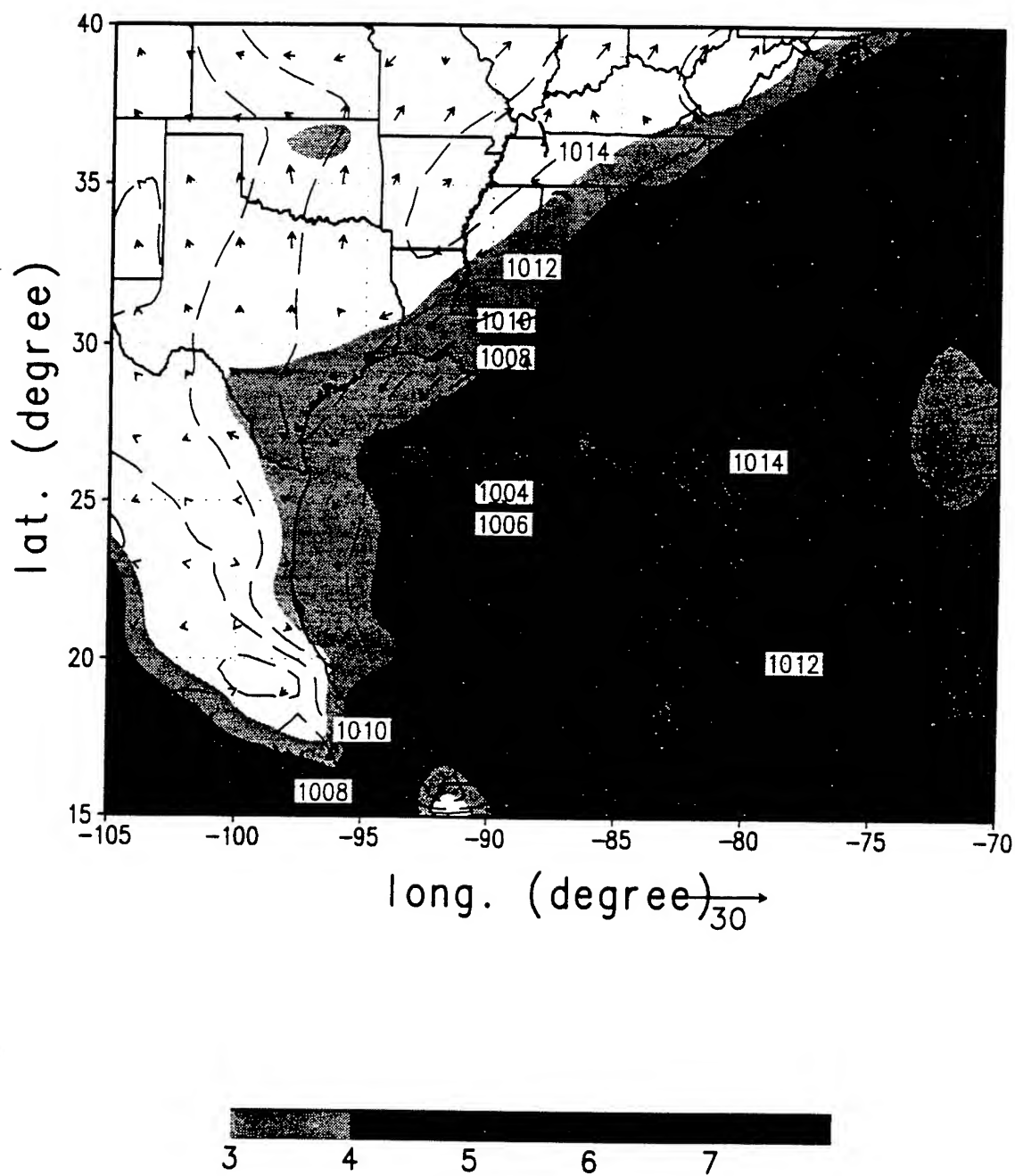


Figure 10.1 Sea level pressure (mb), 950 mb wind vectors (ms^{-1}) and integrated water vapor (cm) of Exp. ODW2 at 12 hour.

simulation of Florence. At 12 hour, comparing Figs. 9.4 and 9.5, the weakened westerly trough resulted in a reduction of the strength of the outflow jet of Florence in this numerical experiment by 6.9 ms^{-1} or about 15%. The weakened trough and outflow jet of Florence were responsible for a 2 mb minimum SLP increase and a 5.0 ms^{-1} or 15% maximum surface wind reduction of Florence's intensity. Fig. 9.6 showed that the weakened outflow jet also resulted in weaker convection in the core region at 10-15 hour or 8-13 hours before the model storm reached its highest intensity. The weaker convection is consistent with the reduction in the storm intensity. The weakened upper level westerly trough was also responsible for the reduction of the eddy AMF convergence in this numerical experiment (Table 9.2). Cross-section diagnosis of this experiment revealed a weaker secondary circulation in the entrance of the outflow jet and a weaker reversed one in the exit region.

This numerical experiment suggested that the approaching of the upper level westerly jet was important to the intensification of Florence's inner core convection between 1000 and 1500 UTC September 9 and therefore the deepening of the minimum SLP between 1200 and 2400 UTC September 9. On the other hand, the strong vertical shear associated with the upper level westerly trough might prevent Florence from further intensifying. Merrill (1988 a and b) suggested that the upper level environmental interactions with tropical cyclones, in general, contribute

negatively to intensity changes. His conclusion was based upon two observations: 1) maximum intensity of tropical cyclones are limited by the potential which the sea surface temperature can provide (Emanuel, 1986), and tropical cyclones rarely reaches to their potential maximum intensity; 2) Increasing vertical shear is usually accompanied with the approaching of the upper level westerly trough and works against the intensification of tropical cyclones. However, for Florence, because it made landfall three hours after it reached its maximum intensity, it was difficult to fully determine whether or not the upper level westerly trough had a positive effect on the intensification. Nevertheless, the result from this numerical experiment suggested that the upper level westerly trough's contribution was important to the intensification of Florence.

10.2 Future Research.

A major limitation of the ODW observations is that they do not provide the information above 400 mb because of the altitude limitations of the NOAA WP-3D. Details observations of the three-dimensional structure of the outflow layer of tropical cyclones are extremely scarce. Dropsonde data collected from 200 mb to surface by the recent TCM-90 and 92 experiments (Elsberry and Abbey, 1990) may be proven to be very useful in the study of the interactions between upper level environments and tropical cyclones (DeMaria et al., 1993).

Future studies should include the utilization of the dynamic initialization (Hoke and Anthes, 1977) or the four-dimensional data assimilation (Harms et al, 1992) to avoid the spin-up problem in the early hours of the model integration. A tropical cyclone model with nested grids should also be used in order to accommodate the non-uniform resolution of the ODW data. Because Florence made landfall at 0200 UTC 10 September, three hours after it reached its maximum intensity, the interactions between Florence and the upper level westerly trough occurred in a relatively short period of time (less than a day). Therefore, it is rather difficult to study the full extent of the interactions. A real case study of the interactions between tropical cyclones and their upper level environments in the Atlantic or Pacific Oceans would be valuable.

In any case study, the question arises whether or not the behavior shown is relevant to a large group of tropical cyclones. More studies need to be performed to explore the detailed mechanisms related to the interactions between upper level environments and tropical cyclones.

11. LIST OF REFERENCES.

- Alaka, M. A., 1961: The occurrence of anomalous winds and their significance. *Mon. Wea. Rev.*, **89**, 482-494.
- , 1962: On the occurrence of dynamic instability in incipient and developing hurricanes. National Hurricanes Research Projects, Rept. No. 50, U. S. Weather Bureau, Washington, D. C., 51-56.
- Alliss, R. J., S. Raman and S. Chang, 1992: Special Sensor Microwave/Imager (SSM/I) observation of Hurricane Hugo (1989), *Mon. Wea. Rev.*, **120**, 2723-2737.
- , G. D. Sandlin, S. W. Chang and S. Raman, 1993: Application of SSM/I data in the analysis of Hurricane Florence (1988). *J. Appl. Meteor.*, **32**, 1581-1591.
- Anthes, R. A., 1972: Development of asymmetries in a three dimensional numerical model of the tropical cyclone. *Mon. Wea. Rev.*, **100**, 461-476.
- , 1974: The Dynamics and Energetics of Mature Tropical Cyclones. *Reviews of Geophysics and Space Physics*, **12**, No. 3, 495-522.
- , and J. E. Hoke, 1975: The effect of horizontal divergence and the latitude variation of the Coriolis parameter on the drift of a model hurricane. *Mon. Wea. Rev.*, **103**, 757-763.
- , 1977: Hurricane model experiments with a new cumulus parameterization scheme, *Mon. Wea. Rev.*, **105**, 287-300.

- , 1982: Tropical Cyclones: Their Evolution, Structure and Effects. American Meteorological Society. Vol. 19, No. 41, 208 pages.
- Barnes, S. L., 1964: A technique for maximizing details in numerical weather map analysis. *J. Appl. Meteor.*, **3**, 396-409.
- , 1973: Mesoscale objective analysis using weighted time-series observations. NOAA Tech. Memo. ERL NSSL-62, National Severe Storms Laboratory, 1313 Halley Circle, Norman, OK 73069, (NTIS COM-73-10781), 60pp.
- Bender, M. A., R. J. Ross, Y. Kurihara and R. E. Tuleya, 1991: Improvements in tropical cyclone track and intensity forecasts using a bogus vortex. Preprints, *19th Conf. on Hurricanes and Tropical Meteorology*, Miami, Amer. Meteor. Soc., 324-325.
- Black, P. G. and R.A. Anthes, 1971: On the asymmetric structure of the tropical cyclone outflow Layer. *J. Atmos. Sci.*, **28**, 1348-1366.
- Blackadar, A. K., 1976: Modeling the nocturnal boundary layer. Preprints. *Third Symposium on Atmospheric Turbulent, Diffusion and Air Quality*, Raleigh, Amer. Meteor. Soc., 46-49.
- Bourke, W. and J. L. McGregor, 1983: A nonlinear normal mode initialization scheme for a limited area prediction model. *Mon. Wea. Rev.*, **111**, 2285-2297.
- Businger, J. A., J. C. Wyngaard, Y. Izumi and E. F. Bradley, 1971: Flux profile relationship in the atmospheric surface layer. *J. Atmos. Sci.*, **28**, 181-189.

- Challa, M. and R. L. Pfeffer, 1980: Effects of eddy fluxes of angular momentum on model hurricane development. *J. Atmos. Sci.*, **37**, 1603-1618.
- and -----, 1990: The formation of Atlantic hurricanes from cloud clusters and depressions. *J. Atmos. Sci.*, **47**, 909-927.
- Chang, S. W., K. Brehme, R. V. Madala and K. D. Sashegyi, 1989: A numerical study of the east coast snowstorm of 10-12 February 1983. *Mon. Wea. Rev.*, **117**, 1768-1778.
- , S., R. J. Alliss, S. Raman and J. J. Shi, 1993: SSM/I observations of ERICA/IOP 4 marine cyclone: A comparison with in situ observations and model simulation. *Mon. Wea. Rev.*, **121**, 2452-2464.
- and T. R. Holt, 1993: Impact of assimilating SSM/I rainfall rates on numerical prediction of winter cyclones. *Mon. Wea. Rev.*, in press.
- Charney, J. G. and Eliassen, A., 1964: On the growth of the hurricane depression. *J. Atmos. Sci.*, **21**, 68-75.
- Chen, L. and W. M. Gray, 1984: Global view of the upper level outflow patterns associated with tropical cyclone intensity changes during FGGE. paper presented at the 15th Technical Conference on Hurricanes and Tropical Meteorology, AMS, January 9-13, Miami, Florida.
- Davidson, N. E., K. Puri, 1992: Tropical prediction using dynamic nudging, satellite-defined convective heat sources, and a cyclone bogus. *Mon. Wea. Rev.*, **120**, 2501-2522.

- DeMaria, M., S. D. Aberson and K. V. Ooyama, 1992: A nested spectral model for hurricane track forecasting. *Mon. Wea. Rev.*, **120**, 1628-1643.
- , J.-J. Baik and J. Kaplan, 1993: Upper-level eddy angular momentum fluxes and tropical cyclone intensity change. *J. Atmos. Sci.*, **50**, 1133-1147.
- Detering, H. W. and D. Etling, 1985: Application of the E- ϵ turbulence model to the atmospheric boundary layer. *Bound. Layer. Meteor.*, **33**, 113-133.
- DiMego, G., 1988: The National Meteorological Center regional analysis system. *Mon. Wea. Rev.*, **116**, 977-1000.
- Elsberry, R. L. and R. F. Abbey, Jr., 1991: Overview of the tropical cyclone motion (TCM-90) field experiment. Preprints, 19th Conf. Hurricanes and Tropical meteorology, Miami, Amer. Meteor. Soc., 1-6.
- Emanuel, K. A., 1986: An air-sea interaction theory for tropical cyclones. Part I: Steady -state maintenance. *J. Atmos. Sci.*, **43**, 585-604.
- Fiorino, M. and T. T. Warner, 1981: Incorporating surface winds and rainfall rates into the initialization of a mesoscale hurricane model. *Mon. Wea. Rev.*, **109**, 1914-1929.
- Frank, W. M., 1977a: The structure and energetics of the tropical cyclone, Part I: storm structure. *Mon. Wea. Rev.*, **105**, 1119-1135.
- , 1977b: The structure and energetics of the tropical cyclone,

Part II: dynamics and energetics. *Mon. Wea. Rev.*, **105**, 1136-1150.

Franklin, J. L. and M. DeMaria, 1992: The impact of Omega Dropwindsonde Observations on barotropic hurricane track forecasts. *Mon. Wea. Rev.*, **120**, 381-391. *Mon. Wea. Rev.*, **121**, 2433-2451.

-----, S. J. Lord, S. E. Feuer and F. D. Marks, Jr., 1993: The kinematic structure of Hurricane Gloria (1985) determined from nested analyses dropwindsonde and doppler radar data.

Haltiner, G. J. and R. T. Williams, 1980: Numerical Prediction and Dynamic Meteorology. 2nd ed., John Wiley and Sons, New York, 477pp.

Harms, D. E., 1985: Application of an objective analysis scheme to mesoscale observational network design. M.S. Thesis, North Carolina State University, Raleigh, NC, 91 pp.

-----, K. Sashegyi, R. V. Madala and S. Raman, 1992: Four dimensional data assimilation of GALE data using a multivariate analysis scheme and a mesoscale model with diabatic initialization. NRL Memorandum report 4223-92-7147. [Available from NRL, Washington, D.C. 20375.]

Hoke, J. E. and R. A. Anthes, 1977: Dynamic Initialization of a three-dimensional primitive-equation model of Hurricane Alma of 1962. *Mon. Wea. Rev.*, **105**, 1266-1280.

-----, N. M. Phillips, G. J. DiMego, J. J. Tuccillo and J. G. Sela, 1989: The regional analysis and forecast system of the National

- Meteorological Center. *Wea. Forecasting*, **4**, 323-334.
- Holland, G. J., 1983: Angular momentum transports in tropical cyclones, *Quart. J. R. Met. Soc.*, **109**, 187-209.
- and R. T. Merrill, 1984: On the dynamics of tropical cyclone structural changes. *Quart. J. R. Met. Soc.*, **110**, 723-745.
- Hollinger, J. P., 1991: DMSP Special Sensor Microwave/Imager Calibration, Final Report Vol. II. (available from the author at Naval Research Laboratory, Washington, DC 20375).
- Holt, T, S. W. Chang and S. Raman, 1990: A numerical study of the coastal cyclogenesis in GALE IOP 2: Sensitivity to PBL parameterizations. *Mon. Wea. Rev.*, **118**, 234-257.
- Kaplan, J. and J. L. Franklin, 1991: The relationship between the motion of tropical storm Florence (1988) and its environmental flow. Preprints, *19th Conf. on Hurricanes and Tropical Meteorology*, Amer. Meteor. Soc., Miami.
- Koch, S. E., M. des Jardins and P. J. Kocin, 1981: The GEMPAK Barnes objective analysis scheme. NASA Tech. Memo. 83851, NASA/GLAS, Greenbelt, MD 20771, 56 pp.
- , S. E., M. DesJardins and P. J. Kocin. 1983: An interactive Barnes objective scheme for use with satellite and conventional data. *J. Climate Appl. Meteor.*, **22**, 1487-1503.
- Krishnamurti, T. N., S. Low-Nam and R. J. Pasch, 1983: Cumulus parameterization and rainfall rates II. *Mon. Wea. Rev.*, **111**, 815-828.
- Lawrence, M. B. and J. M. Gross, 1989: Atlantic hurricane season of

1988. *Mon. Wea. Rev.*, **117**, 2248-2259.
- Lord, S. J., 1991: A bogusing system for vortex circulations in the National Meteorological Center global forecast model. Preprints, *19th Conf. on Hurricanes and Tropical Meteorology*, Miami, Amer. Meteor. Soc., 328-330.
- McBride, J., 1981: Observational analysis of tropical cyclone formation. Part III: budget analysis. *J. Atmos. Sci.*, **38**, 1152-1166.
- Madala, R. V. and S. A. Piacsek, 1975: Numerical simulation of asymmetric hurricanes on a beta-plane with vertical shear, *Tellus*, **27**, 453-468.
- , 1981: Efficient time integration schemes for atmospheric and ocean models. Chpt. 4, Finite Difference Techniques for Vectorized Fluid Dynamic Calculations. Springer-Verlag, pp 56-74.
- , S. W. Chang, U. C. Mohanty, S. C. Madan, R. K., Paliwal, V. B. Sarin, T. Holt and S. Raman, 1987: Description of the naval research laboratory limited-area dynamical Weather prediction model . NRL Technical Report No. 5992, Washington, D.C., 131pp.
- Manabe, S., J. Smagorinsky and R. F. Strickler, 1965: Simulated Climatology of a general circulation model with a hydrologic cycle. *Mon. Wea. Rev.*, **93**, 769-798.
- Merrill, R. T., 1984: Structure of the tropical cyclone outflow layer. Proceedings of the 15th Technical Conference on Hurricanes

- and Tropical Meteorology, AMS, January 9-13, Miami, Florida.
- , 1988a: Characteristics of the upper-tropospheric environmental flow around Hurricanes, *J. Atmos. Sci.*, **45**, 1665-1677.
- , 1988b: Environmental influences on hurricane intensification. *J. Atmos. Sci.*, **45**, 1678-1687.
- Miller, B. I., 1963: The three-dimensional wind structure around a tropical cyclone. National Hurricane Research Project, Rept. No. 15, 41 pp.
- Molinari, J., 1982: Numerical hurricane prediction using remotely-sensed rainfall rates. *Mon. Wea. Rev.*, **110**, 553-571.
- and D. Vollaro, 1989: External influences on hurricane intensity. Part I: outflow layer eddy angular momentum fluxes. *J. Atmos. Sci.*, **46**, 1093-1105.
- and -----, 1990: External influences on hurricane intensity. Part II: vertical structure and response of the hurricane vortex. *J. Atmos. Sci.*, **47**, 1902-1918.
- Neumann, C. J., 1981: Trends in forecasting the tracks of Atlantic tropical cyclones. *Bull. Amer. Meteor. Soc.*, **62**, 1473-1485.
- Ooyama, K. V., 1987: Numerical experiments of study and transient jets with a simple Model of the hurricane outflow layer. Preprints, the 17th Conference on Hurricanes and Tropical Meteorology, AMS, April 7-10, Miami, Florida.
- , 1992: Scale controlled objective analysis. *Mon. Wea. Rev.*, **115**, 2479-2506.

- Palmen, E. and H. Riehl, 1957: Budget of angular momentum and kinetic energy in tropical cyclones. *J. Meteor.*, **14**, 150-159.
- , and C. W. Newton, 1969: Atmospheric Circulation Systems. Academic Press, 111 Fifth Ave., New York, NY, 603pp.
- Perkey, D. J. and C. W. Kreitzberg, 1976: A time dependent lateral boundary scheme for limited-area primitive equation models. *Mon. Wea. Rev.*, **104**, 744-755
- Pfeffer, R. L., 1958: Concerning the mechanisms of hurricanes. *J. Meteor.*, **15**, 113-119.
- and M. Challa, 1981: A numerical study of the role of eddy fluxes of momentum in the development of Atlantic hurricanes. *J. Atmos. Sci.*, **38**, 2393-2398
- Rodgers, E. B., J. Stout and J. Steranka, 1986: Upper-tropospheric and lower-stratospheric dynamics associated with tropical cyclones as Inferred from total ozone measurements. Postprints, The Second Conference on Satellite Meteorology/Remote Sensing and Applications, AMS, Williamsburg, Virginia.
- , S. W. Chang, J. Stout, J. Steranka and J. J. Shi, 1991: Satellite observations of variations in tropical cyclone convection caused by upper-tropospheric troughs. *J. Appl. Meteor.*, **30**, 1163-1184.
- Sadler, J. C., 1976: The role of the tropical upper-tropospheric trough in early season typhoon development. *Mon. Wea. Rev.*, **104**, 1266-1278.

- , 1978: Mid-season typhoon development and intensity changes and the tropical upper-tropospheric trough. *Mon. Wea. Rev.*, **106**, 1137-1152.
- Sashegyi, K. D. and R. V. Madala, 1993: Application of vertical-mode initialization to a limited-area model in flux form. *Mon. Wea. Rev.*, **121**, 207-220.
- , D. E. Harms, R. V. Madala and S. Raman, 1993: Application of Bratseth scheme for the analysis of GALE data using a mesoscale model. *Mon. Wea. Rev.*, **121**, 2331-2350.
- Shi, J. J. , S. W. Chang and S. Raman, 1990: A numerical study of the outflow layer of tropical cyclones. *Mon. Wea. Rev.*, **118**, 2042-2055.
- Steranka, J., E. B. Rodgers and R. C. Gentry, 1986: The relationship between satellite measured convection burst and tropical cyclone intensification. *Mon. Wea. Rev.*, **114**, 1539-1546.
- Tuleya, R. E. and Y. Kurihara, 1981: A numerical study on the effects of environmental flow on tropical storm genesis. *Mon. Wea. Rev.*, **109**, 2487-2506.
- Uccellini, L. W., P. J. Kocin, R. A. Petersen, C. H. Wash, and K. F. Brill, 1984: The President's day cyclone of 18-19 February 1979: synoptic overview and analysis of the subsynoptic jet streak influencing the pre-cyclogenetic period. *Mon. Wea. Rev.*, **112**, 31-55.
- Velden, C. S., W. S. Olsen and B. A. Roth, 1989: Tropical cyclone center-fixing using SSM/I data. Preceding, Fourth Conference

on Satellite Meteorology and Oceanography, J36-J39, San
Diego, CA.

Appendix J

Enhancement of Objective Analysis of Hurricane Florence (1988) with Dropsonde Data

Enhancement of Objective Analysis of Hurricane Florence (1988) with Dropsonde Data

Jainn-Jong Shi¹, Simon Chang, Keith Sashegyi² and Sethu Raman¹

Naval Research Laboratory, Washington, DC 20375

1. North Carolina State University, Raleigh, NC 27695.
2. Science Applications International Corp., McLean, VA 22102.

1. Introduction.

The accurate description of the initial conditions in numerical simulations of the tropical cyclone always suffers from two main difficulties. The first is the lack of observational data over tropical oceans. The second is, even when the data is available, the inability to utilize all the data available in the analysis. A total of 51 Omega-DropWindsonde (ODW) data were collected by AOML/HRD in the Synoptic Flow Experiment for Hurricane Florence on 8-9 September, 1988. This make realistic description of the initial conditions for the numerical simulation of Florence possible. Fig. 1 shows the two flight routes, the locations and the release time of the ODW dropsonde data. Although the release time of the ODW dropsonde data ranged from 1817Z on 08/09/88 to 0247Z on 09/09/88, it was determined for this preliminary study that all data would be used to enhanced the NMC 2.5° analyses at 00Z on 09/09/88, which are bi-cubically interpolated onto a grid of 0.5° resolution in longitude and latitude, matching the average spacing of the ODW data.

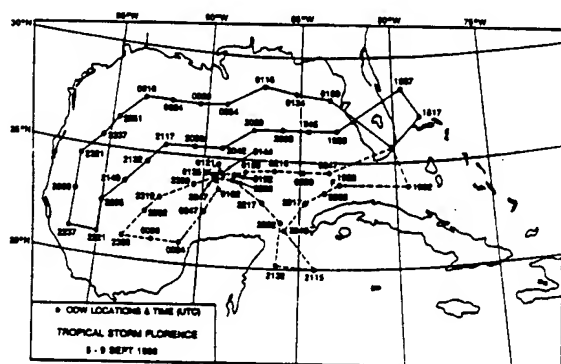


Fig. 1 The flight routes and the ODW drops' location and time of the Synoptic Flow Experiment for Hurricane Florence (1988).

The objective analysis scheme of the Naval Research Laboratory (NRL) limited-area model includes three stages. The first is the consistency check and the data smoothing in vertical direction. The second is the data quality control. The third is the Barnes objective analysis scheme. The purpose of the analysis is to provide the initial conditions to the prediction model with

minimum noise and error relative to the observations. The objective analysis scheme has been modified by adding an optional third pass into the Barnes scheme to incorporate the comparatively high density of the ODW data.

The objective of this article is to describes the objective analysis and to show how much the ODW data can be used to enhance the the NMC 2.5° RAFS analyses of Hurricane Florence (1988) by using the objective analysis. The objective analysis scheme will be introduced in Section 2 and the result will be shown in Section 3.

2. Analysis.

2.1 Step 1: Consistency check and smoothing in the vertical direction.

The observations will first be checked for the hydrostatic consistency. If not, geopotential height of that observation is recomputed according to the temperature and the surface pressure at the same location. The data is also smoothed in the vertical direction to filter out noises which have the scale smaller than the model's vertical resolution. In this step, if the surface pressure of the data is less than 1000 mb, the 1000 mb level data is obtained by an extrapolation.

2.2 Step 2: Quality control.

In Step 2, there are two quality control checks which are adopted from DiMego (1988). The first one is a "gross" check to examines the magnitude of the observed data and to reject any report which is non-meteorological. The second one is a "buddy" check which detect any observation data which is inconsistent with those from surrounding station and may result in an unrealistic analysis. The "buddy check" is performed on all the report locations. At each location, the observation data has to agree with at least half of the reports within 7.5° (or an equivalent distant) for the mid-latitude cyclone and 3.0° for tropical cyclone. Observed data fail in the "buddy" check are deleted from the original data set. The radius of the "buddy" check depends on the data resolution and the nature of the weather phenomena which the prediction model intends to include.

Two more tasks are done in this step to speed up the Barnes scheme in the next step. The first is to create in the data rich areas super observations which are generated by taking average of the data values and the data

locations. This will reduce the computation required in the Barnes scheme. The second is to put bogus data reports with wind perfect analysis in the area which has no data report. This will help to vectorize the codes of the Barnes scheme for the super computer computation. In this step, the average minimum station spacing Δn , which will be used in the Barnes scheme, is also computed. The information in Fig. 1 has also been used to set up the analysis domain and resolution of the Barnes scheme. In this experiment, the average minimum station spacing Δn is 135.0 km in the first two and 67.5 km in the third pass. The critical radius (or cutoff radius) are 864 km and 432 km for the first two and the third pass, respectively. The calculations of Δn and the critical radius are based on the GEMPAK (Koch et al., 1981).

2.3 Step 3: Barnes Scheme.

A modified Barnes objective analysis scheme (Koch et al., 1981; Koch, 1983; Harms, 1985), which is a two-pass successive correction method with an optional third-pass correction for the high resolution data area, is used for the analysis. Before starting the objective analysis, a bi-linear interpolation is applied to interpolate the background data from the grid points to the data locations and then computes the corrections by subtracting the background data from the observed data. The modified Barnes scheme is then performed on the corrections. After the analysis is done, the corrections which are on the grid points will be added to the background data to get the enhanced field. The domain of the analysis grid is from 78° to 99° W and from 18° to 32° N, which covers all the ODW drop locations. Fig. 2 shows the analysis domain for the all three passes of the Barnes scheme. As it is shown in the next section, the analyses after the first two passes failed to show the details of Florence's structure which can be resolved by the ODW data. That is why the third pass has been added into the Barnes objective analysis scheme. For the third pass, the analyses after the first two passes will be used as the background data. More details of the third pass are described in the next section.

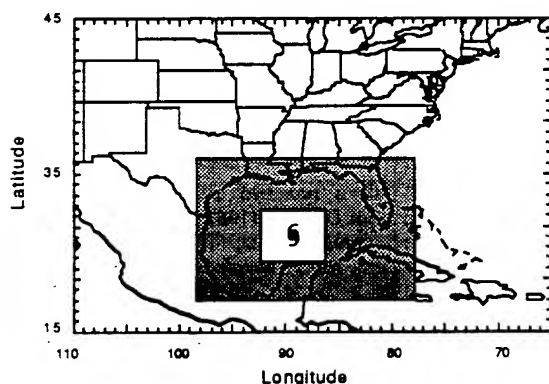


Fig. 2 The analysis domain for three passes of the Barnes scheme. The shaded area is the domain for the first and second pass. The plain area inside the shaded area is the domain for the third pass.

3. Result from performing the analysis component on the dropsonde data of Hurricane Florence (1988).

Fig. 3 shows the sea level pressures and surface temperatures and Fig. 4 shows the 1000 mb geopotential heights and wind vectors from the NMC 2.5° analyses. Fig. 5 and 6 show the sea level pressures and the 1000 mb geopotential heights and wind vectors from the enhanced analyses with the ODW dropsonde data analyzed by the Barnes scheme with only two passes. These figures show that there is a well organized tropical storm in the Gulf of Mexico which is poorly defined on NMC 2.5° analyses. The two-pass enhanced analyses with the ODW data have already shown the hurricane in more detail and provide better analyses.

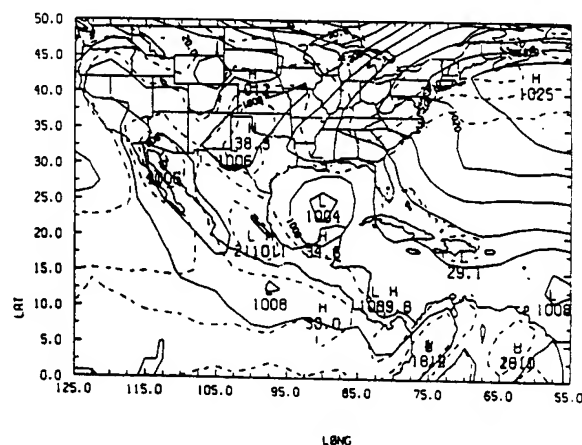


Fig. 3 The sea level pressures and surface temperatures from the NMC 2.5° Analyses at 00Z on 9/9/88. The solid lines are isobars and the dashed lines are isotherms.

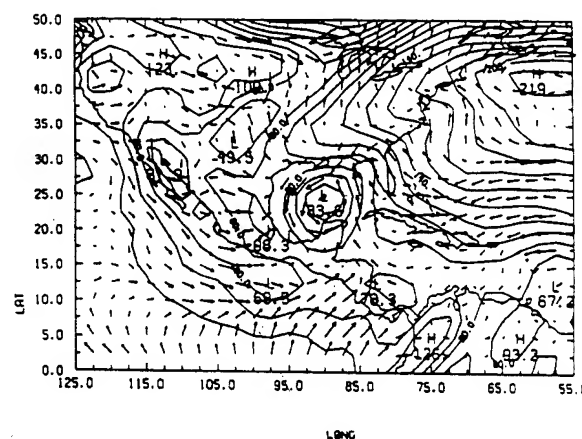


Fig. 4 Same as Fig. 3 except for the 1000 mb geopotentials and wind vectors.

Although the ODW data at some locations near the hurricane center have surface pressure of 994 mb and 1000 mb geopotential height of -54 m, it is felt that more information can still be extracted out from the ODW data. We suspect that the "buddy" check has deleted those extreme data (e.g., low surface pressure, low geopotential height and strong wind) near the center in the conventional two-pass analysis. Because the scale of the

center is small, if the "buddy" check is skipped, those extreme data near the center will affect the grid points away from the center and then results in a weaker pressure gradient and an unrealistic circulation pattern. It is also obvious from Fig. 1 that the data resolution near the hurricane center is about twice of that away from the center. The average station spacing near the center is about 0.7° while it is about 1.5° away from the center. To resolve the nature of the small scale of the center and the high ODW dropsonde data resolution near the center, a third-pass in the Barnes scheme is employed over a 5° by 6° box with a resolution of $1/6^\circ$ centered around Florence (Fig. 2) and with a weighting function of smaller scale than its counterpart in the first two passes. As it is shown in the previous section, Δn used in the third pass is 67.5 km, half of that in the first two passes.

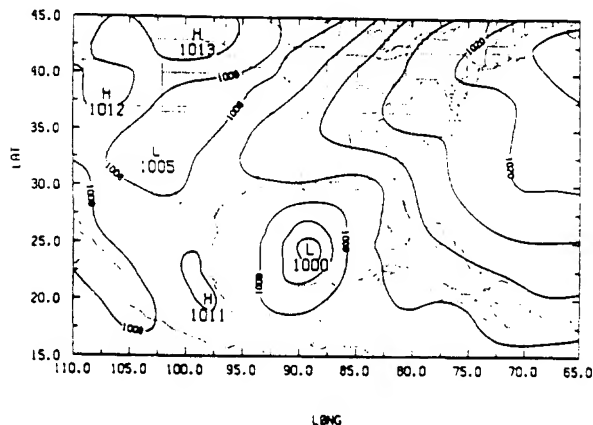


Fig. 5 The enhanced sea level pressures after two passes of the Barnes objective analysis scheme.

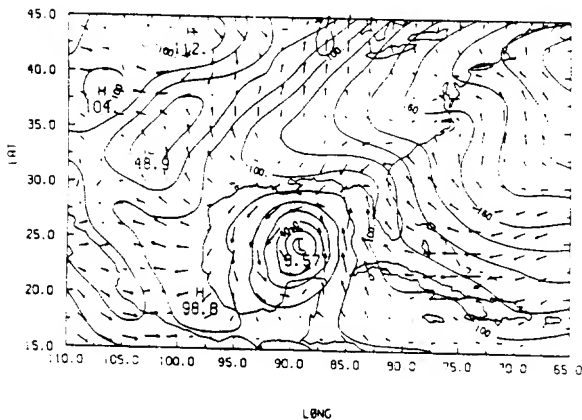


Fig. 6 Same as Fig. 5 except for the 1000 mb geopotentials and wind vectors.

As it is mentioned before, the analyses after the first two passes are used as the background data. The ODW dropsonde data inside the third pass domain without the "buddy" check are used in the analysis. Because the third pass is carried out over a smaller region covering only the hurricane center, this will ensure that the analysis is confined within the drop region and result in a better representation of the inner region structure.

Fig. 7 shows the sea level pressures and Fig. 8 shows the 1000 mb geopotential heights and wind vectors after the third pass. Comparing both figures to Fig. 5 and 6. The central pressure and the 1000 mb geopotential height are modified from 1000 mb and 3.57 m to 994 mb and -53.20 m, respectively. At the mean time, the general pattern of Florence is preserved. In the future, numerical simulations of Hurricane Florence (1988) will be conducted using the enhanced analysis fields.

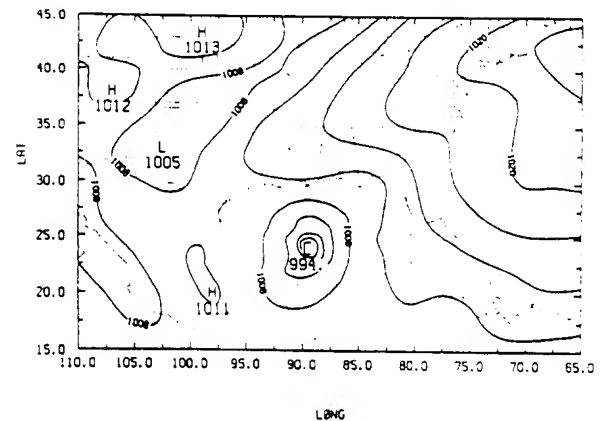


Fig. 7 The enhanced sea level pressures after the third pass of the Barnes objective analysis scheme.

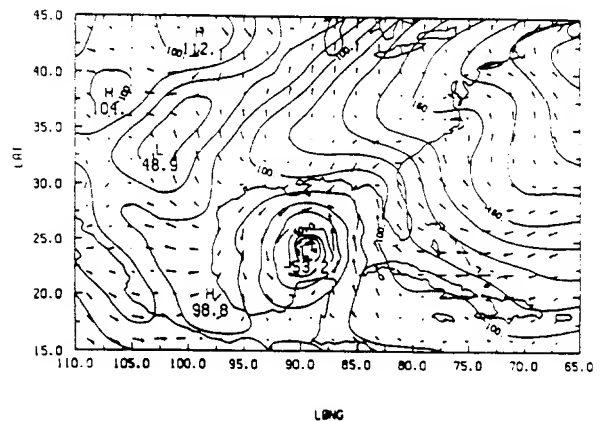


Fig. 8 Same as Fig. 7 except for the 1000 mb geopotentials and wind vectors.

References

- DiMego, G., 1988: The National Meteorological Center regional analysis system. *Mon. Wea. Rev.*, **116**, 977-1000.
- Harms, D. E., 1985: Application of an objective analysis scheme to mesoscale observational network design. M.S. Thesis, North Carolina State University, Raleigh, NC, 91 pp.
- Koch, S. E., 1983: An interactive Barnes objective scheme for use with satellite and conventional data. *J. Climate Appl. Meteor.*, **22**, 1487-1503.
- Koch, S. E., M. des Jardins and P. J. Kocin, 1981: The GEMPAK Barnes objective analysis scheme. NASA Tech. Memo. 83851, NASA/GLAS, Greenbelt, MD 20771, 56 pp.

Appendix K

**Special Sensor Microwave/Imager (SSM/I)
Observations of Hurricane Hugo (1989)**

Special Sensor Microwave/Imager (SSM/I) Observations of Hurricane Hugo (1989)

RANDALL J. ALLISS AND SETHU RAMAN

Department of Marine, Earth and Atmospheric Sciences, North Carolina State University, Raleigh, North Carolina

SIMON W. CHANG

Naval Research Laboratory, Washington, D.C.

(Manuscript received 21 November 1991, in final form 25 March 1992)

ABSTRACT

Data from the Special Sensor Microwave/Imager (SSM/I) on board a Defense Meteorological Satellite Program (DMSP) spacecraft have been used to study the precipitation patterns associated with Hurricane Hugo (1989). Results indicate the intensification of Hugo was associated with increases in SSM/I-derived total latent heat release and increases in heavier rainfall rates near the storm center. This study also shows that SSM/I rainfall rates prior to the landfall of Hugo at Charleston, South Carolina, compared favorably with raingage observations. Additionally, data from the 85-GHz channel was used to monitor the extent of convection near the storm's center. As Hugo intensified, the areal coverage of deep convection increased. Furthermore, the 85-GHz brightness-temperature imagery was useful in determining the location of Hugo's low-level center. These results indicate the potential of using SSM/I data in the analysis and prediction of tropical cyclones in an operational environment.

1. Introduction

Due to the scarcity of conventional, in situ meteorological data over the open oceans, passive microwave radiometry has the potential to become an important source of observations of tropical weather systems, especially tropical cyclones. The primary advantage of these instruments is that the microwave radiation can penetrate the overlying cirrus clouds with little attenuation, thereby revealing structural details—particularly those areas of deep convection—not always depicted by visible and infrared images. Recently, remote sensing of tropical cyclones from space has been enhanced via the Special Sensor Microwave/Imager (SSM/I), which rides on board a polar-orbiting Defense Meteorological Satellite Program (DMSP) spacecraft. The SSM/I is a joint U.S. Navy–Air Force operational instrument that measures critical atmospheric, oceanographic, and land parameters. Potential applications of SSM/I data to the operational analysis of tropical weather systems have been described by a number of recent papers (e.g., Felde and Glass 1991; Goodberlet et al. 1989; Negri et al. 1989; Rao et al. 1991; Rappaport 1991; Sandlin and Spangler 1989; Velden et al. 1989). Rappaport and Black (1989) point out important SSM/I limitations, such as relatively

infrequent overpasses of tropical cyclones, navigational errors, and limitations imposed by poor spatial resolution of various SSM/I sensors.

It is well remembered that Hurricane Hugo made landfall at Charleston, South Carolina, and caused tremendous damage along the United States southeast coastal region, as well as in the Caribbean islands. In this paper, rainfall rates derived from algorithms using the brightness temperatures (BT) of radiation are used to examine the precipitation patterns observed in Hugo. Since the maintenance of tropical cyclones is dependent upon the release of latent heat, remote sensing of latent heat release becomes important. The use of passive microwave radiometry in observing the latent heat release in tropical cyclones was valuable in monitoring the moisture budget of these storms (Adler and Rodgers 1977). This study compares SSM/I-derived rainfall rates and other rainfall parameters with the observed intensity of the storm. Quantitative results of the spatial variations of the area-averaged rain rate in the inner and outer core regions of Hugo and their relationship to changes in storm-scale precipitation patterns are presented. SSM/I rainfall rates are also compared to raingage observations made near the path of Hugo during landfall in the Carolinas.

Accurate estimates of tropical cyclone centers are always important in storm analysis and prediction. Velden et al. (1989) indicated that the location of centers of cyclonic storms could be estimated with greater precision and consistency using 85-GHz imagery, compared to using conventional visible images, which

Corresponding author address: Dr. Sethu Raman, Department of Marine, Earth and Atmospheric Sciences, Box 8208, North Carolina State University, Raleigh, NC 27695-8202.

are limited by dense cloud overcast and by nighttime hours. When using the Geostationary Operational Environmental Satellite (GOES) imagery alone, there is occasionally great uncertainty in the location of tropical cyclone centers (Mayfield et al. 1988). Because microwave radiation at 85 GHz is sensitive to convective clouds and precipitation over oceanic regions, 85-GHz imagery is also examined to observe the storm structure as related to Hugo's intensity and to estimate the location of the center near the surface.

2. SSM/I characteristics and capabilities

Since its launch in June 1987, the first DMSP SSM/I has monitored the development and course of approximately 75% of the tropical storms and hurricanes that have occurred worldwide (Sandlin and Spangler 1989). The SSM/I completes 14.1 revolutions per day along a near-sun-synchronous track at an altitude of 833 km. It has an inclination angle of 98.8° and an orbital period of 102.0 min. The SSM/I uses a conical scanner with an angle of incidence of 53° . With an observational swath width of 1400 km, there is an 89% probability of viewing a storm in the tropics at least once per day. With the recent launch of the second SSM/I, this probability has increased to 99%, and the probability of at least two passes per day has increased to 89%. The chance of at least three passes per day is currently 59% (Velden et al. 1989). Figure 1 shows the coverage and orbital track of one SSM/I in 24 h. The shaded regions indicate possible data gaps in a 24-h period.

Radiation measured by the SSM/I comes from three sources—atmospheric emission, emission from the earth's surface, and atmospheric emission reflected from the earth's surface. For microwave radiation, significant attenuation can be caused by water vapor, oxygen, and liquid water (both in the form of cloud water and rain). Clouds or rain, however, also considerably increase the atmospheric emission. In extreme cases, clouds or rain totally obscure the surface, such that the microwave radiation is related only to atmospheric phenomena.

The SSM/I frequencies are 19.4, 22.2, 37.0, and 85.5 GHz. Through the proper choice of instrumental parameters (wavelength, polarization, and viewing angle), it is possible to establish useful relations between the BTs measured by the multifrequency radiometers and specific atmospheric parameters of interest. The rain-rate algorithm used in this study is described by Olson (1989) and Hollinger (1991). It was developed using a combination of the 85-GHz horizontal (H) and vertical (V), 37-GHz (V), 22-GHz (V) and (H), and the 19-GHz (V) channels. In general, the SSM/I observes a region of rain as an area of high BTs over the otherwise cold (in terms of BTs) ocean. The basis of the rain-rate algorithm over the ocean is that initially the 19- and 37-GHz BTs increase as rain rates increase

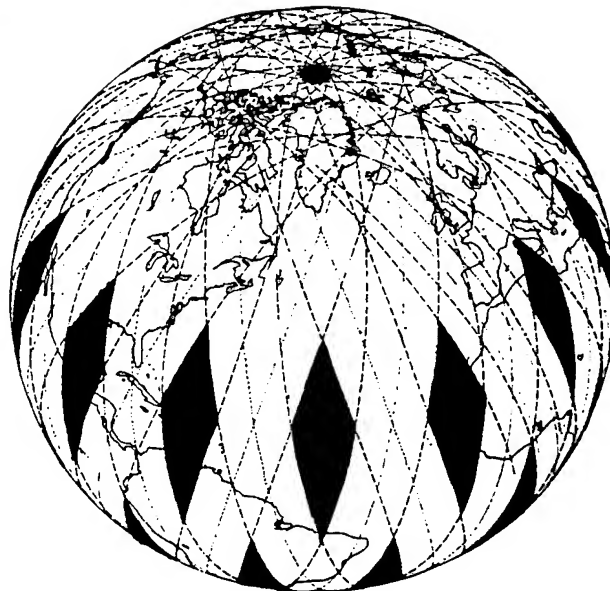


FIG. 1. Ground coverage of SSM/I in 24 h (from Hollinger 1989). Shaded areas indicated data gaps. Dashed lines indicate the boundaries of the swath. Dotted lines indicate the nadir.

up to a moderate rain rate, after which the BTs decrease as the rain rates increase further. This reduction in BTs for larger rain-rate values is due to the scattering by the large raindrops or to hail present in heavy rain, or both.

Hollinger (1991) describes the detailed procedure for determining rain rates from BTs. Pixels within ± 100 km of the coast were not processed because the field of view contained data from both sea and land surfaces resulting in large gradients in the estimated fields over coastal regions. Fortunately, this problem was minimized in our study because all but one SSM/I swath covered the open oceans. Because the 85-GHz (H) channel was not operating during this period, an alternate algorithm was used. Following Hollinger (1991), rainfall rates over the ocean were computed using

$$R = \exp(5.10196 - 0.05378T_{37V} + 0.2766T_{37H} + 0.01373T_{19V}) - 2.0 \text{ mm h}^{-1}, \quad (1)$$

whereas for rainfall rates over land, we applied

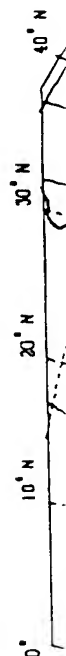
$$R = \exp(-17.76849 - 0.09612T_{37V} + 0.15678T_{19V}) - 1.0 \text{ mm h}^{-1}, \quad (2)$$

where R is the rainfall rate and T_{85V} , T_{85H} , T_{37V} , T_{22V} , and T_{19V} are the BTs of the 85-GHz (V), 85-GHz (H), 37-GHz (V), 22-GHz (V), and 19-GHz (V) polarized channels, respectively. If the formulas produced a rainfall rate less than zero, then the rain-rate value was set to zero.

All
by co
additi
specif
(Sand
requir
rainfa
(Holl
tween
becau
comm
were
graph
vance
tory.
proje

3. A

As
cane
follo
tropi
teorc
ber 2



FIG

All SSM/I products have been statistically validated by comparisons with ground-truth measurements. In addition, all products are expected to be accurate within specification approximately 67% ($\pm 1 \sigma$) of the time (Sandlin and Spangler 1989). The SSM/I specifications require 5 mm h^{-1} accuracy in standard deviation for rainfall-rate estimates between 0 and 25 mm h^{-1} (Hollinger 1991). There is an inherent uncertainty between 10 and 25 km in the registration of the image because of navigational errors (Sandlin 1991, personal communication). The SSM/I data used in this study were obtained through the Fleet Numerical Oceanographic Center and preprocessed at the Center for Advanced Space Sensing of the Naval Research Laboratory. Preprocessing entails resampling, smoothing, and projecting the data into grid format.

3. A synoptic description of Hurricane Hugo

As described in Case and Mayfield (1990), Hurricane Hugo, over the period of 10–22 September 1989, followed a course that was typical for North Atlantic tropical cyclones (Fig. 2). Hugo was detected by Meteorological Satellite (Meteosat) imagery on 9 September as an area of disturbed weather moving west off

the coast of Africa. A tropical depression developed out of this disturbed area while moving westward across the tropical Atlantic. Embedded in the low-latitude easterlies, this depression strengthened and was named a tropical storm on 11 September by the National Hurricane Center (NHC). On 13 September, while still located some 3000 km east of the Caribbean Sea, the storm intensified to hurricane strength. On 15 September, U.S. Air Force reconnaissance aircraft made its first flight into the center of Hugo and found a minimum central pressure of 918 mb and maximum sustained surface winds of about 72 m s^{-1} . As Hugo approached the Leeward Islands, it slowed and began to turn toward the west-northwest. On 17 September, the center passed directly over the island of Guadeloupe. A turn toward the northwest followed as the center passed over St. Croix and over the eastern tip of Puerto Rico on 18 September. As Hugo exited the Caribbean, its movement maintained a general track toward the northwest. Figure 3 shows the minimum central pressure and maximum winds as a function of time obtained from NHC best-track data.

During the 30 h prior to landfall in South Carolina, Hugo began to accelerate toward the northwest. Final landfall occurred at 0400 UTC 22 September, just

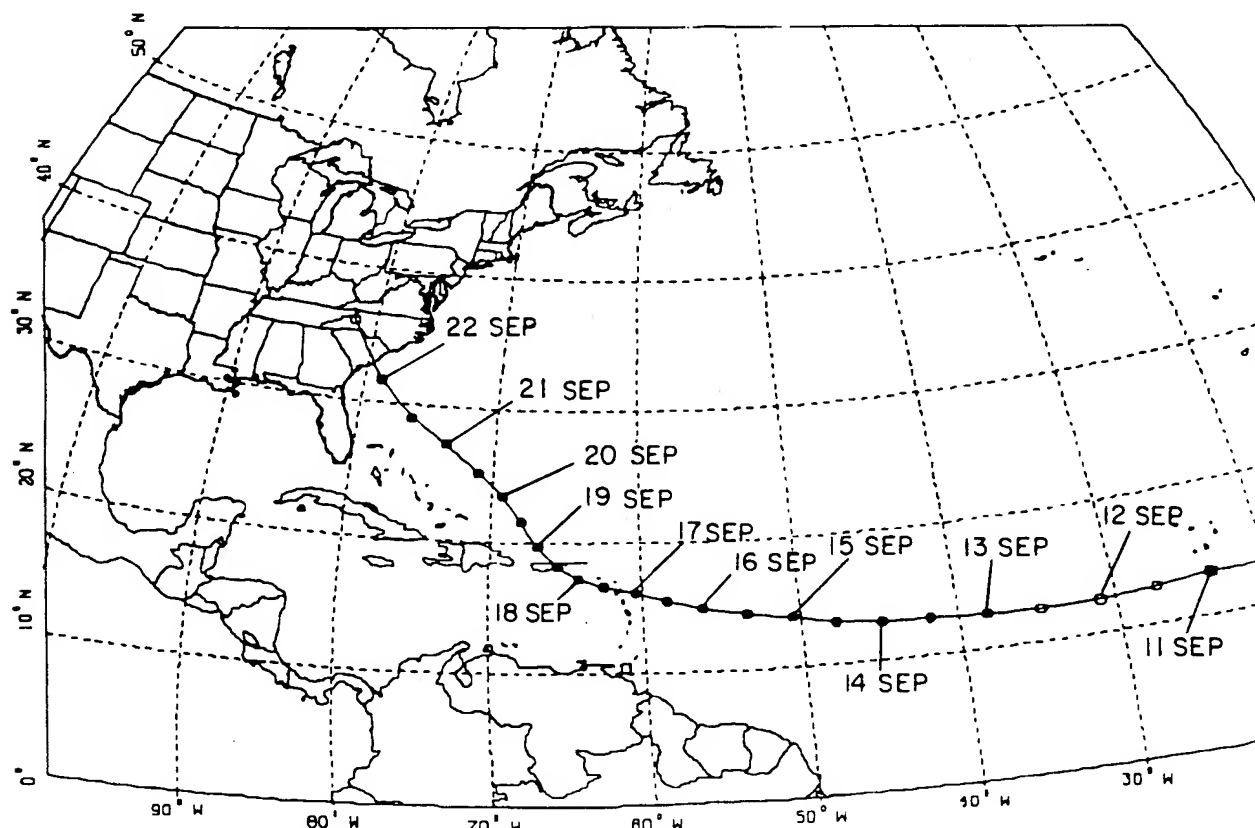


FIG. 2. Track of Hurricane Hugo from depression stage through final landfall: X = tropical depression stage, O = tropical storm stages, and ● = hurricane stages. Labels indicate location at 0000 UTC for each day.

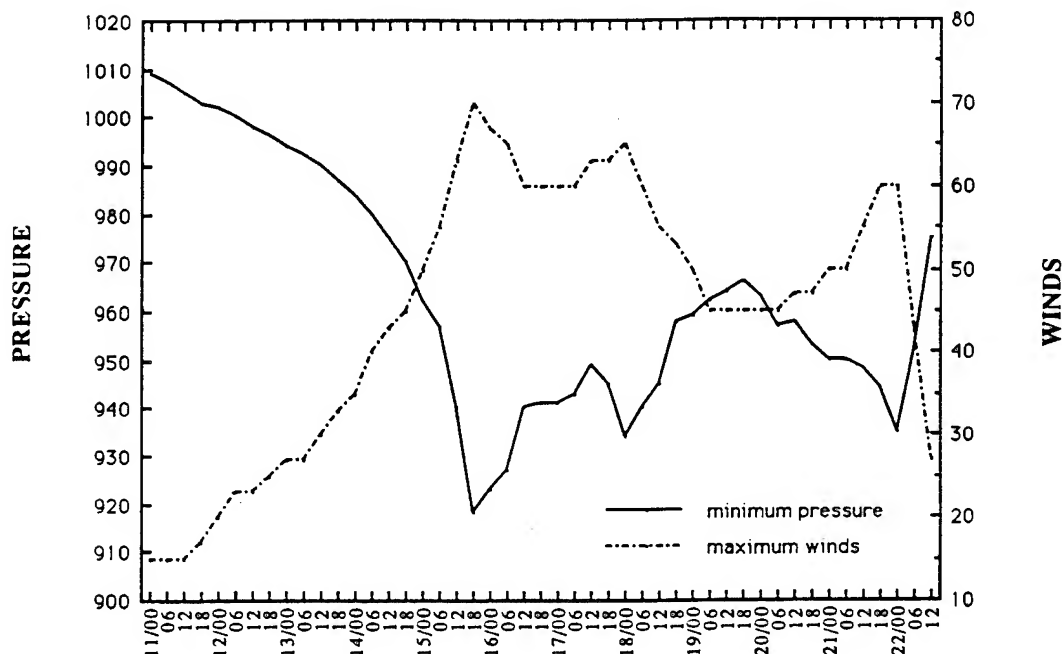


FIG. 3. Time series (UTC) of minimum central sea level pressure (mb) and maximum sustained wind speeds (m s^{-1}) obtained from NHC best-track data.

north of Charleston, South Carolina. Reintensification 30 h prior to landfall, along with a large translational speed, was responsible for the significant storm surge and severe damage along the South Carolina coastline. Based on U.S. Air Force reconnaissance reports, NHC estimated maximum sustained surface winds of 60 m s^{-1} just prior to landfall (Powell et al. 1991). By 1200 UTC 22 September, Hugo had weakened but maintained tropical-storm strength as it passed Charlotte, North Carolina. A turn toward the north occurred thereafter, and on 23 September, Hugo became extratropical in character (Case and Mayfield 1990).

4. Hugo precipitation pattern derived from SSM/I data

SSM/I observations were obtained from Hugo's predepression stage through final landfall. Figure 4a reveals SSM/I rain rates around 0700 UTC 10 September, just prior to Hugo's classification as a tropical depression. Two areas of convection with moderate rainfall rates ($10\text{--}15 \text{ mm h}^{-1}$) were observed to the southeast of the Cape Verde Islands. Over the next 13 h, according to Meteosat imagery, the two areas of convection merged. SSM/I rain rates at 2000 UTC

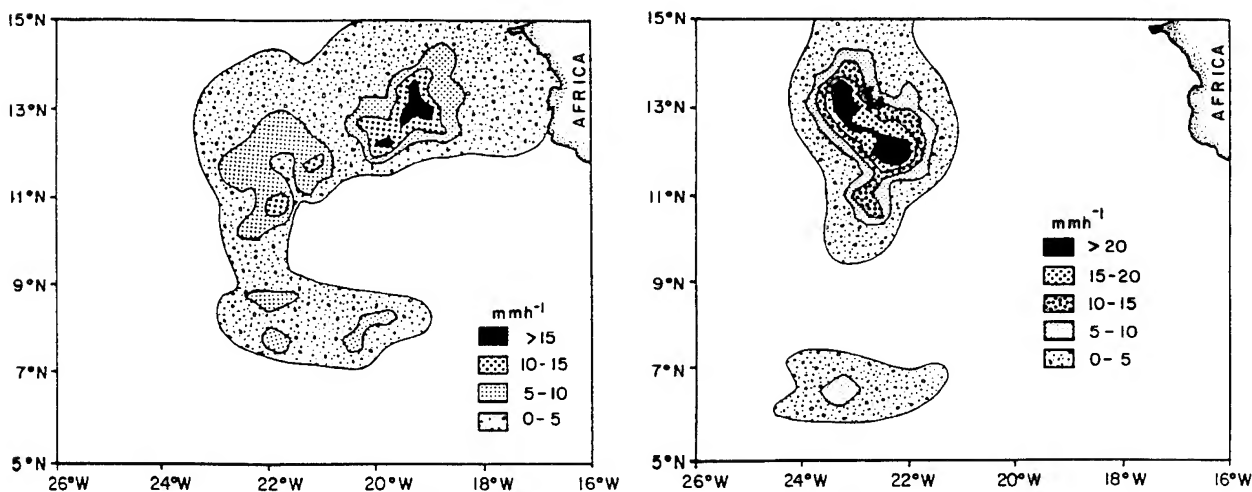


FIG. 4. (a) SSM/I rainfall rates at 0700 UTC 10 September. (b) Rainfall rates at 2000 UTC 10 September.

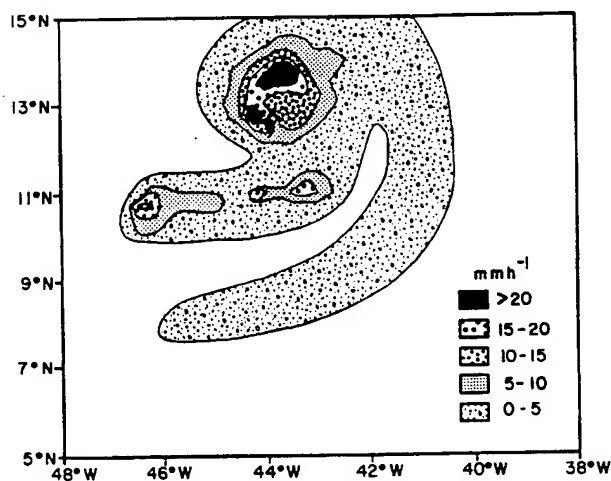


FIG. 5. SSM/I rainfall rates at 2100 UTC 13 September.

also showed one area of convection with some curvature in the rain pattern (Fig. 4b). Coverage by SSM/I was available 3 days later on 13 September. At this time, NHC had classified the storm as a hurricane with estimated maximum sustained winds of 33 m s^{-1} . The precipitation pattern showed an organized area of convection around the center of Hugo (Fig. 5). Figure 5 shows the approximate location of Hugo as determined from NHC best-track data. A large rainband also extended to the south and west of the storm's inner-core region. This rainband was several hundred kilometers long and approximately 100 km wide. This rainband was similar to those observed by Willoughby et al. (1984).

Hugo underwent a period of explosive deepening just prior to the arrival of the first NOAA P-3 aircraft on 15 September (Black and Marks 1991). The central pressure at 0900 UTC was estimated to be 949 mb, with maximum sustained winds near 60 m s^{-1} (see Fig. 3, Black and Marks 1991). SSM/I rain-rate imagery at 0900 UTC showed a large area of high rainfall rates associated with the inner-core region of the storm (Fig. 6a). What appeared to be an eyewall with high rain rates was also observed around the center, with the most intense precipitation (rates greater than 25 mm h^{-1}) occurring in the northwest region of the eyewall. The radius of the eyewall, measured using 85-GHz imagery, was 24 km. The SSM/I pass on 13 September did not show an eyewall or intense precipitation around its center, suggesting that the precipitation field was not as well organized. A spiral band at 0900 UTC was also evident in the rain-rate pattern to the north of the hurricane center. These bands curved inward toward the center of circulation. Their importance to intensity changes has been shown in Willoughby et al. (1982), who reported that large intensity changes can result from contraction and reformation of concentric, convective rings around the eye. SSM/I observations

between 1000 UTC 10 September and 0900 UTC 15 September, if available to forecasters, may have assisted in the analysis of Hugo since airborne reconnaissance was not available.

The scene at 2200 UTC 15 September captured Hugo at near maximum intensity. According to U.S. Air Force reconnaissance, a central pressure of 918 mb and sustained winds in excess of 70 m s^{-1} were observed just prior to the SSM/I observation (see Fig. 3, Black and Marks 1991). Figure 6b reveals an intense and tightly wrapped eyewall with a radius of 9 km as measured from the 85-GHz imagery. There is also the presence of a concentric ring at a radius of 91 km from the center. It appears that this concentric ring developed in the period between the two SSM/I observations on 15 September. The 85-GHz imagery showed that the circular rainband structure contracted 15 km between 0900 and 2200 UTC 22 September. Figure 6c shows the time-composite radar reflectivity structure of Hugo from P-3 aircraft (courtesy of M. Black) valid at 1730 UTC. This time composite was 4.5 h prior to the SSM/I observation. The radar reflectivities depict the presence of an inner eyewall and what appeared to be a developing secondary eyewall at a larger radius. These features were similar to the SSM/I imagery seen in Fig. 6b. The large spiral rainband to the west and southwest of the hurricane was observed in both the SSM/I imagery and the aircraft radar composite. This band observed in earlier SSM/I passes was most likely the same feature that had remained quasi-stationary relative to the moving cyclone over a number of days.

At 2200 UTC 16 September, Hugo was less than 200 km from the island of Guadeloupe. The center of Hugo, as depicted in the rain-rate imagery, was denoted by the light blue circular region where rain-rate values less than 10 mm h^{-1} were observed (Fig. 6d). This region was surrounded by two tightly curved areas of precipitation with rainfall rates greater than 25 mm h^{-1} . Furthermore, the double eyewall configuration seen earlier was no longer present. The U.S. Air Force reconnaissance estimated a pressure of 941 mb during this time—an increase of 23 mb in 24 h. While an eyewall cycle may have occurred during this period, it is impossible to determine from two consecutive SSM/I rain-rate imagery if indeed this process took place. The disappearance of the inner eye usually marks the end of a period of intensification and the beginning of a weakening phase, as suggested by Willoughby et al. (1982).

During the subsequent 48 h, Hugo passed over the Leeward Islands (Fig. 2) and crossed the eastern tip of Puerto Rico. SSM/I rain-rate imagery at 2300 UTC 18 September (not shown) revealed that Hugo's precipitation pattern was less organized. Rain rates at 1000 UTC 19 September showed a large rainband extending east and south from the inner-core region (Fig. 7a). The areas of most intense rain at this time were in a semicircle extending west to east around the center.

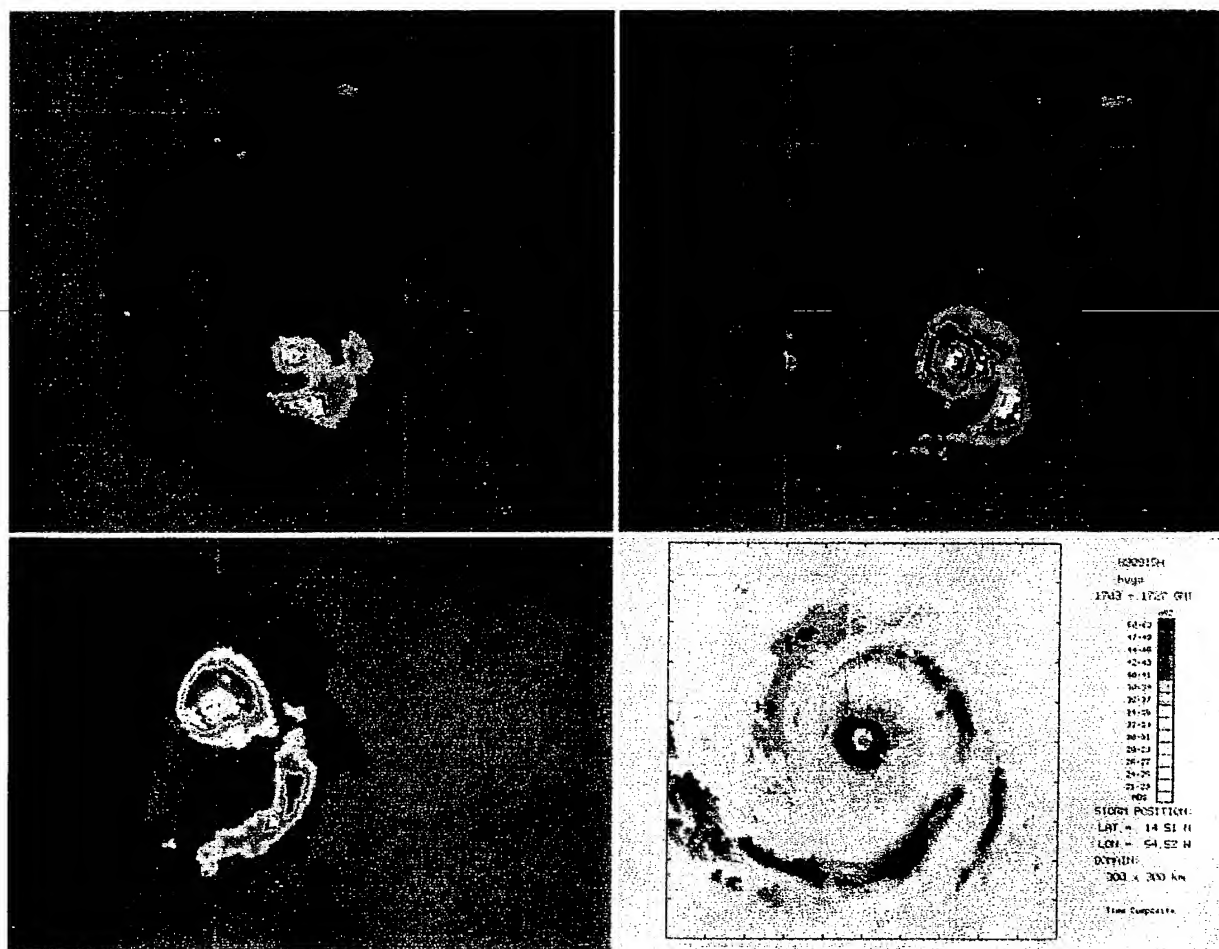


FIG. 6. (a) SSM/I rainfall rates imaged at 0900 UTC 15 September. The imagery shows a considerable increase in organization and convection around the center than in the previous image. A spiral band within the inner-core region has encompassed the center. The white horizontal-vertical lines indicate 20°N and 40°W , respectively. (b) The pass at 2200 UTC 15 September captures Hugo at near maximum intensity. The white horizontal-vertical lines indicate 20°N and 40° and 50°W , respectively. (c) Radar time composite for 1709-1727 UTC 15 September. Reflectivity intensities are denoted by shades of gray represented in the legend (image courtesy of M. Black, Hurricane Research Division-NOAA/AOML). (d) SSM/I rainfall rates at 2200 UTC 16 September. The vertical line indicates 50°W . All color rainfall rate imagery shows rain rates in 5 mm h^{-1} increments. Indigo represents rates less than 5 mm h^{-1} , royal blue $5\text{--}10 \text{ mm h}^{-1}$, light blue $10\text{--}15 \text{ mm h}^{-1}$, green $15\text{--}20 \text{ mm h}^{-1}$, red $20\text{--}25 \text{ mm h}^{-1}$, and white greater than 25 mm h^{-1} .

Additionally, no intense rain rates were retrieved in the southeast quadrant of the storm. Both the effects of landfall and the presence of an upper low just south of Hispaniola may have produced some of the observed precipitation patterns by inhibiting the outflow. The pass at 2300 UTC on the same day showed that Hugo was located north of the Dominican Republic (Fig. 7b). A closed center in the rainfall pattern was observed, which was reflected by a minimum in rainfall. Rates greater than 20 mm h^{-1} were present to the east of this rainfall minimum. A large rainband emanating from the western inner-core region was also observed. Within this outer rainband, isolated areas of deep convection with high rain rates were imaged by SSM/I. The precipitation at 2300 UTC appeared to be better

organized than in the SSM/I pass 13 h earlier (Fig. 7a).

Hugo's precipitation pattern was again determined by an SSM/I pass at 0000 UTC 22 September. During this pass, the center of the storm was 200 km southeast of Charleston, South Carolina. Rain rates greater than 25 mm h^{-1} were observed in a partial circle in the northern quadrants of the eyewall around a region of low rainfall rates (Fig. 8a). This region of low rain rates was approximately coincident with U.S. Air Force reconnaissance estimates of the storm center. A large rainband connected to the inner-core region of Hugo was also noted during this pass with embedded areas of rain rates greater than 20 mm h^{-1} . Figure 8b shows the southeast composite radar centered at Charleston.

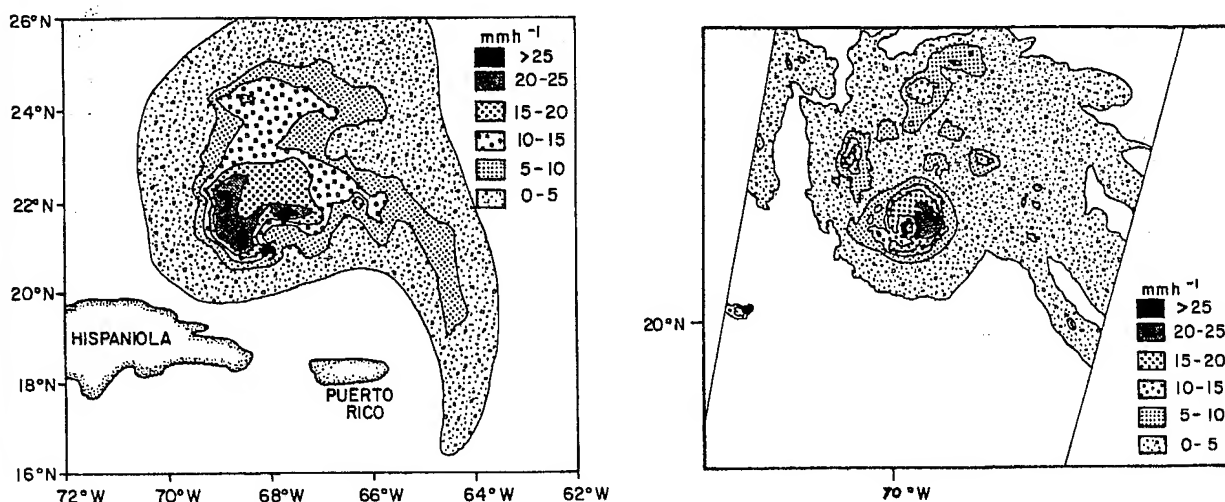


FIG. 7. (a) SSM/I rainfall rates at 1000 UTC 19 September, depict Hugo several hundred kilometers to the north of Puerto Rico. The deepest convection at this time is confined to the north and west of the center of circulation. (b) The ascending pass at 2300 UTC 19 September reveals newly formed convection to the east of the center.

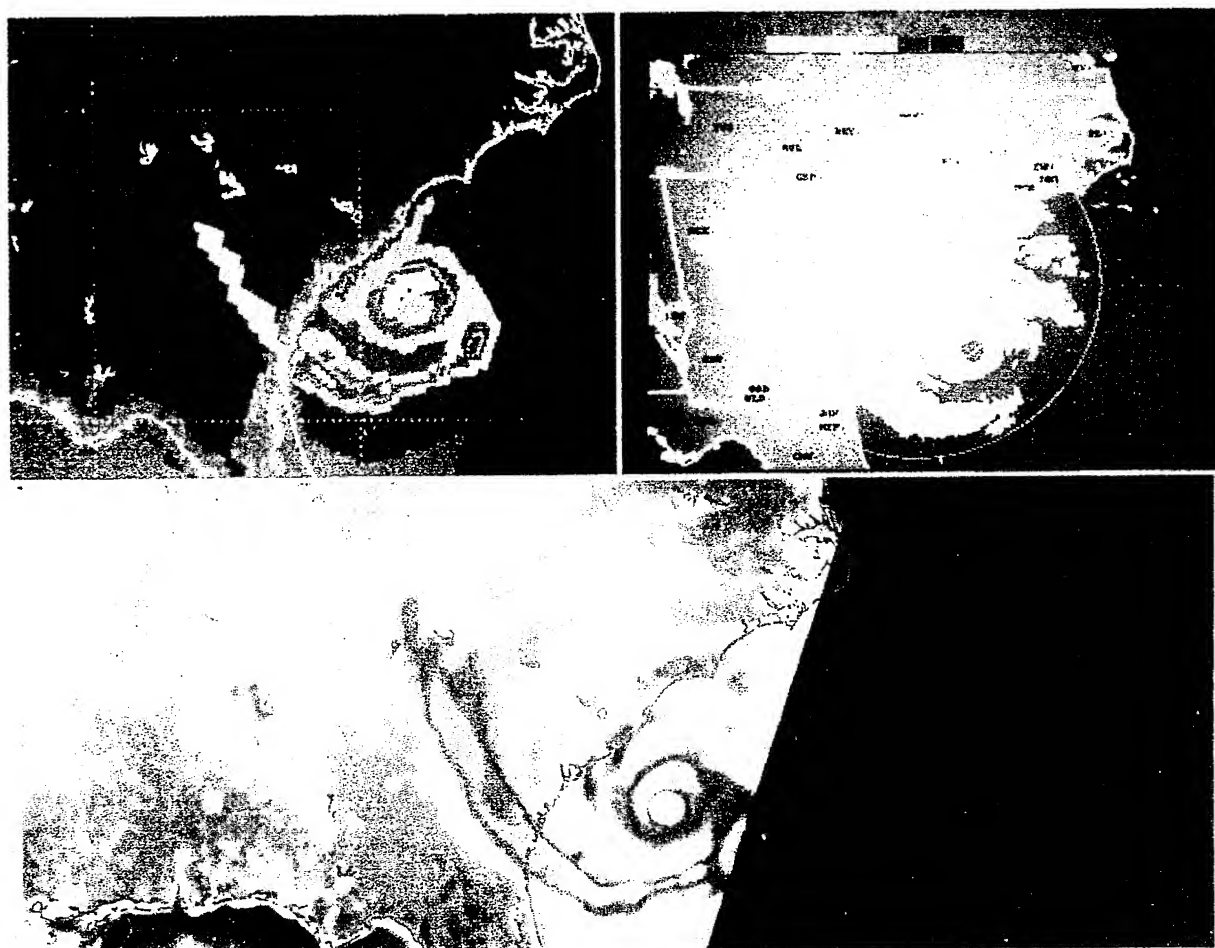


FIG. 8. (a) SSM/I rainfall rates (0000 UTC 22 September), 4 h prior to landfall. (b) Southeast radar composite at 0000 UTC 22 September reveals a similar pattern to the SSM/I rainfall rates. The legend at the top refers to the VIP levels indicating precipitation intensity. (c) SSM/I 85 GHz at 0000 UTC 22 September. Blue and turquoise shades indicate areas of deep convection. Areas shaded in white represent low-precipitating regions, like within the eye of Hugo.

The digital video integrator processor (DVIP) levels are indicated by the color code at the top of Fig. 8b. Radar observations and SSM/I rainfall rates showed a similar structure of the mesoscale rainfall patterns. In particular, the heavy precipitation occurring in the eyewall region, and the heavy rain observed in the rainband southeast of Savannah, Georgia, were also observed in the SSM/I and composite radar precipitation patterns. A quantitative comparison of SSM/I rain rates with radar-estimated rain rates was not conducted for this study. Instead, a comparison of SSM/I rain rates with raingage-measured rain amounts was performed and will be discussed in the next section. The 85-GHz imagery showed the organization of Hugo's convection (Fig. 8c). The purple, light blue, and yellow shaded regions indicate where the deepest convection was taking place, which was approximately coincident with the precipitation pattern seen in the radar composite (Fig. 8b).

5. Comparison between SSM/I and raingage observations

Due to the timely overpass of the SSM/I just prior to landfall in South Carolina, a quantitative comparison of SSM/I rainfall rates with raingage data along the southeast coastline was made. The SSM/I observation at 0000 UTC 22 September was used for this comparison. A 4-h period between 0000 UTC and 0400 UTC was selected for this comparison. In order to obtain the total precipitation expected from one SSM/I observation, the rain-rate field was first interpolated to a grid with a resolution of 0.5° in longitude and latitude. Next, the entire field was moved at 1-h intervals according to the best track obtained from NHC, with the rain values at each grid point being accumulated. The precipitation pattern of Hugo was assumed to be in steady state during the period, although the actual rain pattern probably changed. Only a 1-mb drop in the central pressure was noted in the NHC best-track data between 0000 UTC and landfall.

Figure 9a shows the 4-h predicted accumulated precipitation over the area of interest following the above procedure. Also shown is the track plotted every hour over the entire period. Maximum rainfall occurred at and near the area of landfall, as well as over central Georgia, the latter associated with a highly convective rainband (Fig. 8a). Maximum values of 89 mm were estimated on the coast near Charleston, South Carolina, and about 83 mm along the southeast Georgia coastline. A minimum in rainfall was also observed extending along the Savannah River.

Hourly precipitation data throughout North and South Carolina, Georgia, Tennessee, and Virginia were obtained from hourly reporting raingage stations. The raingages were located at sites operated by the National Weather Service, the Federal Aviation Administration, and cooperative observers. Standard raingage types in-

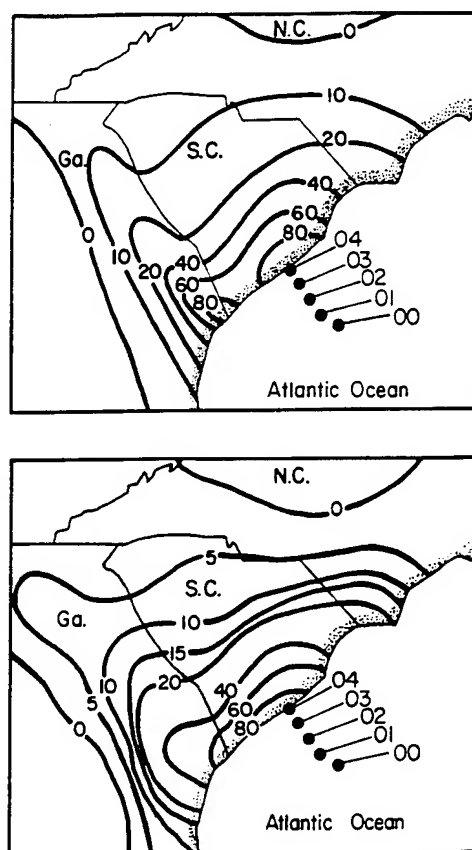


FIG. 9. (a) Four-hour SSM/I predicted rainfall (mm) for the period 0000–0400 UTC 22 September 1989. (b) Four-hour raingage totals (mm) for the same period. The track of Hugo is displayed and labeled for each hour.

clude Fischer–Porter, tipping bucket, and universal. Rain rates observed by surface raingages along the South Carolina coast were comparable to SSM/I rain rates. Charleston observed rain rates greater than 20 mm h^{-1} at 0000 UTC. SSM/I rain rates showed an area of 25 mm h^{-1} impinging on the Charleston coast around 0000 UTC. Observing stations in central Georgia along a quasi-stationary rainband all reported rain rates in excess of 10 mm h^{-1} around 0000 UTC. This supported SSM/I observations.

Rainfall totals from raingages for the same 4-h period as the SSM/I observations were compiled and interpolated onto a grid using a two-pass Barnes's scheme with a 0.5° resolution in longitude and latitude. Figure 9b shows the areal distribution of total rainfall for the 4-h period. Values in excess of 80 mm were obtained along the South Carolina coastal area near Charleston, with Charleston reporting 87 mm. These values decreased inland with increasing distance from the coastline. A slight minimum in rainfall occurred along the South Carolina and Georgia border. The observed rainfall totals over this area were similar to those predicted by SSM/I. Alliss et al. (1991) discussed in more

data
rates
land

6. S
a. 1

T
for
and
cent
from
ove:

wh
 $\times 1$
 $\times 1$
the
inte
of r.
rain
also
with
7
km
 $\times 1$
of?
Adi
typ
due
eac
rate
Ad

detail the comparison between SSM/I-derived rainfall rates and raingage observations during the time of landfall.

6. SSM/I-derived rainfall parameters

a. Total latent heat release

The total latent heat release (TLHR) was computed for eight observations for circular areas of 111-, 222-, and 444-km radius from the center of circulation. The center of circulation for all calculations was determined from an analysis of the 85-GHz imagery. The TLHR over an area is given by (Rodgers and Adler 1981)

$$\text{TLHR} = L\rho \int_A R da, \quad (3)$$

where ρ is the density of rainwater assumed to be $1.0 \times 10^3 \text{ kg m}^{-3}$, L the latent heat of condensation ($2.5 \times 10^6 \text{ J kg}^{-1}$), da the incremental area (27 km^2), R the rainfall rate at each grid point, and A the area of integration. Additionally, the ratio of the contribution of rainfall by rates greater than 10 mm h^{-1} to the total rainfall (RIP) within a 222-km radius of the center was also computed. Only passes providing full coverage within this area were chosen for the study.

The time-averaged TLHR within 111, 222, and 444 km of the center of circulation were 2.4×10^{14} , 9.1×10^{14} , and $16.6 \times 10^{14} \text{ W}$, respectively. The estimate of TLHR within 444 km of the center by Rodgers and Adler (1981) for 12 observations of western Pacific typhoons was $8.7 \times 10^{14} \text{ W}$. This difference may be due in part to the difference in the number of cases for each study, the differences in resolution of the rain rates, and the fact that Hugo was stronger than average. Additionally, all rainfall rates calculated by Rodgers

and Adler were less than 10 mm h^{-1} . The estimates obtained by Rodgers and Adler, as well as ours, appear to be reasonable given the large variation in the amount of heat that tropical cyclones release.

Viewing the TLHR as a function of time is very useful in observing the intensity changes of Hugo. Figure 10 shows a plot of TLHR computed within a circular area of radius 111 km from the center for nine SSM/I passes. The top of the figure shows the maximum winds (m s^{-1}) and minimum central pressure (mb). These values were obtained from the NHC best-track data and from public advisories issued by NHC. In addition to TLHR, values of RIP were also computed.

As shown in Fig. 10, from 10 to 15 September, the value of TLHR within 111 km (TLHR111) more than doubled, increasing from $1.9 \times 10^{14} \text{ W}$ during depression stage to $4.2 \times 10^{14} \text{ W}$ observed during the 2200 UTC 15 September pass. A value of $3.0 \times 10^{14} \text{ W}$ was calculated for the 2200 UTC 16 September pass. This represented a slight decrease over the 24-h period and was coincident with a decrease in Hugo's intensity as reflected in the maximum wind and minimum pressure. Between 16 and 18 September, Hugo underwent several intensity changes, which could not be resolved by TLHR111 due to the lack of SSM/I observations during that period. Calculations performed on the two SSM/I passes of 19 September yielded values of 1.40×10^{14} and $1.45 \times 10^{14} \text{ W}$, respectively. Hugo's intensity also remained unchanged during this day, as suggested by the minimum pressure and maximum wind. Between 0000 UTC 19 September and 0000 UTC 22 September, Hugo reintensified, which was also reflected in the increase of TLHR111. A value of $2.95 \times 10^{14} \text{ W}$ was reached for the 0000 UTC 22 September pass.

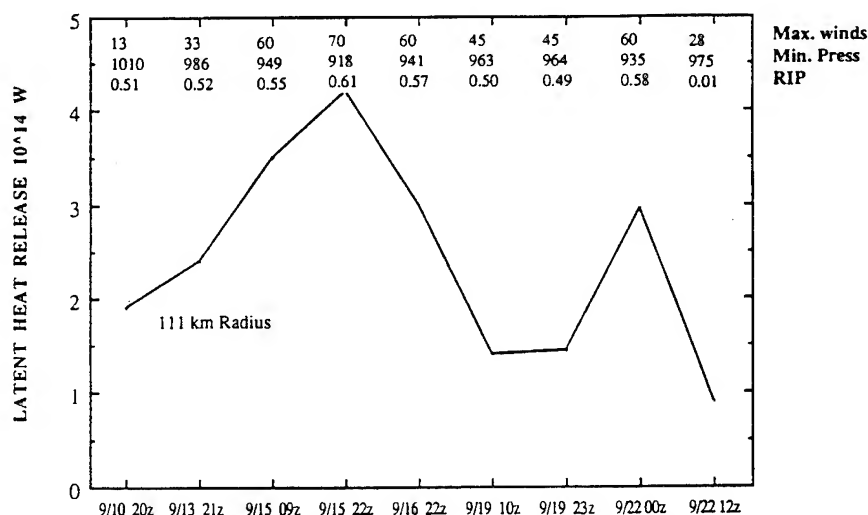


FIG. 10. Total latent heat release (TLHR) as a function of time. Calculations are for a circular area of 111-km radius from the center. Maximum wind (m s^{-1}), minimum pressure (mb), and the fraction of rainfall contributed by rainfall rates greater than 10 mm h^{-1} (RIP) are also displayed as a function of time. Wind and pressure information obtained from the NHC best-track data.

The TLHR111 of the SSM/I pass 8 h after landfall (1200 UTC 22 September) yielded a value of 0.9×10^{14} W. The sudden drop in TLHR during this 12-h period was most likely due to the landfall of Hugo at 0400 UTC. Rodgers and Adler (1981), who performed similar calculations, observed a 24-h lag between the maximum TLHR and intensity. Rodgers et al. (1991) found a lag of 32 h between the convective enhancement and intensity for Hurricane Irene (1981). Unfortunately, any lag present in Hugo's TLHR and intensity could not be determined from these SSM/I passes due to missing orbits and because the storm was sometimes located between adjacent swaths. Based on the availability of SSM/I imagery at 12 h, or longer intervals, it appeared that the TLHR were in phase with the observed intensity. Hopefully, with more frequent SSM/I observations in the future, along with reconnaissance data, a lag can be determined more definitively.

b. Other intensity parameters

The intensification of Hugo during this period was also evident in other SSM/I-derived rainfall parameters (Fig. 10). The RIP increased from 0.51 to 0.61 between 10 and 15 September. The reintensification of Hugo, which commenced 2 days prior to landfall, was also reflected in the RIP variations. RIP values increased from 0.49 to 0.58 between 2300 UTC 19 September and 0000 UTC 22 September. During this period of intensification, the central pressure of Hugo dropped approximately 30 mb (Fig. 3). A *t* test was conducted to determine the statistical significance between pressure and RIP. A correlation coefficient of -0.926 was obtained and was significant at the 1% level. Thus, as Hugo's surface pressure dropped, the contribution of SSM/I-determined RIP increased. Likewise, during times of weakening, a decrease in the RIP values was observed.

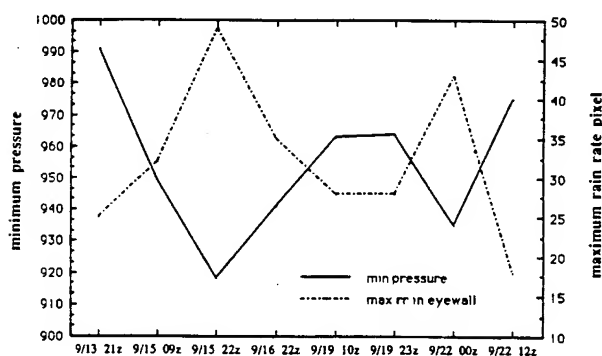


FIG. 11. Maximum rainfall rate within the eyewall region as a function of minimum central pressure. During the two maximum intensity periods, SSM/I observations show a maximum in rainfall rate within the eyewall region.

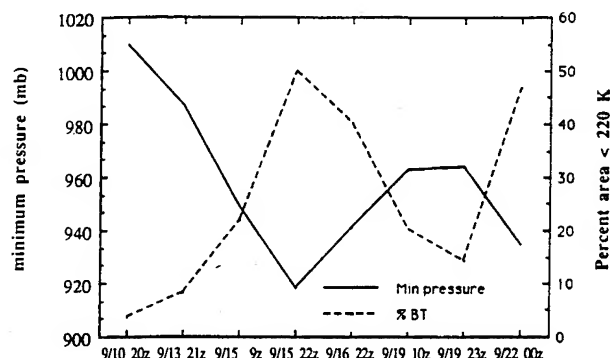


FIG. 12. Minimum central pressure (mb) and the percentage of 85-GHz brightness temperatures less than 220 K within a circular area of radius 111 km as a function of time.

Another method to relate the intensity of the storm with SSM/I rain rates was to compare the maximum SSM/I rain rate at a pixel in and near the eyewall region with the observed minimum central pressure. Only SSM/I passes where the storm was of hurricane status were used for this comparison. This was done to avoid times in which a distinct inner circulation or eyewall was not present. As shown in Fig. 11, when the central pressure in the storm decreased, the maximum rain rate observed by SSM/I increased in all cases. Two maxima in rain rate coincided with the two lowest pressure measurements. During these two passes, the maxima in rain rates were found to be 49 and 43 mm h^{-1} , corresponding to minimum pressures estimated by NHC of 918 and 935 mb, respectively. Since the temporal resolution was poor, the lag between the convection and minimum pressure could not be determined, as discussed before. A correlation coefficient between the maximum rain rate and minimum pressure was calculated to be -0.90 . This suggests a high probability that the two fields were related. Additional cases, however, are needed to verify this preliminary result and to determine the lag.

Examining the horizontally polarized 85-GHz BTs around the storm center may also be indicative of the storm's intensity. Wilheit et al. (1982) and Spencer et al. (1988) have shown that, at microwave frequencies near 85 GHz, large ice and water particles present in convective precipitation scatter the upwelling energy, resulting in cold BTs relative to the warm ocean background. As a storm intensifies, the areal coverage of deep convection around the center should increase. Because 85-GHz BTs less than 220 K are associated with heavy precipitation, a comparison between the central pressure and percentage of 85-GHz BTs less than 220 K can be examined. The calculations were performed over a circular area with a radius from the center of 111 km. Figure 12 shows that in all cases, as the central pressure decreased, the percent area of 85-GHz BT less than 220 K increased, while during times of increasing pressure, a decrease in the percentage was

TABLE 1. Percent areal coverage of rainfall and the percent contribution of rainfall (in parentheses) for four rainfall-rate categories (mm h^{-1}) within a radius of 200 km from the center during an intensification episode. Also shown are the minimum central pressures (mb) observed during each time.

SSM/I pass	Minimum pressure	SSM/I rainfall rates			
		<5	5–15	15–25	>25
1000 UTC 10 September	1010	67 (47)	25 (33)	8 (20)	0 (0)
0900 UTC 15 September	949	39 (13)	47 (55)	11 (24)	3 (8)
2200 UTC 15 September	918	32 (6)	35 (38)	28 (46)	5 (10)

noted. A correlation of -0.93 was found between the two parameters at the 0.4% confidence level. Felde and Glass (1991) found similar behavior for western Pacific typhoons during both intensification and weakening stages.

7. Rain-rate statistics

a. General characteristics

The contributions of rainfall within specified rain-rate categories and the areal coverage of these rain rates were examined during a period of intensification. The objective was to see how the contribution and areal coverage of rainfall changed during these times. Table 1 shows the percent areal coverage of rainfall and the percent contribution of rainfall (in parentheses) for four rain-rate categories within 200 km of the center. In addition, the central pressures obtained from NHC best-track data are shown for comparison purposes. Figure 2 shows the pressure decrease that took place between 10 and 15 September. The SSM/I observation (1000 UTC 10 September) during tropical-depression stage showed that there was little organization of the storm's convection. Table 1 shows that rain rates less than 5 mm h^{-1} occur in 67% of the area and contribute approximately 47% to the total rainfall during this period. No rain rates greater than 25 mm h^{-1} were observed during depression stage. The second SSM/I observation (0900 UTC 15 September) showed that rates less than 5 mm h^{-1} now occurred only in 39% of the area. The increasingly important contribution of heavier precipitation was evident at this time. Rates greater than 25 mm h^{-1} occurred in 3% of the area and contributed to 8% of the total rainfall. The third observation of Hugo, 13 h later (2200 UTC 15 September), showed an even larger contribution of rates greater than 15 mm h^{-1} . Rates less than 5 mm h^{-1} occurred in only 32% of the area, as compared to 67% of the area during the first observation. Precipitation with intensity between 15 and 25 mm h^{-1} occurred in 28% of the area, but contributed to 46% of the total. By 2200 UTC, Hugo's intensity had peaked. It appears that as the storm intensified, there was a shift toward heavier precipitation within the radius of 200 km. These observations were also consistent with the RIP

values, which showed the contribution of rates greater than 10 mm h^{-1} to the total storm rainfall.

b. Spatial variations of rainfall

Rainfall rates averaged over time and space were calculated for four circular areas with radii 60, 111, 222, 333, and 444 km from the center. Data from six SSM/I overpasses during hurricane stage were used. The time-averaged mean rain rate within these circular areas was 14.5, 12.1, 8.8, 5.6, and 4.0 mm h^{-1} , respectively. Large variations of these rain rates existed for individual times according to the observed intensity during that period. Within 60 km of the center, precipitation averaged from a minimum of 5.9 mm h^{-1} to a maximum of 19.5 mm h^{-1} observed at 0900 UTC 15 September. Marks (1985) points out that the average rain rate in the eyewall of Hurricane Allen increased as the eyewall radius decreased during the concentric eyewall cycle described by Willoughby et al. (1982). Due to the coarse resolution of SSM/I rainfall rates (25 km), compared to that of radar data (used by Willoughby 1982), a determination of whether or not the rain rate increased with decreasing eyewall radius was impossible.

The average spatial distribution of rainfall rate as a function of distance from the center of circulation was computed for various stages of development. Additionally, the average rainfall rate by quadrant oriented relative to the storm track was also computed. Figure 13 shows the average rainfall rate for each 20-km radius from the center during the intensification phase between 10 and 15 September. The figure shows that as Hugo intensified, the maximum average rainfall rate increased. It is evident that the convection surged toward smaller radii between 10 and 15 September. Due to the lack of SSM/I observations between these times, however, the detailed fashion of the contraction could not be determined. We do note, however, that the maximum average rain rate increased from 9 mm h^{-1} at depression stage at a radius of 50 km to 19 mm h^{-1} during the hurricane stage at a radius of 30 km. During the 2200 UTC 15 September pass there were three separate maxima in rainfall rates. Values of 16, 14.5, and 15 mm h^{-1} were observed at a radius of 30, 70, and 130 km, respectively. The inner two maxima supported

Percent area < 220 K

Pressure

19 23z 9/22 00z

the percentage of
within a circular

ty of the storm
the maximum
eyewall region
pressure. Only
hurricane status
done to avoid
ion or eyewall
hen the central
maximum rain
all cases. Two
he two lowest
wo passes, the
be 49 and 43
pressures esti-
ectively. Since
ag between the
uld not be de-
tion coefficient
imum pres-
uggests a high
ed. Additional
is preliminary

1 85-GHz BTs
dicative of the
nd Spencer et
ve frequencies
cles present in
velling energy,
n ocean back-
al coverage of
ould increase.
are associated
n between the
GHz BTs less
ulations were
adius from the
in all cases, as
ent area of 85-
e during times
percentage was

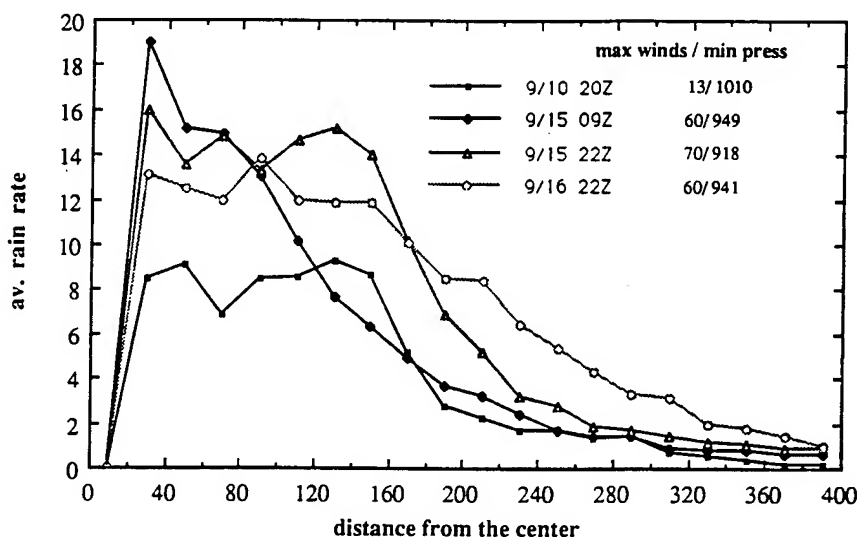


FIG. 13. (a) Mean rainfall rate (mm h^{-1}) as a function of radial distance (km) from the center during the intensification period that occurred between 10 and 15 September.

the observation of two concentric convective rings that were observed in the SSM/I imagery and in the P-3 radar composite (Figs. 6b,c). The SSM/I rain-rate imagery 24 h later (2200 UTC 16 September) showed that the two concentric rings no longer existed. This was also evident in Fig. 13, which showed a single maximum rain rate of 14 mm h^{-1} at a radius of 90 km.

The time-averaged rain rate by quadrant within 75 km of the center relative to the storm motion is shown in Fig. 14. These values are averages of six observations

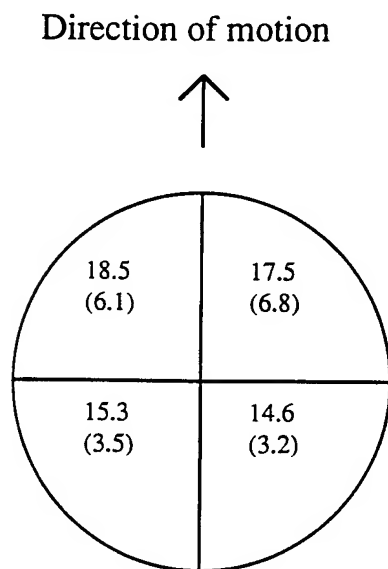


FIG. 14. Time-averaged rainfall rate (mm h^{-1}) and standard deviations (in parentheses) for a circular area of radius 75 km from the center, viewed by quadrant, relative to the storm motion.

of Hugo during the hurricane stage. The numbers in parentheses represent the standard deviations for each quadrant. The distribution is such that 30% of the total rainfall occurred in the left front (LF) quadrant and 26% occurred in the right front (RF) quadrant. It appears that the rain rates in both the left rear (LR) and right rear (RR) quadrants fluctuated much less than those in the other quadrants, with standard deviations of 3.5 and 3.2 mm h^{-1} , respectively. This was much less than those for the LF and RF quadrants. This suggests that the front semicircle (in the direction of motion) had more rain intensity changes than the rear semicircle. Burpee and Black (1989) suggest that translational speeds of hurricanes appear to be one of several factors that may determine the orientation of the precipitation patterns. Shapiro (1983) found that the axisymmetric convection distribution within the eyewall was related to the asymmetries in the boundary-layer convergence, which in turn was associated with the translation of the storm. Since Hugo had translational speeds ranging from 3 to greater than 10 m s^{-1} , storm motion may have caused the particular distribution shown here.

8. SSM/I center fixing

Velden et al. (1989) and Sandlin and Spangler (1989) have both shown the usefulness of 85-GHz imagery in locating the centers of tropical cyclones. Additionally, NHC began processing 85-GHz data during October 1989, and has developed several applications for its use. Rappaport (1991) points out that the data has, in general, been accepted for operational use. For this study, nine cases were examined. An estimation of the location of the center was determined in several ways. If no eye was present, the estimate from the 85-

GHz imagery was made by locating the center of the low-level circulation as defined by the tightly wrapped convection near the storm center. If an eye was present, not only was the location of such a center estimated, but the maximum BT in that region was also located. Figure 15a shows the 85-GHz imagery of Hugo around 1000 UTC 19 September. Figure 15b shows the GOES

enhanced infrared image for the same time (GOES visible imagery was unavailable due to darkness). The SSM/I image showed a tightly curved convective band to the north of Puerto Rico, just northeast of 21.0°N, 68.0°W. This location was approximately coincident with the NHC public advisory, which indicated that the center of Hugo was at about 21.2°N, 67.7°W near

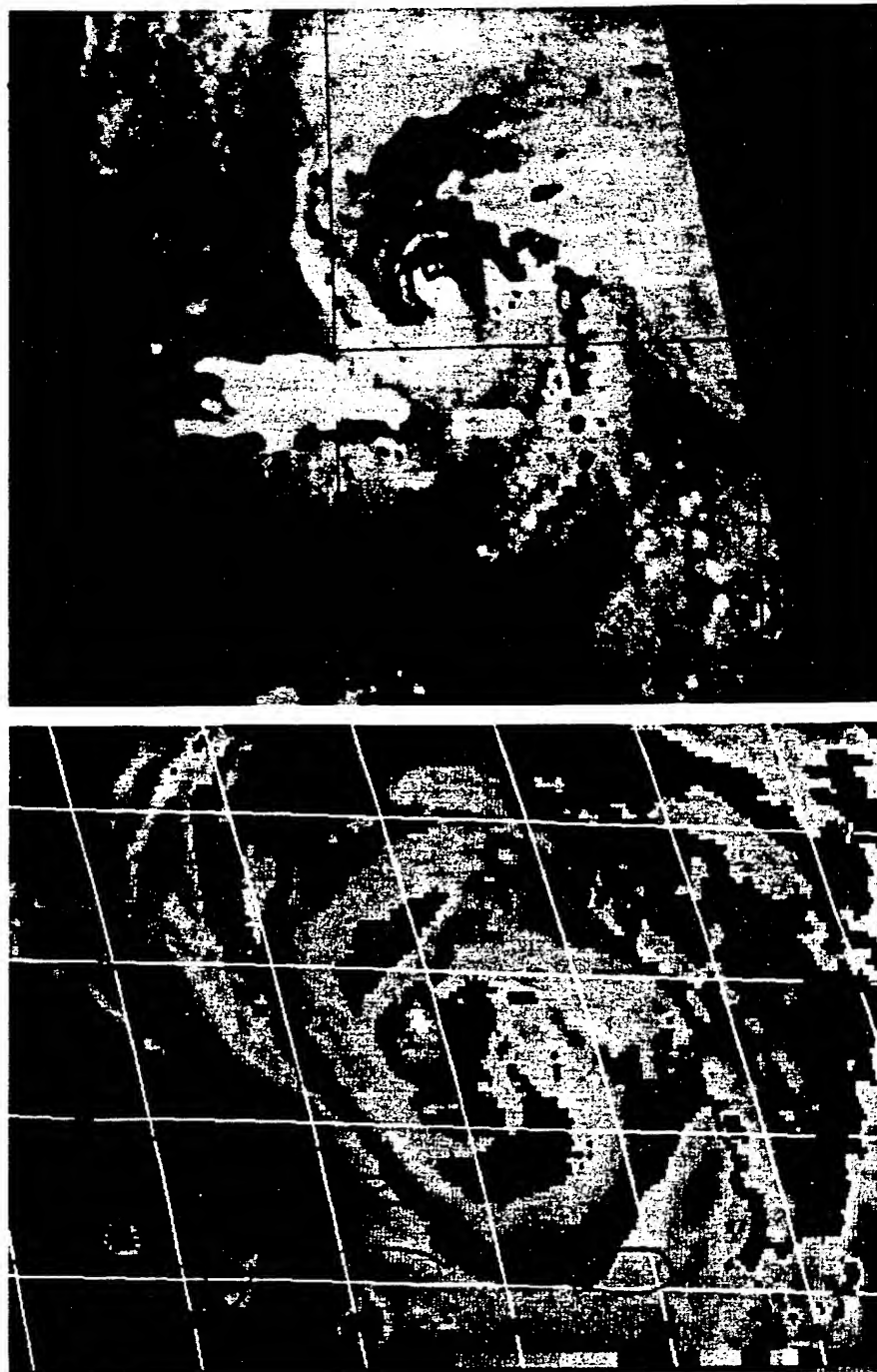


FIG. 15. Hurricane Hugo at 1000 UTC 19 September 1989, as seen by (a) SSM/I 85-GHz imagery and (b) GOES infrared imagery.

e numbers in
tions for each
0% of the total
quadrant and
adrant. It ap-
ear (LR) and
uch less than
rd deviations
is was much
nts. This sug-
ection of mo-
than the rear
suggest that
to be one of
orientation of
3) found that
on within the
he boundary-
sociated with
had transla-
an 10 m s^{-1} ,
ticular distri-

nd Spangler
85-GHz im-
yclones. Ad-
z data during
applications
that the data
onal use. For
n estimation
ed in several
from the 85-

TABLE 2. The average difference (km) between the NHC low-level center, extrapolated to SSM/I time, and the center estimated from SSM/I 85-GHz imagery.

NHC method of determination	NHC-SSM/I difference (km)
GOES only (three cases)	32
Reconnaissance and GOES (six cases)	12
Combined average (nine cases)	18

1000 UTC. Neither the banding areas of convection nor the center could be inferred in the GOES imagery. The infrared image was dominated by a large area of cirrus clouds obscuring the center.

A comparison was made between the NHC best-track positions and the estimated SSM/I center (Table 2). These positions were determined from reconnaissance and satellite measurements. All NHC positions were extrapolated to the time the SSM/I scan crossed the position of the proposed center (SSM/I time). The extrapolation was conducted using the NHC advisories, which contained information on speed and direction of movement. The extrapolation did not take into account unsteady motion between best-track positions or for trochoidal motions; thus, some error may have been introduced. The extrapolations performed, however, did not exceed 1 h; therefore, any bias is assumed to be small. As listed in Table 2, the average difference between SSM/I and NHC estimates, when reconnaissance information was not available, was 32 km. This average dropped to 12 km when the NHC estimate used information from reconnaissance flights. This suggests that SSM/I estimations of the low-level center were more comparable to NHC estimates when reconnaissance information was available at NHC. For all nine observations, the average difference was 18 km. While limited in availability and subject to image interpretation, SSM/I 85-GHz imagery may provide supplemental information to enhance existing satellite capabilities. This preliminary examination also suggests a potential for reduced positioning errors, especially during times when high clouds cover the system's low-level center.

9. Conclusions

Data from the SSM/I on board the DMSP F-8 spacecraft have been used to study the various storm-structure features observed in Hugo. Rainfall rates and 85-GHz imagery were instrumental in observing Hugo's convective organization and precipitation patterns. Assuming data becomes available at shorter time intervals, a potentially valuable application of SSM/I might be to estimate minimum central pressure and maximum winds from the rain-rate imagery, analogous to the Dvorak (1975) technique. Additionally, rainfall rates measured by SSM/I just prior to landfall strongly

support those observed at reporting stations along the Georgia-South Carolina coastlines. These results indicate that rain data obtained by SSM/I may be useful in providing forecasts for precipitation amounts over coastal areas as tropical cyclones make landfall.

It was found that the TLHR calculated from SSM/I rainfall rates was comparable to estimates made by Rodgers and Adler (1981), who studied other tropical cyclones using the Nimbus Electrically Scanning Microwave Radiometer (ESMR-5). Furthermore, observations showed that as the TLHR increased with time, so did the intensity of Hugo. Because of the poor temporal resolution, any lag present between the TLHR and the intensity was impossible to determine. The contribution of heavier rainfall rates to the total storm rainfall (RIP) was calculated and observed to increase as Hugo intensified. It was found that higher rainfall rates occurred closer to the inner-core region during times of intensification. The areal coverage of higher rainfall rates was also observed to increase during times of intensification. Maximum rainfall rates in the eyewall region were found to increase as the minimum observed central pressure decreased. Poor temporal resolution prevented an estimation of the lag between the convection and minimum pressure. With three sensors currently in orbit, more frequent observations of tropical cyclones might help in determining this lag time.

The utility of SSM/I 85-GHz imagery in estimating the location of the low-level circulation has also been demonstrated in this study. The usefulness of SSM/I data for this application was most beneficial when the eye of Hugo was obscured by clouds and at night when GOES visible imagery was unavailable. Furthermore, in the event that GOES becomes inoperative, or during times when no airborne reconnaissance data is available, SSM/I observations may become increasingly important for operational use.

Acknowledgments. We thank Glenn Sandlin of Naval Research Laboratory for processing the SSM/I data, for providing us with the SSM/I imagery, and for invaluable discussions on the SSM/I data characteristics. We also wish to thank Kevin Schrab and Ronald Weglarz of North Carolina State University for their helpful suggestions. This research was supported by an NRL Basic Research Grant and ONR Grant N0001492AF00002.

REFERENCES

- Adler, R. F., and E. B. Rodgers. 1977: Satellite-observed latent heat release in a tropical cyclone. *Mon. Wea. Rev.*, **105**, 956-963.
- Alliss, R. A., S. Raman, and S. W. Chang. 1991: A comparison of rainfall rates and intensity during Hurricane Hugo using SSM/I observations. *Proc., 19th Conf. on Hurricanes and Tropical Meteorology*, Miami, Amer. Meteor. Soc., 391-395.
- Black, P. G., and F. D. Marks. 1991: The structure of an eyewall meso-vortex in Hurricane Hugo (1989). *Proc., 19th Conf. on Hurricanes and Tropical Meteorology*, Miami, Amer. Meteor. Soc., 579-582.

- Burpee, R. W., and M. L. Black, 1989: Temporal and spatial variations of rainfall near the centers of two tropical cyclones. *Mon. Wea. Rev.*, **117**, 2204–2209.
- Case, R. A., and M. B. Mayfield, 1990: Atlantic hurricane season of 1989. *Mon. Wea. Rev.*, **118**, 1171–1175.
- Dvorak, V. R., 1975: Tropical cyclone intensity analysis and forecasting from satellite imagery. *Mon. Wea. Rev.*, **103**, 420–430.
- Felde, G. W., and M. Glass, 1991: SSM/I brightness temperatures analysis of tropical cyclones. *Proc., 19th Conf. on Hurricanes and Tropical Meteorology*, Miami, Amer. Meteor. Soc., 400–404.
- Goodberlet, M. A., C. T. Swift, and J. C. Wilkerson, 1989: Remote sensing of ocean surface winds with the Special Sensor Microwave/Imager. *J. Geophys. Res.*, **94**, 547–555.
- Hollinger, J. P., 1989: DMSP Special Sensor Microwave/Imager Calibration Validation. Final Report, Vol. I, 51 pp. [Available from J. P. Hollinger, Naval Research Laboratory, Washington, DC 20375.]
- , 1991: DMSP Special Sensor Microwave/Imager Calibration Validation. Final Report, Vol. II, 106 pp. [Available from J. P. Hollinger, Naval Research Laboratory, Washington, DC 20375.]
- Marks, F. D., Jr., 1985: Evolution of the structure of precipitation in hurricane Allen (1980). *Mon. Wea. Rev.*, **113**, 1268–1285.
- Mayfield, M., C. J. McAdie, and A. Pike, 1988: A preliminary evaluation of the dispersion of tropical cyclone position and intensity estimates determined from satellite imagery. NOAA National Hurricane Center Research Paper, 16 pp.
- Negri, A. J., R. F. Adler, and C. D. Kummerow, 1989: False-color display of Special Sensor Microwave/Imager (SSM/I) data. *Bull. Amer. Meteor. Soc.*, **70**, 146–151.
- Olson, W. S., 1989: Physical retrieval of rainfall rates over the ocean by multispectral microwave radiometry-application to tropical cyclones. *J. Geophys. Res.*, **94**, 2267–2280.
- Powell, M. D., P. P. Dodge, and M. L. Black, 1992: The landfall of Hurricane Hugo in the Carolinas. *Wea. Forecasting*, **6**, 379–399.
- Rao, G. V., P. D. MacArthur, and J. H. McCoy, 1991: The SSM/I latent heat release and brightness temperature anomalies associated with tropical cyclones and their utility in predicting intensity changes of tropical storms. *Proc., 19th Conf. on Hurricanes and Tropical Meteorology*, Miami, Amer. Meteor. Soc., 175–178.
- Rappaport, E. N., 1991: Operational applications of SSM/I data at the National Hurricane Center. *Proc., 19th Conf. on Hurricanes and Tropical Meteorology*, Miami, Amer. Meteor. Soc., 179–183.
- , and P. G. Black, 1989: The utility of Special Sensor Microwave/Imager data in the operational analysis of tropical cyclones. *Proc., Fourth Conf. on Satellite Meteorology and Oceanography*, San Diego, Amer. Meteor. Soc., J21–J24.
- Rodgers, E. B., and R. F. Adler, 1981: Tropical cyclone rainfall characteristics as determined from a satellite passive microwave radiometer. *Mon. Wea. Rev.*, **109**, 506–521.
- , S. Chang, J. Stout, J. Steranka, and J. J. Shi, 1991: Satellite observations of variations in tropical cyclone convection caused by upper-tropospheric troughs. *J. Appl. Meteor.*, **30**, 1163–1184.
- Sandlin, G. D., and D. J. Spangler, 1989: SSM/I imagery, center-fixes, and wind fields for tropical cyclones. Naval Research Laboratory Report, 18 pp. [Available from G. D. Sandlin, Naval Research Laboratory, Washington, D.C. 20375.]
- Shapiro, L. J., 1983: The asymmetric boundary layer flow under a translating hurricane. *J. Atmos. Sci.*, **40**, 1984–1998.
- Spencer, R. W., H. M. Goodman, and R. E. Hood, 1989: Precipitation retrieval over land and ocean with the SSM/I: Identification and characteristics of the scattering signal. *J. Atmos. Oceanic Technol.*, **6**, 254–273.
- Velden, C. S., W. S. Olson, and B. A. Roth, 1989: Tropical cyclone center-fixing using SSM/I Data. *Proc., Fourth Conf. on Satellite Meteorology and Oceanography*, San Diego, Amer. Meteor. Soc., J36–J39.
- Wilheit, T. T., A. T. C. Chang, J. L. King, E. B. Rodgers, R. A. Nieman, B. M. Drupp, A. S. Milman, J. S. Stratigos, and H. Siddalingaiah, 1982: Microwave radiometric observations near 19.35, 92, and 183 GHz of precipitation in Tropical Storm Cora. *J. Appl. Meteor.*, **21**, 1137–1145.
- Willoughby, H. E., J. A. Clos, and M. G. Shoreibah, 1982: Concentric eye walls, secondary wind maxima, and the evolution of the hurricane vortex. *J. Atmos. Sci.*, **39**, 395–411.
- , F. D. Marks, Jr., and R. J. Feinberg, 1984: Stationary and moving convective bands in hurricanes. *J. Atmos. Sci.*, **41**, 3189–3192.

Appendix L

**Sensitivity of Monsoon Rainfall Predictions
to Initialization Procedures**

Sensitivity of monsoon rainfall predictions to initialization procedures

K. Alapaty^a, R.V. Madala^b and S. Raman^a

^a*Department of Marine, Earth and Atmospheric Sciences, North Carolina State University, Raleigh, NC 27695, USA*

^b*Naval Research Laboratory, Washington, D.C. 20375, USA*

(Received November 2, 1992; revised and accepted March 18, 1993)

ABSTRACT

Prediction of orographic-convective rainfall during an active monsoon period is studied with an adiabatic and a diabatic vertical mode initialization schemes. A nested grid mesoscale model is used to perform two numerical simulations. In the diabatic initialization scheme, vertical distribution of latent heat released in convective clouds is obtained using the Kuo scheme from analyzed rainfall rates. Results indicate that the model predicted significantly higher rainfall rates when the initial conditions are obtained using a diabatic initialization scheme. Also, predicted rainfall rates are persistently higher almost throughout the period of simulation with a considerable increase during the first nine hours of integration when initial conditions are obtained from a diabatic initialization scheme. Use of diabatic initialization scheme lead to the prediction of stronger winds, stronger circulation patterns associated with the cumulus convection and higher latent heat fluxes from surrounding oceans, leading to higher rainfall rates.

RÉSUMÉ

On étudie la prévision de précipitation orographique convective pendant une période active de mousson à l'aide de schémas avec initialisation en mode vertical adiabatique et diabatique. On utilise un modèle de mésoéchelle à grilles emboîtées afin de réaliser deux simulations numériques. Dans le schéma à initialisation diabatique, la distribution verticale de la chaleur latente libérée dans les nuages convectifs est obtenue à l'aide du schéma de Kuo à partir de l'analyse des taux de précipitation. Les résultats montrent que le modèle prédit des taux de précipitation nettement plus élevés lorsque les conditions initiales sont obtenues par un schéma d'initialisation diabatique. De plus, dans ce cas, les taux prévus de précipitation sont plus élevés pendant pratiquement toute la période de simulation, avec une augmentation considérable dans les neuf premières heures d'intégration. L'utilisation d'un tel schéma conduit à la prévision de vents plus rapides, d'une circulation plus forte associée à la convection nuageuse et d'un flux de chaleur latente plus élevé à partir des océans, le tout conduisant à des taux de précipitation plus forts.

INTRODUCTION

Short range prediction of rainfall in the regional and global scale models is mainly affected by the inaccuracies in the input data namely, the divergence,

moisture and the mass fields. A numerical study of the effect of initial moisture analysis on the rainfall predictions (Wolcott and Warner, 1981) indicates that the most realistic amounts of rainfall are produced when a saturation constraint was imposed by the use of satellite and surface-based observations. Also, it was found (Wolcott and Warner, 1981) that the cumulus convection in the model sustains only in the presence of proper convergence field in the initialized initial conditions. Using a general circulation model, Mohanty et al. (1986) studied the impact of diabatic heating on the initialization of divergent circulations in the tropics. They also found that the initial large-scale divergent circulations were not retained during the forecast period unless the model was forced to generate a diabatic heating sufficiently similar to the observed heating. Puri (1987) studied the use of tropical diabatic heating information for initial state specification and found that the persistence of dynamical balance during model integrations is strongly dependent on the compatibility between the specified heating during initialization and the heating during the model integration. One of the shortcomings in these studies is the a priori assumption of the magnitude and the vertical distribution of heating rates used in the diabatic initialization schemes. To alleviate this problem, satellite-based data such as infrared and visible imagery data (Turpeinen et al., 1990) or outgoing longwave radiation data (Puri and Miller, 1990) are used to estimate the initial convective heating rates for use in the initialization schemes.

During the monsoon season, the westcoast of India is one of the regions where large rainfall rates are observed. Analyzed rainfall data for the monsoon region (Krishnamurti et al., 1983) indicate maximum rates of about 200 mm d^{-1} along the westcoast of India. Though there exists some uncertainty in the analyzed rainfall rates, (pers. commun. with T.N. Krishnamurti), these provide an unique opportunity to study the effects of initialization procedures on a model forecast. The objective of this paper is to study the effects of diabatic and adiabatic initialization procedures on the monsoon rainfall prediction using a nested grid mesoscale model.

THE MODEL

A nested grid model developed at the Naval Research Laboratory and North Carolina State University is used for numerical simulations. It is a primitive equation model written in pressure-based terrain-following σ -coordinate system having a one-way interacting nested grid network. Physics included in the model are for convective and nonconvective precipitation, and atmospheric boundary layer processes. Atmospheric radiation is not considered because of the relatively short model integration time (48 h). Convective precipitation is parameterized using modified Kuo scheme (Kuo, 1974; Anthes, 1977). Nonconvective precipitation occurs in the model when super satura-

tion is reached on the resolvable scale. Excess moisture precipitates into lower model layers and evaporates or falls to the surface. A dry convective adjustment scheme, which conserves total static energy, is included in the model above the atmospheric boundary layer to remove superadiabatic lapse rates. There are ten uniform vertical levels in the model and the lowest layer represent the boundary layer. For the horizontal differencing, a staggered grid network (Arakawa C-grid) is used with p_s , q , T , ϕ , and σ specified at the same horizontal points, and u and v are interlaced between them, where p_s is the surface pressure, q the specific humidity, T the temperature, ϕ the geopotential, σ the vertical velocity, u the zonal wind and v the meridional wind. Horizontal grid resolutions in the coarse-grid mesh (CGM) and the fine-grid mesh (FGM) domains are 1.5° and 0.5° , respectively. Figure 1 shows the simulation domain for the CGM and the FGM. The CGM domain covers from 37.5° E to 112.5° E and 20.5° S to 42.5° N and the FGM domain from 56.5° E to 100.0° E and 3.0° S to 28.5° N. Envelop topography was obtained from the navy $10'$ global topography data for 1.5° and 0.5° horizontal resolutions. Model sea surface temperatures (SST) were obtained from the 1° resolution global climatological values based on a 10 year average for the month of July. Davies scheme (1976, 1983) is employed to provide lateral boundary conditions. At the model top and bottom, the boundary condition for σ is assumed zero. A split-explicit method is used for the model integrations with

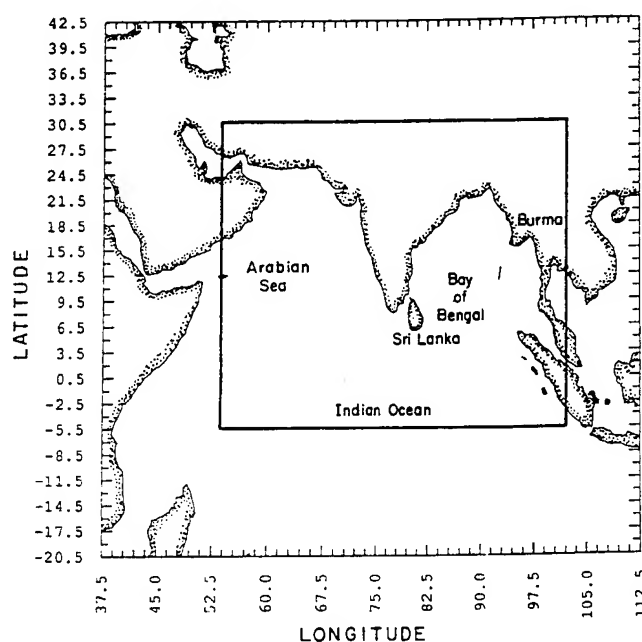


Fig. 1. Model domain of simulation in the coarse grid mesh and the fine grid mesh.

time steps of 300 s and 100 s, in the coarse-grid mesh and the fine-grid mesh domains, respectively. The First GARP Global Experiment (FGGE) level III A data is used to specify the initial conditions.

INITIALIZATION PROCEDURE

An adiabatic vertical mode initialization (AVMI) scheme developed at the Naval Research Laboratory was used to develop a diabatic version (DVMI) of the scheme. To incorporate the latent heat forcing into the AVMI scheme,

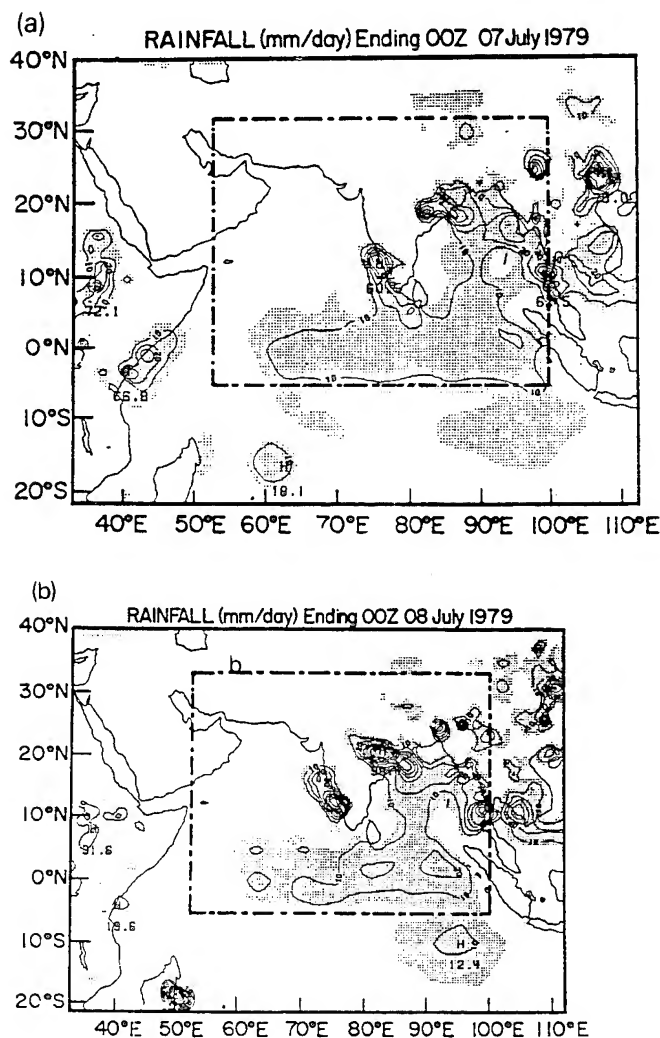


Fig. 2. Analyzed accumulated rainfall distribution by Krishnamurti et al. (1983) for the days (a) 7 and (b) 8 July 1979. Rainfall maximum is located offshore of westcoast of India.

a reverse Kuo scheme was used. Figure 2a and b shows the analyzed accumulated rainfall distribution (Krishnamurti et al., 1983) ending at 00 UTC 7 and 8 July 1979, respectively, for the simulation domain. Dashed box indicates the nested domain. Rainfall rates over the land were obtained from more than 3000 rain gages using a successive correction objective analysis procedure. Rainfall rates over the oceanic region were estimated from the satellite brightness. Though the analyzed rainfall rates over the oceanic region are subject to uncertainties, seaward increase of rainfall indicates that the maximum rainfall associated with the Western Ghats during this period was located just offshore. Rainfall over the Bay of Bengal and eastern India was due to the monsoon depression. Since the rainfall received over the simulation domain was almost due to the cumulus convection, large scale rainfall is thus negligible. Since hourly rainfall rates are not readily available, it is assumed that the previous day of the starting time of simulation has a constant rate of rainfall throughout that day. This constant rainfall rate is converted into convective heating using the reverse Kuo scheme for use in the diabatic initialization scheme. Further, model produced convective heating rates and rainfall for the first three hours of simulation are merged with the corresponding rates from the diabatic initialization scheme. A nonlinear weighting factor (α) is employed where $\alpha = 1$ at $t = 0$ and $\alpha = 0$ at $t = 3$ h. The relation is given by:

$$R_m = \alpha R_i + (1 - \alpha) R_c \quad (1)$$

where R_i is the convective rainfall rate used in the DVMI, R_c the model-produced convective rainfall rate, R_m the merged rain rate, and α is given by:

$$\alpha = 1 - [1 + \sin(\pi t/3) - (\pi/2)]/2 \quad (2)$$

The above relations allow the influence of the initialized heating and rain rates to approach to zero in a smooth manner. This procedure is done only for the diabatic initialization case.

SYNOPTIC CONDITIONS AND NUMERICAL EXPERIMENTS

During the simulation period (00 UTC 6 to 00 UTC 8 July 1979), monsoon was active and the winds were steady along the westcoast of India. Western Ghats, the mountain range is located about 100 km inland from the westcoast of India. Low level winds approached the westcoast of India almost perpendicular to the Western Ghats. Orographically lifted air generally triggers convective instability over this region, leading to large rainfall rates. A monsoon depression was located over the Burma Coast at 00 UTC 6 July 1979 and moved westward during the next 48 h.

Two numerical simulations are performed for 48 h starting at 00 UTC 6 July 1979. In the first experiment, initial conditions are balanced using the

fine-grid mesh
(FGGE) level III

developed at the
version (DVMI)
AVMI scheme,

1983) for the days
ist of India.

adiabatic vertical mode initialization scheme while in the second experiment the diabatic vertical mode initialization scheme is used. The coastline in the simulation domain is determined by the model topography data. Thick and bold contours with bold zeros in all plots represent the coastline. Since the coarse-grid model is primarily used to capture the large scale circulations associated with the monsoon flow and also to provide the boundary conditions for the fine-grid model, we present only the results obtained from the fine-grid model simulations. Since the horizontal resolution of the FGGE data is too coarse (2.5°), the monsoon depression can not be represented adequately. The analyzed wind speeds, vorticity and divergence associated with the monsoon depression are very weak in the initial conditions.

RESULTS AND DISCUSSION

Model-predicted rainfall using adiabatic and diabatic VMI schemes are compared with the observations. We refer the results obtained using the adiabatic VMI scheme to as AB case and those obtained using the diabatic VMI to as DB case. As mentioned before, because of some uncertainty in the analyzed rainfall maxima, only spatial distribution of the predicted rainfall is compared with the observations.

Comparison of rainfall rates

Figure 3a and b shows the predicted accumulated rainfall at the end of the first day of simulation (ending at 00 UTC 7 July) for the AB case and the DB case, respectively. It can be noticed that predicted rainfall in both the cases are somewhat similar. For the DB case, areal coverage of predicted rainfall is larger with higher rainfall maximum than that for the AB case. Predicted maximum in both cases exists offshore of the west coast of India with a rate of 74 and 107 mm d^{-1} , for the AB case and DB case, respectively. Comparing with the observations (Fig. 2a), the predicted offshore rainfall maximum seems to be higher for both cases and spatial distribution is somewhat similar. As mentioned earlier, estimated rainfall rates over the oceans are subject to errors, only spatial distribution of observed rainfall is compared with the model predictions rather than the reported maximum rates. Predicted rainfall distribution due to the model's monsoon depression (off the Burma coast) and over the Bay of Bengal in the DB case compares better with the observations (Fig. 2a) than with that for the AB case. In both the AB and DB cases, model does not predict rainfall northeast of India (closer to the east coast) while observations indicate a rainfall rate of 50 mm d^{-1} . Predicted circulation patterns associated with the predicted monsoon depression indicated horizontal convergence but cumulus convection did not sustain because of the advection of relatively drier air from the north. Also, vertical cross sec-

SENSITIV

(a)

LATITUDE

28.
27.
25.
24.
22.
21.
19.
18.
16.
15.
13.
12.
10.
9.
7.
6.
4.
3.
1.
0.
-1.
-3.

(b)

LATITUDE

28.
27.
25.
24.
22.
21.
19.
18.
16.
15.
13.
12.
10.
9.
7.
6.
4.
3.
1.
0.
-1.
-3.

Fig. 3. P
in the D

tions o
(not st
contin
to the
Pred
and th
over th
predict

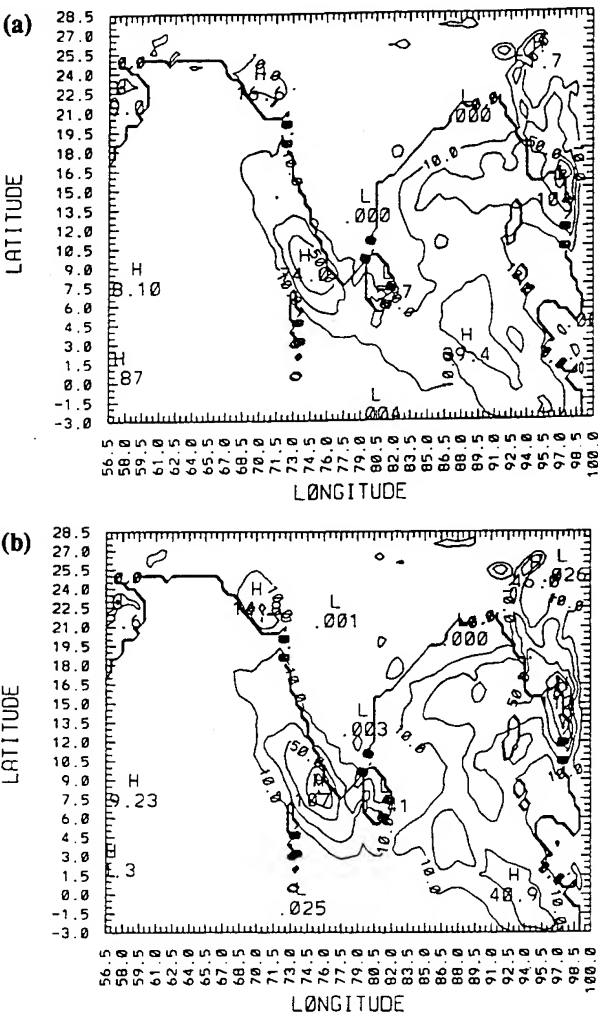


Fig. 3. Predicted rainfall for a period of 24 h ending 00 UTC 7 July (a) in the AB case and (b) in the DB case, respectively. Contour intervals are 10, 25, 50, 75, 100, 125 mm d⁻¹.

tions of the relative humidity at different times during the model integration (not shown) indicated low values, particularly over the northern Indian sub-continent. Uncertainties in the moisture filed in the analyzed FGGE data lead to the poor prediction of rainfall associated with the monsoon depression.

Predicted rainfall rates for the second day of simulation for the AB case and the DB case are shown in Fig. 4a and b, respectively. Predicted rainfall over the oceanic regions is higher in the DB case than in the AB case. Again, predicted rainfall offshore of westcoast of India is higher in the DB case (187

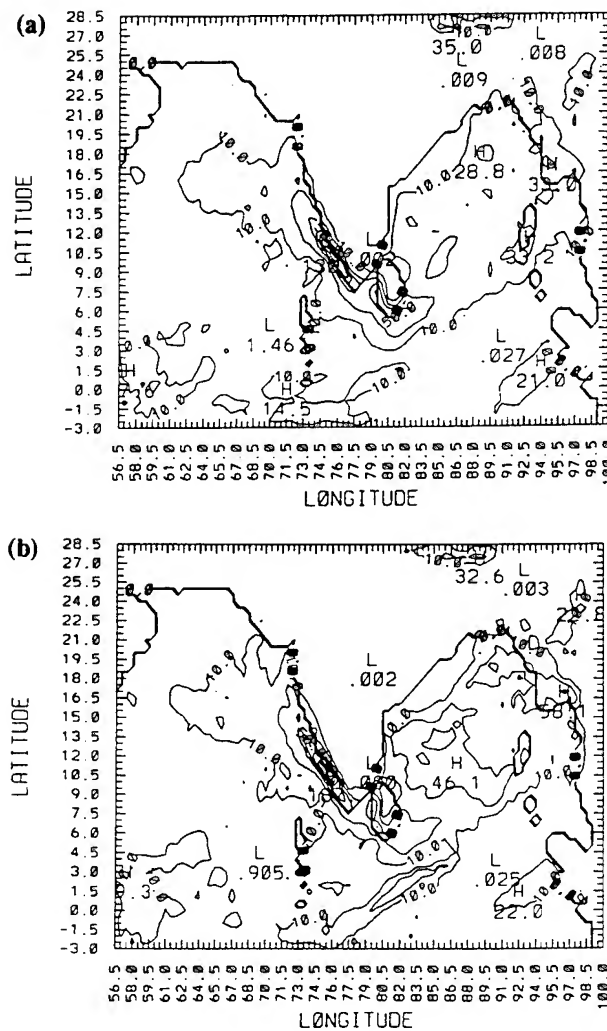


Fig. 4. Predicted rainfall for a period of 24 h ending 00 UTC 8 July (a) in the AB case and (b) in the DB case, respectively. Contour intervals are 10, 25, 50, 75, 100, 125, 150, 175, 200 mm d^{-1} .

mm d^{-1}) than that predicted in the AB case (130 mm d^{-1}) while spatial distribution is similar. Also, comparing with the observed rainfall (Fig. 2b) both the AB and DB cases predict higher rainfall rates and spatial distribution of rainfall in both cases is somewhat comparable to that in the observations. Again, similar to the previous day, in both cases the model did not predict rainfall over the land (over foot hills of Western Ghats closer to the west coast, northeast India closer to the east coast) and is due to the presence of drier

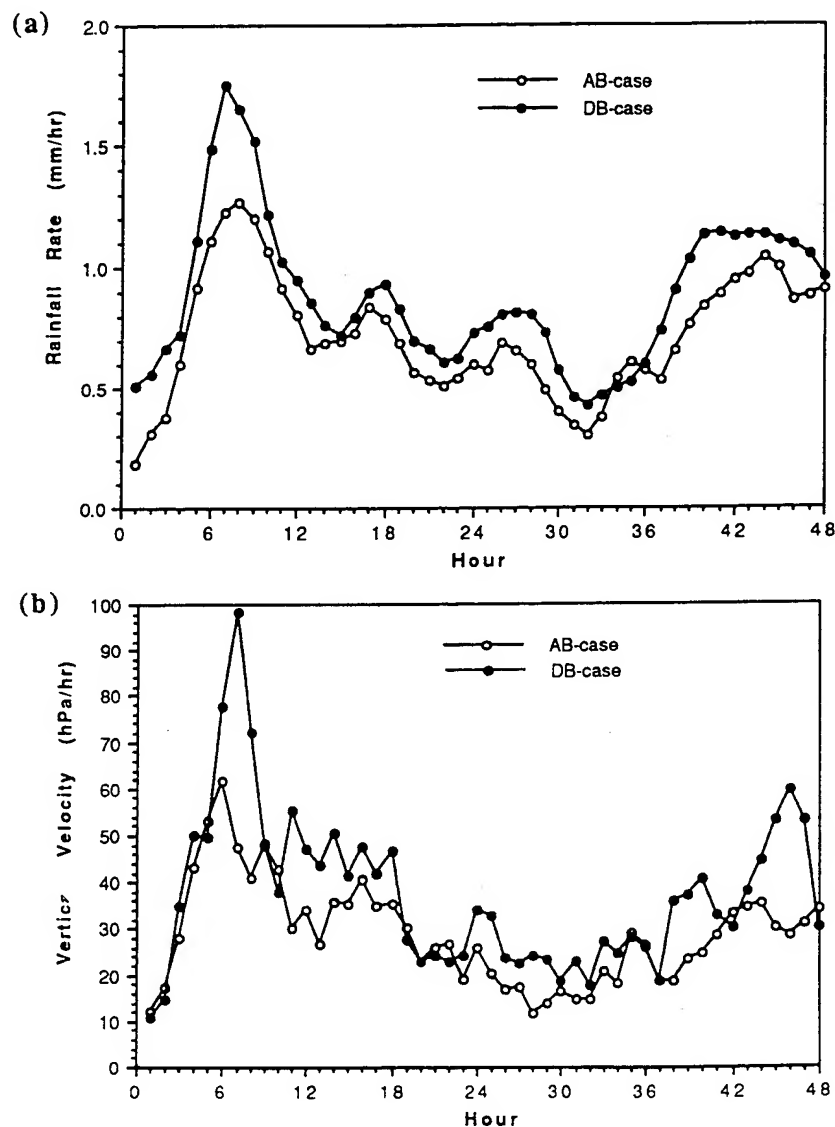


Fig. 5. Temporal variation of (a) area averaged convective rainfall for the area between 6° to 20° N and 70.5° to 76.5° E in the AB case and the DB case, respectively, and (b) domain maximum vertical velocity (ω) for the region 6° to 20° N and 70.5° to 76.5° E at the end of each hour of simulation.

layers. Essentially, predicted rainfall rates are higher for the DB case for both days of simulation, indicating the influence of the diabatic initialization procedure.

To further investigate the effects of the diabatic initialization on the model forecast, area average of accumulated convective rainfall for an area between 6° to 20° N and 70.5° to 76.5° E covering most of the rainfall region near the Western Ghats is considered. Figure 5a shows the temporal variation of area averaged accumulated convective rainfall for the AB case (circles) and for the DB case (dots). During the first nine hours of simulation, predicted area averaged rainfall rates are much higher for the DB case than those in the AB case. This result is due to the enhanced convergence in the lower layers in the DB case where initial conditions are obtained using the diabatic VMI scheme. Also, in the DB case area averaged rainfall is almost persistently higher compared to that in the AB case. This indicates the improvement of model predictions in the DB case where diabatic initialization is used. Signature of the model spinup can be clearly seen in the Fig. 5a where predicted convective rainfall peaks to a maximum at about seven hours starting from the initial time. Also, spinup time required by the model is almost the same for both the simulations. These results are consistent with the results found in other studies mentioned earlier. Also, Turpeinen et al. (1990) found that the diabatic initialization had little impact on the reduction of the spinup time unless the humidity field in the initial conditions was enhanced. Puri and Miller (1990) used the Betts–Miller scheme and rainfall rates derived from the OLR data to initialize the initial moisture field and their results also indicated that reduction in the spinup time occurred only when diabatic initialization and moisture adjustments are performed together.

Figure 5b shows the temporal variation of domain maximum vertical velocity (minimum ω velocity) with in the region considered above for the AB and DB cases. Some noise is present since only instantaneous values of vertical velocities are considered. The vertical velocity field also shows similar behavior to that in the rainfall shown in the Fig. 5a, indicating the presence of model spinup during the early hours of numerical integration. This result also supports the argument (Puri and Miller, 1990; Turpeinen et al., 1990) that diabatic initialization may help in increasing the predicted rainfall rates with no reduction of the spinup time associated with the model.

Comparison of surface moisture fluxes and winds

As mentioned before, the predicted area averaged rainfall and domain maximum vertical velocities for the DB case are almost persistently higher than those in the AB case. Particularly, during the first twelve hours of simulation these are considerably higher. These results indicate that the amount of moisture available for precipitation in the DB case seems to be higher than that in the AB case. To confirm this, accumulated evaporation from the oceans for each day of simulation are considered. Figure 6a and b shows the spatial distribution of latent heat fluxes (averaged for 24 h) for the AB case and the

in the model area between the region near the equator (areas) and for the predicted area in the AB layers in the MI scheme. higher compared model prediction of the convective in the initial for both the other studies the diabatic unless the Miller (1990) OLR data to that reduction and moist vertical velocity for the AB values of vertical winds similar to the presence of this result (Alapaty et al., 1990) rainfall rates

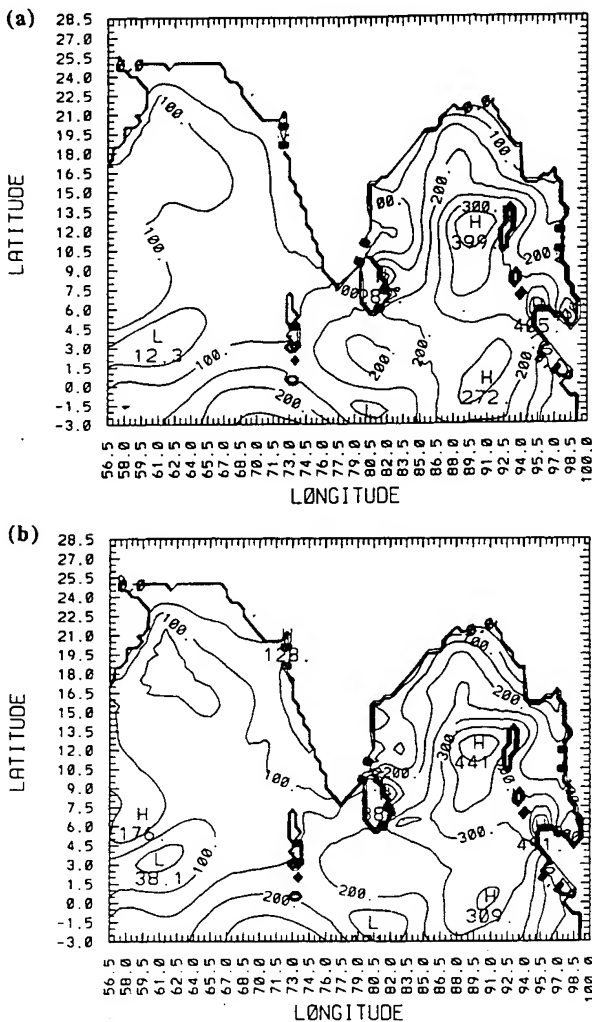


Fig. 6. Spatial distribution of predicted latent heat fluxes at the end of 24 h of simulation (a) in the AB case and (b) in the DB case, respectively. Contour interval is 50 W m^{-2} .

DB case, respectively for the first day of simulation. Increase in the latent heat fluxes over the central Arabian sea, Indian Ocean and the central Bay of Bengal can be noticed. In general, there is an increase in latent heat fluxes of about 40 W m^{-2} can be seen over these regions.

In the diabatic initialization scheme, analyzed rainfall rates are used in estimating the convective heating rates and its vertical distributions. To that effect an additional term is added in the system of equations where calculation of the divergence is of primary interest. As one would expect, the spatial

and domain are much higher than the amount of rainfall over the oceans in the spatial case and the

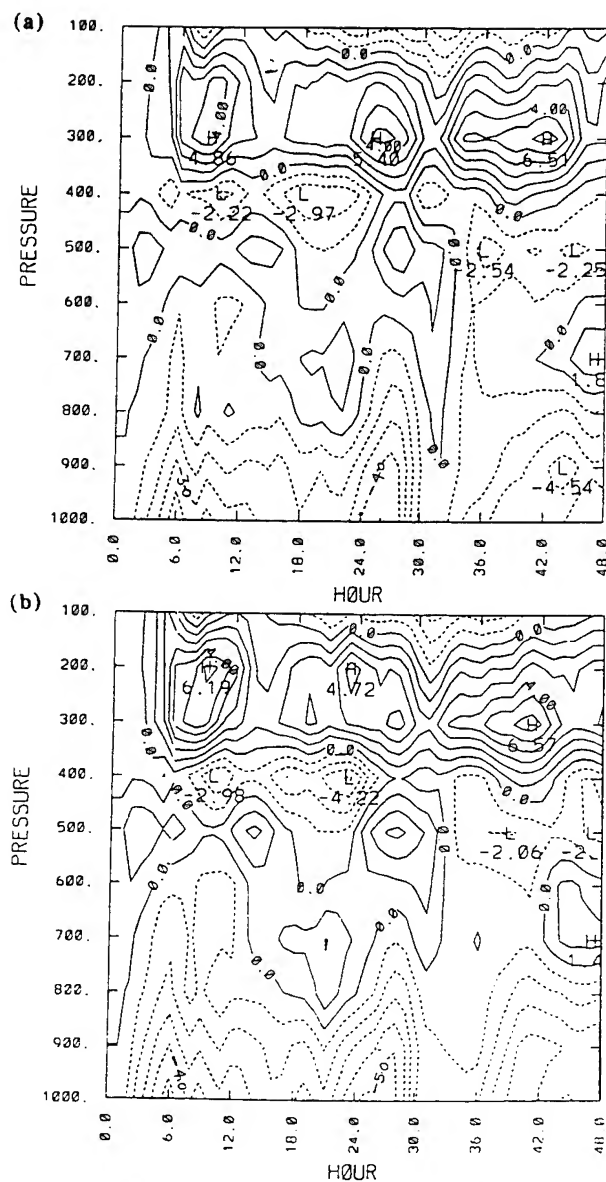


Fig. 7. The height-time section of area averaged divergence for the area between 6° to 20° N and 70.5° to 76.5° E (a) in the AB case and (b) in the DB case, respectively. Contour interval is $1.0 \times 10^{-4} \text{ h}^{-1}$.

distribution of the wind field in the initial conditions for the DB case is different than that for the AB case. Increased convergence in the lower layers (and corresponding increase in the divergence in the upper layers) over the regions of observed rainfall caused local accelerations of the wind for the DB case. The presence of persistently stronger winds over these regions in the DB case lead to the increase in the evaporation from the oceans. Spatial distri-

SENSIT

butic
activ
those
wind
in th
of ve
pred
day
diffe

Fu
tions
genc
are s
the a
DB
the u
stor
conv
AB
M
cases
with
soon
d⁻¹
the r
ditio
socia
very
adeq
oluti
fall a

CON

To
latio
abat
is us
lyze
put
cate
alm
proc
patt
eval

bution of winds over the Bay of Bengal and Arabian sea for the convectively active regions in the DB case are slightly stronger (about 1.5 m s^{-1}) than those in the AB case during the period of simulation. The differences in the wind fields lead to the differences in the latent heat fluxes. Vertical velocities in the DB case are higher than in the AB case and also larger areal coverage of vertical velocities in the DB case is consistent with the areal increase in the predicted rainfall shown in Fig. 3b. Comparison of these fields for the second day of simulation also indicate somewhat similar results, in agreement with differences in the predicted rainfall in the AB and the DB cases.

Further, to compare differences in the circulation patterns time-height sections of the area averaged (between 6° to 20° N and 70.5° to 76.5° E) divergence field for the AB case and the DB case, respectively are considered and are shown in the Fig. 7a and b. During the first twelve hours of simulation, the area averaged convergence in the lower layers is relatively higher in the DB case than that in the AB case. Consistently, area averaged divergence in the upper layers during this period is also higher in the DB case, indicating stronger vertical circulations. During the rest of the simulation period also convergence in the lower layers is slightly stronger in the DB case than in the AB case.

Model prediction of monsoon depression is similar in both AB and the DB cases and location of the predicted depression (not shown) is in agreement with the observations. Since the analyzed rainfall over the location of monsoon depression at the starting time of integration is very small ($\sim 10 \text{ mm d}^{-1}$), differences of the computed vorticity and divergence associated with the monsoon depression between the AB and the DB cases in the initial conditions are negligible. Also, computed vorticity and divergence maximum associated with the model's monsoon depression in both AB and DB cases are very weak compared to those in the observations. Monsoon depression is not adequately resolved in the initial conditions and this is due to the coarse resolution of the FGGE data. These problems lead to the poor prediction of rainfall associated with the monsoon depression in both the AB and DB cases.

CONCLUSIONS

To study the effects of the initialization procedure on the numerical simulation of monsoon rainfall, two different initial states are specified using adiabatic and diabatic vertical mode initialization schemes. A nested grid model is used to perform simulations for the period 00 UTC 6 July to 8 July. Analyzed rainfall rates for the previous day of starting time are utilized to compute the initial convective heating rates using the Kuo scheme. Results indicate that (a) diabatic initialization helps in predicting higher rainfall rates almost throughout the simulation period, (b) differences in the initialization procedures lead to the prediction of relatively stronger winds and circulation patterns associated with the cumulus convection which in turn increased the evaporation from the surrounding oceanic regions and (c) spinup time re-

between 6° to 20° N
Contour interval

DB case is dif-
lower layers
ers) over the
id for the DB
ons in the DB
patial distri-

mains the same whether initial conditions are prepared using adiabatic or diabatic initialization schemes.

These results also suggest that a proper moisture initialization scheme in conjunction with diabatic initialization scheme may help in improving the model rainfall prediction particularly over the land areas. Also, to improve the model forecast of rainfall associated with the monsoon depression, augmentation of data in the initial conditions is required. Our future work is to incorporate a moisture initialization scheme similar to the one used by Puri and Miller (1990) in to the diabatic initialization scheme and to study its impact on the model forecast and the spinup time.

ACKNOWLEDGEMENTS

This work was supported in part by the Naval Research Laboratory, Washington, D.C. and in part by the Division of International Programs, National Science Foundation under the grant INT-9008926. Computer resources were provided by the North Carolina Supercomputing Center, Research Triangle Park, NC.

REFERENCES

- Anthes, R.A., 1977. A cumulus parameterization scheme utilizing a one-dimensional cloud model. *Mon. Weather Rev.*, 105: 207-286.
- Davies, H.C., 1976. A lateral boundary formulation for multi-level prediction models. *Q. J. R. Meteorol. Soc.*, 102: 405-418.
- Davies, H.C., 1983. Limitations of some common lateral boundary schemes used in regional NWP models. *Mon. Weather Rev.*, 111: 1002-1012.
- Krishnamurti, T.N., Cocke, S., Pasch, R. and Low-Nam, S., 1983. Precipitation estimates from rainguage and satellite observations: Summer MONEX. *Dep. Meteorol., Florida State Univ.*, 377 pp.
- Kuo, H.L., 1974. Further studies of the parameterization of the influence of cumulus convection on large-scale flow. *J. Atmos. Sci.*, 31: 1232-1240.
- Mohanty, U.C., Kasahara, A. and Errico, R., 1986. The impact of diabatic heating on the initialization of divergent circulations in a global forecast model. *J. Meteorol. Soc. Jpn.*, 64(6): 805-817.
- Puri, K. and Miller, M.J., 1990. The use of satellite data in the specification of convective heating for diabatic initialization and moisture adjustment in numerical weather prediction models. *Mon. Weather Rev.*, 118: 67-93.
- Puri, K., 1987. Some experiments on the use of tropical diabatic heating information for initial state specification. *Mon. Weather Rev.*, 115: 1394-1406.
- Turpeinen, O.M., Garand, L., Benoit, R. and Roch, M., 1990. Diabatic initialization of the Canadian regional finite-element (RFE) model using satellite data. Part I: Methodology and application to a winter storm. *Mon. Weather Rev.*, 118: 1381-1395.
- Turpeinen, O.M., 1990. Diabatic initialization of the Canadian regional finite-element (RFE) model using satellite data. Part II: Sensitivity to humidity enhancement, Latent-heating profile and rain rates. *Mon. Weather Rev.*, 118: 1396-1407.
- Wolcott, S.W. and Warner, T.T., 1981. A moisture analysis procedure utilizing surface and satellite data. *Mon. Weather Rev.*, 113: 1989-1998.